An investigation of magma mingling and potential magma mixing during the intrusion of mafic melts into metasediments undergoing partial melting in the Dalradian series of eastern Scotland

by

Helena Michaela Fest

Thesis presented in partial fulfilment of the requirements for the degree of

MASTER OF EARTH SCIENCE IN THE FACULTY OF SCIENCE

at Stellenbosch University

Date: March 2022

Department of Earth Science, Stellenbosch University

Supervisor: Prof. Gary Stevens

Co-Supervisors: Prof. Jean-François Moyen

Dr. Axel Gerdes

DECLARATION

By submitting this thesis electronically, I declare that the entirety of the work contained therein is my own, original work, that I am the sole author thereof (save to the extent explicitly otherwise stated), that reproduction and publication thereof by Stellenbosch University will not infringe any third party rights and that I have not previously in its entirety or in part submitted it for obtaining any qualification. This thesis is submitted in fulfilment of a Master of Science in the department of Earth Science, Stellenbosch University.

Full name: Helena Michaela Fest

Date: March 2022

ABSTRACT

In order to understand the evolution and differentiation of the Earth, the petrogenesis of chemically evolved intermediate to felsic rocks which are characteristic of Earth's continental crust, is of fundamental importance. The generation of granitic melts by melting of source rock, and the segregation and upwards migration of these melts are main mechanisms driving the differentiation of the crust. The frequent exposure of granitoids in close relation with mafic rocks has led many studies to discuss the involvement of mantle derived mafic melts in the petrogenesis of granitic material. Processes of mingling and mixing of magmas from different sources are popular hypothesised mechanisms to explain chemical and isotopic variabilities of co-magmatic granitoids, often inferred to occur in mid- to lower crustal zones where mantle derived mafic magmas interact with crustal derived felsic melts. However, geological exposures of partial melting zones and granitic melt production in corelation with mafic intrusions with indicative textures for mingling and mixing processes are scarce and poorly constrained. A coastal section in north-east Scotland is interpreted to expose a crustal sequence of in situ anatexis, interspersed with numerous mingled intrusions varying from mafic to felsic in composition. The magmatic rocks along the coastal section of Inzie Head show a variety of field and textural evidence indicative of magma interaction processes, ranging from interconnected vein networks, pillow-like structures, enclaves and schlieren, to gradual changes in colour and grain sizes along contact domains. In order to investigate the potential of processes such as magma mingling and mixing in the petrogenesis of granitoids, this study presents a combination of different geo-analytical techniques: field and petrographic observations of the different rock types, whole rock and mineral chemistries, combined in situ U-Pb and Lu-Hf isotopic analyses of zircon, as well as in-situ apatite and whole rock analyses of Sm-Nd and Rb-Sr isotopic signatures. Magma mixing models were formulated to investigate if additions of chosen end-members can account for the chemical and isotopic compositions observed in the hypothetical mixed rocks. Geochronological constrains suggest co-magmatic behaviour over a period of 30 myr coinciding with crustal anatexis of the metasedimentary sequence and the in situ derivation of leucosomes within the crustal domain. The intrusion of multiple mafic magma batches is suggested to have promoted crustal anatexis and maintained a partially molten state over a prolonged period in the crustal domain, promoting processes of magma interaction. The zircon Hf and apatite Sr and Nd isotopic compositions of the different rocks are characterized by a high degree of variability within the individual samples. The mixing models can account for the variable chemical and isotopic compositions of the different rocks. The study concluded that the first addition of dioritic magmas resulted in the elevation of the overall heat budget in the crustal sequence, whereby magma interaction was limited to diffusional processes along sharp contact domains. Succeeding intrusions of dioritic material into the crustal zone resulted in gradual contact domains and larger scale mixing processes shaping the exposed igneous rocks. It was furthermore concluded that mixing and hybridisation was more efficient where granitic material invaded the mafic intrusions, forming hybrid vein networks.

OPSOMMING

Die petrogenese van chemies geëvolueerde intermediêre tot felsiese gesteentes wat kenmerkend is van die Aarde se kontinentale kors is van fundamentele belang om die evolusie en differensiasie van die Aarde te verstaan. Die generering van granitiese smeltings deur die smelting van 'n brongesteentes, en die segregasie en opwaartse migrasie van hierdie smelte is hoofmeganismes wat die differensiasie van die kors aandryf. Die gereelde blootstelling van granitoïede in noue verband met mafiese gesteentes het daartoe gelei dat baie studies die betrokkenheid van mantel-afgeleide mafiese smelte in die petrogenese van granitiese materiaal bespreek. Vermengingsprosesse van magmas van verskillende bronne is gewilde hipotetiese meganismes om chemiese en isotopiese veranderlikhede van ko-magmatiese granitoïede te verduidelik, wat dikwels afgelei word om in middel tot laer kors sones plaas te vind waar mantel-afgeleide mafiese magmas in wisselwerking tree met kors-afgeleide felsiese smelte. Geologiese blootstelling van gedeeltelike smeltsones en granitiese smeltproduksie in korrelasie met mafiese indringings met aanduidingstekstures vir vermenging en mengprosesse is egter skaars en swak beperk. 'n Kusgedeelte in noordoos-Skotland word geïnterpreteer om 'n korsvolgorde van in situ anateksis bloot te lê, wat afgewissel word met talle gemengde indringings wat wissel van mafiese tot felsiese samestelling. Die magmatiese gesteentes langs die kusgedeelte van Inzie Head toon 'n verskeidenheid veld- en tekstuurbewyse wat aanduidend is van magma-interaksieprosesse, wat wissel van onderling gekoppelde aarnetwerke, kussingagtige strukture, enklawes en schlieren, tot geleidelike veranderinge in kleur en korrelgroottes langs kontakdomeine. Om die potensiaal van magmavermenging en vermengingsprosesse in die petrogenese van granitoïede te ondersoek, bied hierdie studie 'n kombinasie van verskillende geo-analitiese tegnieke aan: veld- en petrografiese waarnemings van die verskillende gesteentes, heelgesteentes en minerale chemieë, gekombineer in situ U-Pb en Lu-Hf isotopiese ontledings van sirkoon, sowel as in situ apatiet en heelgesteentes ontledings van Sm-Nd en Rb-Sr isotopiese handtekeninge. Mengmodelle is geformuleer om te ondersoek of toevoegings van gekose eindlede die chemiese en isotopiese samestellings wat in die hipotetiese gemengde gesteentes waargeneem is, kan verantwoord. Geochronologiese beperkings dui op ko-magmatiese gedrag oor 'n tydperk van 30 miljoen jaar wat saamval met kors anateksis van die metasedimentêre volgorde en die in situ afleiding van leukosome binne die korsdomein. Daar word voorgestel dat die indringing van veelvuldige mafiese magma-groepe kors anateksis bevorder het en 'n gedeeltelik gesmelte toestand oor 'n lang tydperk in die korsdomein gehandhaaf het, wat prosesse van magma-interaksie bevorder het. Die sirkoon Hf en apatiet Sr en Nd isotopiese samestellings van die verskillende gesteentes word gekenmerk deur 'n hoë mate van variasie binne die individuele monsters. Die mengmodelle kan verantwoording doen vir die veranderlike chemiese en isotopiese samestellings wat waargeneem word. Die studie het tot die gevolgtrekking gekom dat die eerste toevoeging van dioritiese magmas gelei het tot die verhoging van die algehele hittebegroting in die korsvolgorde, waardeur magma-interaksie beperk is tot diffusieprosesse langs skerp kontakdomeine. Opeenvolgende indringing van dioritiese materiaal in die kors sone het gelei tot geleidelike kontakdomeine en groterskaalse mengprosesse wat die blootgestelde stollingsgesteentes gevorm het. Daar is verder tot die gevolgtrekking gekom dat vermenging en hybridisasie meer doeltreffend was waar granitiese materiaal die mafiese indringings binnegedring het en hibriede aarnetwerke gevorm het.

TABLE OF CONTENTS

LIST OF FIGURES

Chapter 1 – Introduction

Chapter 2 – Geological Setting

Chapter 4 – Results

Chapter 5 – Discussion

LIST OF TABLES

Chapter 3 – Methodology

Chapter 4 – Results

Chapter 5 – Discussion

ACKNOWLEDGEMENTS

First and foremost, I would like to thank my supervisor Gary Stevens for the opportunity to complete this MSc in Stellenbosch and helping me progress as a researcher during that time. Thank you for your patience and guidance for my development throughout this journey. I would also like to thank my co-supervisor Jean-François Moyen for providing me with the knowledge and skills necessary to undertake this study. I would like to thank my second co-supervisor Axel Gerdes for the guidance and insight into the intricacies of isotopic systems. Thank you for all your help and encouragement. I would furthermore like to thank everyone form the CAF at Stellenbosch for the help and support. Thank you to everyone from FIERCE at Frankfurt a.M. for all the help and a source of advice. Lastly, to my friends, family and partner, that have supported me throughout most of this journey. I am grateful to each of you for being guiding lights in the darkest times.

FUNDING CONTRIBUTORS

I would like to thank the South African National Research Foundation (NRF) for funding this research in the form of grant funding to Professor Gary Stevens via the SARChI programme and an MSc bursary to Helena Fest.

CHAPTER 1 INTRODUCTION

A fundamental mechanism in understanding the evolution of the Earth concerns the formation of granitoid rocks, which are characteristic of Earth´s continental crust (Sawyer, 1998). The chemical composition of evolved felsic melts is not in equilibrium with the generally ultramafic composition of the mantle and by definition cannot be a direct derivation of mantle melting (Rudnick, 1995). In contrast with the ultramafic mantle, the average continental crust is intermediate in composition and characterized by a chemical stratigraphy that ranges from more mafic to intermediate lower layers to felsic and granite dominated upper layers (Rudnick and Fountain, 1995). The generation, segregation and upwards migration of granitic melts, are the main mechanisms driving the differentiation of Earth's continental crust and are thus fundamental in understanding its evolution (Brown, 2013; Brown and Rushmer, 2006; Sawyer et al., 2011). Different petrogenetic scenarios have been proposed to explain the derivation of granitic melts and the compositional variabilities associated with granitoids exposed on Earth's surface, whereby theories regarding the involvement and potential contribution of the mantle differ largely in nature. The formation of exposed migmatite terranes has been correlated to variable degrees of crustal anatexis, associated with the derivation and migration of granitic melts (Brown, 2013; Johnson et al., 2015; Sawyer, 1998; Stevens et al., 1997). Zones of major partial melting have been evoked at lower to mid-crustal levels or at the crustal base, where important processes for granitic melt generation and crustal differentiation are prevalent (Annen et al., 2006; Hildreth and Moorbath, 1988). However, the potential and efficiency of partial melting processes and generation of granitic melts is largely dependent on temperature (T), pressure (P) and fluid conditions as well as the composition of the source.

1.1 PARTIAL MELTING AND THE ORIGIN OF HEAT

Partial melting describes the progressive change of a solid rock into a two-component system, consistent of solid fractions and melt (Sawyer, 1999). The solid fraction, generally referred to as restite or residuum, comprises of new minerals that formed as solid products and refractory minerals that did not participate in the melting reactions. The degree of anatexis and generated melt gradually increases with rising temperatures, decreasing the volume of the solid fraction, thus lowering the bulk viscosity and promoting crustal differentiation (Sawyer, 1999). The efficient melt separation from the solid residuum results in the formation of leucocratic segregations, which may be reflected as leucosomes. The generation, separation and upwards extraction of granitic magmas inevitably results in local and regional heterogeneities within the crust as the upward migration of granitic magmas ultimately contributes to a more evolved upper continental crust, whereby a refractory zone, dominated by melt-depleted residuum, is generated in lower crustal levels (Brown, 2013; Vielzeuf et al., 1990). Anatectic processes are promoted by a sufficient increase in temperature, relative to the prevailing pressure and fluid conditions, where reactant mineral assemblages become unstable and undergo melt-producing reactions (Sawyer, 1999). However, a typical geotherm in the continental crust with an average thickness of ca. 35 km, is generally insufficient to generate high enough temperatures that are amenable for partial melting of common crustal rocks (Petford et al., 2000).

Two different source domains have been considered as the origin of heat necessary to drive crustal anatexis: I) internal heat production within the crust; II) advective heat input from the mantle into the crust. Considering internal heat production within a thickened crust may rise temperatures sufficiently high for partial melting to occur. The internal heat production is largely driven by radiogenic heat producing elements (e.g. U, Th and K) in an enriched crust and aided by deep burial and incubation over a prolonged period with the re-establishment of disrupted isotherms. This process is thus favourable in tectonically active geological settings, such as collision zones. However, it has been argued that such anatectic events have a high potential to stall early in their evolution with relatively little melt production, as insufficient heat is available to achieve voluminous melts and efficient crustal differentiation (Clemens et al., 2020; Petford et al., 2000; Thompson and Connolly, 1995). Conversely, heat transfer from intruding or underplating hot, mantle-derived magmas can result in a steep increase of the overall heat budget in adjacent crustal lithologies and thus may induce comprehensive melting reactions in various rocks (Bergantz, 1989; Huppert and Sparks, 1988). The intrusion of mantle-derived magmas can be expected to furthermore result in the production of granitic melts through cooling and differentiation of the mafic material (Annen et al., 2006; Moyen, 2020). Considering the mantle as a key provider of heat

necessary for granitoid melt generation, different petrogenetic scenarios have been proposed, where mantle contributions are evaluated in various roles.

1.1.1 THE INVOLVEMENT OF THE MANTLE

In a variety of geological settings, the involvement of the mantle is proposed in multiple petrogenetic scenarios for granite derivation, that are largely distinct by three main mechanisms: I) the addition of heat necessary provided by the mantle; II) the prevailing fluid conditions; III) the main source of derived material. Considering the mantle solely as a contributor of heat by intrusions or underplating of mafic magmas may create high-temperature, low-pressure conditions in overlying crustal rocks. Experimental constrains on natural rock lithologies under temperature conditions achieved by mafic underplating, demonstrated the production of voluminous granitic melts under fluid-absent, granulite metamorphic conditions. The heat transfer from hot mantle magmas may induce partial melting through the dehydration and breakdown of hydrous minerals (e.g. micas or amphibole) in the absence of a 'free' fluid phase. Fluid-absent incongruent partial melting of hydrous minerals within lower crustal layers generally occurs at higher temperatures >800°C (Clemens et al., 2016; Clemens and Vielzeuf, 1987; Stevens and Clemens, 1993; Vielzeuf and Montel, 1994). Phase equilibria modelling and experimental constrains on partial melting of (meta-)sedimentary protoliths under fluid-absent conditions successfully demonstrated muscovite and biotite dehydration reactions as the main melt-generating factors to produce peraluminous granitoids (Stevens et al., 1997; Vielzeuf and Holloway, 1988; Vielzeuf and Montel, 1994). Furthermore, phase equilibria studies and geochemical trends produced by modelling of major and trace element compositions have postulated genetic links between exposed granites and surrounding (meta-)sedimentary lithologies (Johnson et al., 2003, 2001b, 2001a).

Field and textural evidence in migmatite terrains have been related to variable degrees of crustal anatexis (Sawyer, 1999). Thereafter, a low melt fraction results in the formation of metatexite migmatites and small isolated pockets of melt, where pre-migmatization textures may be preserved (Brown, 1973; Sawyer, 1999). Melt pockets enlarge with increasing degrees of anatexis and eventually form an interconnected network promoting permeability and movement of melt. The formation of diatexite migmatites with flow structures, schlieren or vein like leucosome textures are evidence for higher degrees of partial melting and higher melt fractions, where pre-migmatization textures are usually lost (Brown, 1973; Sawyer, 1999). Although mantle heat is considered as a contributing element in this crustal recycling scenario, the addition of mantle derived material and potential of chemical magma mixing is regarded as negligible or absent. The experimental melting of a protolith of average pelitic composition have successfully demonstrated the generation of strongly peraluminous granitic melts (Mayne et al., 2019; Stevens et al., 1997). Granitoid rocks with strongly peraluminous compositions are commonly referred to as S-type to imply their (meta-)sedimentary source as they require a source of peraluminous character, e.g. compositions of an average pelite. In this scenario, chemical and isotopic variations in granitoid rocks are explained by partial melting of various crustal lithologies. Thus, metaluminous to weakly peraluminous granitoids, commonly referred to as I-type, are proposed to represent magmas with entrained peritectic clinopyroxene, derived from melting of pre-existing, (meta-)igneous crustal rocks.

A second petrogenetic scenario proposes for the formation of anatectic zones the contribution of heat and fluids derived from underplating of hydrous mantle-derived magmas. Fluid-fluxed or fluid-present melting conditions are induced by ascending water, which is exsolved by the cooling and fractionation of underplating hydrous basaltic magmas (Collins et al., 2020). The ascending water thus has the potential to lower the solidus and trigger melting in overlying crustal rocks or pre-existing mafic underplates. As the influx of water allows for efficient melt generation at lower temperatures, resulting melt-loss recording migmatites may form under (upper) amphibolite facies conditions (Carvalho et al., 2016; Collins et al., 2016; Weinberg and Hasalová, 2015). In this scenario, the reworking and contribution of crustal material is not a necessity, as the generation of voluminous granodioritic magmas can be achieved by the melting of pre-existing mafic underplates, describing the conversion of a mantle-derived source into new formed continental crust (Collins et al., 2020). Multiple inputs of basaltic magmas may create pro-longed melting conditions and can account for repeated episodes of granitoid magma injections into upper crustal layers. The migration and intrusion of hot and hydrous, felsic to intermediate magmas may furthermore induce dehydration reaction and fluid-fluxed partial melting in overlying crustal layers, potentially forming mid-crustal anatectic zones in the absence of a direct mantle contribution (Schwindinger and Weinberg, 2017). Phase stability modelling based on partial melting of metapelitic rocks under fluid

excess conditions have concluded, generation of substantial amounts of melt at relatively low temperatures of ca. 710°C (Mayne et al., 2019). However, the majority of resulting modelled melt compositions along the modelled P-T paths have been described as generally uncommon or absent within the natural rock record.

A third petrogenetic scenario for the generation of granitoids considers the contribution of crustal and mantle-derived material and the potential for magma mixing (Huppert and Sparks, 1988; Janoušek et al., 2004; Perugini and Poli, 2012). Intruding mantle-derived magmas crystallize while cooling down within the colder crustal environment and form evolved melts through fractional crystallization. The emplacement of significant volumes of mantle-derived magma may induce partial melting in surrounding crustal rocks as heat and possibly fluids are released while the magma crystallizes (Annen et al., 2006). Zones of anatexis and granitic melt derivation that stand in relation with mantle-derived intrusions or underplates may promote the possibility of mechanical and chemical interaction of contrasting magmas. Thus, compositional variabilities of granitoids in co-magmatic suites have been explained by mixing and hybridization of contrasting magmas at deeper crustal levels before their ascent and emplacement in present exposures.

1.2 THE POTENTIAL OF MAGMA MINGLING AND MIXING PROCESSES IN THE GENERATION OF GRANITOIDS

Based on different approaches (field observations, petrographic evidence, chemical and isotopic constrains), various authors proposed magma mingling and mixing as crucial processes in granitoid petrogenesis (Baxter and Feely, 2002; Collins, 1996; Foden et al., 2002; Janoušek et al., 2004; Zeh et al., 2020). Numerous exposures of granitic bodies that are mingled with mafic to intermediate rocks in the geological field allude to chemical interaction of the different magmas (El Desouky et al., 1996; Johnson et al., 2001b; Perugini and Poli, 2012; Pietranik and Koepke, 2009; Weinberg et al., 2021). Typical field exposures ascribed to magma mixing and mingling include dispersions or enclaves of darker-coloured, more mafic magmas in a lighter-coloured, more felsic host, as well as syn-plutonic dykes, back-veining and net-veining textures, intermingled schlieren and sheets or flow-structures of contrasting domains. Although mixing and mingling are frequently associated, the two processes are commonly differentiated based on the extent of physical and chemical magma interaction (Perugini and Poli, 2012; Weinberg et al., 2021). Thereafter, mingling describes the mechanical interaction and material exchange of participating magmas, preserving their individual characters and resulting in the juxtaposition of distinct domains with diverse composition. Magma mixing refers to the chemical interaction of magmas that may accompany the mingling process to form hybrid magma compositions where the individuality of the contrasting magmas is progressively lost (Johnson and Barnes, 2006; Weinberg et al., 2021). Chilled contact margins of contrasting rocks or enclaves have been explained by quenching of hotter magma against a cooler, felsic host, recording the efficient mechanical mingling of contrasting magmas, whereas porphyritic or (larger-scale) gradual hybridization textures have been inferred to resemble chemically mixed hybrid zones (Baxter and Feely, 2002; Słaby et al., 2008). Mineral phases crystallizing in magma mixing systems have been postulated to show distinct petrographic features, disequilibrium textures and compositional changes, as a result of the open magmatic system behaviour (Baxter and Feely, 2002; Hibbard, 1991; Janoušek et al., 2000). A single identified texture may not be characteristic for mixing processes, yet the assemblage and combination of such microtextures is inferred to be representative for magma mixing and mingling processes.

Numerous textures have been attributed to mixing processes of which twelve frequently observed textures have been summarized by Hibbard, 1991: (1) rapakivi and (2) antirapakivi textures; rapakivi textures describe K-feldspar crystals, which are rimmed by plagioclase. Quenching of the more mafic system may lead to the growth of plagioclase on K-feldspar crystals that are derived from the felsic magma. Conversely, antirapakivi textures define the mantling of K-feldspar on plagioclase crystals, which were formed in the mafic magma. (3) poikilitic or oikocrystic quartz and K-feldspar; This texture describes small mafic crystals (e.g. amphibole, biotite and/ or calcic plagioclase), generated by quenching of the more mafic system, that are poikilitically included in larger K-feldspar and quartz crystals, which crystallized later in a more felsic, hybrid system. (4) biotite or amphibole inclusion zones within K-feldspar phenocrysts; Although similar to the poikilitic textures (3), this texture is attributed to result if K-feldspar forms as a relatively early phase in a more felsic system, which is brought into contact with a more mafic magma, containing crystallized biotite or amphibole phases. Further growth of the K-feldspar results in the inclusion and zonal arrangement of the rimmed, mafic

minerals. (5) Sphene-feldspar ocelli; The texture describes biotite or amphibole absent zones around sphene crystals, consistent of plagioclase, K-feldspar and quartz. The sphene crystals in the centre of the broadly spherical shaped aggregates, typically show ophitic textures with small lathes of more calcic plagioclase (anorthite). Attributed to mixing, the close relation of sphene and calcic plagioclase lathes derives from undercooling of a more mafic system. Crystallization of K-felspar, quartz and more sodic plagioclase (albite) results from the subsequent mixing with a more felsic magma. (6) blade-shaped biotite crystals; bladed shapes define atypical morphologies of biotite crystals, resulting from physical growth restrictions. Mixing of a more mafic melt with a crystal-rich, more felsic system may trigger biotite crystallization, whereby the crystalline phases restrict the growth of the crystallizing biotite phase. (7) acicular and mixed apatite morphologies; The growth of apatite with acicular shapes, rather than the more usual stubby prismatic shapes, is attributed to the rapid growth in a quenched more mafic system upon mingling and mixing with a cooler, more felsic magma. Furthermore, the coexistence of both apatite morphologies has also been explained by mixing and mingling of magmas (Baxter & Feely, 2002). (8) small lath-shaped plagioclase morphologies; Plagioclase may form small laths of more calcic composition in a quenched, more mafic magma system. Mixing with a more felsic magma results in the growth of more sodic plagioclase rims, (if not protected by larger host crystals, e.g. K-feldspar), whereby abrupt step zoning of core and rim, reflects the late-stage equilibration of the magma mixing scenario. (9) (anorthite) spike zones in albitic plagioclase; Zones of more calcic plagioclase within albitic plagioclase crystals, may result from mixing of a sodic plagioclase into a more mafic melt or by adding mafic melt into the felsic system, capable to crystalize anorthitic plagioclase. The return to the growth of more sodic plagioclase which forms the zonation, may be achieved by the equilibration of the new hybrid system or by a second event, which could reintroduce the crystal into a more felsic system. (10) boxy cellular plagioclase morphologies; Dissolution reactions of anorthitic plagioclase within a melt of more felsic composition, may result in growth zoning of more sodic plagioclase within the anorthitic cores. During subsequent equilibration of the hybrid system, an enclosing rim may form around the commonly rounded cores. (11) spongy cellular plagioclase textures; the generation of spongy plagioclase textures has been attributed to the partial resorption of the crystal. Heat transfer from the more mafic system, may promote reactive dissolution or direct partial melting of a plagioclase crystal, which formed in a more felsic system. (12) Quartz ocelli; This texture describes phenocrysts of generally rounded quartz, rimmed by finer grains of mafic minerals (e.g. biotite and amphibole). The mixing concept is similar as described for texture (4). This texture has also been identified with phenocrysts of plagioclase. In addition to the summarized textures by Hibbard (1991), authors attributed amphibole clots or resorbed biotite inclusions in amphibole to represent local mixing scenarios (Janoušek et al., 2000).

Chemical and isotopic variabilities within rocks from proposed suites of magma interaction, have been inferred to record the chemical mixing of crustal and mantle-derived melts (Chappell, 1996; Janoušek et al., 2004; Laurent et al., 2017; Zeh et al., 2020). Besides strongly peraluminous S-type granites, granitoids varying from weakly peraluminous to metaluminous compositions often show an increase in maficity that might be explainable by mixing with mafic melts. Thus, rocks of assumed hybrid compositions that form linear trends in binary mixing scenarios between defined mafic and crustal end-members, have been interpreted to result from variable degrees of mixing between the contrasting magmas (Barbarin, 2005; Janoušek et al., 2004; Weidendorfer et al., 2014). As the trace element composition of accessory phases (e.g. zircon, monazite, apatite or titanite) are highly sensitivity to the magma conditions, the importance of common accessory minerals in understanding a rocks petrogenesis has been demonstrated, using various minerals and isotope systems (Gerdes and Zeh, 2009; Laurent et al., 2017; Laurent and Zeh, 2015; Zeh et al., 2013, 2009). In-situ analyses of stable and radiogenic isotopes, as well as the combined evaluation of two or more systems, have been used to identify magmatic source domains, potential co-magmatic behaviour or petrological processes involved (Gerdes and Zeh, 2009; Zeh et al., 2009). Thereafter, based on the combined evaluation of in-situ U-Pb and Lu-Hf isotopic analyses on single zircon grains, studies have determined the timing of magma crystallization or metamorphic events (Gerdes and Zeh, 2009; Zeh et al., 2009). The combined isotopic signatures may furthermore provide evidence to distinguish between crustal recycling and the input from a juvenile mantle source or whether both processes contributed to the magma generation (Blichert-Toft and Albarède, 2008; Couzinié et al., 2019; Gerdes and Zeh, 2009, 2006; Vervoort et al., 2000; Zeh et al., 2009).

The Sm-Nd or Rb-Sr isotopic systems of whole-rock and mineral phases have been used to identify melting events or chemical changes in the magmatic source (Fisher et al., 2020; Laurent et al., 2017). During partial melting events, the radiogenic parental isotopes Sm and Lu behave as rather compatible elements relative to their respective daughter isotopes Nd and Hf, resulting in a commonly observed correlation, defined as the terrestrial array (Bouvier et al., 2008; Patchett

et al., 2004; Vervoort and Kemp, 2016). The identification of systematic changes in different isotopic systems in co-magmatic suites has therefore the potential to record the nature of crustal and/ or mantle end-member reservoirs and thus may help to reveal magmatic mixing processes (Zeh et al., 2020). Unlike juvenile isotopic values that are generally characteristic for primary, mantle-derived melts, studies have identified more evolved and therefore presumably older isotopic signatures at the time of granite emplacement, suggesting their derivation from melting of pre-existing crustal lithologies. In-situ U-Pb dating of zircon grains from granitoid rocks revealing older and younger domains within zircon crystals of single samples, may indicate possible inheritance of older zircon domains from pre-existing crustal rocks. Conversely, isotope analyses of granitoids revealing primitive isotopic signatures without evidence for crustal inheritance have been related to the derivation of primary mantle-derived material. However, various granitoids exposed on Earth's crust are characterized by 'hybridic' (mantle- and crustal-like) isotopic signatures, that might not be explained by a single source domain. Yet, mixing processes of contrasting magmas with distinctly primitive and evolved isotopic signatures might explain the wide range in chemical and isotopic compositions displayed by studied granitoids.

Authors have raised critical arguments and introduced various contradicting models, opposing the magma mingling and mixing theory. Field exposures and geochemical trends have been described as ambiguous and not inevitably indicative for interactions of crustal and mantle magmas. Thus, interpretations on genetic links in simple mixing scenarios are potentially subjective to the compositions of the chosen end-members, which might not be representative of the true end-member geochemistry. Inconsistencies between chemical mixing trends of major elements, trace elements and isotope compositions have been observed and interpreted to contradict potential magma mixing scenarios (Clemens and Stevens, 2012; Farina et al., 2014). Furthermore, other petrological processes, such as fractional crystallization, the entrainment of peritectic minerals, restite unmixing or country-rock assimilation and contamination, have been demonstrated to cause local compositional and isotopic variations or chemical trends and thus argued to provide equivocal geochemical evidence (Clemens and Stevens, 2012; Farina et al., 2012; Villaros et al., 2012). To successfully decipher whether magma mixing processes participated in granitoid petrogenesis, the comparison of major and trace element compositions with the concentration of several isotopic systems is of high importance. Arguments against magma mixing are furthermore largely based on the different physical properties of mafic and felsic magmas, hindering chemical interactions when assuming a magma mixing scenario with a mantle-derived magma of average basaltic composition and a crustal magma of average rhyolitic composition. Experiments have demonstrated the prospect and efficiency of magma mixing to be largely dependent on the viscosity and density of the participating end-members, as well as their respective magma and solidus temperatures. Thus, magma mixing and hybridization is argued to be most efficient when the participating magmas are characterized by low viscosities or liquid behaviour, whereby most homogenous hybrid compositions are an expected result from mixing of similar end-members (Perugini and Poli, 2012; Poli et al., 1996; Sparks and Marshall, 1986). The chemical interaction is thereafter limited by the cooling and crystallization of mafic magmas when in contact with cooler felsic magmas, as the increase in viscosity by the thermal equilibration of the end-members inhibits chemical mixing and hybridization processes (Sparks and Marshall, 1986). However, multiple petrogenetic scenarios have been proposed to overcome the imposed physical disparities of contrasting magmas.

1.2.1 CRUSTAL MIXING ZONES AS POTENTIAL BIRTHPLACES OF GRANITOIDS

Besides the physical features of contrasting magmas, exerts the timespan that the system spent in a partially molten state and the potential for the subsequent development of chemical heterogeneities, important controls on the efficiency of magma mixing (Perugini and Poli, 2012; Petrelli et al., 2011, 2006; Poli et al., 1996; Sparks and Marshall, 1986; Spera et al., 2016; Weinberg et al., 2021). Frequently invoked scenarios revolve largely around crustal zones of major partial melting or magma mushes, where amenable conditions for magma mixing and hybridization processes are achieved (Annen et al., 2006; Hildreth and Moorbath, 1988; Schwindinger and Weinberg, 2017; Weinberg et al., 2021). Mixing processes of contrasting magmas have been postulated to be subject to chaotic dynamics, where chemical homogenization is largely dependent on efficient mechanical mingling and subsequent diffusion-driven chemical equilibration (Ottino et al., 1988; Petrelli et al., 2011). Thereafter, the generation of thermal and chemical gradients between magmas may promote chemical mixing processes (fig. 1; Perugini and Poli, 2012). The replenishment of a magmatic system by episodic intrusions of hot mafic magmas may create thermal gradients and prolonged melting conditions, whereby thermal gradients in a partially molten system are associated with compositional gradients and mixing processes (fig. 1 – a & d).

Compositional gradients might be furthermore induced by fractional crystallization as well as country rock assimilation and contamination of magmas, having the potential to trigger chemical mixing and hybridization processes (fig. 1 – b & c). The processes proposed have the potential to occur simultaneously, enhancing the possibility of larger-scale mixing in magmatic systems.

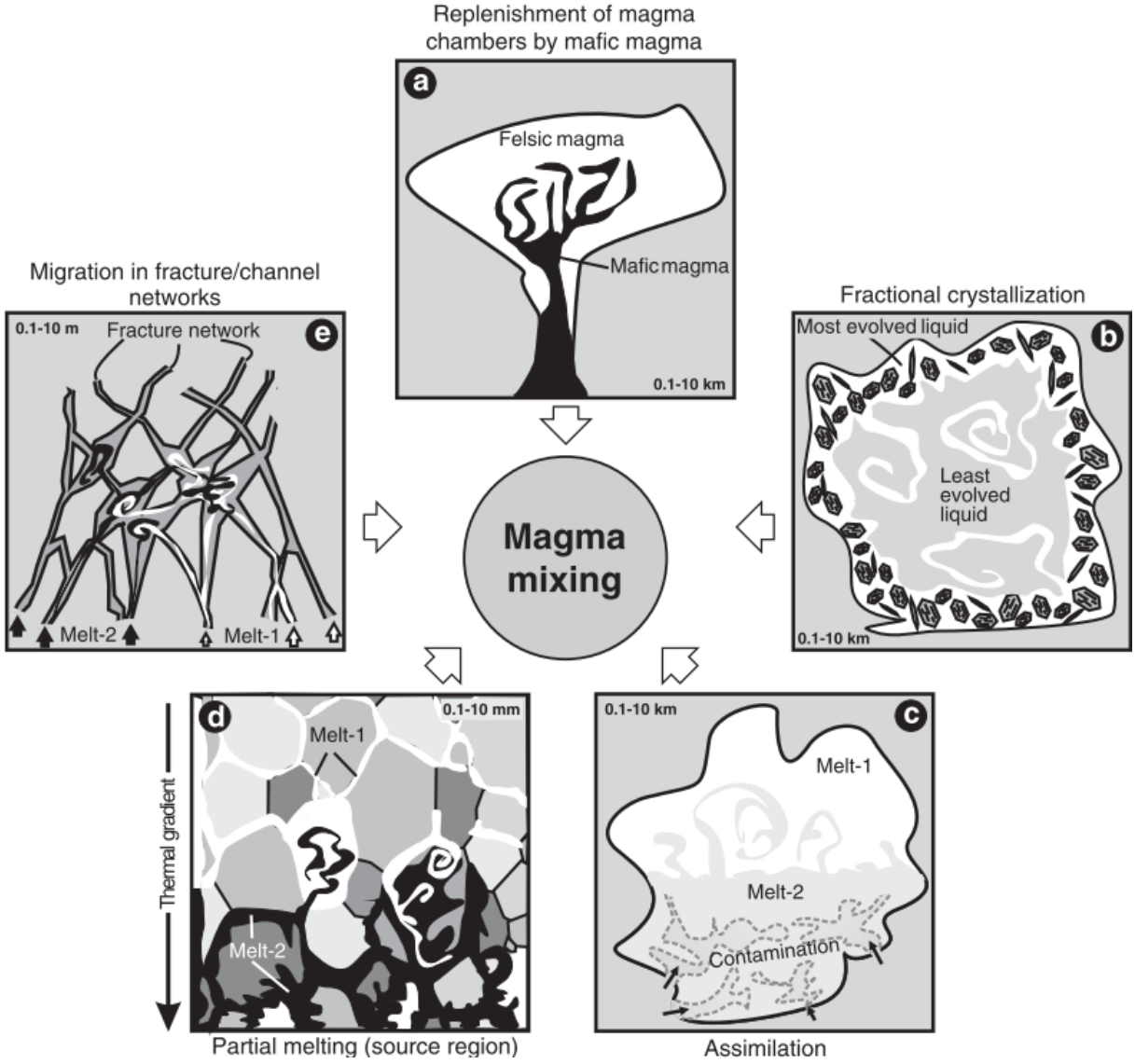

Figure 1 – Schematic visualisation of petrological processes with the potential to generate thermal or compositional gradients promoting the possibility of magma mixing processes; a) the replenishment of magma chambers by heat and material provided by intruding mafic magmas; b) fractional crystallization along cooler margins of the magmatic system, generating compositional gradients towards the inner domain of a magma; c) contamination through the assimilation of country-rock, generating compositional gradients and inducing magma mixing; d) thermal gradients in a partial melting region promoting chemical gradients and magma mixing; e) mixing resulting from melt migration in a network of fractures or channels; adapted from Perugini and Poli, 2012; after de Campos et al., 2011

In addition to major partial melting zones, magma mush zones have been proposed as important long-term magmatic reservoirs, where remobilization and mixing of magmas may be promoted (Weinberg et al., 2021). Magma mushes are generally defined as permeable mixtures consistent of solids and interstitial melt. In a magma mush, induced physical differences between contrasting magmas may be overcome, as the permeability of mushes allows for the invasion of external melts. Thus, multiple opportunities are provided for reactions with the solid crystals and interactions between different melts, promoting chemical mixing and hybridization processes (Weinberg et al., 2021). Weather chaotic mixing dynamics or magma mushes are the predominating petrogenetic processes, the dynamic nature of magma mixing may result in the coexistence of well-mixed hybrid magmas with poorly homogenized domains (Morgavi et al., 2013; Perugini and Poli, 2000). However, the mixing of magmas does not necessarily require sources from contrasting domains, as

mixing processes may take place between magmas derived from similar sources and thus comparable composition, whereby the contribution of mixing processes might be enigmatic. The possibility of mixing and hybridization processes between felsic magmas derived from different sources has been suggested in mid-crustal zones of felsic magma interaction (Schwindinger and Weinberg, 2017). Here, magmas generated by combined in-situ muscovite dehydration and fluid-fluxed melting of sediments, mingle and mix with intruding felsic magmas derived from lower crustal layers. Compositional variabilities and complex relationship of mingled granitoids are explained by mixing processes of the crustal magmas without the direct involvement of the mantle (Schwindinger and Weinberg, 2017).

Mixing and hybridisation processes of magmas from different sources are generally inferred to occur in zones within the mid to lower crust, prior to rise or uplift of the studied samples. Thus, frequently used models are the hypothesised MASH zones (melting, assimilation, storage and homogenization after Hildreth and Moorbath, 1988, or melting, assimilation, segregation and homogenization, re-defined after Pearce, 1996) or the similar deep crustal hot zones (Annen et al., 2006), to imply magma interaction at unexposed crustal levels. In such models, partial melting or remelting of lower crustal rocks is caused by the input of mantle-derived mafic magmas, which stall and partially crystallize at the crustal base or within lower crustal layers, where mixing and homogenization between contrasting magmas may be induced by the generation of thermal gradients (fig. 2). The concept of underplating and early stalling of ascending mafic magmas relies on the fundamental concept that crustal rocks of overall lower densities act as a density filter for the mafic magmas of higher densities (e.g. Richards, 2003). The accumulation, cooling and fractional crystallization of ponding mantle-derived magmas, forming layers of ultramafic cumulates, represents a significant addition of heat, causing partial melting of rocks from the lower crustal layers (fig. 2). A regionally limited zone of mingling and mixing, in form of intensive magma interaction and chemical exchange between crust- and mantle-derived melts may be provoked, producing melts of intermediate to felsic composition (Annen et al., 2006; Hildreth and Moorbath, 1988; Richards, 2003). Pyroxene-dominated cumulates remain within the deeper crust, whereas the resulting intermediate to felsic magmas ascend to shallower crustal levels, resulting in crustal differentiation (fig. 2). The varying chemical and isotopic compositions of the ascending magmas are suggested to be a direct result of convoluted and complex magma mixing and mingling processes and the invasion of magmas with increasingly evolved compositions into heated crustal layers. The continued magma input may control the intensity and duration of the mafic underplating and crustal anatexis (Richards, 2003).

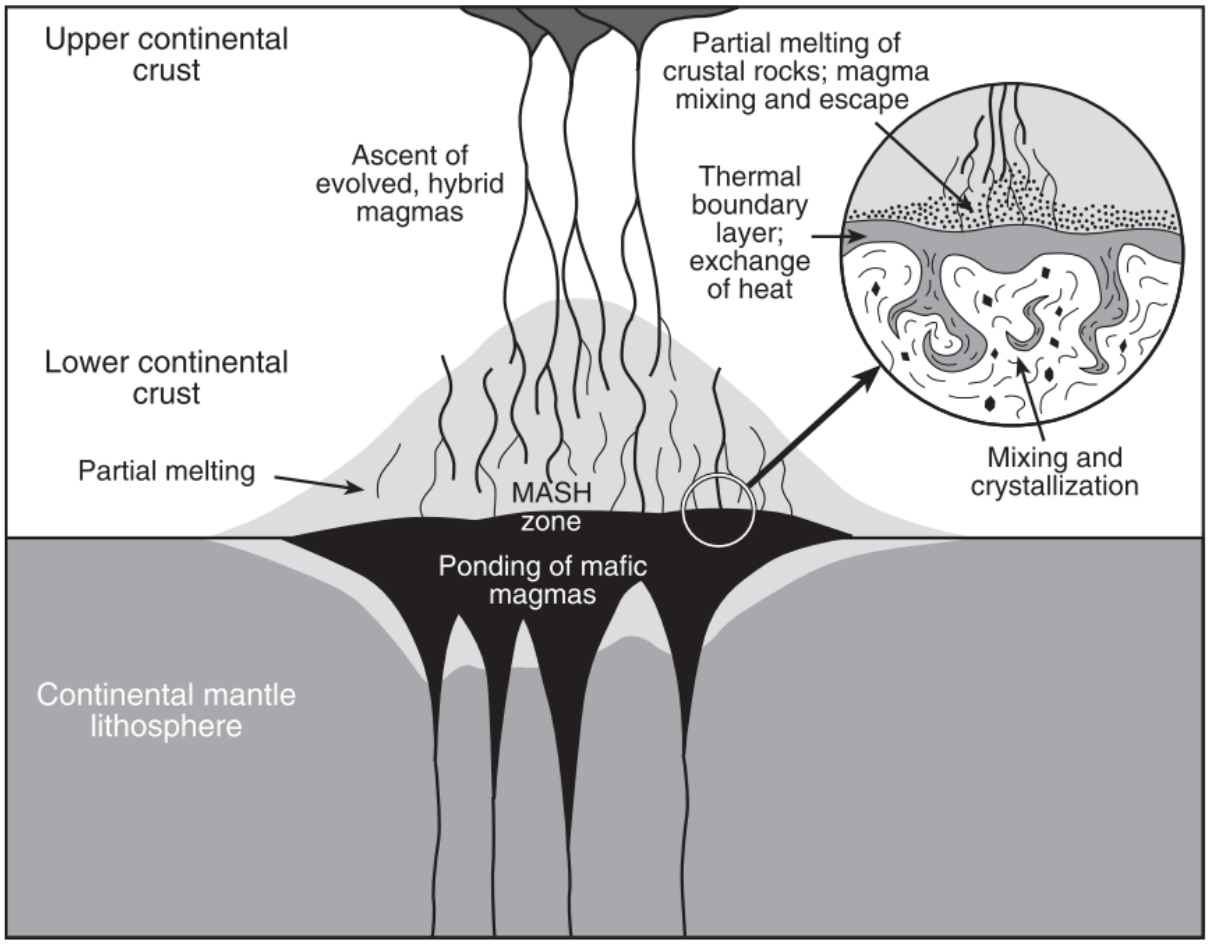

Figure 2 – Schematic visualisation of mafic underplating and the generation of a MASH zone within lower crustal layers. The advective heat input from mantle derived magmas creates a zone of partially molten material where mixing and mingling of crustal and mantle derived melts is promoted along the thermal and compositional gradients. Evolved magmas may escape, ascent and solidify in upper crustal layers; Adapted from Richards, 2003*; after* Hildreth, 1981*;* Huppert and Sparks, 1988

As exposed lower or mid crustal sites of in-situ anatexis and continuous magmatic systems with magma interactions are rare, the efficiency and actual existence of MASH or deep crustal hot zone scenarios during granite petrogenesis remains enigmatic (e.g. Clemens and Stevens, 2016). Besides the described physical differences of the contrasting melts, adds the possibility of relatively fast melt extraction rates of smaller melt volumes in sites of partial melting, another main point of critic (Clemens and Stevens, 2016). Faster extraction of smaller melts may lead to their ascend without further stalling or storage, providing insufficient time for mixing or homogenization processes in deeper crustal levels. Furthermore, large-scale, deep-crustal mixing models are generally based on numerical modelling and experimental data, whereas geological field evidence is generally inferred to represent single parts of the magmatic system. Geological sites where MASH zones have been postulated, are often allocated to represent the uppermost stages of the large-scale magmatic system (Hildreth and Moorbath, 1988; Walker et al., 2015). Furthermore, most studies are based on granitoid exposures with mafic pillow, enclave or syn-plutonic dyke textures, occasionally with signs of hybridisation, whereas sites of granitic melt generation and potential MASH zone processes are scarce. Geological features of metasedimentary lithologies, recording mafic intrusions and granitic melt production are poorly constrained. Such structures are often suggested to be largely destroyed by re-equilibration processes or hidden within deeper crustal levels. Thus, the actual existence of crustal mixing zones and whether such zones and associated processes could play a key role in the petrogenesis of granitoid magmas remain in question.

1.3 STUDY CONTEXT

To investigate whether mixing processes between contrasting magmas in hypothesised crustal zones of magma interaction could play a dominant role in the petrogenesis of granitoids this study aims to identify potential genetic links between magmatic rocks of diverse compositions. To provide insights into a probable zone of magma interaction processes, mingling and potential mixing relations between crustal and mantle-derived magmas within a crustal domain of partial melting need to be identified. A coastal exposure of migmatitic metasediments in NE Scotland comprises of numerous igneous intrusions and intermingled bodies of dioritic to granitic compositions. The uplifted (upper) amphibolite to granulite metamorphic sequence, with textures identified for in-situ partial melting, opens the possibility to record a potential mid crustal zone, where interaction between mantle and crustal-derived melts may have occurred. The exposed sequence along the coastal section, termed the Inzie Head Gneiss Formation, lies within the Buchan Block, a geologically distinct area within the Grampian Terrane of north-eastern Scotland. Metasedimentary rocks of the Buchan Block are generally correlated with lithologies of the Dalradian Supergroup, a major unit comprising the Grampian Terrane. However, distinguish structural, magmatic, metamorphic and sedimentological differences the Buchan Block from the rest of the Grampian Terrane (Johnson et al., 2017 and references there in). Outcrops of metasedimentary rocks, granitoids and associated ultramafic to mafic intrusions of the Buchan Block, form a broadly horseshoe-shaped pattern, which is bound by a regional shear zone system.

The Buchan Block is the type locality for low pressure, high temperature regional metamorphism, associated with higher geothermal gradients. Established peak metamorphic conditions, around 470 Ma, have been related to crustal anatexis and deformation, as well as the broadly concurrent emplacement of the ultramafic to mafic intrusions and voluminous granitoid bodies (Carty et al., 2012; Johnson et al., 2003, 2001b, 2001a; Viete et al., 2013, 2010). Exposures of metatexites, diatexites and leucosome bodies along the costal section of Inzie Head are interspersed with igneous rocks of dioritic to granitic compositions. Previous studies have postulated a genetic link between exposed granitoid bodies of Inzie Head and the surrounding (metasedimentary) migmatites, of which they are potentially derived from (Johnson et al., 2003). The intermingled relationships of mafic and felsic bodies within the Inzie Head Formation might record a temporal overlap in local anatexis, granitoid formation and the emplacement of dioritic magmas. If mafic melts were the source of heat, then the successive generation of mantle-derived intrusions and/ or underplates could have driven local anatexis and the generation of granitic melts. Thereafter, if crustal melts escaped their metasedimentary source to mingle, mix and hybridise with mantle melts to produce a range of granitoid compositions that were possibly extracted, then the field area chosen for this study has the potential to represent a mid-crustal MASH zone.

This study aims to explore the bulk compositional consequences of magma mixing to investigate suggested genetic links and the potential of chemical mixing in the evolution of the exposed mingled rocks by: (1) the categorization of potentially mixed and unmixed rocks based on field and textural evidence, bulk-rock chemistry, mineral chemistry and petrographic characteristics; (2) the establishment of age relations by U-Pb geochronology of zircon grains and comparison with established ages; (3) examining the isotopic signatures and potential relations of the rocks based on Lu-Hf isotopic compositions of zircon grains, as well as Sm-Nd and Rb-Sr isotope data of apatite grains to identify the magmatic source domain; and (4) the comparison of whole-rock Sm-Nd and Rb-Sr isotopic signatures of rocks from Inzie Head with rocks of the wider Buchan Block area. The establishment of the potential source domain, genetic links and possible mixing relations of contrasting rocks can provide insights into a probable zone of magma interaction and hybridization. Understandings of potential chemical and isotopic mixing scenarios and the exposure of a prospective crustal mixing zone thus may contribute to comprehend processes driving large granitoid formations

CHAPTER 2 GEOLOGICAL SETTING

The syn to post collisional magmatic rocks of the Inzie Head coastal section were emplaced during the Caledonian orogeny, which formed the early to mid-Palaeozoic Caledonian orogenic belt in north-eastern Europe. A shift in plate tectonic movements in the early Palaeozoic, resulted in the formation of a subduction zone along the margin of the Laurentian continent and the rapid closing of the Iapetus Ocean (Chew and Strachan, 2014). The convergence of Baltica and the microcontinent Avalonia towards Laurentia, ultimately led to a continent-continent collision, succeeding uplift and the formation of the Caledonian orogenic belt. The Caledonian orogeny is generally separated into specific events, of which the mid-Ordovician, Grampian Event is of most relevance for rocks of Grampian Terrain in northern Scotland. The Grampian Terrain, a major crustal block that was amalgamated during the Caledonian Orogeny, forms a NE-SW trending belt, extending from the Shetland Islands in the NE to north-western Ireland in the SW (fig. 3; Chew and Strachan, 2014; Stephenson et al., 2013b)(Chew and Strachan, 2014; Stephenson et al., 2013b). It is bound by two major structural features, the Highland Boundary Fault in the SE and the Great Glen Fault in the NW (fig. 3; Stephenson et al., 2013b). The mid-Neoproterozoic to early Ordovician Dalradian Supergroup constitutes a major unit of the Grampian Terrain in north-eastern Scotland. The Supergroup is largely comprised of clastic metasedimentary rocks, recording a range of changing sedimentation environments, as well as varying degrees of metamorphic and complex structural processes (Stephenson et al., 2013a, 2013b). Early sedimentation of the Supergroup largely reflects the deposition in rift-basins within the supercontinent Rodinia, recording the increasing instability within the supercontinent, as well as its subsequent breakup and the development of the Iapetus Ocean, between the newly separated continents of Laurentia, Baltica and Gondwana (Cawood et al., 2001; Fettes, 2013).

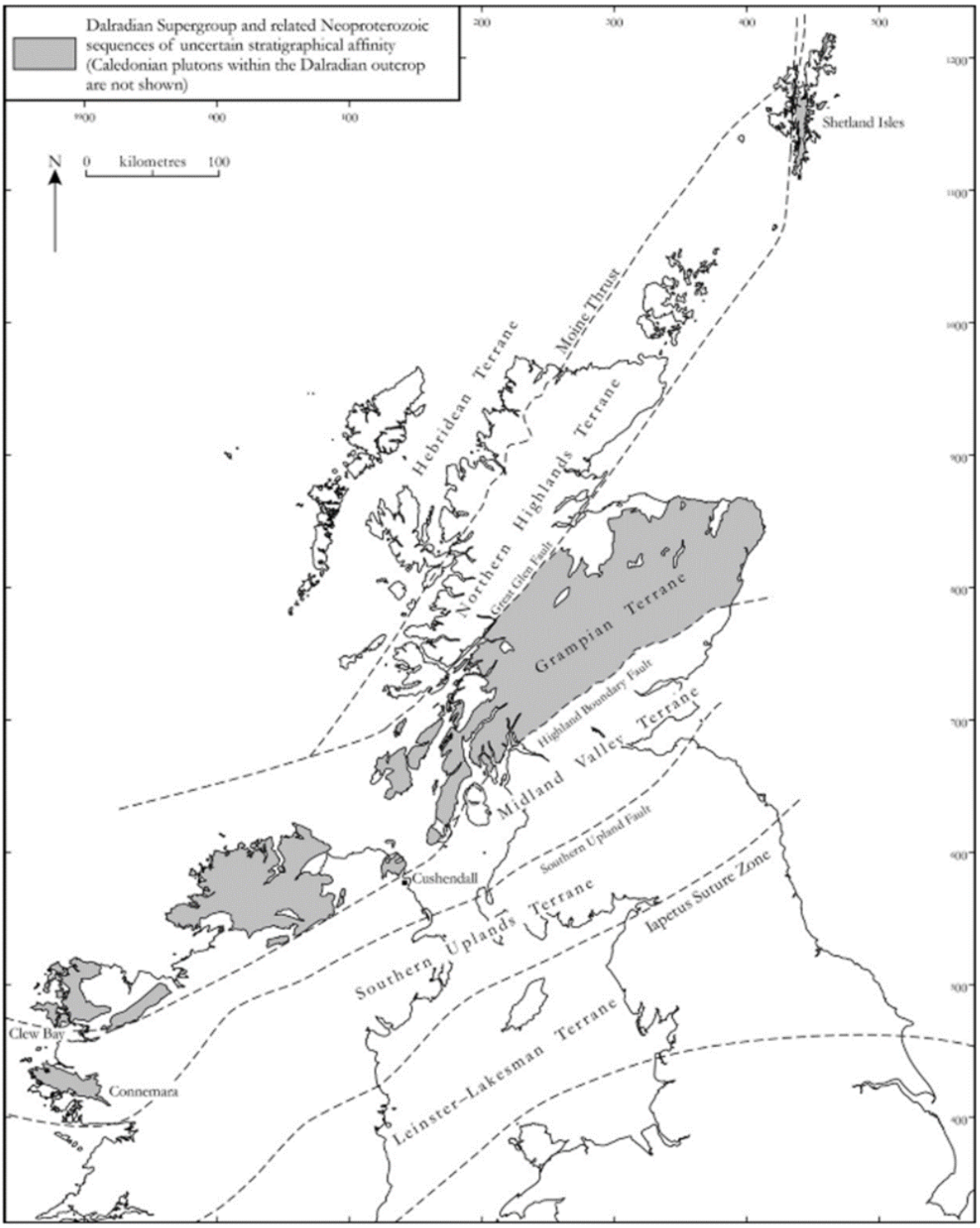

Figure 3 – Schematic map of the geological terranes on the British Isles showing the distribution of Caledonian terranes and bounding faults; Highlighted in grey is the Dalradian Supergroup within the Grampian Terrane; Adapted from Stephenson et al., 2013a

Commencing around 488 Ma and lasting until ca. 461 Ma, the Grampian Orogeny is widely attributed to the collision of an arc terrane with the Laurentian margin (Viete et al., 2013). Major phases of crustal thickening during the orogeny led to peak deformation and metamorphism of rocks within the wider Scottish Grampian Terrane between 475 – 465 Ma (Dewey, 2005). The regional metamorphic activity resulted in a zonal pattern of varying metamorphic facies across the Scottish Grampian Terrane, indicated by different index minerals within the metamorphosed pelitic rocks of the Dalradian strata (fig. 4). Rocks of suitable composition show an increase in metamorphic grade from lower, greenschist facies in the south-west, to higher metamorphic grades of mid-amphibolite facies in the north-east (fig. 4). The prograde

metamorphic sequence of classical Barrovian-type (medium-pressure) regional metamorphism was established in reference to identified index minerals, that are indicative for the different metamorphic conditions within metapelitic rocks along the progressive metamorphic zones: chlorite -> biotite -> garnet -> staurolite -> kyanite -> sillimanite (Barrow, 1912, 1893). In addition to the Barrovian metamorphic zones, a second zonal facies pattern has been recognized in the north-east of the Scottish Grampian Terrane, indicative for low-pressure, high-temperature metamorphic conditions (Harte and Hudson, 1979; Read, 1952). The so-termed Buchan-type metamorphism is characterized by a variation of the progressive index mineral sequence: chlorite -> biotite -> cordierite -> andalusite -> sillimanite. The different mineral transitions of the aluminosilicates polymorphs within the progressive mineral sequences form a key element in characterizing the peak metamorphic conditions, as the phase stability of andalusite, kyanite and sillimanite are largely dependent on the prevailing temperature (T) and pressure (P) conditions.

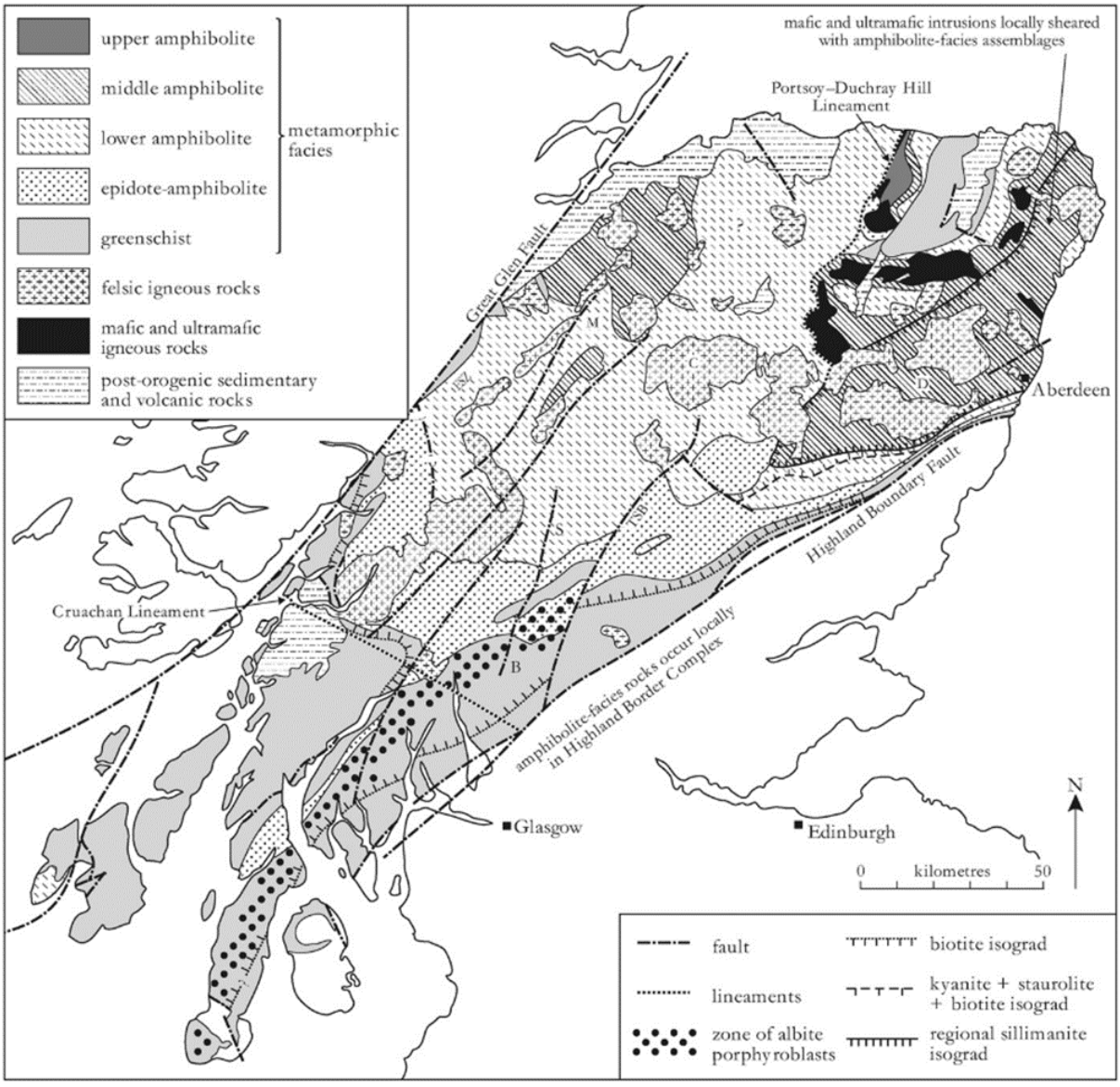

Figure 4 – Schematic map of the metamorphic facies distribution within the Scottish Grampian Terrane. Black square indicates the Buchan Block area; Adapted from Stephenson et al., 2013a*; from* Fettes et al., 1985*; by* Stephenson and Gould, 1995*;* Strachan et al., 2002

The formation of sillimanite after andalusite in Buchan-type metamorphism, requires an increase in temperature while pressures are not exceeding 4 – 4.5 kbar. Conversely, an increase in temperature at higher pressures above ca. 4.5 kbar results in the stability of kyanite and the mineral transition kyanite -> sillimanite, as seen in the Barrovian-type metamorphosed rocks. Maximum P-T conditions for the Barrovian metamorphosed terrane were estimated at 7 – 8 kbar and 500 – 600°C for lower metamorphic grades, increasing to 7 – 10 kbar and 650 – 800°C in higher metamorphic grades,

indicated by the presence of kyanite in the mineral assemblages (Chew and Strachan, 2014; Phillips et al., 1999). The required moderate geothermal gradient (dT/dP) for Barrovian metamorphic activity, is generally associated with regional metamorphism during continent-continent orogenic events. Geochronological constrains estimated broadly contemporaneous metamorphic activity of the Barrovian and Buchan type (Johnson et al., 2017; Oliver, 2001; Viete et al., 2013). Thus, the south-west to north-east transition from an overall moderate-P/T gradient, characteristic for Barrovian metamorphism, to high-T/low-P conditions suitable for Buchan-type metamorphism, requires a steep increase in the prevailing geothermal gradient or decrease of local pressure conditions (Stephenson et al., 2013a). However, the transition of metamorphic conditions, the cause of the high heat flow, associated magmatism and origin of complex migmatite formations within the Buchan Block region, remain enigmatic (Chew and Strachan, 2014).

2.1 Regional geological setting of the Buchan Block

The Buchan Block area of the north-eastern Scottish Grampian Terrane (fig. 5) is bound in the west and south by two major shear zones: (1) The E-W trending Deeside Lineament, west of Aberdeen, forming the southern margin and (2) the NNE-SSW trending Portsoy-Duchray-Hill (PDH) Lineament, running south of Portsoy, defining the western margin (fig. 5).

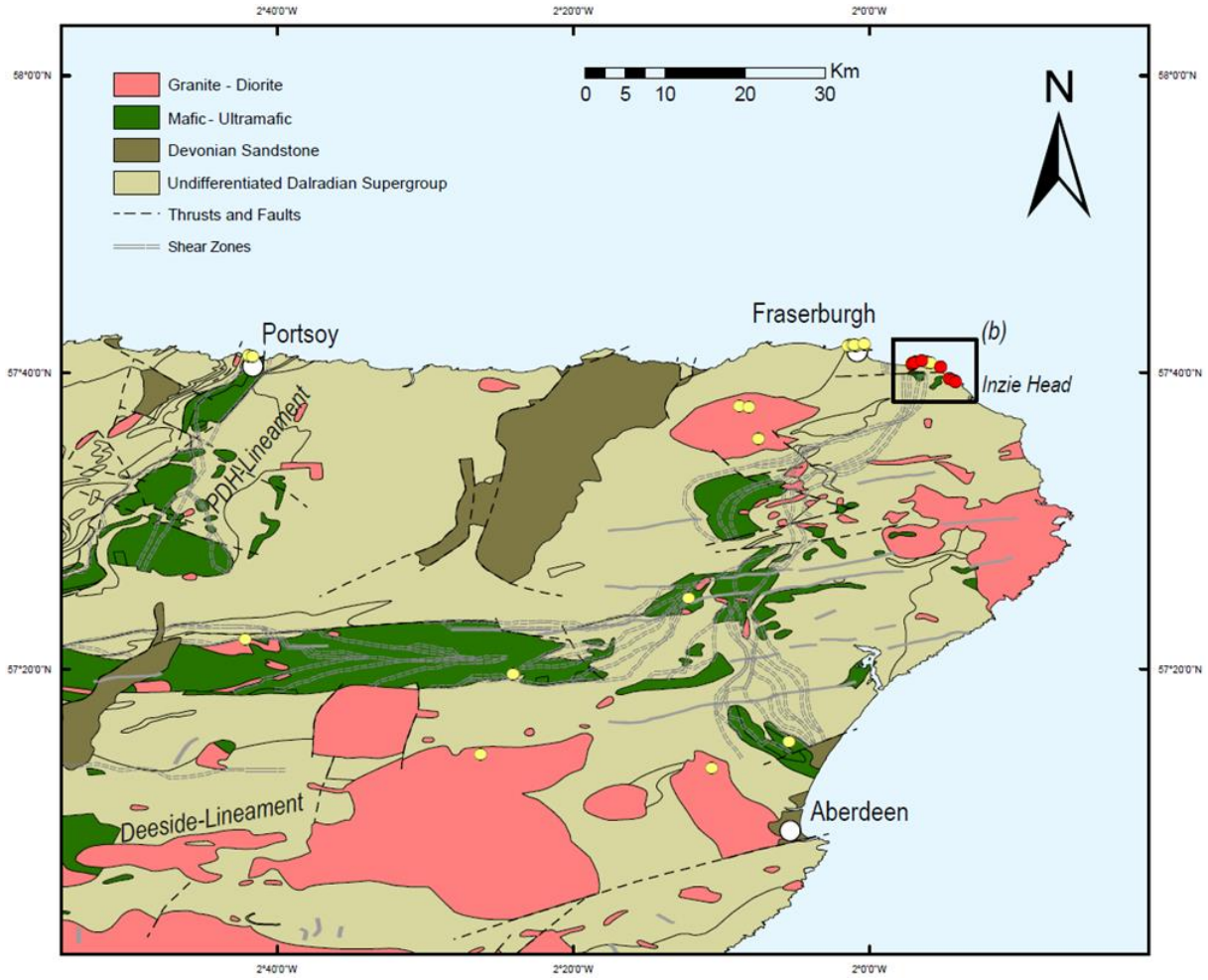

Figure 5 – Major geological features within the Buchan Block terrane; Black rectangle indicates the coastal section of the Inzie Head Gneiss Formation. Sample localities of this study are marked in red (sample group 1) and yellow (sample group 2) and referred to in table 1. Modified after Johnson et al., 2017*; Map projection in WGS84*

Buchan metamorphic activity within the area reached upper amphibolite to granulite facies conditions, with inferred pressure conditions along the metamorphic gradient between ca. 2 – 4.5 kbar and increasing temperatures along the

sequence from ca. 650°C to ≥ 800°C (Johnson et al., 2015, 2003, 2001b, 2001a). In addition to the distinct Buchan-type metamorphic activity, significant differences in structural, sedimentological and magmatic evolution distinguish the Buchan Block area from the rest of the Grampian Terrain (Stephenson et al., 2013b). Large exposures of (ultra-) mafic to intermediate intrusions, generally termed the Grampian Basic Suite, are absent elsewhere in the Scottish Grampian Terrane and form an exclusive occurrence within the Buchan Block (fig. 4). Mafic magma emplacement occurred between ca. 475 – 470 Ma, broadly contemporaneous with established peak metamorphic activity of the region (Viete et al., 2013). Based on the trace element chemistry and low initial $^{87}Sr/^{86}Sr$ isotopic ratios around 0.706, the roots of a calc-alkaline arc has been suggested as source domain of the mafic rocks (Oliver, 2001; Pankhurst, 1970; Thompson, 1985). The Grampian Basic Suite is largely constituted of gabbroic rocks, that were emplaced during the Grampian regional metamorphic event as a planar and sub-horizontal sheet (Viete et al., 2010). The emplacement of the gabbroic sheet resulted in contact metamorphism of surrounding country rocks, estimated at temperatures of 700 – 850 °C and pressures of 4-5 kbar which is equivalent to a crustal depth of ca 15 – 18 km (Droop and Charnley, 1985). The current outcrop pattern of the gabbroic rocks was formed during large-scale folding following the peak metamorphic activity in the Buchan Block domain (Fettes, 1970). Previous studies emphasized the Buchan Block as an area, characterized by least crustal thickening, relative to the rest of the Grampian Terrane. Positive anomalies of gravity and magnetic survey data have been correlated with the observed geological features of the area (Johnson et al., 2017; Trewin and Rollin, 2002). Thus, the exposed mafic intrusions of the Grampian Basic Suite and major shear zones are clearly delineated and a broad gravity high of the area is consistent with a comparatively thin lithosphere relative to the rest of the Grampian Terrane.

Syn to late-tectonic metaluminous to peraluminous granitoid bodies are dispersed throughout the Buchan Block domain. During the Grampian orogenic event, widespread magmatic activity between ca 475 – 465 Ma resulted in the emplacement of voluminous granitic bodies. These Grampian aged granites have been described as peraluminous and formed within major shear zones which enclose the Grampian Basic Suite. These granites have been suggested to derive from partial melting processes in the mid-crust, showing crustal like initial $^{87}Sr/^{86}Sr$ isotopic signatures and inherited zircon populations (Harmon, 1984; Johnson et al., 2003; Kneller and Aftalion, 1987). A later uplifting and exhumation phase, starting at ca. 460 Ma and following the peak metamorphism, resulted in the extensive exposure and rapid cooling of the metamorphic belt. After peak metamorphic activity, post tectonic granite emplacement commenced around 455 Ma, suggested to have formed in response to decompressional melting of the thickened continental crust. Their mineralogy and chemical characteristics have been described as largely similar to the granites formed around 470 Ma, with crustal-like isotopic signatures (Oliver et al., 2008). A minority of granitoids emplaced around 455 Ma and after, have been described with low peraluminous to metaluminous compositions and/ or low initial $^{87}Sr/^{86}Sr$ isotopic ratios, that are inconsistent with crustal derivation (Oliver, 2001; Oliver et al., 2008). The complex, ca. 5 km long coastal section of Inzie Head at the north-eastern end of the Buchan Block area exposes metamorphosed migmatite sequence, which is interspersed with numerous syn to post-collisional igneous bodies of granitic to dioritic composition. The igneous exposures are characterized by complex intermingled relations of rocks that differ significantly in composition and textures. Metatexites, diatexites and leucosome exposures, constitute the so-termed Inzie Head Gneiss Formation, recording amphibolite to granulite facies conditions (fig. 5).

2.2 REGIONAL GEOLOGICAL SETTING OF THE INZIE HEAD FORMATION

The Inzie Head Formation is exposed along a coastal section broadly from Cairnbulg to St. Combs, where a metamorphosed sedimentary sequence constitutes of variably migmatized pelites, semipelites and psammites (fig. 6). Identified metamorphic mineral assemblages suggest amphibolite to granulite facies conditions during peak metamorphism, with an increase in metamorphic grade from the NW to the SE.

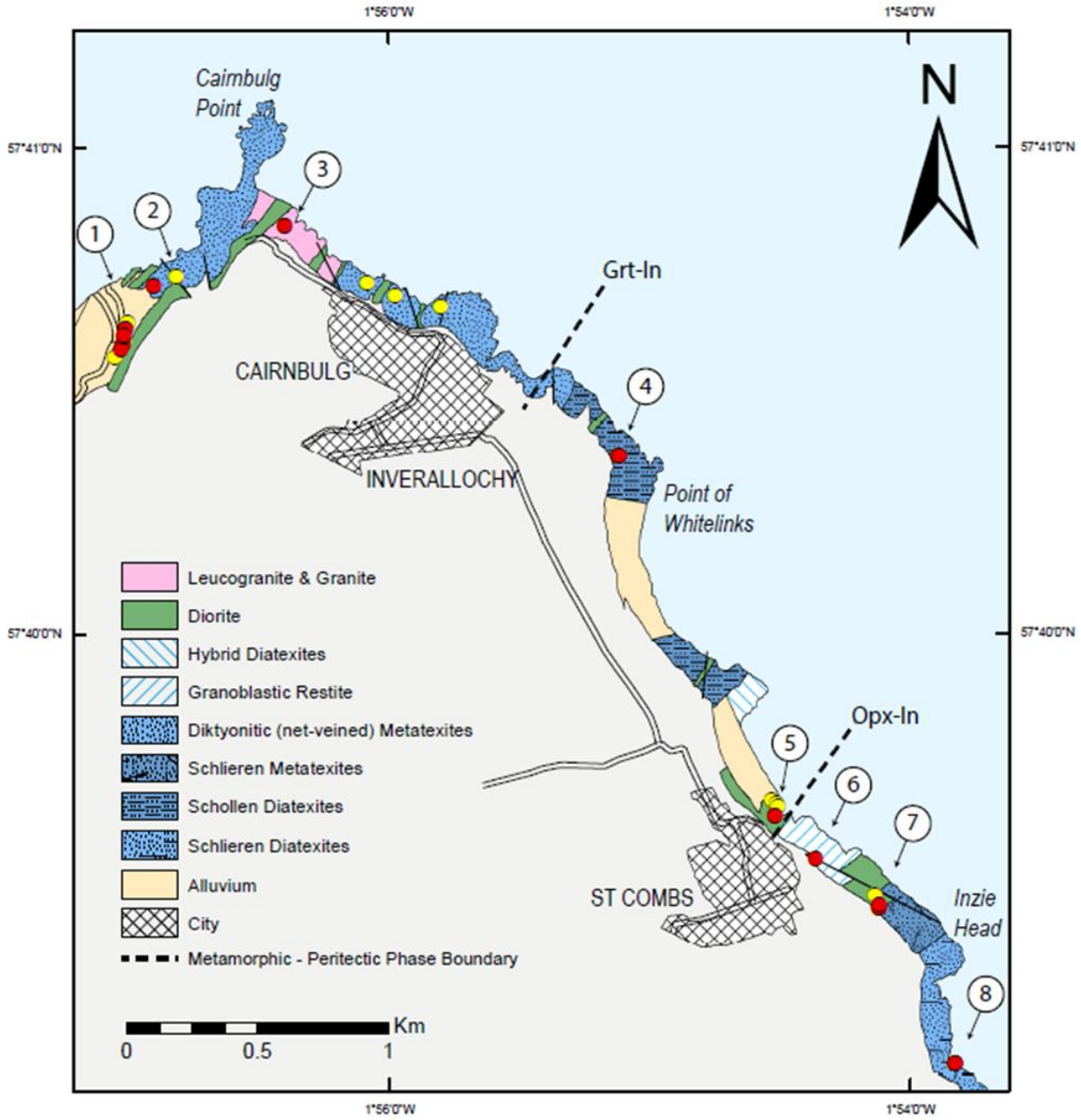

Figure 6 – Major geological units of the Inzie Head Gneiss Formation and main granite and diorite exposures. Yellow and red dots indicate sample localities which are highlighted by the numbers and referred to in table 1. Modified after Johnson et al., 2001b

Low peak metamorphic pressures of maximum 4.5 kbar have been inferred for the coastal section, with the potential for near isobaric conditions around 3 kbar, whereas temperatures possibly exceeded 800°C at the highest metamorphic grades (Johnson et al., 2015, 2001a). The migmatites throughout the section show variable degrees of in-situ anatexis and melt segregation, that resulted in variably sized leucocratic segregations. Based on different mineralogical characteristics, three main leucosome types have been distinguished: cordierite-bearing leucosome (L-crd), garnet-bearing leucosome (L-gt) and orthopyroxene-bearing leucosome (L-opx). Cordierite, garnet and orthopyroxene porphyroblasts within the different leucosomes are used as indicator minerals, inferred to have formed during local anatexis as peritectic phases, which were in equilibrium with the formed melt. An overall increase in size and abundance of the leucosome segregations from the NW to SE of the section, is concomitant with changing migmatite morphologies. Furthermore, correlating with the prograde metamorphic grade form NW to SE, form the different leucosome types a zonal sequence, whereafter the coastal section has been distinguished into three main zones (Johnson et al., 2001b). Figure 7 illustrates the different leucosome zones of the Inzie Head crustal section, as inferred prior to uplifting and later stage processes (Johnson et al., 2001b).

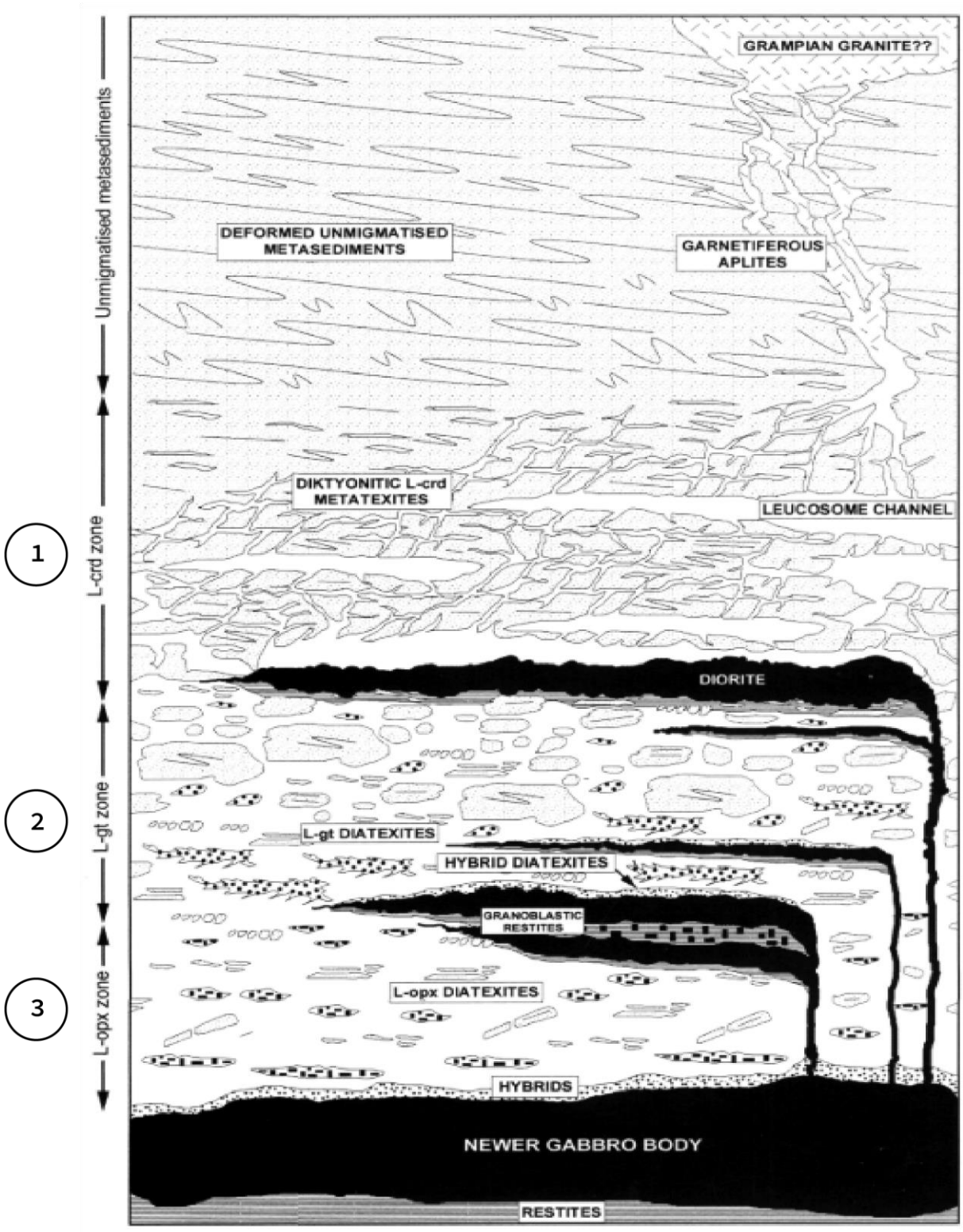

Figure 7 – Schematic drawing of the Inzie Head coastal section prior to uplift; Adapted from Johnson et al., 2001b*; The Newer Gabbro body refers to the Grampian Basic Suite*

The first zone (1) is located at the NW end of the section and defines the lowest metamorphic grade, where migmatites expose net-veined and schollen metatexitic morphologies. Leucosome bodies within this section contain porphyroblastic cordierite, which further continues throughout the migmatized coastal section. Further SE, metamorphic grades and melt fractionation increased and the occurrence of L-gt defines the second zone (2) (fig. 6 & 7). The L-grt mingles with the L-crd type and exposed diatexitic migmatites contain fragments of semi-digested pelitic schollen. The highest metamorphic grade is defined in the third zone (3), at the SE end of the coastal section, where schlieren diatexites are exposed. L-opx occurs and mingles locally with L-crd dominated schlieren, whereas the L-grt type and pelitic schollen are largely absent

at this grade. The mingling features of the different leucosome types at the different metamorphic grades, have been interpreted to represent coeval melt emplacement (Johnson et al., 2001a, 2001b). Later-stage retrogression of the metamorphic sections resulted in substantial pseudomorphic replacement of the high-grade mineral assemblages by chlorite and sericite.

Previous authors noticed frequent interconnections from the leucosome segregations to granitic bodies, which are dispersed throughout the coastal section and range from cm to more than hundreds of m in size (Johnson et al., 2003). A genetic link between the migmatites and granite bodies has been postulated, based on geochemical and petrographic constrains, as well as thermodynamic modelling of phase relations (Johnson et al., 2003, 2001a, 2001b). Thereafter, leucosome and granites derived from a common crustal source, as a result of efficient in-situ partial melting of the sedimentary host rocks, whereby leucosome bodies are interpreted as frozen in-situ melts and channel ways through which granitic melt migrated upwards. Studies have compared the composition of granites from Inzie Head and the wider Buchan Block area with experimentally determined melt compositions of metapelite protoliths under fluid-absent conditions, noticing many approximating compositions. Studies have argued that the significant amount of L-crd produced melt required a considerable incursion of excess fluid and proposed a two-stage model. Thereafter, partial melting has occurred initially under fluid present conditions at pressures of ca. 2.8 kbar and temperatures around 650°C (Johnson et al., 2015). The incursion of excess fluid necessary is suggested to have derived from dehydration melting of the surrounding metasedimentary crustal rocks, induced by the emplacement of a hot mafic magma and associated deformation. Following fluid-absent conditions are recorded within rocks towards the SE of the section, where the increasing metamorphic gradient suggests rising temperatures that possibly exceeded 775°C.

Dark-coloured sheets of dioritic composition are evident throughout the Inzie Head section, ranging from ca. 10 cm to 300 m in size (fig. 6; Johnson et al., 2001b). The (micro-)dioritic bodies commonly crosscut the migmatite sequence and earlier structures. Previous studies proposed the derivation of the diorite intrusions from an underlying mafic mass, which is represented by the (ultra-)mafic exposures of the Grampian Basic Suite (Johnson et al., 2001b). As clinopyroxene is absent in the Inzie Head diorites, their mineralogical resemblance to uralitized gabbros has been emphasized. Furthermore, the development of leucosome has been suggested to have enhanced marginally to the diorite sheets, preferentially along their upper margins, as leucosome proportions in place are generally enlarged (fig. 7). The intermingled field relations of the contrasting rocks have been explained to represent a temporal overlap in melt generation and the intrusion of diorites. Furthermore, interconnected veins and wispy tongues or veins of felsic compositions frequently penetrate or separate angular and lobate pillows of diorites. Mingling relations of the diorite intrusions and granitic bodies are evident throughout the section, with contact margins varying from sharp to diffuse and gradational. Previous studies proposed the derivation of diorites by multiple intrusions, emphasizing that darker-coloured, more mafic domains of the diorites crosscut lighter-coloured, earlier domains, regarded to have been subject to hybridization processes (Stephenson et al., 2013b). In place, potentially hybridized, intermediate domains form veins crosscutting through granitic bodies. Exposures of gradational contact margins, which range from mm to tens of m in size, show variable colour and grain size variations, as well as finely porphyritic textures, invoking the possibility of chemical mixing during magma petrogenesis.

Zircon U-Pb geochronological age constrains suggest a coeval relationship between granite magma activity and metamorphic processes around 470 Ma, coherent with the field observations. Conversely, previous studies constrained a zircon U-Pb crystallization age of 490 Ma for a diorite sample from the Inzie Head Formation, contradicting a derivation from the ca. 470 Ma Grampian Basic Suite (Johnson et al., 2017). Thereafter, a first peak of the high dT/ dP Buchan metamorphic activity, together with mafic magma emplacement, has been proposed to have occurred at ca. 490 Ma, in the early phases or preceding the Grampian orogenic event (Johnson et al., 2017). Constrains on the Hf isotopic signature of the same diorite sample, yielded evolved, sub-chondritic epsilon (ε) values, varying between –8 to –13, which have been proposed to reflect in-situ crustal contamination of the intruding diorites (Johnson et al., 2017). The obtained εHf values were further converted to represent epsilon Nd (εNd) values and compared to previously determined isotopic fields of Dalradian metasediments and Caledonian granites of Ordovician age (fig. 8). Thereafter, the constrained εNd isotopic composition of the diorite sample yielded a signature at the juvenile end of the metasedimentary field, within error overlapping with the Ordovician granites (fig. 8).

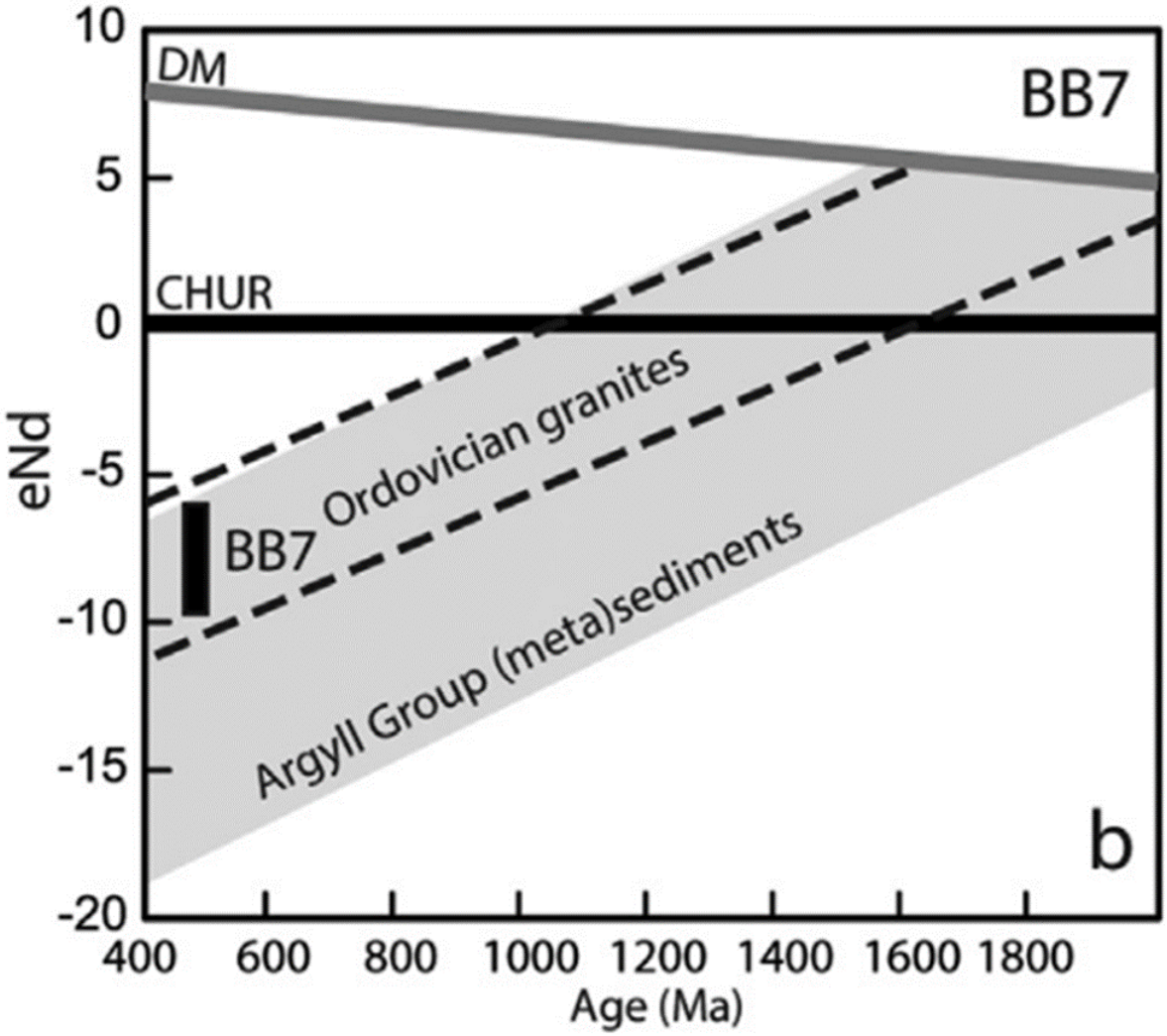

Figure 8 – Isotopic εNd diagram showing values of a diorite (BB7) in comparison with εNd values of granites with overlapping age and (meta-)sediments from the surrounding Grampian terrane; Adapted from Johnson et al., 2017

CHAPTER 3 METHODOLOGY

In the scope of this project, various steps were undertaken to investigate the petrogenesis of the sampled rocks from Inzie Head and the wider Buchan Block domain.

3.1 FIELD WORK AND SAMPLING

The sampling was undertaken in two field trips by Prof. Gary Stevens in the year 2015 (sample group 1 = SG1) and Prof. Jean-François Moyen and Dr. Mathew Mayne in the year 2016 (sample group 2 = SG2). The sample localities are shown in fig 5 & 6 (red dots reflect SG1 and yellow dots resemble SG2) and are summarized in table 1. All seventy-four samples were prepared and analysed for whole-rock major and trace element compositions. Sample set 1 comprises of samples from the Inzie Head section, of which a selection was further prepared and analysed for petrographic and mineral geochemical constrains, as well as mineral isotopic compositions. Sample set 2 constitute of rocks from the Inzie Head section and additional samples from the wider Buchan Block area, where a selection was prepared and analyses for whole rock isotopic compositions.

TABLE 1 – SUMMARY OF ALL SAMPLES, SAMPLE LOCATIONS AND RESPECTIVE ANALYTICAL STEPS (IH = SAMPLES OBTAINED FROM THE INZIE HEAD COASTAL SECTION; PORT = SAMPLES OBTAINED AROUND THE PORTSOY AREA; FRAS = SAMPLES OBTAINED AROUND THE FRASERBURGH AREA; BB = SAMPLES OBTAINED INLAND WITHIN THE WIDER BUCHAN BLOCK AREA); A) THIN SECTION, B) WHOLE ROCK MAJOR AND TRACE ELEMENT CHEMISTRY, C) MINERAL CHEMISTRY, D) ZIRCON U-PB ISOTOPE ANALYSES, E) ZIRCON LU-HF ISOTOPE ANALYSES, F) APATITE SM-ND ISOTOPE ANALYSES, G) APATITE RB-SR ISOTOPE ANALYSES, H) WHOLE ROCK SM-ND AND RB-SR ISOTOPE ANALYSES

	Sample ID	Rock Type	Mingling Features	Lat.	Long.	Field Location	Sample Group	ThinS.[a]	WR[b] ME+TE	Min.[c] Chem.	Zr.[d] U/Pb	Zr.[e] Lu/Hf	Ap.[f] Sm/Nd	Ap.[g] Rb/Sr	WR[h] Isot.
Inzie Head															
	s1A	Gabbroic Diorite		57.676	-1.95032	IH - 1	SG1	X	X	X					
	s1B	Granodiorite	M	57.676	-1.95032	IH - 1	SG1	X	X	X	X	X	X	X	
	s1C	Granite	M	57.676	-1.95032	IH - 1	SG1	X	X						
	s1Da	Granite	M	57.676	-1.95045	IH - 1	SG1	X	X	X	X	X	X	X	
	s1Db	Monzonite	M	57.676	-1.95045	IH - 1	SG1	X	X	X					
	s1E	Metapelite		57.677	-1.95013	IH - 1	SG1	X	X						
	s1F	Granite		57.677	-1.95013	IH - 1	SG1	X	X	X	X	X		X	
	s1G	Granodiorite	M	57.677	-1.95025	IH - 1	SG1	X	X						
	s1H	Granodiorite	M	57.677	-1.95022	IH - 1	SG1	X	X	X	X	X	X	X	
	s034	Granite	M	57.677	-1.95014	IH - 1	SG2		X						
	s035	Migmatite	M	57.676	-1.95034	IH - 1	SG2		X						
	s036	Granite	M	57.676	-1.95096	IH - 1	SG2		X						
	s037	Migmatite	M	57.676	-1.95096	IH - 1	SG2		X						X
	s038	Granite	M	57.676	-1.95096	IH - 1	SG2		X						
	s2A	Migmatitic Metapelite		57.679	-1.94835	IH - 2	SG1	X	X	X	X	X	X	X	
	s2B	Granite		57.679	-1.94835	IH - 2	SG1	X	X		X	X	X	X	
	s039	Migmatite		57.679	-1.94701	IH - 2	SG2		X						X
	s3B	(Leuco-) Granite		57.681	-1.93997	IH - 3	SG1	X	X	X	X	X	X	X	
	s040	Migmatite		57.678	-1.93481	IH - 3-4	SG2		X						X
	s041	Granite	M	57.678	-1.93301	IH - 3-4	SG2		X						
	s042	Migmatitic Metapelite		57.678	-1.93012	IH - 3-4	SG2		X						
	s4A	Grt-bearing Diatexite		57.673	-1.9186	IH - 4	SG1	X	X	X					
	s4B	Grt-bearing Diatexite		57.673	-1.9186	IH - 4	SG1	X	X						
	s4D	Grt-bearing Leucosome		57.673	-1.9186	IH - 4	SG1	X	X		X	X	X	X	
	s5A	Diorite	M	57.66	-1.90863	IH - 5	SG1	X	X	X	X	X		X	
	s5Ba	Granite	M	57.66	-1.90863	IH - 5	SG1	X	X	X	X	X	X	X	
	s5Bb	Diorite	M	57.66	-1.90863	IH - 5	SG1	X	x	X	X	X	X	X	
	s043	Gabbroic Diorite	M	57.661	-1.90895	IH - 5	SG2		X						
	s044	Gabbroic Diorite	M	57.661	-1.90875	IH - 5	SG2		X						X
	s045	Granite	M	57.661	-1.90865	IH - 5	SG2		X						X
	s046	Diorite		57.66	-1.90853	IH - 5	SG2		X						X
	s6	Residuum-rich Diatexitic Metapelite		57.659	-1.90605	IH - 6	SG1	X	X						
	s7A	Diorite		57.657	-1.90198	IH - 7	SG1	X	X	X	X	X	X	X	
	s7B	Granite		57.657	-1.90198	IH - 7	SG1	X	X		X	X	X	X	
	s047	Quartz-Monzonite	M	57.657	-1.90238	IH - 7	SG2		X						X
	s8A	Metapelite with Crd-Porphyroblast		57.65	-1.88888	IH - 8	SG1	X	X						
	s8B	Metapelite with Grt-Porphyroblast		57.65	-1.88888	IH - 8	SG1	X	X						
	s8C	Migmatitic Metapelite		57.65	-1.88888	IH - 8	SG1	X	X						
	s8Da	Granite	M	57.65	-1.88888	IH - 8	SG1	X	X	X	X	X	X	X	
	s8Db	Diorite	M	57.65	-1.88888	IH - 8	SG1	X	X	X	X	X	X	X	
Wider Buchan Block Area															
	s005	Granite		57.629	-2.14517	BB	SG2		X						
	s006	Granite		57.627	-2.13429	BB	SG2		X						
	s007	Granite		57.592	-2.12389	BB	SG2		X						
	s009	Granite		57.592	-2.12389	BB	SG2		X						
	s013	Granite		57.37	-2.70152	BB	SG2		X						X
	s015	Granite		57.237	-2.43622	BB	SG2		X						
	s016	Granite		57.251	-2.08942	BB	SG2		X						
	s008	Gabbro		57.414	-2.2025	BB	SG2		X						X
	s010	Gabbro		57.328	-2.39912	BB	SG2		X						X
	s011	Gabbro		57.328	-2.40019	BB	SG2		X						
	s012	Gabbro		57.328	-2.40019	BB	SG2		X						
	s017	Gabbro		57.251	-2.08942	BB	SG2		X						
	s049	Gabbro		57.685	-2.69702	Port	SG2		X						
	s050	Gabbro		57.685	-2.69702	Port	SG2		X						X
	s051	Gabbro		57.685	-2.6974	Port	SG2		X						
	s052	Gabbro		57.685	-2.69304	Port	SG2		X						
	s053	Gabbro		57.685	-2.69304	Port	SG2		X						
	s054	Anorthosite		57.685	-2.69304	Port	SG2		X						
	s028	Granite		57.696	-2.01414	Fras	SG2		X						X
	s030	Granite		57.697	-2.01561	Fras	SG2		X						
	s020	Granite		57.697	-2.0228	Fras	SG2		X						X
	s022	Granite		57.696	-2.01393	Fras	SG2		X						
	s032	Granite		57.699	-2.00456	Fras	SG2		X						
	s029	Metapelite		57.696	-2.01414	Fras	SG2		X						X
	s033	Migmatitic Metapelite		57.699	-2.00456	Fras	SG2		X						
	s018	Psammite		57.697	-2.02064	Fras	SG2		x						
	s019	Psammite		57.697	-2.02178	Fras	SG2		X						
	s021	Pelite/ Psammite		57.696	-2.01399	Fras	SG2		X						
	s023	Pelite		57.696	-2.01393	Fras	SG2		X						
	s024	Pelite		57.698	-2.01812	Fras	SG2		X						
	s025	Calc Silicate		57.698	-2.01615	Fras	SG2		X						
	s026	Psammite		57.697	-2.01489	Fras	SG2		X						
	s027	Calc Silicate		57.697	-2.01452	Fras	SG2		X						
	s031	Calc Silicate		57.698	-2.00445	Fras	SG2		X						

3.2 WHOLE ROCK MAJOR AND TRACE ELEMENT GEOCHEMISTRY

Both sample groups were prepared at the Central Analytic Facility (CAF) of Stellenbosch University, South Africa and analysed in two different runs. In preparation for whole-rock major and trace analyses, a jaw crusher and tungsten swing mill were used to achieve fine powders of each sample, which were further prepared into fused glass discs. Major elemental compositions were determined by X-ray Fluorescence Spectrometry (XRF) using a PANanalytical Axios Wavelength Dispersive spectrometer, fitted with a Rh tube, scintillation detector and a gas-flow proportional counting detector. Known compositions of control standards (BE-N, JB-1, BHVO-1, WITS-B, DISKO-1, JG-1, HUSG, WITS-G and NIM-G) were used for calibration procedures and quality controls (accuracy and precision) of the analyses. The known compositions are treated as unknown, whereby a relative derivation from the reference composition of less than 1% is regarded as acceptable.

Whole-rock trace element compositions were determined on fused glass discs by Laser Ablation Inductively Coupled Plasma Mass Spectrometry (LA-ICP-MS), using a Resolution 193 nm Excimer laser ablation system, which is connected to an Agilent 7700 (sample set 1) or 8800 (sample set 2) ICP-MS. Ablation on sample set 1 was performed on two spots of 100 µm per sample in He gas at a flow rate of 0.30 L/min at a frequency of 10 Hz and energy of 2.5 J/cm^2. Before the introduction into the plasma of the ICP, a carrier gas of Ar (at 1 L/min) and N (at 0.003 L/min) was added. Two spots of 104 µm per sample were analysed for sample set 2 in He gas at a flow rate of 0.45 L/min at a frequency of 8 Hz and energy of 3 J/cm^2. A carrier gas of 0.8 L/min Ar and 0.004 L/min N were added before the introduction into the ICP. The analysed trace element concentrations were quantified using NIST 610 as calibration standards and certified quality control standards (BHVO and BCR glasses and powders, produced by the USGS, Dr S. Wilson, Denver, CO), which were run in standard bracketing every 15 – 20 samples, throughout the sequence. The acquired data was processed using Iolite (v 3.65), distributed by the School of Earth Sciences from the University of Melbourne and further handled using Microsoft Excel.

3.3 MAJOR ELEMENT MINERAL CHEMISTRY

Petrographic and chemical analyses of thirty-one thin sections of sample set 1 were analysed at the Central Analytic Facility of the Stellenbosch University, South Africa. First constrains on mineral assemblages were drawn under polarisation microscopy, to identify textures of interest. Furthermore, carbon coated thin sections were analysed for the chemical signatures of individual minerals. Major element compositions were identified by quantitative energy-dispersion X-ray spectroscopy (EDS) using a ZEISS EVO MA15 VP scanning electron microscope (SEM) with an Oxford Instrument (max 20mm2) detector and the Oxford INCA software. Beam conditions during the quantitative analyses were 20 kV accelerating voltage and 1.0 A probe current, with a specimen beam current at -20.00 nA and a working distance of 8.5 mm. The accuracy of the chemical analyses was verified by using relevant Astimex Scientific mineral standards of known compositions, treated as unknowns to compare the mineral stoichiometries. Mineral formulae were calculated in Microsoft Excel, whereby analyses falling outside of ±0.02 of ideal stoichiometry were rejected.

3.4 MINERAL IN-SITU ISOTOPE ANALYSES

15 samples of sample set 1 were prepared for in-situ mineral analyses at the CAF at Stellenbosch University, South Africa. The samples were prepared using a jaw crusher and disc mill, followed by sieving. A Super Panner was used for the gravitational separation of minerals, according to their distinct density differences, followed by magnetic separation with a Frantz separator. The remaining samples underwent heavy liquid separation, using Tetrabromoethane (TBE) and Iodomethane (MEI). Approximately 100 zircon and 100 apatite crystals were hand-picked per sample under a binocular microscope and mounted in 25 mm epoxy resin discs, which were grinded till exposure, polished and carbon coated for further processing under a ZEISS MERLIN SEM. Cathodoluminescence (CL), backscatter electron (BSE) and secondary electron (SE) imagery were obtained at 11na with 10 kV and 10 mm working distance.

3.4.1 IN-SITU U-PB ISOTOPE ANALYSES OF ZIRCON

Internal structures of zircon were investigated and zones of interest identified using CL and BSE images, prior to further laser ablation analyses. Zircon U-Pb isotope analyses were acquired at the CAF by using a Thermo Scientific Element2 single collector high magnetic sector field inductively coupled plasma mass spectrometer (SC-SF-ICP-MS), coupled to an ASI Resolution laser ablation system. Zircon U-Pb data was obtained by single spot ablation under continuous He gas flow of 0.35 L/min, with a spot size of 26 µm and a fluence of 2.0 J/cm^2. Calibration standards were performed using GJ-1 (Jackson et al., 2004) as a primary reference material, Plešovice (Sláma et al., 2008) and 91500 (Wiedenbeck et al., 1995) as secondary reference materials, which were analysed in standard bracketing between groups of 13 samples throughout the sequence. The employed methods for analyses and data processing followed the methods described by Gerdes and Zeh (2009, 2006) and Frei and Gerdes (2009). No common Pb correction was applied to the data and age uncertainties are quoted in 2σ. Data reduction was performed using the Iolite data reduction software package and further processed with Isoplot/Ex 3.0 (Ludwig, 2003).

3.4.2 IN-SITU LU-HF ISOTOPE ANALYSES OF ZIRCON

In-situ Lu-Hf isotope analyses were performed, when possible, on the same zircon grains as analysed for U-Pb age data. Lu-Hf isotopes were analysed at the Goethe-University Frankfurt, Germany, by laser ablation multi collector inductively coupled plasma mass spectrometry (LA-MC-ICP-MS). A Resonetics 193 nm Excimer (Compex Pro 102F) laser system with a S155 ablation was coupled to a Thermo Scientific Neptune. The same methods were applied as described in Gerdes and Zeh (2009, 2006) and Zeh and Gerdes (2012). Calibration, accuracy and reproducibility were ensured by repeated analyses of GJ-1 and Plešovice zircon reference materials, throughout the sequence (n=30 and 20, respectively), expressed in mean with two standard deviation uncertainties. Whenever possible, ablation spots, usually between 40-60 µm in size, were super-imposed on the U-Pb laser ablated spots. Thus, initial $^{176}Hf/^{177}Hf$ and εHf were calculated, using the previously identified $^{206}Pb/^{238}U$ or $^{207}Pb/^{206}Pb$ ages and were based on a ^{176}Lu decay constant of 1.867×10^{-11} year^{-1} (Scherer et al., 2001) and chondrite uniform reservoir (CHUR) parameters of $^{176}Lu/^{177}Hf = 0.0336$ and $^{176}Hf/^{177}Hf = 0.282785$ (Bouvier et al., 2008). Positive or negative $\varepsilon Hf_{(t)}$ values refer to the enrichment or depletion of Hf at a given time, relative to the CHUR expresses as 0.

3.4.3 IN-SITU SM-ND AND RB-SR ISOTOPE ANALYSES OF APATITE

In-situ Sm-Nd and Rb-Sr isotope analyses on apatite grains were performed at the Goethe-University Frankfurt, Germany by LA-MC-ICP-MS with a Resonetics Excimer laser system (as described above), coupled to a Thermo Scientific Neptune. $^{147}Sm/^{144}Nd$ and $^{87}Rb/^{86}Sr$ isotopic analyses were performed on different apatite grains, due to analytical difficulties. Sm-Nd isotope ratios were analysed with 40-72 µm spot sizes, at a laser frequency of 5-8 Hz and energy density of 6 J cm^{-2}. Laser ablation for Rb-Sr was performed with spot sizes between 72-86 µm, at a laser frequency of 10 Hz and energy density of 4 J cm^{-2}. The applied method is described in detail in Wilson et al. (2017). The raw data was corrected for gas blank and isobaric interferences from Kr, Rb, Er and Yb isotopes. The internal $^{86}Sr/^{88}Sr$ was used for mass bias correction of Sr isotopes. Sodalime glass NIST SRM-612 were used to estimate and correct for the Rb/Sr interelement fractionation and the difference between the Rb and Sr mass bias. Plagioclase MIR and different grains of Durango apatite (named here DUR-1, -2 and -3) were used as quality controls throughout the sequences.

3.4.4 WHOLE ROCK SM-ND AND RB-SR ISOTOPE ANALYSES

Fourteen samples were selected from sample set 2 and prepared fine rock powders were sent to the University of Cape Town, South Africa for whole rock $^{147}Sm/^{144}Nd$ and $^{87}Rb/^{86}Sr$ isotope analyses. JG-2 and JNdi-1 (Tanaka et al., 2000) were used as reference materials and calibration standards for Sm-Nd analyses and JG-2 and NIST987 for Rb-Sr analyses. Calculations are based on present-day CHUR values of $^{143}Nd/^{144}Nd = 0.512638$; $^{147}Sm/^{144}Nd = 0.1967$ and present-day depleted mantle (DM) values of $^{143}Nd/^{144}Nd = 0.51315$; $^{147}Sm/^{144}Nd = 0.2137$. Present-day bulk silicate earth (BSE) values of $^{87}Sr/^{86}Sr = 0.705$ and $^{87}Rb/^{86}Sr = 0.09$ were used for further calculations.

CHAPTER 4 RESULTS

Although samples were collected throughout the Buchan Block area, the main focus was set on the coastal section of Inzie Head, south-east of Fraserburgh (fig. 5 and 6). Thus, from a total of seventy-four samples, forty samples were collected from along the coastal section (table 1). Photos of field exposures were taken by Prof. Gary Stevens and Dr. Mathew Mayne.

4.1 FIELD RELATIONS

The Inzie Head Gneiss Formation is largely comprised of metamorphosed pelites, semi-pelites and calcsilicates, showing varying degrees of anatexis. Metatexitic migmatites at the NW end of the section contain variably sized elongated patches and lenses of leucocratic segregations, locally folded and stretched forming interconnected vein networks or stromatic layers (fig. 9 – a). Networks of leucocratic segregations separate foliated schlieren and angular to elongated schollen of variable size (fig. 9 – b). The schlieren are biotite dominated resembling restite, whereas the schollen compare to the surrounding metapelitic rocks with locally preserved relict layering or bedding (fig. 9 – c). The schollen generally appear parallel to the dominant foliation of the migmatites but some outcrops expose rotated schollen, which lie at a high angle, giving these domains a more chaotic and rather diatexitic character. The leucocratic segregations are white to pale grey in colour and increase in volume and abundance towards the SE. Here, the intermingled texture of L-crd and L-grt is of chaotic nature, containing dark coloured diffuse patches and schlieren of residuum (fig. 9 – d). Garnet porphyroblasts are locally replaced or show coronas of fine-grained intergrowth of phyllosilicates (fig. 9 – e). At the SE end of the section, metatexitic and diatexitic migmatites containing schlieren of L-crd, which mingles with the darker grey L-opx, whereas angular and elongated schollen are generally absent. The exposed mingling features are seemingly less chaotic as schlieren and patches appear to widely follow preferred flow directions (fig. 9 – f). The leucosome segregations throughout the section are frequently connected to larger granitoid exposures.

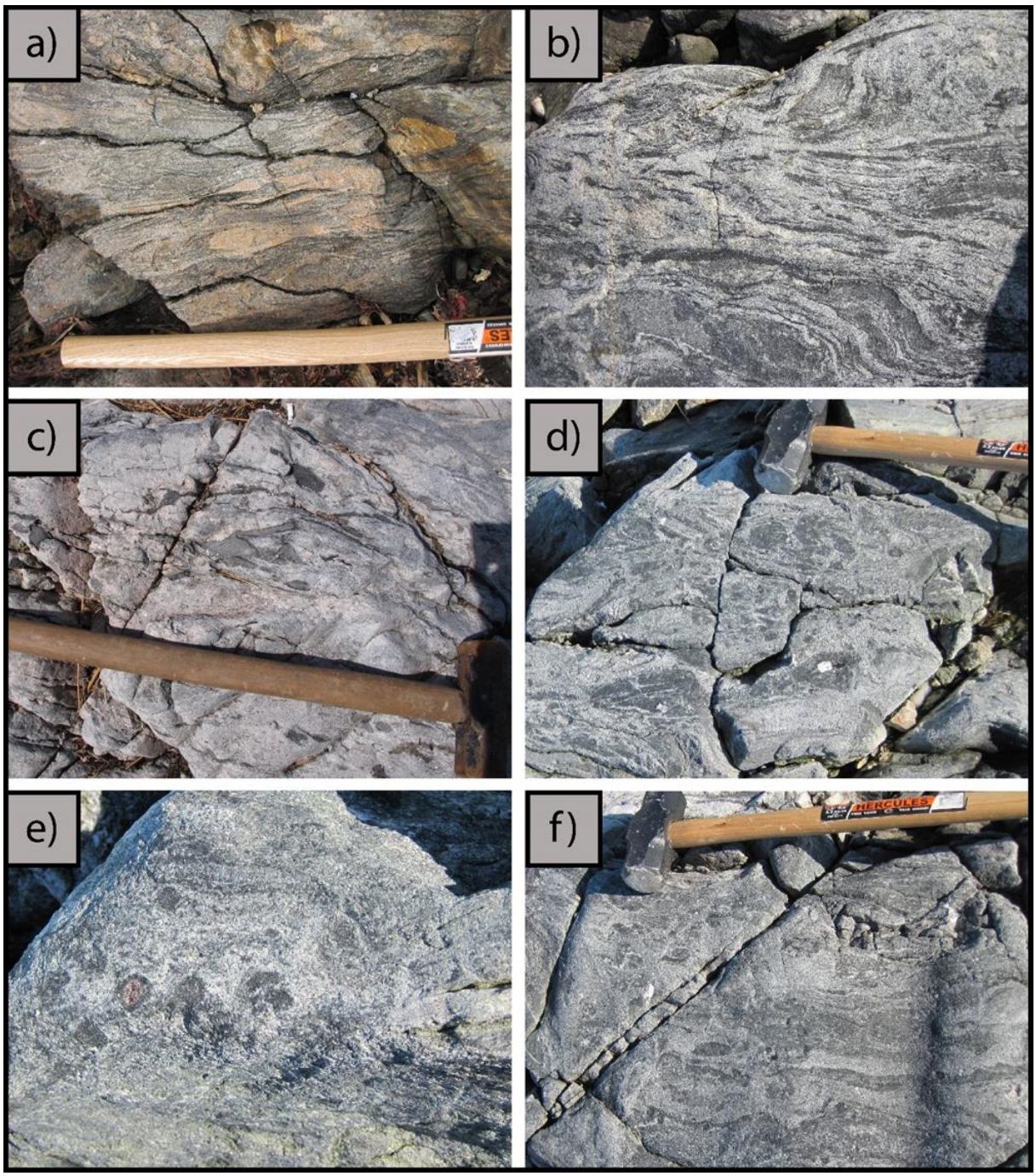

Figure 9 – Field relations of Inzie Head migmatites; a) Elongated patches of leucocratic segregations in migmatite; b) Leucocratic segregations separating locally rotated schollen; c) Metapelitic fragments in leucosome; d) Diatexite containing mingled L-crd and L-grt; e) Garnet porphyroblasts with variable sized coronas and replacement textures byfine-grained intergrowth of phyllosilicates; f) migmatite with flow structures of schlieren and patches

Granitoids are exposed throughout the migmatite sequence, distinct in colour and grain size from the leucosome segregations. From pale leucogranitic to pink and red in colour, granitoids are exposed as veins and larger sheets, with medium to coarse-grained, generally equigranular textures (fig. 10). The granitoid exposures vary in size from tens of cm to several hundred m in size, sporadically containing mafic schlieren, which are dominated by biotite crystals (fig. 10 – a). Granitic sheets are tentatively larger towards the NW of the coastal section, where granitoid bodies range up to ca. 300 m in size. Contacts to adjacent migmatite exposures are generally sharp and lack fine-grained margins (fig. 10 – b & c). Invading granitic veins locally transgress the sharp contacts and intrude into the migmatites, where they connect to leucosome patches, forming gradual transitions, making a clear distinction between leucosome and granite difficult (fig. 10 – b). Variable sized sheets of dark coloured diorite are exposed throughout the section, ranging between tens to hundreds of m across. The fine to medium-grained, mostly equigranular diorites are dark-greenish in colour and thus distinct from the surrounding migmatites and

granitoids (fig. 10 – c). The sheets seemingly cross-cut the migmatite exposures and earlier structures, showing sharp contacts with margins lacking gradual or finer grained domains that would suggest chilling.

Figure 10 – Field relations of Inzie Head granitoids; a) Mafic clot (biotite-dominated) within fine to medium grained granitoid; b) Contact of migmatite and granitoid with continuous veins connecting to leucosome segregations; c) Contact between migmatite and granitoid on the right (indicated by dashed white line) and between granitoid and diorite on the left (indicated by white arrows)

Along the coastal section, the diorite outcrops are commonly exposed in close relation with granitic or leucocratic material, showing a variety of mingling features (fig. 11). A common occurrence are back-veining structures of granitoids, where veins of granitic material penetrate and invade into the diorites (fig. 11 – a-c). The granitic veins form local vein-networks separating angular fragments or lobate pillows of diorite, giving the appearance of a breccia-like system (fig. 11 – c). The abundance of intruding granitic veins generally decrease towards the centre of larger diorite exposures. Contact margins range from sharp, wispy and diffuse to gradational, where colour and grain sizes show gradual changes with distance to the contact (fig. 11 – c-e). Darker, more mafic compositions of diorite are generally found within the centre of larger intrusions, whereas the outer domains are frequently characterized by slightly lighter, grey colours. Such transition from darker to paler diorites vary from sharp to gradual in nature (fig. 11 – d). In addition, porphyritic textures are evident within some mingled diorites and granitoids, defined by larger feldspar crystals that are embedded within an otherwise rather equigranular textures (fig. 11 – e-f).

Figure 11 – Examples of mingled field relations at Inzie Head; a) & b) Granitic veins in diorite, separating angular and lobate diorite fragments c) Colour and grain size variation in the invading granitic vein system and the mafic exposure d) sharp contact of darker and paler mafic domains, cross-cut by a felsic vein; e) Diorite and granitoid contact with granitoid containing large feldspar crystals and diorite containing small, flame-like fractions of granitic material in close proximity to the contact; f) porphyritic feldspar crystals within diorite

4.2 PETROGRAPHY

Petrographic analyses of thirty-one thin sections were conducted on samples from the Inzie Head coastal section. A main focus was set to identify textures, indicative for mixing of contrasting magmas. Thus, the samples were first categorized into groups, based on the presence or lack of macroscopic mingling and mixing features (table 1). Granitic and dioritic samples with no evident mingled field relations or macroscopic evidence that would suggest mixing of magmas, constitute groups (1) and (2), respectively. This classification does not preclude the possibility that the samples might have formed by mixing of

magmas derived from different sources but were of similar composition. Samples with macroscopic mingling features that indicate a potential for magma mixing scenarios are categorized in group (3). Leucosome segregations form a distinct separate group (4).

4.2.1 GROUP (1) – MACROSCOPICALLY UNMINGLED AND UNMIXED GRANITOIDS

In absence of evident field or hand sample textures, suggestive for mingling with contrasting magmas, selected granitic samples were categorized into group (1). The (fine to) medium-grained granitic rocks, with major minerals constituting of K-feldspar (20 – 40 %), plagioclase (20 – 30 %), quartz (25 – 40 %) and biotite (5 – 15 %), exhibit hypidiomorphic to allotriomorphic, inequigranular textures (fig. 12). The groundmass with an average grain size between 1.5 to 3 mm, contains dispersed larger crystals of sub- to anhedral K-feldspar, ranging up to ca. 5 mm in length (fig. 12 – a & b). K-feldspar (K-fsp) crystals display patchy tartan twinning and/or discontinuous, irregular perthite lamellae and patches (fig. 13 – a). Multiple embayments of quartz and plagioclase display interlocking and intergrowing textures, which emphasize the generally curved and lobate grain boundaries. The larger, phenocrystic grains contain inclusions of anhedral biotite and/or quartz, either in weak zonal arrangement or dispersed throughout the sample (fig. 12 – a). Finer-grained, rounded to lath-shaped crystals of plagioclase are frequently mantled by, or included within, K-feldspar, forming antirapakivi-like textures (fig. 12 – b). Subhedral to anhedral plagioclase grains within the samples groundmass show irregular and interlobating grain boundaries, sporadically with intergrowth textures of lobate quartz (fig. 12 – c). Fine intergrowth textures with lobate quartz located on plagioclase grain boundaries occasionally form lobes of myrmekite that intrude into K-fsp crystals.

Plagioclase grains, generally with simple or multiple twinning, display weakly defined concentric zoning and/or patchy dissolution patterns (fig. 12 c – e). Concentric zoning patterns are evident in a minority of plagioclase grains, accentuated by zonal alteration and sericitization (fig. 12 c & d). The accentuation of certain domains emphasizes the compositional zoning patterns, formed during growth of the plagioclase grains. The majority of plagioclase grains in the granitic samples is characterized by alteration, corrosion and associated sericitization, spreading along microstructures and grain boundaries or in patches throughout plagioclase grains (fig. 12 – e). Weakly defined dissolution textures and irregular patches of K-feldspar are characteristic for this plagioclase type, whereas plagioclases with concentric zoning patterns are generally absent in K-fsp patches. Biotite with weakly to well-developed chloritization, and minor muscovite (<5 Vol.-%) within the groundmass, form flakes or lath shaped crystals, occasionally in intergrown relation. The grains generally show weak to moderate resorption and appear with discontinuous and locally restricted alignment of preferred orientations, indicating a weak foliation. Anhedral to interstitial quartz with undulous extinction, occurs with sutured grain boundaries and local subgrain formation. Occasional lobate and vermicular inclusions of quartz within K-feldspar form runic or graphic intergrowth textures (fig. 12 – f). Accessory minerals include abundant zircon and apatite, as well as minor rutile, monazite and opaque minerals, e.g. pyrite. Ti-Oxide and minor allanite were found as accessory mineral phases within sample s3B, the latter, as a euhedral inclusion in plagioclase with antiperthite patches.

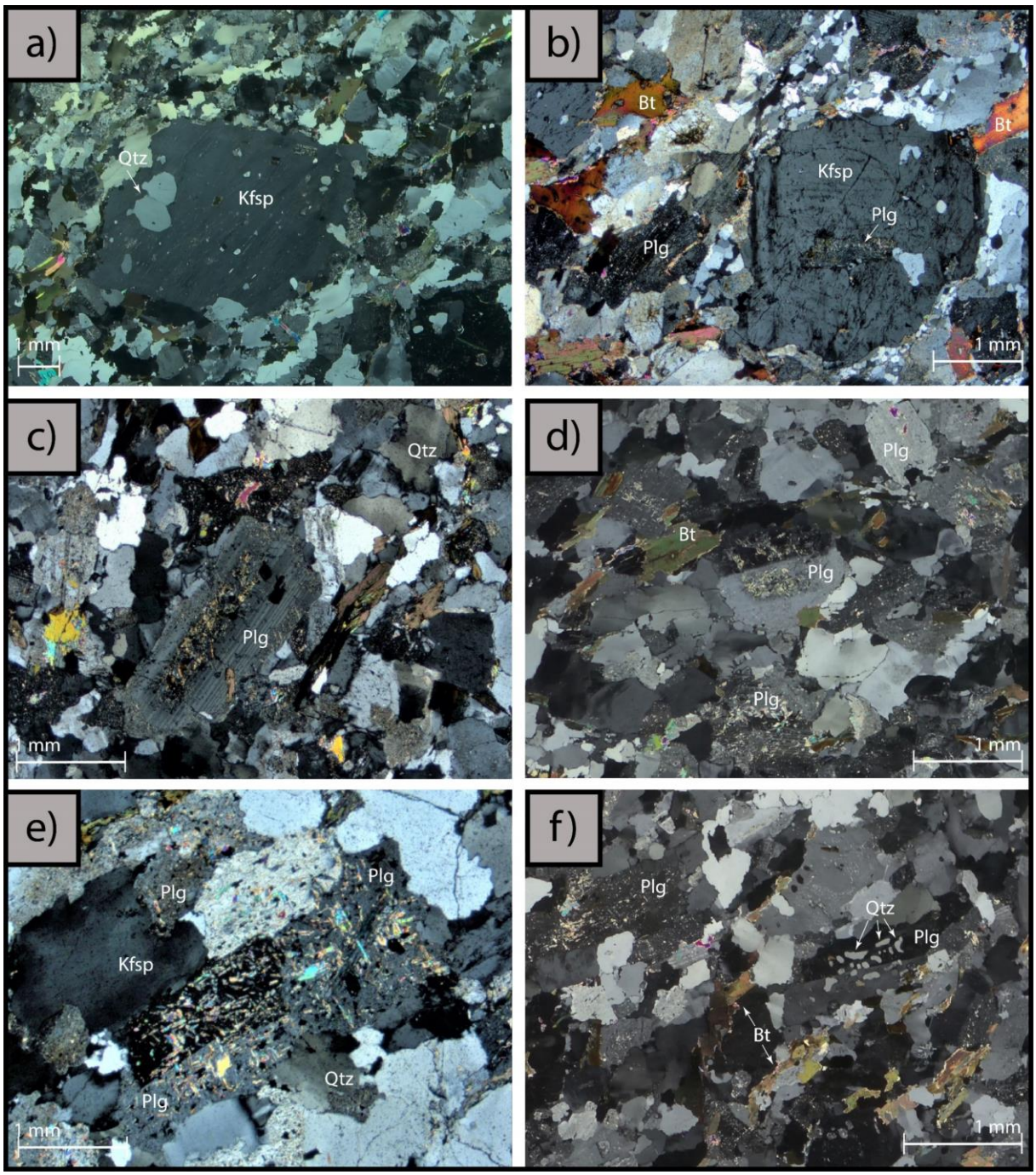

Figure 12 – Images of textural characteristic in unmingled granite samples s1F, s2B, s3B and s7B; a) Pokilitic K-feldspar containing quartz, plagioclase, biotite and apatite inclusions; b) Antirapakivi texture – lath shaped plagioclase mantle by K-feldspar; c) Concentric zoning patterns of core and alternating rims in plagioclase, compositional differences are highlighted by alteration; d) Alteration textures in different plagioclase grains; e) Plagioclase with sericitization and replacement textures; f) Runic intergrowth of quartz in plagioclase; All images were obtained using light microscopy

4.2.2 GROUP (2) – MACROSCOPICALLY UNMINGLED AND UNMIXED DIORITES

Selected dioritic samples in absence of evident macroscopic mingling or mixing textures are categorized in group (2). The fine to medium-grained rocks, with hypidiomorphic to allotriomorphic textures, are mainly composed of plagioclase (30 – 40 Vol.-%), hornblende (35 – 45 Vol.-%), biotite (25 – 30 Vol.-%), lesser quartz (10 – 15 Vol.-%) and minor titanite (5-10 Vol.-%), as well as apatite, zircon, pyrite and minor allanite as accessory minerals (all with < 5 Vol.-%). Microporphyritic textures within the rocks are defined by polycrystalline aggregates of light green hornblende, ranging up to ca. 3 mm in length, set in

a fine-grained groundmass with an average grain size of < 1 mm (fig. 13 – a). Finer hornblende grains within the groundmass frequently show signs of resorption along grain boundaries. Most polycrystalline clots have overall rounded to elongated shapes, with a seemingly random orientation of crystals that show lamellar or patchy exsolution patterns (fig. 13 – b+c). Some clots with well-defined shapes have an apparent gradation of hornblende grains within, where subhedral crystals are enclosed by finer, irregular shaped grains (fig. 13 – b). The hornblende clots may contain subhedral to euhedral, embedded or embayed, crystals of biotite, showing replacement textures. Pokilitic intergrowth of titanite is predominantly found along grain margins or in close relation with biotite-absent hornblende clots (fig. 13 – c+d). The -hornblende-titanite textures are associated with anhedral plagioclase and minor quartz, whereas biotite is characteristically absent in direct vicinity to these domains (fig. 13 – d). The absence of biotite is generally locally restricted to the titanite-centred, ocellar-like textures. The described titanite-ocellar structures are distributed sporadically. The dioritic samples show allotriomorphic to elongated plagioclase crystals within the groundmass and dispersed lathes, that can range up to 1.5 mm in length. The larger plagioclase grains are characterized by weakly defined concentric zoning or patchy dissolution and alteration patterns. Compositional, concentric zoning is emphasized by domain restricted alteration and corrosion patterns of inner core domains, creating sieve-like textures (fig. 13 – e+f). Surrounding rims and smaller plagioclase grains within the groundmass frequently contain abundant embayments and inclusions of groundmass minerals, occasionally defining pokilitic to sub-dendritic textures. Quartz in the dioritic samples occurs as an anhedral crystal phase, interstitial along grain boundaries and microstructures. Occasionally, quartz embayments show lobate intergrowth textures with nearly optical continuity (fig. 13 – b+c+f).

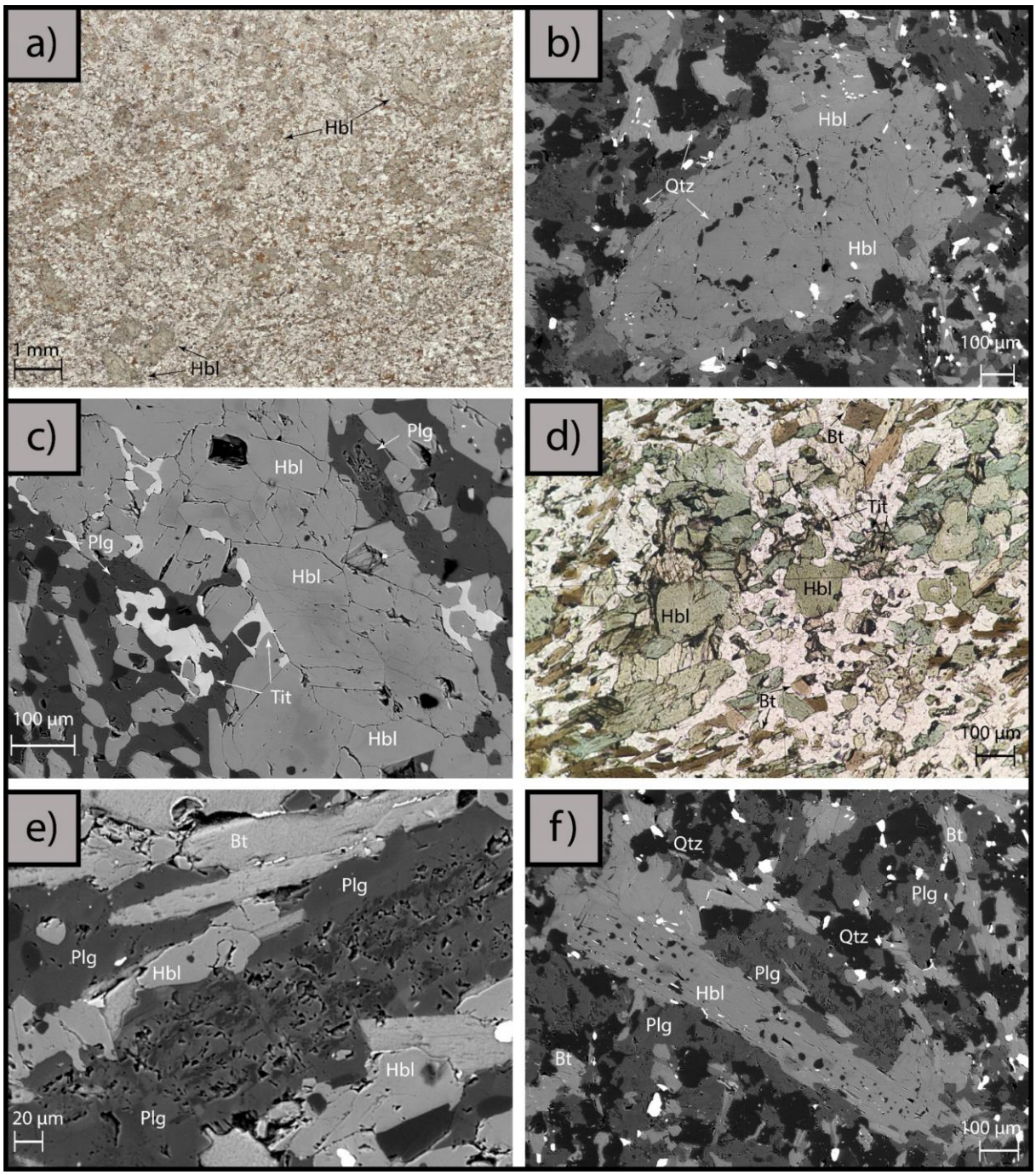

Figure 13 – Images of textural characteristic in unmingled diorite samples s1A and s7A; a) Hornblende cluster defining microporphyritic textures in diorite (image obtained by light microscopy); b) Hornblende cluster with concentric inclusions of quartz (BSE image obtained with SE microscopy); c) Pokilitic intergrowth texture of titanite (light) with hornblende cluster with compositional patterns (light grey), chemical zoning in enclosed plagioclase grain in top right corner (BSE image obtained with SE microscopy); d) Hornblende-titanite cluster which is absent in biotite, biotite (brown) is evident in the surrounding matrix (image obtained by light microscopy); e) Chemical variation in plagioclase grain (BSE image obtained with SE microscopy); f) Plagioclase nearly enclosed by hornblende (BSE image obtained with SE microscopy)

4.2.3 GROUP (3) – MACROSCOPICALLY MINGLED AND POTENTIALLY MIXED SAMPLES

Samples with evident macroscopic features, indicative for mingling and possible mixing processes, are categorized in group (3). The samples were obtained within the direct contact of contrasting rocks or within the associated hybridic domains. The petrographic analyses of contact samples reveal contrasting textures of the juxtaposed felsic and mafic domains (fig. 14 – a-c). The medium-grained, felsic sample domains are characterized by hypidiomorphic to allotriomorphic, generally

inequigranular textures. The main constituent minerals are plagioclase (25-45 Vol.-%), quartz (30-45 Vol.-%) and biotite (5-20 Vol.-%), whereas K-feldspar (0-40 Vol.-%) is highly variable. The contrasting fine-grained, mafic sections show varying equigranular to microporphyritc, biotite-dominated textures. The mafic domains are comprised of biotite (30-65 Vol.-%) and abundant plagioclase (20-50 Vol. %), with occasional minor hornblende (5-15 Vol.-%) and/ or quartz (5-20 Vol.%).

Sharp to wispy contacts of the contrasting domains are clearly delineated in samples s1D and s8D, originating from the NW and SE ends of the section, respectively (fig. 14 – a-c). Minor quartz forms an interstitial and anhedral phase within the otherwise biotite and plagioclase dominated mafic domains. Minor hornblende occurs within certain distance from the contact margin to the felsic domain, forming weakly-defined clots with biotite replacement textures. With increasing proximity towards the contact, the clots become solely biotite bearing and hornblende is absent. Biotite grains with locally restricted preferred orientations, show flow alignments with subordinate orientated lathes of plagioclase. This is especially well-developed in sample s8D, where a mafic wisp seemingly intrudes the felsic domain (fig. 14 – b). Chloritization of biotite is generally absent within the mafic domains whereas biotite crystals, within the intruding wisp of sample s8D, have increasing degrees of chloritization with the depth. The chloritization of biotite is comparable with weak to moderately chloritized biotite found in the felsic domain. Subhedral accessory titanite within the mafic sample domain occurs along grain boundaries, enclosed within biotite or in pokilitic intergrowth with biotite and minor quartz. Allotriomorphic plagioclase within the mafic sample domains is characterized by concentric zoning patterns, showing signs of domain restricted alteration and patchy cellular dissolution textures, emphasizing the inner domains, which are overgrown by irregular rims (fig. 14 – c). Domain restricted alteration of inner cores increases in intensity towards the contact zones of the juxtaposed felsic domains.

Contrastingly, the majority of plagioclase grains within the felsic sample section and in proximity to the contact are generally lacking concentric zoning patterns and appear rather featureless (fig. 14 – a+c). The featureless grains show characteristic albite twinning and signs of sericitization, located along grain boundaries and microcracks. A second plagioclase type appears within a small distance to the contact and is characterized by concentric zoning patterns, either showing multiple concentric zones or patchy dissolution textures within inner core domains (fig. 14 – d+e). With increasing distance to the contact, a minority of larger plagioclase grains show domain restricted alteration, emphasizing the inner domains (fig. 14 – f). The surrounding, unaltered and irregular rims frequently enclose grains of fine K-feldspar or quartz. K-feldspar is absent in direct proximity to the contact margin of the contrasting sections but within the felsic domain, K-fsp grains increase in size and abundance with increasing distance to the contact. K-feldspar first appears as an anhedral and interstitial phase containing perthite lamellae or as patches enclosed in featureless plagioclase grains, occasionally zonally arranged. Grain boundaries between plagioclase and K-feldspar grains are generally intergrown, showing nearly dendritic features. With increasing distance to the contact, subhedral K-feldspar grains are characterized by weak to well-developed tartan twinning, frequently containing inclusions of anhedral to lath shaped plagioclases, forming antirapakivi textures (fig. 14 – f). Occasional lobes of myrmikite intergrowth textures of quartz and plagioclase seemingly intrude into K-feldspar crystals. With the absence of K-feldspar in direct proximity to the contact margin, plagioclase and quartz predominate, occasionally with lobate or vermicular intergrowth textures. The contact with the biotite-rich mafic domain is characterized by a continuous interlocking of crystals. Apatite and zircon are frequent inclusions in plagioclase and quartz of both domains, with locally restricted trails of apatite close to the contact. Accessory allanite found within felsic samples is generally euhedral in shape and occasionally found as inclusions within K-feldspar or plagioclase (fig. 14 – b). Conversely, allanite within the mafic domain, appears as subhedral crystals and close to the contact, in poikilitic intergrowth with biotite.

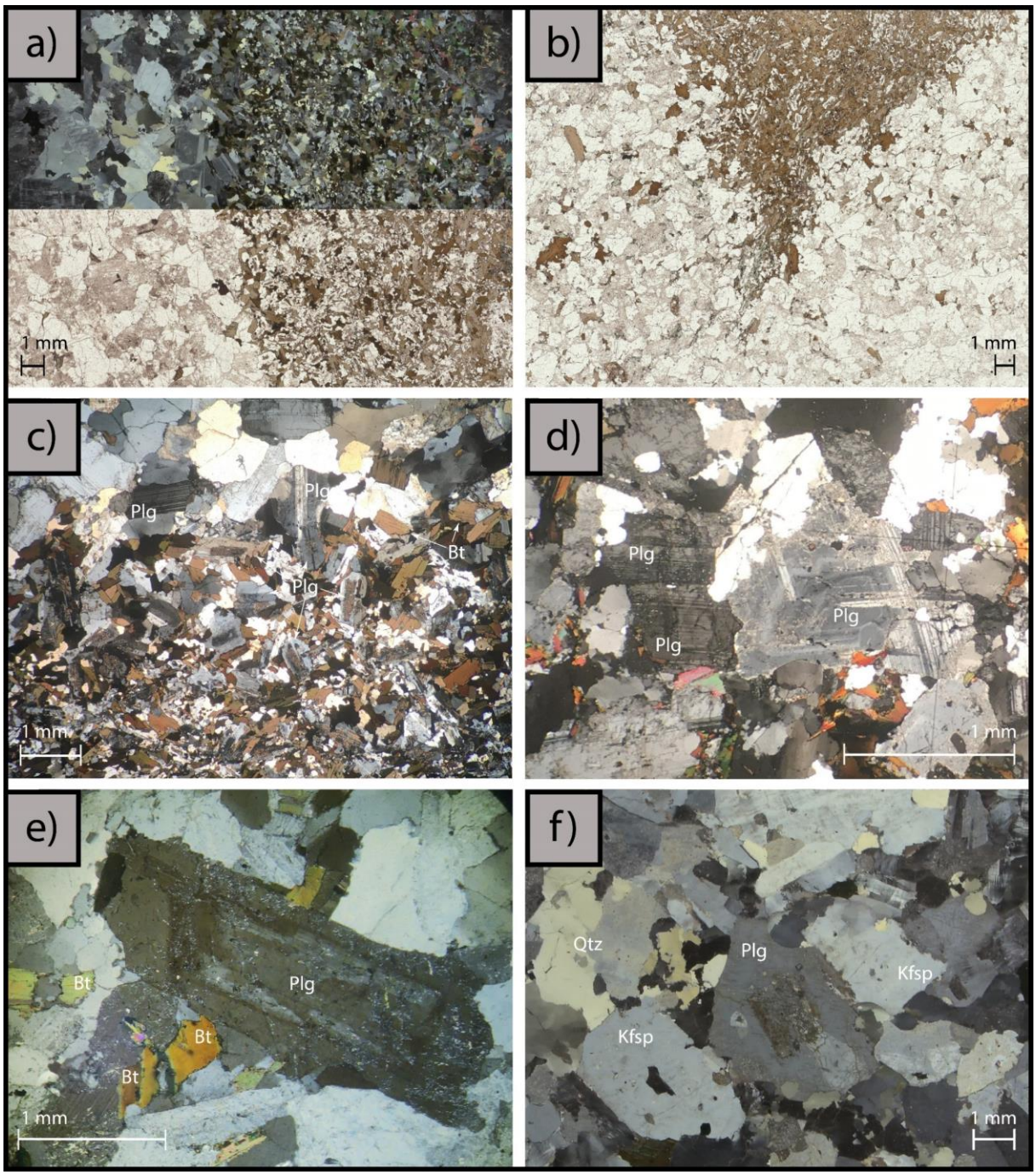

Figure 14 – Images of textural characteristic in mingled samples s1D and s8D; a) sharply delineated contact between felsic (left) and mafic (right) domain; b) Biotite-dominated mafic wisp (top) within felsic domain; c) Plagioclase textures along a sharply delineated contact with interlocking crystals of mafic and felsic domains; d) Concentric zoning patterns in plagioclase of the felsic domain; e) Concentric and patchy dissolution patterns within plagioclase of the felsic domain; f) Domain restricted alteration in plagioclase (centre) and antirapakivi texture in K-fsp (bottom left) of the felsic domain; All images were obtained by light microscopy

The contact margin of the contrasting felsic and mafic domains in sample s5B is characterized by a gradational transition zone, which is evident on a hand sample scale (fig. 15 – a). The transition from the medium-grained felsic section to the fine-grained mafic domain is characterized by a decrease in the abundance of quartz and overall average grain size, accompanied by an increase in the abundance of biotite. Hornblende grains appear within distance to the felsic domain, forming inclusions in plagioclase rims or showing signs of biotite replacement textures (fig. 15 – b). K-feldspar is absent throughout the gradational contact zone. The felsic domain is thus dominated by plagioclase and quartz with minor biotite and accessory pyrite. Anhedral pyrite occurs as dispersed accessory grains in close relation with biotite and as a pyrite band which intrudes the transition zone. Subhedral to anhedral plagioclase occurring throughout the contact domain show concentric and patchy zoning patterns or appear rather featureless (fig. 15 – b+c). Signs of alteration are variable, ranging from minor sericitization along microstructures to replacement textures, predominantly found within inner domains. Alteration of plagioclase grains

increases towards the more mafic domain where epidote replacement textures are associated with patches of K-feldspar. Plagioclase alteration as well as biotite chloritization are enhanced in close proximity to the pyrite band. Accessory titanite occurs in close relation to the pyrite dominated band and dispersed throughout the gradual contact domain, generally in pokilitic relation with plagioclase and quartz (fig. 15 – d).

The petrographic analyses of two samples (s1G and s1H), obtained from intrusive felsic veins with frayed and wispy contact relationships to the dioritic host rocks, show comparable mineral textures as the other mingled samples of group (3). The felsic domains of both samples are overall similar and predominated by plagioclase, K-feldspar, quartz and biotite, differing from the plagioclase and biotite dominated mafic domains, which contain variable hornblende. A fine-grained, intrusive mafic wisp in sample s1H, constitutes of moderately aligned biotite and allotriomorphic plagioclase (fig. 15 – e). Plagioclase grains within appear featureless and homogenic in composition, lacking compositional zoning patterns. Weak signs of sericitization are restricted to grain boundaries and microcracks. The developed alignment of biotite forms a preferred orientation, parallel along the felsic contact, with deeper intruding wisps maintaining the same alignment (fig. 15 – e). The interlocking of crystals along the contact is locally restricted and gradual changes in the mineral assemblage or average grain size within the contact domain is generally absent. Thus, contrastingly to the contact domains described above, K-feldspar within the felsic section of sample s1G and s1H is present in direct contact to the mafic domains. K-feldspar forms subhedral to anhedral crystals, showing minor patchy zoning patterns and intergrowth textures along grain boundaries with plagioclase (fig. 15 – f). Grains are generally elongated to poikilitic in shape, containing abundant inclusions of groundmass minerals, whereby lobate inclusions of quartz are predominating, forming runic intergrowth textures. Furthermore, the mantling of K-feldspar grains around plagioclase forming antirapakivi textures, is a frequent occurrence throughout the felsic domain (fig. 16. – a). Myrmikite intergrowth textures of plagioclase and quartz occur in close relation to K-feldspar grains.

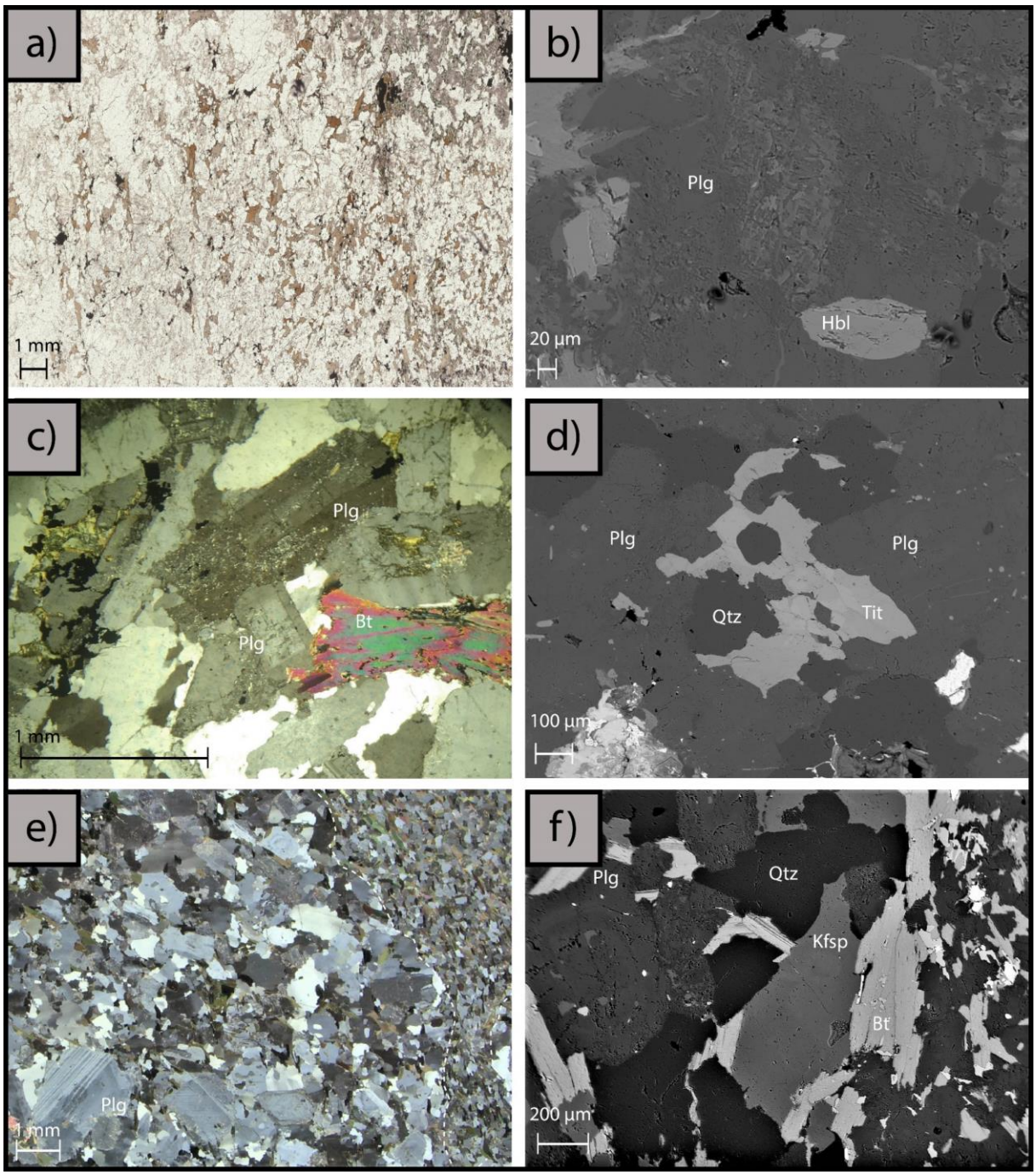

Figure 15 – Images of textural characteristic in mingled samples s1H and s5B; All images on the left were obtained by light microscopy, all images on the right were obtained using a SEM; a) gradual contact between felsic domain (left) and mafic domain (towards the right); b) plagioclase with strongly altered, rounded inner domain, elliptic hornblende (light grey; bottom right) grain enclosed within the rim of the plagioclase; c) Plagioclase textures within the gradual contact zone; d) Pokilitic titanite within the gradual contact zone; e) textural differences of a felsic domain and intruding mafic wisp; f) Concentric compositional zoning in plagioclase (left) and patchy compositional zoning in K-fsp (dark grey in centre)

Plagioclase grains in the felsic sample sections of sample s1G and s1H show a variety of different concentric and patchy zoning patterns. Compositional variations form complex concentric zoning patterns, commonly with multiple rim domains (fig. 15 – f; fig. 16 – b+c). Compositional concentric zoning patterns define subangular to rounded cores that are surrounded by rims containing abundant inclusions or lobate intergrowth of quartz. Larger plagioclase grains occasionally show compositional spike patches and inclusions of apatite in the outer rim domains (fig. 16 – b). Patchy dissolution and domain restricted corrosion and sericitization textures are weak to moderately defined, emphasizing microcracks and core domains, which frequently contain dispersed antiperthite patches. Dispersed synneusis textures of plagioclase grains include up to 4 distinguishable crystals, with grain boundaries generally in near optical continuity (fig. 16 – c). Preferred orientations of biotite with weak signs of chloritization are locally restricted and dispersed clots contain anhedral titanite mantling around

Fe-Oxide within the centre. Accessory titanite, with less than 5 Vol.-%, forms anhedral crystals in both domains of the samples. Titanite is generally dispersed, frequently in poikilitic relation with or nearly mantling around plagioclase grains in direct proximity of the contact domain (fig. 16 – d). Other accessory minerals include ilmenite, zircon and anhedral allanite, the latter showing disturbed inner oscillatory zoning and epidote overgrowth. Apatite, with mixed morphologies of stubby and prismatic crystals, occurs as inclusions within and along grain boundaries of plagioclase and biotite.

The mafic domains within sample s1G, show fine-grained schlieren or bands of contact-parallel aligned biotite juxtaposed to the contrasting felsic, coarser-grained section (fig. 16 – e). Phenocrysts of plagioclase and quartz, with local biotite-rich boarders as well as clots of hornblende, define a microporphyritic texture within the mafic domains. The plagioclase phenocrysts are generally characterized by concentric zoning patterns, as seen within the adjacent felsic domain. Sample s1B represents a distinctly lighter-coloured section of a mafic outcrop, characterized by colour and grain size variation towards a juxtaposed granitoid. The texture is predominated by biotite and plagioclase over quartz and K-feldspar. Plagioclase occurs as finer grained, groundmass forming minerals and as larger crystals, ranging up to 2 mm in length, forming a microporphyritic texture accompanied by schlieren of biotite (fig. 16 – f). The plagioclase grains are characterized by similar complex zoning patterns as described for the felsic domains of sample s1H and s1G (fig. 17 – a+b). Contrastingly, K-feldspar and quartz are less abundant in sample s1B and form interstitial and anhedral crystal phases. K-feldspar frequently shows signs of compositional zoning along rims or in patches throughout the grain, as well as fine inclusions of plagioclase, forming antirapakivi textures (fig. 17 – c). Bladed and flaky shapes of biotite show resorption textures along grain margins and allanite grains form a subhedral, accessory phase with epidote overgrowth.

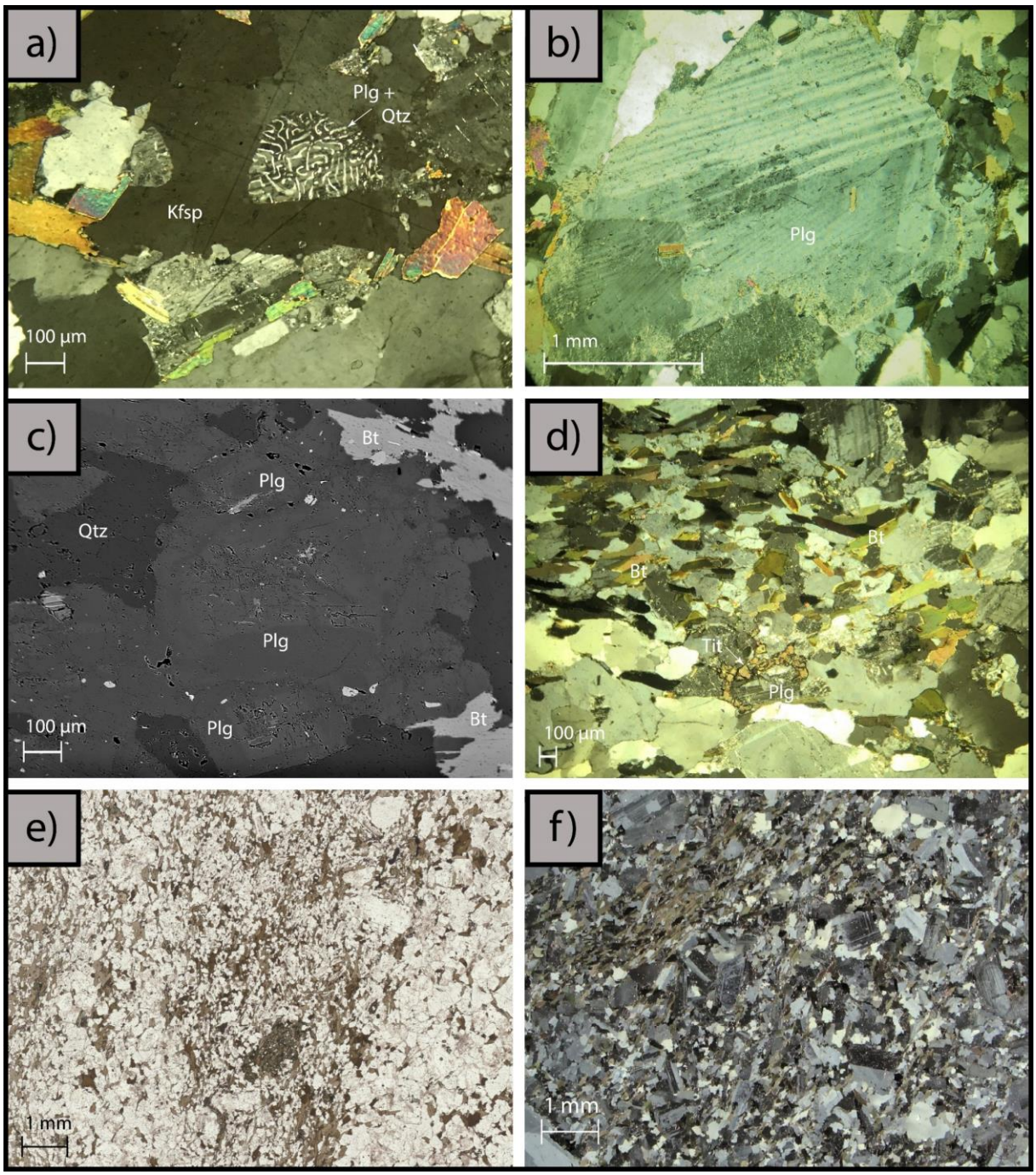

Figure 16 – Images of textural characteristic in mingled samples s1B, s1G and s1H; a) Myrmikite textures within plagioclase, enclosed within K-fsp creating antirapakivi texture (image obtained by light microscopy); b) Concentric compositional zoning in plagioclase (image obtained by light microscopy); c) Compositional zoning patterns in plagioclases (image obtained using a SEM); d) Plagioclase nearly mantled by titanite at wispy contact of mafic and felsic domain (image obtained by light microscopy); e) Alternating mafic schlieren in granitic vein, schlieren containing cluster of hornblende (image obtained by light microscopy); f) Biotite-dominated discontinuous schlieren and porphyroblastic plagioclase (image obtained by light microscopy)

Sample s5A was obtained from the mingled diorite with intruding felsic veins and porphritic feldspar, as described in the field relations (fig. 11 – f). The fine-grained groundmass is K-feldspar absent and composed of plagioclase, hornblende, biotite and minor quartz, with dispersed larger plagioclase grains defining a porphyritic texture (fig. 17 – d+e). The large plagioclase grains appear poikiloblastic, containing abundant dispersed or zonally arranged lobate to subangular inclusions of hornblende and quartz (fig. 17 – e+f). Zonally arranged inclusions of apatite and minor poikilitic intergrown titanite emphasize the compositional concentric zoning textures. Patchy dissolution textures within the core domain are enclosed by rims of differing composition (fig. 17 – e+f). Fine grained quartz occurs in close relation along the grain boundaries of large plagioclase. Accessory titanite forms anhedral crystals, frequently in poikilitic relation within hornblende, plagioclase and quartz

dominated clusters, which are absent in biotite. Accessory phases furthermore include zircon, allanite, pyrite and apatite, the latter showing mixed morphologies of prismatic and stubby crystals throughout the section.

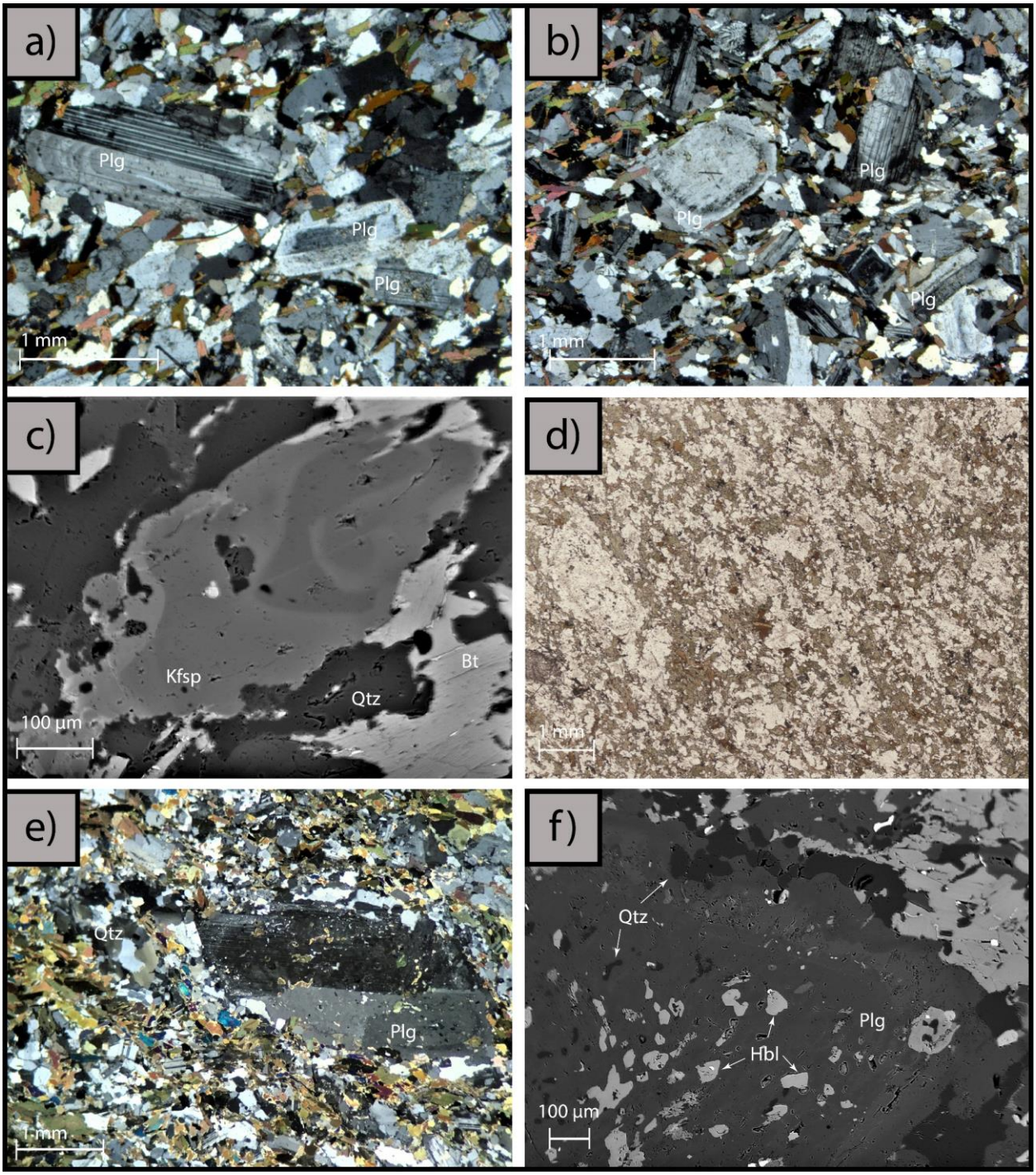

Figure 17 – Images of textural characteristic in mingled samples s1B and s5A; a) Alternating plagioclase zoning and alteration textures (image obtained by light microscopy); b) Alternating plagioclase zoning and alteration textures (image obtained by light microscopy); c) Anhedral K-feldspar showing compositional zoning patterns (image obtained using a SEM); d) Porphyroblastic plagioclase set in a fine-grained groundmass (image obtained by light microscopy); e) Poikioblastic plagioclase containing abundant, zonally arranged inclusions and fine-grained quartz cluster (image obtained by light microscopy); f) inner textures of poikioblastic plagioclase (image obtained using a SEM)

4.2.4 GROUP (4) – LEUCOSOME

The obtained garnet-bearing leucosome samples are characterized by inequigranular, porphyritic textures and categorized in group (4). Subhedral to anhedral garnet porphyroblasts, which range up to ca. 2 cm in diameter, are set in a fine to medium-grained groundmass, comprised of plagioclase, quartz, cordierite, biotite, K-feldspar and muscovite (fig. 18). The generally inclusion free garnet porphyroblasts show cracks filled with coarse biotite grains and are surrounded by variably sized alteration coronas (fig. 18 – a). The coronas comprise of fine-grained phyllosilicates, associated with coarse-grained biotite, minor quartz, feldspar and muscovite (fig. 18 – b). The coarse-grained flakes and lathes of biotite are characterized by strong chloritization features (fig. 18 – b+c). As white mica forms the predominant phase within the fine intergrowth texture, the corona textures may be characterized as a pseudomorphic alteration product, described as pinite. The corona texture is suggestive for a replacement of garnet under higher temperatures by a stable mineral phase, here probably cordierite. The replacement of cordierite by fine-grained alteration products is evident throughout grains within the groundmass (fig. 18 – d). The coarse-grained pseudomorphed grains are largely to fully replaced by the fine-grained intergrowth of phyllosilicates, whereby unaltered remnants of cordierite are generally absent. Quartz with undulose extinction and weakly defined subgrain formation, occurs as an anhedral to interstitial crystal phase (fig. 18 – d). Plagioclase and K-feldspar are highly altered and occur in frequent intergrowth with quartz, muscovite and biotite.

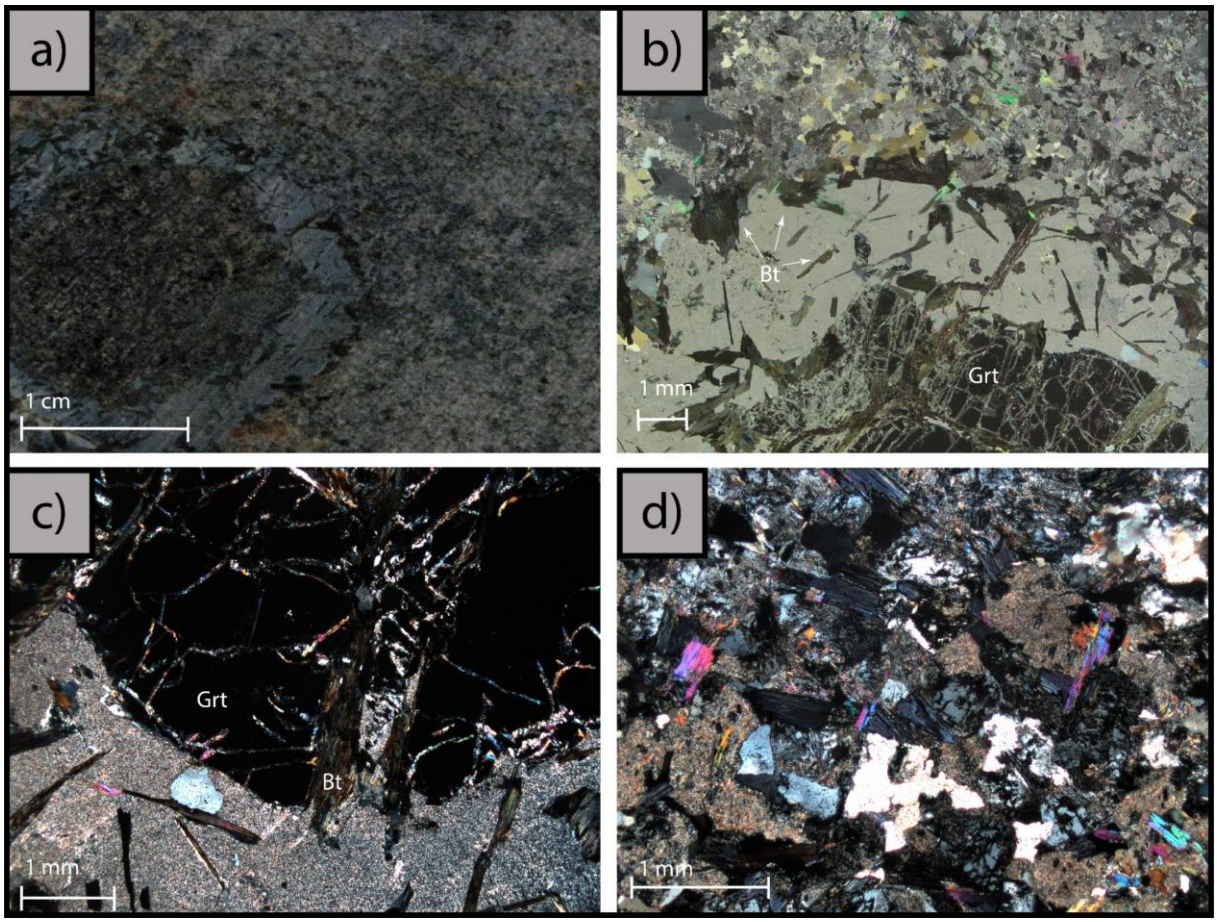

Figure 18 – Images of textural characteristic in leucosome sample s4D; a) Garnet porphyroblasts with corona texture in medium to coarse-grained groundmass; b) Corona texture around garnet porphyroblasts (image obtained by light microscopy); c) Textural relation of garnet and minerals associated with the surrounding corona (image obtained by light microscopy); d) mineral textures of minerals comprising the groundmass (image obtained by light microscopy)

4.3 MAJOR ELEMENT CHEMISTRY

A total of seventy-four samples was analysed for major and trace element compositions, forty-four of the samples are of igneous origin and thirty samples are derived from sedimentary and migmatization processes. Samples with evident contacts between contrasting rocks, were separated and analysed individually. The lighter coloured, felsic domains are hereafter indicated by an "a" (s1Da, s5Ba and s8Da) and the darker-coloured, mafic domains indicated by a "b" (s1Db, s5Bb and s8Db). The full set of analyses can be found in appendix I.

Based on their major elemental geochemistry, the forty-four igneous samples were classified on a Total Alkali-Silica (TAS) diagram (fig. 19 – a). The samples are characterized by mafic to felsic compositions, ranging in SiO_2 contents from 42.9 – 76.5 wt.-%, that classify within gabbroic, dioritic, granodioritic and granitic discrimination fields (fig. 19 – a). The colour code in fig. 19 was applied according to the respective TAS geochemical discriminating field, whereas the symbology follows the macroscopic and microscopic characterizations of the mingled and unmingled groups. Unmingled granitic and dioritic samples of the Inzie Head section are shown as filled triangles and squares, respectively. Samples with evidence for possible mixing and mingling are represented by diamond shapes. Samples obtained from the surrounding Buchan Block area, are represented by unfilled shapes, following the same colour symbology code. The granitic samples obtained from the Fraserburgh area are distinguished by purple colours. The samples delineate a positive trend, whereby the majority of samples fall beneath the alkaline-subalkaline dividing line. The majority of samples follows the characteristic calc-alkaline trend with a minority of outliers falling within the field of the tholeiite series on an AFM diagram (after Irvine and Baragar, 1971). To reflect the amount of Al in relation to the feldspar phases, the samples were plotted on an A/CNK (Al/Ca+Na+K) versus A/NK (Al/Na+K) diagram (after Shand, 1943). Excess Al implicates the need for Al-excess minerals (e.g. Al-silicates, cordierite, garnet, muscovite or biotite) to crystallize, whereas a deficiency in Al implies the crystallization of Al-deficient minerals (e.g. amphibole or pyroxene). Furthermore, the A/CNK versus A/NK diagram visualizes the balance of Ca to Na+K, roughly reflecting the proportions of plagioclase and K-feldspar. The granitic rocks are characterized by peraluminous A/CNK ratios between ca. 1.05 – 1.2, whereby a minority of samples delineate a negative trend with the granodioritic samples that are characterized by A/CNK ratios between ca. 1 – 1.1 (fig. 19 – c). The negative trend is further extended by the mafic samples of metaluminous composition.

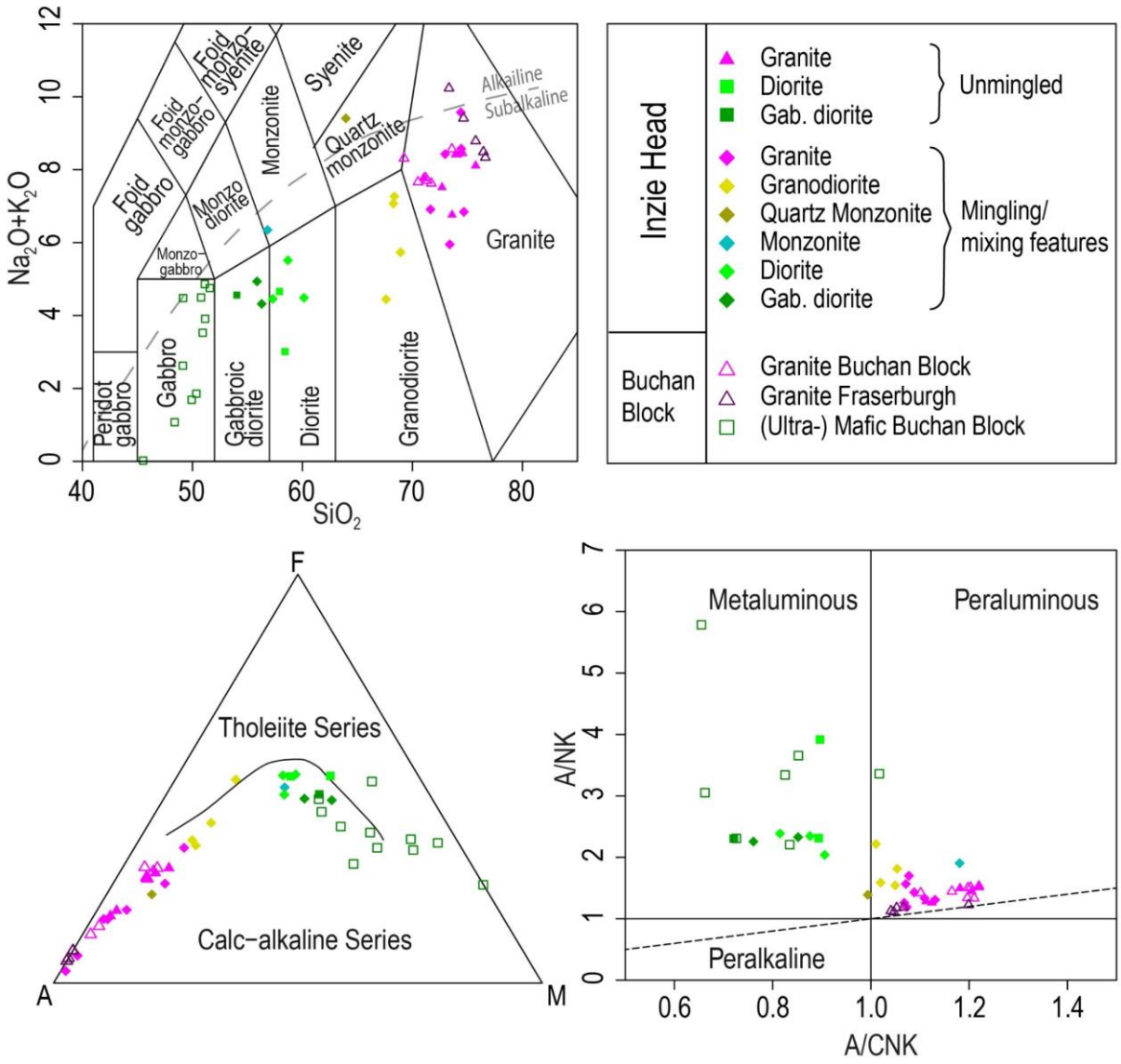

Figure 19 – Whole-rock major elemental discrimination diagrams of the studied igneous rocks: a) TAS-diagram after Middlemost (1994) *grey dashed line represents alkaline/ subalkaline discrimination trend; b) AFM-diagram after* Irvine and Baragar (1971)*; c) A/NK vs. A/CNK diagram after* Shand (1943)

Major element compositions of the full sample set (n = 74) are plotted on binary silica versus oxide (Haker) diagrams (fig. 20). Three different correlation coefficients (R^2) are presented: R^2_{IH} = igneous rocks from Inzie Head, R^2_{IH+} = igneous samples combined with metapelites and migmatites from Inzie Head and R^2_{ALL} = full sample set of rocks from Inzie Head, Fraserburgh and the wider Buchan Block area. Whole-rock major element compositions of the different igneous rocks from Inzie Head are generally well correlated in CaO, FeO_t, MgO, MnO and TiO_2, delineating negative trends with R^2_{IH} values between 0.82 – 0.93 (fig. 20). Conversely, fairly poor correlations are evident for Al_2O_3, K_2O and Na_2O contents (R^2_{IH} = 0.11 – 0.44). The correlation slightly increases for Al_2O_3 and Na_2O (R^2_{IH+} = 0.5 and 0.19) when considering the metapelitic migmatites (fig. 20), whereas the correlation of K_2O decreases drastically (R^2_{IH+} = 0.07). A decrease in correlation is furthermore evident for whole rock compositions in CaO, FeO_t, MgO, MnO and TiO_2 (R^2_{IH+} = 0.24 – 0.87). Considering all samples, obtained from Inzie Head and from the Buchan Block area, further decreases the correlation in Al_2O_3, FeO_t, MgO, MnO, Na_2O and TiO_2 (R^2_{ALL} = 0.12 – 0.59), but causes a slight increase in CaO and K_2O (R^2_{ALL} = 0.4 and 0.18).

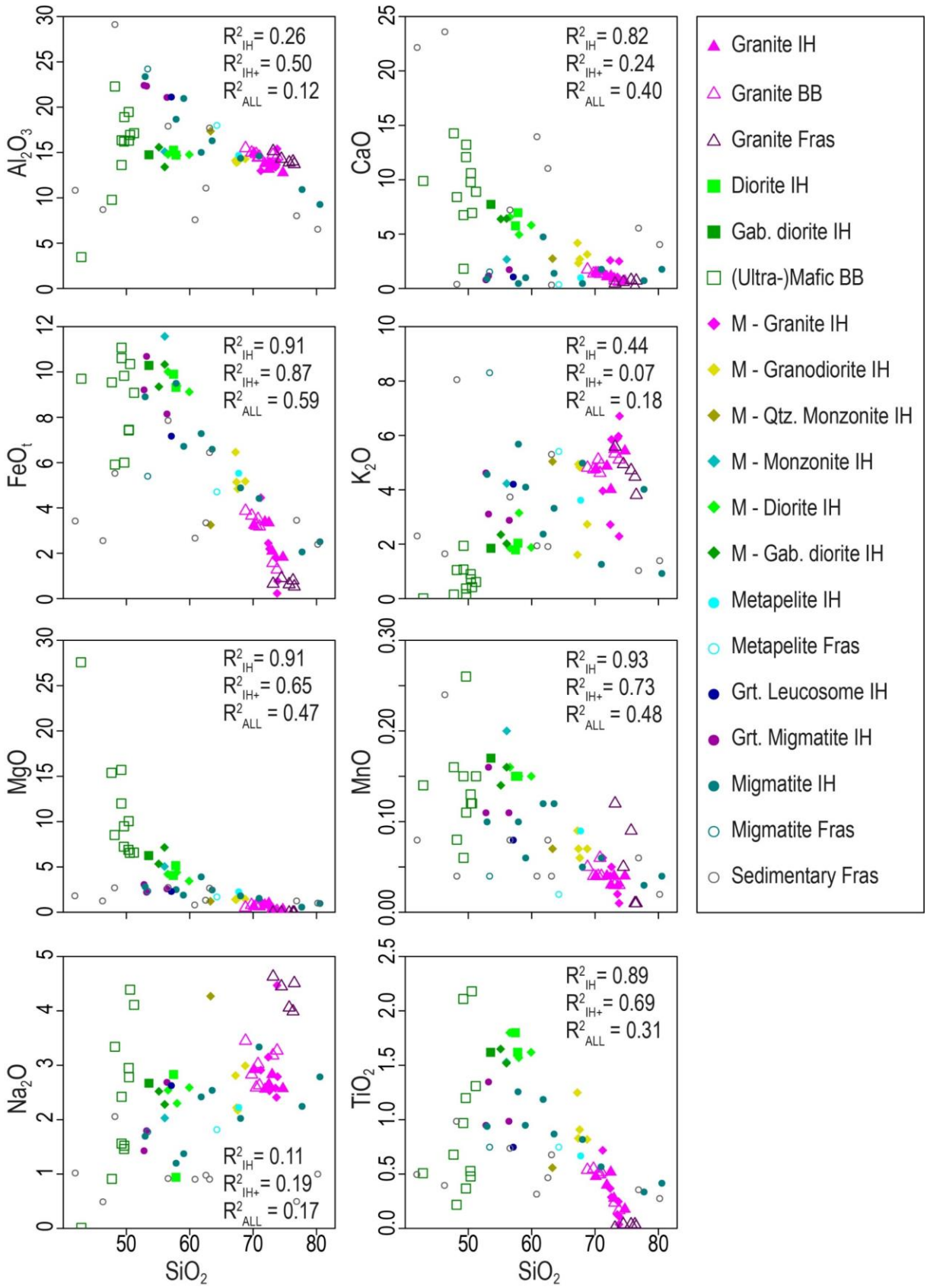

Figure 20 – Haker-diagrams of whole-rock major element compositions versus silica content; M= Samples with mingling/ mixing features, IH = samples obtained from the Inzie Head coastal section, BB = samples obtained from the wider Buchan Block area, Fras = samples obtained around Fraserburgh

4.3.1 UNMINGLED SAMPLES

Felsic samples of Inzie Head, without prevailing mixing and mingling features, fall exclusively in the granite field of the TAS-diagram (SiO_2 = 70.1 – 74.7 wt.-%; Na_2O+K_2O = 6.66 – 8.31 wt.-%). With Al_2O_3 and CaO contents between 12.8 – 13.8 wt.-% and 0.69 – 1.57 wt.-%, respectively, plot the samples within the lower end of the peraluminous field (fig. 19 – c). Most major elements of the granite samples are weakly to well, negative correlated with respect to SiO_2. An exception form K_2O and Na_2O, where the concentrations show an overall increase with decreasing silica content (fig. 20). The unmingled rocks from Inzie Head with more mafic compositions, plot within the diorite and gabbroic diorite fields of the TAS diagram (fig. 19 – a; SiO_2 = 53.6 – 57.8 wt.-%; Na_2O+K_2O = 2.98 – 4.62 wt.-%). Higher Al_2O_3 (14.7 – 15.3 wt.-%) and CaO (5.76 – 7.73 wt.-%) contents, move these samples into the metaluminous field (fig. 19 – c). A relatively strong depletion in Na_2O of sample s7A (0.94 wt.-%), shifts this sample higher in the metaluminous field (fig. 19 – c and fig. 20). As expected for mafic rocks, FeO_t (9.32 – 10.3 wt.-%), MgO (4.09 – 6.28 wt.-%), MnO (0.15 – 0.17 wt.-%) and TiO_2 (1.62 – 1.80 wt.-%) contents are relatively elevated, compared to the granitic rocks (fig. 20).

4.3.2 MINGLED AND POTENTIALLY MIXED SAMPLES

Of the twenty-one samples from Inzie Head with mingling and/ or potential mixing features, seven samples plot within the granite TAS-field (SiO_2 = 71.2 – 73.9 wt.-%; Na_2O+K_2O = 5.87 – 9.50 wt.-%). Two samples (s1Da and s8Da), that were separated from the contrasting mafic domains, fall within the granite classification. Most major element concentrations are comparable but with a higher variability than the given range in compositions of the unmingled granitic rocks (fig. 20). Samples s8Da and s045 show a relative enrichment in CaO content (2.50 – 2.58 wt.-%) and lower K_2O concentrations (2.29 – 2.72 wt.-%). Four samples, with possible mixing and/ or mingling features plot in the granodiorite field of the TAS-diagram (SiO_2 = 67.2 – 68.8 wt.-%; Na_2O+K_2O = 4.42 – 7.16 wt.-%). The granodiorites all fall within the lower peraluminous field, with overall similar Al_2O_3 content (13.9 – 14.3 wt.-%) to the granitic rocks, whereas relatively higher CaO contents (2.33 – 4.18 wt.-%) shift the samples closer towards the metaluminous field (fig. 19 – c). The felsic sample s5Ba, that was separated from the more mafic domain, is comparatively enriched in TiO_2 (1.25 wt.-%) and depleted in K_2O (1.61 wt.-%) (fig. 20).

Two of the mafic samples that were separated (s5Bb and s8Db) plot with three other samples in the diorite and gabbroic diorite fields of the TAS-diagram (SiO_2 = 55.1 – 59.9 wt.-%; Na_2O+K_2O = 4.30 – 5.45 wt.-%). All five samples fall into the metaluminous field, with Na_2O (2.28 – 2.59 wt.-%) and K_2O (1.86 – 2.35 wt.-%) contents, whereby sample s8Db is with an elevated K_2O content of 3.15 wt.-% relatively enriched to the other dioritic rocks (fig. 20). CaO (4.95 – 6.57 wt.-%), FeO_t (9.12 – 10.3 wt.-%), MgO (3.48 – 7.18 wt.-%), MnO (0.14 – 0.16 wt.-%) and TiO_2 (1.52 – 1.80 wt.-%) concentrations are elevated, relative to the granitic and granodioritic samples (fig. 20). Two samples, s047 and s1Db, plot unlike any other igneous sample within the quartz monzonite and monzonite fields of the TAS-diagram, respectively (fig. 19 – a). Relatively high Al_2O_3 (17.4 wt.-%), CaO (2.74 wt.-%), Na_2O (4.27 wt.-%) contents and comparatively lower silica (SiO_2 = 63.3 wt.-%) of sample s045, discriminates the sample from the granitic rocks and shifts the sample into the metaluminous field. Although MgO (5.08 wt.-%), TiO_2 (1.53 wt.-%) and silica (56.1 wt.-%) contents of the monzonite sample s1Db are comparable to the diorite samples, the sample is discriminated by the other major element concentrations. The comparatively high K_2O (4.23 wt.-%) with low CaO (2.67 wt.-%) and Na_2O (2.03 wt.-%) concentrations, shift the sample into the peraluminous field and closer to the granitic samples. The FeO_t (11.6 wt.-%) and MnO (0.20 wt.-%) compositions are higher than observed for any other of the igneous rocks from Inzie Head (fig. 20).

4.3.3 (META-)SEDIMENTARY AND MIGMATITE SAMPLES

The silica content of the metapelitic migmatite samples is highly variable, ranging from 53.0 – 80.8 wt.-%. The wide range in FeO_t (2.06 – 10.7 wt.-%), Al_2O_3 (9.27 – 23.4 wt.-%), Na_2O (1.20- 3.34 wt.-%), K_2O (0.93 – 5.68 wt.-%) and MnO (0.03 – 0.16 wt.-%) overlaps with the observed concentrations of the igneous samples (fig. 20). The obtained CaO contents (0.47 – 1.79 wt.-%) are relatively uniform and within range of the granites, whereas TiO_2 (0.34 – 1.35 wt.-%) and MgO (0.63 – 3.96 wt.-%) contents fall in between the given concentrations of the dioritic and granitic samples (fig. 20). The sedimentary

and migmatitic rocks from the Fraserburgh area are similar in the given spread of MgO (0.88 – 2.81 wt.-%) and TiO_2 (0.28 – 0.99 wt.-%) contents, falling between most diorite and granite samples, yet showing a much wider range in Al_2O_3 (6.54 – 29.1 wt.-%), CaO (0.32 – 23.6 wt.-%), MnO (0.02 – 0.24 wt.-%) and SiO_2 (42.1 – 80.4 wt.-%) relative to the metapelitic migmatites from Inzie Head.

4.3.4 IGNEOUS SAMPLES OF THE SURROUNDING BUCHAN BLOCK

Five of the igneous samples from the Fraserburgh area, fall within the upper end of the granite field in the TAS-diagram (SiO_2 = 73.2 – 76.5 wt.-%; Na_2O+K_2O = 8.32 – 10.2 wt.-%). The granitic rocks from Fraserburgh are relatively high in Na_2O contents (3.99 – 4.63 wt.-%), but generally lower in CaO (0.15 – 0.78 wt.-%), FeO_t (0.53 – 0.90 wt.-%) and TiO_2 (0.01 – 0.04 wt.-%), relative to the granitoid rocks from Inzie Head. The felsic igneous rocks of the wider Buchan Block area document similar major element geochemistry, as granitoid samples from Inzie Head (SiO_2 = 68.8 – 73.8 wt.-%; Na_2O+K_2O = 7.55 – 8.51 wt.-%). The felsic rocks of this study are mostly defining negative trends in silica versus oxide plots, whereas the mafic rocks from the wider Buchan Block area show weakly defined but contrasting positive trends (fig. 20). The mafic to ultramafic samples from the wider Buchan Block area, all plot in the gabbroic field of the TAS-diagram (SiO_2 = 47.7 – 51.2 wt.-%; Na_2O+K_2O = 1.06 – 4.81 wt.-%). The mafic rocks are low in K_2O (0.01 – 1.94 wt.-%) and generally higher in CaO (6.74 – 14.3 wt.-%) and MgO (6.58 – 15.7 wt.-%), relative to the other igneous rocks of this study. Al_2O_3 (9.78 – 22.3 wt.-%), MnO (0.06 – 0.26 wt.-%), Na_2O (0.91 – 4.39 wt.-%) and TiO_2 (0.22 – 2.18 wt.-%) contents are highly variably (fig. 20). A single sample (s045) is in comparison discriminated by very low Al_2O_3 (3.46 wt.-%), K_2O (0.01 wt.-%), Na_2O (0.01 wt.-%) and SiO_2 (42.9 wt.-%) compositions, whereas MgO is highly elevated (27.6 wt.-%).

4.4 TRACE ELEMENT CHEMISTRY

All seventy-four samples were analysed for whole-rock trace element compositions. Measured trace element compositions versus the samples maficity ($MgO+FeO_t$) were plotted on binary plots and a selection of diagrams presented in fig. 21. Positive correlations are observed for transition metals, where Ni, Cr, V, Sc and Cu contents generally increase with increasing maficity (Fig. 21). The positive trend is clearly delineated by the felsic and metasedimentary migmatite samples, whereas samples of more mafic compositions are characterized by higher variation in their respective concentration. Mafic to ultramafic rocks of the Buchan Block area, form strong outliers and do not follow the overall positive trend. Plotted concentrations of high-field strength elements (HFSE) and large-ion lithophile elements (LILE) show much more complex inter-relationships (fig. 21). Trace element plots of Rb, Zn, Sr and Th, seemingly show two distinct trends, a positive trend mainly defined by migmatites and/ or granitoids, and a weakly defined negative trend delineated by the more mafic rocks of Inzie Head and mafic to ultramafic rocks of the greater Buchan Block area. Plots of LREE (La+Ce+Pr+Nd+Sm+Eu+Gd) and HREE (Tb+Dy+Ho+Er+Tm+Yb+Lu+Y) against maficity also show the two distinct trends, whereas a cluster formation of the different rock types is evident in La_N/Yb_N versus maficity plot (fig. 21). Granitoid rocks with unmingled and mingled features plot in a tight cluster, showing within defined negative trends. Sedimentary and migmatitic samples form a wider cluster, also showing a weakly defined negative trend, from higher ratios in the sedimentary rocks from Fraserburgh to generally lower ratios in the metapelitic migmatites. More mafic unmingled and mingled rocks of Inzie Head form a tight cluster, without any distinct trends as the obtained ratios are quite similar. The mafic to ultramafic rocks of the wider Buchan Block area plot with slightly higher ratios than the mafic rocks from Inzie Head yet also lack any defined trend (fig. 21).

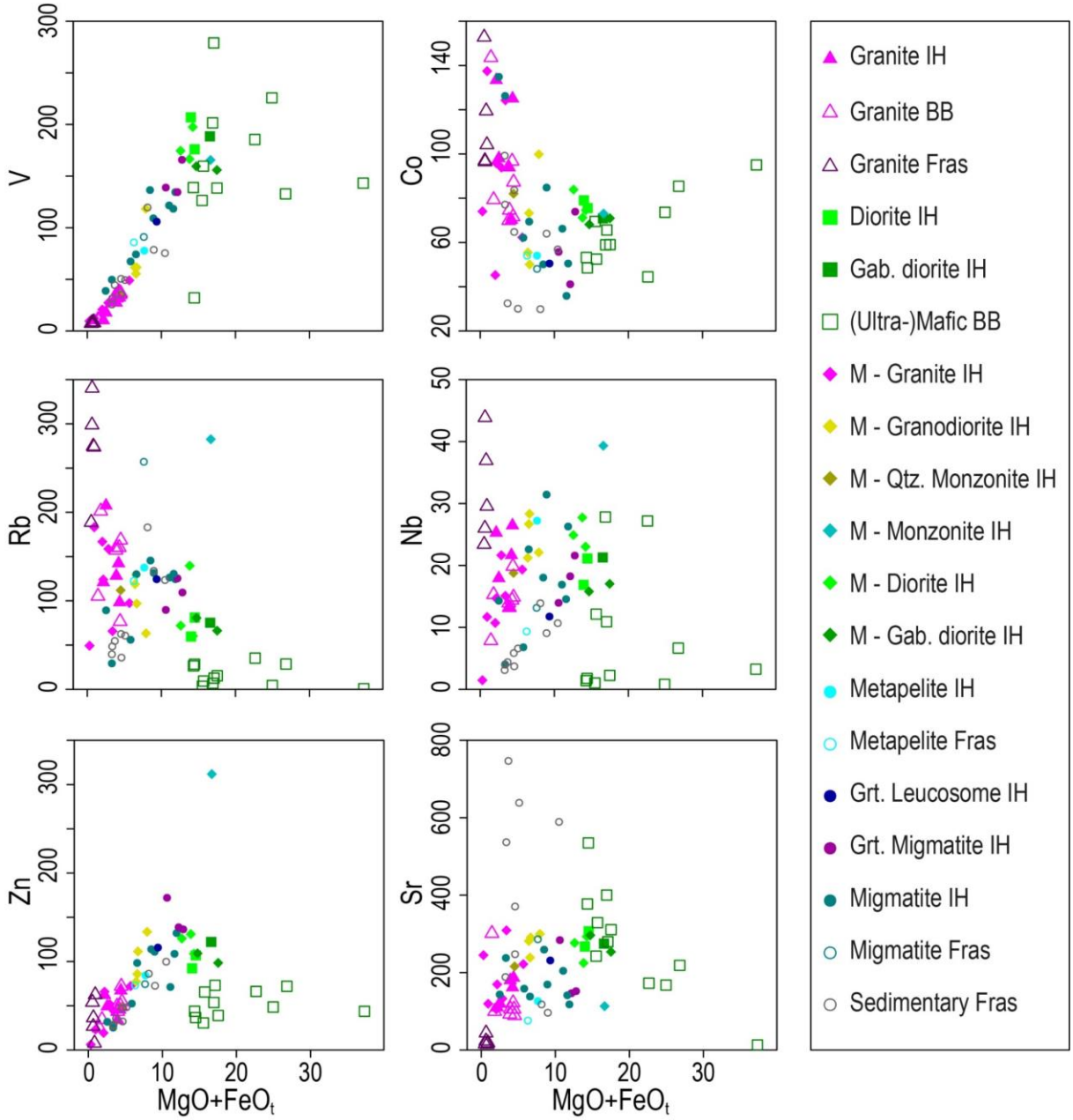

Figure 21 – Binary diagrams of whole-rock trace element concentrations versus maficity (MgO+FeOt); M= Samples with mingling/ mixing features, IH = samples obtained from the Inzie Head coastal section, BB = samples obtained from the wider Buchan Block area, Fras = samples obtained around Fraserburgh

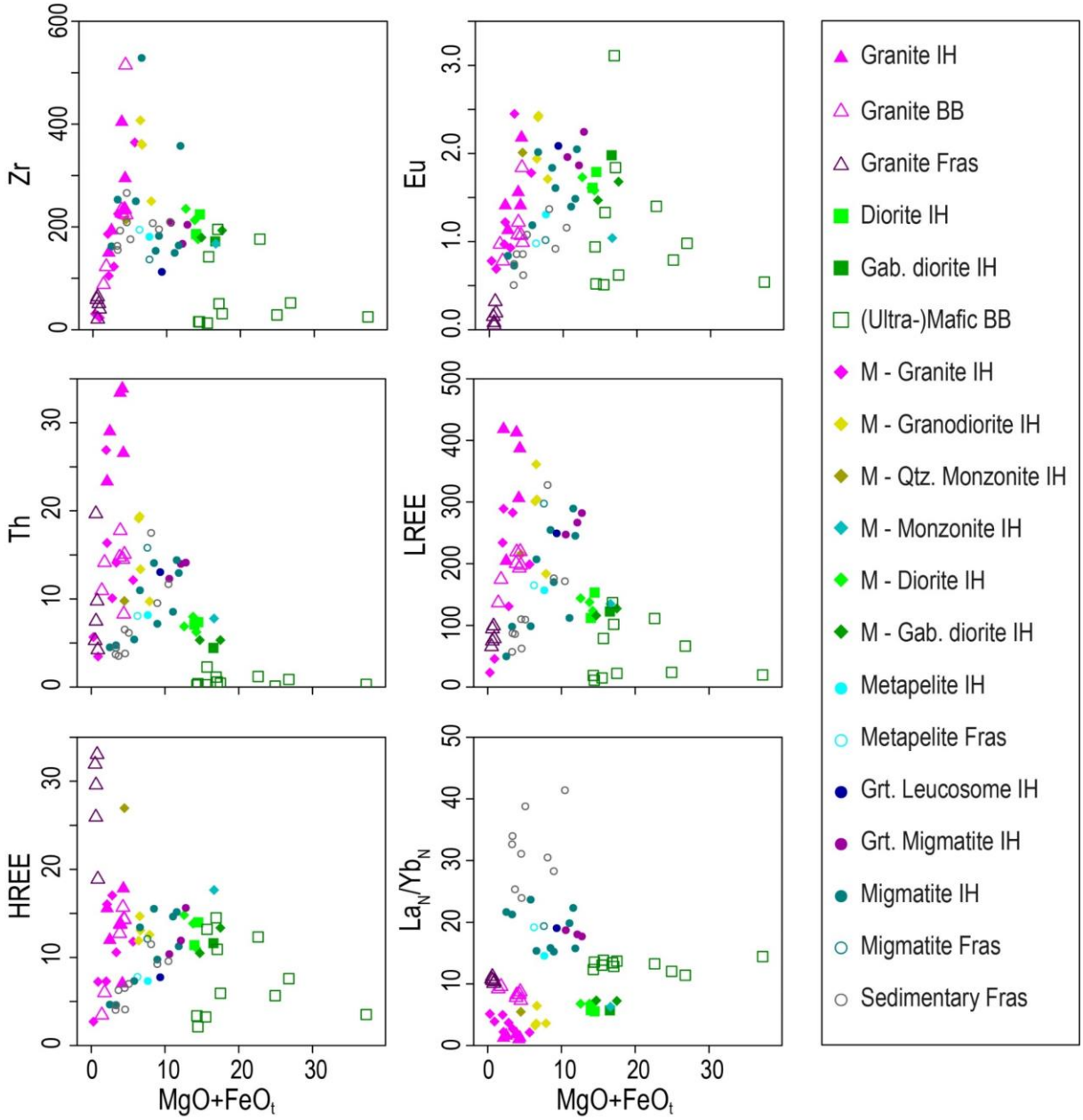

Figure 21 – continued

4.4.1 UNMINGLED SAMPLES

Chondrite-normalized rare earth element (REE) diagrams of the granitic unmingled rocks of Inzie Head show varying concentrations (ΣREE = 216.5 – 433.8) with relatively uniform patterns (fig. 22 – a). Enriched LREE over HREE delineate relatively steep patterns (La_N/Yb_N = 13.5 – 41.4) with markedly negative Eu anomalies (Eu/Eu* = 0.28 – 0.59). N-MORB-normalized patterns of the unmingled granitic rocks from the Inzie Head section show a characteristic zigzag pattern and enrichment in most LILE, relative to expected values of rocks from the upper continental crust (UCC), of which an averaged reference line was added to the plot (fig. 23, after Taylor and McLennan, 1995). However, the unmingled granitic rocks from Inzie Head are relatively enriched in less compatible LREE and some HFSE, such as La, Ce, Nd, Sm and Th, relative to the reference values (fig. 23 – a). N-MORB-normalized values of Sr, P and Ti of the granitic rocks, are below expected values for rocks of the UCC or rocks of the lower continental crust (LCC; after Taylor and McLennan, 1995). The unmingled gabbroic diorite and diorite samples of Inzie Head are characterized by relatively constant chondrite-normalized REE concentrations (ΣREE = 123.3 – 167.2; fig. 22 – a). HREE concentrations of the more mafic rocks are generally comparable

to unmingled granitic rocks, whereas relatively lower LREE contents define flatter patterns (La_N/Yb_N = 6.44 – 8.23). Negative Eu anomalies are weakly defined in the two diorite samples (Eu/Eu* = 0.82 – 0.87), whereas the Eu anomaly is slightly positive (Eu/Eu* = 1.05) in the gabbroic diorite sample. Compared to the unmingled granitic rocks and the UCC line, N-MORB-normalized patterns for the unmingled mafic rocks of the Inzie Head section show a slight depletion in most LILE, except in Sr, and less compatible REE (fig. 23 – a). A strong depletion in Ti and enrichment in Th, as seen in the granitic rocks, is absent in the mafic samples. The chondrite and N-MORB-normalized trace element fields, delineated by the unmingled felsic and mafic samples of Inzie Head, are shown for further comparison in in fig. 22, fig. 23, fig. 24 and fig. 25.

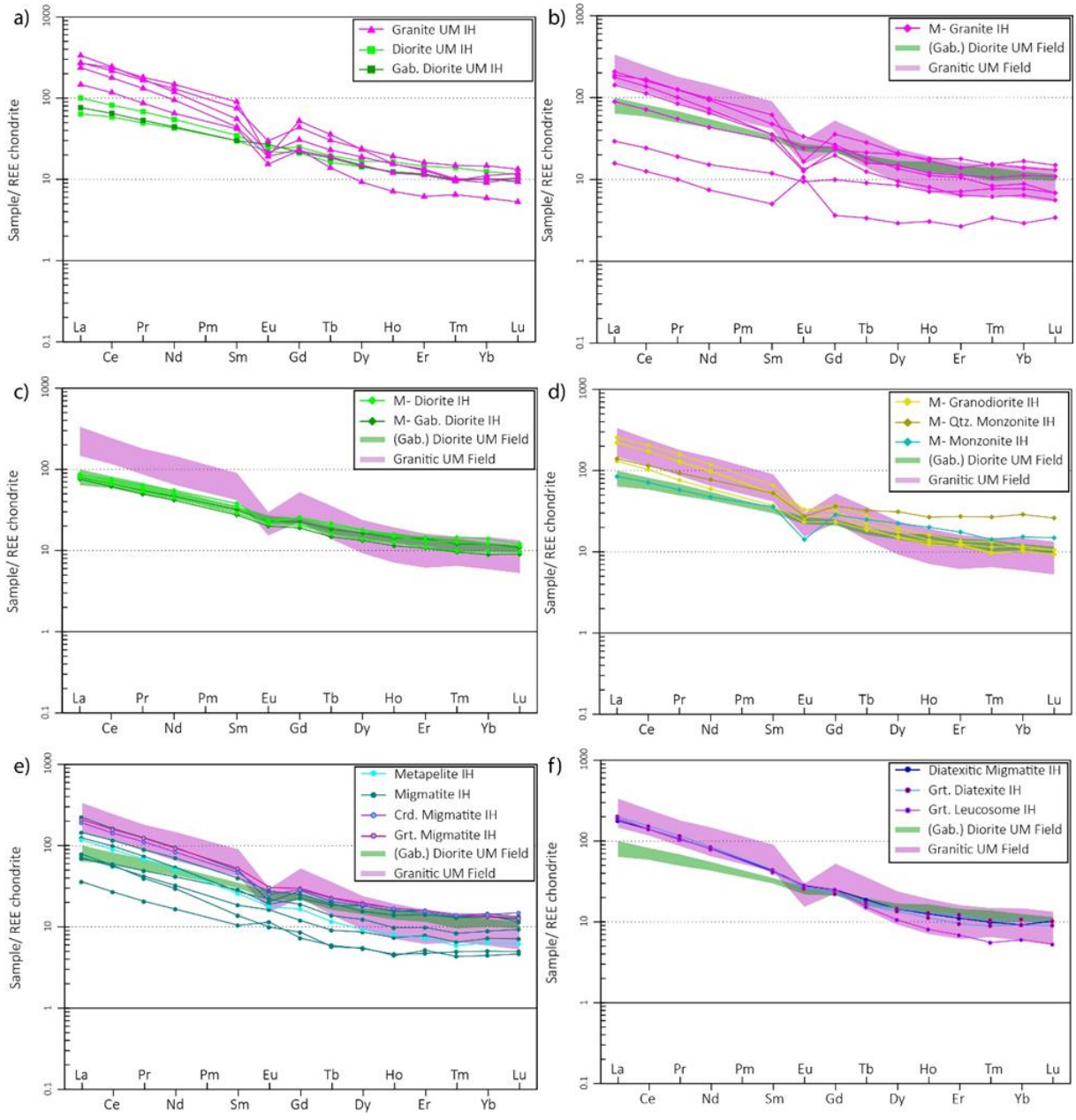

Figure 22 – Chondrite-normalized REE patterns of rocks from the Inzie Head section; a) REE patterns of unmingled rocks; b) REE patterns of mingled granites; c) REE patterns of mingled diorites; d) REE patterns of mingled granodiorites and (quartz-) monzonite; e) REE patterns of metapelite and migmatites; f) REE patterns of diatexitic and leucosome samples; REE Chondrite normalization data used after Anders and Grevesse, 1989

4.4.2 MINGLED AND POTENTIALLY MIXED SAMPLES

Chondrite-normalized patterns of the granitic samples with evident mingling features, are highly variable in their total REE concentration and overall steepness of the patterns (ΣREE = 26.1 – 305.2; La_N/Yb_N = 3.90 – 28.3; fig. 22 – b). Three samples (s1Da, s036, s041) follow the overall pattern delineated by the unmingled granites, with clearly defined negative Eu anomalies (Eu/Eu* = 0.35 – 0.50). However, the relatively lower chondrite normalized LREE contents in sample s036 are similar to the observed concentrations of the more mafic rocks of Inzie Head (fig. 22 – b). Weakly defined negative Eu anomalies are evident in three samples (s1C, s038, s8Da; Eu/Eu* = 0.81 – 0.93). Samples s1C and s8Da fall within the granitic unmingled field in their total REE contents (ΣREE = 210.8 and 293.3), whereas sample s038 plots with comparatively much lower total REE concentration (ΣREE = 52.9). Sample s045, with the lowest total REE concentration (ΣREE = 26.1), shows a distinct positive Eu anomaly (Eu/Eu* = 2.47). N-MORB-normalized patterns of the granitic samples with mingling features, are highly variable (fig.23 – b). With the exception of one or two outliers, the concentrations of Nb, K, Pb, Sr, Eu and the HREE elements are fairly constant and relatively similar to the unmingled granitic rocks. However, N-MORB-normalized concentrations of the LILE and most HFSE are generally variable, with noticeable depletions in the mingled samples (fig. 23 – b). Chondrite-normalized patterns of mingled mafic rocks from Inzie Head generally plot within the same field as delineated by the unmingled mafic rocks (fig. 22 – c); La_N/Yb_N = 6.29 – 8.74; ΣREE = 126.5 – 158.8), with weakly-defined negative Eu anomalies (Eu/Eu* = 0.73 – 0.88). N-MORB-normalized patterns of the mingled diorites and gabbroic diorites of Inzie Head are similar to the unmingled mafic rocks (fig.23 – c). Two samples show strong enrichments in hydrous fluid mobile elements and plot above expected values for the UCC, a diorite enriched in Cs and a gabbroic diorite with a strong U enrichment (fig. 23 – c).

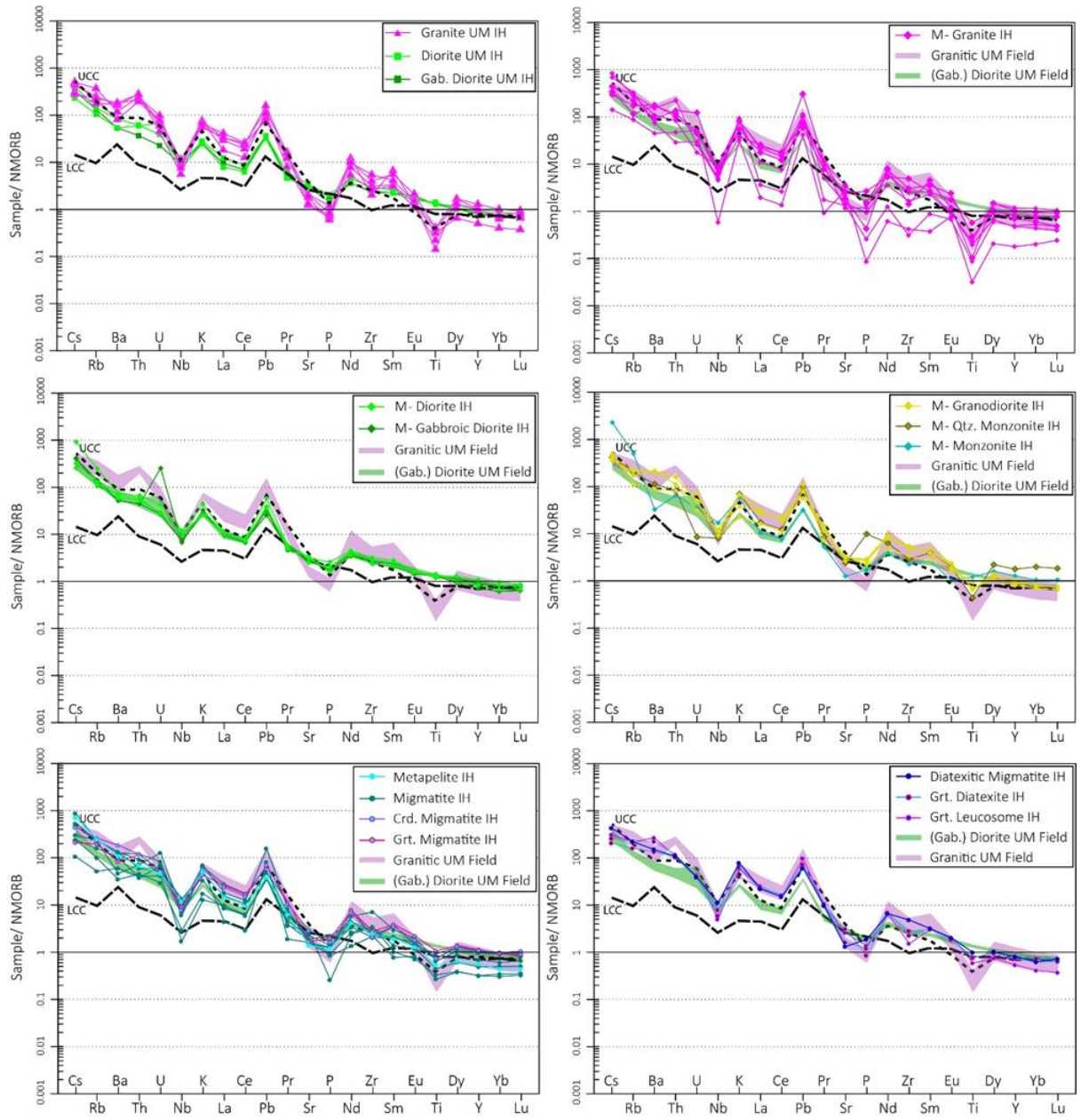

Figure 23 – N-MORB-normalized trace element patterns of rocks from the Inzie Head section; a) trace element patterns of unmingled rocks; b) trace element patterns of mingled granites; c) trace element patterns of mingled diorites; d) trace element patterns of mingled granodiorites and (quartz-) monzonite; e) trace element patterns of metapelite and migmatites; f) trace element patterns of diatexitic and leucosome samples; NMORB normalization data used after Sun and McDonough, 1989

Mingled granodioritic rocks are slightly variable in their LREE contents, but overall similar in their patterns, which generally fall within the delineated field of the unmingled granitic rocks (La_N/Yb_N = 11.4 – 23.7), showing well-defined negative Eu anomalies (Eu/Eu* = 0.65 – 0.80). Relative to other mingled samples, total REE concentrations are mostly higher (ΣREE = 313.1 – 375.9), except for sample s5Ba with ΣREE = 196.28. The granodioritic rocks are overall similar in N-MORB-normalized patterns (fig. 23 – d). Except for Cs and Sr, LILE contents are variable and plot between the unmingled granitic and dioritic samples. The mingled quartz-monzonite sample s047 shows similar chondrite-normalized LREE concentrations as the granitic unmingled samples but is relatively enriched in HREE (La_N/Yb_N = 4.98; fig. 22 – d). The sample shows a depletion in U, giving a low value that plots closely to an expected value for the LCC. However, P and most HREE (Dy, Y, Yb, Lu), are relatively enriched. With relatively lower LREE contents, the mingled monzonite sample (s1Db) plots closer to the mafic unmingled field (La_N/Yb_N = 5.70; ΣREE = 152.5) but with a clearly defined negative Eu anomaly (Eu/Eu* = 0.44). Compared to the unmingled diorite field, the monzonite is relatively enriched in Cs and Rb, but depleted in Ba, where the value lies closer to the average for the LCC.

4.4.3 (META-)SEDIMENTARY AND MIGMATITE SAMPLES

Metapelitic and migmatitic rocks from Inzie Head are characterized by highly variable chondrite-normalized REE patterns, generally enriched in LREE over HREE (La_N/Yb_N = 5.13 – 18.75; ΣREE = 103.1 – 305.0). One sample (s039) is particularly low in total REE concentration, ΣREE = 54.7 (fig. 22 – e). Most samples show weakly to well-defined negative Eu anomalies, whereas two samples (s039 and s041) are distinct through a positive anomaly (Eu/Eu* = 1.08 and 1.30). The diatexitic samples show distinctly steeper chondrite-normalized REE patterns than the migmatite samples (La_N/Yb_N = 19.2 – 21.3). The normalized pattern of the garnet-bearing leucosome sample (s4D) is similar in LREE content to the diatexites but relatively depleted in HREE (La_N/Yb_N = 32.7). N-MORB-normalized concentrations of the metapelite sample (s2A) of Inzie Head follow the given trend line of the UCC, whereas the migmatites are characterized by highly variable concentrations (fig 23 – e). Relative strong depletions of the REE, as well as Nb and P, are evident where samples plot below the LCC line. N-MORB-normalized patterns of the diatexites and garnet-bearing leucosome sample from Inzie Head, follow the UCC trend line (fig. 23 – f). Comparatively, Th enrichment and strong Ti depletion as is seen in granitic samples is absent. Furthermore, Ba is slightly enriched in the garnet-bearing Leucosome and a garnet-bearing diatexites sample. However, variable in their total REE content, unmolten sedimentary samples and the metapelitic migmatites of Fraserburgh are relatively similar in their overall chondrite-normalized patterns (fig.24 – d); ΣREE = 61.7 – 339.9; La_N/Yb_N = 9.60 – 25.4). Weakly to well-defined negative Eu anomalies are evident within all samples (Eu/Eu* = 0.46 – 0.98). The sedimentary and metapelite samples show similar patterns in N-MORB-normalized patterns (fig. 25 – d), with strong depletions in Nb and P.

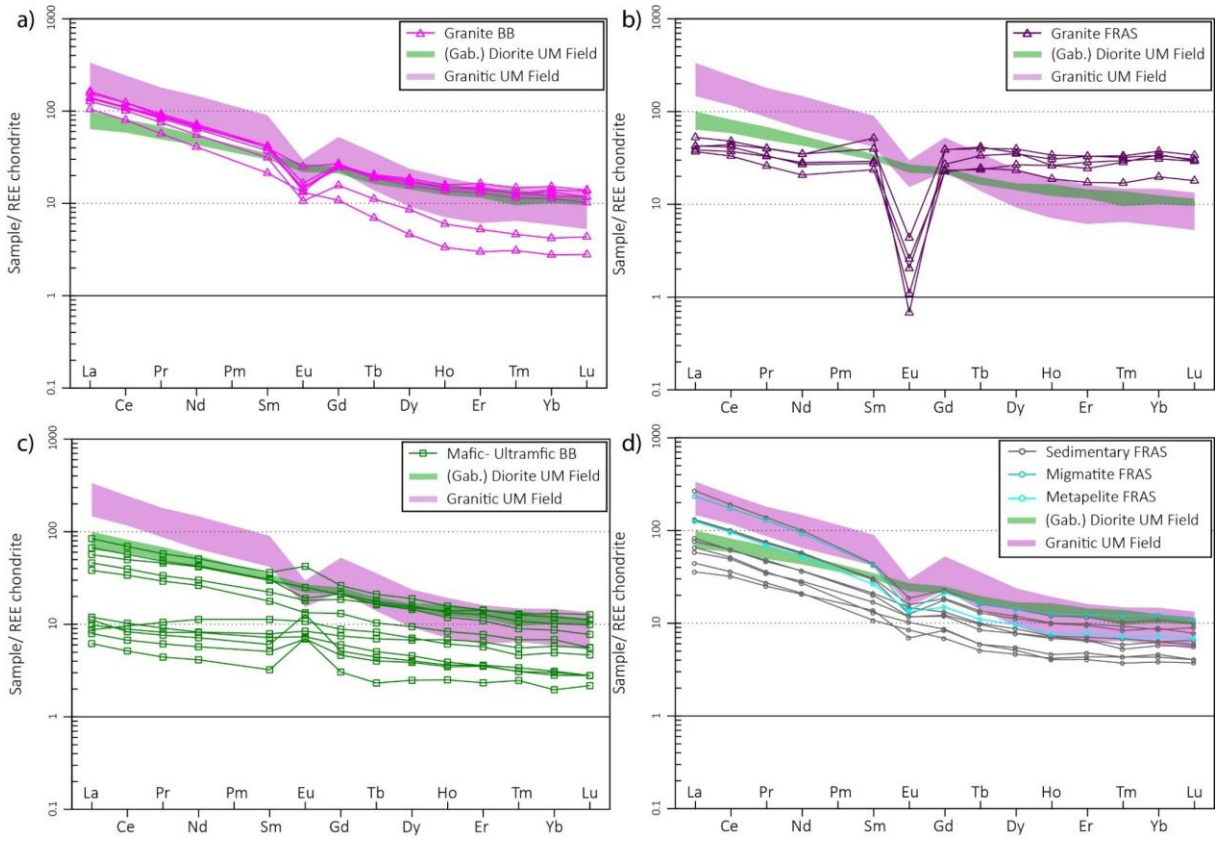

Figure 24 – Chondrite-normalized REE patterns of samples from Fraserburgh and the wider Buchan Block area; a) REE patterns of granitic rocks from the wider Buchan Block area; b) REE patterns of granitic rocks from Fraserburgh; c) REE patterns of (ultra-) mafic rocks from the wider Buchan Block; d) REE patterns of crustal host rocks from Fraserburgh; REE Chondrite normalization data used after Anders and Grevesse, 1989

4.4.4 IGNEOUS SAMPLES OF THE BUCHAN BLOCK

The granitic rocks obtained from around Fraserburgh are distinct in their chondrite-normalized pattern (fig. 24 – b). The relatively uniform patterns are generally flat, with strong Eu anomalies and lower total REE contents than most of the other granitic rocks (La_N/Yb_N = 1.02 – 2.22; Eu/Eu* = 0.02 – 0.11; ΣREE = 97.4 – 132.1). However, chondrite-normalized REE patterns of the granitic samples of the wider Buchan Block area are variable in their REE concentration and mostly similar to the granitic field of the Inzie Head unmingled granites (fig. 24 – a). LREE concentrations are generally in the lower end of the unmingled granitic field, whereas most HREE concentrations are on the upper end of the field (La_N/Yb_N = 9.21 – 13.25; ΣREE = 208.6 – 234.1). Two samples (s015 and s016) show steeper patterns and lower total REE concentrations (La_N/Yb_N = 31.1 – 38.8; ΣREE = 140.0 – 180.6). Negative Eu anomalies are weakly to well-defined (Eu/Eu* = 0.40 – 0.86). N-MORB-normalized patterns of the granitic samples of the Buchan Block area generally follow a similar trend as the unmingled granites from Inzie Head (fig.25 – a). Most HFSE and REE are relatively uniform, whereas most LILE, except K, are variably enriched. However, N-MORB-normalized patterns of the granitic rocks from Fraserburgh differ from the Inzie Head Granites (fig. 25 – b). Strong depletions in Ba, Sr, P, Zr, Eu and Ti form a strong zigzag pattern and a general enrichment in HREE shifts the patterns above the reference lines.

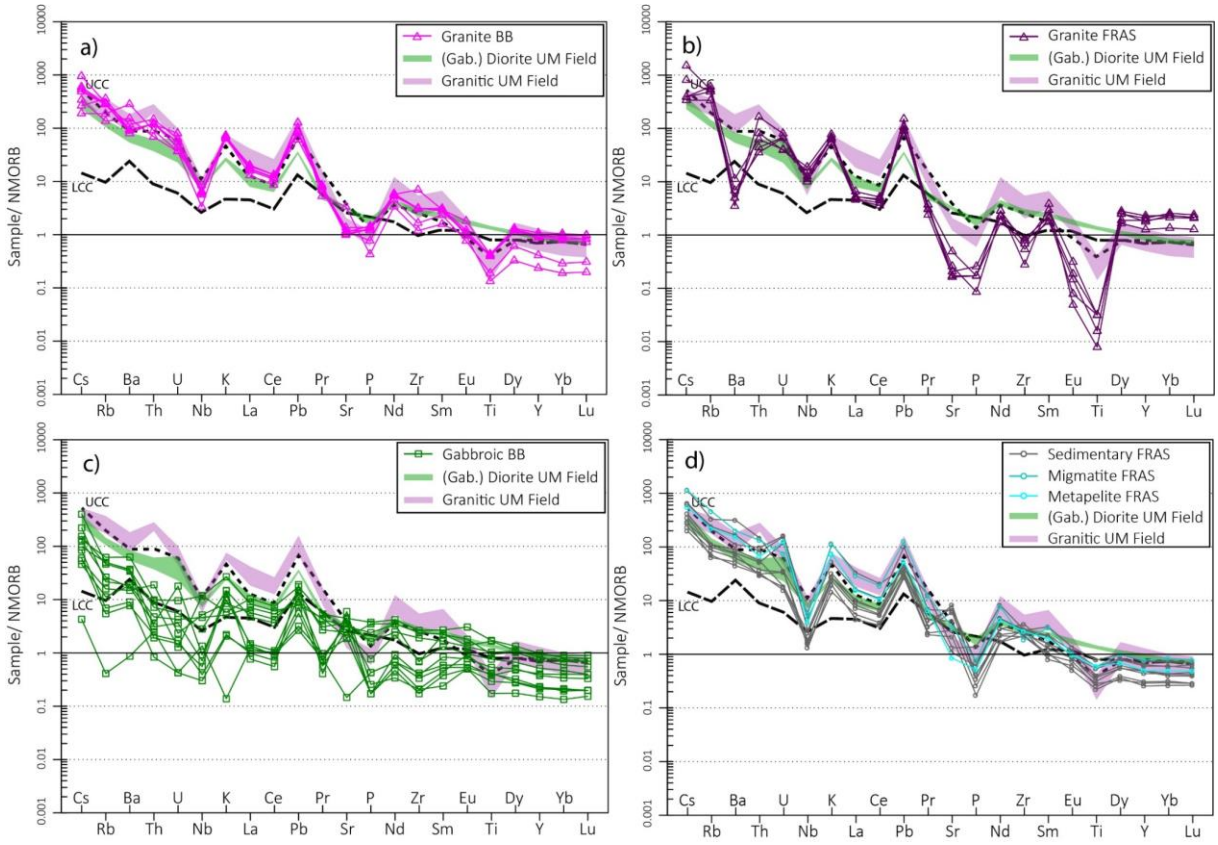

Figure 25 – N-MORB-normalized trace element patterns of samples from Fraserburgh and the wider Buchan Block area; a) trace element patterns of granitic rocks from the wider Buchan Block area; b) trace element patterns of granitic rocks from Fraserburgh; c) trace element patterns of (ultra-) mafic rocks from the wider Buchan Block; d) trace element patterns of crustal host rocks from Fraserburgh; NMORB normalization data used after Sun and McDonough, 1989

Chondrite-normalized REE patterns of the mafic to ultramafic rocks of the surrounding Buchan Block area are highly variable (fig. 24 – c). Except for one sample (s010) are most patterns defined by relatively enriched LREE over HREE (La_N/Yb_N = 2.12 – 8.74). Conversely, sample s010 shows increasing concentrations from La_N to Sm_N (La_N/Yb_N = 1.82). Total REE concentrations are highly variable and mostly lower than the total REE contents of the mafic rocks from Inzie Head (ΣREE = 13.2 – 151.3). Weakly defined negative Eu anomalies (Eu/Eu* = 0.74 – 0.99) are evident in four of the samples, with relatively higher total REE concentration, whereas the other six samples show weakly to well-defined positive Eu anomalies (Eu/Eu* = 1.07 – 2.28). The sample with relatively elevated MgO content plots within the field of mafic and ultramafic rocks with lower total REE concentrations (ΣREE = 23.1). The pattern is similar to most of the mafic to ultramafic

rocks, with a positive Eu anomaly and gradual slope of the chondrite-normalized pattern ($Eu/Eu^* = 1.11$; $La_N/Yb_N = 3.57$). N-MORB-normalized plots of the ultramafic and mafic rocks of the greater Buchan Block area show varying concentrations but generally similar patterns for the HREE (fig. 25 – c). LILE concentrations of the anorthosite sample are relatively depleted, whereas HFSE and REE compositions are similar to the gabbroic samples. Gabbroic samples are characterised by variable enrichments in LILE, plotting with values close and above the LCC line (fig. 25 – c).

4.5 MINERAL CHEMISTRY

Mineral chemical analyses were performed on the variety of different rock types to obtain representative compositions of the individual rock-forming minerals. Plagioclase and biotite are constituting phases within all samples and described below with representative analyses shown in table (1) and (2). As hornblende is absent in the felsic rocks, chemical analyses were acquired on crystals within the mafic, (gabbroic) diorite samples, with representative analyses given in table (3). Garnet-porphyroblasts are exclusively found in the leucosome, with representative analyses shown in table (4). The analytical methods used for data acquisition are described in detail in section 3.3 of the methodology chapter. The full set of analyses for each sample and mineral can be found in Appendix II.

4.5.1 PLAGIOCLASE

TABLE 2: REPRESENTATIVE ANALYSES OF PLAGIOCLASE; ID INDICATES THE DOMAIN OF THE SPOT ANALYSES ON THE PLAGIOCLASE GRAIN, WITH M OR F INDICATING WHETHER THE GRAIN IS LOCATED IN THE MAFIC OR FELSIC DOMAIN OF CONTACT SAMPLES; FORMULA CALCULATED BASED ON 8 OXYGEN; AN IS THE ANORTHITE COMPONENT AN = CA/(CA+NA+K), AB IS THE ALBITE COMPONENT AB = NA/(CA+NA+K) AND OR IS THE ORTHOCLASE COMPONENT OR = K/(CA+NA+K)

Sample	s1A		s1B		s1D		s1F		s1H		s2A		s3B		s4D		s5A		s5B		s7A		s8D	
Spot No.	4	33	45	55	37	63	16	52	14	54	57	86	14	27	44	63	257	366	13	52	18	39	18	50
ID	outer	inner	inner	outer	inner M	outer F	inner	outer	inner F	outer M	inner	outer	outer	outer	inner	outer	inner	inner	inner F	outer M	inner	outer	inner M	inner F
wt.-%																								
SiO_2	59.2	53.3	56.2	60.7	54.0	63.5	63.0	60.3	57.9	60.1	61.3	62.0	65.2	60.4	61.3	61.2	59.6	52.1	55.6	59.2	53.4	48.4	52.4	59.8
TiO_2	0.0	0.0	0.0	0.0	0.0	0.0	0.0	0.0	0.0	0.0	0.0	0.0	0.0	0.0	0.0	0.0	0.0	0.2	0.0	0.0	0.0	0.0	0.0	0.0
Al_2O_3	25.5	29.0	27.4	24.6	28.4	22.6	23.2	25.0	26.5	24.7	24.4	24.4	21.6	25.0	24.5	24.3	25.4	30.1	28.0	25.5	29.5	32.5	29.9	25.4
FeO_t	0.3	0.2	0.0	0.0	0.0	0.0	0.0	0.0	0.0	0.2	0.0	0.0	0.0	0.0	0.0	0.7	0.0	0.2	0.0	0.0	0.0	0.2	0.2	0.0
MgO	0.0	0.0	0.0	0.0	0.0	0.0	0.0	0.0	0.0	0.0	0.0	0.0	0.0	0.0	0.0	0.0	0.0	0.0	0.0	0.0	0.0	0.0	0.0	0.0
CaO	8.0	12.2	9.9	6.6	11.6	4.1	5.1	7.2	9.2	7.4	5.1	4.4	3.5	7.0	5.8	4.5	7.6	13.0	10.8	7.9	12.4	15.9	13.0	7.1
Na_2O	7.3	4.7	6.2	8.2	5.2	9.8	9.0	7.5	6.5	7.6	8.7	9.2	9.7	7.8	7.9	8.4	7.5	4.0	5.6	7.3	4.8	2.5	4.4	7.5
K_2O	0.0	0.0	0.2	0.2	0.0	0.0	0.0	0.0	0.0	0.0	0.2	0.4	0.0	0.1	0.2	0.6	0.1	0.1	0.0	0.1	0.0	0.0	0.0	0.2
Cr_2O_3	0.0	0.2	0.0	0.0	0.0	0.0	0.0	0.0	0.1	0.1	0.0	0.0	0.0	0.0	0.0	0.0	0.0	0.0	0.2	0.0	0.2	0.2	0.0	0.0
Total	100.3	99.6	100.0	100.2	99.2	100.0	100.3	100.0	100.3	100.2	99.7	100.2	100.0	100.3	99.7	99.7	100.3	99.7	100.3	100.1	100.3	99.6	99.9	100.0
Formula																								
Number of ions on the basis of 8 O																								
Si	2.64	2.42	2.52	2.69	2.45	2.80	2.78	2.69	2.59	2.68	2.72	2.73	2.88	2.68	2.74	2.72	2.65	2.37	2.50	2.64	2.41	2.22	2.37	2.67
Al	1.34	1.55	1.45	1.28	1.52	1.17	1.21	1.31	1.40	1.30	1.28	1.26	1.13	1.31	1.29	1.28	1.33	1.62	1.48	1.34	1.57	1.76	1.60	1.33
Ti	0.00	0.00	0.00	0.00	0.00	0.00	0.00	0.00	0.00	0.00	0.00	0.00	0.00	0.00	0.00	0.00	0.00	0.01	0.00	0.00	0.00	0.00	0.00	0.00
Cr	0.00	0.01	0.00	0.00	0.00	0.00	0.00	0.00	0.00	0.01	0.00	0.00	0.00	0.00	0.00	0.00	0.00	0.00	0.01	0.00	0.01	0.01	0.00	0.00
Fe^{3+}	0.01	0.01	0.00	0.00	0.00	0.00	0.00	0.00	0.00	0.01	0.00	0.00	0.00	0.00	0.00	0.02	0.00	0.01	0.00	0.00	0.00	0.01	0.01	0.00
Na	0.63	0.42	0.54	0.70	0.46	0.83	0.77	0.65	0.56	0.66	0.75	0.78	0.83	0.67	0.68	0.73	0.65	0.35	0.49	0.63	0.42	0.22	0.39	0.65
Ca	0.38	0.60	0.48	0.31	0.57	0.19	0.24	0.34	0.44	0.35	0.24	0.21	0.16	0.33	0.28	0.21	0.36	0.64	0.52	0.38	0.60	0.78	0.63	0.34
K	0.00	0.00	0.01	0.01	0.00	0.00	0.00	0.00	0.00	0.00	0.01	0.02	0.00	0.01	0.01	0.04	0.01	0.01	0.00	0.01	0.00	0.00	0.00	0.01
Σ Z	4.01	3.99	3.97	3.97	3.97	3.97	3.99	4.00	3.99	4.00	4.00	3.99	4.00	3.99	4.03	4.07	3.99	4.02	3.98	3.98	3.98	4.00	3.99	4.00
Σ X	1.01	1.01	1.03	1.03	1.03	1.03	1.01	1.00	1.01	1.01	1.00	1.01	1.00	1.01	0.97	0.97	1.01	1.00	1.01	1.02	1.02	1.00	1.02	1.00
Total	5.02	5.01	5.00	5.00	5.00	5.00	5.00	5.00	5.00	5.01	5.00	5.00	5.00	5.00	5.00	5.05	5.00	5.01	4.99	5.00	4.99	5.00	5.01	5.00
Mol.%																								
An	37.67	58.78	46.40	30.46	55.14	18.84	24.04	34.45	43.89	34.77	24.24	20.50	16.43	33.02	28.68	21.93	35.75	63.97	51.64	37.17	59.05	77.99	61.79	33.80
Ab	62.33	41.22	52.68	68.46	44.86	81.16	75.96	65.55	56.11	65.23	74.64	77.51	83.57	66.39	70.17	74.39	63.70	35.20	48.36	62.07	40.95	22.01	38.21	64.80
Or	0.00	0.00	0.92	1.08	0.00	0.00	0.00	0.00	0.00	0.00	1.13	1.99	0.00	0.60	1.14	3.68	0.54	0.83	0.00	0.76	0.00	0.00	0.00	1.41

4.5.1.1 PLAGIOCLASE IN UNMINGLED SAMPLES

Plagioclase grains of unmingled granitic samples from Inzie Head, are characterized by relatively low anorthite and higher albitic compositions, ranging from An_{10} – An_{40} (fig. 26 – a). Plagioclase crystals with zonally arranged alteration surfaces are slightly elevated in An contents, ranging between An_{31} – An_{40}, whereas An contents in unzoned grains are generally lower (An_{10} – An_{30}). However, the majority of plagioclase grains shows weakly-defined, normal chemical zoning of slightly decreasing An contents from core to rim domains (fig. 12 – c+d). Patchy compositional changes within inner domains spike

with comparatively high Ab contents (Ab_{94} – Ab_{98}). In addition, fractures and inner replacement textures are generally related to fine growths of elevated orthoclase component (Or_{94} – Or_{98}).

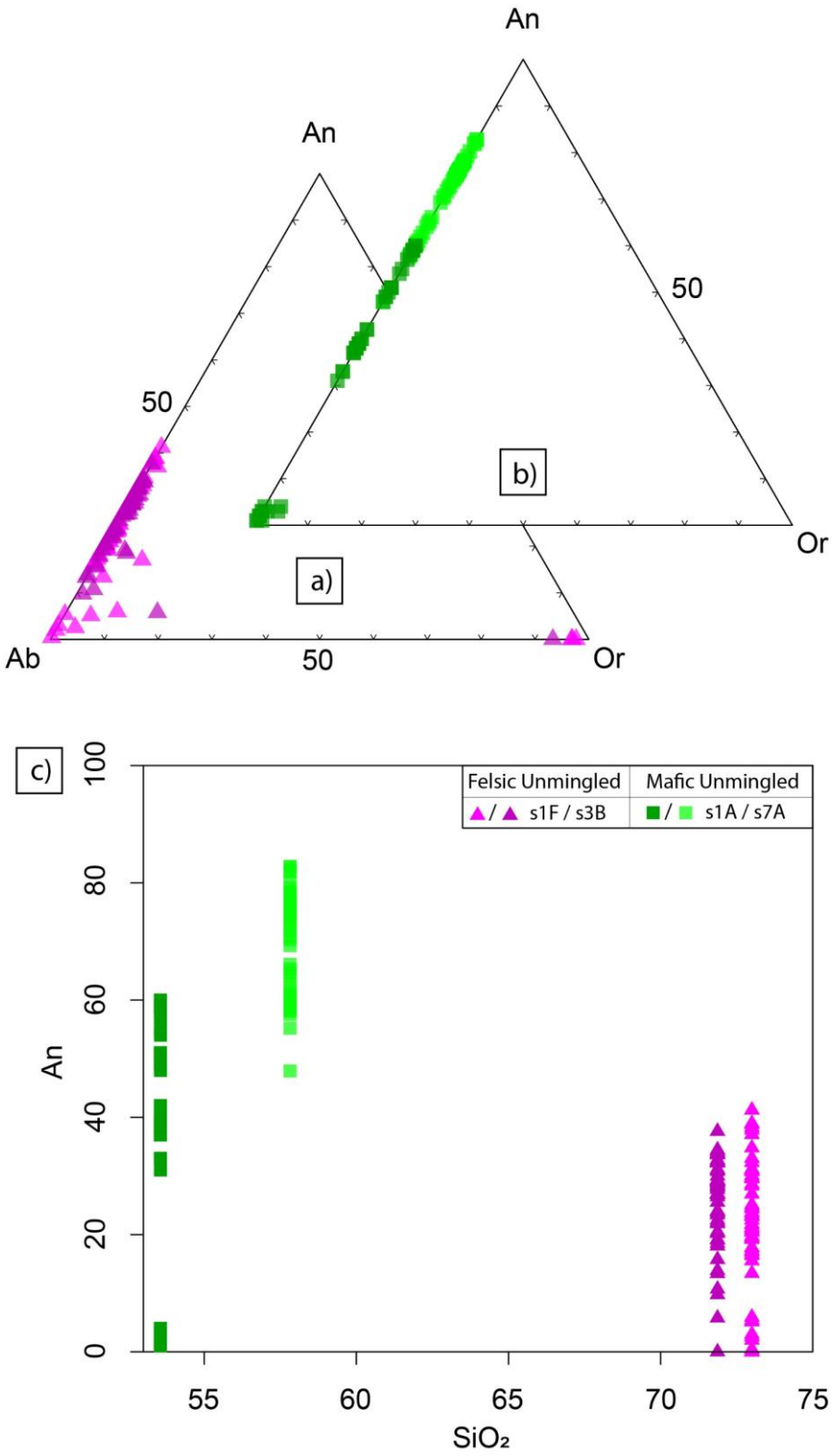

Figure 26 – Feldspar compositions of unmingled rocks in triangle plot (after Irvine and Baragar, 1971*) and binary plot; a) plagioclase compositions in granite samples without mingling features; b) plagioclase compositions in mafic samples without mingling features; c) binary plot of whole rock SiO_2 versus An content of plagioclases from the different unmingled samples*

The majority of plagioclase grains from unmingled mafic samples are distinguished by higher An content relative to plagioclase from granitic samples (fig. 26 – b+c). The overall variation in An content of plagioclase grains from diorite sample

s7A (An_{48} – An_{83}) is characterized by patchy to boxy irregular compositional zones of higher Ab contents (Ab_{34} – Ab_{52}) that are predominantly found within inner domains (fig. 13 – e). Reverse chemical zoning is evident in a minority of grains, where irregular, sodic core like inner areas (An_{59} – An_{64}) are surrounded by rim domains of relatively high An content (An_{79} – An_{83}). Evidence of alteration is primarily found on domains with higher An content whereas albitic patches are generally free of alteration textures. Normal zoning patterns are evident in the majority of plagioclase grains from gabbroic diorite sample s1A, defined by core domains with higher An contents (An_{50} – An_{60}) relative to the surrounding rims (An_{30} – An_{50}). Signs of alteration and patches of high albite content (Ab_{95} – Ab_{99}) are restricted to these calcic cores. The surrounding, irregular rims are notably lower in their Ab component, than the albitic patches within the core domains (fig. 26 – b). Anorthite contents in the dioritic sample s7A are overall higher, in comparison with the more mafic sample s1A (fig. 26 – c).

4.5.1.2 PLAGIOCLASE IN MINGLED AND POTENTIALLY MIXED SAMPLES

Plagioclase within mingled granodioritic rocks (here s1B and s1H) is relatively uniform in composition, for the most part ranging from An_{30} to An_{50} (fig. 27 – a). Patchy and normal chemical zoning patterns are evident within the majority of grains (fig. 16 – b+c). However, a minority of crystals in sample s1H is characterized by complex concentric zoning patterns, where the inner rounded and more calcic core is surrounded by alternating zones of higher albitic and higher anorthitic chemical compositions (fig. 16 – b+c). Plagioclase grains within the microgranular enclave of sample s1H, are relatively consistent in composition (An_{35} – An_{42}) and comparable to plagioclase compositions of the coarser-grained, more felsic section. Plagioclase in sample s5A is predominantly characterized by concentric zones, with cores of primarily elevated An contents (An_{55} – An_{68}), relative to the surrounding rims (An_{36} – An_{55}; fig. 27 – b). Boxy cellular dissolution textures are restricted to calcic core domains. However, a minority of grains are inclusion rich and characterized by patchy compositional changes throughout (fig. 17 – e+f), where a concentric, outer zone of strongly elevated An content (An_{72} – An_{87}) is irregularly overgrown by a sodic outermost rim (An_{16} – An_{25}). Patches of elevated Or contents are restricted along inner fractures.

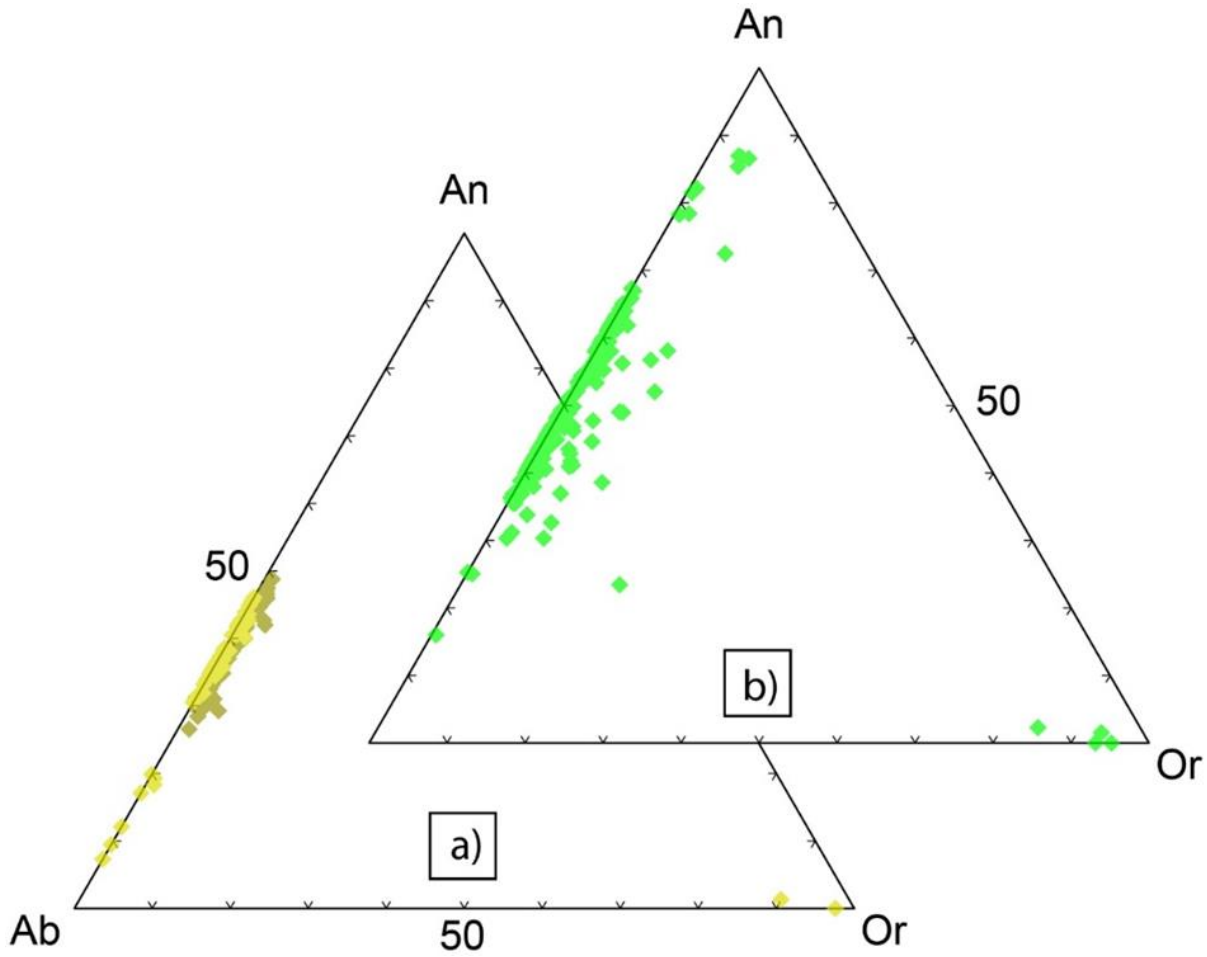

Figure 27 – Feldspar compositions of mingled samples; a) plagioclase compositions of mingled granodioritic samples s1B and s1H; b) plagioclase compositions of mingled dioritic sample s5A

Plagioclase compositions are highly variable throughout the sharp contact of the contrasting domains in sample s1D (fig. 14 – a; fig. 28 – a). Within the mafic domain (s1Db), normal zoning in plagioclases is characterized by altered calcic cores with high An contents (An_{52} – An_{59}), rimmed by plagioclase of higher albite content (An_{33} – An_{46}) (fig. 14 – c). The majority of plagioclase grains in the felsic domain (s1Da) of the sample are unzoned and relatively uniform in An content (An_{18} – An_{24}), with patches of enriched Ab or Or compositions along fractures (fig. 28 – a). Normal concentric zoning patterns are evident in a minority of plagioclase grains, where rounded inner core domains with zonally restricted signs of alteration, are elevated in An content (An_{40} – An_{43}) (fig. 14 – f). The relatively lower An content in surrounding rims (An_{15} – An_{29}), is comparable in composition to the unzoned plagioclase grains. Plagioclase grains within the felsic part of the gradual contact of sample s5B, are predominantly characterized by normal concentric zoning patterns of more calcic cores (An_{49} – An_{55}), surrounded by more sodic (An_{35} – An_{44}) rims (fig. 15 – c; fig. 28 – b). Patches of higher albitic compositions (Ab_{80} – Ab_{92}) are generally restricted to inner fractures. Plagioclase crystals within the more mafic part of the contact, are relatively homogenous in An content and with An_{36} – An_{41} within range of the sodic rims in the felsic domain (fig. 28 – b). However, inner cores are highly altered with elevated Or contents along fractures (Or_{94} – Or_{97}) (fig. 15 – b). Calcic cores of plagioclase grains within the mafic domain of the wispy contact in sample s8D, are relatively elevated in An (An_{57} – An_{62}) with zonally restricted signs of alteration (fig. 28 – c). Surrounding rims are irregular and highly variable in composition, ranging between An_{10} and An_{46}, similar to the An contents of plagioclase rims in the felsic domain of the contact. Plagioclase grains within the felsic domain are predominantly unzoned and relatively homogenous in composition (An_{31} – An_{41}). Replacement textures and patches of elevated albitic (An_{09} – An_{20}) or Or (Or_{92} – Or_{97}) rich components occur along fractures throughout grains. A second and minor plagioclase type within the felsic domains is characterized by normal concentric zoning patterns (fig. 14 – d+e). Rounded and patchy, calcic core domains, with elevated An contents between An_{47} – An_{53}, are surrounded by irregular, more sodic rims (An_{10} – An_{40}).

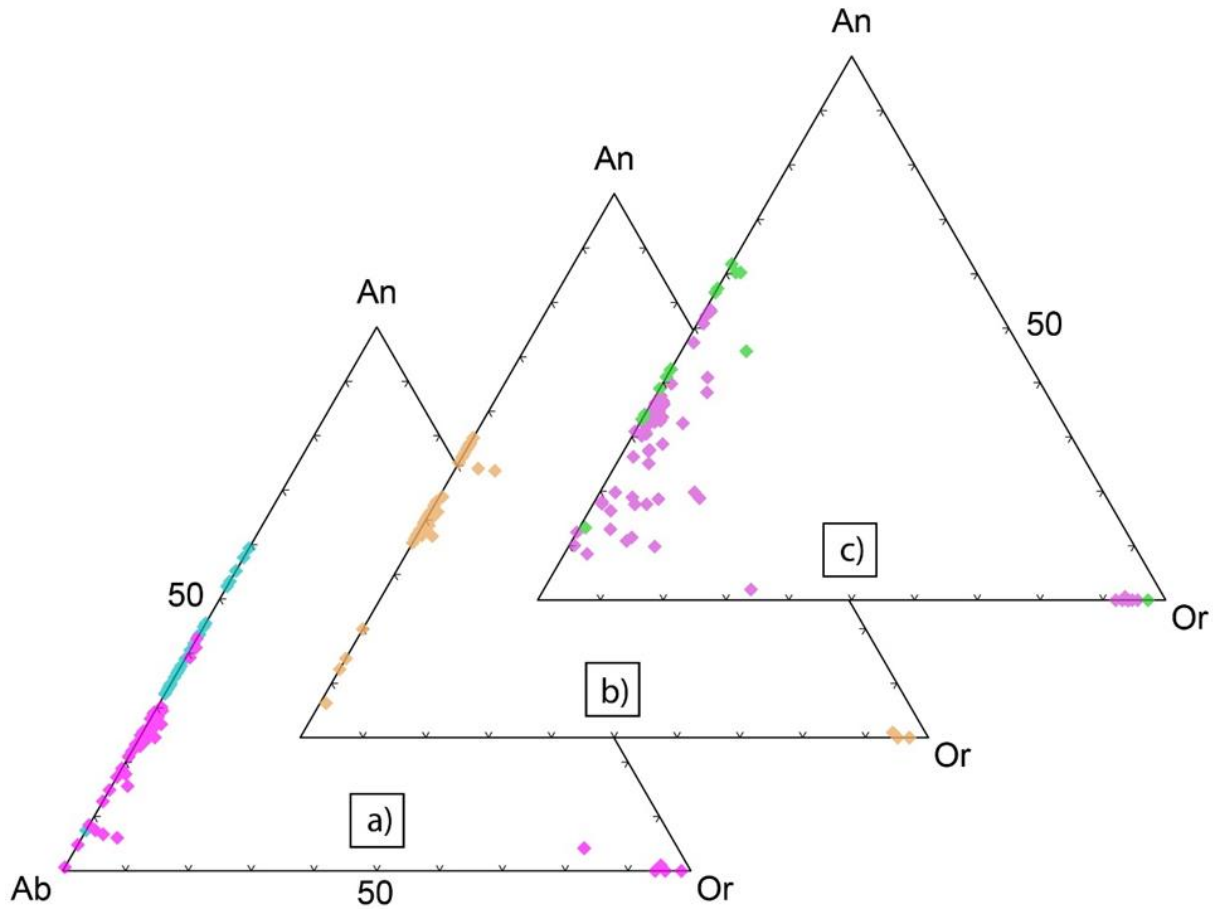

Figure 28 – Feldspar compositions in mingled contact samples; a) plagioclase compositions of the contact sample s1D, plagioclase analysed within the felsic domain (s1Da) are shown in pink and analyses of plagioclases within the mafic domain (s1Db) are shown in blue; b) plagioclase compositions within the gradual contact of sample s5B; c) plagioclase compositions of the contact sample s8D, analyses within the mafic wisp (s8Db) are shown in green and plagioclase analyses of the felsic domain (s8Da) in pink

Plagioclase compositions of grains from metapelite are relatively homogenous (An_{19} – An_{25}), regularly containing low Or contents between Or_{01} – Or_{02} (fig. 29 – a). An values outside of the given, homogenous spread (An_{12} – An_{17} and An_{25} – An_{28}) are generally richer in Or compositions (Or_{03} – Or_{07}) and principally related to alteration along internal fractures. Plagioclase grains of the garnet-bearing leucosome, that have strong signs of alteration along internal fractures and show a wide range in compositions (fig. 29 – b). A small group of relatively homogenous plagioclase compositions, with An contents between An_{24} – An_{30}, contain low Or components (Or_{01} – Or_{02}). However, the majority of plagioclase compositions are characterized by highly variable and relatively enriched Ab and Or content.

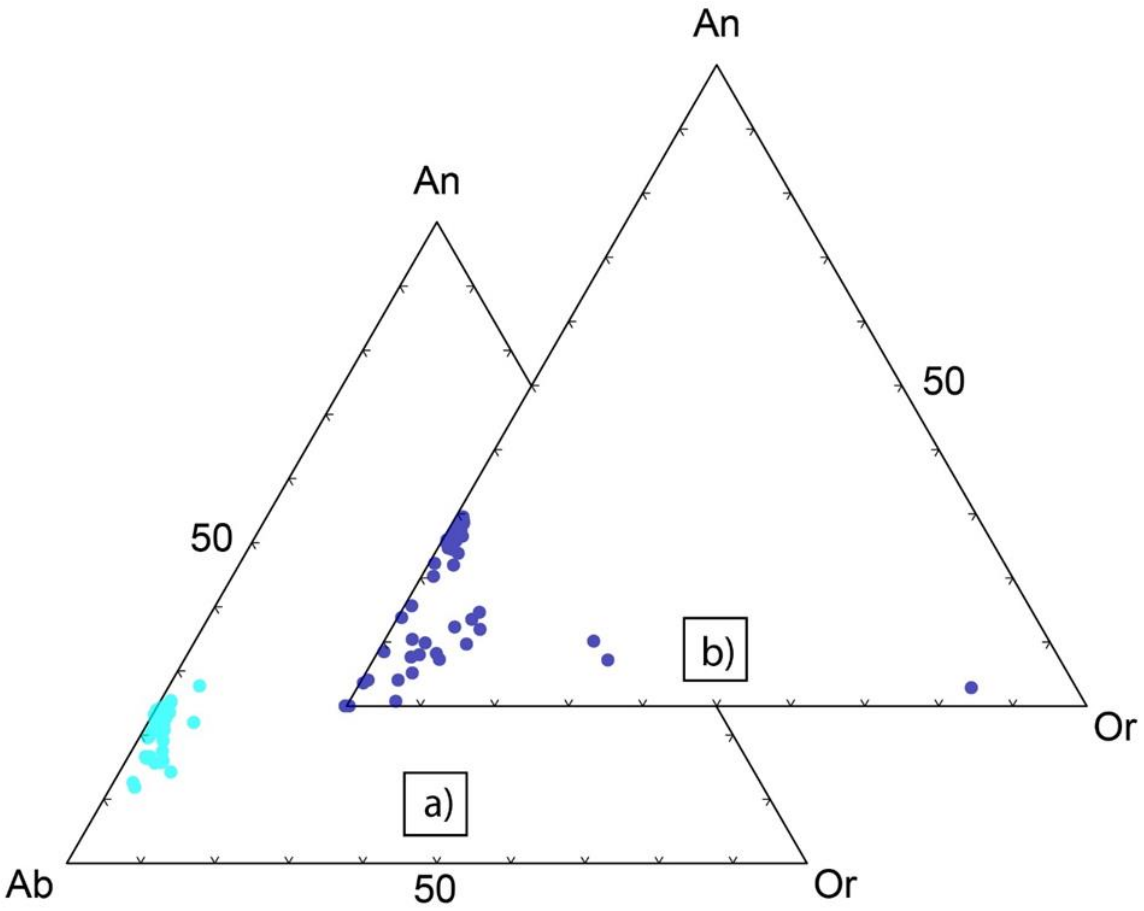

Figure 29 – Feldspar compositions of crustal host rocks; a) Compositions of plagioclase in metapelite; b) Compositions of plagioclase in garnet-bearing leucosome

An overall comparison of the plagioclase compositions from the different samples shows clearly that plagioclase of the metapelite and leucosome are characterized by consistently low anorthite contents (fig. 30). Relative to the crustal host rocks, are the granitic unmingled and mingled samples characterized by a higher variation, ranging into higher anorthite contents. In comparison with the granitic samples, an overall increase in anorthite contents with increasing maficity is weakly defined by the granodiorites and more mafic rocks (fig. 30).

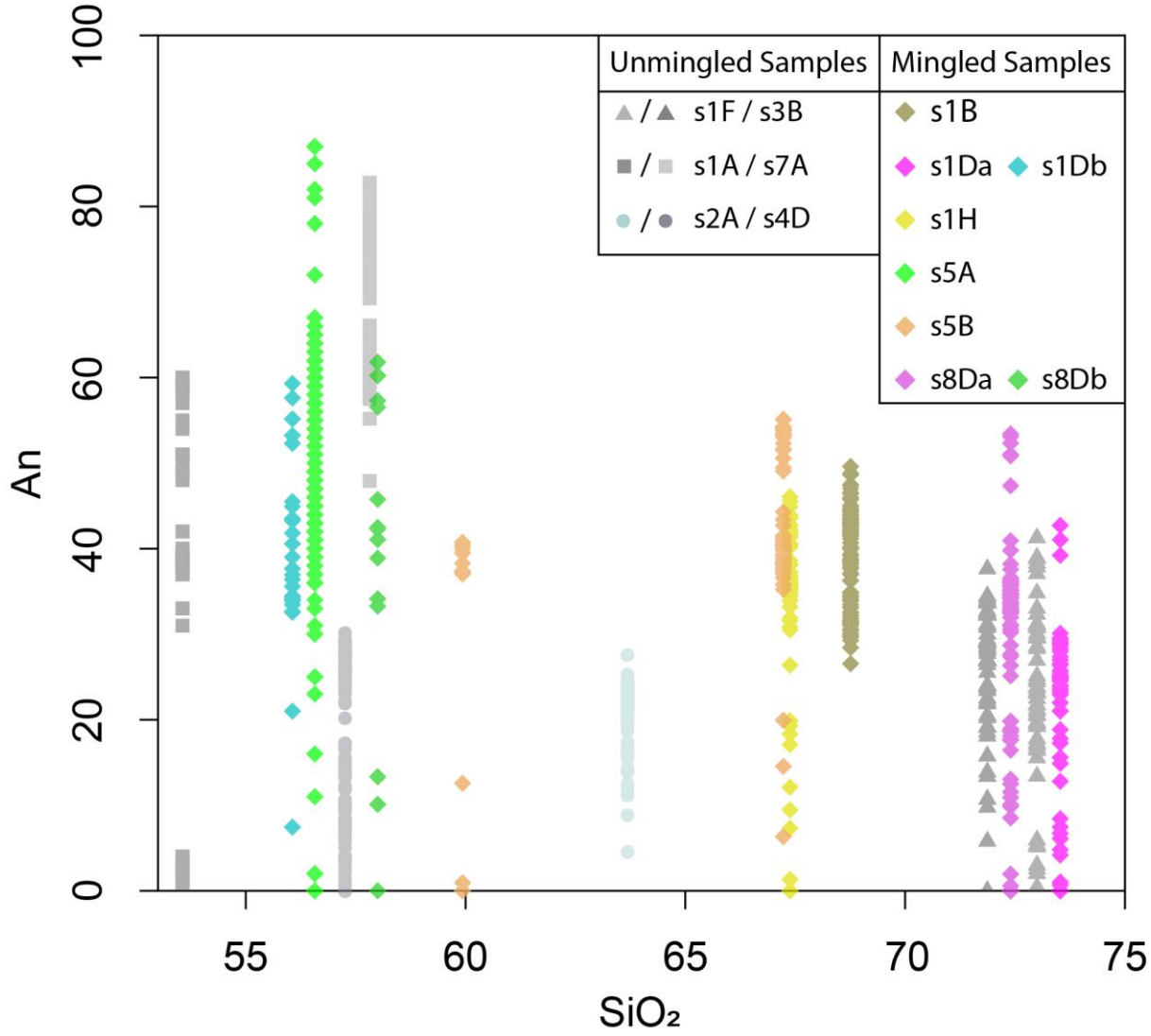

Figure 30 – Binary plot of anorthite component in plagioclases of the different rock types versus whole rock SiO_2; grey squares and triangles represent the unmingled mafic and felsic rocks; respectively, grey circles represent the metapelitic migmatites

4.5.2 BIOTITE

TABLE 3: REPRESENTATIVE ANALYSES OF BIOTITE; ID INDICATES IF THE ANALYSED BIOTITE IS LOCATED WITHIN THE FELSIC (F) OR MAFIC (M) DOMAIN; FORMULA CALCULATED BASED ON 22 OXYGEN

Sample	s1A		s1B		s1D		s1F		s1H		s2A		s3B		s4D		s5A		s5B		s7A		s8D	
Spot No.	1	2	3	5	3	8	2	3	1	6	2	5	2	4	3	15	3	6	5	6	1	4	4	11
ID					F	M			M	F													F	M
wt.-%																								
SiO_2	37.1	37.5	35.9	35.0	35.9	36.2	34.3	34.0	35.4	35.4	33.8	34.0	34.4	34.4	36.5	32.2	36.3	31.3	35.3	35.3	36.9	37.2	36.7	37.0
TiO_2	3.2	3.3	3.0	4.0	3.6	3.3	3.1	3.2	2.5	3.5	4.0	3.4	2.8	3.1	0.9	1.5	2.6	1.5	3.7	3.4	2.3	2.5	3.9	2.6
Al_2O_3	15.6	15.8	16.2	16.1	16.7	15.8	18.5	18.4	16.4	15.4	20.0	18.9	17.3	16.9	24.1	25.4	16.2	17.4	15.6	15.6	16.4	16.1	16.1	16.8
FeO_t	18.5	18.6	23.4	23.3	23.8	21.6	23.3	23.5	23.2	24.1	21.0	21.9	26.9	26.5	22.4	24.9	23.3	26.0	21.6	21.4	18.6	18.4	21.6	21.7
MnO	0.2	0.2	0.3	0.2	0.5	0.3	0.3	0.3	0.4	0.3	0.1	0.1	0.3	0.4	0.0	0.1	0.1	0.1	0.0	0.3	0.0	0.0	0.3	0.3
MgO	10.6	10.6	8.1	7.8	6.3	8.5	5.5	5.4	6.7	6.4	7.3	8.4	4.4	4.2	6.9	9.1	10.5	12.1	8.0	8.3	10.5	10.7	7.9	8.1
CaO	0.0	0.0	0.0	0.0	0.0	0.0	0.0	0.0	0.0	0.0	0.1	0.0	0.0	0.0	0.0	0.0	0.1	0.1	0.0	0.0	0.0	0.0	0.0	0.0
Na_2O	0.2	0.3	0.0	0.0	0.2	0.3	0.0	0.2	0.2	0.2	0.5	0.2	0.2	0.2	0.0	0.0	0.3	0.2	0.2	0.2	0.3	0.2	0.2	0.2
K_2O	9.6	9.6	9.2	9.3	9.2	9.4	9.5	9.5	9.3	9.4	9.6	9.2	9.5	9.3	4.6	2.9	9.4	5.0	9.2	9.2	9.4	9.5	9.5	9.6
Total	95.0	95.8	96.1	95.7	96.2	95.4	94.5	94.7	94.1	94.7	96.2	96.2	95.8	95.0	95.3	96.0	98.8	93.7	93.6	93.6	94.3	94.6	96.1	96.4
Formula																								
Number of ions on the basis of 22 O																								
Si	5.66	5.66	5.54	5.43	5.54	5.57	5.39	5.35	5.59	5.59	5.16	5.21	5.43	5.47	5.39	4.79	5.44	4.96	5.55	5.56	5.65	5.68	5.60	5.64
Al^{IV}	2.34	2.34	2.46	2.57	2.46	2.43	2.61	2.65	2.41	2.41	2.84	2.79	2.57	2.53	2.61	3.21	2.56	3.04	2.45	2.44	2.35	2.32	2.40	2.36
Σ Z	8.00	8.00	8.00	8.00	8.00	8.00	8.00	8.00	8.00	8.00	8.00	8.00	8.00	8.00	8.00	8.00	8.00	8.00	8.00	8.00	8.00	8.00	8.00	8.00
Al^{VI}	0.46	0.47	0.47	0.38	0.58	0.44	0.82	0.78	0.63	0.44	0.75	0.62	0.66	0.64	1.59	1.25	0.31	0.20	0.45	0.45	0.61	0.58	0.50	0.66
Ti	0.37	0.38	0.35	0.47	0.41	0.39	0.36	0.38	0.30	0.42	0.45	0.40	0.34	0.37	0.10	0.16	0.29	0.17	0.44	0.40	0.27	0.29	0.45	0.30
Fe_t	2.36	2.35	3.02	3.02	3.08	2.79	3.06	3.09	3.06	3.17	2.68	2.81	3.56	3.53	2.76	3.09	2.91	3.45	2.84	2.82	2.38	2.34	2.76	2.77
Mn	0.03	0.02	0.04	0.03	0.07	0.04	0.04	0.05	0.05	0.04	0.01	0.01	0.04	0.06	0.00	0.01	0.01	0.01	0.00	0.04	0.00	0.00	0.04	0.04
Mg	2.40	2.38	1.87	1.81	1.46	1.96	1.29	1.27	1.58	1.51	1.66	1.91	1.04	1.01	1.53	2.02	2.35	2.85	1.88	1.94	2.39	2.43	1.79	1.84
Σ X	5.16	5.13	5.28	5.33	5.02	5.18	4.75	4.79	4.99	5.14	4.80	5.13	4.98	4.97	4.39	5.28	5.56	6.48	5.16	5.20	5.04	5.06	5.04	4.95
Ca	0.00	0.00	0.00	0.00	0.00	0.03	0.00	0.00	0.00	0.00	0.02	0.00	0.00	0.00	0.00	0.00	0.02	0.02	0.00	0.00	0.00	0.00	0.00	0.00
Na	0.07	0.09	0.00	0.00	0.06	0.08	0.00	0.07	0.07	0.06	0.15	0.07	0.06	0.05	0.00	0.00	0.08	0.06	0.06	0.07	0.08	0.07	0.05	0.05
K	1.86	1.84	1.81	1.84	1.81	1.84	1.91	1.92	1.88	1.90	1.87	1.81	1.91	1.89	0.86	0.54	1.80	1.02	1.85	1.85	1.83	1.84	1.85	1.86
Σ Y	1.93	1.93	1.81	1.84	1.87	1.95	1.91	1.99	1.95	1.96	2.04	1.88	1.97	1.94	0.86	0.54	1.90	1.10	1.91	1.92	1.91	1.91	1.90	1.91
Total	15.55	15.53	15.56	15.55	15.47	15.57	15.48	15.56	15.57	15.54	15.59	15.63	15.61	15.55	14.84	15.07	15.77	15.78	15.52	15.57	15.56	15.55	15.44	15.52
X_{Fe}	0.50	0.50	0.62	0.63	0.68	0.59	0.70	0.71	0.66	0.68	0.62	0.59	0.77	0.78	0.64	0.61	0.55	0.55	0.60	0.59	0.50	0.49	0.61	0.60

Biotite within mafic and felsic unmingled samples from the Inzie Head section are generally distinct in composition. Biotite crystals in the mafic rocks are characterized by relatively uniform Al^{IV} (~ 2.3 a.p.f.u.) compositions, with Mg (2.3 – 2.5 a.p.f.u.) and Fe (2.3 – 2.5 a.p.f.u.) in approximately equal proportions. Thus, analyses of mafic biotite grains form a relatively tight cluster in the Al^{IV} versus Fe/Fe+Mg diagram, plotting towards phlogopite subgroup compositions (X_{Fe} = ~ 0.5) (fig. 31). An observed increase in Ti content from 0.2 to 0.4 a.p.f.u. is evident from inner to outer domains of the biotite crystals. In comparison, biotite crystals of the unmingled granites are higher in Fe and Al^{IV} contents (3.1 – 3.6 a.p.f.u. and 2.5 – 2.6 a.p.f.u., respectively), with lower Mg proportions (1.0 – 1.6 a.p.f.u.). Thus, biotite compositions of the samples, shift in the Al^{IV} versus Fe/Fe+Mg diagram towards compositions of siderophyllite (X_{Fe} = 0.7 – 0.8) (fig. 31). Ti contents are relatively high (Ti = 0.2 – 0.5 a.p.f.u.) and variable throughout the biotite grains.

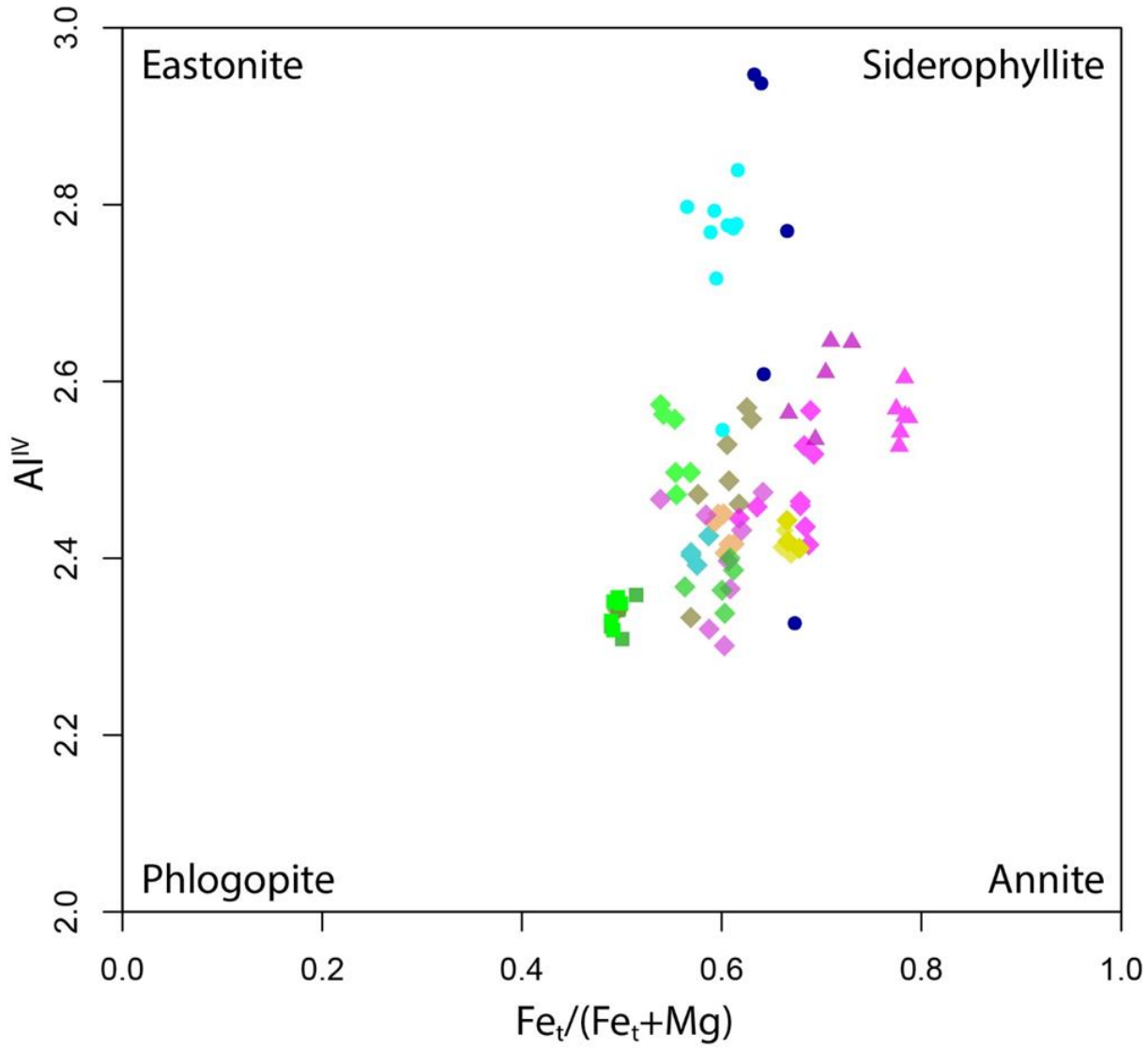

Figure 31 – Binary plot of biotite compositions (in a.p.f.u.) within the different rock types; colours and symbols as seen in the previous figures (fig. 26 – 31)

Biotite compositions of the mingled samples from Inzie Head are highly variable in Al^{IV} (2.3 – 2.6 a.p.f.u.), Mg (1.4 – 2.6 a.p.f.u.) and Fe (2.4/2.6 – 3.2 a.p.f.u.) contents, which overlap with biotite of the granitic and mafic unmingled samples. Thus, the majority of biotite compositions from the mingled samples plot on an Al^{IV} versus Fe/Fe+Mg diagram in between the defined mafic and granitic clusters, with X_{Fe} values of 0.5 – 0.7 a.p.f.u. (fig. 31). Biotite grains within the diffuse contact zone of sample s5B, are relatively uniform in compositions throughout. However, the wispy contact of contrasting domains in sample s8D, is characterized by highly variable biotite compositions in the felsic domain (s8Da), with Al^{IV} and X_{Fe} varying between 2.3 – 2.5 a.p.f.u. and 0.54 – 0.64 a.p.f.u., respectively. Contrastingly, Al^{IV} and X_{Fe} contents in most biotite grains within the mafic part of the sample (s8Db) are comparably less variable (Al^{IV} = 2.3 – 2.4 a.p.f.u. and X_{Fe} = 0.56 – 0.61 a.p.f.u.). Biotite in sample s1D, where the contact between the contrasting rocks is clearly delineated, is characterized by distinct compositions. Biotite grains in the mafic domain of the sample (s1Db) are relatively uniform in composition (fig. 31). Al^{IV} contents of 2.4 a.p.f.u. and X_{Fe} values between 0.57 – 0.59 are relatively lower, compared to biotite grains of the felsic domain. Values for X_{Fe} of biotite within the felsic section, increase from 0.62 to 0.69, with increasing distance to the contact. Thus, defining together with biotite compositions of the mafic domain, a positive trend on the Al^{IV} versus X_{Fe} diagram (fig. 31). Biotite grains from the granodioritic sample s1B, are highly variable in Al^{IV} and X_{Fe} content, ranging between 2.3 – 2.6 a.p.f.u. and 0.5 – 0.63, respectively. Biotite compositions of grains from the granodioritic sample s1H are relatively uniform, with Al^{IV} = 2.4 a.p.f.u. and X_{Fe} = 0.66 – 0.68, showing the same composition as biotite within the mafic microgranular enclave. Altered biotite grains from the metapelite and leucosome samples are highly variable in Al^{IV}, ranging from 2.3 – 3.0 a.p.f.u. (fig. 31). However, X_{Fe} values from the leucosome sample are relatively elevated, ranging between 0.63 – 0.68, compared to

the metapelite sample (X_{Fe} = 0.57 – 0.62). Biotite within the metapelite is relatively enriched in Ti (0.46 – 0.29 a.p.f.u.), whereas biotite from the leucosome sample is generally lower in Ti content (0.04 – 0.1 a.p.f.u.).

4.5.3 HORNBLENDE

TABLE 4: REPRESENTATIVE HORNBLENDE ANALYSES OF THE (GABBROIC) DIORITE SAMPLES; X_{Mg} = Mg/(Mg+Fe^{2+}); FORMULA CALCULATED BASED ON 23 OXYGEN

	s1A		s5A		s5B		s7A	
Spot No.	12	26	1	22	1	2	4	5
wt.-%								
SiO_2	53.0	47.8	49.6	47.4	43.4	42.5	51.4	47.9
TiO_2	0.3	0.8	0.4	0.7	1.3	1.4	0.6	1.1
Al_2O_3	2.6	6.3	5.5	7.2	10.0	10.2	3.9	7.2
FeO_t	13.2	15.9	18.2	19.1	19.5	19.9	15.7	17.2
MnO	0.3	0.4	0.1	0.1	0.6	0.4	0.4	0.4
MgO	14.8	12.1	11.5	10.4	7.6	7.2	13.5	11.6
Cr_2O_3	0.4	0.4	0.0	0.0	0.0	0.0	0.4	0.0
CaO	12.2	11.5	11.9	11.5	11.5	11.2	11.4	10.6
Na_2O	0.4	1.0	0.5	0.6	0.9	1.3	0.5	0.7
K_2O	0.0	0.4	0.4	0.5	1.0	1.1	0.2	0.4
Total	97.1	96.6	98.1	97.5	95.7	95.2	98.0	97.1
Formula								
Number of ions on the basis of 23 O								
Si	7.66	7.08	7.25	7.00	6.70	6.64	7.39	6.98
Al^{IV}	0.34	0.92	0.75	1.00	1.30	1.36	0.61	1.02
Σ T	8.00	8.00	8.00	8.00	8.00	8.00	8.00	8.00
Al^{VI}	0.11	0.18	0.21	0.25	0.51	0.51	0.06	0.22
Ti	0.03	0.09	0.04	0.08	0.14	0.16	0.07	0.12
Fe^{3+}	0.23	0.47	0.49	0.67	0.24	0.17	0.70	0.96
Fe^{2+}	1.36	1.50	1.74	1.69	2.28	2.43	1.18	1.13
Mn	0.04	0.05	0.01	0.01	0.07	0.05	0.05	0.05
Mg	3.18	2.66	2.51	2.29	1.75	1.68	2.90	2.51
Cr	0.04	0.05	0.00	0.00	0.00	0.00	0.04	0.00
Σ C	5.00	5.00	5.00	5.00	5.00	5.00	5.00	5.00
Ca	1.88	1.83	1.87	1.83	1.90	1.88	1.75	1.65
Na	0.12	0.29	0.15	0.16	0.27	0.40	0.13	0.20
K	0.00	0.08	0.07	0.10	0.19	0.21	0.04	0.08
Σ B	2.01	2.21	2.09	2.09	2.36	2.49	1.92	1.94
Total	15.01	15.21	15.09	15.09	15.36	15.49	14.92	14.94
X_{Mg}	0.70	0.64	0.56	0.59	0.43	0.41	0.69	0.71

Chemical compositions of hornblende grains from the mafic samples are characterized by relatively high Ca (> 1.5 a.p.f.u.) and low Na + K (< 0.5 a.p.f.u.) contents, characteristic for calcic amphiboles. According to the amphibole nomenclature after

Leake et al. (1997), the majority of compositions classify as magnesiohornblende, with Si between 6.5 – 7.5 a.p.f.u. and X_{Mg} (Mg/[Mg+Fe2+]) ranging from 0.5 – 0.9 (fig. 32). Several hornblende crystals of the gabbroic diorite sample s1A show chemical zoning patterns, evident as darker patches within the grains (fig 13 – c). Such domains are predominantly found within inner core areas and are characterized by relatively elevated Si contents of 7.5 – 7.7 a.p.f.u., distinctive for actinolite compositions (fig. 32). The higher Si content is inversely proportional with lower Ti, Al_{tot} and Na+K values within these hornblende domains.

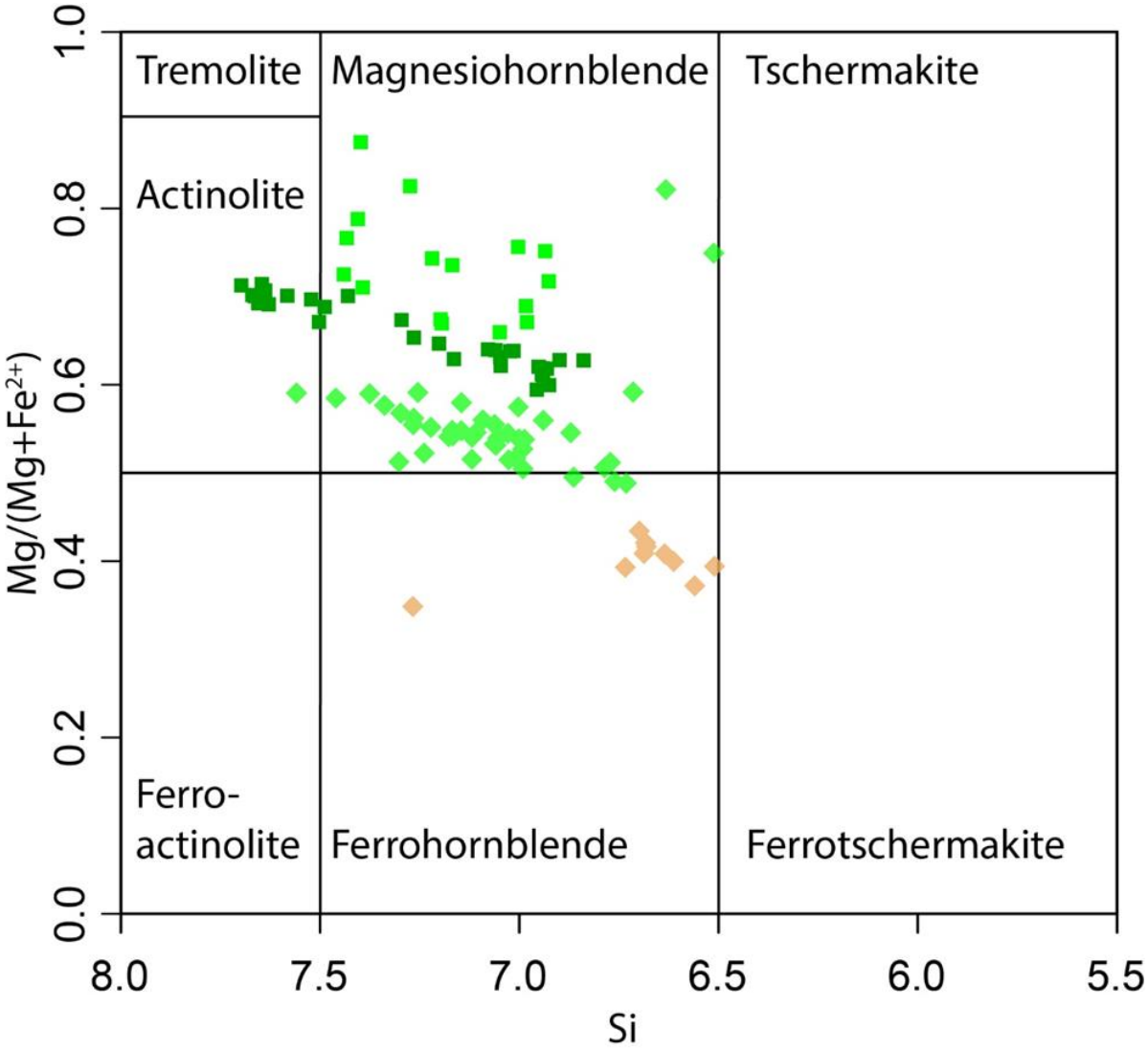

Figure 32 – Binary plot of hornblende compositions (in a.p.f.u.) within the mafic rocks; colours as seen in previous figures (fig. 26 – 31)

Hornblende compositions of mingled samples s5A and s5B are generally lower in X_{Mg}, predominantly ranging between 0.4 – 0.6, with Ti contents between 0.03 – 0.15. Hornblende in the contact sample s5B are distinct by X_{Mg} values below 0.5 characteristic of ferro hornblende compositions, here accompanied by elevated Ti contents of 0.15 – 0.17 a.p.f.u.

4.5.4 GARNET

TABLE 5: REPRESENTATIVE ANALYSES OF GARNET PORPHYROBLASTS; FORMULA CALCULATED BASED ON 12 OXYGEN; ALM REPRESENTS THE ALMANDINE COMPONENT ALM = FE/(FE+MG+MN+CA), PY REPRESENTS THE PYROPE COMPONENT PY = MG/(FE+MG+MN+CA), SP REPRESENTS THE SPESSARTINE COMPONENT SP = MN/(FE+MG+MN+CA), GRO REPRESENTS THE GROSSULAR COMPONENT GRO = CA/(FE+MG+MN+CA)

s4D								
wt.-%								
Spot No.	SiO_2	TiO_2	Al_2O_3	FeO_t	MnO	MgO	CaO	Total
11	37.5	0.0	21.2	36.0	1.3	3.4	0.9	100.2
57	37.0	0.0	20.7	37.0	2.7	1.9	0.8	100.1
Formula								
Number of ions based on 12 O								
Spot No.	Si	Ti	Al	Fe	Mn	Mg	Ca	Total
11	3.01	0.00	2.00	2.42	0.09	0.41	0.08	7.99
57	3.01	0.00	1.98	2.52	0.19	0.23	0.07	8.00

Spot No.	Py	Alm	Gro	Sp	X_{Mg}
11	13.6	81.0	2.5	2.9	8.60
57	7.7	83.7	2.4	6.2	4.90

Garnet porphyroblasts in the garnet-bearing leucosome display minor chemical zoning in terms of the major element chemistry. The high almandine component [X_{Alm} = Fe/(Fe+Mg+Mn+Ca)] increases from an average of X_{Alm} = 81 to X_{Alm} = 83 towards the rims and biotite filled cracks in the inner domain (fig. 33). Corresponding with the increase in X_{Alm}, the spessartine component increases [X_{Spes} = Mn/(Fe+Mg+Mn+Ca)] from X_{Spes} = 3 to X_{Spes} = 4 – 6. A corresponding decrease in the average pyrope component [X_{Pyr} = Mg/(Fe+Mg+Mn+Ca)], from X_{Pyr} = 13 to X_{Pyr} = 10 is evident with the apparent increase in X_{Alm} and X_{Spes} contents (fig. 33). The variability of the relatively low grossular component [X_{Gros} = Ca/(Fe+Mg+Mn+Ca)] is minor and the component is generally uniform throughout the garnet grain.

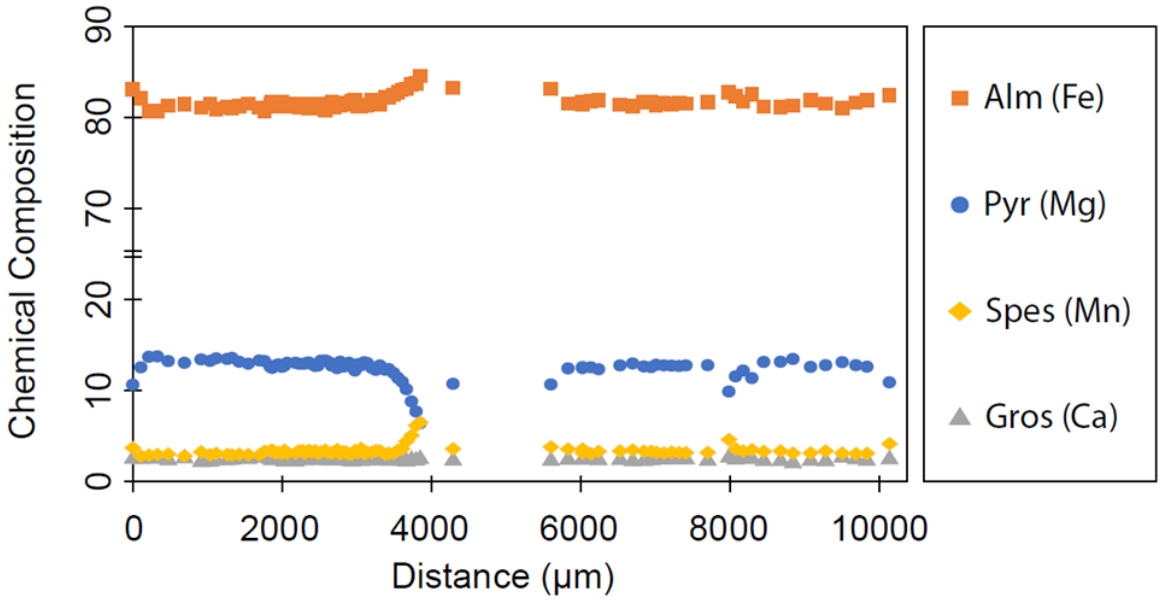

Figure 33 – Diagram showing garnet compositions analysed in traverse throughout a porphyroblasts

4.6 ZIRCON ANALYSES

Fifteen different samples from the Inzie Head coastal section were selected for zircon isotope analyses. Internal textures of separated zircon grains from selected unmingled and mingled igneous samples, as well as metapelitic and leucosome crustal rocks, were examined and domains selected for further analyses.

4.6.1 ZIRCON TEXTURES AND U-PB ISOTOPE ANALYSES

In-situ U-Pb isotope analyses on zircon of the different rock types were performed to establish crystallization ages for each sample and thus to identify potential co-magmatic behaviour, as well as the possibility of inheritance of older or previously formed zircon domains. Internal textures of zircon grains and in-situ isotope analyses are presented below, categorized according to the different rock types. Five hundred and seventy-two U-Pb spot analyses were performed on zircon grains from the fifteen selected samples. The full data set as well as individual Tera-Wasserburg and Wetherill concordance plots can be found in appendix III. Most zircon domains from the thirteen igneous samples are characterized by a wide spread of obtained dates from around 400 – 600 Ma, with a predominant age population density of obtained $^{206}Pb/^{238}U$ dates at ca. 470 Ma. However, eleven of these samples yielded sporadically older $^{206}Pb/^{238}U$ and $^{207}Pb/^{206}Pb$ dates, scattering up to 2.87 Ga. These older dates are indicative for inheritance and represent analyses spots generally taken in core-like or inner areas, often associated with blurred oscillatory zoning or rather featureless domains. For further calculations was the focus set on the younger age population < 600 Ma, as the highest density of concordant measured ages spread from around 430 – 530 Ma.

Approximately half the sample set is characterized by a high number of sub-concordant to highly discordant data points, failing a discordance test of < 5%, which possibly relates to partial lead loss and the presence of a common lead, respectively. Based on the spatial resolution and the ablating spot size, it is not possible to give an unambiguous interpretation of the dates, as mixed analyses of different zircon domains are a likely occurrence, due to the complex internal texture of the grains. The ablation of more than one zircon domain may thus also contribute to the discordant behaviour of the data points. These can likely but not necessarily be related to the observed outer rim structures in the CL images. A strict concordance test as a filter or limiting factor was therefore not applied. Collected data points were drawn on Concordia diagrams and, even though typically used for detrital zircon populations, plotted with the Zircon Age Extractor (ZAE) function of Isoplot (Ludwig, 2012).ZAE plots were solely used for visualization purposes to show the apparent U-Pb age spread of around 30 million years, given within each sample. Figures shown below therefore display the analysed U-Pb dates per sample, colour coded according to their degree of concordance. The quoted uncertainties of the individual analyses are given in 2σ and symbolized by the box heights of in the diagrams. Additionally, were kernel density estimations plotted and added to the ZAE figures, giving an idea of the highest age distribution density of each sample. Taking all of that into account and in combination with the CL images, were representative analyses spots of each sample selected, for calculations of the weighted average $^{206}Pb/^{238}U$ age of the magmatic fraction. Potential metamorphic influences are indicated by Th-U ratios < 0.1 and highlighted on the figures.

4.6.1.1 ZIRCON TEXTURES AND U-PB ANALYSES OF DIORITIC MINGLED AND UNMINGLED SAMPLES

Extracted zircon grains from the dioritic rocks show sub- to anhedral crystal shapes, typically 40 – 120 µm in length. CL images reveal a complex nature of contorted patchy and convoluted inner domains, characterized by a high degree of resorption and overgrowth (fig. 34). Occasionally, concentric zoned or featureless rim-like structures appear, although not uniformly, in bright white to darker grey CL that are either truncating, penetrating or following parallel to the internal structure. Remnants of blurred magmatic oscillatory zoning, as well as potential primary core-like domains are sporadically preserved. The convoluted internal textures of zircon from the unmingled diorite sample s7A (fig. 34 – a) are overall comparable to the internal textures of zircon grains from mingled and/ or mixed samples (fig. 34 – b-d).

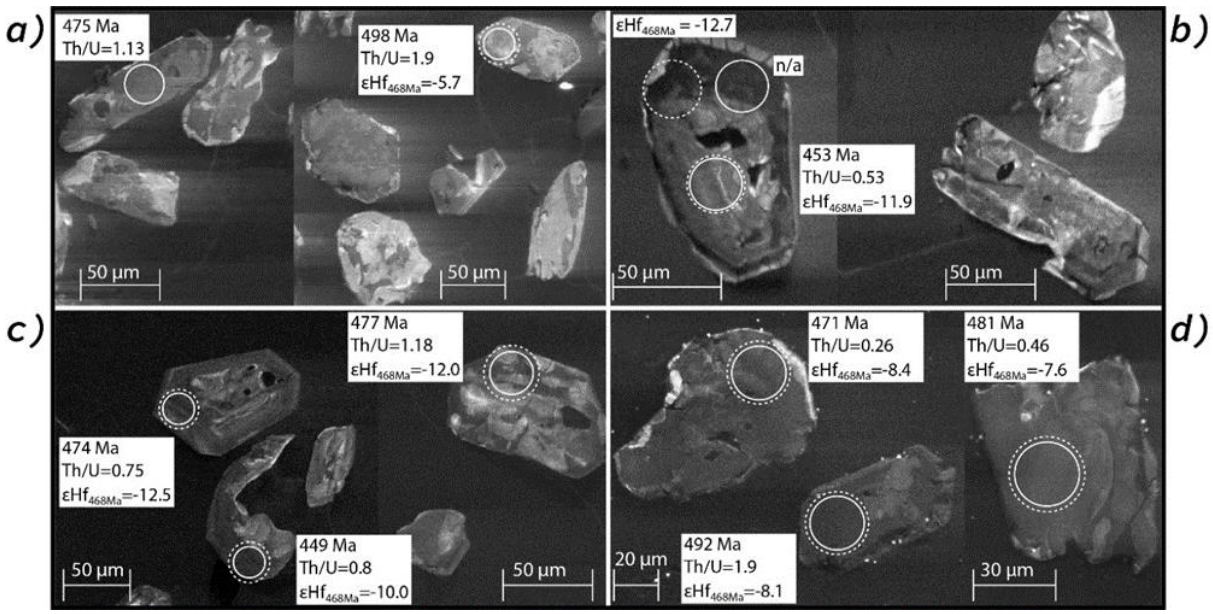

Figure 34 – Cathodoluminescence images with in-situ isotope analyses (white boxes) of separated zircon grains from different mafic samples; a) internal zircon textures of grains from the unmingled diorite sample s7A; b) internal zircon textures of grains from the potentially mixed diorite sample s5A; c) internal zircon textures of grains from the mingled diorite sample s5Bb; d) internal zircon textures of grains from the mingled diorite sample s8Db

One hundred and sixteen $^{206}Pb/^{238}U$ dates < 600 Ma of zircon from the dioritic rocks were obtained and presented in fig. 35. Three data points were neglected, as samples s5Bb, s7A and s8Db each have a single analysis giving a date older than 600 Ma. The nineteen spot analyses of zircon from the unmingled sample s7A range from 461 – 499 Ma in a comparatively small age spread, yielding a crystallization age at 469 ±3 Ma with a mean squared weighted deviation (MSWD) of 1.7 (fig. 35 – a, table 6). Note that a MSWD of > 1.8 – 2.0 usually means that the analyses scatter outside the analytical error and no longer form a uniform age group. However, processes such as Pb-loss or addition of common Pb can cause the elevated MSWD. Compared to zircon from the other dioritic rocks, shows the potentially mixed sample s5A the biggest range in measured U-Pb dates, spreading nearly continuously from 417 – 521 Ma (n=38). Data points are overall less concordant when compared to analyses obtained from the unmingled sample s7A. However, a correlation of discordant analyses with Th/ U ratios < 0.1, that have the potential to indicate metamorphic processes, is not observed, although a tendency towards younger dates (below 440 Ma) can be seen (fig. 35 – b). Weighted mean calculations give a crystallization age of 452 ±4 Ma with an MSWD of 2.5 (table 6). The dioritic domain s5Bb of the gradual contact is characterized by a significant number of highly discordant data points, spreading nearly continuously from 447 – 500 Ma. This sample is the only dioritic sample with Th/U ratios < 0.1 (fig. 35 – c). The calculated crystallization age at 461 ±3 (MSWD=2.8) is slightly older than sample s5A (table 6). U-Pb analyses of the dioritic domain s8Db of the contact sample gives the oldest calculated age of the dioritic rocks at 472 ±2 (MSWD of 1.4). The sample is characterized by a relatively high amount of concordant data points, comparable to the unmingled diorite sample s7A (table 6).

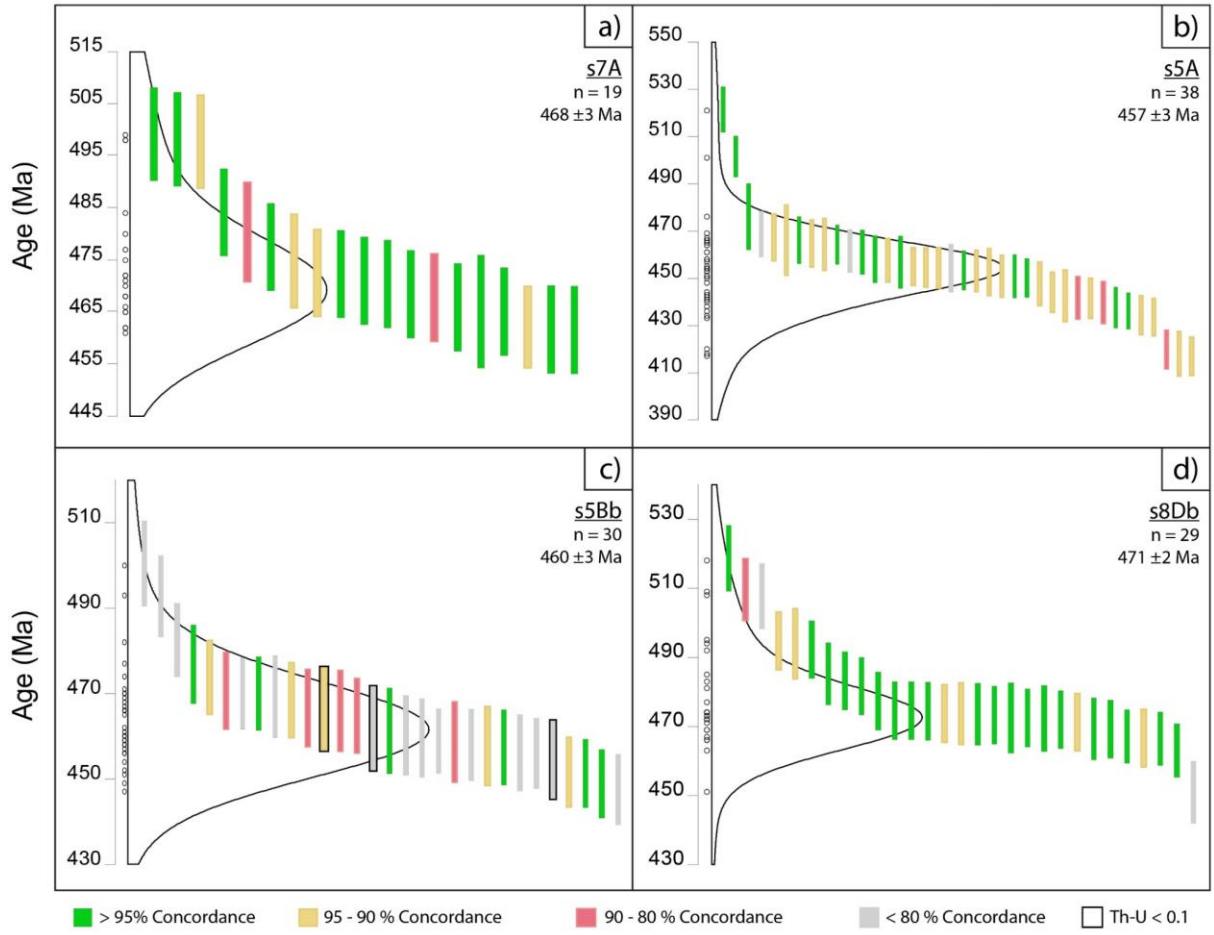

Figure 35 – Measured U-Pb dates of dioritic samples; a) measured age spread of zircon from the unmingled sample s7A; b) measured age spread of zircon from the potentially mixed sample s5A; c) measured age spread of zircon from the mingled sample s5Bb; d) measured age spread of zircon from the mingled sample s8Db; box heights represent 2σ uncertainties

4.6.1.2 ZIRCON TEXTURES AND U-PB ANALYSES OF GRANITIC MINGLED AND UNMINGLED SAMPLES

In comparison to the dioritic samples, zircon grains separated from the granitic samples are generally larger in size, ranging up to ca. 300 µm in length, characterized by euhedral to subhedral crystal shapes (fig. 36). Well-defined to blurred oscillatory zoning patterns, as well as preserved core-like domains are predominating internal textures in zircon grains from the granitic samples (fig. 36). Inner core-like domains are often rounded and expose convoluted and disturbed textures, with weak signs of resorption or blurred primary zoning patterns. Most grains show surrounding rim domains, that either truncate and penetrate the inner core-like areas or surround the inner domain in a nearly indistinguishable pattern. Zircon grains of unmingled and mingled granitic rocks are characterized by overall similar internal textures. A minority of grains from mingled and unmingled granitic samples show patchy and contorted inner domains, comparable to zircon textures of the dioritic samples (fig. 36 – c-e).

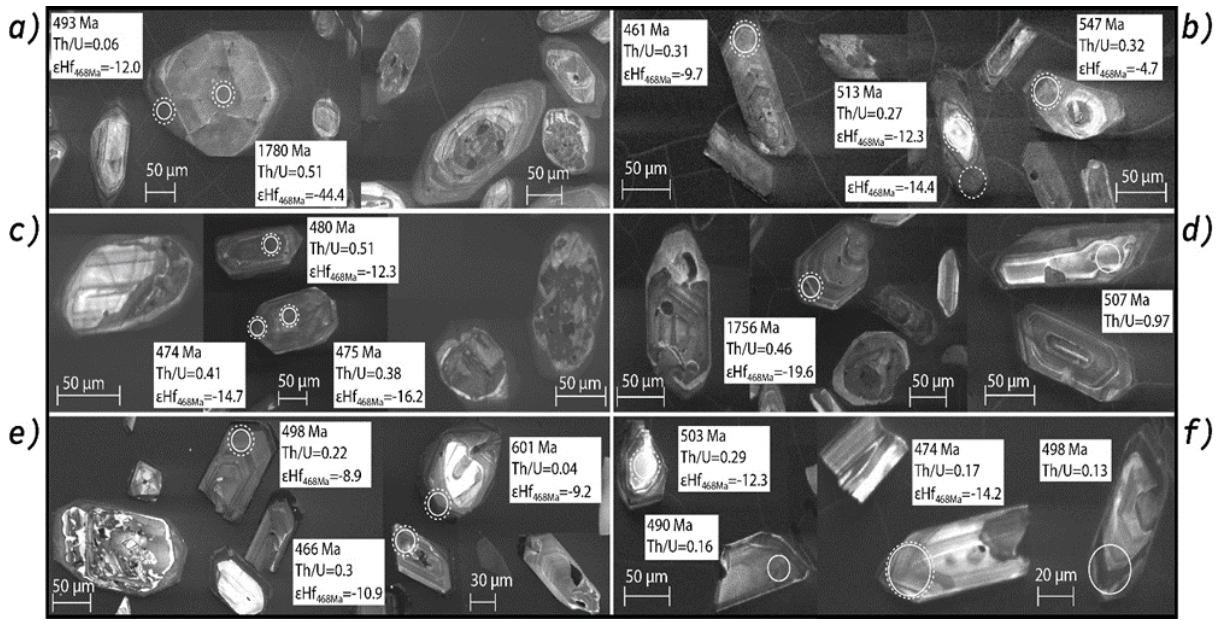

Figure 36 – Cathodoluminescence images with in-situ isotope analyses (white boxes) of separated zircon grains from different granitic samples; a) internal zircon textures of grains from the unmingled granite sample s1F; b) internal zircon textures of grains from the unmingled granite sample s2B; c) internal zircon textures of grains from the unmingled granite sample s3B; d) internal zircon textures of grains from the unmingled granite sample s7B; e) internal zircon textures of grains from the mingled granite sample s1Da; f) internal zircon textures of grains from the mingled granite sample s8Da

Two hundred and sixteen analyses < 600 Ma were attained on zircon from the granitic samples, overall spreading from 446 – 564 Ma, with a single outlying and highly discordant analysis at 404 Ma. Unmingled (fig. 37 – a-d) and mingled (fig. 37 e+f) granitic samples are characterized by wide spreads of measured dates, overall similar to the dioritic rocks. Granite s1F has the highest population (n=12) of excluded analyses with older apparent ages > 600 Ma. The remaining thirty-eight analyses spread from 451 – 532 Ma, with the outlier that was mentioned above at 404 Ma (fig.37 – a). Additionally, is this sample characterized by the highest amount of analyses with Th/U ratios < 0.1 (n=12), which may be linked to the rim textures seen in the CL images. The calculated mean gives a crystallization age at 469 ±3 Ma with an elevated MSWD of 4.2 (table 6). A significant amount of discordant data points were obtained for sample s2B (fig. 37 – b). With analysed dates spreading from 456 – 513 Ma and two slightly older at ~546 Ma, gives this sample a calculated age of 468 ±3 Ma (MSWD=2), similar to sample s1F (table 6). The fifty-six analyses obtained from zircon grains of sample s3B form a seemingly continuous age spread from 446 – 542 Ma. However, when plotted on a Concordia diagram, the spot analyses seem to form two clusters (appendix III). Given no obvious correlation between the analysed dates and the zircon domain identified in the CL, both clusters were calculated separately. This gives a mean age for the younger population of s3B – 1 at 455 ±2 Ma (MSWD=1.17) and for the older cluster s3B – 2 of 475 ±2 Ma (MSWD=1.3). Analysed dates for sample s7B spread from 456 – 524 Ma, giving a calculated age of 476 ±3 with an MSWD of 2.9. With thirty-four analyses, spreading from 466 – 564 Ma, gives the granitic domain s1Da of the mingled contact sample the oldest calculated crystallization age of granitic rocks at 483 ±3 Ma (MSWD=2.2; table 6). The other mingled granitic domain s8Da spreads from 464 – 538 Ma, with a relatively small data set of nineteen U-Pb analyses. In comparison with the dioritic contact domain (s8Db = 472 ±2 Ma) is the calculated crystallization age at 479 ±5 (MSWD=4.8) slightly older but within error overlapping (table 6).

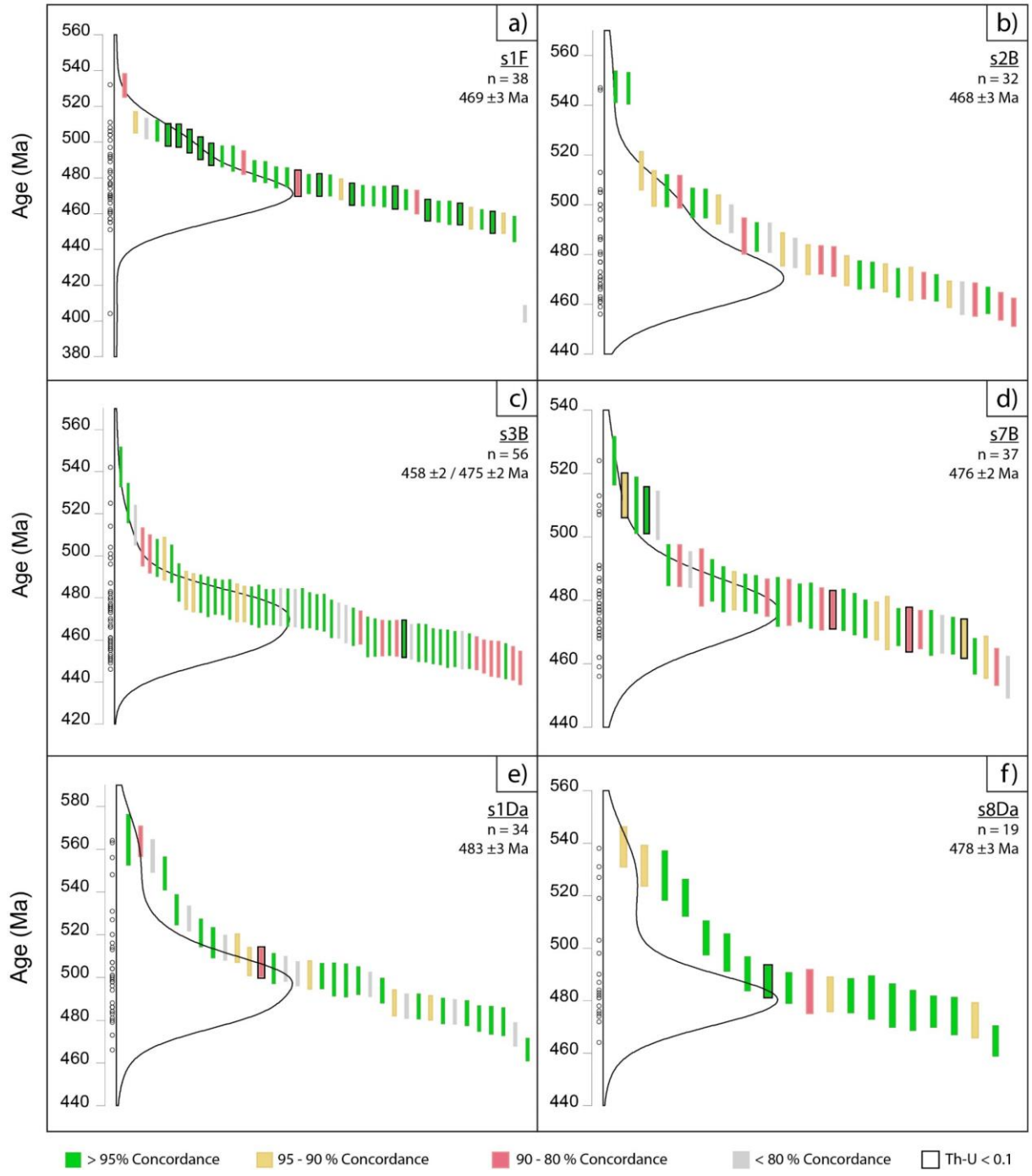

Figure 37 – Measured U-Pb dates of granitic samples; a) measured age spread of zircon from the unmingled sample s1F; b) measured age spread of zircons from the unmingled sample s2B; c) measured age spread of zircon from the unmingled sample s3B; d) measured age spread of zircons from the unmingled sample s7B; e) measured age spread of zircon from the mingled sample s1Da; f) measured age spread of zircon from the mingled sample s8Da; box heights represent 2σ uncertainties

4.6.1.3 ZIRCON TEXTURES AND U-PB ANALYSES OF MINGLED GRANODIORITIC SAMPLES

Zircon grains separated from the granodioritic samples show inner structures that are predominated by inner, core-like and outer, rim-like domains of contrasting CL (fig. 36). The inner, core-like domains reveal blurred oscillatory zoning, wide banded and convoluted patterns or appear featureless, comparable to textures exposed by zircon grains of granitic and dioritic rocks. The complex inner textures are frequently surrounded by thin, asymmetrical rims, that often penetrate the inner domains. Irregular resorption and recrystallization fronts are indicative features for variable degrees of alteration (fig. 36 – a).

Zircon grains are generally around 110 µm in length, occasionally ranging up to ca. 300 µm, with predominantly subhedral crystal shapes.

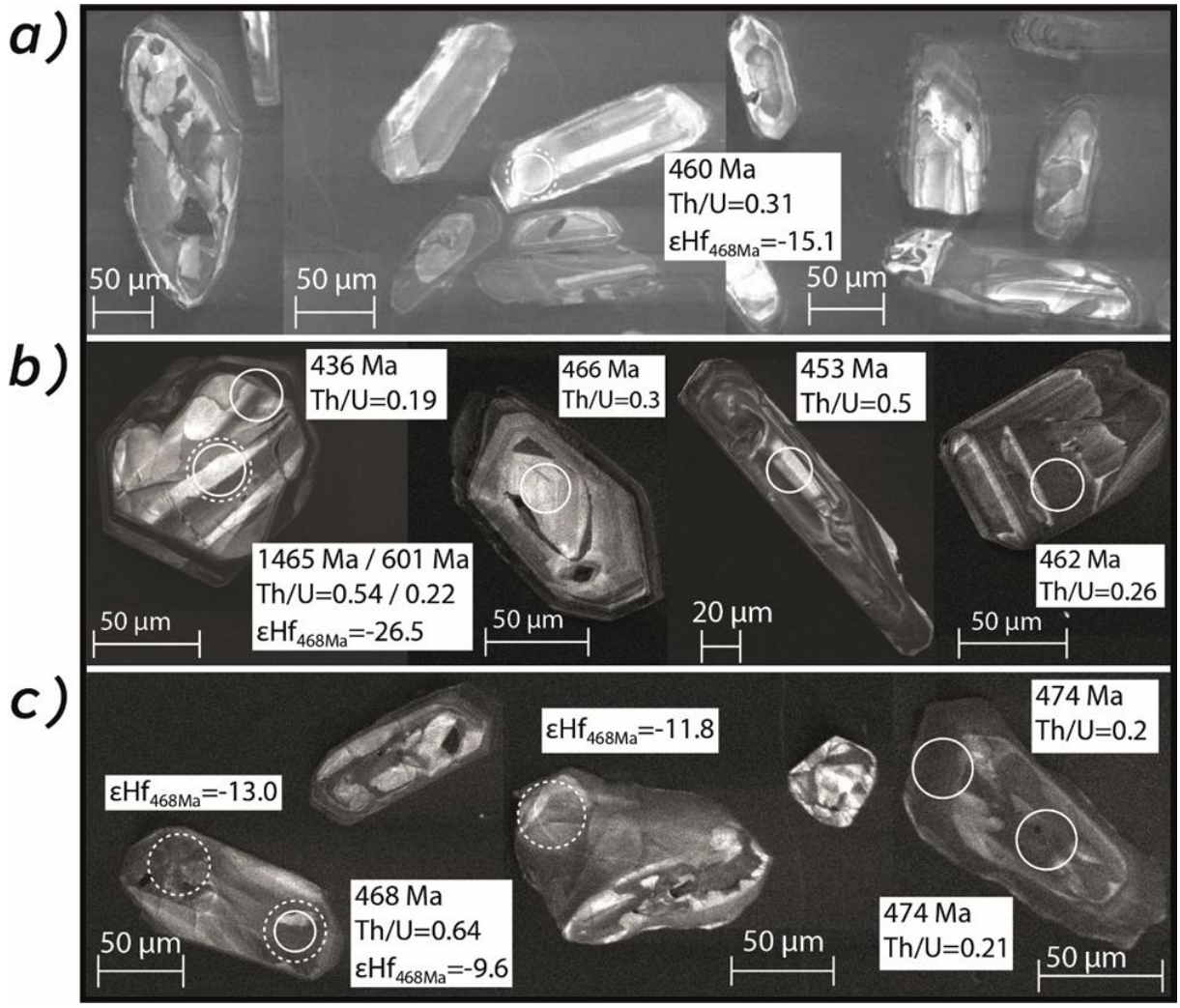

Figure 38 – Cathodoluminescence images with in-situ isotope analyses (white boxes) of separated zircon grains from different granodioritic samples; a) internal zircon textures of grains from the potentially mixed sample s1B; b) internal zircon textures of grains from the potentially mixed sample s1H; c) internal zircon textures of grains from the mingled contact sample s5Ba

Eleven of eighty-one useable analyses of the granodioritic rocks gave measured ages older than 600 Ma, of which seven were obtained from sample s1B. The remaining thirty-three analyses of sample s1B spread from 444 – 575 Ma, giving a calculated age of 463 ±4 Ma with a relatively high MSWD of 4.8 (table 6). Sample s1H has the smallest data set of eleven useable analyses, of which only three data points can be considered as concordant. Ranging from 436 – 518 Ma is the calculated age for this sample at 458 ±4 (MSWD=1.13). Additionally, sample s1H is the only granodioritic rock with no Th/U ratio < 0.1. Similarly, as described for sample s3B above, shows sample s5Ba two clusters with higher proportions of analysed U-Pb dates (fig. 39 – c). Averaged ages were calculated individually, giving an age for the younger population s5Ba – 1 at 448 ±4 Ma (n=11) and for the older population s5Ba – 2 at 475 ±4 Ma (n=11). Th/U ratios < 0.1 were obtained by six analyses, which spread through the given age range. Obtained zircon dates of sample s5Ba show a higher spread than obtained zircon dates of the mafic sample domain s5Bb. Whereas zircon dates spread nearly continuously from 450 to 470 Ma in sample s5Bb, ranges the obtained spread in the granodioritic domain of s5Ba from 440 to 480 Ma.

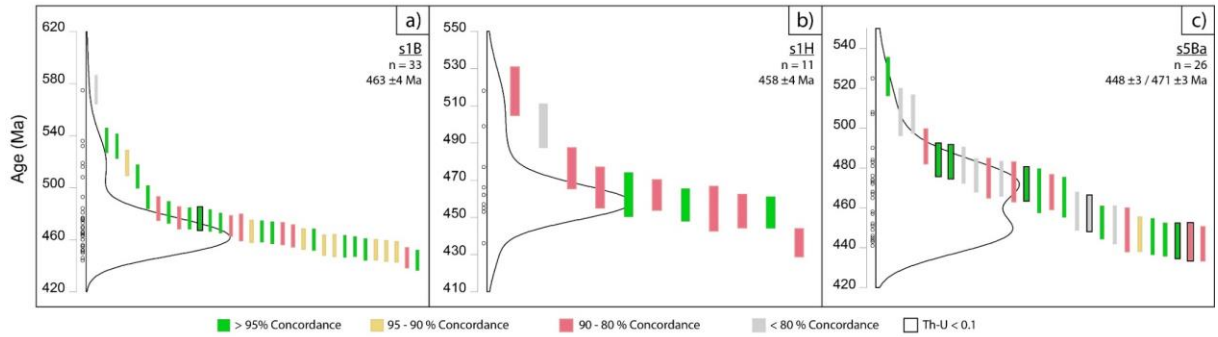

Figure 39 – Measured U-Pb dates of mingled or mixed granodioritic samples; a) measured age spread of zircon from sample s1B; b) measured age spread of zircon from sample s1H; c) measured age spread of zircon from sample s5Ba; box heights represent 2σ uncertainties

TABLE 6: CALCULATED ZIRCON U-PB CRYSTALLIZATION AGES. SAMPLES ARE COLOUR CODED FOR THE INDIVIDUAL ROCK TYPES: GREEN = DIORITE, YELLOW = GRANODIORITE, PINK = GRANITE

Sample	Age	±2σ	MSWD	n/ rejected
s5Ba – 1	448	4	1.6	11/ 0
s5A	457	3	1.5	21/ 0
s1H	458	4	1.1	8/1
S3B – 1	458	2	0.3	15/ 0
s5Bb	460	3	2.7	24/ 0
s1B	463	4	4.8	22/ 0
s2B	468	3	2.0	9/ 0
s7A	468	3	1.5	12/ 0
s1F	469	3	4.2	14/ 0
s8Db	471	2	0.8	19/ 0
s5Ba – 2	471	3	0.7	8/ 0
S3B – 2	475	2	1.3	25/ 0
s7B	476	2	2.4	22/ 0
s8Da	478	3	1.6	10/ 0
s1Da	483	3	2.2	12/1

4.6.1.4 ZIRCON TEXTURES AND U-PB ANALYSES OF METAPELITE AND LEUCOSOME SAMPLES

Zircon grains separated from the metapelite (s2A) and garnet-bearing leucosome (s4D) sample appear with subhedral and regularly rounded crystal shapes (fig. 37). CL images reveal internal textures, with core-like inner areas and an irregularly surrounding domain, comparable to those described for the granites above. Blurred oscillatory zoning to nearly featureless textures, with signs of alteration, are predominant. Crystal sizes range up to ~250 µm (s2A) and ~150 µm (s4D), in length.

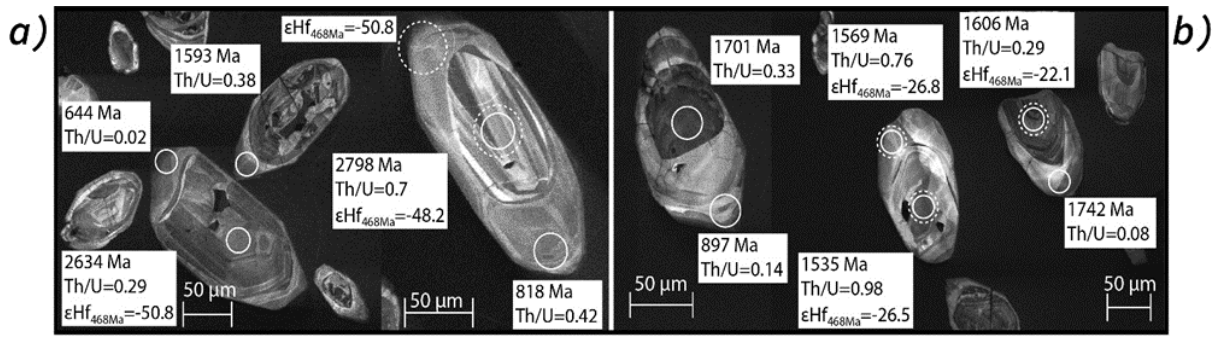

Figure 40 – Cathodoluminescence images with in-situ isotope analyses (white boxes) of separated zircon grains from the metapelite; (a) and leucosome (b) samples

Analysed zircon grains of the metapelitic sample s2A and the leucosome sample s4D are both characterized by similar discontinuous spreads in measured U-Pb and Pb-Pb dates. Obtained analyses of both samples spread from ca. 450 Ma to 2.8 Ga, with two age gaps occurring in between (fig. 41 – a+c). Kernel density estimations form three peaks, of which the youngest peak, between 400 – 600 Ma indicates the most recent event and thus may imply the occurrence of partial melting. Of the seventy-nine isotope analyses from zircon of the metapelitic sample s2A, give nine analyses apparent U-Pb ages < 600 Ma, spreading from 440 – 598 Ma (fig. 41 – b). Six of these analyses are characterized by Th-U ratios < 0.1. Seven of the forty-four zircon analyses attained from the garnet-bearing leucosome sample s4D are younger than 600 Ma, spreading from 463 – 593 Ma (fig. 41 – d). Six of these seven analyses give Th/U ratios < 0.1. The younger zircon ages of both samples are predominated by discordant U-Pb dates.

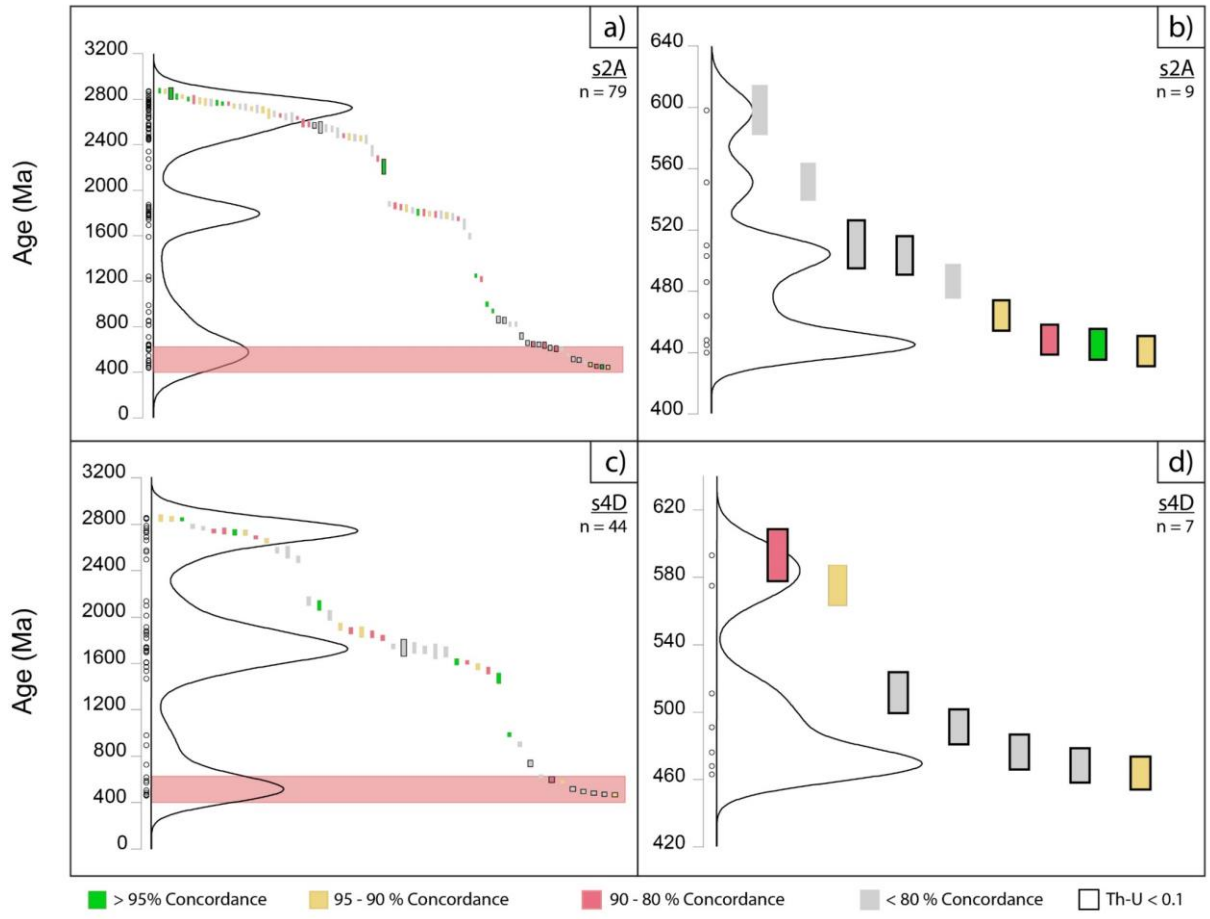

Figure 41 – Measured U-Pb dates of the metapelitic and leucosome samples; a) measured age spread of zircon from the metapelite sample s2A; b) measured ages < 600 Ma of zircon from the metapelite sample s2A; c) measured age spread of zircon from the leucosome sample s4D; d) measured ages < 600 Ma of zircon from the leucosome sample s4D; box heights represent 2σ uncertainties

4.6.2 ZIRCON LU-HF ISOTOPE ANALYSES

A total of three hundred and seventy-two in-situ Lu-Hf isotope spot analyses were performed, whenever possible, on the same zircon domains as previously analysed for U-Pb geochronology. One hundred and sixteen Lu-Hf analyses were obtained on core and rim domains, from fifty-five zircon grains, to reflect the compositional variations within single grains. Measured $^{176}Hf/^{177}Hf$ ratios are calculated to the mean magmatic crystallization age of 468 Ma (εHf_{468} and $^{176}Hf/^{177}Hf_{468}$), representing the evaluated U-Pb age spread, from 448 ±4 to 483 ±3 Ma, of the igneous samples (Table 6). Weighted averages (WA) of given εHf_{468} values, were first calculated including the full data spread of the individual samples (fig. 42 – a, fig. 43 – a, table 7). A second weighted average (WAmag) for each sample was calculated, including only εHf_{468} values of zircon with U-Pb ages, which fall within the given magmatic age spread (fig. 42 – b, fig. 43 – b, table 7). $^{176}Hf/^{177}Hf$ ratios that were calculated to the individual measured U-Pb or Pb-Pb age of the zircon grain, are hereafter referred to as $^{176}Hf/^{177}Hf_t$ and εHf_t. The Hf isotopic signatures of the four dioritic samples, separates them into two distinct groups (fig. 42). The mingled contact sample s8Db and the unmingled diorite sample s7A that delineated a comparatively older age are characterized by a spread of εHf468 values over 5 and 6 ε units, ranging from ca. -6 ($^{176}Hf/^{177}Hf_{468}$ = 0.28233) to -11 and -12 ($^{176}Hf/^{177}Hf_{468}$ = 0.28216), respectively. Their calculated weighted averages at ca. -8 and -7, are the most juvenile values within this data set (fig. 42, fig. 43, table 7). An overall more negative spread in εHf_{468} values of samples s5A and s5Bb is evident in their WA of ca. -12 (fig. 42, table 7). εHf_{468} varies over 6 ε units in sample s5Bb, from -9 to -15, whereas sample s5A shows a larger spread over 9 ε units, from ca. -8 to -17. As most zircon domains in diorite samples fall within the magmatic age bracket, calculated WAmag for diorite samples are almost identical to the calculated WA, showing only slight variations (< 1 ε unit).

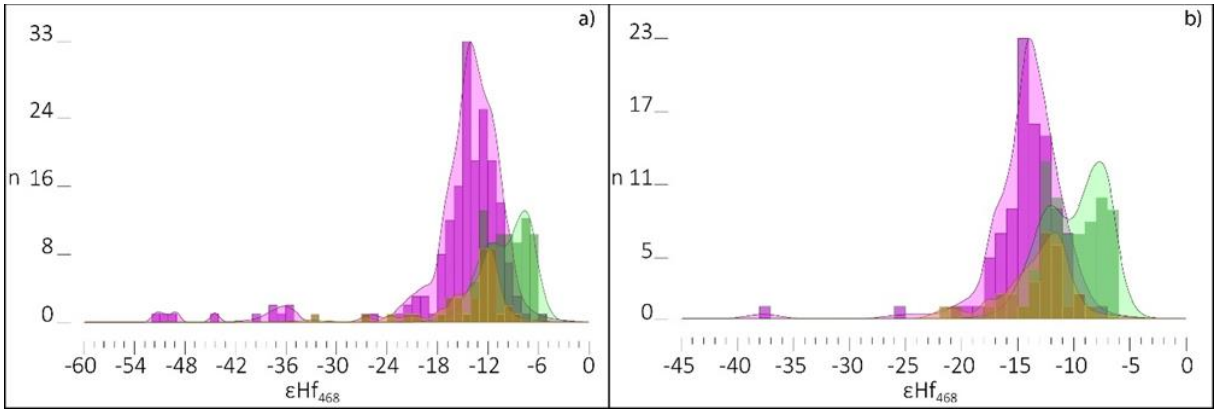

Figure 42 – Obtained spread of εHf_{468} isotopic signatures of the igneous rocks from Inzie Head; Left: probability density plots of εHf_{468} of all zircon domains from granites (pink), diorite (green), and granodiorite (yellow); Right: probability density plots of εHf_{468} of the magmatic zircon fraction

Inherited and magmatic zircon domains of the granitic samples exhibit a wide spread of εHf_{468} values, ranging from -5 to -51 (fig. 42 – a). The main fraction (ca. 87%) of zircon from granitic samples form a near continuous spread in εHf_{468} between ca. -8 and -18 (fig. 42 – a). The spread of εHf_{468} values within individual samples generally varies over 17 to 43 ε units. The contact sample s8Da forms an exception, as strong negative outliers are absent and εHf_{468} values show a significantly smaller spread over 8 ε unit, from -10 to -18 (fig. 43 – a). Calculated WA at ca. -14.5 of the unmingled granite samples s1F, s3B and s7B overlap within error with the WA at -14 of the mingled contact sample s8Da (table 7). However, two samples, the unmingled sample s2B and the mingled contact sample s1Da are characterized by slightly more positive WA values at -11 and -12, respectively, and overlap within error with the more negative values of the mingled dioritic samples s5A and s5Bb (fig. 43 – a, table 7). Establishing the WAmag reduces the MSWD and given spread in ε units within the individual samples. However, the actual WAmag values are generally only slightly differing, with less than 1 ε unit, from the calculated WA of the whole εHf_{468} spread (table 7). The granodioritic sample s5Ba plots, with a WA of ca. -12, in a similar field as the more negative diorites (s5A and s5Bb) and more positive granites (s1Da and s2B). The spread in εHf_{468} over 5 ε units (-8 to -13) in sample s5Ba is notably smaller than the observed scatter over 23 ε units in the granodioritic sample s1B (fig. 43). The main population (88%) of zircon within s1B form a nearly continuous spread from ca. -10 to -18 and the calculated WA (ca. -14) plots within a similar field as most granite samples in this study (table 7). The high MSWD (at 34) of sample s1B is only

slightly reduced to 29, when the WAmag is calculated. Only two εHf values could be obtained for sample s1H, of which only one identifies with a magmatic age < 500 Ma (εHf_{468} = -21).

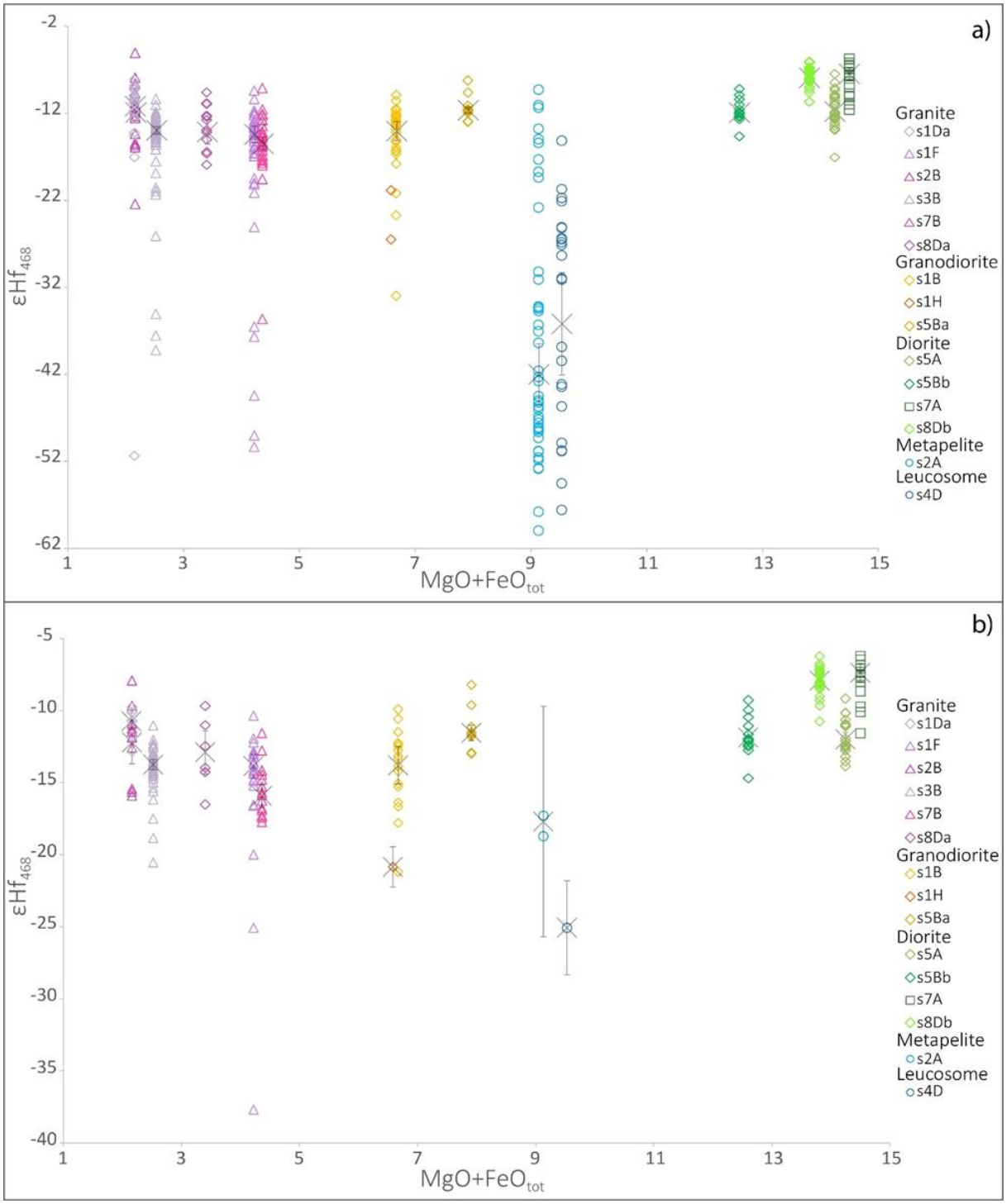

Figure 43 – Calculated εHf_{468} plotted against whole rock $MgO+FeO_{tot}$; a) including εHf468 of all zircon domains and the WA (grey X); b) including εHf468 of the magmatic zircon fraction and the WAmag (grey X)

The metapelite and leucosome samples are both characterized by a high variation of εHf_{468} values. The metapelite sample s2A spreads over 51 ε units from -9 to -60, giving an overall WA of -42 (fig. 43 – a). Two of the three zircon domains with measured U-Pb ages < 500 Ma are within the established magmatic age bracket and have εHf_{468} values between -15 and -19, which give a more positive WAmag of -18 (fig. 43 – b, table 7). A similar heterogeneity of εHf_{468} values is shown within the leucosome sample s4D. Analysed zircon grains vary over 42 ε units, from -15 to -58, with a WA at -36 (Fig. 43 – a, table 7). A single zircon analyses with a magmatic U-Pb < 500 Ma, gives a εHf_{468} value of -25 (Fig. 43 – b). Whereas zircon domains

with older, inherited ages (> 500 Ma) generally show a trend towards more negative ε values, little correlation is observed between the Hf isotopic signatures and the age of inherited domains across the heterogeneity in εHf_{468} for each observed age peak. Analysed zircon domains from the different samples with inherited ages between 800 and 1400 Ma, generally show εHf_{468} values between -9 and -18. This scatter over 9 ε units overlaps with the overall spread of εHf_{468} from magmatic zircon < 500 Ma.

TABLE 7: CALCULATED AVERAGES OF ZIRCON εHf_{468} VALUES; SAMPLES ARE COLOUR CODED FOR THE INDIVIDUAL ROCK TYPES: GREEN = DIORITE, YELLOW = GRANODIORITE, PINK = GRANITE, BLUE = METAPELITE AND LEUCOSOME

Sample	εHf_{468}	±2σ	MSWD	n/rejected	εHf_{468} (mag)	±2σ	MSWD	n/rejected
s7A	-7.4	0.73	5.7	16/0	-7.2	0.62	3.8	15/1
s8Db	-7.9	0.39	5	27/1	-7.8	0.34	3.3	25/2
s1Da	-11.1	0.66	11.7	26/2	-10.8	0.4	2	14/1
s5Ba	-11.6	0.38	1.5	11/1	-11.6	0.38	1.5	11/1
s5A	-11.7	0.47	2.2	32/2	-11.8	0.48	2.2	30/1
s5Bb	-11.9	0.59	1.8	13/1	-11.9	0.59	1.8	13/1
s2B	-11.9	0.85	13	20/1	-12.0	1.3	15	14/1
s1B	-14.0	1.1	34	25/2	-13.6	1.2	29	19/1
s1F	-14.4	0.95	39	42/6	-13.8	0.64	11.1	27/3
s3B	-13.9	0.44	8.8	49/5	-13.8	0.34	4.3	38/4
s8Da	-14.1	1.4	9.6	13/0	-14.5	2	11.8	8/0
s7B	-15.5	0.71	18	30/2	-15.8	0.7	11.3	19/1
s2A	-42.0	3.5	673	43/1	-17.5	1.1	1.12	3/0
s1H	-25.0	31	50	2/0	-20.8	1.4	-	1/0
s4D	-36.2	5.9	897	23/0	-25.1	3.3	-	1/0

εHf calculated to the measured age (εHf_t) of the individual zircon domains, delineate distinct crustal evolution trends (Fig. 44). εHf_t values between ca. 15 (1837 Ma, $^{176}Hf/^{177}Hf_{meas}$ = 0.2820287) and -25 (463 Ma, $^{176}Hf/^{177}Hf_{meas}$ = 0.28178202) for metapelitic and leucosome zircon define, together with zircon domains of the felsic samples, time-evolved εHf_t trends. Such evolution arrays are delineated around 1.3-1.5 Ga and 1.8-2.1 Ga, as well as weakly outlined trends around 2.8 Ga. A single analysis from the unmingled diorite sample s7A, with an older inherited age of 1184 Ma and εHft of 5 ($^{176}Hf/^{177}Hf_{meas}$ = 0.28216565) plots within the evolution array at ca. 1.3-1.5 Ga (Fig. 44). However, such evolutionary trends are not observed for the most positive εHf magmatic values of this data set.

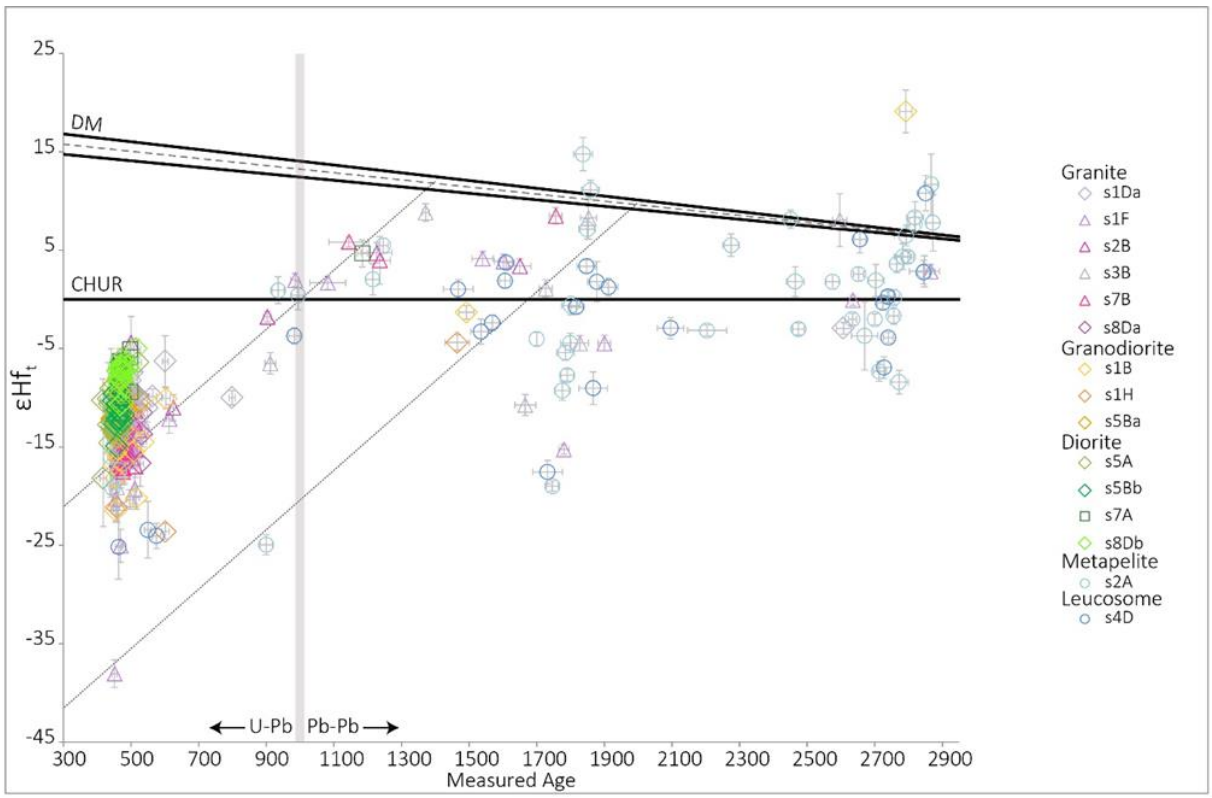

Figure 44 – Plot of εHf$_t$ versus the measured U-Pb and Pb-Pb dates [U-Pb dates are shown to the left of grey line (at 1.0 Ga) and Pb-Pb dates to the right of grey line]; dotted lines indicate crustal evolution trends at 1.4 Ga and 2.0 Ga; Depleted Mantle (DM) arrays (after Blichert-Toft et al., 2002 *and* Griffin et al., 2000)

4.7 APATITE ANALYSES

Rb-Sr and Sm-Nd isotope analyses were conducted on apatites, separated from the same fifteen samples that were selected for zircon analyses. Although potential inner textures of apatite grains (see appendix IV) are an important feature and reported below, the large laser spot size used for apatite analyses (72 – 86 µm for Sr analyses and 40 – 60/ 104 µm for Nd analyses) are generally insufficient to spatially resolve the described small-scale inner patterns (fig. 45). Obtained Sr and Nd isotope ratios are thus usually a result of analyses from more than one apparent apatite domain.

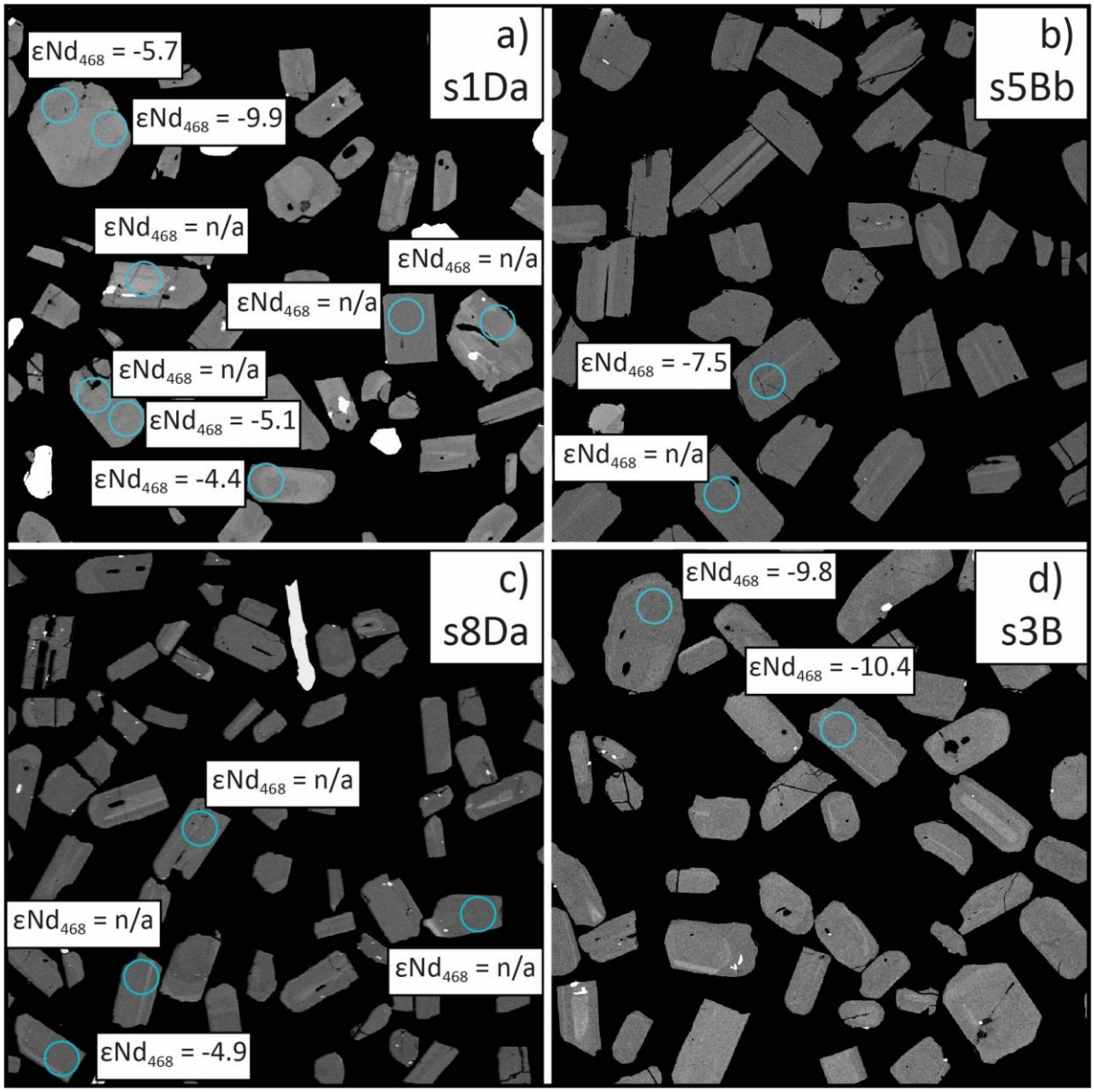

Figure 45 – BSE images with in-situ Sm-Nd isotope analyses of separated apatite grains from different samples; a) internal apatite textures of the mingled granite sample s1Da; b) internal apatite textures of the mingled diorite sample s5Bb; c) internal apatite textures of the mingled granite sample s8Da; d) internal apatite textures of the unmingled granite sample s3B

4.7.1 APATITE TEXTURES AND RB-SR ISOTOPE ANALYSES

Two hundred and twenty-three in-situ Rb-Sr analyses were performed on different apatite grains of the fifteen selected samples. Measured initial $^{87}Sr/^{86}Sr$ isotope ratios are age corrected to the averaged magmatic age of 468 Ma and hereafter reported as Sr_{468}.

4.7.1.1 APATITE TEXTURES AND RB-SR ISOTOPE ANALYSES OF DIORITIC SAMPLES

Apatite grains separated from the unmingled sample s7A and the mingled sample s8Db are characterized by anhedral to irregular, stubby to elongated crystal shapes, varying between 50 – 200 µm in size. Conversely, apatite grains from the mixed and mingled samples s5A and s5Bb are predominated by subhedral, stubby to elongated crystal shapes, ranging in size between 50 – 200 µm, where most grains show apparent inner textures of lamellae that are contrasting in their CL (fig. 45 – b). Isotope analyses of apatites from the diorite samples show a comparatively small but prominent scatter in Sr_{468} values, from 0.7097 to 0.7122, with an outlier at 0.7087 (fig. 46 & 47). The outlying value is the only analyses that was successfully obtained from apatites of the unmingled diorite sample s7A. The highest and thus most evolved Sr_{468} values within the observed spread are given by apatites of the contact sample s8Db, resulting in a weighted average Sr_{468} of 0.7113 ±0.0015 (MSWD=63; n=5; fig. 47, table 8). However, a single outlier gives a much lower value of 0.7097 and is within error not overlapping with the spread of more evolved values (fig. 46). Sr_{468} values of the mixed sample s5A and the contact sample s5Bb yield comparatively lower calculated averages of 0.7102 ±0.0001 (MSWD=0.74; n=7) and 0.7104 ±0.0001 (MSWD=1.5; n=15), respectively (fig. 47, table 8).

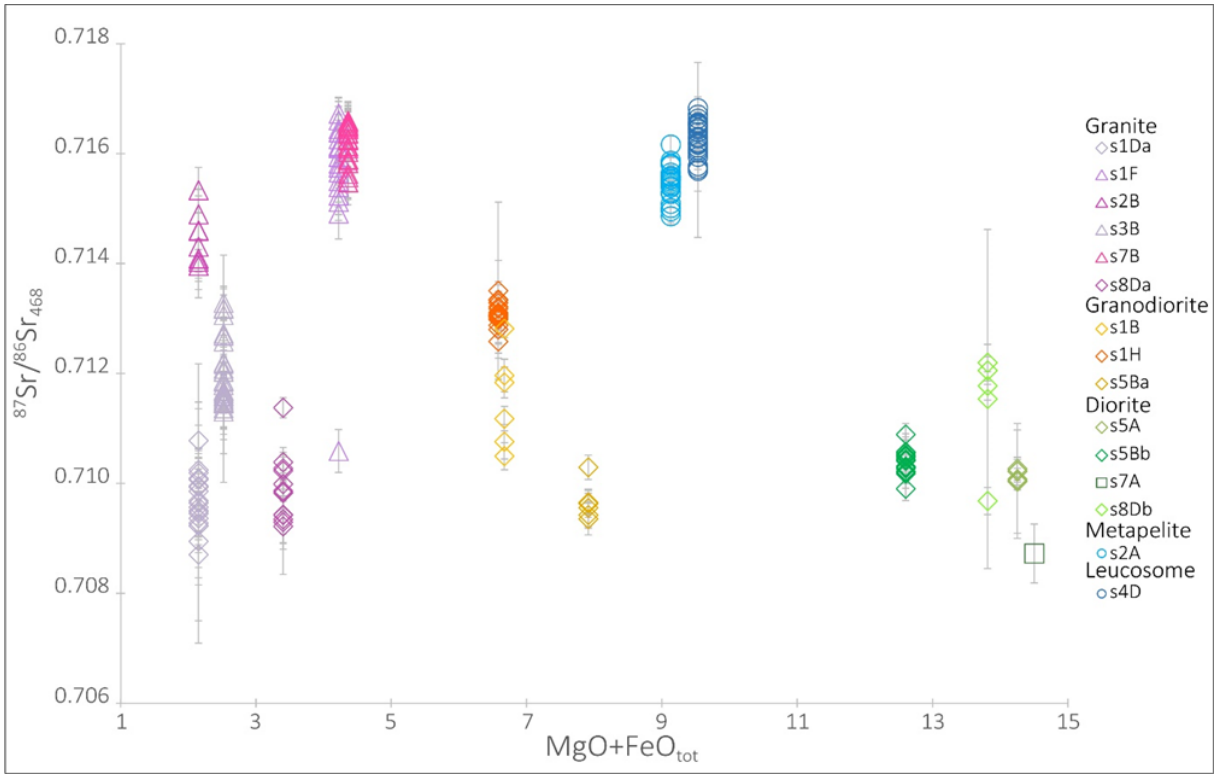

Figure 46 – Binary plot of $^{87}Sr/^{86}Sr_{468}$ isotopic signatures of apatites versus whole rock $MgO+FeO_{tot}$ of the different samples; grey vertical lines represent the uncertainties of each analysis

4.7.1.2 APATITE TEXTURES AND RB-SR ISOTOPE ANALYSES OF GRANODIORITIC SAMPLES

Stubby to elongated and prismatic apatite morphologies are characteristic for all three granodiorite samples (s1B, s1H, s5Ba). Stubby to rounded apatite grains are generally featureless and darker in CL, whereas grains of rather elongated to prismatic shape, usually appear in lighter grey scale with predominant inner lamellae textures. Sample s5Ba as the felsic domain of the gradual contact, shows a relatively homogenous spread, with the lowest Sr_{468} values in the granodioritic sample range from 0.7094 to 0.7103 (fig. 46). The low weighted averaged Sr_{468} of 0.7096 ±0.0002 (MSWD=2.1; n=7) lies below the averaged Sr_{468} values of the dioritic sample domain s5Bb (at 0.7104 ±0.0001; fig. 47, table 8). With higher Sr_{468} values,

ranging from 0.7126 to 0.7135, gives sample s1H a higher averaged Sr_{468} of 0.7131 ±0.0001 (MSWD=1,5; n=16). Sample s1B lies with given values from 0.7105 to 0.7128 and an averaged Sr_{468} value of 0.7118 ±0.0010 (MSWD= 71; n=6), in between the other two granodiorite samples (fig. 46 & 47, table 8).

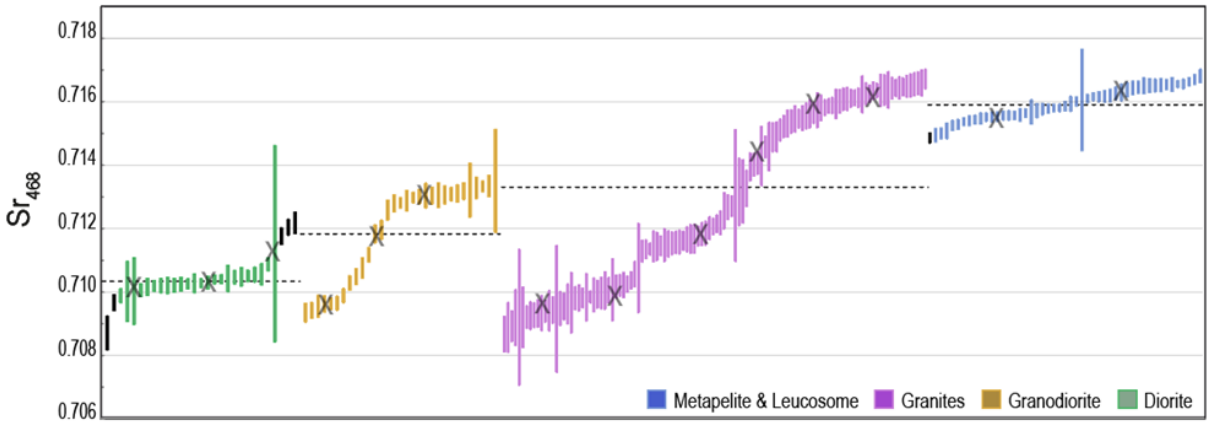

Figure 47 – $^{87}Sr/^{86}Sr_{468}$ isotopic signatures grouped according to rock type; averaged values of the individual samples are represented by grey X; black dotted lines indicate the overall average of all analyses obtained from the different rock types; black boxes represent excluded outliers; box heights represent 2σ uncertainties

4.7.1.3 APATITE TEXTURES AND RB-SR ISOTOPE ANALYSES OF GRANITIC SAMPLES

Apatite grains separated from the unmingled granitic samples (s1F, s2B, s3B and s7B) are predominated by rounded to stubby crystal shapes, with a minority of grains that are characterized by rather elongated shapes. Separated grains range up to 400 µm in size and appear featureless, with thin outermost rims (< 10 µm) of contrasting bright CL (fig. 45 – d). Conversely, apatite grains from the mingled samples s1Da and s8Da are characterized by stubby and rounded to elongated and prismatic needle-like crystal shapes, that do not exceed 250 µm in size. Furthermore, grains may contain fine inclusions as well as inner features, that are weakly defined by lamella and truncating domains of contrasting CL (fig. 45 – a+c). Although the overall spread in Sr_{468} values within the granite samples is relatively large, the mingled samples s1Da and s8Da have a smaller range that define the lower granite boundary of Sr_{468} values (fig. 46). The averaged Sr_{468} of 0.7097 ±0.00020 (MSWD=3.1; n=23) and 0.7099 ±0.0002 (MSWD=4.7; n=13) for samples s1Da and s8Da, respectively, are below the averaged Sr_{468} values of the diorite samples but within range of the mingled sample s5Ba (fig. 47, table 8). Unmingled granitic samples s1F and s7B define the upper boundary of the given value spread, with values ranging between 0.7149 to 0.7167 and 0.7155 to 0.7166 (fig. 46 & 47). A single outlier within sample s1F, gives a lower value of 0.7106 that is in error not overlapping with the higher value spread in the sample (fig. 46). The averaged Sr_{468} values of 0.7160 ±0.00026 (MSWD=8.6; n=18) for sample s1F and 0.7161 ±0.0002 (MSWD=5; n=22) for s7B, are within the highest values of this sample range (fig. 47, table 8). Calculated weighted averages of Sr_{468} for samples s2B and s3B, are within the four distinct averaged values of the granites, yielding values of 0.7145 ±0.0004 (MSWD=5.4; n=8) and 0.7118 ±0.0002 (MSWD=5.1; n=27), respectively (table 8).

TABLE 8: CALCULATED AVERAGES OF APATITE $^{87}Sr/^{86}Sr_{468}$ VALUES; SAMPLES ARE COLOUR CODED FOR THE INDIVIDUAL ROCK TYPES: GREEN = DIORITE, YELLOW = GRANODIORITE, PINK = GRANITE, BLUE = METAPELITE AND LEUCOSOME

Sample	$^{87}Sr/^{86}Sr_{468}$	±2σ	MSWD	n/rejected
s7A	0.7087	0.00053	-	1/0
s5Ba	0.7096	0.00016	2.1	8/1
s1Da	0.7097	0.00020	3.1	23/0
s8Da	0.7099	0.00021	4.6	14/1
s5A	0.7102	0.00010	0.44	6/0
s5Bb	0.7104	0.00007	1.5	17/2
s8Db	0.7113	0.00150	63	5/0
s1B	0.7118	0.00100	71	6/0
s3B	0.7118	0.00017	5.1	28/1
s1H	0.7131	0.00009	1.5	17/1
s2B	0.7145	0.00042	5.4	8/0
s2A	0.7155	0.00010	10.4	23/2
s1F	0.7160	0.00026	8.5	19/1
s7B	0.7161	0.00015	5	22/0
s4D	0.7164	0.00012	10.8	26/0

4.7.1.4 APATITE TEXTURES AND RB-SR ISOTOPE ANALYSES OF METAPELITE AND LEUCOSOME SAMPLES

Rounded and stubby apatite morphologies are predominant within apatites, separated from the metapelitic (s2A) and garnet-bearing leucosome sample (s4D). Apatite grains are generally featureless and in dark grey scale under CL imaging. Fine, rounded inclusions within grains from sample s4D are occasionally in zonal arrangement. The garnet-bearing leucosome sample s4D is characterized by the highest values for Sr_{468}, obtained within this sample set (fig. 46). Values ranging from 0.7157 to 0.7168, yield the highest averaged Sr_{468} of 0.7164 ±0.0001 (MSWD=10.8; n=26) in this study (fig.47, table 8). The comparatively lower Sr_{468} values obtained from apatites of the metapelite sample s2A, range from 0.7149 to 0.7162 and lie within the upper range of the granitic value spread (fig 45). The averaged Sr_{468} of 0.7155 ±0.0001 (MSWD=10.5; n=21) is slightly lower than the highest averaged Sr_{468} values of the unmingled granites s1F and s7B (fig. 47, table 8).

4.7.2 APATITE SM-ND ISOTOPE ANALYSES

One hundred and seventy-eight in-situ Sm-Nd analyses were performed on different apatite grains of the fifteen selected samples. Sm-Nd analyses of apatites from the unmingled granitic sample s1F and the mingled diorite sample s5A were unsuccessful due to the sample integrity during the analytical procedure. Successfully measured initial $^{143}Nd/^{144}Nd$ isotope ratios are age corrected to the averaged magmatic age of 468 Ma and hereafter reported as $^{143}Nd/^{144}Nd_{468}$ and εNd_{468}.

4.7.2.1 APATITE SM-ND ISOTOPE ANALYSES OF DIORITIC SAMPLES

Apatites of the unmingled diorite sample s7A and the mingled sample s8Db show a similar, relatively restricted spread over 2 and 3 εNd_{468} units, respectively (fig. 48). The obtained values vary from -5 ±3 ($^{143}Nd/^{144}Nd_{468}$ ~ 0.51178) to -8 ±3 ($^{143}Nd/^{144}Nd_{468}$ ~ 0.51164), giving calculated weighted averages of ca. -6, with small MSWD below 2 (fig. 49, table 9). However, the two samples are distinct by their respective $^{147}Sm/^{144}Nd$ ratios. Analysed apatites of the mingled sample s8Db show overall lower $^{147}Sm/^{144}Nd$ ratios from 0.148 to 0.227, whereas apatites from the unmingled sample s7A are characterized by a wider spread of higher values from 0.225 to 0.297 (fig. 50). Apatites from the mingled sample s5Bb spread in obtained εNd_{468} over 8 ε units from -5 ±2 to -13 ±2 (fig. 48). The average of -9 ±1 with a higher MSWD=4 of the whole εNd_{468} spread in sample s5Bb, is more negative than the dioritic samples s7A and s8Db (fig. 49). In contrast to the other two dioritic samples, obtained $^{147}Sm/^{144}Nd$ ratios of apatites from the mingled sample s5Bb are lower and relatively uniform, spreading from 0.121 to 0.146 (fig 49).

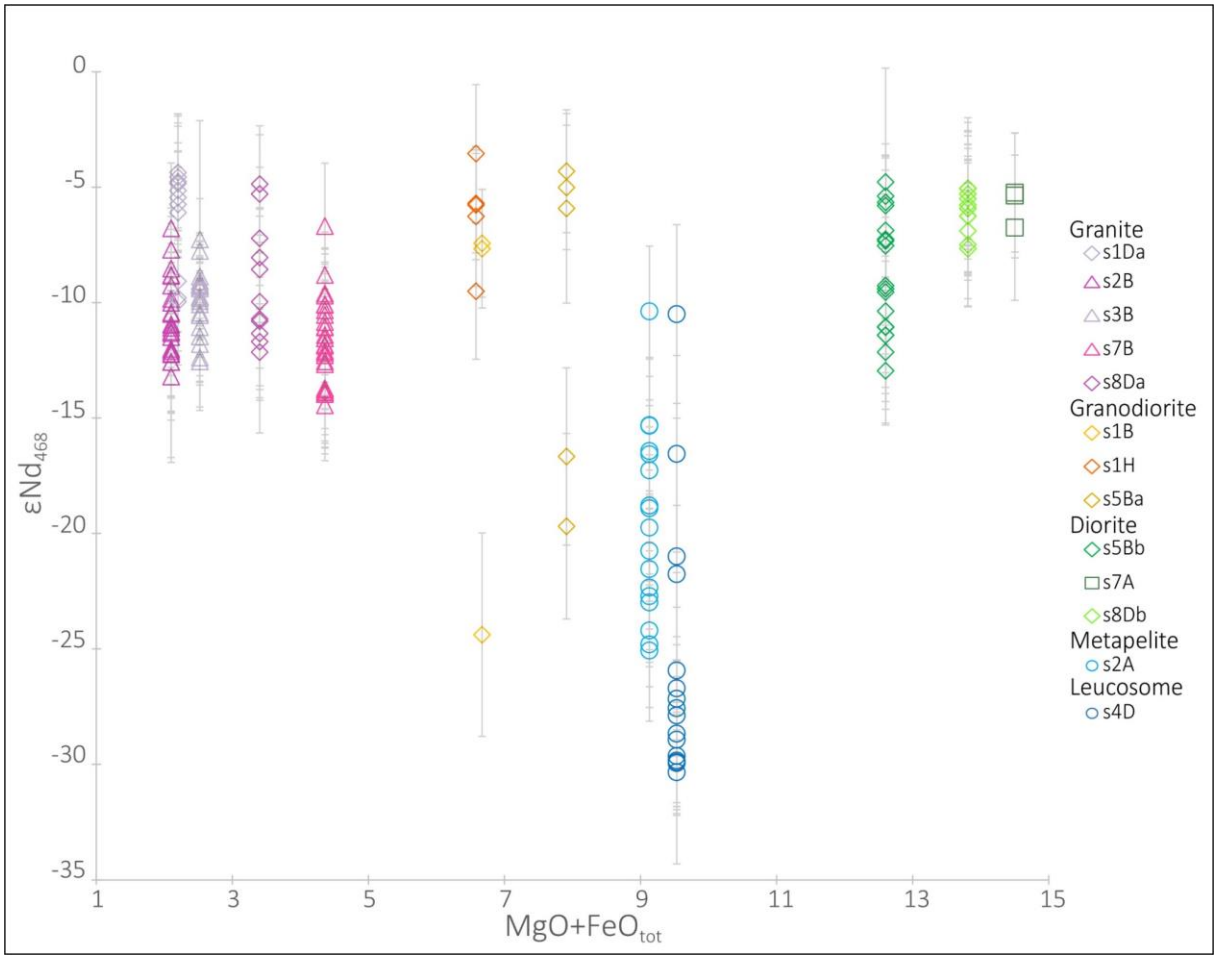

Figure 48 – Binary plot of εNd_{468} isotopic signatures of apatites versus whole rock $MgO+FeO_{tot}$ of the different samples; grey vertical lines represent the uncertainties of each analysis

4.7.2.2 APATITE SM-ND ISOTOPE ANALYSES OF GRANODIORITIC SAMPLES

εNd_{468} values of apatites from the granodioritic samples s1B and s5Ba spread discontinuously over 17 and 16 ε units, respectively (fig. 48). Only three analyses were obtained for sample s1B, with εNd_{468} values at -7±2 and -8±3 and an outlier at -24±4, giving a calculated WA of -10±17 with an MSWD of 25. Obtained εNd_{468} values for sample s5Ba spread discontinuously from -4±3 and -6±4 to -17±4 and -20±4, giving a calculated WA of -9±8 with an MSWD at 17 (fig. 49, table 9). Apatites of sample s5Ba show low $^{147}Sm/^{144}Nd$ ratios, ranging from 0.078 to 0.151, where the given, relatively uniform

ratios of the dioritic contact domain s5Bb fall within (fig. 50). $^{147}Sm/^{144}Nd$ ratios of apatites from sample s1B are higher, spreading from 0.279 to 0.388 (fig. 50). Obtained εNd_{468} values of apatites from sample s1H spread discontinuously from -4±3 to -6±3 and -10±3, giving a calculated WA of -6±2 with an MSWD of 2, which is within error overlapping with the WA of the two diorite samples s7A and s8Db. The obtained $^{147}Sm/^{144}Nd$ ratios of sample s1H are similar to $^{147}Sm/^{144}Nd$ ratios of the unmingled sample s7A, ranging from 0.233 to 0.265.

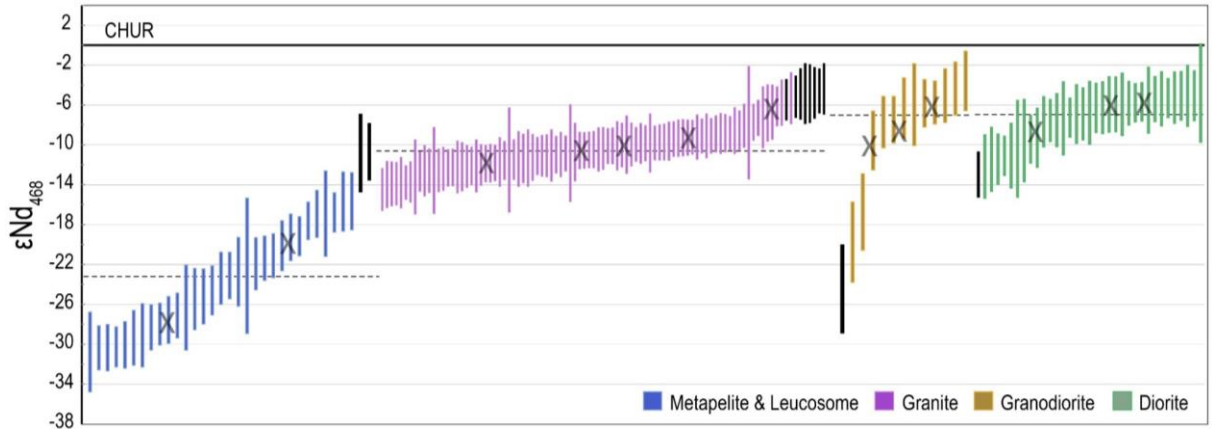

Figure 49 – Spread of εNd468 values grouped according to the different rock types; averaged values of the individual samples are represented by grey X; box heights represent 2σ uncertainties; the dotted lines represent the weighted averages of εNd468 values for the different rock types, whereby black boxes are rejected outliers

4.7.2.3 APATITE SM-ND ISOTOPE ANALYSES OF GRANITIC SAMPLES

With apatite εNd_{468} values, ranging between -4 ±3 and -10±2, comprises the mingled granitic sample s1Da the most positive values within the granitic group (fig. 48). The calculated WA of -6 ±2 is therefore within error overlapping with the two diorite samples s7A and s8Db and the granodioritic sample s1H, whereby the higher MSWD of 3 resembles the higher spread in obtained εNd_{468} values (fig. 49, table 9). $^{147}Sm/^{144}Nd$ ratios vary from 0.393 to 0.453, higher than other samples in this study (fig. 50). The mingled sample s8Da also shows relatively high values in obtained $^{147}Sm/^{144}Nd$ ratios, spreading from 0.299 to 0.366. Both mingled samples, s1Da and s8Da show a slight positive correlation of $^{147}Sm/^{144}Nd$ and $^{143}Nd/^{144}Nd$ ratios (fig. 50). Similar to the mingled dioritic sample s5Bb, εNd_{468} values of sample s8Da show a nearly continuous spread from -5±3 to -12±2, giving a WA of -9±2 with an MSWD at 4 (fig. 49, table 9). The obtained εNd_{468} values of apatites from the unmingled granitic samples s2B, s3B and s7B yield calculated WA of -11±1 (MSWD=2), -10±1 (MSWD=1) and -12±1 (MSWD=1), respectively (table 9). All three samples show similar continuous spreads in εNd_{468} values from -7±2 to -14±2 (fig. 48). With lower values than the two mingled granitic samples (s1Da and s8Da), show the three unmingled samples s2B, s3B and s7B, a similar, relatively narrow range in $^{147}Sm/^{144}Nd$ ratios, from 0.247 to 0.270, 0.242 to 0.260 and 0.253 to 0.290, respectively (fig. 50).

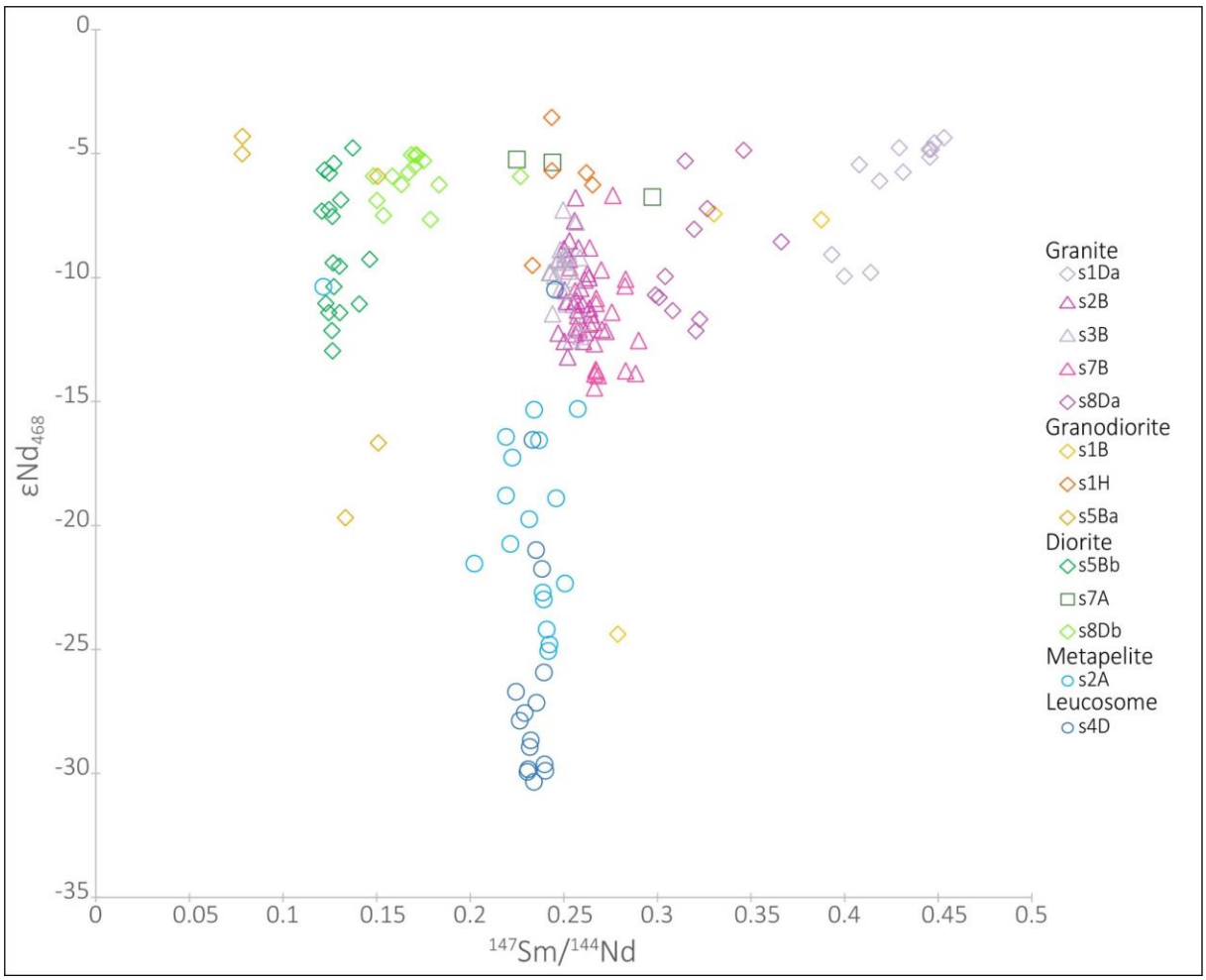

Figure 50 – Binary plot of εNd_{468} versus $^{147}Sm/^{144}Nd$ ratios of apatites from the different samples

4.7.2.4 APATITE SM-ND ISOTOPE ANALYSES OF METAPELITE AND LEUCOSOME SAMPLES

Apatites of the garnet-bearing leucosome sample s4D, exhibit a quite narrow range in $^{147}Sm/^{144}Nd$ ratios, from 0.225 to 0.245 (fig. 50). The spread is slightly lower than seen for the three unmingled granite samples (s2B, s3B and s7B), but within the given range of the metapelitic sample s2A. The range of $^{147}Sm/^{144}Nd$ ratios of apatites from the metapelite sample s2A vary from 0.202 to 0.258 with a major outlier at 0.122. Additionally, shows this outlier a more positive εNd_{468} value of -10±3, compared to the rest of the given spread from -15±3 to -25±3 (fig. 48). This given spread yields a negative WA of -20±2 for the metapelitic sample with a high MSWD of 7 (table 9). εNd_{468} values of apatites from the leucosome sample s4D range from -17±4 to -30±2, with a more positive outlier at -10±4 (fig. 48). The calculated WA of -28±2 (MSWD=5) is the most negative value in this sample set (fig. 49, table 9).

TABLE 9: CALCULATED AVERAGES OF APATITE εNd_{468} VALUES; SAMPLES ARE COLOUR CODED FOR THE INDIVIDUAL ROCK TYPES: GREEN = DIORITE, YELLOW = GRANODIORITE, PINK = GRANITE, BLUE = METAPELITE AND LEUCOSOME

Sample	εNd_{468}	$\pm 2\sigma$	MSWD	n/rejected
s7A	-5.7	1.6	0.7	3/0
s8Db	-6.0	0.7	1.0	14/0
s1H	-6.1	2.4	2.1	5/0
s1Da	-6.3	1.3	3.1	12/0
s5Ba	-8.5	8.3	17	5/0
s5Bb	-8.6	1.3	4.1	18/0
s8Da	-9.2	1.8	4.1	11/0
s1B	-10.0	17.0	25	3/0
s3B	-10.0	0.5	1.3	22/1
s2B	-10.5	0.7	2.0	23/1
s7B	-11.7	0.6	2.5	27/1
s2A	-19.8	1.7	6.8	17/1
s4D	-27.8	1.6	4.6	16/2

4.8 WHOLE ROCK SM-ND AND RB-SR ISOTOPE ANALYSES

Whole rock isotope analyses were performed on ten mafic to felsic igneous samples and four migmatitic metapelites, from the second sample group, which were obtained from the Inzie Head coastal section and the wider Buchan Block area. The highest calculated initial εNd_{468} values of 1.3 ± 0.2 ($^{143}Nd/^{144}Nd$ ~ 0.51253) and -0.6 ±0.2 ($^{143}Nd/^{144}Nd$ ~ 0.51261) were obtained from two mafic samples from the Buchan Block Basic Suite, defining the upper end of εNd_{468} values within this data set (fig. 51, table 10). The mafic samples from the Inzie Head coastal section, as well as a mafic sample from the wider Buchan Block area, yield less juvenile εNd_{468} values between -7 ($^{143}Nd/^{144}Nd$ ~ 0.51210) and -8 ($^{143}Nd/^{144}Nd$ ~ 0.51206). The granitic samples from the wider Buchan Block area, all yield similar εNd_{468} values of -8 ($^{143}Nd/^{144}Nd$ ~ 0.511617) to -9 ($^{143}Nd/^{144}Nd$ ~ 0.51193). Conversely, a mingled granitic sample, that was obtained from the Inzie Head section yields a slightly more positive εNd_{468} values of -7 ($^{143}Nd/^{144}Nd$ ~ 0.51206), comparable to the more negative mafic rocks (fig. 51, table 10). A mingled quartz monzonite from the Inzie Head coastal section yields a distinct, more negative εNd_{468} value of -11 ($^{143}Nd/^{144}Nd$ ~ 0.51189). Migmatitic metapelites from Fraserburgh and the Inzie Head section define the lowest values within this sample spread, ranging between -21 ($^{143}Nd/^{144}Nd$ ~ 0.51130) and -23 ($^{143}Nd/^{144}Nd$ ~ 0.51117). A third migmatite sample from Inzie Head yields a εNd_{468} value of -15, falling between the given granite and migmatite spread (fig. 51, table 10).

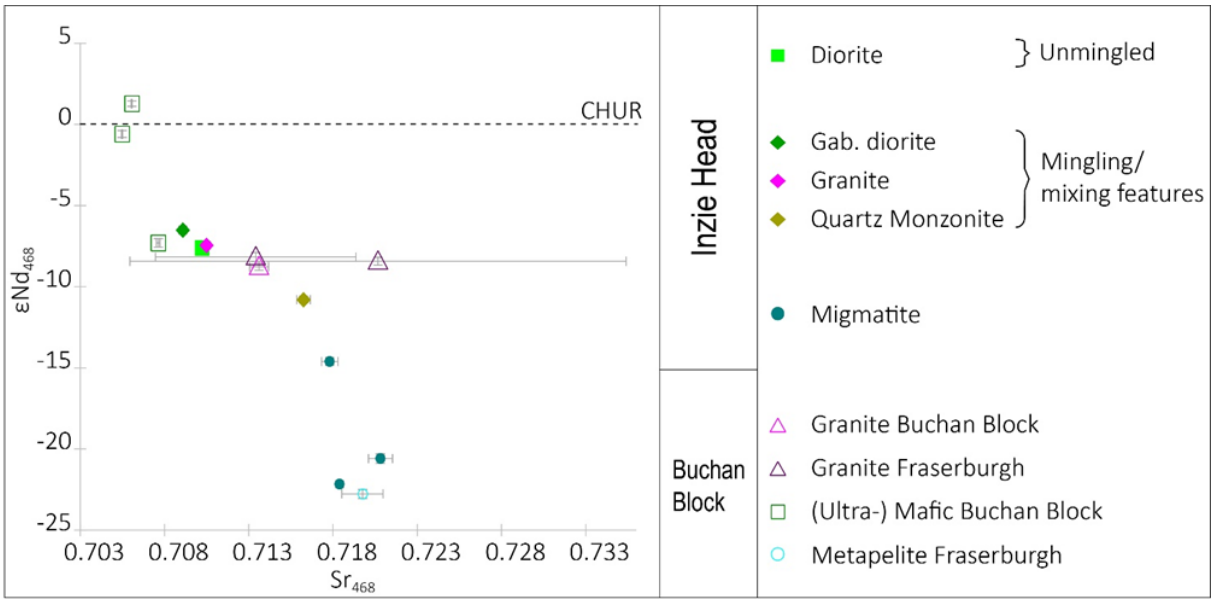

Figure 51 – Binary plot of whole rock εNd_{468} versus Sr_{468} isotopic signatures of samples from Inzie Head and the wider Buchan Block area

The mafic samples, obtained from the wider Buchan Block area, yield comparatively low Sr_{468} values of 0.7055 ±0.00003 and 0.7076 ±0.0001, defining the lowest values in this data set (fig. 51, table 10). The two mafic samples from the Inzie Head coastal section are slightly higher in Sr_{468} values, at 0.7091 ±0.0002 and 0.7102 ±0.0002. The mingled granite sample from the Inzie Head coastal section is again similar in isotopic signature to the dioritic sample, yielding a Sr_{468} value of 0.7105 ± 0.0002 (fig. 51, table 10). The highest Sr_{468} ratios, ranging from 0.7178 ±0.0005 to 0.7208 ±0.0007, were obtained from the migmatitic metapelite samples, as well as a granite sample from the wider Buchan Block area. Sr_{468} values of the two granites from the Buchan Block and the quartz monzonite from Inzie Head vary from 0.7105 ±0.0002 to 0.7163 ±0.0004 (fig. 51, table 10).

TABLE 10: CALCULATED WHOLE ROCK εNd_{468} AND $^{87}Sr/^{86}Sr_{468}$ VALUES; SAMPLES ARE COLOUR CODED FOR THE INDIVIDUAL ROCK TYPES: GREEN = MAFIC ROCKS, ORANGE = QUARTZ MONZONITE, PINK = GRANITE, BLUE = METAPELITIC MIGMATITES

Sample	εNd_{468}	±2σ	$^{87}Sr/^{86}Sr_{468}$	±2σ
s008	-7.3	0.27	0.70763	0.00011
s010	-0.6	0.21	0.70548	0.00003
s013	-8.8	0.22	0.71362	0.00056
s020	-8.2	0.28	0.71341	0.00594
s028	-8.4	0.23	0.72067	0.01473
s029	-22.8	0.28	0.71975	0.00123
s037	-22.2	0.20	0.71839	0.00011
s039	-14.6	0.25	0.71781	0.00048
s040	-20.6	0.28	0.72082	0.00071
s044	-6.5	0.23	0.70909	0.00022
s045	-7.4	0.23	0.71049	0.00016
s046	-7.6	0.30	0.71023	0.00018
s047	-10.8	0.21	0.71625	0.00040
s050	1.3	0.17	0.70606	0.00002

CHAPTER 5 DISCUSSION

Mingling and mixing processes between magmas of different sources are often inferred to occur in MASH zones, postulated at lower, unexposed crustal levels (Annen et al., 2006; Hildreth and Moorbath, 1988). Fundamental in the conceptualization of MASH zones are mantle-derived magmas, that stalled at the crustal base or intruded into crustal layers, acting as providers of heat and material. A sufficient increase in the thermal heat budget has the ability to induce melting processes in adjacent crustal lithologies or previously crystallized mantle additions, creating a zone of local anatexis, where the interaction between magmas of different sources may be promoted (Annen et al., 2006; Collins et al., 2020; Schwindinger and Weinberg, 2017). If heat for partial melting in the crust is supplied by mafic intrusions, studies have concluded that the volume of generated crustal melts cannot exceed the volume of generated granitic melts by differentiation of that same mafic magma (Moyen, 2020). Proposed models have suggested multiple incremental mafic intrusions into crustal levels to create crustal hot zones of magma, heat and volatile accumulation, where intermediate to felsic melts are generated by incomplete crystallization of intruding mafic magmas in combination with remelting of earlier intrusions and partial melting of surrounding crustal lithologies (Annen et al., 2006). The in-situ generation of crustal-derived melts and the partially molten state of the MASH or crustal hot zone has been argued to promote mingling and mixing between contrasting magmas, having the potential to induce chaotic mixing dynamics or magmatic mush systems to form magmas of hybrid composition (Perugini and Poli, 2012; Weinberg et al., 2021). Magmas generated by the contribution of mafic material within dynamic MASH zone environments may separate and ascent to higher crustal levels, proposed to aid the construction of (large) granitoid suites exposed on Earth's surface, describing a crustal growth environment. As mingling and mixing processes are inferred to be driven by complex dynamics, derived rocks in co-magmatic exposures may record variable degrees of magma interaction within single granitoid suites (Perugini and Poli, 2012; Weinberg et al., 2021). Insights into conceptualized MASH zones are bound by the limited number of geological exposures documented to record zones of partial melting, granitic melt formation and interaction of contrasting magmas. The samples in this study from the Inzie Head Formation within the Buchan Block appear to represent an exhumed crustal zone of in-situ anatexis and granitic melt generation, where crustal-derived melts mingled and possibly mixed with intruding mafic magmas. Thus, the exposed relationships of the different rock types within the coastal section of Inzie Head, meet the basic criteria of a crustal MASH zone and in this study serve as a case to investigate the magma interaction processes prevailing within such domains.

5.1 CONSIDERING THE COASTAL SECTION OF INZIE HEAD AS AN EXPOSED MASH ZONE

The Inzie Head migmatitic sequence along the coastal section from Cairnbulg to St. Combs, is interspersed by numerous exposures of intermingled igneous rocks with variable compositions and textures. The complexity of mingling relationships is suggestive for co-magmatic behaviour of the contrasting igneous rocks, characterizing the exposed crustal domain as a zone of potential magma interaction and hybridization processes. The crustal host rocks have been documented to record low-pressure, high-temperature metamorphic conditions, consistent with Buchan-type metamorphism, that resulted in migmatization and partial melting of the sedimentary sequence (Johnson et al., 2003, 2001b, 2001a). Buchan-type metamorphic activity requires the elevation of the normal prevailing geothermal gradient to higher temperatures, while the pressure conditions decrease or remain comparatively low. The high increase in temperature thus required an external source to supplement sufficient heat to drive metamorphic and partial melting processes of the crustal lithologies. Mafic intrusive rocks within the Scottish Grampian Terrane are exclusively found within the high-T metamorphic Buchan Block domain (fig. 4), where constrains from gravity and magnetic anomalies are consistent with the interpretation of an underlying mafic mass beneath a thin lithosphere (Johnson et al., 2017; Viete et al., 2010). The mafic units exposed in the Buchan Block domain are of differing age and have been categorized in two distinct groups, older Dalradian mafic units, formed at ca. 600 Ma, and younger Grampian gabbroic rocks, that were dated to ca. 474 – 470 Ma (Viete et al., 2010). The age of the Grampian gabbroic units is thus consistent with the established timing of peak metamorphic activities in the Buchan domain around 470 Ma, suggesting that the intrusion of the gabbroic magmas as well as the possible intraplating and underplating of similar magmas contributed significantly to the metamorphic heat budget.

Both groups of mafic rocks show REE patterns that are indicative for garnet-absent source regions whereafter a thinned lithosphere of less than 70 km thickness has been construed (Viete et al., 2010). The geochemical compositions of the mafic

rocks have been interpreted to either reflect their derivation from an enriched mantle source or variable amounts of crustal contaminations during ascent and emplacement of the mafic magmas (Viete et al., 2010). Although varying crustal assimilation has the potential to shape the composition of the mafic magmas observed, a clear distinction in geochemical signatures of the two mafic groups has been interpreted to represent different conditions during the melting processes and formation of the mafic magmas (Viete et al., 2010). The older Dalradian units have been interpreted to have formed as products of fluid-present melting of the mantle wedge in an extensional back-arc setting, that developed prior to the onset of the Grampian orogeny. Conversely, the derivation of the younger Grampian units has been related to asthenospheric decompression melting during the Grampian orogeny and were largely formed under fluid-absent conditions. Decompression melting and uprising of the mantle were promoted by syn-orogenic extensional processes and crustal thinning on a lithospheric-scale during the Grampian orogeny (Viete et al., 2010). Consequently, decompression melting may enable mantle derived melts to intrude into crustal layers, whereby the intrusion of mafic magmas into upper crustal layers might be promoted by shear networks formed due to the syn-orogenic structural activities. The dioritic to gabbroic diorite exposures along the Inzie Head section thus possibly derived from the same source as the Buchan Block mafic rocks, representing shallower crustal intrusions that derived from the underlying mafic mass.

The derivation of significant amounts of underplating mantle-derived material, that was emplaced at shallow depth, has the ability to provide heat and fluids necessary to drive in-situ partial melting in overlying or adjacent crustal lithologies, whereby the contribution of mantle-derived material may promote mingling and potential mixing of contrasting magmas within the partially molten system (Perugini and Poli, 2012). This is consistent with leucosome derivations in the Inzie Head Formation, that have been described to have formed preferentially marginal to larger diorite sheets (Johnson et al., 2001b). Field exposures of darker, more mafic diorite intrusions apparently cross-cutting paler-grey granodioritic and possibly earlier hybridized domains are indicative for the intrusion of multiple magma batches into higher crustal levels (fig. 11 – d). The spatial distribution of mafic rocks with variable chemical compositions, juxtaposed by granitoid bodies along the Inzie Head section, suggest that multiple mafic intrusions promoted and possibly maintained partial melting conditions within the system over a prolonged period. Considering that the crustal section was in a partially molten state, magma interaction in form of mingling, mixing and hybridization might have been promoted between the intruding mafic magmas and the crustal derived melts. Previous studies have suggested that an increase in temperature, the resultant partial melting of surrounding metasedimentary rocks by heat transfer and mixing of different magma systems is particularly effective where episodic intrusions of mafic magmas broadly sustain the available thermal heat budget (Perugini and Poli, 2012; Weidendorfer et al., 2014). Increased anatectic melt production may result in decreasing viscosities of the derived magmas, promoting mingling processes and enhancing the potential of chemical mixing of magmas from different sources (Perugini and Poli, 2012). The evidence provided by this study suggests co-magmatic behaviour between the contrasting rocks of Inzie Head, which was accompanied by mingling and possible mixing processes. Given the co-magmatic behaviour and potential for mixing of the contrasting magmas in the Inzie Head domain, the degree to which magma mingling, mixing and hybridization processes shaped the granitic to dioritic exposures must be determined.

5.2 PARTIAL MELTING OF THE CRUSTAL SEQUENCE AND THE DERIVATION OF GRANITOIDS IN THE INZIE HEAD DOMAIN

The Inzie Head Formation is regarded as an important geological exposure, providing insights into the migmatization, partial melting and granitic melt derivation from metasedimentary source rocks, that are significant to the understanding of such processes. Detailed studies on the geochemistry and petrography of the exposed metasedimentary, leucosome and granitic bodies, concluded the in-situ derivation and formation of granitic rocks, that derived from melting of the (mid to upper) crustal sequence (Johnson et al., 2003, 2001a). Constrained peak metamorphic temperatures for the migmatization of pelitic and semipelitic rocks from the Inzie Head section, were sufficiently high to induce partial melting processes. Based on documented peritectic phases and mineral assemblages, studies have concluded an increase in the prevailing metamorphic conditions from upper amphibolite facies in the north-west to granulite metamorphic facies in the south-east of the coastal section. Peak metamorphic conditions of the Inzie Head section have been determined based on equilibrium phase constraints, concluded to have reached 3 – 4.5 kbar and temperatures of minimum 680°C to in excess of 800°C (Johnson et al., 2003, 2001a). The documented low-pressure metamorphism is consistent with pressure conditions expected within mid to upper

crustal levels, equivalent to a depth of ca. 10 – 15 km. However, phase equilibria modelling based on the composition of an average metapelite of the region, determined that the prevailing pressures probably did not exceed 3 kbar, suggesting relatively isobaric heating (Johnson et al., 2015).

Constrains on phase equilibrium modelling suggested that partial melting initially commenced to the west of the Inzie Head section at Fraserburgh under fluid-present conditions, crossing the water saturated solidus at relatively low temperatures. However, limited excess in H_2O resulted in dehydration melting and the incongruent breakdown of hydrous minerals, producing peritectic phases such as garnet (Johnson et al., 2015). Metapelitic rocks exposed along the western shore of the Inzie Head section are generally rich in cordierite and biotite but lack sillimanite and garnet. Whereas the absence in sillimanite is consistent with the modelled compositions, the deficiency in garnet has been explained by the removal of the peritectic phase that derived with the first formed melt (Johnson et al., 2015). Early formed melt must have been sufficient to reach melt connectivity, required for melt segregation, migration and efficient removal of garnet from the system. This is consistent with field exposures, where the initial stages of melt generation are reflected by small leucosome patches and lenses within the metasedimentary horizons, that were capable to form vein networks through which melt migrated upwards into channel ways (Fig. 9). To produce sufficient melt, the authors suggested the addition of small amounts of H_2O, derived from the sub solidus dehydration of nearby rocks of higher solidus temperatures (Johnson et al., 2015). Towards the south-east of the Inzie Head section, peritectic garnet growth has been predicted at temperatures of ca. 760°C followed by its disappearance and the formation of orthopyroxene at ca. 790-800°C at the south-eastern end of the Inzie Head section (Fig. 6). The predominantly diatexitic nature of the migmatites with voluminous leucosome exposures is suggestive for high degrees of partial melting and the production of significant melt fractions above 25 wt.%. An influx of H_2O-rich fluids that mobilized along the network of shear zones has been evoked, to explain the derivation of the substantial amount of melt (Johnson et al., 2015).

Throughout the migmatite sequence, biotite is present even within the highest recorded grades where orthopyroxene is stable. The presence of biotite contradicts the modelled high-grade phase relations, where biotite is predicted to be absent above temperatures of ca. 780°C under pressures of 2.7 – 2.8 kbar (Johnson et al., 2015). The authors suggested that biotite was either exhausted during peak metamorphism and grew during later stage retrogression and/ or that trace components extended the stability of biotite which could not be modelled. The stability of biotite in a partial melting system is generally dependant on the prevailing temperatures and the availability of water in the system (Stevens and Clemens, 1993). In a closed system under fluid-absent partial melting conditions, the stability of biotite may exceed temperatures above 800°C. Conversely, a fluid-present state generally shifts a rocks solidus to lower temperatures and promotes the earlier break down of biotite, whereby biotite would be exceeded below 800°C (Stevens and Clemens, 1993). However, recent studies on fluid-present and fluid-absent partial melting conditions of protoliths with average metapelitic compositions concluded that biotite stability may be extended to above 800°C, when considering an open system of melt extraction (Mayne et al., 2019). Melting reactions under fluid-present conditions would largely consume quartz and plagioclase, whereby plagioclases compositions are enriched in anorthite contents (Mayne et al., 2019). However, the observed mineral assemblage of the Inzie Head metapelitic migmatites is not deficient in quartz or plagioclase. Furthermore, plagioclases are characterized by relatively low anorthite contents below An_{30}, suggesting that these samples underwent fluid-absent partial melting processes. The biotite crystals probably experienced peak metamorphism and were not exhausted by the partial melting reactions. The presence of biotite, locally defining a foliation in the migmatitic rocks, indicates that biotite does not represent a retrograde phase. The coexistence of biotite as a hydrous phase with comparatively anhydrous peritectic garnet and/ or cordierite produced by the partial melting reactions, is suggestive for melt removal from the residuum, preventing back reactions that would destroy the peritectic minerals (Fig. 18; White and Powell, 2010).

Leucosome samples often contain biotite, interpreted to be entrained from the source and/ or are rich in peritectic phases (cordierite, garnet or orthopyroxene) that generally form as solid products from melting reactions consuming hydrous minerals (Johnson et al., 2003, 2001b, 2001a). Consistent with field exposures, the occurrence and abundance of peritectic and/ or entrained material supports the in-situ derivation of leucosomes, as melt migration over significant distances is unlikely to be able to preserve these phases. Thereafter, the leucosome derivations have been interpreted to represent mixtures of variable entrained and/ or peritectic phases together with products of fractional crystallization, accumulated from crystallizing melt, which segregated only short distances before solidification in the present position (Johnson et al., 2003). Based on the geochemistry and petrography of the leucosomes, studies have concluded that variable quantities of melt were lost and moved out of the system into channel ways. This movement of melt into the thicker channel ways was accompanied by fractional crystallization of K-feldspar, forming leucogranitic veins that froze in their present position (Johnson et al., 2003). It was furthermore suggested that some granitic melt that was generated at slightly lower crustal levels, migrated upwards through

the channel ways to ultimately feed larger granitic plutons within the Buchan Block. The composition of larger granitic exposures at Inzie Head and within the Buchan Block area, have been suggested to approximate the compositions of evolved melts that were removed from the system, consistent with their derivation from a peraluminous sedimentary source (Johnson et al., 2003). Chemical compositions obtained from the samples in this study are presented on a B–A discrimination diagram, showing the aluminousity [A = Al-(K+Na+2Ca)] of the samples in relation to the mafic (B = Fe+Mg+Ti) components (after Debon and Le Fort, 1983; Villaseca et al., 1998). The obtained compositions of granitic rocks in this study, form cluster within the lower peraluminous space of the diagram (fig. 52). In relation to the compositions obtained for the migmatites and metasediments, these granitic samples delineate cluster at the thermal minimum defined by experimental melt compositions of pelitic rocks, generated under fluid-absent melting conditions (fig. 52; Vielzeuf and Holloway, 1988).

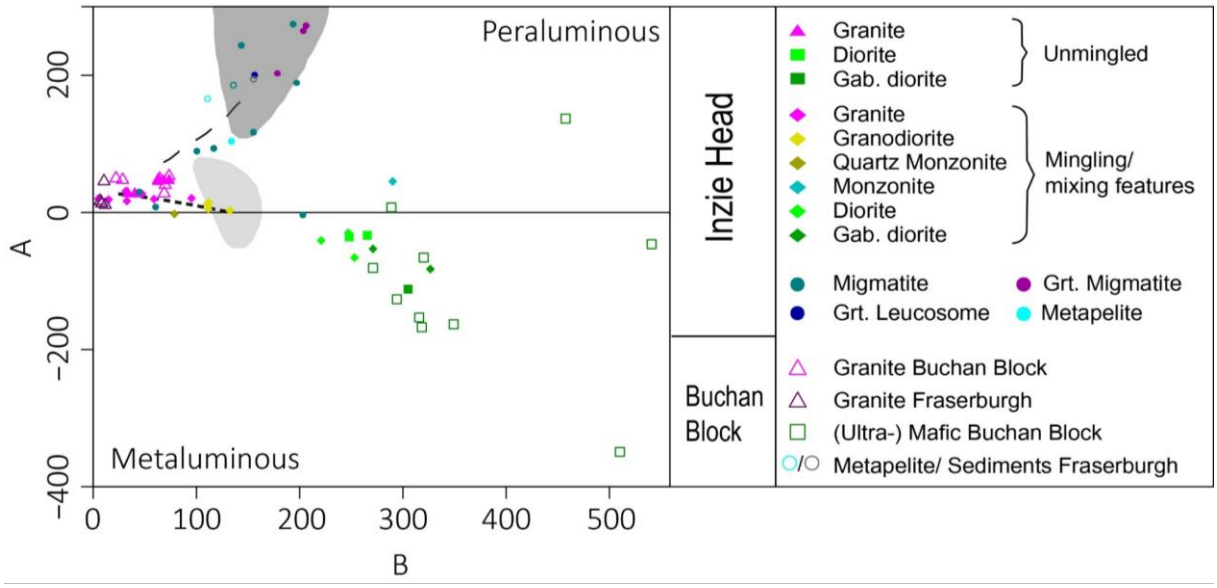

Figure 52 – B–A plot of the Inzie Head and Buchan Block samples (after Villaseca et al., 1998*); Grey fields delineate variable compositions of potential pelitic (dark grey) and (meta-) igneous (light grey) protolith compositions for the derivation of granitic liquids; thin dashed line represents a trajectory of liquids derived from progressive melting of pelitic protoliths (after* Vielzeuf and Holloway, 1988*); thicker dashed line represents the boundary of I- and S-type granites*

The metapelitic, migmatitic and leucosome samples from the crustal sequence at Inzie Head and Fraserburgh are mostly characterized by strongly peraluminous compositions, yielding A/CNK ratios above 1.4. However, the comparatively weak peraluminous chemistry of the granitic bodies with A/CNK ratios between 1.1 and 1.2, is generally inconsistent when considering the migmatite sequence as the only source, as higher A/CNK ratios would be expected for the derived granites. Thus, a possible scenario to explain the weakly peraluminous character of the granitic bodies is mixing of melt which derived from peraluminous metasediments with intruding more mafic material. Although the CaO contents of granitic samples and metapelitic migmatites are overall similar, granites are generally enriched in Na_2O and K_2O contents (fig. 20). The crustal host rocks are characterized by relatively uniform trace element contents of Rb and La that preferentially partition into the melt, whereas the concentrations in granitic rocks are highly variable with a number of granites showing relative enrichments. Granites with mingling and potential mixing features in this study define a slightly negative trend following the I- and S-type discrimination boundary on the B–A diagram (fig. 52). Together with granodioritic samples, delineate the granitic rocks a trend towards compositions suggested to represent melts derived from (meta-)igneous source domains, rather than pelitic protoliths (fig. 52). The same samples delineate with higher CaO and lower K_2O contents a negative trend towards metaluminous compositions on the A/NK vs. A/CNK discrimination diagram (fig. 19) with A/CNK values mostly below 1.1, which is generally regarded as indicative for granitoids derived from (meta-)igneous protoliths. The negative trends delineated by the granitic and granodioritic samples in the B–A plot and the A/NK vs A/CNK diagram are further enhanced and extended by the strongly metaluminous dioritic and gabbroic samples, suggestive for potential mixing processes (fig. 52). The strong correlation and the defined steeper negative trend of the mafic rocks from Inzie Head with the (ultra-)mafic rocks from the wider Buchan Block domain, further indicate the possibility of a genetic link and thus the derivation from a mutual mantle-derived source.

5.3 CONSTRAINS ON THE PREVAILING CONDITIONS WITHIN THE ASSUMED MASH ZONE AND THE POTENTIAL FOR MAGMA MINGLING AND MIXING

The potential for mingling and mixing processes is largely dependent on the rheological properties of the participating magmas, where most efficient mixing can be expected between pure melts or magmas of similar rheological behaviour (Bateman, 1995; Poli et al., 1996; Sparks and Marshall, 1986). Thus, the expected developing crystallinity in a cooling magma system can be regarded to impose large controls on the efficiency of mixing processes, to a degree where magma interaction would be inhibited. The crystal content in magmatic systems is largely governed by the prevailing pressure and temperature conditions, as well as a function of the water activity within the systems (fig. 53). The temperatures of the mafic magmas upon intrusion into the exposed crustal sequence at Inzie Head probably did not exceed 900°C. This upper temperature limit can be constrained based on the presence of biotite in migmatites that are in close proximity to the intrusions. Biotite is unstable at temperatures above 900°C and would thus be expected to be absent in the mineral assemblages of rocks that experienced such high temperatures (Mayne et al., 2019; Stevens and Clemens, 1993). As the solidus of a water-undersaturated magma of average basaltic composition lies above 900°C, sufficient water must have been contained within the mafic Inzie Head magmas prior to their intrusion into the exposed crustal level (fig. 53). Considering the dioritic intrusions at Inzie Head to be related to the Grampian (ultra-)mafic rocks of the wider Buchan Block domain, would suggest that they derived from magmas that resulted from decompression melting of the mantle under fluid undersaturated conditions (Viete et al., 2010). A large number of rocks from the Grampian (ultra-)mafic suites contain pyroxene (clinopyroxene and/ or orthopyroxene), which is consistent with a fluid deficient system. The diorites of the Inzie Head section thus seem to be more hydrous than most of the Grampian (ultra-)mafic rocks but whether this infiltration of fluid occurred at the source or during the ascent of the magmas remains ambiguous.

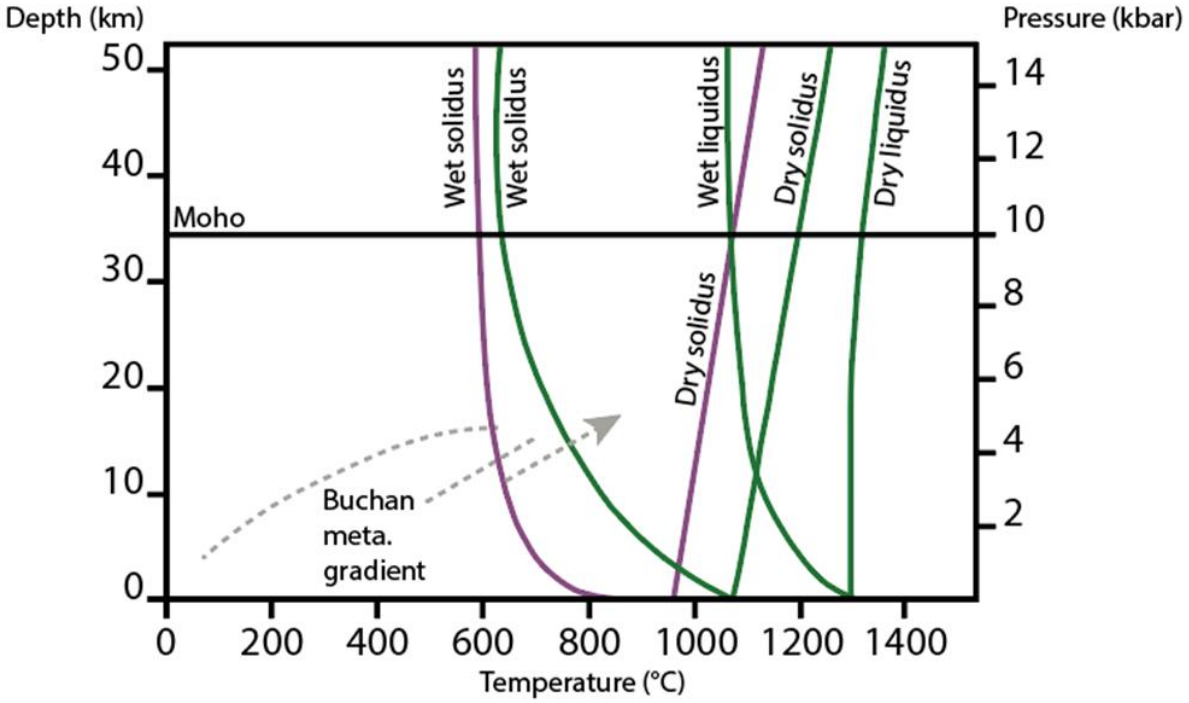

Figure 53 – Water-saturated (wet) and water-undersaturated (dry) solidi for granitic (purple) magmatic systems (after Thompson, 1996*) as well as the solidi and liquidi for gabbroic (green) magmatic systems (after* Lambert and Wyllie, 1972*); Grey dashed lines represent the estimated metamorphic gradients of the Buchan area (after* Turner, 1981*); dashed line with arrow represents the local metamorphic field gradient from Fraserburgh to Inzie Head (after* Johnson et al., 2001a)

To constrain the physical properties of the mingled rocks along Inzie Head, phase abundance models were performed using the whole rock geochemistry of three different samples (fig. 54). Phase abundances of the most mafic Inzie Head diorite were constrained based on a thermodynamic dataset and solution model for ultramafic and mafic rock melting. Phase abundances and compositions were modelled as a function of temperature under set pressure conditions of 4 kbar, representing the upper pressure limit of the sequence. The water content was set to 1.4 wt.-%, sufficient to allow the observed hydrous

mafic minerals to form whilst leaving a small amount of excess water at the solidus. Modelled mineral compositions (appendix VI) were compared with the measured compositions of the observed mineral assemblage of the sample. Most minerals approximate modelled compositions at temperatures around 740 – 780°C, which is overall consistent with the constrained metamorphic temperatures for the Inzie Head section. However, inner core domains of plagioclases are rather coherent with predicted compositions at temperatures between 850 – 860°C. Plagioclase as a mineral with relatively low diffusion rates has the potential to preserve core domains that crystallized early in the magma system and thus possibly record the magma conditions upon intrusion into the exposed section. The relative diffusional inaccessibility of plagioclases removes these core domains from the effective bulk composition. Consequently, plagioclase rims have a higher albite component and the modelled solidus can be expected at a lower temperature than predicted by this model (fig. 54 – a). The preservation of core domains in plagioclases with higher anorthite contents and frequently showing signs of corrosion, is a common feature in the studied magmatic rocks from the Inzie Head section, generally interpreted to reflect magma mingling and mixing of a more felsic and more mafic magma, by the capture of crystals from a compositionally differing magma (Hibbard, 1981; Pietranik and Koepke, 2014, 2009).

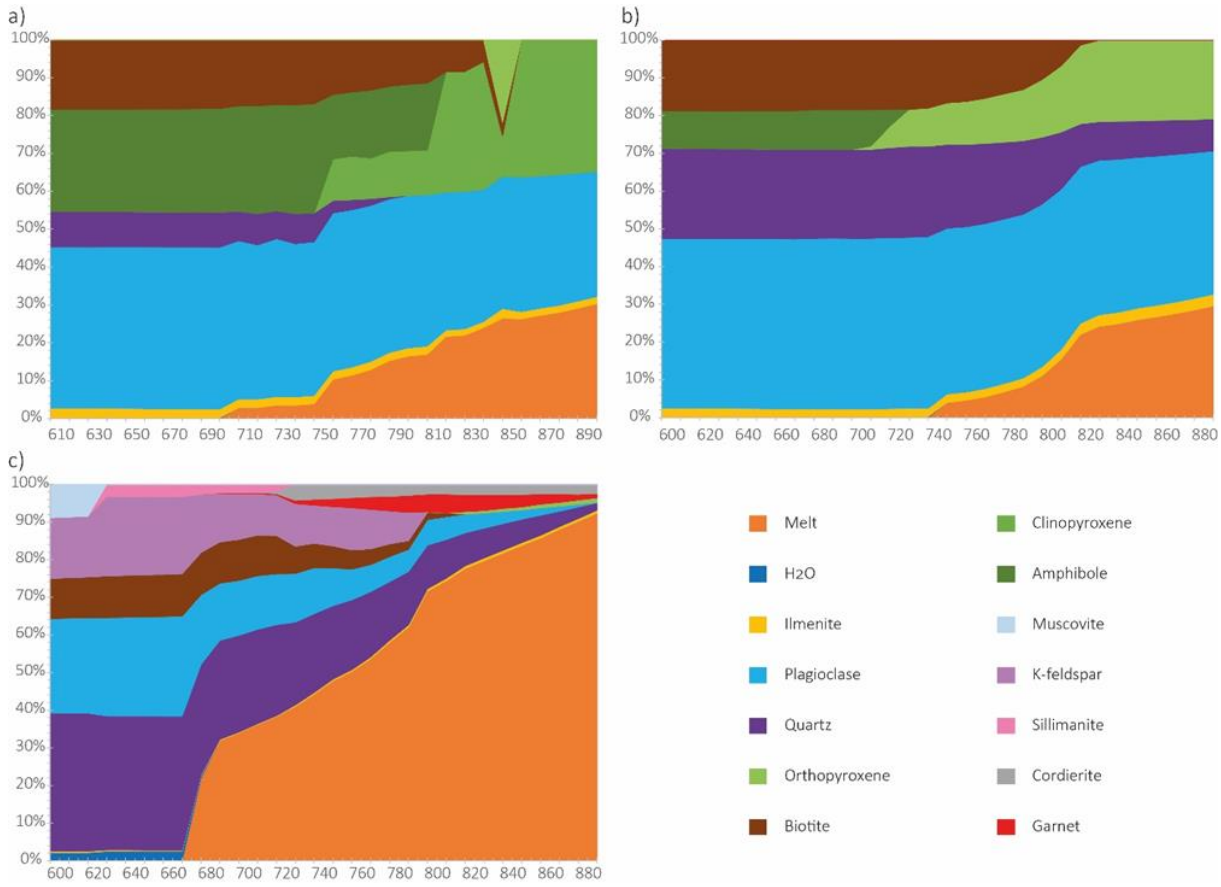

Figure 54 – Phase abundance models for the three different samples; a) phase abundances for the most mafic (gabbroic) diorite; b) phase abundances for the most felsic and mingled diorite; c) phase abundances for an unmingled average granite

Phase abundances for an average unmixed granite from the Inzie Head section were modelled under pressure conditions of 4 kbar, based on a thermodynamic dataset and solution model for melting of rocks with granitic compositions. The water content was set to 3 wt.-% to represent the minimum water composition that would have been buffered by biotite fluid-absent melting conditions (Clemens and Watkins, 2001). Measured phase compositions generally approximate modelled compositions at temperatures between 740 – 790°C, where 44 – 58 wt.% melt fraction is predicted (Fig. 54 - c). The modelled phase abundances show the large discrepancies in the degree of crystallinity for the mafic and felsic system, when considering the given temperature range between 740 – 790°C as the prevailing temperatures in the exposed crustal and potential MASH zone sequence. Whereas the granitic system contains melt fractions around 50 wt.%, the mafic system is characterized by a much higher degree of crystallinity, containing between 4 – 15 wt.% melt (Fig. 54 – a+c). The presumed temperature difference upon intrusion and the low proportion of melt predicted within the mafic system at the prevailing temperature

conditions in the crustal sequence suggest that the partially molten granitic magma was below the solidus of the intruding mafic magma, resulting in quenching and solidification of the hotter mafic magma within the colder crustal environment and limiting or inhibiting mixing processes at the level of exposure. This is consistent with the field evidence, where the chosen mafic sample seemingly cross cuts with a sharp contact an older, potentially hybridized domain.

A third model was based on the composition of the most silicic mingled Inzie Head diorite in this study. Phase abundances were modelled under constant pressure conditions of 4 kbar using a thermodynamic dataset and solution model for melting of intermediate rocks with a set water content at 0.86 wt.%. The measured mineral compositions were obtained within the ca. 10 cm wide gradational contact zone between the granitic and dioritic domains, which could explain the general inconsistency of measured biotite and hornblende compositions with the modelled compositions for these phases. Corroded inner plagioclase domains of higher anorthite contents, that are largely preserved in grains within the granitic domain, are consistent with compositions estimated for higher temperatures >810°C, suggestive for crystal capture by the granitic system. Compositions of the surrounding rim domains and plagioclase compositions of featureless grains within the mafic contact section are again inconsistent with predicted phase compositions. The field and petrological evidence clearly suggests co-magmatic behaviour and thus temperatures above 740°C, whereby the fraction of predicted melt is generally low when considering the inferred temperature range between 740 – 790°C. Under assumed water and pressure conditions for the model, melt fractionations above 810°C rise from ca 15 wt.% to ca. 30 wt.% at 890°C. Higher water activity or lower pressure conditions could result in higher melt fractions in the system, enhancing the possibility of local mixing. However, as the granitic and mafic domains are clearly distinguishable with distance to the contact and as the contact domain with signs of mixing and hybridization is generally limited to tens of cm, mixing and hybridization processes were probably locally restricted. Thus, the gradual contact domain may suggest the formation of a thermal gradient promoting similar rheological and crystallinity conditions along the margin, that were possibly imposed by heating of the granitic domain by the mafic intrusion. Relatively low prevailing pressures of the sequence in the upper crustal setting suggests that the country rocks surrounding the potential MASH zone were relatively cool. Exposures of ineffective mingling as described for the most mafic sample as well as limited mixing and inefficient hybridization of mingling magmas as described for the gradual contact zone could be related to the effective loss of heat to the cooler surrounding environment.

5.4 TEXTURAL AND GEOCHEMICAL EVIDENCE FOR MAGMA INTERACTION PROCESSES

The variety of mingling and potential mixing textures exposed throughout the migmatized coastal sequence are indicative for the complex nature of magma interaction processes, that are shaped by the differences in physical properties as described by the models. Distinct contact domains between rocks of contrasting compositions vary from sharp and chilled to irregular and wispy in nature. Locally, mafic exposures form rounded to angular pillow-like structures that are separated by felsic domains, interpreted to represent the intrusion and quenching of the hotter mafic magma in the colder, felsic environment (Fig. 11). The observed contact domains are consistent with field exposures elsewhere, that have been inferred to resemble the early stages of magma interaction during the replenishment of a felsic magma system by mafic intrusions (Perugini and Poli, 2005). Pillow structures, as well as fingering and wispy textures of mafic into the more felsic magma probably developed as a result of the divergence in temperatures and rheological properties of the two systems. Large differences in the rheological properties of the two systems can be expected when the heat transfer is insufficient, resulting in quenching of the mafic magma in the cooler granitic host magma which inhibits the possibility of mixing and hybridization processes (Weinberg et al., 2021). The differences in the physical and rheological properties may result in viscous dynamics between the high-temperature, low-viscosity mafic intrusions and the colder, high-viscosity crustal material, forming the observed fingering and wispy textures (Fig. 11 – a+e; Perugini and Poli, 2005). This interpretation is consistent with the differences in the modelled physical properties, when considering mafic magma temperatures around 850°C upon intrusion into the colder felsic environment. The colder crustal temperatures around 740 – 790°C would thus force the mafic magma to cool relatively quickly, whereas crustal domains in close proximity probably experienced heating. This would explain why the mafic magma was locally relatively immobile, forming sharp contacts, pillows or wisps into the granitic systems, while mobile granitic melt was able to migrate into the mafic system, forming vein networks that are separating mafic blocks. Flow dynamics in the host rock system and veining of granitic material into the mafic magma may break and separate mafic domains effectively, forming the rounded to angular shaped pillows or enclaves (Weinberg et al., 2021). Considering the crustal system was in a partial molten state upon

intrusion of the mafic magmas, may have provided opportunities for rejuvenation of the partially molten state and the possibility for material exchange (Weinberg et al., 2021).

As mixing processes are most efficient between magmas behaving as liquids, quenching of the mafic magma against a cooler host and the coherent increase in viscosity and crystallinity, decrease the efficiency of chemical magma mixing. The interaction between the contrasting magmas was thus probably locally restricted and limited to the thermal boundary along the contact margin. Consistently, petrographic evidence indicates slight chilling towards the distinct contact margins, with the generation of thermal gradients (Fig. 14 – a-c). Rapid thermal equilibration would be expected to generate uniform textures within the contrasting domains (Kumar et al., 2004). However, gradual changes in grain size and mineral assemblages within both domains along the distinct contact margins are consistent with the generation of thermal gradients within. Described in the petrographic information, these changes are generally locally restricted to the proximity to the contact margin, occurring over tens of centimetres (Fig. 14 – a+c). The mafic domains are characterized by an increase in biotite abundance towards the contact, accompanied by a consistent decrease in the abundance hornblende, which is absent in proximity to the contact (Fig. 14 – a-c). Consistently, the felsic domains show a decrease in abundance and grain size of K-feldspar, which disappears with increasing proximity to the contact margin. The gradual decrease and disappearance of K-feldspar is suggestive for an increase in prevailing temperature, pressure or fluid conditions that influenced diffusion rates and changed the amount of melt present in the systems, resulting in the replacement of K-feldspar by sodium rich plagioclase (Kumar and Pieru, 2010). The change in compositions requires diffusional movement of elements or migration of melts. The disappearance of K-feldspar and increased abundance of biotite towards the contact suggest potassium diffusion, potentially enhanced by mingling dynamics. Diffusion of potassium from the granitic magma into the diorite magma implies some degree of interaction between the contrasting magmas over a certain length of scale. However, the interaction was insufficient to resolve the sharp contact between the two chemically different magmas. This is suggestive for chemical diffusional movement of elements in the melts rather than the movement of melt itself, although the movement of melt could have enhanced the diffusional processes.

Plagioclase grains within mafic domains along sharp contacts are characterized by an increase in grain size, showing resorbed inner cores of higher anorthite content (Fig. 14 – a-c). Grains are overgrown by more sodic rims, which are similar in compositions to the composition of plagioclases within the felsic domain, possibly indicating locally restricted hybridization processes by the addition of melt from the felsic portion of the contact. However, these melt additions were probably limited to small amounts as these changes are restricted to tens of centimetres and insufficient to resolve the sharp contact domains. Most plagioclases within the felsic domain are characterized by relatively uniform compositions, showing vermicular intergrowth textures of quartz along the contact, consistent with K-feldspar replacement processes under changing conditions. Dispersed large crystals of zoned plagioclases occur within the felsic domain only in distance to the contact (Fig. 14 – d-f). Resorbed inner cores of higher anorthite content as seen within the mafic domain of the contact margin are suggestive for mechanical transfer of grains during limited magma mixing processes (Castro, 2001; Pietranik and Koepke, 2014; Ubide et al., 2014). Finer plagioclase grains lacking albitic rim textures but with signs of resorption, are occasionally overgrown by irregular K- feldspar. The petrographic evidence of the sharp contact domains suggests that the generation of a thermal gradient resulted in limited mixing of the two systems, where earlier crystals converted to stable mineral phases under the changing compositions and temperature conditions (Perugini and Poli, 2012; Weidendorfer et al., 2014). Zoned plagioclases thus may represent early crystals which experienced resorption and acted as growth sites of stable mineral phases (Streck, 2008). The zoned plagioclase crystals captured in the felsic domain, are suggestive of limited mechanical transfer of mafic material into the cooler, felsic domains. Conversely, magma mixing and hybridization were probably more efficient in mingled domains where sharp contacts are largely resolved or absent, showing larger-scale compositional and textural changes in adjacent felsic and mafic exposures (Fig. 10 – c; Fig. 11 – c).

Throughout the Inzie Head section, exposures with gradual to complex colour and grain size variations within domains are evident on a metre scale. Felsic veins showing grey hybridized colours that gradually change into lighter coloured domains, form vein structures within mafic exposures, which are characterized by convoluted zones of darker, finer-grained and hybridized lighter coloured, coarser grained domains (Fig. 10 – c; Fig. 11 – c). The hybrid domains are characterized by granodioritic compositions, containing abundant mineral textures indicative for magma mixing and hybridization processes (Baxter and Feely, 2002; Hibbard, 1991; Janoušek et al., 2000). Proposed mineral characteristics for magma mixing and hybridization are abundant, varying from resorption with complex and inverse zoning or anorthitic spike zones in larger plagioclases, irregular compositional zoning in K-feldspar, (anti-)rapakivi textures, bladed-shaped biotite crystals, mixed apatite morphologies to titanite ocelli-like textures within single samples. Furthermore, hornblende cluster within more mafic but weakly defined schlieren, are suggestive of interactions between more mafic material and a more felsic system (Fig. 16 –

e). The observed field exposures and mineral textures are suggestive of granitic material invading into the arriving mafic magma, creating mixed and hybridized domains. Heating of the granitic material by the hotter mafic environment thus would have the potential to overcome the imposed thermal challenge and result in the formation of larger-scale thermal and compositional gradients or magmatic mushes, promoting the chemical interaction of the contrasting magmas. However, in-situ magma mixing and hybridization appears to have been locally restricted within the exposed mid to upper crustal zone. Temperatures within the partially molten domain were probably overall insufficient for the easy addition of mafic contributions into the felsic, crustal system, resulting in the pillow structures and viscos dynamics. Chemical interaction between the contrasting domains appears to have been more successful, where granitic melt invaded the mafic intrusions, adding felsic material into the system and generating the hybridized, granodioritic zones. Interestingly, individual textures that are indicative for magma mixing have been observed in both unmingled granitic and mafic rocks. (Anti-)rapakivi or hornblende-titanite ocelli textures might indicate mixing processes at an earlier stage of their evolution. Earlier mixing scenarios thus could have taken place at lower crustal levels or during the ascent into the upper crustal domain.

Although the observed field exposures are suggestive for effective mixing processes, the range of major and trace element compositions exhibited by the mafic and felsic rocks could be produced by a combination with other processes, such as source controlled compositional variation and fractional crystallization superimposed. However, hybridisation and magma mixing processes are proposed by numerous studies to explain field exposures of gradual colour and grain size changes and the high compositional variations in major-element, trace-element and isotope chemistry observed in studied granitoids (Chappell, 1996; Janoušek et al., 2004; Zeh et al., 2020). Thereafter, major and trace-element concentrations would show mixing arrays in form of linear correlations. Furthermore, isotopic signatures of the different granitoids are considered to show coherent mixing arrays, where most mantle-like isotope ratios correlate with maficity (Clemens and Stevens, 2012). Linear mixing arrays of major and trace-elements versus mg# (100*(MgO/FeO+MgO) [mol.%]) are generally defined, between the magmatic rocks of this study. Previous studies pointed out, that the addition of a mafic magma into a granitic melt, results in a general decrease in K contents and A/CNK ratios, as Ca is coherently increasing with increasing maficity (Stevens et al., 2007). Such element correlations are observed in the magmatic rocks of this study when including the granodioritic, dioritic and gabbroic rocks.

5.5 ISOTOPIC EVIDENCE FOR MAGMA INTERACTION PROCESSES

Field evidence of igneous rocks in the Inzie Head coastal section clearly suggest co-magmatic mingling relationships of magmas with chemically distinct compositions. The use of zircon U-Pb and Pb-Pb dating is thus an important tool to establish the potential of co-magmatic behaviour in order to confirm if mingling or mixing processes occurred during the petrogenesis of the different rock types in the exposed sequence. The potential of zircon to retain the U-Pb isotopic signature of magmas during crystallization provides an opportunity to evaluate the timing of magmatic emplacements as well as assess the potential of inheritance of older, pre-existing zircon domains. The presence of common Pb or later stage alteration processes that may induce Pb loss can have a direct impact on the obtained zircon dates, resulting in significant uncertainties in the U-Pb ages. Given that the evaluated spread in U-Pb and Pb-Pb values is reflective of the local petrogenesis, the highest age population density of magmatic rocks suggests latest magmatic activity and overall co-magmatic behaviour between ca. 450 and 480 Ma. Older zircon dates between 500 Ma and 2.9 Ga are predominantly found within rocks of granitic composition and interpreted to reflect the inheritance of older zircon domains that possibly derived from the source. The distribution of inherited zircon ages within the unmingled granitic rocks is coherent with the age spread given by analysed zircon domains of the metapelite and leucosome samples, possibly suggesting a co-genetic link or a similar source domain for the granitic magmas. Although younger magmatic zircon domains are rare in the metapelite and leucosome samples, a minority of dates that were obtained on rim domains are consistent with the evaluated spread of the dioritic, granodioritic and granitic rocks, suggesting that the timing of partial melting coincided with the emplacement of the igneous rocks. The determined emplacement ages of the individual magmatic samples delineate a period over 30 myr. This evaluated age spread is overall consistent with the established timing of the Grampian orogeny and related metamorphic activity within the Buchan Block from ca. 488 Ma to 461 Ma.

The oldest recorded rocks in this study are exclusively of granitic composition, suggestive of early deeper crustal magmas, possibly formed as a result of the commencing tectonic activity and mafic underplating that intruded into the current level of

exposure. The age determined of a mingled and unmingled diorite from the Inzie Head section are within error consistent with the established timing of Grampian mafic magmatism from 475 to 470 Ma, suggesting a correlation with the emplacement of (ultra-)mafic rocks within the wider Buchan Block domain (fig. 55 – a). Rocks of granodioritic composition are within error overlapping in age with the dioritic intrusions, indicative of close co-magmatic relationships. The trend towards younger ages of 460 – 450 Ma could be an artifact of regional cooling processes, that were prolonged in the potential MASH zone when compared to the established regional cooling (fig. 55 – a). Samples that were obtained in close proximity to each other in the field may vary greatly in age, consistent with the hypothesis of rejuvenation and contribution of multiple intrusions into the crustal MASH zone. The inheritance of single older zircon grains within some dioritic rocks, could either be suggestive for crystal capture and mixing with granitic material or for crustal assimilation upon ascent of the mafic magma. The evaluation and comparison of the obtained Hf isotopic signature with the measured age of the same zircon domains, can give important clues in further understanding potential inheritance (fig. 55 – b). In comparison to the U-Pb isotopic system, the Lu-Hf isotopic composition within zircon has a higher resistance towards later-stage alteration processes and thus, a higher potential to retain the initial isotopic signature of the magma during crystallization. Different Lu-Hf and U-Pb isotopic signatures of zircon within a single sample or single grains, have the potential to provide information about the timing of magmatic or metamorphic events, as well as insights into potential magma sources or crustal recycling processes (Gerdes and Zeh, 2009; Zeh et al., 2009).

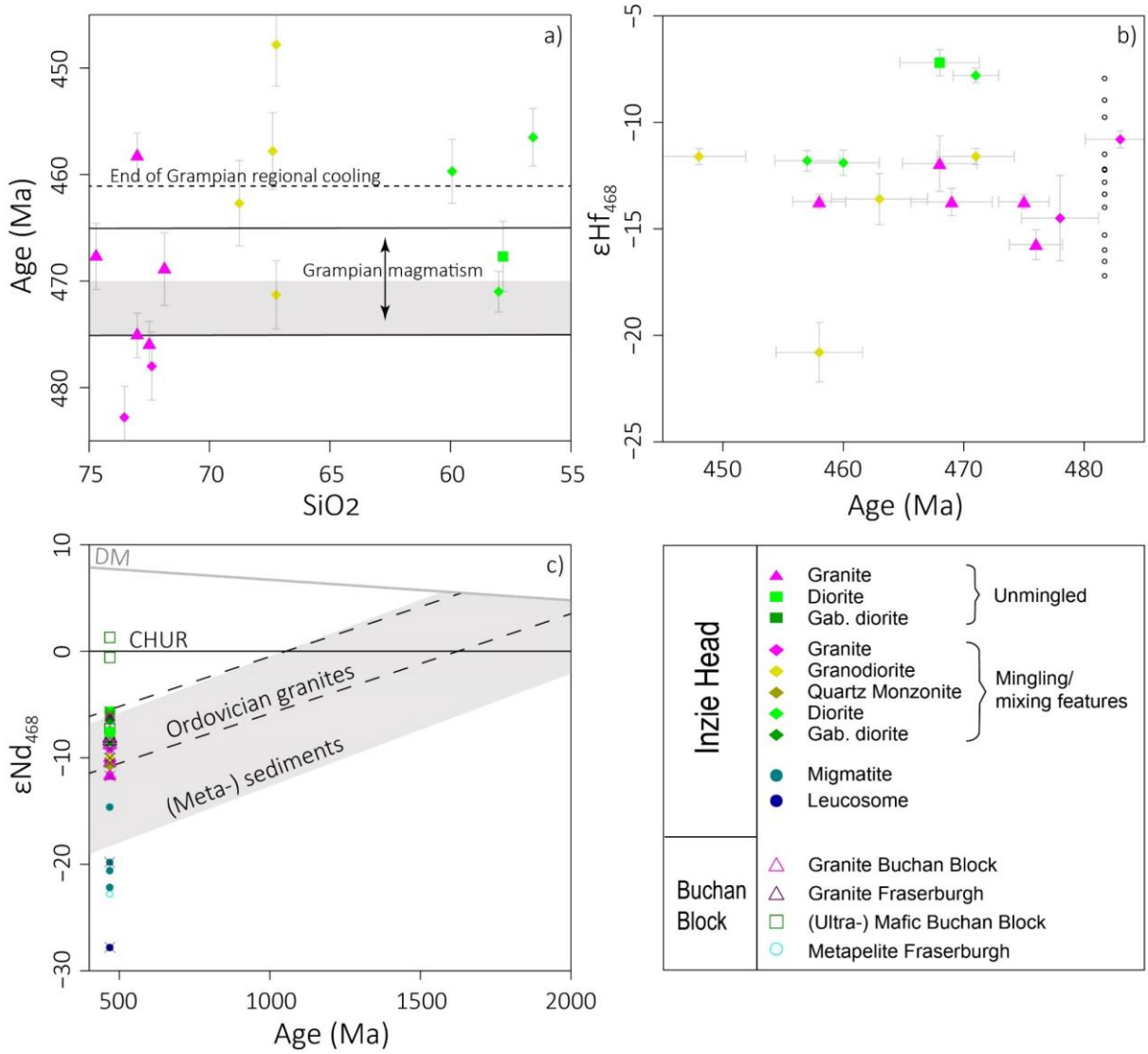

Figure 55 – Comparison of isotopic signatures of the different rocks; a) obtained zircon age spread of the magmatic rocks compared to the established timing of Grampian igneous and tectonic activities, the grey shaded field delineates the established timing of mafic magmatism within the Buchan Block; b) comparison of obtained zircon εHf_{468} with the obtained age of the samples with black dots showing εHf_{486} of previous studies (Johnson et al., 2017)*; c) comparison of the obtained spread in whole rock and apatite (marked with black X) εNd_{468} with established εNd values of rocks from the area*

The obtained εHf_t as a function of the measured U-Pb and Pb-Pb date of the same zircon domain visualizes the high scatter in both isotopic systems in relation to potential inheritance, suggesting several crustal evolution trends (fig. 44). Predominantly defined by analysed zircon domains of the granitic, leucosome and metapelite samples, delineate crustal paths three peaks of zircon growth events at around 1.3 – 1.6 Ga, 1.7 – 2.0 Ga and 2.7 – 2.9 Ga. Thereafter, crustal evolution trends of zircon formed at ca. 1.3 Ga, delineate expected εHf_{468} value of ca. -13 for the average time of emplacement at 468 Ma. The wide scatter towards lower and more evolved εHf_{468} values (down to εHf_{468} = -25 and -38) of the magmatic rocks, in relation to the wide range in obtained U-Pb and Pb-Pb ages, suggests therefore recycling of heterogeneous crustal material (Gerdes and Zeh, 2009; Zeh et al., 2009). This is coherent with averaged εHf_{468} values of -17 and -25 of magmatic zircon overgrowth domains from the metapelite and leucosome sample, respectively. Considering the more positive εHf_{468} values that range up to -5 as a direct result of crustal recycling, would necessitate an evolution trend of zircon formed at ca 1 Ga. However, such a trend is not defined by inherited zircon domains, older than 500 Ma (fig. 44). The comparison of calculated averaged ages and εHf_{468} values for the individual rocks delineates more juvenile εHf_{468} values for the two oldest diorites, whereas the younger diorites are characterized by more evolved values at -12, that are within error overlapping with the given range of granodioritic and granitic samples. The granitic rocks show a tendency towards more evolved εHf_{468} values around -14, consistent with crustal recycling. Estimates of εHf_{468} compositions of a directly mantle-derived unhybridized magma, suggest juvenile values of ca. +15, significantly higher than the most juvenile εHf_{468} values of -7 in this dataset. Previous studies interpreted evolved zircon εHf values, between -8 to -13 at an emplacement age of 486 Ma of a diorite from Inzie Head, to require magma contamination by a crustal component (fig.55 – b; Johnson et al., 2017).Although the more juvenile εHf_{468} values at -7 and -8 of the two older diorites are already fairly crustal, these values are distinct and not overlapping within error with the more evolved signatures of the other magmatic rocks. The more juvenile values of these diorites suggest little in-situ crustal contamination and thus might indicate the derivation of magma from a hybridized or contaminated mantle source, which was emplaced into a relatively cold crust where magma interaction was largely inhibited. This interpretation is thus consistent with the observed field relations of the samples, where sharp contact domains have been observed to juxtaposed rocks. Conversely the lower εHf_{468} values of the two younger diorites could represent their emplacement into a partially molten, hotter crustal domain, where magma interaction or crystal capture could have been responsible for the hybridization and lowering of the isotopic composition. This interpretation is consistent with the overall similar spread in εHf_{468} values observed within the gradually hybridized contact domain of the dioritic and granodioritic domains. A trend of more juvenile values with increasing maficity is thus weakly defined by the magmatic rocks, that are not overlapping within error (fig. 56 – a).

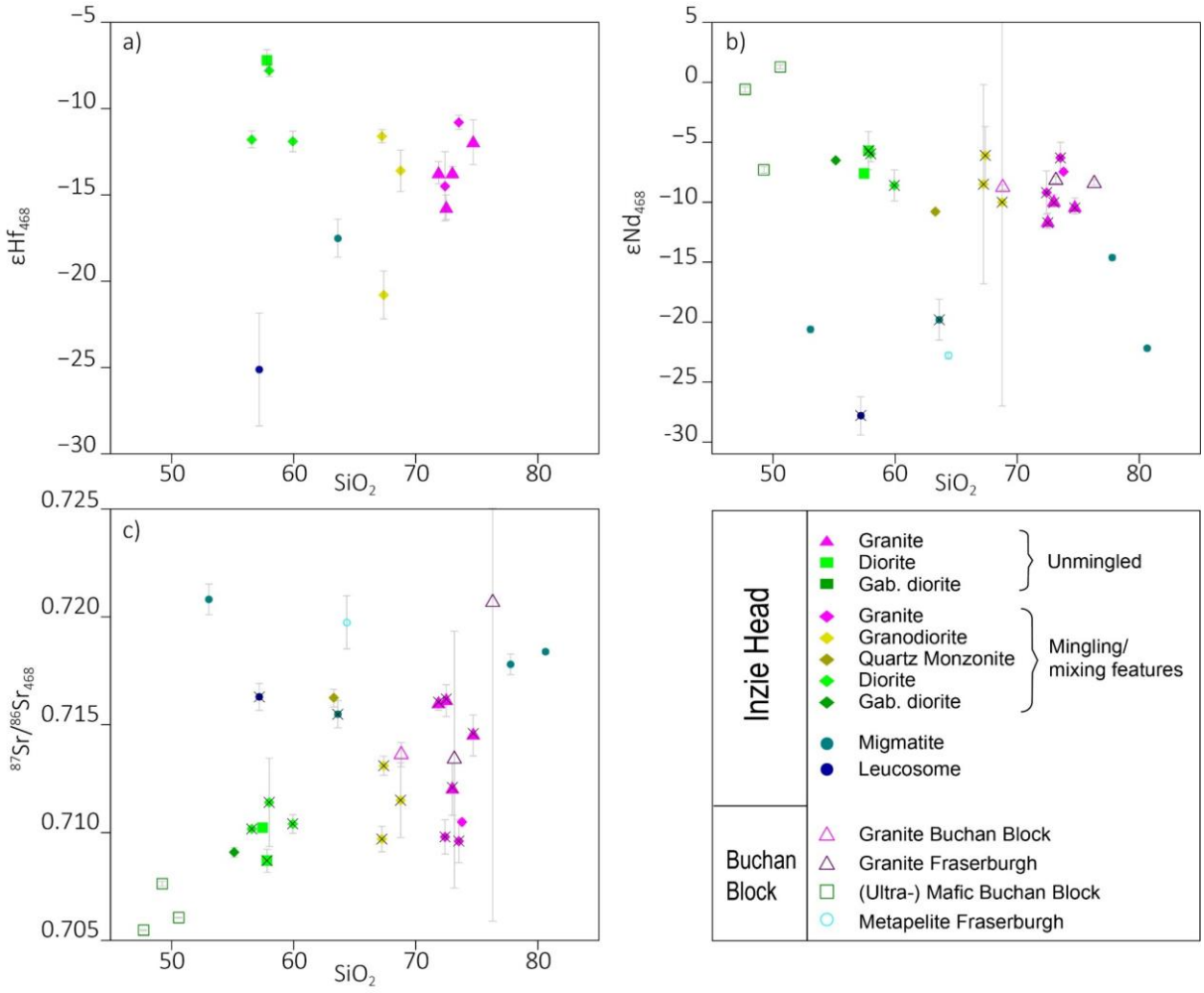

Figure 56 – Comparison of obtained isotopic values with whole rock SiO_2; a) obtained zircon εHf_{468} versus SiO_2; b) obtained whole rock and apatite (marked with black X) εNd_{468} versus SiO_2; c) obtained whole rock and apatite (marked with black X) $^{87}Sr/^{86}Sr_{468}$ versus SiO_2

This observation is consistent with obtained Sr and Nd isotopic compositions of apatites from the magmatic rocks, where the mafic unmingled sample s7A is characterized by the most juvenile isotopic values (fig. 56). However, a clear trend of more juvenile values with increasing maficity is largely rendered by the isotopic signatures of mingled granitic and granodioritic samples that are overlapping within error and the large uncertainties of the calculated averages. The wide scatter of εNd_{468} values of apatites observed in individual samples leads to large uncertainties of the calculated averages. The most juvenile εNd_{468} values in this study do not represent expected εNd_{468} values of an unmetasomatized, directly mantle-derived melt, estimated at around + 9. The highest whole rock εNd_{468} values at +1 and -1 in this study were obtained from two gabbroic rocks from the Buchan Block domain, whereas the most juvenile apatite εNd_{468} value of diorites from the Inzie Head section are at -5 and thus much more evolved. Previous studies delineated fields of εNd values for the Grampian granites and (meta-) sedimentary rocks of the Grampian terrane (fig. 55 – c; Johnson et al., 2017). Most magmatic samples are with averaged εNd_{468} values of apatites and whole rocks between -6 to -12, within the delineated granite and metasediment fields (fig. 55 – c). However, the two oldest diorite samples that also showed more juvenile zircon εHf_{468} values, as well as a mingled granite and granodiorite have slightly more radiogenic apatite εNd_{468} values around -6 and with two whole rock analyses of gabbroic samples from the Buchan Block domain at +1 and -1, lie above and at the edge of the juvenile end of the delineated fields. Throughout all isotopic systems, most migmatite and leucosome samples represent the evolved end of the given isotopic spreads and fall below the delineated field with significantly more evolved εNd_{468} values than expected.

$Sr_{(i)}$ isotopic signatures of granitoids are another important feature to discriminate between granite origins, as potential metasedimentary source domains are generally characterized by evolved $^{87}Sr/^{86}Sr$ ratios. Granitic magmas derived from recycling of an evolved crustal source will therefore have a comparably high $Sr_{(i)}$ ratio, whereas a more juvenile source will be reflected in lower $Sr_{(i)}$ isotopic ratios. The obtained spread of whole rock Sr_{468} values of the granitic rocks in this data set are within error overlapping with $Sr_{(i)}$ isotopic signatures determined in previous studies, which categorized the Grampian

Granites into two geochemically and isotopically distinct suits according to a sudden change in initial $^{87}Sr/^{86}Sr$ ratios at 435 Ma (Oliver, 2001). They determined that $Sr_{(i)}$ ratios between ca. 0.711 – 0.733 of older, peraluminous granites with Grampian ages between 480 – 435 Ma, are significantly higher than the $Sr_{(i)}$ values (ca. 0.704 – 0.708) of the younger, metaluminous to weakly peraluminous granites of 435 - 400 Ma. Previous studies suggested contributions of mafic, mantle-derived melts to explain lower initial Sr and higher εNd isotopic signatures of the metaluminous younger granites (Oliver, 2001). However, there is no evidence for such an isotopic and geochemical temporal correlation in this study.

The isotopic compositions of apatites of granitic to dioritic samples from Inzie Head, all yield relatively evolved Sr_{468} ratios, ranging above 0.708. Only the whole rock Sr_{468} analyses of gabbroic rocks from the wider Buchan Block display isotopic ratios around 0.706, consistent with previously determined $Sr_{(i)}$ isotopic ratios of rocks from the Grampian Basic Suite within the Buchan Block, which are suggested to represent their origin in the roots of a calc-alkaline arc (Oliver, 2001; Pankhurst, 1970). Although such values are closer to the Bulk Silicate Earth value of 0.704, the obtained isotopic ratios of the mafic rocks are generally not describable as directly mantle-derived, unless the mantle was previously hybridized or crustal contamination occurred during the petrogenesis of the magma. Whole rock Sr_{468} ratios of most migmatite and metapelite samples in this study are characterized by evolved values ranging from 0.718 to 0.721 and are broadly consistent with previously established initial $^{87}Sr/^{86}Sr$ ratios of ca. 0.718 (Pankhurst, 1974). The evolved isotopic signatures of the crustal host rocks cannot account for the more juvenile isotopic compositions of the magmatic samples, suggesting limited contributions from the exposed crustal sequence (Oliver, 2001). However, the lower Sr_{468} isotopic ratios in combination with higher εNd_{468} and εHf_{468} values of the unmingled granites, relative to the crustal host rocks in this study, could reflect hybridisation of an evolved crustal-derived melt by a more juvenile, mantle-derived melt (fig. 57).

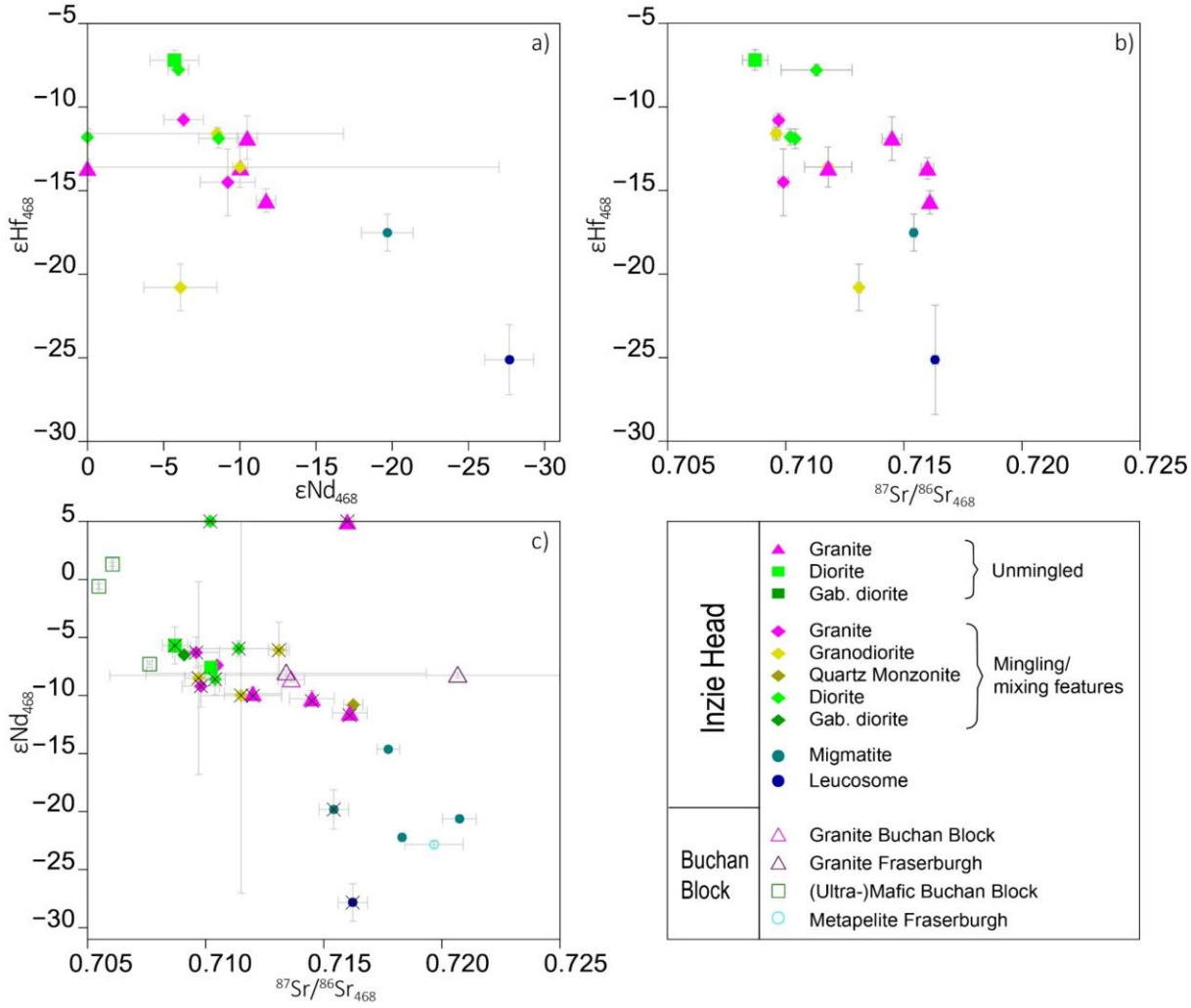

Figure 57 – Comparison of obtained isotopic values; a) obtained zircon εHf_{468} versus apatite εNd_{468} values; b) obtained zircon εHf_{468} versus apatite Sr_{468}; c) obtained εNd_{468} versus $^{87}Sr/^{86}Sr_{468}$ values of whole rock and apatites (marked with black X)

$^{87}Sr/^{86}Sr_{468}$ signatures of apatites from the migmatite and leucosome samples of this study are characterized by evolved averaged values around 0.716, which is within error overlapping with the most evolved values of unmingled granitic rocks. Granitic and dioritic rocks that lack mingling features are more often rather distinct in their isotopic signatures. This is furthermore consistent for samples that expose sharp contacts to juxtaposed contrasting domains. Although the dioritic domain s8Db of the wispy contact is characterized by more juvenile εHf_{468} and εNd_{468} values that are comparable to the unmingled diorite sample s7A, the higher Sr_{468} value is rather unexpected. Inconsistencies in the Sr isotopic composition when compared to the εNd and εHf values could be explained by controls of different diffusional properties between the two magmatic systems. At a given temperature, diffusion rates of Sr, Nd or Hf isotopes may vary greatly within different minerals (Brady and Cherniak, 2010; Cherniak, 2010). Different diffusion rates could furthermore explain more juvenile values in mingled granitic and granodioritic rocks and might correlate with diffusion driven compositional changes as observed along the distinct contact margins. Samples where field exposures of gradual contact domains indicate the potential for local magma mixing are characterized by highly variable isotopic compositions and similar averaged values that are generally overlapping within error. Apatites from the granitic samples with mingling features cluster at more juvenile Sr_{468} values around 0.710, that are within error overlapping with the Sr_{468} isotopic values of the dioritic samples from Inzie Head. Such systematic changes of chemical compositions with the isotopic signatures of all rocks and the observed field relations, could be suggestive for limited magma interaction processes.

5.6 CONSTRAINS ON POTENTIAL MIXING SCENARIOS

To further investigate the potential of magma mixing processes in the petrogenesis of the magmatic rocks in this study, multicomponent mixing tests with different end-member compositions were defined to investigate the observed major element, trace element and isotopic compositions. Using the obtained granitic compositions of rocks without evident mingling features, supposedly reflecting granitic melts derived from crustal melting, as the felsic end-member and the mafic, gabbroic compositions of this data set as the mafic end-member. As a dioritic magma composition does not represent a mafic, directly-mantle derived magma, unless the mantle domain was previously hybridised or mixing occurred already within the source domain, all rocks of dioritic composition are considered as hybrids or mixed rocks. Thus, mixing results suggest an input of ca. 16 – 22 % of felsic melt, to achieve the observed dioritic compositions, if the initial composition was comparable with the gabbroic composition. Conversely little mafic input is needed, ca. 9 – 12 %, if the weakly peraluminous, granodioritic samples were originally of a more granitic composition when compared to those derived from the partial melting of a metasedimentary source. Significantly less mafic input, between 2 – 8 %, is needed to describe the granitic compositions that show evident mingling features and follow the I-S-type boundary in the B-A diagram. The regression coefficients (expressed in R^2 values) of most rocks with mingling and/ or mixing features are largely between 0.9 and 1, suggesting potential mixing correlations, disregarding the chosen endmembers. Interestingly, R^2 values of the dioritic contact domains of samples s5Bb and s8Db, are generally lower at around 0.8 and thus less well correlated. This could stand in relation with the unmingled diorite sample s7A that shows relatively low < 0.7 R^2 values and can thus not be described as a mixed rock with the variable chosen end member compositions in these mixing tests.

Binary mixing tests of the isotopic systems aim to further investigate potential genetic links between the different magmatic rocks, as well as the migmatites and metapelites. $^{143}Nd/^{144}Nd$, $^{176}Hf/^{177}Hf$ and $^{87}Sr/^{86}Sr$ isotopic ratios of the magmatic rocks from Inzie Head delineate variable linear trends when plotted against the whole rock 1/Nd, 1/Hf and 1/Sr, respectively, to visualize the chemical compositions in relation to the isotopic signatures of the samples (fig. 58). The delineation of linear trends is suggestive for mixing relationships between the different magma sources to achieve the observed scatter in compositions of potentially mixed rocks. The isotopic compositions of the migmatites were used as an indicator for the isotopic signature derived from the crustal source as the felsic end-member composition and the gabbroic rocks as the mafic end-members (table 11). The $^{87}Sr/^{86}Sr$ versus 1/Sr plot visualizes defined linear trends between the fields delineated by the surrounding crustal host rocks and the gabbroic rocks from the Buchan Block area. Higher $Sr_{(i)}$ ratios of unmingled granites are close to the evolved values of the crustal host rocks, suggesting little to no input from a more juvenile source (fig. 58 – a). However, mingled magmatic rocks, all shift with lower $Sr_{(i)}$ ratios towards the more juvenile end. The linear trends towards lower values are suggestive to derive from a more juvenile source, rather than complete derivation from the surrounding crust. The mixing scenarios involving the $^{143}Nd/^{144}Nd$ ratios are broadly coherent with the suggested mixing relations by the $Sr_{(i)}$ isotopic signatures of the samples, delineating several linear mixing trends, as a result of highly variable $^{143}Nd/^{144}Nd$ isotopic

ratios (fig. 58 – b). Conversely, mixing scenarios of Hf isotopic zircon signatures of the rocks are highly variable and inconsistent with the other two isotopic systems (fig. 58 – c). This could be explained by the lack of Hf isotopic compositions of the gabbroic rocks from the Buchan Block domain. Thus, the Hf isotopic compositions of the most juvenile diorite samples were used to constrain the potential of mixing, which might not be representative of the true end-members composition.

TABLE 11: ISOTOPIC AND TRACE ELEMENT COMPOSITIONS OF CHOSEN END-MEMBERS FOR MIXING CALCULATIONS

Sample ID	Rock type	$^{87}Sr/^{86}Sr_{468}$	±2σ	$^{143}Nd/^{144}Nd_{468}$	±2σ	1/Sr	1/Nd
s010	Gabbro	0.70548	0.00003	0.51261	0.00000	0.00596	0.14782
s029	Metapelite	0.71975	0.00123	0.51117	0.00000	0.01310	0.03191
s037	Migmatite	0.71839	0.00011	0.51118	0.00000	0.00420	0.05666
s039	Migmatite	0.71781	0.00048	0.51167	0.00000	0.00693	0.10106
s040	Migmatite	0.72082	0.00071	0.51130	0.00000	0.00705	0.01768
s050	Gabbro	0.70606	0.00002	0.51253	0.00000	0.00250	0.03265

Sample ID	Rock type	$^{176}Hf/^{177}Hf_{468}$	±2σ	1/Hf
s7A	Diorite	0.28228	0.00002	0.17699
s8Db	Diorite	0.28227	0.00001	0.17167
s4D	Grt.-Leucosome	0.28178	0.00006	0.33445
s2A	Metapelite	0.28200	0.00003	0.22346
s1H	Granodiorite	0.28190	0.00004	0.10724
s5Bb	Diorite	0.28216	0.00002	0.15924

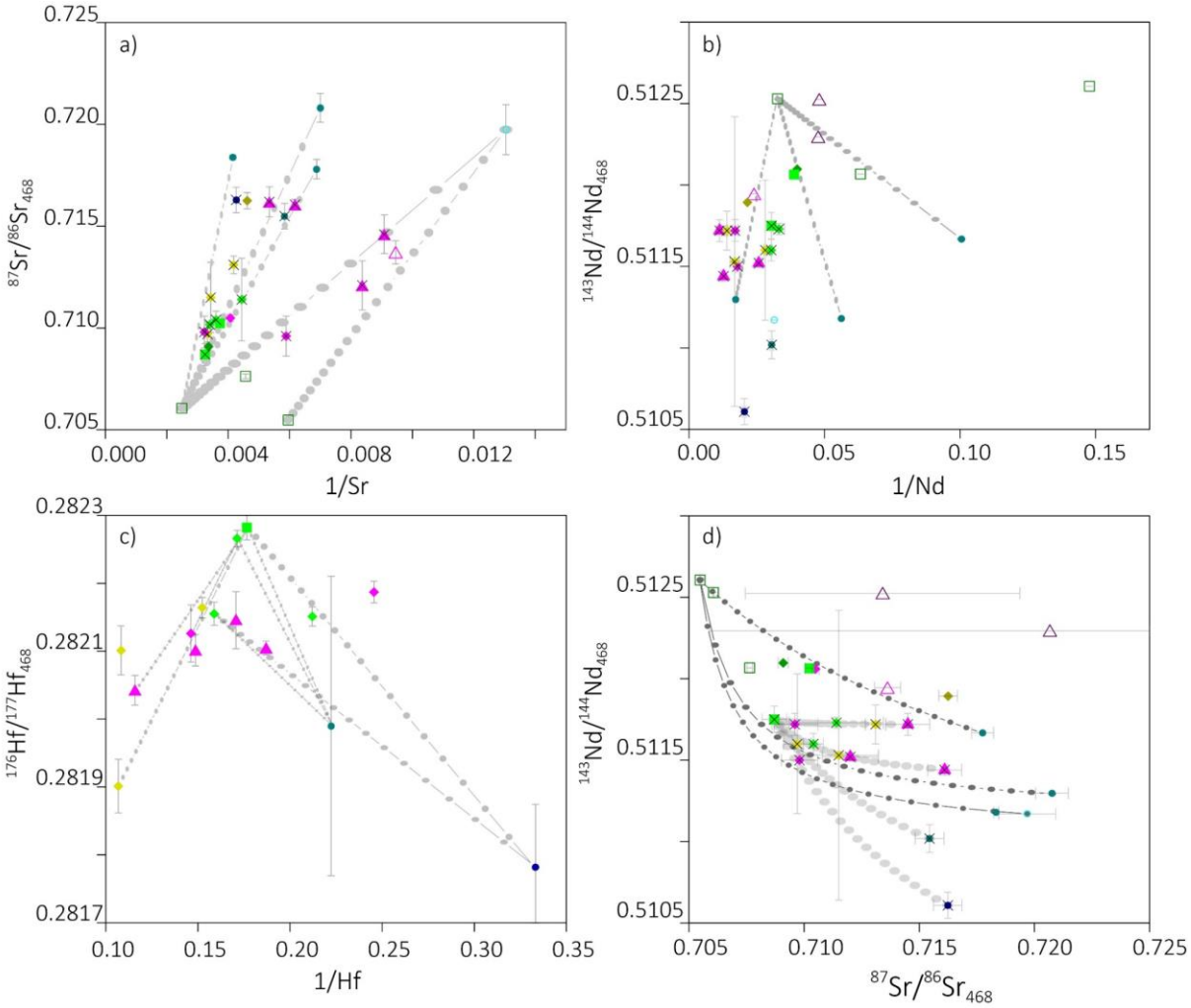

Figure 58 – Calculated mixing relations of the different isotopic systems; a) mixing relations of whole rock isotopic Sr_{468} values, apatite isotopic signatures are plotted for comparison and marked with black X; b) mixing relations of whole rock isotopic Nd_{468} values, apatite isotopic signatures are plotted for comparison and marked with black X; c) mixing relations of zircon isotopic Hf_{468} values; d) mixing hyperbolas between whole rock Nd_{468} and Sr_{468} isotopic signatures (dark grey dotted lines) as well as between apatite (marked with black X) Nd_{468} and Sr_{468} isotopic signatures (light grey dotted lines); Symbol and colour coding as in fig. 57

Potential mixing relations between the contrasting isotopic source domains are furthermore highlighted in mixing scenarios involving both isotopic systems. Mixing hyperbolas calculated based on the Nd and Sr isotopic ratios, delineate several possible mixing scenarios, which account for the variable isotopic compositions of the magmatic rocks. Varying isotopic signatures and trace element contents of the mafic rocks in this study, might suggest a potential inhomogeneous mantle source or crustal contamination during the petrogenesis of the rocks (Laurent et al., 2017). Studies have proposed a mantle source domain, previously enriched or contaminated by subduction processes of sedimentary rocks, to explain geochemical and isotopic compositions of similar dioritic samples (Laurent et al., 2014; Laurent and Zeh, 2015). Varying isotopic compositions might therefore reflect an isotopically heterogenous source, rather than mixing processes of contrasting magmas at crustal levels. However, periodic injection and emplacement of mafic magmas might promote interactions of different magma batches over a prolonged time enabling possible magma interaction and accounting for observed similar isotopic signatures in rocks that expose textural evidence suggested to derive from mixing. The isotopic signatures obtained from apatites of contrasting domains from the wispy contact sample s8D, are distinct. This is coherent with field observations, of wispy but clearly delineated contact margins. However, similar isotopic signatures of the granodioritic and dioritic domains of the gradual contact sample s5B, might suggest a direct correlation to the diffuse nature of the contact between the two chemically distinct domains. The isotopic signatures of zircon and apatites from the two domains show a similar highly variable spread, suggesting the preservation of small-scale heterogeneities on a larger outcrop scale. In addition, possible mixing or hybridization of these two samples is suggested by the weakly peraluminous and granodioritic character of s5Ba. Furthermore, sample s5Bb has a weaker metaluminous character than the other dioritic samples. Previous studies pointed out, that magma mixing processes can preserve smaller scale heterogeneities, even in presumably well-mixed, hybrid domains

(Laurent et al., 2017). Appropriate temperature conditions are crucial for the efficient interaction and mixing of contrasting magmas, as viscosity contrasts are high. Viscosity estimates based on experimental constrains for dioritic and granodioritic/ granitic rocks of broadly similar chemical composition from the Matok Pluton, suggest a lowering of viscosity contrasts at temperatures above 850°C, which is consistent with the modelled temperatures of the mafic intrusions in this study. The variety of magma interaction textures as seen in the field might therefore suggest differing equilibration temperatures. The older diorite intrusions at ca. 470 Ma, might reflect early intrusions into a colder but partially molten domain, resulting in sharp and wispy mingling textures. Higher temperatures differences would limit magma interactions, preserving distinct isotopic and geochemical signatures, as seen for the contact in s8D. Incremental or periodic replenishing of mafic magmas or intrusions at a later stage into a hotter crust may promote local mixing and hybridization of differing magmas (Laurent et al., 2017). Field and isotopic evidence of the younger diorite s5Bb suggests mafic magma interactions of the contrasting domains. The two distinct age peaks of s5Ba might reflect an early partially molten state and following re-equilibration of the isotopic systems or a continuous process, in coherence with textural evidence as seen in CL images of the zircon domains.

CHAPTER 6 CONCLUSION AND RECOMMENDATION

The Inzie Head coastal section within the Buchan Block domain is regarded to represent an exposed upper crustal domain of in-situ partial melting, where interaction processes between crustal and mantle derived magmas shaped the observed rock exposures. Geochronological constrains provide evidence for long-lived syn to post-collisional magmatism from 483±3 to 448±4 Ma within the Inzie Head domain, broadly contemporaneous with the established timing of the Grampian Orogenic event. The prolonged magmatic activity over a period of ca. 30 myr coincided with crustal anatexis of the metasedimentary sequence and the in-situ derivation of exposed leucosome. The constrained ages of two dioritic rocks are within error overlapping with the established timing of mafic magmatism within the Buchan Block domain and proposed to represent upper crustal intrusions that derived from mafic underplating beneath a thinned lithosphere. The intrusion of multiple mafic magma batches with estimated temperatures around 850 – 900°C are suggested to have acted as providers of heat to promote fluid-absent partial melting reactions within the upper crustal sequence and probably maintained a partially molten state within the domain over a prolonged period. Partial melting of the metapelitic sequence resulted in the formation of metatexitic to diatexitic migmatites and the in-situ derivation of leucosomes, which are rich in peritectic minerals such as garnet. The partially molten state of the crustal domain is suggested to have promoted mingling processes between the contrasting magmas.

Magma interaction within the Inzie Head domain was characterized by complex dynamics which resulted in highly diverse mingling and mixing relationships. The first emplacement of granitic rocks into the Inzie Head sequence was followed by dioritic intrusions. These comparatively older diorites show either no mingling features or sharp to wispy contact margins to adjacent granitic rocks and are distinct in their Hf isotopic signatures. These diorites are regarded to have cooled relatively quickly upon intrusion into the colder upper crustal environment, resulting in limited mingling features. Thus, mixing processes in form of crystal capture and diffusion driven re-equilibration were locally restricted to the vicinity of the contact margins. The older diorites are furthermore characterized by crustal-like isotopic signatures, that are overlapping within error with values obtained from mingled granodioritic and granitic rock exposures. It is thus suggested that the dioritic material derived from a contaminated or hybridized mantle source or that mixing processes occurred at the source domain, within a deeper and unexposed crustal level. The comparatively younger diorites are highly variable and more evolved in their isotopic signatures, which are within error overlapping with the calculated ages and isotopic averages of the granodioritic and granitic exposures. These diorites are suggested to have intruded into a crustal environment where the heat budget was already elevated, as mingling and mixing features are enhanced. Observed field exposures with gradual contact domains and mineral textures suggest that mixing was more efficient, where granitic material invaded into the younger dioritic magmas, as heating of the granitic material by the hotter mafic magmas promotes the interaction of the contrasting magmas. The granodioritic domains are generally in close relation with the diorite exposures, overlapping in constrained ages and isotopic signatures and thus possibly represent efficiently hybridized domains.

The chemical and isotopic compositions of granitic rocks in this study are interpreted to be inconsistent with the direct derivation from the surrounding crustal host rocks. Although the inherited zircon population within the igneous rocks show an overall similar spread as the detrital zircon population of the metapelitic and leucosome rocks, crustal evolution trends of obtained U-Pb and Lu-Hf isotopic compositions cannot account for the more juvenile signatures observed in zircon of the dioritic and granitic rocks. However, designed mixing models between mafic and felsic end-members, can account for the observed range in chemical and isotopic compositions of the different rocks. This is consistent with observed field observations and mineral textures, which are indicative for mixing scenarios. It is thus proposed that mixing and hybridization processes were involved in shaping the observed range in compositions. Little input of a juvenile mafic melt would suffice to generate the weakly peraluminous compositions observed in the granitic rocks with tendencies towards more juvenile isotopic signatures. Furthermore, little input of a strongly evolved felsic magma could explain the tendency towards more evolved isotopic signatures in dioritic rocks. The evaluation of field exposures and mineral textures in combination with the chemical and isotopic signatures of the different rocks indicates that in-situ mixing between contrasting magmas could have been a limited but dominant mechanism during the petrogenesis of the younger magmatic rocks of Inzie Head. The Inzie Head domain is thus proposed to represent an upper crustal MASH zone of limited magma interaction, as the heat budget within the system was probably insufficient to promote extensive mixing over a large area for a prolonged time. Initial mixing and mingling processes are proposed to have taken place at a deeper crustal level or at the source domain, shaping the chemical and isotopic compositions of the older diorites and granites in this study. To further comprehend the possibility of mixing and

hybridisation processes within the exposed section, stable isotope studies of the different rocks would be suggested. In addition, an in-depth study of in-situ isotope compositions of accessory minerals along the contact margins to investigate gradual changes would be recommended. This study did not obtain whole rock and mineral isotopic compositions on the same rocks, which could provide important clues on the petrogenesis of the studied rocks.

REFERENCES

Anders, E., Grevesse, N., 1989. Abundances of the elements: Meteoritic and solar. Geochim. Cosmochim. Acta 53, 197–214. https://doi.org/10.1016/0016-7037(89)90286-X

Annen, C., Blundy, J.D., Sparks, R.S.J., 2006. The genesis of intermediate and silicic magmas in deep crustal hot zones. J. Petrol. 47, 505–539. https://doi.org/10.1093/petrology/egi084

Barbarin, B., 2005. Mafic magmatic enclaves and mafic rocks associated with some granitoids of the central Sierra Nevada batholith, California: Nature, origin, and relations with the hosts. Lithos 80, 155–177. https://doi.org/10.1016/j.lithos.2004.05.010

Barrow, G., 1912. On the geology of lower dee-side and the southern highland border. Proc. Geol. Assoc. 23, 274–290. https://doi.org/10.1016/S0016-7878(12)80018-6

Barrow, G., 1893. On an Intrusion of Muscovite-biotite Gneiss in the South-eastern Highlands of Scotland, and its accompanying Metamorphism. Q. J. Geol. Soc. London 49, 330–358. https://doi.org/10.1144/GSL.JGS.1893.049.01-04.52

Bateman, R., 1995. The interplay between crystallization, replenishment and hybridization in large felsic magma chambers. Earth Sci. Rev. 39, 91–106. https://doi.org/10.1016/0012-8252(95)00003-S

Baxter, S., Feely, M., 2002. Magma mixing and mingling textures in granitoids: examples from the Galway Granite, Connemara, Ireland. Mineral. Petrol. 76, 63–74. https://doi.org/10.1007/s007100200032

Bergantz, G.W., 1989. Underplating and partial melting: Implications for melt generation and extraction. Science (80-.). 245, 1093–1095. https://doi.org/10.1126/science.245.4922.1093

Blichert-Toft, J., Albarède, F., 2008. Hafnium isotopes in Jack Hills zircons and the formation of the Hadean crust. Earth Planet. Sci. Lett. 265, 686–702. https://doi.org/10.1016/j.epsl.2007.10.054

Blichert-Toft, J., Boyet, M., Télouk, P., Albarède, F., 2002. 147Sm-143Nd and 176Lu-176Hf in eucrites and the differentiation of the HED parent body. Earth Planet. Sci. Lett. 204, 167–181. https://doi.org/10.1016/S0012-821X(02)00976-7

Bouvier, A., Vervoort, J.D., Patchett, P.J., 2008. The Lu-Hf and Sm-Nd isotopic composition of CHUR: Constraints from unequilibrated chondrites and implications for the bulk composition of terrestrial planets. Earth Planet. Sci. Lett. 273, 48–57. https://doi.org/10.1016/j.epsl.2008.06.010

Brady, J.B., Cherniak, D.J., 2010. Diffusion in minerals: An overview of published experimental diffusion data. Rev. Mineral. Geochemistry 72, 899–920. https://doi.org/10.2138/rmg.2010.72.20

Brown, M., 2013. Granite: From genesis to emplacement. Bull. Geol. Soc. Am. 125, 1079–1113. https://doi.org/10.1130/B30877.1

Brown, M., 1973. The definition of metatexis, diatexis and migmatite. Proc. Geol. Assoc. 84, 371–382. https://doi.org/10.1016/S0016-7878(73)80021-5

Brown, M., Rushmer, T., 2006. Evolution and Differentiation of the Continental Crust. Cambridge Cambridge Univ. Press.

Carty, J.P., Connelly, J.N., Hudson, N.F.C., Gale, J.F.W., 2012. Constraints on the timing of deformation, magmatism and metamorphism in the dalradian of NE Scotland. Scottish J. Geol. 48, 103–117. https://doi.org/10.1144/sjg2012-407

Carvalho, B.B., Sawyer, E.W., Janasi, V.A., 2016. Crustal reworking in a shear zone: Transformation of metagranite to migmatite. J. Metamorph. Geol. 34, 237–264. https://doi.org/10.1111/jmg.12180

Castro, A., 2001. Plagioclase morphologies in assimilation experiments. Implications for disequilibrium melting in the generation of granodiorite rocks. Mineral. Petrol. 71, 31–49. https://doi.org/10.1007/s007100170044

Cawood, P.A., McCausland, P.J.A., Dunning, G.R., 2001. Opening Iapetus: Constraints from the Laurentian margin in Newfoundland. Bull. Geol. Soc. Am. 113, 443–453. https://doi.org/10.1130/0016-7606(2001)113<0443:OICFTL>2.0.CO;2

Chappell, B.W., 1996. Magma mixing and the production of compositional variation within granite suites: Evidence from the granites of southeastern Australia. J. Petrol. 37, 449–470. https://doi.org/10.1093/petrology/37.3.449

Cherniak, D.J., 2010. Diffusion in Accessory Minerals: Zircon, Titanite, Apatite, Monazite and Xenotime. Rev. Mineral. Geochemistry 72, 827–869. https://doi.org/10.2138/rmg.2010.72.18

Chew, D.M., Strachan, R.A., 2014. The laurentian caledonides of Scotland and Ireland. Geol. Soc. Spec. Publ. 390, 45–91. https://doi.org/10.1144/SP390.16

Clemens, J.D., Maas, R., Waight, T.E., Kunneke, L.K., 2016. Genesis of felsic plutonic magmas and their igneous enclaves: The Cobaw batholith of southeastern Australia. J. Geol. 124, 293–311. https://doi.org/10.1086/685509

Clemens, J.D., Stevens, G., 2016. Melt segregation and magma interactions during crustal melting: Breaking out of the matrix. Earth-Science Rev. 160, 333–349. https://doi.org/10.1016/j.earscirev.2016.07.012

Clemens, J.D., Stevens, G., 2012. What controls chemical variation in granitic magmas? Lithos 134–135, 317–329.

https://doi.org/10.1016/J.LITHOS.2012.01.001

Clemens, J.D., Stevens, G., Bryan, S.E., 2020. Conditions during the formation of granitic magmas by crustal melting – Hot or cold; drenched, damp or dry? Earth-Science Rev. 200. https://doi.org/10.1016/j.earscirev.2019.102982

Clemens, J.D., Vielzeuf, D., 1987. Constraints on melting and magma production in the crust. Earth Planet. Sci. Lett. 86, 287–306. https://doi.org/10.1016/0012-821X(87)90227-5

Clemens, J.D., Watkins, J.M., 2001. The fluid regime of high-temperature metamorphism during granitoid magma genesis. Contrib. to Mineral. Petrol. 140, 600–606. https://doi.org/10.1007/s004100000205

Collins, W.J., 1996. Lachlan Fold Belt granitoids: Products of three-component mixing. Trans. R. Soc. Edinburgh, Earth Sci. 87, 171–181. https://doi.org/10.1017/s0263593300006581

Collins, W.J., Huang, H.Q., Jiang, X., 2016. Water-fluxed crustal melting produces Cordilleran batholiths. Geology 44, 143–146. https://doi.org/10.1130/G37398.1

Collins, W.J., Murphy, J.B., Johnson, T.E., Huang, H.Q., 2020. Critical role of water in the formation of continental crust. Nat. Geosci. 13, 331–338. https://doi.org/10.1038/s41561-020-0573-6

Couzinié, S., Laurent, O., Chelle-Michou, C., Bouilhol, P., Paquette, J.L., Gannoun, A.M., Moyen, J.F., 2019. Detrital zircon U–Pb–Hf systematics of Ediacaran metasediments from the French Massif Central: Consequences for the crustal evolution of the north Gondwana margin. Precambrian Res. 324, 269–284. https://doi.org/10.1016/j.precamres.2019.01.016

de Campos, C.P., Perugini, D., Ertel-Ingrisch, W., Dingwell, D.B., Poli, G., 2011. Enhancement of magma mixing efficiency by chaotic dynamics: An experimental study. Contrib. to Mineral. Petrol. 161, 863–881. https://doi.org/10.1007/s00410-010-0569-0

Debon, F., Le Fort, P., 1983. A chemical–mineralogical classification of common plutonic rocks and associations. Trans. R. Soc. Edinb. Earth Sci. 73, 135–149. https://doi.org/10.1017/S0263593300010117

Dewey, J.F., 2005. Orogeny can be very short. Proc. Natl. Acad. Sci. U. S. A. 102, 15286–15293. https://doi.org/10.1073/pnas.0505516102

Droop, G.T.R., Charnley, N.R., 1985. Comparative geobarometry of pelitic hornfelses associated with the Newer Gabbros: a preliminary study. J. Geol. Soc. London 142, 53–62. https://doi.org/10.1144/gsjgs.142.1.0053

El Desouky, M., Feely, M., Mohr, P., 1996. Diorite-granite magma mingling and mixing along the axis of the Galway Granite batholith, Ireland. J. Geol. Soc. London. 153, 361–374. https://doi.org/10.1144/gsjgs.153.3.0361

Farina, F., Stevens, G., Gerdes, A., Frei, D., 2014. Small-scale Hf isotopic variability in the Peninsula pluton (South Africa): the processes that control inheritance of source 176Hf/177Hf diversity in S-type granites. Contrib. to Mineral. Petrol. 168, 1–18. https://doi.org/10.1007/s00410-014-1065-8

Farina, F., Stevens, G., Villaros, A., 2012. Multi-batch, incremental assembly of a dynamic magma chamber: The case of the Peninsula pluton granite (Cape Granite Suite, South Africa). Mineral. Petrol. 106, 193–216. https://doi.org/10.1007/s00710-012-0224-8

Fettes, D.J., 2013. Dalradian structure and metamorphism. Edinburgh Geol. 53, 10–15.

Fettes, D.J., 1970. The structural and metamorphic state of the Dalradian rocks and their bearing on the age of emplacement of the basic sheet. Scottish J. Geol. 6, 108–118. https://doi.org/10.1144/sjg06010108

Fettes, D.J., Long, C.B., Bevins, R.E., Max, M.D., Oliver, G.J.H., Primmer, T.J., Thomas, L.J., Yardley, B.W.D., 1985. Grade and time of metamorphism in the Caledonide Orogen of Britain and Ireland. Geol. Soc. Mem. 9, 41–53. https://doi.org/10.1144/GSL.MEM.1985.009.01.03

Fisher, C.M., Bauer, A.M., Vervoort, J.D., 2020. Disturbances in the Sm–Nd isotope system of the Acasta Gneiss Complex—Implications for the Nd isotope record of the early Earth. Earth Planet. Sci. Lett. 530, 1–10. https://doi.org/10.1016/j.epsl.2019.115900

Foden, J.D., Elburg, M.A., Turner, S.P., Sandiford, M., O'Callaghan, J., Mitchell, S., 2002. Granite production in the Delamerian Orogen, South Australia. J. Geol. Soc. London. 159, 557–575. https://doi.org/10.1144/0016-764901-099

Frei, D., Gerdes, A., 2009. Precise and accurate in situ U-Pb dating of zircon with high sample throughput by automated LA-SF-ICP-MS. Chem. Geol. 261, 261–270. https://doi.org/10.1016/j.chemgeo.2008.07.025

Gerdes, A., Zeh, A., 2009. Zircon formation versus zircon alteration - New insights from combined U-Pb and Lu-Hf in-situ LA-ICP-MS analyses, and consequences for the interpretation of Archean zircon from the Central Zone of the Limpopo Belt. Chem. Geol. 261, 230–243. https://doi.org/10.1016/j.chemgeo.2008.03.005

Gerdes, A., Zeh, A., 2006. Combined U-Pb and Hf isotope LA-(MC-)ICP-MS analyses of detrital zircons: Comparison with SHRIMP and new constraints for the provenance and age of an Armorican metasediment in Central Germany. Earth Planet. Sci. Lett. 249, 47–61. https://doi.org/10.1016/j.epsl.2006.06.039

Griffin, W.L., Pearson, N.J., Belousova, E., Jackson, S.E., Van Achterbergh, E., O'Reilly, S.Y., Shee, S.R.,

2000. The Hf isotope composition of cratonic mantle: LAM-MC-ICPMS analysis of zircon megacrysts in kimberlites. Geochim. Cosmochim. Acta 64, 133–147. https://doi.org/10.1016/S0016-7037(99)00343-9

Harmon, R.S., 1984. Stable isotope geochemistry of Caledonian granitoids from the British Isles and East Greenland. Phys. Earth Planet. Inter. 35, 105–120. https://doi.org/10.1016/0031-9201(84)90037-2

Harte, B., Hudson, N.F.C., 1979. Pelite facies series and the temperatures and pressures of Dalradian metamorphism in E Scotland. Geol. Soc. Spec. Publ. London 8, 323–337. https://doi.org/10.1144/GSL.SP.1979.008.01.36

Hibbard, M.J., 1991. Textural anatomy of twelve magma-mixed granitoid systems: In: Enclaves and granite petrology Didier, J., Barbarin, B. (Eds). Elsevier, Amsterdam Dev Petrol, 431–444.

Hibbard, M.J., 1981. The magma mixing origin of mantled feldspars. Contrib. to Mineral. Petrol. 76, 158–170. https://doi.org/10.1007/BF00371956

Hildreth, W., 1981. Gradients in Silicic Magma Chambers: Implications for Lithospheric Magmatism. J. Geophys. Res. 86, 10153–10192.

Hildreth, W., Moorbath, S., 1988. Crustal contributions to arc magmatism in the Andes of Central Chile. Contrib. to Mineral. Petrol. 98, 455–489. https://doi.org/10.1007/BF00372365

Huppert, H.E., Sparks, R.S.J., 1988. The generation of granitic magmas by intrusion of basalt into continental crust. J. Petrol. 29, 599–624. https://doi.org/10.1093/petrology/29.3.599

Irvine, T.N., Baragar, W.R.A., 1971. A Guide to the Chemical Classification of the Common Volcanic Rocks. Can. J. Earth Sci. 8, 523–548. https://doi.org/10.1139/e71-055

Jackson, S.E., Pearson, N.J., Griffin, W.L., Belousova, E.A., 2004. The application of laser ablation-inductively coupled plasma-mass spectrometry to in situ U-Pb zircon geochronology. Chem. Geol. 211, 47–69. https://doi.org/10.1016/j.chemgeo.2004.06.017

Janoušek, V., Bowes, D.R., Braithwaite, C.J.R., Rogers, G., 2000. Micro structural and mineralogical evidence for limited involvement of magma mixing in the petrogenesis of a Hercynian high-K calc-alkaline intrusion: The Kozárovice granodiorite, Central Bohemian Pluton, Czech Republic. Trans. R. Soc. Edinburgh, Earth Sci. 91, 15–26. https://doi.org/10.1017/S0263593300007264

Janoušek, V., Braithwaite, C.J.R., Bowes, D.R., Gerdes, A., 2004. Magma-mixing in the genesis of Hercynian calc-alkaline granitoids: An integrated petrographic and geochemical study of the Sázava intrusion, Central Bohemian Pluton, Czech Republic. Lithos 78, 67–99. https://doi.org/10.1016/j.lithos.2004.04.046

Johnson, K., Barnes, C.G., 2006. Magma mixing and mingling in the Grayback pluton, Klamath Mountains, Oregon. Spec. Pap. Geol. Soc. Am. 410, 247–267. https://doi.org/10.1130/2006.2410(12)

Johnson, T.E., Hudson, N.F.., Droop, G.T.R., 2001a. Partial melting in the Inzie Head gneisses: The role of water and a petrogenetic grid in KFMASH applicable to anatectic pelitic migmatites. J. Metamorph. Geol. 19, 99–118. https://doi.org/10.1046/j.0263-4929.2000.00292.x

Johnson, T.E., Hudson, N.F.C., Droop, G.T.R., 2003. Evidence for a genetic granite – migmatite link in the Dalradian of NE Scotland. J. Geol. Soc. London 160, 447–457.

Johnson, T.E., Hudson, N.F.C., Droop, G.T.R., 2001b. Melt segregation structures within the lnzie Head gneisses of the northeastern Dalradian. Scottish J. Geol. 37, 59–72. https://doi.org/10.1144/sjg37020059

Johnson, T.E., Kirkland, C.L., Reddy, S.M., Fischer, S., 2015. Grampian migmatites in the Buchan Block, NE Scotland. J. Metamorph. Geol. 33, 695–709. https://doi.org/10.1111/jmg.12147

Johnson, T.E., Kirkland, C.L., Viete, D.R., Fischer, S., Reddy, S.M., Evans, N.J., McDonald, B.J., 2017. Zircon geochronology reveals polyphase magmatism and crustal anatexis in the Buchan Block, NE Scotland: Implications for the Grampian Orogeny. Geosci. Front. 8, 1469–1478. https://doi.org/10.1016/j.gsf.2017.02.002

Kneller, B.C., Aftalion, M., 1987. The isotopic and structural age of the Aberdeen Granite. J. Geol. Soc. London 144, 717–721. https://doi.org/10.1144/gsjgs.144.5.0717

Kumar, S., Pieru, T., 2010. Petrography and major elements geochemistry of microgranular enclaves and neoproterozoic granitoids of south Khasi, Meghalaya: Evidence of magma mixing and alkali diffusion. J. Geol. Soc. India 76, 345–360. https://doi.org/10.1007/s12594-010-0106-9

Kumar, S., Rino, V., Pal, A.B., 2004. Typology and geochemistry of microgranular enclaves hosted in Malanjkhand granitoids, Central India. J. Geol. Soc. India 64, 277–292.

Lambert, I.B., Wyllie, P.J., 1972. Melting of Gabbro (Quartz Eclogite) with Excess Water to 35 Kilobars, with Geological Applications. J. Geol. 80, 693–708. https://doi.org/10.1086/627795

Laurent, O., Rapopo, M., Stevens, G., Moyen, J.F., Martin, H., Doucelance, R., Bosq, C., 2014. Contrasting petrogenesis of Mg-K and Fe-K granitoids and implications for post-collisional magmatism: Case study from the Late-Archean Matok pluton (Pietersburg block, South Africa). Lithos 196–197, 131–149.

https://doi.org/10.1016/j.lithos.2014.03.006

Laurent, O., Zeh, A., 2015. A linear Hf isotope-age array despite different granitoid sources and complex Archean geodynamics: Example from the Pietersburg block (South Africa). Earth Planet. Sci. Lett. 430, 326–338. https://doi.org/10.1016/j.epsl.2015.08.028

Laurent, O., Zeh, A., Gerdes, A., Villaros, A., Gros, K., Słaby, E., 2017. How do granitoid magmas mix with each other? Insights from textures, trace element and Sr–Nd isotopic composition of apatite and titanite from the Matok pluton (South Africa). Contrib. to Mineral. Petrol. 172, 1–22. https://doi.org/10.1007/s00410-017-1398-1

Ludwig, K.R., 2003. A Geochronological Toolkit for Microsoft Excel. Berkeley Geochronol. Center, Spec. Publ. 5, 71.

Mayne, M.J., Stevens, G., Moyen, J.F., 2019. A phase equilibrium investigation of selected source controls on the composition of melt batches generated by sequential melting of an average metapelite. Geol. Soc. London Spec. Publ. 491, 223–241. https://doi.org/10.1144/SP491-2018-121

Middlemost, E.A.K., 1994. Naming materials in the magma/igneous rock system. Earth-Science Rev. 37, 215–224. https://doi.org/10.1016/0012-8252(94)90029-9

Morgavi, D., Perugini, D., De Campos, C.P., Ertel-Ingrisch, W., Dingwell, D.B., 2013. Morphochemistry of patterns produced by mixing of rhyolitic and basaltic melts. J. Volcanol. Geotherm. Res. 253, 87–96. https://doi.org/10.1016/j.jvolgeores.2012.12.007

Moyen, J.-F., 2020. Granites and crustal heat budget. Geol. Soc. Spec. Publ. 491, 77–100. https://doi.org/10.1144/SP491-2018-148

Oliver, G.J.H., 2001. Reconstruction of the grampian episode in Scotland: Its place in the caledonian orogeny. Tectonophysics 332, 23–49. https://doi.org/10.1016/S0040-1951(00)00248-1

Oliver, G.J.H., Wilde, S.A., Wan, Y., 2008. Geochronology and geodynamics of Scottish granitoids from the late neoproterozoic break-up of Rodinia to Palaeozoic collision. J. Geol. Soc. London 165, 661–674. https://doi.org/10.1144/0016-76492007-105

Ottino, J.M., Leong, C.W., Rising, H., Swanson, P.D., 1988. Morphological structures produced by mixing in chaotic flows. Nature 333, 419–425. https://doi.org/10.1038/333419a0

Pankhurst, R.J., 1974. Rb-Sr Whole-Rock chronology of Caledonian events in Northeast Scotland. Bull. Geol. Soc. Am. 85, 345–350. https://doi.org/10.1130/0016-7606(1974)85<345:RWCOCE>2.0.CO;2

Pankhurst, R.J., 1970. The geochronology of the basic igneous complexes. Scottish J. Geol. 6, 83–107. https://doi.org/10.1144/sjg06010083

Patchett, P.J., Vervoort, J.D., Söderlund, U., Salters, V.J.M., 2004. Lu-Hf and Sm-Nd isotopic systematics in chondrites and their constraints on the Lu-Hf properties of the Earth. Earth Planet. Sci. Lett. 222, 29–41. https://doi.org/10.1016/j.epsl.2004.02.030

Pearce, J., 1996. Source of Granitic rocks. Episodes 19, 120–125.

Perugini, D., Poli, G., 2012. The mixing of magmas in plutonic and volcanic environments: Analogies and differences. Lithos 153, 261–277. https://doi.org/10.1016/j.lithos.2012.02.002

Perugini, D., Poli, G., 2005. Viscous fingering during replenishment of felsic magma chambers by continuous inputs of mafic magmas: Field evidence and fluid-mechanics experiments. Geology 33, 5–8. https://doi.org/10.1130/G21075.1

Perugini, D., Poli, G., 2000. Chaotic dynamics and fractals in magmatic interaction processes: a different approach to the interpretation of mafic microgranular enclaves. Earth Planet. Sci. Lett. 175, 93–103. https://doi.org/10.1016/s0012-821x(00)00039-x

Petford, N., Cruden, A.R., McCaffrey, K.J.W., Vigneresse, J.L., 2000. Granite magma formation, transport and emplacement in the Earth's crust. Nature 408, 669–673. https://doi.org/10.1038/35047000

Petrelli, M., Perugini, D., Poli, G., 2011. Transition to chaos and implications for time-scales of magma hybridization during mixing processes in magma chambers. Lithos 125, 211–220. https://doi.org/10.1016/j.lithos.2011.02.007

Petrelli, M., Perugini, D., Poli, G., 2006. Time-scales of hybridisation of magmatic enclaves in regular and chaotic flow fields: Petrologic and volcanologic implications. Bull. Volcanol. 68, 285–293. https://doi.org/10.1007/s00445-005-0007-8

Phillips, E.R., Highton, A.J., Hyslop, E.K., Smith, M., 1999. The timing and P-T conditions of regional metamorphism in the Central Highlands, Scotland. J. Geol. Soc. London. 156, 1183–1193. https://doi.org/10.1144/gsjgs.156.6.1183

Pietranik, A., Koepke, J., 2014. Plagioclase transfer from a host granodiorite to mafic microgranular enclaves: diverse records of magma mixing. Mineral. Petrol. 108, 681–694. https://doi.org/10.1007/s00710-014-0326-6

Pietranik, A., Koepke, J., 2009. Interactions between dioritic and granodioritic magmas in mingling zones: Plagioclase record of mixing, mingling and subsolidus interactions in the Gęsiniec Intrusion, NE Bohemian Massif, SW Poland. Contrib. to Mineral. Petrol. 158, 17–36. https://doi.org/10.1007/s00410-

008-0368-z

Poli, G., Tommasini, S., Halliday, A.N., 1996. Trace element and isotopic exchange during acid-basic magma interaction processes. Trans. R. Soc. Edinburgh, Earth Sci. 87, 225–232. https://doi.org/10.1017/s0263593300006635

Read, B.H.H., 1952. Metamorphism and Migmatisation in the Ythan Valley , Aberdeenshire. Trans. Edinburgh Geol. Soc. 15, 265–279.

Richards, J.P., 2003. Tectono-magmatic precursors for porphyry Cu-(Mo-Au) deposit formation. Econ. Geol. 98, 1515–1533. https://doi.org/10.2113/gsecongeo.98.8.1515

Rudnick, R.L., 1995. Making continental crust. Nature 378, 603–605.

Rudnick, R.L., Fountain, D.M., 1995. Nature and composition of the continental crust: a lower crustal perspective. Rev. Geophys. 33, 267–309.

Sawyer, E.W., 1999. Criteria for the recognition of partial melting. Phys. Chem. Earth 24, 269–279. https://doi.org/10.1016/S1464-1895(99)00029-0

Sawyer, E.W., 1998. Formation and evolution of granite magmas during crustal reworking: the significance of diatexites. J. Petrol. 39, 1147–1167. https://doi.org/10.1093/petroj/39.6.1147

Sawyer, E.W., Cesare, B., Brown, M., 2011. When the continental crust melts. Elements 7, 229–234. https://doi.org/10.2113/gselements.7.4.229

Scherer, E., Münker, C., Mezger, K., 2001. Calibration of the lutetium-hafnium clock. Science (80-.). 293, 683–687. https://doi.org/10.1126/science.1061372

Schwindinger, M., Weinberg, R.F., 2017. A felsic MASH zone of crustal magmas — Feedback between granite magma intrusion and in situ crustal anatexis. Lithos 284–285, 109–121. https://doi.org/10.1016/j.lithos.2017.03.030

Shand, S.J., 1943. Eruptive Rocks. Their Genesis, Composition, Classification, and Their Relation to Ore-Deposits with a Chapter on Meteorite. John Wiley Sons, New-York 444. https://doi.org/10.1097/00010694-194807000-00012

Słaby, E., Götze, J., Wörner, G., Simon, K., Wrzalik, R., Śmigielski, M., 2008. K-feldspar phenocrysts in microgranular magmatic enclaves: A cathodoluminescence and geochemical study of crystal growth as a marker of magma mingling dynamics. Lithos 105, 85–97. https://doi.org/10.1016/j.lithos.2008.02.006

Sláma, J., Košler, J., Condon, D.J., Crowley, J.L., Gerdes, A., Hanchar, J.M., Horstwood, M.S.A., Morris, G.A., Nasdala, L., Norberg, N., Schaltegger, U., Schoene, B., Tubrett, M.N., Whitehouse, M.J., 2008. Plešovice zircon - A new natural reference material for U-Pb and Hf isotopic microanalysis. Chem. Geol. 249, 1–35. https://doi.org/10.1016/j.chemgeo.2007.11.005

Sparks, R.S.J., Marshall, L.A., 1986. Thermal and mechanical constraints on mixing between mafic and silicic magmas. J. Volcanol. Geotherm. Res. 29, 99–124. https://doi.org/10.1016/0377-0273(86)90041-7

Spera, F.J., Schmidt, J.S., Bohrson, W.A., Brown, G.A., 2016. Dynamics and thermodynamics of magma mixing: Insights from a simple exploratory model. Am. Mineral. 101, 627–643. https://doi.org/10.2138/am-2016-5305

Stephenson, D., Gould, D., 1995. British Regional Geology: The Grampian Highlands. HMSO Br. Geol. Surv. London 261. https://doi.org/10.1086/624615

Stephenson, D., Mendum, J.R., Fettes, D.J., Leslie, A.G., 2013a. The Dalradian rocks of Scotland: An introduction. Proc. Geol. Assoc. 124, 3–82. https://doi.org/10.1016/j.pgeola.2012.06.002

Stephenson, D., Mendum, J.R., Fettes, D.J., Smith, C.G., Gould, D., Tanner, P.W.G., Smith, R.A., 2013b. The Dalradian rocks of the north-east Grampian Highlands of Scotland. Proc. Geol. Assoc. 124, 318–392. https://doi.org/10.1016/j.pgeola.2012.07.011

Stevens, G., Clemens, J.D., 1993. Fluid-absent melting and the roles of fluids in the lithosphere: a slanted summary? Chem. Geol. 108, 1–17. https://doi.org/10.1016/0009-2541(93)90314-9

Stevens, G., Clemens, J.D., Droop, G.T.R., 1997. Melt production during granulite-facies anatexis: Experimental data from “primitive” metasedimentary protoliths. Contrib. to Mineral. Petrol. 128, 352–370. https://doi.org/10.1007/s004100050314

Stevens, G., Villaros, A., Moyen, J.F., 2007. Selective peritectic garnet entertainment as the origin of geochemical diversity in S-type granites. Geology 35, 9–12. https://doi.org/10.1130/G22959A.1

Strachan, R.A., Smith, M., Harris, A.L., Fettes, D.J., 2002. The Northern Highland and Grampian Terranes. Geol. Scotl. 81–148.

Streck, M.J., 2008. Mineral textures and zoning as evidence for open system processes. Rev. Mineral. Geochemistry 69, 595–622. https://doi.org/10.2138/rmg.2008.69.15

Sun, S.S., McDonough, W.F., 1989. Chemical and isotopic systematics of oceanic basalts: Implications for mantle composition and processes. Geol. Soc. Spec. Publ. 42, 313–345. https://doi.org/10.1144/GSL.SP.1989.042.01.19

Tanaka, T., Togashi, S., Kamioka, H., Amakawa, H., Kagami, H., Hamamoto, T., Yuhara, M., Orihashi, Y., Yoneda, S., Shimizu, H., Kunimaru, T., Takahashi, K., Yanagi, T., Nakano, T., Fujimaki, H., Shinjo, R., Asahara, Y., Tanimizu, M., Dragusanu,

C., 2000. JNdi-1: A neodymium isotopic reference in consistency with LaJolla neodymium. Chem. Geol. 168, 279–281. https://doi.org/10.1016/S0009-2541(00)00198-4

Taylor, S.R., McLennan, S.M., 1995. The geochemical evolution crust of the continental crust. Rev. Mineral. Geochemistry 33, 241–265.

Thompson, A.B., 1996. Fertility of crustal rocks during anatexis. Trans. R. Soc. Edinburgh, Earth Sci. 87, 1–10. https://doi.org/10.1017/s0263593300006428

Thompson, A.B., Connolly, J.A.D., 1995. Melting of the continental crust: Some thermal and petrological constraints on anatexis in continental collision zones and other tectonic settings. J. Geophys. Res. 100, 15565–15579.

Thompson, R.N., 1985. Model for Grampian tract evolution. Nature 314, 562. https://doi.org/10.1038/314562a0

Trewin, N.H., Rollin, K., 2002. In: Trewin, N.H. (Ed.), The Geology of Scotland. Geol. Soc. London, Geology of Series 1–25.

Turner, F.J., 1981. Metamorphic petrology: Mineralogical, field, and tectonic aspects , p. (2nd Ed. New York, McGraw- Hill 524.

Ubide, T., Galé, C., Larrea, P., Arranz, E., Lago, M., Tierz, P., 2014. The relevance of crystal transfer to magma mixing: A case study in composite dykes from the central pyrenees. J. Petrol. 55, 1535–1559. https://doi.org/10.1093/petrology/egu033

Vervoort, J.D., Kemp, A.I.S., 2016. Clarifying the zircon Hf isotope record of crust – mantle evolution. Chem. Geol. 425, 65–75. https://doi.org/10.1016/j.chemgeo.2016.01.023

Vervoort, J.D., Patchett, P.J., Albarède, F., Blichert-Toft, J., Rudnick, R., Downes, H., 2000. Hf-Nd isotopic evolution of the lower crust. Earth Planet. Sci. Lett. 181, 115–129. https://doi.org/10.1016/S0012-821X(00)00170-9

Vielzeuf, D., Clemens, J.D., Pin, C., Moinet, E., 1990. Granites, granulites, and crustal differentiation. In: D. Vielzeuf P. Vidal (Eds), Granulites Crustal Differ. NATO ASI Ser. Kluwer Acad. Publ. Dordr. 59–86. https://doi.org/10.1007/978-94-009-2055-2

Vielzeuf, D., Holloway, J.R., 1988. Experimental determination of the fluid-absent melting relations in the pelitic system. Contrib. to Mineral. Petrol. 98, 257–276. https://doi.org/10.1007/bf00375178

Vielzeuf, D., Montel, J.M., 1994. Partial melting of metagreywackes. Part I. Fluid-absent experiments and phase relationships. Contrib. to Mineral. Petrol. 117, 375–393. https://doi.org/10.1007/BF00307272

Viete, D.R., Oliver, G.J.H., Fraser, G.L., Forster, M.A., Lister, G.S., 2013. Timing and heat sources for the Barrovian metamorphism, Scotland. Lithos 177, 148–163. https://doi.org/10.1016/j.lithos.2013.06.009

Viete, D.R., Richards, S.W., Lister, G.S., Oliver, G.J.H., Banks, G.J., 2010. Lithospheric-scale extension during Grampian orogenesis in Scotland. Geol. Soc. Spec. Publ. 335, 121–160. https://doi.org/10.1144/SP335.7

Villaros, A., Buick, I.S., Stevens, G., 2012. Isotopic variations in S-type granites: An inheritance from a heterogeneous source? Contrib. to Mineral. Petrol. 163, 243–257. https://doi.org/10.1007/s00410-011-0673-9

Villaseca, C., Barbero, L., Rogers, G., 1998. Crustal origin of Hercynian peraluminous granitic batholiths of central Spain: petrological, geochemical and isotopic (Sr, Nd) constraints. Lithos 43, 55–79. https://doi.org/10.1016/S0024-4937(98)00002-4

Walker, B.A., Bergantz, G.W., Otamendi, J.E., Ducea, M.N., Cristofolini, E.A., 2015. A MASH zone revealed: The mafic complex of the Sierra Valle Fértil. J. Petrol. 56, 1863–1896. https://doi.org/10.1093/petrology/egv057

Weidendorfer, D., Mattsson, H.B., Ulmer, P., 2014. Dynamics of magma mixing in partially crystallized magma chambers: Textural and petrological constraints from the basal complex of the Austurhorn intrusion (SE Iceland), Journal of Petrology. https://doi.org/10.1093/petrology/egu044

Weinberg, R.F., Hasalová, P., 2015. Water-fluxed melting of the continental crust: A review. Lithos 212–215, 158–188. https://doi.org/10.1016/j.lithos.2014.08.021

Weinberg, R.F., Vernon, R.H., Schmeling, H., 2021. Processes in mushes and their role in the differentiation of granitic rocks. Earth-Science Rev. https://doi.org/10.1016/j.earscirev.2021.103665

White, R.W., Powell, R., 2010. Retrograde melt-residue interaction and the formation of near-anhydrous leucosomes in migmatites. J. Metamorph. Geol. 28, 579–597. https://doi.org/10.1111/j.1525-1314.2010.00881.x

Wiedenbeck, M., Allé, P., Corfu, F., Griffin, W.L., Meier, M., Oberli, F., von Quadt, A., Roddick, J.C., Spiegel, W., 1995. Three Natural Zircon Standards for U-Th-Pb, Lu-Hf, Trace Element and REE Analyses. Geostand. Newsl. 19, 1–23. https://doi.org/10.1111/j.1751-908X.1995.tb00147.x

Wilson, A.H., Zeh, A., Gerdes, A., 2017. In situ Sr isotopes in plagioclase and trace element systematics in the lowest part of the eastern Bushveld Complex: Dynamic processes in an evolving magma chamber. J. Petrol. 58, 327–360. https://doi.org/10.1093/petrology/egx018

Zeh, A., Gerdes, A., 2012. U-Pb and Hf isotope record of detrital zircons from gold-bearing sediments of the

Pietersburg Greenstone Belt (South Africa)-Is there a common provenance with the Witwatersrand Basin? Precambrian Res. 204–205, 46–56. https://doi.org/10.1016/j.precamres.2012.02.013

Zeh, A., Gerdes, A., Barton, J.M., 2009. Archean accretion and crustal evolution of the kalahari craton - The zircon age and Hf isotope record of granitic rocks from barberton/ swaziland to the francistown arc, Journal of Petrology. https://doi.org/10.1093/petrology/egp027

Zeh, A., Gerdes, A., Heubeck, C., 2013. U-Pb and Hf isotope data of detrital zircons from the barberton greenstone belt: Constraints on provenance and Archaean Crustal evolution. J. Geol. Soc. London. 170, 215–223. https://doi.org/10.1144/jgs2011-162

Zeh, A., Wilson, A.H., Gudelius, D., Gerdes, A., 2020. Hafnium isotopic composition of the bushveld complex requires mantle melt–upper crust mixing: New evidence from zirconology of mafic, felsic and metasedimentary rocks. J. Petrol. 60, 2169–2200. https://doi.org/10.1093/petrology/egaa004

APPENDICES

APPENDIX I: WHOLE-ROCK GEOCHEMISTRY

TABLE 1: MAJOR ELEMENT GEOCHEMISTRY IN WT.-%; BDL = BELOW DETECTION LIMIT; L.O.I = WEIGHT LOSS OR GAIN AT 1000°C; Fe_2O_3 REPRESENTS TOTAL FE IN THE SAMPLE

	Sample ID	Rock Type	Sample Group	Field Location	Al_2O_3	CaO	Cr_2O_3	Fe_2O_3	K_2O	MgO	MnO	Na_2O	P_2O_5	SiO_2	TiO_2	L.O.I.	Sum
Inzie Head																	
	s1A	Gabbroic Diorite	SG1	IH - 1	14.74	7.73	0.02	10.29	1.85	6.28	0.17	2.67	0.22	53.56	1.62	0.80	99.95
	s1B	Granodiorite	SG1	IH - 1	14.29	3.13	bdl	5.17	2.73	1.50	0.07	2.99	0.31	68.76	0.82	0.46	100.23
	s1C	Granite	SG1	IH - 1	12.98	1.57	bdl	4.45	3.96	1.23	0.06	2.91	0.31	71.22	0.72	0.87	100.28
	s1Da	Granite	SG1	IH - 1	13.38	1.05	bdl	1.81	5.89	0.34	0.02	2.58	0.05	73.53	0.13	0.39	99.17
	s1Db	Monzonite	SG1	IH - 1	15.08	2.67	0.01	11.57	4.23	5.08	0.20	2.03	0.20	56.06	1.53	1.25	99.91
	s1E	Metapelite	SG1	IH - 1	14.70	0.99	0.01	5.54	3.62	2.31	0.09	2.23	0.14	67.93	0.67	1.41	99.64
	s1F	Granite	SG1	IH - 1	13.77	1.07	bdl	3.38	4.87	0.84	0.04	2.56	0.07	71.87	0.40	0.66	99.53
	s1G	Granodiorite	SG1	IH - 1	13.98	2.70	bdl	4.84	4.83	1.59	0.06	2.17	0.34	67.59	0.91	0.52	99.53
	s1H	Granodiorite	SG1	IH - 1	13.89	2.33	bdl	5.14	4.94	1.44	0.07	2.22	0.33	67.38	0.83	0.60	99.17
	s034	Granite	SG2	IH - 1	14.92	1.47	0.00	3.24	4.76	0.67	0.04	2.92	0.10	70.13	0.48	0.69	99.42
	s035	Migmatite	SG2	IH - 1	15.05	4.76	0.00	7.29	2.38	3.96	0.12	2.42	0.16	62.00	1.19	0.78	100.11
	s036	Granite	SG2	IH - 1	14.02	1.18	0.00	2.19	5.85	0.66	0.05	2.53	0.11	72.59	0.29	0.71	100.18
	s037	Migmatite	SG2	IH - 1	9.27	1.79	0.00	2.51	0.93	1.01	0.04	2.79	0.03	80.75	0.42	0.58	100.12
	s038	Granite	SG2	IH - 1	14.10	0.71	0.00	0.77	6.71	0.16	0.03	2.79	0.03	73.86	0.11	0.49	99.76
	s2A	Migmatitic Metapelite	SG1	IH - 2	16.33	1.41	0.01	6.60	3.33	2.53	0.12	2.54	0.26	63.73	0.87	1.80	99.53
	s2B	Granite	SG1	IH - 2	12.77	0.69	bdl	1.82	5.43	0.34	0.04	2.57	0.08	74.71	0.18	0.47	99.10
	s039	Migmatite	SG2	IH - 2	10.94	0.75	0.00	2.06	4.02	0.63	0.03	2.25	0.10	77.89	0.34	0.62	99.63
	s3B	(Leuco-) Granite	SG1	IH - 3	13.62	0.91	bdl	2.09	5.48	0.43	0.04	2.83	0.09	73.00	0.28	0.48	99.25
	s040	Migmatite	SG2	IH - 3-4	23.39	0.89	0.01	8.92	4.57	2.88	0.10	1.70	0.14	53.17	0.94	3.99	100.70
	s041	Granite	SG2	IH - 3-4	13.64	0.90	0.00	1.78	5.97	0.25	0.03	2.41	0.14	73.69	0.25	0.83	99.89
	s042	Migmatitic Metapelite	SG2	IH - 3-4	14.64	1.76	0.00	4.43	1.26	1.57	0.06	3.34	0.11	71.16	0.57	1.40	100.30
	s4A	Grt-bearing Diatexite	SG1	IH - 4	22.41	0.82	0.02	9.21	4.63	3.13	0.11	1.43	0.14	53.00	0.95	3.87	99.72
	s4B	Grt-bearing Diatexite	SG1	IH - 4	21.12	1.75	0.02	8.15	2.88	2.63	0.11	2.69	0.10	56.62	0.99	2.95	100.01
	s4D	Grt-bearing Leucosome	SG1	IH - 4	21.13	1.08	0.01	7.18	4.21	2.35	0.08	2.63	0.16	57.30	0.75	2.94	99.82
	s5A	Diorite	SG1	IH - 5	14.78	6.57	bdl	10.01	1.86	4.24	0.16	2.54	0.19	56.57	1.80	1.42	100.14
	s5Ba	Granite	SG1	IH - 5	14.11	4.18	bdl	6.46	1.61	1.45	0.09	2.81	0.26	67.23	1.25	0.67	100.12
	s5Bb	Diorite	SG1	IH - 5	14.77	5.81	bdl	9.12	1.88	3.48	0.15	2.59	0.30	59.93	1.62	0.93	100.58
	s043	Gabbroic Diorite	SG2	IH - 5	13.40	6.42	0.03	10.33	2.02	7.18	0.16	2.28	0.20	56.05	1.52	0.83	100.42
	s044	Gabbroic Diorite	SG2	IH - 5	15.58	6.38	0.00	9.35	2.35	5.37	0.14	2.52	0.20	55.13	1.65	1.35	100.02
	s045	Granite	SG2	IH - 5	15.40	2.50	0.00	0.23	2.29	0.07	0.01	4.47	0.01	73.79	0.04	1.32	100.13
	s046	Diorite	SG2	IH - 5	15.25	5.76	0.00	9.90	1.79	4.09	0.15	2.83	0.17	57.45	1.80	1.18	100.37
	s6	Residuum-rich Diatexitic Metapelite	SG1	IH - 6	18.69	0.48	0.01	9.51	5.68	2.56	0.10	1.20	0.22	58.06	1.26	2.31	100.08
	s7A	Diorite	SG1	IH - 7	14.71	6.96	0.01	9.32	2.04	5.18	0.15	0.94	0.24	57.82	1.62	0.65	99.64
	s7B	Granite	SG1	IH - 7	13.15	1.14	bdl	3.34	4.01	1.02	0.03	2.65	0.14	72.50	0.52	0.80	99.30
	s047	Quartz-Monzonite	SG2	IH - 7	17.35	2.74	0.00	3.25	5.04	1.25	0.07	4.27	1.15	63.29	0.56	0.86	99.83
	s8A	Metapelite with Crd-Porphyroblast	SG1	IH - 8	20.98	1.01	0.01	6.73	4.11	1.95	0.06	1.38	0.19	59.23	0.95	2.96	99.56
	s8B	Metapelite with Grt-Porphyroblast	SG1	IH - 8	22.35	1.16	0.02	10.70	3.12	2.28	0.16	1.80	0.23	53.40	1.35	3.36	99.93
	s8C	Migmatitic Metapelite	SG1	IH - 8	14.37	0.47	0.01	4.90	4.99	1.87	0.05	2.03	0.15	68.20	0.82	1.50	99.36
	s8Da	Granite	SG1	IH - 8	13.81	2.58	bdl	2.44	2.72	0.96	0.04	3.15	0.18	72.40	0.37	0.54	99.19
	s8Db	Diorite	SG1	IH - 8	14.67	4.95	bdl	9.38	3.15	4.43	0.15	2.30	0.24	58.00	1.57	0.91	99.75
Buchan Block																	
	s005	Granite	SG2	BB	14.99	1.37	0.00	3.66	4.75	0.84	0.04	2.83	0.15	69.77	0.55	1.06	100.01
	s006	Granite	SG2	BB	14.52	1.36	0.00	3.18	4.92	0.68	0.04	2.63	0.15	71.00	0.52	1.01	100.01
	s007	Granite	SG2	BB	14.82	1.39	0.00	3.21	5.11	0.73	0.04	2.59	0.14	70.50	0.50	0.90	99.93
	s009	Granite	SG2	BB	14.43	1.33	0.00	3.51	4.62	0.79	0.06	3.02	0.16	70.78	0.50	0.85	100.05
	s013	Granite	SG2	BB	15.47	1.74	0.00	3.87	4.81	0.55	0.05	3.45	0.09	68.81	0.54	0.55	99.93
	s015	Granite	SG2	BB	14.57	0.62	0.00	1.28	5.11	0.16	0.03	3.27	0.05	73.79	0.17	0.92	99.97
	s016	Granite	SG2	BB	14.75	0.73	0.00	1.57	5.33	0.24	0.03	3.18	0.17	73.12	0.24	0.67	100.03
	s008	Gabbro	SG2	BB	13.62	6.74	0.11	11.07	1.07	15.72	0.15	1.56	0.09	49.24	0.97	0.64	100.98
	s010	Gabbro	SG2	BB	9.78	14.26	0.08	9.54	0.15	15.40	0.16	0.91	0.02	47.71	0.68	2.04	100.73
	s011	Gabbro	SG2	BB	19.47	9.77	0.00	7.42	0.90	6.91	0.13	2.95	0.02	50.37	0.53	2.16	100.63
	s012	Gabbro	SG2	BB	16.21	12.07	0.04	9.83	0.37	7.26	0.26	1.46	0.28	49.64	1.20	1.51	100.13
	s017	Gabbro	SG2	BB	18.90	13.22	0.10	6.00	0.16	9.51	0.11	1.52	0.02	49.67	0.37	0.77	100.35
	s049	Gabbro	SG2	Port	16.35	1.81	0.01	10.61	1.94	12.02	0.06	2.42	0.41	49.25	2.11	3.95	100.94
	s050	Gabbro	SG2	Port	16.94	6.94	0.02	10.35	0.42	6.58	0.12	4.39	0.44	50.59	2.18	1.34	100.31
	s051	Gabbro	SG2	Port	22.28	8.40	0.02	5.91	1.05	8.55	0.08	3.34	0.03	48.19	0.22	2.71	100.78
	s052	Gabbro	SG2	Port	16.30	10.60	0.17	7.45	0.71	10.07	0.12	2.78	0.05	50.41	0.48	1.47	100.61
	s053	Gabbro	SG2	Port	17.13	8.89	0.02	9.08	0.61	6.61	0.15	4.11	0.19	51.22	1.31	1.31	100.63
	s054	Anorthosite	SG2	Port	3.46	9.88	0.40	9.70	0.01	27.58	0.14	0.01	0.05	42.89	0.51	6.02	100.65
	s028	Granite	SG2	Fras	14.01	0.15	0.00	0.80	4.48	0.00	0.01	3.99	0.02	76.30	0.04	0.65	100.45
	s030	Granite	SG2	Fras	14.30	0.59	0.00	0.90	4.94	0.00	0.05	4.45	0.03	74.47	0.04	0.31	100.08
	s020	Granite	SG2	Fras	15.15	0.45	0.00	0.65	5.58	0.00	0.12	4.63	0.02	73.16	0.01	0.38	100.15
	s022	Granite	SG2	Fras	13.71	0.72	0.00	0.53	3.81	0.00	0.01	4.51	0.02	76.50	0.02	0.30	100.13
	s032	Granite	SG2	Fras	13.90	0.78	0.00	0.63	4.72	0.00	0.09	4.06	0.01	75.69	0.04	0.13	100.05
	s029	Metapelite	SG2	Fras	18.00	0.38	0.01	4.72	5.42	1.76	0.02	1.82	0.06	64.47	0.75	2.72	100.13
	s033	Migmatitic Metapelite	SG2	Fras	24.22	1.54	0.01	5.41	8.31	2.41	0.04	1.78	0.09	53.57	0.75	1.91	100.04
	s018	Psammite	SG2	Fras	8.06	5.57	0.00	3.47	1.04	1.30	0.06	0.50	0.03	77.04	0.36	2.10	99.53
	s019	Psammite	SG2	Fras	8.73	23.60	0.00	2.57	1.66	1.30	0.24	0.49	0.04	46.46	0.40	15.44	100.93
	s021	Pelite/ Psammite	SG2	Fras	17.74	0.32	0.00	6.45	5.31	2.70	0.04	0.91	0.07	63.33	0.68	2.49	100.04
	s023	Pelite	SG2	Fras	29.12	0.42	0.02	5.54	8.06	2.76	0.04	2.06	0.16	48.38	0.99	2.75	100.30
	s024	Pelite	SG2	Fras	11.08	11.05	0.00	3.35	1.92	1.39	0.08	0.98	0.04	62.74	0.47	6.51	99.61
	s025	Calc Silicate	SG2	Fras	6.54	4.06	0.00	2.40	1.40	1.08	0.02	1.00	0.02	80.39	0.28	2.00	99.19
	s026	Psammite	SG2	Fras	7.59	13.95	0.00	2.68	1.95	0.88	0.04	0.91	0.05	61.00	0.32	9.65	99.02
	s027	Calc Silicate	SG2	Fras	10.85	22.17	0.00	3.43	2.31	1.86	0.08	1.02	0.08	42.11	0.50	15.53	99.94
	s031	Calc Silicate	SG2	Fras	17.94	7.24	0.01	7.86	3.75	2.81	0.08	0.92	0.08	56.78	0.74	1.27	99.48

TABLE 2: TRACE ELEMENT GEOCHEMISTRY IN PPM

	Sample ID	Rock Type	Sample Group	Field Location	Sc	V	Cr	Co	Ni	Cu	Zn	Rb	Sr	Y	Zr	Nb	Mo
Inzie Head																	
	s1A	Gabbroic Diorite	SG1	IH - 1	23.77	188.63	148.06	70.90	91.76	22.07	122.14	74.73	274.93	23.67	171.78	21.22	1.22
	s1B	Granodiorite	SG1	IH - 1	15.35	61.69	24.65	50.08	20.54	44.43	111.39	96.33	290.87	24.65	359.70	28.28	0.77
	s1C	Granite	SG1	IH - 1	14.14	49.03	19.76	62.30	16.60	23.44	72.24	96.86	222.02	22.67	364.34	19.27	0.73
	s1Da	Granite	SG1	IH - 1	9.04	17.74	9.28	95.93	8.26	18.21	65.88	123.44	169.64	28.69	104.77	14.62	1.14
	s1Db	Monzonite	SG1	IH - 1	26.16	165.72	120.27	73.06	74.15	24.61	312.04	281.82	113.28	35.87	167.15	39.30	0.55
	s1E	Metapelite	SG1	IH - 1	15.22	78.24	108.31	54.07	49.50	17.17	84.66	137.41	126.54	15.62	181.02	27.22	0.57
	s1F	Granite	SG1	IH - 1	12.22	38.61	36.06	70.20	19.85	13.56	45.59	141.76	161.73	13.96	234.86	21.60	1.84
	s1G	Granodiorite	SG1	IH - 1	10.59	61.49	23.04	55.44	19.70	15.02	77.22	118.26	281.68	22.48	407.30	21.17	0.89
	s1H	Granodiorite	SG1	IH - 1	13.74	55.44	21.58	73.25	18.55	10.37	85.94	128.76	238.85	29.09	361.69	26.62	0.84
	s034	Granite	SG2	IH - 1	6.82	27.48	11.10	93.90	8.50	8.08	33.95	127.70	180.25	27.63	404.20	13.05	1.16
	s035	Migmatite	SG2	IH - 1	14.79	121.75	68.60	66.35	50.95	13.53	71.35	126.00	205.00	28.46	149.95	16.88	0.69
	s036	Granite	SG2	IH - 1	6.03	27.29	12.45	93.85	9.63	11.41	51.80	158.05	132.75	33.12	122.85	21.58	0.40
	s037	Migmatite	SG2	IH - 1	6.55	49.86	50.10	126.35	21.65	10.65	25.55	29.10	238.10	8.91	253.95	3.98	0.39
	s038	Granite	SG2	IH - 1	3.46	12.22	11.60	137.45	9.40	7.80	23.10	182.45	119.60	13.73	23.01	11.60	0.34
	s2A	Migmatitic Metapelite	SG1	IH - 2	16.24	109.51	102.46	84.89	47.25	27.73	111.56	131.05	169.91	19.30	182.70	31.44	0.87
	s2B	Granite	SG1	IH - 2	11.45	10.41	10.09	133.40	12.93	18.43	62.16	120.37	110.04	28.24	149.76	25.22	4.10
	s039	Migmatite	SG2	IH - 2	5.79	39.04	36.70	134.90	17.10	11.04	31.95	88.85	144.30	8.95	162.35	14.24	1.38
	s3B	(Leuco-) Granite	SG1	IH - 3	9.04	17.81	12.23	98.07	10.36	5.29	49.21	206.99	119.44	26.15	193.22	17.87	0.55
	s040	Migmatite	SG2	IH - 3-4	14.01	118.81	119.35	35.96	63.85	67.69	109.15	130.35	141.80	28.90	164.05	14.51	0.89
	s041	Granite	SG2	IH - 3-4	4.29	20.75	10.30	45.25	9.70	11.40	19.20	166.20	105.00	13.13	186.10	10.63	1.06
	s042	Migmatitic Metapelite	SG2	IH - 3-4	9.86	67.52	72.35	62.27	29.35	11.18	52.50	55.74	159.45	13.69	250.05	6.71	0.45
	s4A	Grt-bearing Diatexite	SG1	IH - 4	21.75	134.96	151.65	41.22	73.12	45.51	138.97	125.23	147.60	23.05	167.72	18.20	0.70
	s4B	Grt-bearing Diatexite	SG1	IH - 4	19.70	139.16	158.82	55.85	74.88	31.25	172.51	89.43	284.18	20.61	208.50	13.90	0.63
	s4D	Grt-bearing Leucosome	SG1	IH - 4	16.18	106.35	115.99	50.52	63.39	17.88	116.24	123.99	231.91	15.05	113.08	11.68	0.79
	s5A	Diorite	SG1	IH - 5	23.29	197.69	56.08	74.60	63.59	29.44	108.73	59.71	293.34	22.97	175.89	22.96	1.21
	s5Ba	Granite	SG1	IH - 5	15.03	118.37	11.38	99.86	15.69	42.02	133.61	62.70	299.87	26.03	249.94	22.03	0.90
	s5Bb	Diorite	SG1	IH - 5	21.47	174.65	43.13	83.89	47.55	21.87	126.09	71.43	276.87	30.15	235.30	24.84	1.18
	s043	Gabbroic Diorite	SG2	IH - 5	19.09	156.05	223.00	70.93	124.40	33.58	98.45	65.72	253.70	25.34	193.10	16.95	0.92
	s044	Gabbroic Diorite	SG2	IH - 5	17.49	159.60	62.80	68.15	79.80	37.55	109.20	80.08	296.60	19.92	179.30	15.71	1.49
	s045	Granite	SG2	IH - 5	1.12	9.53	8.40	74.05	6.15	7.60	6.15	48.80	245.20	5.00	30.90	1.36	0.49
	s046	Diorite	SG2	IH - 5	18.73	207.05	41.55	79.03	54.45	36.25	92.30	59.11	267.45	21.89	186.00	16.78	0.78
	s6	Residuum-rich Diatexitic Metapelite	SG1	IH - 6	20.16	134.68	127.45	50.53	65.86	28.18	132.68	124.22	118.85	22.51	358.16	26.25	0.58
	s7A	Diorite	SG1	IH - 7	22.36	176.11	88.46	75.53	51.62	19.68	106.99	80.51	307.02	28.71	224.39	21.07	1.26
	s7B	Granite	SG1	IH - 7	11.79	32.34	18.41	125.07	16.32	19.25	67.31	97.82	187.02	36.08	294.58	26.40	2.24
	s047	Quartz-Monzonite	SG2	IH - 7	8.34	35.82	20.35	82.05	12.63	11.54	48.95	111.40	216.15	49.79	214.10	18.71	1.07
	s8A	Metapelite with Crd-Porphyroblast	SG1	IH - 8	22.24	136.84	131.94	50.16	62.53	33.75	114.37	145.26	260.07	30.42	154.19	18.02	0.50
	s8B	Metapelite with Grt-Porphyroblast	SG1	IH - 8	26.07	166.27	136.07	73.98	64.65	42.78	136.84	109.01	152.54	31.74	204.60	21.56	0.99
	s8C	Migmatitic Metapelite	SG1	IH - 8	13.80	74.62	96.51	69.48	34.59	18.03	98.48	129.79	138.49	27.24	529.48	22.55	1.03
	s8Da	Granite	SG1	IH - 8	9.05	28.07	10.81	124.28	16.01	6.70	44.07	65.17	309.35	19.49	225.36	15.00	0.79
	s8Db	Diorite	SG1	IH - 8	21.45	166.64	72.10	71.21	42.25	21.72	131.03	138.99	224.91	28.45	213.18	27.68	1.18
Buchan Block																	
	s005	Granite	SG2	BB	8.46	36.69	18.10	87.30	10.54	17.32	54.55	168.10	89.08	27.25	223.75	14.80	0.31
	s006	Granite	SG2	BB	7.88	34.73	17.95	69.97	9.08	15.93	49.60	156.60	92.88	24.30	232.90	13.86	0.36
	s007	Granite	SG2	BB	8.31	32.03	16.15	74.60	8.92	18.45	43.65	159.65	105.95	26.64	227.05	13.12	0.33
	s009	Granite	SG2	BB	8.40	37.81	19.15	96.75	10.61	31.46	50.05	159.65	122.30	30.35	233.85	14.33	0.41
	s013	Granite	SG2	BB	7.91	35.25	10.70	71.63	6.99	17.62	72.05	76.15	105.72	24.90	514.85	19.79	0.69
	s015	Granite	SG2	BB	3.06	10.95	8.75	143.60	8.40	8.21	24.90	104.70	301.50	6.62	87.85	7.77	0.34
	s016	Granite	SG2	BB	2.95	12.79	8.35	79.35	5.10	8.15	34.40	200.75	99.80	11.50	122.70	15.22	0.32
	s008	Gabbro	SG2	BB	17.97	132.90	749.15	85.40	355.35	49.32	72.00	28.03	218.75	14.45	52.16	6.55	0.34
	s010	Gabbro	SG2	BB	54.34	226.00	499.65	73.65	91.10	57.55	48.55	3.87	167.75	10.54	28.62	0.70	0.34
	s011	Gabbro	SG2	BB	27.48	139.00	60.40	53.21	19.99	21.46	43.75	26.00	377.40	6.30	15.44	1.29	0.36
	s012	Gabbro	SG2	BB	37.04	279.20	292.85	65.62	84.25	57.30	73.15	12.15	279.95	20.51	50.43	10.82	0.50
	s017	Gabbro	SG2	BB	29.25	126.50	681.10	69.52	77.55	74.15	30.50	3.04	242.70	5.92	12.76	0.91	0.32
	s049	Gabbro	SG2	Port	21.70	185.60	133.25	44.44	39.75	8.87	66.20	34.74	172.72	23.10	176.25	27.12	0.83
	s050	Gabbro	SG2	Port	24.04	201.70	136.40	58.91	45.90	101.95	53.65	6.33	400.55	27.51	195.10	27.76	3.69
	s051	Gabbro	SG2	Port	4.61	32.09	150.25	48.48	174.35	11.60	36.65	27.88	535.40	4.22	15.23	1.65	0.38
	s052	Gabbro	SG2	Port	39.85	138.50	1047.50	59.01	137.75	63.23	38.95	14.83	310.90	11.31	31.06	2.14	0.54
	s053	Gabbro	SG2	Port	26.10	159.70	173.05	52.46	69.25	49.50	65.50	8.89	329.20	25.57	141.80	12.05	1.10
	s054	Anorthosite	SG2	Port	39.31	143.30	2491.50	95.05	738.75	47.80	43.70	0.23	13.15	6.51	24.85	3.14	0.34
	s028	Granite	SG2	Fras	6.34	8.67	8.70	119.50	11.68	15.57	7.75	274.05	14.65	64.25	50.70	36.90	1.15
	s030	Granite	SG2	Fras	5.76	7.97	7.80	104.20	10.95	7.94	62.50	273.00	18.60	35.50	40.00	29.50	0.60
	s020	Granite	SG2	Fras	2.60	7.55	8.60	96.45	40.65	16.05	36.45	339.50	44.10	49.90	20.57	43.85	0.57
	s022	Granite	SG2	Fras	3.92	7.38	8.65	152.80	9.55	10.70	53.95	188.10	15.51	57.75	58.75	23.35	0.43
	s032	Granite	SG2	Fras	3.86	8.02	10.75	97.00	6.70	10.55	26.65	298.00	23.31	52.80	63.95	25.95	0.48
	s029	Metapelite	SG2	Fras	11.83	86.28	90.80	54.19	46.80	15.81	73.25	122.10	76.36	13.84	194.85	9.25	0.52
	s033	Migmatitic Metapelite	SG2	Fras	16.50	91.21	106.10	48.08	48.65	48.15	74.50	256.60	286.85	21.48	137.15	13.10	1.15
	s018	Psammite	SG2	Fras	5.35	35.39	41.45	83.78	20.35	21.89	32.50	35.43	248.50	8.13	209.20	3.65	0.38
	s019	Psammite	SG2	Fras	6.62	44.74	51.35	32.63	23.31	15.01	35.80	54.45	748.10	13.51	193.20	4.32	0.39
	s021	Pelite/ Psammite	SG2	Fras	12.40	78.96	85.45	64.15	45.50	43.87	72.85	133.45	97.21	16.80	195.60	9.04	0.56
	s023	Pelite	SG2	Fras	20.92	120.00	140.40	30.03	60.75	9.59	86.35	182.85	118.60	20.26	207.75	13.86	0.51
	s024	Pelite	SG2	Fras	7.63	50.74	56.50	64.79	26.16	20.26	47.65	62.19	371.75	12.21	266.75	5.77	0.58
	s025	Calc Silicate	SG2	Fras	3.74	25.90	28.55	99.40	15.55	16.00	27.40	39.15	189.65	7.16	163.25	3.07	0.45
	s026	Psammite	SG2	Fras	5.09	31.76	32.70	77.30	20.65	19.46	28.80	48.14	538.15	8.55	155.80	3.90	0.58
	s027	Calc Silicate	SG2	Fras	7.54	49.63	54.95	30.13	28.00	19.38	48.55	60.61	639.90	13.69	176.35	6.52	0.60
	s031	Calc Silicate	SG2	Fras	11.98	75.51	89.80	56.89	58.50	41.77	99.90	123.05	589.75	17.91	210.30	10.59	1.11

TABLE 2 CONTINUED

	Sample ID	Rock Type	Sample Group	Field Location	Cs	Ba	La	Ce	Pr	Nd	Sm	Eu	Gd	Tb	Dy	Ho	Er
Inzie Head																	
	s1A	Gabbroic Diorite	SG1	IH - 1	2.31	339.64	23.66	52.38	6.50	26.57	5.84	1.98	5.61	0.87	4.67	0.89	2.45
	s1B	Granodiorite	SG1	IH - 1	2.64	1346.79	69.13	138.73	15.97	59.35	10.32	2.43	8.26	1.05	5.69	1.00	2.58
	s1C	Granite	SG1	IH - 1	2.08	1115.47	44.06	90.68	10.25	38.90	6.90	1.78	6.43	0.75	4.79	0.86	2.37
	s1Da	Granite	SG1	IH - 1	3.08	572.20	58.15	134.46	15.30	58.81	11.99	1.22	9.24	1.34	6.75	1.21	2.91
	s1Db	Monzonite	SG1	IH - 1	16.06	205.42	26.25	57.80	7.05	28.37	6.98	1.04	7.41	1.18	7.22	1.44	3.67
	s1E	Metapelite	SG1	IH - 1	4.95	682.18	36.29	72.05	8.25	30.13	5.00	1.31	4.27	0.55	2.98	0.58	1.51
	s1F	Granite	SG1	IH - 1	3.02	1023.15	73.62	143.66	16.09	56.89	8.62	1.41	6.06	0.66	2.98	0.51	1.29
	s1G	Granodiorite	SG1	IH - 1	2.49	1354.72	67.56	140.38	15.57	58.23	10.05	1.94	7.47	0.93	4.83	0.88	2.51
	s1H	Granodiorite	SG1	IH - 1	2.91	1271.85	79.46	165.99	19.27	71.47	12.81	2.41	9.80	1.32	6.29	1.16	2.84
	s034	Granite	SG2	IH - 1	1.96	1159.00	103.72	196.65	20.85	71.34	10.77	1.56	7.95	1.09	6.07	1.11	2.80
	s035	Migmatite	SG2	IH - 1	6.11	293.15	21.34	47.66	5.96	24.75	5.57	1.40	5.80	0.88	5.81	1.14	3.15
	s036	Granite	SG2	IH - 1	5.86	681.50	27.65	57.76	6.68	25.93	5.95	0.93	6.02	1.01	6.53	1.28	3.75
	s037	Migmatite	SG2	IH - 1	0.74	378.75	24.23	46.07	4.81	17.65	2.68	0.73	2.22	0.27	1.77	0.32	1.08
	s038	Granite	SG2	IH - 1	4.82	468.00	9.08	19.61	2.31	9.10	2.31	0.69	2.57	0.43	2.72	0.51	1.50
	s2A	Migmatitic Metapelite	SG1	IH - 2	3.69	813.25	38.53	79.40	8.94	32.30	5.29	1.61	4.89	0.65	3.97	0.70	2.06
	s2B	Granite	SG1	IH - 2	3.33	508.40	83.72	191.34	21.94	88.71	17.53	1.41	13.55	1.69	7.51	1.12	2.70
	s039	Migmatite	SG2	IH - 2	1.69	639.00	11.10	21.68	2.51	9.90	2.04	0.84	1.88	0.28	1.74	0.33	0.99
	s3B	(Leuco-) Granite	SG1	IH - 3	3.55	752.28	45.53	94.39	10.58	38.89	8.15	1.13	5.86	0.90	4.84	0.86	2.37
	s040	Migmatite	SG2	IH - 3-4	3.17	799.30	69.16	130.42	15.19	56.57	9.69	1.49	7.26	0.97	5.86	1.12	3.35
	s041	Granite	SG2	IH - 3-4	3.05	967.50	54.75	110.80	12.22	43.30	6.92	0.97	5.10	0.59	3.06	0.58	1.34
	s042	Migmatitic Metapelite	SG2	IH - 3-4	1.67	220.35	21.96	44.75	5.11	19.29	3.60	1.19	3.10	0.43	2.78	0.53	1.64
	s4A	Grt-bearing Diatexite	SG1	IH - 4	1.82	1407.28	62.49	122.94	14.12	50.79	8.53	1.87	6.14	0.81	4.70	0.93	2.57
	s4B	Grt-bearing Diatexite	SG1	IH - 4	1.44	863.52	58.72	113.20	12.83	47.34	7.97	1.96	5.74	0.76	4.36	0.81	1.98
	s4D	Grt-bearing Leucosome	SG1	IH - 4	2.18	1678.13	58.97	113.14	13.09	47.91	8.08	2.09	6.49	0.72	3.40	0.58	1.44
	s5A	Diorite	SG1	IH - 5	1.80	371.74	24.41	53.27	6.54	26.85	5.60	1.58	5.30	0.76	4.43	0.91	2.30
	s5Ba	Granite	SG1	IH - 5	3.42	555.30	40.67	83.11	9.30	35.60	7.25	1.71	6.06	0.88	4.95	0.94	2.63
	s5Bb	Diorite	SG1	IH - 5	2.26	422.88	26.43	61.13	7.76	32.94	7.39	1.73	6.58	1.03	5.81	1.14	3.07
	s043	Gabbroic Diorite	SG2	IH - 5	2.93	322.95	24.83	53.96	6.72	28.10	6.22	1.68	5.86	0.87	5.27	1.03	2.92
	s044	Gabbroic Diorite	SG2	IH - 5	2.81	328.70	23.47	49.73	6.04	25.04	5.34	1.47	4.92	0.70	4.27	0.82	2.24
	s045	Granite	SG2	IH - 5	0.99	283.50	4.89	10.13	1.22	4.46	0.98	0.78	0.94	0.16	0.94	0.22	0.56
	s046	Diorite	SG2	IH - 5	1.61	342.20	19.82	47.39	6.02	25.80	5.82	1.61	5.47	0.77	4.58	0.88	2.42
	s6	Residuum-rich Diatexitic Metapelite	SG1	IH - 6	2.99	947.38	55.18	112.68	12.65	48.28	8.34	2.05	6.46	0.89	4.63	0.90	2.32
	s7A	Diorite	SG1	IH - 7	2.86	526.08	31.01	65.99	8.32	32.88	6.77	1.79	6.46	0.93	5.42	1.18	3.04
	s7B	Granite	SG1	IH - 7	2.19	1100.27	84.60	175.56	20.15	78.45	14.65	2.18	11.31	1.43	7.65	1.38	3.38
	s047	Quartz-Monzonite	SG2	IH - 7	2.91	711.35	43.34	92.61	11.36	46.39	10.29	2.01	9.46	1.53	10.04	1.92	5.73
	s8A	Metapelite with Crd-Porphyroblast	SG1	IH - 8	3.07	1160.80	58.92	114.78	13.52	49.73	9.10	1.84	7.46	1.06	6.08	1.22	3.30
	s8B	Metapelite with Grt-Porphyroblast	SG1	IH - 8	1.47	521.46	64.41	127.65	15.03	55.52	10.20	2.25	7.71	1.08	6.35	1.21	3.35
	s8C	Migmatitic Metapelite	SG1	IH - 8	2.11	831.41	44.79	93.46	10.83	42.12	7.75	2.02	6.49	0.92	4.99	1.00	2.97
	s8Da	Granite	SG1	IH - 8	2.40	1073.69	64.11	128.88	15.20	55.99	9.25	2.45	6.87	0.86	4.36	0.80	2.22
	s8Db	Diorite	SG1	IH - 8	6.41	461.50	27.01	58.14	7.26	30.16	6.81	1.61	6.66	0.96	5.73	1.07	2.77
Buchan Block																	
	s005	Granite	SG2	BB	6.65	500.95	42.96	88.02	10.50	40.25	8.19	0.99	6.85	0.95	5.73	1.07	2.99
	s006	Granite	SG2	BB	3.44	562.80	43.74	89.67	10.66	40.79	7.83	1.08	6.62	0.89	5.06	0.99	2.73
	s007	Granite	SG2	BB	3.78	740.80	48.41	99.99	11.36	43.23	8.18	1.22	6.77	0.93	5.49	1.07	2.96
	s009	Granite	SG2	BB	4.19	593.90	42.44	87.21	10.11	38.52	7.28	1.07	6.32	0.97	6.00	1.14	3.46
	s013	Granite	SG2	BB	2.39	964.05	50.75	99.82	10.85	41.68	7.80	1.84	6.99	0.90	5.49	1.05	3.16
	s015	Granite	SG2	BB	1.33	1778.00	32.52	64.60	6.95	24.53	4.16	0.97	2.80	0.33	1.49	0.24	0.63
	s016	Granite	SG2	BB	1.86	587.00	39.55	81.70	9.18	33.25	6.12	0.78	4.06	0.53	2.77	0.43	1.10
	s008	Gabbro	SG2	BB	0.68	227.75	11.86	27.36	3.57	15.80	3.46	0.98	3.39	0.49	3.04	0.60	1.63
	s010	Gabbro	SG2	BB	0.59	57.00	2.71	7.76	1.28	6.77	2.20	0.79	2.29	0.39	2.29	0.44	1.20
	s011	Gabbro	SG2	BB	1.08	215.55	3.46	6.71	0.93	4.29	1.18	0.94	1.33	0.21	1.30	0.26	0.76
	s012	Gabbro	SG2	BB	1.55	118.50	17.56	40.32	5.61	25.08	5.81	1.84	5.43	0.77	4.66	0.85	2.30
	s017	Gabbro	SG2	BB	0.42	48.40	2.46	5.44	0.75	3.43	0.99	0.51	1.20	0.19	1.25	0.25	0.74
	s049	Gabbro	SG2	Port	0.93	394.85	20.75	45.96	5.87	25.64	5.94	1.40	5.54	0.83	5.08	0.96	2.67
	s050	Gabbro	SG2	Port	0.32	116.65	26.15	56.01	7.05	30.63	7.08	3.11	6.77	1.00	6.10	1.13	3.01
	s051	Gabbro	SG2	Port	2.81	233.95	1.92	4.16	0.54	2.48	0.63	0.52	0.79	0.11	0.80	0.18	0.49
	s052	Gabbro	SG2	Port	0.87	107.95	3.70	8.28	1.11	4.95	1.54	0.62	1.94	0.33	2.18	0.49	1.35
	s053	Gabbro	SG2	Port	0.38	93.70	14.27	32.05	4.08	17.97	4.35	1.33	4.81	0.79	4.87	1.00	2.97
	s054	Anorthosite	SG2	Port	0.03	5.48	3.04	7.18	1.00	4.90	1.40	0.54	1.56	0.24	1.47	0.28	0.75
	s028	Granite	SG2	Fras	2.71	31.35	16.35	38.70	4.91	20.98	7.71	0.32	10.10	1.89	12.73	2.44	6.94
	s030	Granite	SG2	Fras	5.68	43.00	13.25	33.58	4.08	16.16	5.38	0.19	5.83	1.16	7.51	1.35	3.62
	s020	Granite	SG2	Fras	2.74	70.95	13.08	35.46	4.87	20.80	10.08	0.05	10.01	1.97	11.55	1.89	5.13
	s022	Granite	SG2	Fras	2.37	31.15	11.45	26.78	3.16	12.43	4.61	0.15	6.99	1.59	11.30	2.20	6.91
	s032	Granite	SG2	Fras	10.55	22.00	11.96	30.02	4.01	16.91	5.68	0.08	6.00	1.12	8.61	1.88	5.98
	s029	Metapelite	SG2	Fras	3.83	942.00	38.71	77.07	8.45	31.34	5.12	0.98	3.86	0.52	3.12	0.55	1.64
	s033	Migmatitic Metapelite	SG2	Fras	7.83	1259.00	72.05	139.47	15.64	55.81	8.18	1.02	5.53	0.77	4.60	0.90	2.58
	s018	Psammite	SG2	Fras	2.03	329.55	13.72	28.96	3.31	12.58	2.09	0.62	1.77	0.24	1.49	0.30	0.91
	s019	Psammite	SG2	Fras	2.45	464.25	17.97	39.62	4.21	16.97	3.28	0.86	3.09	0.40	2.49	0.49	1.37
	s021	Pelite/ Psammite	SG2	Fras	4.31	1037.80	40.50	81.19	9.14	34.55	5.68	0.92	4.64	0.61	3.60	0.71	1.99
	s023	Pelite	SG2	Fras	7.95	1978.50	82.77	153.30	16.81	59.74	8.48	1.37	5.88	0.76	4.56	0.86	2.43
	s024	Pelite	SG2	Fras	2.92	555.25	25.41	49.50	5.81	21.80	3.90	0.86	3.17	0.46	2.51	0.51	1.38
	s025	Calc Silicate	SG2	Fras	1.39	279.75	11.09	25.78	3.05	12.30	2.67	0.51	2.18	0.28	1.64	0.29	0.85
	s026	Psammite	SG2	Fras	1.62	387.50	20.24	41.42	4.34	16.15	2.52	0.75	2.23	0.28	1.76	0.33	1.00
	s027	Calc Silicate	SG2	Fras	1.94	483.15	23.50	50.15	5.62	22.03	4.09	1.08	3.41	0.47	2.80	0.52	1.48
	s031	Calc Silicate	SG2	Fras	4.59	691.05	39.48	78.27	8.85	33.51	5.90	1.16	4.78	0.64	3.83	0.72	2.06

TABLE 2 CONTINUED

	Sample ID	Rock Type	Sample Group	Field Location	Tm	Yb	Lu	Hf	Ta	Pb	Th	U	LREE	HREE	La_N/Yb_N	Sum REE	Ce/Y
Inzie Head																	
	s1A	Gabbroic Diorite	SG1	IH - 1	0.32	2.10	0.33	4.34	0.94	10.99	4.44	1.07	122.52	11.62	5.70	152.54	2.21
	s1B	Granodiorite	SG1	IH - 1	0.32	2.14	0.30	9.20	0.80	17.07	13.37	1.45	304.18	13.07	6.44	123.33	5.63
	s1C	Granite	SG1	IH - 1	0.34	2.34	0.35	9.97	0.53	17.73	12.14	2.10	198.98	11.80	2.12	28.06	4.00
	s1Da	Granite	SG1	IH - 1	0.50	2.91	0.42	4.07	1.61	91.66	16.36	5.77	289.17	16.03	2.22	97.37	4.69
	s1Db	Monzonite	SG1	IH - 1	0.46	3.19	0.48	4.53	1.69	9.45	7.78	1.66	134.88	17.65	6.29	158.78	1.61
	s1E	Metapelite	SG1	IH - 1	0.19	1.34	0.20	4.75	0.75	11.70	8.19	2.18	157.28	7.35	14.60	92.25	4.61
	s1F	Granite	SG1	IH - 1	0.21	1.23	0.17	6.71	1.04	26.72	33.88	2.82	306.35	7.04	1.02	97.54	10.29
	s1G	Granodiorite	SG1	IH - 1	0.31	2.16	0.30	10.40	0.51	23.75	19.13	2.36	301.18	11.90	3.24	13.18	6.25
	s1H	Granodiorite	SG1	IH - 1	0.43	2.32	0.34	9.33	1.23	23.77	19.38	2.27	361.20	14.68	3.57	23.14	5.71
	s034	Granite	SG2	IH - 1	0.33	2.11	0.30	10.47	0.72	22.58	33.40	2.12	412.82	13.80	1.82	29.45	7.12
	s035	Migmatite	SG2	IH - 1	0.43	2.88	0.37	4.51	1.40	10.69	8.59	5.96	112.48	14.65	19.90	256.95	1.67
	s036	Granite	SG2	IH - 1	0.49	3.50	0.48	4.16	2.19	30.36	10.08	0.83	130.92	17.04	3.69	22.22	1.74
	s037	Migmatite	SG2	IH - 1	0.14	0.93	0.15	7.11	0.23	10.83	4.79	1.98	98.38	4.65	21.29	258.16	5.17
	s038	Granite	SG2	IH - 1	0.25	1.61	0.22	1.15	1.38	33.85	3.47	1.40	45.65	7.24	3.90	52.91	1.43
	s2A	Migmatitic Metapelite	SG1	IH - 2	0.27	1.85	0.30	4.48	1.57	15.29	7.19	2.47	170.95	9.79	15.24	185.89	4.11
	s2B	Granite	SG1	IH - 2	0.32	1.90	0.34	5.85	0.91	37.40	23.33	3.52	418.18	15.57	1.26	123.94	6.78
	s039	Migmatite	SG2	IH - 2	0.16	1.05	0.16	4.74	0.91	24.50	4.55	3.17	49.93	4.70	21.66	313.12	2.42
	s3B	(Leuco-) Granite	SG1	IH - 3	0.31	2.33	0.38	5.34	0.96	32.68	29.01	4.61	204.51	11.98	1.61	132.13	3.61
	s040	Migmatite	SG2	IH - 3-4	0.45	3.02	0.43	4.88	1.09	14.45	14.43	3.86	289.76	15.19	22.37	317.27	4.51
	s041	Granite	SG2	IH - 3-4	0.20	1.34	0.18	5.49	0.80	31.95	26.90	1.22	234.05	7.29	4.98	242.42	8.44
	s042	Migmatitic Metapelite	SG2	IH - 3-4	0.21	1.51	0.23	6.95	0.51	11.52	5.45	1.38	98.99	7.34	23.71	375.91	3.27
	s4A	Grt-bearing Diatexite	SG1	IH - 4	0.34	2.25	0.33	4.67	0.79	19.39	14.03	1.93	266.86	11.93	18.04	103.05	5.33
	s4B	Grt-bearing Diatexite	SG1	IH - 4	0.29	1.91	0.29	5.49	0.70	21.99	12.34	1.82	247.74	10.39	18.75	164.65	5.49
	s4D	Grt-bearing Leucosome	SG1	IH - 4	0.18	1.25	0.17	2.99	0.64	29.26	13.05	2.01	249.76	7.75	19.08	404.72	7.52
	s5A	Diorite	SG1	IH - 5	0.32	2.04	0.31	4.71	1.04	11.63	6.25	1.36	123.53	11.05	6.72	112.58	2.32
	s5Ba	Granite	SG1	IH - 5	0.37	2.47	0.34	6.55	1.52	34.69	9.72	3.37	183.68	12.58	3.61	92.06	3.19
	s5Bb	Diorite	SG1	IH - 5	0.47	2.91	0.39	6.28	1.22	17.36	6.88	1.29	143.95	14.81	6.78	123.43	2.03
	s043	Gabbroic Diorite	SG2	IH - 5	0.39	2.53	0.35	5.48	1.16	7.67	5.33	1.25	127.35	13.36	7.24	151.31	2.13
	s044	Gabbroic Diorite	SG2	IH - 5	0.31	1.86	0.29	4.96	0.92	9.75	5.33	11.91	116.00	10.48	7.32	54.66	2.50
	s045	Granite	SG2	IH - 5	0.11	0.61	0.11	1.52	0.28	12.50	5.67	2.44	23.40	2.71	5.13	127.14	2.03
	s046	Diorite	SG2	IH - 5	0.31	2.13	0.31	5.35	1.14	9.81	7.09	3.18	111.92	11.40	5.74	74.01	2.17
	s6	Residuum-rich Diatexitic Metapelite	SG1	IH - 6	0.32	1.92	0.33	9.19	0.98	18.24	12.99	1.84	245.64	11.30	15.76	298.45	5.01
	s7A	Diorite	SG1	IH - 7	0.45	2.61	0.37	5.65	1.12	10.94	7.37	1.85	153.20	13.98	5.55	26.11	2.30
	s7B	Granite	SG1	IH - 7	0.48	3.07	0.43	8.60	1.48	47.54	26.56	3.78	386.88	17.82	1.28	100.61	4.87
	s047	Quartz-Monzonite	SG2	IH - 7	0.87	6.03	0.84	6.33	1.46	28.95	9.77	0.40	215.43	26.95	5.47	147.96	1.86
	s8A	Metapelite with Crd-Porphyroblast	SG1	IH - 8	0.45	2.98	0.48	3.95	1.05	21.10	14.08	2.43	255.34	15.55	15.86	304.98	3.77
	s8B	Metapelite with Grt-Porphyroblast	SG1	IH - 8	0.45	2.83	0.41	5.52	1.20	19.94	14.16	2.46	282.77	15.66	17.75	173.32	4.02
	s8C	Migmatitic Metapelite	SG1	IH - 8	0.42	2.77	0.40	13.68	1.16	47.34	10.99	2.21	207.44	13.46	15.36	181.57	3.43
	s8Da	Granite	SG1	IH - 8	0.27	1.85	0.22	6.82	1.13	21.90	14.11	2.31	282.74	10.58	2.70	18.03	6.61
	s8Db	Diorite	SG1	IH - 8	0.41	2.55	0.37	5.83	1.45	10.83	7.98	2.00	137.63	13.85	6.80	140.73	2.04
Buchan Block																	
	s005	Granite	SG2	BB	0.42	2.76	0.38	6.79	1.15	38.24	15.07	2.10	197.75	14.29	7.33	151.51	3.23
	s006	Granite	SG2	BB	0.37	2.36	0.33	7.02	0.96	26.53	14.74	2.06	200.37	12.73	7.80	134.17	3.69
	s007	Granite	SG2	BB	0.42	2.53	0.38	6.77	1.05	25.84	17.76	3.00	219.14	13.76	8.23	167.22	3.75
	s009	Granite	SG2	BB	0.48	3.19	0.45	6.92	1.05	24.52	14.49	2.57	192.94	15.69	8.28	134.62	2.87
	s013	Granite	SG2	BB	0.41	2.92	0.44	13.47	0.89	18.35	8.29	1.71	219.71	14.36	8.74	126.50	4.01
	s015	Granite	SG2	BB	0.10	0.58	0.09	3.14	0.36	38.40	10.95	1.75	136.52	3.47	9.21	208.64	9.77
	s016	Granite	SG2	BB	0.15	0.88	0.14	4.10	1.29	25.90	14.14	3.76	174.62	6.00	9.60	61.68	7.10
	s008	Gabbro	SG2	BB	0.22	1.43	0.18	1.81	0.35	4.12	0.86	0.26	66.41	7.59	11.40	196.28	1.89
	s010	Gabbro	SG2	BB	0.15	1.03	0.15	1.09	0.05	0.95	0.10	0.02	23.78	5.66	12.03	234.10	0.74
	s011	Gabbro	SG2	BB	0.11	0.65	0.09	0.51	0.09	2.16	0.23	0.07	18.82	3.37	12.33	116.90	1.07
	s012	Gabbro	SG2	BB	0.29	1.81	0.25	1.73	0.43	2.75	0.57	0.20	101.64	10.92	12.83	213.12	1.97
	s017	Gabbro	SG2	BB	0.10	0.63	0.09	0.43	0.05	1.66	0.26	0.08	14.77	3.24	13.04	210.80	0.92
	s049	Gabbro	SG2	Port	0.35	2.12	0.32	4.18	1.69	2.35	1.19	0.45	111.07	12.32	13.25	232.94	1.99
	s050	Gabbro	SG2	Port	0.41	2.50	0.36	4.73	1.76	5.23	1.13	0.06	136.78	14.50	13.43	117.00	2.04
	s051	Gabbro	SG2	Port	0.08	0.41	0.07	0.40	0.09	5.74	0.37	0.17	11.03	2.13	13.53	216.52	0.98
	s052	Gabbro	SG2	Port	0.18	1.21	0.18	0.89	0.13	3.31	0.43	0.84	22.13	5.93	13.69	270.92	0.73
	s053	Gabbro	SG2	Port	0.42	2.74	0.41	3.61	0.74	3.86	2.27	0.11	78.85	13.19	13.84	305.21	1.25
	s054	Anorthosite	SG2	Port	0.10	0.59	0.09	0.76	0.17	0.80	0.30	0.02	19.62	3.52	14.42	180.76	1.10
	s028	Granite	SG2	Fras	1.04	7.04	0.98	3.91	5.33	32.10	9.77	1.84	99.06	33.04	10.07	106.33	0.60
	s030	Granite	SG2	Fras	0.55	4.13	0.58	2.96	3.10	27.95	4.23	3.11	78.46	18.89	10.37	92.30	0.95
	s020	Granite	SG2	Fras	0.92	7.18	0.95	3.04	10.79	26.80	7.48	1.89	94.34	29.58	10.55	67.16	0.71
	s022	Granite	SG2	Fras	1.08	7.80	1.09	4.90	3.08	31.35	5.27	3.18	65.57	31.94	10.78	212.06	0.46
	s032	Granite	SG2	Fras	0.96	6.46	0.94	4.12	2.53	45.25	19.67	3.76	74.64	25.93	11.20	220.93	0.57
	s029	Metapelite	SG2	Fras	0.23	1.51	0.22	5.22	0.54	15.79	8.08	5.93	165.52	7.80	19.23	278.81	5.57
	s033	Migmatitic Metapelite	SG2	Fras	0.39	2.57	0.35	3.94	0.85	38.14	15.85	3.48	297.68	12.15	19.41	309.86	6.49
	s018	Psammite	SG2	Fras	0.14	0.90	0.13	5.89	0.22	9.06	3.84	0.73	63.03	4.12	23.99	293.33	3.56
	s019	Psammite	SG2	Fras	0.17	1.20	0.18	5.31	0.26	10.18	3.53	0.83	85.99	6.30	25.36	339.87	2.93
	s021	Pelite/ Psammite	SG2	Fras	0.27	1.84	0.25	5.66	0.56	11.84	9.53	7.34	176.62	9.27	28.29	241.35	4.83
	s023	Pelite	SG2	Fras	0.33	2.26	0.32	5.88	0.89	12.73	17.52	1.66	328.34	11.51	30.51	433.78	7.57
	s024	Pelite	SG2	Fras	0.19	1.31	0.19	7.54	0.36	9.62	6.57	0.85	110.43	6.54	31.12	180.64	4.05
	s025	Calc Silicate	SG2	Fras	0.12	0.80	0.12	4.57	0.18	8.04	3.74	1.60	57.57	4.09	32.66	257.51	3.60
	s026	Psammite	SG2	Fras	0.14	0.96	0.13	4.34	0.25	15.04	4.47	1.58	87.64	4.60	34.03	426.65	4.85
	s027	Calc Silicate	SG2	Fras	0.22	1.32	0.21	4.90	0.41	15.59	6.16	5.66	109.86	7.01	38.82	139.99	3.66
	s031	Calc Silicate	SG2	Fras	0.30	1.78	0.29	6.16	0.67	30.07	11.72	7.58	171.94	9.62	41.44	313.40	4.37

APPENDIX II: MINERAL CHEMISTRY

TABLE 1: REPRESENTATIVE ANALYSES OF PLAGIOCLASE

Sample	s1A					s1B					s1D					s1F				
Spot No.	04	05	32	33	47	01	22	45	55	78	11	25	37	63	73	6	16	22	42	52
ID	outer	inner	outer	inner	outer	inner	outer	inner	outer	outer	inner C	inner M	inner M	outer F	outer F	outer	inner	outer	inner	outer
wt.-%																				
SiO_2	59.2	52.8	56.1	53.3	58.7	57.5	59.0	56.2	60.7	61.5	61.1	56.6	54.0	63.5	67.2	66.2	63.0	62.8	61.6	60.3
TiO_2	0.0	0.0	0.0	0.0	0.0	0.0	0.0	0.0	0.0	0.0	0.0	0.0	0.0	0.0	0.0	0.0	0.0	0.0	0.0	0.0
Al_2O_3	25.5	29.0	27.8	29.0	25.9	26.9	25.6	27.4	24.6	24.5	24.0	26.4	28.4	22.6	20.0	21.0	23.2	23.1	23.7	25.0
FeO_t	0.3	0.3	0.2	0.2	0.2	0.0	0.0	0.0	0.0	0.0	0.0	0.2	0.0	0.0	0.0	0.0	0.0	0.0	0.0	0.0
MgO	0.0	0.0	0.0	0.0	0.0	0.0	0.0	0.0	0.0	0.0	0.0	0.0	0.0	0.0	0.0	0.0	0.0	0.0	0.0	0.0
CaO	8.0	12.4	10.7	12.2	8.3	9.3	8.0	9.9	6.6	6.1	6.3	9.4	11.6	4.1	1.1	2.9	5.1	4.0	6.0	7.2
Na_2O	7.3	4.6	5.8	4.7	7.2	6.6	7.6	6.2	8.2	8.3	8.3	6.2	5.2	9.8	11.9	10.1	9.0	9.0	8.5	7.5
K_2O	0.0	0.0	0.0	0.0	0.0	0.1	0.2	0.2	0.2	0.3	0.1	0.0	0.0	0.0	0.0	0.0	0.0	0.8	0.0	0.0
Cr_2O_3	0.0	0.2	0.0	0.2	0.1	0.0	0.0	0.0	0.0	0.0	0.0	0.0	0.0	0.0	0.0	0.0	0.0	0.1	0.2	0.0
Total	100.3	99.3	100.6	99.6	100.5	100.3	100.3	100.0	100.2	100.8	99.8	98.8	99.2	100.0	100.2	100.3	100.3	99.8	100.0	100.0
Formula																				
Number of ions on the basis of 8 O																				
Si	2.64	2.41	2.51	2.42	2.61	2.57	2.62	2.52	2.69	2.71	2.72	2.57	2.45	2.80	2.92	2.91	2.78	2.78	2.73	2.69
Ti	0.00	0.00	0.00	0.00	0.00	0.00	0.00	0.00	0.00	0.00	0.00	0.00	0.00	0.00	0.00	0.00	0.00	0.00	0.00	0.00
Al	1.34	1.56	1.47	1.55	1.36	1.41	1.34	1.45	1.28	1.27	1.26	1.42	1.52	1.17	1.02	1.09	1.21	1.21	1.24	1.31
Cr	0.00	0.01	0.00	0.01	0.01	0.00	0.00	0.00	0.00	0.00	0.00	0.00	0.00	0.00	0.00	0.00	0.00	0.00	0.01	0.00
Fe^{3+}	0.01	0.01	0.01	0.01	0.01	0.00	0.00	0.00	0.00	0.00	0.00	0.01	0.00	0.00	0.00	0.00	0.00	0.00	0.00	0.00
Mn	0.00	0.00	0.00	0.00	0.00	0.00	0.00	0.00	0.00	0.00	0.00	0.00	0.00	0.00	0.00	0.00	0.00	0.00	0.00	0.00
Mg	0.00	0.00	0.00	0.00	0.00	0.00	0.00	0.00	0.00	0.00	0.00	0.00	0.00	0.00	0.00	0.00	0.00	0.00	0.00	0.00
Na	0.63	0.41	0.51	0.42	0.62	0.57	0.65	0.54	0.70	0.71	0.71	0.55	0.46	0.83	1.00	0.86	0.77	0.77	0.73	0.65
Ca	0.38	0.61	0.51	0.60	0.40	0.44	0.38	0.48	0.31	0.29	0.30	0.46	0.57	0.19	0.05	0.14	0.24	0.19	0.29	0.34
K	0.00	0.00	0.00	0.00	0.00	0.01	0.01	0.01	0.01	0.02	0.01	0.00	0.00	0.00	0.00	0.00	0.00	0.04	0.00	0.00
Σ Z	3.99	3.99	3.98	3.99	3.98	3.98	3.96	3.97	3.97	3.98	3.98	3.99	3.97	3.97	3.95	4.00	3.99	3.99	3.98	4.00
Σ X	1.01	1.01	1.02	1.01	1.02	1.02	1.04	1.03	1.03	1.02	1.02	1.01	1.03	1.03	1.05	1.00	1.01	1.01	1.02	1.00
Total cat.	5.00	5.00	5.00	5.00	5.00	5.00	5.00	5.00	5.00	5.00	5.00	5.00	5.00	5.00	5.00	5.00	5.00	5.00	5.00	5.00
Mol.-%																				
An	37.67	59.95	50.19	58.78	38.90	43.37	36.25	46.40	30.46	28.43	29.52	45.50	55.14	18.84	4.81	13.87	24.04	19.09	28.32	34.45
Ab	62.33	40.05	49.81	41.22	61.10	56.05	62.75	52.68	68.46	69.97	69.84	54.50	44.86	81.16	95.19	86.13	75.96	76.63	71.68	65.55
Or	0.00	0.00	0.00	0.00	0.00	0.58	1.00	0.92	1.08	1.61	0.64	0.00	0.00	0.00	0.00	0.00	0.00	4.28	0.00	0.00

TABLE 1 CONTINUED

Sample	s1H					s2A					s3B					s4D				
Spot No.	14	24	37	46	54	16	43	57	86	135	2	14	27	44	52	07	37	44	51	63
ID	inner F	outer F	outer F	inner M	outer M	outer	inner	inner	outer	outer	outer	outer	outer	inner	inner	outer	outer	inner	outer	outer
wt.-%																				
SiO_2	57.9	59.6	68.0	57.8	60.1	62.2	61.3	61.3	62.0	63.0	64.3	65.2	60.4	61.6	59.0	62.7	66.8	61.3	59.1	61.2
TiO_2	0.0	0.0	0.0	0.0	0.0	0.0	0.0	0.0	0.0	0.0	0.0	0.0	0.0	0.0	0.0	0.0	0.0	0.0	0.0	0.0
Al_2O_3	26.5	24.9	20.2	26.3	24.7	24.1	24.6	24.4	24.4	23.6	22.4	21.6	25.0	24.5	25.9	23.8	21.7	24.5	28.3	24.3
FeO_t	0.0	0.0	0.0	0.2	0.2	0.0	0.0	0.0	0.0	0.2	0.0	0.0	0.0	0.0	0.0	0.3	0.3	0.0	0.3	0.7
MgO	0.0	0.0	0.0	0.0	0.0	0.0	0.0	0.0	0.0	0.0	0.0	0.0	0.0	0.0	0.0	0.0	0.0	0.0	0.0	0.0
CaO	9.2	7.4	1.6	8.7	7.4	4.7	5.3	5.1	4.4	3.3	4.4	3.5	7.0	6.6	8.2	3.0	0.8	5.8	2.0	4.5
Na_2O	6.5	7.5	11.2	6.6	7.6	9.1	8.6	8.7	9.2	9.3	9.4	9.7	7.8	8.0	7.1	8.4	9.9	7.9	6.6	8.4
K_2O	0.0	0.0	0.0	0.0	0.0	0.2	0.3	0.2	0.4	0.9	0.0	0.0	0.1	0.0	0.0	1.9	0.8	0.2	4.6	0.6
Cr_2O_3	0.1	0.0	0.0	0.0	0.1	0.0	0.0	0.0	0.0	0.0	0.0	0.0	0.0	0.0	0.0	0.0	0.0	0.0	0.0	0.0
Total	100.3	99.4	101.0	99.6	100.2	100.3	100.2	99.7	100.2	100.3	100.5	100.0	100.3	100.7	100.2	100.0	100.2	99.7	100.9	99.7
Formula																				
Number of ions on the basis of 8																				
Si	2.59	2.68	2.95	2.60	2.68	2.74	2.71	2.72	2.73	2.77	2.83	2.88	2.68	2.72	2.63	2.78	2.94	2.74	2.60	2.72
Ti	0.00	0.00	0.00	0.00	0.00	0.00	0.00	0.00	0.00	0.00	0.00	0.00	0.00	0.00	0.00	0.00	0.00	0.00	0.00	0.00
Al	1.40	1.32	1.03	1.40	1.30	1.25	1.28	1.28	1.26	1.22	1.16	1.13	1.31	1.28	1.36	1.24	1.12	1.29	1.47	1.28
Cr	0.00	0.00	0.00	0.00	0.01	0.00	0.00	0.00	0.00	0.00	0.00	0.00	0.00	0.00	0.00	0.00	0.00	0.00	0.00	0.00
Fe^{3+}	0.00	0.00	0.00	0.01	0.01	0.00	0.00	0.00	0.00	0.01	0.00	0.00	0.00	0.00	0.00	0.01	0.01	0.00	0.01	0.02
Mn	0.00	0.00	0.00	0.00	0.00	0.00	0.00	0.00	0.00	0.00	0.00	0.00	0.00	0.00	0.00	0.00	0.00	0.00	0.00	0.00
Mg	0.00	0.00	0.00	0.00	0.00	0.00	0.00	0.00	0.00	0.00	0.00	0.00	0.00	0.00	0.00	0.00	0.00	0.00	0.00	0.00
Na	0.56	0.65	0.94	0.58	0.66	0.78	0.74	0.75	0.78	0.79	0.80	0.83	0.67	0.69	0.62	0.72	0.84	0.68	0.56	0.73
Ca	0.44	0.35	0.07	0.42	0.35	0.22	0.25	0.24	0.21	0.16	0.21	0.16	0.33	0.31	0.39	0.14	0.04	0.28	0.09	0.21
K	0.00	0.00	0.00	0.00	0.00	0.01	0.02	0.01	0.02	0.05	0.00	0.00	0.01	0.00	0.00	0.11	0.05	0.01	0.26	0.04
Σ Z	3.99	3.99	3.98	4.00	3.99	3.99	3.99	4.00	3.99	4.00	3.99	4.00	3.99	4.00	3.99	4.03	4.07	4.03	4.08	4.03
Σ X	1.01	1.01	1.02	1.00	1.01	1.01	1.01	1.00	1.01	1.00	1.01	1.00	1.01	1.00	1.01	0.97	0.93	0.97	0.92	0.97
Total cat.	5.00	5.00	5.00	5.00	5.00	5.00	5.00	5.00	5.00	5.00	5.00	5.00	5.00	5.00	5.00	5.00	5.00	5.00	5.00	5.00
Mol.-%																				
An	43.89	35.09	7.31	42.21	34.77	21.80	24.91	24.24	20.50	15.67	20.61	16.43	33.02	31.12	38.82	14.59	4.04	28.68	10.10	21.93
Ab	56.11	64.91	92.69	57.79	65.23	76.88	73.31	74.64	77.51	79.22	79.39	83.57	66.39	68.88	61.18	74.55	90.82	70.17	61.37	74.39
Or	0.00	0.00	0.00	0.00	0.00	1.32	1.78	1.13	1.99	5.11	0.00	0.00	0.60	0.00	0.00	10.86	5.14	1.14	28.54	3.68

TABLE 1 CONTINUED

Sample	s5A					s5B					s7A					s8D				
Spot No.	111	173	257	326	366	02	13	17	32	52	16	18	32	39	45	15	18	36	50	75
ID	inner	outer	inner	inner	inner	outer F	inner F	inner C	inner M	outer M	outer	inner	outer	outer	inner	outer M	inner M	outer F	inner F	inner F
wt.-%																				
SiO_2	54.8	56.5	59.6	47.8	52.1	58.5	55.6	59.0	54.4	59.2	47.6	53.4	52.0	48.4	50.4	55.1	52.4	61.9	59.8	55.5
TiO_2	0.0	0.0	0.0	0.0	0.2	0.0	0.0	0.0	0.0	0.0	0.0	0.0	0.0	0.0	0.0	0.0	0.0	0.1	0.0	0.0
Al_2O_3	28.6	27.3	25.4	32.7	30.1	26.2	28.0	25.8	28.3	25.5	32.9	29.5	30.8	32.5	31.3	27.9	29.9	24.2	25.4	28.5
FeO_t	0.0	0.3	0.0	0.0	0.2	0.0	0.0	0.0	0.0	0.0	0.2	0.0	0.0	0.2	0.0	0.9	0.2	0.0	0.0	0.0
MgO	0.0	0.0	0.0	0.0	0.0	0.0	0.0	0.0	0.0	0.0	0.0	0.0	0.0	0.0	0.0	0.9	0.0	0.0	0.0	0.0
CaO	11.2	9.7	7.6	16.2	13.0	8.7	10.8	8.3	11.2	7.9	16.9	12.4	13.8	15.9	14.5	8.7	13.0	5.2	7.1	10.7
Na_2O	5.4	6.2	7.5	2.4	4.0	7.0	5.6	7.0	5.3	7.3	1.9	4.8	3.9	2.5	3.3	4.6	4.4	7.9	7.5	5.6
K_2O	0.1	0.1	0.1	0.1	0.1	0.0	0.0	0.0	0.0	0.1	0.0	0.0	0.0	0.0	0.0	1.6	0.0	0.3	0.2	0.1
Cr_2O_3	0.0	0.0	0.0	0.0	0.0	0.2	0.2	0.1	0.2	0.0	0.2	0.2	0.1	0.2	0.0	0.0	0.0	0.0	0.0	0.0
Total	100.1	100.0	100.3	99.2	99.7	100.6	100.3	100.2	99.5	100.1	99.7	100.3	100.5	99.6	99.6	99.8	99.9	99.7	100.0	100.4
Formula																				
Number of ions on the basis of 8 O																				
Si	2.47	2.54	2.65	2.20	2.37	2.60	2.50	2.63	2.47	2.64	2.19	2.41	2.35	2.22	2.31	2.50	2.37	2.77	2.67	2.49
Ti	0.00	0.00	0.00	0.00	0.01	0.00	0.00	0.00	0.00	0.00	0.00	0.00	0.00	0.00	0.00	0.00	0.00	0.00	0.00	0.00
Al	1.51	1.44	1.33	1.78	1.62	1.37	1.48	1.36	1.51	1.34	1.79	1.57	1.64	1.76	1.69	1.49	1.60	1.28	1.33	1.50
Cr	0.00	0.00	0.00	0.00	0.00	0.01	0.01	0.01	0.01	0.00	0.01	0.01	0.01	0.01	0.00	0.00	0.00	0.00	0.00	0.00
Fe^{3+}	0.00	0.01	0.00	0.00	0.01	0.00	0.00	0.00	0.00	0.00	0.01	0.00	0.00	0.01	0.00	0.03	0.01	0.00	0.00	0.00
Mn	0.00	0.00	0.00	0.00	0.00	0.00	0.00	0.00	0.00	0.00	0.00	0.00	0.00	0.00	0.00	0.00	0.00	0.00	0.00	0.00
Mg	0.00	0.00	0.00	0.00	0.00	0.00	0.00	0.00	0.00	0.00	0.00	0.00	0.00	0.00	0.00	0.06	0.00	0.00	0.00	0.00
Na	0.47	0.54	0.65	0.22	0.35	0.61	0.49	0.61	0.47	0.63	0.17	0.42	0.34	0.22	0.29	0.40	0.39	0.68	0.65	0.49
Ca	0.54	0.46	0.36	0.80	0.64	0.41	0.52	0.40	0.54	0.38	0.83	0.60	0.67	0.78	0.71	0.42	0.63	0.25	0.34	0.52
K	0.00	0.00	0.01	0.01	0.01	0.00	0.00	0.00	0.00	0.01	0.00	0.00	0.00	0.00	0.00	0.09	0.00	0.02	0.01	0.01
Σ Z	3.98	3.99	3.99	3.98	4.00	3.98	3.99	3.99	3.99	3.98	3.99	3.98	3.99	4.00	3.99	4.08	3.98	4.05	4.00	3.99
Σ X	1.02	1.01	1.01	1.02	1.00	1.02	1.01	1.01	1.01	1.02	1.01	1.02	1.01	1.00	1.01	0.92	1.02	0.95	1.00	1.01
Total cat.	5.00	5.00	5.00	5.00	5.00	5.00	5.00	5.00	5.00	5.00	5.00	5.00	5.00	5.00	5.00	5.00	5.00	5.00	5.00	5.00
Mol.-%																				
An	53.05	46.15	35.75	78.27	63.97	40.53	51.64	39.34	53.80	37.17	82.75	59.05	66.10	77.99	70.76	45.76	61.79	26.34	33.80	51.00
Ab	46.53	53.43	63.70	21.09	35.20	59.47	48.36	60.66	46.20	62.07	17.25	40.95	33.90	22.01	29.24	43.89	38.21	71.60	64.80	48.23
Or	0.42	0.42	0.54	0.64	0.83	0.00	0.00	0.00	0.00	0.76	0.00	0.00	0.00	0.00	0.00	10.34	0.00	2.06	1.41	0.77

TABLE 2: REPRESENTATIVE ANALYSES OF BIOTITE

Sample	s1A					s1B					s1D					s1F				
Spot No.	01	02	03	04	05	02	03	04	05	08	03	05	08	12	13	01	02	03	04	05
ID											F	F	C	M	M					
wt.-%																				
SiO_2	37.1	37.5	37.0	36.7	36.4	35.5	35.9	35.7	35.0	36.0	35.9	35.4	35.3	36.2	36.3	34.5	34.3	34.0	34.4	33.4
TiO_2	3.2	3.3	3.4	2.8	3.3	3.9	3.0	3.0	4.0	3.0	3.6	3.7	3.7	3.3	2.5	2.0	3.1	3.2	2.7	3.1
Al_2O_3	15.6	15.8	15.0	15.5	15.2	16.4	16.2	17.2	16.1	16.9	16.7	15.9	15.4	15.8	16.1	18.0	18.5	18.4	17.2	17.3
FeO_t	18.5	18.6	18.7	18.3	19.1	23.8	23.4	22.5	23.3	22.5	23.8	24.0	23.1	21.6	21.4	23.7	23.3	23.5	24.0	25.1
MnO	0.2	0.2	0.3	0.0	0.1	0.3	0.3	0.3	0.2	0.2	0.5	0.5	0.4	0.3	0.4	0.2	0.3	0.3	0.2	0.2
MgO	10.6	10.6	10.5	10.7	10.1	7.8	8.1	8.2	7.8	8.2	6.3	6.4	7.4	8.5	9.1	6.6	5.5	5.4	6.0	5.2
CaO	0.0	0.0	0.0	0.0	0.0	0.0	0.0	0.0	0.0	0.0	0.0	0.0	0.0	0.0	0.0	0.0	0.0	0.0	0.0	0.0
Na_2O	0.2	0.3	0.0	0.2	0.2	0.0	0.0	0.0	0.0	0.0	0.2	0.0	0.3	0.3	0.2	0.2	0.0	0.2	0.0	0.2
K_2O	9.6	9.6	9.5	9.2	9.4	9.1	9.2	9.2	9.3	9.3	9.2	9.6	9.3	9.4	9.3	8.7	9.5	9.5	9.5	9.4
Total	95.0	95.8	94.3	93.3	93.8	96.8	96.1	96.2	95.7	96.1	96.2	95.5	94.8	95.4	95.2	94.0	94.5	94.7	94.0	93.8
Formula																				
Number of ions on the basis of 22 O																				
Si	5.66	5.66	5.69	5.68	5.64	5.44	5.54	5.47	5.43	5.51	5.54	5.54	5.54	5.57	5.60	5.44	5.39	5.35	5.47	5.36
Al^{IV}	2.34	2.34	2.31	2.32	2.36	2.56	2.46	2.53	2.57	2.49	2.46	2.46	2.46	2.43	2.40	2.56	2.61	2.65	2.53	2.64
Σ Z	8.00	8.00	8.00	8.00	8.00	8.00	8.00	8.00	8.00	8.00	8.00	8.00	8.00	8.00	8.00	8.00	8.00	8.00	8.00	8.00
Al^{VI}	0.46	0.47	0.41	0.50	0.41	0.41	0.47	0.58	0.38	0.57	0.58	0.47	0.39	0.44	0.51	0.78	0.82	0.78	0.68	0.62
Ti	0.37	0.38	0.39	0.33	0.38	0.45	0.35	0.35	0.47	0.35	0.41	0.43	0.43	0.39	0.30	0.24	0.36	0.38	0.33	0.38
Fe_t	2.36	2.35	2.40	2.36	2.48	3.05	3.02	2.89	3.02	2.88	3.08	3.13	3.03	2.79	2.76	3.12	3.06	3.09	3.19	3.37
Mn	0.03	0.02	0.03	0.00	0.02	0.03	0.04	0.03	0.03	0.02	0.07	0.07	0.05	0.04	0.05	0.02	0.04	0.05	0.03	0.03
Mg	2.40	2.38	2.40	2.46	2.34	1.79	1.87	1.88	1.81	1.86	1.46	1.48	1.74	1.96	2.09	1.56	1.29	1.27	1.41	1.24
Σ X	5.16	5.13	5.22	5.16	5.22	5.32	5.27	5.15	5.33	5.12	5.02	5.11	5.25	5.17	5.19	4.94	4.75	4.78	4.96	5.02
Ca	0.00	0.00	0.00	0.00	0.00	0.00	0.00	0.00	0.00	0.00	0.00	0.03	0.00	0.03	0.00	0.03	0.00	0.00	0.00	0.00
Na	0.07	0.09	0.00	0.06	0.06	0.00	0.00	0.00	0.00	0.00	0.06	0.00	0.08	0.08	0.06	0.06	0.00	0.07	0.00	0.06
K	1.86	1.84	1.86	1.81	1.85	1.79	1.81	1.80	1.84	1.83	1.81	1.90	1.86	1.84	1.82	1.75	1.91	1.92	1.92	1.92
Σ Y	1.92	1.93	1.86	1.87	1.91	1.79	1.81	1.80	1.84	1.83	1.87	1.94	1.94	1.95	1.88	1.84	1.91	1.99	1.92	1.98
Total	15.54	15.52	15.49	15.52	15.54	15.52	15.55	15.53	15.55	15.52	15.46	15.52	15.57	15.57	15.59	15.56	15.49	15.55	15.56	15.62
X_{Fe}	0.50	0.50	0.50	0.49	0.51	0.63	0.62	0.61	0.63	0.61	0.68	0.68	0.64	0.59	0.57	0.67	0.70	0.71	0.69	0.73

TABLE 2 CONTINUED

Sample	s1H					s2A					s3B					s4D				
Spot No.	01	03	04	05	06	01	02	05	06	09	01	02	03	04	05	02	03	07	15	17
ID	M	M	F	F	F															
wt.-%																				
SiO_2	35.4	35.3	35.1	35.4	35.2	33.9	33.8	34.0	34.9	34.7	33.6	34.4	34.4	34.4	34.0	35.7	36.5	31.7	32.2	31.1
TiO_2	2.5	3.2	2.8	3.5	3.4	4.0	4.0	3.4	3.6	3.7	3.2	2.8	3.4	3.1	2.5	0.7	0.9	2.5	1.5	2.1
Al_2O_3	16.4	15.9	15.8	15.4	15.3	19.6	20.0	18.9	19.9	19.5	16.6	17.3	17.3	16.9	17.3	24.6	24.1	20.6	25.4	20.2
FeO_t	23.2	23.2	24.0	24.1	23.7	20.3	21.0	21.9	20.7	21.7	26.6	26.9	26.2	26.5	26.5	25.4	22.4	28.1	24.9	28.9
MnO	0.4	0.3	0.3	0.3	0.3	0.1	0.1	0.1	0.1	0.1	0.4	0.3	0.5	0.4	0.3	0.1	0.0	0.1	0.1	0.1
MgO	6.7	6.4	6.8	6.4	6.7	7.2	7.3	8.4	7.8	8.4	4.0	4.4	4.1	4.2	4.2	7.1	6.9	8.5	9.1	9.5
CaO	0.0	0.0	0.0	0.0	0.0	0.0	0.1	0.0	0.0	0.0	0.0	0.0	0.0	0.0	0.0	0.0	0.0	0.0	0.0	0.0
Na_2O	0.2	0.3	0.0	0.2	0.2	0.4	0.5	0.2	0.3	0.3	0.0	0.2	0.3	0.2	0.0	0.0	0.0	0.0	0.0	0.2
K_2O	9.3	9.4	9.3	9.4	9.3	9.7	9.6	9.2	8.8	8.8	9.3	9.5	9.3	9.3	9.3	3.7	4.6	5.4	2.9	4.8
Total	94.1	93.8	94.1	94.7	94.0	95.2	96.2	96.2	96.1	97.1	93.8	95.8	95.4	95.0	94.2	97.3	95.3	96.8	96.0	96.9
Formula																				
Number of ions on the basis of 22 O																				
Si	5.59	5.60	5.56	5.59	5.58	5.23	5.16	5.21	5.28	5.23	5.44	5.43	5.44	5.47	5.46	5.23	5.39	4.87	4.79	4.79
Al^{IV}	2.41	2.40	2.44	2.41	2.42	2.77	2.84	2.79	2.72	2.77	2.56	2.57	2.56	2.53	2.54	2.77	2.61	3.13	3.21	3.21
Σ Z	8.00	8.00	8.00	8.00	8.00	8.00	8.00	8.00	8.00	8.00	8.00	8.00	8.00	8.00	8.00	8.00	8.00	8.00	8.00	8.00
Al^{VI}	0.63	0.56	0.51	0.44	0.44	0.79	0.75	0.62	0.84	0.69	0.61	0.66	0.66	0.64	0.73	1.47	1.59	0.60	1.25	0.46
Ti	0.30	0.38	0.34	0.42	0.40	0.46	0.45	0.40	0.41	0.42	0.39	0.34	0.40	0.37	0.31	0.08	0.10	0.29	0.16	0.25
Fe_t	3.06	3.07	3.18	3.17	3.15	2.61	2.68	2.81	2.62	2.73	3.61	3.56	3.47	3.53	3.56	3.11	2.76	3.61	3.09	3.72
Mn	0.05	0.04	0.04	0.04	0.04	0.01	0.01	0.01	0.01	0.01	0.06	0.04	0.07	0.06	0.05	0.01	0.00	0.01	0.01	0.01
Mg	1.58	1.52	1.60	1.51	1.58	1.64	1.66	1.91	1.77	1.89	0.97	1.04	0.96	1.01	1.01	1.55	1.53	1.95	2.02	2.18
Σ X	4.99	5.00	5.15	5.14	5.17	4.73	4.80	5.13	4.80	5.06	5.02	4.98	4.90	4.97	4.93	4.75	4.39	5.86	5.29	6.16
Ca	0.00	0.00	0.03	0.00	0.00	0.00	0.02	0.00	0.00	0.00	0.00	0.00	0.00	0.00	0.00	0.00	0.00	0.00	0.00	0.00
Na	0.07	0.08	0.00	0.06	0.06	0.13	0.15	0.07	0.09	0.08	0.00	0.06	0.10	0.05	0.00	0.00	0.00	0.00	0.00	0.07
K	1.88	1.90	1.87	1.90	1.89	1.90	1.87	1.81	1.69	1.69	1.92	1.91	1.89	1.89	1.90	0.70	0.86	1.05	0.54	0.95
Σ Y	1.95	1.97	1.90	1.96	1.94	2.02	2.04	1.88	1.78	1.77	1.92	1.97	1.99	1.94	1.90	0.70	0.86	1.05	0.54	1.02
Total	15.57	15.53	15.56	15.54	15.55	15.54	15.60	15.63	15.42	15.51	15.55	15.60	15.54	15.54	15.55	14.92	14.84	15.51	15.08	15.64
X_{Fe}	0.66	0.67	0.67	0.68	0.67	0.61	0.62	0.59	0.60	0.59	0.79	0.77	0.78	0.78	0.78	0.67	0.64	0.65	0.61	0.63

TABLE 2 CONTINUED

Sample	s5A					s5B					s7A					s8D				
Spot No.	03	04	05	06	08	02	03	04	05	06	01	02	03	04	05	02	04	06	09	11
ID																F	F	F	M	M
wt.-%																				
SiO_2	36.3	36.9	37.0	31.3	37.3	35.4	35.4	35.1	35.3	35.3	36.9	36.6	37.0	37.2	37.0	37.5	36.7	36.7	37.2	37.0
TiO_2	2.6	1.8	3.0	1.5	2.5	3.7	3.4	3.8	3.7	3.4	2.3	2.2	1.9	2.5	2.3	3.2	3.9	4.1	1.5	2.6
Al_2O_3	16.2	17.1	16.3	17.4	16.6	15.6	15.5	15.5	15.6	15.6	16.4	16.6	16.8	16.1	16.5	16.5	16.1	16.5	18.0	16.8
FeO_t	23.3	24.3	23.3	26.0	23.3	21.6	21.4	21.1	21.6	21.4	18.6	18.1	18.0	18.4	18.3	21.2	21.6	22.1	20.9	21.7
MnO	0.1	0.1	0.1	0.1	0.1	0.0	0.3	0.2	0.0	0.3	0.0	0.1	0.0	0.0	0.0	0.2	0.3	0.4	0.3	0.3
MgO	10.5	11.6	9.9	12.1	10.5	7.7	7.9	8.0	8.0	8.3	10.5	10.3	10.5	10.7	10.6	7.8	7.9	7.6	9.1	8.1
CaO	0.1	0.0	0.0	0.1	0.0	0.0	0.0	0.0	0.0	0.0	0.0	0.0	0.0	0.0	0.0	0.0	0.0	0.0	0.0	0.0
Na_2O	0.3	0.2	0.3	0.2	0.3	0.2	0.2	0.3	0.2	0.2	0.3	0.3	0.3	0.2	0.2	0.2	0.2	0.3	0.0	0.2
K_2O	9.4	7.6	9.5	5.0	9.1	9.2	9.2	9.2	9.2	9.2	9.4	9.5	9.4	9.5	9.5	9.4	9.5	9.4	8.8	9.6
Total	98.8	99.6	99.4	93.7	99.7	93.3	93.4	93.0	93.6	93.6	94.3	93.7	93.9	94.6	94.4	96.2	96.1	96.9	95.7	96.4
Formula																				
Number of ions on the basis of 22 O																				
Si	5.44	5.43	5.50	4.96	5.50	5.58	5.59	5.55	5.55	5.56	5.65	5.64	5.67	5.68	5.65	5.70	5.60	5.57	5.63	5.64
Al^{IV}	2.56	2.57	2.50	3.04	2.50	2.42	2.41	2.45	2.45	2.44	2.35	2.36	2.33	2.32	2.35	2.30	2.40	2.43	2.37	2.36
Σ Z	8.00	8.00	8.00	8.00	8.00	8.00	8.00	8.00	8.00	8.00	8.00	8.00	8.00	8.00	8.00	8.00	8.00	8.00	8.00	8.00
Al^{VI}	0.31	0.39	0.35	0.20	0.39	0.48	0.48	0.44	0.45	0.45	0.61	0.66	0.70	0.58	0.62	0.65	0.50	0.52	0.84	0.66
Ti	0.29	0.20	0.34	0.17	0.28	0.44	0.40	0.45	0.44	0.40	0.27	0.25	0.22	0.29	0.27	0.36	0.45	0.47	0.17	0.30
Fe_t	2.91	2.99	2.90	3.45	2.88	2.85	2.83	2.79	2.84	2.82	2.38	2.33	2.31	2.34	2.34	2.69	2.76	2.80	2.64	2.77
Mn	0.01	0.01	0.01	0.01	0.01	0.00	0.04	0.02	0.00	0.04	0.00	0.02	0.00	0.00	0.00	0.03	0.04	0.05	0.04	0.04
Mg	2.35	2.55	2.20	2.85	2.32	1.80	1.86	1.88	1.88	1.94	2.39	2.37	2.41	2.43	2.42	1.77	1.79	1.71	2.05	1.84
Σ X	5.57	5.75	5.45	6.48	5.48	5.09	5.12	5.15	5.16	5.20	5.04	4.97	4.94	5.05	5.02	4.86	5.05	5.02	4.90	4.95
Ca	0.02	0.00	0.00	0.02	0.00	0.00	0.00	0.00	0.00	0.00	0.00	0.00	0.00	0.00	0.00	0.00	0.00	0.00	0.00	0.00
Na	0.08	0.05	0.07	0.06	0.08	0.06	0.07	0.09	0.06	0.07	0.08	0.08	0.08	0.07	0.06	0.06	0.05	0.07	0.00	0.05
K	1.80	1.43	1.80	1.02	1.71	1.86	1.86	1.85	1.85	1.85	1.83	1.86	1.83	1.84	1.86	1.82	1.85	1.81	1.69	1.86
Σ Y	1.90	1.48	1.87	1.10	1.79	1.92	1.92	1.94	1.92	1.92	1.91	1.94	1.91	1.91	1.92	1.88	1.90	1.89	1.69	1.90
Total	15.77	15.63	15.67	15.78	15.67	15.49	15.53	15.53	15.52	15.56	15.56	15.57	15.55	15.54	15.56	15.40	15.45	15.43	15.44	15.51
X_{Fe}	0.55	0.54	0.57	0.55	0.55	0.61	0.60	0.60	0.60	0.59	0.50	0.50	0.49	0.49	0.49	0.60	0.61	0.62	0.56	0.60

TABLE 3: REPRESENTATIVE ANALYSES OF HORNBLENDE

Sample	s1A					s5A					s5B					s7A				
Spot No.	02	08	12	16	26	01	07	20	22	23	01	02	03	06	07	02	04	05	13	14
wt.-%																				
SiO_2	49.4	51.4	53.0	51.6	47.8	49.5	45.5	49.7	47.4	45.4	43.4	42.5	42.5	41.4	42.8	51.8	51.4	47.9	52.2	47.8
TiO_2	0.7	0.4	0.3	0.3	0.8	0.4	1.3	0.7	0.7	1.1	1.2	1.4	1.4	1.4	1.4	0.5	0.6	1.1	0.4	1.0
Al_2O_3	5.2	3.7	2.6	2.7	6.3	5.5	9.2	5.6	7.2	7.9	10.0	10.2	9.6	10.7	9.6	3.3	3.9	7.2	2.8	7.5
FeO_t	15.1	14.0	13.2	13.2	15.9	18.2	19.4	17.8	19.1	19.0	19.5	19.9	19.7	20.4	20.1	16.4	15.7	17.2	17.0	17.6
MnO	0.4	0.3	0.3	0.3	0.4	0.1	0.1	0.1	0.1	0.1	0.6	0.4	0.4	0.5	0.4	0.5	0.4	0.4	0.5	0.4
MgO	12.8	14.0	14.8	14.6	12.1	11.5	9.3	11.5	10.4	9.7	7.6	7.2	7.4	6.4	6.9	13.6	13.5	11.6	14.1	11.5
Cr_2O_3	0.4	0.3	0.4	0.3	0.4	0.0	0.0	0.0	0.0	0.0	0.0	0.0	0.0	0.0	0.0	0.4	0.4	0.0	0.2	0.2
CaO	11.8	12.0	12.2	12.2	11.5	11.9	12.0	12.2	11.5	11.5	11.5	11.2	11.5	11.2	11.3	10.4	11.4	10.6	9.6	10.3
Na_2O	0.8	0.6	0.4	0.4	1.0	0.5	1.0	0.7	0.6	0.6	0.9	1.3	0.9	1.1	0.9	0.3	0.5	0.7	0.4	0.9
K_2O	0.3	0.2	0.0	0.1	0.4	0.4	0.9	0.4	0.5	0.7	1.0	1.0	0.9	1.0	0.9	0.0	0.2	0.4	0.0	0.3
Total	96.8	96.9	97.1	95.8	96.6	98.1	98.8	98.7	97.5	96.0	95.7	95.2	94.1	94.2	94.3	97.3	98.0	97.1	97.4	97.3
Formula																				
Number of ions on the basis of 23 O																				
Si	7.27	7.49	7.66	7.58	7.08	7.25	6.76	7.26	7.00	6.87	6.70	6.64	6.68	6.56	6.73	7.41	7.39	6.98	7.40	6.93
Al^{IV}	0.73	0.51	0.34	0.42	0.92	0.75	1.24	0.74	1.00	1.13	1.30	1.36	1.32	1.44	1.27	0.56	0.61	1.02	0.48	1.07
Σ T	8.00	8.00	8.00	8.00	8.00	8.00	8.00	8.00	8.00	8.00	8.00	8.00	8.00	8.00	8.00	7.97	8.00	8.00	7.87	8.00
Al^{VI}	0.17	0.12	0.11	0.06	0.18	0.21	0.38	0.23	0.25	0.27	0.51	0.51	0.46	0.56	0.51	0.00	0.06	0.22	0.00	0.20
Ti	0.07	0.05	0.03	0.04	0.09	0.04	0.15	0.07	0.08	0.13	0.14	0.16	0.17	0.17	0.16	0.06	0.07	0.12	0.04	0.10
Fe^{3+}	0.37	0.33	0.23	0.26	0.47	0.49	0.27	0.23	0.67	0.59	0.24	0.17	0.22	0.16	0.14	1.18	0.70	0.96	1.59	1.15
Fe^{2+}	1.49	1.38	1.36	1.37	1.50	1.74	2.14	1.95	1.69	1.82	2.28	2.43	2.37	2.54	2.51	0.78	1.18	1.13	0.43	0.98
Mn	0.05	0.04	0.04	0.03	0.05	0.01	0.01	0.01	0.01	0.01	0.07	0.05	0.05	0.06	0.06	0.06	0.05	0.05	0.06	0.05
Mg	2.81	3.05	3.18	3.21	2.66	2.51	2.06	2.50	2.29	2.19	1.75	1.68	1.73	1.50	1.62	2.90	2.90	2.51	2.99	2.49
Cr	0.05	0.03	0.04	0.03	0.05	0.00	0.00	0.00	0.00	0.00	0.00	0.00	0.00	0.00	0.00	0.05	0.04	0.00	0.02	0.03
Σ C	5.00	5.00	5.00	5.00	5.00	5.00	5.00	5.00	5.00	5.00	5.00	5.00	5.00	5.00	5.00	5.03	5.00	5.00	5.13	5.00
Ca	1.87	1.87	1.88	1.93	1.83	1.87	1.92	1.92	1.83	1.86	1.90	1.88	1.93	1.91	1.91	1.59	1.75	1.65	1.46	1.60
Na	0.21	0.17	0.12	0.13	0.29	0.15	0.29	0.21	0.16	0.16	0.27	0.40	0.26	0.35	0.28	0.09	0.13	0.20	0.11	0.24
K	0.06	0.03	0.00	0.02	0.08	0.07	0.17	0.08	0.10	0.13	0.19	0.21	0.17	0.21	0.18	0.00	0.04	0.08	0.00	0.05
Σ B	2.14	2.07	2.01	2.07	2.21	2.09	2.38	2.21	2.09	2.16	2.36	2.49	2.37	2.46	2.37	1.69	1.92	1.94	1.57	1.89
Total	15.14	15.07	15.01	15.07	15.21	15.09	15.38	15.21	15.09	15.16	15.36	15.49	15.37	15.46	15.37	14.69	14.92	14.94	14.57	14.89
X_{Mg}	0.65	0.69	0.70	0.70	0.64	0.59	0.49	0.56	0.57	0.55	0.43	0.41	0.42	0.37	0.39	0.79	0.71	0.69	0.87	0.72

TABLE 4: TRAVERSE ANALYSES ALONG A GARNET PORPHYROBLAST; THE DISTANCE BETWEEN ANALYSES SPOTS IS GIVEN IN MM

Sample	s4D																					
Spot No.	01	02	03	04	05	06	07	08	09	10	11	12	13	14	15	16	17	18	19	20	21	22
wt.-%																						
SiO_2	36.6	37.1	37.2	37.0	36.2	37.1	37.3	37.7	36.6	37.8	37.5	37.0	37.2	37.1	37.0	37.0	36.9	37.3	37.5	36.6	37.5	37.0
TiO_2	0.0	0.0	0.0	0.0	0.0	0.0	0.0	0.0	0.0	0.0	0.0	0.0	0.0	0.1	0.0	0.0	0.0	0.1	0.0	0.0	0.0	0.0
Al_2O_3	20.5	21.1	20.9	20.6	20.4	20.6	21.0	21.2	20.6	21.3	21.2	20.6	20.8	20.8	20.6	20.9	20.7	20.9	20.9	20.5	21.2	20.8
FeO_t	36.9	36.4	36.1	35.6	35.8	36.2	36.3	36.5	36.3	36.0	36.0	36.3	36.2	36.1	36.0	36.8	36.2	36.3	36.3	36.3	36.5	36.5
MnO	1.6	1.2	1.3	1.3	1.3	1.2	1.5	1.3	1.4	1.3	1.3	1.3	1.3	1.3	1.5	1.5	1.5	1.4	1.4	1.4	1.5	1.4
MgO	2.7	3.1	3.4	3.4	3.3	3.3	3.4	3.3	3.4	3.4	3.4	3.3	3.2	3.3	3.3	3.2	3.1	3.2	3.2	3.1	3.2	3.3
CaO	0.9	0.9	0.9	0.9	0.8	0.9	0.8	0.8	0.9	0.8	0.9	0.9	0.9	0.9	1.0	0.9	0.8	1.0	1.0	0.9	0.8	0.9
Total	99.2	99.9	99.8	98.8	97.9	99.4	100.3	100.8	99.0	100.6	100.2	99.4	99.6	99.6	99.4	100.3	99.3	100.2	100.2	98.9	100.7	99.9
Number of ions on the basis of 12 O																						
Mg	0.32	0.38	0.41	0.41	0.40	0.39	0.40	0.40	0.41	0.40	0.41	0.40	0.39	0.40	0.40	0.38	0.38	0.38	0.39	0.38	0.38	0.40
Al	1.97	2.01	1.98	1.98	1.98	1.98	1.99	1.99	1.98	2.00	2.00	1.97	1.98	1.98	1.97	1.99	1.99	1.98	1.98	1.98	2.00	1.98
Si	3.00	2.99	3.00	3.01	2.99	3.01	3.00	3.01	2.99	3.02	3.01	3.00	3.01	3.00	3.00	2.99	3.00	3.00	3.01	3.00	3.00	2.99
Ca	0.08	0.08	0.08	0.08	0.08	0.08	0.07	0.07	0.07	0.07	0.08	0.08	0.08	0.08	0.08	0.08	0.07	0.08	0.08	0.08	0.07	0.08
Ti	0.00	0.00	0.00	0.00	0.00	0.00	0.00	0.00	0.00	0.00	0.00	0.00	0.00	0.01	0.00	0.00	0.00	0.01	0.00	0.00	0.00	0.00
Cr	0.00	0.00	0.00	0.00	0.00	0.00	0.00	0.00	0.00	0.00	0.00	0.00	0.00	0.00	0.00	0.00	0.00	0.00	0.00	0.00	0.00	0.00
Mn	0.11	0.08	0.09	0.09	0.09	0.09	0.10	0.09	0.10	0.09	0.09	0.09	0.09	0.09	0.10	0.10	0.10	0.10	0.10	0.10	0.10	0.10
Fe_t	2.53	2.46	2.43	2.43	2.47	2.46	2.44	2.44	2.48	2.40	2.42	2.46	2.45	2.44	2.45	2.48	2.46	2.44	2.44	2.48	2.44	2.47
Tot. cat.	8.02	8.00	8.00	8.00	8.02	8.00	8.01	7.99	8.03	7.98	7.99	8.01	8.00	8.00	8.01	8.02	8.01	8.00	8.00	8.01	8.00	8.02
Py	10.63	12.54	13.71	13.75	13.23	13.05	13.41	13.26	13.53	13.48	13.59	13.16	12.96	13.29	13.24	12.63	12.49	12.72	12.87	12.60	12.73	13.05
Alm	83.05	82.05	80.67	80.66	81.27	81.45	81.03	81.47	80.92	81.09	80.96	81.20	81.51	81.04	80.65	81.42	81.62	81.33	81.19	81.63	81.49	81.23
Gro	2.61	2.58	2.71	2.62	2.47	2.67	2.28	2.30	2.44	2.45	2.52	2.65	2.58	2.73	2.77	2.58	2.44	2.74	2.74	2.61	2.33	2.58
Sp	3.70	2.83	2.90	2.97	3.03	2.83	3.28	2.97	3.11	2.98	2.94	3.00	2.95	2.94	3.34	3.38	3.46	3.22	3.20	3.15	3.45	3.14
X_{Mg}	6.70	7.90	8.70	8.73	8.37	8.24	8.49	8.36	8.57	8.53	8.60	8.33	8.18	8.43	8.43	8.00	7.90	8.07	8.16	7.97	8.05	8.27
Distance	0	107	214	330	471	693	916	1033	1117	1265	1329	1426	1546	1694	1766	1840	1867	1902	1948	1998	2031	2069

TABLE 4 CONTINUED

Sample	s4D																					
Spot No.	23	24	25	26	27	28	29	30	31	32	33	34	35	36	37	38	39	40	41	42	43	44
wt.-%																						
SiO_2	37.2	37.4	37.2	37.0	37.5	37.3	36.9	37.3	37.7	37.3	37.5	37.4	37.3	36.9	37.6	37.2	36.8	37.3	37.4	37.3	37.4	37.5
TiO_2	0.0	0.0	0.0	0.0	0.0	0.0	0.0	0.0	0.0	0.0	0.0	0.0	0.0	0.0	0.0	0.0	0.0	0.0	0.0	0.0	0.0	0.0
Al_2O_3	21.2	21.0	21.0	21.1	20.9	21.3	21.0	21.1	20.9	21.0	21.0	21.1	20.9	21.1	21.0	21.1	20.7	21.0	21.2	21.1	20.9	21.1
FeO_t	36.0	36.3	36.3	36.3	36.4	36.3	36.4	36.4	36.4	36.4	36.7	36.5	36.9	36.3	36.3	36.0	36.0	36.7	36.8	36.5	36.6	36.9
MnO	1.4	1.5	1.5	1.4	1.5	1.5	1.5	1.4	1.5	1.5	1.4	1.4	1.5	1.5	1.4	1.4	1.4	1.4	1.4	1.5	1.4	1.6
MgO	3.2	3.3	3.2	3.2	3.3	3.3	3.2	3.2	3.4	3.4	3.3	3.2	3.3	3.1	3.3	3.1	3.1	3.3	3.2	3.1	3.3	3.3
CaO	0.8	0.9	0.9	0.9	0.9	0.9	0.9	0.9	0.9	0.9	0.9	0.9	1.0	0.9	0.9	0.9	0.9	0.8	0.8	0.9	0.9	0.8
Total	99.9	100.4	100.1	99.9	100.6	100.6	99.8	100.3	100.7	100.6	100.8	100.5	100.9	99.9	100.5	99.8	99.0	100.5	100.8	100.4	100.5	101.3
Number of ions on the basis of 12 O																						
Mg	0.39	0.39	0.39	0.39	0.39	0.39	0.38	0.38	0.40	0.40	0.40	0.38	0.40	0.38	0.39	0.38	0.38	0.40	0.39	0.37	0.39	0.39
Al	2.01	1.99	2.00	2.01	1.98	2.01	2.00	2.00	1.97	1.99	1.98	2.00	1.97	2.01	1.98	2.00	1.99	1.98	2.00	2.00	1.98	1.98
Si	3.00	3.00	3.00	2.99	3.01	2.99	2.99	3.00	3.01	3.00	3.00	3.00	2.99	2.99	3.02	3.00	3.00	3.00	2.99	3.00	3.00	3.00
Ca	0.07	0.08	0.08	0.08	0.08	0.08	0.08	0.08	0.08	0.08	0.07	0.07	0.08	0.08	0.07	0.08	0.08	0.07	0.07	0.07	0.08	0.07
Ti	0.00	0.00	0.00	0.00	0.00	0.00	0.00	0.00	0.00	0.00	0.00	0.00	0.00	0.00	0.00	0.00	0.00	0.00	0.00	0.00	0.00	0.00
Cr	0.00	0.00	0.00	0.00	0.00	0.00	0.00	0.00	0.00	0.00	0.00	0.00	0.00	0.00	0.00	0.00	0.00	0.00	0.00	0.00	0.00	0.00
Mn	0.09	0.10	0.10	0.09	0.10	0.10	0.10	0.09	0.10	0.10	0.10	0.10	0.10	0.11	0.09	0.10	0.10	0.09	0.09	0.10	0.10	0.11
Fe_t	2.43	2.44	2.45	2.45	2.44	2.44	2.46	2.45	2.44	2.44	2.45	2.45	2.48	2.46	2.43	2.43	2.46	2.47	2.46	2.46	2.46	2.46
Tot. cat.	7.99	8.00	8.01	8.01	8.00	8.00	8.01	8.00	8.00	8.01	8.01	8.00	8.02	8.01	7.99	7.99	8.01	8.01	8.01	8.00	8.01	8.01
Py	13.04	12.95	12.93	12.97	13.09	12.94	12.68	12.73	13.28	13.29	13.16	12.73	12.93	12.45	13.17	12.64	12.68	13.05	12.86	12.20	12.90	12.77
Alm	81.48	81.06	81.16	81.41	80.97	81.09	81.34	81.46	80.96	80.74	81.16	81.63	81.04	81.53	81.28	81.52	81.38	81.51	81.77	81.91	81.24	81.21
Gro	2.32	2.61	2.50	2.49	2.50	2.69	2.60	2.69	2.50	2.54	2.47	2.46	2.76	2.51	2.48	2.54	2.72	2.39	2.31	2.49	2.65	2.38
Sp	3.16	3.38	3.41	3.13	3.44	3.29	3.37	3.13	3.27	3.42	3.21	3.18	3.28	3.51	3.07	3.30	3.23	3.04	3.06	3.40	3.21	3.64
X_{Mg}	8.24	8.23	8.20	8.20	8.32	8.21	8.04	8.06	8.42	8.45	8.33	8.04	8.21	7.89	8.33	8.00	8.04	8.24	8.10	7.71	8.18	8.10
Distance	2180	2226	2275	2309	2355	2394	2446	2479	2521	2576	2617	2663	2700	2738	2779	2822	2861	2899	2939	2978	3017	3057

TABLE 4 CONTINUED

Sample	s4D																					
Spot No.	45	46	47	48	49	50	51	52	53	54	55	56	57	58	59	60	61	62	63	64	65	66
wt.-%																						
SiO_2	37.4	37.4	37.4	37.1	37.3	36.8	37.4	37.1	37.4	37.7	37.1	37.2	37.0	36.4	37.2	37.1	37.0	37.2	36.9	37.2	37.4	37.6
TiO_2	0.0	0.0	0.0	0.0	0.0	0.0	0.0	0.0	0.0	0.0	0.0	0.0	0.0	0.0	0.0	0.0	0.0	0.0	0.0	0.0	0.0	0.0
Al_2O_3	20.9	21.2	21.4	21.1	21.1	20.7	21.0	21.0	21.1	21.0	20.8	21.0	20.7	20.3	21.1	21.0	21.0	21.0	20.9	20.9	20.8	21.4
FeO_t	36.4	36.1	36.7	36.7	37.0	36.4	36.9	36.4	37.0	37.1	37.4	37.2	37.0	37.1	36.9	37.0	37.0	36.8	36.2	36.8	36.4	36.6
MnO	1.4	1.4	1.4	1.5	1.5	1.3	1.4	1.4	1.5	1.6	2.0	2.2	2.7	2.8	1.6	1.7	1.6	1.4	1.6	1.4	1.5	1.5
MgO	3.3	3.2	3.1	3.1	3.3	3.1	3.1	3.0	2.9	2.8	2.6	2.2	1.9	1.6	2.7	2.7	3.2	3.2	3.1	3.2	3.1	3.2
CaO	0.9	0.8	0.9	0.9	0.9	0.9	0.8	0.9	0.9	0.8	0.8	0.9	0.8	0.9	0.8	0.8	0.9	0.9	0.9	0.9	0.9	0.9
Total	100.3	100.2	100.9	100.5	101.1	99.0	100.7	99.7	100.8	101.1	100.7	100.6	100.1	99.1	100.3	100.4	100.7	100.5	99.6	100.3	100.0	101.2
Number of ions on the basis of 12 O																						
Mg	0.39	0.39	0.37	0.37	0.39	0.37	0.37	0.36	0.34	0.33	0.31	0.26	0.23	0.19	0.32	0.32	0.38	0.38	0.38	0.38	0.37	0.38
Al	1.98	2.01	2.01	2.00	1.99	1.99	1.99	2.00	2.00	1.98	1.98	1.99	1.98	1.98	2.01	2.00	1.99	1.99	1.99	1.98	1.98	2.01
Si	3.01	3.00	2.99	2.99	2.99	3.00	3.00	3.00	3.00	3.02	3.00	3.00	3.01	3.00	3.00	3.00	2.98	2.99	3.00	3.00	3.01	3.00
Ca	0.07	0.07	0.07	0.08	0.08	0.08	0.07	0.08	0.07	0.07	0.07	0.07	0.07	0.08	0.07	0.07	0.08	0.08	0.08	0.08	0.07	0.07
Ti	0.00	0.00	0.00	0.00	0.00	0.00	0.00	0.00	0.00	0.00	0.00	0.00	0.00	0.00	0.00	0.00	0.00	0.00	0.00	0.00	0.00	0.00
Cr	0.00	0.00	0.00	0.00	0.00	0.00	0.00	0.00	0.00	0.00	0.00	0.00	0.00	0.00	0.00	0.00	0.00	0.00	0.00	0.00	0.00	0.00
Mn	0.09	0.10	0.10	0.10	0.10	0.09	0.09	0.09	0.10	0.11	0.13	0.15	0.19	0.20	0.11	0.11	0.11	0.10	0.11	0.09	0.10	0.10
Fe_t	2.45	2.43	2.45	2.47	2.47	2.48	2.48	2.47	2.48	2.48	2.53	2.51	2.51	2.56	2.49	2.50	2.49	2.47	2.46	2.48	2.46	2.44
Tot. cat.	8.00	7.99	8.00	8.01	8.02	8.01	8.00	8.00	8.00	7.99	8.01	8.00	8.00	8.01	8.00	8.00	8.03	8.01	8.01	8.01	8.00	8.00
Py	13.11	13.01	12.47	12.28	12.76	12.30	12.36	11.93	11.40	10.98	10.14	8.80	7.69	6.41	10.73	10.67	12.43	12.56	12.46	12.56	12.33	12.76
Alm	81.33	81.34	81.85	81.73	81.36	82.19	82.13	82.46	82.71	83.02	83.11	83.63	83.73	84.53	83.24	83.12	81.49	81.73	81.45	81.77	81.87	81.39
Gro	2.45	2.42	2.47	2.58	2.49	2.49	2.39	2.51	2.44	2.40	2.33	2.49	2.42	2.57	2.43	2.41	2.51	2.54	2.52	2.60	2.48	2.48
Sp	3.11	3.23	3.21	3.41	3.39	3.02	3.12	3.11	3.45	3.60	4.42	5.08	6.16	6.49	3.60	3.80	3.56	3.17	3.56	3.08	3.32	3.36
X_{Mg}	8.29	8.23	7.87	7.77	8.09	7.74	7.78	7.50	7.18	6.90	6.40	5.57	4.90	4.08	6.74	6.72	7.88	7.94	7.90	7.93	7.79	8.08
Distance	3101	3141	3203	3258	3310	3380	3431	3495	3550	3608	3667	3736	3795	3850	4292	5602	5833	6026	6026	6137	6242	6531

TABLE 4 CONTINUED

Sample	s4D																					
Spot No.	67	68	69	70	71	72	73	74	75	76	77	78	79	80	81	82	83	84	85	86	87	88
wt.-%																						
SiO_2	37.0	37.1	37.2	36.7	37.1	36.7	37.2	37.4	36.9	37.3	37.3	37.8	37.4	36.9	37.5	37.2	36.6	37.1	37.6	37.3	36.9	37.5
TiO_2	0.0	0.0	0.0	0.1	0.0	0.0	0.0	0.0	0.0	0.0	0.0	0.0	0.0	0.0	0.0	0.0	0.0	0.0	0.0	0.0	0.0	0.0
Al_2O_3	20.8	21.1	21.2	20.7	20.8	20.7	21.0	21.0	20.8	21.3	21.1	21.5	21.3	21.0	21.1	20.8	20.7	21.0	21.2	20.9	20.8	20.9
FeO_t	36.5	36.7	36.6	36.5	36.5	36.4	36.2	36.3	36.2	37.2	37.1	36.9	36.7	36.4	36.3	36.5	36.5	36.6	36.6	36.4	36.5	36.9
MnO	1.5	1.5	1.5	1.4	1.4	1.4	1.4	1.4	1.4	2.0	1.6	1.5	1.5	1.5	1.5	1.4	1.4	1.5	1.4	1.3	1.4	1.8
MgO	3.3	3.2	3.2	3.2	3.2	3.2	3.2	3.2	3.2	2.5	2.9	3.1	2.8	3.3	3.3	3.4	3.2	3.2	3.3	3.2	3.2	2.7
CaO	0.8	0.8	0.9	0.9	0.9	0.9	0.9	0.9	0.8	1.0	0.9	1.0	0.9	0.8	0.8	0.8	0.8	0.8	1.0	0.9	0.8	0.9
Total	99.9	100.4	100.5	99.7	99.9	99.4	99.9	100.2	99.4	101.2	100.9	101.7	100.7	99.9	100.5	100.0	99.2	100.3	101.2	100.0	99.6	100.7
Number of ions on the basis of 12 O																						
Mg	0.39	0.38	0.38	0.39	0.39	0.39	0.38	0.38	0.38	0.30	0.35	0.37	0.34	0.40	0.40	0.41	0.38	0.39	0.39	0.38	0.38	0.33
Al	1.98	2.00	2.00	1.98	1.99	1.99	2.00	1.99	1.99	2.01	2.00	2.01	2.02	2.00	1.99	1.98	1.99	2.00	1.99	1.99	1.99	1.98
Si	3.00	2.99	2.99	2.98	3.00	2.99	3.00	3.01	3.00	2.99	2.99	3.00	2.99	2.98	3.00	3.00	2.99	2.99	3.00	3.01	3.00	3.01
Ca	0.07	0.07	0.07	0.08	0.08	0.08	0.08	0.08	0.07	0.08	0.08	0.08	0.08	0.07	0.07	0.07	0.07	0.07	0.08	0.08	0.07	0.08
Ti	0.00	0.00	0.00	0.01	0.00	0.00	0.00	0.00	0.00	0.00	0.00	0.00	0.00	0.00	0.00	0.00	0.00	0.00	0.00	0.00	0.00	0.00
Cr	0.00	0.00	0.00	0.00	0.00	0.00	0.00	0.00	0.00	0.00	0.00	0.00	0.00	0.00	0.00	0.00	0.00	0.00	0.00	0.00	0.00	0.00
Mn	0.11	0.10	0.10	0.10	0.10	0.10	0.10	0.10	0.10	0.14	0.11	0.10	0.10	0.10	0.10	0.09	0.10	0.10	0.09	0.09	0.09	0.13
Fe_t	2.47	2.47	2.46	2.48	2.47	2.48	2.44	2.44	2.46	2.49	2.49	2.45	2.46	2.46	2.44	2.46	2.49	2.47	2.44	2.45	2.48	2.48
Tot. cat.	8.01	8.01	8.01	8.02	8.01	8.02	8.00	8.00	8.00	8.01	8.01	8.00	8.00	8.02	8.00	8.01	8.02	8.01	8.00	8.00	8.01	8.00
Py	12.97	12.63	12.56	12.84	12.75	12.73	12.69	12.77	12.79	9.87	11.57	12.20	11.38	13.13	13.16	13.48	12.59	12.78	13.11	12.77	12.63	10.89
Alm	81.21	81.65	81.66	81.33	81.55	81.44	81.56	81.49	81.63	82.75	82.30	81.68	82.53	81.18	81.12	81.26	81.85	81.51	81.00	81.61	81.87	82.38
Gro	2.35	2.37	2.44	2.59	2.55	2.58	2.55	2.56	2.38	2.75	2.55	2.75	2.58	2.37	2.37	2.14	2.41	2.36	2.75	2.55	2.40	2.57
Sp	3.48	3.35	3.33	3.24	3.15	3.25	3.19	3.18	3.20	4.62	3.59	3.37	3.51	3.32	3.36	3.12	3.15	3.35	3.14	3.07	3.10	4.16
X_{Mg}	8.22	7.99	7.94	8.13	8.06	8.06	8.03	8.08	8.08	6.27	7.31	7.73	7.18	8.31	8.34	8.51	7.94	8.08	8.32	8.07	7.96	6.90
Distance	6700	6851	6948	7016	7120	7219	7320	7414	7705	7990	8078	8180	8299	8457	8681	8846	9084	9286	9507	9690	9838	10142

APPENDIX III: ZIRCON ANALYSES

TABLE 1: ZIRCON ISOTOPE SPOT ANALYSES; UNCERTAINTIES ARE REPORTED IN ±2σ

Sample	Rock type	Identifier U-Pb	$^{207}Pb/^{206}Pb$	2σ	$2\sigma_{sys}$	$^{206}Pb/^{238}U$	2σ	$2\sigma_{sys}$	$^{207}Pb/^{235}U$	2σ	$2\sigma_{sys}$	Concordance (%) 206/238 - 207/235	Concordance (%) 206/238 - 207/206	Identifier Lu-Hf	$^{176}Hf/^{177}Hf_t$	2σ	εHf_t	2σ	Date (Ma)	$^{176}Hf/^{177}Hf_{468}$	2σ	εHf_{468}	2σ
s1B	Granodiorite	s1B - 01	992	37	38	626	11	15	710	16	18	88	63										
s1B	Granodiorite	s1B - 03	931	32	34	464	8	12	551	12	15	84	50										
s1B	Granodiorite	s1B - 04	653	31	33	460	8	11	493	11	13	93	71	Us316	0.282099	0.000022	-14.0	0.8	460	0.282099	0.000022	-13.9	0.8
s1B	Granodiorite	s1B - 05	490	36	38	455	8	11	461	11	13	99	93	Us313	0.282059	0.000023	-15.6	0.8	455	0.282059	0.000023	-15.3	0.8
s1B	Granodiorite	s1B - 06	1465	48	49	575	11	15	790	18	21	73	39										
s1B	Granodiorite	s1B - 07	681	65	66	519	10	13	548	16	18	95	76	Us314	0.282149	0.000024	-10.9	0.8	519	0.282150	0.000024	-12.0	0.8
s1B	Granodiorite	s1B - 08	462	38	40	455	8	12	455	11	13	100	98	Us315	0.281892	0.000033	-21.5	1.2	455	0.281892	0.000033	-21.2	1.2
s1B	Granodiorite	s1B - 08b	541	32	34	516	9	13	521	12	14	99	95	Us315b	0.281891	0.000033	-20.1	1.2	516				
s1B	Granodiorite	s1B - 09	534	18	21	476	8	12	486	10	12	98	89	Us317	0.282113	0.000074	-13.2	2.6	476	0.282114	0.000074	-13.3	2.6
s1B	Granodiorite	s1B - 11	556	29	31	475	8	12	488	11	13	97	85	Us319	0.282144	0.000028	-12.1	1.0	475	0.282144	0.000028	-12.3	1.0
s1B	Granodiorite	s1B - 13	771	91	91	469	10	13	522	19	21	90	61										
s1B	Granodiorite	s1B - 14	784	64	65	603	12	16	642	19	21	94	77	Us318	0.282121	0.000030	-10.1	1.1	603	0.282125	0.000030	-12.9	1.1
s1B	Granodiorite	s1B - 15	512	17	20	532	9	13	526	11	14	101	104										
s1B	Granodiorite	s1B - 16	870	23	26	477	8	12	550	12	15	87	55										
s1B	Granodiorite	s1B - 18	604	50	52	452	8	11	477	13	14	95	75	Us321	0.282028	0.000025	-16.7	0.9	452	0.282028	0.000025	-16.4	0.9
s1B	Granodiorite	s1B - 19	922	18	21	470	8	11	555	12	14	85	51										
s1B	Granodiorite	s1B - 20	833	28	30	446	8	11	515	12	14	87	54										
s1B	Granodiorite	s1B - 21	632	35	37	450	8	11	480	11	13	94	71	Us322	0.282119	0.000025	-13.5	0.9	450	0.282119	0.000025	-13.2	0.9
s1B	Granodiorite	s1B - 22	730	14	18	456	8	11	503	10	13	90	62	Us323	0.282138	0.000030	-12.7	1.1	456	0.282138	0.000030	-12.5	1.1
s1B	Granodiorite	s1B - 23	664	52	53	493	9	12	523	14	16	94	74	Us324	0.282160	0.000019	-11.1	0.7	493	0.282161	0.000019	-11.7	0.7
s1B	Granodiorite	s1B - 24	509	31	33	536	9	13	530	12	14	101	105	Us327	0.282038	0.000015	-14.5	0.5	536	0.282040	0.000015	-15.9	0.5
s1B	Granodiorite	s1B - 26	536	21	24	444	8	11	458	10	12	97	83	Us326	0.282211	0.000023	-10.4	0.8	444	0.282210	0.000023	-9.9	0.8
s1B	Granodiorite	s1B - 27	774	55	56	484	9	12	542	15	17	89	62										
s1B	Granodiorite	s1B - 29	569	18	21	508	9	13	518	11	13	98	89	Us328	0.282029	0.000050	-15.4	1.8	508	0.282030	0.000050	-16.3	1.8
s1B	Granodiorite	s1B - 30	681	26	29	466	8	12	503	11	13	93	68										
s1B	Granodiorite	s1B - 31	1446	16	19	1088	18	26	1212	19	23	90	75										
s1B	Granodiorite	s1B - 32	1320	34	36	975	17	24	1086	21	25	90	74										
s1B	Granodiorite	s1B - 33	2432	10	14	1308	21	30	1798	22	27	73	54										
s1B	Granodiorite	s1B - 34	866	43	44	463	8	12	534	14	16	87	53										
s1B	Granodiorite	s1B - 35	1492	22	24	1222	36	41	1320	27	30	93	82	Us330	0.281799	0.000020	-1.3	0.7	1492	0.281820	0.000020	-23.7	0.7
s1B	Granodiorite	s1B - 36	708	24	27	451	8	11	494	11	13	91	64	Us329	0.282143	0.000048	-12.7	1.7	451	0.282143	0.000048	-12.3	1.7
s1B	Granodiorite	s1B - 37	2792	18	20	2396	39	53	2612	25	31	92	86	Us331	0.281524	0.000061	19.1	2.2	2792	0.281558	0.000061	-33.0	2.1
s1B	Granodiorite	s1B - 39	629	60	61	455	8	12	484	14	16	94	72	Us332	0.281988	0.000017	-18.1	0.6	455	0.281988	0.000017	-17.8	0.6
s1B	Granodiorite	s1B - 40	497	15	19	481	8	12	481	10	12	100	97	Us336	0.282165	0.000035	-11.2	1.2	481	0.282165	0.000035	-11.5	1.2
s1B	Granodiorite	s1B - 41	577	34	36	466	8	12	483	11	13	96	81	Us333	0.282142	0.000021	-12.4	0.7	466	0.282142	0.000021	-12.3	0.7
s1B	Granodiorite	s1B - 42	607	58	59	476	8	12	495	14	15	96	78	Us334	0.282019	0.000039	-16.5	1.4	476	0.282019	0.000039	-16.7	1.4
s1B	Granodiorite	s1B - 43	507	22	25	465	8	12	470	10	12	99	92	Us335	0.282130	0.000047	-12.8	1.7	465	0.282130	0.000047	-12.8	1.7
s1B	Granodiorite	s1B - 45	552	31	33	452	8	12	469	11	13	97	82	Us339	0.282192	0.000022	-10.9	0.8	452	0.282191	0.000022	-10.6	0.8
s1B	Granodiorite	s1B - 47	530	19	22	473	8	11	480	10	12	98	89	Us338	0.282996	0.000192	18.0	6.8	473	0.282996	0.000192	17.9	6.8
s1B	Granodiorite	s1B - 48	618	54	55	460	8	12	484	14	16	95	74	Us337	0.282065	0.000025	-15.2	0.9	460	0.282065	0.000025	-15.1	0.9
s1B	Granodiorite	s1B - n/a1												Us325	0.282088	0.000024	-13.7	0.9	493	0.282089	0.000024	-14.2	0.9

TABLE 1 CONTINUED

Sample	Rock type	Identifier U-Pb	$^{207}Pb/^{206}Pb$	2σ	$2\sigma_{sys}$	$^{206}Pb/^{238}U$	2σ	$2\sigma_{sys}$	$^{207}Pb/^{235}U$	2σ	$2\sigma_{sys}$	Concordance (%) 206/238 - 207/235	Concordance (%) 206/238 - 207/206	Identifier Lu-Hf	$^{176}Hf/^{177}Hf_t$	2σ	εHf_t	2σ	Date (Ma)	$^{176}Hf/^{177}Hf_{468}$	2σ	εHf_{468}	2σ
s1Da	Granite	s1Da - 01	646	42	44	488	6	10	518	9	12	94	76	Us142	0.282207	0.000025	-9.6	0.9	488	0.282208	0.000025	-10.0	0.9
s1Da	Granite	s1Da - 05	698	61	62	501	7	11	538	12	15	93	72										
s1Da	Granite	s1Da - 06	529	31	33	548	8	12	544	8	11	101	104	Us143	0.282127	0.000040	-11.0	1.4	548	0.282132	0.000040	-12.7	1.4
s1Da	Granite	s1Da - 08	522	65	66	564	12	15	555	16	18	102	108	Us146	0.282151	0.000022	-9.9	0.8	564	0.282153	0.000022	-11.9	0.8
s1Da	Granite	s1Da - 09	530	53	54	479	7	11	487	9	12	98	90	Us145	0.282131	0.000060	-12.5	2.1	479	0.282131	0.000060	-12.7	2.1
s1Da	Granite	s1Da - 10	600	51	52	483	6	10	501	10	12	96	81	Us149	0.282205	0.000044	-9.8	1.6	483	0.282205	0.000044	-10.1	1.6
s1Da	Granite	s1Da - 11	509	27	29	516	7	11	515	7	11	100	101	Us150	0.282183	0.000016	-9.8	0.6	516	0.282184	0.000016	-10.8	0.6
s1Da	Granite	s1Da - 12	1573	65	66	556	8	12	803	20	22	69	35										
s1Da	Granite	s1Da - 14	578	21	24	484	6	10	502	7	10	96	84										
s1Da	Granite	s1Da - 15	966	31	33	507	7	11	599	8	12	85	52										
s1Da	Granite	s1Da - 16	1212	32	33	484	6	10	634	9	13	76	40										
s1Da	Granite	s1Da - 17	496	34	36	499	8	12	497	8	11	100	101	Us154	0.282168	0.000018	-10.7	0.6	499	0.282169	0.000018	-11.4	0.6
s1Da	Granite	s1Da - 18	627	33	35	486	6	10	512	7	10	95	78	Us153	0.282193	0.000021	-10.1	0.7	486	0.282194	0.000021	-10.5	0.7
s1Da	Granite	s1Da - 19	522	53	54	481	6	10	487	10	12	99	92	Us152	0.282197	0.000020	-10.1	0.7	481	0.282197	0.000020	-10.4	0.7
s1Da	Granite	s1Da - 21	761	52	53	513	7	11	562	13	16	91	67	Us155	0.282156	0.000044	-10.8	1.6	513	0.282158	0.000044	-11.8	1.6
s1Da	Granite	s1Da - 22	2404	23	25	527	6	11	1054	11	17	50	22	Us156	0.282203	0.000020	-9.9	0.7	480	0.282203	0.000020	-10.1	0.7
s1Da	Granite	s1Da - 23	778	39	40	507	7	11	559	10	13	91	65	Us157	0.282194	0.000033	-9.6	1.2	507	0.282195	0.000033	-10.4	1.2
s1Da	Granite	s1Da - 24	588	27	30	601	8	13	597	8	12	101	102	Us159	0.282228	0.000073	-6.3	2.6	601	0.282231	0.000073	-9.2	2.6
s1Da	Granite	s1Da - 25	518	38	40	494	6	10	497	8	11	99	95	Us160	0.282133	0.000048	-12.1	1.7	494	0.282134	0.000048	-12.6	1.7
s1Da	Granite	s1Da - 26	498	30	32	520	7	11	517	7	11	101	105	Us162	0.282077	0.000016	-13.5	0.6	520	0.282078	0.000016	-14.6	0.6
s1Da	Granite	s1Da - 28	518	53	54	480	7	11	485	10	12	99	93	Us163	0.282181	0.000033	-10.7	1.2	480	0.282182	0.000033	-10.9	1.2
s1Da	Granite	s1Da - 29	604	18	22	498	7	11	515	6	10	97	83	Us164	0.282086	0.000069	-13.6	2.4	498	0.282087	0.000069	-14.3	2.4
s1Da	Granite	s1Da - 32	537	41	43	531	7	12	530	10	12	100	99	Us167	0.282226	0.000020	-9.0	0.7	486	0.282226	0.000020	-9.3	0.7
s1Da	Granite	s1Da - 33	567	41	42	498	8	12	511	10	12	98	88	Us165	0.282237	0.000051	-8.3	1.8	498	0.282238	0.000051	-8.9	1.8
s1Da	Granite	s1Da - 34	650	39	40	486	6	10	515	9	11	94	75										
s1Da	Granite	s1Da - 35	2608	22	24	2577	30	48	2594	16	24	99	99	Us169	0.281026	0.000017	-2.9	0.6	2608	0.281039	0.000017	-51.4	0.6
s1Da	Granite	s1Da - 36	1014	31	32	563	7	12	661	11	14	85	56										
s1Da	Granite	s1Da - 37	534	49	50	500	6	11	505	10	12	99	94										
s1Da	Granite	s1Da - 40	530	45	47	486	6	10	493	9	12	99	92	Us171	0.282185	0.000018	-10.4	0.6	486	0.282185	0.000018	-10.8	0.6
s1Da	Granite	s1Da - 41	1221	66	66	504	6	11	657	18	20	77	41										
s1Da	Granite	s1Da - 42	1391	76	77	496	6	10	691	21	23	72	36										
s1Da	Granite	s1Da - 45	1195	30	31	501	6	10	651	10	13	77	42										
s1Da	Granite	s1Da - 46	1442	29	31	514	6	11	723	9	13	71	36										
s1Da	Granite	s1Da - 47	522	49	51	504	7	11	507	10	12	99	97	Us172	0.282258	0.000032	-7.4	1.1	504	0.282259	0.000032	-8.2	1.1
s1Da	Granite	s1Da - 51	1274	52	53	473	6	10	639	13	16	74	37										
s1Da	Granite	s1Da - 53	533	27	29	466	5	10	478	6	10	97	87	Us158	0.282182	0.000025	-10.9	0.9	466	0.282182	0.000025	-10.9	0.9
s1Da	Granite	s1Da - 54	1091	24	26	799	9	16	879	9	14	91	73	Us161	0.281998	0.000021	-10.0	0.7	799	0.282007	0.000021	-17.1	0.7
s1Da	Granite	s1Da-n/a1												Us147	0.282196	0.000034	-9.7	1.2	500	0.282196	0.000034	-10.4	1.2
s1Da	Granite	s1Da-n/a2												Us148	0.282227	0.000221	-9.0	7.8	480	0.282228	0.000221	-9.3	7.8
s1Da	Granite	s1Da-n/a3												Us173	0.282154	0.000044	-11.6	1.6	480	0.282154	0.000044	-11.9	1.6

TABLE 1 CONTINUED

Sample	Rock type	Identifier U-Pb	$^{207}Pb/^{206}Pb$	2σ	$2\sigma_{sys}$	$^{206}Pb/^{238}U$	2σ	$2\sigma_{sys}$	$^{207}Pb/^{235}U$	2σ	$2\sigma_{sys}$	Concordance (%) 206/238 - 207/235	Concordance (%) 206/238 - 207/206	Identifier Lu-Hf	$^{176}Hf/^{177}Hf_t$	2σ	εHf_t	2σ	Date (Ma)	$^{176}Hf/^{177}Hf_{468}$	2σ	εHf_{468}	2σ
s1F	Granite	s1F - 01	581	29	31	483	6	10	499	7	10	97	83	Us005	0.282021	0.000020	-16.3	0.7	483	0.282021	0.000020	-16.6	0.7
s1F	Granite	s1F - 02	1602	26	28	1473	18	30	1524	14	21	97	92	Us006	0.281874	0.000021	3.9	0.7	1602	0.281893	0.000021	-21.1	0.7
s1F	Granite	s1F - 03	541	49	50	451	7	11	464	10	12	97	83	Us007	0.281426	0.000040	-38.1	1.4	451	0.281426	0.000040	-37.7	1.4
s1F	Granite	s1F - 04	605	33	35	469	6	10	492	7	10	95	78	Us008	0.281782	0.000047	-25.0	1.7	469	0.281782	0.000047	-25.1	1.7
s1F	Granite	s1F - 05	2635	16	18	2347	25	43	2507	14	22	94	89	Us009	0.281088	0.000014	-0.1	0.5	2635	0.281105	0.000014	-49.0	0.5
s1F	Granite	s1F - 06	691	28	30	455	6	10	493	6	10	92	66	Us010	0.281926	0.000032	-20.3	1.1	455	0.281925	0.000032	-20.0	1.1
s1F	Granite	s1F - 07	503	29	31	492	6	10	493	7	10	100	98	Us011	0.282126	0.000035	-12.4	1.2	492	0.282127	0.000035	-12.9	1.2
s1F	Granite	s1F - 08	516	27	29	457	6	10	466	6	9	98	89	Us012	0.282024	0.000042	-16.8	1.5	457	0.282023	0.000042	-16.5	1.5
s1F	Granite	s1F - 09	570	33	35	455	6	10	474	8	11	96	80	Us050	0.282104	0.000022	-14.0	0.8	455	0.282104	0.000022	-13.7	0.8
s1F	Granite	s1F - 10	872	55	56	477	7	11	549	12	14	87	55										
s1F	Granite	s1F - 11	1113	26	28	685	9	15	792	10	14	87	62	Us014	0.282081	0.000047	-14.4	1.7	470	0.282081	0.000047	-14.5	1.7
s1F	Granite	s1F - 12	1900	19	21	1843	20	35	1869	12	20	99	97	Us013	0.281447	0.000022	-4.4	0.8	1900	0.281459	0.000022	-36.5	0.8
s1F	Granite	s1F - 13	768	78	79	466	7	10	518	16	18	90	61										
s1F	Granite	s1F - 14	735	56	57	613	9	14	637	13	16	96	83	Us015	0.282056	0.000041	-12.1	1.5	613	0.282060	0.000041	-15.2	1.5
s1F	Granite	s1F - 15	1028	47	48	985	13	21	995	16	20	99	96	Us016	0.282217	0.000019	2.0	0.7	985	0.282225	0.000019	-9.4	0.7
s1F	Granite	s1F - 16	790	35	37	489	7	11	545	9	12	90	62										
s1F	Granite	s1F - 18	738	46	48	457	6	10	507	10	12	90	62	Us017	0.282070	0.000026	-15.1	0.9	457	0.282070	0.000026	-14.9	0.9
s1F	Granite	s1F - 19	745	21	24	511	6	11	555	6	10	92	69	Us018	0.281919	0.000044	-19.2	1.6	511	0.281921	0.000044	-20.2	1.6
s1F	Granite	s1F - 20	503	24	27	504	6	11	502	6	10	100	100	Us019	0.282043	0.000036	-15.0	1.3	504	0.282044	0.000036	-15.8	1.3
s1F	Granite	s1F - 21	1137	31	32	532	7	11	662	9	13	80	47										
s1F	Granite	s1F - 22	495	50	51	461	7	10	466	9	11	99	93	Us020	0.282198	0.000033	-10.5	1.2	461	0.282198	0.000033	-10.4	1.2
s1F	Granite	s1F - 23	553	29	31	476	6	10	488	6	9	98	86	Us021	0.282084	0.000067	-14.2	2.4	476	0.282084	0.000067	-14.4	2.4
s1F	Granite	s1F - 24	491	19	22	480	5	10	482	5	9	100	98	Us022	0.282118	0.000036	-12.9	1.3	480	0.282119	0.000036	-13.2	1.3
s1F	Granite	s1F - 26	527	20	23	501	6	11	505	6	10	99	95	Us023	0.282041	0.000035	-15.2	1.2	501	0.282042	0.000035	-15.9	1.2
s1F	Granite	s1F - 27	797	21	24	508	6	11	564	6	10	90	64										
s1F	Granite	s1F - 28	522	31	33	476	6	10	484	7	10	98	91	Us025	0.282091	0.000021	-13.9	0.8	476	0.282091	0.000021	-14.1	0.8
s1F	Granite	s1F - 29	1082	53	54	1064	14	23	1069	18	22	99	98	Us024	0.282147	0.000019	1.7	0.7	1082	0.282160	0.000019	-11.7	0.7
s1F	Granite	s1F - 30	584	28	30	480	6	10	498	7	10	96	82	Us026	0.282128	0.000020	-12.6	0.7	480	0.282128	0.000020	-12.8	0.7
s1F	Granite	s1F - 31	1002	24	26	404	5	9	506	6	10	80	40										
s1F	Granite	s1F - 32	505	28	31	468	6	10	473	6	10	99	93	Us027	0.282061	0.000033	-15.2	1.2	468	0.282061	0.000033	-15.2	1.2
s1F	Granite	s1F - 33	2865	13	15	2799	28	49	2835	12	22	99	98	Us028	0.281018	0.000020	2.8	0.7	2865	0.281069	0.000020	-50.3	0.7
s1F	Granite	s1F - 34	2745	17	19	2065	23	39	2427	13	21	85	75										
s1F	Granite	s1F - 35	522	33	35	470	6	10	478	8	10	98	90	Us029	0.282072	0.000029	-14.7	1.0	470	0.282072	0.000029	-14.8	1.0
s1F	Granite	s1F - 36	563	31	33	471	6	10	486	6	10	97	84	Us034	0.282145	0.000022	-12.1	0.8	471	0.282145	0.000022	-12.2	0.8
s1F	Granite	s1F - 37	492	43	44	470	6	10	472	8	11	99	96	Us035	0.282104	0.000022	-13.6	0.8	470	0.282104	0.000022	-13.7	0.8
s1F	Granite	s1F - 38	692	26	28	474	6	10	513	6	10	92	68	Us036	0.282153	0.000030	-11.8	1.1	474	0.282153	0.000030	-11.9	1.1
s1F	Granite	s1F - 39	487	38	39	462	6	10	467	8	10	99	95	Us037	0.282124	0.000016	-13.1	0.6	462	0.282124	0.000016	-13.0	0.6
s1F	Granite	s1F - 40	502	25	27	506	6	11	505	6	10	100	101	Us038	0.282011	0.000020	-16.1	0.7	506	0.282012	0.000020	-16.9	0.7
s1F	Granite	s1F - 42	506	21	24	460	5	10	467	5	9	98	91	Us039	0.282108	0.000053	-13.7	1.9	460	0.282108	0.000053	-13.5	1.9
s1F	Granite	s1F - 44	472	25	28	493	6	10	489	6	9	101	104	Us040	0.282150	0.000023	-11.5	0.8	493	0.282151	0.000023	-12.0	0.8
s1F	Granite	s1F - 45	1780	15	18	1601	17	31	1678	11	19	95	90	Us041	0.281220	0.000014	-15.2	0.5	1780	0.281235	0.000014	-44.4	0.5
s1F	Granite	s1F - 46	585	66	67	491	7	11	505	13	15	97	84	Us042	0.282119	0.000033	-12.6	1.2	491	0.282119	0.000033	-13.1	1.2
s1F	Granite	s1F - 47	992	42	44	637	9	14	718	12	15	89	64										
s1F	Granite	s1F - 48	591	34	36	461	6	10	483	8	10	96	78	Us046	0.282122	0.000027	-13.2	1.0	461	0.282122	0.000027	-13.0	1.0
s1F	Granite	s1F - 49	462	21	24	497	6	10	491	6	9	101	108	Us043	0.282034	0.000018	-15.5	0.6	497	0.282035	0.000018	-16.1	0.6
s1F	Granite	s1F - 50	511	38	40	484	6	10	489	8	11	99	95	Us047	0.282091	0.000033	-13.8	1.2	484	0.282091	0.000033	-14.1	1.2
s1F	Granite	s1F - 51	497	21	24	477	6	10	480	5	9	99	96	Us048	0.282127	0.000024	-12.6	0.8	477	0.282127	0.000024	-12.8	0.8
s1F	Granite	s1F - 52	473	21	24	504	6	10	498	6	9	101	107	Us045	0.282109	0.000023	-12.7	0.8	504	0.282110	0.000023	-13.5	0.8
s1F	Granite	s1F - 53	1540	31	33	1430	18	29	1474	15	21	97	93	Us044	0.281922	0.000020	4.1	0.7	1540	0.281940	0.000020	-19.5	0.7
s1F	Granite	s1F - 54	574	37	38	470	6	10	488	8	11	96	82	Us049	0.282088	0.000033	-14.2	1.2	470	0.282088	0.000033	-14.2	1.2

TABLE 1 CONTINUED

Sample	Rock type	Identifier U-Pb	$^{207}Pb/^{206}Pb$	2σ	$2\sigma_{sys}$	$^{206}Pb/^{238}U$	2σ	$2\sigma_{sys}$	$^{207}Pb/^{235}U$	2σ	$2\sigma_{sys}$	Concordance (%) 206/238 - 207/235	Concordance (%) 206/238 - 207/206	Identifier Lu-Hf	$^{176}Hf/^{177}Hf_t$	2σ	εHf_t	2σ	Date (Ma)	$^{176}Hf/^{177}Hf_{468}$	2σ	εHf_{468}	2σ
s1H	Granodiorite	s1H - 02	501	91	96	462	12	15	477	17	19	97	92										
s1H	Granodiorite	s1H - 03	933	65	73	466	11	14	557	14	18	84	50										
s1H	Granodiorite	s1H - 07	970	39	41	462	8	12	560	11	14	82	48										
s1H	Granodiorite	s1H - 09	978	60	63	518	13	17	620	18	22	84	53										
s1H	Granodiorite	s1H - 11	842	48	51	455	12	14	532	11	14	85	54										
s1H	Granodiorite	s1H - 15	558	46	49	453	9	12	474	10	12	95	81										
s1H	Granodiorite	s1H - 16	1348	61	62	499	12	15	692	17	21	72	37										
s1H	Granodiorite	s1H - 17	482	54	55	457	9	12	464	11	15	98	95	Us451	0.281901	0.000039	-21.1	1.4	457	0.281901	0.000039	-20.8	1.4
s1H	Granodiorite	s1H - 18	983	66	68	453	9	12	557	16	21	81	46										
s1H	Granodiorite	s1H - 19	1465	36	37	1298	28	35	1367	19	26	95	89	Us452	0.281730	0.000022	-4.4	0.8	1465	0.281742	0.000022	-26.5	0.8
s1H	Granodiorite	s1H - 19b	884	30	32	601	11	15	668	12	15	90	68	Us452 (2)	0.281740	0.000022	-23.6	0.8	601				
s1H	Granodiorite	s1H - 20	790	29	31	436	8	10	500	9	12	87	55										
s1H	Granodiorite	s1H - 21	822	53	57	477	11	14	544	12	15	88	58										

TABLE 1 CONTINUED

Sample	Rock type	Identifier U-Pb	$^{207}Pb/^{206}Pb$	2σ	$2\sigma_{sys}$	$^{206}Pb/^{238}U$	2σ	$2\sigma_{sys}$	$^{207}Pb/^{235}U$	2σ	$2\sigma_{sys}$	Concordance (%) 206/238 - 207/235	206/238 - 207/206	Identifier Lu-Hf	$^{176}Hf/^{177}Hf_t$	2σ	εHf_t	2σ	Date (Ma)	$^{176}Hf/^{177}Hf_{468}$	2σ	εHf_{468}	2σ
s2A	Metapelite	s2A - 02	2819	25	26	2833	46	60	2819	21	31	100	100	Us174	0.281204	0.000045	8.3	1.6	2819	0.281233	0.000045	-44.5	1.6
s2A	Metapelite	s2A - 03	2190	44	45	598	16	20	1068	21	22	56	27										
s2A	Metapelite	s2A - 04	2669	24	27	2091	47	59	2400	26	37	87	78										
s2A	Metapelite	s2A - 05	2549	43	47	1489	47	55	1985	37	48	75	58										
s2A	Metapelite	s2A - 06	2442	37	39	1591	41	49	1996	25	32	80	65										
s2A	Metapelite	s2A - 07	1206	89	91	634	19	22	789	36	50	80	53										
s2A	Metapelite	s2A - 08	2783	25	27	2568	50	66	2696	22	30	95	92	Us177	0.281115	0.000037	4.4	1.3	2783	0.281147	0.000037	-47.5	1.3
s2A	Metapelite	s2A - 09	2457	28	313	1252	30	38	1775	26	37	71	51										
s2A	Metapelite	s2A - 10	2758	14	20	2628	39	57	2702	17	26	97	95	Us176	0.281015	0.000022	0.2	0.8	2758	0.281026	0.000022	-51.8	0.8
s2A	Metapelite	s2A - 100	2798	17	19	2686	41	59	2750	18	26	98	96	Us219	0.281104	0.000016	4.3	0.6	2798	0.281129	0.000016	-48.2	0.6
s2A	Metapelite	s2A - 101	634	63	66	464	9	13	498	14	19	93	73	Us218	0.282002	0.000039	-17.4	1.4	464	0.282001	0.000039	-17.3	1.4
s2A	Metapelite	s2A - 102	2767	29	31	1704	39	49	2252	26	27	76	62										
s2A	Metapelite	s2A - 103	1716	53	55	714	18	22	1014	24	32	70	42										
s2A	Metapelite	s2A - 104	2867	19	21	2603	41	58	2750	19	28	95	91	Us217	0.281266	0.000087	11.7	3.1	2867	0.281316	0.000087	-41.6	3.1
s2A	Metapelite	s2A - 105	1094	66	67	503	12	15	631	18	23	80	46										
s2A	Metapelite	s2A - 11	2703	24	25	2494	42	58	2614	20	27	95	92	Us175	0.281100	0.000046	1.9	1.6	2703	0.281117	0.000046	-48.6	1.6
s2A	Metapelite	s2A - 14	1783	33	35	1113	21	28	1366	18	25	81	62										
s2A	Metapelite	s2A - 16	2772	27	29	2584	44	60	2689	22	32	96	93	Us178	0.280764	0.000033	-8.4	1.2	2772	0.280797	0.000033	-59.9	1.2
s2A	Metapelite	s2A - 17	2652	15	19	2338	37	52	2508	18	28	93	88	Us179	0.281152	0.000020	2.6	0.7	2652	0.281166	0.000020	-46.9	0.7
s2A	Metapelite	s2A - 18	2670	39	41	2472	57	71	2590	28	33	95	93	Us186	0.280964	0.000097	-3.7	3.5	2670	0.281033	0.000097	-51.6	3.4
s2A	Metapelite	s2A - 19	2847	44	45	2910	88	105	2894	41	43	101	102	Us185	0.281031	0.000044	2.9	1.6	2847	0.281097	0.000044	-49.3	1.6
s2A	Metapelite	s2A - 20	2543	31	32	1375	38	45	1906	29	40	72	54										
s2A	Metapelite	s2A - 21	2587	31	32	2141	44	58	2381	25	34	90	83										
s2A	Metapelite	s2A - 22	2636	39	40	1924	48	58	2299	28	34	84	73										
s2A	Metapelite	s2A - 23	1799	29	31	1614	33	43	1697	19	24	95	90	Us188	0.281513	0.000028	-4.4	1.0	1799	0.281524	0.000028	-34.2	1.0
s2A	Metapelite	s2A - 24	1473	77	81	510	15	18	732	22	27	70	35										
s2A	Metapelite	s2A - 29	2713	17	19	2486	39	56	2613	17	23	95	92	Us187	0.280834	0.000028	-7.3	1.0	2713	0.280858	0.000028	-57.8	1.0
s2A	Metapelite	s2A - 30	2011	42	43	857	21	26	1260	25	28	68	43										
s2A	Metapelite	s2A - 31	1801	27	29	1788	28	41	1797	18	28	99	99	Us190	0.281619	0.000026	-0.6	0.9	1801	0.281637	0.000026	-30.2	0.9
s2A	Metapelite	s2A - 32	1785	26	27	1464	26	36	1602	17	25	91	82	Us192	0.281494	0.000021	-5.4	0.8	1785	0.281509	0.000021	-34.7	0.8
s2A	Metapelite	s2A - 33	1790	19	21	1645	27	38	1710	15	23	96	92	Us191	0.281426	0.000017	-7.7	0.6	1790	0.281443	0.000017	-37.1	0.6
s2A	Metapelite	s2A - 38	2765	21	22	2726	42	60	2746	19	29	99	99	Us189	0.281106	0.000025	3.6	0.9	2765	0.281123	0.000025	-48.4	0.9
s2A	Metapelite	s2A - 39	1762	28	29	1373	27	36	1535	19	27	89	78										
s2A	Metapelite	s2A - 41	2575	19	20	2193	36	50	2398	19	26	91	85	Us193	0.281181	0.000021	1.8	0.7	2575	0.281199	0.000021	-45.7	0.7
s2A	Metapelite	s2A - 42	1837	28	29	1663	28	40	1741	19	29	96	91	Us194	0.282029	0.000048	14.8	1.7	1837	0.282067	0.000048	-15.0	1.7
s2A	Metapelite	s2A - 43	1875	20	22	1449	23	33	1632	16	24	89	77										
s2A	Metapelite	s2A - 45	1696	45	47	1010	25	31	1255	27	38	80	60										
s2A	Metapelite	s2A - 46	2535	24	25	1230	25	33	1799	20	29	68	49										
s2A	Metapelite	s2A - 47	2730	21	23	1938	33	46	2352	19	27	82	71										
s2A	Metapelite	s2A - 48	1134	45	47	644	15	19	772	20	25	83	57										
s2A	Metapelite	s2A - 49	2634	12	20	2286	35	50	2472	17	26	92	87	Us195	0.281035	0.000016	-2.0	0.6	2634	0.281055	0.000016	-50.8	0.6
s2A	Metapelite	s2A - 50	1593	24	27	1050	21	28	1243	17	21	84	66										
s2A	Metapelite	s2A - 52	2640	26	29	1797	36	47	2224	24	30	81	68										
s2A	Metapelite	s2A - 53	1483	49	51	653	15	19	876	23	33	75	44										
s2A	Metapelite	s2A - 54	759	60	62	448	9	12	504	13	16	89	59										
s2A	Metapelite	s2A - 56	2872	20	23	2808	48	64	2850	22	29	99	98	Us198	0.281153	0.000081	7.8	2.9	2872	0.281190	0.000081	-46.0	2.9
s2A	Metapelite	s2A - 57	675	71	73	440	9	12	481	15	17	91	65	Us197	0.282056	0.000116	-16.0	4.1	440	0.282055	0.000116	-15.4	4.1
s2A	Metapelite	s2A - 58	1583	27	28	551	12	16	800	14	17	69	35										
s2A	Metapelite	s2A - 59	2818	15	19	2595	38	56	2725	17	26	95	92	Us196	0.281185	0.000034	7.7	1.2	2818	0.281219	0.000034	-45.0	1.2
s2A	Metapelite	s2A - 61	1169	38	41	603	15	19	739	20	28	82	52										
s2A	Metapelite	s2A - 63	1535	35	37	820	19	23	1043	18	23	79	53										
s2A	Metapelite	s2A - 65	1655	54	56	611	14	17	898	24	32	68	37										
s2A	Metapelite	s2A - 66	2726	27	29	2031	44	56	2397	25	35	85	75										
s2A	Metapelite	s2A - 67	2204	58	59	2257	43	59	2232	34	63	101	102	Us201	0.281285	0.000016	-3.1	0.6	2204	0.281295	0.000016	-42.3	0.6
s2A	Metapelite	s2A - 68	2451	21	23	2233	36	48	2347	18	27	95	91	Us200	0.281441	0.000026	8.1	0.9	2451	0.281464	0.000026	-36.3	0.9
s2A	Metapelite	s2A - 70	2756	15	20	2471	36	53	2632	17	26	94	90	Us199	0.280964	0.000024	-1.7	0.8	2756	0.280997	0.000024	-52.8	0.8
s2A	Metapelite	s2A - 71	2342	46	50	1220	30	38	1698	34	45	72	52										
s2A	Metapelite	s2A - 73	1849	24	35	1637	30	40	1730	17	25	95	89	Us203	0.281806	0.000028	7.2	1.0	1849	0.281845	0.000028	-22.8	1.0
s2A	Metapelite	s2A - 75	2275	24	25	1963	34	46	2118	20	28	93	86	Us205	0.281482	0.000032	5.5	1.1	2275	0.281521	0.000032	-34.3	1.1
s2A	Metapelite	s2A - 76	2474	17	21	2123	37	51	2308	20	28	92	86	Us206	0.281112	0.000017	-3.0	0.6	2474	0.281132	0.000017	-48.1	0.6
s2A	Metapelite	s2A - 77	2567	17	20	1576	28	38	2050	18	26	77	61										
s2A	Metapelite	s2A - 78	2738	17	19	2544	39	56	2651	18	27	96	93	Us202	0.281029	0.000017	0.2	0.6	2738	0.281053	0.000017	-50.9	0.6
s2A	Metapelite	s2A - 79	1215	20	24	1085	18	26	1132	13	20	96	89	Us207	0.282072	0.000045	2.0	1.6	1215	0.282101	0.000045	-13.8	1.6
s2A	Metapelite	s2A - 80	1246	14	24	1242	19	28	1246	13	19	100	100	Us208	0.282149	0.000022	5.5	0.8	1246	0.282170	0.000022	-11.3	0.8
s2A	Metapelite	s2A - 81	491	51	52	445	9	12	456	10	13	97	91	Us212	0.281962	0.000065	-19.2	2.3	445	0.281961	0.000065	-18.7	2.3
s2A	Metapelite	s2A - 82	1145	87	94	486	11	14	629	21	28	77	42										
s2A	Metapelite	s2A - 83	1746	18	21	1439	23	33	1570	15	22	92	82	Us210	0.281137	0.000014	-19.0	0.5	1746	0.281157	0.000014	-47.2	0.5
s2A	Metapelite	s2A - 84	1776	23	25	1611	27	38	1686	16	24	96	91	Us211	0.281391	0.000027	-9.3	1.0	1776	0.281406	0.000027	-38.4	1.0
s2A	Metapelite	s2A - 85	2793	35	37	2394	60	69	2628	30	39	91	86	Us209	0.281169	0.000029	6.5	1.0	2793	0.281213	0.000029	-45.2	1.0
s2A	Metapelite	s2A - 89	1859	26	27	1637	30	41	1740	18	26	94	88	Us213	0.281912	0.000028	11.1	1.0	1859	0.281943	0.000028	-19.4	1.0
s2A	Metapelite	s2A - 90	1820	23	25	1430	26	36	1595	17	24	90	79										
s2A	Metapelite	s2A - 91	982	31	33	935	18	24	949	14	19	99	95	Us215	0.282220	0.000038	0.9	1.4	935	0.282228	0.000038	-9.3	1.4
s2A	Metapelite	s2A - 92	1018	36	38	994	19	26	1002	15	21	99	98	Us214	0.282167	0.000041	0.4	1.5	994	0.282178	0.000041	-11.1	1.5
s2A	Metapelite	s2A - 93	2501	41	42	1322	37	43	1845	26	35	72	53										
s2A	Metapelite	s2A - 94	2178	32	33	852	21	26	1324	24	33	64	39										
s2A	Metapelite	s2A - 95	2709	34	35	1362	35	43	1986	24	31	69	50										
s2A	Metapelite	s2A - 96	1879	32	34	641	13	17	994	15	21	64	34										
s2A	Metapelite	s2A - 98	2465	26	28	2331	45	58	2411	23	27	97	95	Us216	0.281254	0.000043	1.8	1.5	2465	0.281281	0.000043	-42.8	1.5
s2A	Metapelite	s2A - 99	1664	36	37	818	19	24	1088	18	25	75	49	Us220	0.281512	0.000028	-24.9	1.0	900	0.281517	0.000028	-34.5	1.0
s2A	Metapelite	s2A-n/a1												Us184	0.280991	0.000015	-2.0	0.6	2700	0.280999	0.000015	-52.8	0.5
s2A	Metapelite	s2A-n/a2												Us204	0.281588	0.000019	-4.0	0.7	1700	0.281611	0.000019	-31.1	0.7

TABLE 1 CONTINUED

Sample	Rock type	Identifier U-Pb	$^{207}Pb/^{206}Pb$	2σ	$2\sigma_{sys}$	$^{206}Pb/^{238}U$	2σ	$2\sigma_{sys}$	$^{207}Pb/^{235}U$	2σ	$2\sigma_{sys}$	Concordance (%) 206/238 - 207/235	Concordance (%) 206/238 - 207/206	Identifier Lu-Hf	$^{176}Hf/^{177}Hf_t$	2σ	εHf_t	2σ	Date (Ma)	$^{176}Hf/^{177}Hf_{468}$	2σ	εHf_{468}	2σ
s2B	Granite	s2B - 01	1025	33	35	456	6	10	562	9	12	81	44										
s2B	Granite	s2B - 02	701	41	42	498	6	10	535	9	12	93	71										
s2B	Granite	s2B - 04	517	37	39	505	7	11	504	7	10	100	98										
s2B	Granite	s2B - 06	694	23	26	470	6	10	508	6	9	93	68										
s2B	Granite	s2B - 07	972	37	39	477	6	10	573	10	13	83	49										
s2B	Granite	s2B - 09	569	31	33	500	6	10	511	7	10	98	88	Us055	0.282347	0.000074	-4.4	2.6	500	0.282348	0.000074	-5.0	2.6
s2B	Granite	s2B - 09b												Us056	0.282166	0.000024	-10.8	0.8	500	0.282166	0.000024	-11.5	0.8
s2B	Granite	s2B - 10	619	29	31	473	6	10	499	7	10	95	76	Us054	0.282135	0.000080	-12.5	2.8	473	0.282135	0.000080	-12.6	2.8
s2B	Granite	s2B - 12	816	25	27	505	7	11	566	8	11	89	62										
s2B	Granite	s2B - 13	838	28	30	625	11	15	671	10	14	93	75	Us059	0.282080	0.000037	-11.0	1.3	625	0.282084	0.000037	-14.4	1.3
s2B	Granite	s2B - 14	745	21	24	463	5	10	513	6	9	90	62	Us057	0.282049	0.000049	-15.7	1.7	463	0.282049	0.000049	-15.6	1.7
s2B	Granite	s2B - 14b	745	21	24	463	5	10	513	6	9	90	62	Us058	0.282155	0.000072	-12.0	2.6	463	0.282155	0.000072	-11.9	2.6
s2B	Granite	s2B - 16	2078	29	30	906	11	19	1317	14	19	69	44										
s2B	Granite	s2B - 17	585	26	28	471	6	10	489	6	10	96	81	Us061	0.282054	0.000023	-15.4	0.8	471	0.282054	0.000023	-15.4	0.8
s2B	Granite	s2B - 18	1365	38	39	462	7	10	647	11	14	71	34										
s2B	Granite	s2B - 20	576	26	29	466	5	10	483	6	10	97	81	Us063	0.282267	0.000084	-8.0	3.0	466	0.282267	0.000084	-7.9	3.0
s2B	Granite	s2B - 22	492	17	21	471	5	10	473	5	9	100	96	Us062	0.282182	0.000044	-10.8	1.6	471	0.282182	0.000044	-10.9	1.6
s2B	Granite	s2B - 24	531	25	28	547	7	11	544	7	10	101	103	Us064	0.282354	0.000151	-3.0	5.4	547	0.282358	0.000151	-4.7	5.4
s2B	Granite	s2B - 27	960	46	47	461	7	10	554	12	14	83	48										
s2B	Granite	s2B - 28	768	42	44	506	7	11	557	11	13	91	66	Us067	0.282164	0.000024	-10.7	0.8	506	0.282165	0.000024	-11.5	0.8
s2B	Granite	s2B - 29	530	38	39	468	6	10	478	8	11	98	88	Us068	0.282568	0.000934	2.7	33.1	468	0.282568	0.000934	2.7	33.1
s2B	Granite	s2B - 30	905	45	46	487	7	11	568	9	12	86	54										
s2B	Granite	s2B - 31	516	26	28	461	5	10	471	6	9	98	89	Us069	0.282217	0.000026	-9.8	0.9	461	0.282217	0.000026	-9.7	0.9
s2B	Granite	s2B - 33	1363	51	52	494	6	10	679	14	17	73	36										
s2B	Granite	s2B - 36	591	25	28	500	6	11	515	6	10	97	85										
s2B	Granite	s2B - 37	745	40	41	481	7	11	529	9	12	91	65	Us072	0.282041	0.000035	-15.6	1.3	481	0.282041	0.000035	-15.9	1.3
s2B	Granite	s2B - 39	636	42	44	486	6	10	512	9	12	95	76	Us070	0.282246	0.000076	-8.2	2.7	486	0.282247	0.000076	-8.6	2.7
s2B	Granite	s2B - 40	468	33	35	486	6	10	483	7	10	101	104	Us074	0.282176	0.000021	-10.7	0.8	486	0.282176	0.000021	-11.1	0.8
s2B	Granite	s2B - 41	632	60	61	468	7	10	495	11	13	94	74	Us073	0.282205	0.000150	-10.1	5.3	468	0.282205	0.000150	-10.1	5.3
s2B	Granite	s2B - 44	1650	33	34	1649	21	34	1647	18	23	100	100	Us077	0.281830	0.000021	3.4	0.8	1650	0.281857	0.000021	-22.4	0.8
s2B	Granite	s2B - 45	1152	51	52	480	6	10	614	12	15	78	42										
s2B	Granite	s2B - 47	722	37	38	477	6	10	523	8	11	91	66	Us076	0.282156	0.000025	-11.6	0.9	477	0.282156	0.000025	-11.8	0.9
s2B	Granite	s2B - 48	778	30	32	459	6	10	515	7	11	89	59										
s2B	Granite	s2B - 50	856	40	41	477	6	10	547	9	12	87	56										
s2B	Granite	s2B - 51	760	31	33	467	5	10	519	7	11	90	61										
s2B	Granite	s2B - 52	1226	46	47	1186	16	25	1196	17	21	99	97	Us060	0.282141	0.000029	4.8	1.0	1226	0.282164	0.000029	-11.6	1.0
s2B	Granite	s2B - 53	701	41	42	513	8	12	547	10	13	94	73	Us065	0.282140	0.000026	-11.4	0.9	513	0.282141	0.000026	-12.3	0.9
s2B	Granite	s2B - 54	1047	38	39	903	11	19	945	13	17	96	86	Us075	0.282164	0.000014	-1.8	0.5	903	0.282171	0.000014	-11.3	0.5
s2B	Granite	s2B - 55	542	35	37	546	7	11	543	8	11	101	101										
s2B	Granite	s2B-n/a1												Us066	0.282084	0.000282	-14.3	10.0	470	0.282084	0.000282	-14.4	10.0
s2B	Granite	s2B-n/a2												Us079	0.282173	0.000018	-11.0	0.7	477	0.282173	0.000018	-11.2	0.7

TABLE 1 CONTINUED

Sample	Rock type	Identifier U-Pb	$^{207}Pb/^{206}Pb$	2σ	$2\sigma_{sys}$	$^{206}Pb/^{238}U$	2σ	$2\sigma_{sys}$	$^{207}Pb/^{235}U$	2σ	$2\sigma_{sys}$	Concordance (%) 206/238 - 207/235	Concordance (%) 206/238 - 207/206	Identifier Lu-Hf	$^{176}Hf/^{177}Hf_t$	2σ	εHf_t	2σ	Date (Ma)	$^{176}Hf/^{177}Hf_{468}$	2σ	εHf_{468}	2σ
s3B	Granite (Leuco-)	s3B - 01	2740	27	28	2163	41	53	2461	30	35	88	79										
s3B	Granite (Leuco-)	s3B - 03	515	34	36	470	9	12	473	12	14	99	91	Us398	0.282083	0.000054	-14.4	1.9	470	0.282083	0.000054	-14.4	1.9
s3B	Granite (Leuco-)	s3B - 04	693	31	33	477	9	12	512	13	15	93	69	Us399	0.282066	0.000064	-14.8	2.2	477	0.282067	0.000064	-15.0	2.2
s3B	Granite (Leuco-)	s3B - 06	1100	29	31	501	9	12	618	14	16	81	46										
s3B	Granite (Leuco-)	s3B - 07	2596	21	23	2367	40	54	2478	26	31	96	91	Us395	0.281343	0.000075	8.1	2.7	2596	0.281382	0.000075	-39.2	2.7
s3B	Granite (Leuco-)	s3B - 08	813	28	30	449	8	11	509	12	14	88	55										
s3B	Granite (Leuco-)	s3B - 10	1008	28	30	912	16	22	934	18	21	98	90	Us396	0.282025	0.000031	-6.5	1.1	912	0.282035	0.000031	-16.1	1.1
s3B	Granite (Leuco-)	s3B - 11	511	50	51	458	9	12	463	13	15	99	90	Us397	0.282121	0.000067	-13.3	2.4	458	0.282121	0.000067	-13.1	2.4
s3B	Granite (Leuco-)	s3B - 15	485	36	38	455	8	12	457	12	13	100	94	Us401	0.282119	0.000043	-13.4	1.5	455	0.282119	0.000043	-13.2	1.5
s3B	Granite (Leuco-)	s3B - 17	643	35	37	475	9	12	500	12	14	95	74	Us400	0.282115	0.000035	-13.1	1.3	475	0.282115	0.000035	-13.3	1.3
s3B	Granite (Leuco-)	s3B - 19	1124	28	30	459	8	12	584	14	16	79	41										
s3B	Granite (Leuco-)	s3B - 20	1827	26	28	1712	30	40	1754	25	29	98	94	Us406	0.281494	0.000022	-4.4	0.8	1827	0.281500	0.000022	-35.1	0.8
s3B	Granite (Leuco-)	s3B - 21	578	33	35	496	9	12	508	12	14	98	86	Us407	0.281898	0.000028	-20.3	1.0	496	0.281898	0.000028	-20.9	1.0
s3B	Granite (Leuco-)	s3B - 22	1520	48	49	714	13	18	935	22	24	76	47										
s3B	Granite (Leuco-)	s3B - 23	639	35	37	475	9	12	500	12	14	95	74	Us408	0.282110	0.000035	-13.3	1.2	475	0.282111	0.000035	-13.4	1.2
s3B	Granite (Leuco-)	s3B - 26	1011	31	32	461	8	12	561	13	15	82	46										
s3B	Granite (Leuco-)	s3B - 29	1666	31	32	1335	22	31	1461	22	27	91	80	Us404	0.281421	0.000030	-10.7	1.1	1666	0.281430	0.000030	-37.5	1.1
s3B	Granite (Leuco-)	s3B - 30	487	31	33	473	8	12	472	11	13	100	97	Us405	0.282089	0.000020	-14.1	0.7	473	0.282089	0.000020	-14.2	0.7
s3B	Granite (Leuco-)	s3B - 31	859	37	38	451	8	12	521	13	15	87	52										
s3B	Granite (Leuco-)	s3B - 32	1465	60	61	469	8	12	676	20	22	69	32										
s3B	Granite (Leuco-)	s3B - 33	515	80	81	480	10	13	482	16	18	100	93	Us403	0.282107	0.000018	-13.3	0.6	480	0.282107	0.000018	-13.5	0.6
s3B	Granite (Leuco-)	s3B - 34	556	63	64	476	10	13	486	14	16	98	86	Us402	0.282108	0.000032	-13.3	1.1	476	0.282108	0.000032	-13.5	1.1
s3B	Granite (Leuco-)	s3B - 35	460	43	45	461	10	13	458	12	14	101	100	Us412	0.282049	0.000030	-15.8	1.1	461	0.282049	0.000030	-15.6	1.1
s3B	Granite (Leuco-)	s3B - 36	495	42	44	459	9	12	461	12	14	99	93	Us411	0.282179	0.000061	-11.2	2.1	459	0.282179	0.000061	-11.0	2.1
s3B	Granite (Leuco-)	s3B - 38	596	30	32	460	8	12	480	11	13	96	77	Us409	0.281910	0.000056	-20.7	2.0	460	0.281910	0.000056	-20.5	2.0
s3B	Granite (Leuco-)	s3B - 42	1372	10	14	1356	21	31	1356	19	24	100	99	Us413	0.282162	0.000025	8.8	0.9	1372	0.282198	0.000025	-10.3	0.9
s3B	Granite (Leuco-)	s3B - 43	1121	28	30	504	9	13	628	14	16	80	45	Us414	0.282058	0.000024	-15.2	0.8	470	0.282058	0.000024	-15.3	0.8
s3B	Granite (Leuco-)	s3B - 48	530	49	50	450	8	11	460	12	14	98	85	Us416	0.282127	0.000031	-13.3	1.1	450	0.282127	0.000031	-12.9	1.1
s3B	Granite (Leuco-)	s3B - 49	625	24	26	487	9	12	509	12	14	96	78	Us417	0.282071	0.000022	-14.4	0.8	487	0.282071	0.000022	-14.8	0.8
s3B	Granite (Leuco-)	s3B - 50	499	46	48	480	8	12	480	12	14	100	96	Us415	0.282085	0.000017	-14.1	0.6	480	0.282085	0.000017	-14.3	0.6
s3B	Granite (Leuco-)	s3B - 51	853	46	47	446	8	11	516	13	15	87	52										
s3B	Granite (Leuco-)	s3B - 54	1727	19	21	1435	24	33	1553	22	26	92	83	Us418	0.281716	0.000025	1.1	0.9	1727	0.281753	0.000025	-26.1	0.9
s3B	Granite (Leuco-)	s3B - 56	491	30	32	475	9	12	475	11	13	100	97	Us422	0.282100	0.000017	-13.7	0.6	475	0.282100	0.000017	-13.8	0.6
s3B	Granite (Leuco-)	s3B - 57	673	25	28	477	8	12	509	11	13	94	71	Us423	0.282090	0.000026	-14.0	0.9	477	0.282090	0.000026	-14.2	0.9
s3B	Granite (Leuco-)	s3B - 58	472	31	33	482	9	12	477	11	13	101	102	Us419	0.282094	0.000017	-13.7	0.6	482	0.282094	0.000017	-14.0	0.6
s3B	Granite (Leuco-)	s3B - 59	486	38	40	476	9	12	476	12	14	100	98	Us420	0.282080	0.000030	-14.3	1.1	476	0.282080	0.000030	-14.5	1.1
s3B	Granite (Leuco-)	s3B - 61	1311	57	58	514	10	13	686	20	22	75	39										
s3B	Granite (Leuco-)	s3B - 62	765	36	37	482	9	12	530	13	15	91	63	Us427	0.282079	0.000033	-14.2	1.2	482	0.282080	0.000033	-14.5	1.2
s3B	Granite (Leuco-)	s3B - 63	1116	31	33	455	9	12	578	13	15	79	41										
s3B	Granite (Leuco-)	s3B - 64	585	40	42	456	9	12	475	14	16	96	78	Us429	0.282135	0.000028	-12.8	1.0	456	0.282135	0.000028	-12.6	1.0
s3B	Granite (Leuco-)	s3B - 65	567	41	42	457	8	12	473	12	14	97	81	Us428	0.281958	0.000079	-19.1	2.8	457	0.281958	0.000079	-18.8	2.8
s3B	Granite (Leuco-)	s3B - 66	468	51	52	475	10	13	470	13	15	101	101	Us430 (1)	0.282089	0.000043	-14.0	1.5	475	0.282089	0.000043	-14.2	1.5
s3B	Granite (Leuco-)	s3B - 67	1853	24	26	1500	25	35	1647	22	27	91	81	Us426	0.281836	0.000061	8.3	2.2	1853	0.281888	0.000061	-21.3	2.2
s3B	Granite (Leuco-)	s3B - 69	969	57	58	453	8	11	547	16	18	83	47										
s3B	Granite (Leuco-)	s3B - 70	488	58	59	456	8	12	459	13	15	99	93	Us425	0.282150	0.000023	-12.3	0.8	456	0.282150	0.000023	-12.0	0.8
s3B	Granite (Leuco-)	s3B - 71	534	49	50	461	8	12	470	13	15	98	86	Us424	0.282139	0.000018	-12.6	0.6	461	0.282139	0.000018	-12.4	0.6
s3B	Granite (Leuco-)	s3B - 73	688	34	36	499	10	13	530	12	14	94	72	Us430 (2)	0.282089	0.000043	-13.5	1.5	499	0.282089	0.000043	-14.2	1.5
s3B	Granite (Leuco-)	s3B - 75	484	23	26	480	8	12	478	11	13	100	99	Us433	0.282143	0.000021	-12.0	0.8	480	0.282143	0.000021	-12.3	0.8
s3B	Granite (Leuco-)	s3B - 77	496	24	27	475	8	12	476	11	13	100	96	Us432	0.282034	0.000026	-16.0	0.9	475	0.282034	0.000026	-16.2	0.9
s3B	Granite (Leuco-)	s3B - 78	490	24	27	474	8	12	474	10	12	100	97	Us431	0.282075	0.000026	-14.6	0.9	474	0.282075	0.000026	-14.7	0.9
s3B	Granite (Leuco-)	s3B - 79	614	54	55	473	9	12	493	14	15	96	77	Us434	0.282105	0.000040	-13.5	1.4	473	0.282105	0.000040	-13.6	1.4
s3B	Granite (Leuco-)	s3B - 81	797	41	43	451	8	12	508	13	15	89	57										
s3B	Granite (Leuco-)	s3B - 82	774	25	27	483	9	12	533	12	14	91	62	Us438	0.282123	0.000024	-12.6	0.9	483	0.282124	0.000024	-13.0	0.9
s3B	Granite (Leuco-)	s3B - 83	1152	28	30	467	9	12	599	14	16	78	41	Us439	0.282123	0.000033	-12.9	1.2	470	0.282124	0.000033	-13.0	1.2
s3B	Granite (Leuco-)	s3B - 84	493	28	30	466	9	12	468	11	13	100	94										
s3B	Granite (Leuco-)	s3B - 85	794	45	46	461	8	12	518	13	15	89	58										
s3B	Granite (Leuco-)	s3B - 86	590	28	31	475	8	12	494	12	14	96	81	Us436	0.282098	0.000023	-13.7	0.8	475	0.282099	0.000023	-13.9	0.8
s3B	Granite (Leuco-)	s3B - 87	1044	33	34	452	8	11	561	13	15	81	43										
s3B	Granite (Leuco-)	s3B - 89	535	29	31	499	9	12	502	11	13	99	93	Us435	0.282088	0.000031	-13.6	1.1	499	0.282088	0.000031	-14.2	1.1
s3B	Granite (Leuco-)	s3B - 93	793	21	24	466	8	11	522	11	14	89	59										
s3B	Granite (Leuco-)	s3B - 94	526	34	36	525	10	13	522	12	14	101	100	Us447	0.282155	0.000036	-10.6	1.3	525	0.282156	0.000036	-11.8	1.3
s3B	Granite (Leuco-)	s3B - 95	470	38	40	479	10	13	475	12	14	101	102	Us446	0.282087	0.000027	-14.0	1.0	479	0.282087	0.000027	-14.3	1.0
s3B	Granite (Leuco-)	s3B - 96	503	31	33	456	8	12	462	11	13	99	91	Us445	0.282057	0.000025	-15.6	0.9	456	0.282056	0.000025	-15.4	0.9
s3B	Granite (Leuco-)	s3B - 98	545	60	61	461	9	12	473	15	16	97	85	Us444	0.282173	0.000183	-11.4	6.5	461	0.282173	0.000183	-11.2	6.5
s3B	Granite (Leuco-)	s3B - 99	589	33	35	542	9	13	549	12	15	99	92	Us448	0.282075	0.000027	-13.0	1.0	542	0.282076	0.000027	-14.7	1.0
s3B	Granite (Leuco-)	s3B - n/a1												Us421	0.282101	0.000023	-13.7	0.8	470	0.282101	0.000023	-13.8	0.8
s3B	Granite (Leuco-)	s3B - n/a2												Us410	0.281996	0.000049	-17.5	1.7	470	0.281996	0.000049	-17.5	1.7

TABLE 1 CONTINUED

Sample	Rock type	Identifier U-Pb	$^{207}Pb/^{206}Pb$	2σ	$2\sigma_{sys}$	$^{206}Pb/^{238}U$	2σ	$2\sigma_{sys}$	$^{207}Pb/^{235}U$	2σ	$2\sigma_{sys}$	Concordance (%) 206/238 - 207/235	Concordance (%) 206/238 - 207/206	Identifier Lu-Hf	$^{176}Hf/^{177}Hf_t$	2σ	εHf_t	2σ	Date (Ma)	$^{176}Hf/^{177}Hf_{t68}$	2σ	εHf_{t68}	2σ
s4D	Leucosome	s4D - 01	2096	39	41	2000	37	49	2046	24	34	98	95	Us221	0.281362	0.000030	-2.9	1.1	2096	0.281393	0.000030	-38.9	1.1
s4D	Leucosome	s4D - 02	1695	42	45	1273	37	43	1443	30	39	88	75										
s4D	Leucosome	s4D - 03	1712	29	31	1011	19	26	1259	16	23	80	59										
s4D	Leucosome	s4D - 04	1817	23	25	1546	28	38	1664	17	25	93	85	Us222	0.281604	0.000018	-0.8	0.6	1817	0.281616	0.000018	-31.0	0.6
s4D	Leucosome	s4D - 05	1912	28	31	1787	30	43	1843	18	27	97	93	Us223	0.281599	0.000025	1.2	0.9	1912	0.281611	0.000025	-31.1	0.9
s4D	Leucosome	s4D - 07	2844	18	20	2692	41	55	2780	18	28	97	95	Us224	0.281031	0.000034	2.8	1.2	2844	0.281056	0.000034	-50.8	1.2
s4D	Leucosome	s4D - 08	2762	16	20	2154	34	48	2481	17	22	87	78										
s4D	Leucosome	s4D - 09	2557	49	51	1673	45	54	2112	31	39	79	65										
s4D	Leucosome	s4D - 10	2839	12	20	2723	39	55	2791	16	24	98	96										
s4D	Leucosome	s4D - 11	2724	18	20	2566	37	54	2655	18	26	97	94	Us226	0.281023	0.000018	-0.3	0.6	2724	0.281054	0.000018	-50.8	0.6
s4D	Leucosome	s4D - 12	2572	22	24	1508	32	41	2015	23	32	75	59										
s4D	Leucosome	s4D - 13	2851	26	28	2699	54	72	2791	26	32	97	95	Us227	0.281252	0.000051	10.8	1.8	2851	0.281271	0.000051	-43.1	1.8
s4D	Leucosome	s4D - 14	2727	21	23	2610	42	59	2678	19	25	97	96	Us228	0.280836	0.000031	-6.9	1.1	2727	0.280863	0.000031	-57.6	1.1
s4D	Leucosome	s4D - 15	2135	37	38	1040	20	27	1463	20	26	71	49										
s4D	Leucosome	s4D - 18	2739	22	23	2308	42	56	2543	21	27	91	84	Us234	0.281031	0.000020	0.3	0.7	2739	0.281081	0.000020	-49.9	0.7
s4D	Leucosome	s4D - 19	1440	40	43	511	12	15	723	15	22	71	35										
s4D	Leucosome	s4D - 20	2780	17	20	1823	31	43	2314	19	27	79	66										
s4D	Leucosome	s4D - 21	1732	44	46	1385	34	42	1532	25	33	90	80	Us229	0.281186	0.000033	-17.6	1.2	1732	0.281199	0.000033	-45.7	1.2
s4D	Leucosome	s4D - 23	1867	42	43	1741	36	45	1799	24	29	97	93	Us235	0.281339	0.000046	-9.0	1.6	1867	0.281348	0.000046	-40.4	1.6
s4D	Leucosome	s4D - 25	2656	17	19	2436	39	54	2555	18	25	95	92	Us237	0.281249	0.000039	6.1	1.4	2656	0.281264	0.000039	-43.4	1.4
s4D	Leucosome	s4D - 26	1216	62	63	491	10	13	647	17	22	76	40	Us238	0.281777	0.000081	-23.4	2.9	550	0.281779	0.000081	-25.2	2.9
s4D	Leucosome	s4D - 27	936	75	76	593	15	18	675	23	30	88	63										
s4D	Leucosome	s4D - 28	1549	94	95	468	10	13	715	27	42	65	30										
s4D	Leucosome	s4D - 29	1733	64	65	1264	37	44	1448	28	31	87	73										
s4D	Leucosome	s4D - 30	1061	24	26	983	17	23	1011	13	20	97	93	Us236	0.282058	0.000023	-3.7	0.8	983	0.282062	0.000023	-15.1	0.8
s4D	Leucosome	s4D - 31	1847	28	29	1542	29	39	1677	19	26	92	83	Us244	0.281701	0.000018	3.4	0.6	1847	0.281724	0.000018	-27.1	0.6
s4D	Leucosome	s4D - 33	1610	24	26	1554	24	34	1580	16	24	98	97	Us243	0.281865	0.000021	3.8	0.7	1610	0.281877	0.000021	-21.7	0.7
s4D	Leucosome	s4D - 34	1569	24	27	1458	23	33	1504	16	24	97	93	Us241	0.281719	0.000023	-2.4	0.8	1569	0.281733	0.000023	-26.8	0.8
s4D	Leucosome	s4D - 35	1535	30	31	1376	24	33	1438	18	24	96	90	Us240	0.281716	0.000036	-3.3	1.3	1535	0.281741	0.000036	-26.5	1.3
s4D	Leucosome	s4D - 36	1606	16	23	1374	22	32	1468	13	20	94	86	Us242	0.281816	0.000022	1.9	0.8	1606	0.281866	0.000022	-22.1	0.8
s4D	Leucosome	s4D - 37	1742	20	23	1363	23	32	1516	15	23	90	78										
s4D	Leucosome	s4D - 38	1468	44	45	1433	30	39	1448	22	30	99	98	Us239	0.281881	0.000027	1.0	1.0	1468	0.281905	0.000027	-20.7	1.0
s4D	Leucosome	s4D - 39	1669	48	49	622	13	17	906	18	24	69	37										
s4D	Leucosome	s4D - 41	1701	63	64	1269	41	48	1448	28	39	88	75										
s4D	Leucosome	s4D - 42	1718	38	39	897	19	24	1172	19	25	77	52										
s4D	Leucosome	s4D - 44	2009	40	41	1039	27	33	1409	26	34	74	52										
s4D	Leucosome	s4D - 47	1808	71	72	476	10	13	795	23	31	60	26										
s4D	Leucosome	s4D - 48	828	61	65	575	12	16	638	17	23	90	69	Us245	0.281743	0.000036	-24.0	1.3	575	0.281746	0.000036	-26.3	1.3
s4D	Leucosome	s4D - 49	1878	28	30	1556	28	38	1704	18	26	91	83	Us246	0.281637	0.000057	1.8	2.0	1878	0.281689	0.000057	-28.3	2.0
s4D	Leucosome	s4D - 50	645	70	72	463	9	12	502	14	17	92	72	Us247	0.281782	0.000092	-25.2	3.3	463	0.281782	0.000092	-25.1	3.3
s4D	Leucosome	s4D - 51	2740	14	20	2451	37	53	2610	17	27	94	89	Us248	0.280912	0.000015	-3.9	0.5	2740	0.280950	0.000015	-54.5	0.5
s4D	Leucosome	s4D - 52	2685	12	21	2211	34	49	2468	16	25	90	82										
s4D	Leucosome	s4D - 53	1962	39	40	731	19	23	1118	25	34	65	37										
s4D	Leucosome	s4D - 54	2493	27	28	1451	29	38	1934	22	28	75	58										

TABLE 1 CONTINUED

Sample	Rock type	Identifier U-Pb	$^{207}Pb/^{206}Pb$	2σ	$2\sigma_{sys}$	$^{206}Pb/^{238}U$	2σ	$2\sigma_{sys}$	$^{207}Pb/^{235}U$	2σ	$2\sigma_{sys}$	Concordance (%) 206/238 - 207/235	Concordance (%) 206/238 - 207/206	Identifier Lu-Hf	$^{176}Hf/^{177}Hf_t$	2σ	εHf_t	2σ	Date (Ma)	$^{176}Hf/^{177}Hf_{t68}$	2σ	εHf_{t68}	2σ
s5A	Diorite	s5A - 04	718	31	34	458	9	12	508	9	12	90	64	Us249	0.282099	0.000048	-14.1	1.7	458	0.282099	0.000048	-13.9	1.7
s5A	Diorite	s5A - 06	981	55	56	440	9	12	541	11	14	81	45										
s5A	Diorite	s5A - 07	531	41	43	451	9	12	465	8	11	97	85	Us251	0.282179	0.000063	-11.4	2.2	451	0.282179	0.000063	-11.0	2.2
s5A	Diorite	s5A - 08	586	29	32	434	8	11	461	9	11	94	74	Us250	0.282151	0.000031	-12.8	1.1	434	0.282150	0.000031	-12.0	1.1
s5A	Diorite	s5A - 09	513	50	54	466	10	13	477	11	14	98	91	Us252	0.282182	0.000065	-11.0	2.3	466	0.282182	0.000065	-10.9	2.3
s5A	Diorite	s5A - 11	696	46	49	467	10	13	510	10	13	92	67	Us253	0.282203	0.000060	-10.2	2.1	467	0.282203	0.000060	-10.2	2.1
s5A	Diorite	s5A - 12	1038	52	53	461	9	12	578	14	18	80	44	Us254	0.282203	0.000047	-10.2	1.7	467	0.282203	0.000047	-10.2	1.7
s5A	Diorite	s5A - 13	822	39	41	420	8	11	490	10	13	86	51										
s5A	Diorite	s5A - 14	825	46	48	442	9	12	512	11	11	86	54										
s5A	Diorite	s5A - 15	655	41	43	441	9	11	480	9	13	92	67	Us256	0.282250	0.000116	-9.1	4.1	441	0.282249	0.000116	-8.5	4.1
s5A	Diorite	s5A - 16	680	54	55	464	11	14	506	11	14	92	68	Us255	0.282118	0.000105	-13.3	3.7	464	0.282118	0.000105	-13.2	3.7
s5A	Diorite	s5A - 17	519	28	29	501	9	13	505	8	11	99	97	Us257	0.282198	0.000073	-9.6	2.6	501	0.282199	0.000073	-10.3	2.6
s5A	Diorite	s5A - 18	573	42	43	461	9	12	481	10	13	96	80	Us259	0.282140	0.000029	-12.5	1.0	461	0.282140	0.000029	-12.4	1.0
s5A	Diorite	s5A - 19	610	62	65	466	15	17	493	12	16	95	76										
s5A	Diorite	s5A - 21	591	22	25	454	9	12	481	8	11	95	77	Us258	0.282148	0.000056	-12.4	2.0	454	0.282148	0.000056	-12.1	2.0
s5A	Diorite	s5A - 22	579	47	48	417	8	11	446	10	13	94	72	Us261	0.282232	0.000062	-10.3	2.2	417	0.282231	0.000062	-9.2	2.2
s5A	Diorite	s5A - 24	608	36	37	451	9	12	479	9	12	94	74	Us262	0.282130	0.000077	-13.1	2.7	451	0.282130	0.000077	-12.8	2.7
s5A	Diorite	s5A - 25	663	46	47	454	8	12	493	11	14	92	69	Us266	0.282130	0.000028	-13.1	1.0	454	0.282130	0.000028	-12.8	1.0
s5A	Diorite	s5A - 26	575	46	49	454	10	13	478	11	14	95	79	Us265	0.282190	0.000064	-10.9	2.3	454	0.282190	0.000064	-10.6	2.3
s5A	Diorite	s5A - 27	1396	45	46	469	10	12	663	12	16	71	34										
s5A	Diorite	s5A - 28	684	31	32	455	8	12	497	8	12	92	66	Us264	0.282177	0.000032	-11.4	1.1	455	0.282177	0.000032	-11.1	1.1
s5A	Diorite	s5A - 29	528	30	33	436	8	11	453	8	11	96	83	Us263	0.282211	0.000043	-10.6	1.5	436	0.282210	0.000043	-9.9	1.5
s5A	Diorite	s5A - 31	580	37	38	521	10	13	535	10	15	98	90	Us267	0.282275	0.000027	-6.4	1.0	521	0.282277	0.000027	-7.6	1.0
s5A	Diorite	s5A - 32	673	53	56	443	11	14	481	11	12	92	66	Us268	0.282209	0.000046	-10.5	1.6	443	0.282209	0.000046	-10.0	1.6
s5A	Diorite	s5A - 33	563	64	65	476	14	17	493	14	14	97	85										
s5A	Diorite	s5A - 34	698	37	39	448	9	12	492	10	13	91	64										
s5A	Diorite	s5A - 36	568	25	27	450	8	12	473	8	10	95	79	Us271	0.282118	0.000050	-13.6	1.8	450	0.282118	0.000050	-13.2	1.8
s5A	Diorite	s5A - 37	506	39	41	458	10	13	469	10	13	98	90	Us272	0.282134	0.000079	-12.8	2.8	458	0.282134	0.000079	-12.6	2.8
s5A	Diorite	s5A - 38	580	29	31	453	8	12	476	8	11	95	78	Us274	0.282179	0.000031	-11.3	1.1	453	0.282179	0.000031	-11.0	1.1
s5A	Diorite	s5A - 39	650	28	30	433	8	11	472	8	11	92	67	Us275	0.282226	0.000105	-10.1	3.7	433	0.282225	0.000105	-9.4	3.7
s5A	Diorite	s5A - 40	488	33	35	438	9	11	448	8	9	98	90	Us276	0.282095	0.000122	-14.6	4.3	438	0.282095	0.000122	-14.0	4.3
s5A	Diorite	s5A - 41	579	30	32	444	9	11	470	8	11	94	77	Us273	0.282138	0.000034	-13.0	1.2	444	0.282138	0.000034	-12.5	1.2
s5A	Diorite	s5A - 43	664	34	36	453	9	12	490	10	14	92	68	Us284	0.282154	0.000112	-12.2	4.0	453	0.282153	0.000112	-11.9	4.0
s5A	Diorite	s5A - 44	593	49	51	453	10	13	480	12	14	94	76	Us277	0.282148	0.000054	-12.5	1.9	453	0.282148	0.000054	-12.1	1.9
s5A	Diorite	s5A - 45	515	44	45	457	11	12	466	9	12	98	89	Us278	0.282141	0.000072	-12.6	2.6	457	0.282141	0.000072	-12.4	2.6
s5A	Diorite	s5A - 46	610	44	45	418	10	12	452	10	12	93	69	Us279	0.282008	0.000138	-18.2	4.9	418	0.282007	0.000138	-17.1	4.9
s5A	Diorite	s5A - 49	512	29	32	464	8	12	473	8	11	98	91	Us286	0.282108	0.000040	-13.6	1.4	464	0.282108	0.000040	-13.5	1.4
s5A	Diorite	s5A - 50	651	42	43	465	10	12	497	11	13	93	71	Us287	0.282231	0.000074	-9.2	2.6	465	0.282231	0.000074	-9.2	2.6
s5A	Diorite	s5A-n/a1												Us285	0.282130	0.000071	-13.1	2.5	453	0.282130	0.000071	-12.7	2.5

TABLE 1 CONTINUED

Sample	Rock type	Identifier U-Pb	$^{207}Pb/^{206}Pb$	2σ	$2\sigma_{sys}$	$^{206}Pb/^{238}U$	2σ	$2\sigma_{sys}$	$^{207}Pb/^{235}U$	2σ	$2\sigma_{sys}$	Concordance (%) 206/238 - 207/235	Concordance (%) 206/238 - 207/206	Identifier Lu-Hf	$^{176}Hf/^{177}Hf_t$	2σ	εHf_t	2σ	Date (Ma)	$^{176}Hf/^{177}Hf_{468}$	2σ	εHf_{468}	2σ
s5Ba	Granodiorite	s5Ba - 04	917	41	42	441	9	11	527	10	13	84	48										
s5Ba	Granodiorite	s5Ba - 06	1346	24	26	476	8	12	660	10	15	72	35										
s5Ba	Granodiorite	s5Ba - 08	1070	59	64	457	9	12	581	16	20	79	43										
s5Ba	Granodiorite	s5Ba - 13	627	35	37	446	9	12	478	9	13	93	71	Us301	0.282161	0.000059	-12.1	2.1	446	0.282160	0.000059	-11.7	2.1
s5Ba	Granodiorite	s5Ba - 15	524	39	40	452	8	12	466	9	11	97	86	Us302	0.282259	0.000075	-8.6	2.7	452	0.282258	0.000075	-8.2	2.7
s5Ba	Granodiorite	s5Ba - 16	466	15	26	484	8	11	482	7	10	100	104	Us304	0.282164	0.000022	-11.2	0.8	484	0.282165	0.000022	-11.5	0.8
s5Ba	Granodiorite	s5Ba - 17	517	29	33	444	8	11	456	8	11	97	86	Us303	0.282164	0.000016	-12.1	0.6	444	0.282164	0.000016	-11.6	0.6
s5Ba	Granodiorite	s5Ba - 17b	505	31	33	525	10	13	522	8	11	101	104	Us303b	0.282163	0.000016	-10.3	0.6	525				
s5Ba	Granodiorite	s5Ba - 18	491	47	48	443	9	11	454	10	13	98	90	Us307	0.282153	0.000025	-12.5	0.9	443	0.282153	0.000025	-11.9	0.9
s5Ba	Granodiorite	s5Ba - 24	601	50	51	465	10	13	489	10	12	95	77	Us308	0.282125	0.000038	-13.0	1.3	465	0.282125	0.000038	-12.9	1.3
s5Ba	Granodiorite	s5Ba - 25	878	43	44	443	9	12	522	11	14	85	50										
s5Ba	Granodiorite	s5Ba - 26	795	37	39	473	10	13	533	10	12	89	59										
s5Ba	Granodiorite	s5Ba - 27	2609	14	20	1727	28	40	2164	15	23	80	66										
s5Ba	Granodiorite	s5Ba - 28	2200	17	20	862	16	22	1336	16	22	65	39										
s5Ba	Granodiorite	s5Ba - 29	1517	55	56	507	10	13	743	17	25	68	33										
s5Ba	Granodiorite	s5Ba - 32	1653	53	54	508	12	15	776	21	22	65	31										
s5Ba	Granodiorite	s5Ba - 35	825	48	50	467	9	12	537	13	14	87	57										
s5Ba	Granodiorite	s5Ba - 37	944	43	44	490	9	12	582	12	17	84	52										
s5Ba	Granodiorite	s5Ba - 39	585	33	35	445	9	12	468	9	12	95	76										
s5Ba	Granodiorite	s5Ba - 40	1180	87	90	458	10	12	607	20	25	75	39										
s5Ba	Granodiorite	s5Ba - 41	1804	48	49	481	9	12	791	18	23	61	27										
s5Ba	Granodiorite	s5Ba - 42	893	44	46	449	11	14	532	11	14	84	50										
s5Ba	Granodiorite	s5Ba - 43	1261	63	64	474	9	12	646	19	29	73	38										
s5Ba	Granodiorite	s5Ba - 44	873	47	49	474	10	13	552	12	16	86	54										
s5Ba	Granodiorite	s5Ba - 48	1102	35	37	451	10	13	578	11	14	78	41										
s5Ba	Granodiorite	s5Ba - 49	576	47	49	468	11	14	489	12	14	96	81	Us310	0.282218	0.000074	-9.6	2.6	468	0.282218	0.000074	-9.6	2.6
s5Ba	Granodiorite	s5Ba - 51	478	18	28	472	8	12	473	7	10	100	99	Us306	0.282164	0.000022	-11.4	0.8	472	0.282164	0.000022	-11.5	0.8
s5Ba	Granodiorite	s5Ba - 52	481	16	26	483	8	12	483	7	10	100	100	Us305	0.282175	0.000015	-10.8	0.5	483	0.282176	0.000015	-11.1	0.5
s5Ba	Granodiorite	s5Ba-n/a1												Us311	0.282158	0.000024	-12.2	0.9	449	0.282158	0.000024	-11.8	0.9
s5Ba	Granodiorite	s5Ba-n/a2												Us312	0.282124	0.000040	-13.4	1.4	450	0.282123	0.000040	-13.0	1.4

TABLE 1 CONTINUED

Sample	Rock type	Identifier U-Pb	$^{207}Pb/^{206}Pb$	2σ	$2\sigma_{sys}$	$^{206}Pb/^{238}U$	2σ	$2\sigma_{sys}$	$^{207}Pb/^{235}U$	2σ	$2\sigma_{sys}$	Concordance (%) 206/238 - 207/235	Concordance (%) 206/238 - 207/206	Identifier Lu-Hf	$^{176}Hf/^{177}Hf_t$	2σ	εHf_t	2σ	Date (Ma)	$^{176}Hf/^{177}Hf_{468}$	2σ	εHf_{468}	2σ
s5Bb	Diorite	s5Bb - 02	574	33	34	477	9	12	493	9	12	97	83	Us288	0.282152	0.000045	-11.8	1.6	477	0.282152	0.000045	-12.0	1.6
s5Bb	Diorite	s5Bb - 03	2052	60	61	469	10	13	858	25	34	55	23										
s5Bb	Diorite	s5Bb - 04	1084	66	67	460	9	13	586	18	22	78	42										
s5Bb	Diorite	s5Bb - 05	641	47	48	458	9	11	492	10	13	93	71	Us289	0.282151	0.000044	-12.2	1.6	458	0.282151	0.000044	-12.0	1.6
s5Bb	Diorite	s5Bb - 06	1825	59	60	500	10	13	832	23	29	60	27										
s5Bb	Diorite	s5Bb - 08	485	30	32	470	8	12	473	8	11	99	97	Us290	0.282130	0.000024	-12.7	0.8	470	0.282130	0.000024	-12.7	0.8
s5Bb	Diorite	s5Bb - 09	628	39	41	452	8	12	484	9	13	93	72	Us291	0.282141	0.000040	-12.7	1.4	452	0.282141	0.000040	-12.4	1.4
s5Bb	Diorite	s5Bb - 10	584	54	55	466	10	12	491	12	13	95	80	Us292	0.282148	0.000035	-12.2	1.2	466	0.282148	0.000035	-12.1	1.2
s5Bb	Diorite	s5Bb - 12	1302	51	52	470	9	12	649	15	13	72	36										
s5Bb	Diorite	s5Bb - 13	898	43	44	471	9	12	553	10	15	85	52										
s5Bb	Diorite	s5Bb - 14	1023	67	71	454	9	12	570	19	26	80	44	Us299	0.282152	0.000035	-12.2	1.3	459	0.282151	0.000035	-12.0	1.3
s5Bb	Diorite	s5Bb - 15	1569	51	53	493	10	13	743	17	24	66	31										
s5Bb	Diorite	s5Bb - 16	675	46	49	468	9	12	509	10	13	92	69	Us295	0.282161	0.000084	-11.6	3.0	468	0.282161	0.000084	-11.6	3.0
s5Bb	Diorite	s5Bb - 17	654	25	27	474	9	12	505	8	11	94	72	Us294	0.282137	0.000037	-12.4	1.3	474	0.282137	0.000037	-12.5	1.3
s5Bb	Diorite	s5Bb - 19	568	24	27	449	8	11	470	7	10	95	79	Us293	0.282209	0.000038	-10.4	1.4	449	0.282209	0.000038	-10.0	1.4
s5Bb	Diorite	s5Bb - 20	754	44	46	459	9	12	517	12	14	89	61										
s5Bb	Diorite	s5Bb - 24	1022	65	66	467	9	12	580	16	22	80	46										
s5Bb	Diorite	s5Bb - 25	1027	64	73	465	9	12	579	17	25	80	45										
s5Bb	Diorite	s5Bb - 27	1489	31	34	482	9	12	701	12	17	69	32										
s5Bb	Diorite	s5Bb - 31	1569	48	49	456	8	12	699	15	20	65	29										
s5Bb	Diorite	s5Bb - 33	588	38	41	457	9	12	481	9	12	95	78	Us296	0.282075	0.000025	-14.9	0.9	457	0.282075	0.000025	-14.7	0.9
s5Bb	Diorite	s5Bb - 35	570	35	37	451	8	11	472	8	11	95	79	Us297	0.282229	0.000088	-9.6	3.1	451	0.282228	0.000088	-9.3	3.1
s5Bb	Diorite	s5Bb - 36	1259	45	48	456	9	12	621	12	16	73	36										
s5Bb	Diorite	s5Bb - 37	851	35	36	466	10	12	540	11	14	86	55										
s5Bb	Diorite	s5Bb - 38	1124	48	49	458	8	12	590	12	17	78	41										
s5Bb	Diorite	s5Bb - 40	2334	48	50	1376	34	42	1801	33	44	76	59										
s5Bb	Diorite	s5Bb - 41	1195	39	40	460	9	13	609	13	17	76	39										
s5Bb	Diorite	s5Bb - 43	1042	77	80	447	8	11	567	19	24	79	43										
s5Bb	Diorite	s5Bb - 46	533	39	43	461	10	13	475	10	12	97	87	Us298	0.282195	0.000072	-10.6	2.5	461	0.282195	0.000072	-10.5	2.5
s5Bb	Diorite	s5Bb - 49	1164	30	32	459	8	11	598	10	14	77	39										
s5Bb	Diorite	s5Bb - 50	1101	52	53	462	10	13	589	13	16	78	42										
s5Bb	Diorite	s5Bb-n/a1												Us300	0.282178	0.000032	-11.3	1.1	459	0.282178	0.000032	-11.1	1.1

TABLE 1 CONTINUED

Sample	Rock type	Identifier U-Pb	$^{207}Pb/^{206}Pb$	2σ	$2\sigma_{sys}$	$^{206}Pb/^{238}U$	2σ	$2\sigma_{sys}$	$^{207}Pb/^{235}U$	2σ	$2\sigma_{sys}$	Concordance (%) 206/238 - 207/235	Concordance (%) 206/238 - 207/206	Identifier Lu-Hf	$^{176}Hf/^{177}Hf_t$	2σ	εHf_t	2σ	Date (Ma)	$^{176}Hf/^{177}Hf_{t68}$	2σ	εHf_{t68}	2σ
s7A	Diorite	s7A - 01	519	16	19	484	8	12	487	11	13	99	93										
s7A	Diorite	s7A - 02	661	27	29	475	9	12	507	11	13	94	72										
s7A	Diorite	s7A - 03	548	15	19	468	8	12	479	11	13	98	85	Us345	0.282163	0.000084	-11.6	3.0	468	0.282163	0.000084	-11.6	3.0
s7A	Diorite	s7A - 04	492	15	19	499	9	12	494	10	12	101	101	Us346	0.282205	0.000064	-9.4	2.3	499	0.282207	0.000064	-10.0	2.3
s7A	Diorite	s7A - 06	577	18	22	471	8	12	487	11	13	97	82										
s7A	Diorite	s7A - 11	523	18	21	466	8	12	472	10	12	99	89										
s7A	Diorite	s7A - 15	590	17	21	498	9	12	510	10	13	98	84	Us349	0.282328	0.000029	-5.1	1.0	498	0.282329	0.000029	-5.7	1.0
s7A	Diorite	s7A - 21	666	29	31	472	8	12	501	12	14	94	71	Us351	0.282296	0.000019	-6.8	0.7	472	0.282296	0.000019	-6.9	0.7
s7A	Diorite	s7A - 22	507	24	26	462	8	12	465	10	12	99	91	Us350	0.282297	0.000033	-7.0	1.2	462	0.282297	0.000033	-6.8	1.2
s7A	Diorite	s7A - 23	536	22	25	461	8	12	469	10	12	98	86	Us352	0.282245	0.000028	-8.8	1.0	461	0.282245	0.000028	-8.7	1.0
s7A	Diorite	s7A - 26	867	27	29	468	8	12	536	12	15	87	54										
s7A	Diorite	s7A - 27	709	31	33	462	8	11	499	11	13	93	65	Us353	0.282264	0.000029	-8.1	1.0	462	0.282264	0.000029	-8.0	1.0
s7A	Diorite	s7A - 29	599	18	21	470	8	12	487	11	13	97	79	Us354	0.282215	0.000064	-9.7	2.3	470	0.282215	0.000064	-9.7	2.3
s7A	Diorite	s7A - 35	521	22	25	477	8	12	479	10	12	100	92	Us355	0.282205	0.000060	-9.9	2.1	477	0.282205	0.000060	-10.1	2.1
s7A	Diorite	s7A - 37	502	21	24	465	11	13	464	12	14	100	93	Us357	0.282284	0.000047	-7.4	1.6	465	0.282284	0.000047	-7.3	1.6
s7A	Diorite	s7A - 39	635	20	23	472	8	12	496	11	13	95	74	Us356	0.282272	0.000035	-7.6	1.2	472	0.282272	0.000035	-7.7	1.2
s7A	Diorite	s7A - 42	1184	15	19	1076	19	26	1102	18	22	98	91	Us358	0.282166	0.000039	4.7	1.4	1184	0.282181	0.000039	-10.9	1.4
s7A	Diorite	s7A - 44	958	28	30	480	10	13	567	14	17	85	50										
s7A	Diorite	s7A - 45	492	11	16	465	8	12	463	10	12	100	95										
s7A	Diorite	s7A - 48	745	33	35	498	9	12	538	12	15	93	67	Us360	0.282304	0.000027	-5.9	0.9	498	0.282305	0.000027	-6.6	0.9
s7A	Diorite	s7A-n/a1												Us347	0.282307	0.000030	-6.4	1.0	471	0.282307	0.000030	-6.5	1.0
s7A	Diorite	s7A-n/a2												Us361	0.282315	0.000029	-6.2	1.0	467	0.282315	0.000029	-6.2	1.0
s7A	Diorite	s7A-n/a3												Us362	0.282276	0.000030	-7.6	1.1	467	0.282276	0.000030	-7.6	1.1

TABLE 1 CONTINUED

Sample	Rock type	Identifier U-Pb	$^{207}Pb/^{206}Pb$	2σ	$2\sigma_{sys}$	$^{206}Pb/^{238}U$	2σ	$2\sigma_{sys}$	$^{207}Pb/^{235}U$	2σ	$2\sigma_{sys}$	Concordance (%) 206/238 - 207/235	Concordance (%) 206/238 - 207/206	Identifier Lu-Hf	$^{176}Hf/^{177}Hf_t$	2σ	εHf_t	2σ	Date (Ma)	$^{176}Hf/^{177}Hf_{t68}$	2σ	εHf_{t68}	2σ
s7B	Granite	s7B - 01	725	83	84	473	8	12	519	16	17	91	65										
s7B	Granite	s7B - 03	778	71	72	471	7	11	526	15	17	89	61										
s7B	Granite	s7B - 05	742	43	44	468	6	10	517	9	12	90	63	Us085	0.282016	0.000021	-16.8	0.7	468	0.282016	0.000021	-16.8	0.7
s7B	Granite	s7B - 07	460	43	45	469	6	10	466	8	11	101	102	Us087	0.282091	0.000015	-14.1	0.5	469	0.282091	0.000015	-14.1	0.5
s7B	Granite	s7B - 08	440	92	93	483	7	11	475	16	17	102	110										
s7B	Granite	s7B - 09	1561	60	61	456	7	10	689	16	18	66	29										
s7B	Granite	s7B - 10	1144	59	60	1064	15	23	1085	19	23	98	93	Us086	0.282224	0.000014	5.8	0.5	1144	0.282233	0.000014	-9.1	0.5
s7B	Granite	s7B - 12	472	55	56	478	7	11	477	10	12	100	101	Us090	0.282047	0.000080	-15.4	2.8	478	0.282048	0.000080	-15.7	2.8
s7B	Granite	s7B - 14	943	44	45	491	7	11	577	11	14	85	52										
s7B	Granite	s7B - 15	507	42	44	462	6	10	468	8	11	99	91	Us089	0.282031	0.000034	-16.4	1.2	462	0.282031	0.000034	-16.2	1.2
s7B	Granite	s7B - 16	492	39	40	482	6	10	484	8	11	100	98	Us093	0.282042	0.000025	-15.5	0.9	482	0.282043	0.000025	-15.8	0.9
s7B	Granite	s7B - 16												Us094						0.281484	0.000027	-35.6	1.0
s7B	Granite	s7B - 17	488	97	98	479	8	11	479	17	18	100	98	Us092	0.282164	0.000066	-11.3	2.3	479	0.282164	0.000066	-11.6	2.3
s7B	Granite	s7B - 18	488	54	55	479	6	10	480	11	13	100	98	Us091	0.281998	0.000017	-17.2	0.6	479	0.281998	0.000017	-17.4	0.6
s7B	Granite	s7B - 19	492	43	44	471	6	10	474	8	10	99	96	Us099	0.282059	0.000030	-15.2	1.1	471	0.282059	0.000030	-15.3	1.1
s7B	Granite	s7B - 21	582	55	56	486	7	11	502	10	13	97	84	Us095	0.282082	0.000019	-14.1	0.7	486	0.282082	0.000019	-14.5	0.7
s7B	Granite	s7B - 21b	582	55	56	486	7	11	502	10	13	97	84	Us096	0.282060	0.000024	-14.8	0.9	486	0.282060	0.000024	-15.2	0.9
s7B	Granite	s7B - 22	472	59	60	474	6	10	472	10	12	101	100	Us098	0.282002	0.000015	-17.1	0.5	474	0.282002	0.000015	-17.3	0.5
s7B	Granite	s7B - 25	1356	24	26	490	6	10	677	9	13	72	36										
s7B	Granite	s7B - 26	992	39	41	459	6	10	558	9	12	82	46										
s7B	Granite	s7B - 27	518	80	81	470	7	11	477	14	16	99	91	Us101	0.282012	0.000028	-16.9	1.0	470	0.282012	0.000028	-16.9	1.0
s7B	Granite	s7B - 28	718	37	39	483	6	10	527	9	12	92	67	Us105	0.282090	0.000020	-13.8	0.7	483	0.282090	0.000020	-14.2	0.7
s7B	Granite	s7B - 29	518	68	69	508	7	11	510	13	15	100	98	Us102	0.282111	0.000015	-12.5	0.5	508	0.282111	0.000015	-13.4	0.5
s7B	Granite	s7B - 29b												Us103						0.282145	0.000022	-12.2	0.8
s7B	Granite	s7B - 29c												Us104						0.282053	0.000022	-15.5	0.8
s7B	Granite	s7B - 31	920	26	28	477	6	10	561	7	11	85	52										
s7B	Granite	s7B - 32	545	45	46	524	8	12	526	10	12	100	96	Us107	0.282078	0.000021	-13.3	0.7	524	0.282080	0.000021	-14.5	0.7
s7B	Granite	s7B - 36	952	61	62	481	6	10	572	14	16	84	51										
s7B	Granite	s7B - 37	688	48	49	513	7	11	545	11	13	94	75	Us108	0.282031	0.000027	-15.2	1.0	513	0.282031	0.000027	-16.2	1.0
s7B	Granite	s7B - 37b												Us109	0.281982	0.000031	-17.0	1.1	513	0.281982	0.000031	-18.0	1.1
s7B	Granite	s7B - 38	629	50	51	462	7	10	491	11	13	94	73	Us110	0.282130	0.000071	-12.9	2.5	462	0.282129	0.000071	-12.8	2.5
s7B	Granite	s7B - 40	1119	49	50	628	10	15	746	14	17	84	56										
s7B	Granite	s7B - 41	515	76	77	510	9	13	508	15	16	100	99	Us111	0.282148	0.000048	-11.2	1.7	510	0.282149	0.000048	-12.1	1.7
s7B	Granite	s7B - 44	614	57	58	491	7	11	512	11	13	96	80	Us113	0.282128	0.000069	-12.3	2.4	491	0.282129	0.000069	-12.8	2.4
s7B	Granite	s7B - 46	1756	19	21	1654	18	32	1698	12	20	97	94	Us114	0.281905	0.000024	8.5	0.8	1756	0.281937	0.000024	-19.6	0.8
s7B	Granite	s7B - 47	574	51	53	477	7	11	494	11	13	96	83	Us115	0.281999	0.000046	-17.2	1.6	477	0.281999	0.000046	-17.4	1.6
s7B	Granite	s7B - 48	1241	58	58	469	6	10	623	14	16	75	38										
s7B	Granite	s7B - 49	556	48	50	476	7	11	489	9	11	97	86	Us116	0.281989	0.000027	-17.5	1.0	476	0.281990	0.000027	-17.7	1.0
s7B	Granite	s7B - 50	778	58	59	477	7	11	533	13	15	89	61										
s7B	Granite	s7B - 51	813	41	42	471	6	10	531	9	12	89	58										
s7B	Granite	s7B - 52	844	102	103	479	7	11	548	23	24	87	57										
s7B	Granite	s7B - 53	484	47	48	482	6	10	482	9	11	100	100	Us097	0.282071	0.000017	-14.5	0.6	482	0.282072	0.000017	-14.8	0.6
s7B	Granite	s7B - 54	1478	82	83	507	8	12	724	24	25	70	34										
s7B	Granite	s7B - 55	742	53	54	473	6	10	522	11	13	91	64	Us100	0.282081	0.000074	-14.4	2.6	473	0.282082	0.000074	-14.5	2.6
s7B	Granite	s7B - 56	1236	31	33	1145	16	25	1172	14	19	98	93	Us112	0.282113	0.000068	4.0	2.4	1236	0.282130	0.000068	-12.7	2.4
s7B	Granite	s7B - 57	878	94	95	487	9	12	557	19	20	87	56										

TABLE 1 CONTINUED

Sample	Rock type	Identifier U-Pb	$^{207}Pb/^{206}Pb$	2σ	$2\sigma_{sys}$	$^{206}Pb/^{238}U$	2σ	$2\sigma_{sys}$	$^{207}Pb/^{235}U$	2σ	$2\sigma_{sys}$	Concordance (%) 206/238 - 207/235	206/238 - 207/206	Identifier Lu-Hf	$^{176}Hf/^{177}Hf_t$	2σ	εHf_t	2σ	Date (Ma)	$^{176}Hf/^{177}Hf_{468}$	2σ	εHf_{468}	2σ
s8Da	Granite	s8Da - 01	644	34	36	472	7	11	502	7	10	94	73	Us117	0.282217	0.000073	-9.6	2.6	472	0.282217	0.000073	-9.7	2.6
s8Da	Granite	s8Da - 02	552	48	50	475	6	10	487	9	11	98	86										
s8Da	Granite	s8Da - 03	629	78	79	476	8	11	498	14	16	96	76	Us118	0.282095	0.000069	-13.8	2.4	476	0.282095	0.000069	-14.0	2.4
s8Da	Granite	s8Da - 05	460	107	107	481	8	12	477	18	20	101	104	Us124	0.282024	0.000071	-16.2	2.5	481	0.282024	0.000071	-16.5	2.5
s8Da	Granite	s8Da - 06	611	83	83	474	7	11	495	15	17	96	78	Us125	0.282088	0.000062	-14.1	2.2	474	0.282088	0.000062	-14.2	2.2
s8Da	Granite	s8Da - 07	537	45	47	498	7	11	506	9	12	98	93										
s8Da	Granite	s8Da - 09	464	43	45	503	7	11	497	9	11	101	108	Us128	0.282141	0.000043	-11.6	1.5	503	0.282142	0.000043	-12.3	1.5
s8Da	Granite	s8Da - 10	507	42	44	490	7	11	492	8	11	99	97										
s8Da	Granite	s8Da - 14	611	23	25	487	6	10	509	6	10	96	80	Us130	0.282018	0.000021	-16.3	0.7	487	0.282018	0.000021	-16.7	0.7
s8Da	Granite	s8Da - 15	563	67	68	519	7	11	526	12	14	99	92	Us132	0.282181	0.000060	-9.8	2.1	519	0.282182	0.000060	-10.9	2.1
s8Da	Granite	s8Da - 18	578	44	45	484	6	10	499	9	12	97	84										
s8Da	Granite	s8Da - 19	1069	96	97	483	8	12	600	22	24	80	45										
s8Da	Granite	s8Da - 20	518	68	69	481	7	11	488	12	14	99	93	Us133	0.282179	0.000071	-10.7	2.5	481	0.282179	0.000071	-11.0	2.5
s8Da	Granite	s8Da - 24	604	43	45	464	6	10	487	9	11	95	77	Us135	0.282138	0.000024	-12.6	0.8	464	0.282138	0.000024	-12.5	0.8
s8Da	Granite	s8Da - 33	768	39	41	482	7	11	535	9	12	90	63										
s8Da	Granite	s8Da - 37	787	51	53	531	8	12	577	11	14	92	67	Us138	0.282063	0.000069	-13.7	2.4	531	0.282128	0.000038	-12.8	1.3
s8Da	Granite	s8Da - 37b	787	51	53	531	8	12	577	11	14	92	67	Us137	0.282125	0.000038	-11.5	1.3	531	0.282065	0.000069	-15.1	2.4
s8Da	Granite	s8Da - 38	646	112	113	527	9	13	547	20	21	96	82	Us140	0.281981	0.000066	-16.7	2.3	527	0.281982	0.000066	-18.0	2.3
s8Da	Granite	s8Da - 40	549	90	90	478	8	12	489	16	17	98	87										
s8Da	Granite	s8Da - 51	742	43	44	538	8	12	579	10	13	93	73										
s8Da	Granite	s8Da-n/a1												Us119	0.282088	0.000057	-14.1	2.0	474	0.282088	0.000057	-14.2	2.0

TABLE 1 CONTINUED

Sample	Rock type	Identifier U-Pb	$^{207}Pb/^{206}Pb$	2σ	$2\sigma_{sys}$	$^{206}Pb/^{238}U$	2σ	$2\sigma_{sys}$	$^{207}Pb/^{235}U$	2σ	$2\sigma_{sys}$	Concordance (%) 206/238 - 207/235	206/238 - 207/206	Identifier Lu-Hf	$^{176}Hf/^{177}Hf_t$	2σ	εHf_t	2σ	Date (Ma)	$^{176}Hf/^{177}Hf_{468}$	2σ	εHf_{468}	2σ
s8Db	Diorite	s8Db - 01	764	32	33	474	8	12	519	12	14	91	62	Us364	0.282281	0.000021	-7.3	0.7	474	0.282282	0.000021	-7.4	0.7
s8Db	Diorite	s8Db - 02	954	27	29	509	9	13	591	13	15	86	53										
s8Db	Diorite	s8Db - 04	510	18	21	485	9	12	482	11	13	101	95	Us363	0.282294	0.000018	-6.6	0.6	485	0.282294	0.000018	-6.9	0.6
s8Db	Diorite	s8Db - 05	2099	55	56	451	9	12	836	24	26	54	21										
s8Db	Diorite	s8Db - 06	654	22	24	466	8	12	493	11	13	95	71	Us365	0.282264	0.000040	-8.0	1.4	466	0.282264	0.000040	-8.0	1.4
s8Db	Diorite	s8Db - 07	772	29	31	471	8	12	519	12	14	91	61	Us366	0.282254	0.000022	-8.3	0.8	471	0.282254	0.000022	-8.4	0.8
s8Db	Diorite	s8Db - 08	606	17	20	492	8	12	506	10	13	97	81	Us367	0.282260	0.000065	-7.6	2.3	492	0.282261	0.000065	-8.1	2.3
s8Db	Diorite	s8Db - 09	591	28	30	469	9	12	484	12	14	97	79	Us368	0.282261	0.000019	-8.1	0.7	469	0.282261	0.000019	-8.1	0.7
s8Db	Diorite	s8Db - 10	681	29	31	494	10	13	523	13	15	94	73	Us370	0.282276	0.000021	-7.0	0.7	494	0.282276	0.000021	-7.6	0.7
s8Db	Diorite	s8Db - 11	522	23	26	481	8	12	481	11	13	100	92	Us369	0.282275	0.000022	-7.3	0.8	481	0.282275	0.000022	-7.6	0.8
s8Db	Diorite	s8Db - 12	532	17	20	474	8	12	477	10	12	99	89	Us371	0.282278	0.000051	-7.4	1.8	474	0.282278	0.000051	-7.5	1.8
s8Db	Diorite	s8Db - 14	613	19	22	463	8	11	482	11	13	96	76										
s8Db	Diorite	s8Db - 17	495	21	24	472	10	13	469	11	13	101	95	Us373	0.282217	0.000019	-9.6	0.7	472	0.282217	0.000019	-9.7	0.7
s8Db	Diorite	s8Db - 18	534	13	17	473	8	12	477	10	12	99	89										
s8Db	Diorite	s8Db - 20	1252	19	22	824	15	21	936	17	21	88	66	Us375	0.282186	0.000018	-10.7	0.6	470	0.282187	0.000018	-10.7	0.6
s8Db	Diorite	s8Db - 22	1160	38	39	508	10	13	634	16	18	80	44										
s8Db	Diorite	s8Db - 23	647	16	19	518	10	13	536	11	14	97	80	Us376	0.282316	0.000028	-5.0	1.0	518	0.282317	0.000028	-6.1	1.0
s8Db	Diorite	s8Db - 24	514	24	27	467	8	11	469	10	12	99	91	Us378	0.282250	0.000021	-8.5	0.7	467	0.282250	0.000021	-8.5	0.7
s8Db	Diorite	s8Db - 25	511	18	21	473	9	12	474	10	12	100	93	Us377	0.282285	0.000024	-7.1	0.8	473	0.282285	0.000024	-7.2	0.8
s8Db	Diorite	s8Db - 26	503	13	17	483	8	12	480	10	12	101	96	Us379	0.282235	0.000017	-8.7	0.6	483	0.282235	0.000017	-9.0	0.6
s8Db	Diorite	s8Db - 27	591	17	21	474	8	12	488	11	13	97	80	Us384	0.282260	0.000038	-8.0	1.3	474	0.282260	0.000038	-8.1	1.3
s8Db	Diorite	s8Db - 28	569	11	16	472	8	12	482	10	12	98	83	Us386	0.282262	0.000020	-8.0	0.7	472	0.282263	0.000020	-8.1	0.7
s8Db	Diorite	s8Db - 29	529	14	18	466	8	11	471	10	12	99	88	Us387	0.282228	0.000025	-9.3	0.9	466	0.282228	0.000025	-9.3	0.9
s8Db	Diorite	s8Db - 34	544	19	23	477	8	12	483	10	12	99	88	Us388	0.282186	0.000058	-10.6	2.0	477	0.282187	0.000058	-10.7	2.0
s8Db	Diorite	s8Db - 36	652	23	25	474	9	12	500	12	14	95	73	Us389	0.282299	0.000019	-6.6	0.7	474	0.282299	0.000019	-6.8	0.7
s8Db	Diorite	s8Db - 37	481	16	19	472	8	12	468	10	12	101	98	Us390	0.282294	0.000038	-6.9	1.3	472	0.282294	0.000038	-6.9	1.3
s8Db	Diorite	s8Db - 39	583	18	21	474	8	12	488	11	13	97	81	Us391	0.282314	0.000029	-6.1	1.0	474	0.282314	0.000029	-6.2	1.0
s8Db	Diorite	s8Db - 42	547	28	30	469	8	12	476	11	13	99	86	Us392	0.282258	0.000025	-8.2	0.9	469	0.282258	0.000025	-8.2	0.9
s8Db	Diorite	s8Db - 49	688	34	36	495	8	12	526	13	15	94	72	Us393	0.282281	0.000034	-6.8	1.2	495	0.282281	0.000034	-7.4	1.2
s8Db	Diorite	s8Db - 50	570	25	27	472	10	13	484	12	14	98	83	Us394	0.282294	0.000025	-6.9	0.9	472	0.282294	0.000025	-7.0	0.9
s8Db	Diorite	s8Db - n/a1												Us372	0.282288	0.000033	-7.3	1.2	463	0.282288	0.000033	-7.2	1.2
s8Db	Diorite	s8Db - n/a2												Us385	0.282288	0.000042	-7.1	1.5	470	0.282288	0.000042	-7.1	1.5

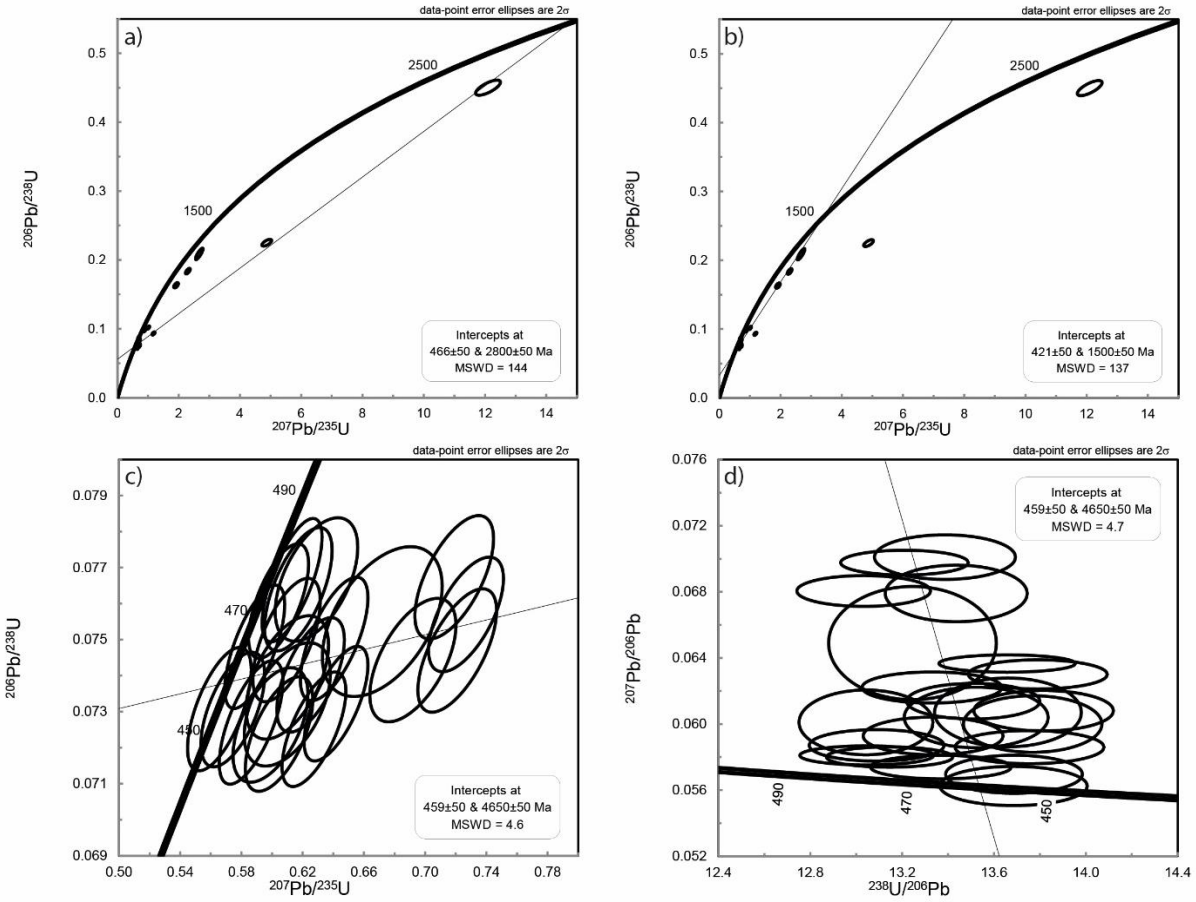

Figure 1 – Concordia plots of zircon isotope spot analyses of sample s1B a) Wetherill plot off all zircon analyses with anchored intercept at 2.8 Ga; b) Wetherill plot of all zircon analyses and anchored intercept at 1.5 Ga; c) Wetherill plot of zircon analyses < 500 Ma selected for age calculation; d) Tera-Wasserburg plot of zircon analyses < 500 Ma selected for age calculation

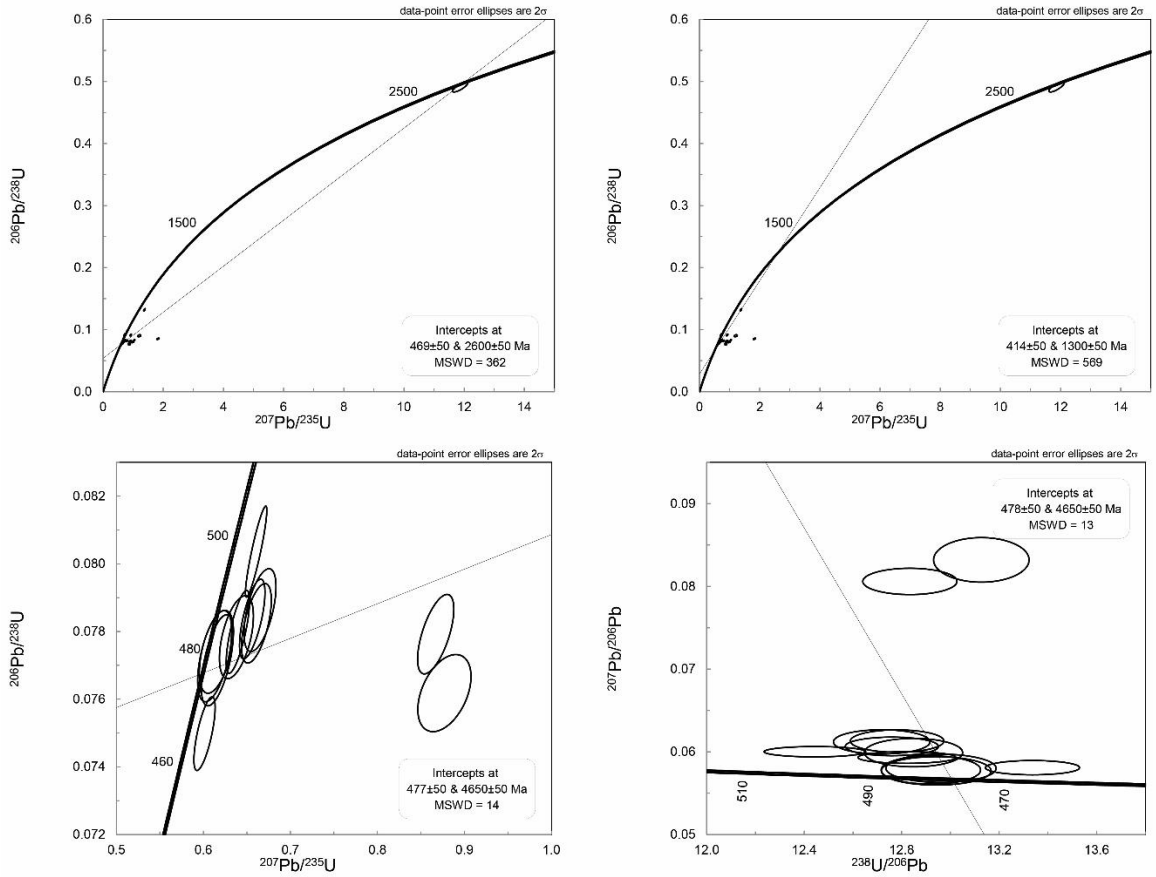

Figure 2 – Concordia plots of zircon isotope spot analyses of sample s1Da a) Wetherill plot off all zircon analyses with anchored intercept at 2.6 Ga; b) Wetherill plot of all zircon analyses and anchored intercept at 1.3 Ga; c) Wetherill plot of zircon analyses < 500 Ma selected for age calculation; d) Tera-Wasserburg plot of zircon analyses < 500 Ma selected for age calculation

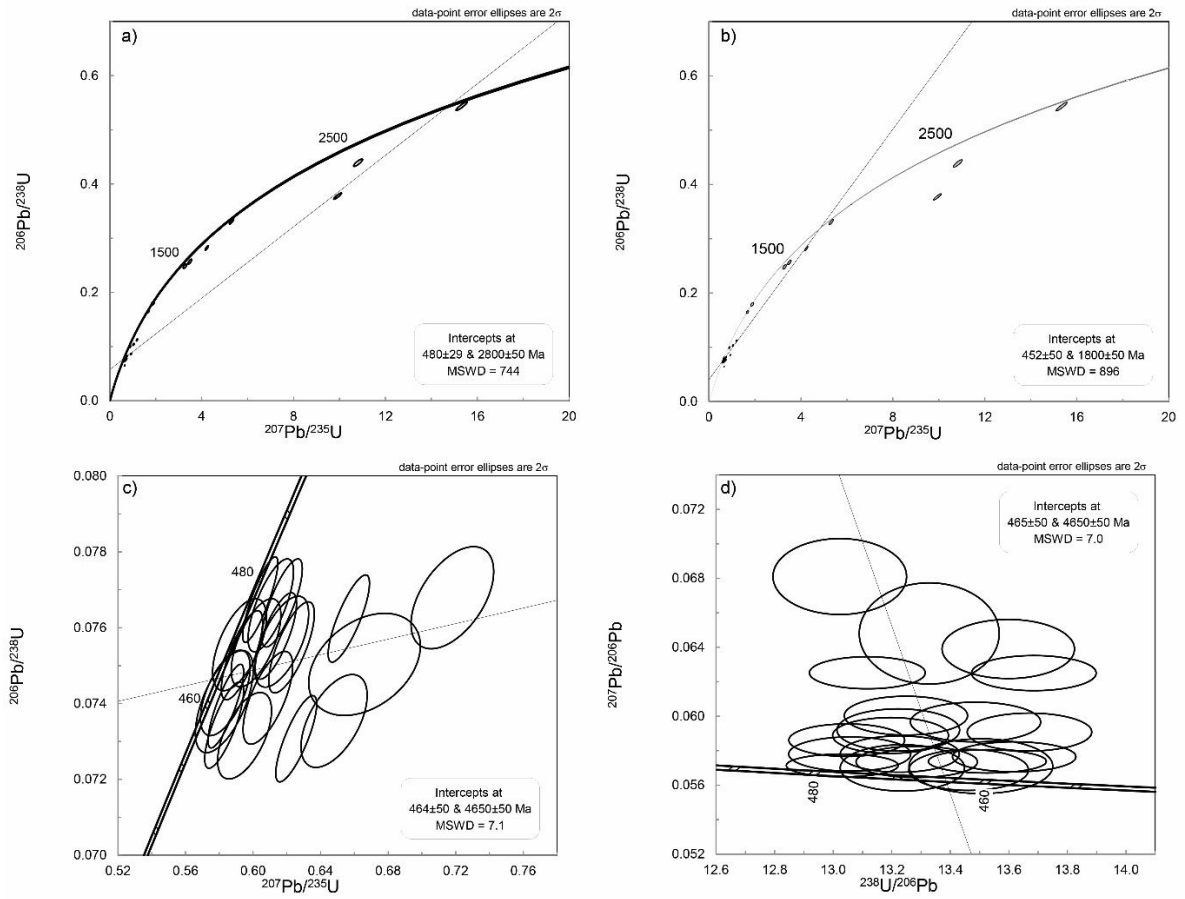

Figure 3 – Concordia plots of zircon isotope spot analyses of sample s1F a) Wetherill plot off all zircon analyses with anchored intercept at 2.8 Ga; b) Wetherill plot of all zircon alayses and anchored intercept at 1.8 Ga; c) Wetherill plot of zircon analyses < 500 Ma selected for age calculation; d) Tera-Wasserburg plot of zircon analyses < 500 Ma selected for age calculation

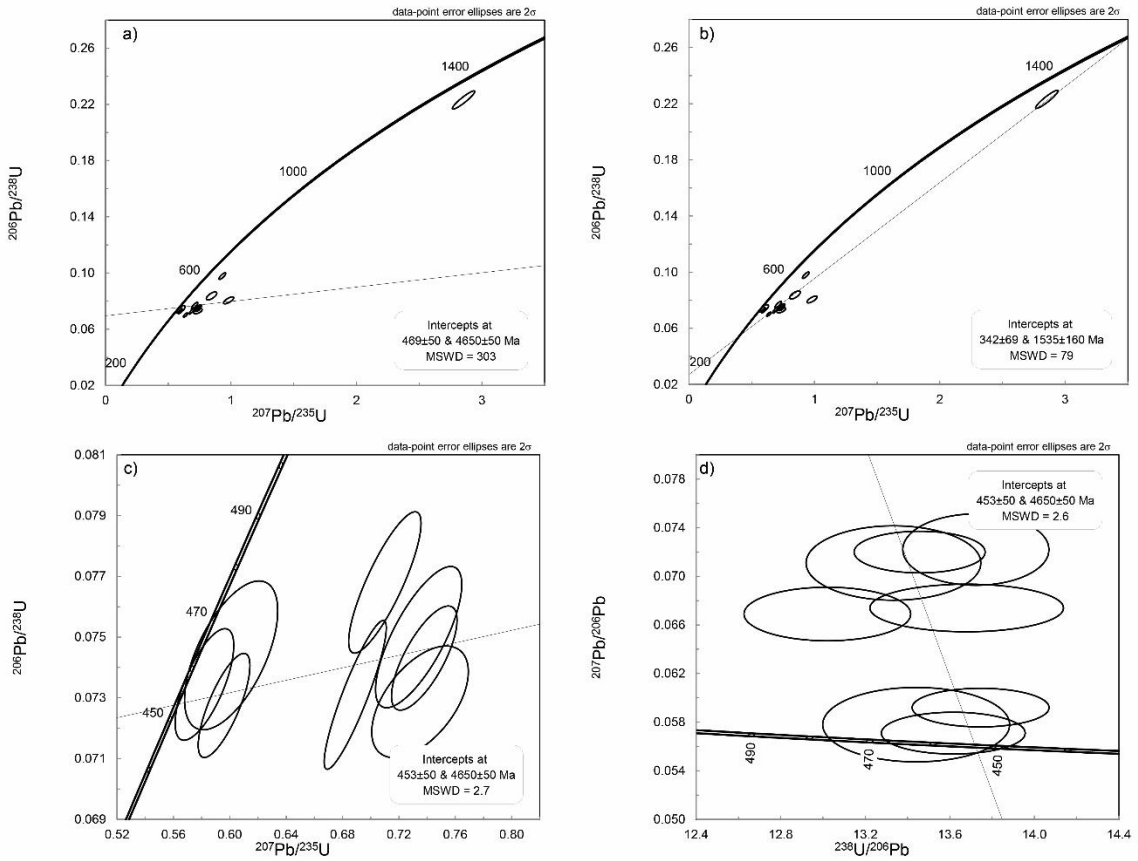

Figure 4 – Concordia plots of zircon isotope spot analyses of sample s1H a) Wetherill plot off all zircon analyses with anchored intercept at 4.65 Ga; b) Wetherill plot of all zircon analyses and anchored intercept at 1535 Ma; c) Wetherill plot of zircon analyses < 500 Ma selected for age calculation; d) Tera-Wasserburg plot of zircon analyses < 500 Ma selected for age calculation

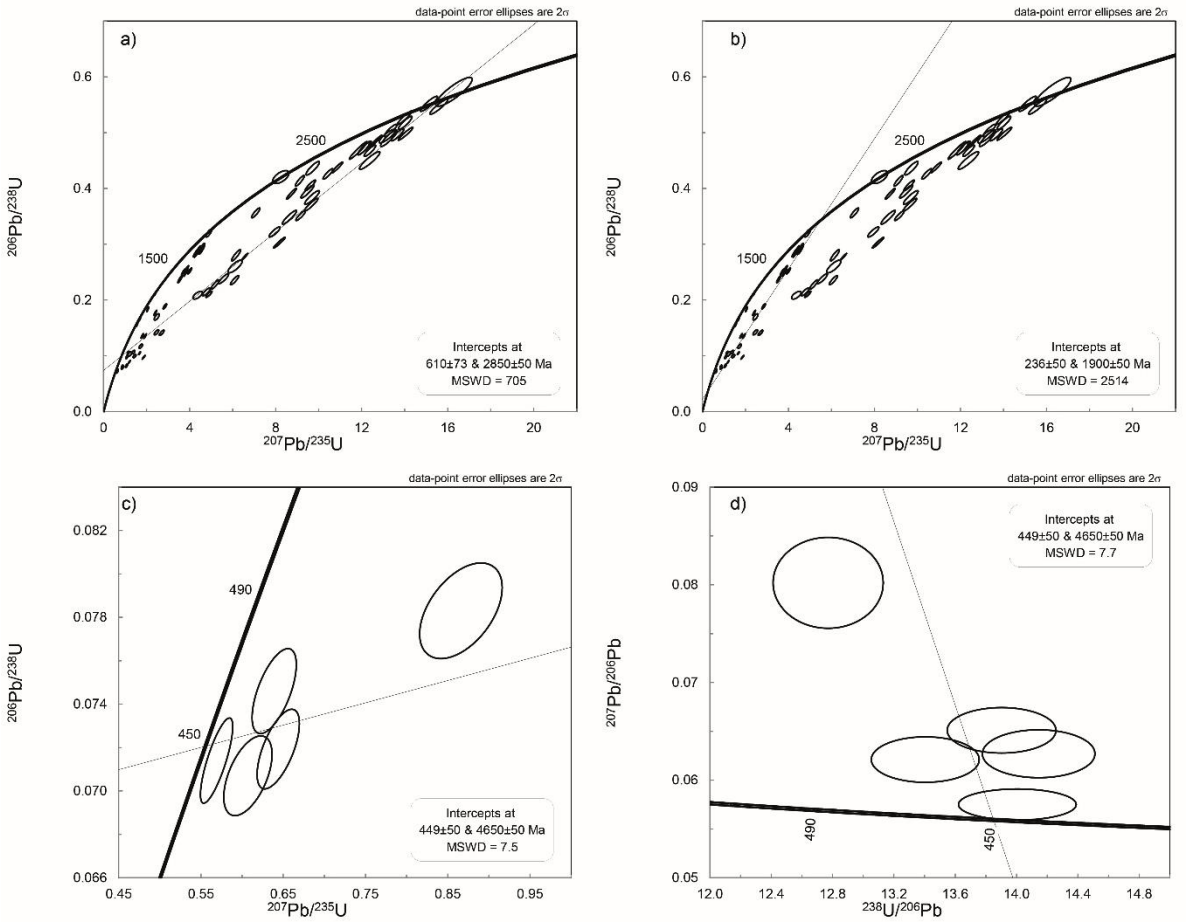

Figure 5 – Concordia plots of zircon isotope spot analyses of sample s2A a) Wetherill plot off all zircon analyses with anchored intercept at 2.85 Ga; b) Wetherill plot of all zircon analyses and anchored intercept at 1.9 Ga; c) Wetherill plot of zircon analyses < 500 Ma; d) Tera-Wasserburg plot of zircon analyses < 500 Ma

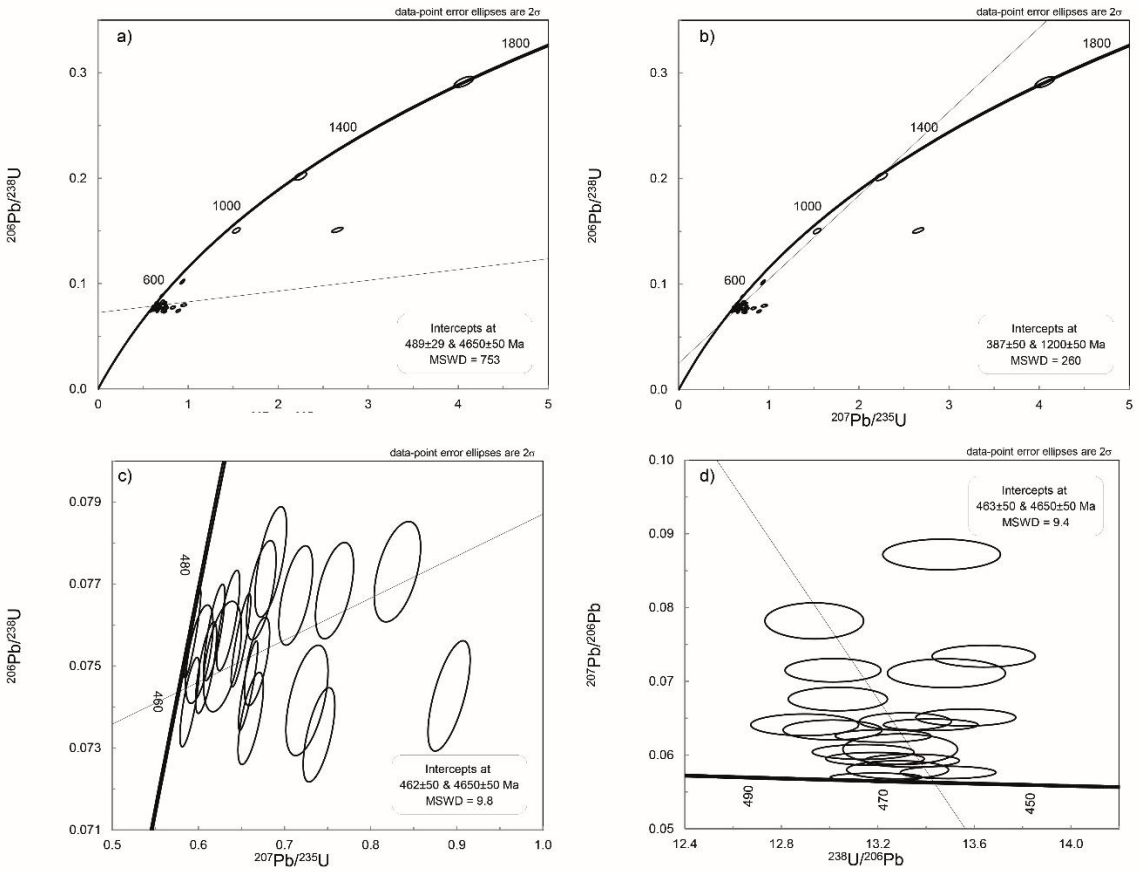

Figure 6 – Concordia plots of zircon isotope spot analyses of sample s2B a) Wetherill plot off all zircon analyses with anchored intercept at 4.65 Ga; b) Wetherill plot of all zircon analyses and anchored intercept at 1.2 Ga; c) Wetherill plot of zircon analyses < 500 Ma selected for age calculation; d) Tera-Wasserburg plot of zircon analyses < 500 Ma selected for age calculation

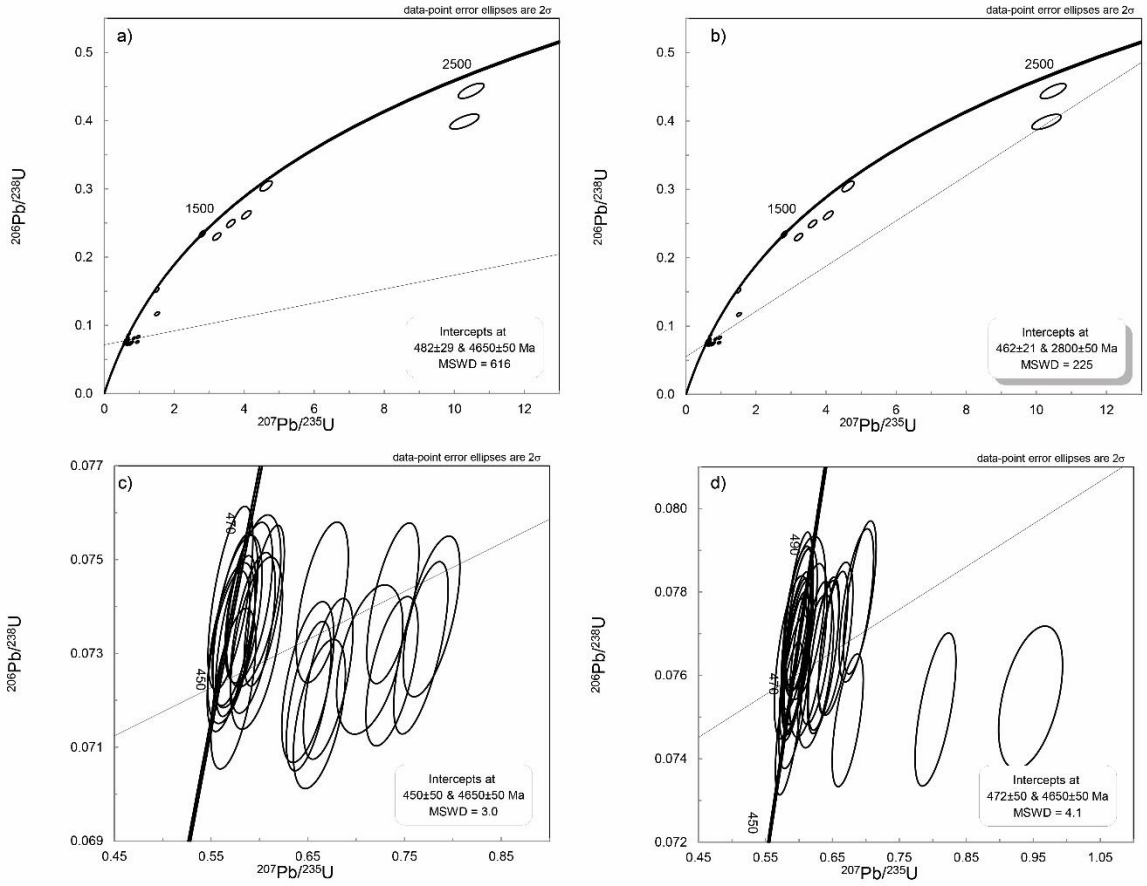

Figure 7 – Concordia plots of zircon isotope spot analyses of sample s3B a) Wetherill plot off all zircon analyses with anchored intercept at 4.65 Ga; b) Wetherill plot of all zircon analyses and anchored intercept at 2.8 Ga; c) Wetherill plot of zircon analyses < 500 Ma selected for age calculation of s3B-1; d) Wetherill plot of zircon analyses < 500 Ma selected for age calculation of s3B-2

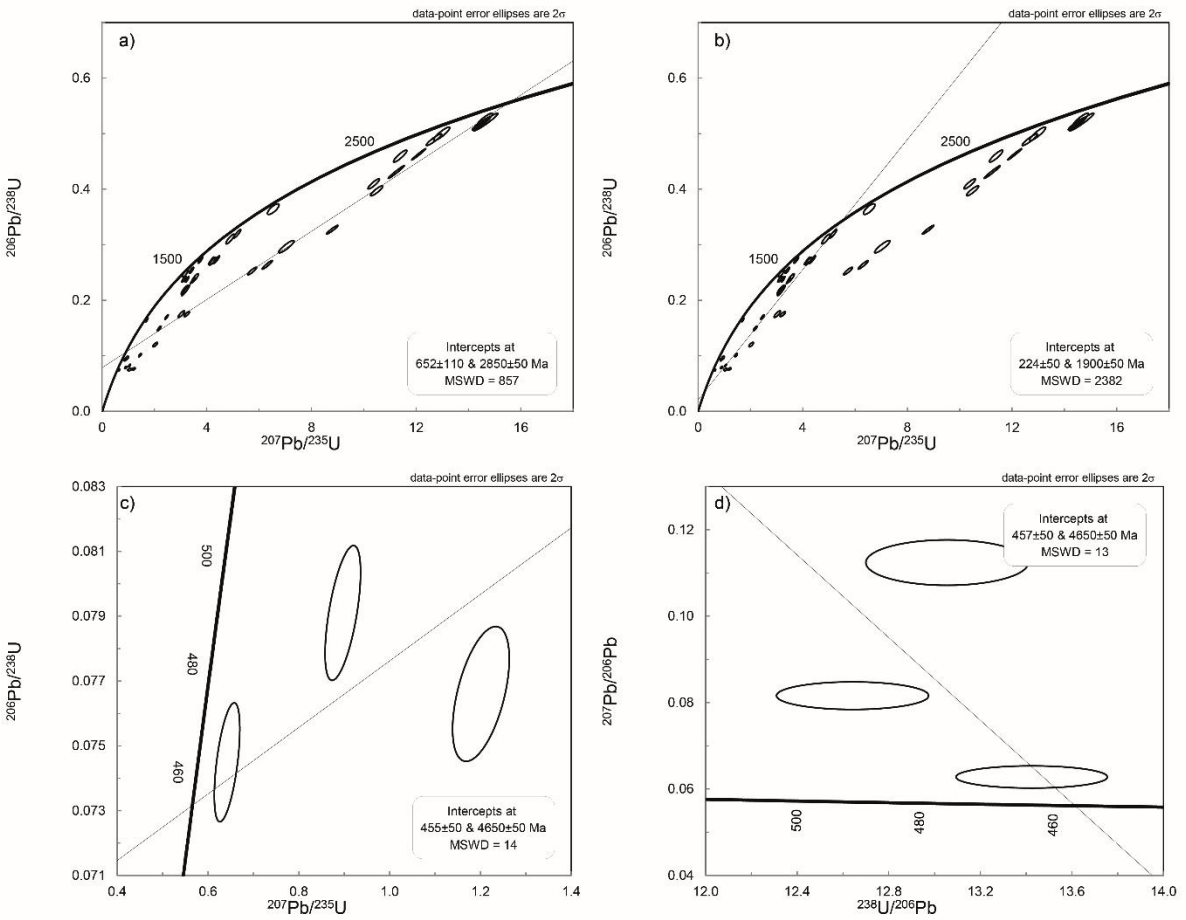

Figure 8 – Concordia plots of zircon isotope spot analyses of sample s4D a) Wetherill plot off all zircon analyses with anchored intercept at 2.85 Ga; b) Wetherill plot of all zircon analyses and anchored intercept at 1.9 Ga; c) Wetherill plot of zircon analyses < 500 Ma; d) Tera-Wasserburg plot of zircon analyses < 500 Ma

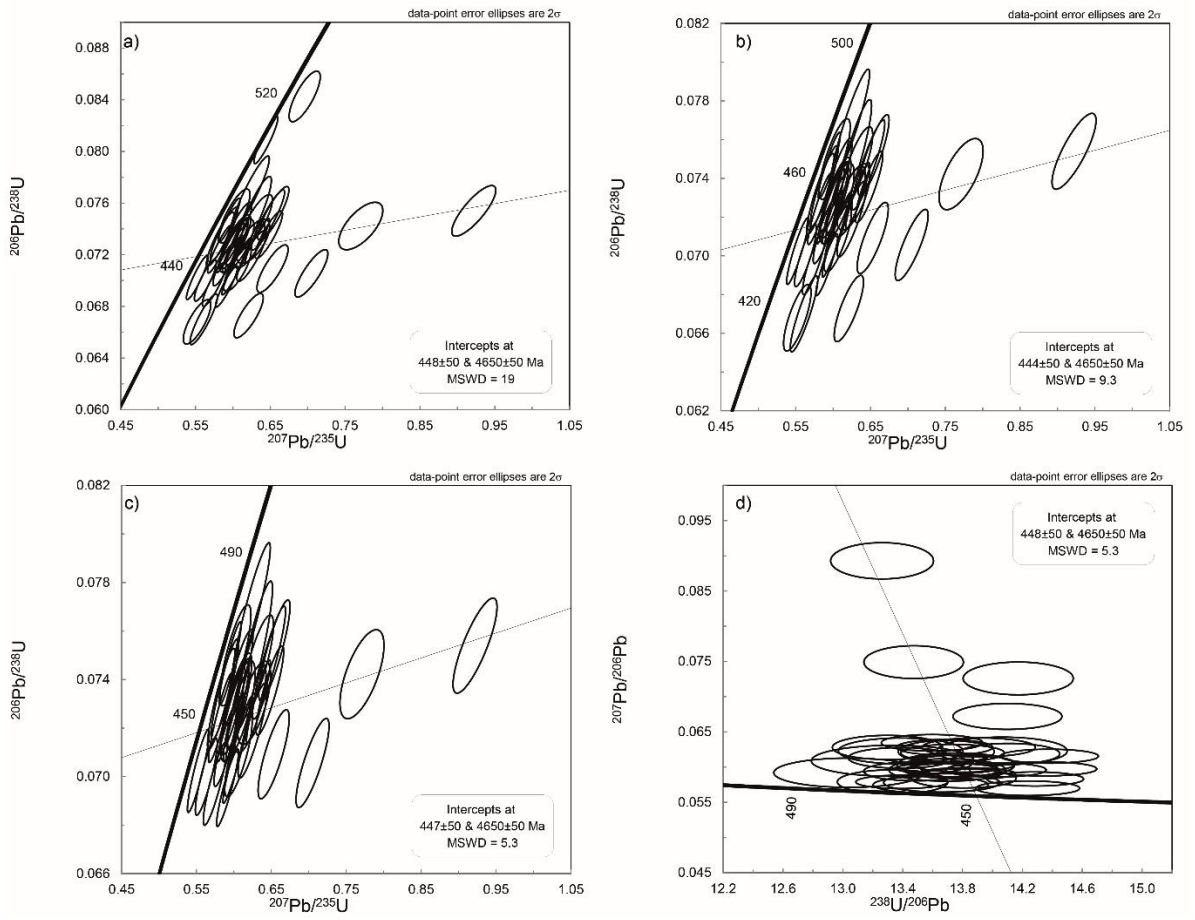

Figure 9 – Concordia plots of zircon isotope spot analyses of sample s5A a) Wetherill plot off all zircon analyses with anchored intercept at 4.65 Ga; b) Wetherill plot of zircon analyses < 500 Ma anchored at 4.65 Ga; c) Wetherill plot of zircon analyses < 500 Ma selected for age calculation; d) Tera-Wasserburg plot of zircon analyses < 500 Ma selected for age calculation

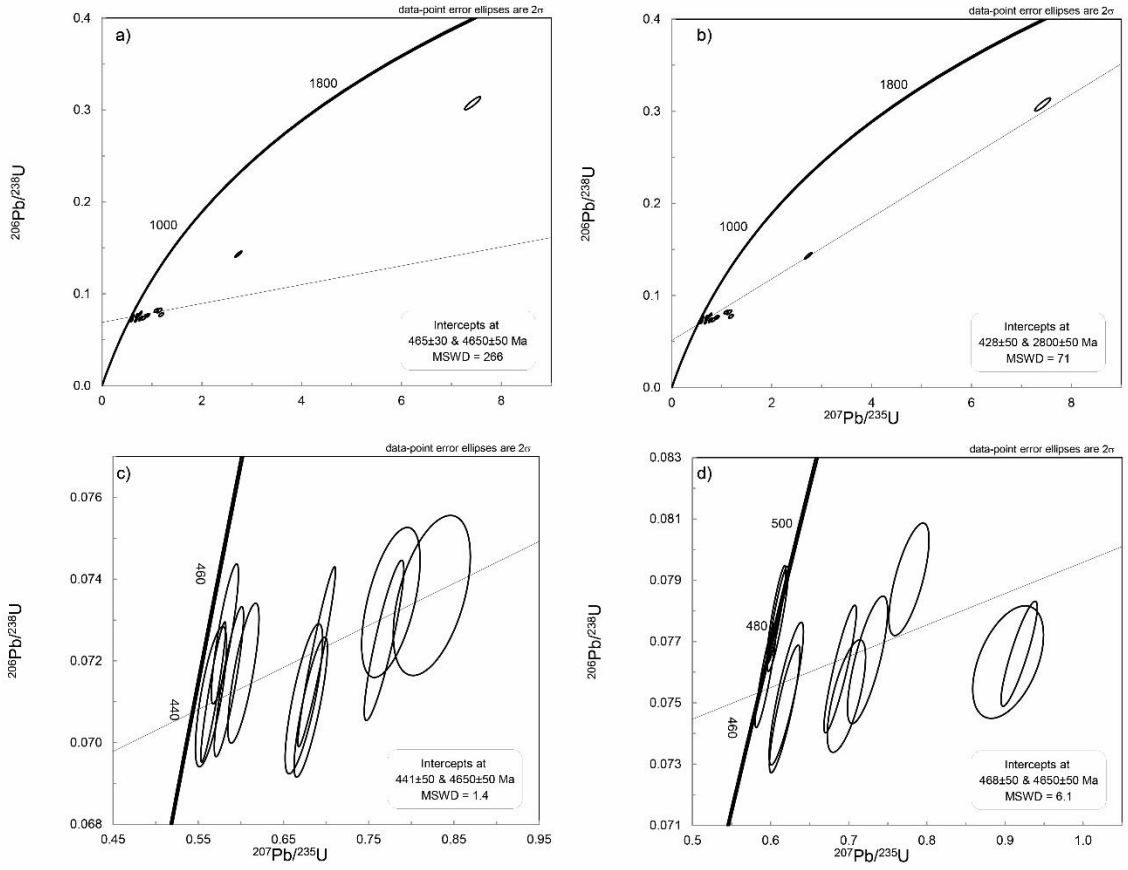

Figure 10 – Concordia plots of zircon isotope spot analyses of sample s5Ba a) Wetherill plot off all zircon analyses with anchored intercept at 4.65 Ga; b) Wetherill plot of all zircon analyses and anchored intercept at 2.8 Ga; c) Wetherill plot of zircon analyses < 500 Ma selected for age calculation of s5Ba-1; d) Wetherill plot of zircon analyses < 500 Ma selected for age calculation of s5Ba-2

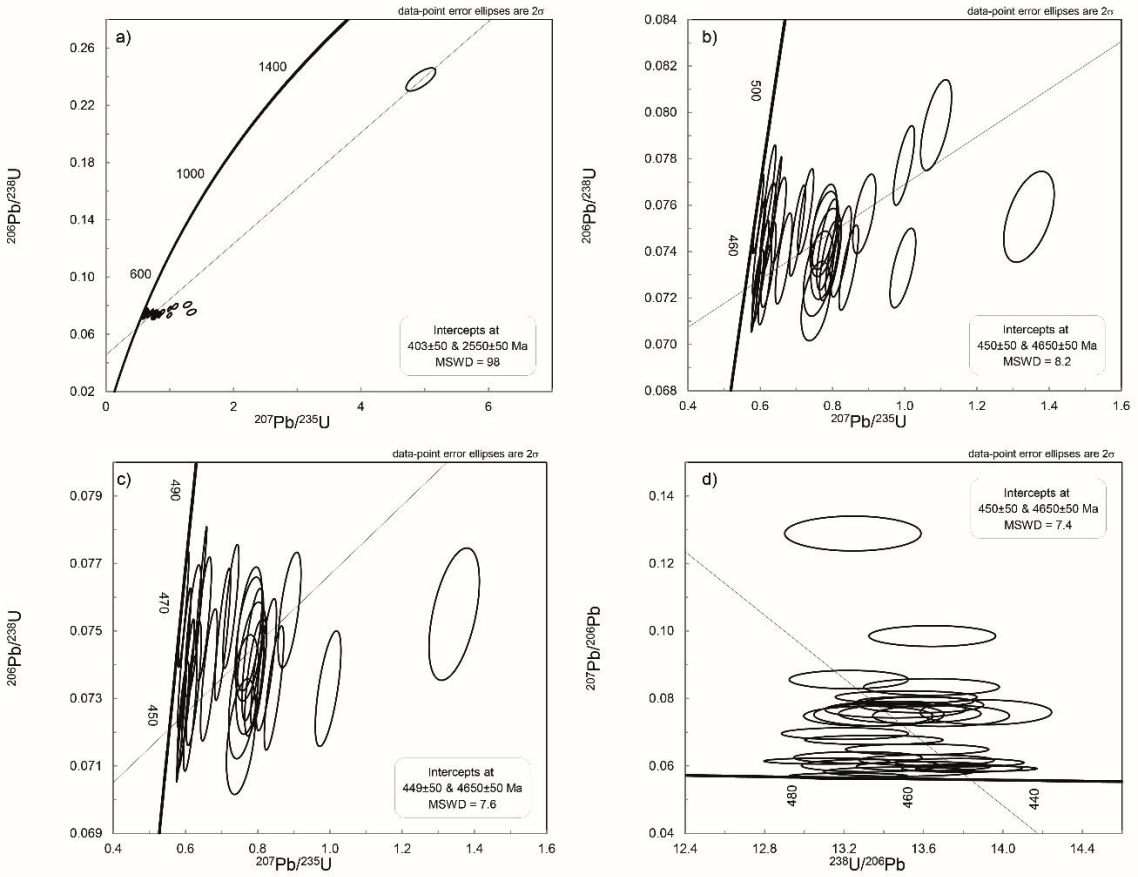

Figure 11 – Concordia plots of zircon isotope spot analyses of sample s5Bb a) Wetherill plot off all zircon analyses with anchored intercept at 2.55 Ga; b) Wetherill plot of zircon analyses < 500 Ma and anchored intercept at 4.65 Ga; c) Wetherill plot of zircon analyses < 500 Ma selected for age calculation; d) Tera-Wasserburg plot of zircon analyses < 500 Ma selected for age calculation

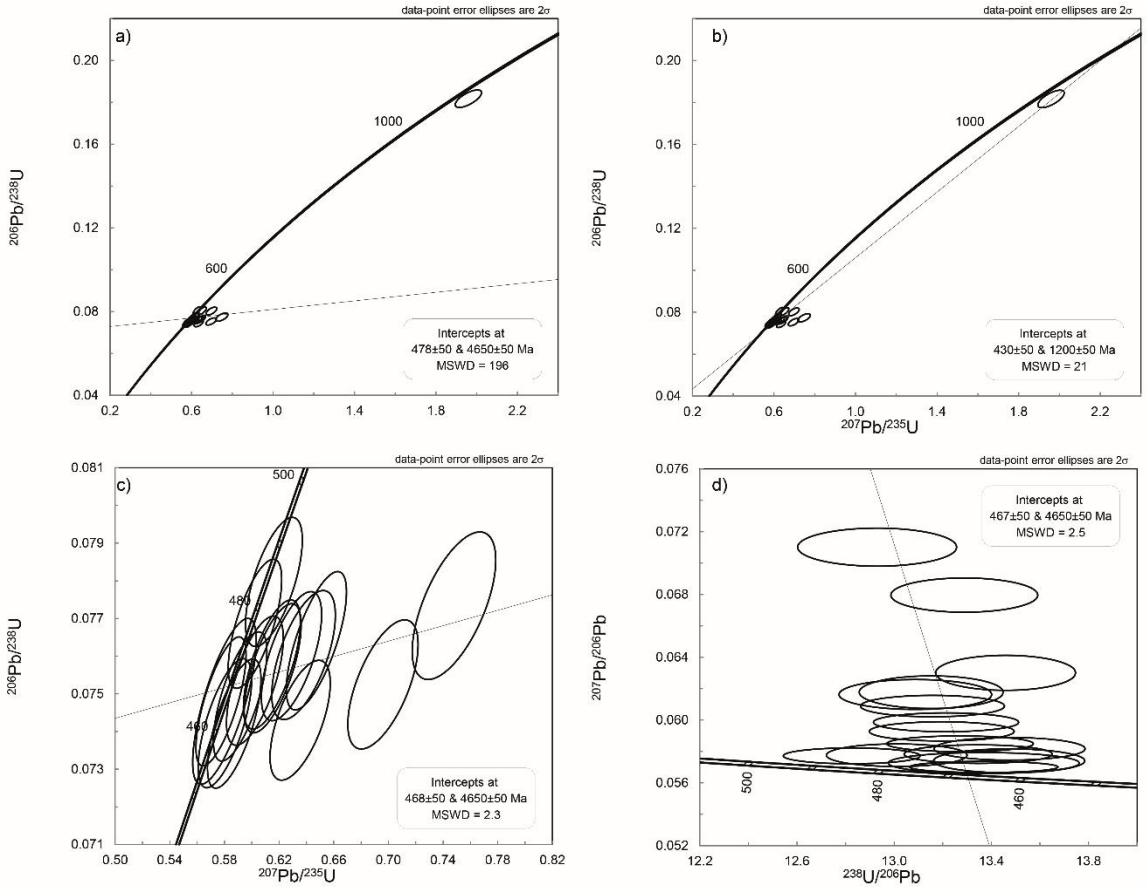

Figure 12 – Concordia plots of zircon isotope spot analyses of sample s7A a) Wetherill plot off all zircon analyses with anchored intercept at 4.65 Ga; b) Wetherill plot of all zircon analyses and anchored intercept at 1.2 Ga; c) Wetherill plot of zircon analyses < 500 Ma selected for age calculation; d) Tera-Wasserburg plot of zircon analyses < 500 Ma selected for age calculation

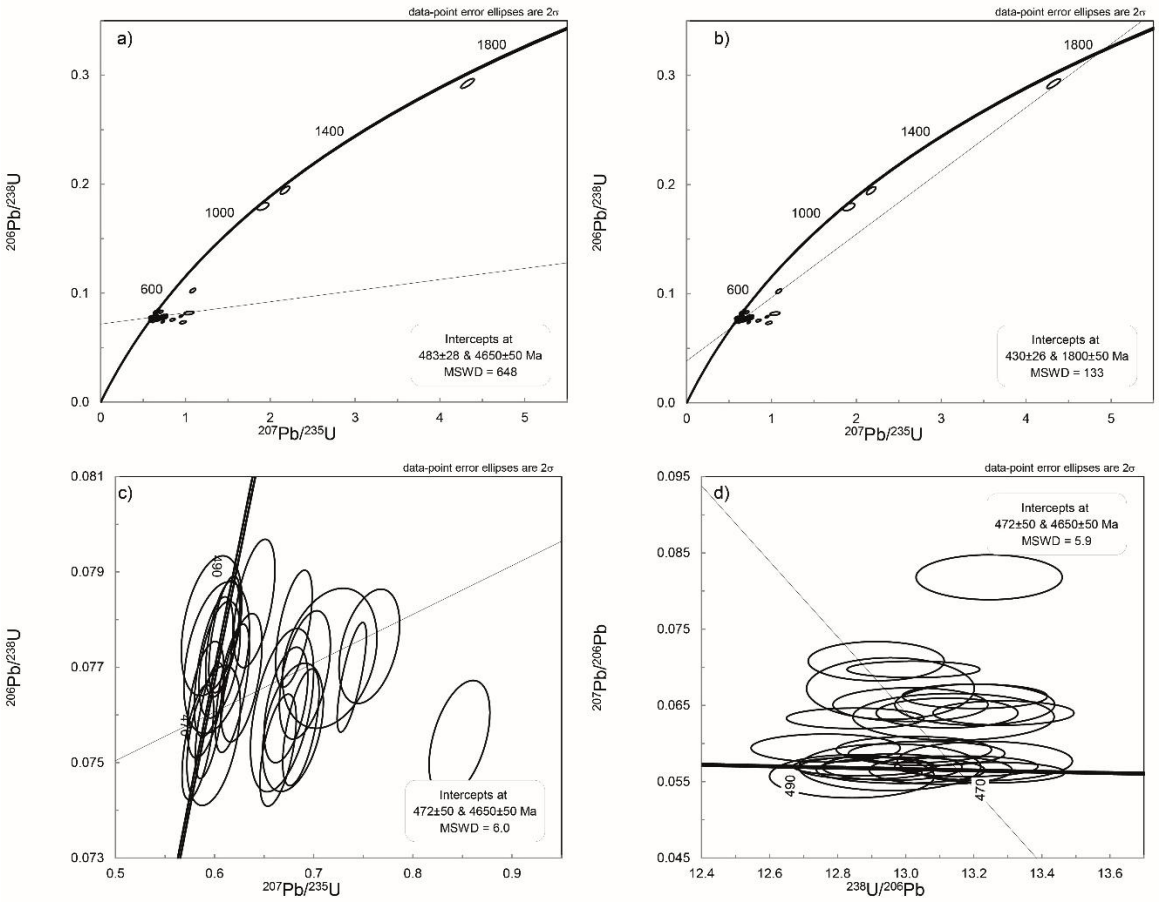

Figure 13 – Concordia plots of zircon isotope spot analyses of sample s7B a) Wetherill plot off all zircon analyses with anchored intercept at 4.65 Ga; b) Wetherill plot of all zircon analyses and anchored intercept at 1.8 Ga; c) Wetherill plot of zircon analyses < 500 Ma selected for age calculation; d) Tera-Wasserburg plot of zircon analyses < 500 Ma selected for age calculation

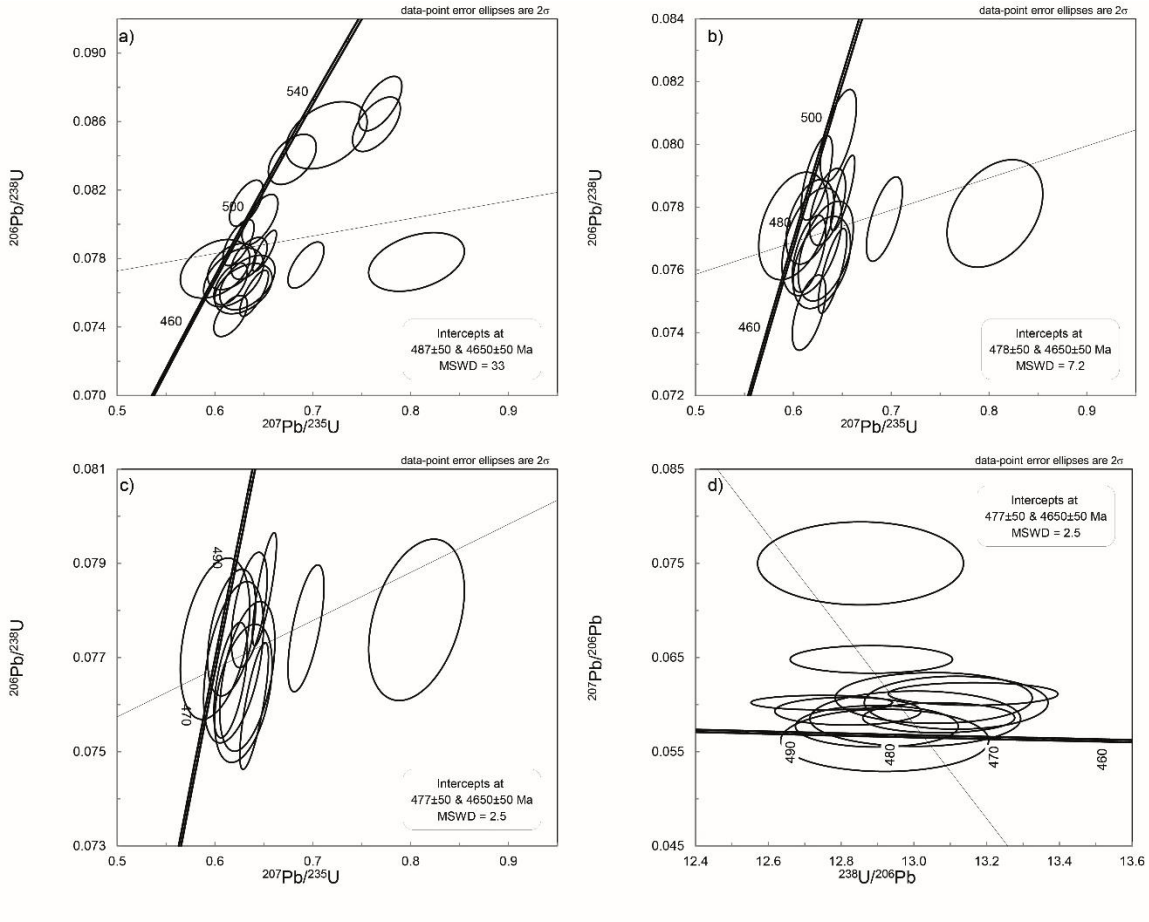

Figure 14 – Concordia plots of zircon isotope spot analyses of sample s8Da a) Wetherill plot of all zircon analyses with anchored intercept at 4.65 Ga; b) Wetherill plot of zircon analyses < 500 Ma and anchored intercept at 4.65 Ga; c) Wetherill plot of zircon analyses < 500 Ma selected for age calculation; d) Tera-Wasserburg plot of zircon analyses < 500 Ma selected for age calculation

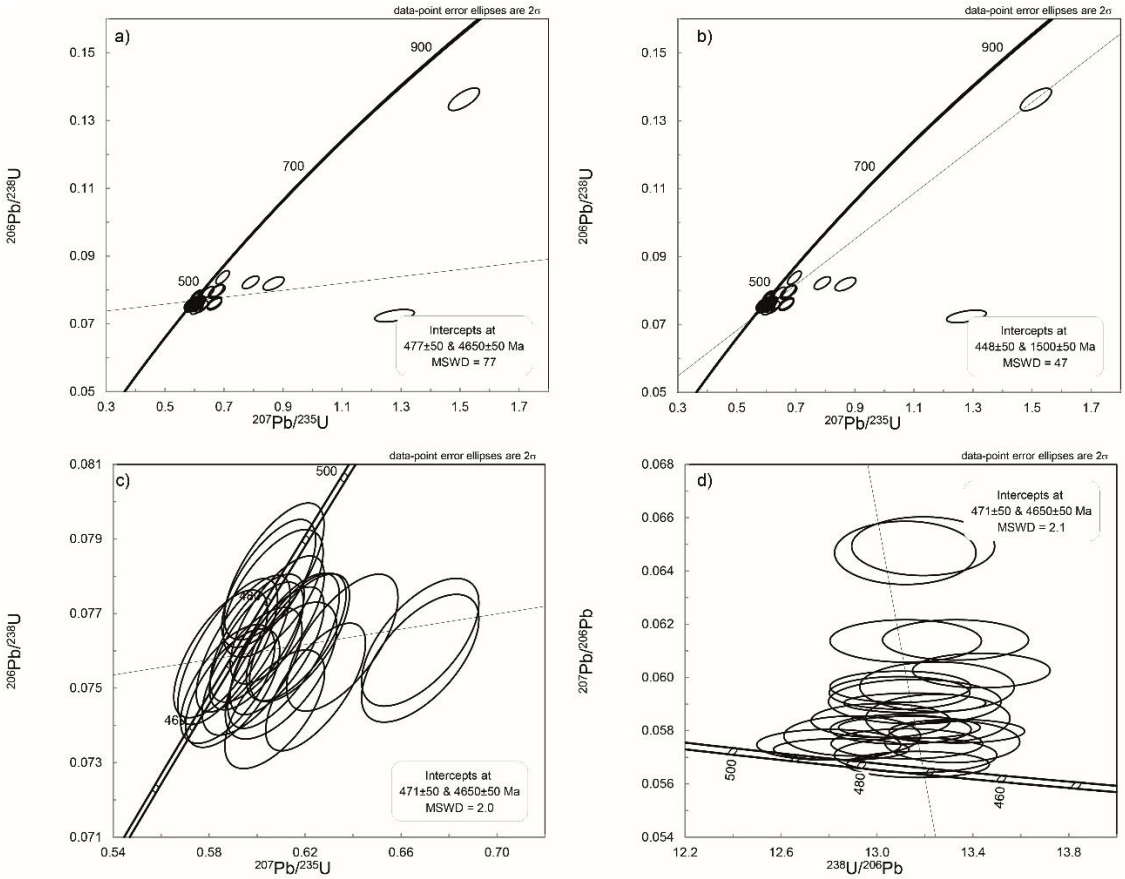

Figure 15 – Concordia plots of zircon isotope spot analyses of sample s8Db a) Wetherill plot of all zircon analyses with anchored intercept at 4.65 Ga; b) Wetherill plot of zircon analyses < 500 Ma and anchored intercept at 1.5 Ga; c) Wetherill plot of zircon analyses < 500 Ma selected for age calculation; d) Tera-Wasserburg plot of zircon analyses < 500 Ma selected for age calculation

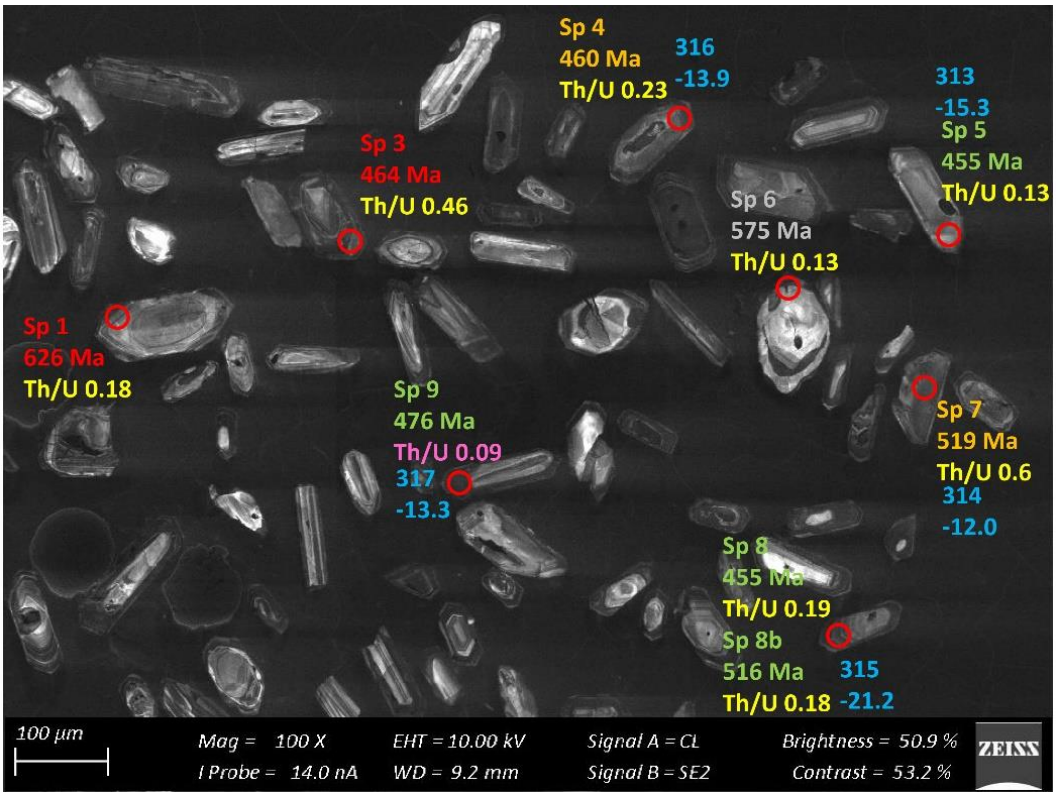

Figure 16 – Zircon Isotope spot analyses of sample s1B; U-Pb analyses are colour coded according to concordance; blue writing indicates the Hf identifier with the respective εHf_{468} values

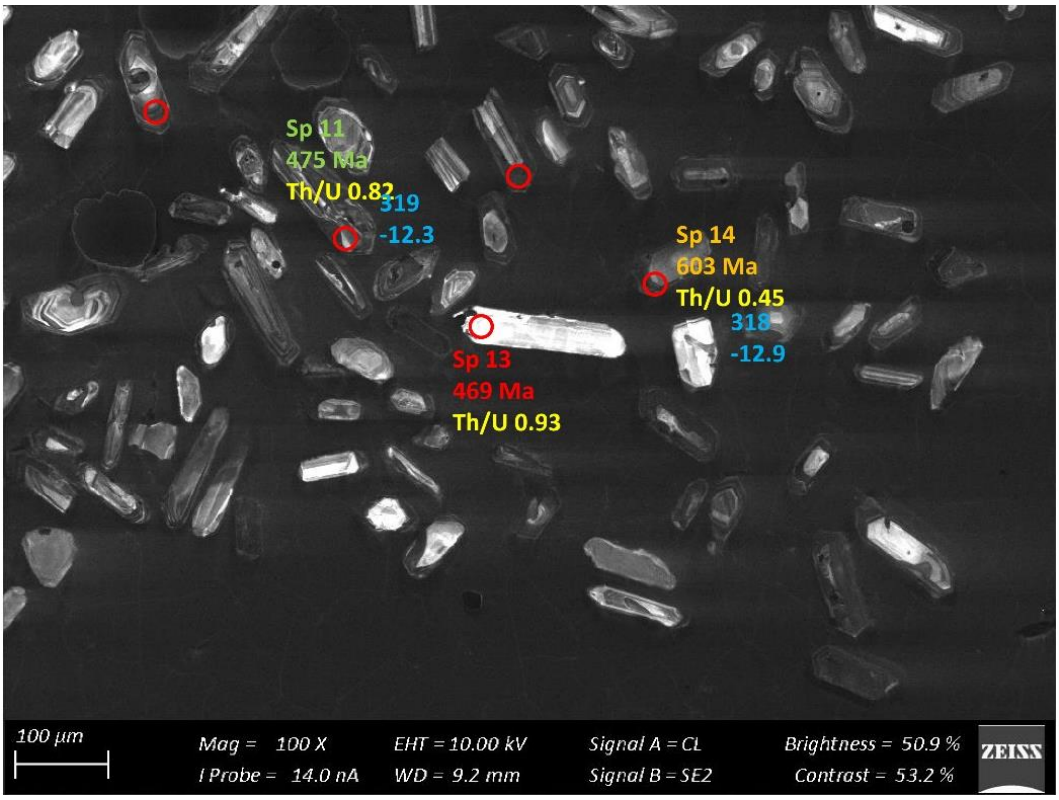

Figure 17 – Zircon Isotope spot analyses of sample s1B; U-Pb analyses are colour coded according to concordance; blue writing indicates the Hf identifier with the respective εHf_{468} values

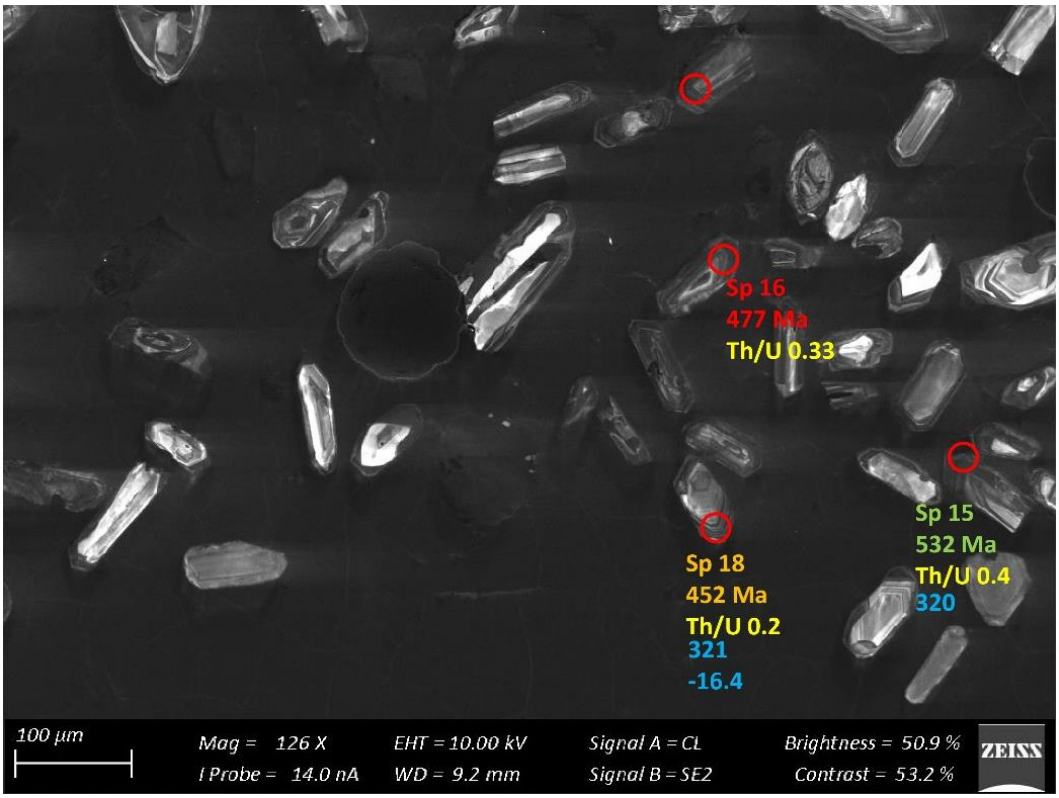

Figure 18 – Zircon Isotope spot analyses of sample s1B; U-Pb analyses are colour coded according to concordance; blue writing indicates the Hf identifier with the respective εHf_{468} values

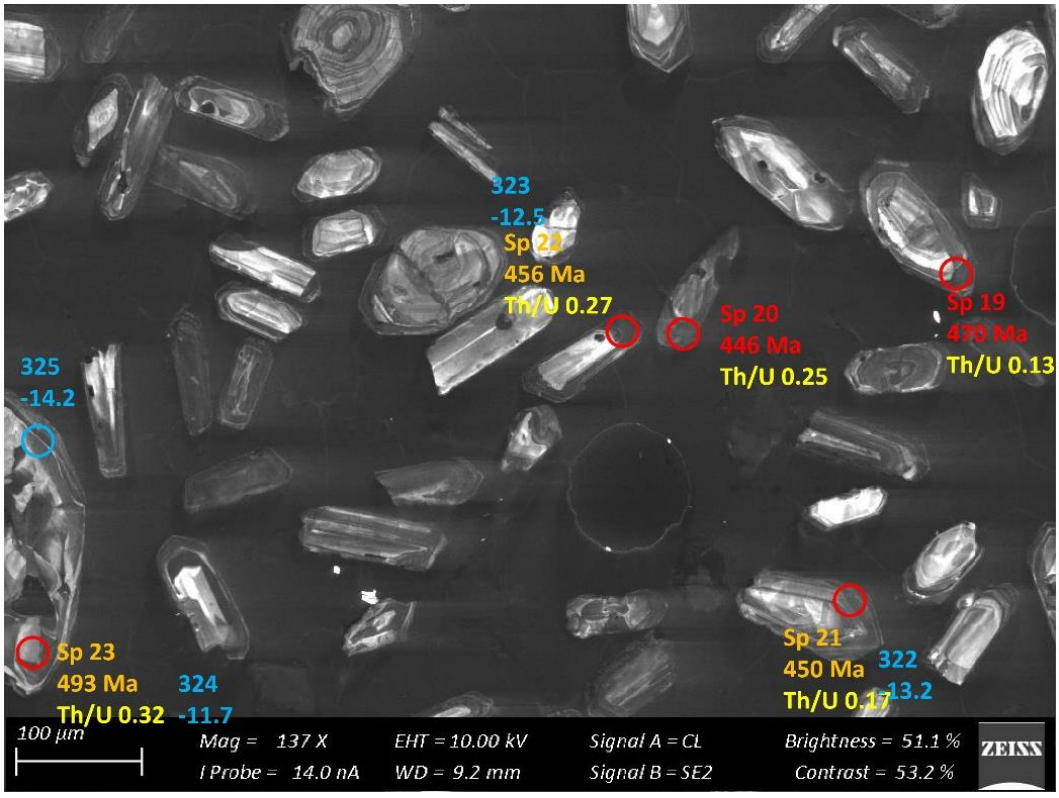

Figure 19 – Zircon Isotope spot analyses of sample s1B; U-Pb analyses are colour coded according to concordance; blue writing indicates the Hf identifier with the respective εHf_{468} values

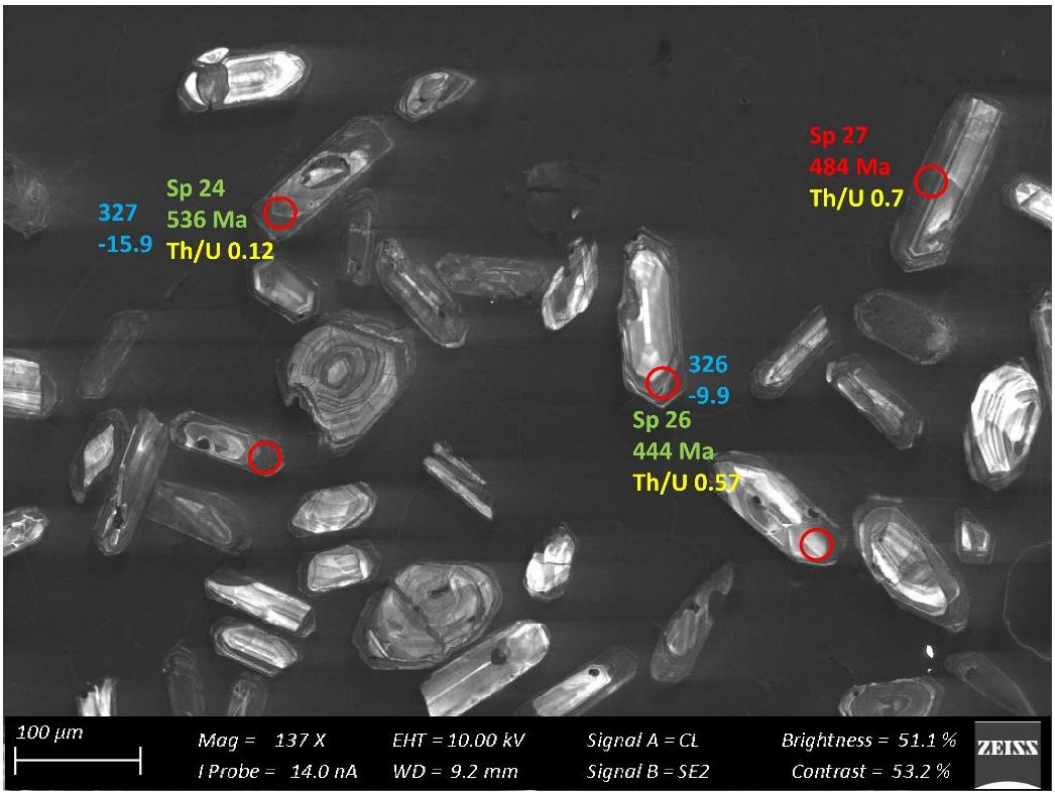

Figure 20 – Zircon Isotope spot analyses of sample s1B; U-Pb analyses are colour coded according to concordance; blue writing indicates the Hf identifier with the respective εHf_{468} values

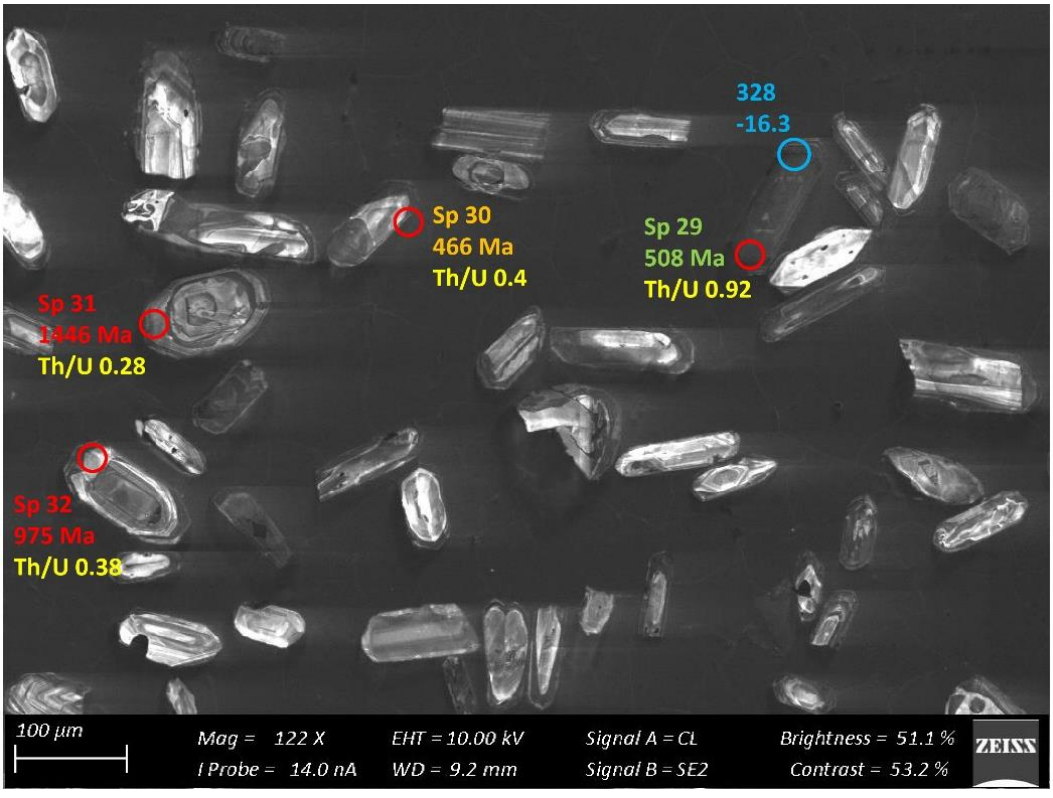

Figure 21 – Zircon Isotope spot analyses of sample s1B; U-Pb analyses are colour coded according to concordance; blue writing indicates the Hf identifier with the respective εHf_{468} values

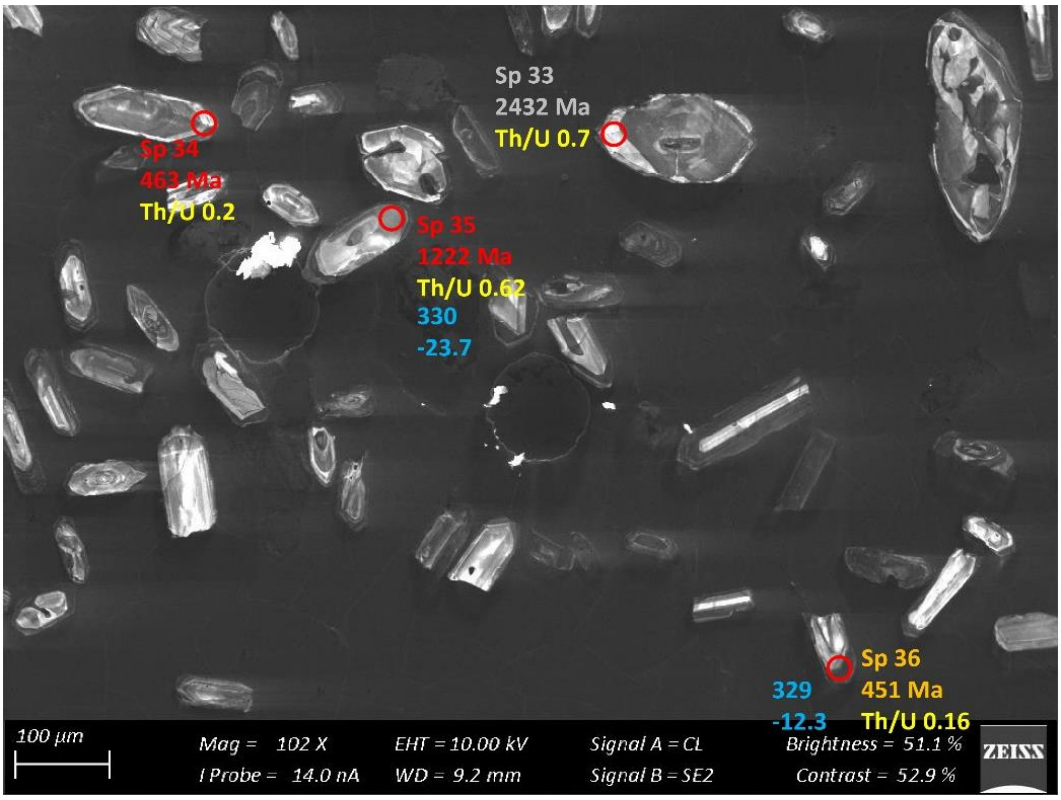

Figure 22 – Zircon Isotope spot analyses of sample s1B; U-Pb analyses are colour coded according to concordance; blue writing indicates the Hf identifier with the respective εHf_{468} values

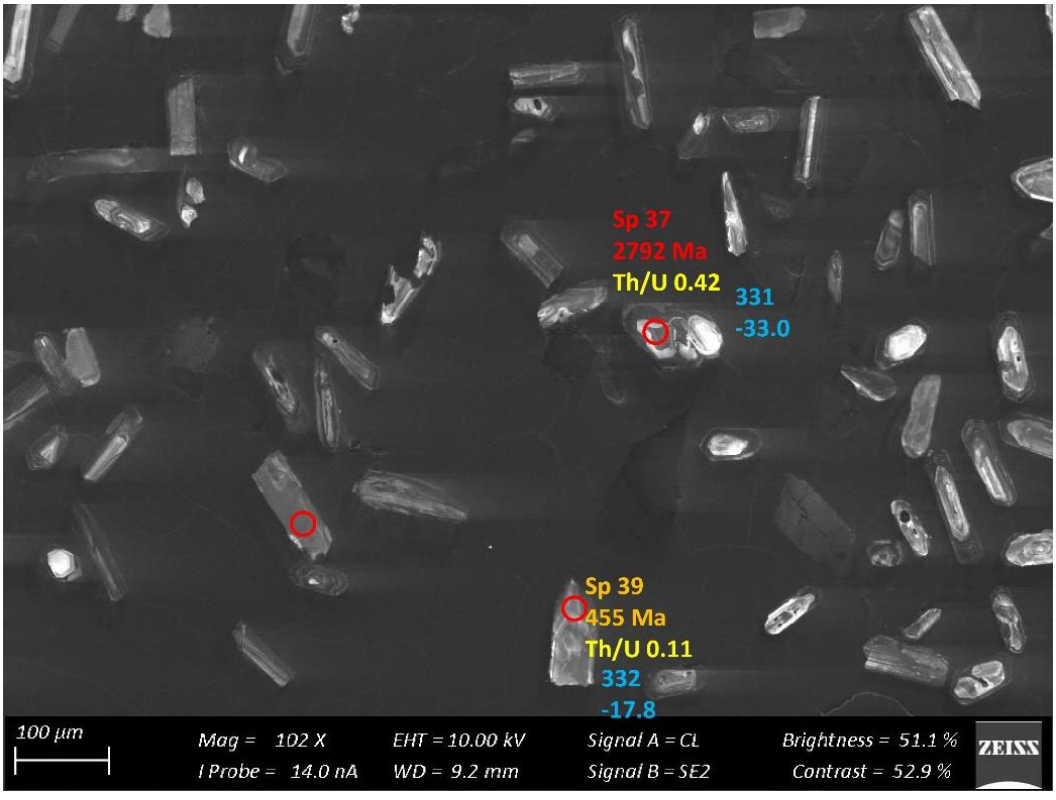

Figure 23 – Zircon Isotope spot analyses of sample s1B; U-Pb analyses are colour coded according to concordance; blue writing indicates the Hf identifier with the respective εHf_{468} values

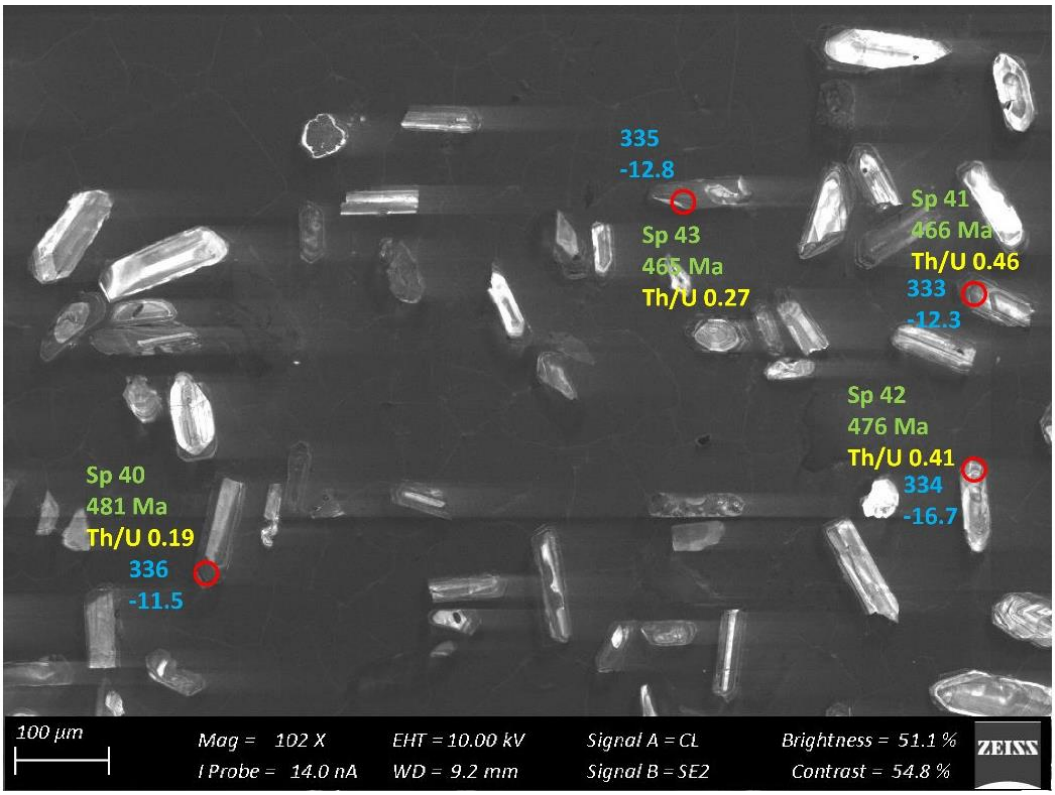

Figure 24 – Zircon Isotope spot analyses of sample s1B; U-Pb analyses are colour coded according to concordance; blue writing indicates the Hf identifier with the respective εHf_{468} values

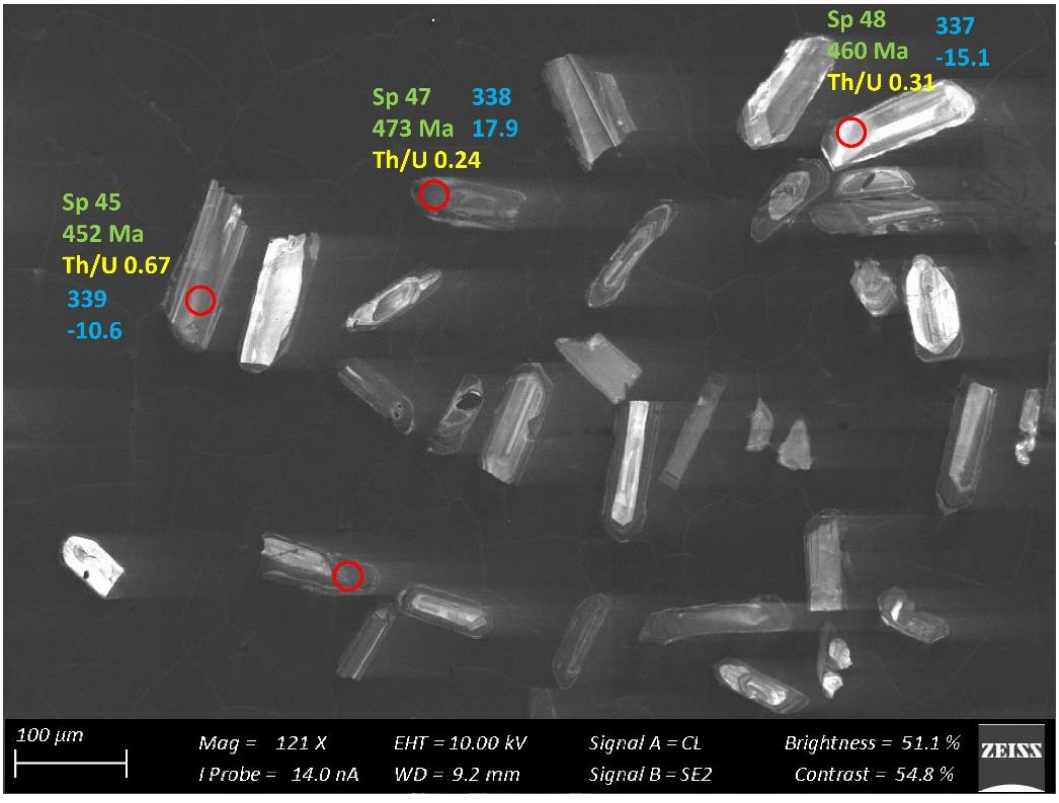

Figure 25 – Zircon Isotope spot analyses of sample s1B; U-Pb analyses are colour coded according to concordance; blue writing indicates the Hf identifier with the respective εHf_{468} values

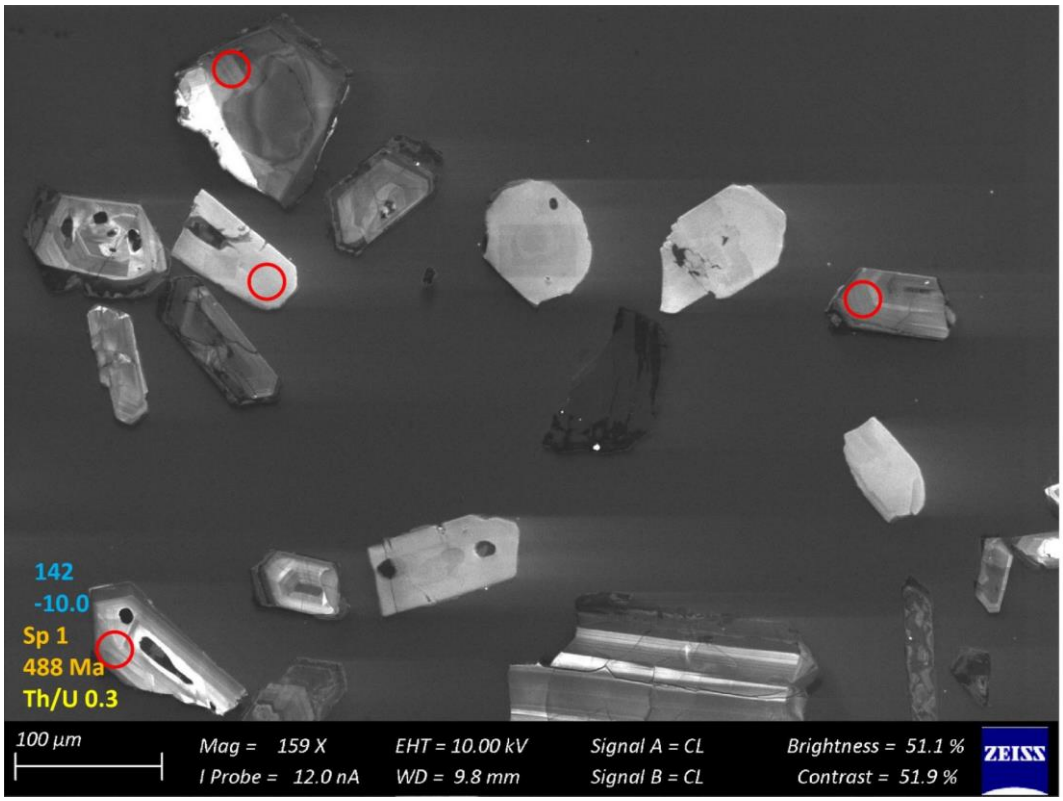

Figure 26 – Zircon Isotope spot analyses of sample s1Da; U-Pb analyses are colour coded according to concordance; blue writing indicates the Hf identifier with the respective εHf_{468} values

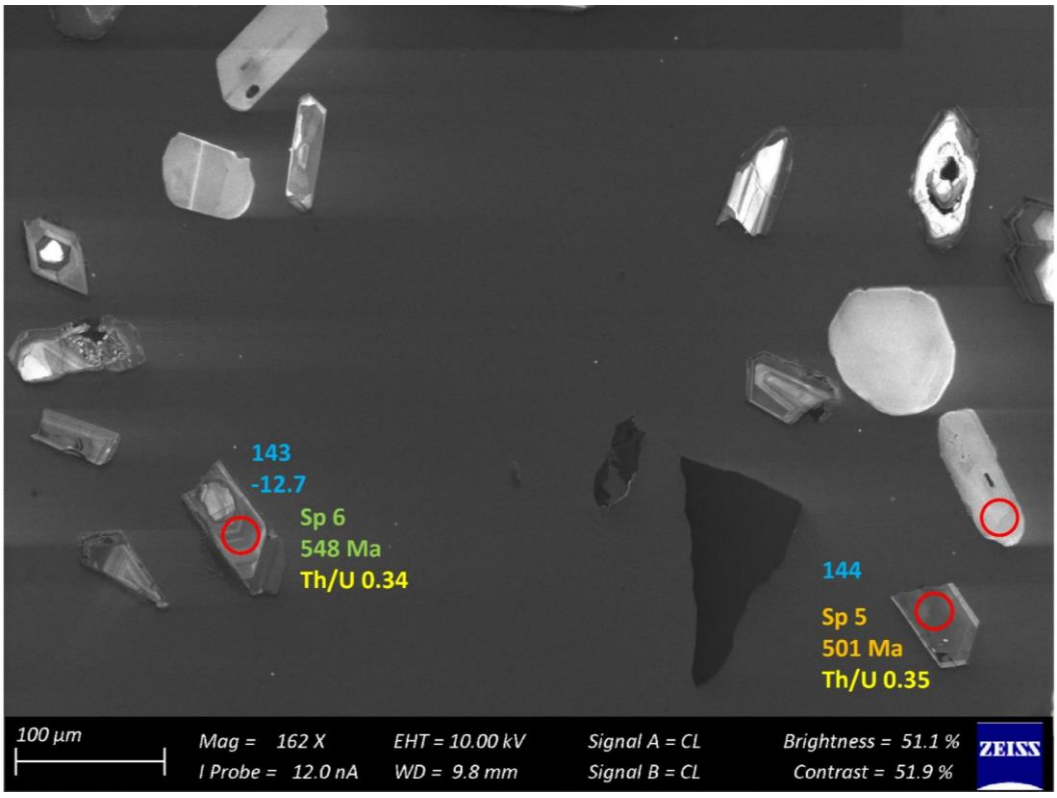

Figure 27 – Zircon Isotope spot analyses of sample s1Da; U-Pb analyses are colour coded according to concordance; blue writing indicates the Hf identifier with the respective εHf_{468} values

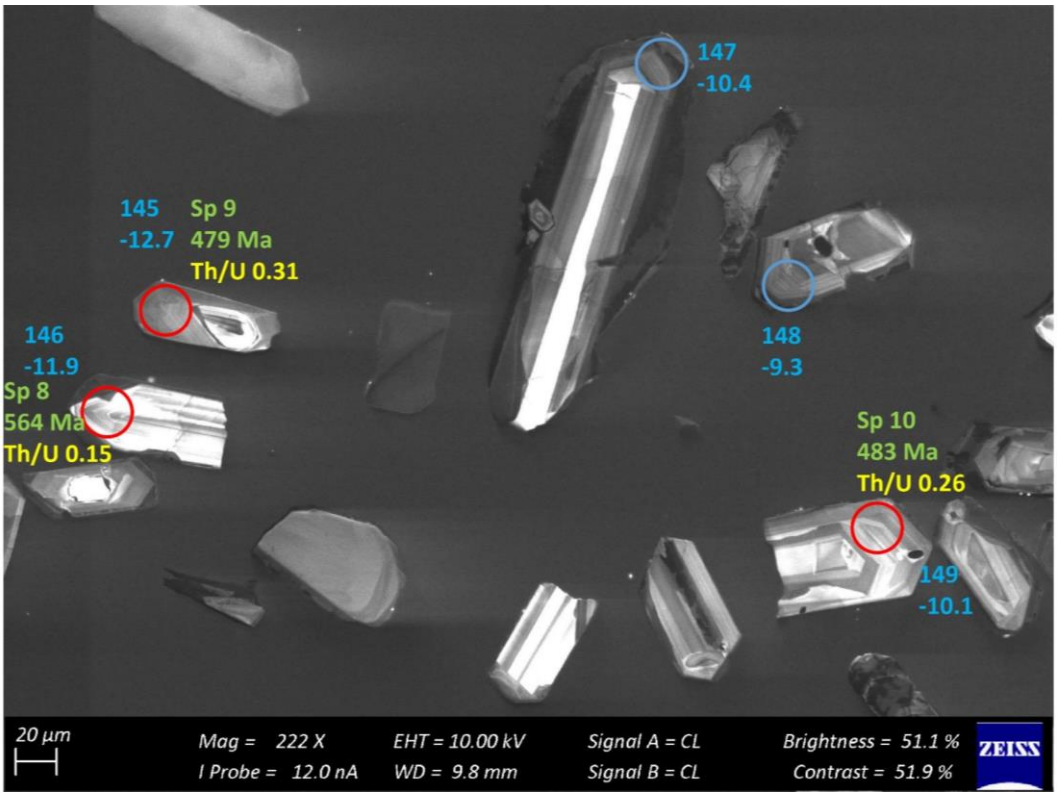

Figure 28 – Zircon Isotope spot analyses of sample s1Da; U-Pb analyses are colour coded according to concordance; blue writing indicates the Hf identifier with the respective εHf_{468} values

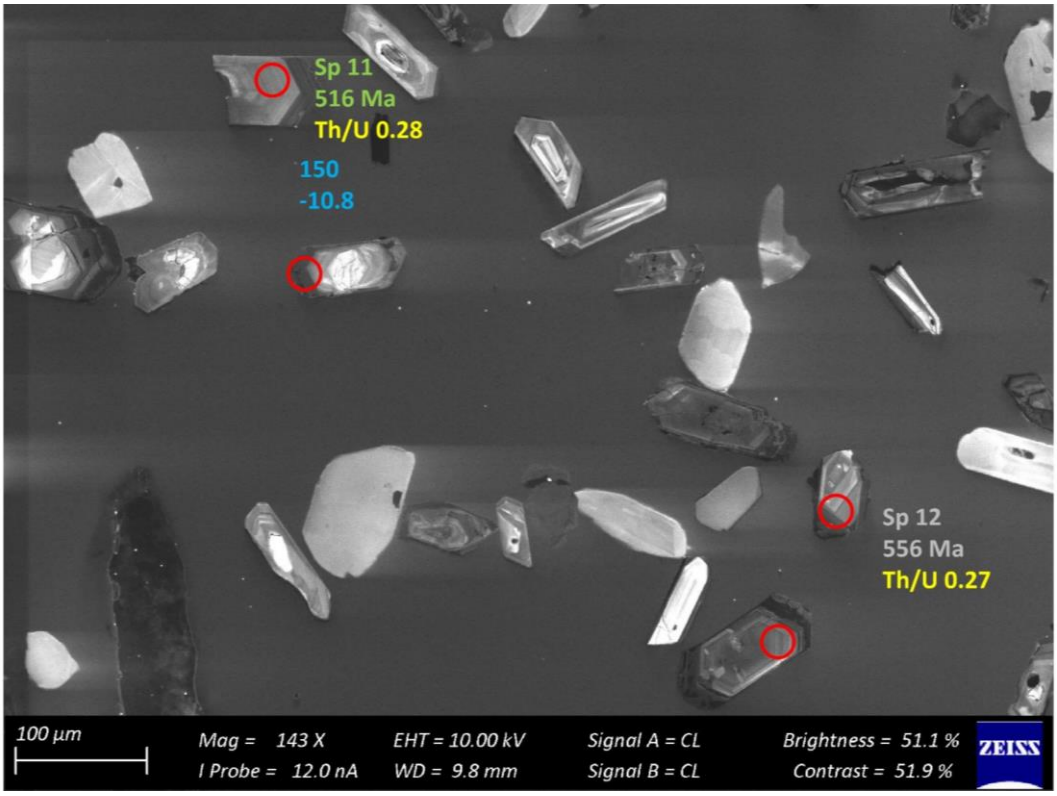

Figure 29 – Zircon Isotope spot analyses of sample s1Da; U-Pb analyses are colour coded according to concordance; blue writing indicates the Hf identifier with the respective εHf_{468} values

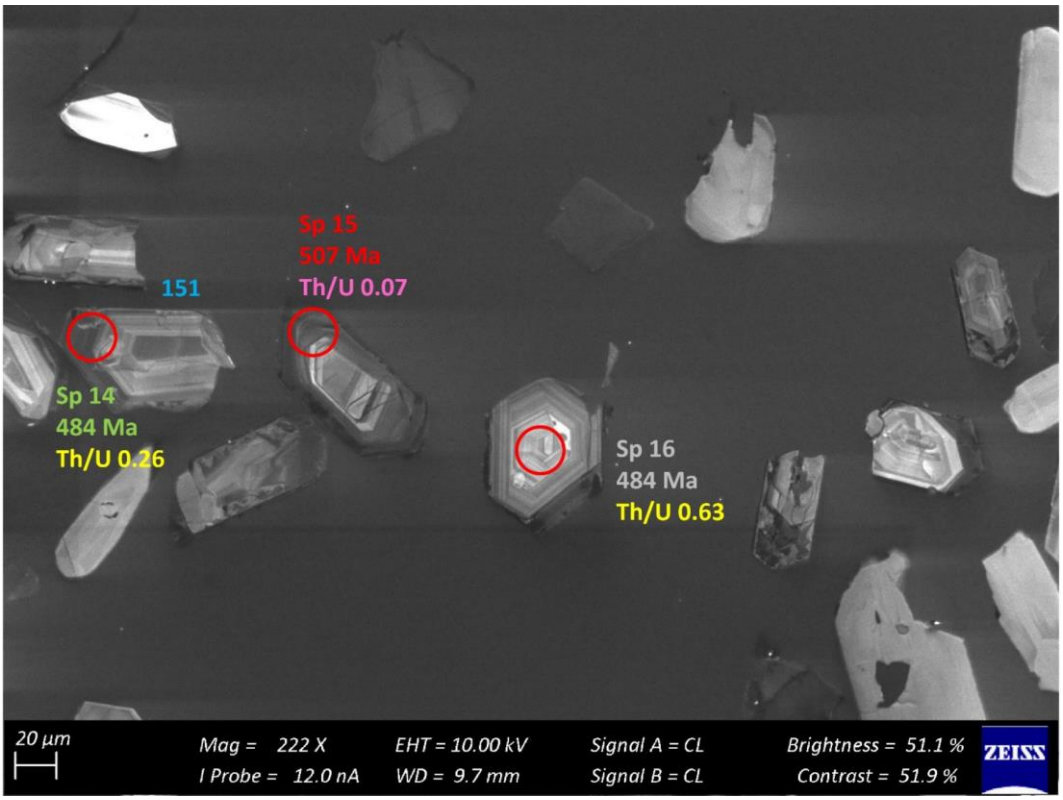

Figure 30 – Zircon Isotope spot analyses of sample s1Da; U-Pb analyses are colour coded according to concordance; blue writing indicates the Hf identifier with the respective εHf_{468} values

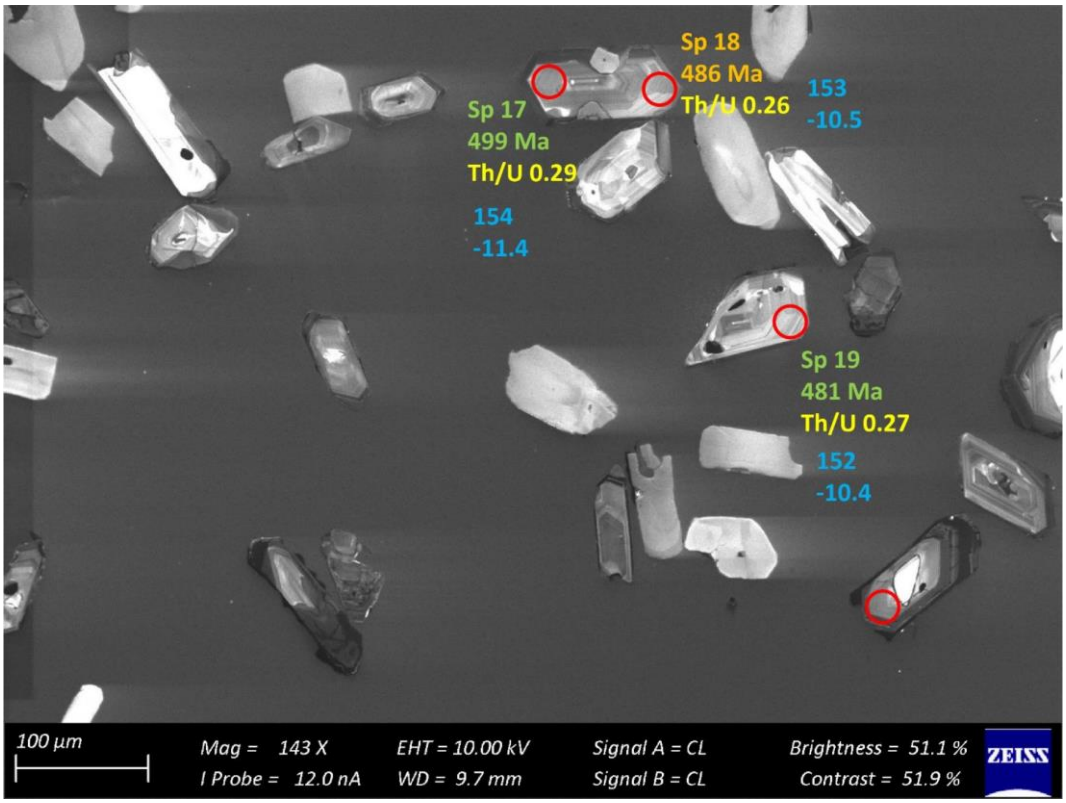

Figure 31 – Zircon Isotope spot analyses of sample s1Da; U-Pb analyses are colour coded according to concordance; blue writing indicates the Hf identifier with the respective εHf_{468} values

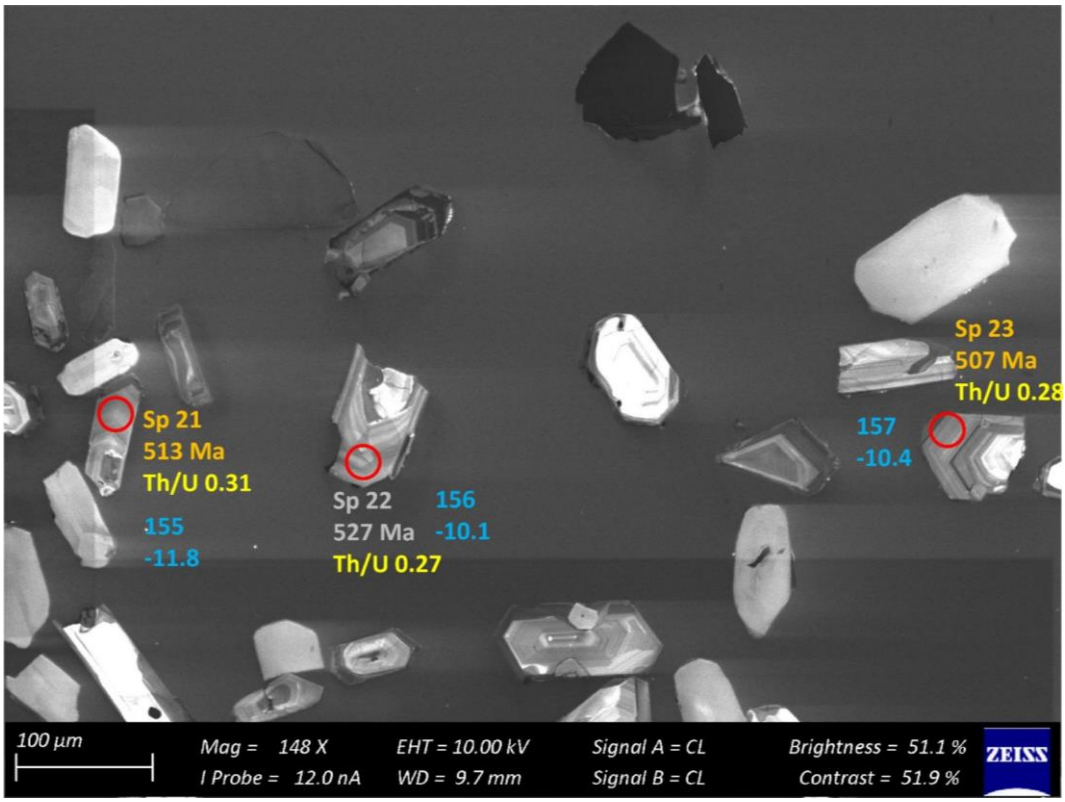

Figure 32 – Zircon Isotope spot analyses of sample s1Da; U-Pb analyses are colour coded according to concordance; blue writing indicates the Hf identifier with the respective εHf_{468} values

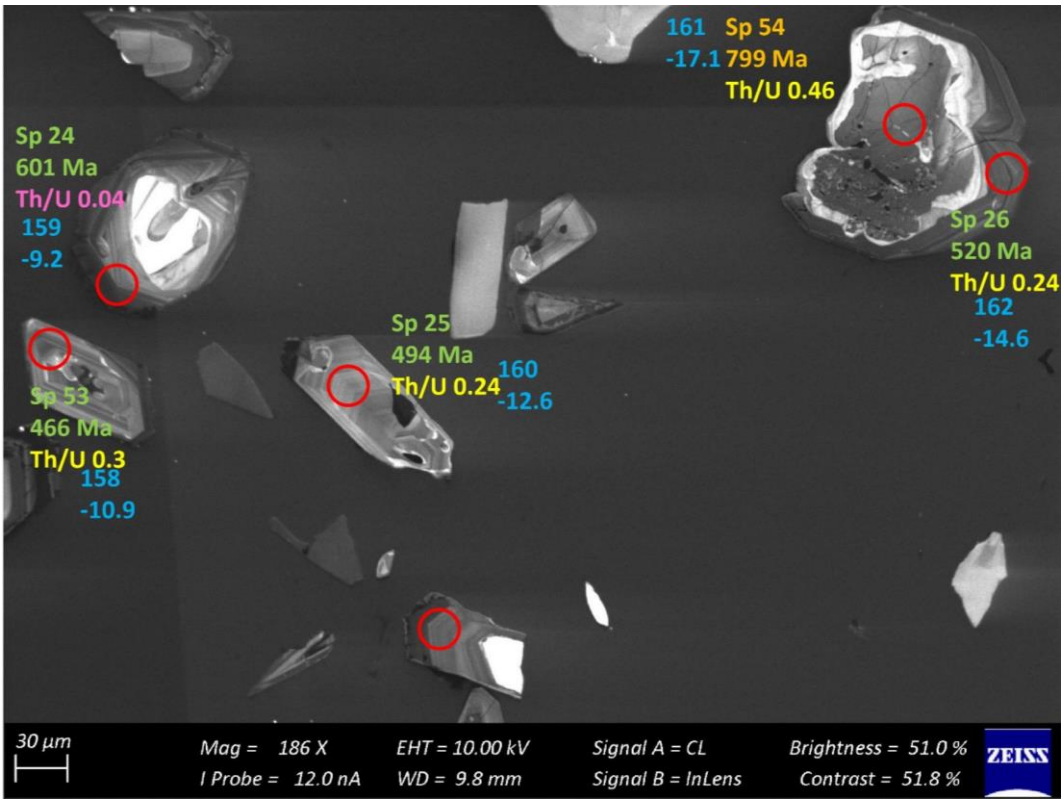

Figure 33 – Zircon Isotope spot analyses of sample s1Da; U-Pb analyses are colour coded according to concordance; blue writing indicates the Hf identifier with the respective εHf_{468} values

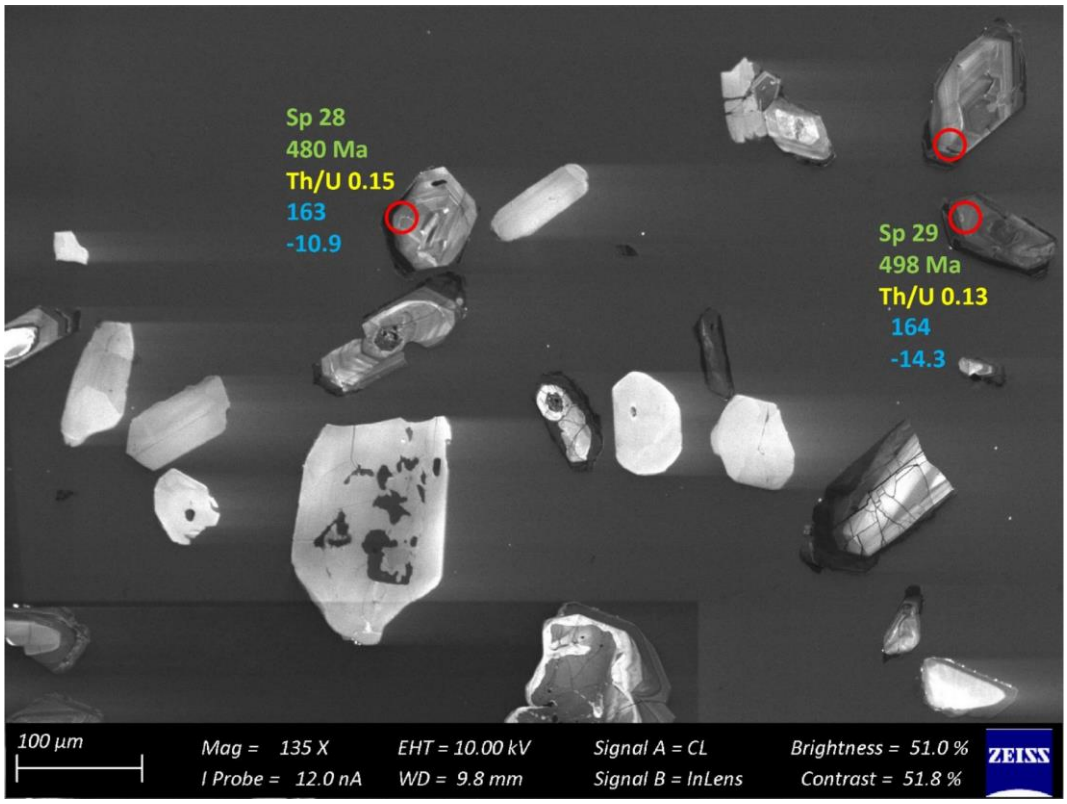

Figure 34 – Zircon Isotope spot analyses of sample s1Da; U-Pb analyses are colour coded according to concordance; blue writing indicates the Hf identifier with the respective εHf_{468} values

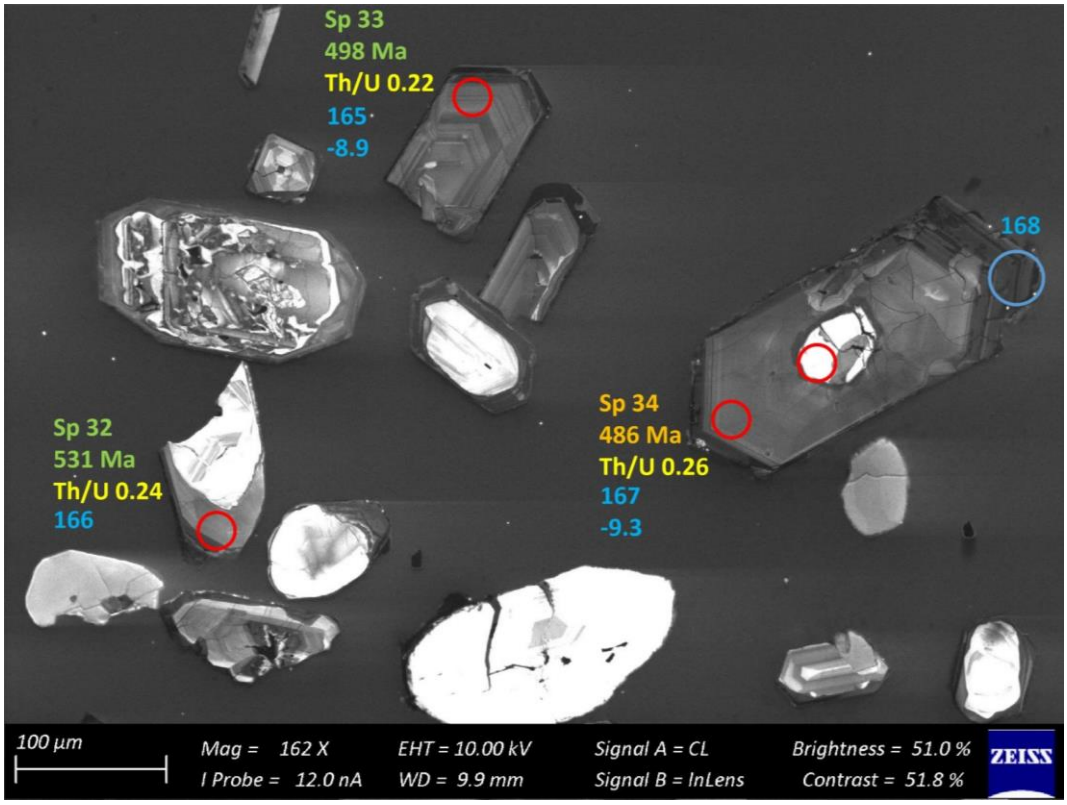

Figure 35 – Zircon Isotope spot analyses of sample s1Da; U-Pb analyses are colour coded according to concordance; blue writing indicates the Hf identifier with the respective εHf_{468} values

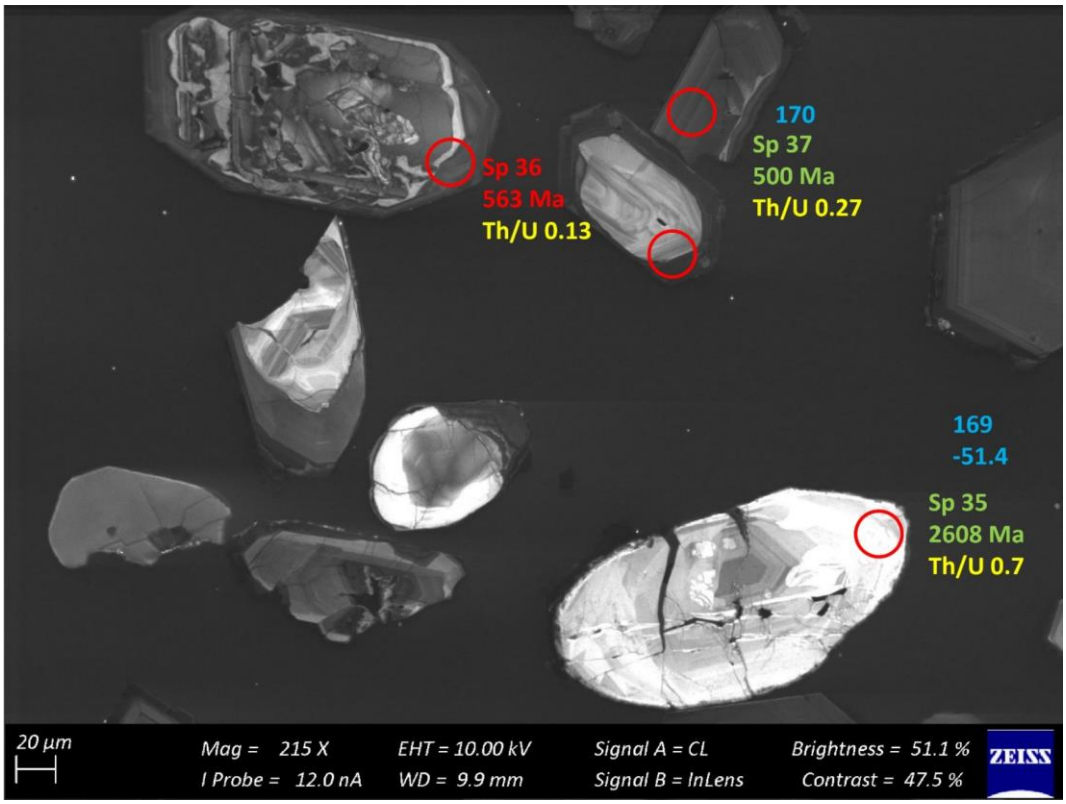

Figure 36 – Zircon Isotope spot analyses of sample s1Da; U-Pb analyses are colour coded according to concordance; blue writing indicates the Hf identifier with the respective εHf_{468} values

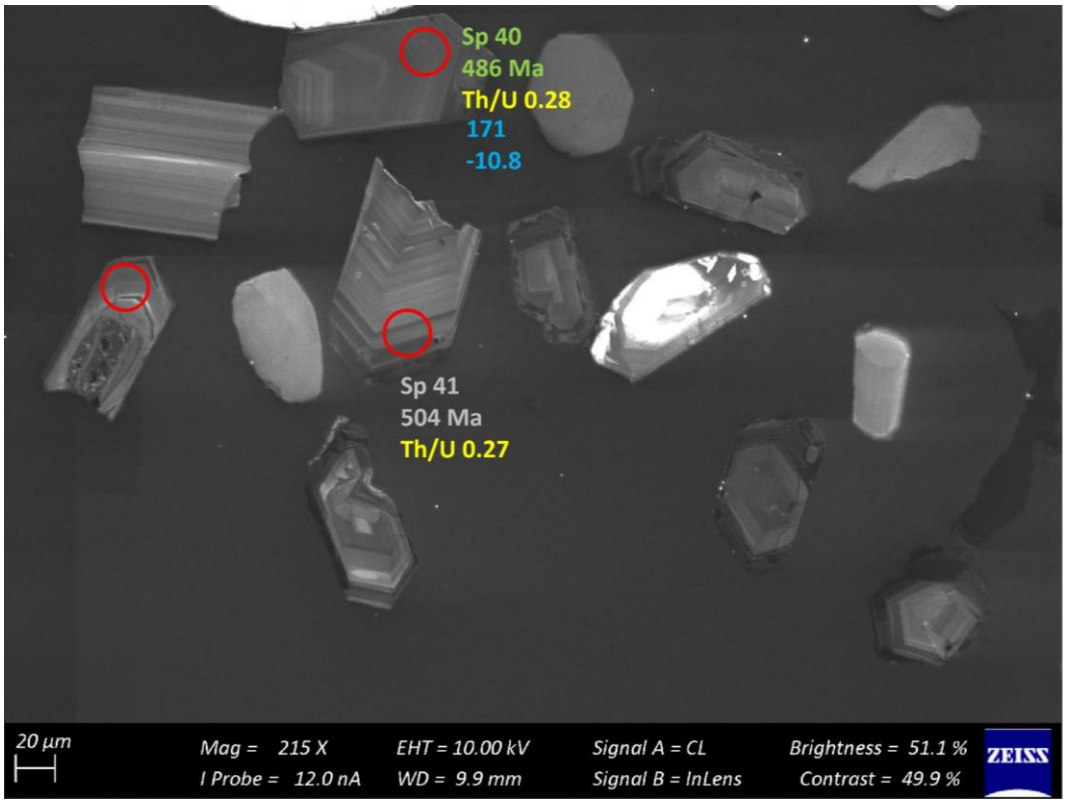

Figure 37 – Zircon Isotope spot analyses of sample s1Da; U-Pb analyses are colour coded according to concordance; blue writing indicates the Hf identifier with the respective εHf_{468} values

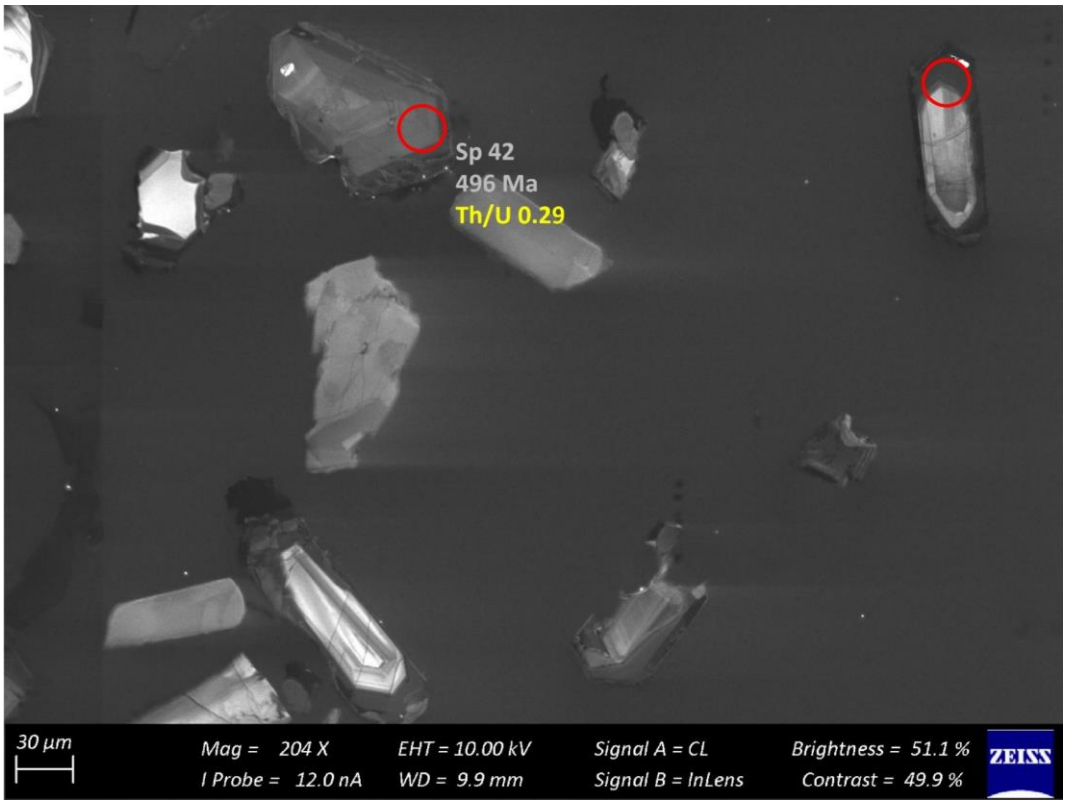

Figure 38 – Zircon Isotope spot analyses of sample s1Da; U-Pb analyses are colour coded according to concordance; blue writing indicates the Hf identifier with the respective εHf_{468} values

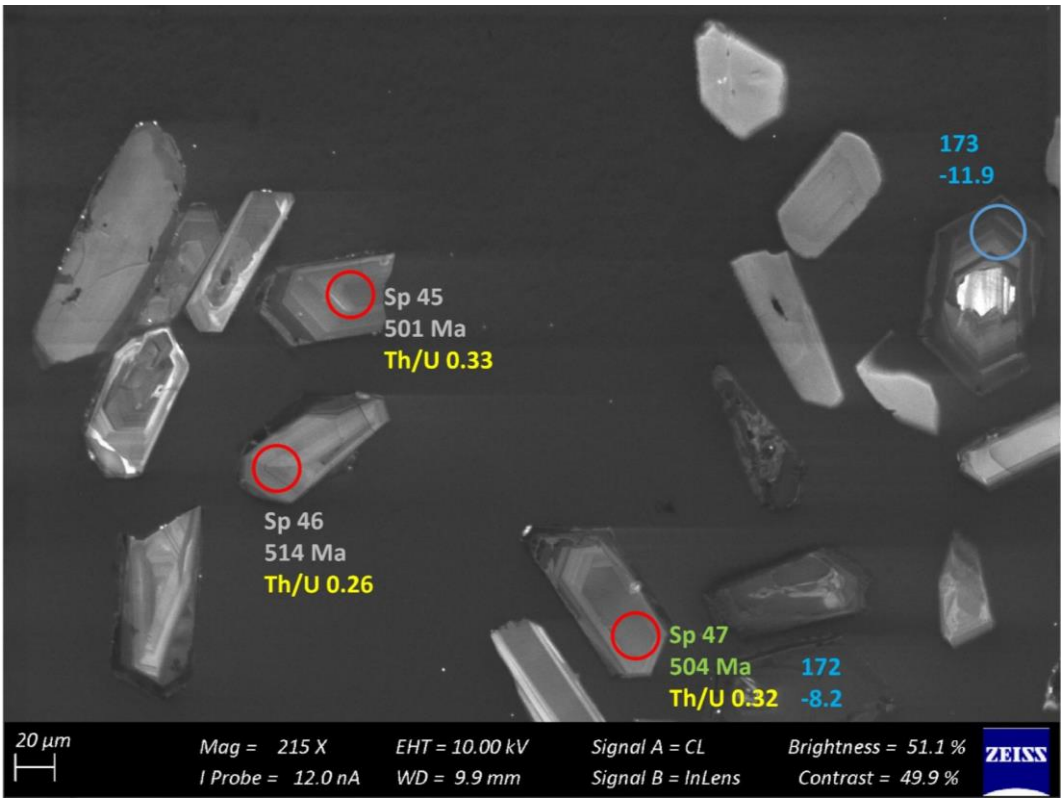

Figure 39 – Zircon Isotope spot analyses of sample s1Da; U-Pb analyses are colour coded according to concordance; blue writing indicates the Hf identifier with the respective εHf_{468} values

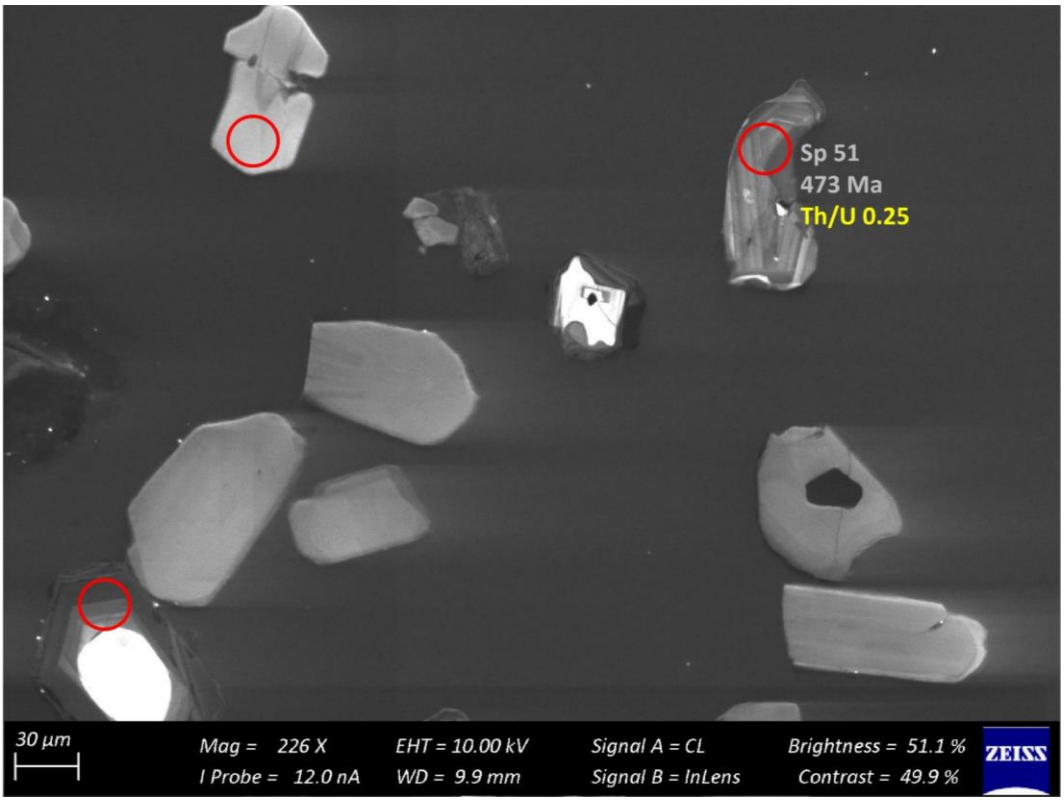

Figure 40 – Zircon Isotope spot analyses of sample s1Da; U-Pb analyses are colour coded according to concordance; blue writing indicates the Hf identifier with the respective εHf_{468} values

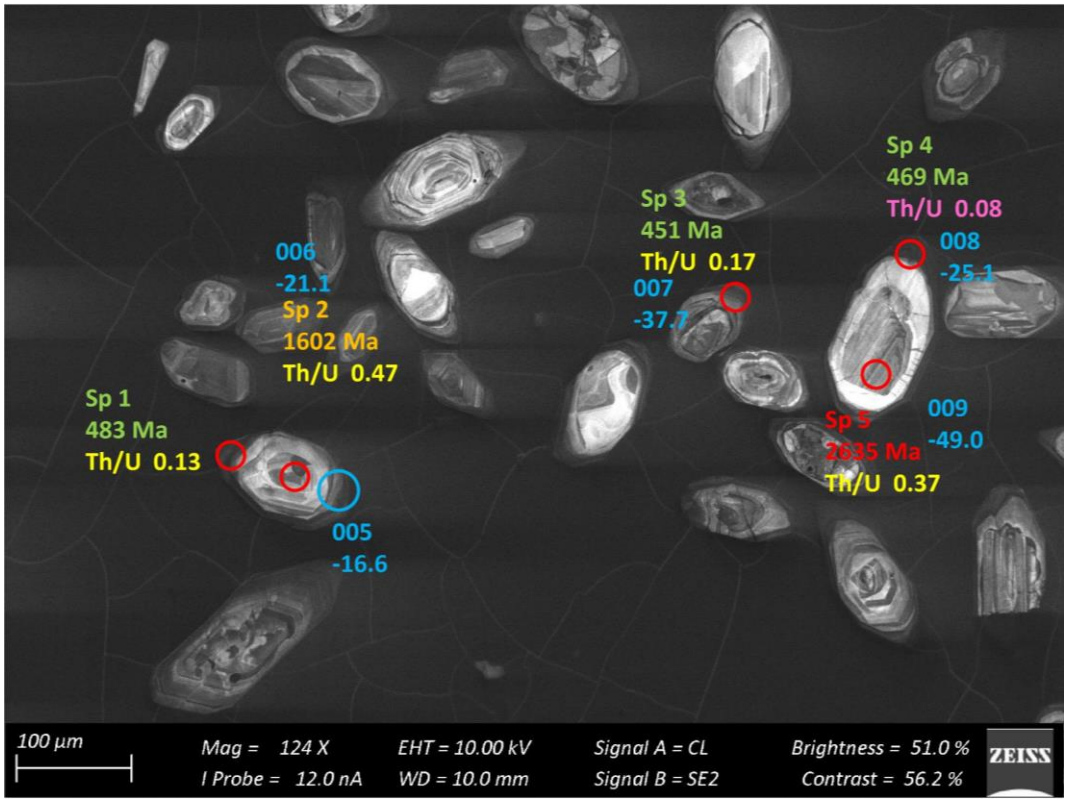

Figure 41 – Zircon Isotope spot analyses of sample s1F; U-Pb analyses are colour coded according to concordance; blue writing indicates the Hf identifier with the respective εHf_{468} values

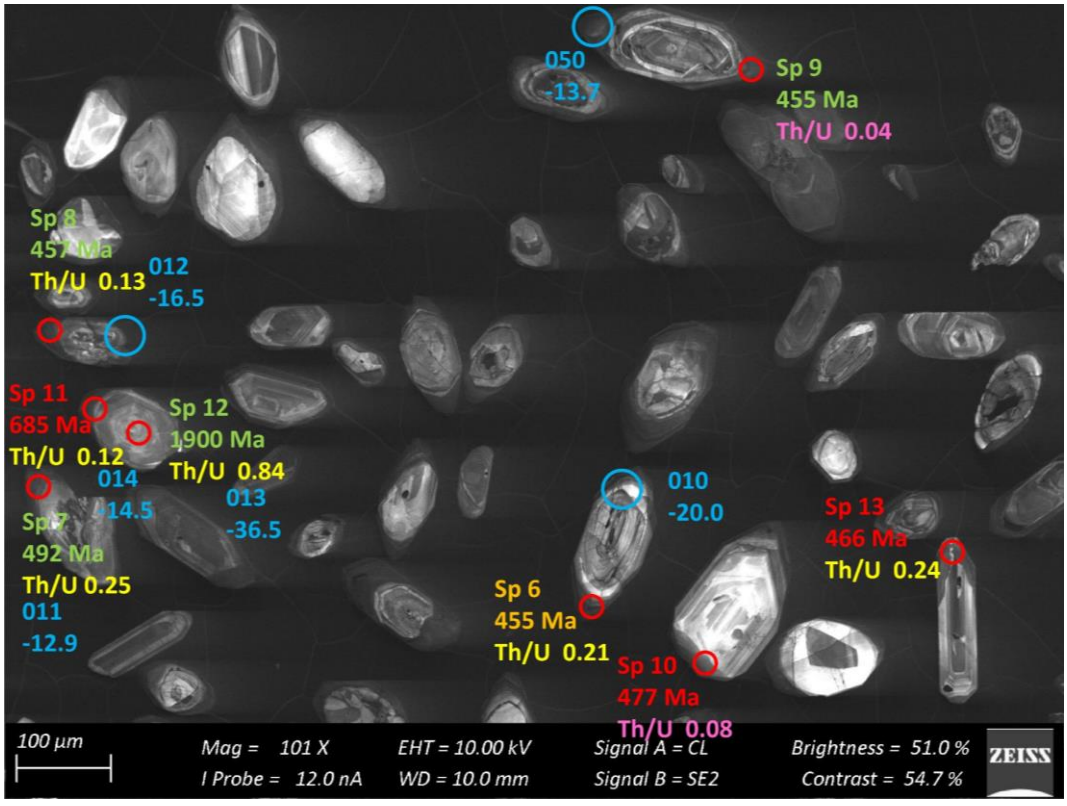

Figure 42 – Zircon Isotope spot analyses of sample s1F; U-Pb analyses are colour coded according to concordance; blue writing indicates the Hf identifier with the respective εHf_{468} values

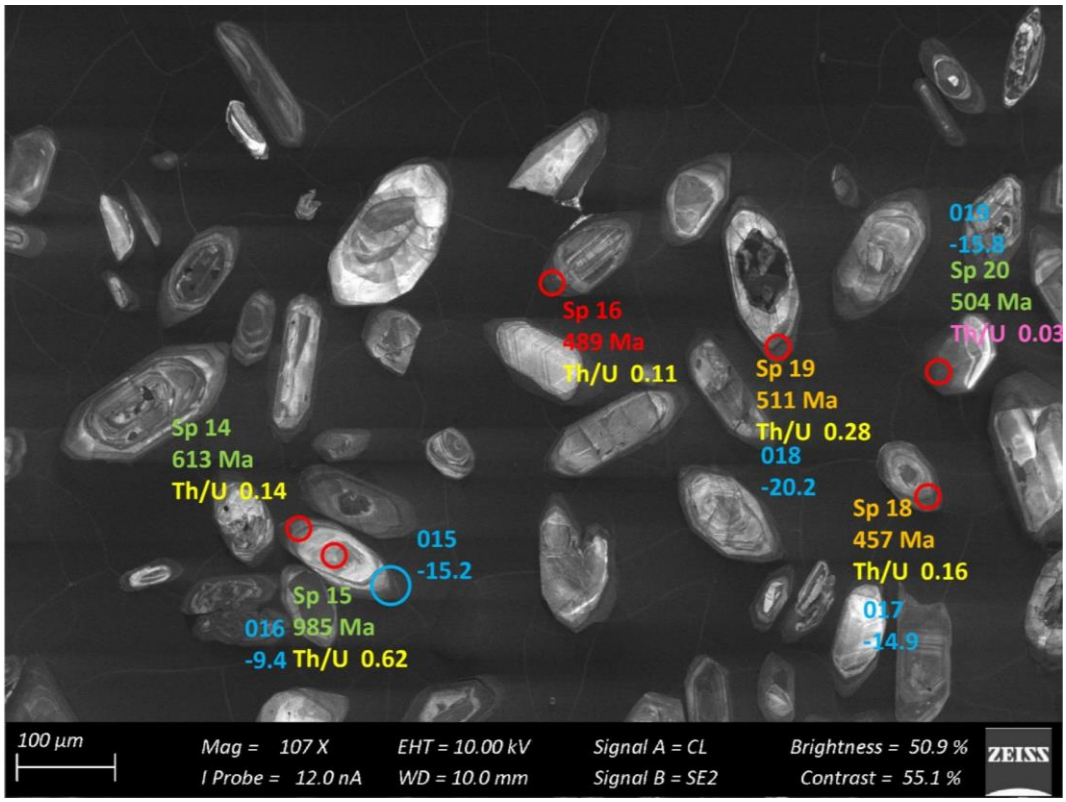

Figure 43 – Zircon Isotope spot analyses of sample s1F; U-Pb analyses are colour coded according to concordance; blue writing indicates the Hf identifier with the respective εHf_{468} values

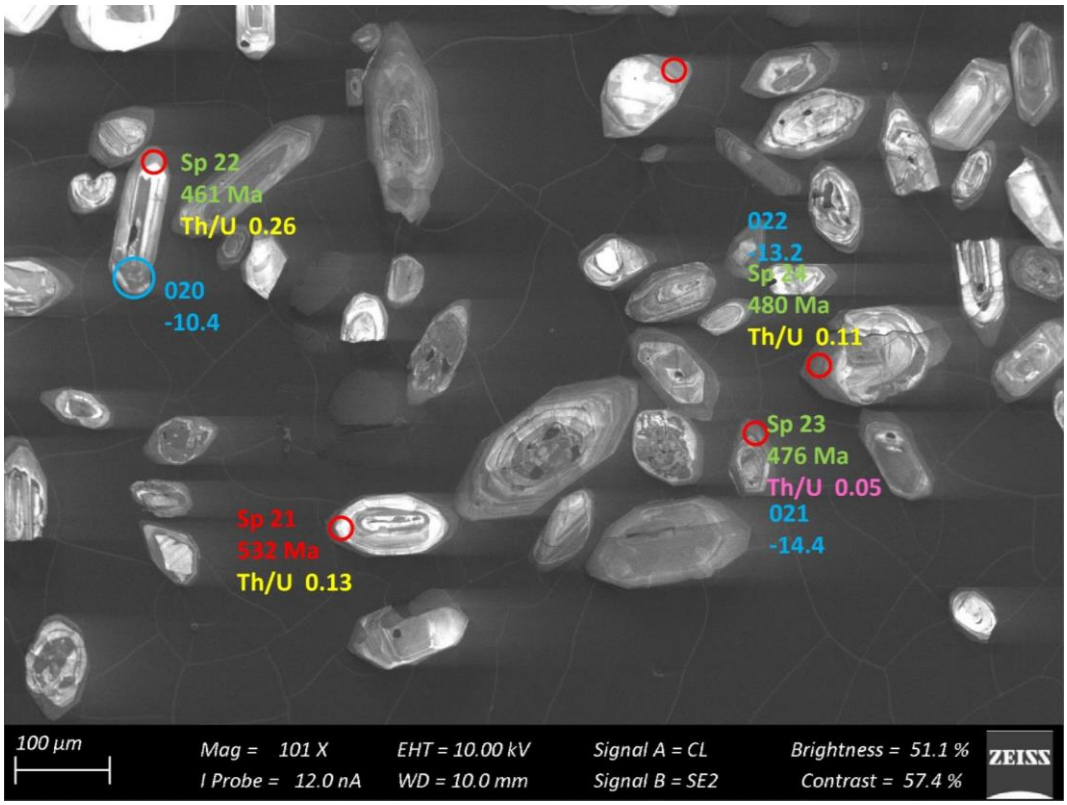

Figure 44 – Zircon Isotope spot analyses of sample s1F; U-Pb analyses are colour coded according to concordance; blue writing indicates the Hf identifier with the respective εHf_{468} values

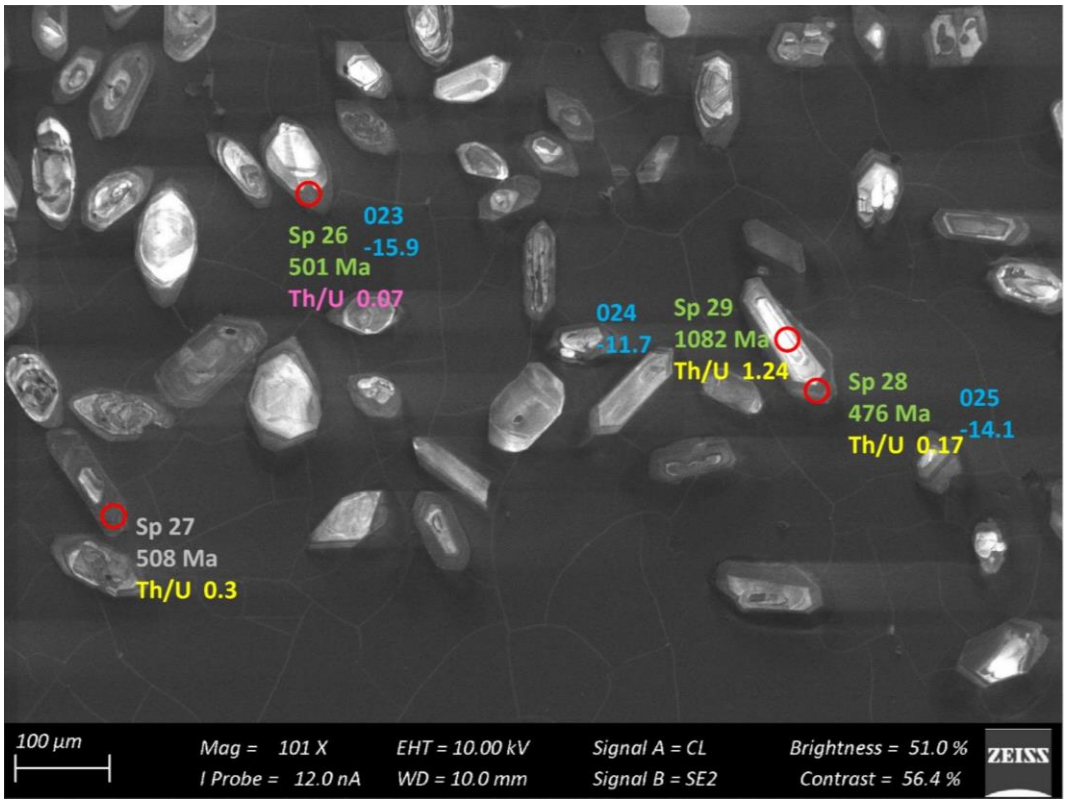

Figure 45 – Zircon Isotope spot analyses of sample s1F; U-Pb analyses are colour coded according to concordance; blue writing indicates the Hf identifier with the respective εHf_{468} values

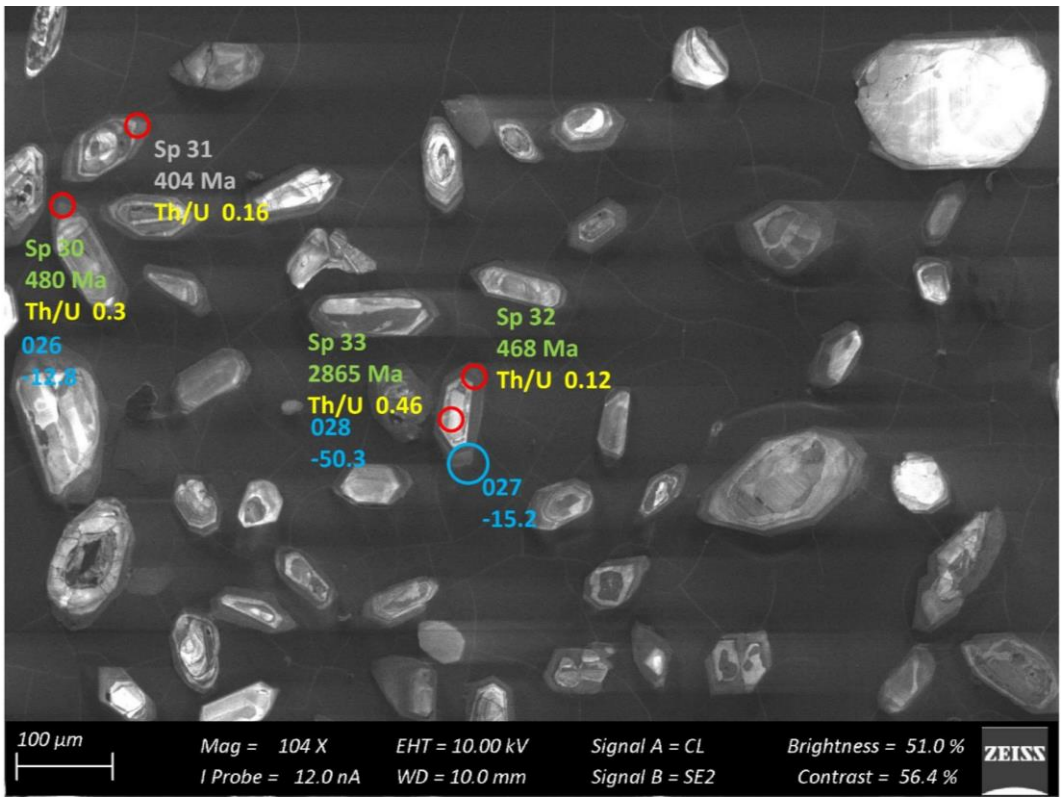

Figure 46 – Zircon Isotope spot analyses of sample s1F; U-Pb analyses are colour coded according to concordance; blue writing indicates the Hf identifier with the respective εHf_{468} values

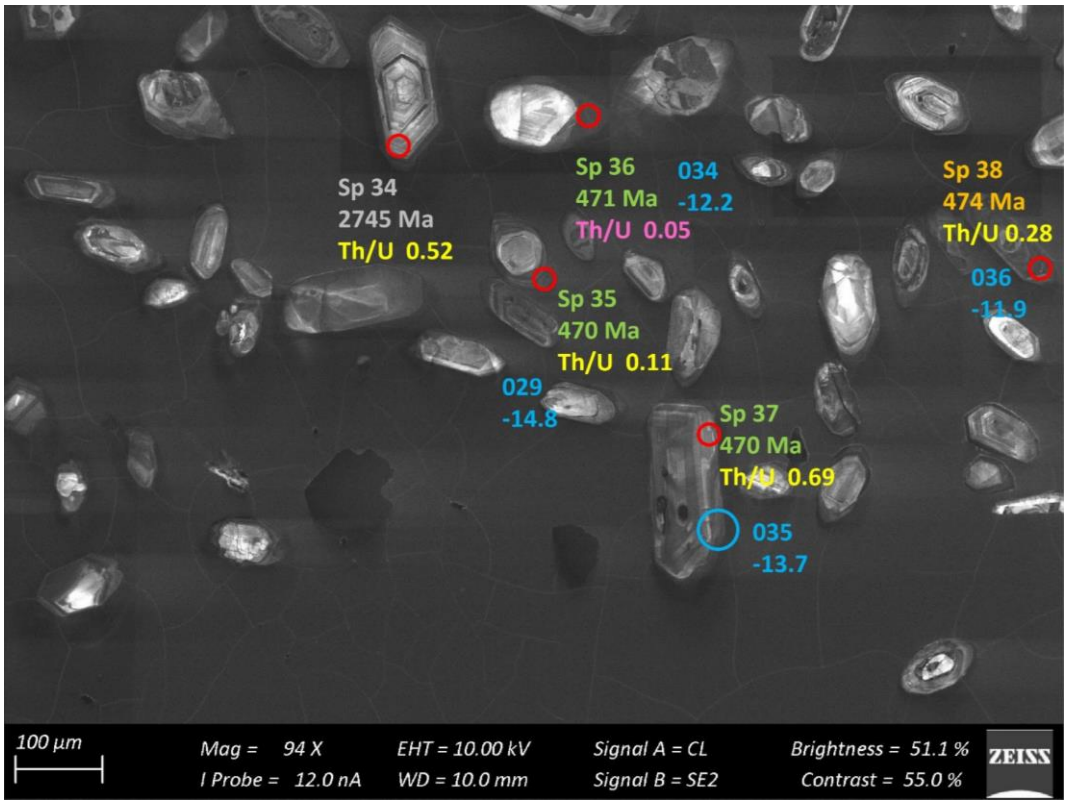

Figure 47 – Zircon Isotope spot analyses of sample s1F; U-Pb analyses are colour coded according to concordance; blue writing indicates the Hf identifier with the respective εHf_{468} values

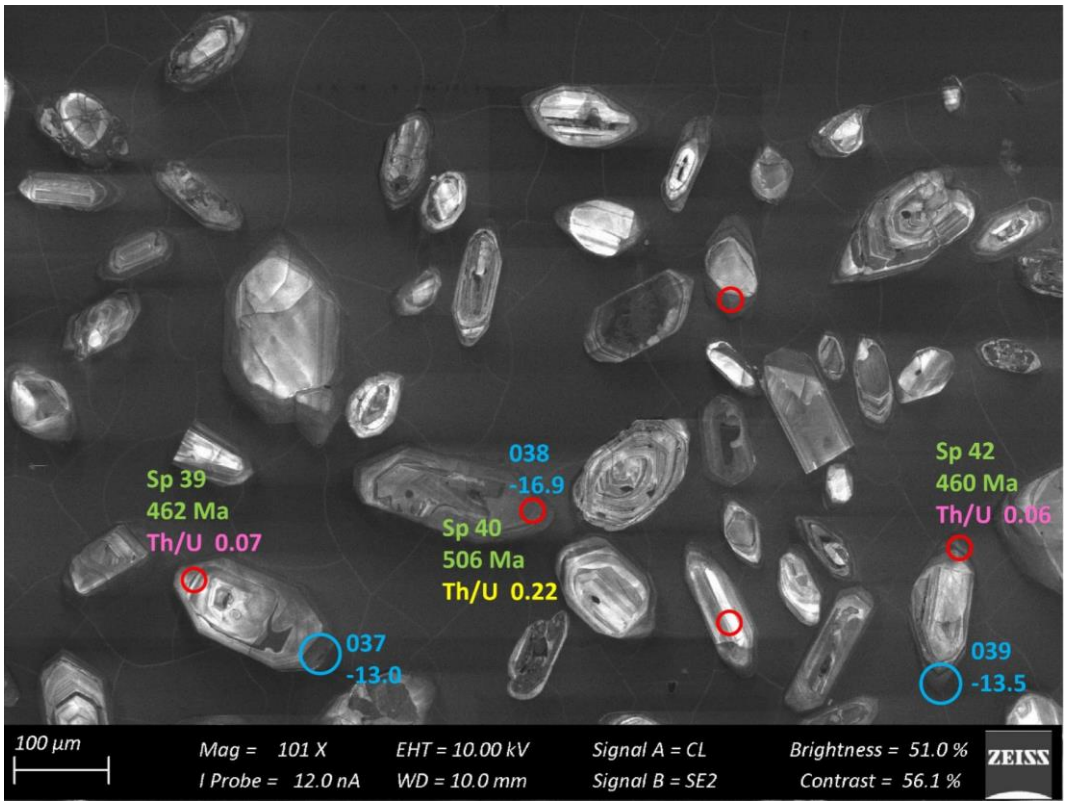

Figure 48 – Zircon Isotope spot analyses of sample s1F; U-Pb analyses are colour coded according to concordance; blue writing indicates the Hf identifier with the respective εHf_{468} values

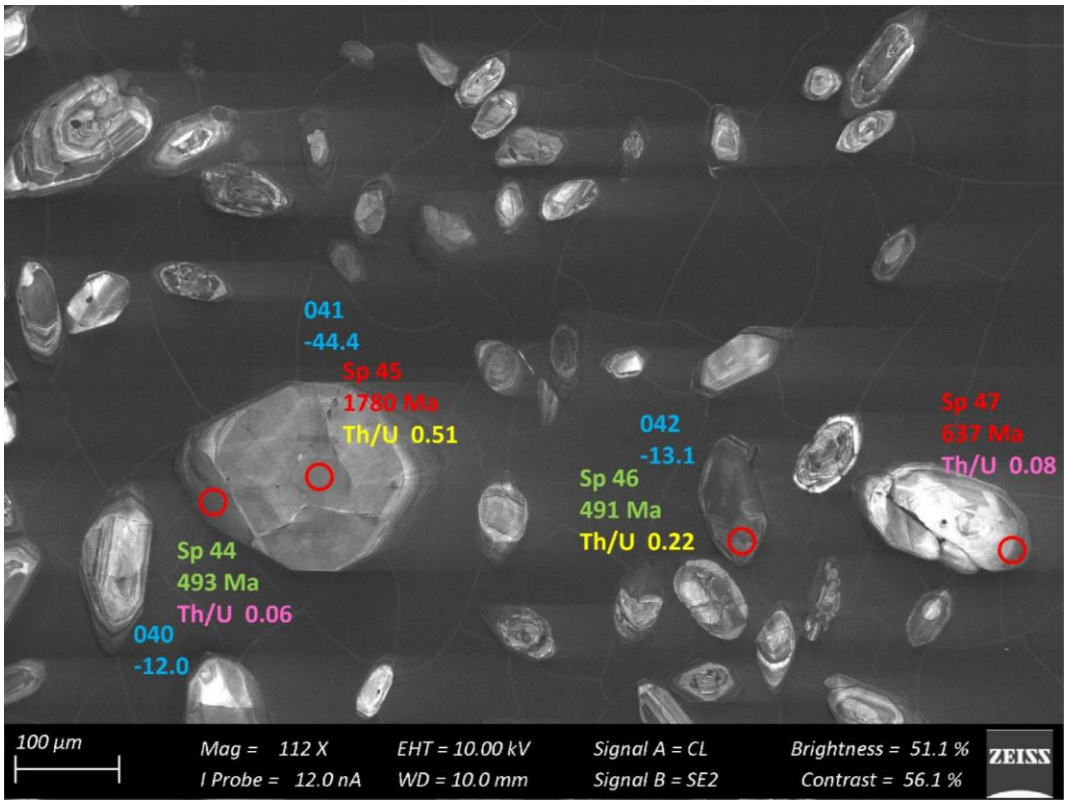

Figure 49 – Zircon Isotope spot analyses of sample s1F; U-Pb analyses are colour coded according to concordance; blue writing indicates the Hf identifier with the respective εHf_{468} values

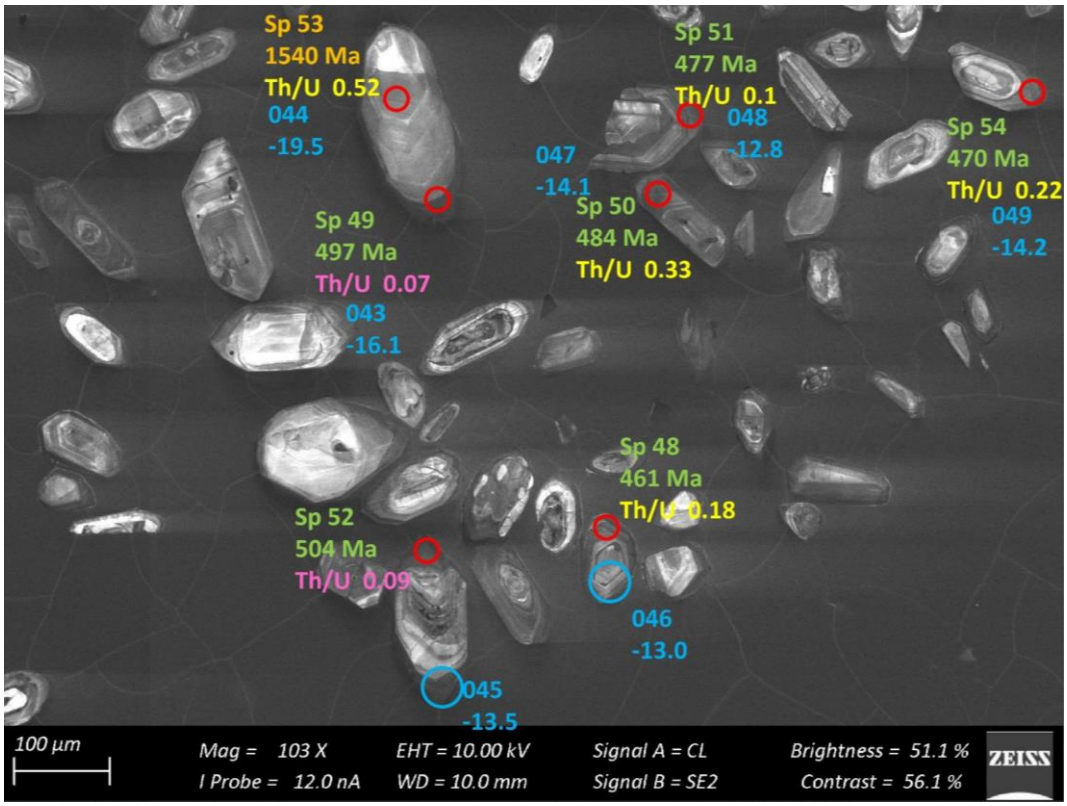

Figure 50 – Zircon Isotope spot analyses of sample s1F; U-Pb analyses are colour coded according to concordance; blue writing indicates the Hf identifier with the respective εHf_{468} values

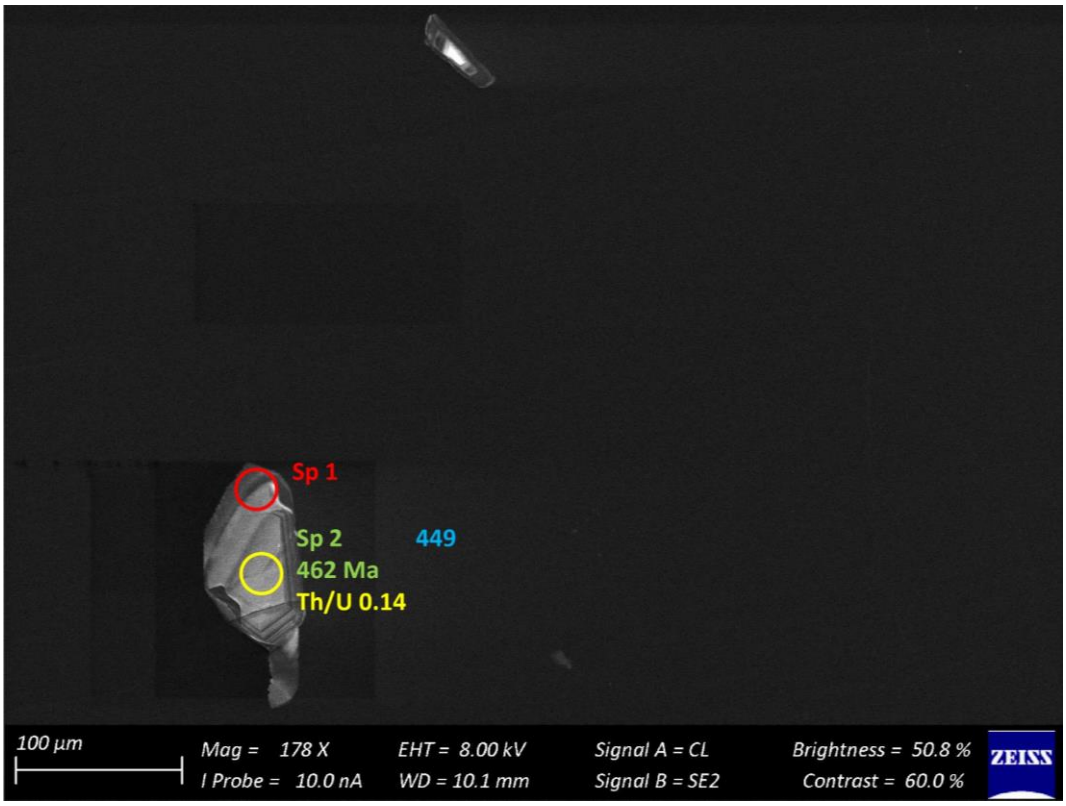

Figure 51 – Zircon Isotope spot analyses of sample s1H; U-Pb analyses are colour coded according to concordance; blue writing indicates the Hf identifier with the respective εHf_{468} values

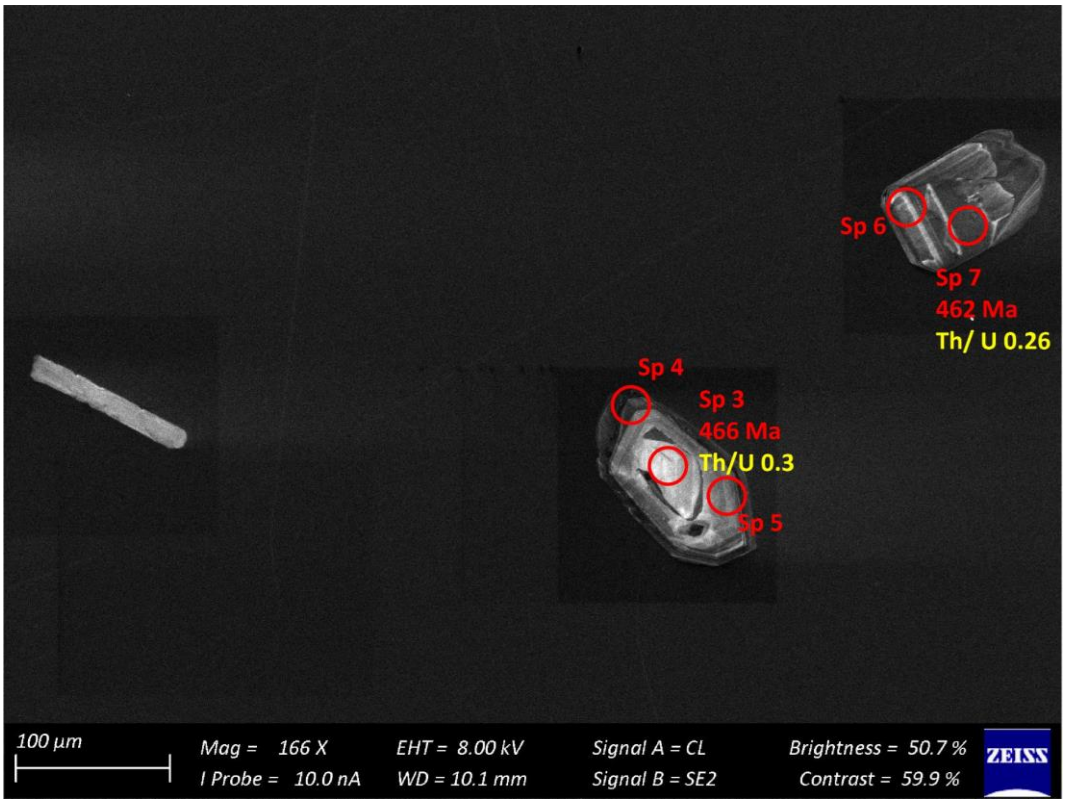

Figure 52 – Zircon Isotope spot analyses of sample s1H; U-Pb analyses are colour coded according to concordance; blue writing indicates the Hf identifier with the respective εHf_{468} values

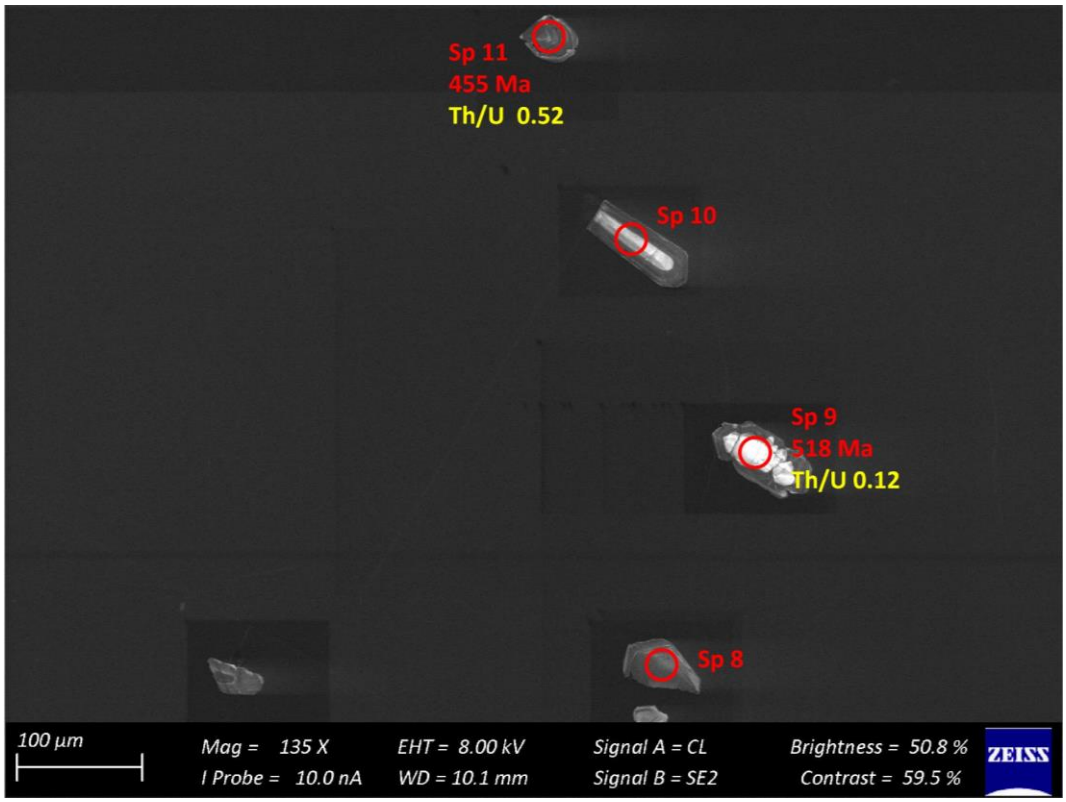

Figure 53 – Zircon Isotope spot analyses of sample s1H; U-Pb analyses are colour coded according to concordance; blue writing indicates the Hf identifier with the respective εHf_{468} values

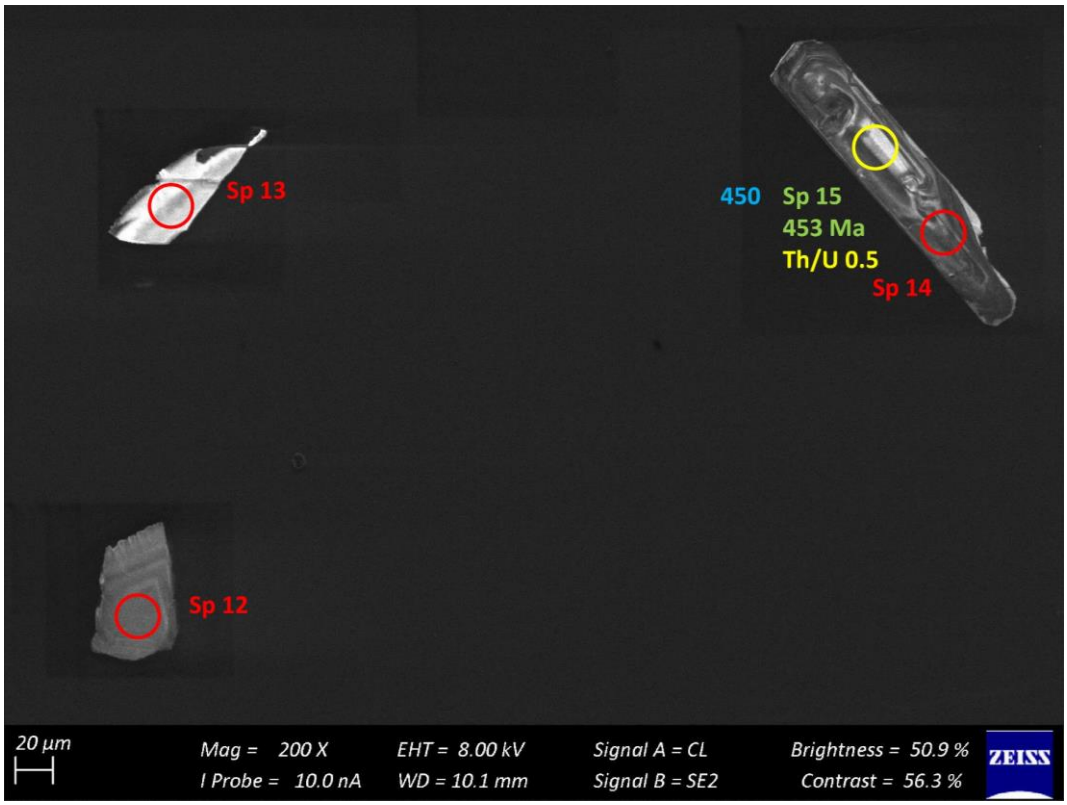

Figure 54 – Zircon Isotope spot analyses of sample s1H; U-Pb analyses are colour coded according to concordance; blue writing indicates the Hf identifier with the respective εHf_{468} values

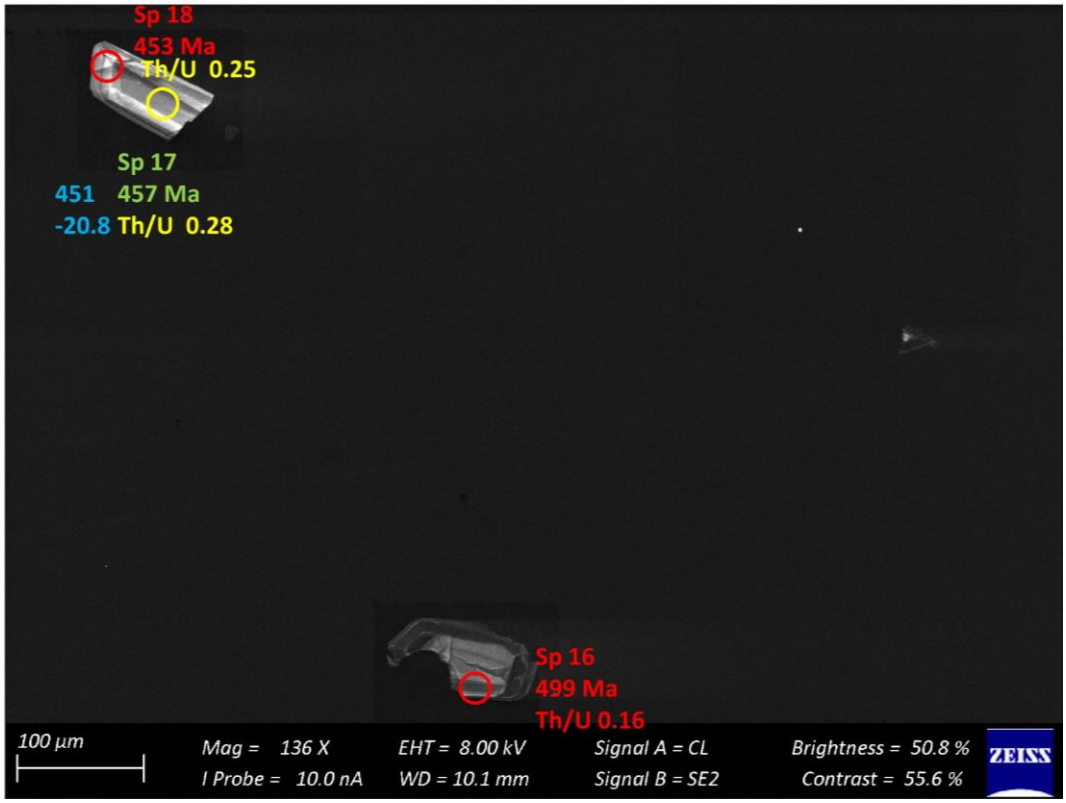

Figure 55 – Zircon Isotope spot analyses of sample s1H; U-Pb analyses are colour coded according to concordance; blue writing indicates the Hf identifier with the respective εHf$_{468}$ values

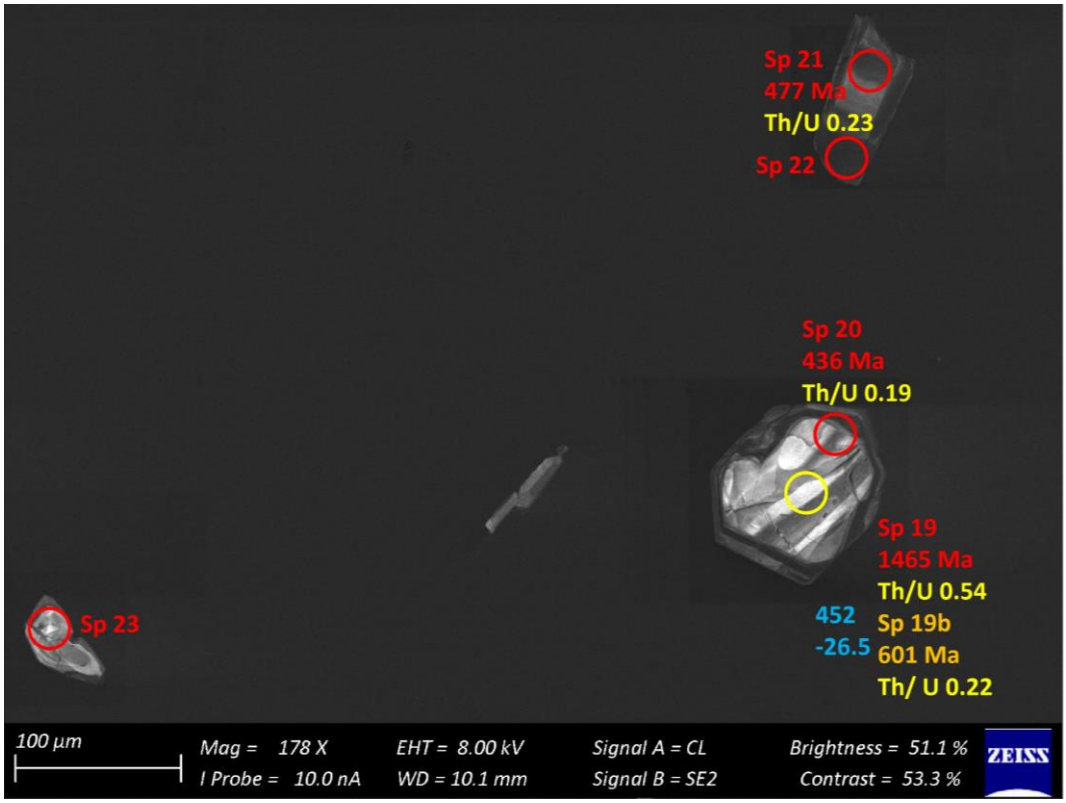

Figure 56 – Zircon Isotope spot analyses of sample s1H; U-Pb analyses are colour coded according to concordance; blue writing indicates the Hf identifier with the respective εHf$_{468}$ values

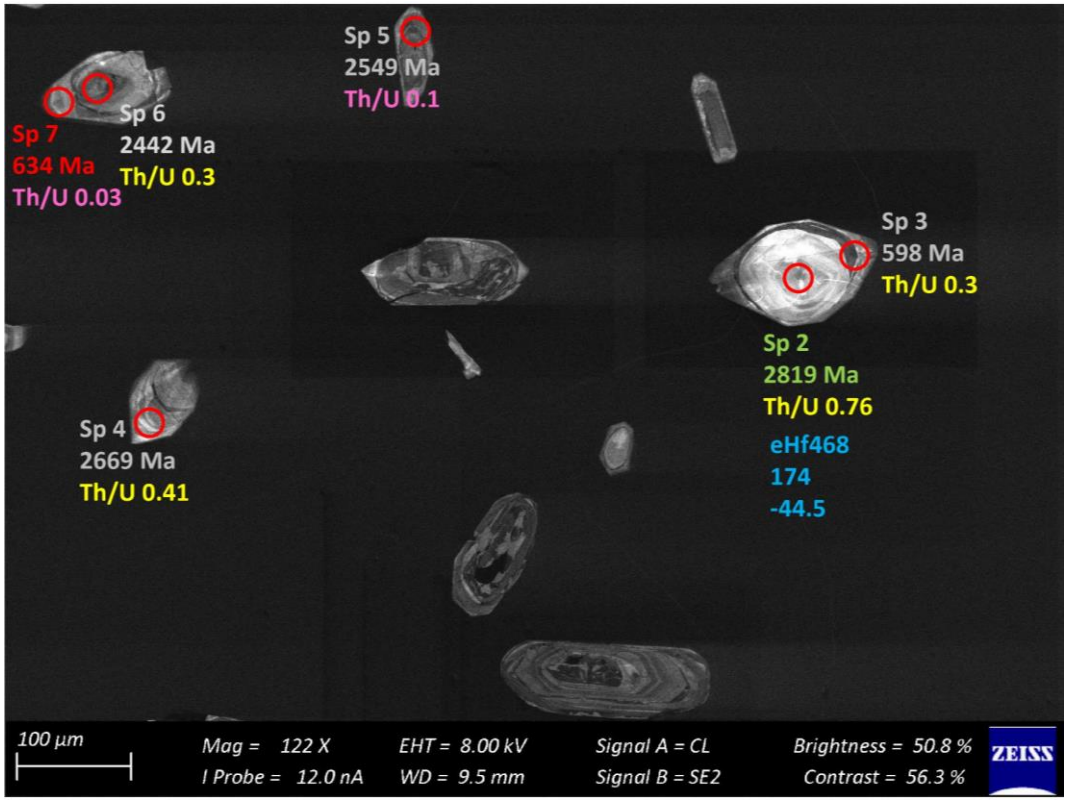

Figure 57 – Zircon Isotope spot analyses of sample s2A; U-Pb analyses are colour coded according to concordance; blue writing indicates the Hf identifier with the respective εHf_{468} values

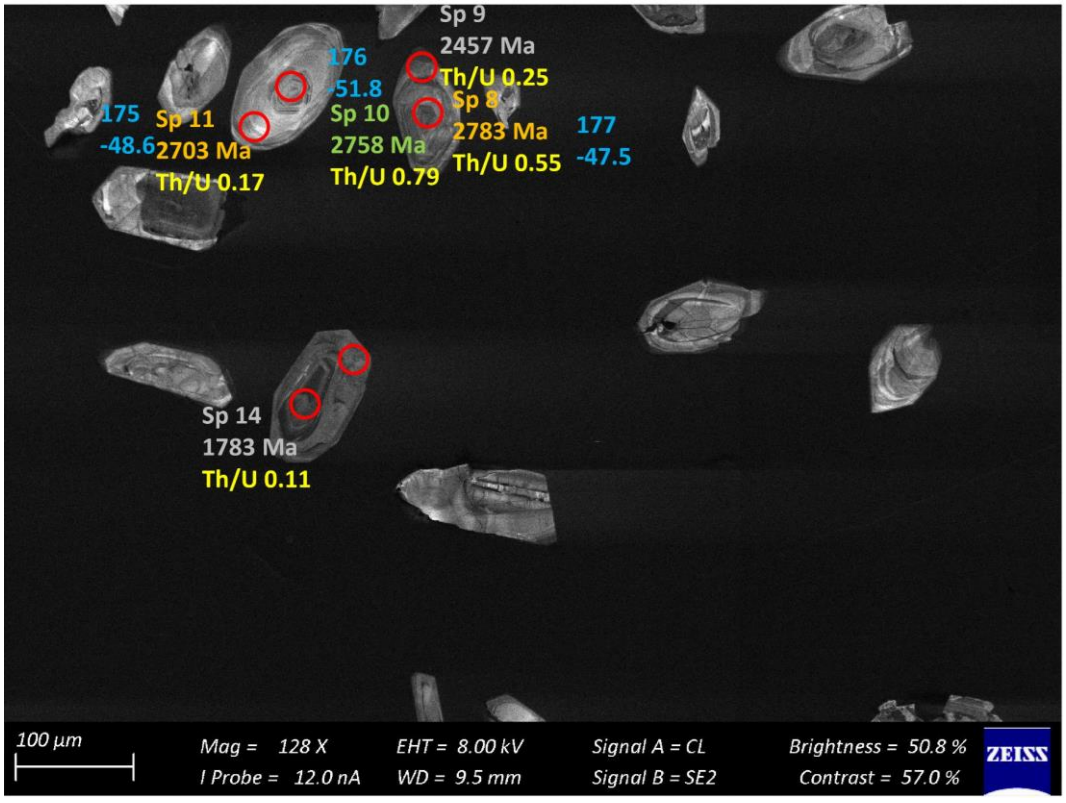

Figure 58 – Zircon Isotope spot analyses of sample s2A; U-Pb analyses are colour coded according to concordance; blue writing indicates the Hf identifier with the respective εHf_{468} values

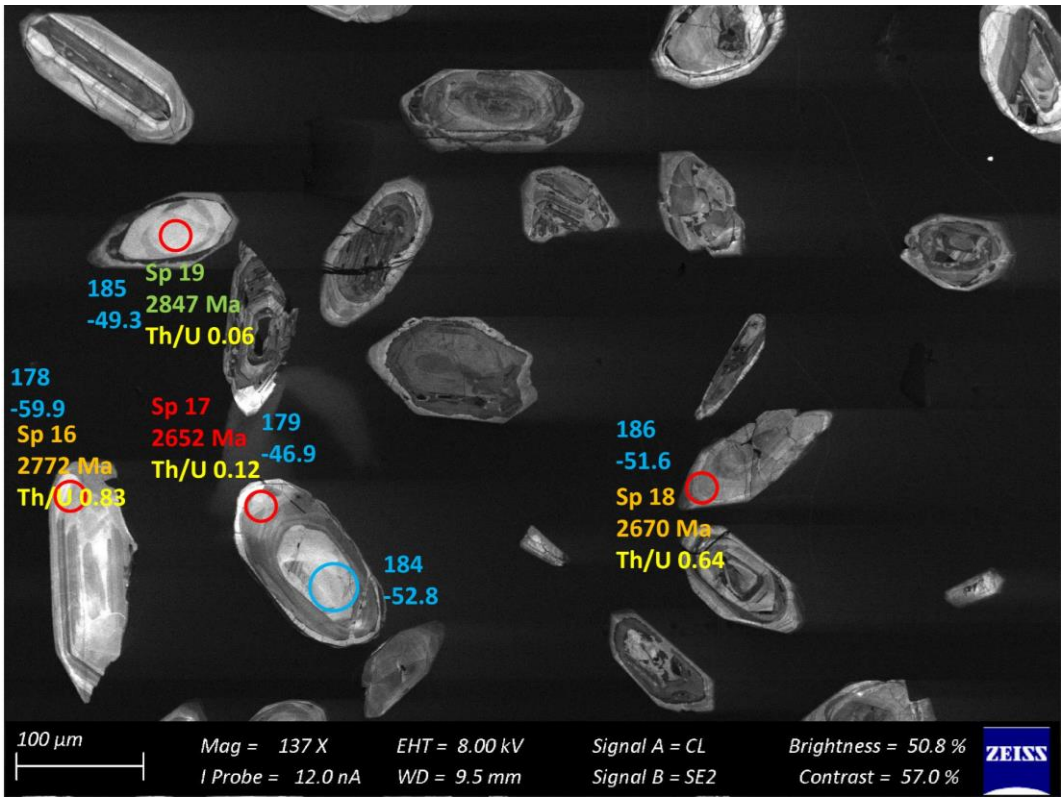

Figure 59 – Zircon Isotope spot analyses of sample s2A; U-Pb analyses are colour coded according to concordance; blue writing indicates the Hf identifier with the respective εHf_{468} values

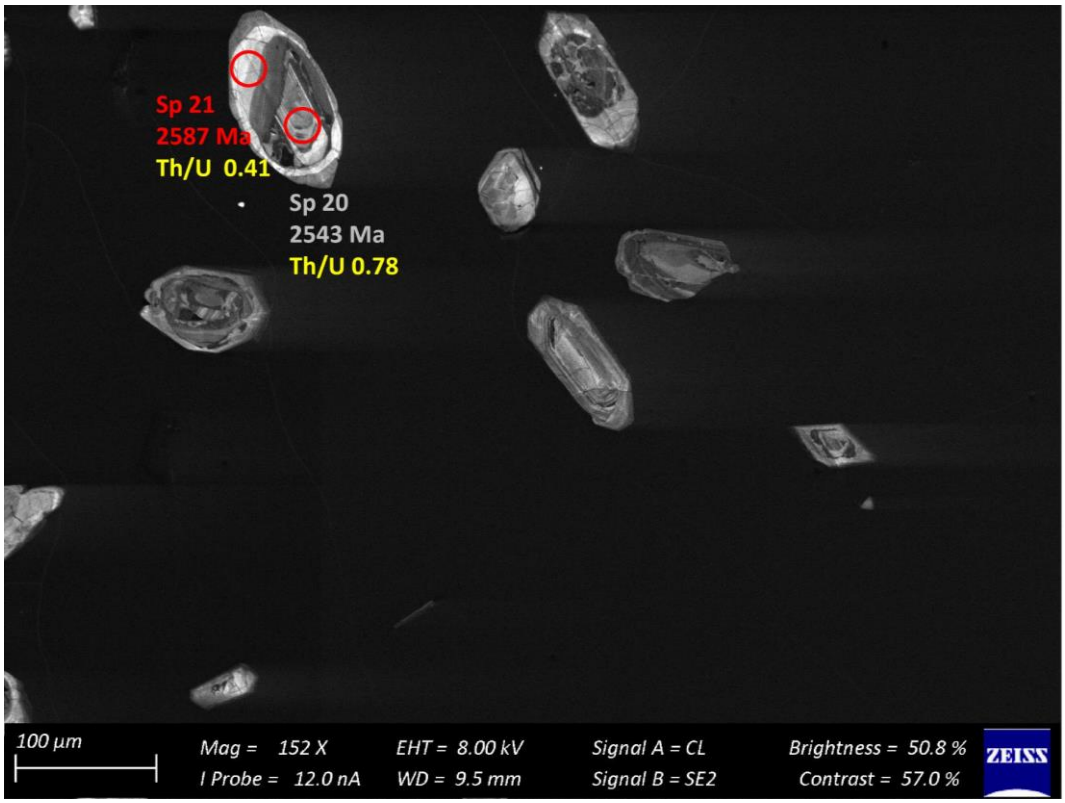

Figure 60 – Zircon Isotope spot analyses of sample s2A; U-Pb analyses are colour coded according to concordance; blue writing indicates the Hf identifier with the respective εHf_{468} values

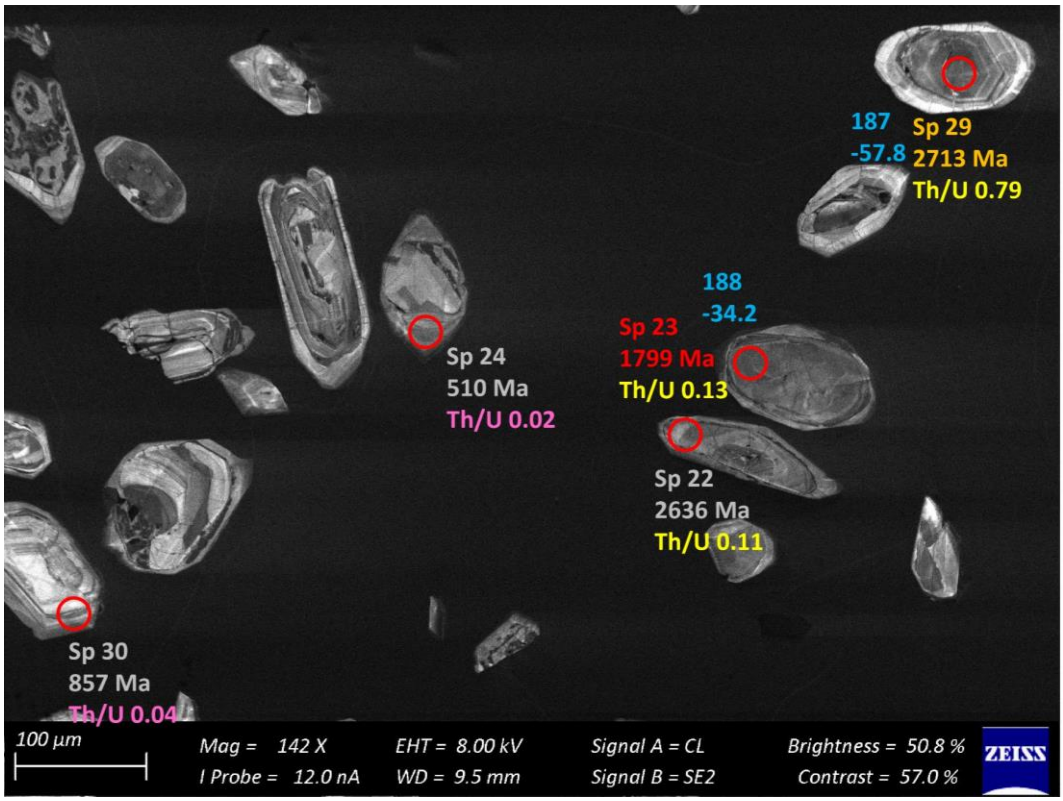

Figure 61 – Zircon Isotope spot analyses of sample s2A; U-Pb analyses are colour coded according to concordance; blue writing indicates the Hf identifier with the respective εHf_{468} values

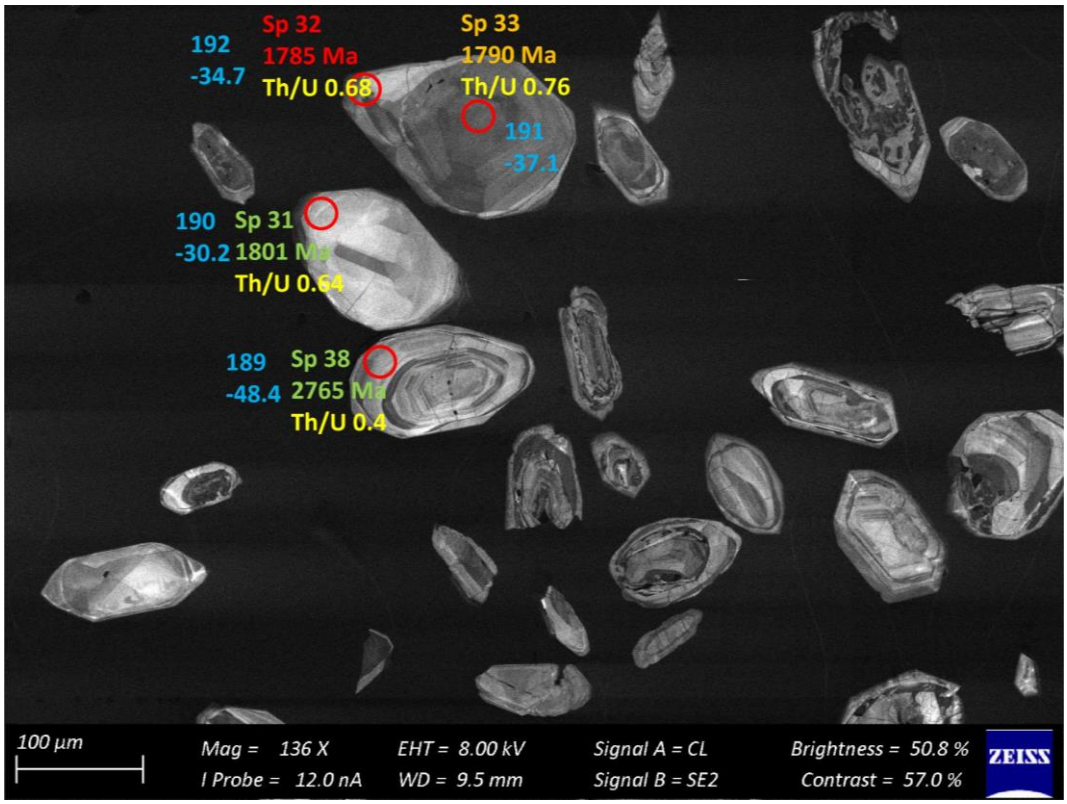

Figure 62 – Zircon Isotope spot analyses of sample s2A; U-Pb analyses are colour coded according to concordance; blue writing indicates the Hf identifier with the respective εHf_{468} values

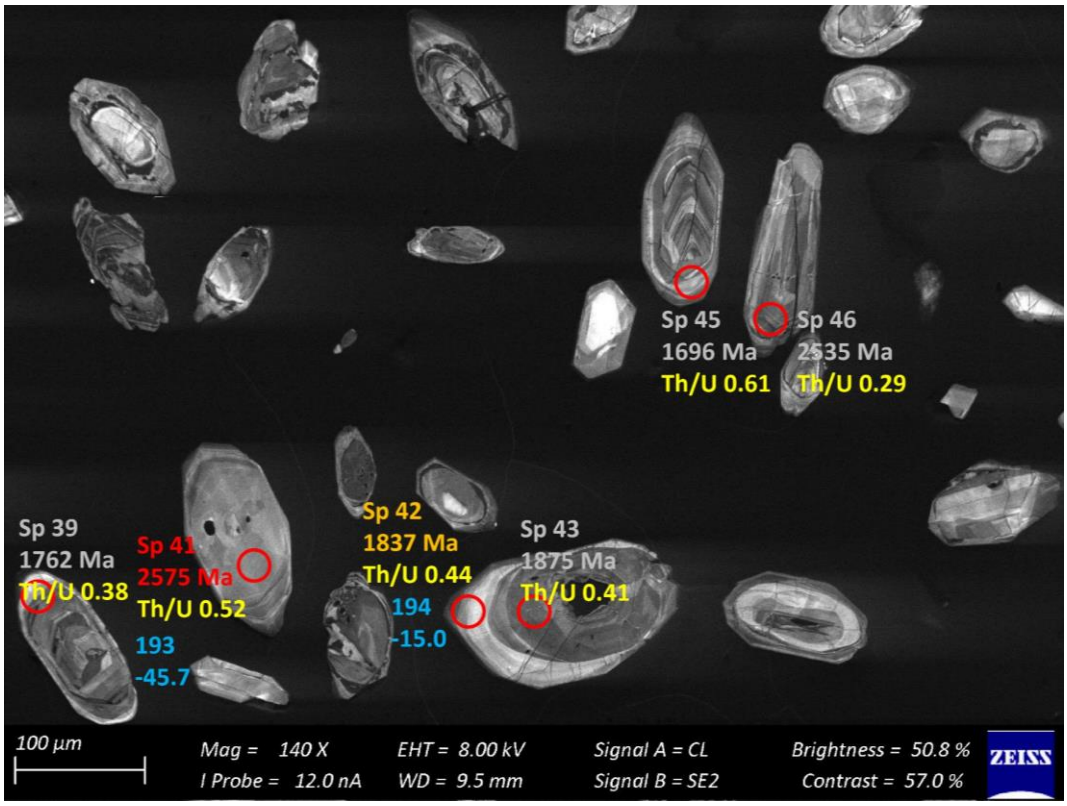

Figure 63 – Zircon Isotope spot analyses of sample s2A; U-Pb analyses are colour coded according to concordance; blue writing indicates the Hf identifier with the respective εHf_{468} values

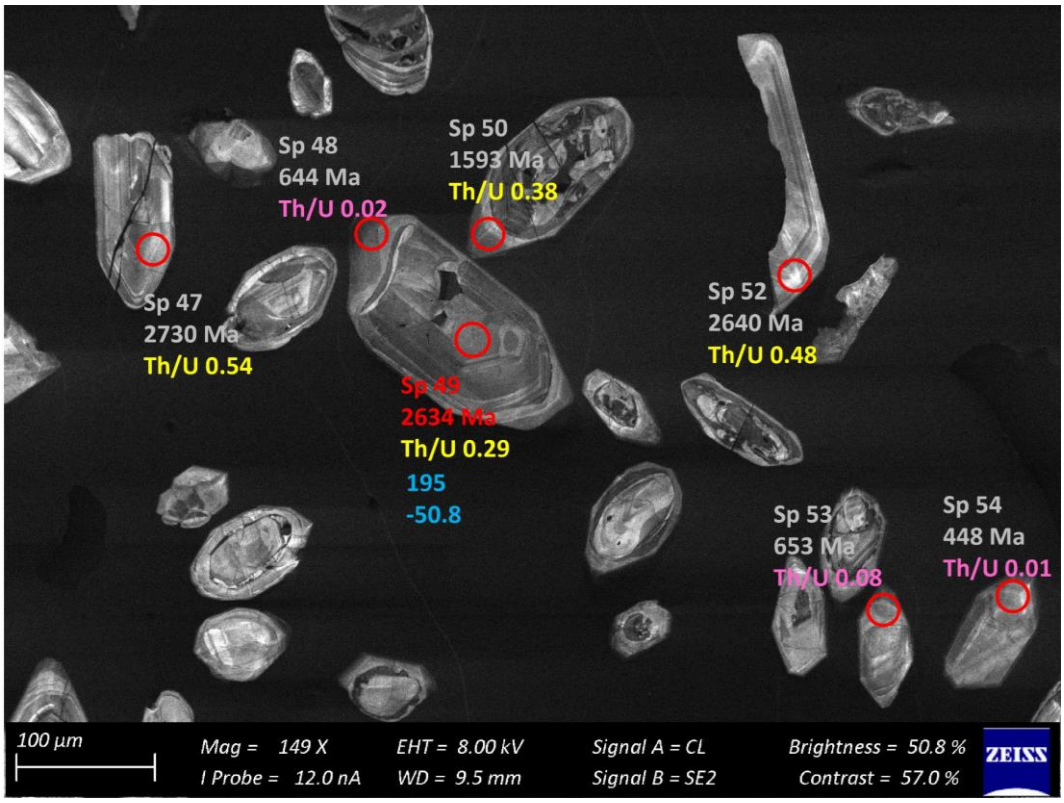

Figure 64 – Zircon Isotope spot analyses of sample s2A; U-Pb analyses are colour coded according to concordance; blue writing indicates the Hf identifier with the respective εHf_{468} values

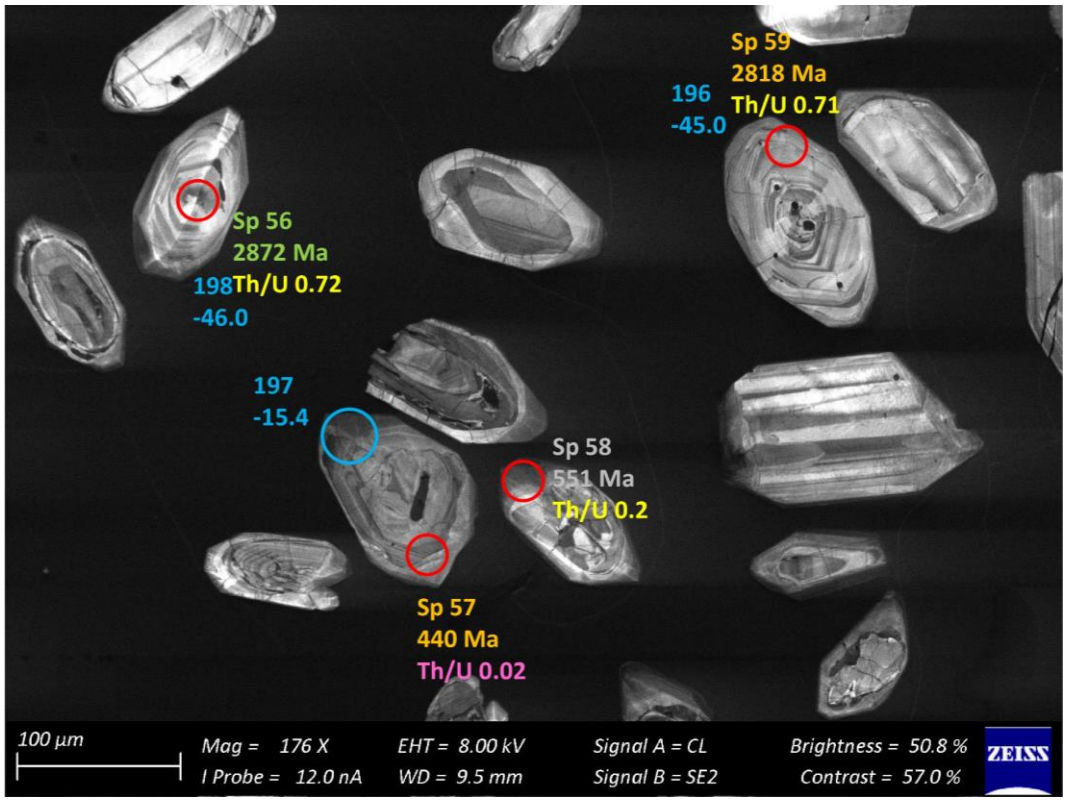

Figure 65 – Zircon Isotope spot analyses of sample s2A; U-Pb analyses are colour coded according to concordance; blue writing indicates the Hf identifier with the respective εHf_{468} values

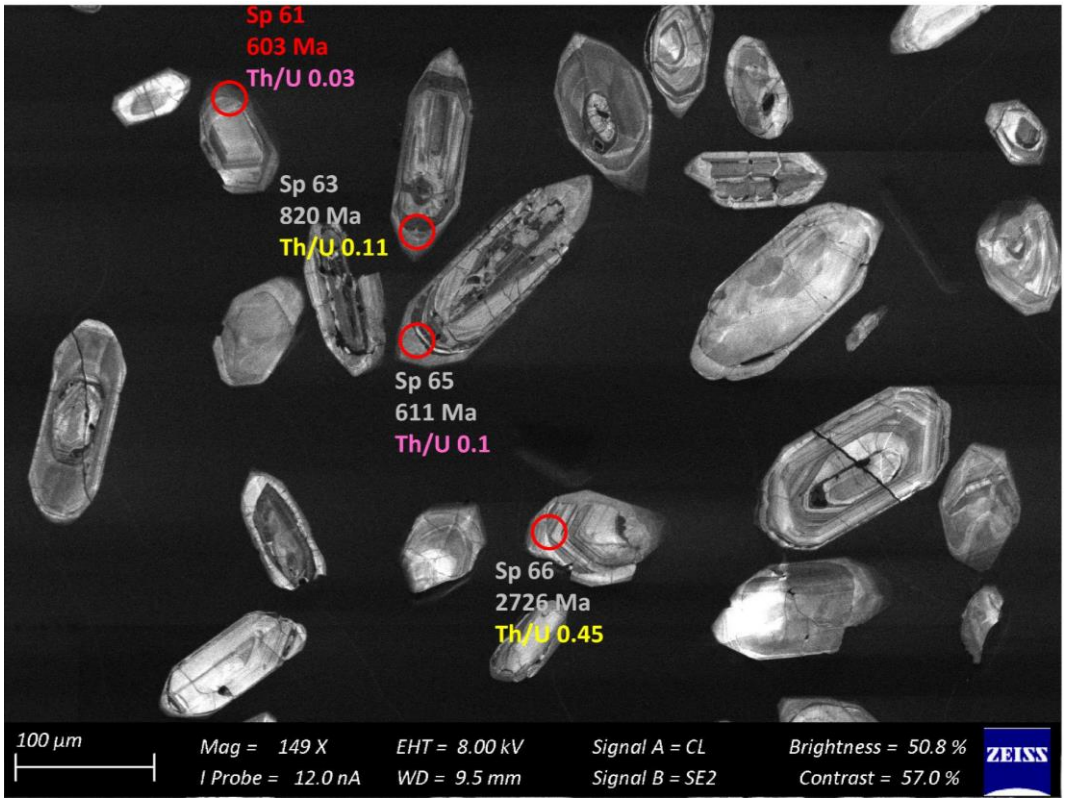

Figure 66 – Zircon Isotope spot analyses of sample s2A; U-Pb analyses are colour coded according to concordance; blue writing indicates the Hf identifier with the respective εHf_{468} values

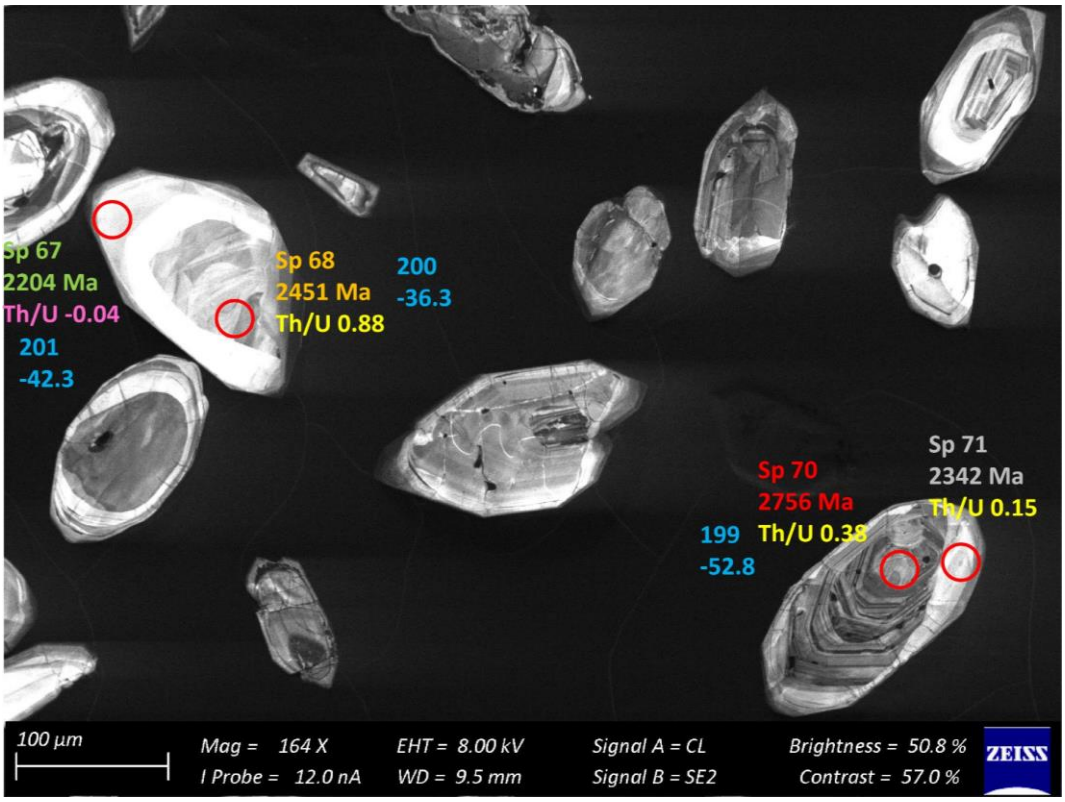

Figure 67 – Zircon Isotope spot analyses of sample s2A; U-Pb analyses are colour coded according to concordance; blue writing indicates the Hf identifier with the respective εHf_{468} values

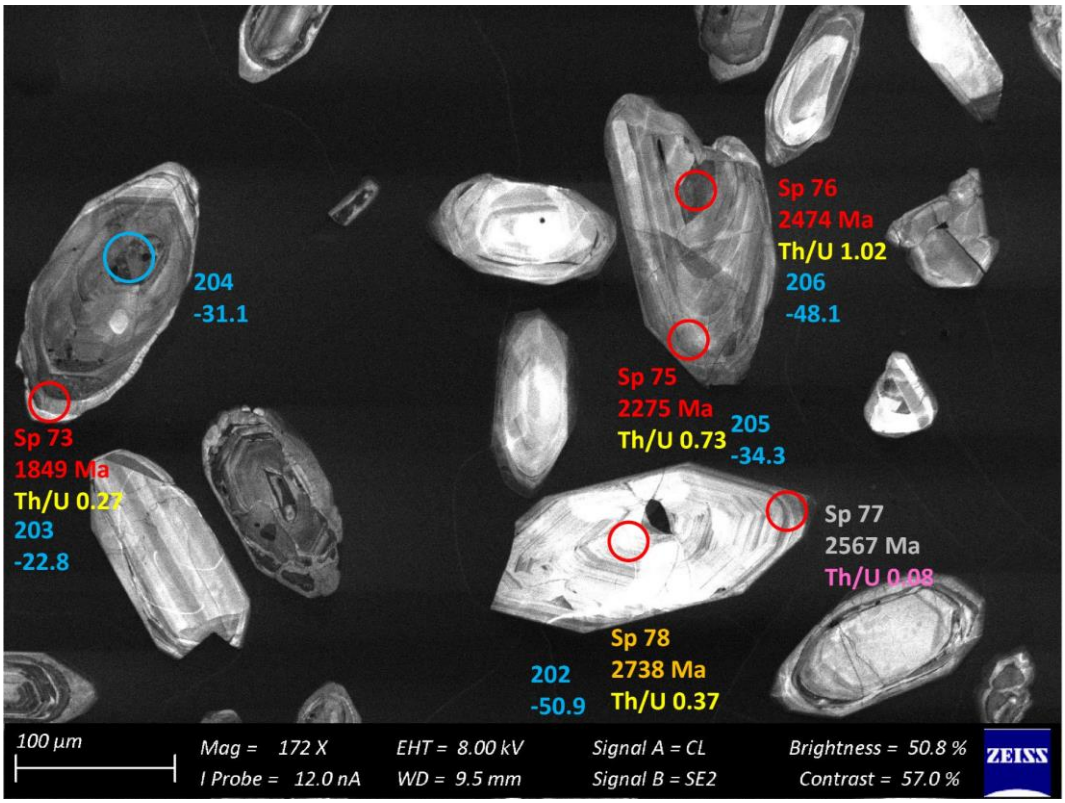

Figure 68 – Zircon Isotope spot analyses of sample s2A; U-Pb analyses are colour coded according to concordance; blue writing indicates the Hf identifier with the respective εHf_{468} values

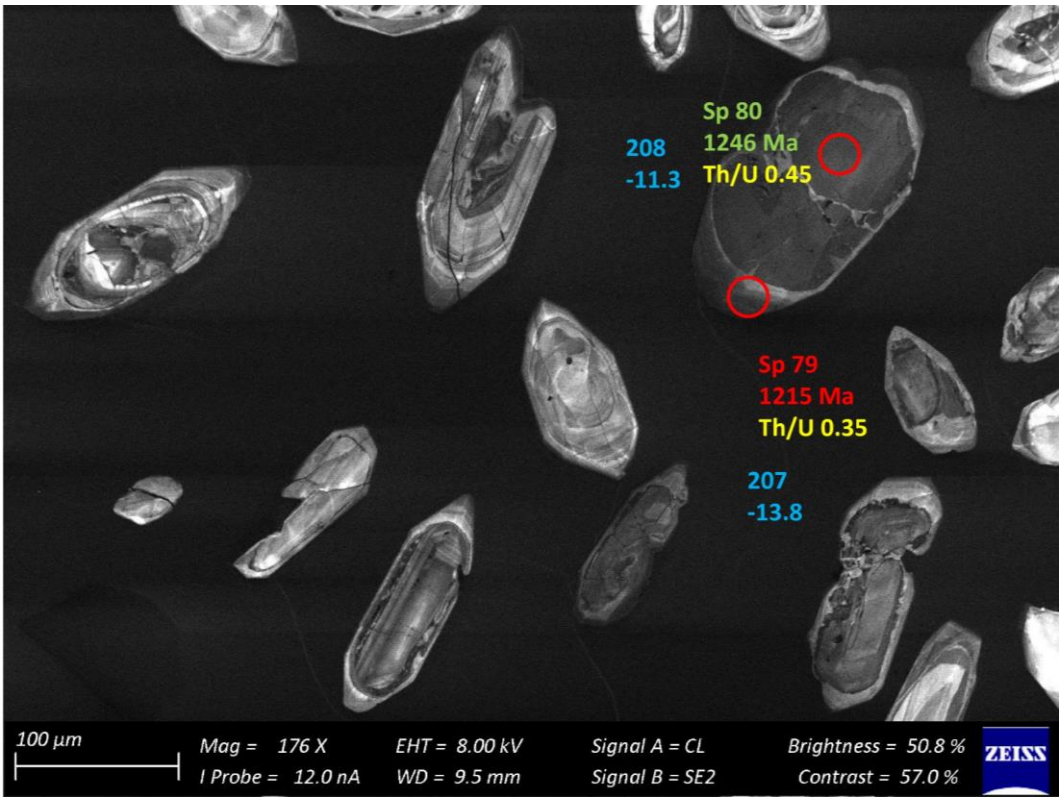

Figure 69 – Zircon Isotope spot analyses of sample s2A; U-Pb analyses are colour coded according to concordance; blue writing indicates the Hf identifier with the respective εHf_{468} values

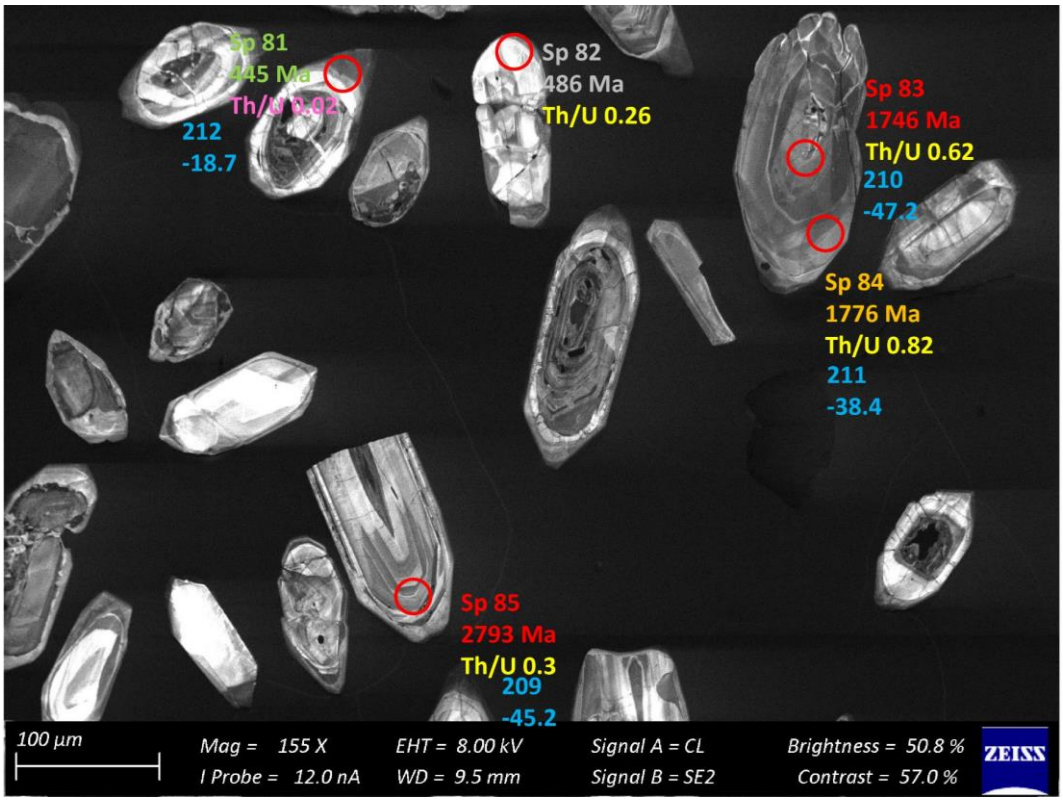

Figure 70 – Zircon Isotope spot analyses of sample s2A; U-Pb analyses are colour coded according to concordance; blue writing indicates the Hf identifier with the respective εHf_{468} values

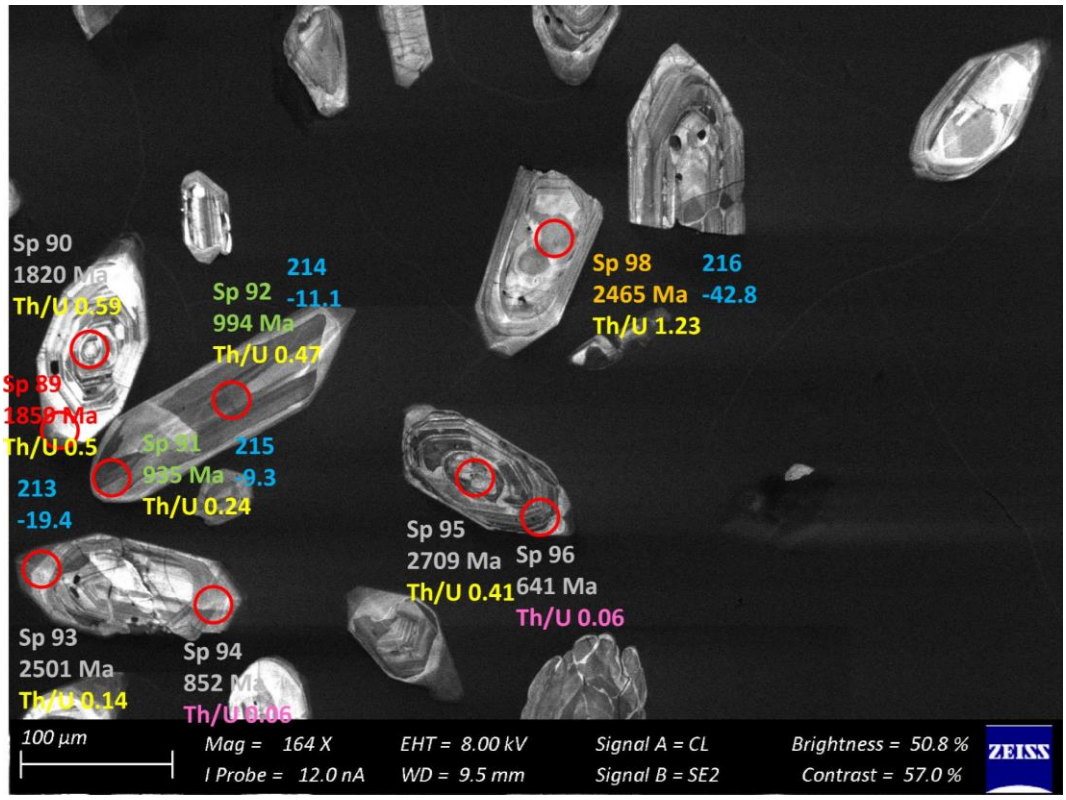

Figure 71 – Zircon Isotope spot analyses of sample s2A; U-Pb analyses are colour coded according to concordance; blue writing indicates the Hf identifier with the respective εHf_{468} values

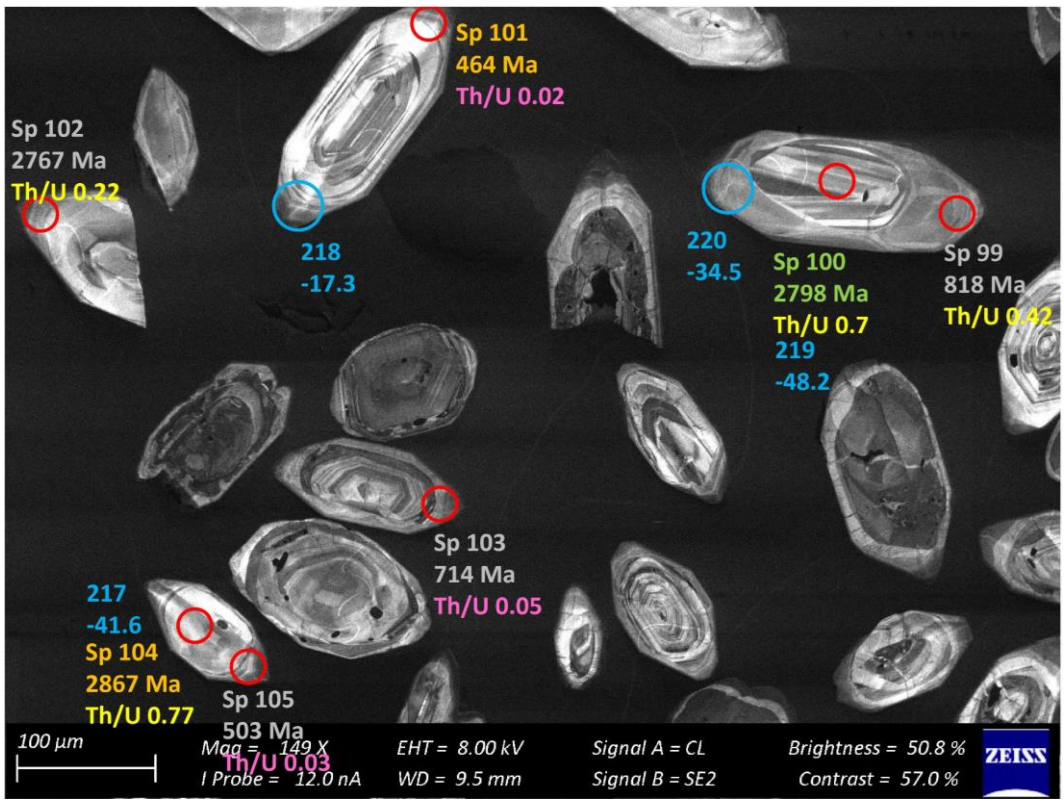

Figure 72 – Zircon Isotope spot analyses of sample s2A; U-Pb analyses are colour coded according to concordance; blue writing indicates the Hf identifier with the respective εHf_{468} values

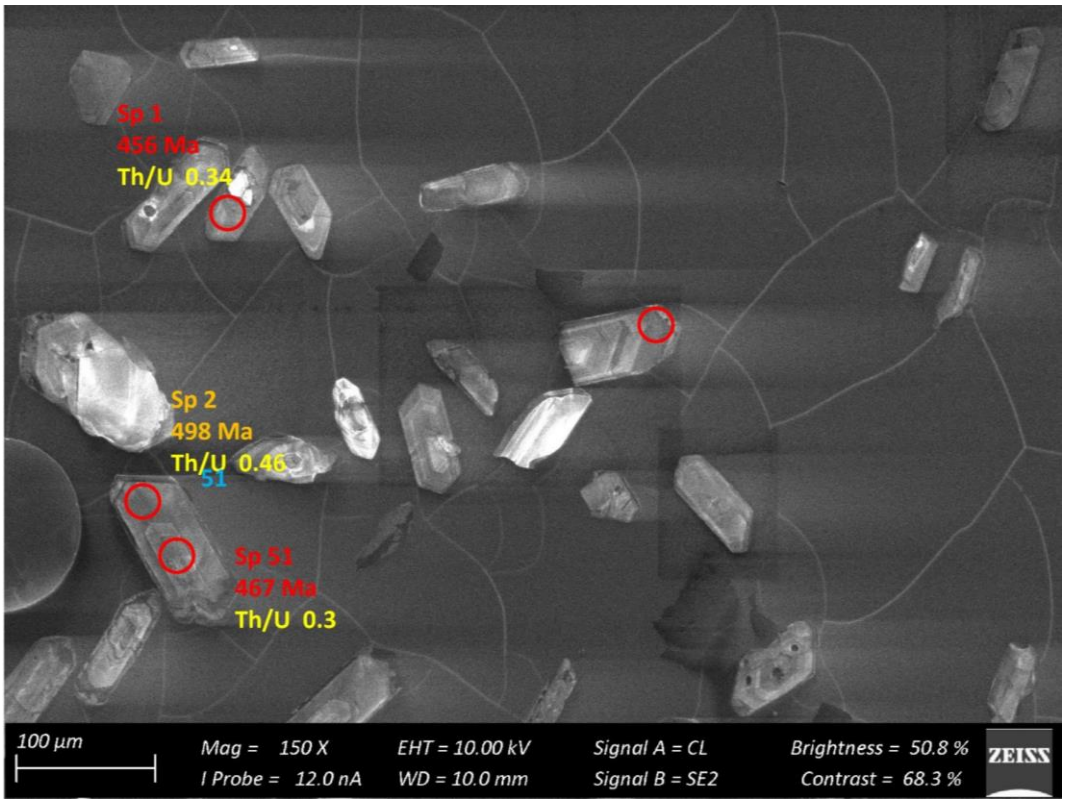

Figure 73 – Zircon Isotope spot analyses of sample s2B; U-Pb analyses are colour coded according to concordance; blue writing indicates the Hf identifier with the respective εHf_{468} values

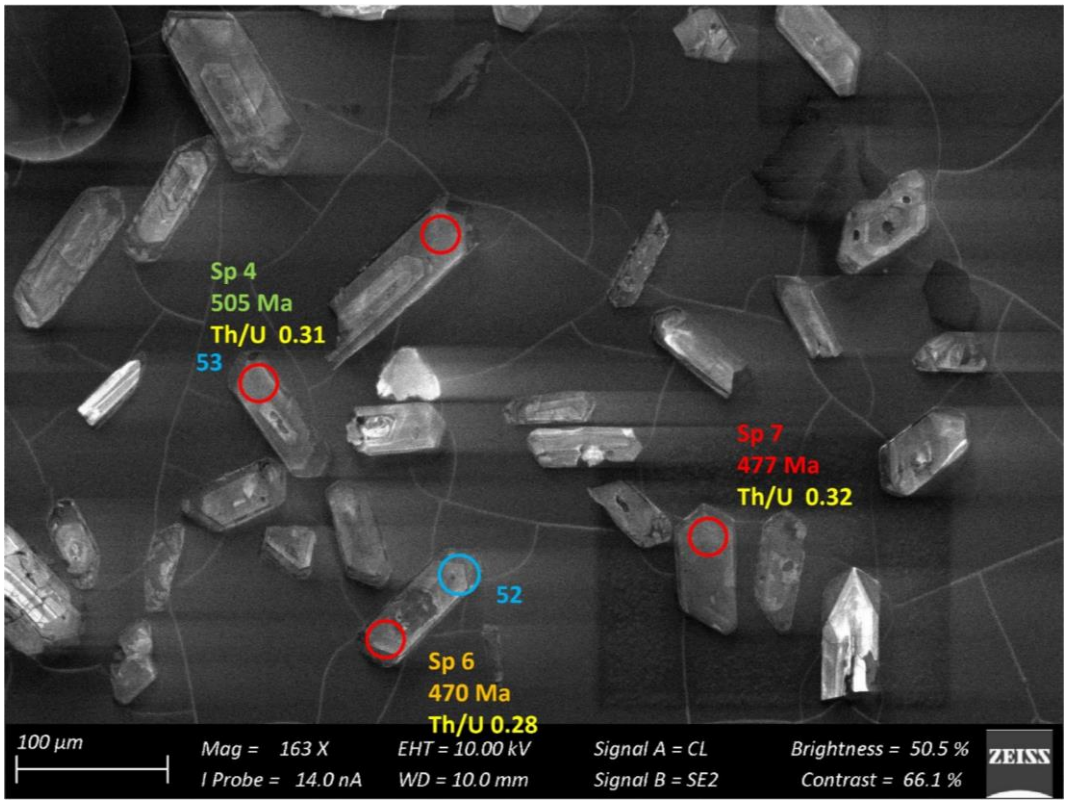

Figure 74 – Zircon Isotope spot analyses of sample s2B; U-Pb analyses are colour coded according to concordance; blue writing indicates the Hf identifier with the respective εHf_{468} values

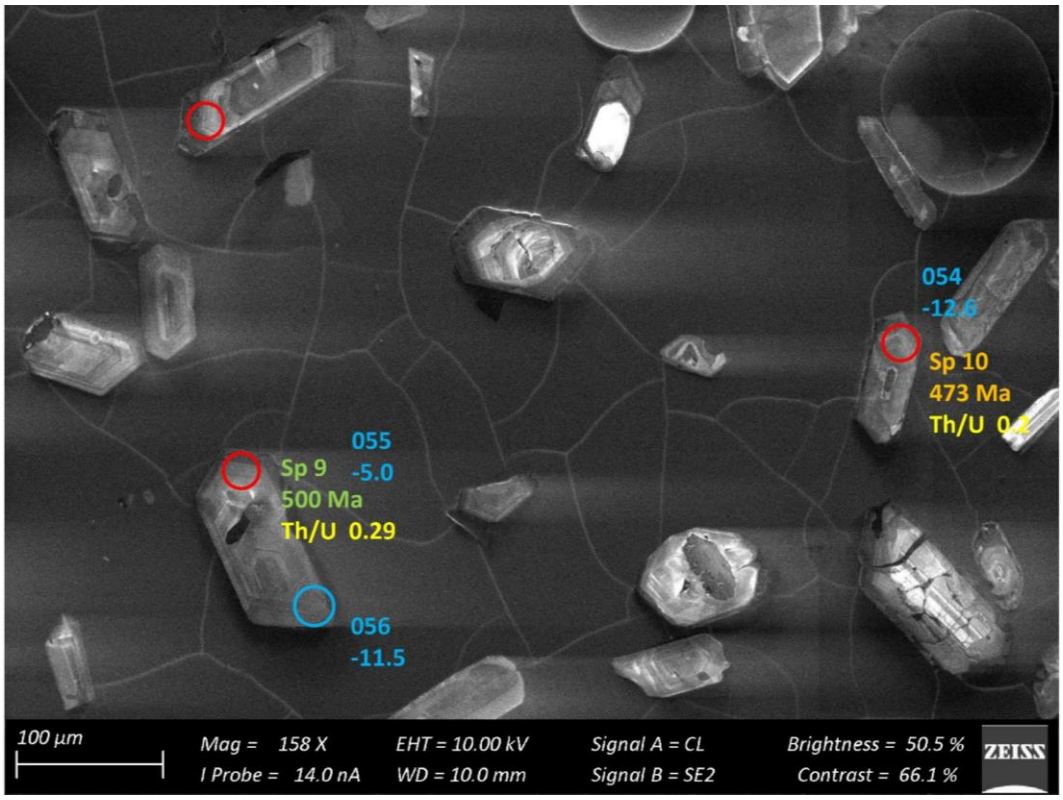

Figure 75 – Zircon Isotope spot analyses of sample s2B; U-Pb analyses are colour coded according to concordance; blue writing indicates the Hf identifier with the respective εHf_{468} values

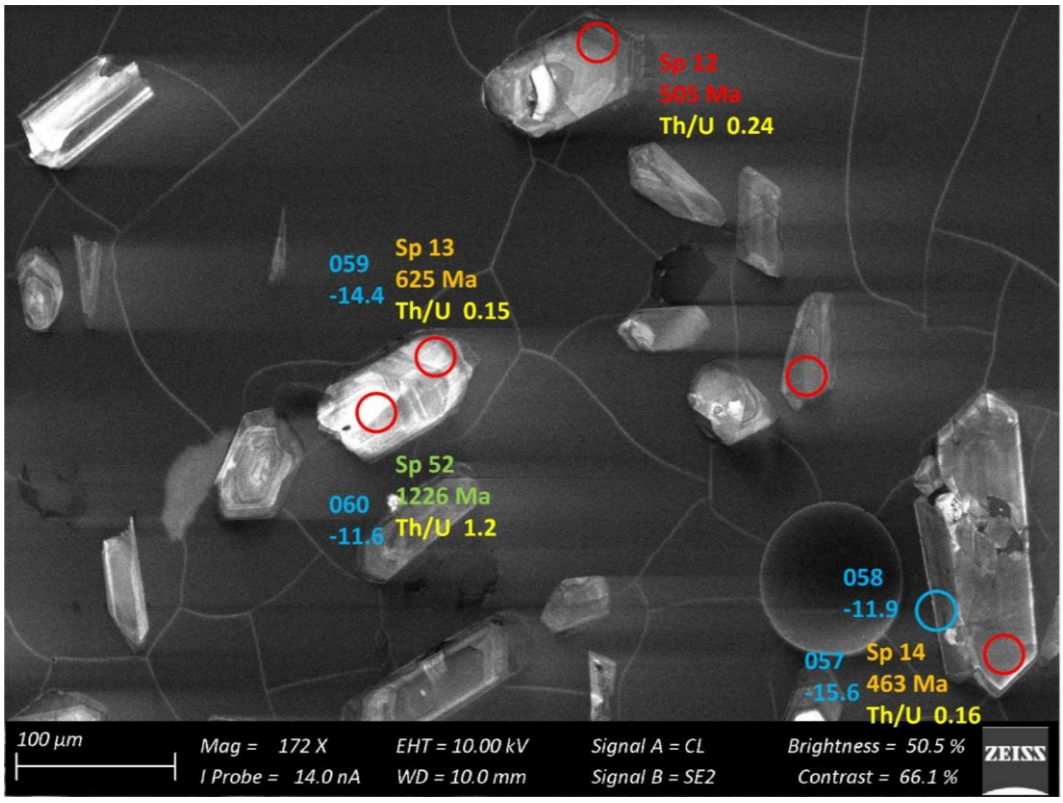

Figure 76 – Zircon Isotope spot analyses of sample s2B; U-Pb analyses are colour coded according to concordance; blue writing indicates the Hf identifier with the respective εHf_{468} values

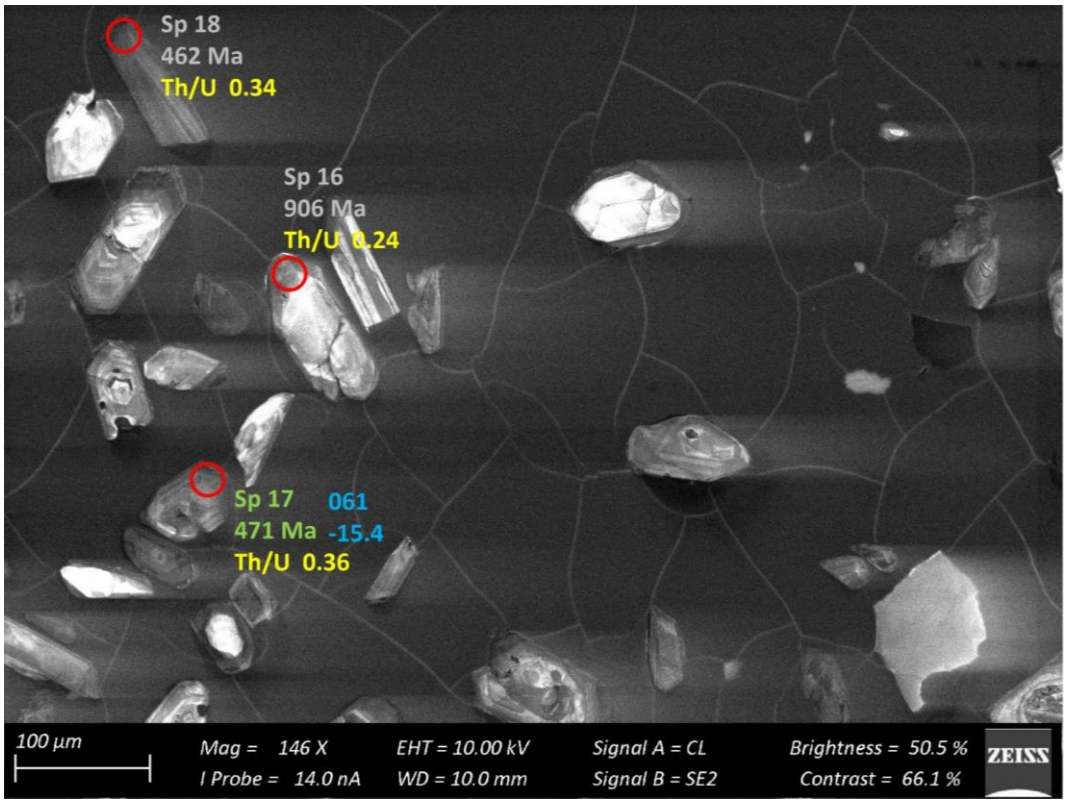

Figure 77 – Zircon Isotope spot analyses of sample s2B; U-Pb analyses are colour coded according to concordance; blue writing indicates the Hf identifier with the respective εHf_{468} values

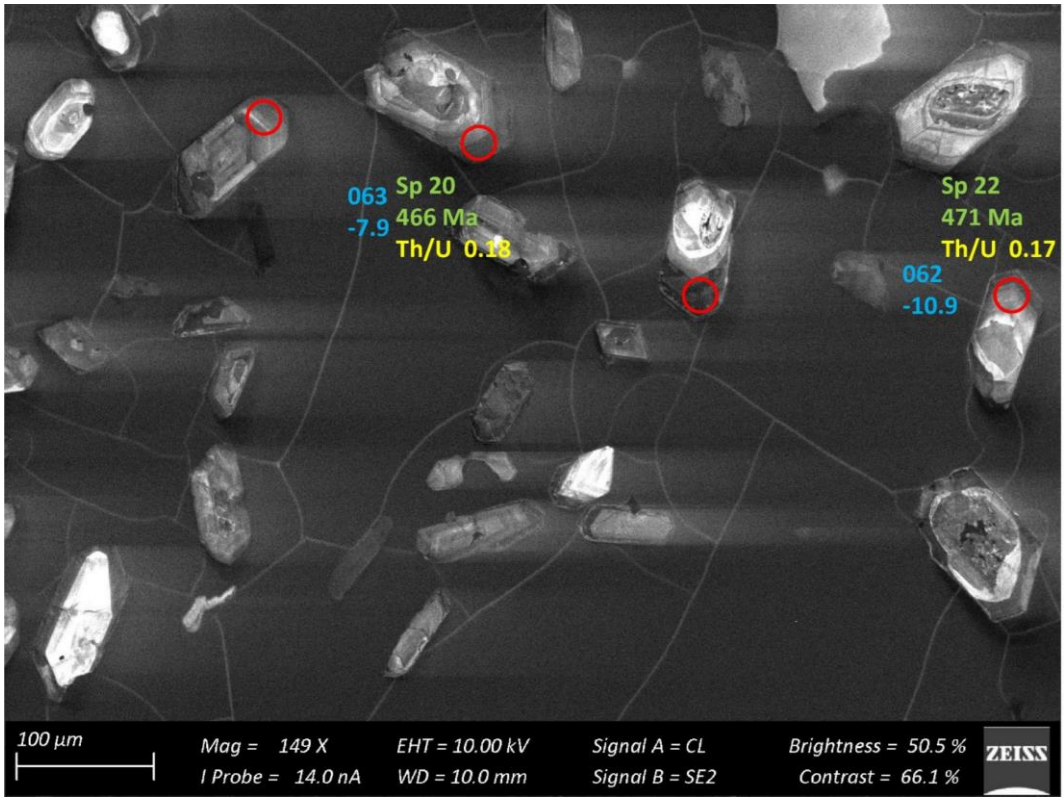

Figure 78 – Zircon Isotope spot analyses of sample s2B; U-Pb analyses are colour coded according to concordance; blue writing indicates the Hf identifier with the respective εHf_{468} values

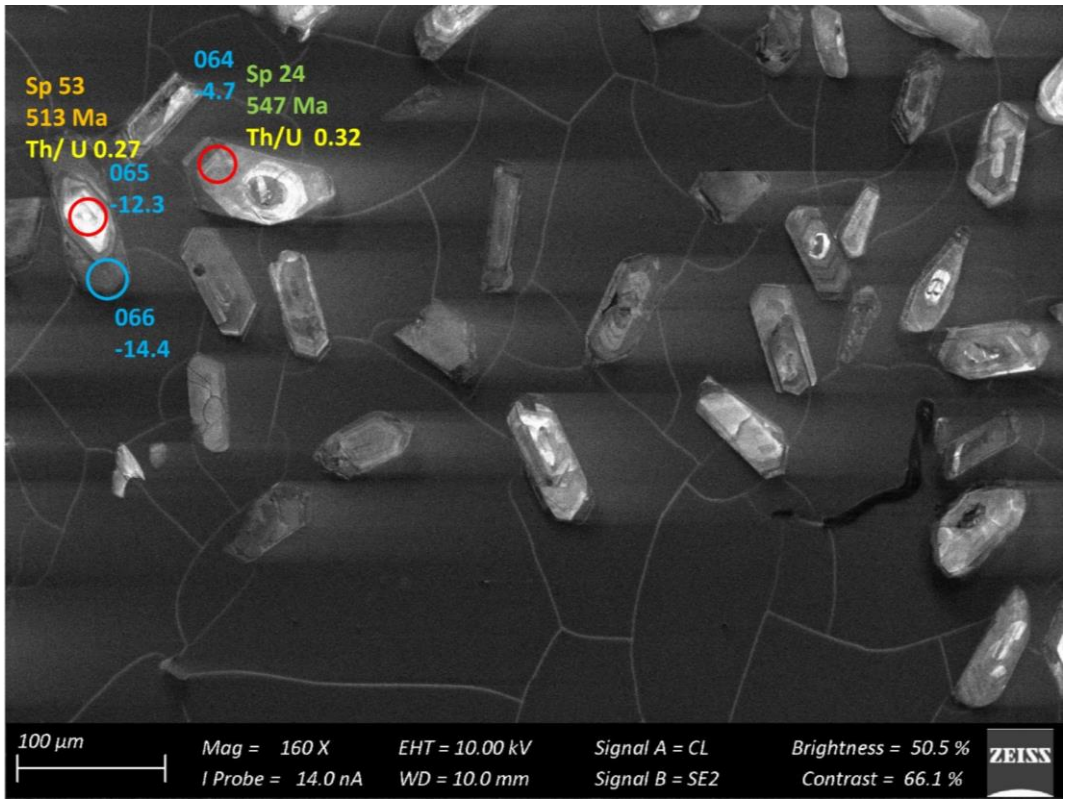

Figure 79 – Zircon Isotope spot analyses of sample s2B; U-Pb analyses are colour coded according to concordance; blue writing indicates the Hf identifier with the respective εHf_{468} values

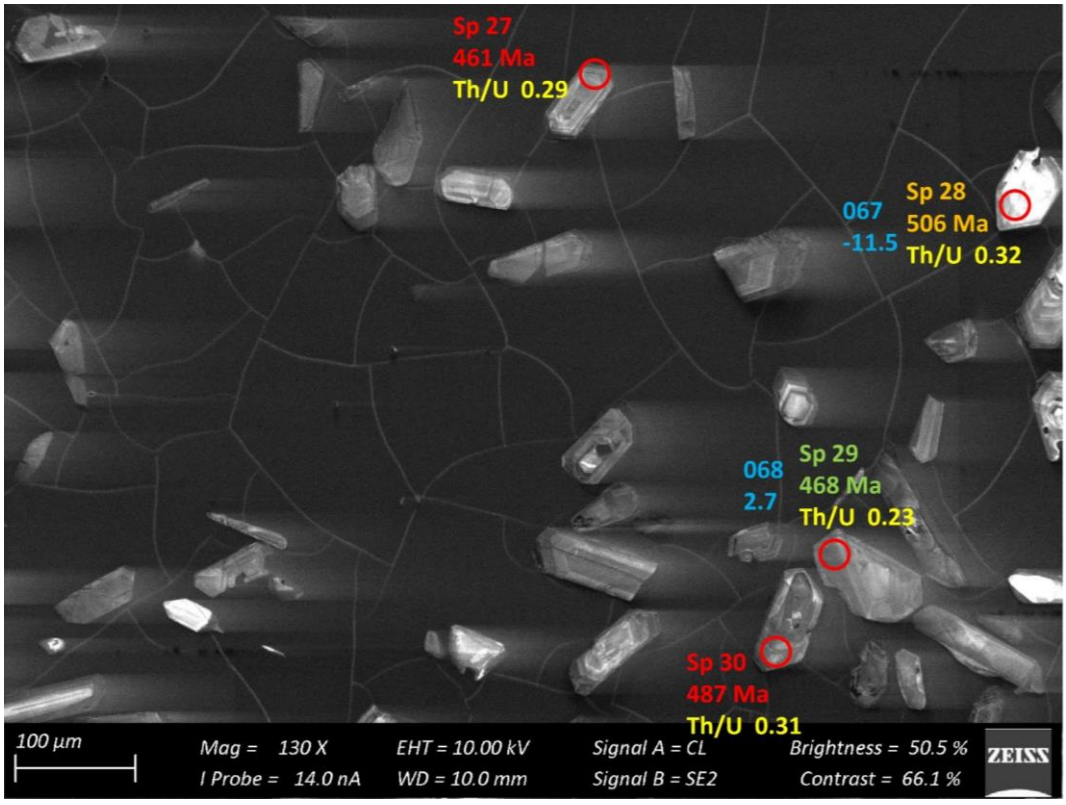

Figure 80 – Zircon Isotope spot analyses of sample s2B; U-Pb analyses are colour coded according to concordance; blue writing indicates the Hf identifier with the respective εHf_{468} values

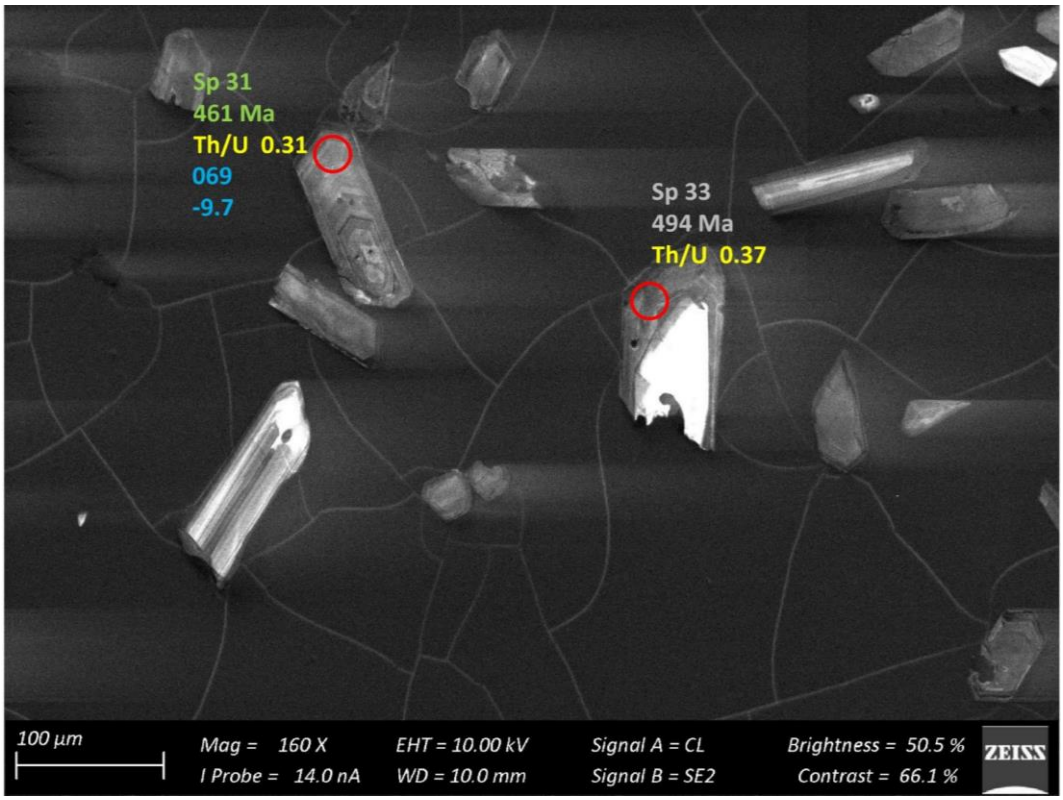

Figure 81 – Zircon Isotope spot analyses of sample s2B; U-Pb analyses are colour coded according to concordance; blue writing indicates the Hf identifier with the respective εHf_{468} values

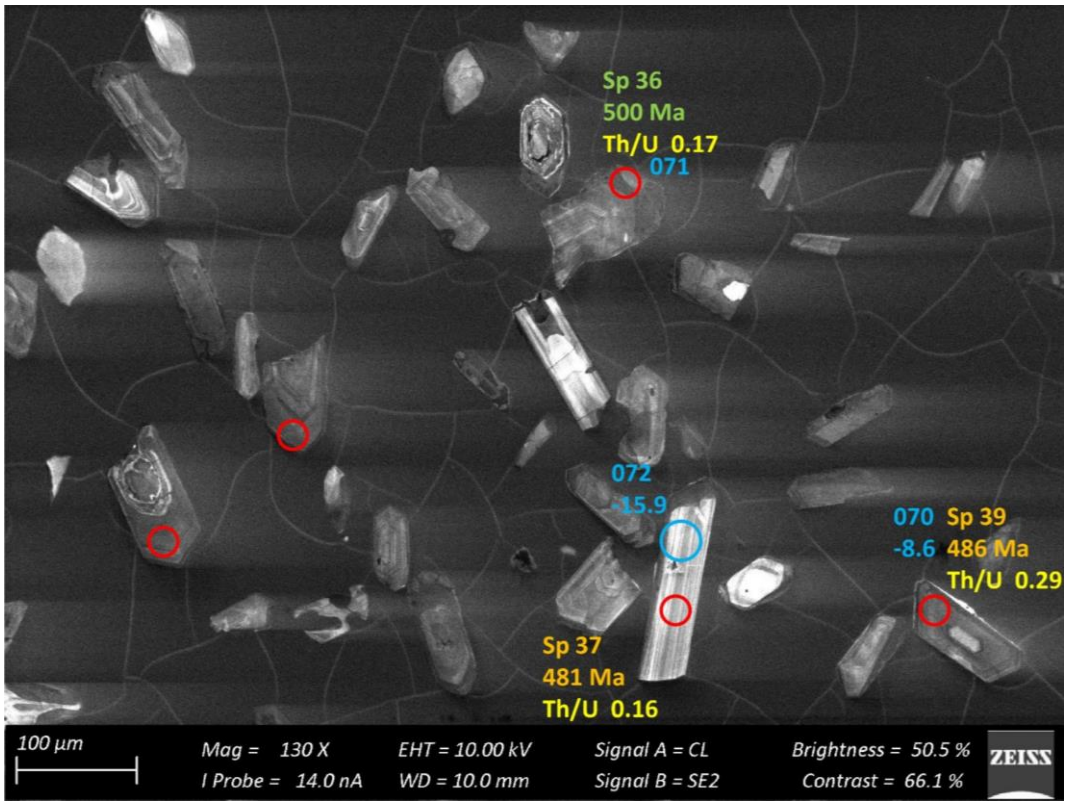

Figure 82 – Zircon Isotope spot analyses of sample s2B; U-Pb analyses are colour coded according to concordance; blue writing indicates the Hf identifier with the respective εHf_{468} values

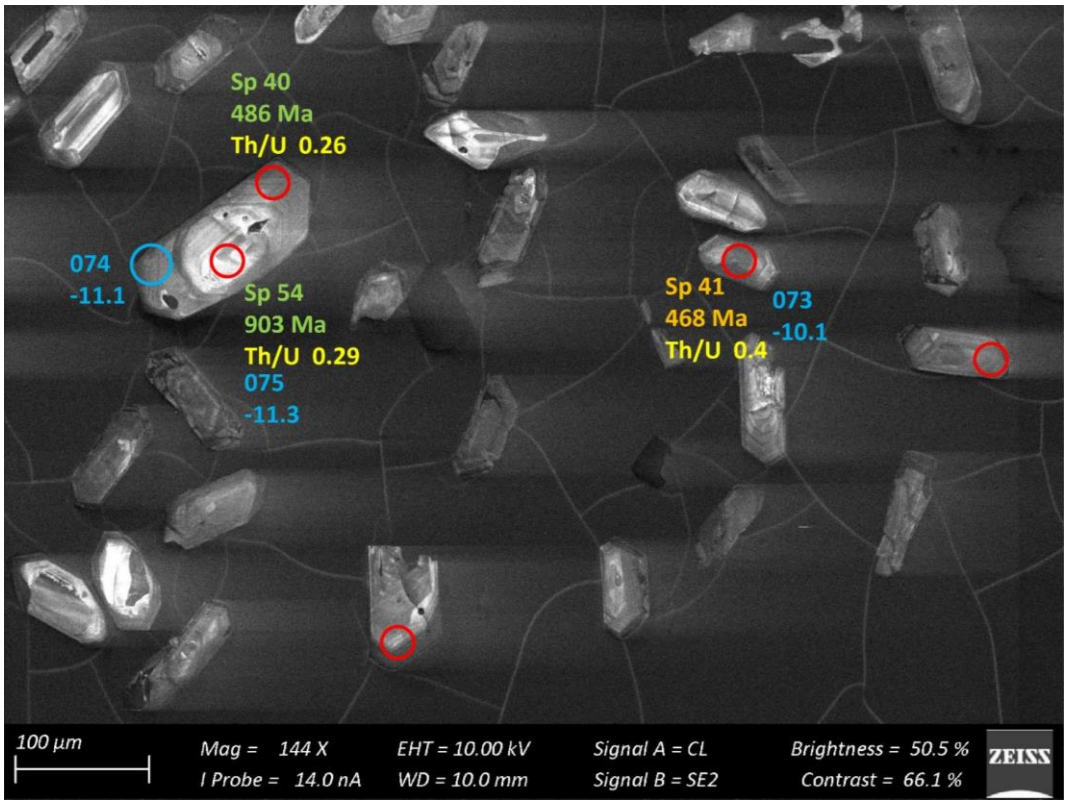

Figure 83 – Zircon Isotope spot analyses of sample s2B; U-Pb analyses are colour coded according to concordance; blue writing indicates the Hf identifier with the respective εHf_{468} values

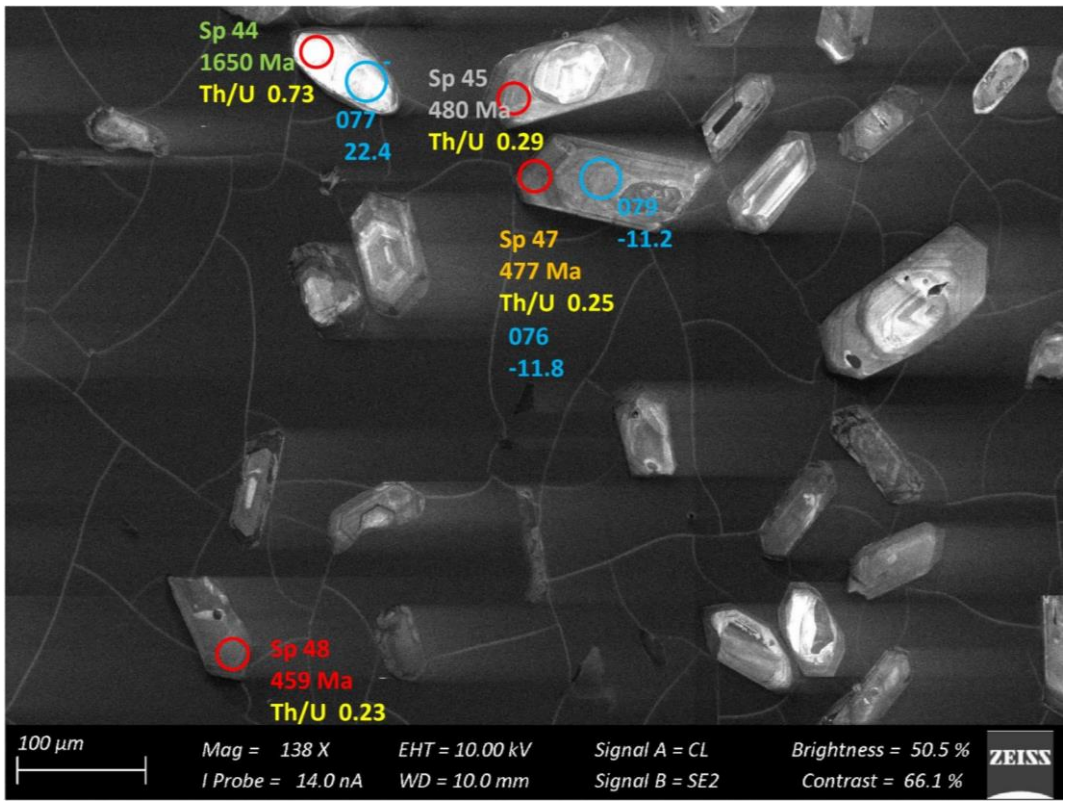

Figure 84 – Zircon Isotope spot analyses of sample s2B; U-Pb analyses are colour coded according to concordance; blue writing indicates the Hf identifier with the respective εHf_{468} values

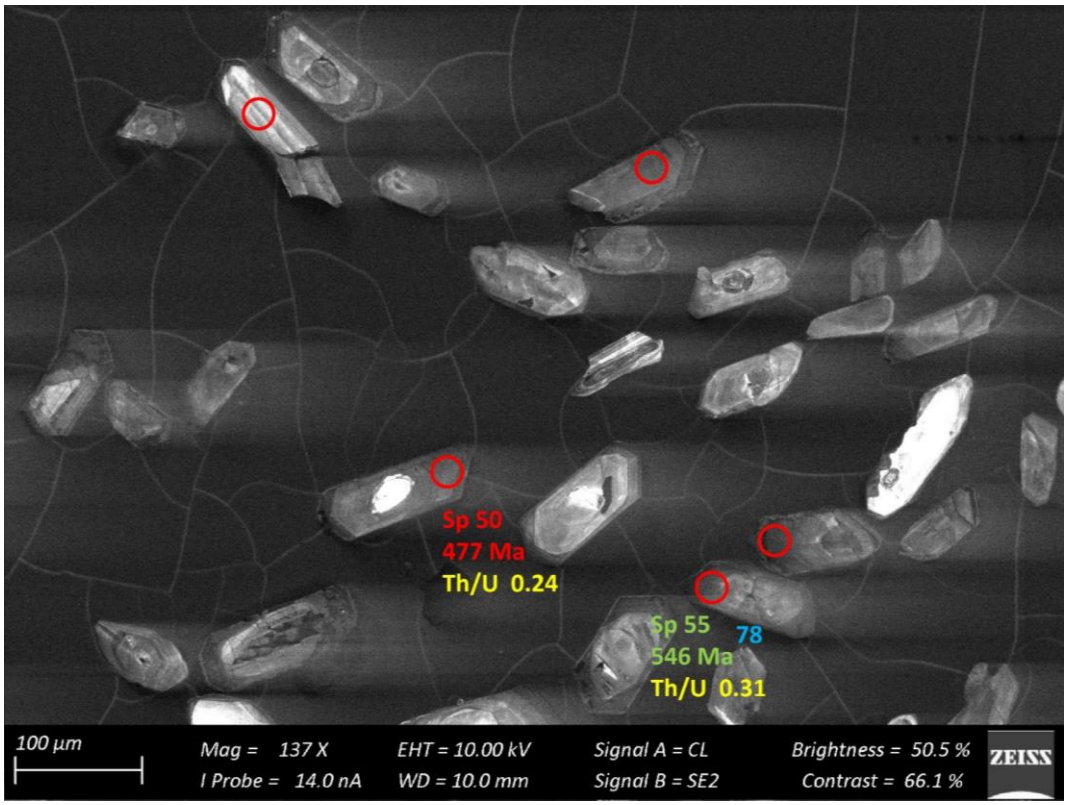

Figure 85 – Zircon Isotope spot analyses of sample s2B; U-Pb analyses are colour coded according to concordance; blue writing indicates the Hf identifier with the respective εHf_{468} values

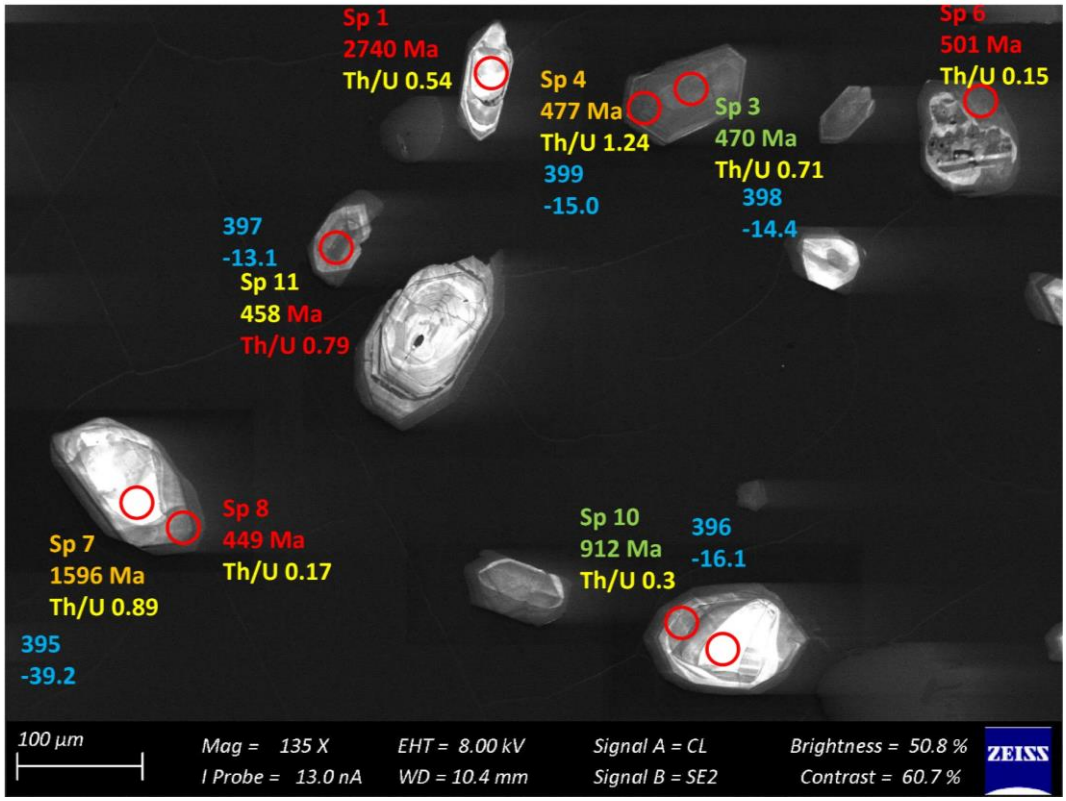

Figure 86 – Zircon Isotope spot analyses of sample s3B; U-Pb analyses are colour coded according to concordance; blue writing indicates the Hf identifier with the respective εHf_{468} values

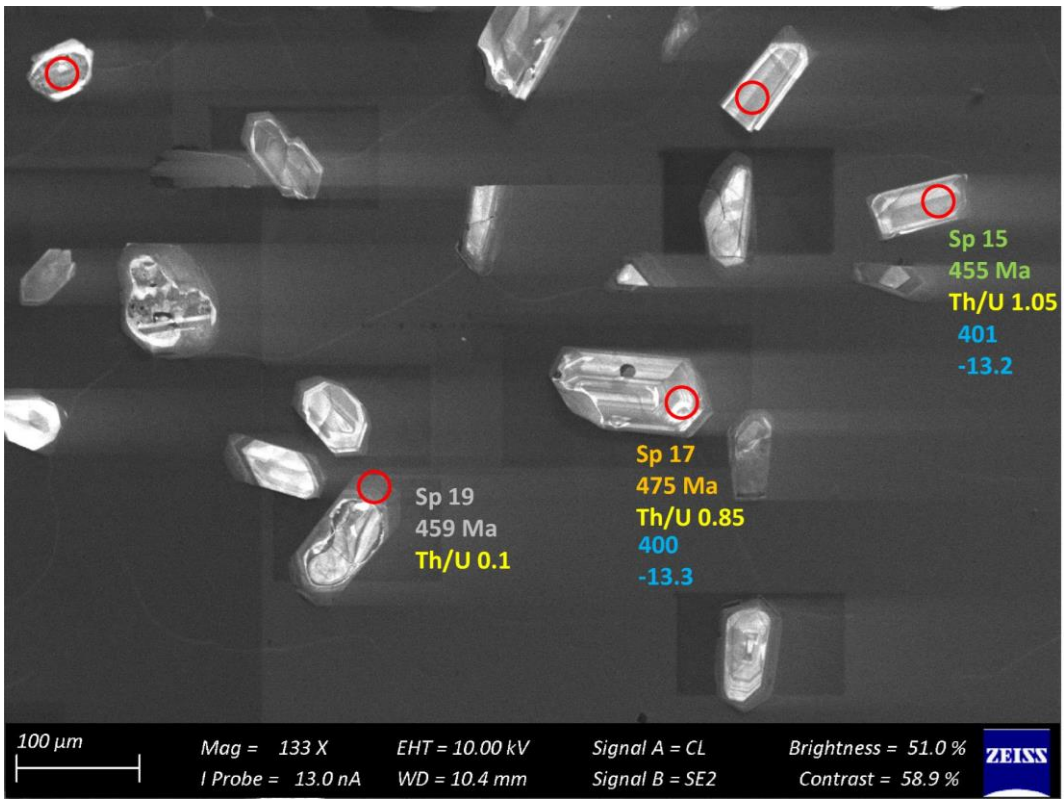

Figure 87 – Zircon Isotope spot analyses of sample s3B; U-Pb analyses are colour coded according to concordance; blue writing indicates the Hf identifier with the respective εHf_{468} values

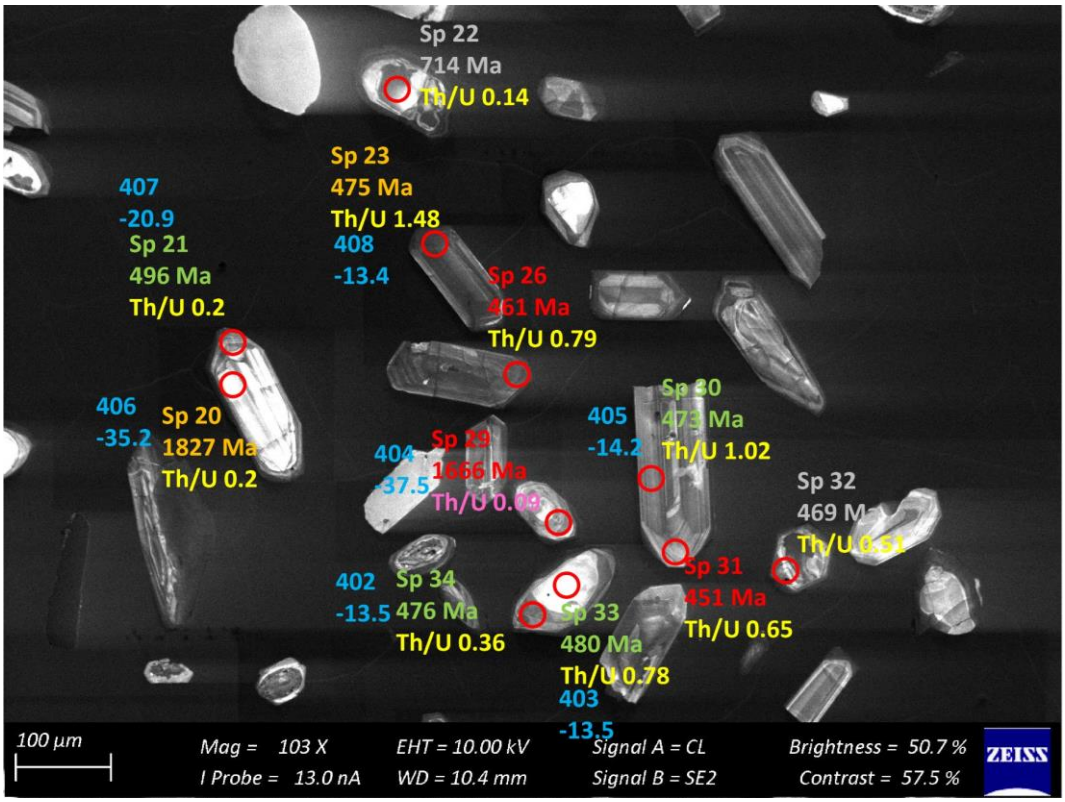

Figure 88 – Zircon Isotope spot analyses of sample s3B; U-Pb analyses are colour coded according to concordance; blue writing indicates the Hf identifier with the respective εHf_{468} values

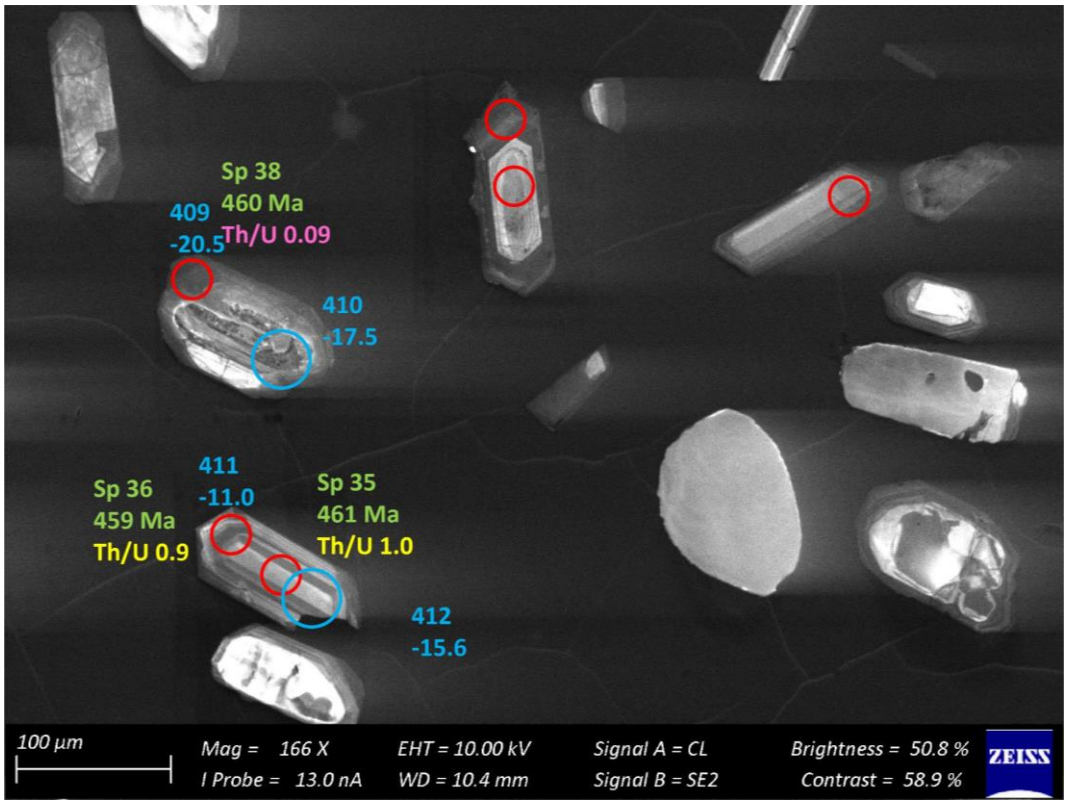

Figure 89 – Zircon Isotope spot analyses of sample s3B; U-Pb analyses are colour coded according to concordance; blue writing indicates the Hf identifier with the respective εHf_{468} values

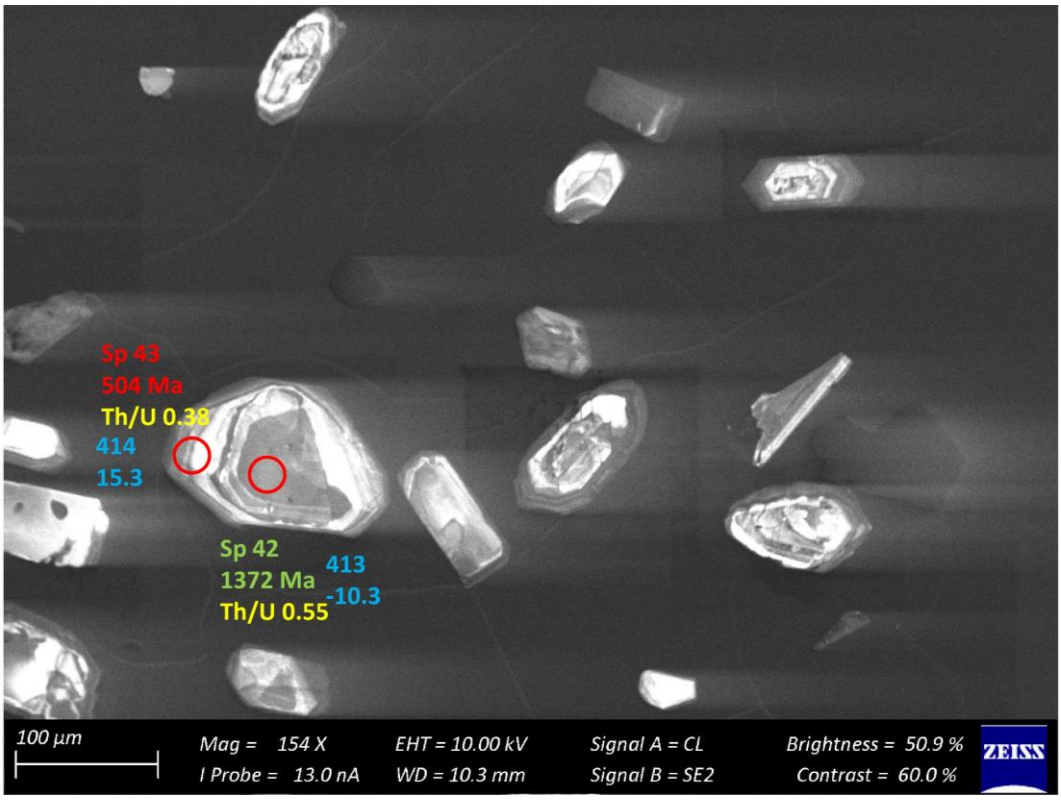

Figure 90 – Zircon Isotope spot analyses of sample s3B; U-Pb analyses are colour coded according to concordance; blue writing indicates the Hf identifier with the respective εHf_{468} values

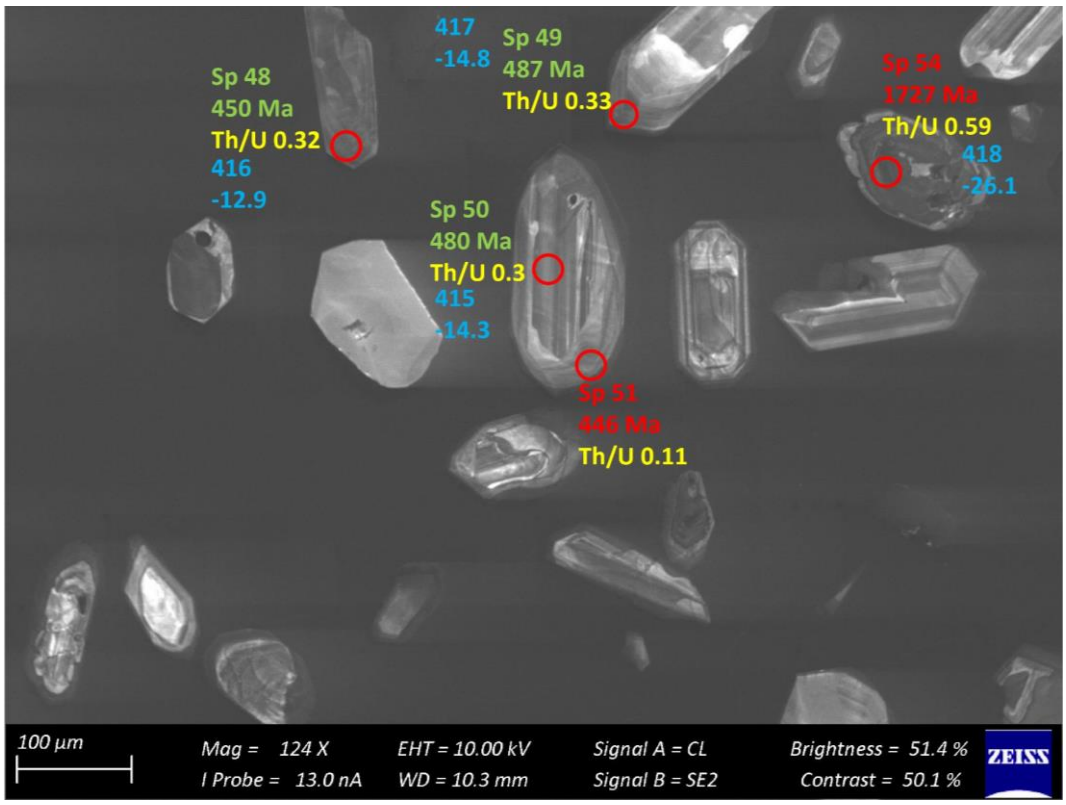

Figure 91 – Zircon Isotope spot analyses of sample s3B; U-Pb analyses are colour coded according to concordance; blue writing indicates the Hf identifier with the respective εHf_{468} values

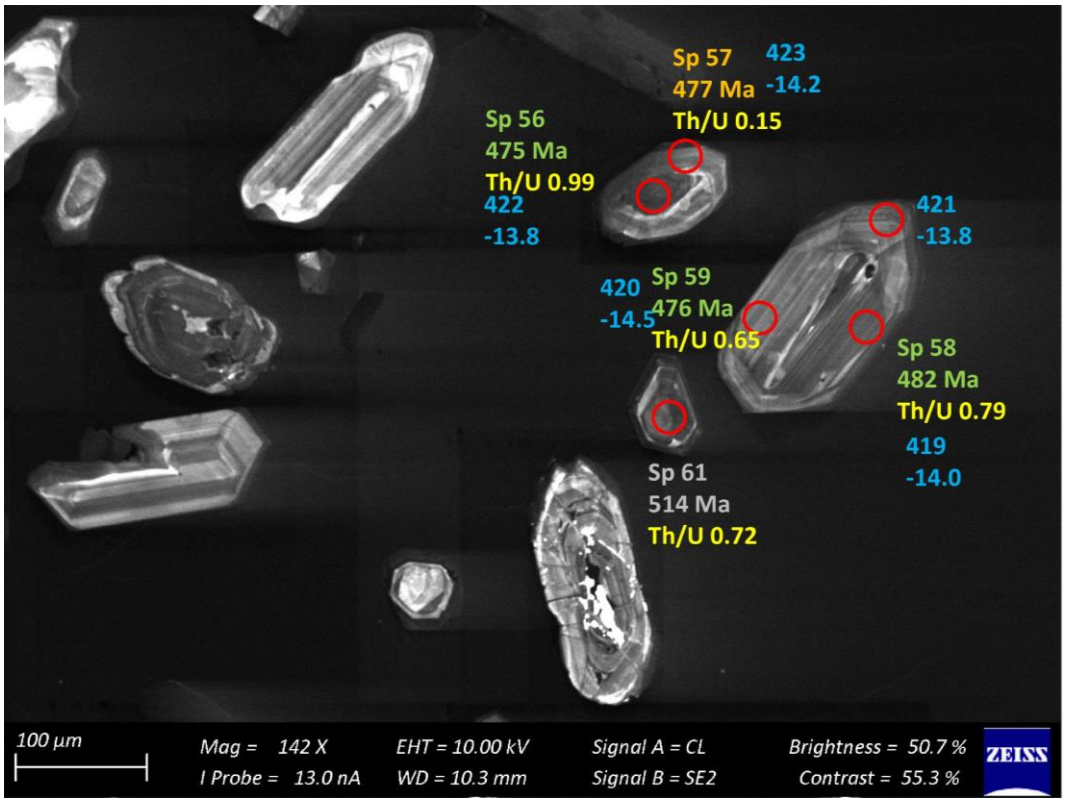

Figure 92 – Zircon Isotope spot analyses of sample s3B; U-Pb analyses are colour coded according to concordance; blue writing indicates the Hf identifier with the respective εHf_{468} values

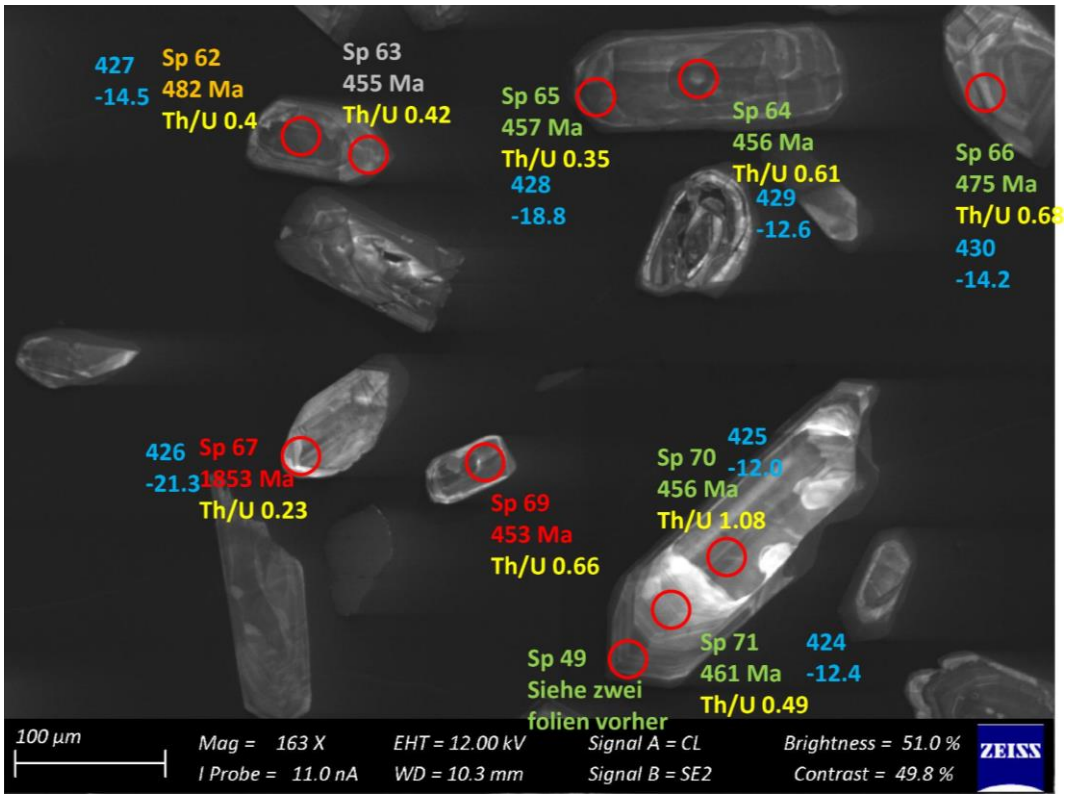

Figure 93 – Zircon Isotope spot analyses of sample s3B; U-Pb analyses are colour coded according to concordance; blue writing indicates the Hf identifier with the respective εHf_{468} values

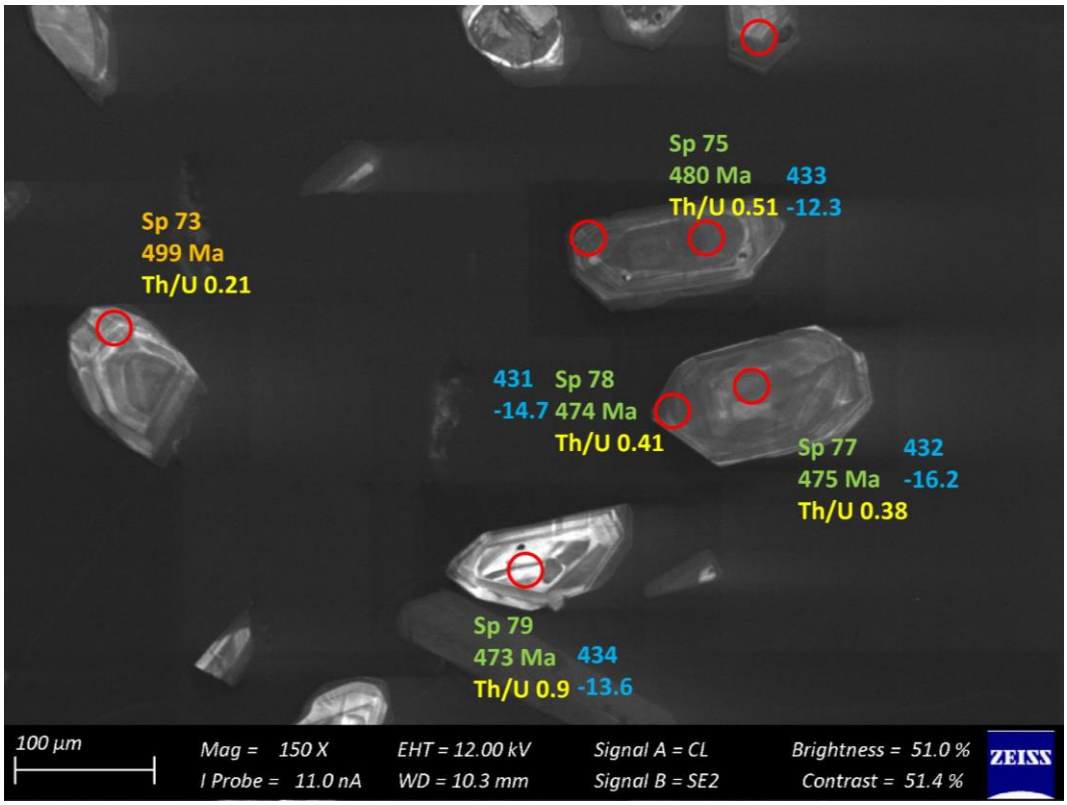

Figure 94 – Zircon Isotope spot analyses of sample s3B; U-Pb analyses are colour coded according to concordance; blue writing indicates the Hf identifier with the respective εHf_{468} values

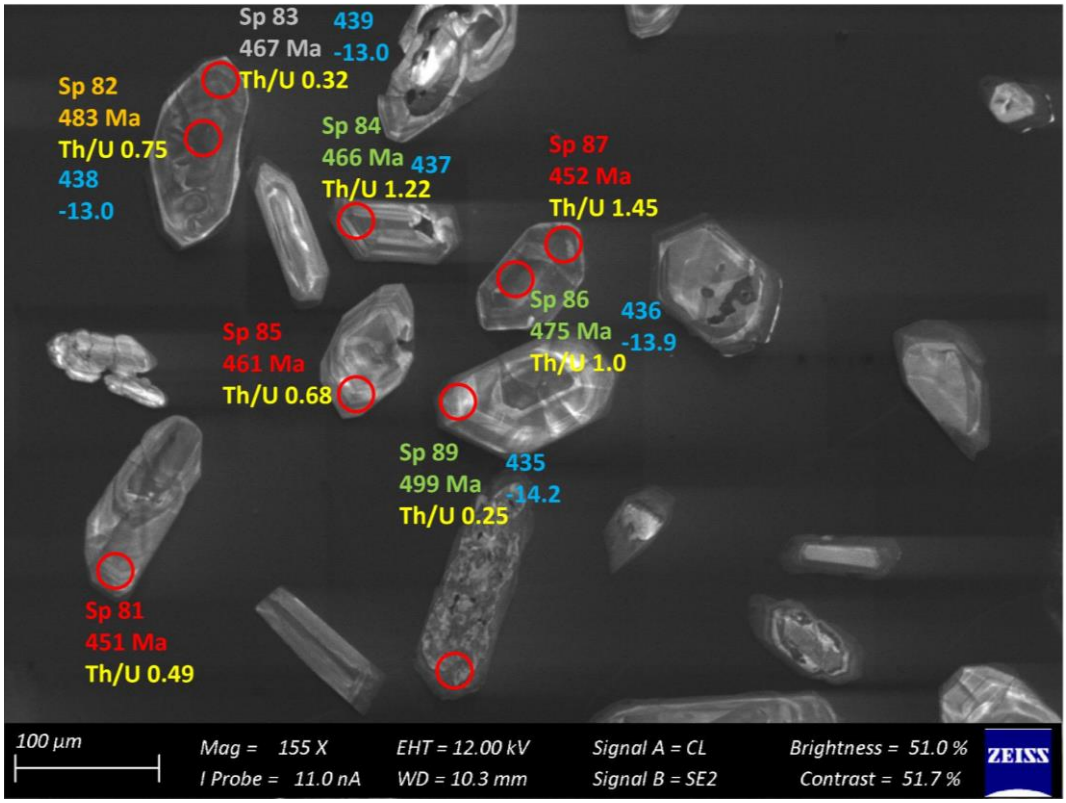

Figure 95 – Zircon Isotope spot analyses of sample s3B; U-Pb analyses are colour coded according to concordance; blue writing indicates the Hf identifier with the respective εHf_{468} values

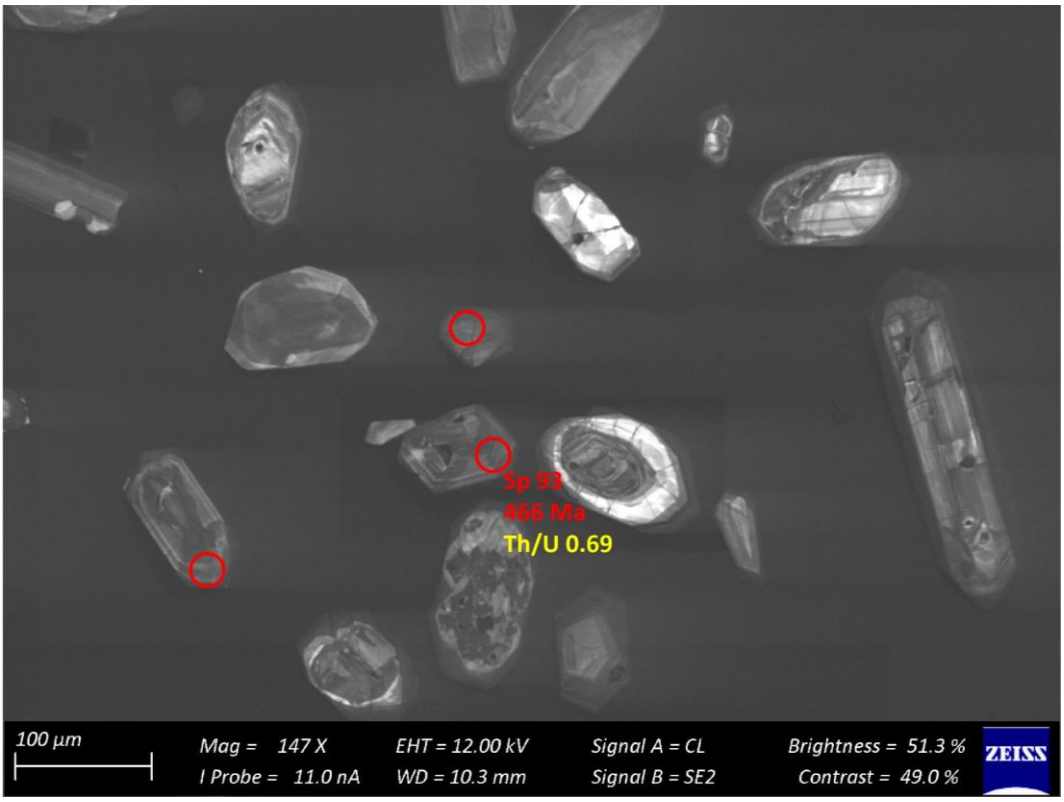

Figure 96 – Zircon Isotope spot analyses of sample s3B; U-Pb analyses are colour coded according to concordance; blue writing indicates the Hf identifier with the respective εHf_{468} values

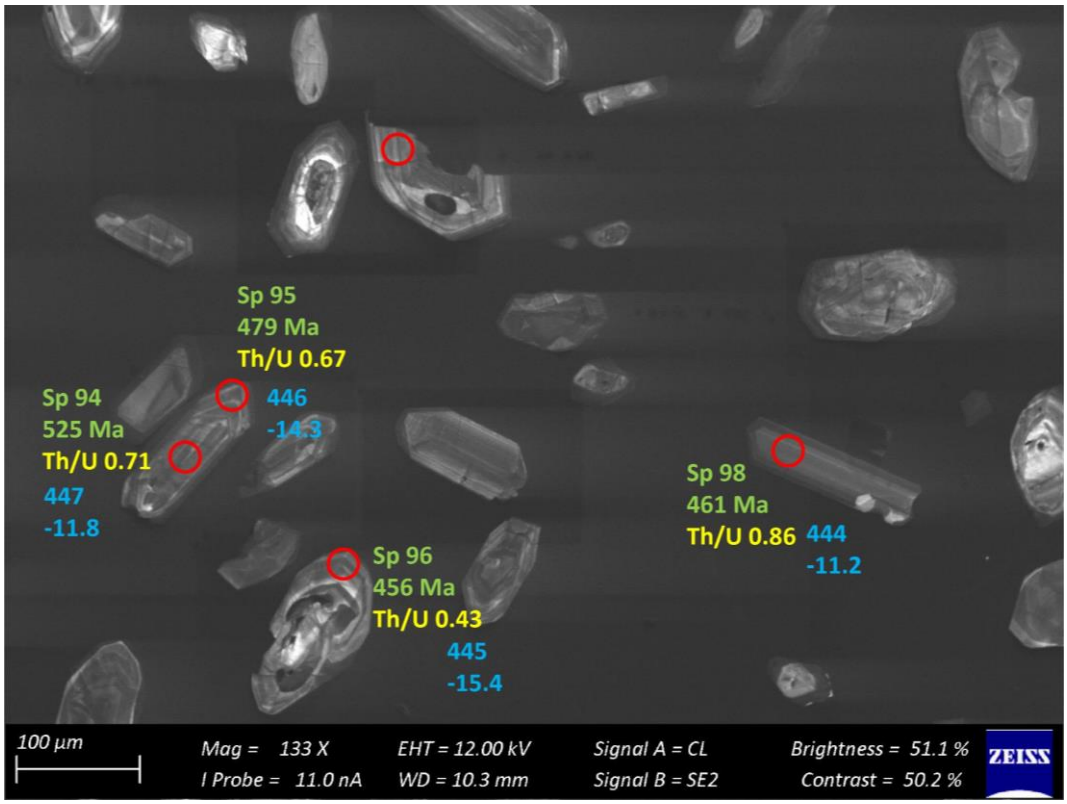

Figure 97 – Zircon Isotope spot analyses of sample s3B; U-Pb analyses are colour coded according to concordance; blue writing indicates the Hf identifier with the respective εHf_{468} values

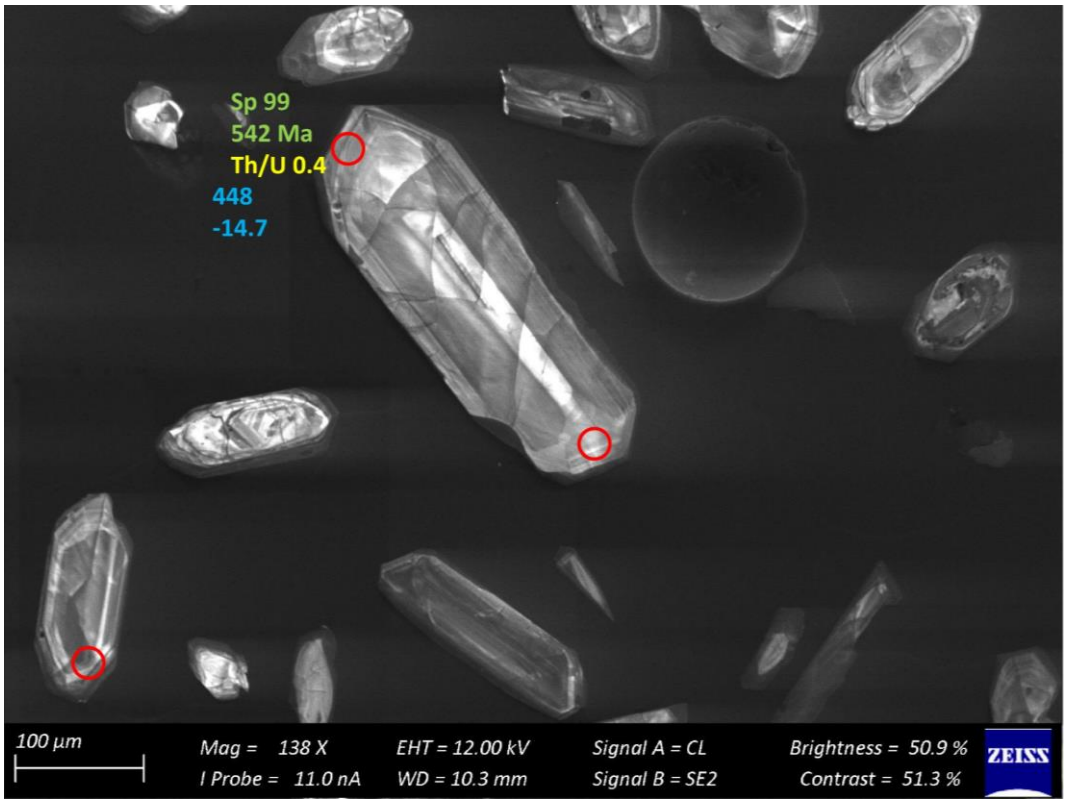

Figure 98 – Zircon Isotope spot analyses of sample s3B; U-Pb analyses are colour coded according to concordance; blue writing indicates the Hf identifier with the respective εHf_{468} values

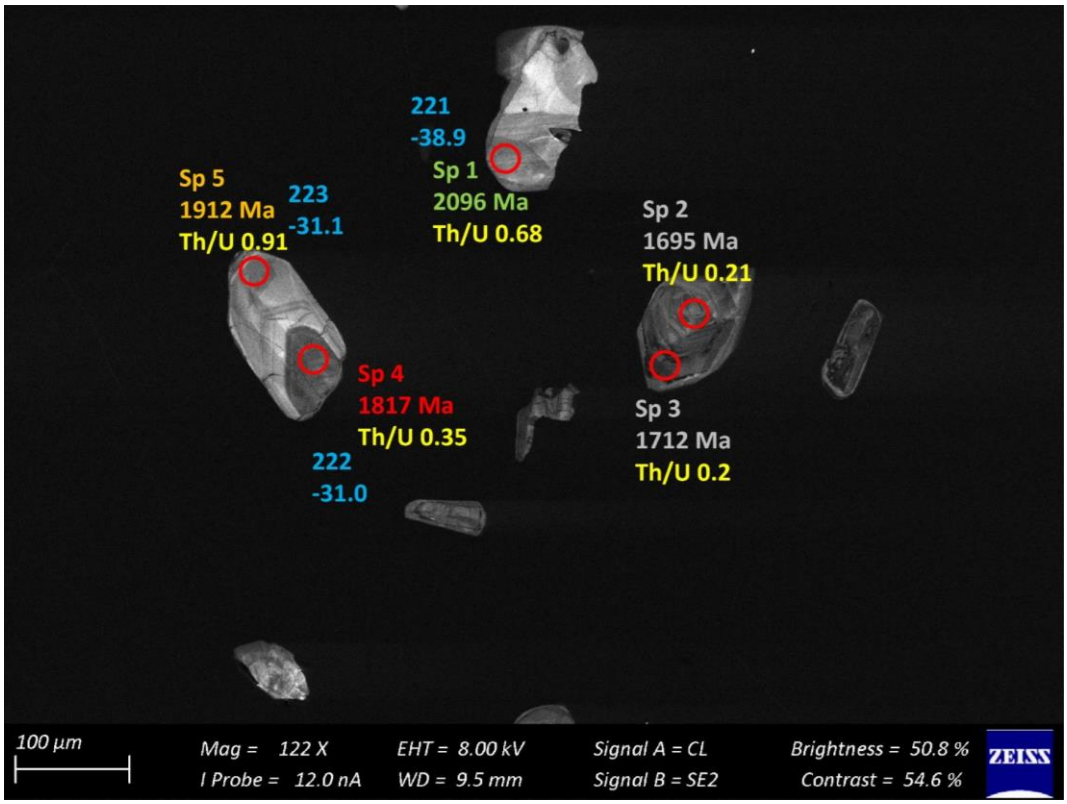

Figure 99 – Zircon Isotope spot analyses of sample s4D; U-Pb analyses are colour coded according to concordance; blue writing indicates the Hf identifier with the respective εHf_{468} values

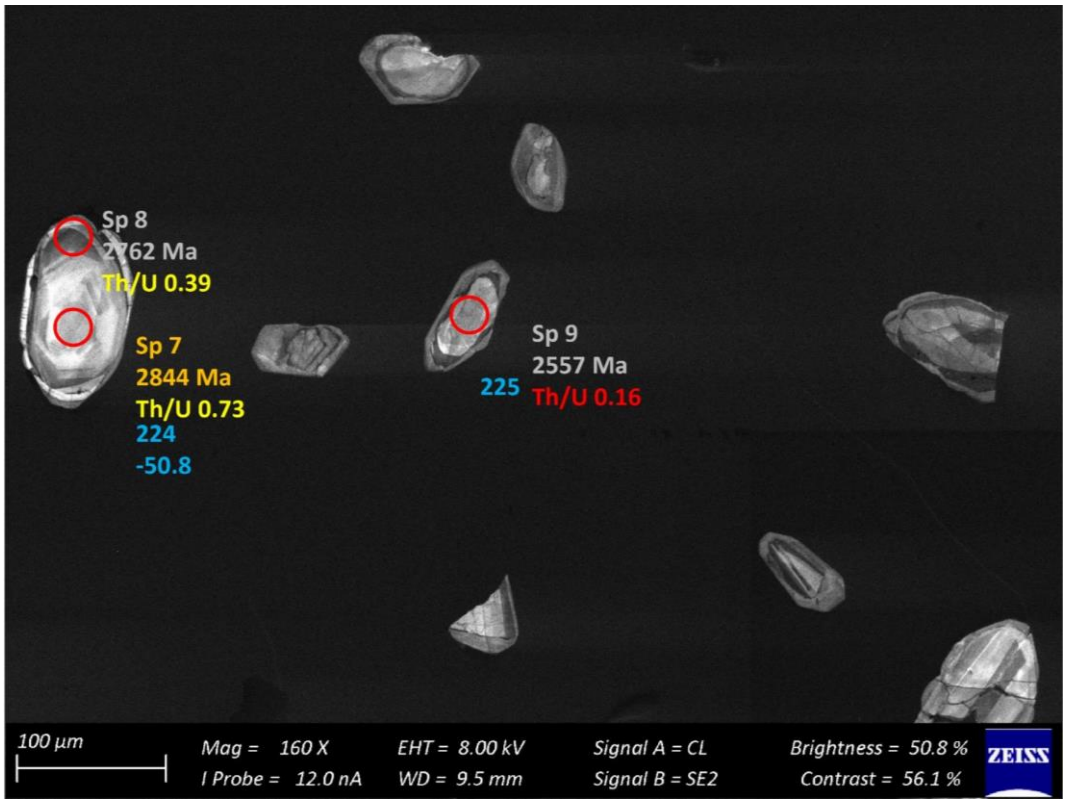

Figure 100 – Zircon Isotope spot analyses of sample s4D; U-Pb analyses are colour coded according to concordance; blue writing indicates the Hf identifier with the respective εHf_{468} values

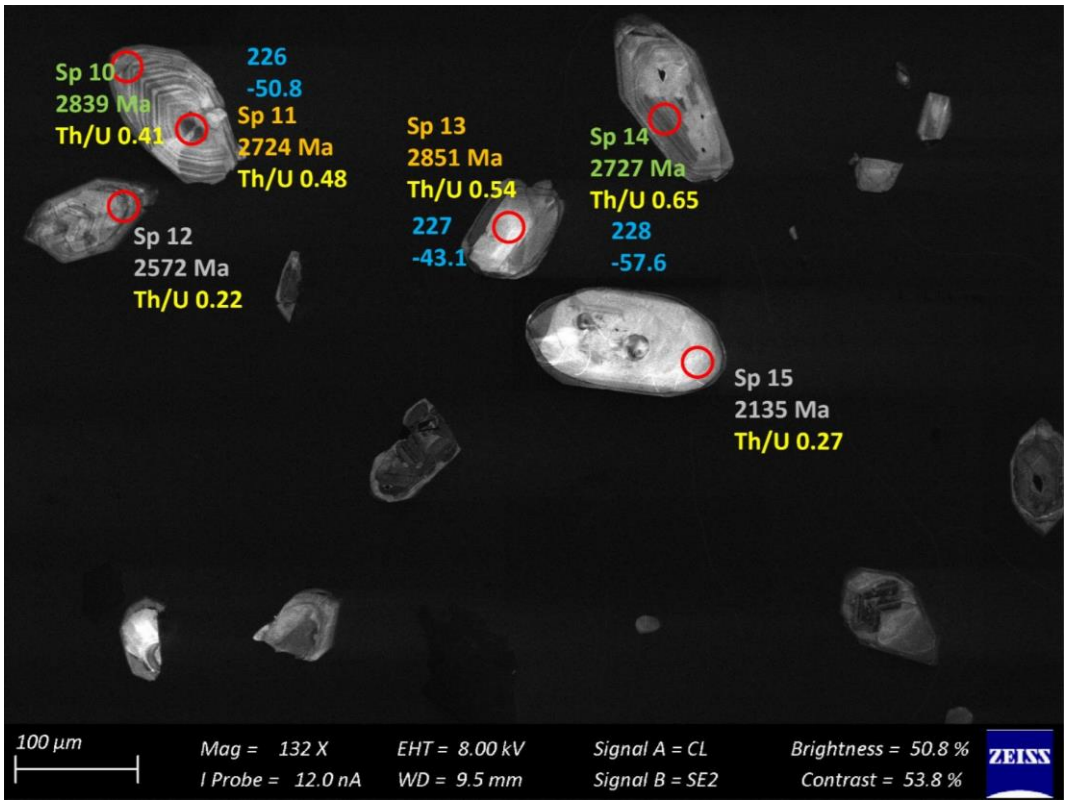

Figure 101 – Zircon Isotope spot analyses of sample s4D; U-Pb analyses are colour coded according to concordance; blue writing indicates the Hf identifier with the respective εHf_{468} values

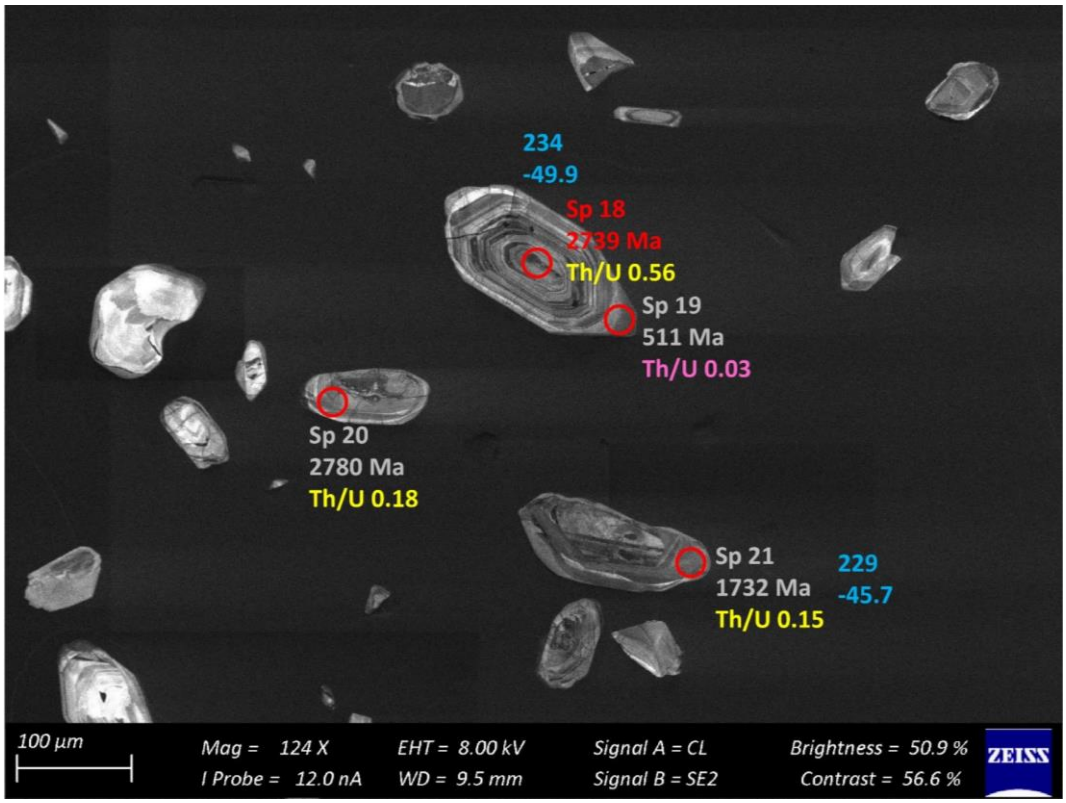

Figure 102 – Zircon Isotope spot analyses of sample s4D; U-Pb analyses are colour coded according to concordance; blue writing indicates the Hf identifier with the respective εHf_{468} values

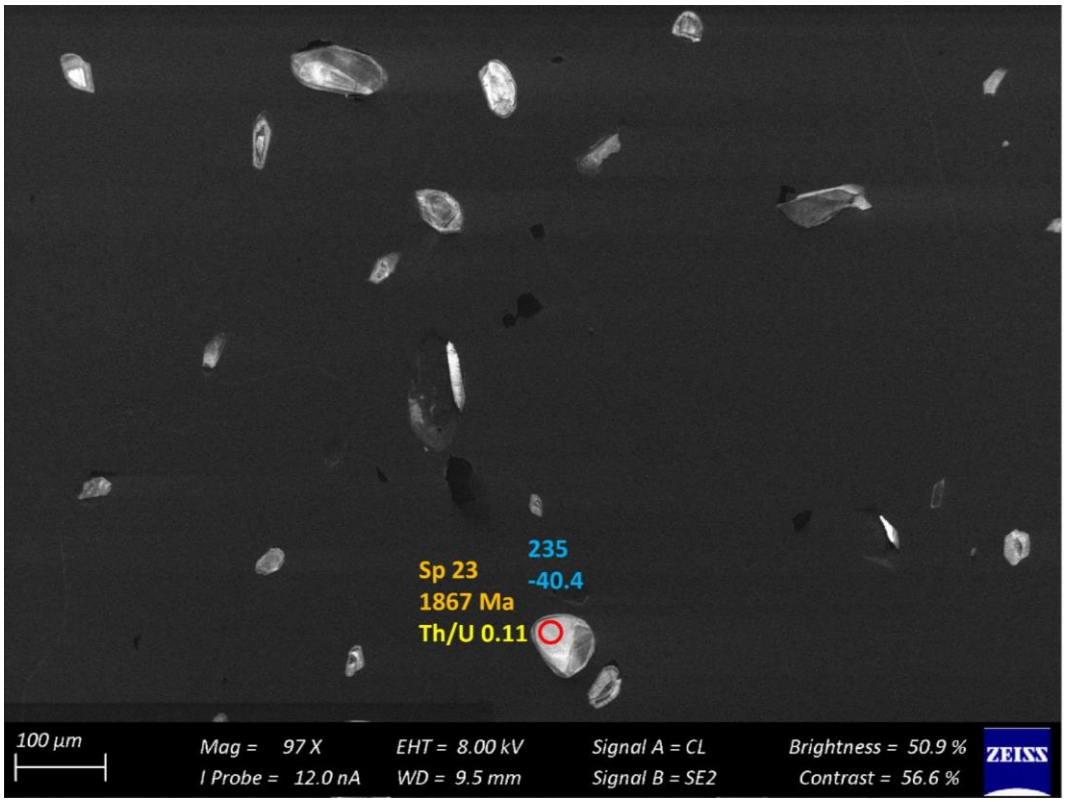

Figure 103 – Zircon Isotope spot analyses of sample s4D; U-Pb analyses are colour coded according to concordance; blue writing indicates the Hf identifier with the respective εHf_{468} values

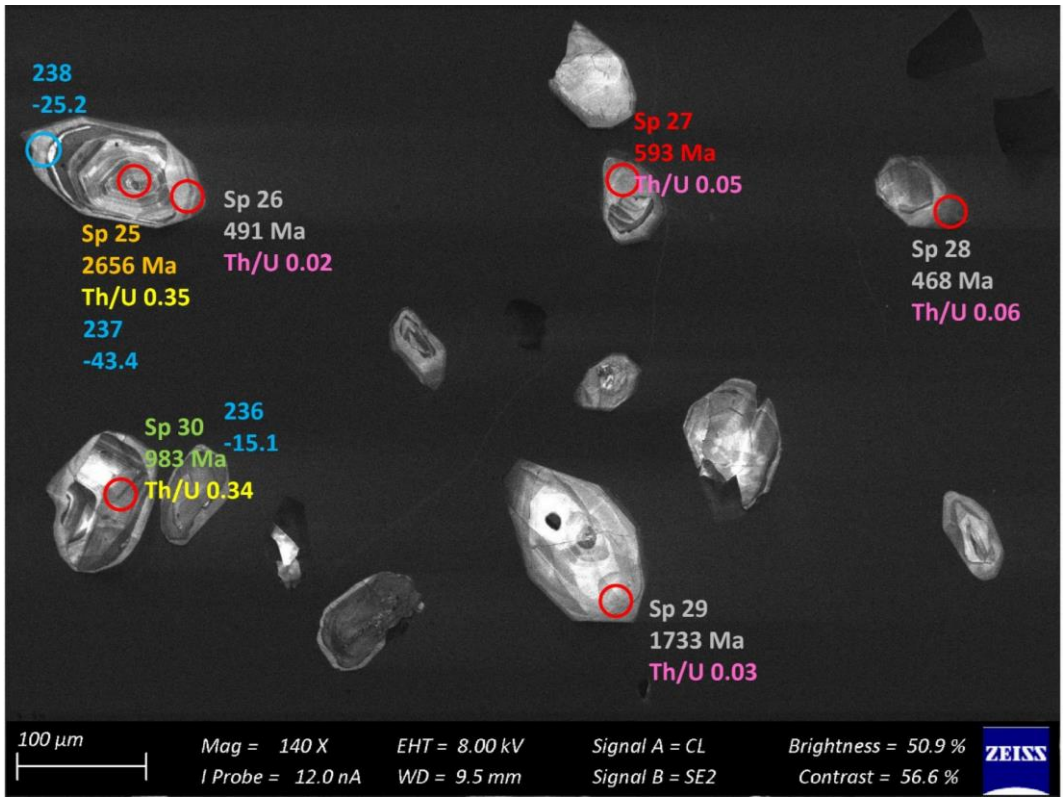

Figure 104 – Zircon Isotope spot analyses of sample s4D; U-Pb analyses are colour coded according to concordance; blue writing indicates the Hf identifier with the respective εHf_{468} values

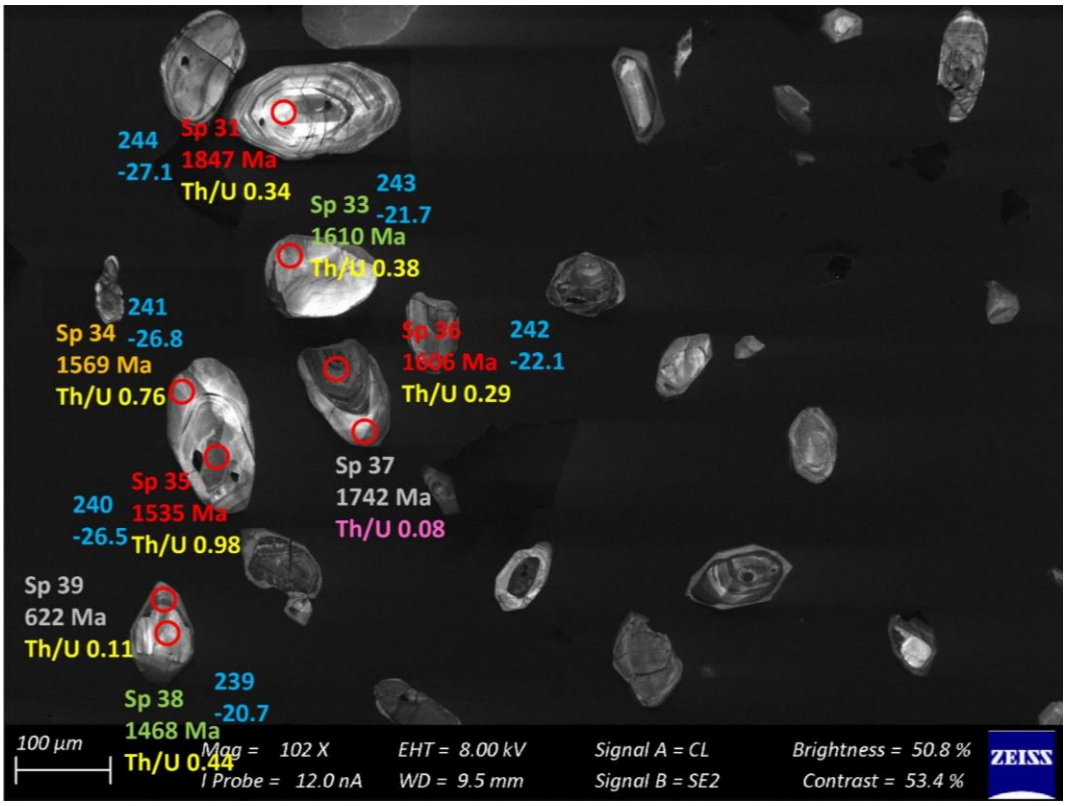

Figure 105 – Zircon Isotope spot analyses of sample s4D; U-Pb analyses are colour coded according to concordance; blue writing indicates the Hf identifier with the respective εHf_{468} values

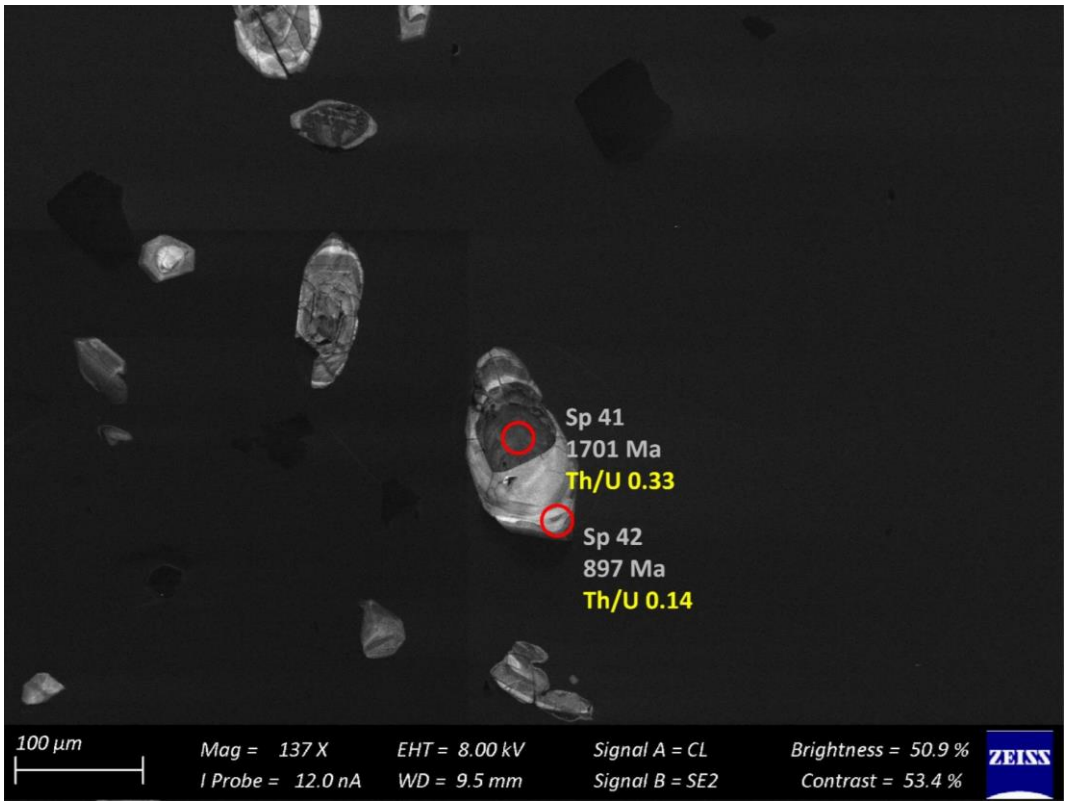

Figure 106 – Zircon Isotope spot analyses of sample s4D; U-Pb analyses are colour coded according to concordance; blue writing indicates the Hf identifier with the respective εHf_{468} values

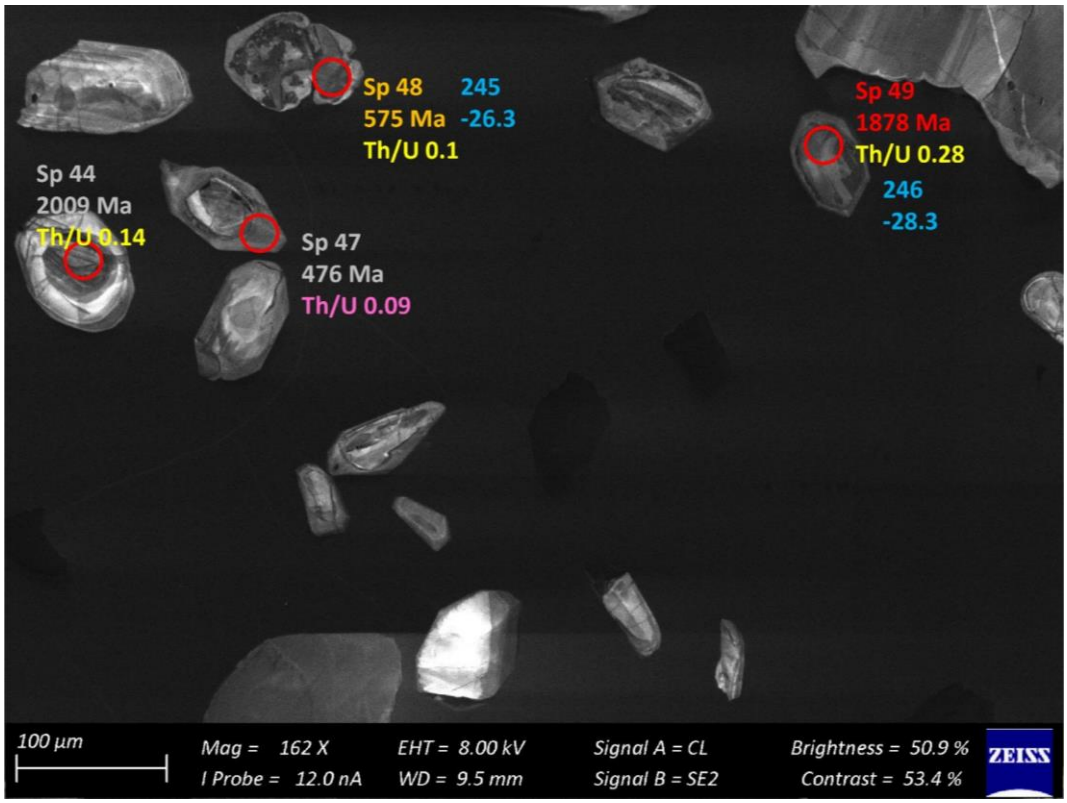

Figure 107 – Zircon Isotope spot analyses of sample s4D; U-Pb analyses are colour coded according to concordance; blue writing indicates the Hf identifier with the respective εHf_{468} values

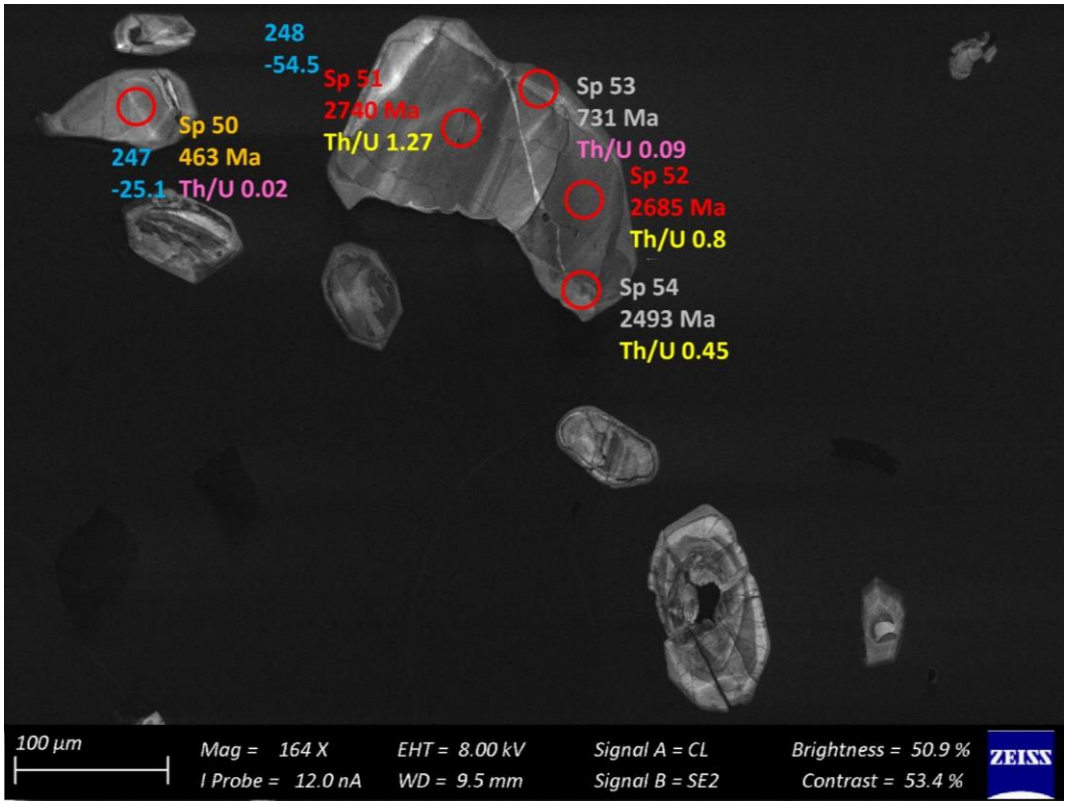

Figure 108 – Zircon Isotope spot analyses of sample s4D; U-Pb analyses are colour coded according to concordance; blue writing indicates the Hf identifier with the respective εHf_{468} values

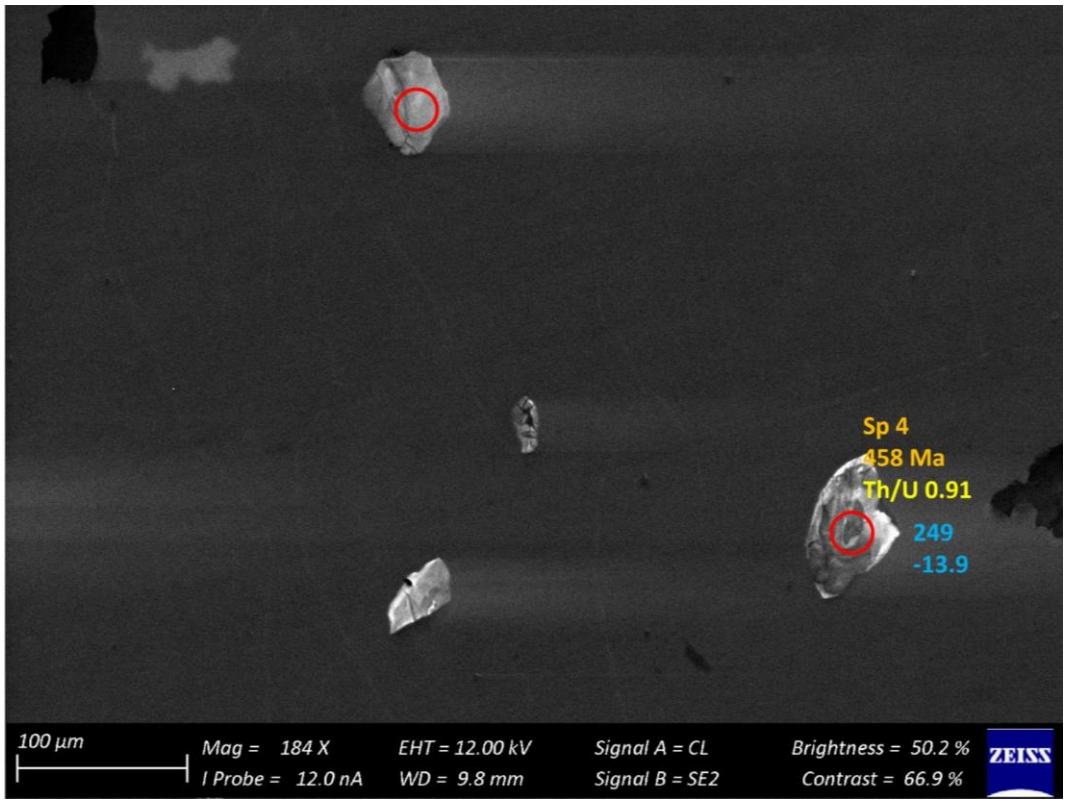

Figure 109 – Zircon Isotope spot analyses of sample s5A; U-Pb analyses are colour coded according to concordance; blue writing indicates the Hf identifier with the respective εHf_{468} values

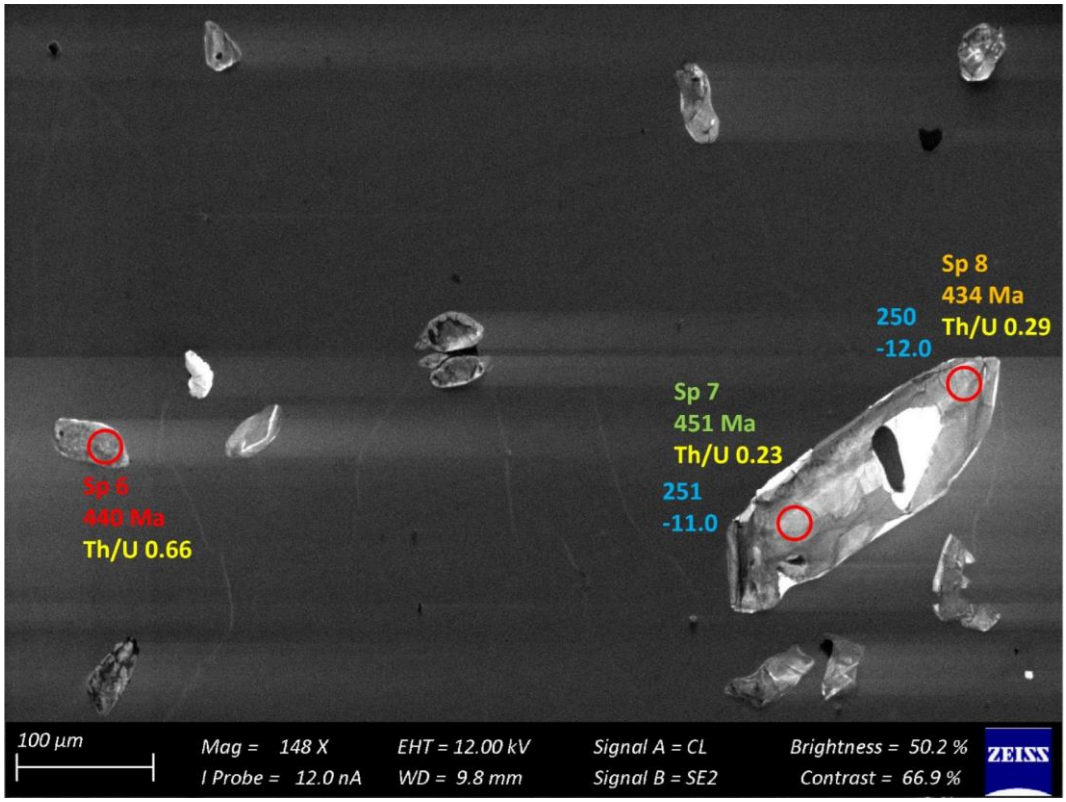

Figure 110 – Zircon Isotope spot analyses of sample s5A; U-Pb analyses are colour coded according to concordance; blue writing indicates the Hf identifier with the respective εHf_{468} values

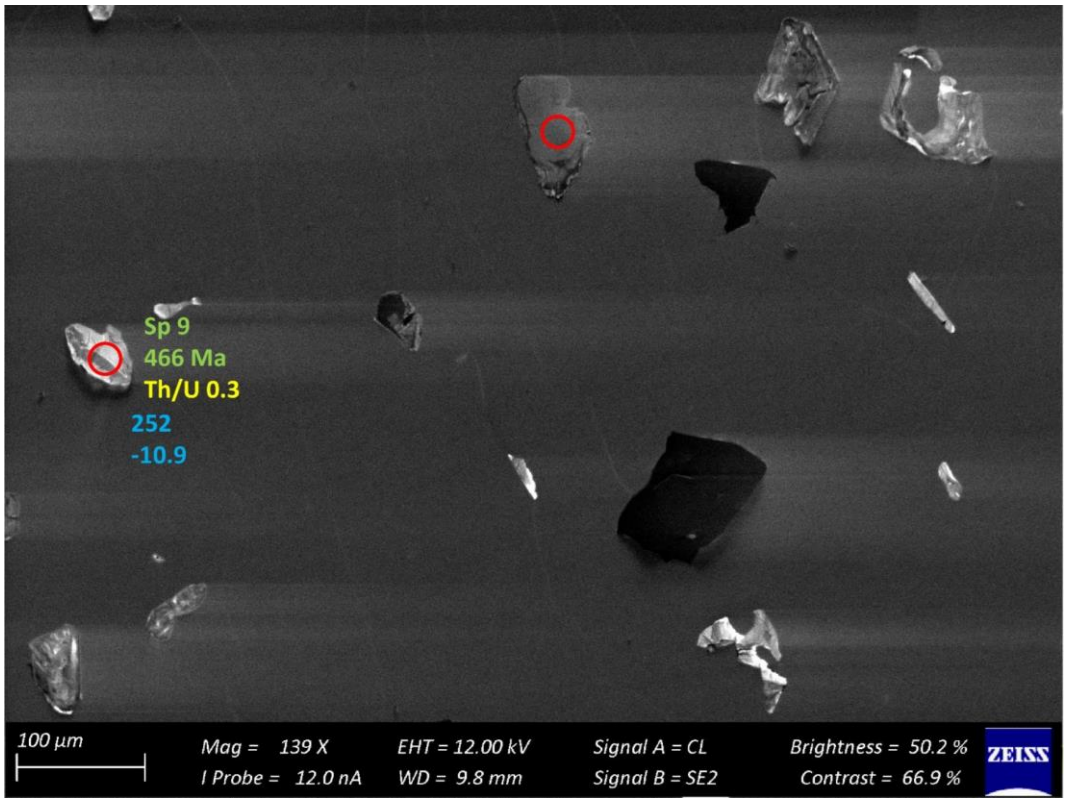

Figure 111 – Zircon Isotope spot analyses of sample s5A; U-Pb analyses are colour coded according to concordance; blue writing indicates the Hf identifier with the respective εHf_{468} values

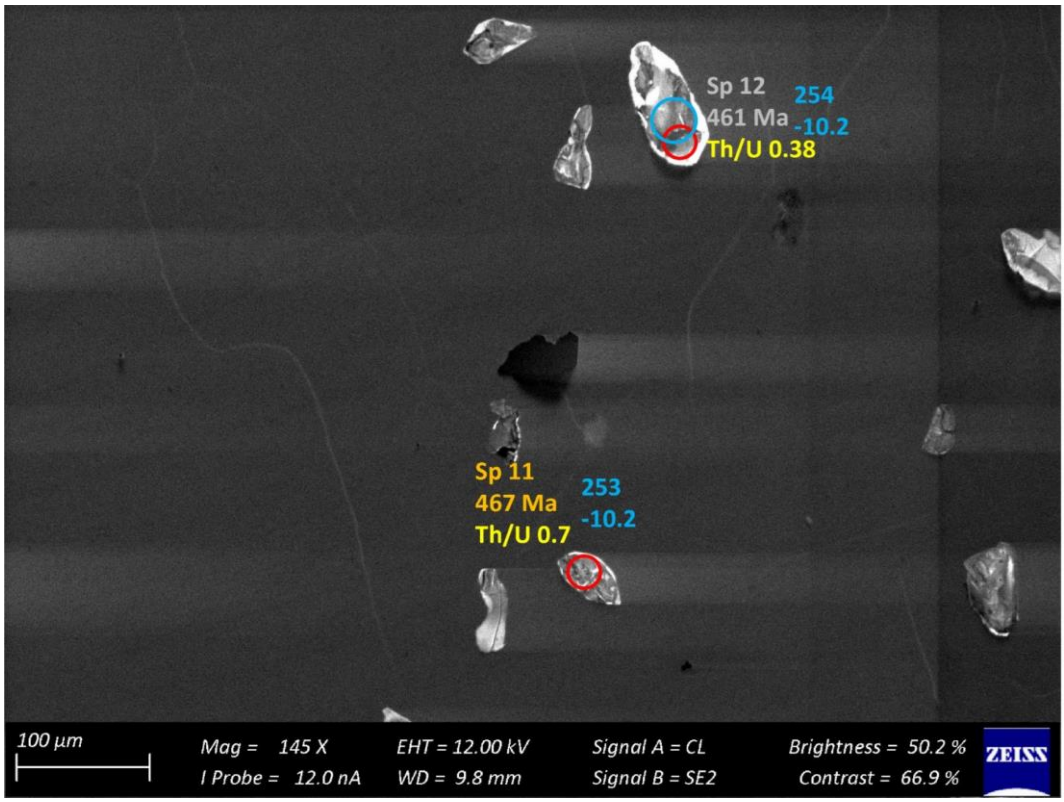

Figure 112 – Zircon Isotope spot analyses of sample s5A; U-Pb analyses are colour coded according to concordance; blue writing indicates the Hf identifier with the respective εHf_{468} values

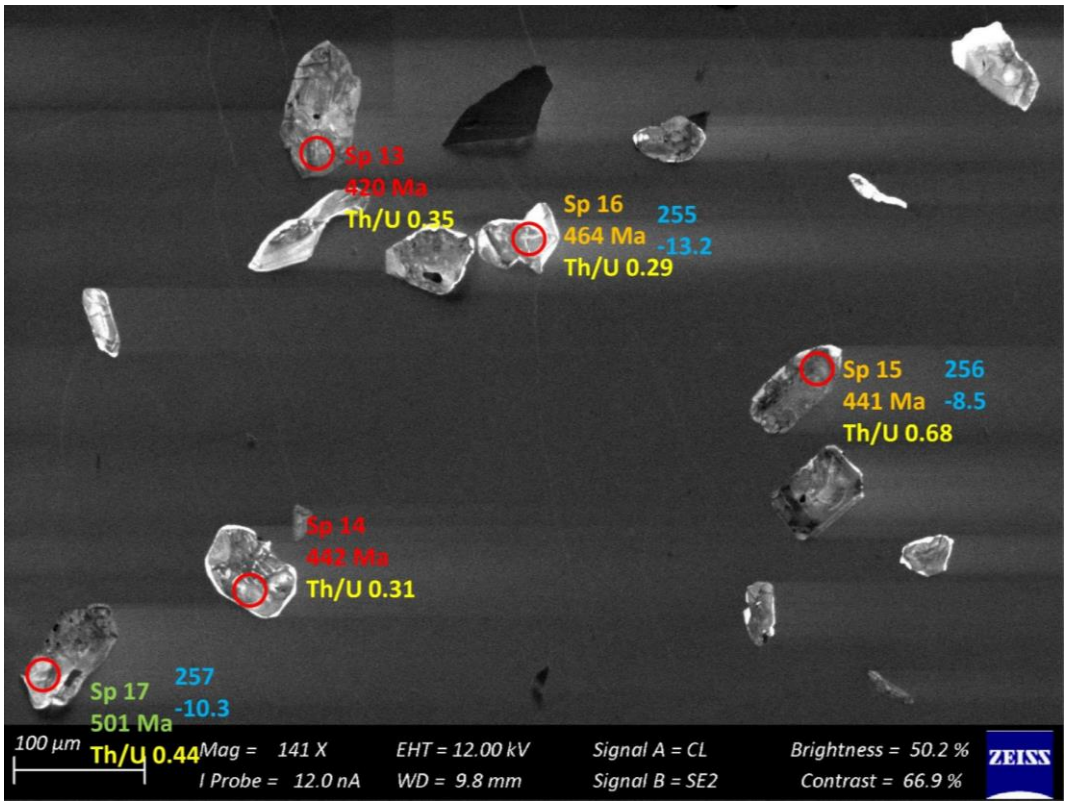

Figure 113 – Zircon Isotope spot analyses of sample s5A; U-Pb analyses are colour coded according to concordance; blue writing indicates the Hf identifier with the respective εHf_{468} values

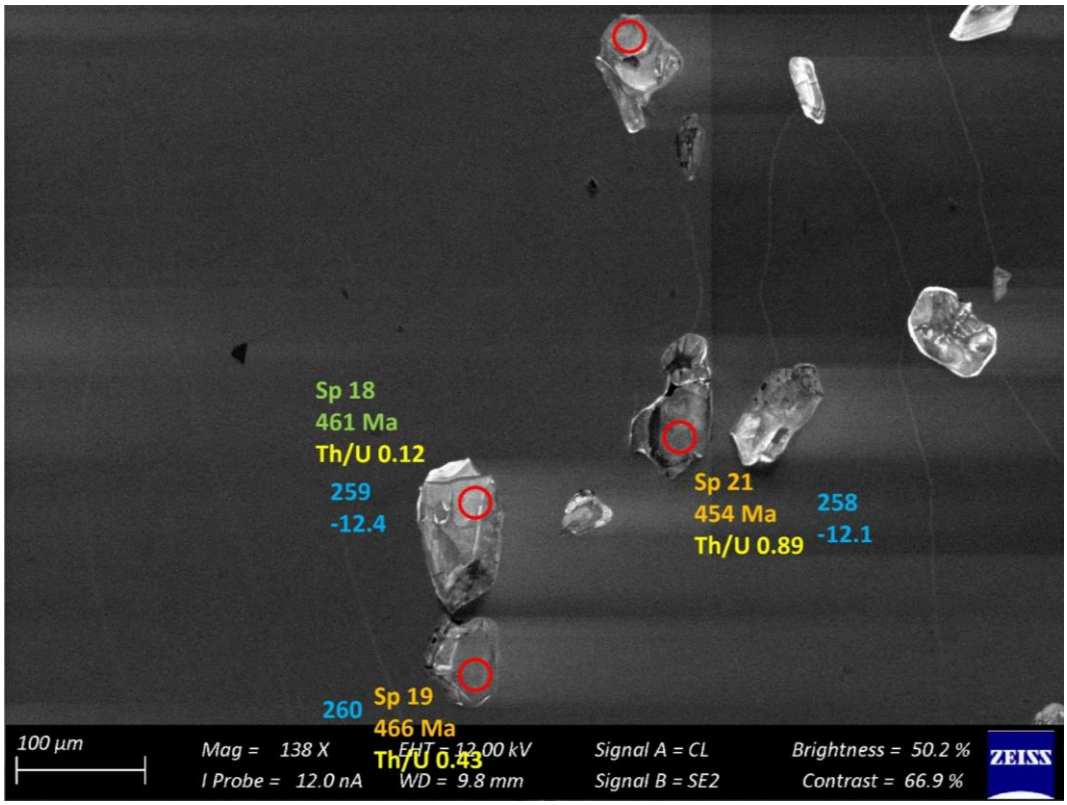

Figure 114 – Zircon Isotope spot analyses of sample s5A; U-Pb analyses are colour coded according to concordance; blue writing indicates the Hf identifier with the respective εHf_{468} values

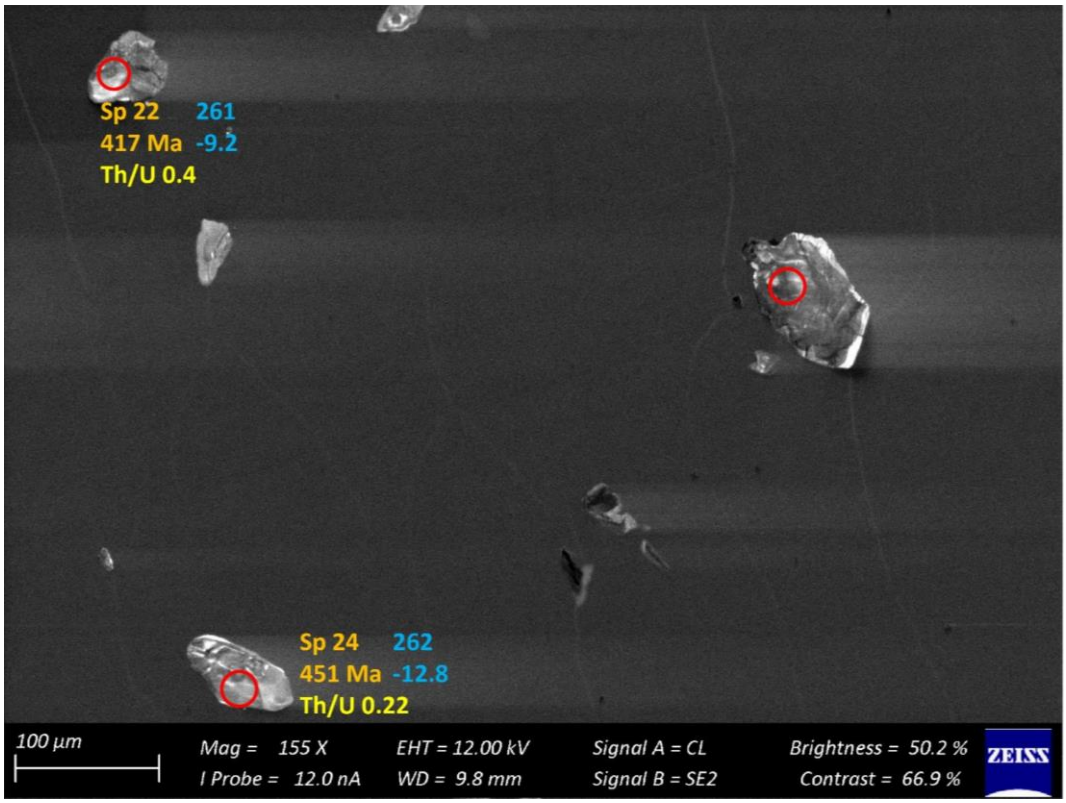

Figure 115 – Zircon Isotope spot analyses of sample s5A; U-Pb analyses are colour coded according to concordance; blue writing indicates the Hf identifier with the respective εHf_{468} values

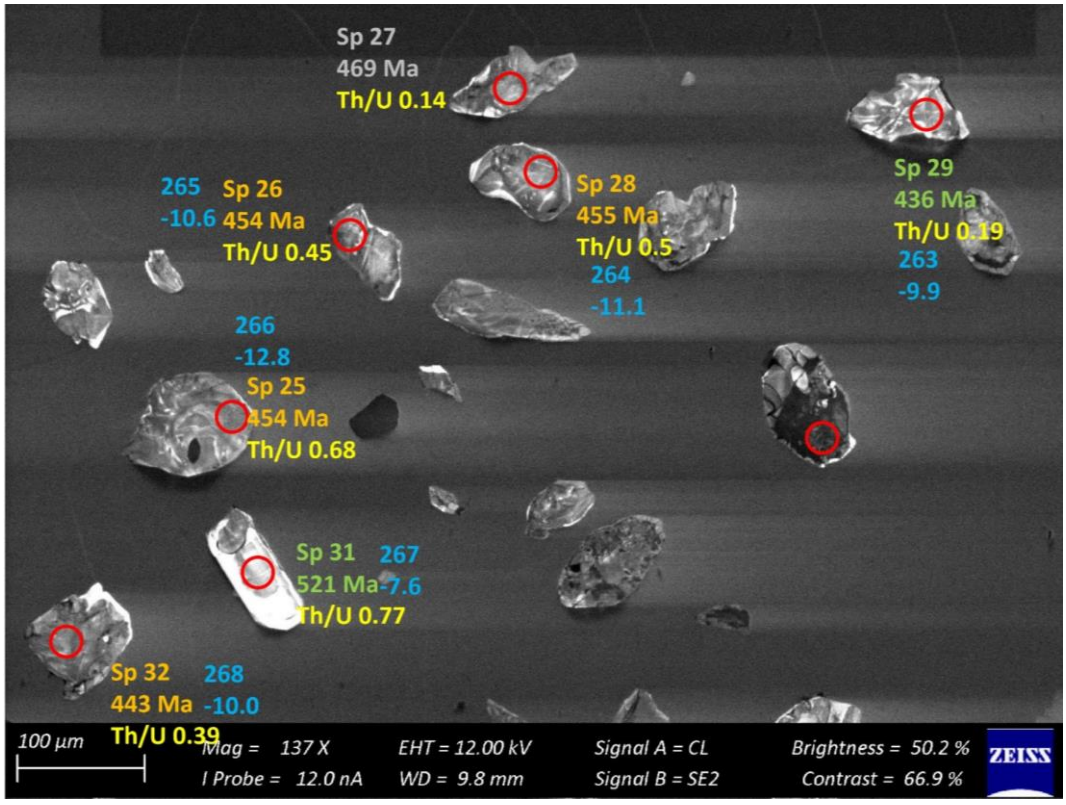

Figure 116 – Zircon Isotope spot analyses of sample s5A; U-Pb analyses are colour coded according to concordance; blue writing indicates the Hf identifier with the respective εHf_{468} values

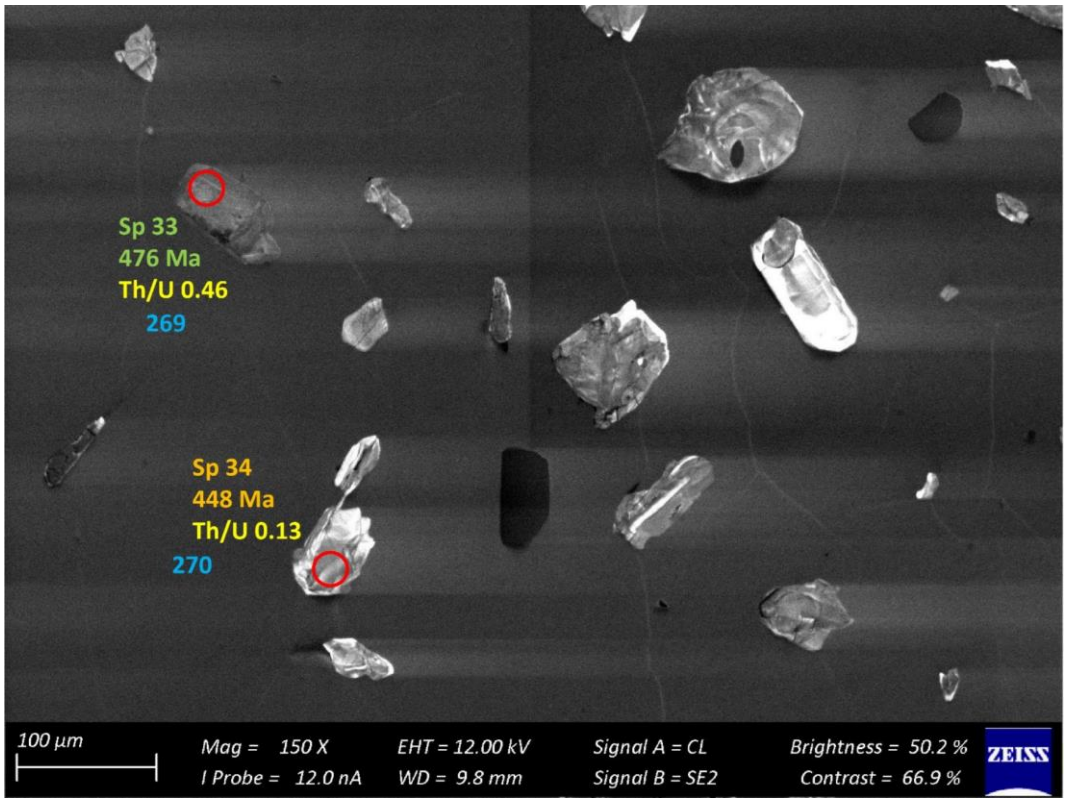

Figure 117 – Zircon Isotope spot analyses of sample s5A; U-Pb analyses are colour coded according to concordance; blue writing indicates the Hf identifier with the respective εHf_{468} values

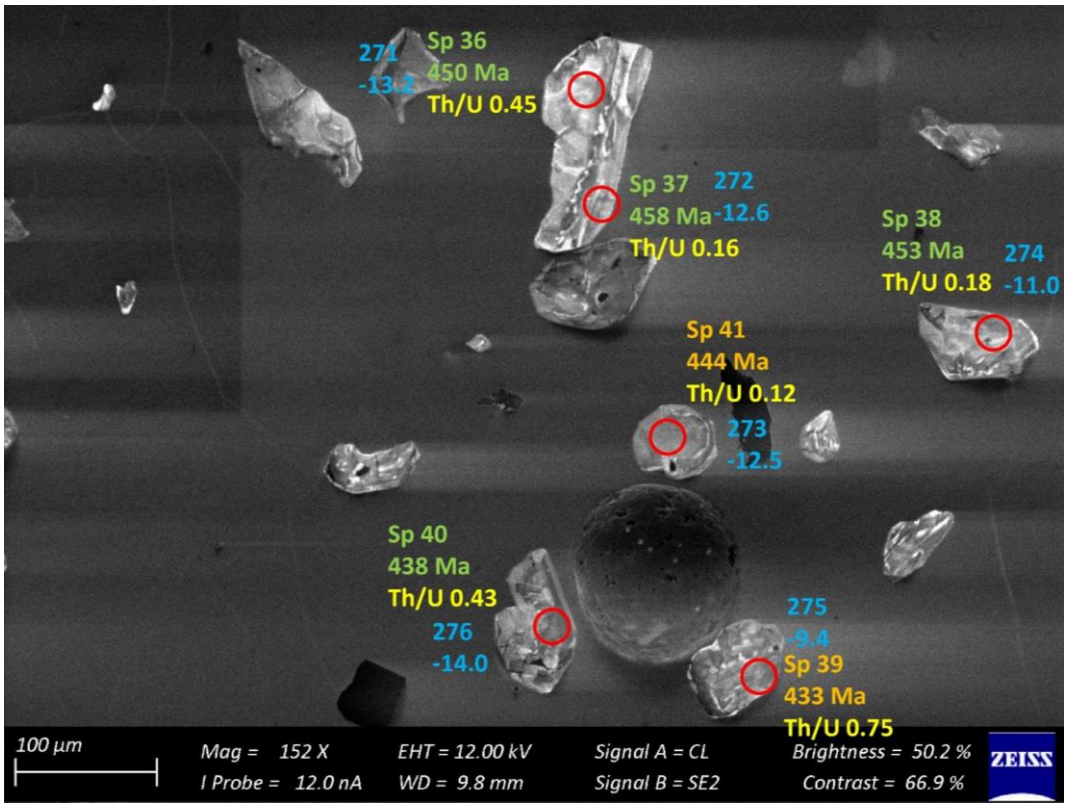

Figure 118 – Zircon Isotope spot analyses of sample s5A; U-Pb analyses are colour coded according to concordance; blue writing indicates the Hf identifier with the respective εHf_{468} values

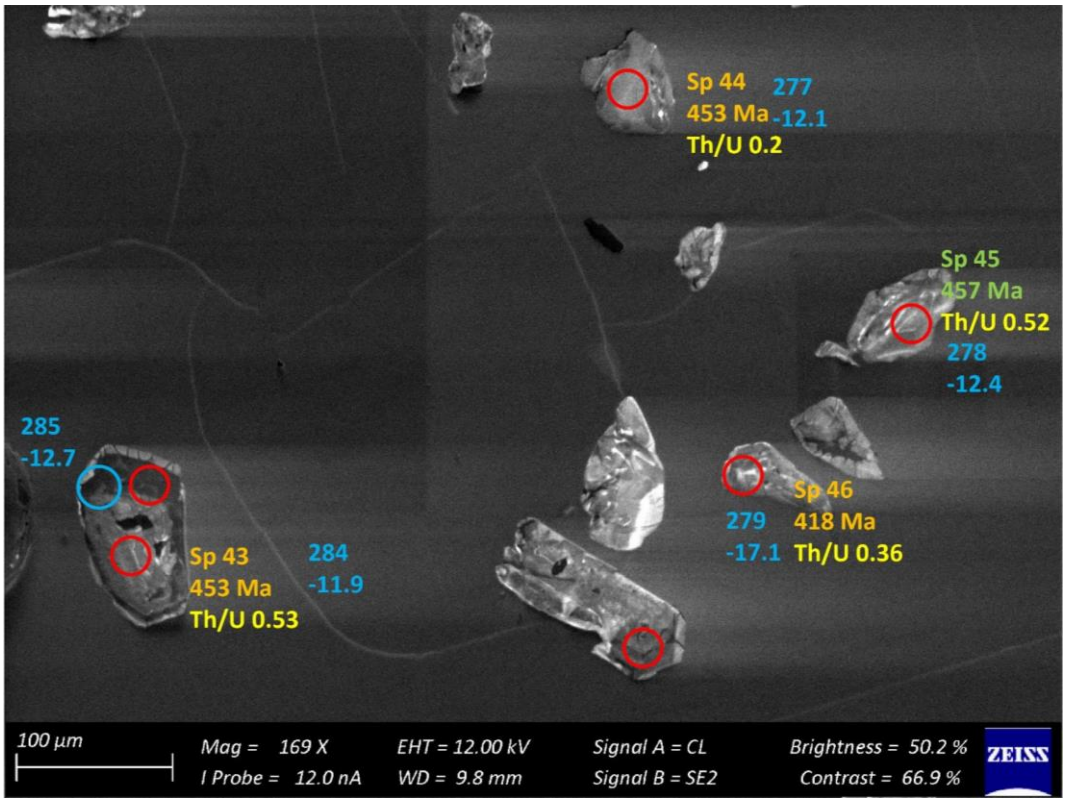

Figure 119 – Zircon Isotope spot analyses of sample s5A; U-Pb analyses are colour coded according to concordance; blue writing indicates the Hf identifier with the respective εHf_{468} values

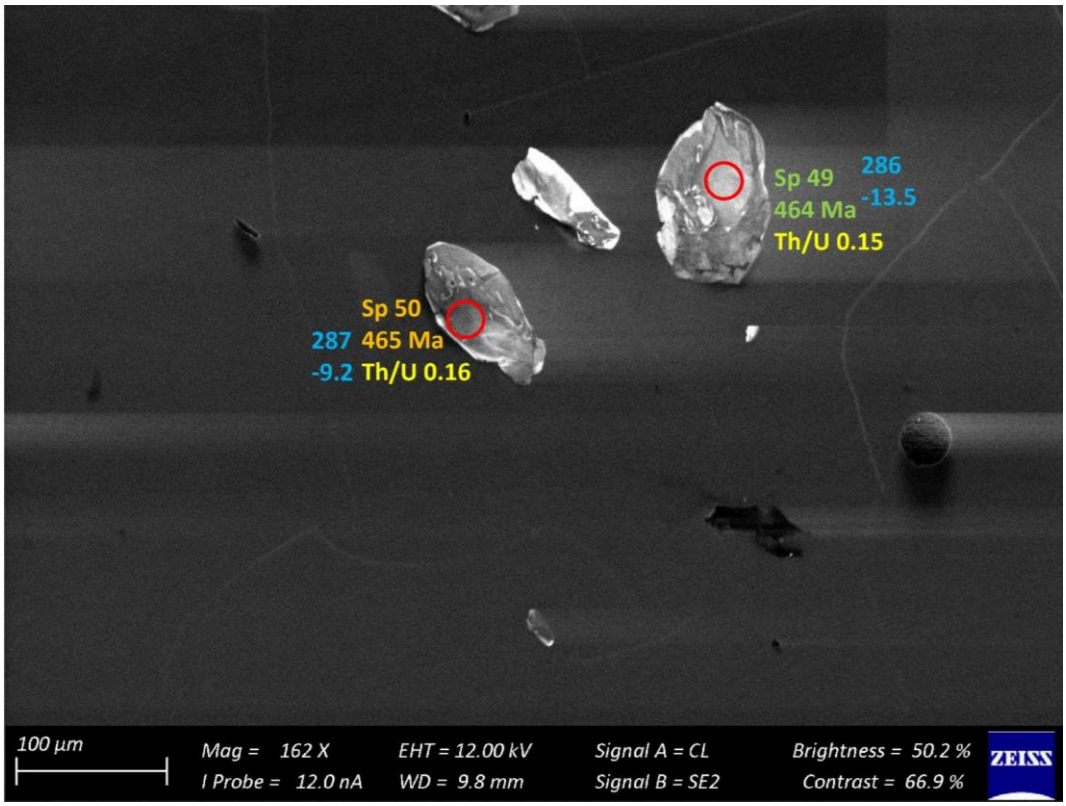

Figure 120 – Zircon Isotope spot analyses of sample s5A; U-Pb analyses are colour coded according to concordance; blue writing indicates the Hf identifier with the respective εHf_{468} values

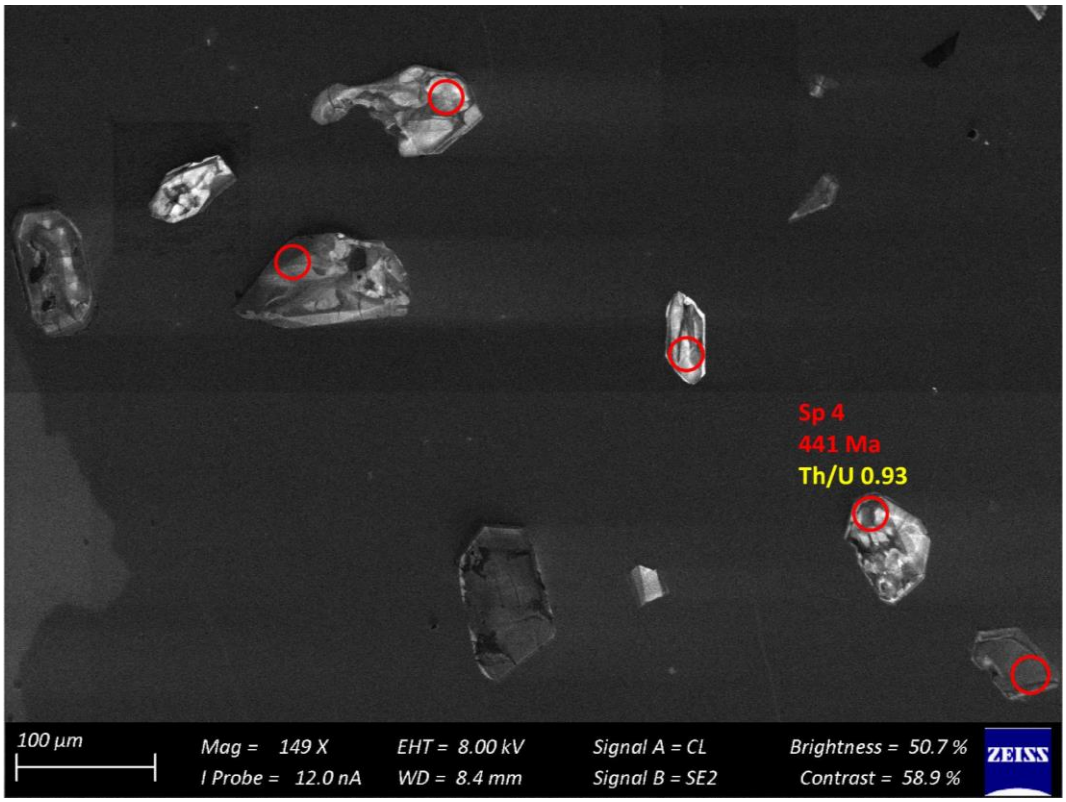

Figure 121 – Zircon Isotope spot analyses of sample s5Ba; U-Pb analyses are colour coded according to concordance; blue writing indicates the Hf identifier with the respective εHf_{468} values

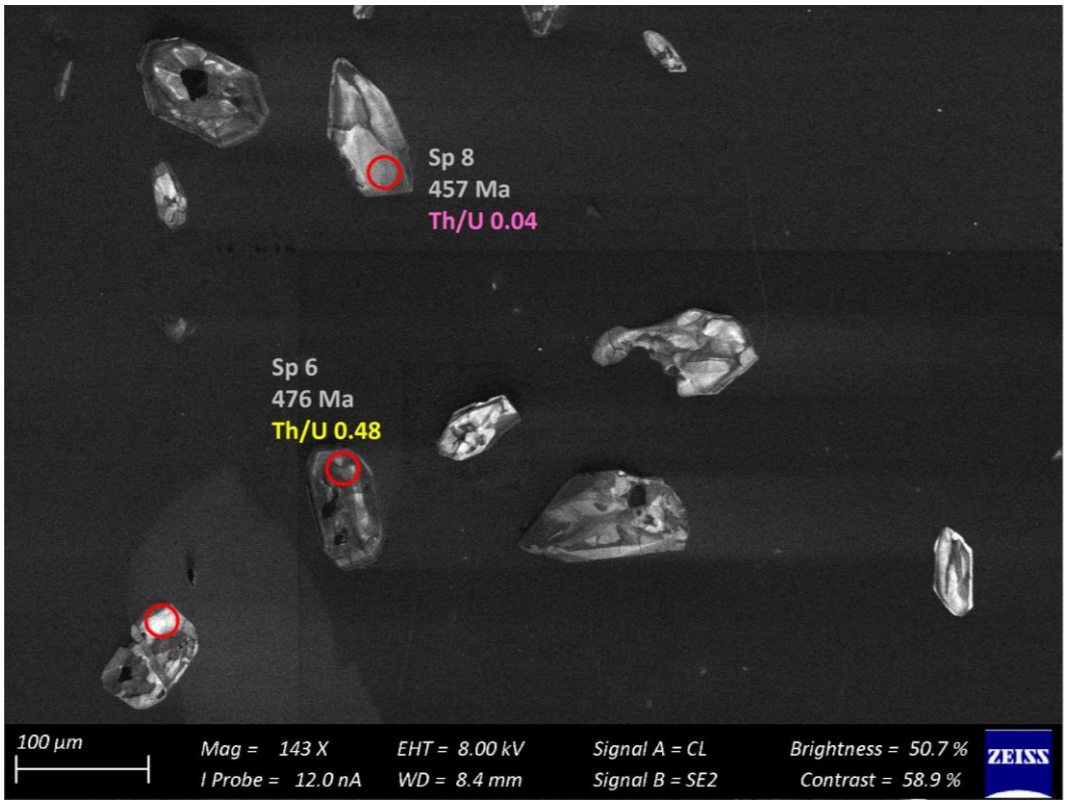

Figure 122 – Zircon Isotope spot analyses of sample s5Ba; U-Pb analyses are colour coded according to concordance; blue writing indicates the Hf identifier with the respective εHf_{468} values

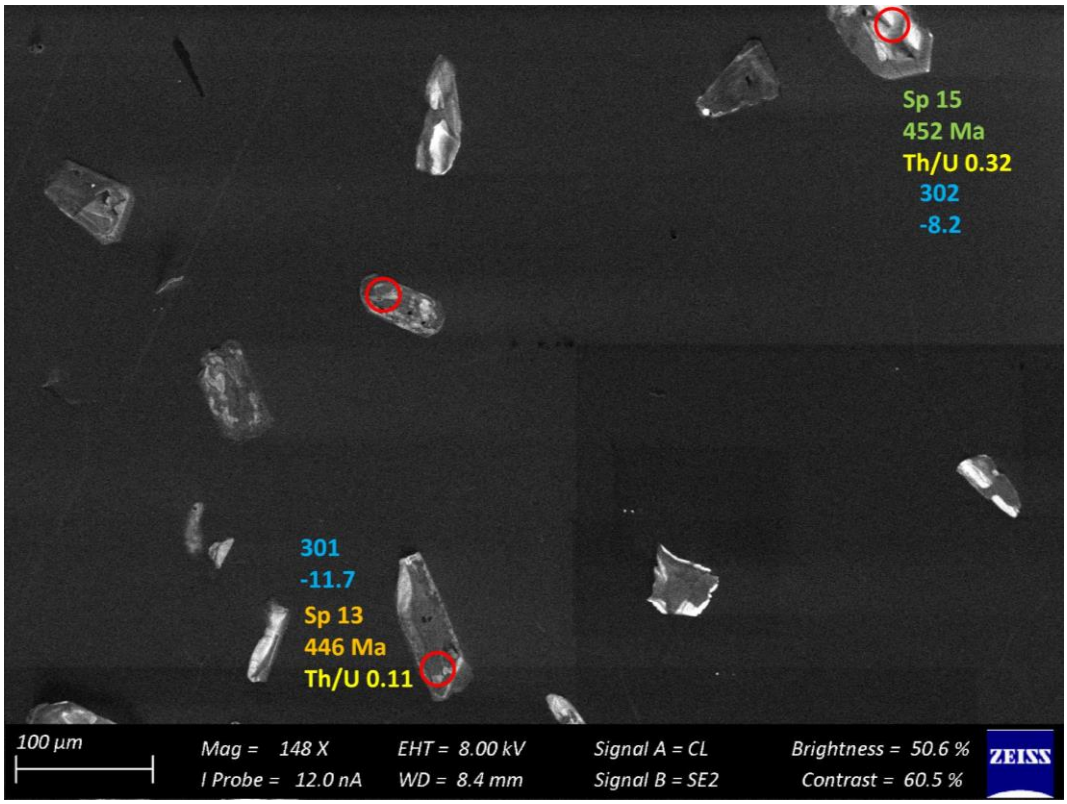

Figure 123 – Zircon Isotope spot analyses of sample s5Ba; U-Pb analyses are colour coded according to concordance; blue writing indicates the Hf identifier with the respective εHf$_{468}$ values

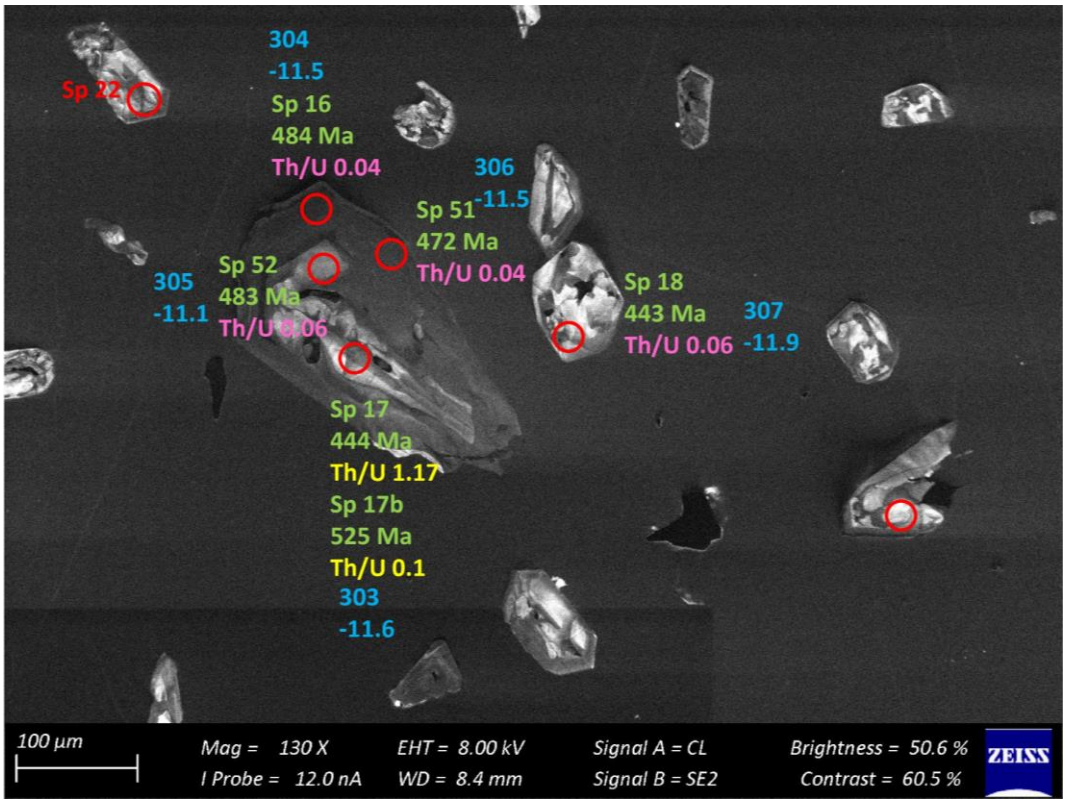

Figure 124 – Zircon Isotope spot analyses of sample s5Ba; U-Pb analyses are colour coded according to concordance; blue writing indicates the Hf identifier with the respective εHf$_{468}$ values

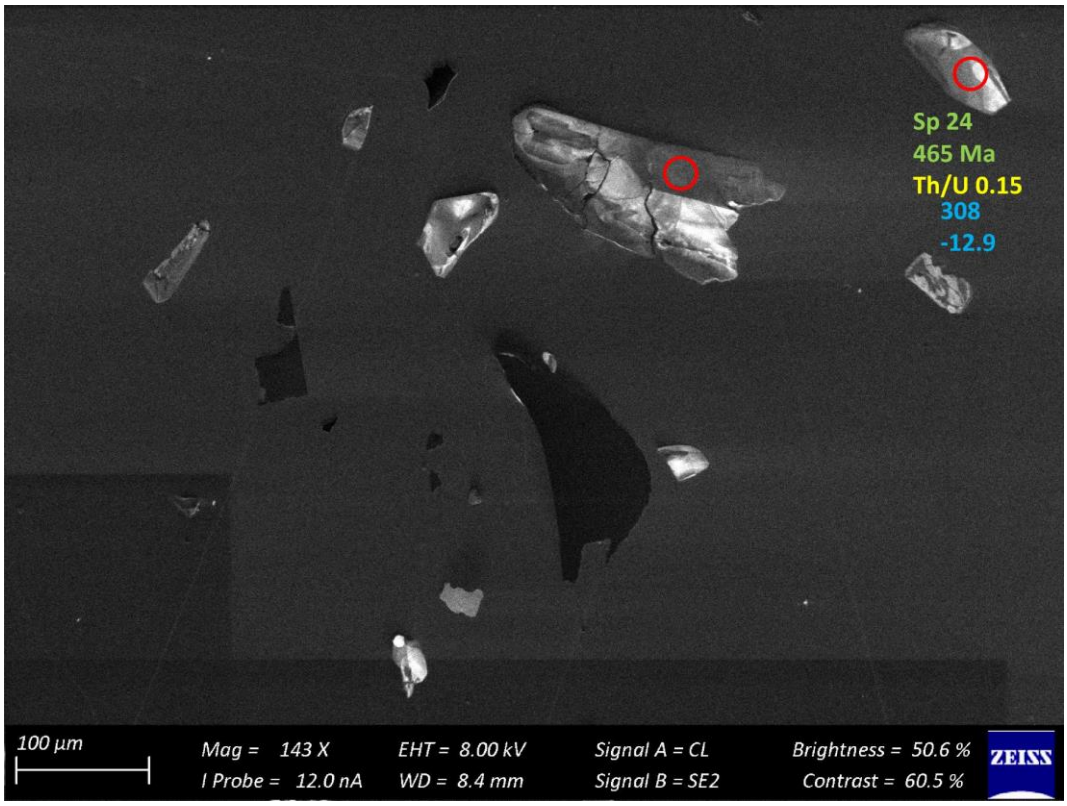

Figure 125 – Zircon Isotope spot analyses of sample s5Ba; U-Pb analyses are colour coded according to concordance; blue writing indicates the Hf identifier with the respective εHf_{468} values

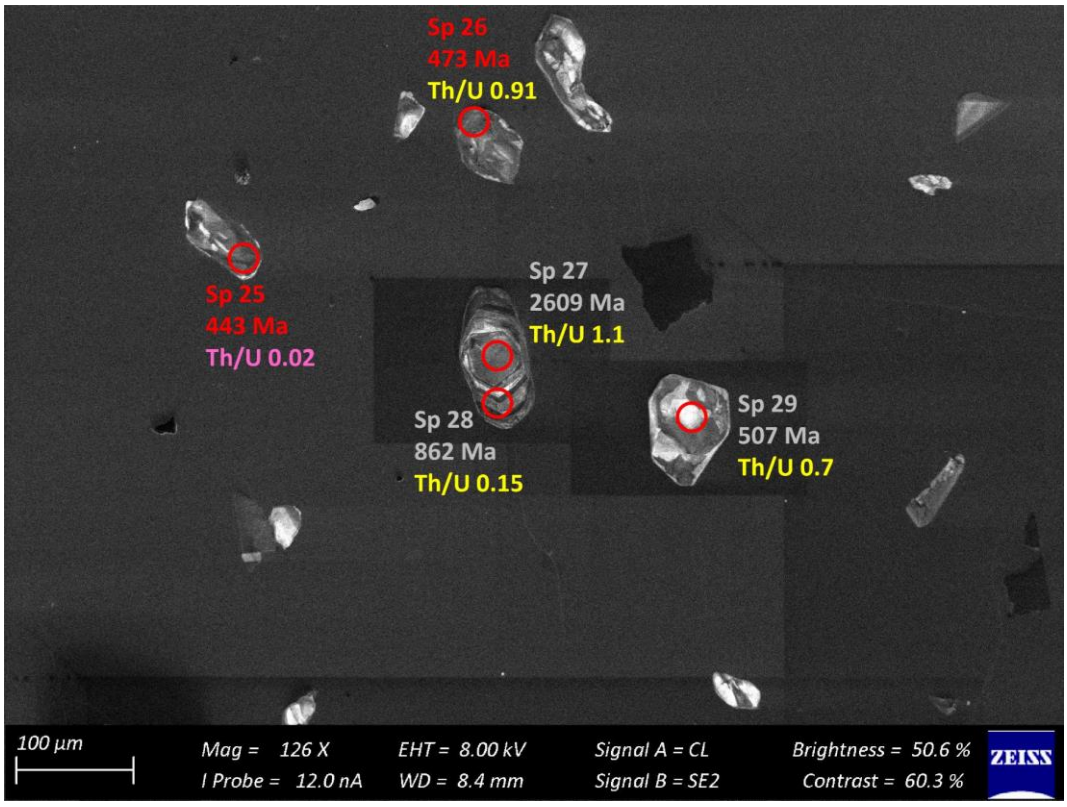

Figure 126 – Zircon Isotope spot analyses of sample s5Ba; U-Pb analyses are colour coded according to concordance; blue writing indicates the Hf identifier with the respective εHf_{468} values

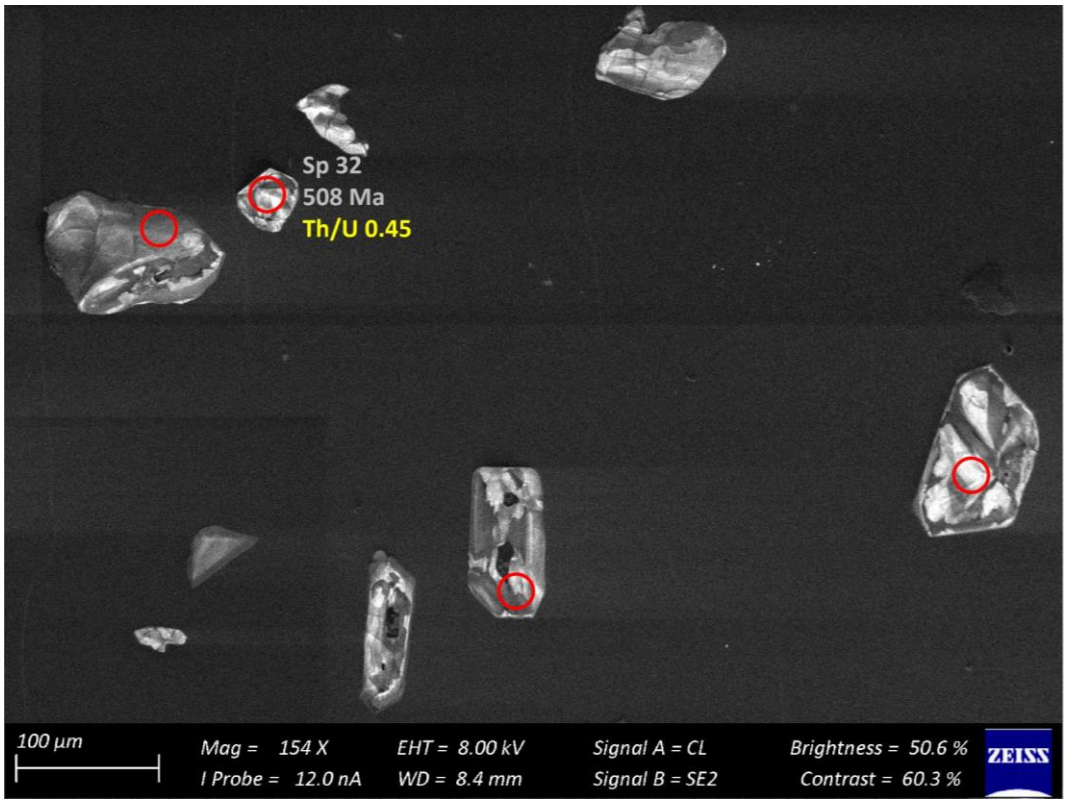

Figure 127 – Zircon Isotope spot analyses of sample s5Ba; U-Pb analyses are colour coded according to concordance; blue writing indicates the Hf identifier with the respective εHf_{468} values

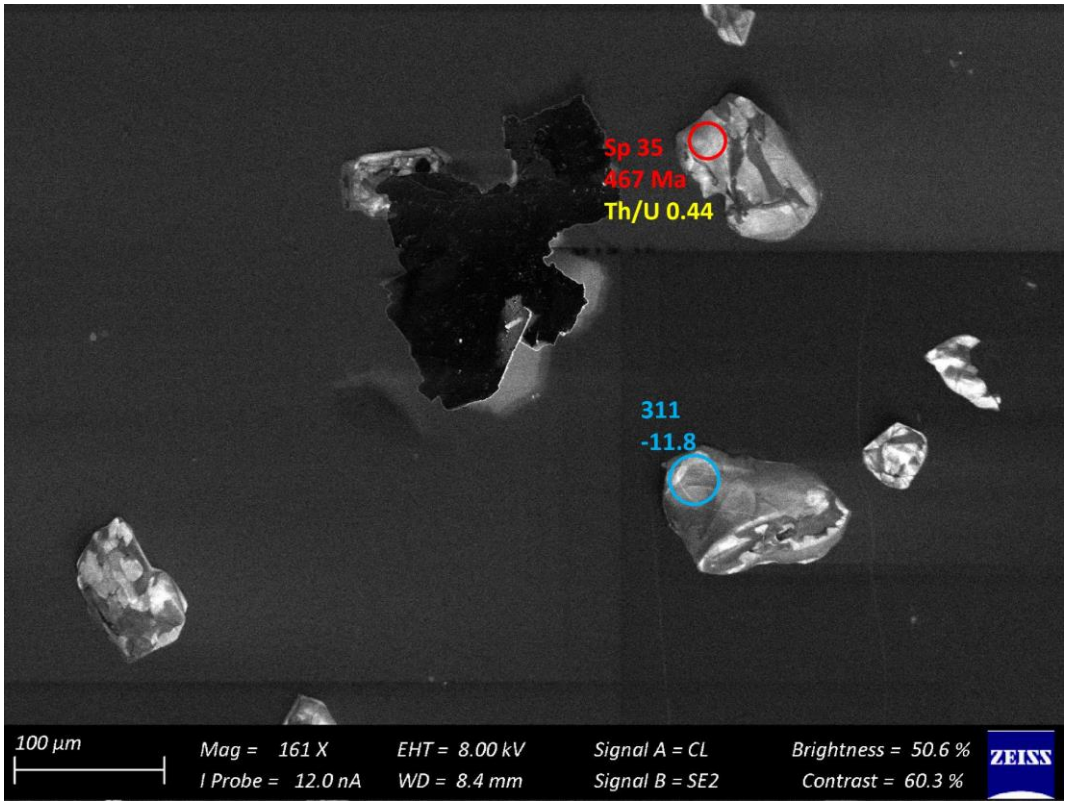

Figure 128 – Zircon Isotope spot analyses of sample s5Ba; U-Pb analyses are colour coded according to concordance; blue writing indicates the Hf identifier with the respective εHf_{468} values

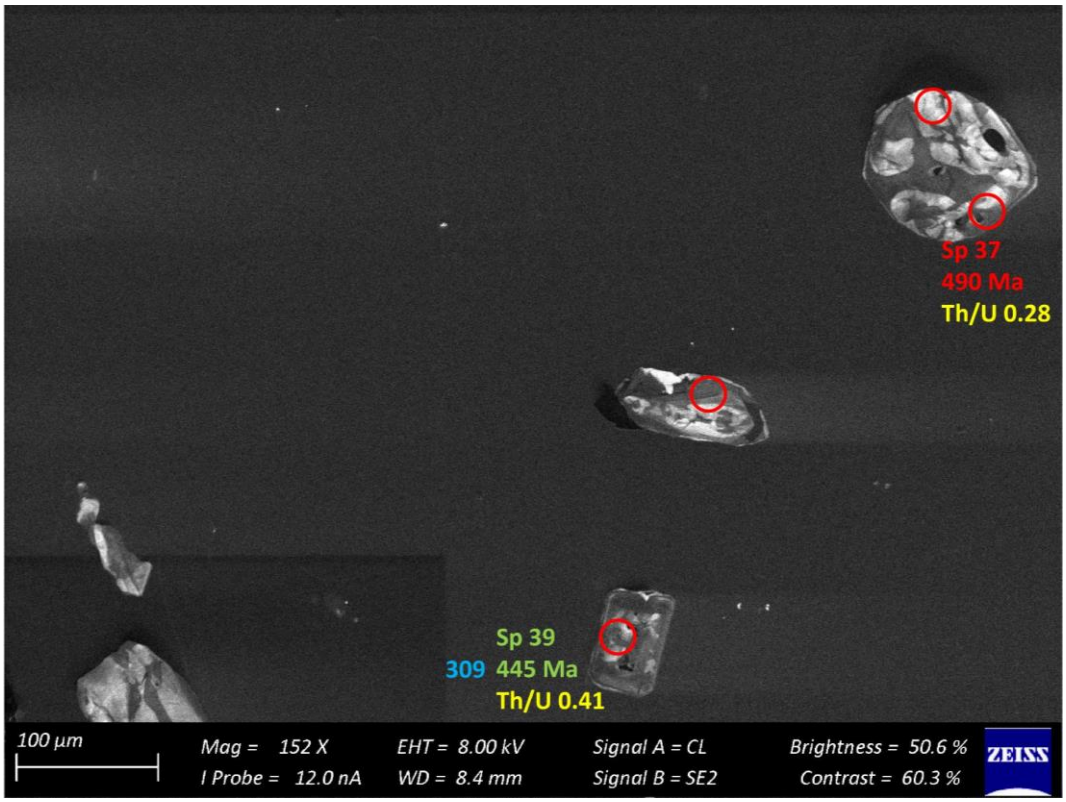

Figure 129 – Zircon Isotope spot analyses of sample s5Ba; U-Pb analyses are colour coded according to concordance; blue writing indicates the Hf identifier with the respective εHf_{468} values

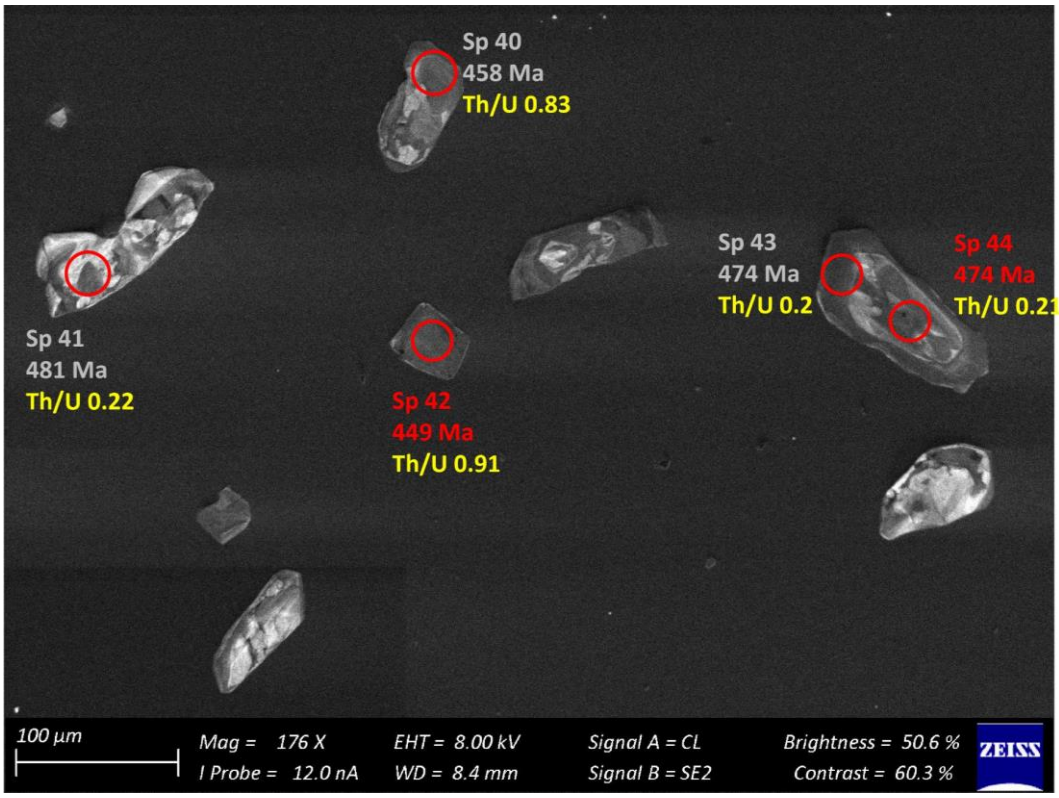

Figure 130 – Zircon Isotope spot analyses of sample s5Ba; U-Pb analyses are colour coded according to concordance; blue writing indicates the Hf identifier with the respective εHf_{468} values

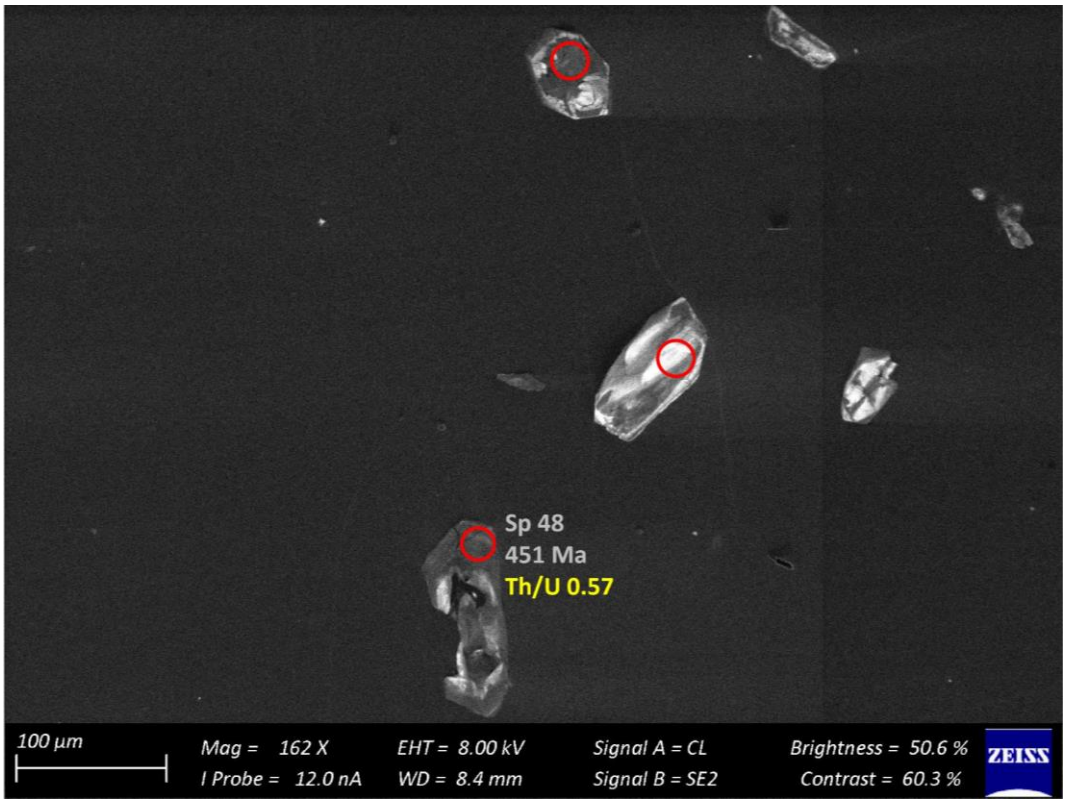

Figure 131 – Zircon Isotope spot analyses of sample s5Ba; U-Pb analyses are colour coded according to concordance; blue writing indicates the Hf identifier with the respective εHf_{468} values

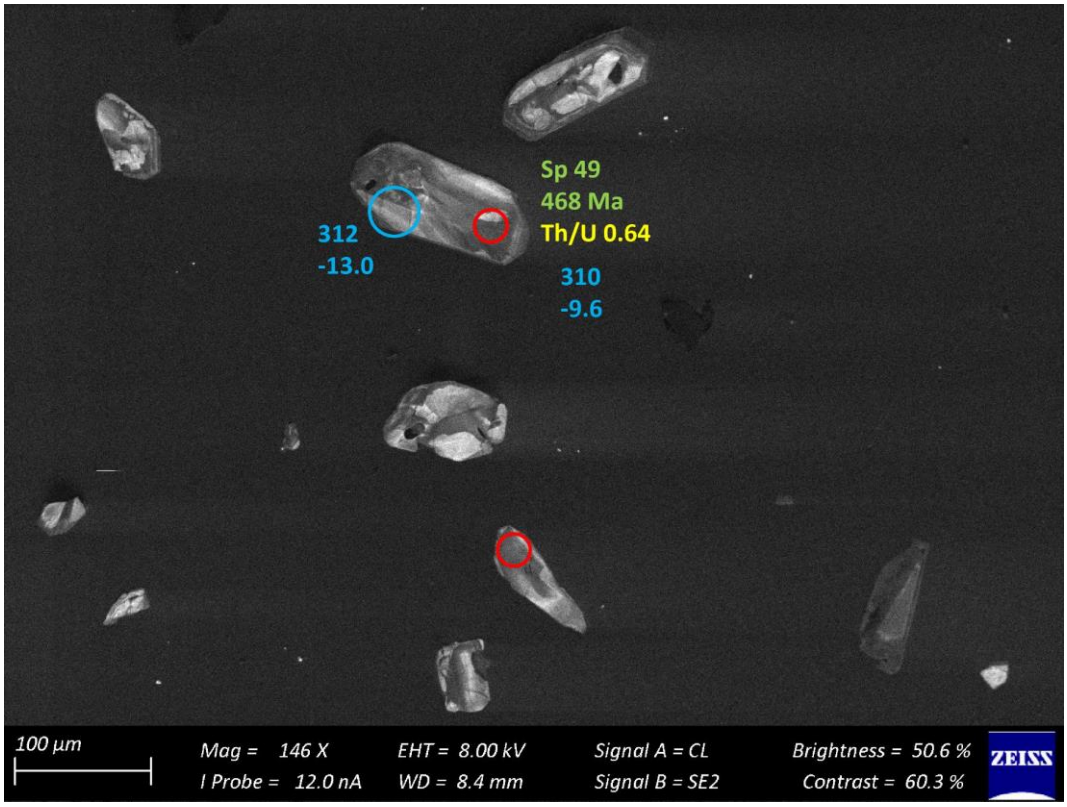

Figure 132 – Zircon Isotope spot analyses of sample s5Ba; U-Pb analyses are colour coded according to concordance; blue writing indicates the Hf identifier with the respective εHf_{468} values

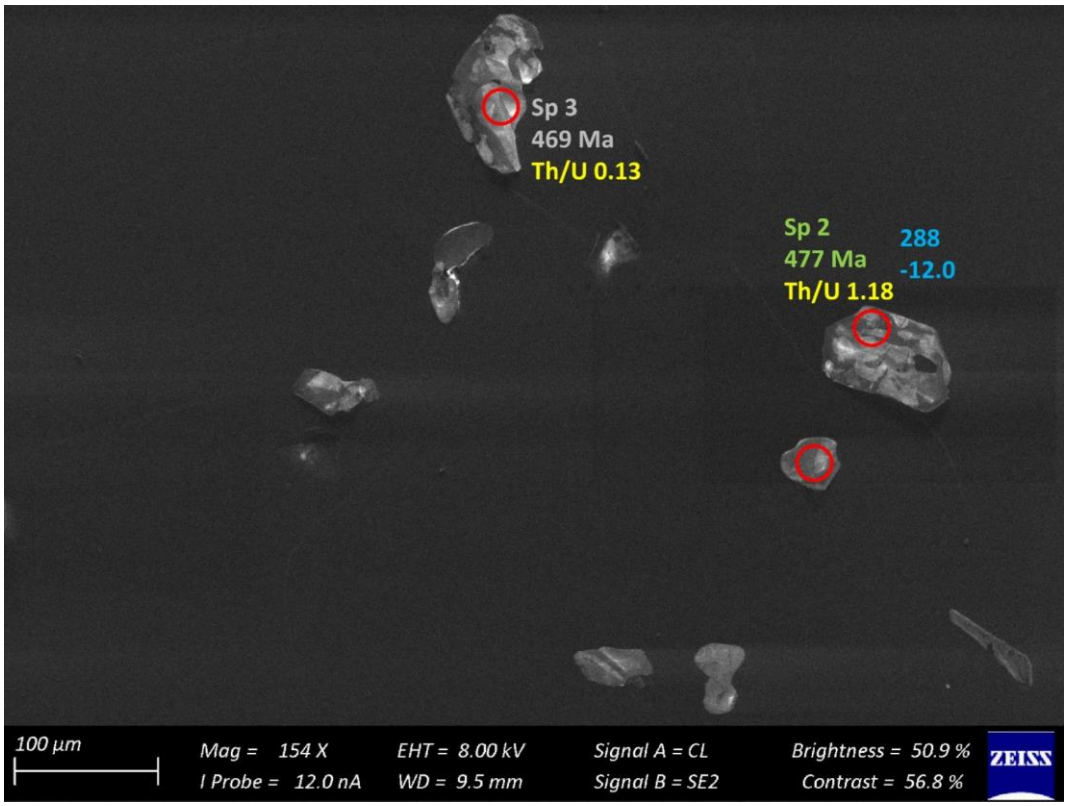

Figure 133 – Zircon Isotope spot analyses of sample s5Bb; U-Pb analyses are colour coded according to concordance; blue writing indicates the Hf identifier with the respective εHf_{468} values

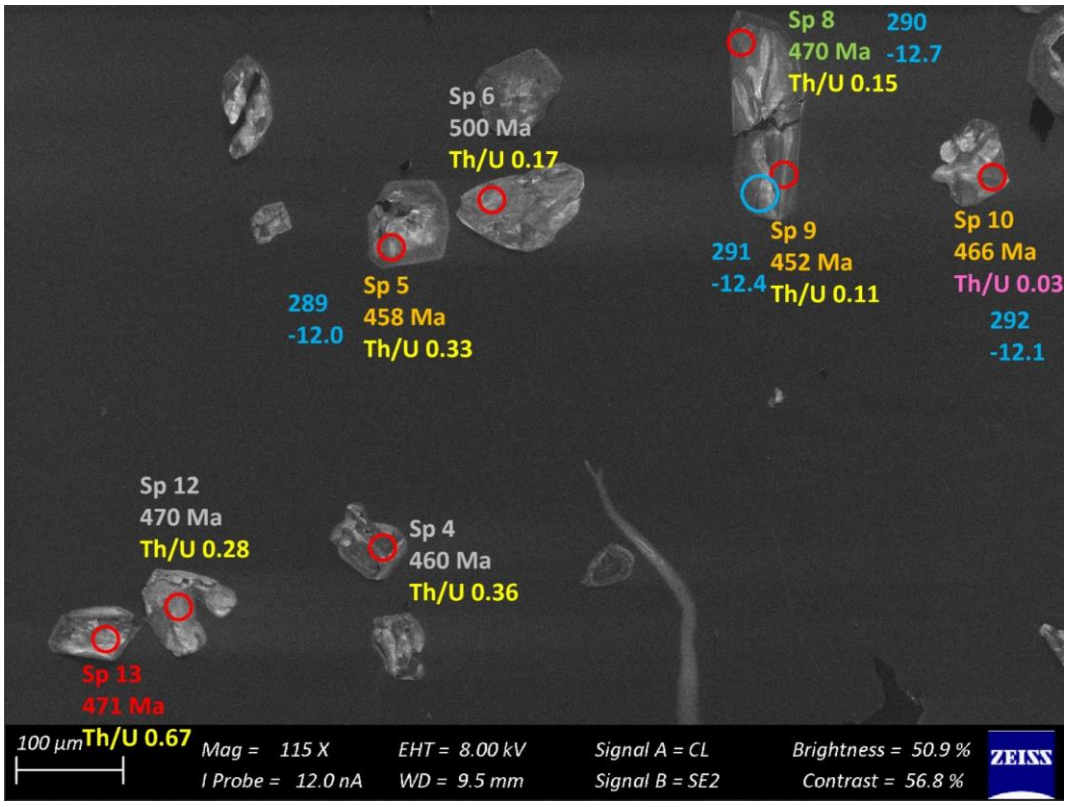

Figure 134 – Zircon Isotope spot analyses of sample s5Bb; U-Pb analyses are colour coded according to concordance; blue writing indicates the Hf identifier with the respective εHf_{468} values

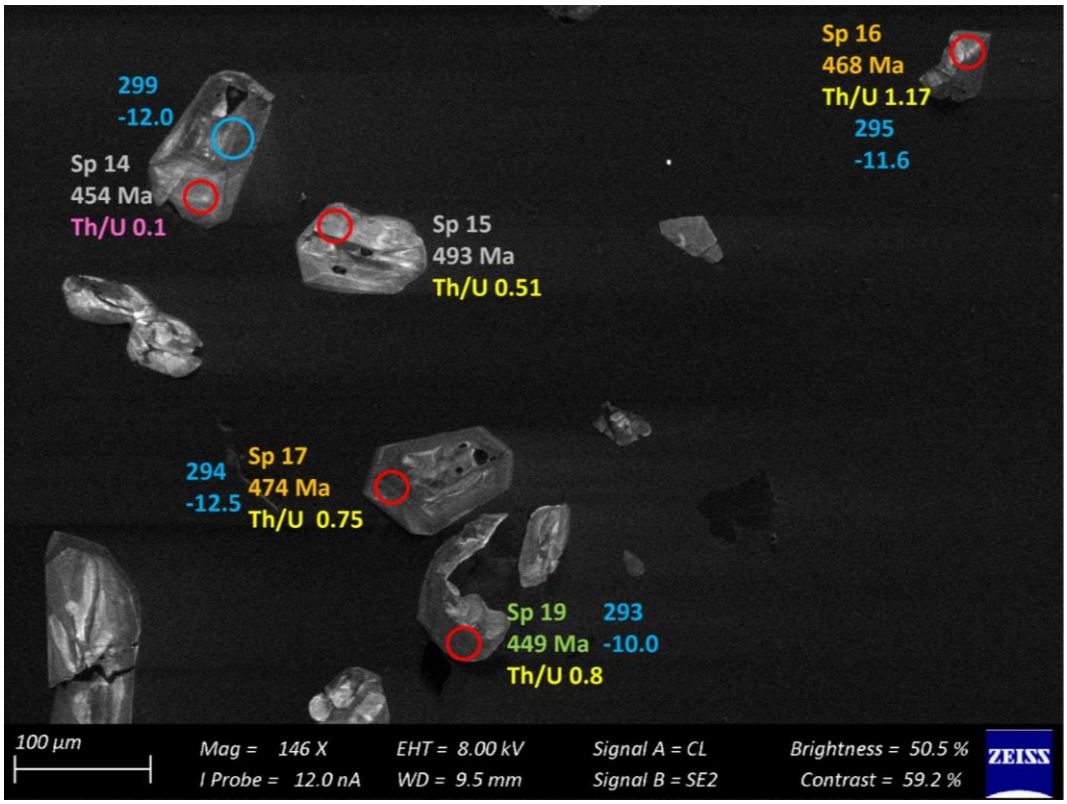

Figure 135 – Zircon Isotope spot analyses of sample s5Bb; U-Pb analyses are colour coded according to concordance; blue writing indicates the Hf identifier with the respective εHf_{468} values

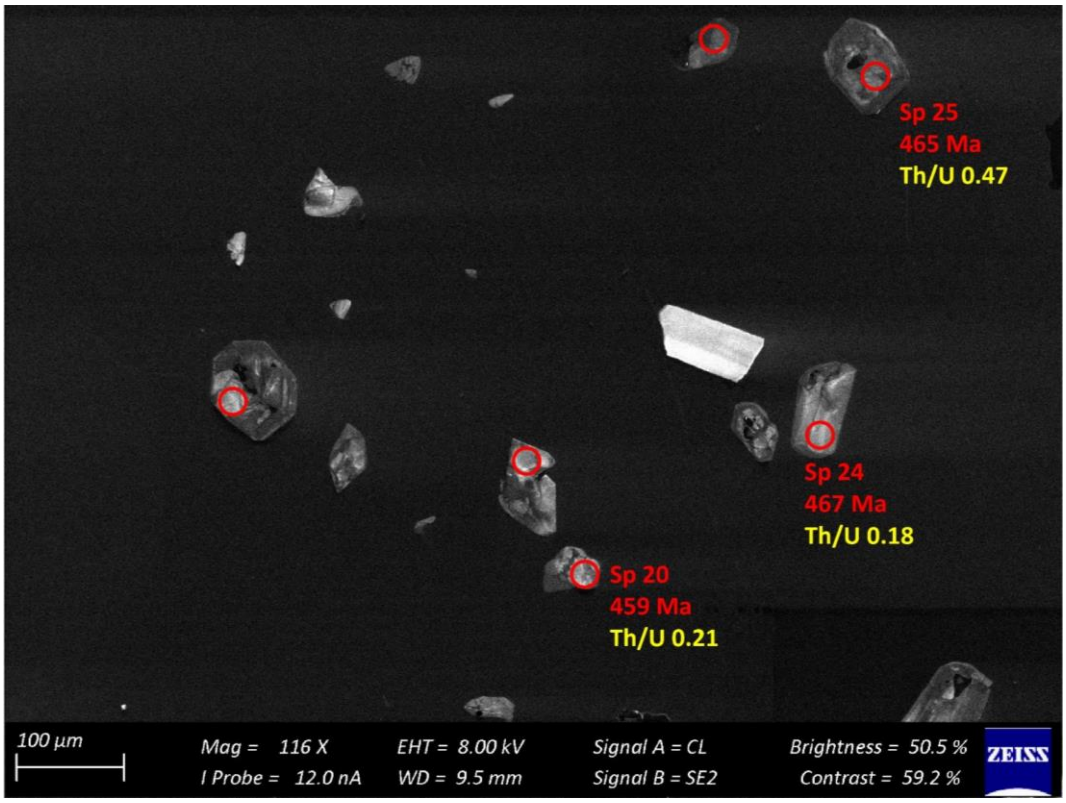

Figure 136 – Zircon Isotope spot analyses of sample s5Bb; U-Pb analyses are colour coded according to concordance; blue writing indicates the Hf identifier with the respective εHf_{468} values

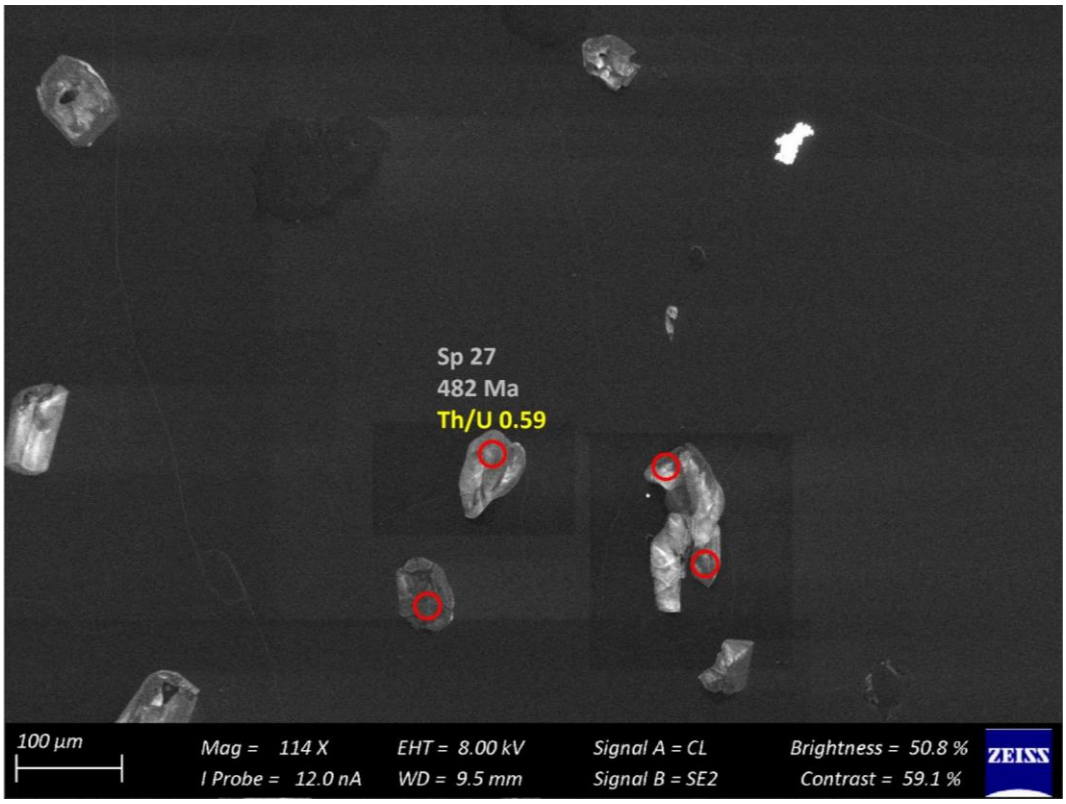

Figure 137 – Zircon Isotope spot analyses of sample s5Bb; U-Pb analyses are colour coded according to concordance; blue writing indicates the Hf identifier with the respective εHf_{468} values

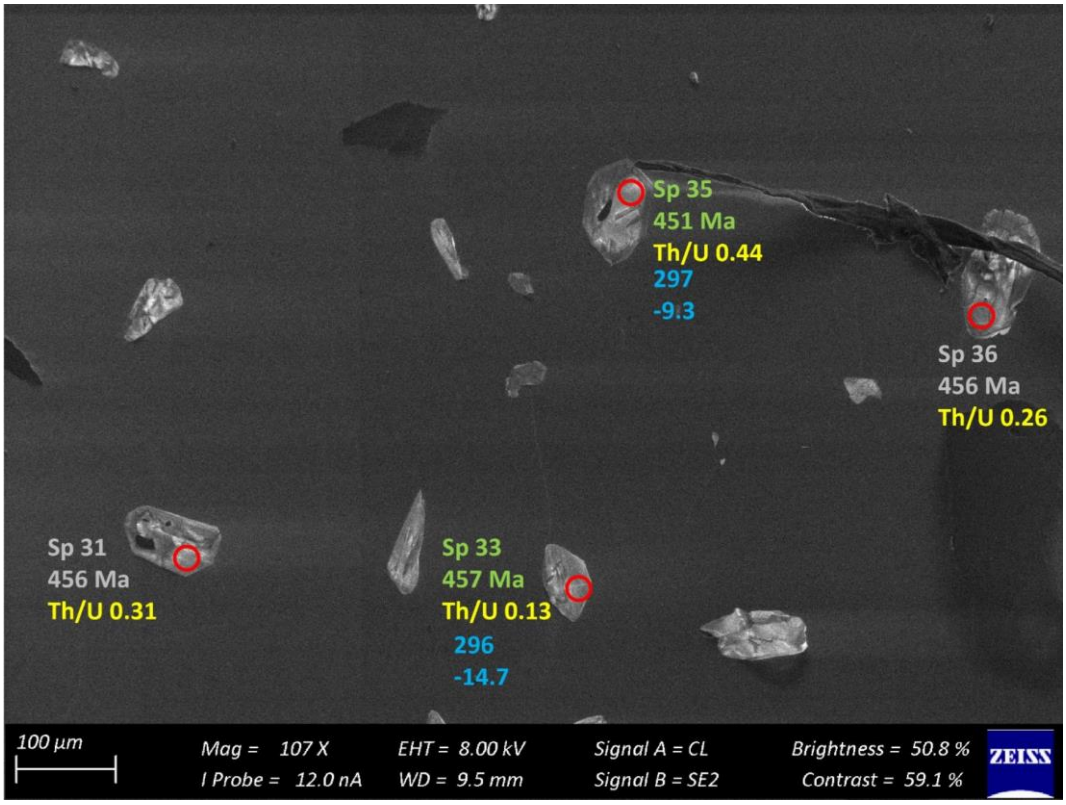

Figure 138 – Zircon Isotope spot analyses of sample s5Bb; U-Pb analyses are colour coded according to concordance; blue writing indicates the Hf identifier with the respective εHf_{468} values

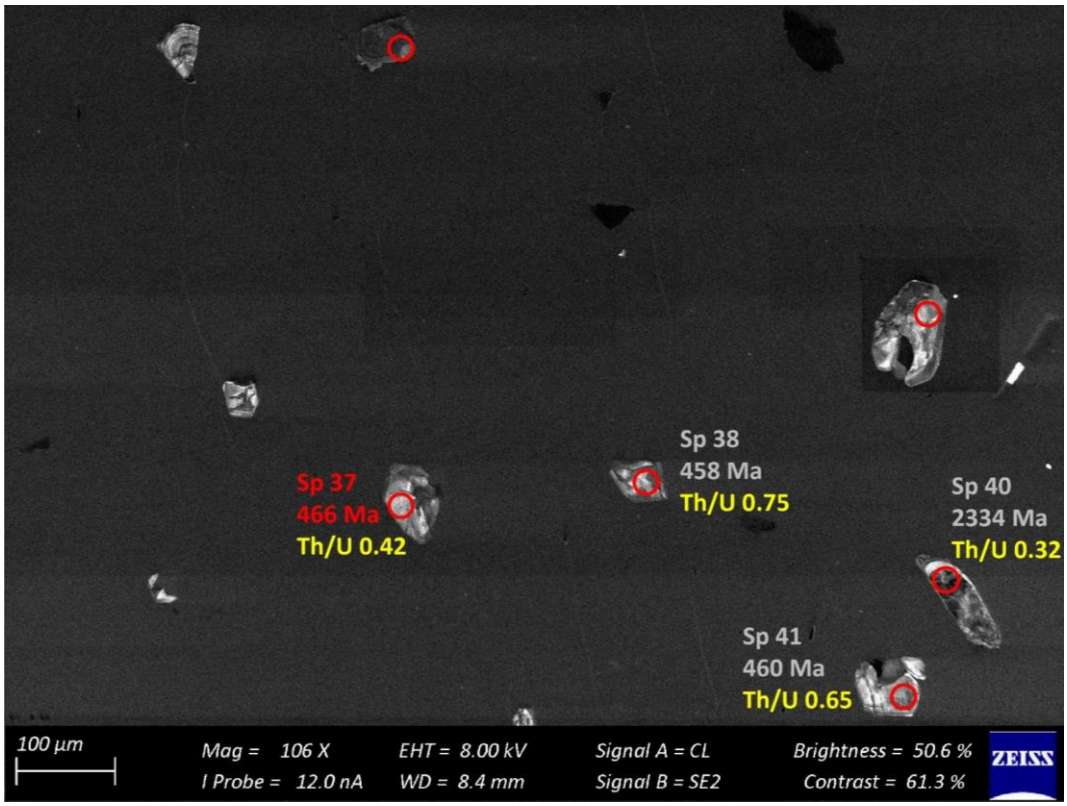

Figure 139 – Zircon Isotope spot analyses of sample s5Bb; U-Pb analyses are colour coded according to concordance; blue writing indicates the Hf identifier with the respective εHf_{468} values

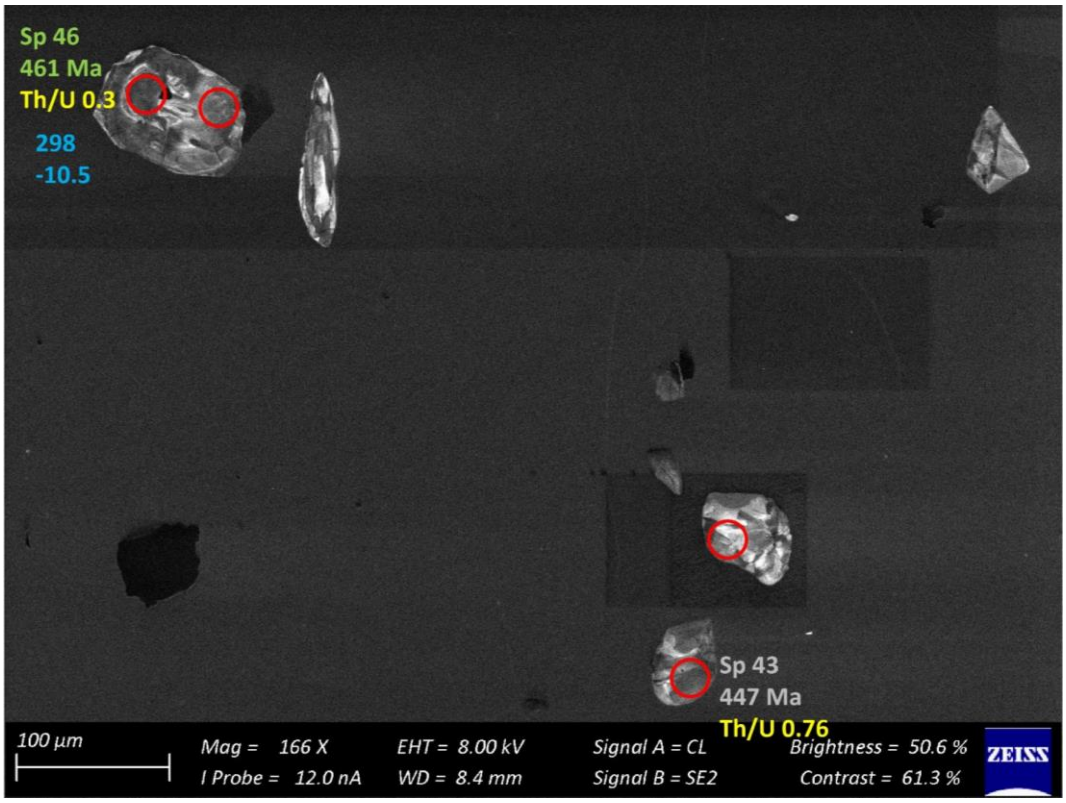

Figure 140 – Zircon Isotope spot analyses of sample s5Bb; U-Pb analyses are colour coded according to concordance; blue writing indicates the Hf identifier with the respective εHf_{468} values

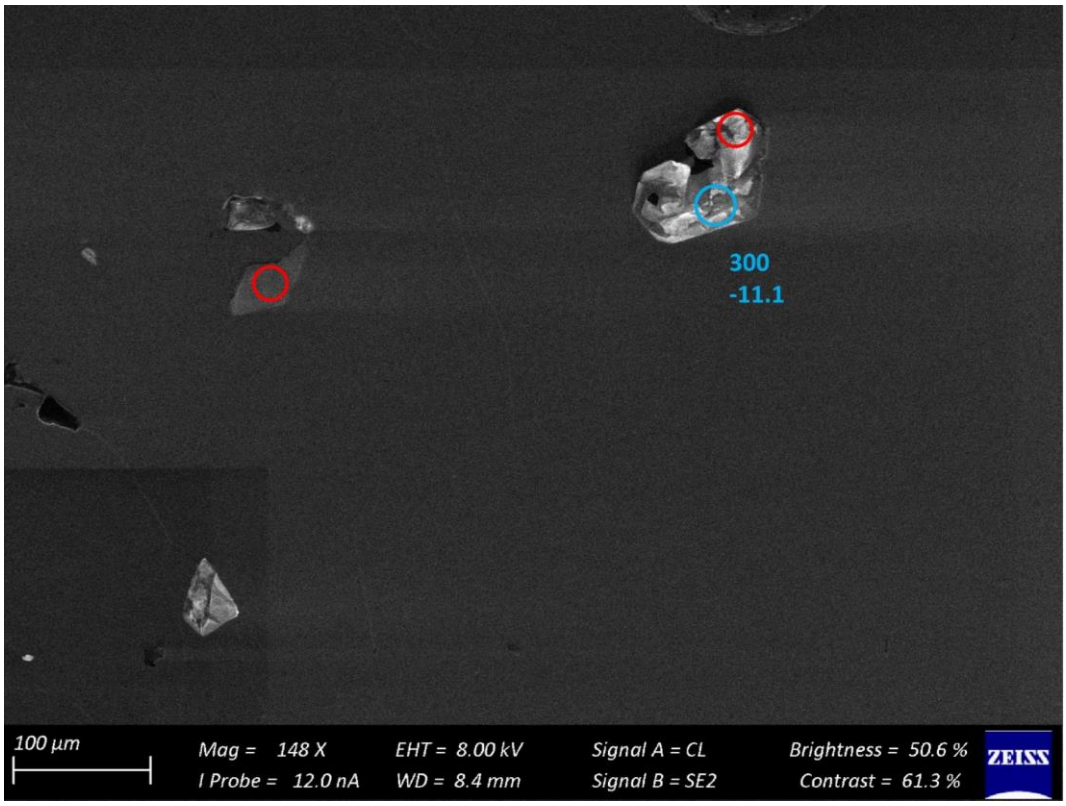

Figure 141 – Zircon Isotope spot analyses of sample s5Bb; U-Pb analyses are colour coded according to concordance; blue writing indicates the Hf identifier with the respective εHf_{468} values

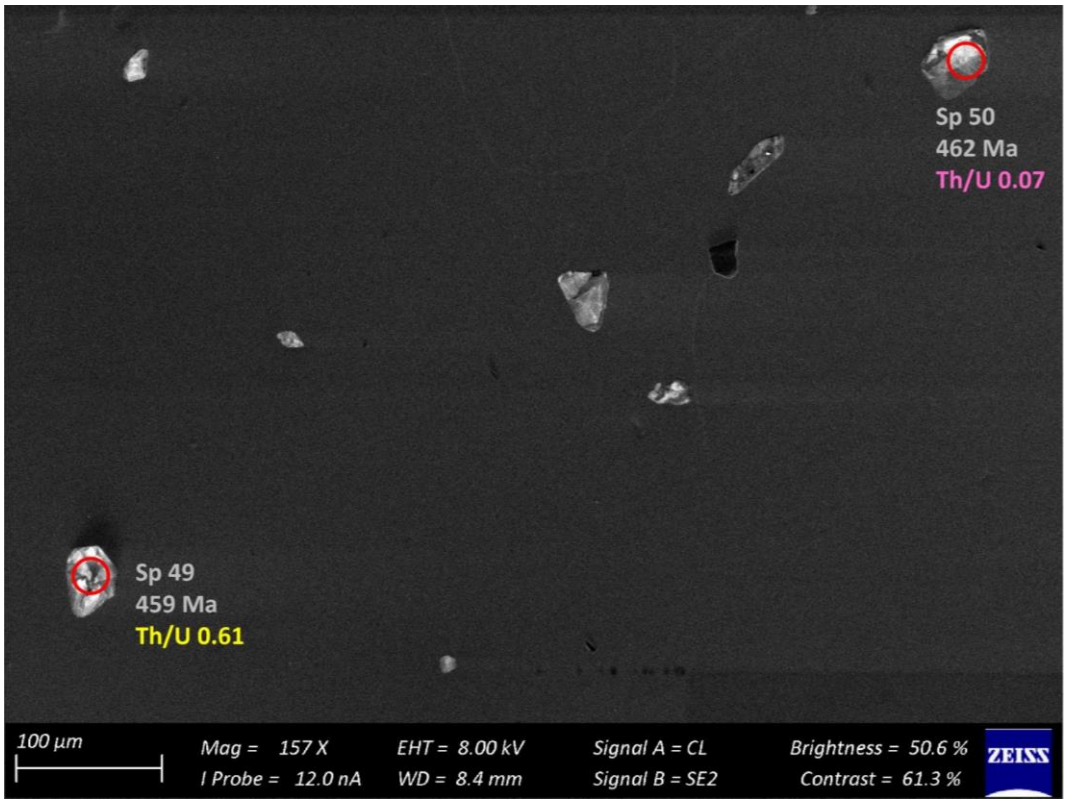

Figure 142 – Zircon Isotope spot analyses of sample s5Bb; U-Pb analyses are colour coded according to concordance; blue writing indicates the Hf identifier with the respective εHf_{468} values

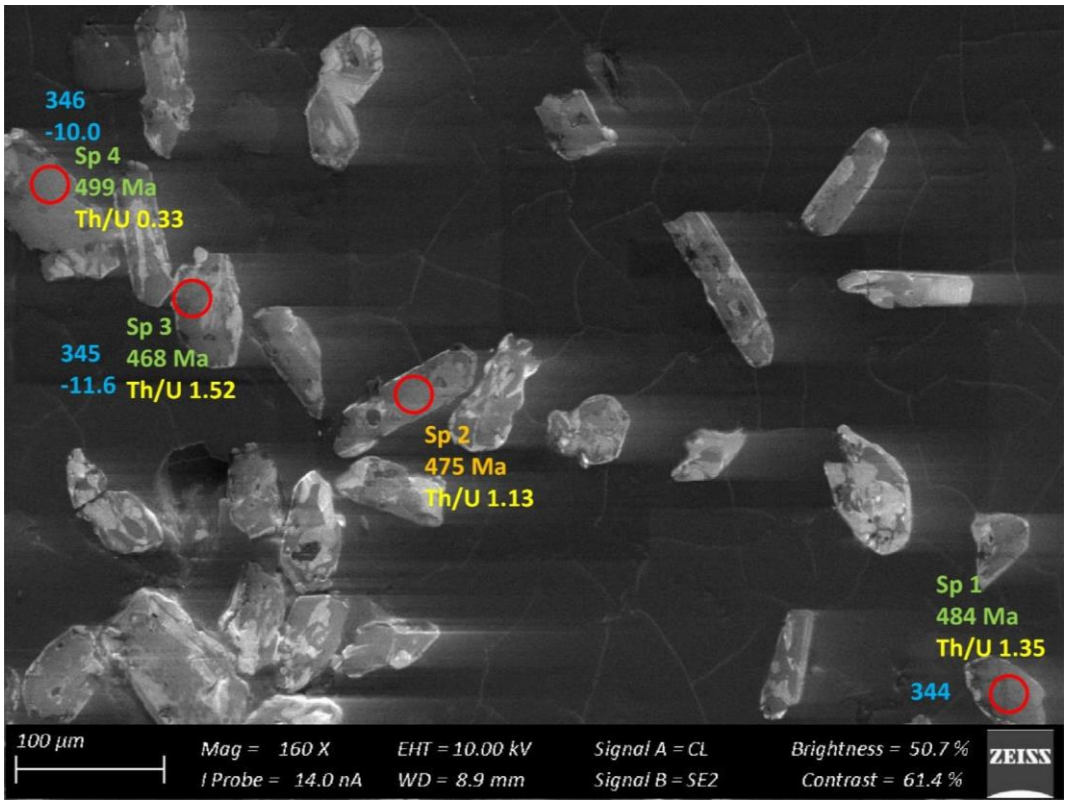

Figure 143 – Zircon Isotope spot analyses of sample s7A; U-Pb analyses are colour coded according to concordance; blue writing indicates the Hf identifier with the respective εHf_{468} values

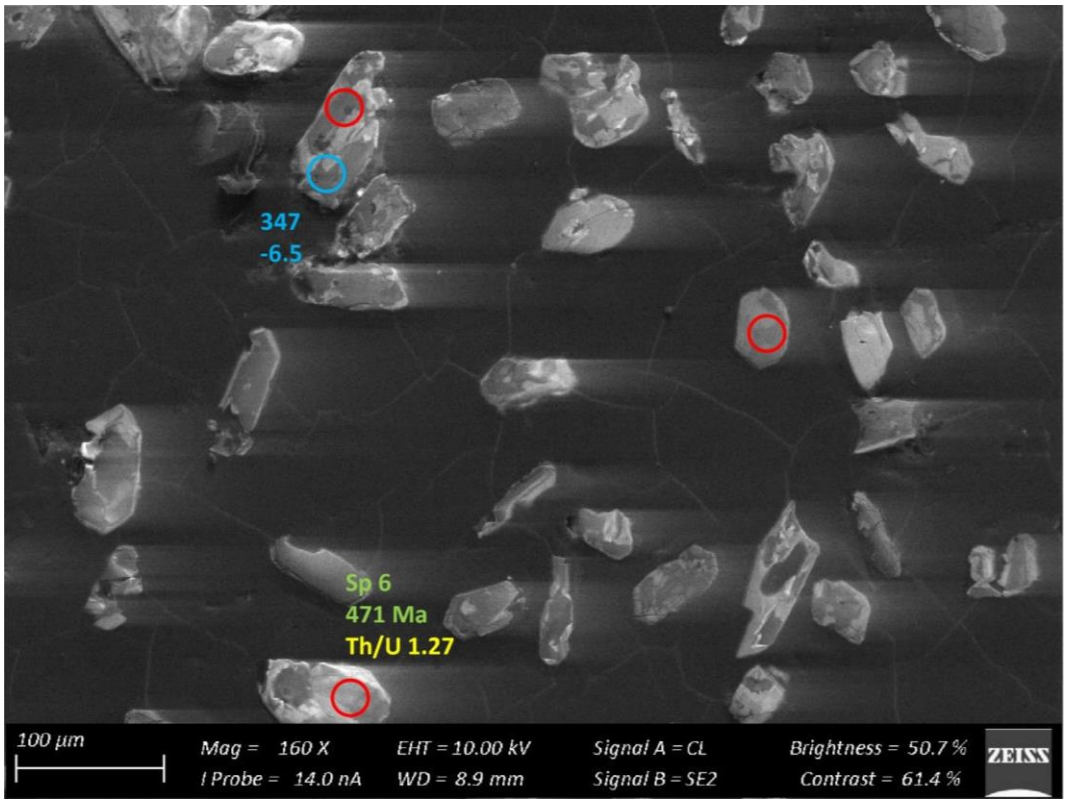

Figure 144 – Zircon Isotope spot analyses of sample s7A; U-Pb analyses are colour coded according to concordance; blue writing indicates the Hf identifier with the respective εHf_{468} values

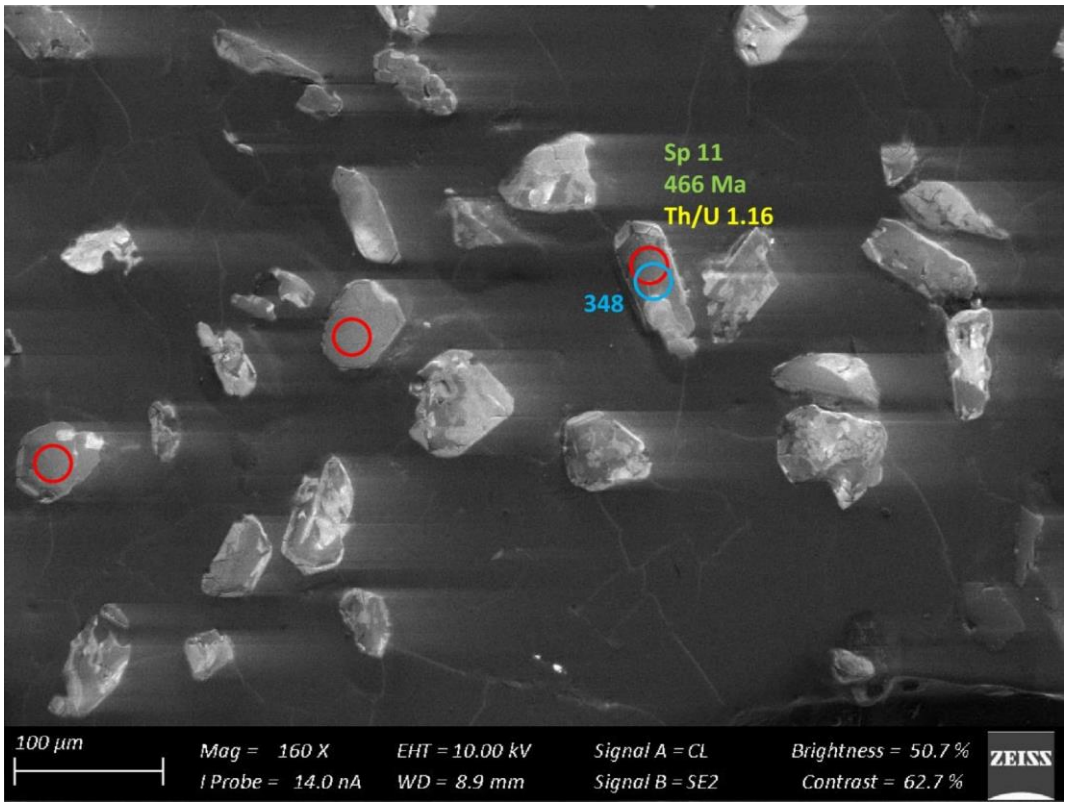

Figure 145 – Zircon Isotope spot analyses of sample s7A; U-Pb analyses are colour coded according to concordance; blue writing indicates the Hf identifier with the respective εHf$_{468}$ values

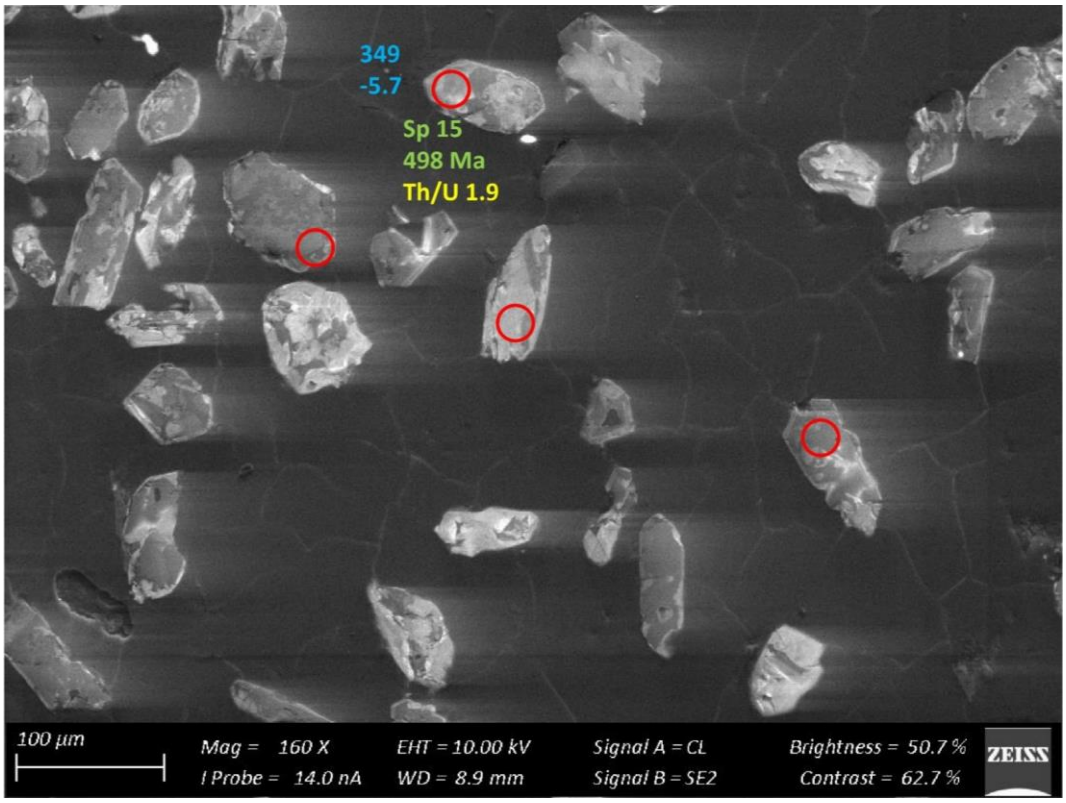

Figure 146 – Zircon Isotope spot analyses of sample s7A; U-Pb analyses are colour coded according to concordance; blue writing indicates the Hf identifier with the respective εHf$_{468}$ values

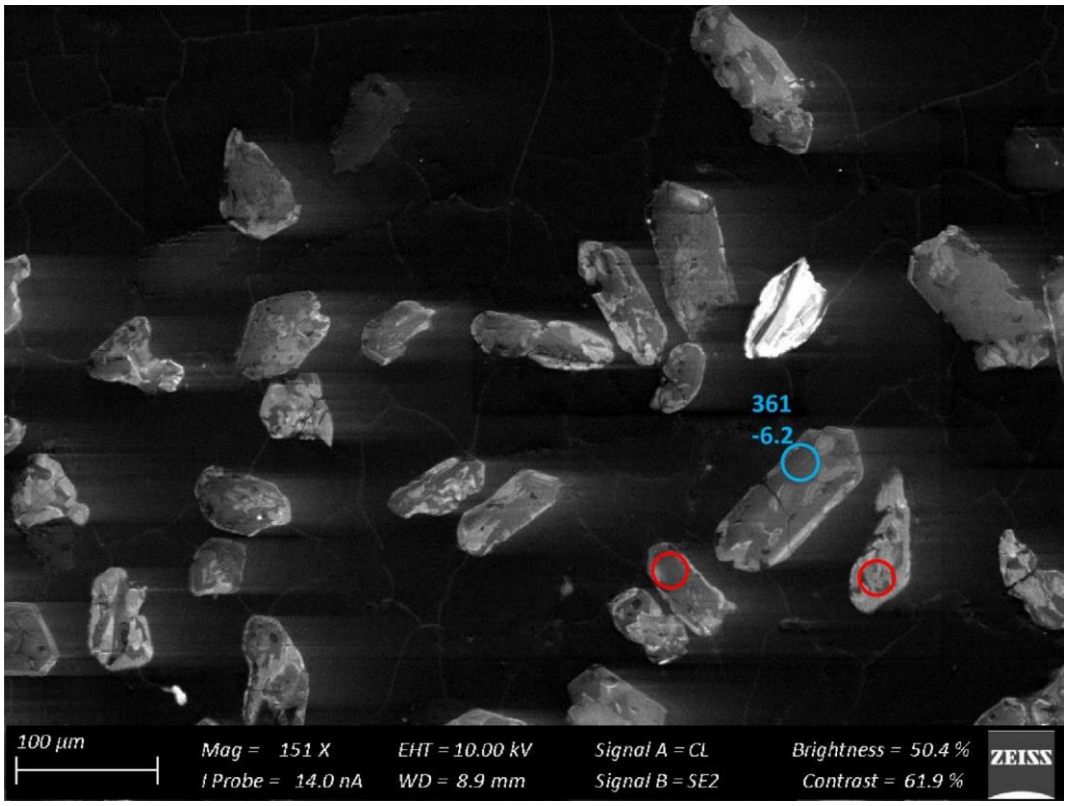

Figure 147 – Zircon Isotope spot analyses of sample s7A; U-Pb analyses are colour coded according to concordance; blue writing indicates the Hf identifier with the respective εHf$_{468}$ values

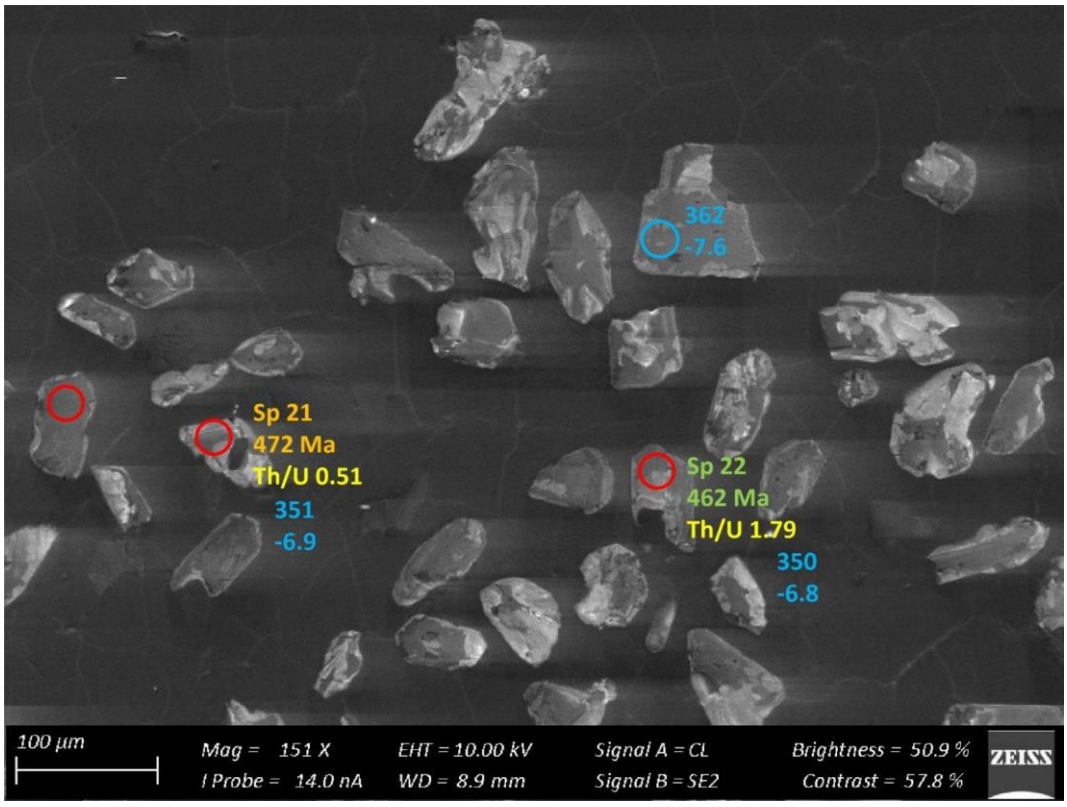

Figure 148 – Zircon Isotope spot analyses of sample s7A; U-Pb analyses are colour coded according to concordance; blue writing indicates the Hf identifier with the respective εHf$_{468}$ values

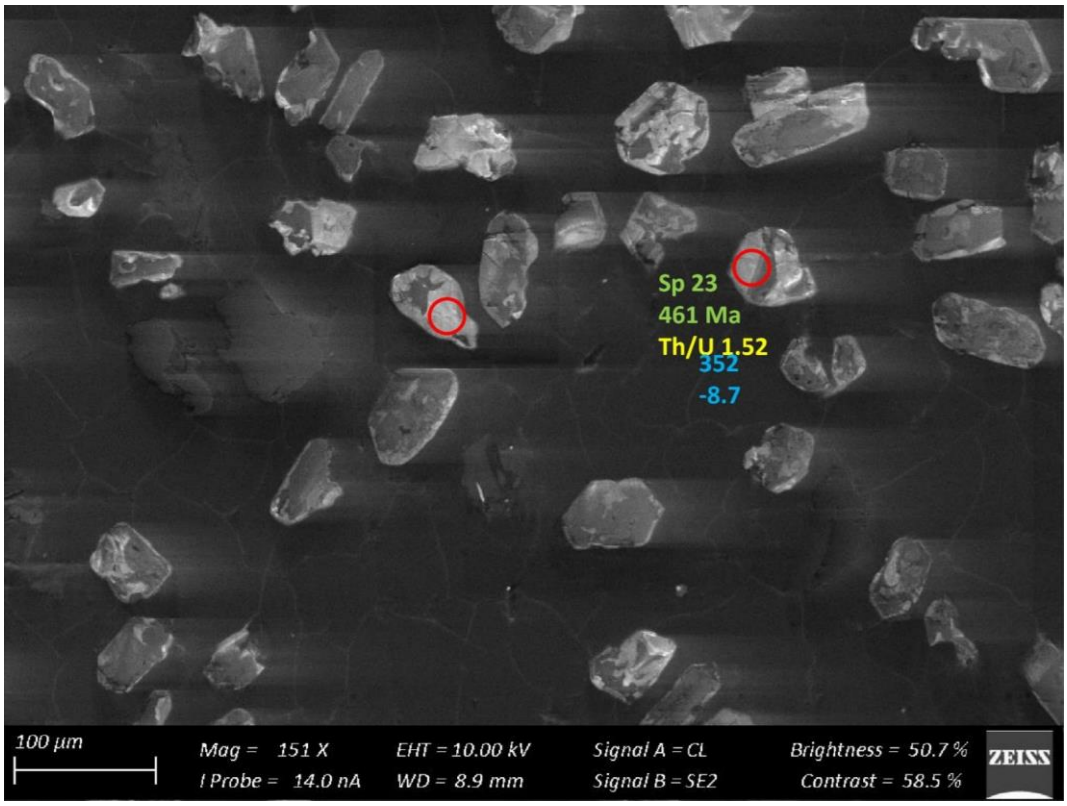

Figure 149 – Zircon Isotope spot analyses of sample s7A; U-Pb analyses are colour coded according to concordance; blue writing indicates the Hf identifier with the respective εHf_{468} values

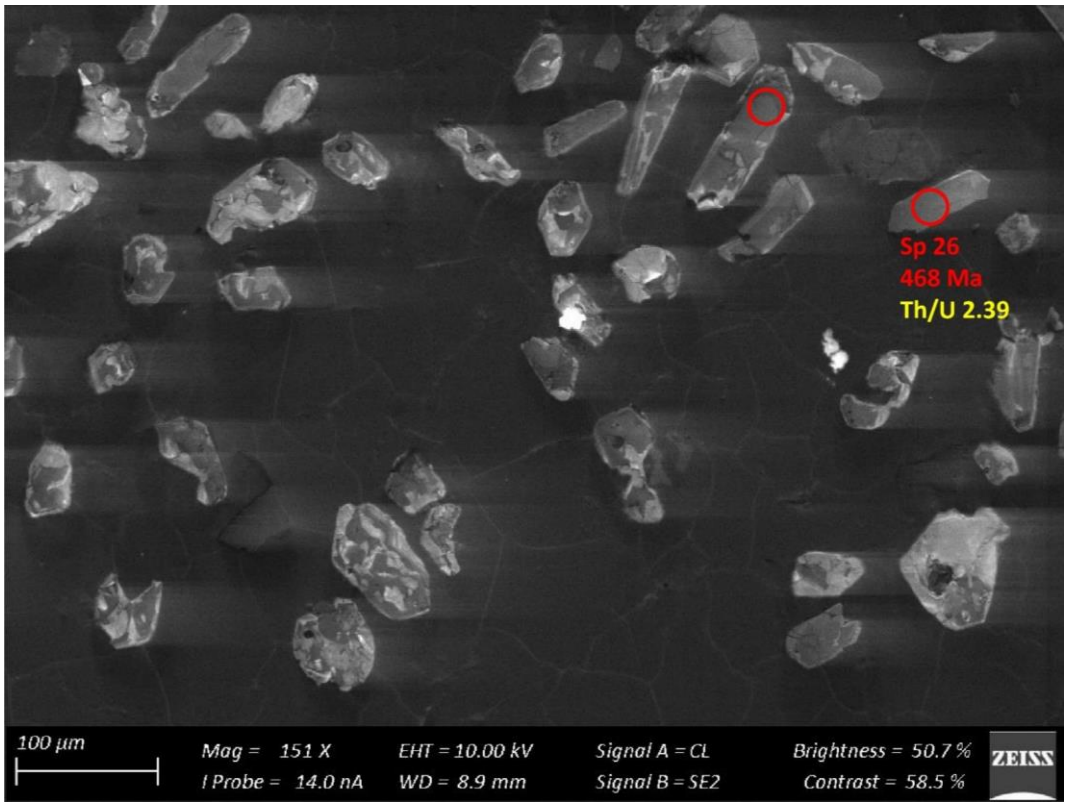

Figure 150 – Zircon Isotope spot analyses of sample s7A; U-Pb analyses are colour coded according to concordance; blue writing indicates the Hf identifier with the respective εHf_{468} values

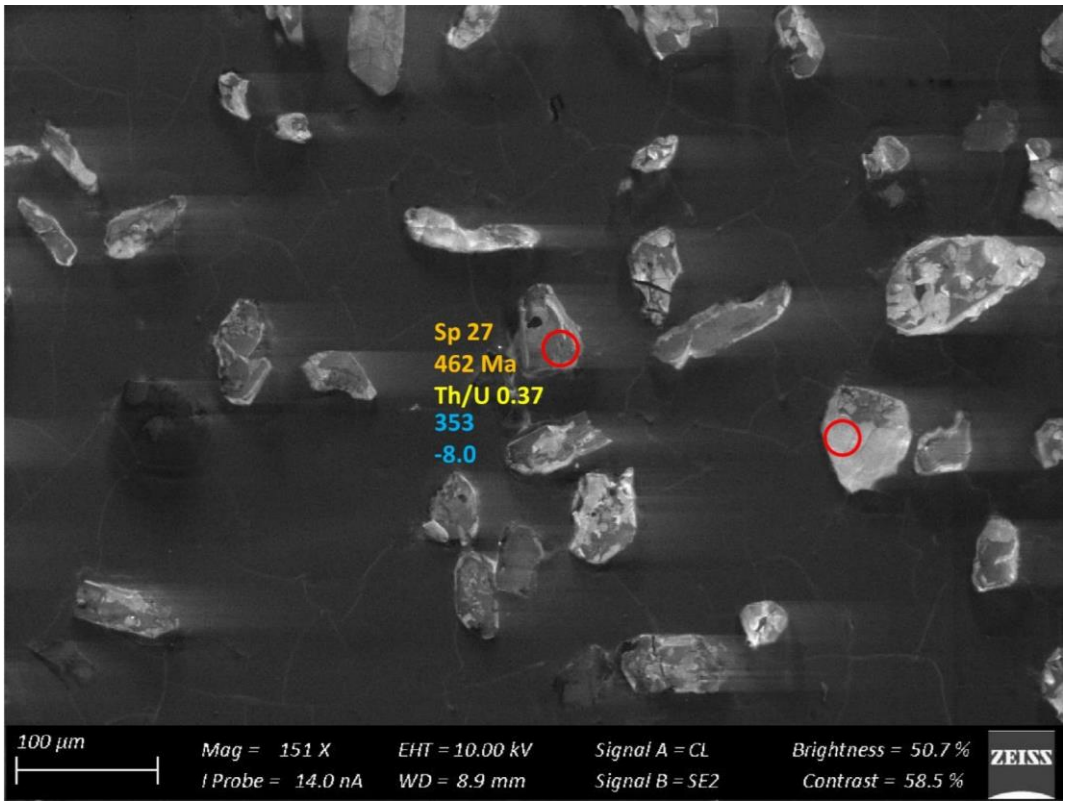

Figure 151 – Zircon Isotope spot analyses of sample s7A; U-Pb analyses are colour coded according to concordance; blue writing indicates the Hf identifier with the respective εHf_{468} values

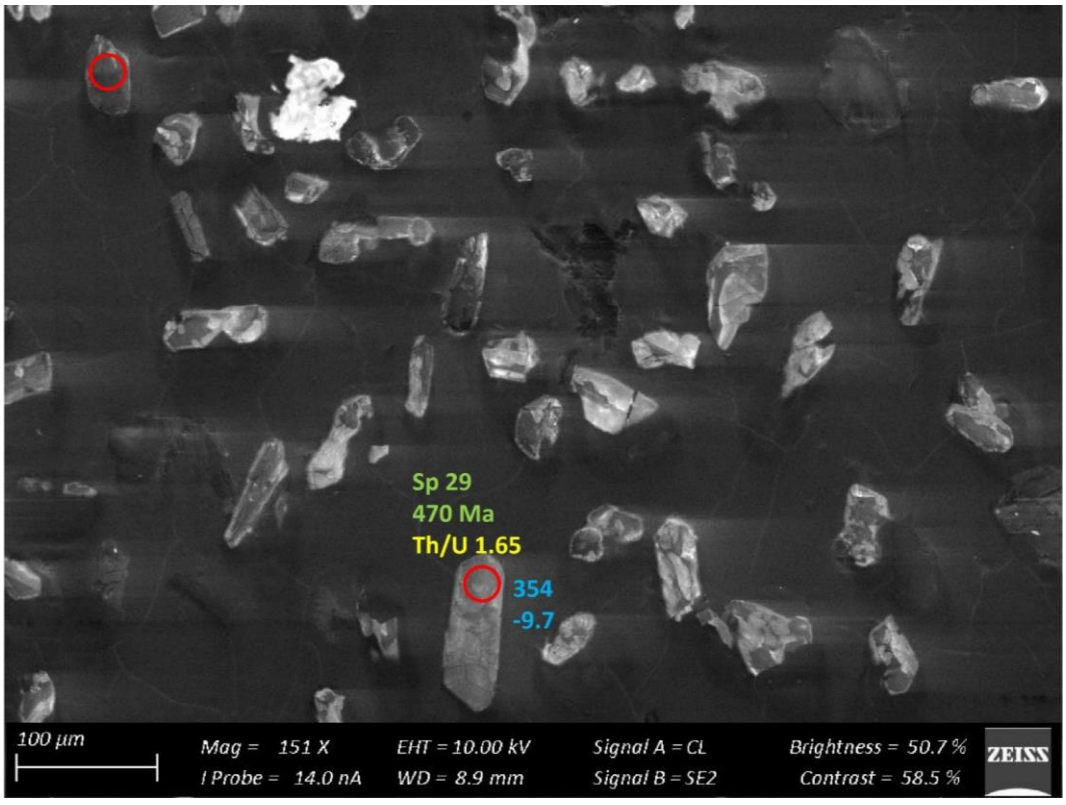

Figure 152 – Zircon Isotope spot analyses of sample s7A; U-Pb analyses are colour coded according to concordance; blue writing indicates the Hf identifier with the respective εHf_{468} values

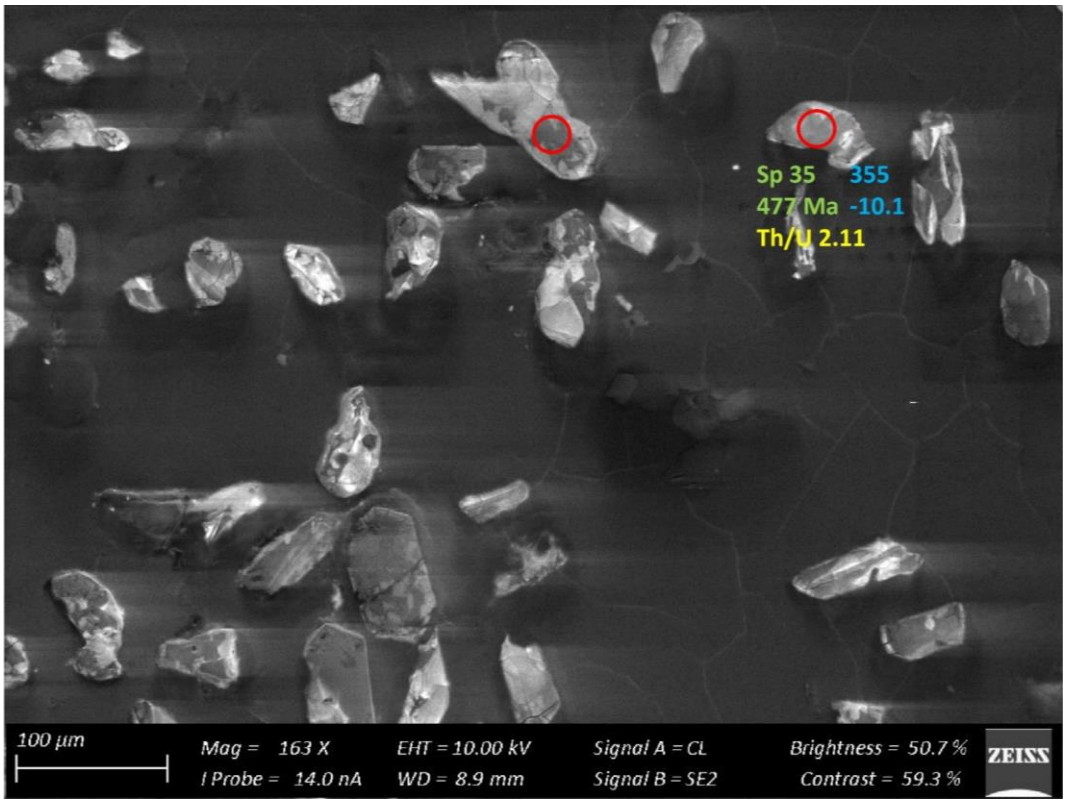

Figure 153 – Zircon Isotope spot analyses of sample s7A; U-Pb analyses are colour coded according to concordance; blue writing indicates the Hf identifier with the respective εHf_{468} values

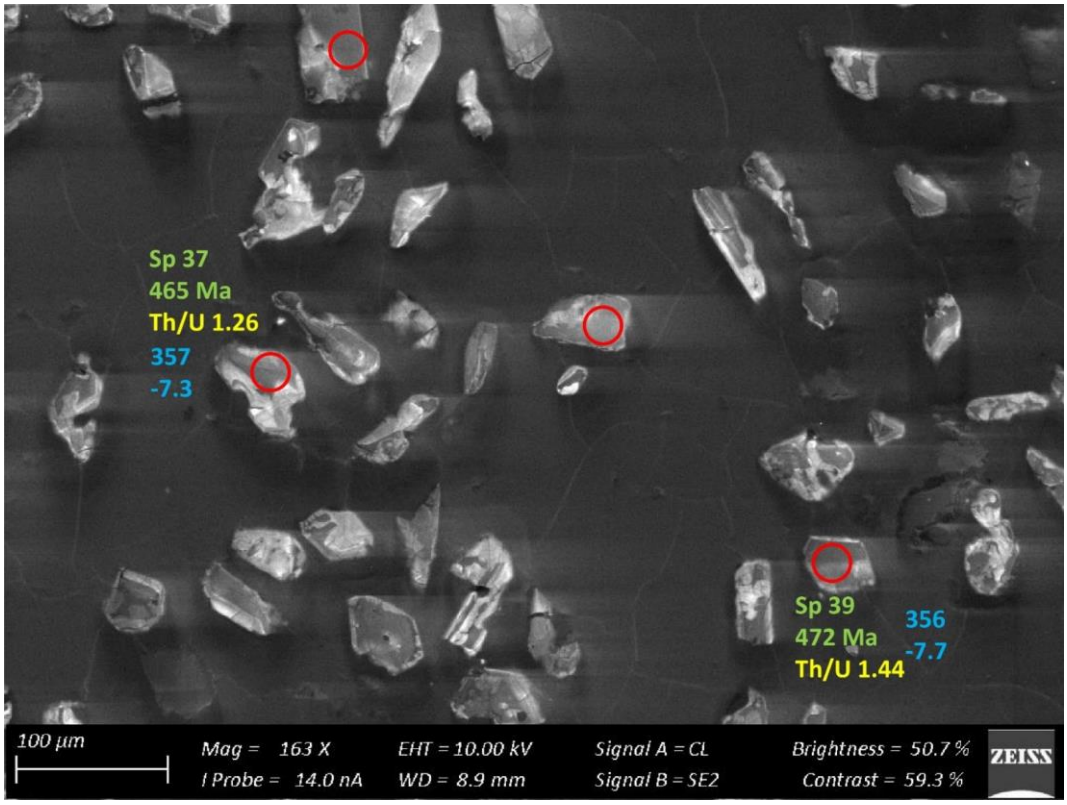

Figure 154 – Zircon Isotope spot analyses of sample s7A; U-Pb analyses are colour coded according to concordance; blue writing indicates the Hf identifier with the respective εHf_{468} values

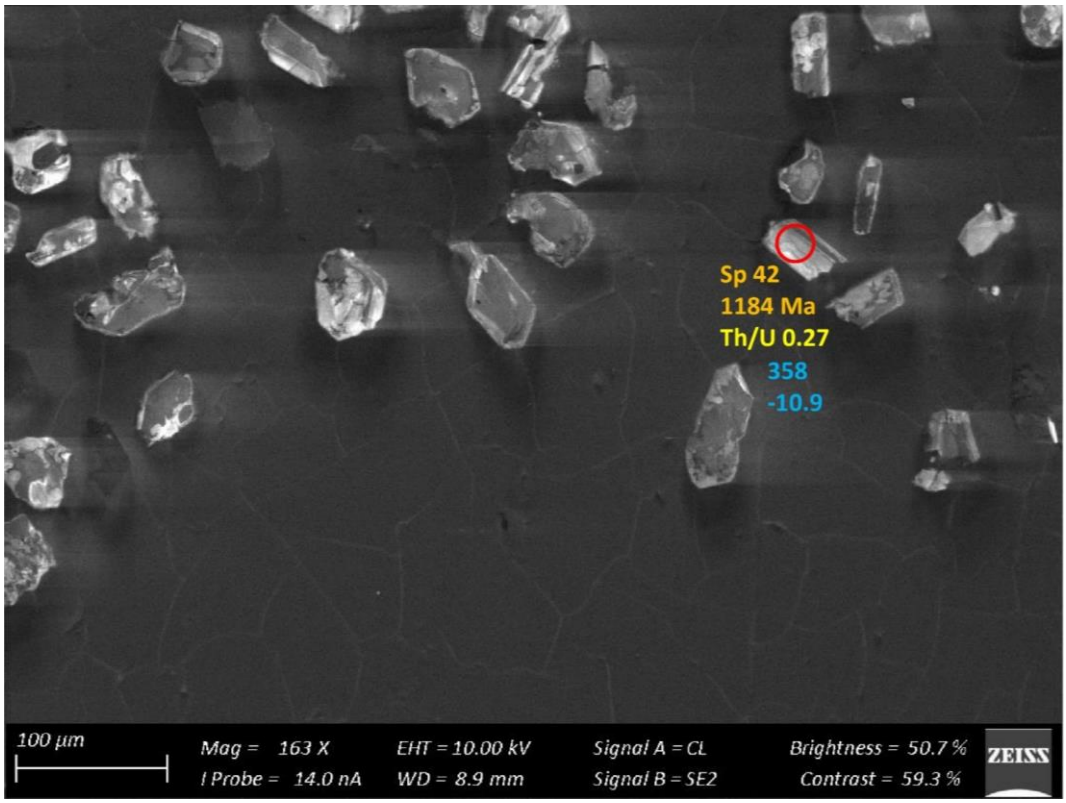

Figure 155 – Zircon Isotope spot analyses of sample s7A; U-Pb analyses are colour coded according to concordance; blue writing indicates the Hf identifier with the respective εHf_{468} values

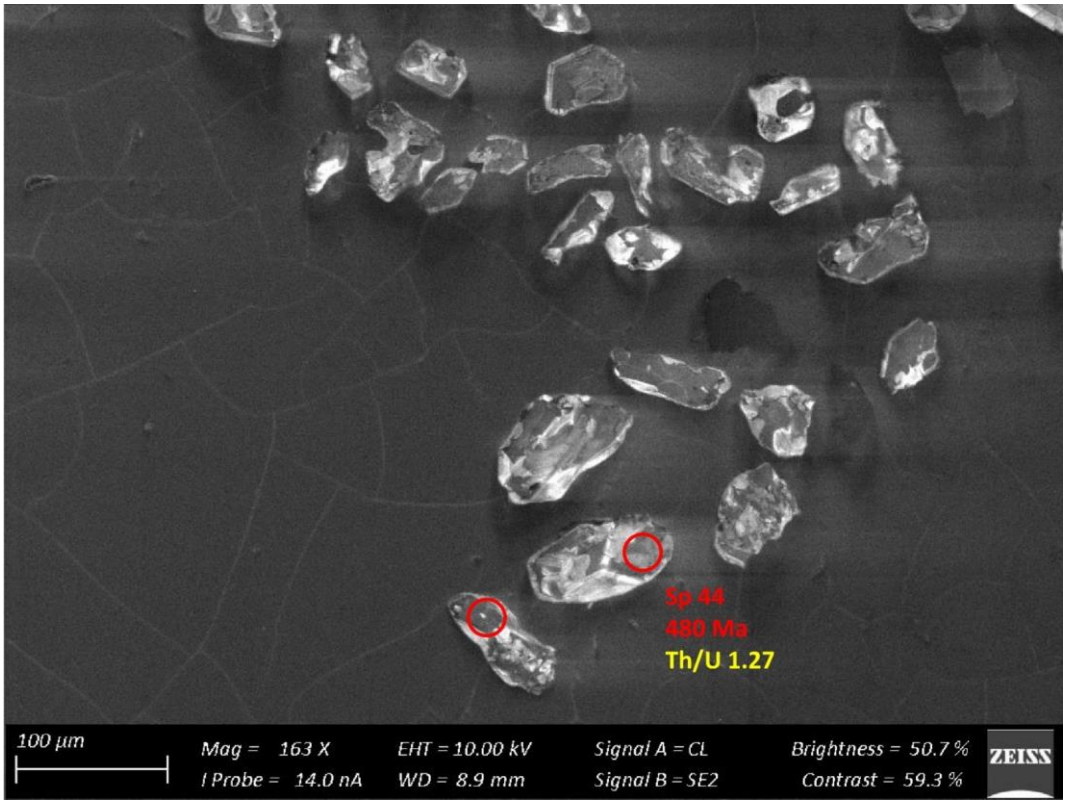

Figure 156 – Zircon Isotope spot analyses of sample s7A; U-Pb analyses are colour coded according to concordance; blue writing indicates the Hf identifier with the respective εHf_{468} values

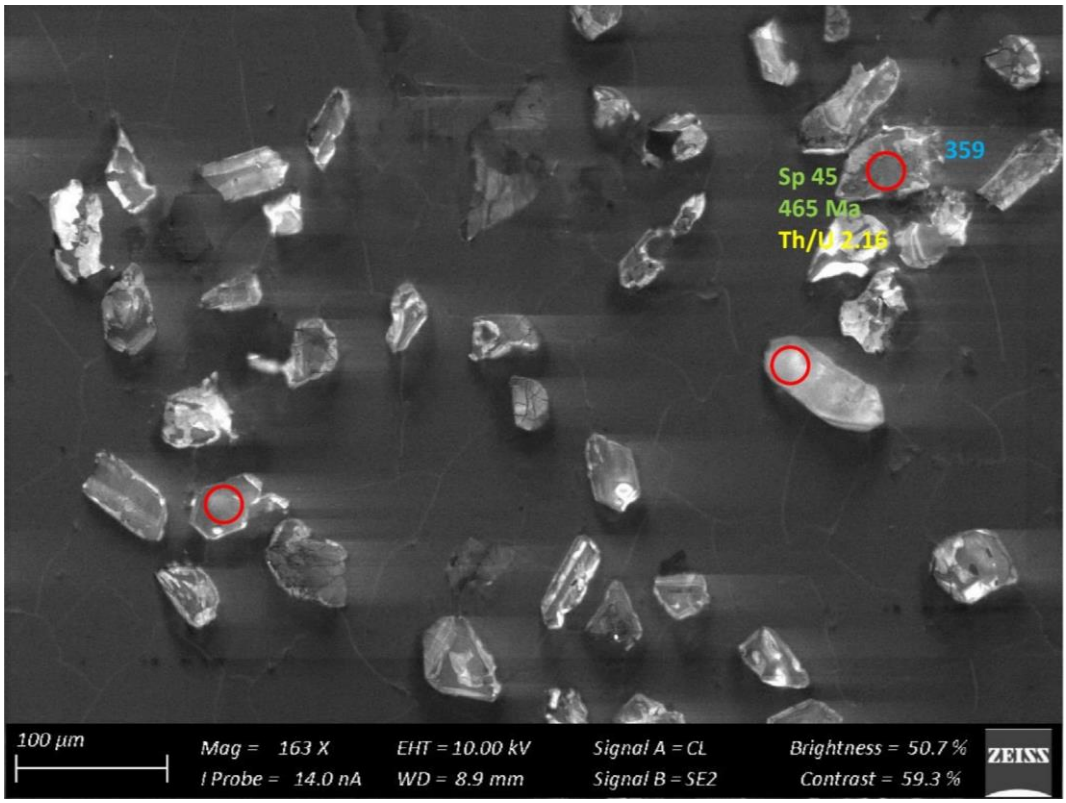

Figure 157 – Zircon Isotope spot analyses of sample s7A; U-Pb analyses are colour coded according to concordance; blue writing indicates the Hf identifier with the respective εHf_{468} values

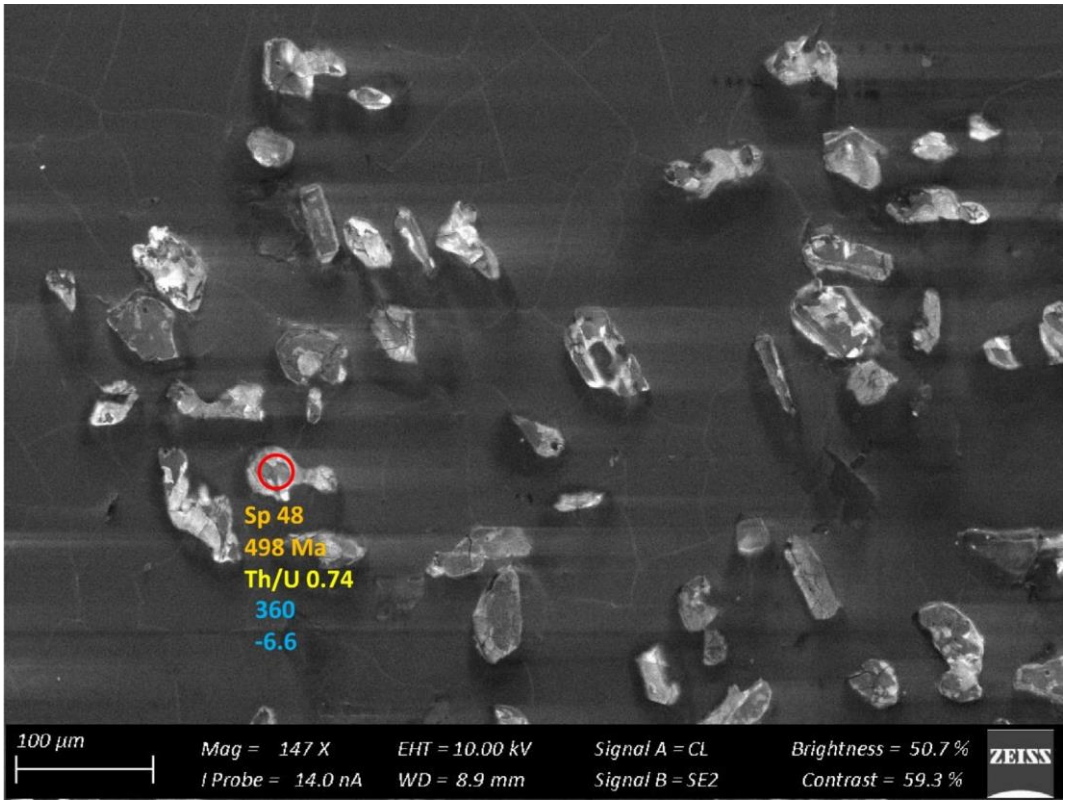

Figure 158 – Zircon Isotope spot analyses of sample s7A; U-Pb analyses are colour coded according to concordance; blue writing indicates the Hf identifier with the respective εHf_{468} values

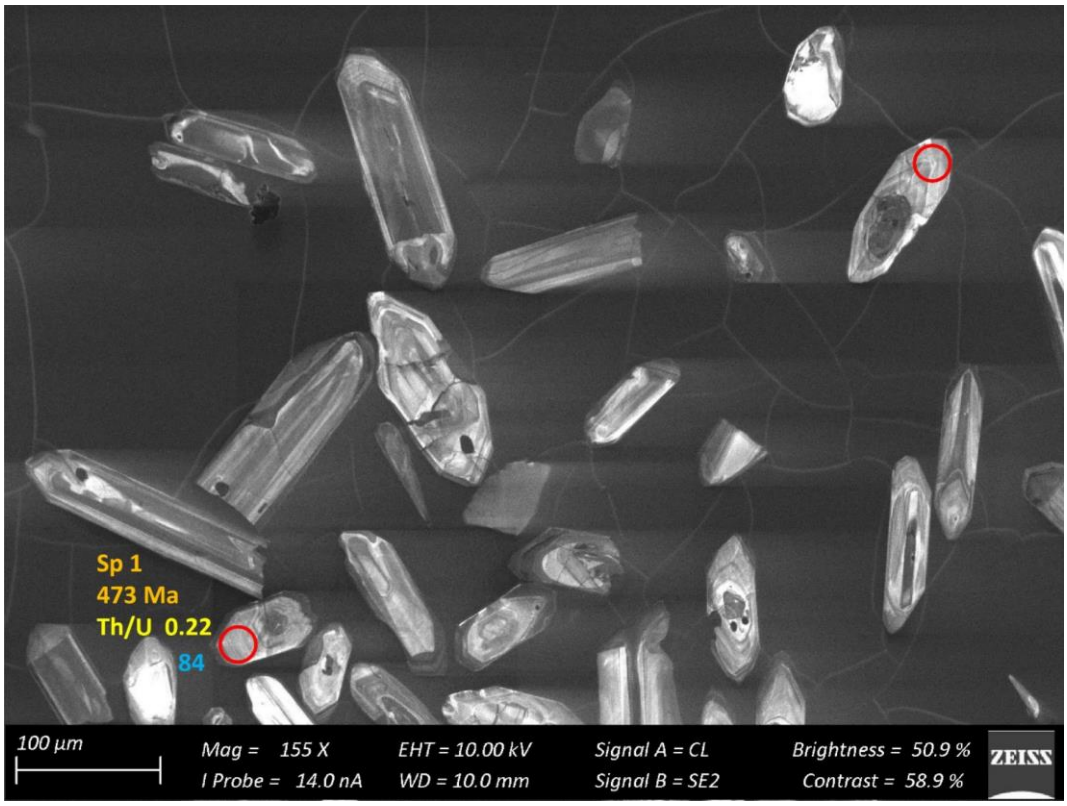

Figure 159 – Zircon Isotope spot analyses of sample s7B; U-Pb analyses are colour coded according to concordance; blue writing indicates the Hf identifier with the respective εHf_{468} values

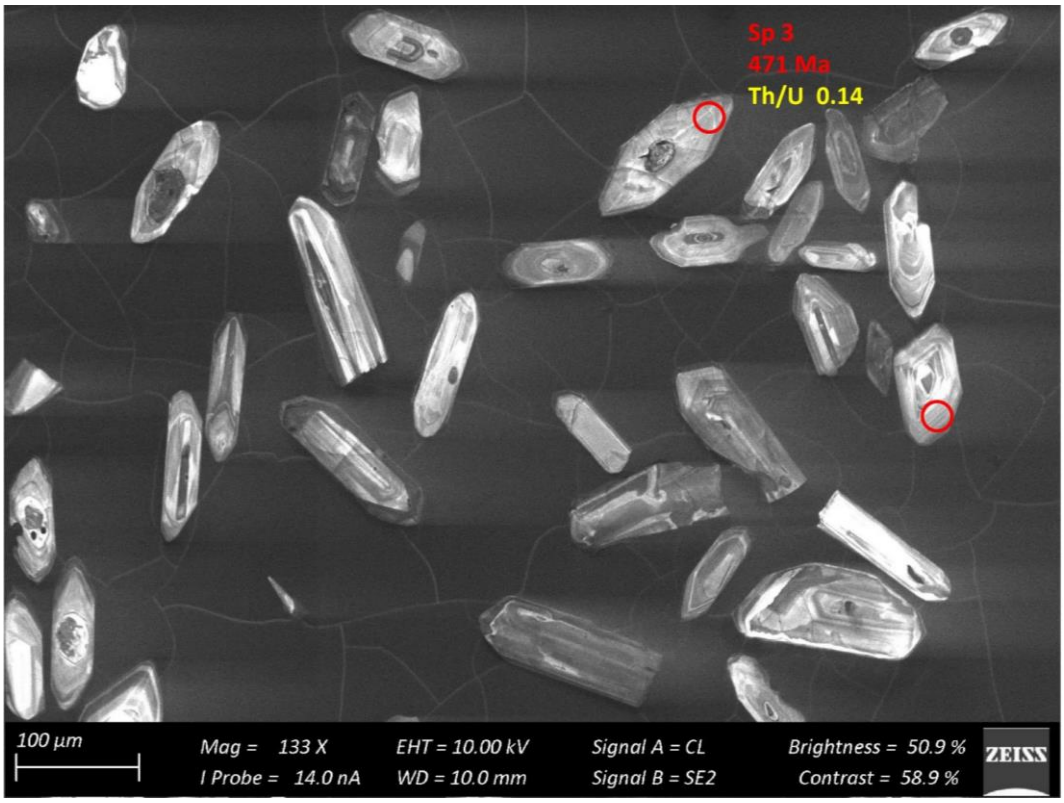

Figure 160 – Zircon Isotope spot analyses of sample s7B; U-Pb analyses are colour coded according to concordance; blue writing indicates the Hf identifier with the respective εHf_{468} values

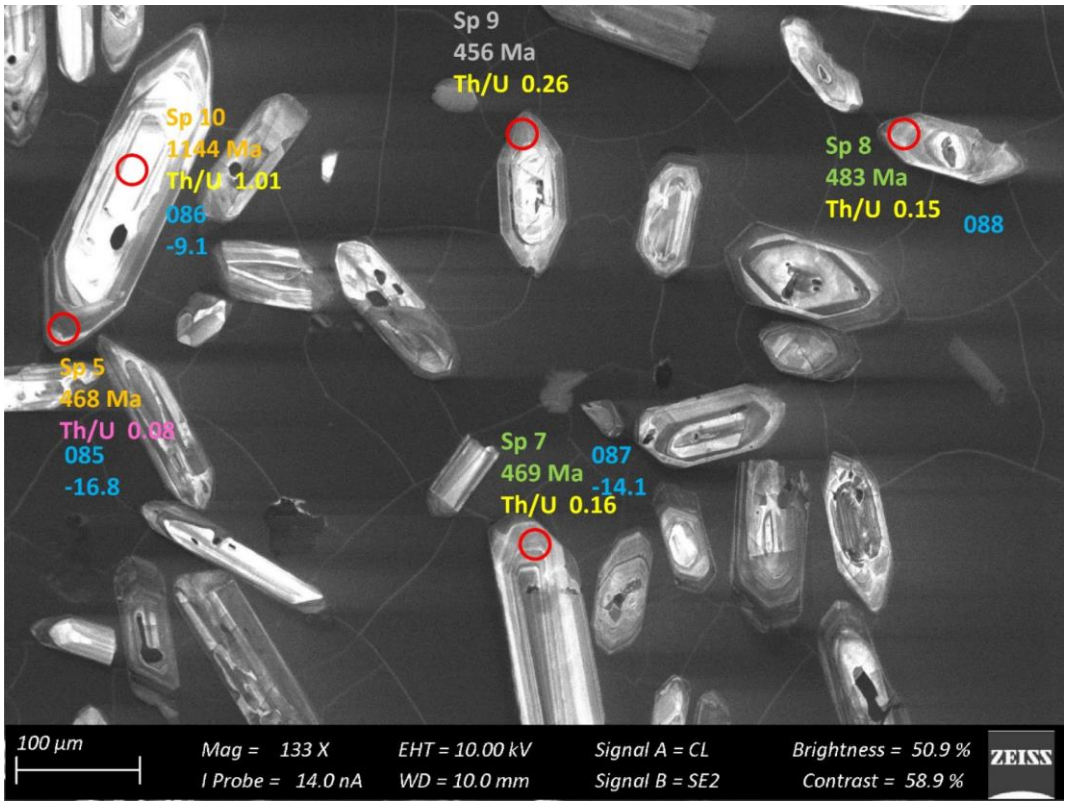

Figure 161 – Zircon Isotope spot analyses of sample s7B; U-Pb analyses are colour coded according to concordance; blue writing indicates the Hf identifier with the respective εHf_{468} values

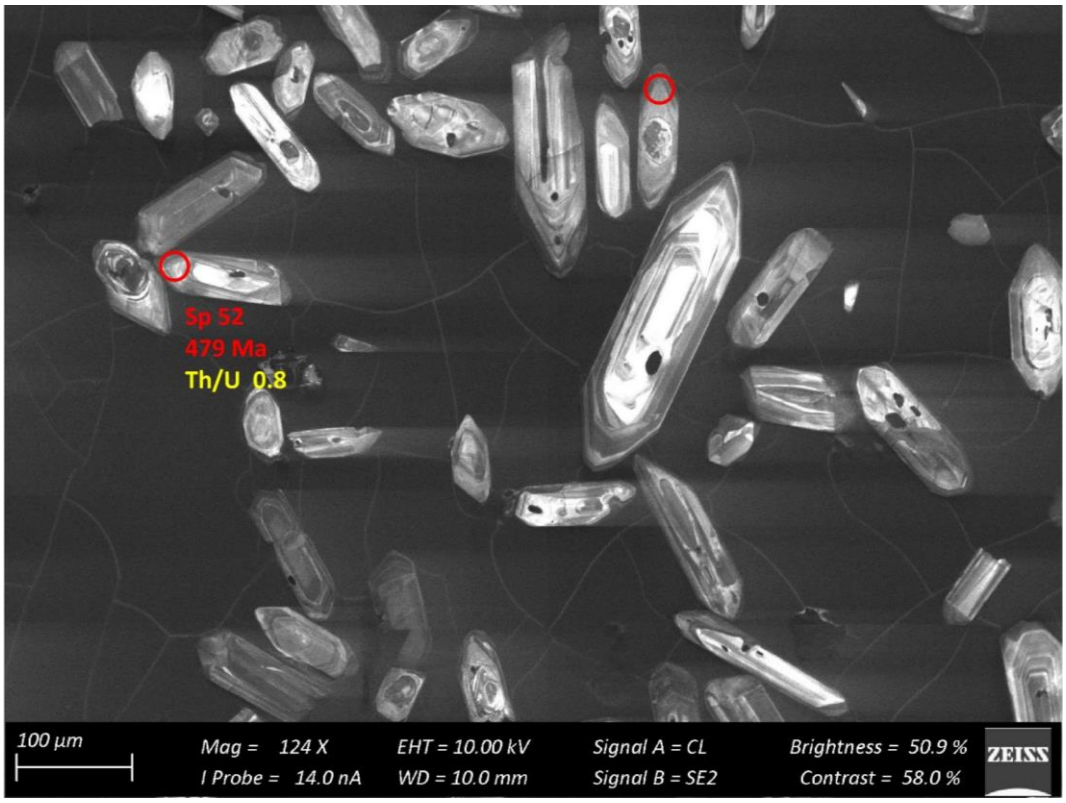

Figure 162 – Zircon Isotope spot analyses of sample s7B; U-Pb analyses are colour coded according to concordance; blue writing indicates the Hf identifier with the respective εHf_{468} values

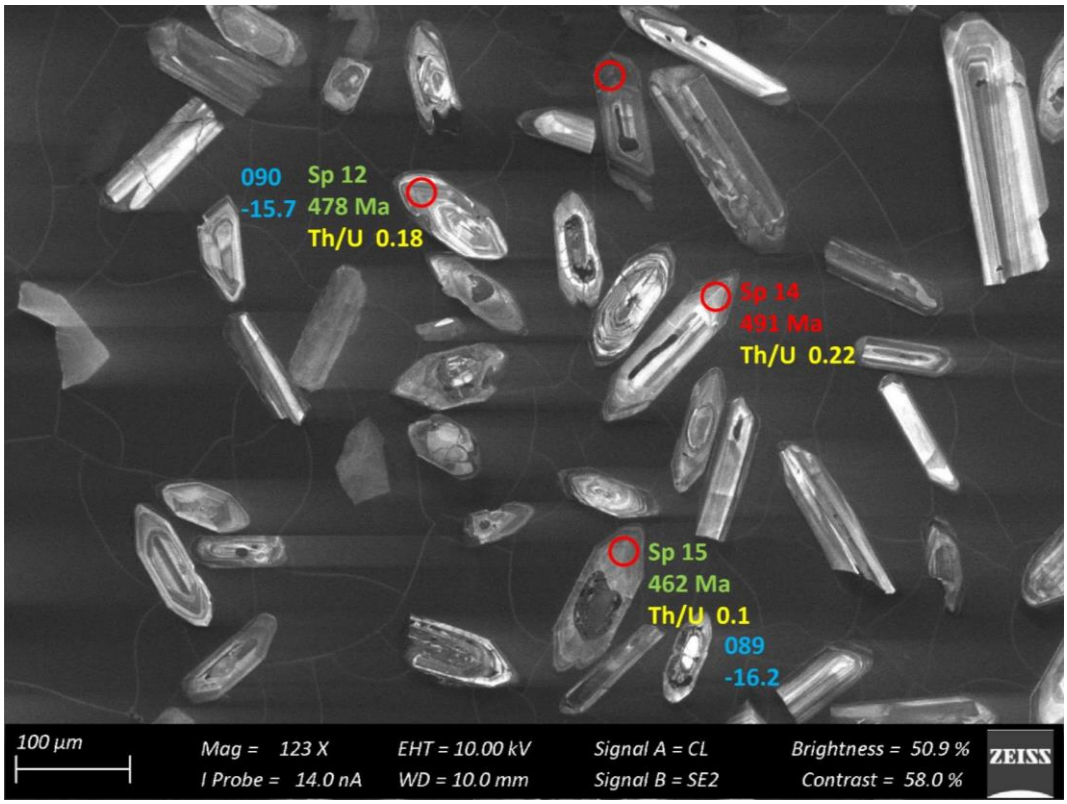

Figure 163 – Zircon Isotope spot analyses of sample s7B; U-Pb analyses are colour coded according to concordance; blue writing indicates the Hf identifier with the respective εHf_{468} values

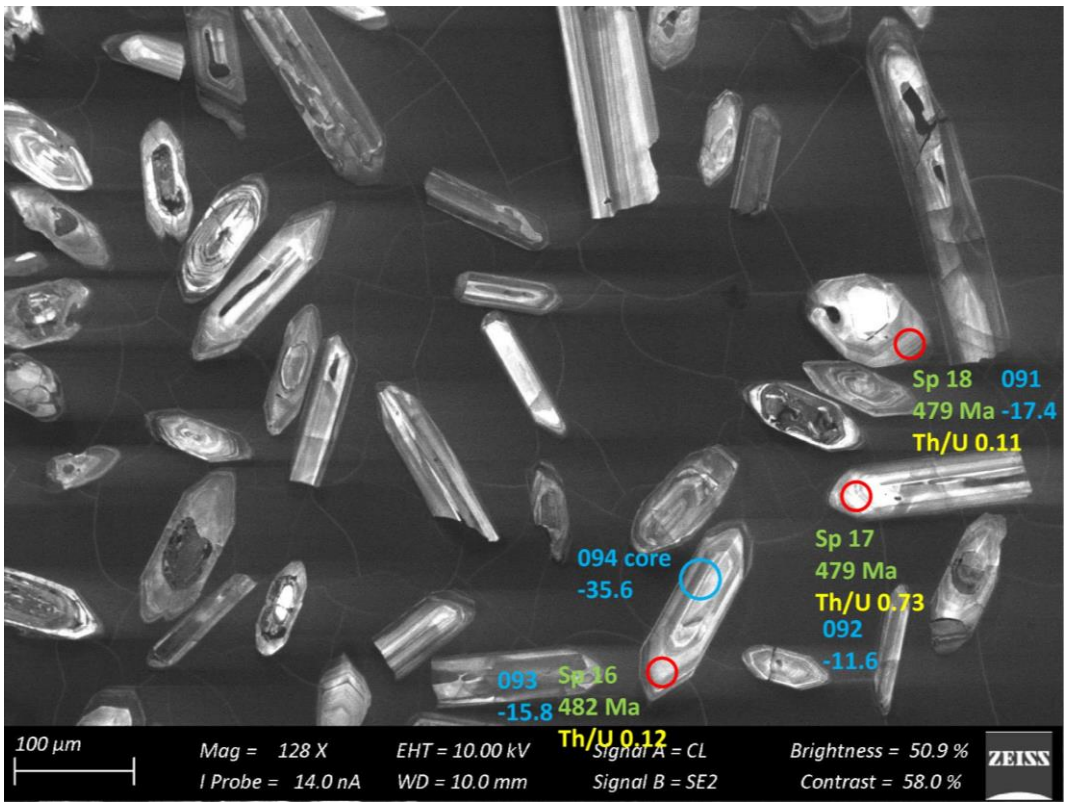

Figure 164 – Zircon Isotope spot analyses of sample s7B; U-Pb analyses are colour coded according to concordance; blue writing indicates the Hf identifier with the respective εHf_{468} values

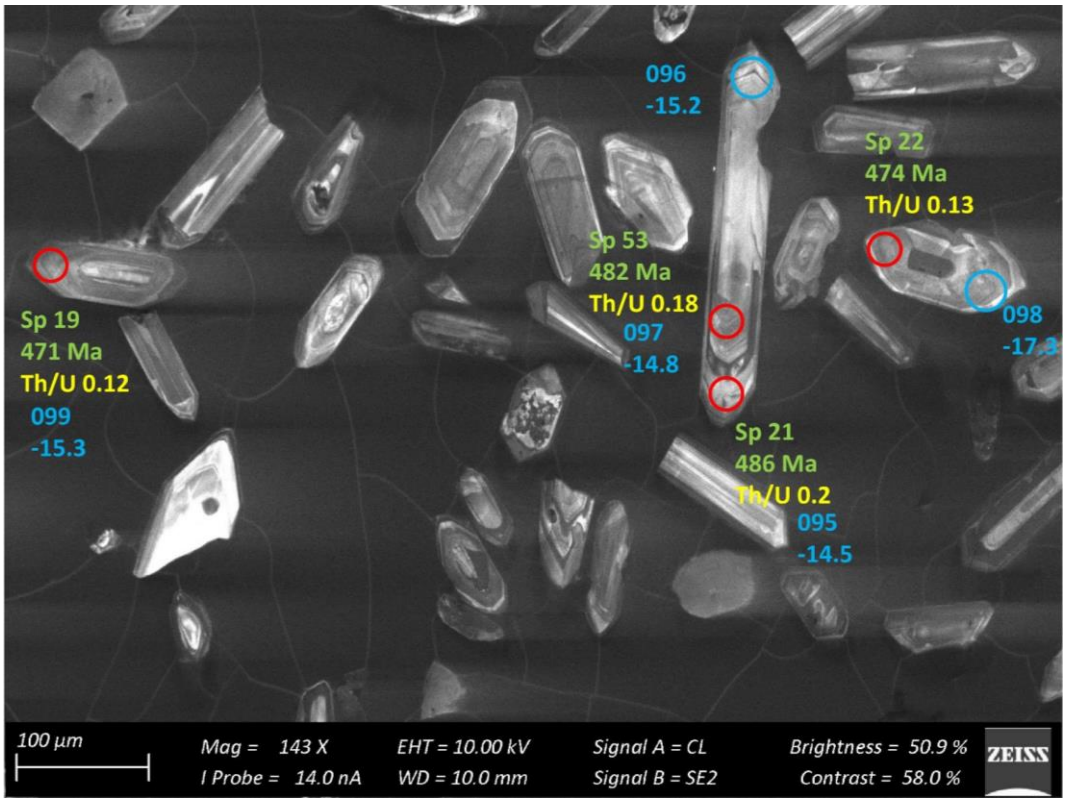

Figure 165 – Zircon Isotope spot analyses of sample s7B; U-Pb analyses are colour coded according to concordance; blue writing indicates the Hf identifier with the respective εHf_{468} values

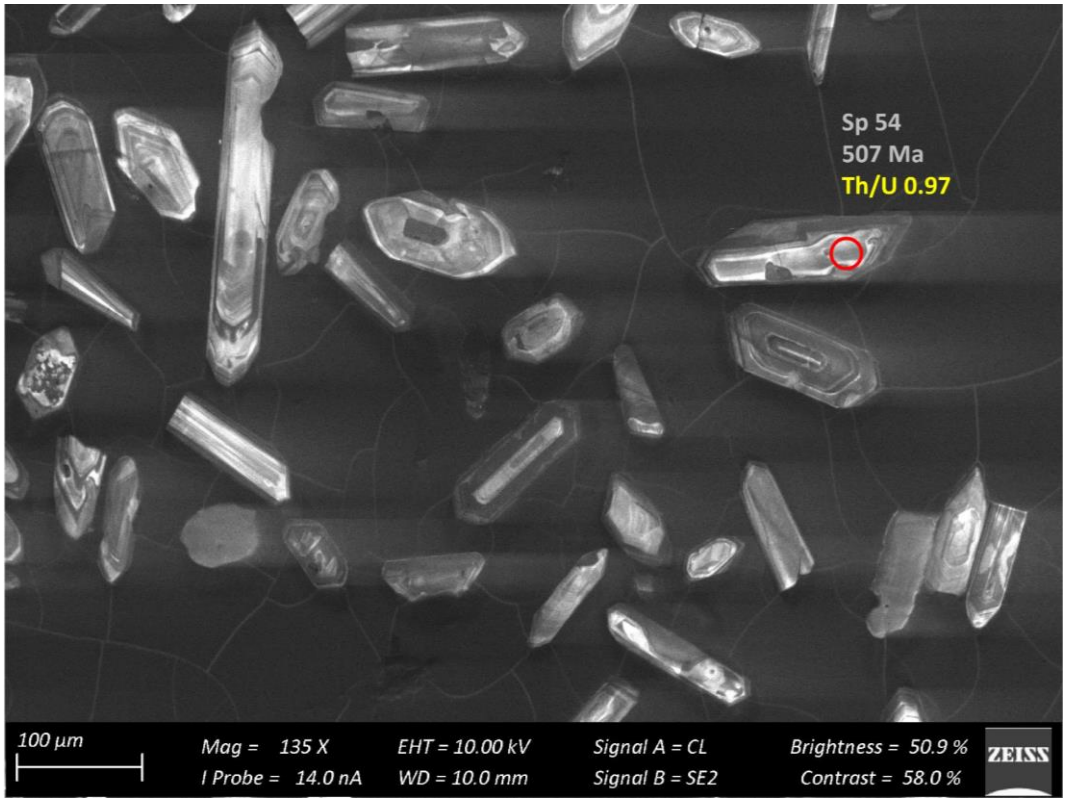

Figure 166 – Zircon Isotope spot analyses of sample s7B; U-Pb analyses are colour coded according to concordance; blue writing indicates the Hf identifier with the respective εHf_{468} values

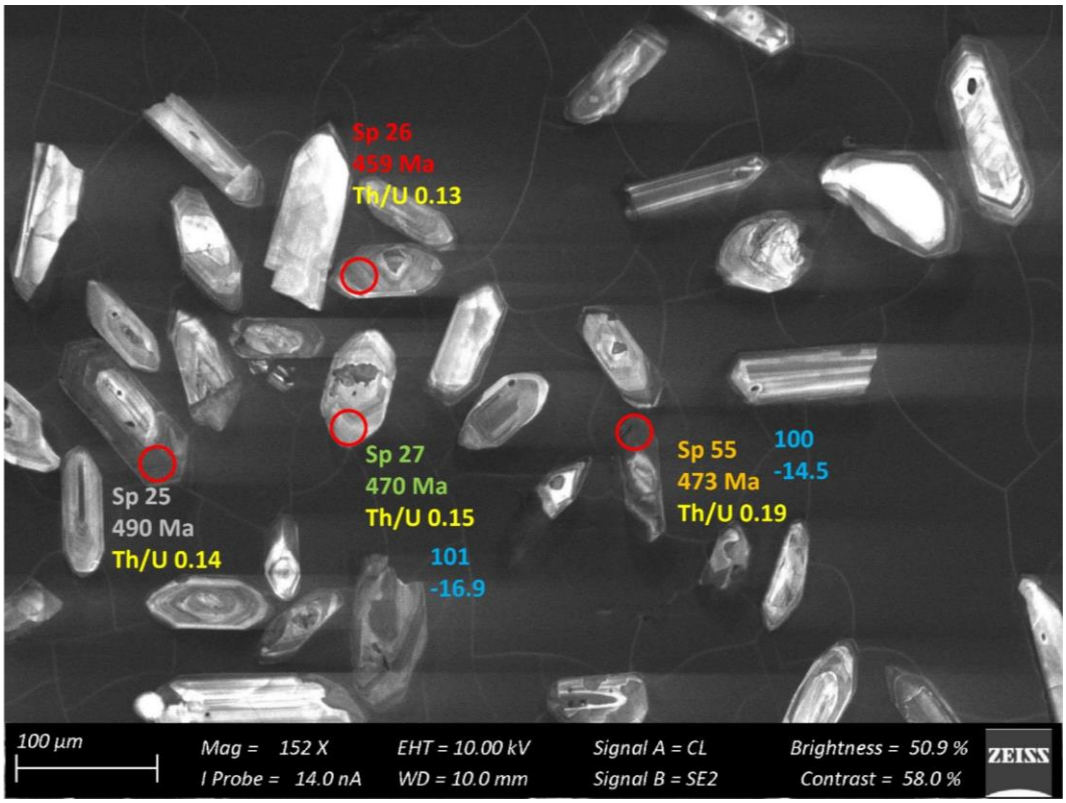

Figure 167 – Zircon Isotope spot analyses of sample s7B; U-Pb analyses are colour coded according to concordance; blue writing indicates the Hf identifier with the respective εHf_{468} values

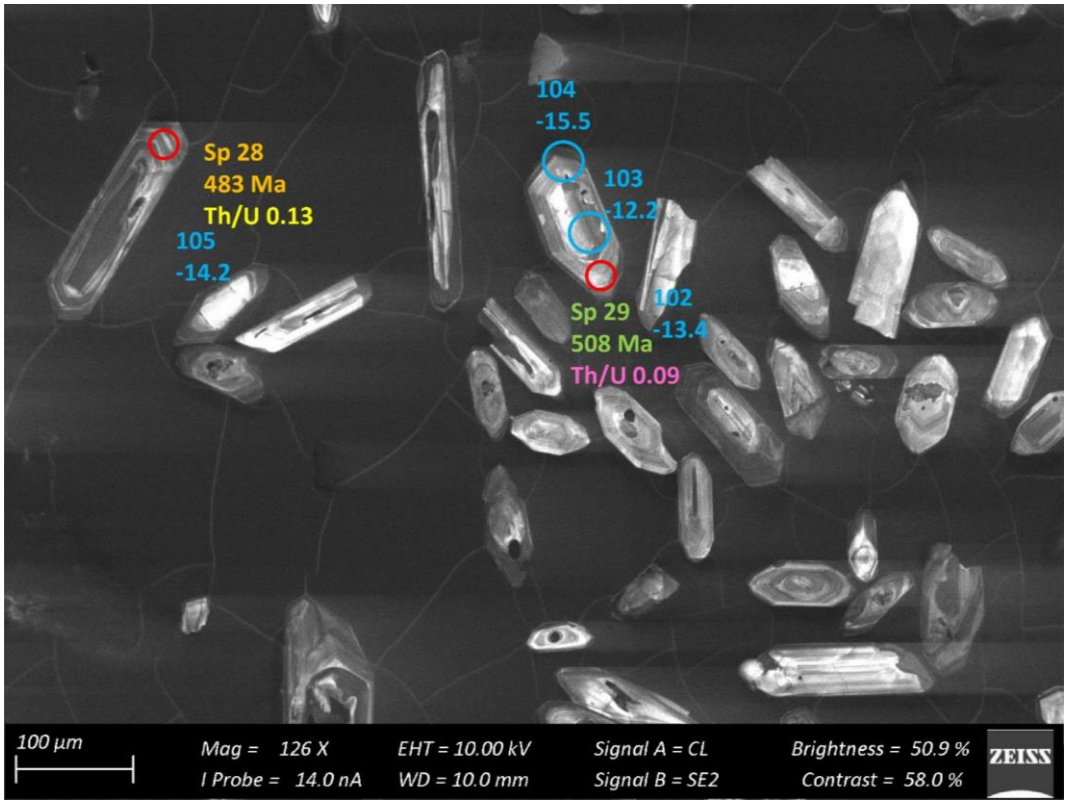

Figure 168 – Zircon Isotope spot analyses of sample s7B; U-Pb analyses are colour coded according to concordance; blue writing indicates the Hf identifier with the respective εHf_{468} values

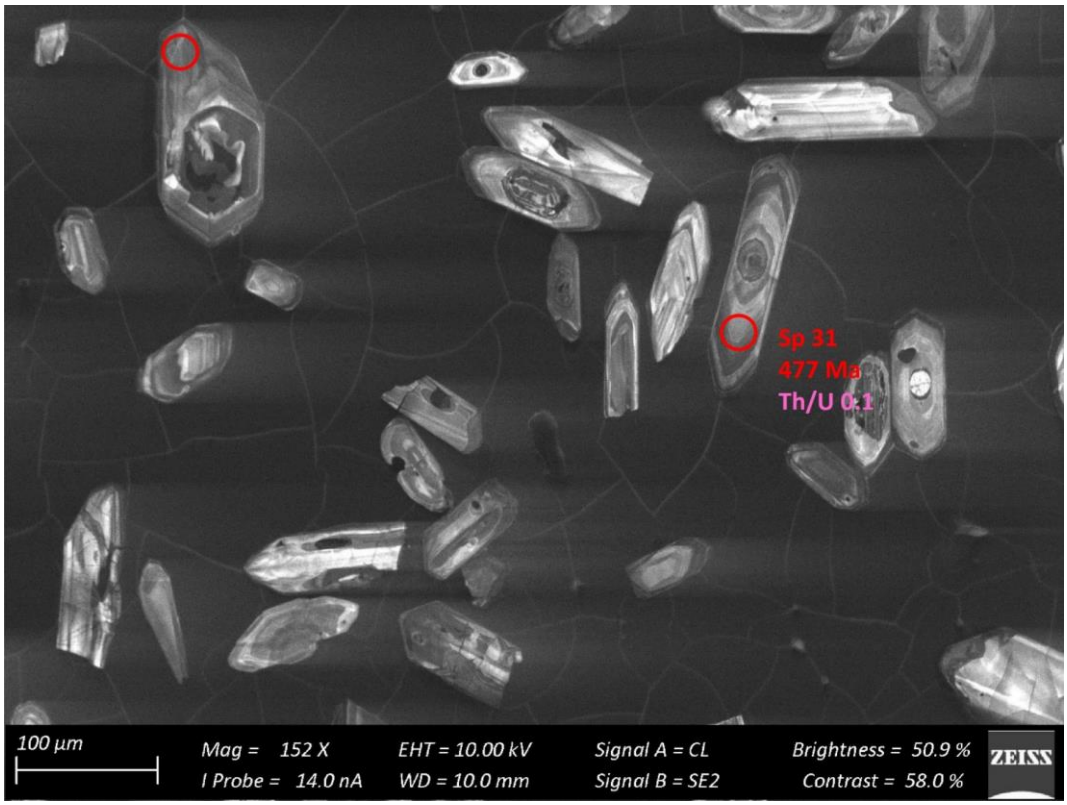

Figure 169 – Zircon Isotope spot analyses of sample s7B; U-Pb analyses are colour coded according to concordance; blue writing indicates the Hf identifier with the respective εHf$_{468}$ values

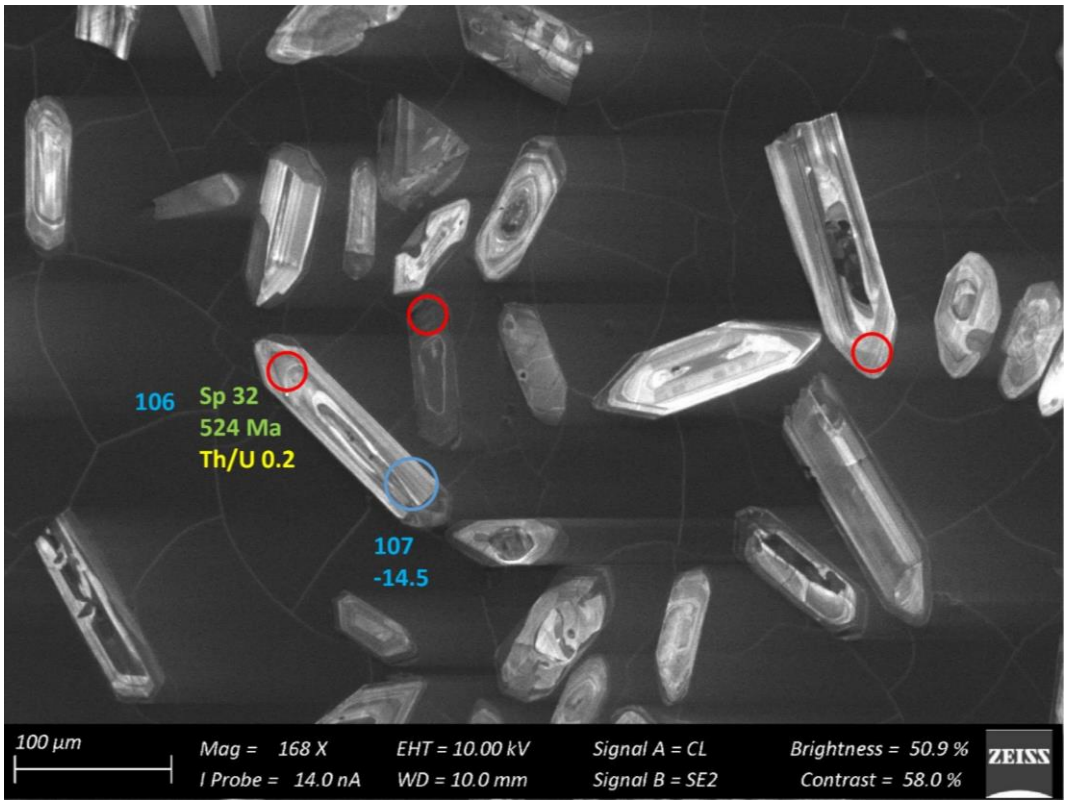

Figure 170 – Zircon Isotope spot analyses of sample s7B; U-Pb analyses are colour coded according to concordance; blue writing indicates the Hf identifier with the respective εHf$_{468}$ values

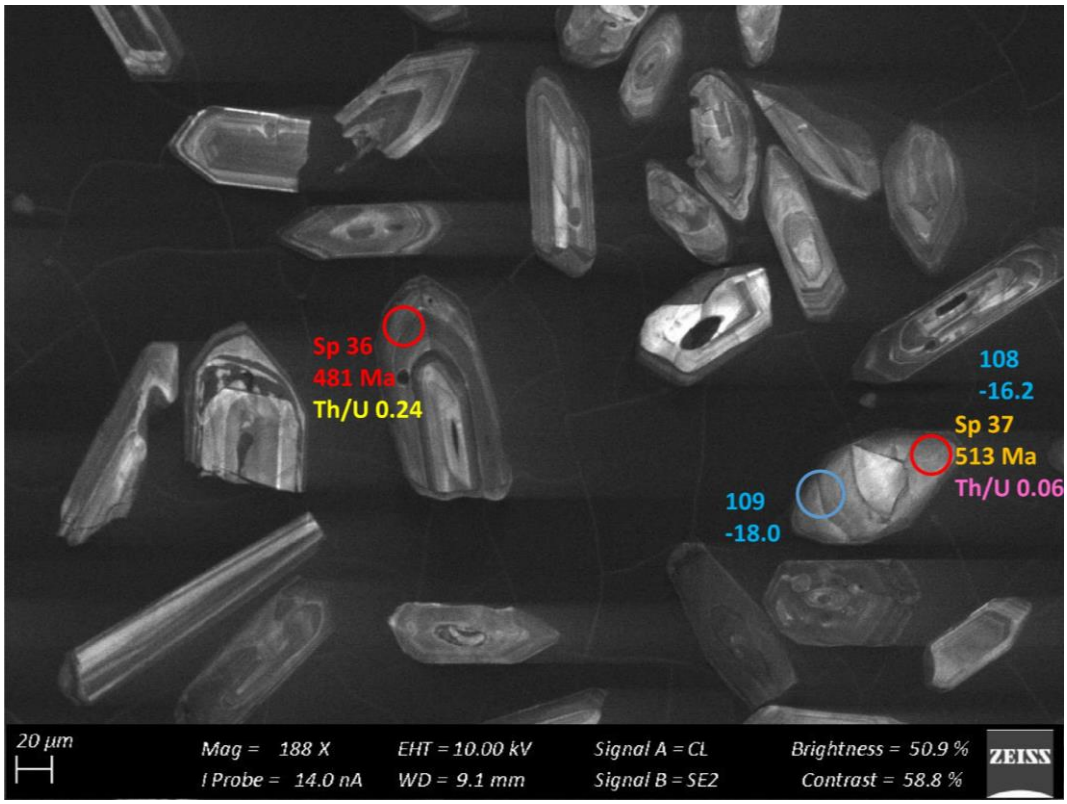

Figure 171 – Zircon Isotope spot analyses of sample s7B; U-Pb analyses are colour coded according to concordance; blue writing indicates the Hf identifier with the respective εHf_{468} values

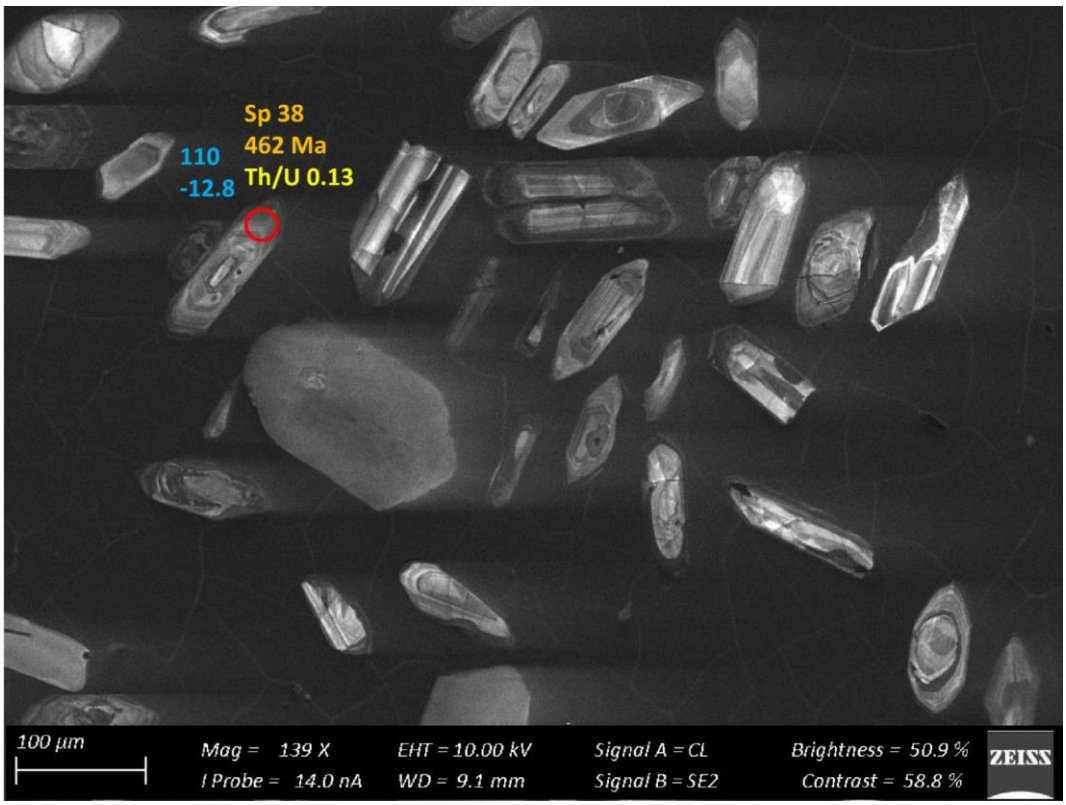

Figure 172 – Zircon Isotope spot analyses of sample s7B; U-Pb analyses are colour coded according to concordance; blue writing indicates the Hf identifier with the respective εHf_{468} values

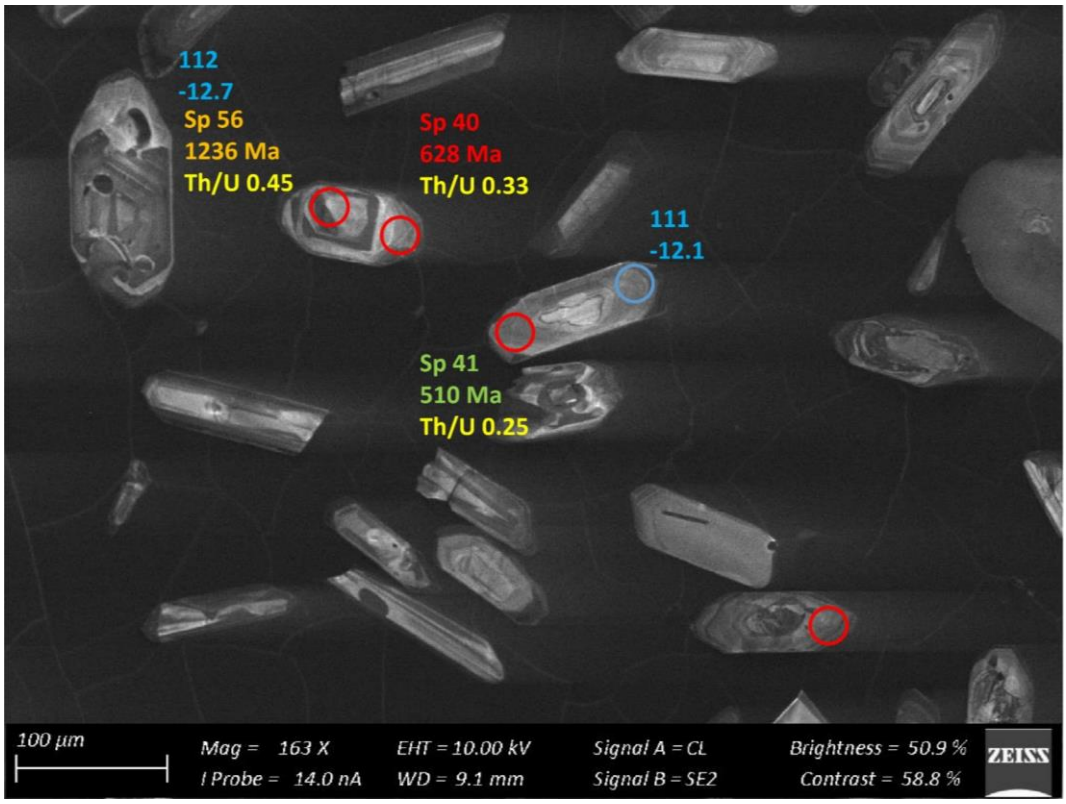

Figure 173 – Zircon Isotope spot analyses of sample s7B; U-Pb analyses are colour coded according to concordance; blue writing indicates the Hf identifier with the respective εHf_{468} values

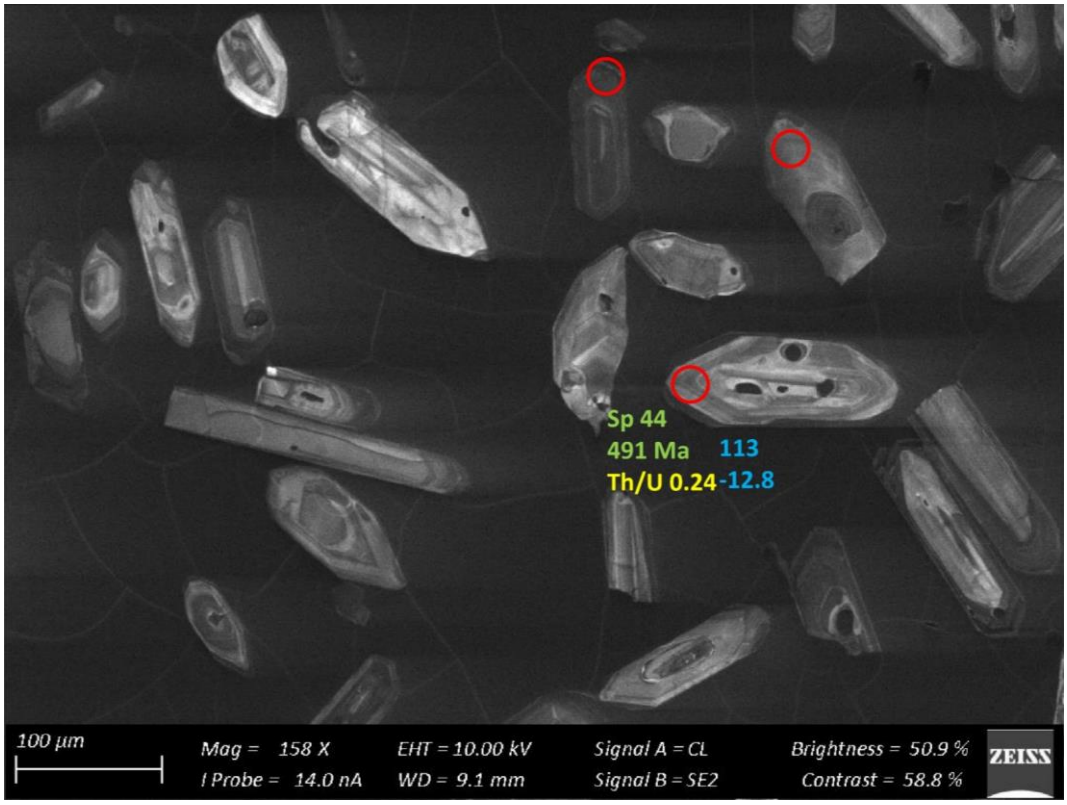

Figure 174 – Zircon Isotope spot analyses of sample s7B; U-Pb analyses are colour coded according to concordance; blue writing indicates the Hf identifier with the respective εHf_{468} values

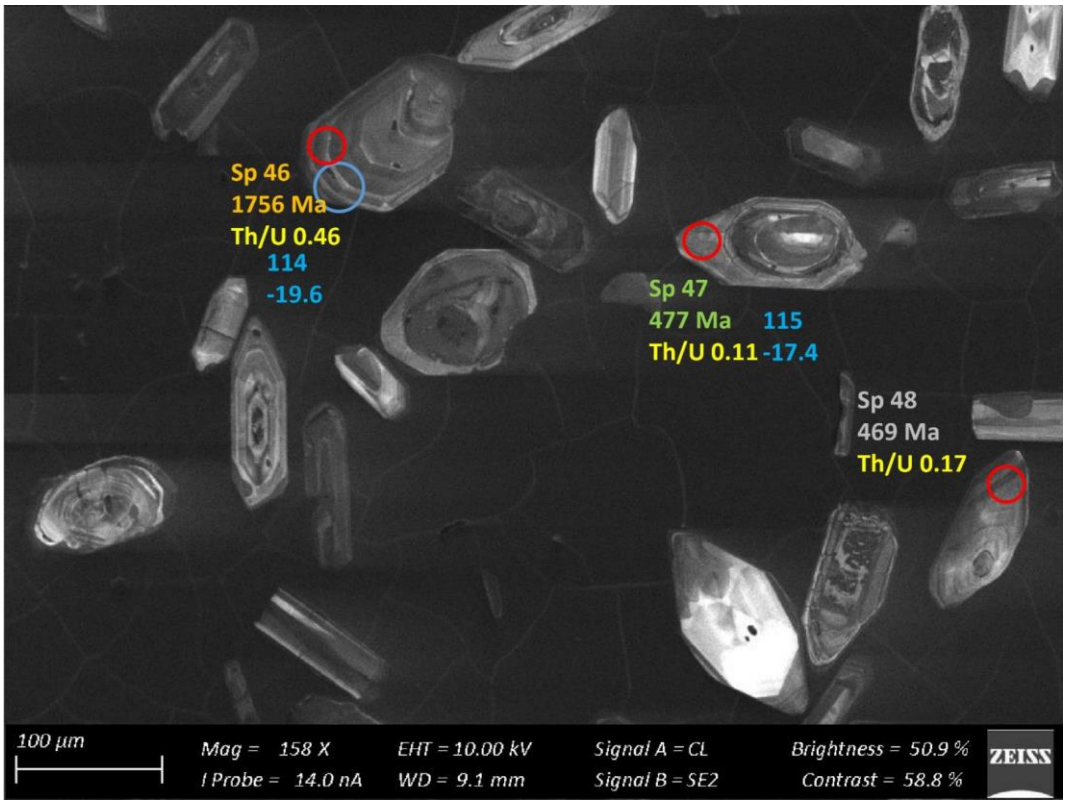

Figure 175 – Zircon Isotope spot analyses of sample s7B; U-Pb analyses are colour coded according to concordance; blue writing indicates the Hf identifier with the respective εHf_{468} values

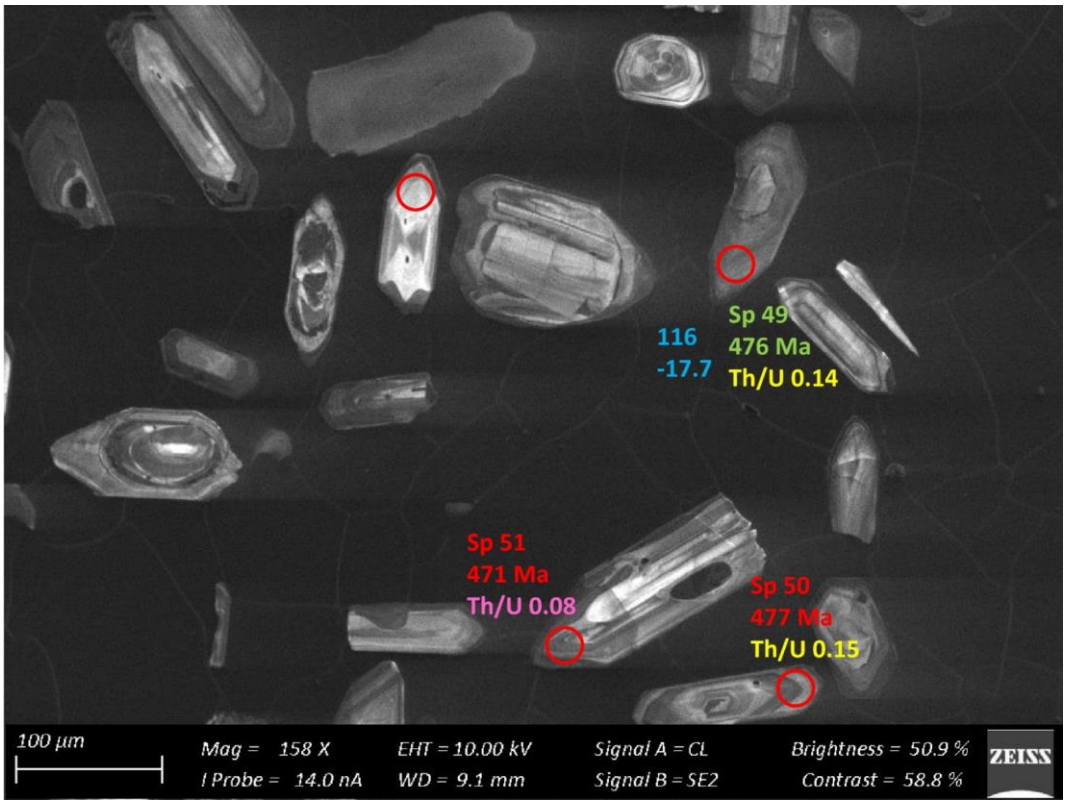

Figure 176 – Zircon Isotope spot analyses of sample s7B; U-Pb analyses are colour coded according to concordance; blue writing indicates the Hf identifier with the respective εHf_{468} values

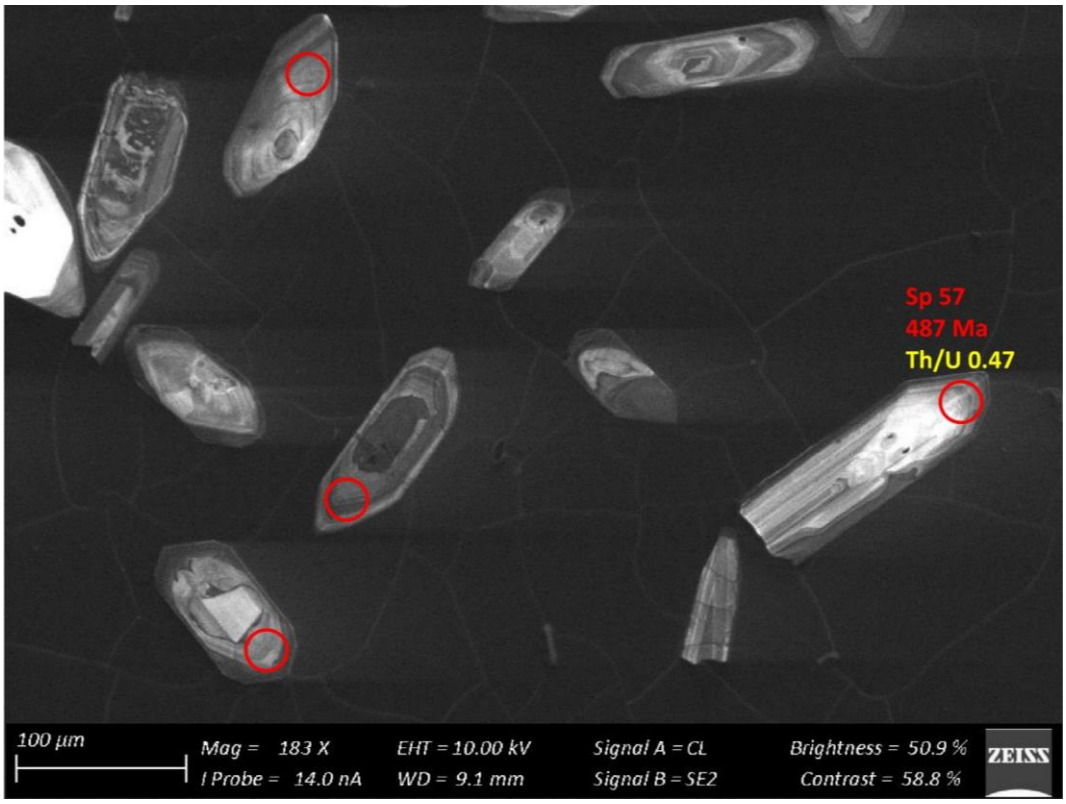

Figure 177 – Zircon Isotope spot analyses of sample s7B; U-Pb analyses are colour coded according to concordance; blue writing indicates the Hf identifier with the respective εHf_{468} values

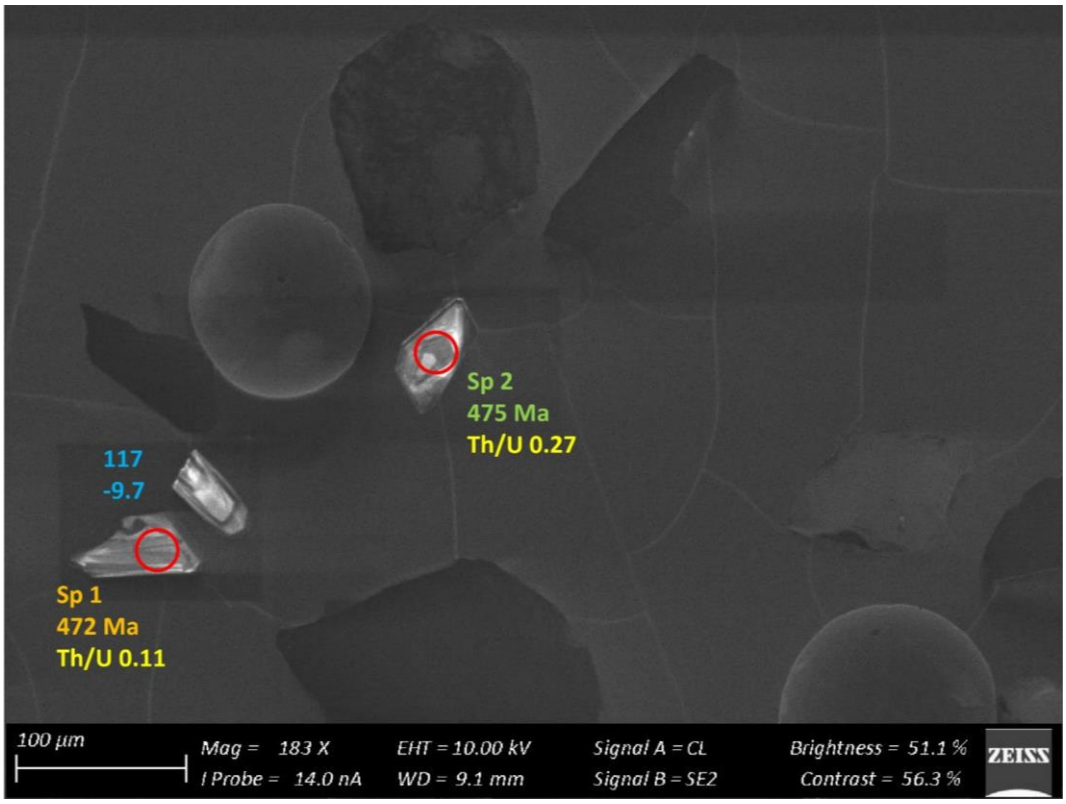

Figure 178 – Zircon Isotope spot analyses of sample s8Da; U-Pb analyses are colour coded according to concordance; blue writing indicates the Hf identifier with the respective εHf_{468} values

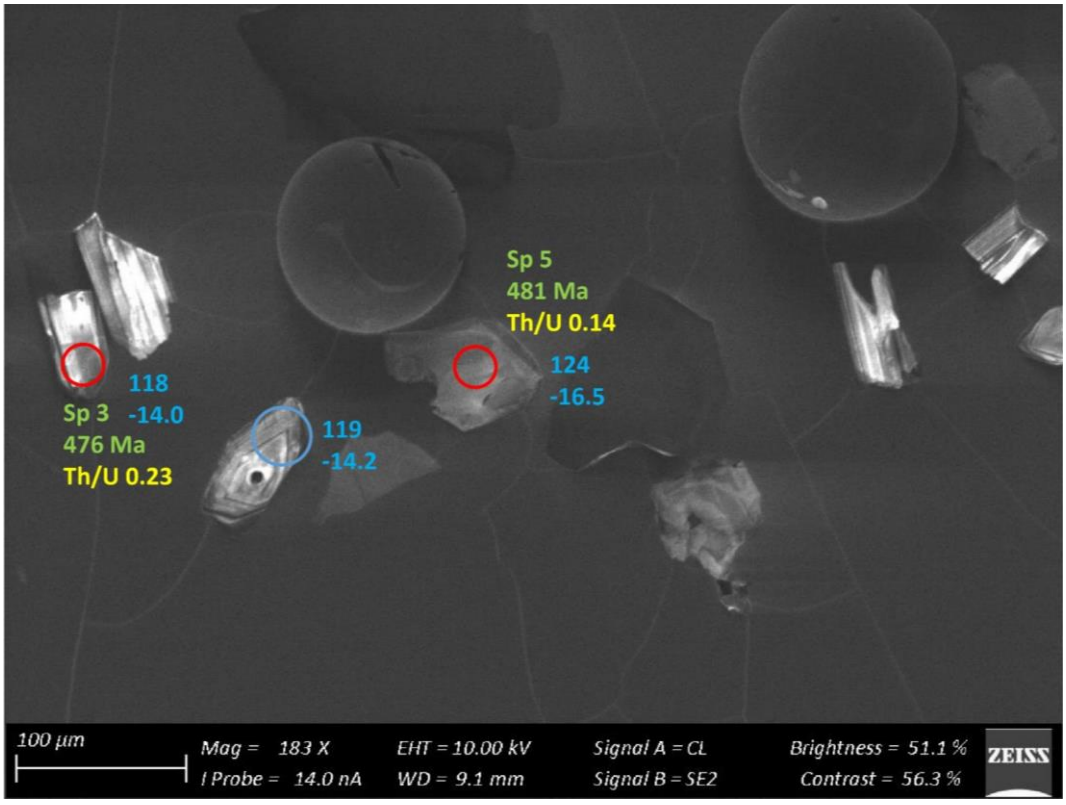

Figure 179 – Zircon Isotope spot analyses of sample s8Da; U-Pb analyses are colour coded according to concordance; blue writing indicates the Hf identifier with the respective εHf_{468} values

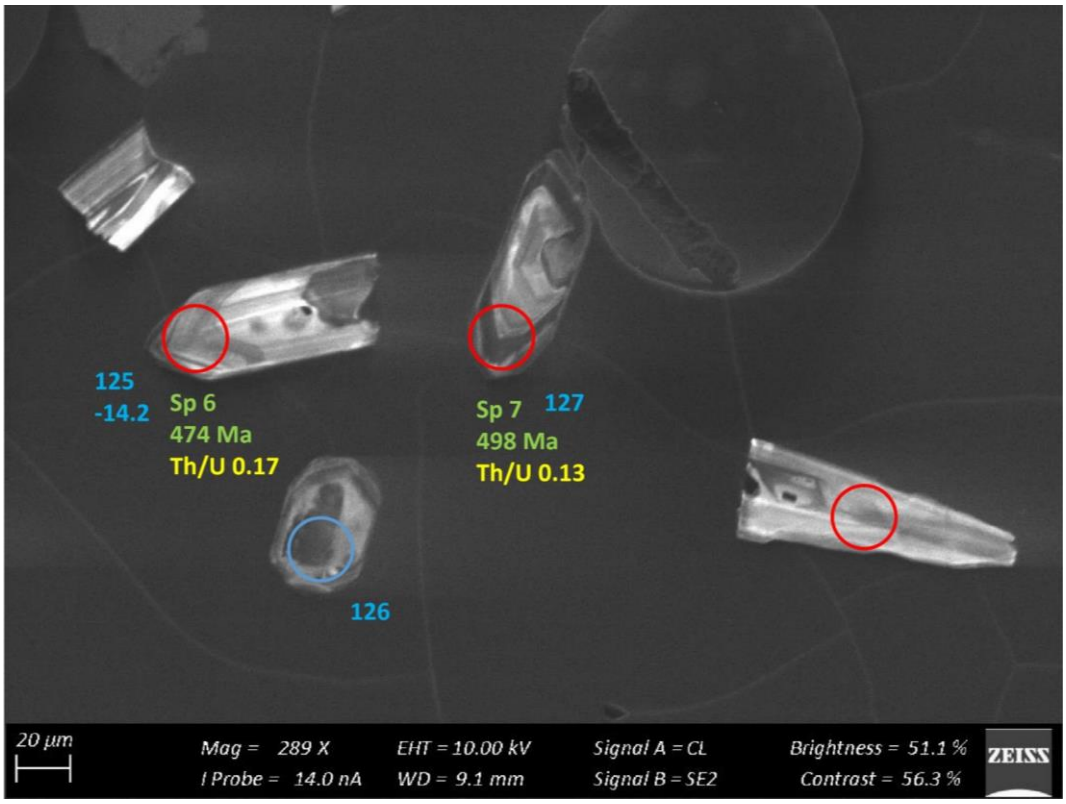

Figure 180 – Zircon Isotope spot analyses of sample s8Da; U-Pb analyses are colour coded according to concordance; blue writing indicates the Hf identifier with the respective εHf_{468} values

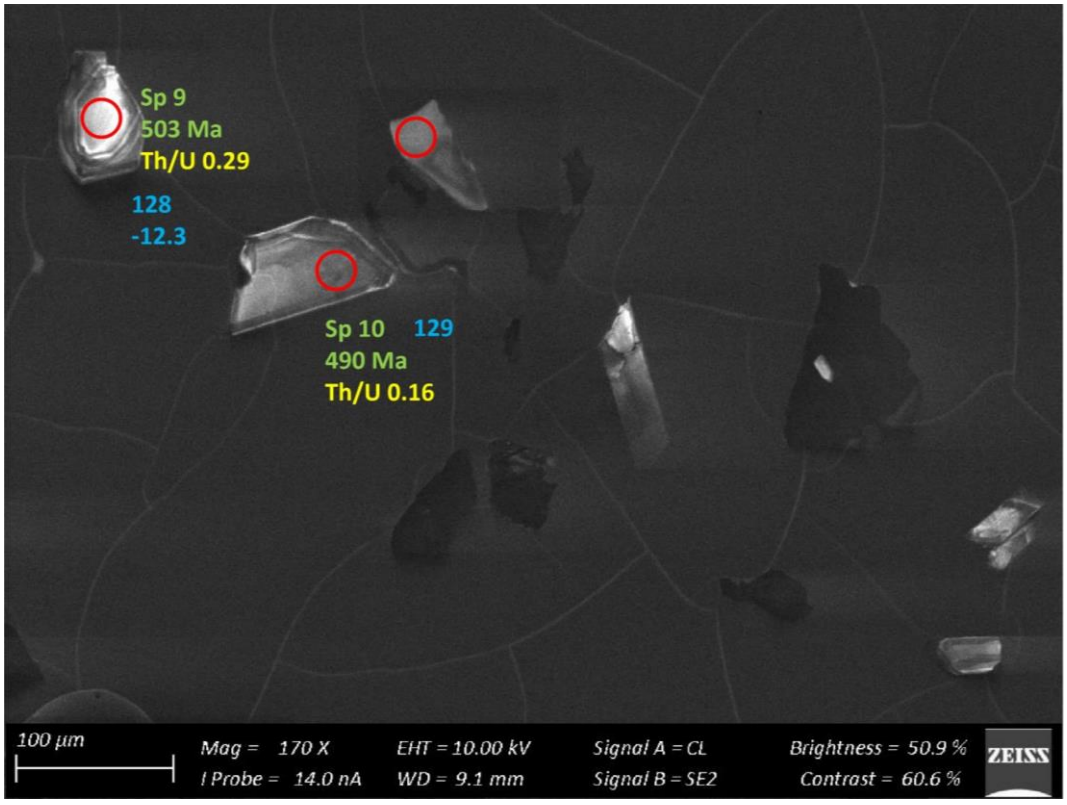

Figure 181 – Zircon Isotope spot analyses of sample s8Da; U-Pb analyses are colour coded according to concordance; blue writing indicates the Hf identifier with the respective εHf_{468} values

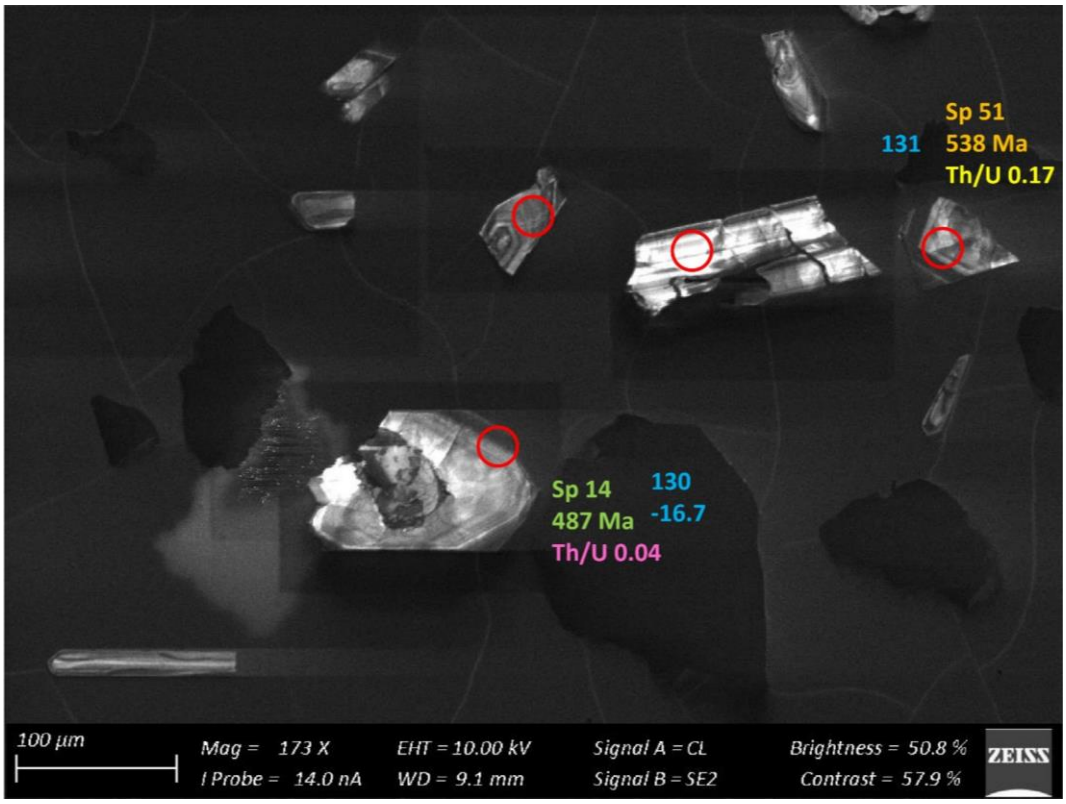

Figure 182 – Zircon Isotope spot analyses of sample s8Da; U-Pb analyses are colour coded according to concordance; blue writing indicates the Hf identifier with the respective εHf_{468} values

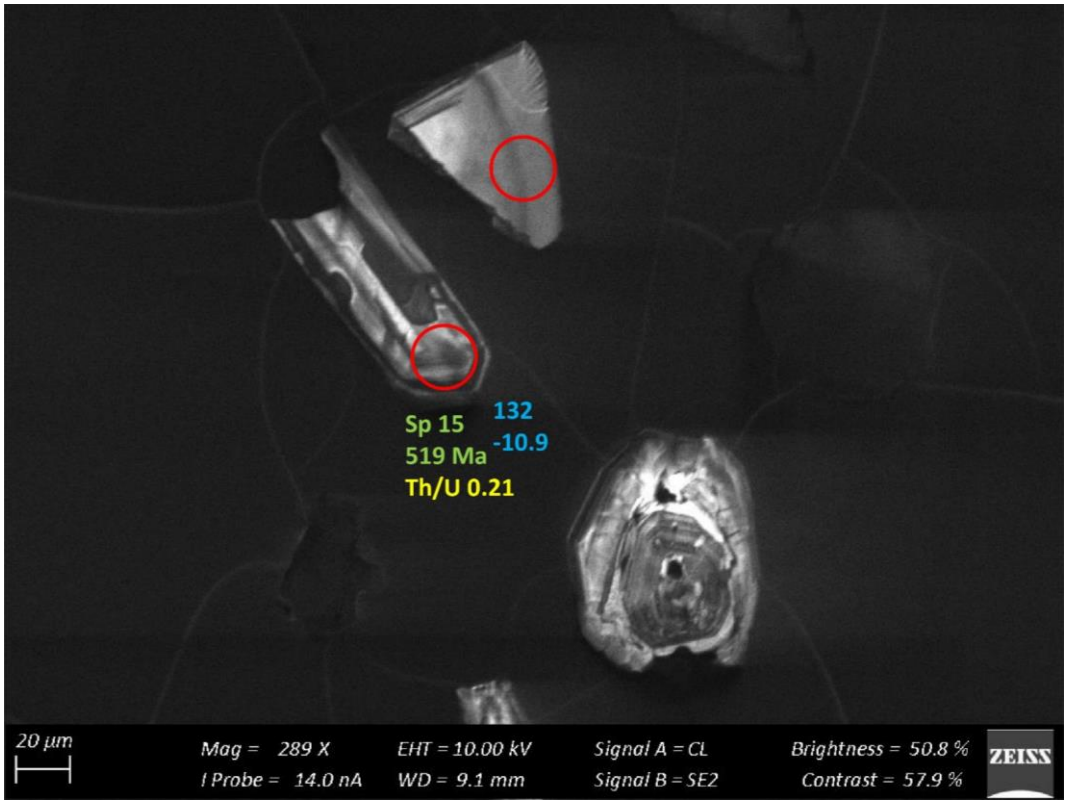

Figure 183 – Zircon Isotope spot analyses of sample s8Da; U-Pb analyses are colour coded according to concordance; blue writing indicates the Hf identifier with the respective εHf_{468} values

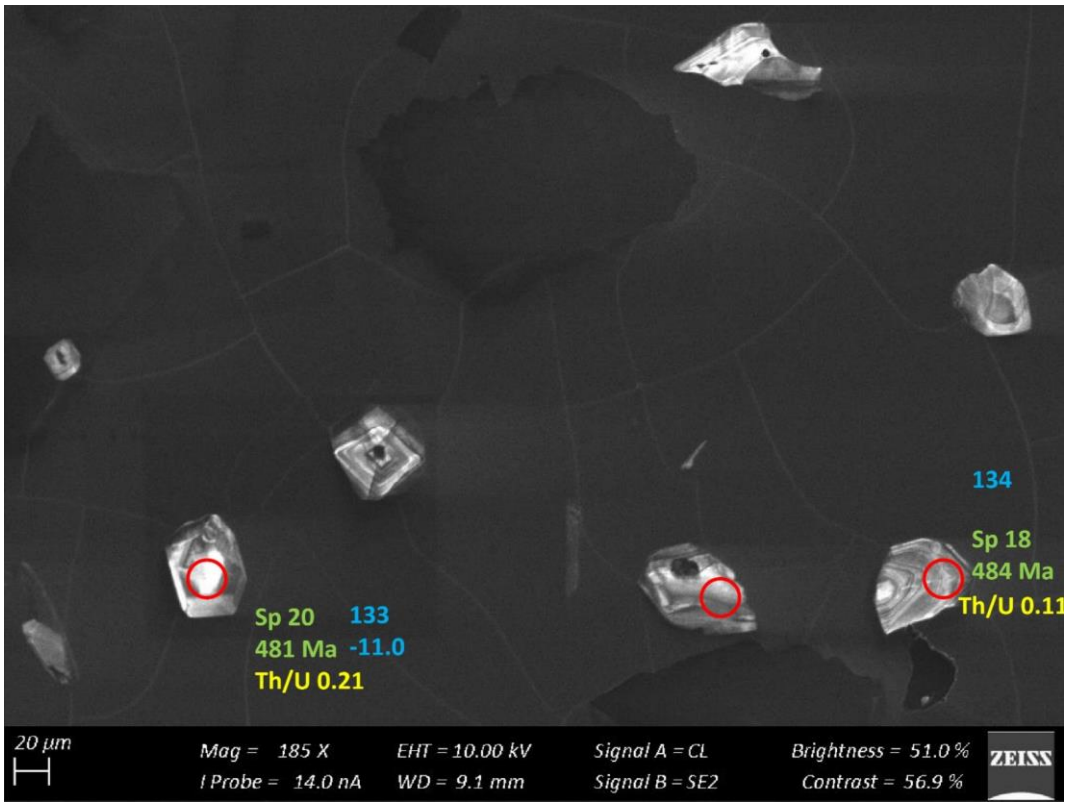

Figure 184 – Zircon Isotope spot analyses of sample s8Da; U-Pb analyses are colour coded according to concordance; blue writing indicates the Hf identifier with the respective εHf_{468} values

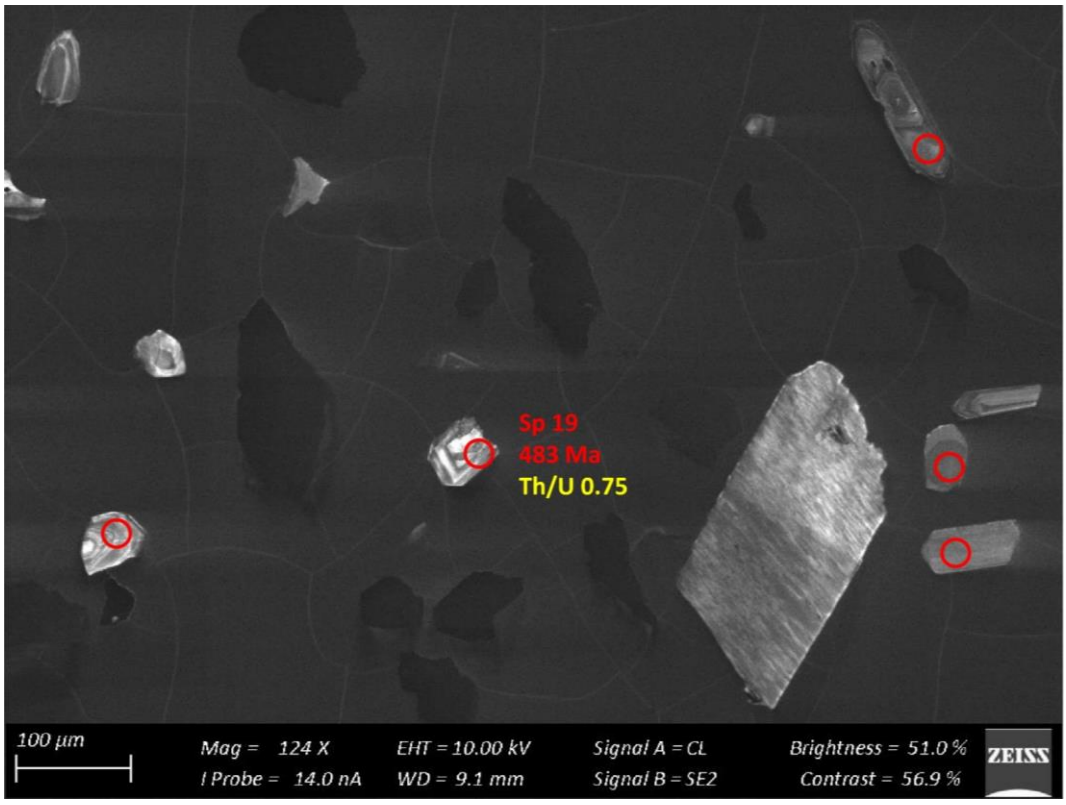

Figure 185 – Zircon Isotope spot analyses of sample s8Da; U-Pb analyses are colour coded according to concordance; blue writing indicates the Hf identifier with the respective εHf_{468} values

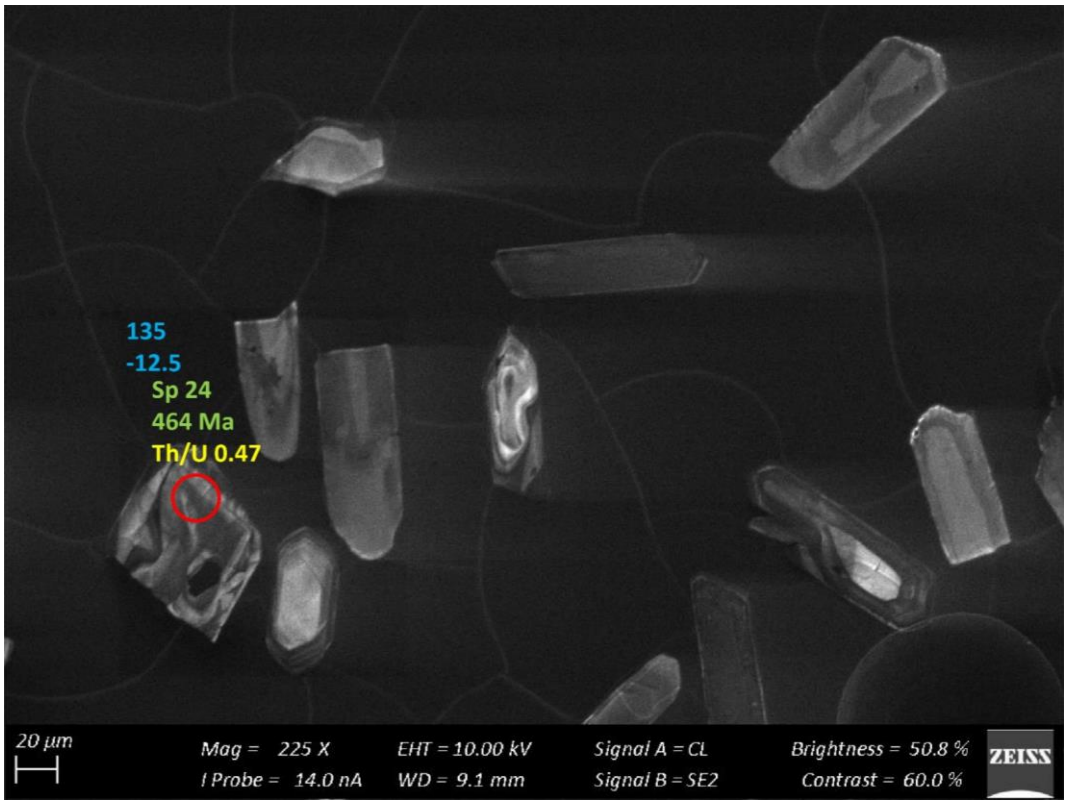

Figure 186 – Zircon Isotope spot analyses of sample s8Da; U-Pb analyses are colour coded according to concordance; blue writing indicates the Hf identifier with the respective εHf_{468} values

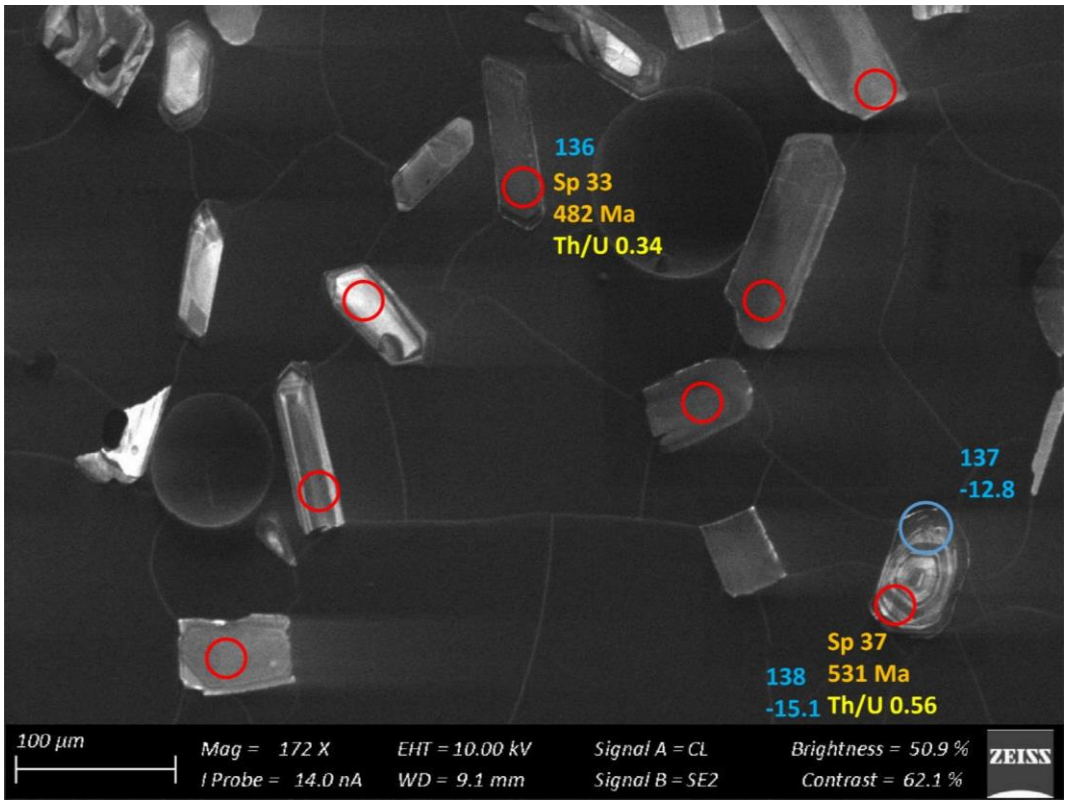

Figure 187 – Zircon Isotope spot analyses of sample s8Da; U-Pb analyses are colour coded according to concordance; blue writing indicates the Hf identifier with the respective εHf_{468} values

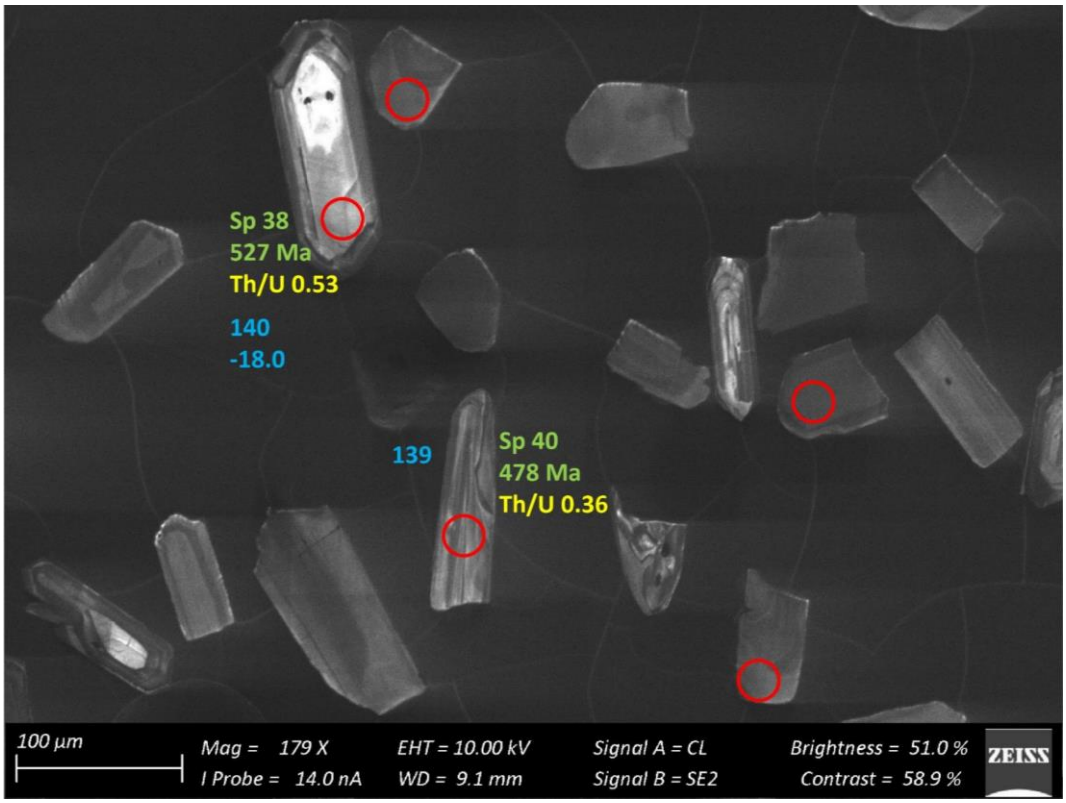

Figure 188 – Zircon Isotope spot analyses of sample s8Da; U-Pb analyses are colour coded according to concordance; blue writing indicates the Hf identifier with the respective εHf_{468} values

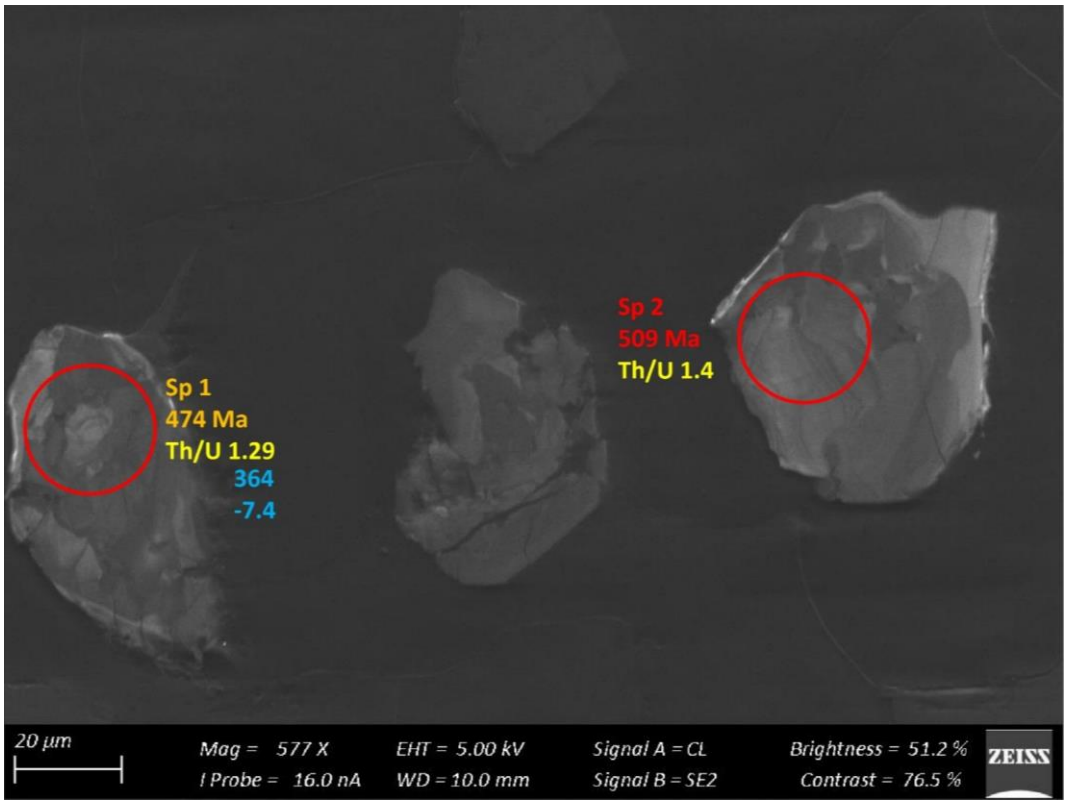

Figure 189 – Zircon Isotope spot analyses of sample s8Db; U-Pb analyses are colour coded according to concordance; blue writing indicates the Hf identifier with the respective εHf_{468} values

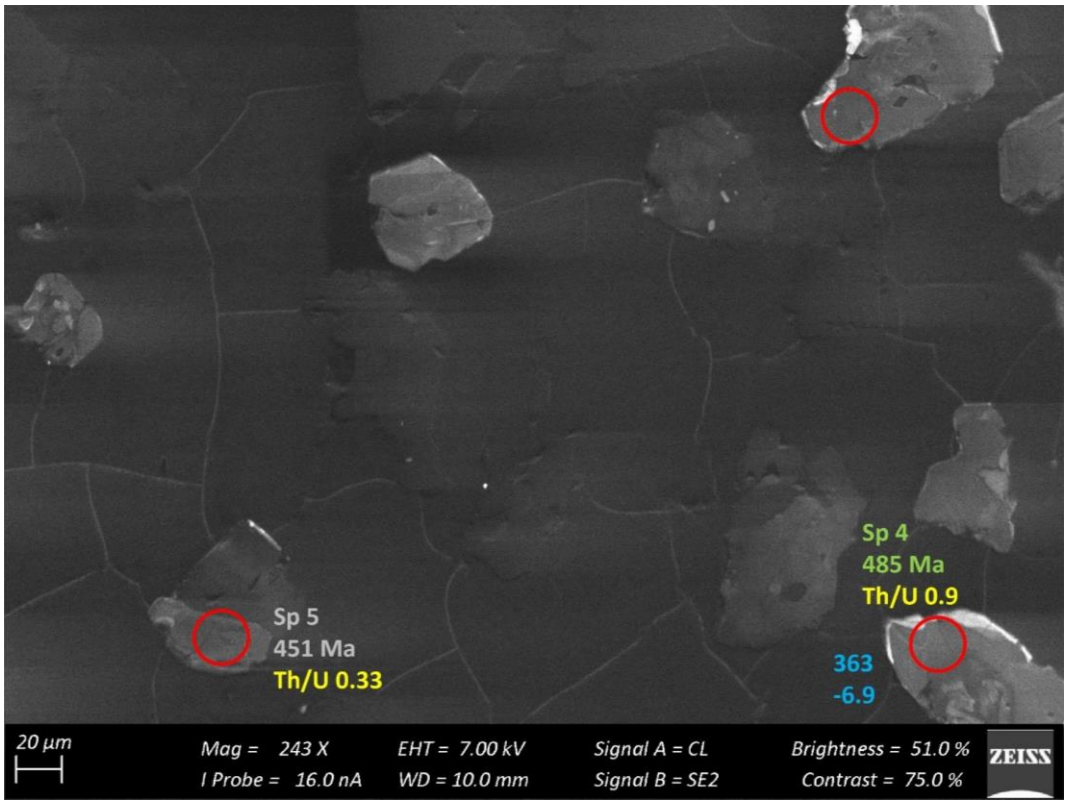

Figure 190 – Zircon Isotope spot analyses of sample s8Db; U-Pb analyses are colour coded according to concordance; blue writing indicates the Hf identifier with the respective εHf_{468} values

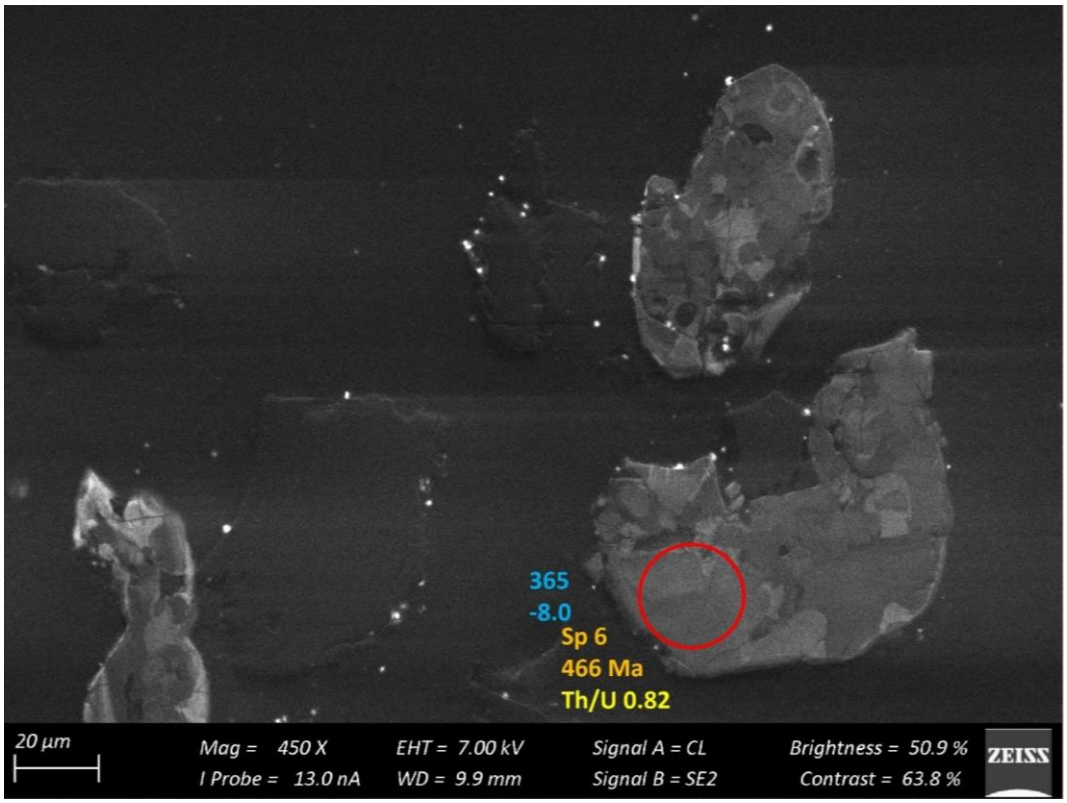

Figure 191 – Zircon Isotope spot analyses of sample s8Db; U-Pb analyses are colour coded according to concordance; blue writing indicates the Hf identifier with the respective εHf_{468} values

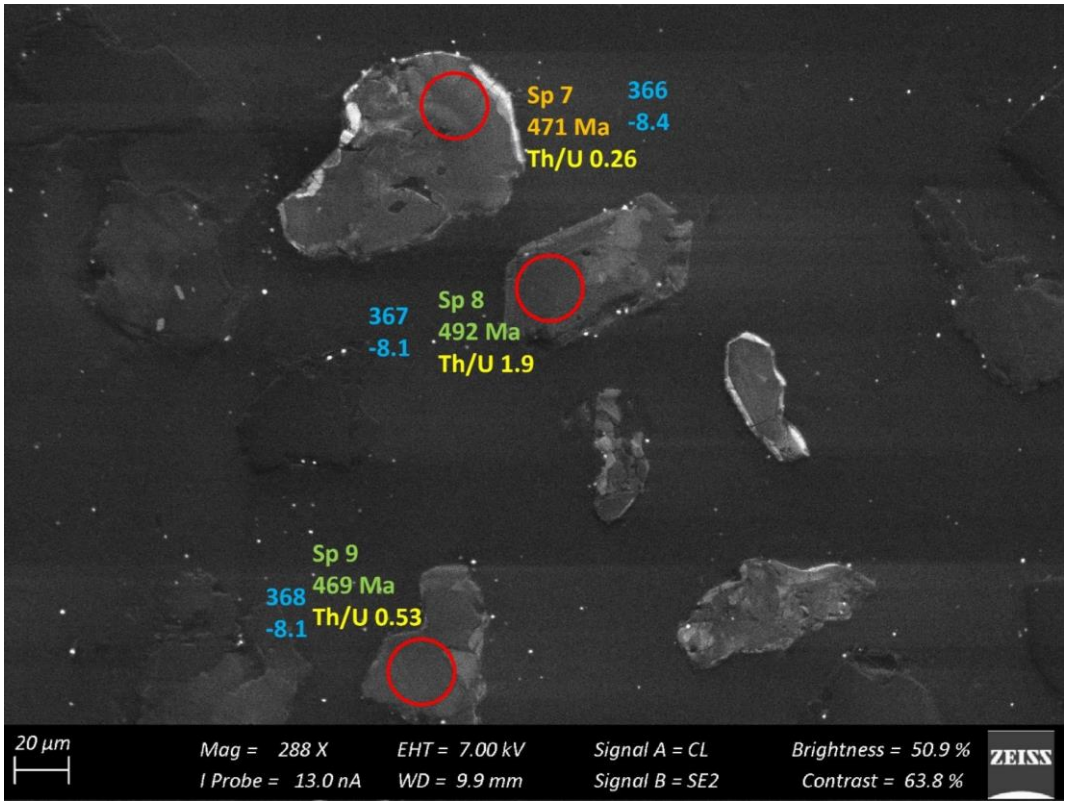

Figure 192 – Zircon Isotope spot analyses of sample s8Db; U-Pb analyses are colour coded according to concordance; blue writing indicates the Hf identifier with the respective εHf_{468} values

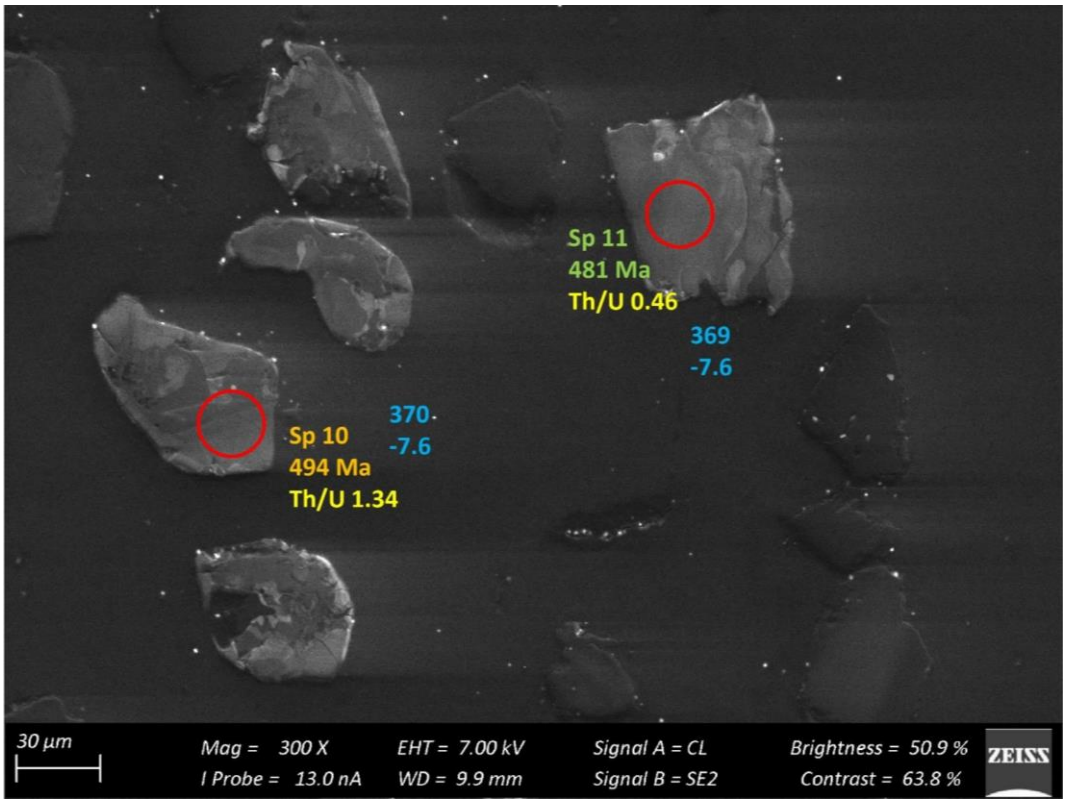

Figure 193 – Zircon Isotope spot analyses of sample s8Db; U-Pb analyses are colour coded according to concordance; blue writing indicates the Hf identifier with the respective εHf_{468} values

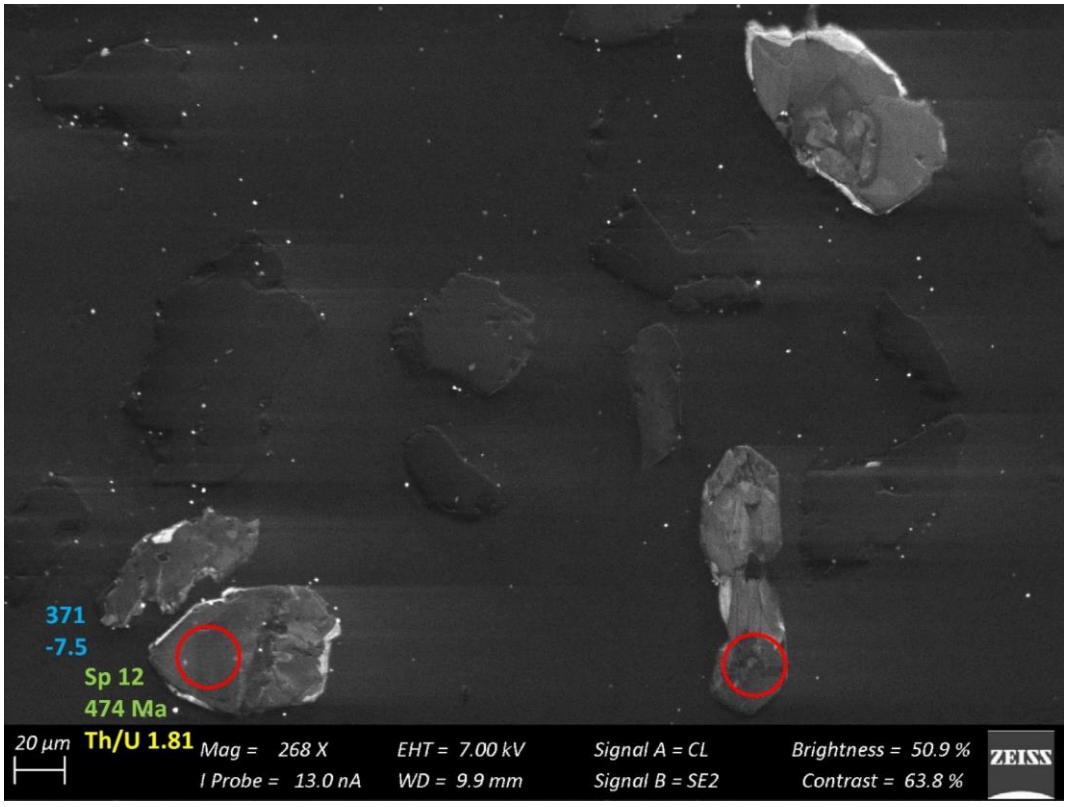

Figure 194 – Zircon Isotope spot analyses of sample s8Db; U-Pb analyses are colour coded according to concordance; blue writing indicates the Hf identifier with the respective εHf_{468} values

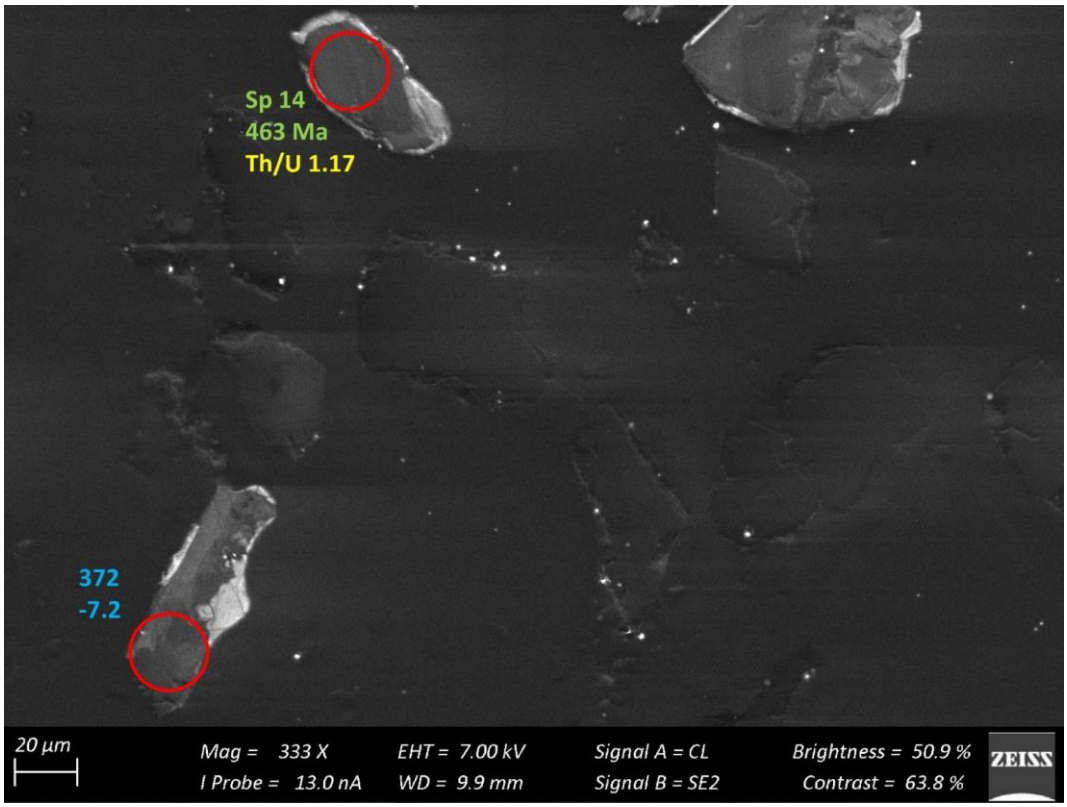

Figure 195 – Zircon Isotope spot analyses of sample s8Db; U-Pb analyses are colour coded according to concordance; blue writing indicates the Hf identifier with the respective εHf$_{468}$ values

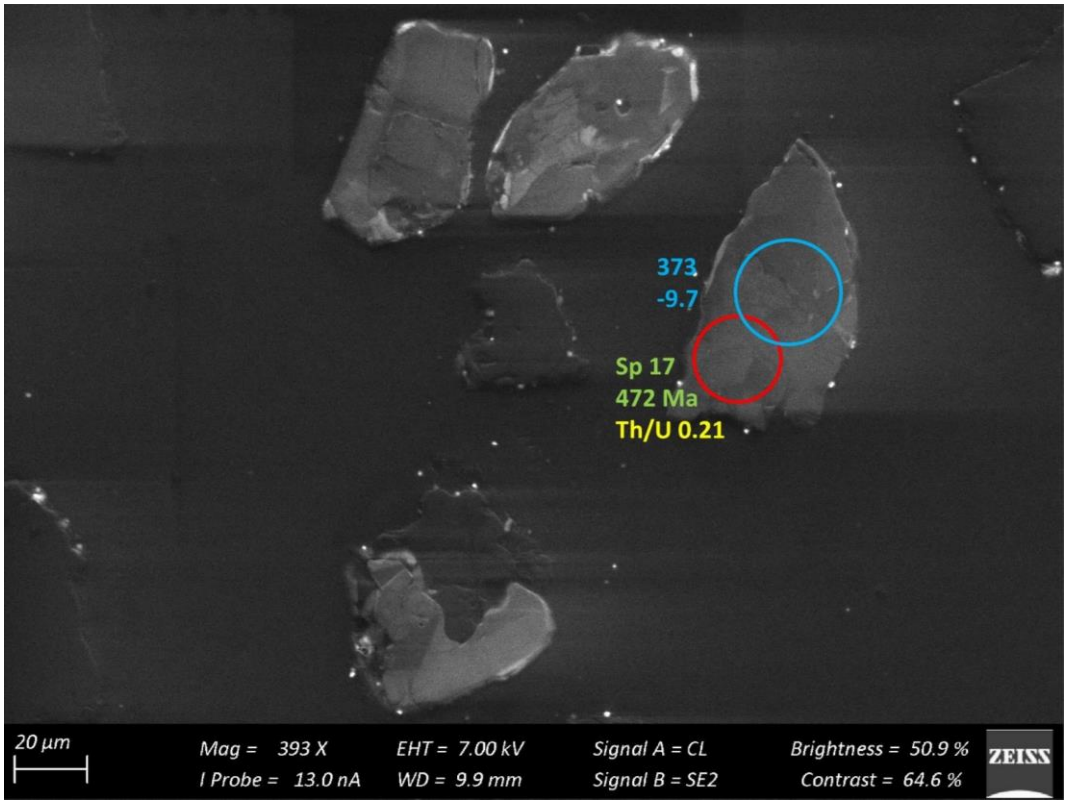

Figure 196 – Zircon Isotope spot analyses of sample s8Db; U-Pb analyses are colour coded according to concordance; blue writing indicates the Hf identifier with the respective εHf$_{468}$ values

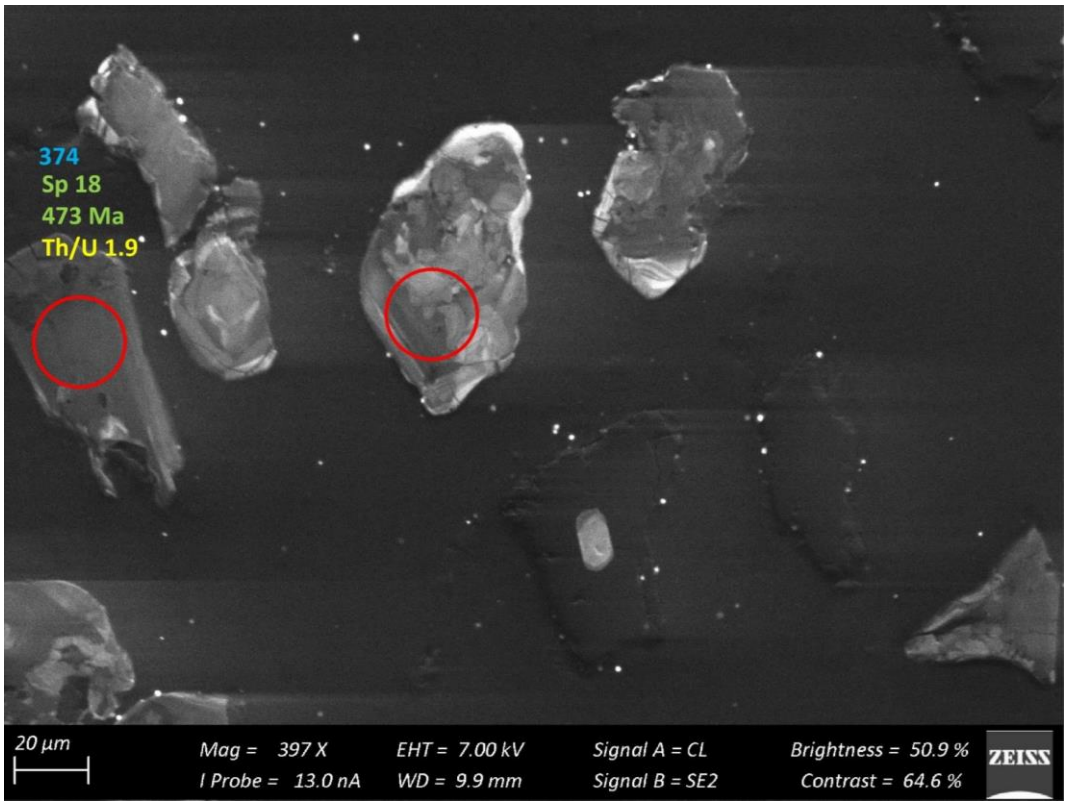

Figure 197 – Zircon Isotope spot analyses of sample s8Db; U-Pb analyses are colour coded according to concordance; blue writing indicates the Hf identifier with the respective εHf$_{468}$ values

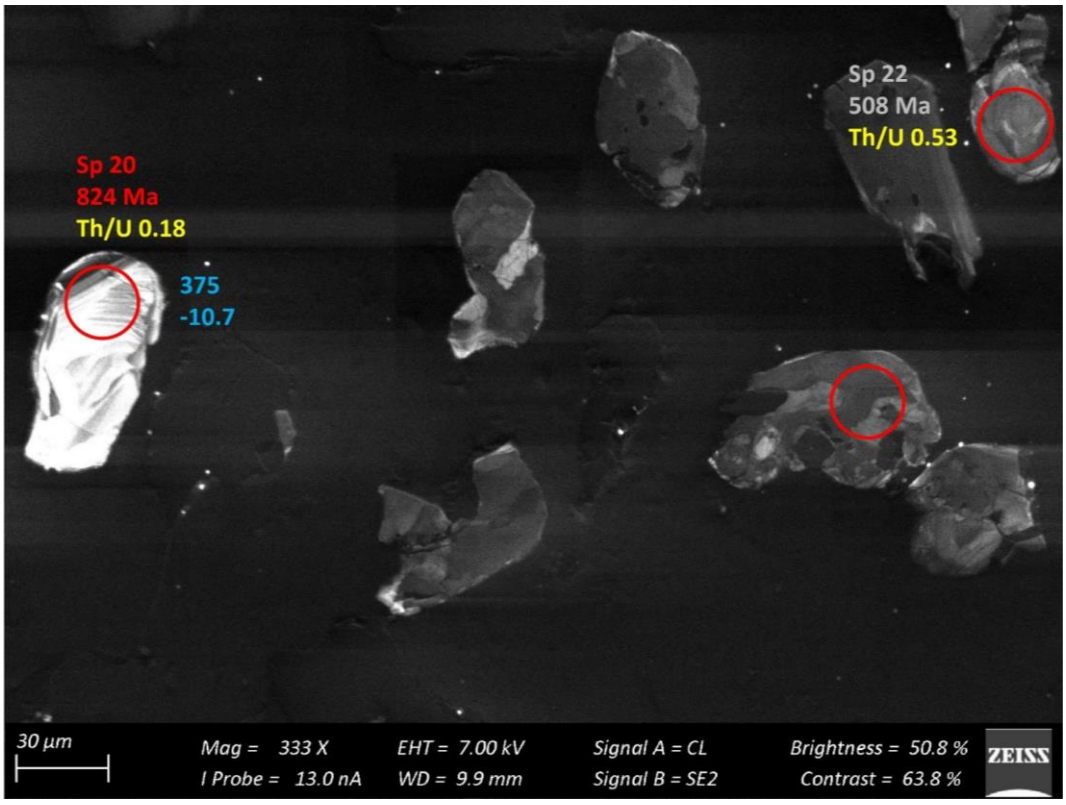

Figure 198 – Zircon Isotope spot analyses of sample s8Db; U-Pb analyses are colour coded according to concordance; blue writing indicates the Hf identifier with the respective εHf$_{468}$ values

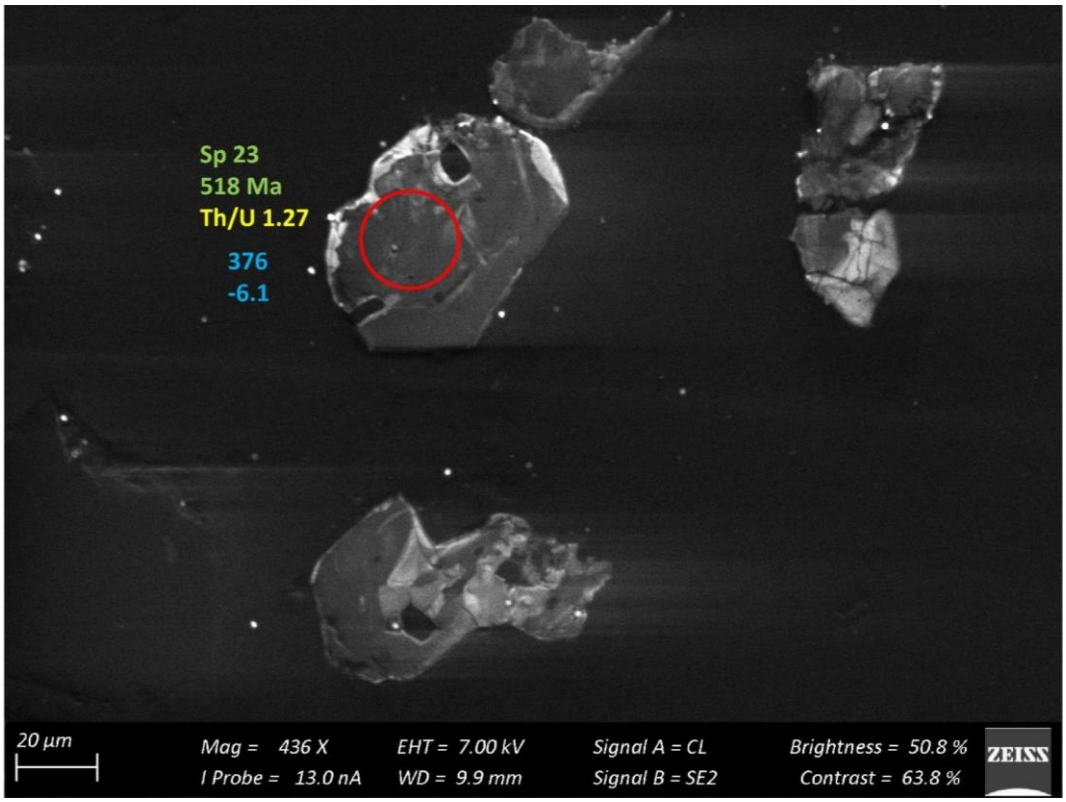

Figure 199 – Zircon Isotope spot analyses of sample s8Db; U-Pb analyses are colour coded according to concordance; blue writing indicates the Hf identifier with the respective εHf_{468} values

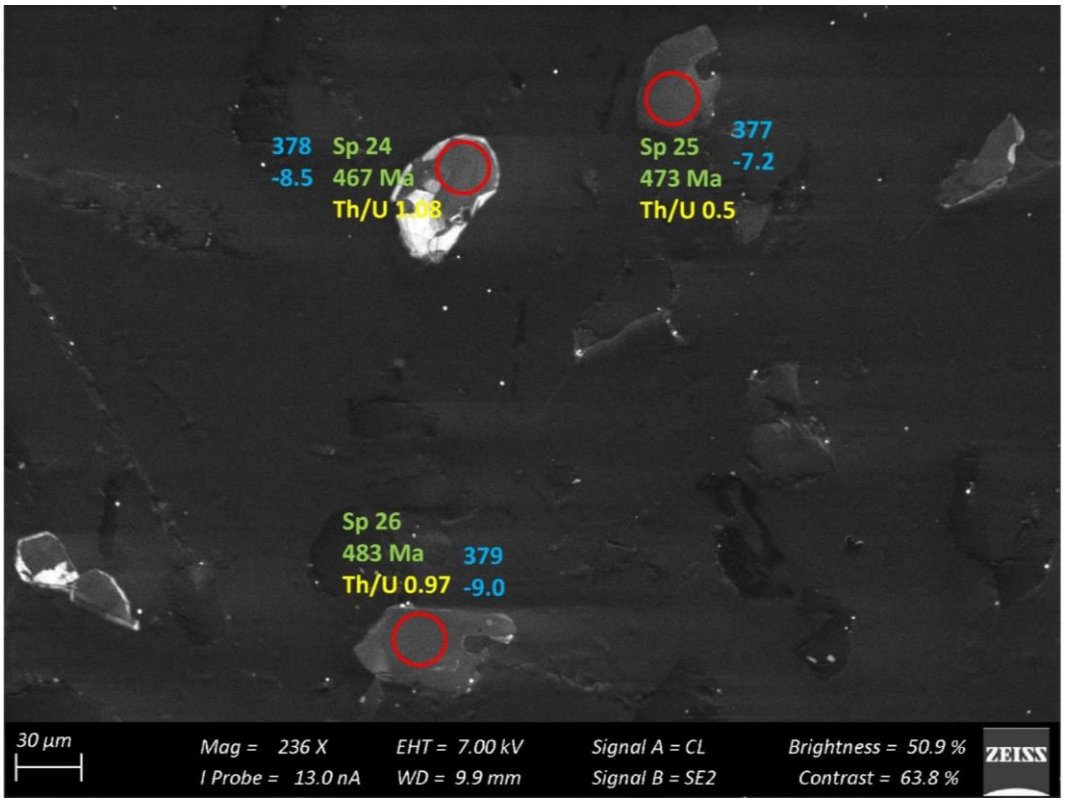

Figure 200 – Zircon Isotope spot analyses of sample s8Db; U-Pb analyses are colour coded according to concordance; blue writing indicates the Hf identifier with the respective εHf_{468} values

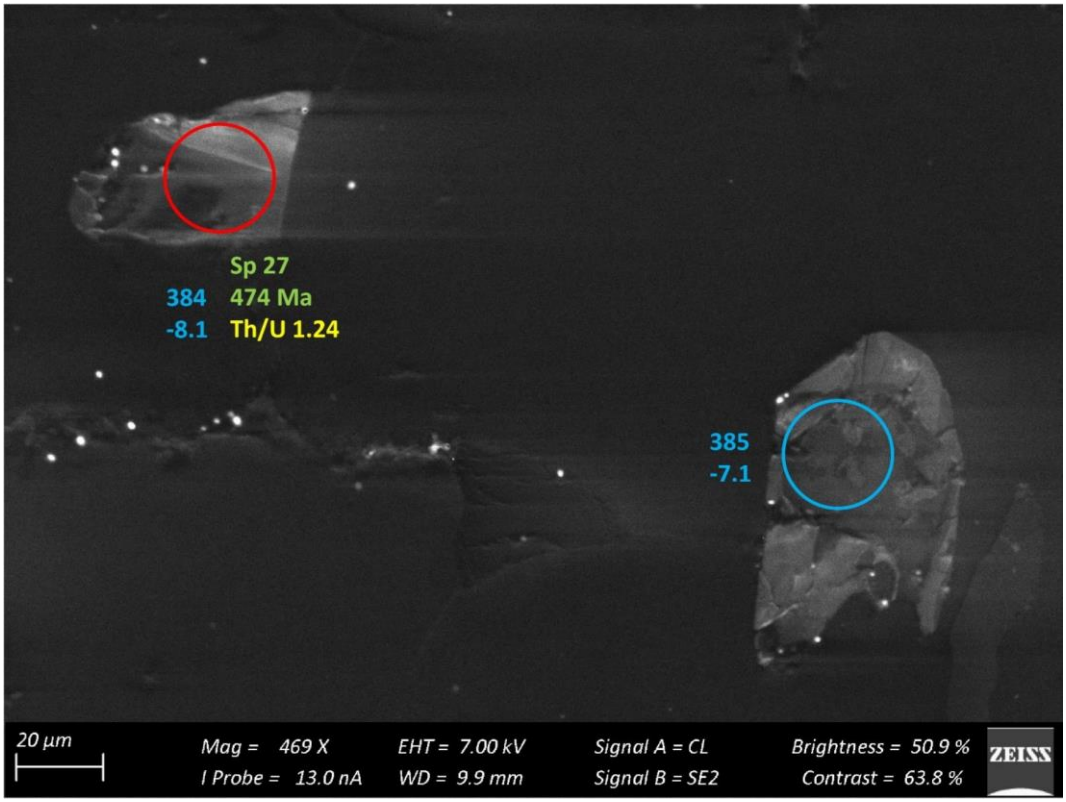

Figure 201 – Zircon Isotope spot analyses of sample s8Db; U-Pb analyses are colour coded according to concordance; blue writing indicates the Hf identifier with the respective εHf_{468} values

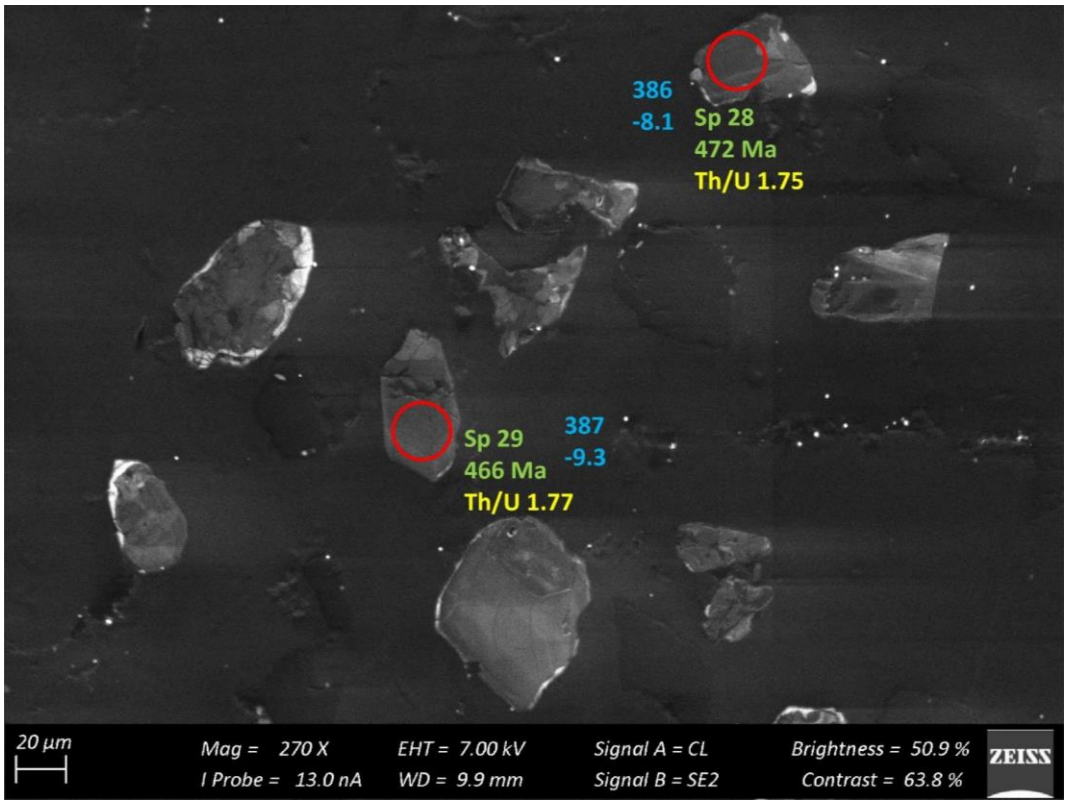

Figure 202 – Zircon Isotope spot analyses of sample s8Db; U-Pb analyses are colour coded according to concordance; blue writing indicates the Hf identifier with the respective εHf_{468} values

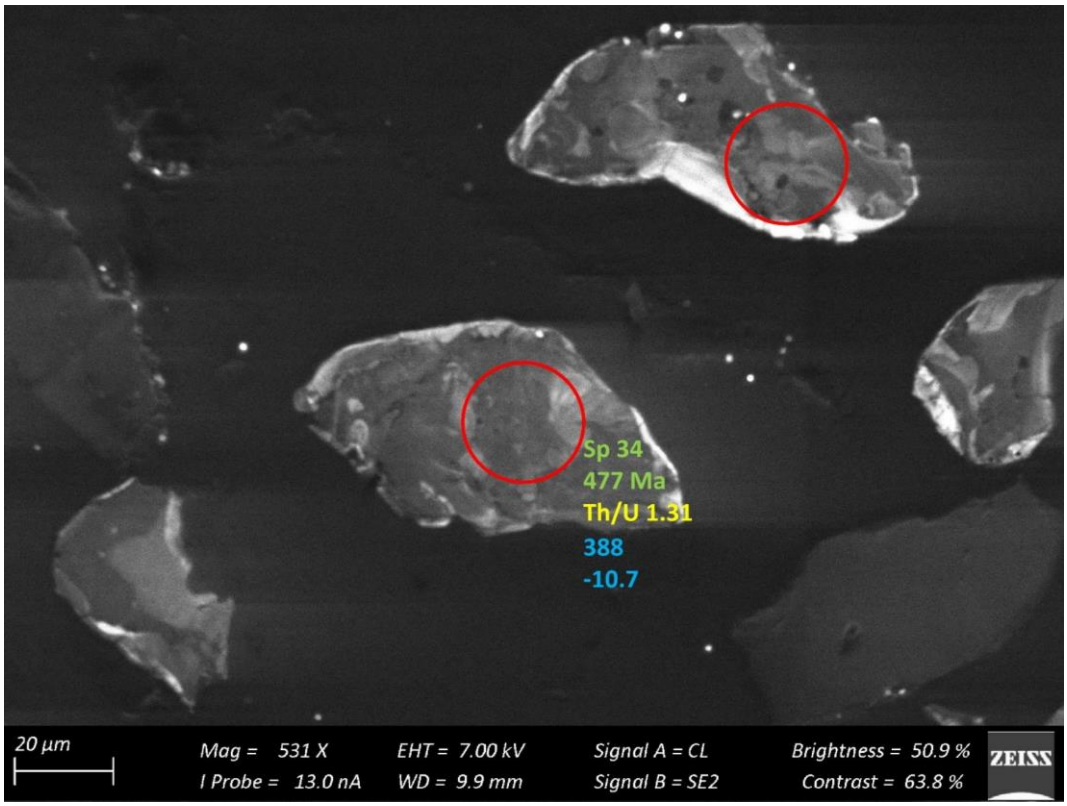

Figure 203 – Zircon Isotope spot analyses of sample s8Db; U-Pb analyses are colour coded according to concordance; blue writing indicates the Hf identifier with the respective εHf_{468} values

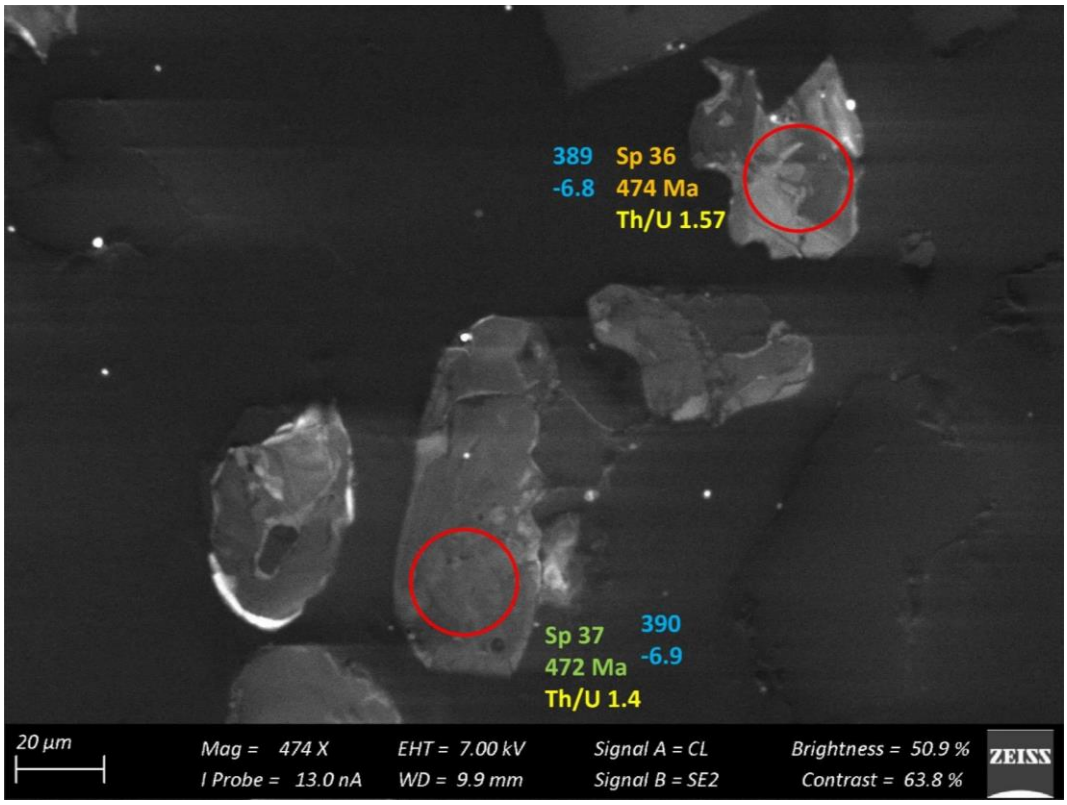

Figure 204 – Zircon Isotope spot analyses of sample s8Db; U-Pb analyses are colour coded according to concordance; blue writing indicates the Hf identifier with the respective εHf_{468} values

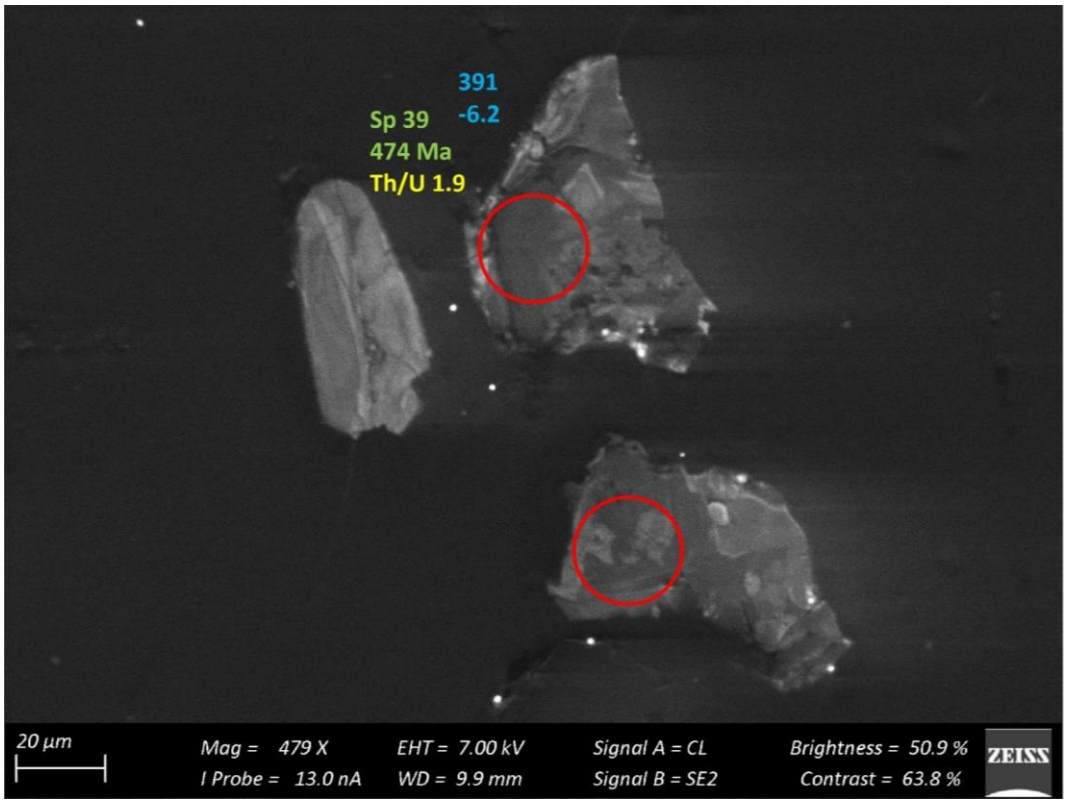

Figure 205 – Zircon Isotope spot analyses of sample s8Db; U-Pb analyses are colour coded according to concordance; blue writing indicates the Hf identifier with the respective εHf_{468} values

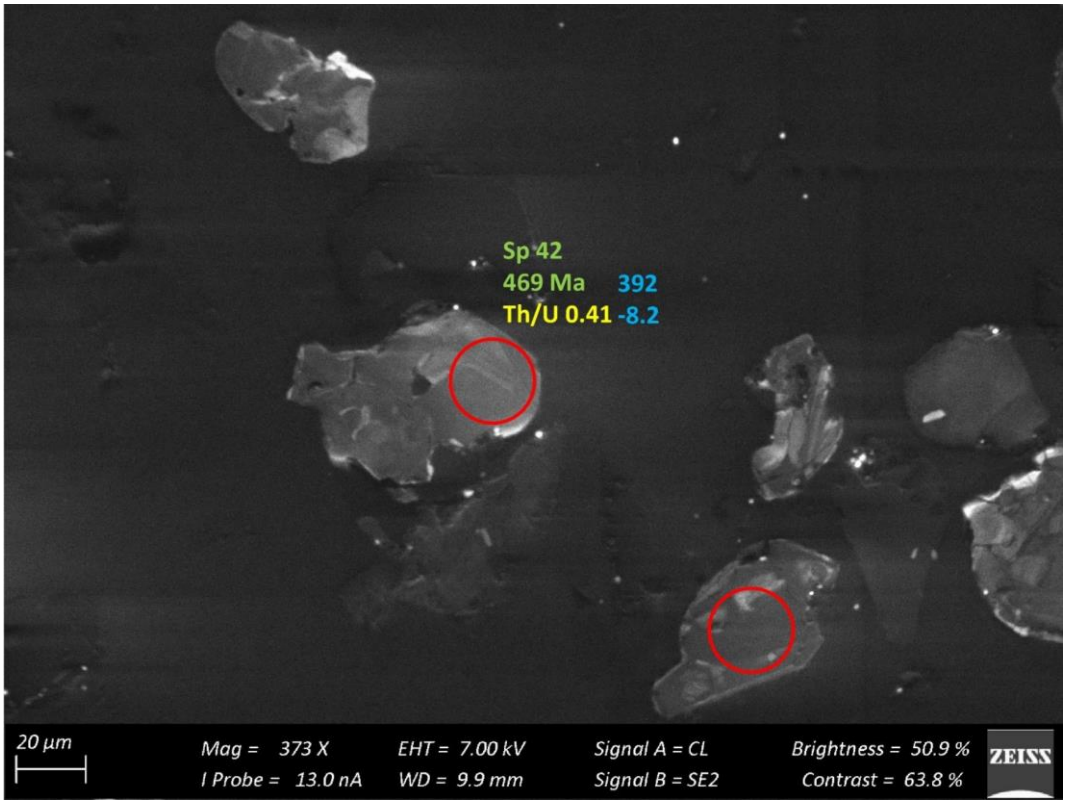

Figure 206 – Zircon Isotope spot analyses of sample s8Db; U-Pb analyses are colour coded according to concordance; blue writing indicates the Hf identifier with the respective εHf_{468} values

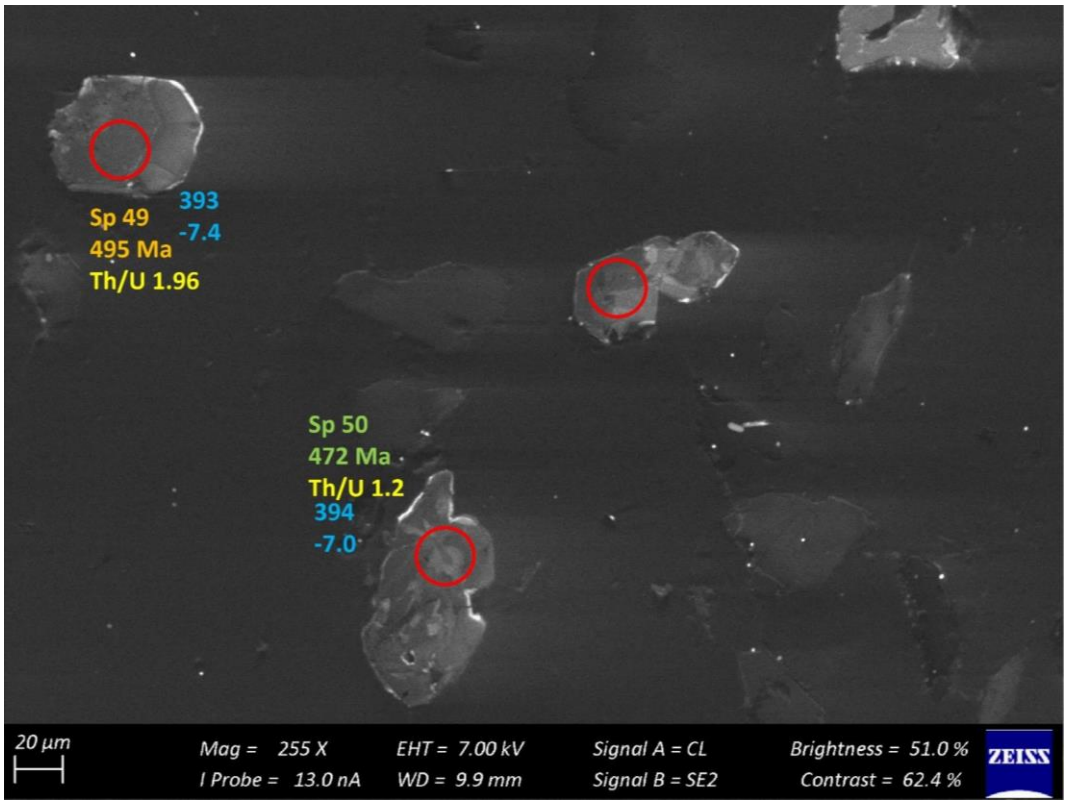

Figure 207 – Zircon Isotope spot analyses of sample s8Db; U-Pb analyses are colour coded according to concordance; blue writing indicates the Hf identifier with the respective εHf_{468} values

APPENDIX IV: APATITE ANALYSES

TABLE 1: APATITE $^{147}Sm/^{144}Nd$ ISOTOPE SPOT ANALYSES; VALUES CALCULATED TO THE AVERAGE MAGMATIC AGE OF 468 MA ARE INDICATED; IDENTIFIER WITH THE INDICATION -C OR -R INDICATE ANALYSES OBTAINED FROM CENTRE OR RIM DOMAINS OF THE GRAIN, RESPECTIVELY

Sample	Rock type	Identifier	$^{147}Sm/^{144}Nd$	$^{143}Nd/^{144}Nd$	$^{143}Nd/^{144}Nd_{468}$	$\pm 2\sigma$	εNd_{468}	$\pm 2\sigma$
s1B	Granodiorite	Us238	0.388	0.51283	0.51164	0.026	-7.7	2.6
s1B	Granodiorite	Us241	0.279	0.51164	0.51079	0.044	-24.4	4.4
s1B	Granodiorite	Us242	0.330	0.51267	0.51165	0.023	-7.4	2.3

Sample	Rock type	Identifier	$^{147}Sm/^{144}Nd$	$^{143}Nd/^{144}Nd$	$^{143}Nd/^{144}Nd_{468}$	$\pm 2\sigma$	εNd_{468}	$\pm 2\sigma$
s1Da	Granite	Us146	0.448	0.51318	0.51180	0.022	-4.6	2.2
s1Da	Granite	Us149	0.445	0.51315	0.51179	0.030	-4.8	3.0
s1Da	Granite	Us151	0.446	0.51316	0.51179	0.029	-4.8	2.9
s1Da	Granite	Us153	0.446	0.51314	0.51177	0.021	-5.1	2.1
s1Da	Granite	Us154	0.431	0.51306	0.51174	0.023	-5.7	2.3
s1Da	Granite	Us157	0.419	0.51301	0.51172	0.020	-6.1	2.0
s1Da	Granite	Us159	0.400	0.51275	0.51153	0.022	-9.9	2.2
s1Da	Granite	Us160	0.453	0.51320	0.51181	0.025	-4.4	2.5
s1Da	Granite	Us161	0.414	0.51280	0.51153	0.029	-9.8	2.9
s1Da	Granite	Us162	0.408	0.51301	0.51176	0.020	-5.4	2.0
s1Da	Granite	Us165	0.429	0.51311	0.51179	0.025	-4.8	2.5
s1Da	Granite	Us170	0.393	0.51278	0.51157	0.022	-9.1	2.2

Sample	Rock type	Identifier	$^{147}Sm/^{144}Nd$	$^{143}Nd/^{144}Nd$	$^{143}Nd/^{144}Nd_{468}$	$\pm 2\sigma$	εNd_{468}	$\pm 2\sigma$
s1H	Granodiorite	Us102	0.262	0.51254	0.51174	0.024	-5.8	2.4
s1H	Granodiorite	Us103	0.244	0.51249	0.51174	0.022	-5.7	2.2
s1H	Granodiorite	Us104	0.244	0.51260	0.51185	0.030	-3.5	3.0
s1H	Granodiorite	Us105	0.265	0.51253	0.51171	0.030	-6.3	3.0
s1H	Granodiorite	Us106	0.233	0.51226	0.51155	0.029	-9.5	2.9

TABLE 1 CONTINUED

Sample	Rock type	Identifier	$^{147}Sm/^{144}Nd$	$^{143}Nd/^{144}Nd$	$^{143}Nd/^{144}Nd_{468}$	±2σ	εNd_{468}	±2σ
s2A	Metapelite	Us084	0.219	0.51175	0.51107	0.020	-18.8	2.0
s2A	Metapelite	Us085	0.241	0.51153	0.51080	0.024	-24.2	2.4
s2A	Metapelite	Us086	0.239	0.51160	0.51087	0.023	-22.7	2.3
s2A	Metapelite	Us087	0.122	0.51188	0.51150	0.028	-10.4	2.8
s2A	Metapelite	Us088	0.242	0.51151	0.51077	0.027	-24.8	2.7
s2A	Metapelite	Us090	0.202	0.51155	0.51093	0.026	-21.5	2.6
s2A	Metapelite	Us091	0.232	0.51173	0.51102	0.025	-19.7	2.5
s2A	Metapelite	Us092	0.219	0.51187	0.51119	0.020	-16.4	2.0
s2A	Metapelite	Us093	0.239	0.51159	0.51086	0.026	-23.0	2.6
s2A	Metapelite	Us094	0.221	0.51165	0.51097	0.022	-20.7	2.2
s2A	Metapelite	Us095	0.251	0.51166	0.51089	0.034	-22.3	3.4
s2A	Metapelite	Us097	0.223	0.51183	0.51115	0.019	-17.3	1.9
s2A	Metapelite	Us098	0.246	0.51182	0.51107	0.023	-18.9	2.3
s2A	Metapelite	Us099	0.237	0.51191	0.51119	0.023	-16.6	2.3
s2A	Metapelite	Us101	0.234	0.51197	0.51125	0.030	-15.3	3.0
s2A	Metapelite	Us102	0.258	0.51204	0.51125	0.029	-15.3	2.9
s2A	Metapelite	Us104	0.242	0.51149	0.51075	0.031	-25.1	3.1

TABLE 1 CONTINUED

Sample	Rock type	Identifier	$^{147}Sm/^{144}Nd$	$^{143}Nd/^{144}Nd$	$^{143}Nd/^{144}Nd_{468}$	±2σ	εNd_{468}	±2σ
s2B	Granite	Us176	0.262	0.51221	0.51141	0.026	-12.2	2.6
s2B	Granite	Us177	0.265	0.51226	0.51145	0.052	-11.5	5.2
s2B	Granite	Us178	0.257	0.51225	0.51146	0.028	-11.3	2.8
s2B	Granite	Us179	0.260	0.51219	0.51139	0.025	-12.6	2.5
s2B	Granite	Us184	0.247	0.51217	0.51141	0.018	-12.2	1.8
s2B	Granite	Us185	0.256	0.51242	0.51164	0.018	-7.7	1.8
s2B	Granite	Us186	0.264	0.51227	0.51146	0.023	-11.2	2.3
s2B	Granite	Us187	0.260	0.51226	0.51147	0.019	-11.1	1.9
s2B	Granite	Us189	0.252	0.51213	0.51136	0.037	-13.2	3.7
s2B	Granite	Us191	0.251	0.51224	0.51147	0.018	-11.0	1.8
s2B	Granite	Us192	0.250	0.51216	0.51139	0.022	-12.6	2.2
s2B	Granite	Us193	0.253	0.51237	0.51160	0.020	-8.5	2.0
s2B	Granite	Us194	0.256	0.51247	0.51169	0.028	-6.8	2.8
s2B	Granite	Us195	0.258	0.51238	0.51158	0.017	-8.8	1.7
s2B	Granite	Us196	0.259	0.51230	0.51150	0.022	-10.4	2.2
s2B	Granite	Us197	0.263	0.51234	0.51153	0.020	-9.8	2.0
s2B	Granite	Us198	0.257	0.51226	0.51148	0.022	-10.9	2.2
s2B	Granite	Us199	0.253	0.51234	0.51156	0.018	-9.3	1.8
s2B	Granite	Us200	0.250	0.51235	0.51158	0.020	-8.8	2.0
s2B	Granite	Us201	0.270	0.51225	0.51142	0.026	-12.1	2.6
s2B	Granite	Us202	0.256	0.51221	0.51142	0.020	-12.0	2.0
s2B	Granite	Us203	0.251	0.51227	0.51150	0.018	-10.5	1.8
s2B	Granite	Us204	0.263	0.51233	0.51152	0.022	-10.0	2.2

TABLE 1 CONTINUED

Sample	Rock type	Identifier	$^{147}Sm/^{144}Nd$	$^{143}Nd/^{144}Nd$	$^{143}Nd/^{144}Nd_{468}$	±2σ	εNd_{468}	±2σ
s3B	Granite	Us059	0.251	0.51233	0.51156	0.017	-9.2	1.7
s3B	Granite	Us060	0.247	0.51232	0.51156	0.018	-9.3	1.8
s3B	Granite	Us061	0.251	0.51234	0.51157	0.017	-9.1	1.7
s3B	Granite	Us062	0.257	0.51242	0.51164	0.057	-7.8	5.6
s3B	Granite	Us063	0.256	0.51230	0.51152	0.018	-10.1	1.8
s3B	Granite	Us064	0.253	0.51235	0.51157	0.017	-9.1	1.7
s3B	Granite	Us065	0.250	0.51243	0.51166	0.018	-7.3	1.8
s3B	Granite	Us066	0.250	0.51232	0.51155	0.017	-9.4	1.7
s3B	Granite	Us067	0.254	0.51217	0.51139	0.021	-12.5	2.1
s3B	Granite	Us068	0.253	0.51231	0.51154	0.018	-9.7	1.8
s3B	Granite	Us069	0.242	0.51228	0.51153	0.018	-9.8	1.8
s3B	Granite	Us070-C	0.259	0.51220	0.51140	0.021	-12.4	2.1
s3B	Granite	Us070-R	0.259	0.51236	0.51156	0.022	-9.2	2.2
s3B	Granite	Us071	0.260	0.51223	0.51143	0.018	-11.8	1.8
s3B	Granite	Us072	0.244	0.51220	0.51145	0.020	-11.5	2.0
s3B	Granite	Us073	0.248	0.51232	0.51156	0.018	-9.2	1.8
s3B	Granite	Us074	0.248	0.51234	0.51158	0.018	-8.9	1.8
s3B	Granite	Us075	0.252	0.51224	0.51147	0.021	-11.1	2.1
s3B	Granite	Us076	0.245	0.51228	0.51153	0.017	-9.9	1.7
s3B	Granite	Us077	0.251	0.51227	0.51150	0.018	-10.5	1.8
s3B	Granite	Us078	0.243	0.51228	0.51153	0.017	-9.8	1.7
s3B	Granite	Us079	0.248	0.51226	0.51150	0.018	-10.4	1.8

TABLE 1 CONTINUED

Sample	Rock type	Identifier	$^{147}Sm/^{144}Nd$	$^{143}Nd/^{144}Nd$	$^{143}Nd/^{144}Nd_{468}$	±2σ	εNd_{468}	±2σ
s4D	Leucosome	Us206	0.238	0.51165	0.51092	0.068	-21.8	6.7
s4D	Leucosome	Us207	0.240	0.51125	0.51052	0.023	-29.6	2.3
s4D	Leucosome	Us209	0.235	0.51168	0.51096	0.022	-21.0	2.2
s4D	Leucosome	Us210	0.245	0.51225	0.51150	0.039	-10.5	3.9
s4D	Leucosome	Us211	0.233	0.51190	0.51119	0.043	-16.5	4.3
s4D	Leucosome	Us213	0.240	0.51144	0.51071	0.042	-25.9	4.2
s4D	Leucosome	Us214	0.240	0.51124	0.51050	0.023	-29.9	2.3
s4D	Leucosome	Us219	0.231	0.51121	0.51050	0.022	-29.9	2.2
s4D	Leucosome	Us220	0.232	0.51126	0.51055	0.027	-28.9	2.7
s4D	Leucosome	Us221	0.225	0.51136	0.51067	0.022	-26.7	2.2
s4D	Leucosome	Us222	0.231	0.51122	0.51051	0.020	-29.8	2.0
s4D	Leucosome	Us224	0.229	0.51133	0.51062	0.021	-27.6	2.1
s4D	Leucosome	Us225	0.234	0.51120	0.51048	0.040	-30.3	4.0
s4D	Leucosome	Us226	0.227	0.51130	0.51061	0.023	-27.9	2.3
s4D	Leucosome	Us227	0.232	0.51128	0.51057	0.032	-28.7	3.2
s4D	Leucosome	Us228	0.236	0.51137	0.51065	0.023	-27.2	2.3

Sample	Rock type	Identifier	$^{147}Sm/^{144}Nd$	$^{143}Nd/^{144}Nd$	$^{143}Nd/^{144}Nd_{468}$	±2σ	εNd_{468}	±2σ
s5Ba	Granodiorite	Us274	0.133	0.51144	0.51103	0.040	-19.7	4.0
s5Ba	Granodiorite	Us278	0.151	0.51219	0.51173	0.041	-5.9	4.1
s5Ba	Granodiorite	Us279	0.151	0.51164	0.51118	0.038	-16.7	3.8
s5Ba	Granodiorite	Us007	0.078	0.51206	0.51181	0.027	-4.3	2.7
s5Ba	Granodiorite	Us008	0.078	0.51202	0.51178	0.027	-5.0	2.7

TABLE 1 CONTINUED

Sample	Rock type	Identifier	$^{147}Sm/^{144}Nd$	$^{143}Nd/^{144}Nd$	$^{143}Nd/^{144}Nd_{468}$	±2σ	εNd_{468}	±2σ
s5Bb	Diorite	Us014	0.123	0.51185	0.51147	0.032	-11.0	3.2
s5Bb	Diorite	Us015	0.125	0.51205	0.51166	0.019	-7.3	1.9
s5Bb	Diorite	Us016	0.127	0.51194	0.51155	0.024	-9.4	2.4
s5Bb	Diorite	Us017	0.137	0.51221	0.51179	0.049	-4.8	4.9
s5Bb	Diorite	Us018	0.126	0.51204	0.51165	0.021	-7.5	2.1
s5Bb	Diorite	Us019	0.141	0.51190	0.51147	0.020	-11.1	2.0
s5Bb	Diorite	Us020	0.131	0.51208	0.51168	0.026	-6.9	2.6
s5Bb	Diorite	Us021	0.125	0.51212	0.51174	0.022	-5.8	2.2
s5Bb	Diorite	Us022	0.130	0.51195	0.51155	0.041	-9.5	4.1
s5Bb	Diorite	Us023	0.130	0.51185	0.51145	0.025	-11.4	2.5
s5Bb	Diorite	Us024	0.146	0.51201	0.51156	0.030	-9.3	3.0
s5Bb	Diorite	Us025	0.127	0.51189	0.51150	0.049	-10.4	4.9
s5Bb	Diorite	Us026	0.126	0.51180	0.51141	0.032	-12.1	3.2
s5Bb	Diorite	Us027	0.127	0.51215	0.51176	0.023	-5.4	2.3
s5Bb	Diorite	Us028	0.126	0.51176	0.51137	0.023	-12.9	2.3
s5Bb	Diorite	Us029	0.122	0.51212	0.51175	0.019	-5.7	1.9
s5Bb	Diorite	Us034	0.124	0.51183	0.51145	0.032	-11.4	3.2
s5Bb	Diorite	Us035	0.121	0.51203	0.51166	0.037	-7.3	3.7

Sample	Rock type	Identifier	$^{147}Sm/^{144}Nd$	$^{143}Nd/^{144}Nd$	$^{143}Nd/^{144}Nd_{468}$	±2σ	εNd_{468}	±2σ
s7A	Diorite	Us246	0.297	0.51260	0.51169	0.031	-6.8	3.1
s7A	Diorite	Us248	0.244	0.51251	0.51176	0.027	-5.4	2.7
s7A	Diorite	Us250	0.225	0.51246	0.51177	0.026	-5.2	2.6

TABLE 1 CONTINUED

Sample	Rock type	Identifier	$^{147}Sm/^{144}Nd$	$^{143}Nd/^{144}Nd$	$^{143}Nd/^{144}Nd_{468}$	±2σ	εNd_{468}	±2σ
s7B	Granite	Us108	0.270	0.51237	0.51154	0.018	-9.7	1.8
s7B	Granite	Us109	0.267	0.51215	0.51133	0.020	-13.7	2.0
s7B	Granite	Us110	0.266	0.51211	0.51130	0.021	-14.4	2.1
s7B	Granite	Us111	0.258	0.51223	0.51144	0.019	-11.5	1.9
s7B	Granite	Us113	0.268	0.51215	0.51133	0.025	-13.8	2.5
s7B	Granite	Us114	0.283	0.51239	0.51152	0.024	-10.1	2.4
s7B	Granite	Us115	0.261	0.51232	0.51152	0.018	-10.1	1.8
s7B	Granite	Us117	0.290	0.51228	0.51139	0.043	-12.5	4.3
s7B	Granite	Us118	0.288	0.51221	0.51133	0.021	-13.9	2.1
s7B	Granite	Us119	0.276	0.51254	0.51169	0.027	-6.7	2.7
s7B	Granite	Us119-C	0.283	0.51237	0.51151	0.021	-10.3	2.1
s7B	Granite	Us119-R	0.283	0.51220	0.51133	0.017	-13.8	1.7
s7B	Granite	Us124	0.264	0.51239	0.51158	0.019	-8.8	1.9
s7B	Granite	Us126	0.268	0.51214	0.51132	0.023	-14.0	2.3
s7B	Granite	Us127	0.253	0.51232	0.51154	0.019	-9.6	1.9
s7B	Granite	Us128	0.266	0.51220	0.51139	0.020	-12.7	2.0
s7B	Granite	Us129	0.273	0.51225	0.51141	0.024	-12.2	2.4
s7B	Granite	Us132	0.267	0.51229	0.51147	0.026	-11.0	2.6
s7B	Granite	Us133	0.258	0.51221	0.51142	0.019	-12.1	1.9
s7B	Granite	Us135	0.267	0.51230	0.51148	0.017	-10.8	1.7
s7B	Granite	Us137	0.266	0.51225	0.51143	0.019	-11.8	1.9
s7B	Granite	Us138	0.267	0.51214	0.51132	0.022	-13.9	2.2
s7B	Granite	Us139	0.276	0.51230	0.51145	0.028	-11.4	2.7
s7B	Granite	Us140	0.264	0.51224	0.51143	0.018	-11.9	1.8
s7B	Granite	Us141	0.256	0.51219	0.51141	0.018	-12.3	1.8
s7B	Granite	Us142	0.256	0.51228	0.51150	0.018	-10.5	1.8
s7B	Granite	Us143	0.255	0.51225	0.51147	0.021	-11.1	2.1

TABLE 1 CONTINUED

Sample	Rock type	Identifier	$^{147}Sm/^{144}Nd$	$^{143}Nd/^{144}Nd$	$^{143}Nd/^{144}Nd_{468}$	±2σ	εNd_{468}	±2σ
s8Da	Granite	Us039	0.327	0.51267	0.51167	0.031	-7.2	3.1
s8Da	Granite	Us041	0.346	0.51285	0.51179	0.025	-4.9	2.5
s8Da	Granite	Us045	0.366	0.51272	0.51160	0.023	-8.6	2.3
s8Da	Granite	Us046	0.321	0.51240	0.51141	0.021	-12.1	2.1
s8Da	Granite	Us047	0.301	0.51240	0.51148	0.049	-10.8	4.9
s8Da	Granite	Us048	0.320	0.51260	0.51162	0.022	-8.0	2.2
s8Da	Granite	Us050	0.323	0.51243	0.51144	0.024	-11.7	2.4
s8Da	Granite	Us051	0.299	0.51240	0.51149	0.029	-10.7	2.9
s8Da	Granite	Us052	0.308	0.51240	0.51145	0.024	-11.3	2.4
s8Da	Granite	Us053	0.304	0.51246	0.51153	0.029	-10.0	2.9
s8Da	Granite	Us056	0.315	0.51273	0.51176	0.026	-5.3	2.6

Sample	Rock type	Identifier	$^{147}Sm/^{144}Nd$	$^{143}Nd/^{144}Nd$	$^{143}Nd/^{144}Nd_{468}$	±2σ	εNd_{468}	±2σ
s8Db	Diorite	Us253	0.158	0.51222	0.51173	0.028	-5.9	2.7
s8Db	Diorite	Us254	0.148	0.51219	0.51173	0.031	-5.9	3.1
s8Db	Diorite	Us255	0.172	0.51230	0.51178	0.031	-5.1	3.1
s8Db	Diorite	Us256	0.154	0.51212	0.51165	0.027	-7.5	2.7
s8Db	Diorite	Us257	0.169	0.51229	0.51178	0.025	-5.0	2.5
s8Db	Diorite	Us260	0.175	0.51230	0.51176	0.020	-5.3	2.0
s8Db	Diorite	Us261	0.167	0.51225	0.51174	0.019	-5.8	1.9
s8Db	Diorite	Us262	0.227	0.51243	0.51173	0.028	-5.9	2.8
s8Db	Diorite	Us263	0.179	0.51219	0.51164	0.025	-7.7	2.5
s8Db	Diorite	Us264	0.150	0.51214	0.51168	0.029	-6.9	2.9
s8Db	Diorite	Us267	0.170	0.51228	0.51175	0.033	-5.5	3.3
s8Db	Diorite	Us268	0.171	0.51230	0.51178	0.025	-5.1	2.4
s8Db	Diorite	Us269	0.163	0.51222	0.51172	0.026	-6.2	2.6
s8Db	Diorite	Us270	0.183	0.51228	0.51172	0.025	-6.3	2.5

TABLE 2: APATITE $^{87}Rb/^{86}Sr$ ISOTOPE SPOT ANALYSES; VALUES CALCULATED TO THE AVERAGE MAGMATIC AGE OF 468 MA ARE INDICATED; IDENTIFIER WITH THE INDICATION -C OR -R INDICATE ANALYSES OBTAINED FROM CENTRE OR RIM DOMAINS OF THE GRAIN, RESPECTIVELY

Sample	Rock type	Identifier	$^{87}Sr/^{86}Sr_{468}$	±2σ	$^{87}Rb/^{86}Sr$	±2σ
s1B	Granodiorite	Us302	0.71281	0.00016	0.00235	0.00149
s1B	Granodiorite	Us307	0.71118	0.00022	0.00199	0.00044
s1B	Granodiorite	Us309	0.71196	0.00030	0.00078	0.00028
s1B	Granodiorite	Us310	0.71183	0.00028	0.06504	0.01563
s1B	Granodiorite	Us338	0.71049	0.00025	0.01751	0.00780
s1B	Granodiorite	Us339	0.71076	0.00031	0.00256	0.00108

Sample	Rock type	Identifier	$^{87}Sr/^{86}Sr_{468}$	±2σ	$^{87}Rb/^{86}Sr$	±2σ
s1Da	Granite	Us314	0.70730	0.00053	0.03553	0.01963
s1Da	Granite	Us315	0.70441	0.00140	0.10272	0.05110
s1Da	Granite	Us316	0.70677	0.00199	0.04389	0.00693
s1Da	Granite	Us317	0.70859	0.00035	0.01032	0.00401
s1Da	Granite	Us318	0.70847	0.00048	0.00774	0.00077
s1Da	Granite	Us319	0.70779	0.00074	0.03330	0.02409
s1Da	Granite	Us320	0.70962	0.00040	0.00731	0.00317
s1Da	Granite	Us321	0.70822	0.00053	0.02760	0.00518
s1Da	Granite	Us323	0.70918	0.00041	0.00433	0.00030
s1Da	Granite	Us324	0.70873	0.00044	0.00889	0.00195
s1Da	Granite	Us325	0.70739	0.00213	0.02957	0.01901
s1Da	Granite	Us326	0.70926	0.00062	0.00616	0.00149
s1Da	Granite	Us327	0.70989	0.00036	0.00481	0.00053
s1Da	Granite	Us328	0.70837	0.00042	0.01935	0.00245
s1Da	Granite	Us329	0.70893	0.00055	0.00691	0.00221
s1Da	Granite	Us330	0.70985	0.00043	0.00167	0.00020
s1Da	Granite	Us331	0.70842	0.00055	0.00453	0.00027
s1Da	Granite	Us332	0.70969	0.00058	0.00601	0.00188
s1Da	Granite	Us333	0.69923	0.00039	0.17765	0.00758
s1Da	Granite	Us334	0.70650	0.00094	0.05142	0.01843
s1Da	Granite	Us335	0.70772	0.00097	0.03822	0.03169
s1Da	Granite	Us336	0.70883	0.00095	0.00646	0.00129
s1Da	Granite	Us337	0.70612	0.00078	0.04500	0.01514

TABLE 2 CONTINUED

Sample	Rock type	Identifier	$^{87}Sr/^{86}Sr_{468}$	±2σ	$^{87}Rb/^{86}Sr$	±2σ
s1F	Granite	Us102	0.71661	0.00041	-0.00002	0.00012
s1F	Granite	Us103	0.71614	0.00030	0.00019	0.00012
s1F	Granite	Us104	0.71610	0.00036	0.00062	0.00059
s1F	Granite	Us105	0.71566	0.00032	0.00586	0.00475
s1F	Granite	Us106	0.71594	0.00046	0.01053	0.00204
s1F	Granite	Us107	0.71550	0.00038	0.01576	0.00944
s1F	Granite	Us108	0.71582	0.00039	0.01416	0.00750
s1F	Granite	Us109	0.71673	0.00030	0.00024	0.00010
s1F	Granite	Us110	0.71612	0.00028	0.00169	0.00095
s1F	Granite	Us111	0.71523	0.00034	0.03781	0.02165
s1F	Granite	Us112	0.71639	0.00047	0.00164	0.00116
s1F	Granite	Us112	0.71512	0.00034	0.07778	0.02240
s1F	Granite	Us113	0.71573	0.00055	0.18176	0.05570
s1F	Granite	Us114	0.71539	0.00036	0.00242	0.00027
s1F	Granite	Us115	0.71059	0.00039	0.00031	0.00016
s1F	Granite	Us116	0.71639	0.00057	0.01494	0.00400
s1F	Granite	Us117	0.71645	0.00026	0.00337	0.00231
s1F	Granite	Us118	0.71491	0.00046	0.04274	0.01371
s1F	Granite	Us119	0.71626	0.00034	0.00467	0.00189
s1F	Granite	Us124	0.71138	0.00018	0.00033	0.00014

TABLE 2 CONTINUED

Sample	Rock type	Identifier	$^{87}Sr/^{86}Sr_{468}$	±2σ	$^{87}Rb/^{86}Sr$	±2σ
s1H	Granodiorite	Us169	0.71306	0.00028	0.00071	0.00045
s1H	Granodiorite	Us170	0.71333	0.00016	0.00036	0.00011
s1H	Granodiorite	Us171	0.71301	0.00022	0.00955	0.00592
s1H	Granodiorite	Us172	0.71298	0.00016	0.00177	0.00025
s1H	Granodiorite	Us173	0.71319	0.00084	0.21663	0.12538
s1H	Granodiorite	Us174	0.71307	0.00020	0.11113	0.04227
s1H	Granodiorite	Us176	0.71350	0.00161	0.02630	0.01336
s1H	Granodiorite	Us178	0.71303	0.00039	0.11559	0.04175
s1H	Granodiorite	Us179	0.71258	0.00031	0.00156	0.00101
s1H	Granodiorite	Us184	0.71305	0.00038	0.04273	0.01590
s1H	Granodiorite	Us185	0.71328	0.00033	0.00777	0.00148
s1H	Granodiorite	Us186	0.71288	0.00032	0.00125	0.00048
s1H	Granodiorite	Us187	0.71280	0.00026	0.00072	0.00030
s1H	Granodiorite	Us188	0.71304	0.00026	0.01053	0.00416
s1H	Granodiorite	Us191	0.71334	0.00033	0.03439	0.02139
s1H	Granodiorite	Us192	0.71317	0.00025	0.03854	0.01820
s1H	Granodiorite	Us193	0.71311	0.00027	0.00145	0.00067

TABLE 2 CONTINUED

Sample	Rock type	Identifier	$^{87}Sr/^{86}Sr_{468}$	±2σ	$^{87}Rb/^{86}Sr$	±2σ
s2A	Metapelite	Us144	0.71565	0.00013	0.00056	0.00019
s2A	Metapelite	Us145	0.71587	0.00014	0.00037	0.00005
s2A	Metapelite	Us146	0.71579	0.00014	0.00140	0.00027
s2A	Metapelite	Us147	0.71558	0.00013	0.00040	0.00007
s2A	Metapelite	Us148	0.71549	0.00017	0.00639	0.00338
s2A	Metapelite	Us149	0.71552	0.00013	0.00071	0.00011
s2A	Metapelite	Us150	0.71617	0.00015	0.00211	0.00067
s2A	Metapelite	Us151	0.71501	0.00016	0.00157	0.00068
s2A	Metapelite	Us152	0.71581	0.00011	0.00068	0.00017
s2A	Metapelite	Us153	0.71554	0.00014	0.00083	0.00021
s2A	Metapelite	Us154	0.71527	0.00015	0.00189	0.00055
s2A	Metapelite	Us155	0.71486	0.00015	0.00429	0.00051
s2A	Metapelite	Us156	0.71553	0.00015	0.00204	0.00100
s2A	Metapelite	Us157	0.71538	0.00012	0.00036	0.00010
s2A	Metapelite	Us158	0.71559	0.00019	0.00040	0.00012
s2A	Metapelite	Us159	0.71496	0.00021	0.00377	0.00085
s2A	Metapelite	Us160	0.71545	0.00013	0.00037	0.00011
s2A	Metapelite	Us161	0.71581	0.00012	0.00026	0.00011
s2A	Metapelite	Us162	0.71558	0.00015	0.00029	0.00007
s2A	Metapelite	Us163	0.71541	0.00015	0.00128	0.00040
s2A	Metapelite	Us164	0.71530	0.00015	0.00115	0.00041
s2A	Metapelite	Us165	0.71509	0.00024	0.00112	0.00022
s2A	Metapelite	Us166	0.71557	0.00014	0.00045	0.00007

Sample	Rock type	Identifier	$^{87}Sr/^{86}Sr_{468}$	±2σ	$^{87}Rb/^{86}Sr$	±2σ
s2B	Granite	Us092	0.71490	0.00045	0.00047	0.00040
s2B	Granite	Us093	0.71396	0.00043	-0.00021	0.00009
s2B	Granite	Us094	0.71403	0.00036	0.00903	0.00375
s2B	Granite	Us095	0.71409	0.00035	0.00025	0.00015
s2B	Granite	Us096	0.71533	0.00042	0.00024	0.00109
s2B	Granite	Us099	0.71460	0.00076	0.00199	0.00117
s2B	Granite	Us100	0.71430	0.00093	0.00361	0.00132
s2B	Granite	Us101	0.71459	0.00034	0.00217	0.00050

TABLE 2 CONTINUED

Sample	Rock type	Identifier	$^{87}Sr/^{86}Sr_{468}$	±2σ	$^{87}Rb/^{86}Sr$	±2σ
s3B	Granite	Us194	0.71170	0.00045	0.04030	0.01358
s3B	Granite	Us195	0.71155	0.00035	0.00295	0.00140
s3B	Granite	Us196	0.71146	0.00044	0.02067	0.01138
s3B	Granite	Us197	0.71137	0.00029	0.00094	0.00012
s3B	Granite	Us198	0.71185	0.00035	0.01274	0.00089
s3B	Granite	Us199	0.71168	0.00039	0.00693	0.00374
s3B	Granite	Us200	0.71218	0.00028	0.00285	0.00155
s3B	Granite	Us201	0.71316	0.00099	0.28622	0.07494
s3B	Granite	Us202	0.71220	0.00037	0.01140	0.00861
s3B	Granite	Us203	0.71179	0.00031	0.00131	0.00014
s3B	Granite	Us204	0.71316	0.00106	0.14060	0.06660
s3B	Granite	Us205	0.71158	0.00034	0.03509	0.01134
s3B	Granite	Us206	0.71159	0.00037	0.02037	0.01191
s3B	Granite	Us207	0.71148	0.00030	0.00416	0.00052
s3B	Granite	Us208	0.71300	0.00207	0.55932	0.20552
s3B	Granite	Us209	0.71273	0.00032	0.00886	0.00359
s3B	Granite	Us210	0.71208	0.00025	0.00652	0.00318
s3B	Granite	Us211	0.71131	0.00034	0.00665	0.00568
s3B	Granite	Us212	0.71164	0.00030	0.00096	0.00011
s3B	Granite	Us213	0.71269	0.00038	0.02657	0.00203
s3B	Granite	Us214	0.71325	0.00057	0.31544	0.03241
s3B	Granite	Us215	0.71257	0.00057	0.11012	0.03617
s3B	Granite	Us216	0.71203	0.00035	0.02741	0.01116
s3B	Granite	Us217	0.71145	0.00048	0.02922	0.01185
s3B	Granite	Us218	0.71169	0.00045	0.02889	0.02247
s3B	Granite	Us219	0.71150	0.00051	0.01109	0.00618
s3B	Granite	Us220	0.71187	0.00037	0.00133	0.00014
s3B	Granite	Us221	0.71153	0.00040	0.04108	0.01708

TABLE 2 CONTINUED

Sample	Rock type	Identifier	$^{87}Sr/^{86}Sr_{468}$	±2σ	$^{87}Rb/^{86}Sr$	±2σ
s4D	Leucosome	Us062	0.71578	0.00018	-0.00003	0.00008
s4D	Leucosome	Us063	0.71655	0.00015	-0.00004	0.00005
s4D	Leucosome	Us064	0.71616	0.00012	0.00005	0.00006
s4D	Leucosome	Us065	0.71671	0.00015	0.00004	0.00006
s4D	Leucosome	Us066	0.71657	0.00011	0.00056	0.00036
s4D	Leucosome	Us067	0.71602	0.00014	0.00041	0.00020
s4D	Leucosome	Us068	0.71664	0.00012	-0.00002	0.00003
s4D	Leucosome	Us069	0.71611	0.00012	0.00000	0.00004
s4D	Leucosome	Us070	0.71651	0.00024	0.00009	0.00005
s4D	Leucosome	Us071	0.71572	0.00022	0.00216	0.00085
s4D	Leucosome	Us072	0.71644	0.00021	0.00006	0.00006
s4D	Leucosome	Us073	0.71618	0.00018	0.00006	0.00006
s4D	Leucosome	Us074	0.71657	0.00015	0.00007	0.00006
s4D	Leucosome	Us075	0.71655	0.00021	0.00009	0.00008
s4D	Leucosome	Us076	0.71652	0.00021	-0.00002	0.00009
s4D	Leucosome	Us077	0.71568	0.00038	0.08768	0.03776
s4D	Leucosome	Us078	0.71607	0.00159	0.00902	0.00798
s4D	Leucosome	Us079	0.71594	0.00023	0.00017	0.00010
s4D	Leucosome	Us084	0.71654	0.00020	0.00040	0.00029
s4D	Leucosome	Us085	0.71682	0.00021	0.00050	0.00042
s4D	Leucosome	Us086	0.71621	0.00019	0.00016	0.00008
s4D	Leucosome	Us087	0.71652	0.00020	-0.00002	0.00006
s4D	Leucosome	Us088	0.71639	0.00023	0.00005	0.00006
s4D	Leucosome	Us089	0.71647	0.00018	0.00010	0.00005
s4D	Leucosome	Us090	0.71628	0.00020	0.00027	0.00008
s4D	Leucosome	Us091	0.71630	0.00026	0.00019	0.00007

Sample	Rock type	Identifier	$^{87}Sr/^{86}Sr_{468}$	±2σ	$^{87}Rb/^{86}Sr$	±2σ
s5A	Diorite	Us285	0.71008	0.00020	0.00487	0.00078
s5A	Diorite	Us287	0.71022	0.00025	0.00567	0.00047
s5A	Diorite	Us288	0.71004	0.00105	0.09580	0.02838
s5A	Diorite	Us294	0.71026	0.00021	0.00308	0.00049
s5A	Diorite	Us295	0.71023	0.00021	0.00052	0.00015
s5A	Diorite	Us298	0.71002	0.00094	0.15982	0.08434

TABLE 2 CONTINUED

Sample	Rock type	Identifier	$^{87}Sr/^{86}Sr_{468}$	±2σ	$^{87}Rb/^{86}Sr$	±2σ
s5Ba	Granodiorite	Us007	0.71029	0.00022	0.00057	0.00007
s5Ba	Granodiorite	Us008	0.70963	0.00025	0.00720	0.00421
s5Ba	Granodiorite	Us012	0.70956	0.00034	0.00244	0.00206
s5Ba	Granodiorite	Us013	0.70943	0.00024	0.00012	0.00007
s5Ba	Granodiorite	Us015	0.70965	0.00022	0.00074	0.00023
s5Ba	Granodiorite	Us019	0.70935	0.00029	0.00040	0.00022
s5Ba	Granodiorite	Us021	0.70964	0.00018	0.00050	0.00057
s5Ba	Granodiorite	Us022	0.70989	0.00022	0.00253	0.00155

Sample	Rock type	Identifier	$^{87}Sr/^{86}Sr_{468}$	±2σ	$^{87}Rb/^{86}Sr$	±2σ
s5Bb	Diorite	Us222	0.71056	0.00023	0.00030	0.00014
s5Bb	Diorite	Us223	0.71089	0.00020	0.00099	0.00051
s5Bb	Diorite	Us224	0.71022	0.00022	0.02022	0.00933
s5Bb	Diorite	Us227	0.71049	0.00029	0.05543	0.01565
s5Bb	Diorite	Us234	0.71029	0.00029	0.00793	0.00300
s5Bb	Diorite	Us236	0.71044	0.00040	0.01717	0.01112
s5Bb	Diorite	Us237	0.71052	0.00017	0.00263	0.00147
s5Bb	Diorite	Us239	0.71057	0.00033	0.02846	0.02321
s5Bb	Diorite	Us240	0.71018	0.00026	0.00028	0.00024
s5Bb	Diorite	Us241	0.71048	0.00021	0.00216	0.00061
s5Bb	Diorite	Us242	0.71020	0.00016	0.00658	0.00283
s5Bb	Diorite	Us243	0.71041	0.00014	0.00026	0.00008
s5Bb	Diorite	Us245	0.71030	0.00013	0.00132	0.00056
s5Bb	Diorite	Us246	0.70990	0.00021	0.05062	0.00457
s5Bb	Diorite	Us247	0.71031	0.00020	0.00162	0.00053
s5Bb	Diorite	Us248	0.71027	0.00015	0.00101	0.00027
s5Bb	Diorite	Us249	0.71042	0.00014	0.00084	0.00012

Sample	Rock type	Identifier	$^{87}Sr/^{86}Sr_{468}$	±2σ	$^{87}Rb/^{86}Sr$	±2σ
s7A	Diorite	Us027	0.70872	0.00053	0.07107	0.01405

TABLE 2 CONTINUED

Sample	Rock type	Identifier	$^{87}Sr/^{86}Sr_{468}$	±2σ	$^{87}Rb/^{86}Sr$	±2σ
s7B	Granite	Us250	0.71583	0.00024	0.00172	0.00048
s7B	Granite	Us251	0.71636	0.00027	0.00294	0.00069
s7B	Granite	Us252	0.71609	0.00035	0.00239	0.00072
s7B	Granite	Us253	0.71627	0.00027	0.01030	0.00461
s7B	Granite	Us254	0.71548	0.00029	0.00409	0.00085
s7B	Granite	Us255	0.71650	0.00034	0.00161	0.00118
s7B	Granite	Us256	0.71588	0.00022	0.00563	0.00349
s7B	Granite	Us257	0.71657	0.00036	0.00433	0.00103
s7B	Granite	Us258	0.71614	0.00024	0.00094	0.00035
s7B	Granite	Us259	0.71644	0.00034	0.00281	0.00136
s7B	Granite	Us260	0.71660	0.00035	0.00139	0.00046
s7B	Granite	Us261	0.71557	0.00040	0.00681	0.00211
s7B	Granite	Us262	0.71624	0.00057	0.08414	0.13325
s7B	Granite	Us263	0.71590	0.00025	0.00388	0.00096
s7B	Granite	Us264	0.71637	0.00022	0.00184	0.00068
s7B	Granite	Us265	0.71649	0.00027	0.00597	0.00195
s7B	Granite	Us266	0.71652	0.00036	0.00347	0.00221
s7B	Granite	Us267	0.71603	0.00036	0.00120	0.00093
s7B	Granite	Us268	0.71548	0.00041	0.00119	0.00038
s7B	Granite	Us269	0.71637	0.00049	0.00213	0.00085
s7B	Granite	Us270	0.71645	0.00035	0.00667	0.00153
s7B	Granite	Us271	0.71563	0.00044	0.00114	0.00016

TABLE 2 CONTINUED

Sample	Rock type	Identifier	$^{87}Sr/^{86}Sr_{468}$	±2σ	$^{87}Rb/^{86}Sr$	±2σ
s8Da	Granite	Us125	0.70983	0.00030	0.01178	0.00381
s8Da	Granite	Us127	0.70933	0.00042	0.08893	0.04074
s8Da	Granite	Us128	0.71039	0.00027	0.00694	0.00395
s8Da	Granite	Us130	0.70982	0.00036	0.04424	0.02092
s8Da	Granite	Us132	0.70929	0.00038	0.00530	0.00197
s8Da	Granite	Us133	0.71023	0.00033	0.01334	0.00406
s8Da	Granite	Us134	0.70943	0.00063	0.02695	0.01305
s8Da	Granite	Us136	0.70987	0.00018	0.01151	0.00681
s8Da	Granite	Us137	0.70922	0.00087	0.00712	0.00342
s8Da	Granite	Us138	0.70999	0.00049	0.00607	0.00573
s8Da	Granite	Us141	0.71027	0.00025	0.00458	0.00043
s8Da	Granite	Us142	0.70983	0.00040	0.00450	0.00129
s8Da	Granite	Us143	0.70942	0.00034	0.00511	0.00178

Sample	Rock type	Identifier	$^{87}Sr/^{86}Sr_{468}$	±2σ	$^{87}Rb/^{86}Sr$	±2σ
s8Db	Diorite	Us050	0.71205	0.00025	0.00419	0.00053
s8Db	Diorite	Us051	0.70968	0.00025	0.02272	0.00472
s8Db	Diorite	Us057	0.71144	0.00308	0.86004	0.83637
s8Db	Diorite	Us059	0.71177	0.00026	0.00260	0.00048
s8Db	Diorite	Us060	0.71219	0.00033	0.05721	0.00782

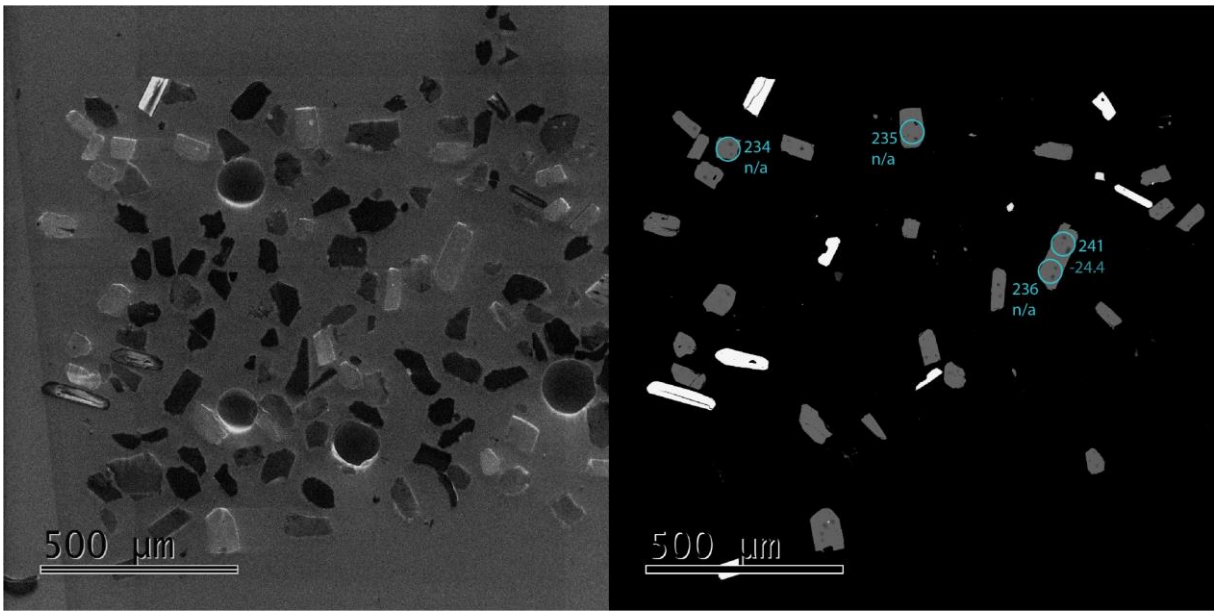

Figure 1 – Apatite εNd spot analyses of sample s1B indicating the analysed spots with the obtained εNd_{468} values

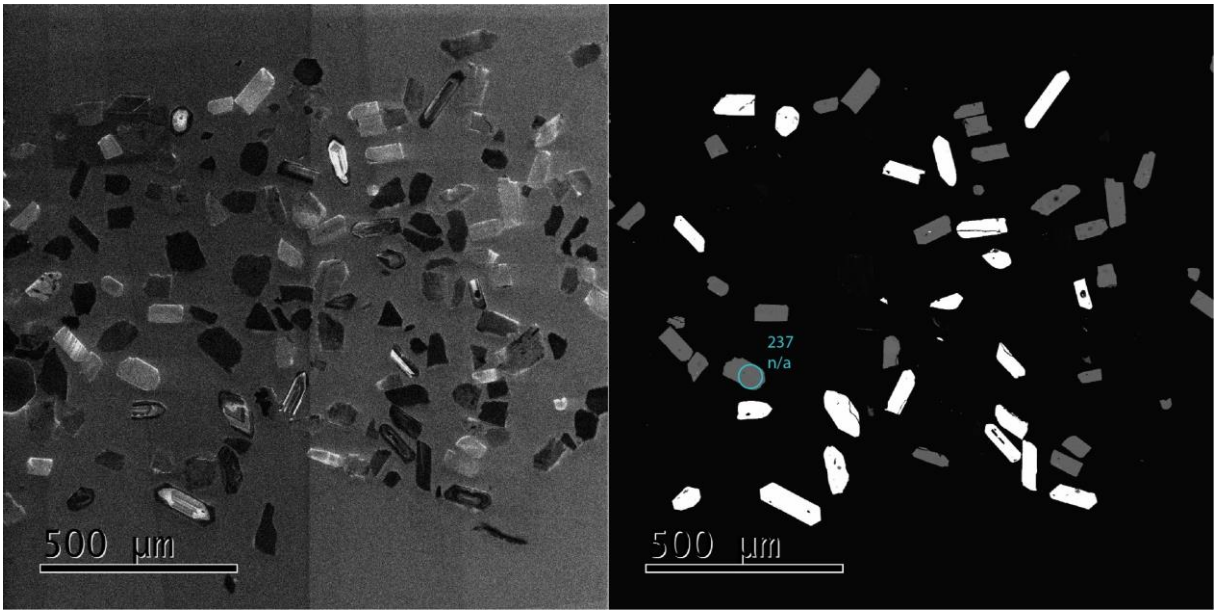

Figure 2 – Apatite εNd spot analyses of sample s1B indicating the analysed spots with the obtained εNd_{468} values

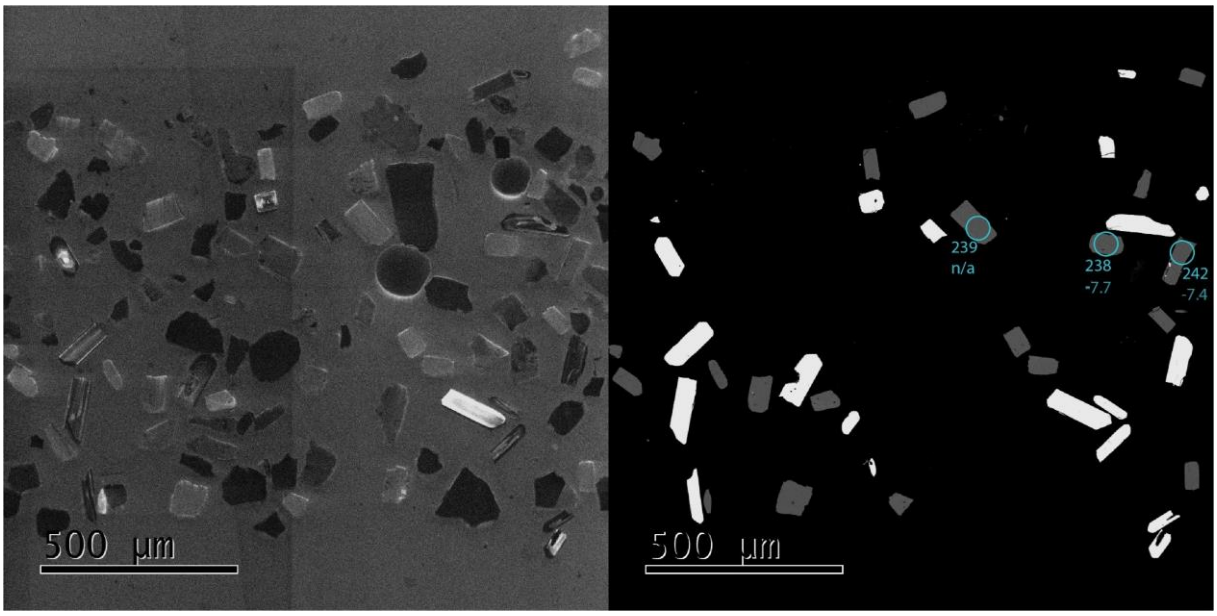

Figure 3 – Apatite εNd spot analyses of sample s1B indicating the analysed spots with the obtained εNd_{468} values

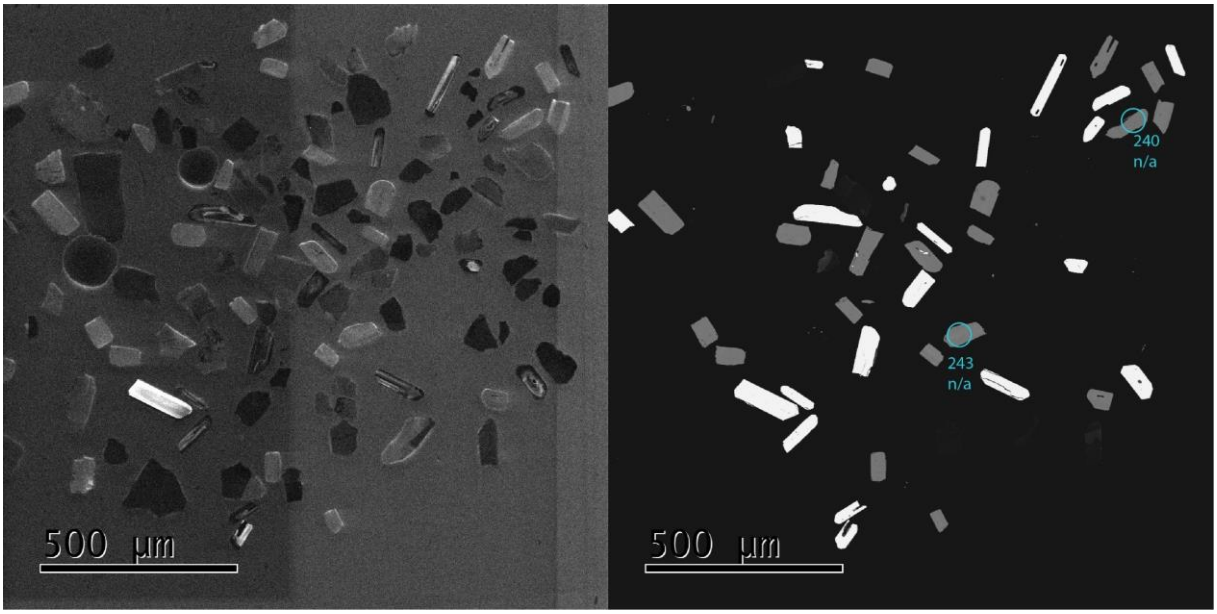

Figure 4 – Apatite εNd spot analyses of sample s1B indicating the analysed spots with the obtained εNd_{468} values

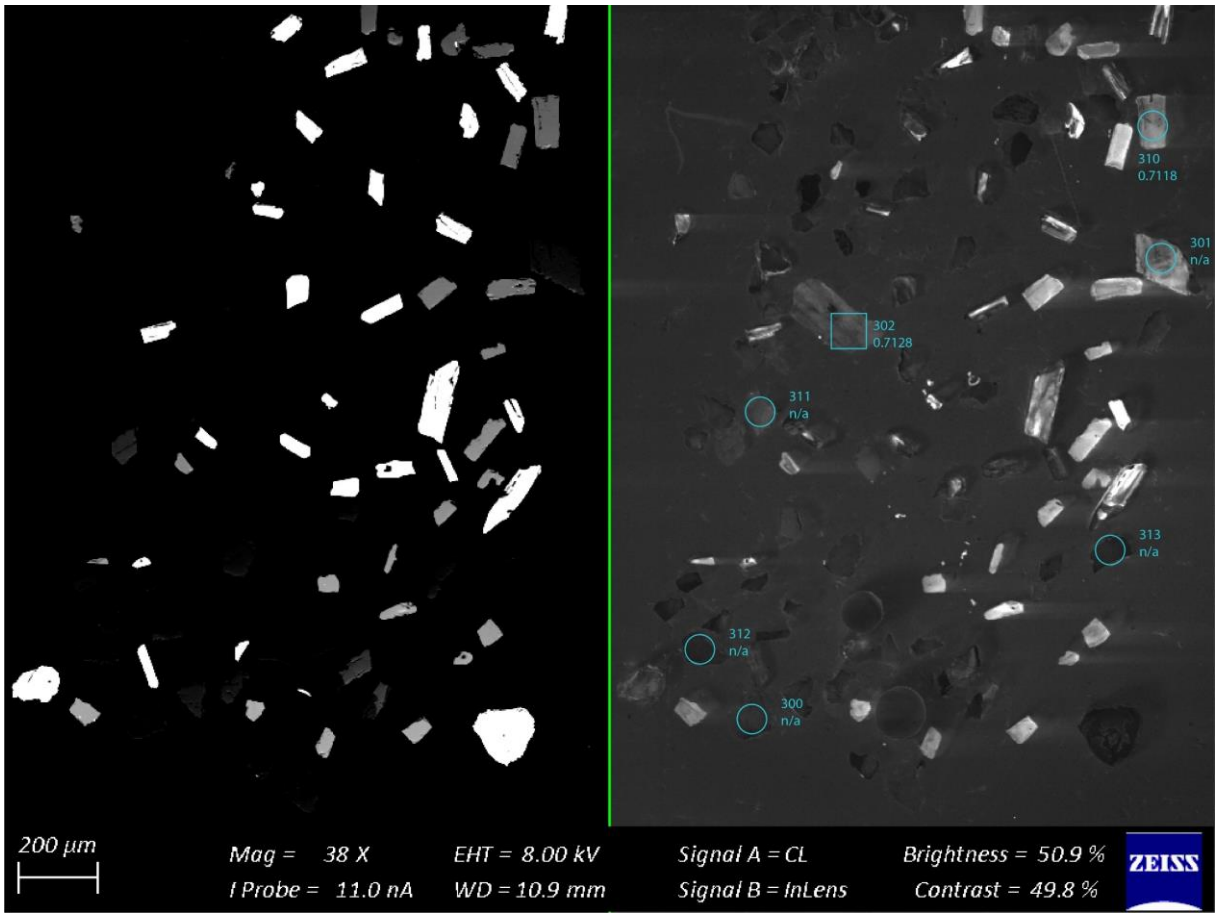

Figure 5 – Apatite spot analyses of sample s1B indicating the analysed spots with the obtained $^{87}Sr/^{86}Sr_{468}$ values

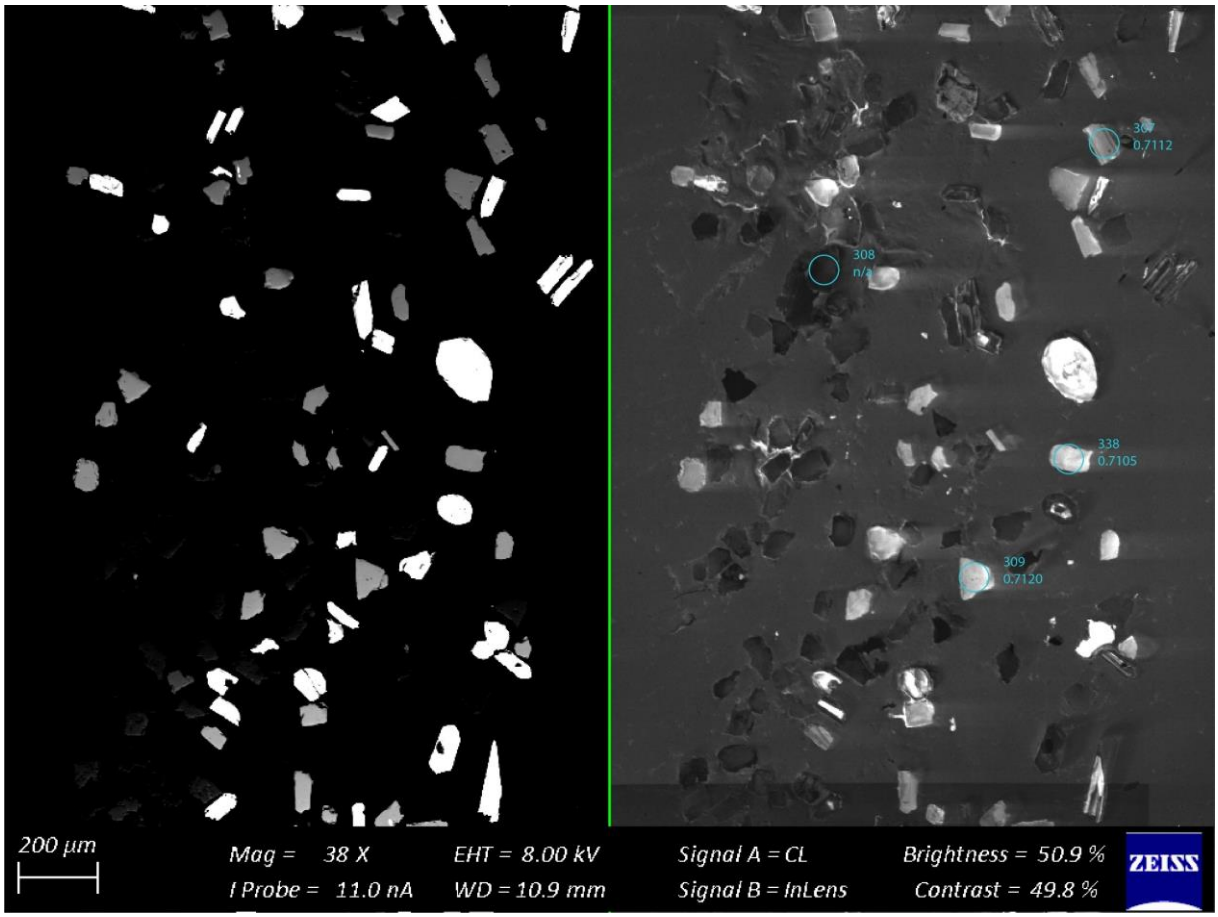

Figure 6 – Apatite spot analyses of sample s1B indicating the analysed spots with the obtained $^{87}Sr/^{86}Sr_{468}$ values

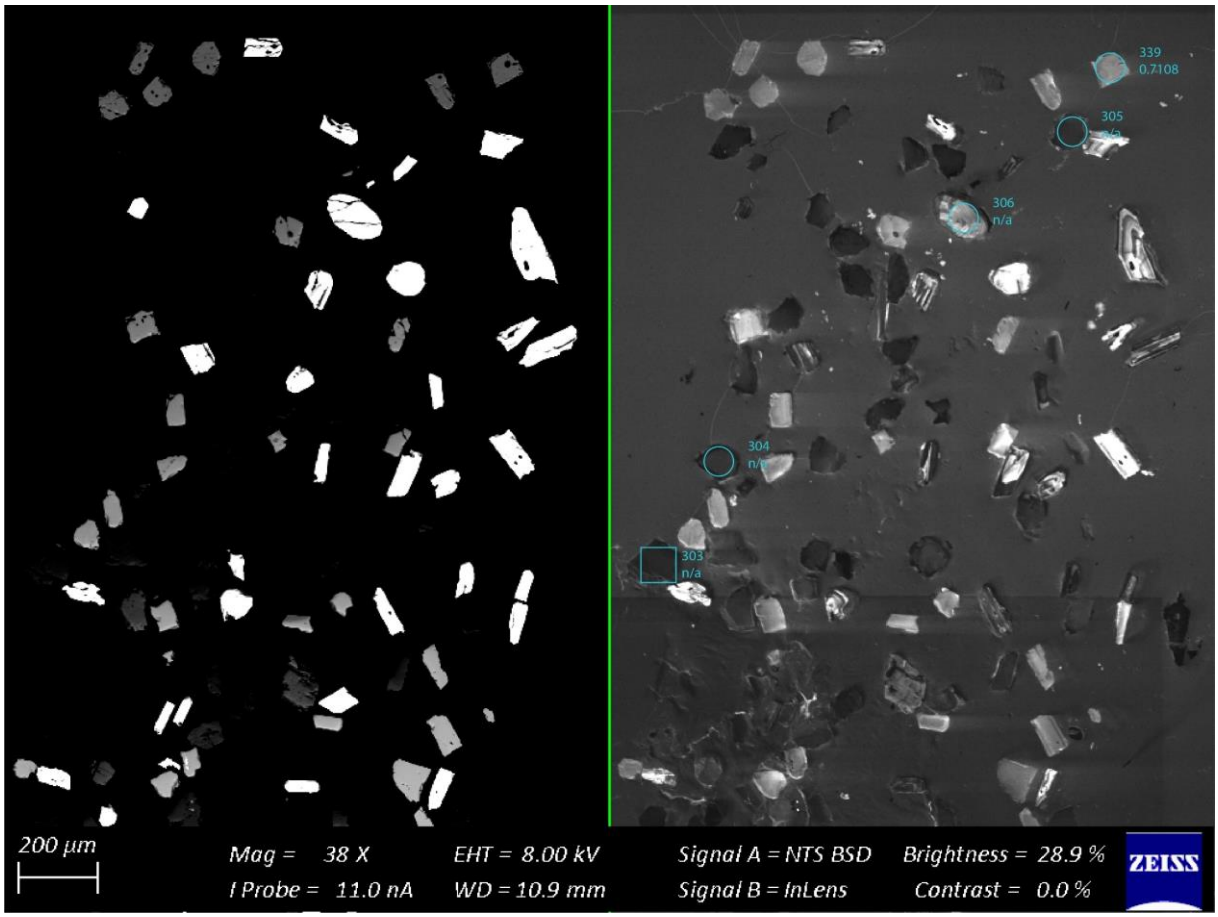

Figure 7 – Apatite spot analyses of sample s1B indicating the analysed spots with the obtained $^{87}Sr/^{86}Sr_{468}$ values

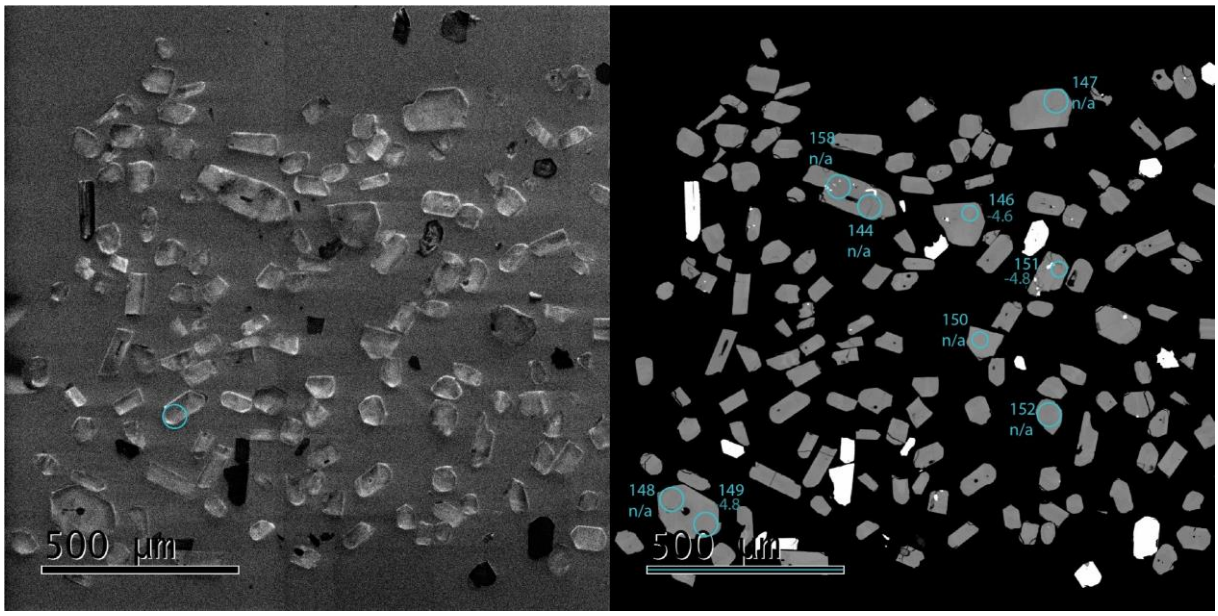

Figure 8 – Apatite εNd spot analyses of sample s1Da indicating the analysed spots with the obtained εNd_{468} values

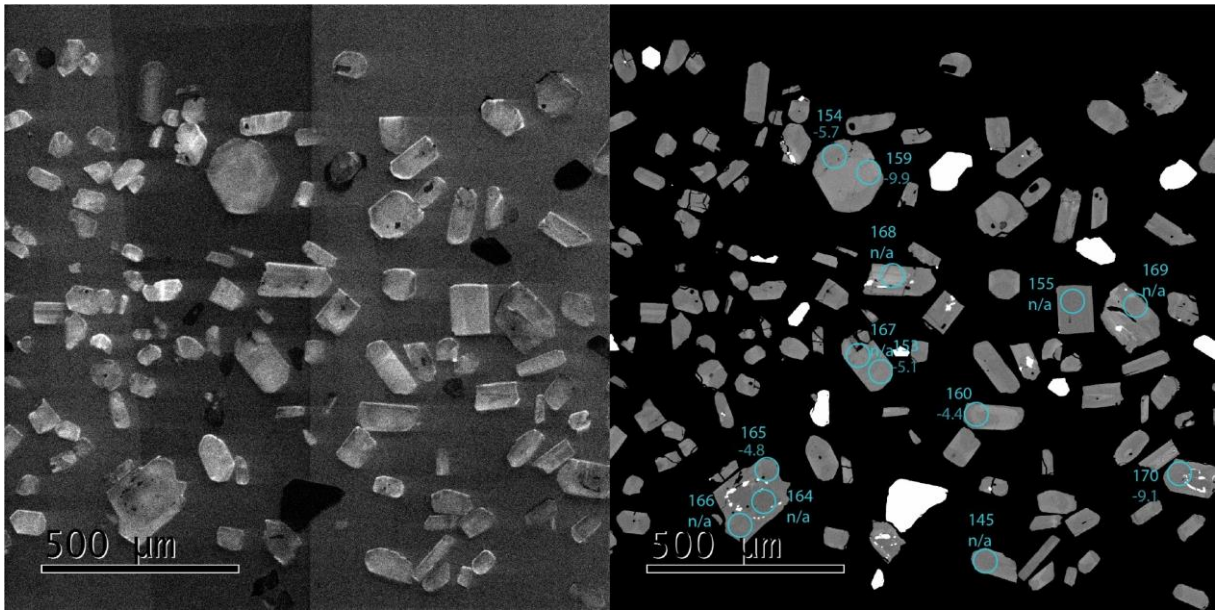

Figure 9 – Apatite εNd spot analyses of sample s1Da indicating the analysed spots with the obtained εNd_{468} values

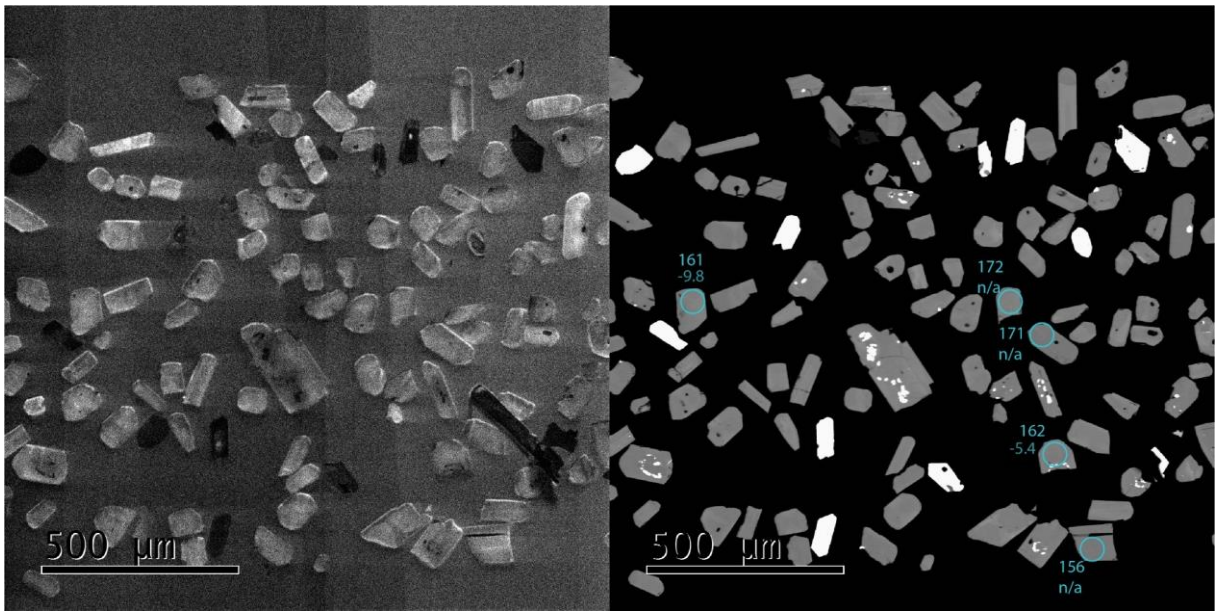

Figure 10 – Apatite εNd spot analyses of sample s1Da indicating the analysed spots with the obtained εNd_{468} values

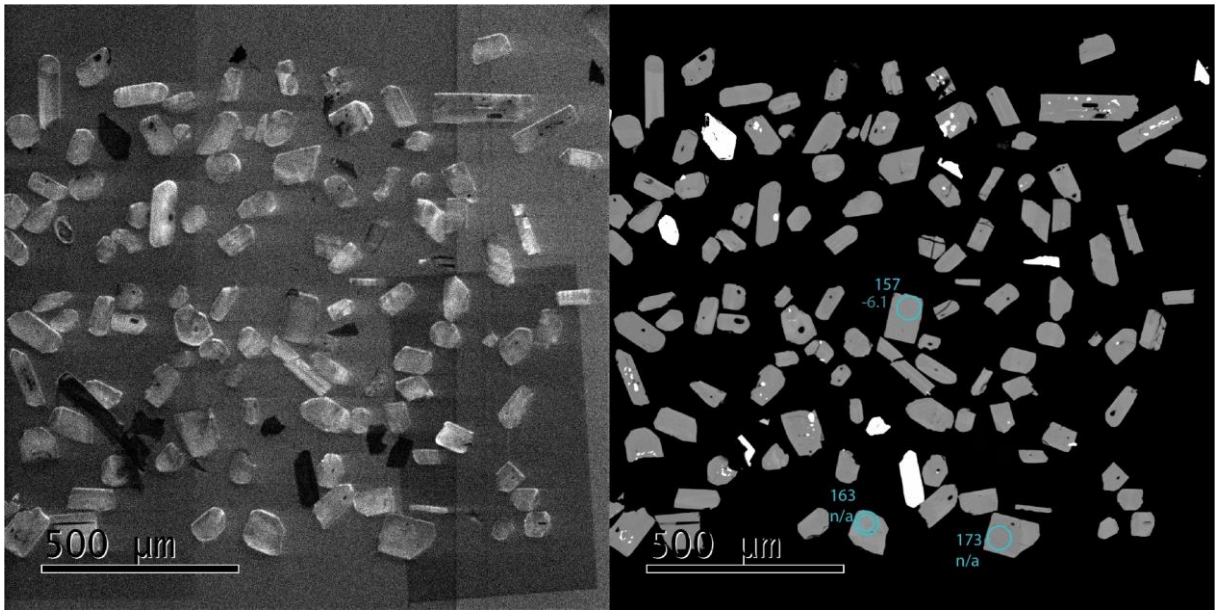

Figure 11 – Apatite εNd spot analyses of sample s1Da indicating the analysed spots with the obtained εNd_{468} values

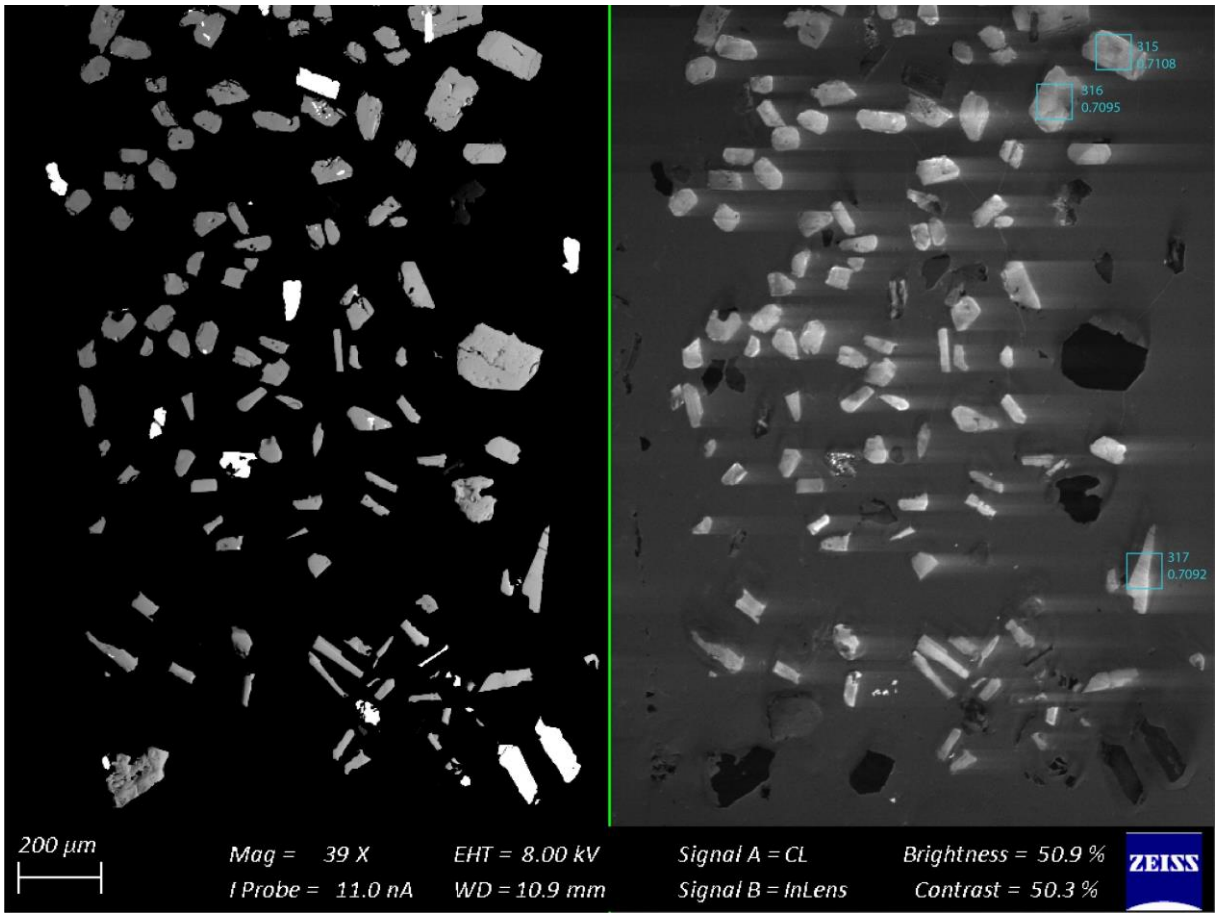

Figure 12 – Apatite spot analyses of sample s1Da indicating the analysed spots with the obtained $^{87}Sr/^{86}Sr_{468}$ values

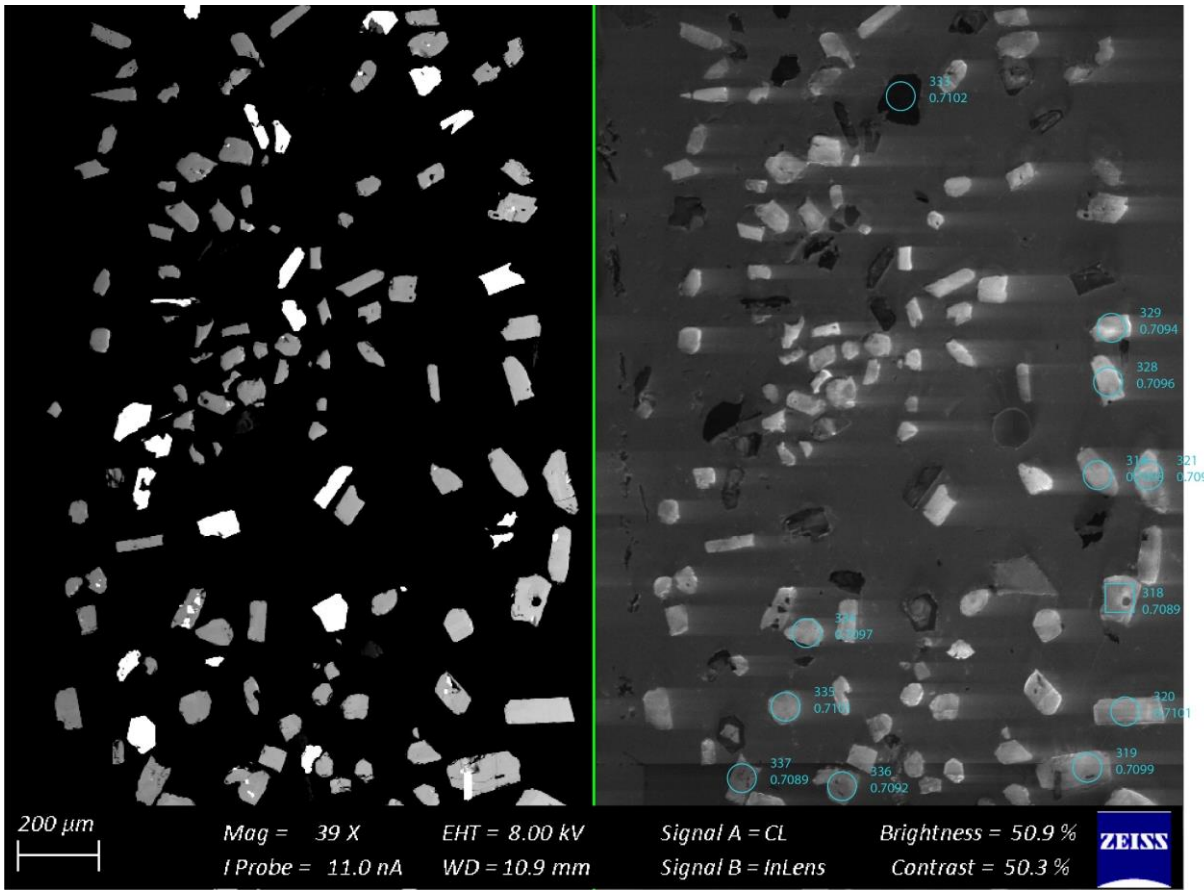

Figure 13 – Apatite spot analyses of sample s1Da indicating the analysed spots with the obtained $^{87}Sr/^{86}Sr_{468}$ values

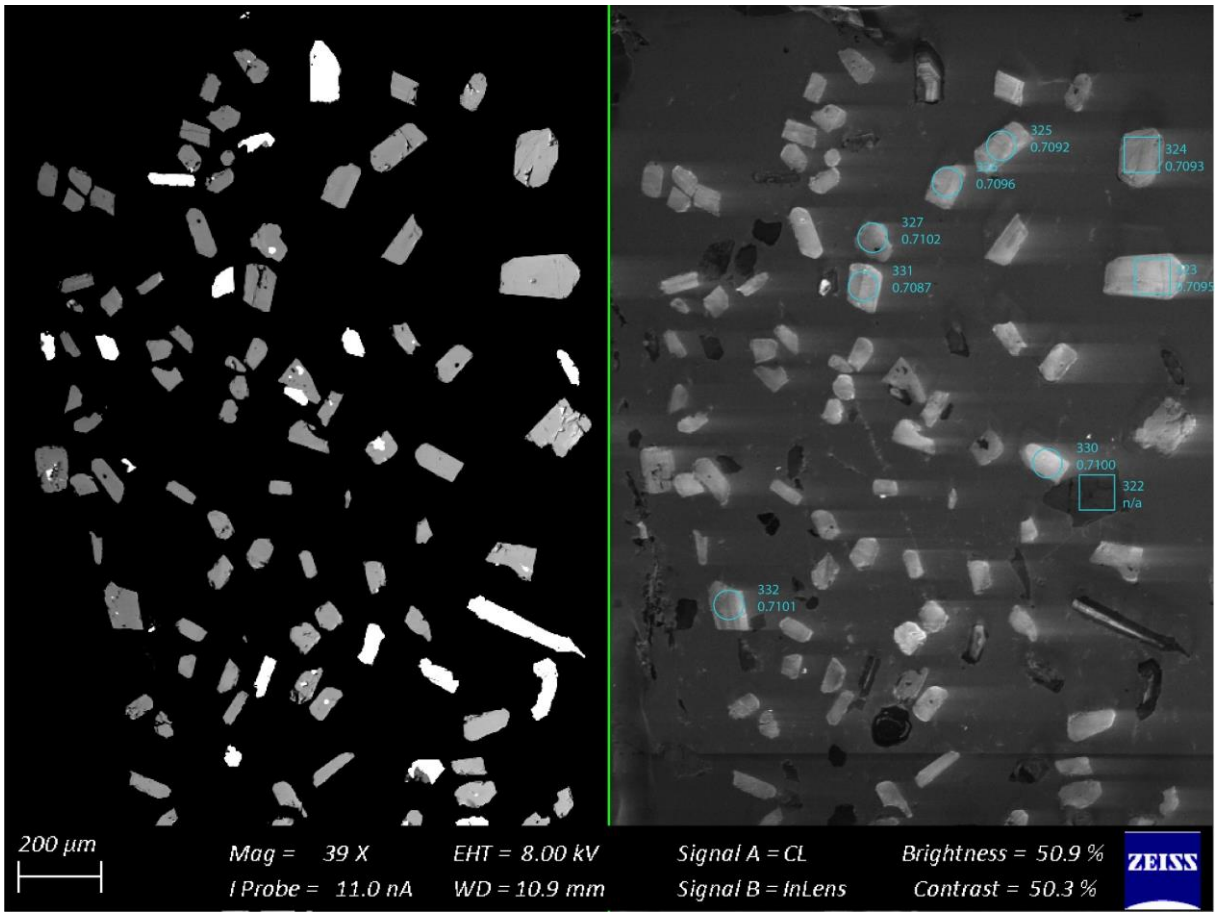

Figure 14 – Apatite spot analyses of sample s1Da indicating the analysed spots with the obtained $^{87}Sr/^{86}Sr_{468}$ values

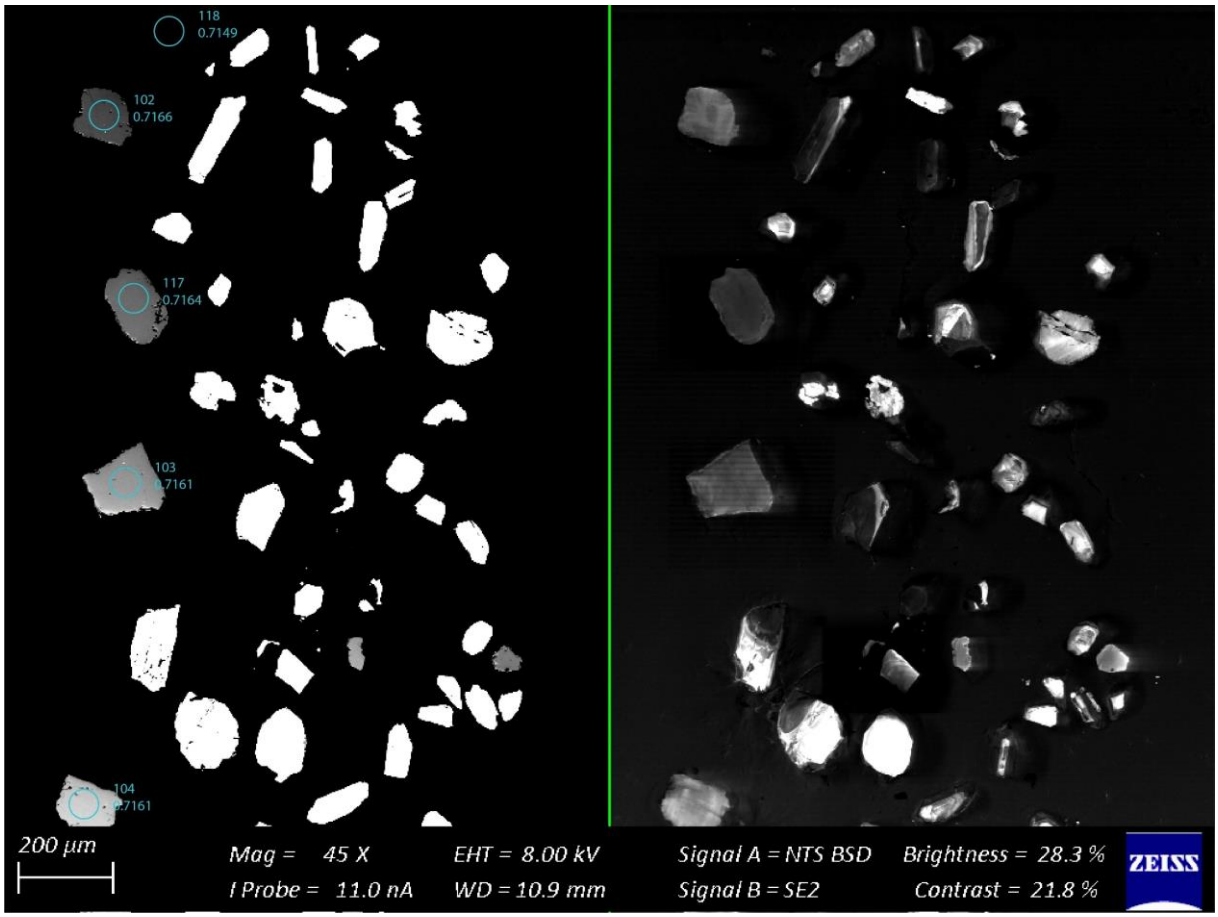

Figure 15 – Apatite spot analyses of sample s1F indicating the analysed spots with the obtained $^{87}Sr/^{86}Sr_{468}$ values

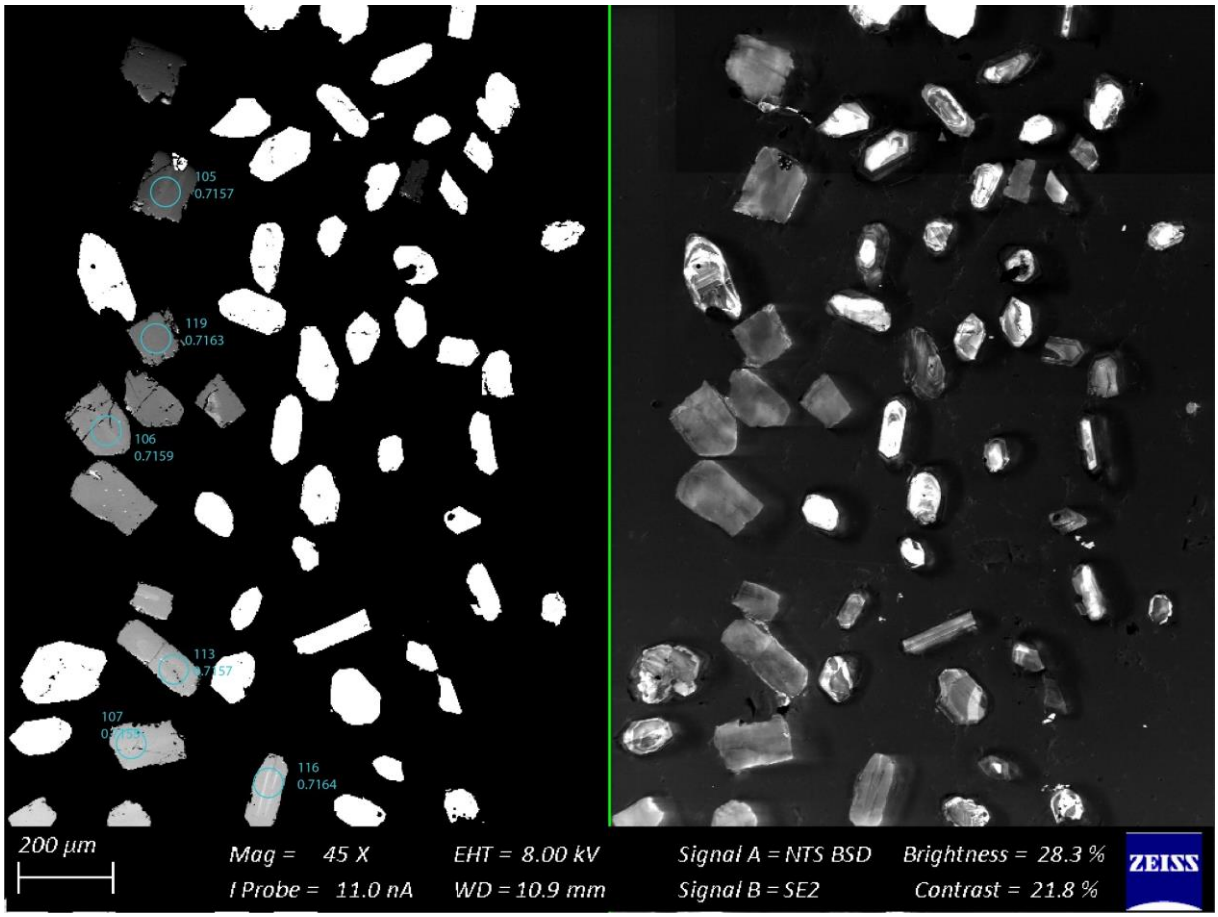

Figure 16 – Apatite spot analyses of sample s1F indicating the analysed spots with the obtained $^{87}Sr/^{86}Sr_{468}$ values

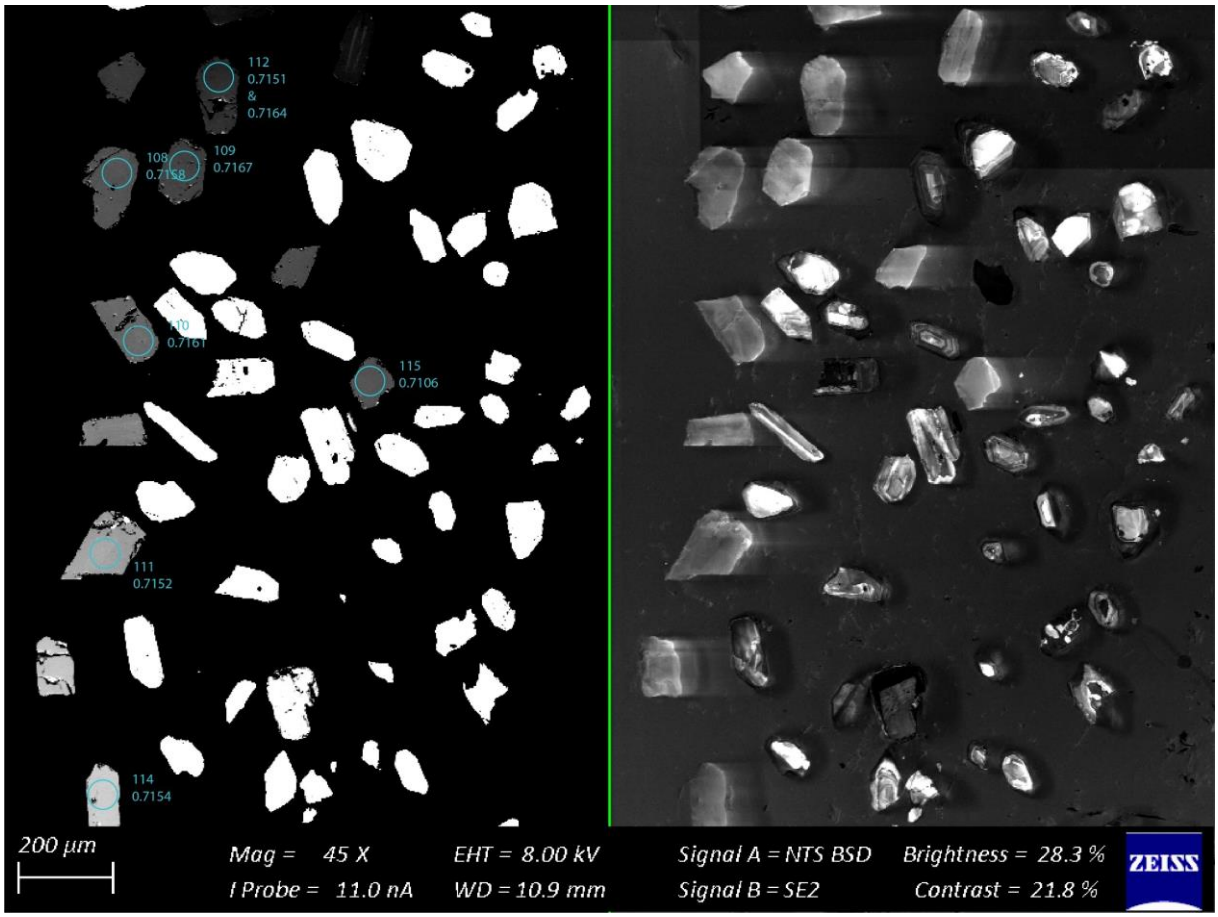

Figure 17 – Apatite spot analyses of sample s1F indicating the analysed spots with the obtained $^{87}Sr/^{86}Sr_{468}$ values

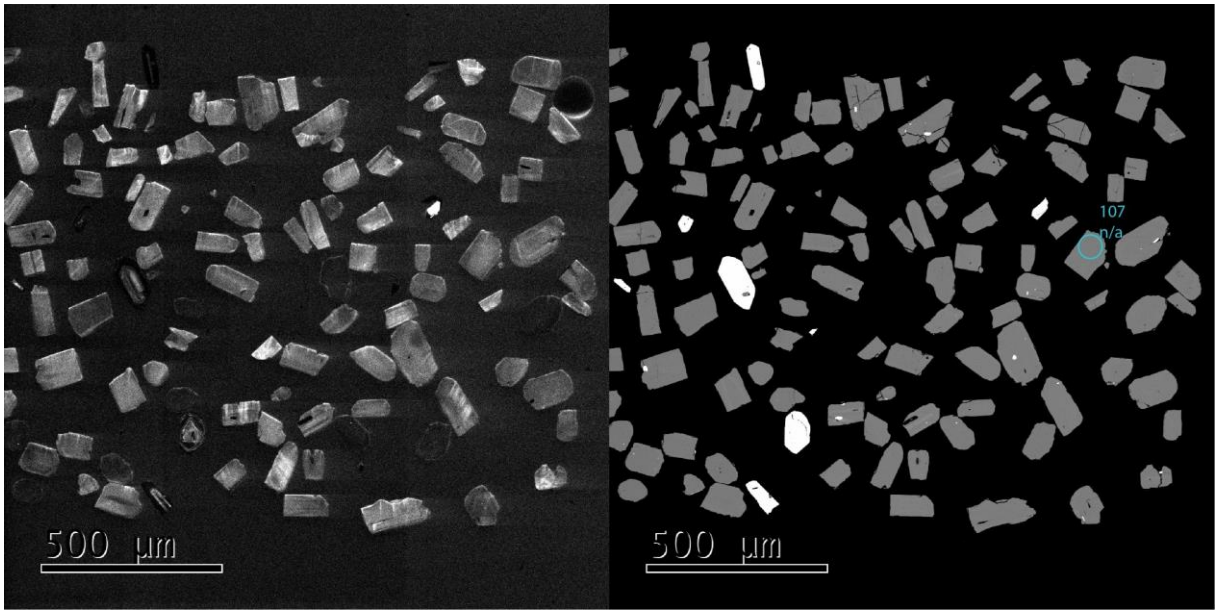

Figure 18 – Apatite εNd spot analyses of sample s1H indicating the analysed spots with the obtained εNd_{468} values

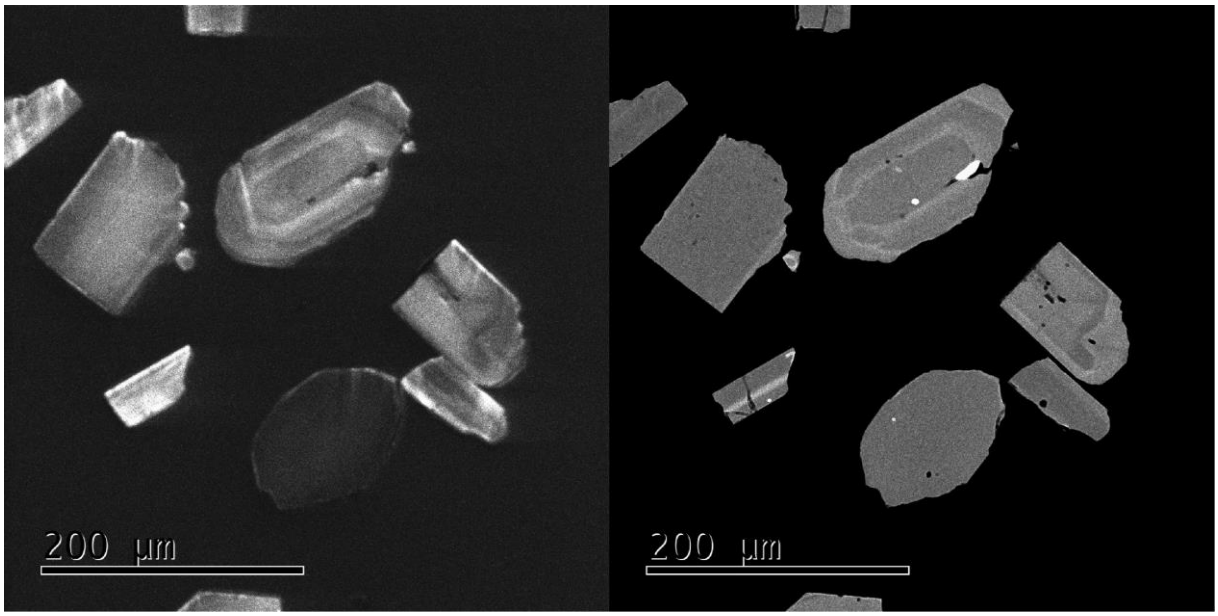

Figure 19 – Apatite εNd spot analyses of sample s1H indicating the analysed spots with the obtained εNd_{468} values

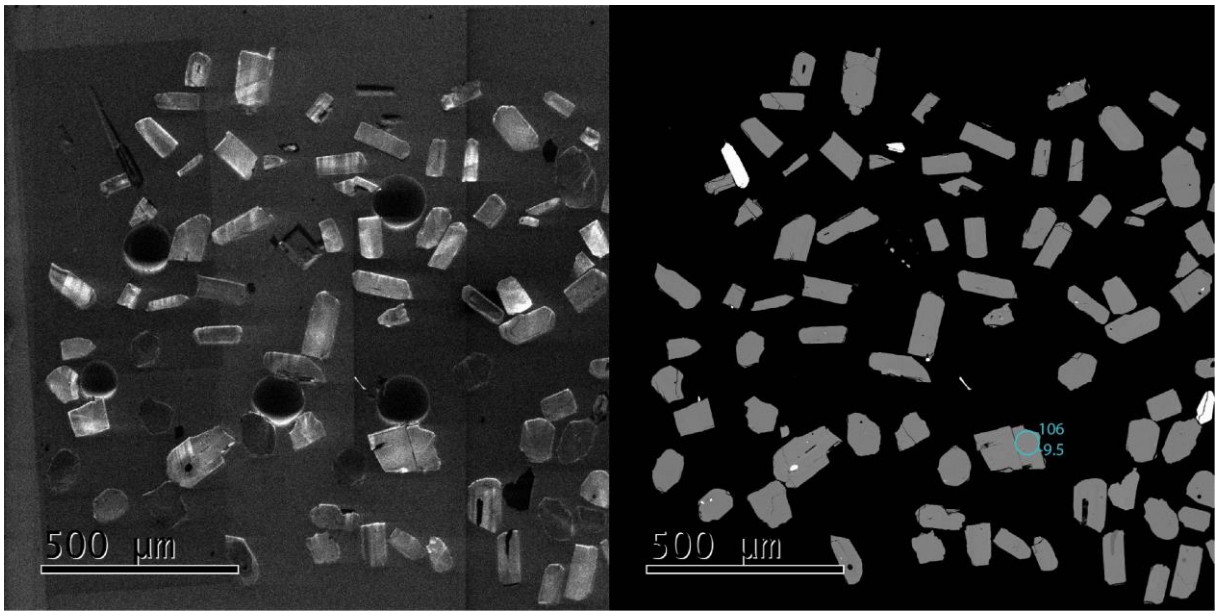

Figure 20 – Apatite εNd spot analyses of sample s1H indicating the analysed spots with the obtained εNd_{468} values

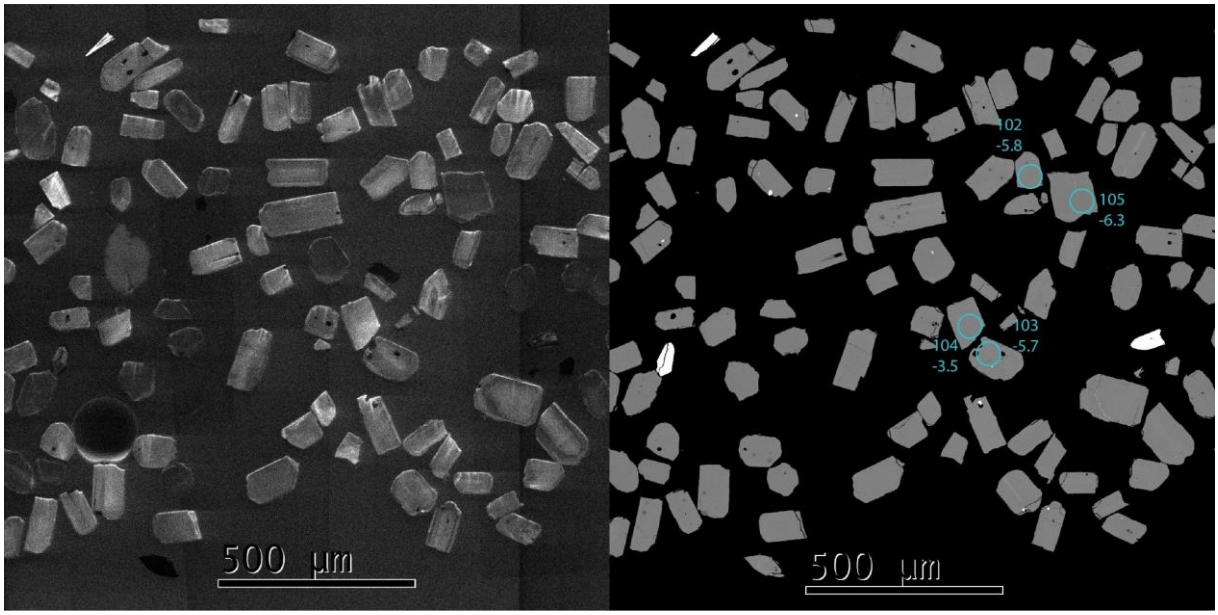

Figure 21 – Apatite εNd spot analyses of sample s1H indicating the analysed spots with the obtained εNd_{468} values

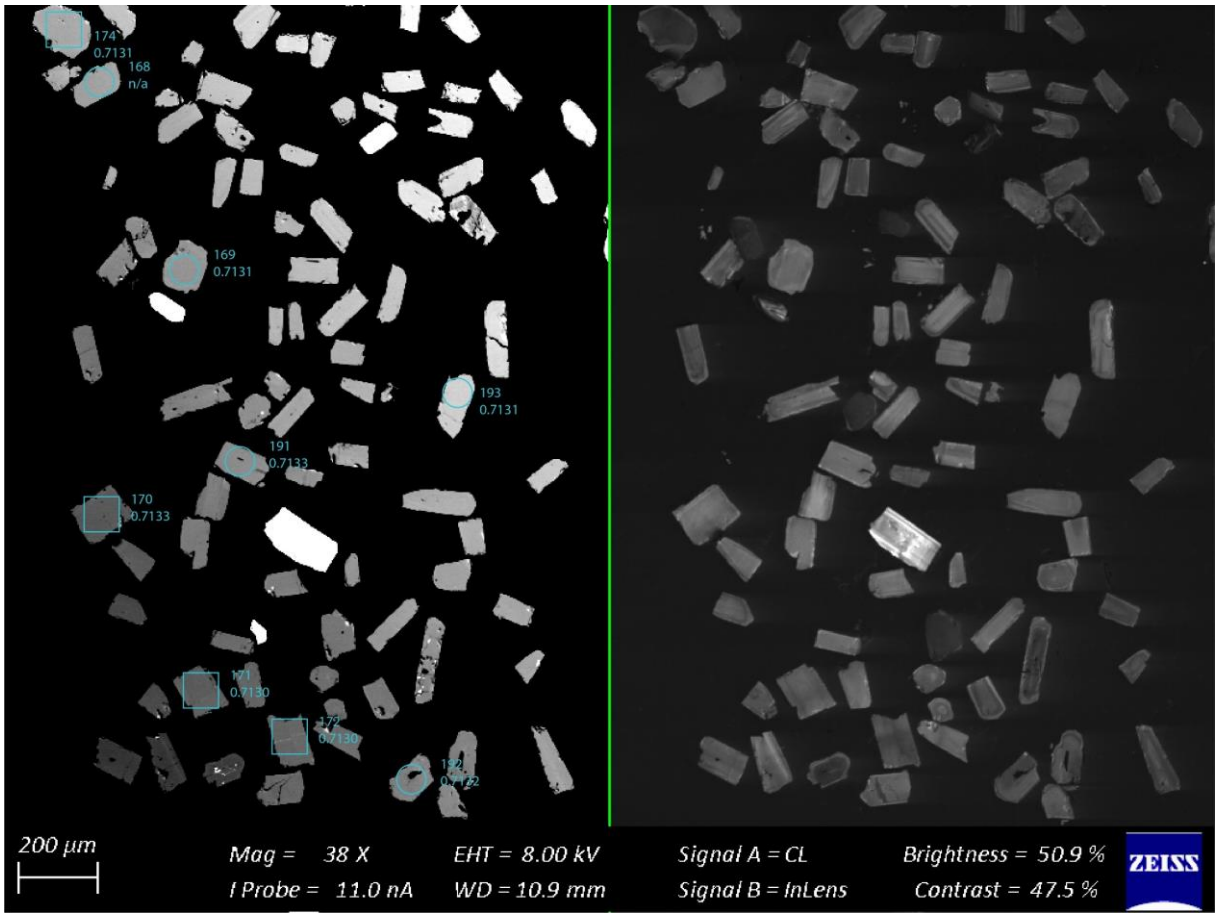

Figure 22 – Apatite spot analyses of sample s1H indicating the analysed spots with the obtained $^{87}Sr/^{86}Sr_{468}$ values

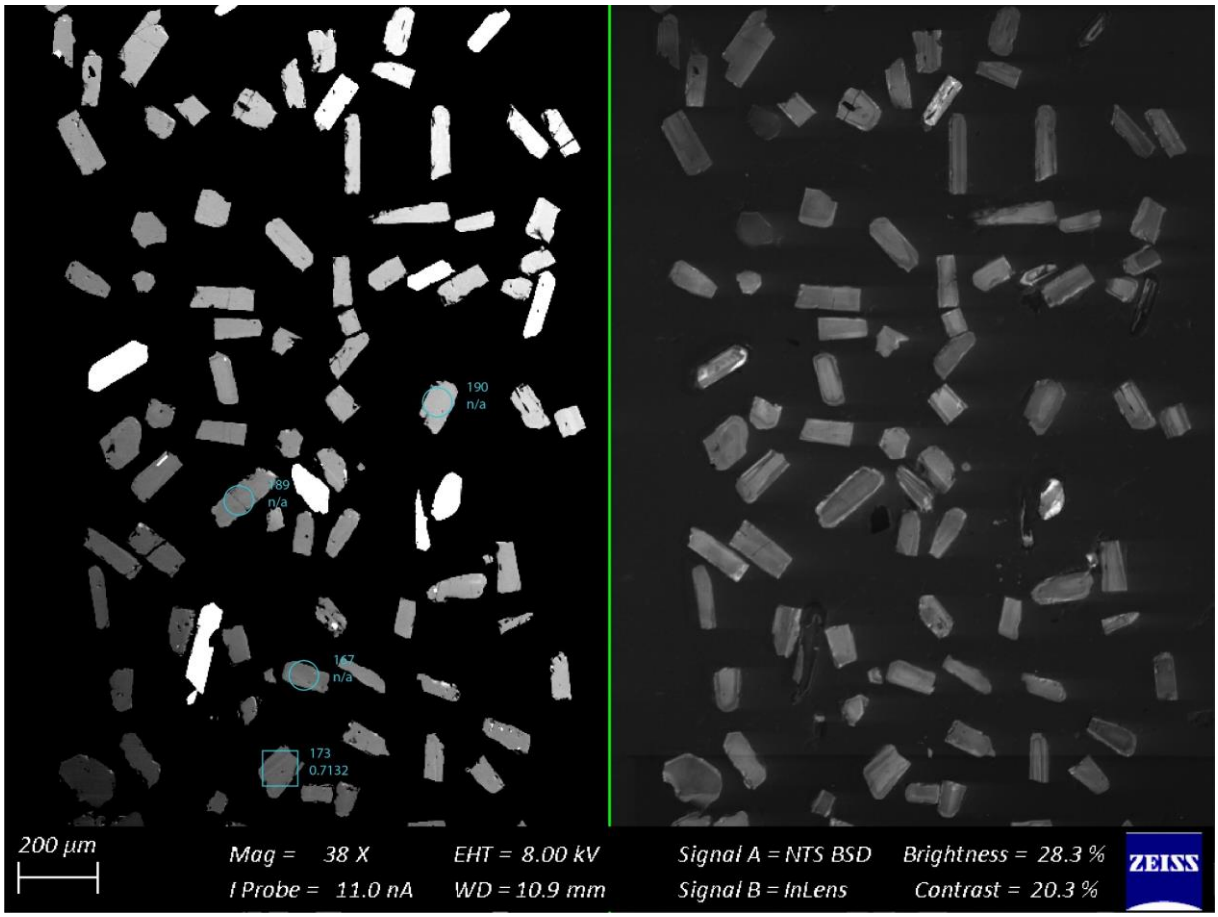

Figure 23 – Apatite spot analyses of sample s1H indicating the analysed spots with the obtained $^{87}Sr/^{86}Sr_{468}$ values

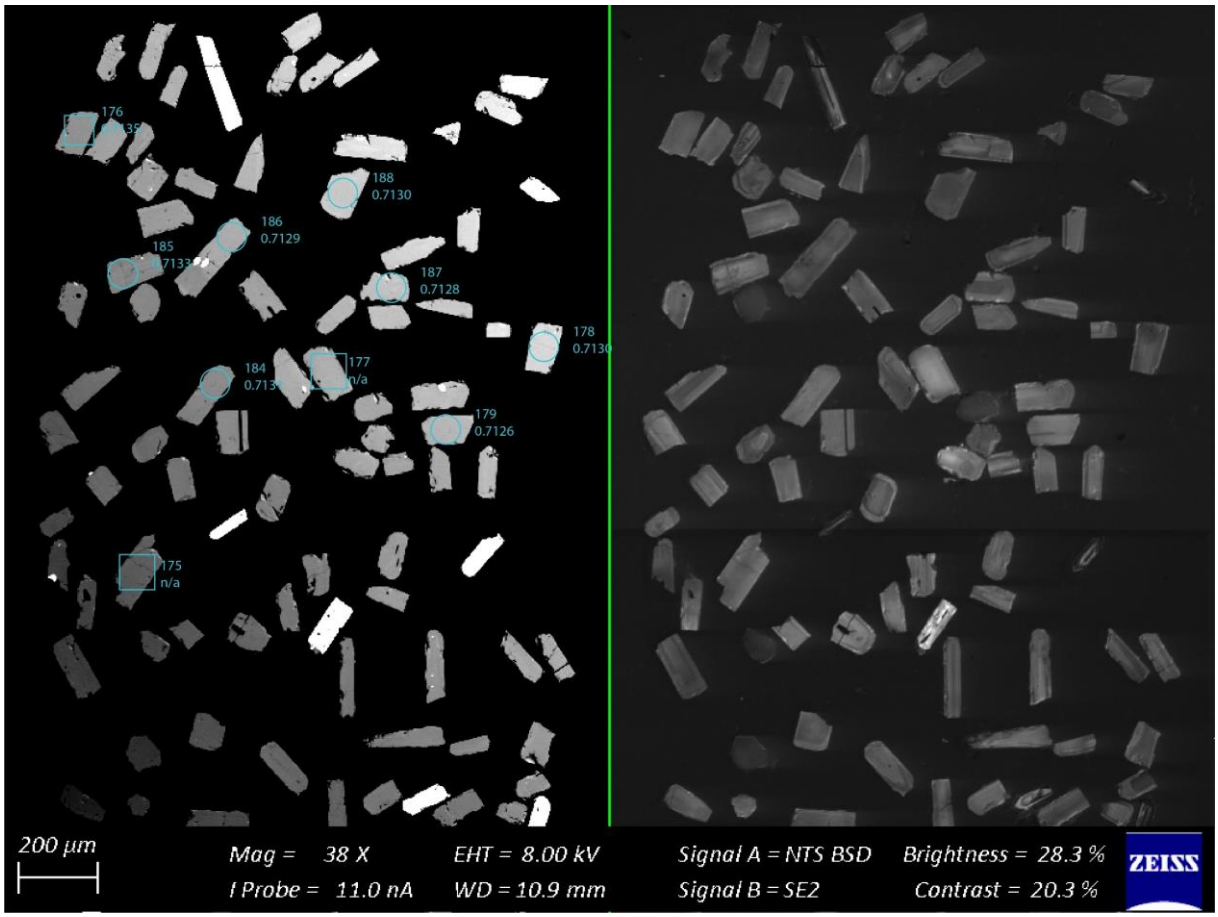

Figure 24 – Apatite spot analyses of sample s1H indicating the analysed spots with the obtained $^{87}Sr/^{86}Sr_{468}$ values

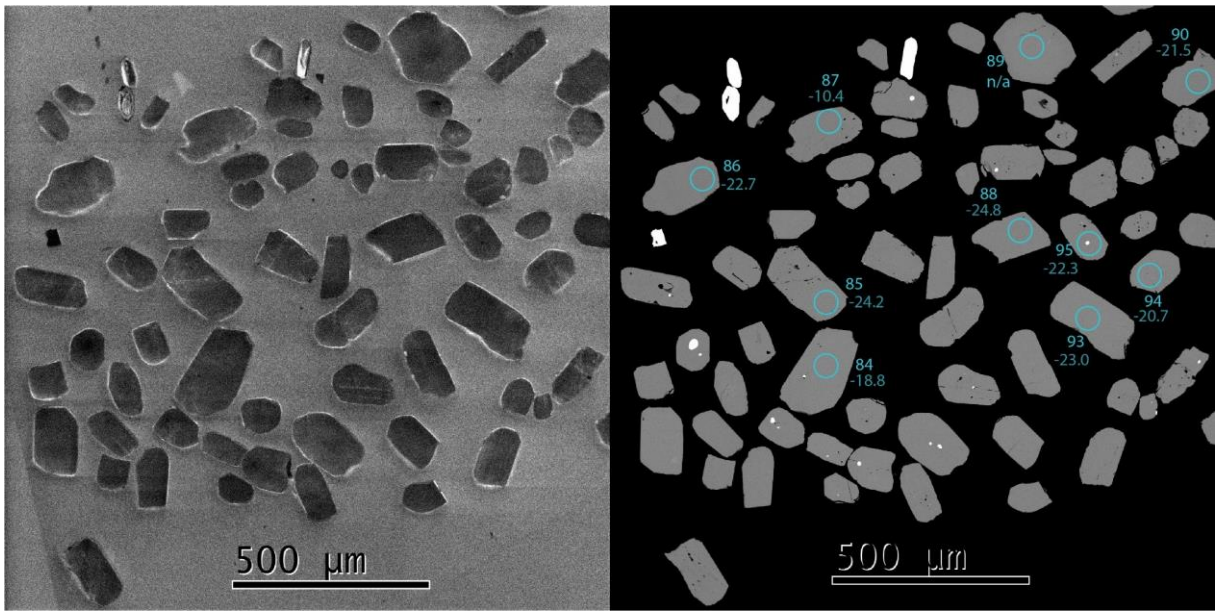

Figure 25 – Apatite εNd spot analyses of sample s2A indicating the analysed spots with the obtained εNd_{468} values

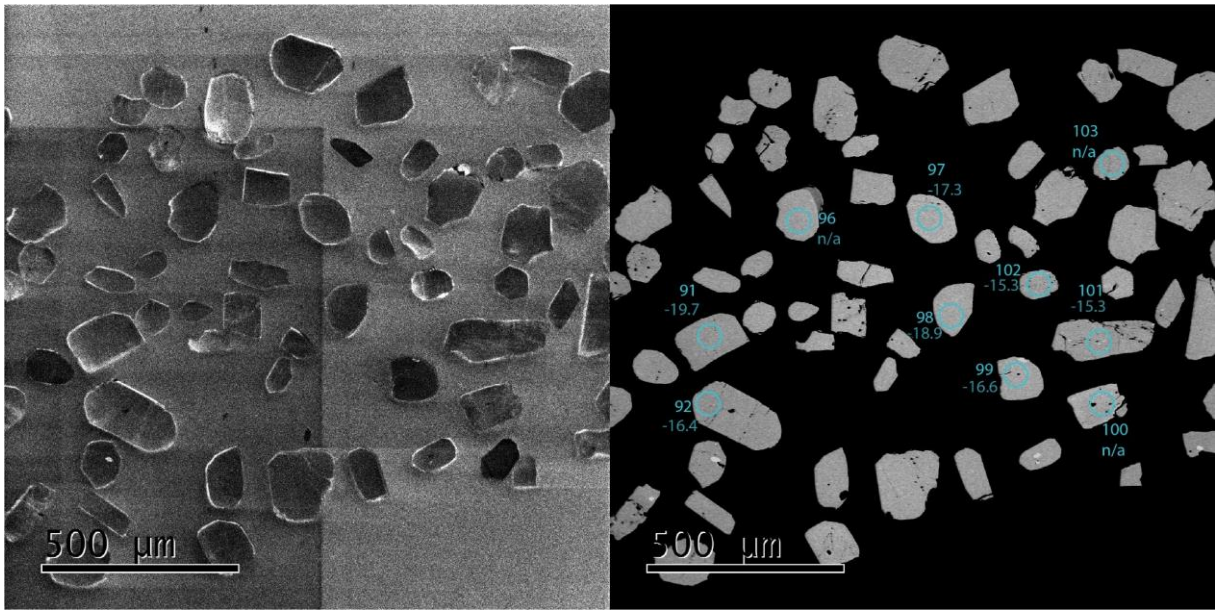

Figure 26 – Apatite εNd spot analyses of sample s2A indicating the analysed spots with the obtained εNd_{468} values

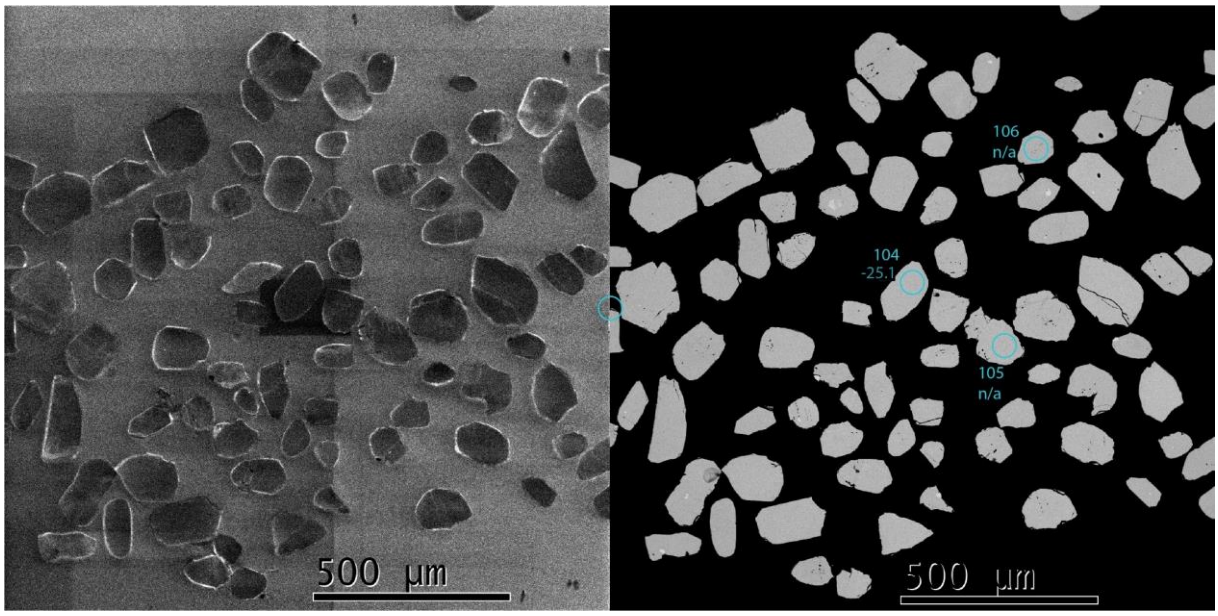

Figure 27 – Apatite εNd spot analyses of sample s2A indicating the analysed spots with the obtained εNd_{468} values

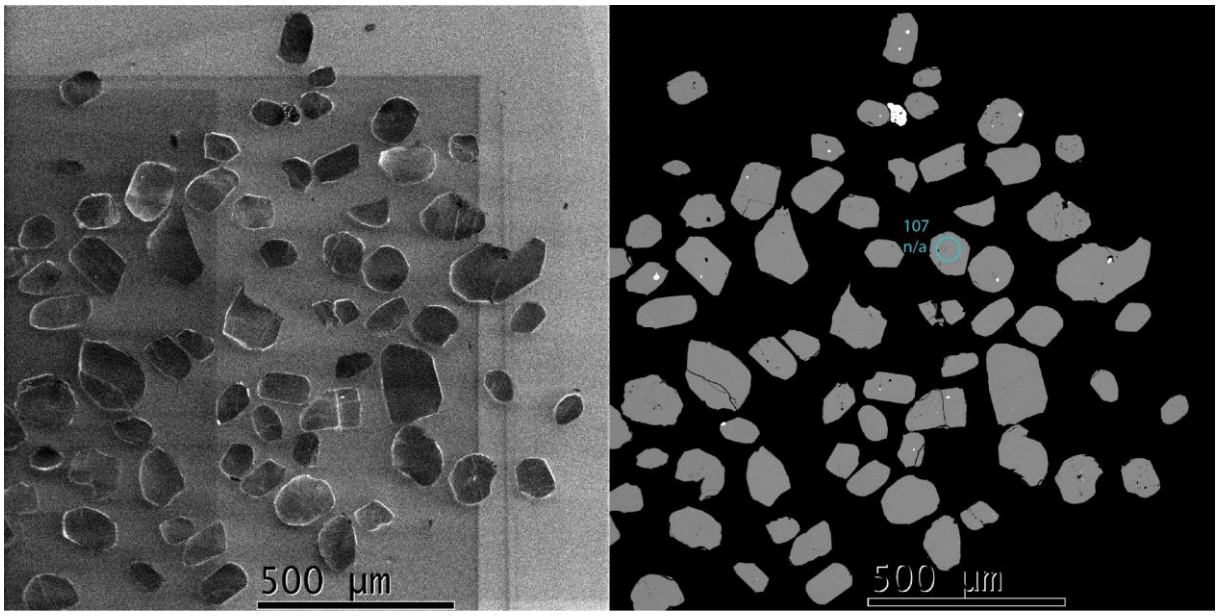

Figure 28 – Apatite εNd spot analyses of sample s2A indicating the analysed spots with the obtained εNd_{468} values

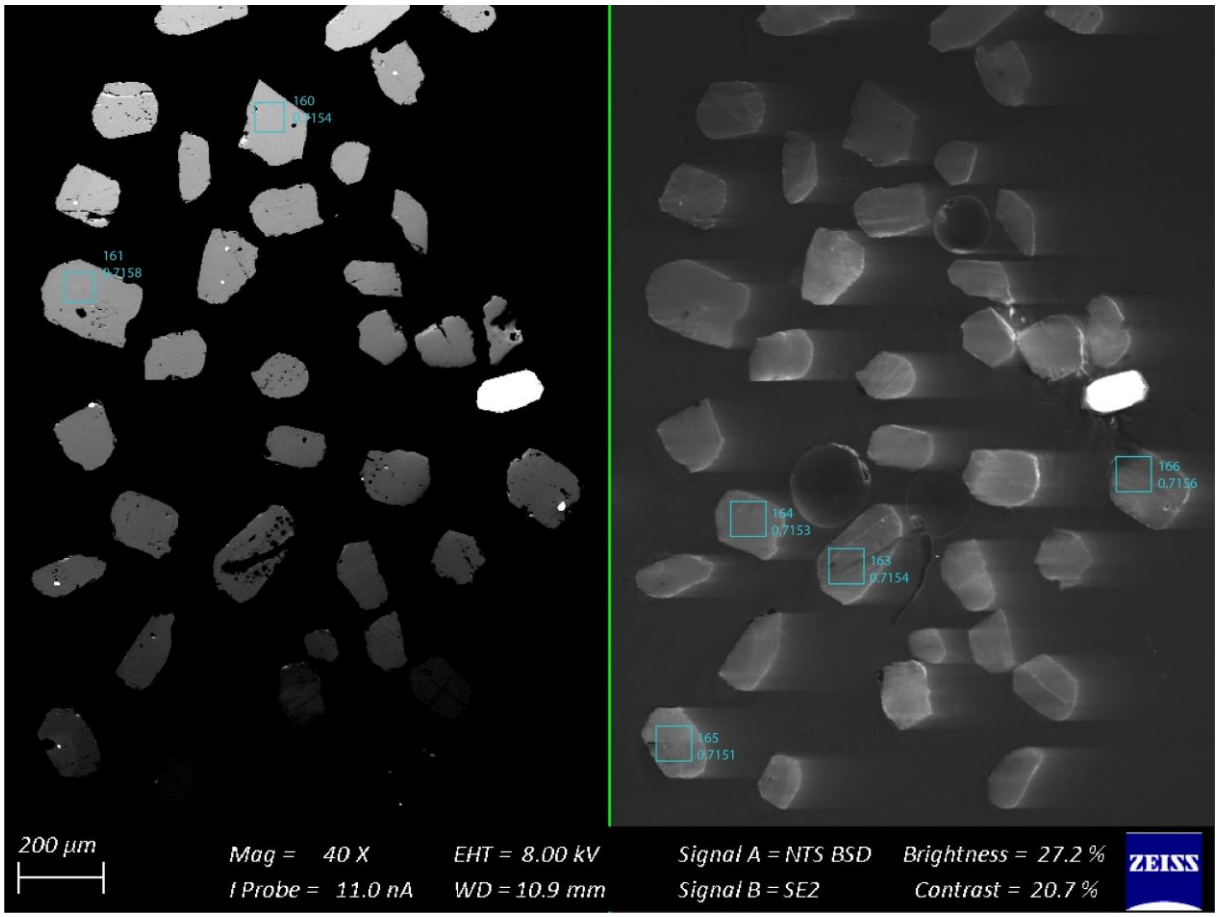

Figure 29 – Apatite spot analyses of sample s2A indicating the analysed spots with the obtained $^{87}Sr/^{86}Sr_{468}$ values

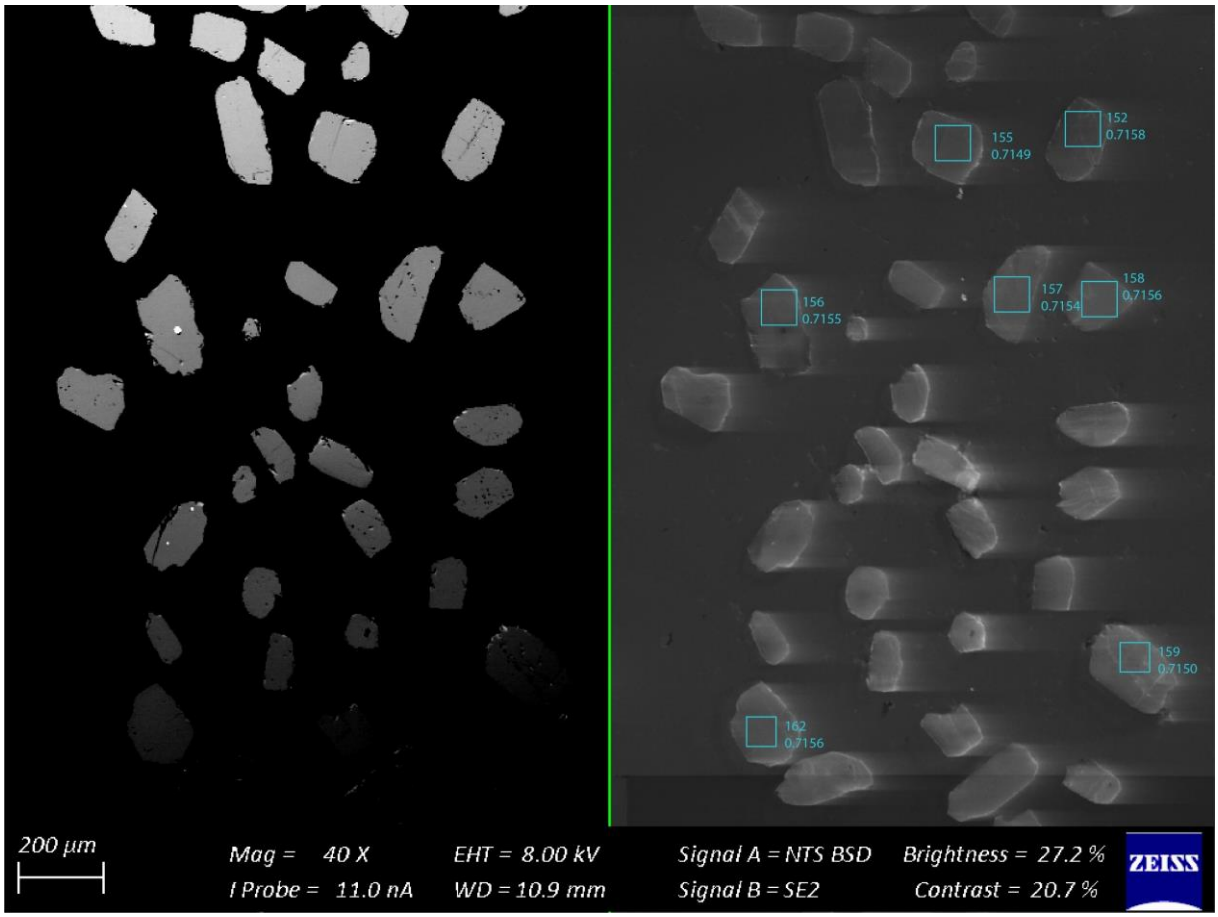

Figure 30 – Apatite spot analyses of sample s2A indicating the analysed spots with the obtained $^{87}Sr/^{86}Sr_{468}$ values

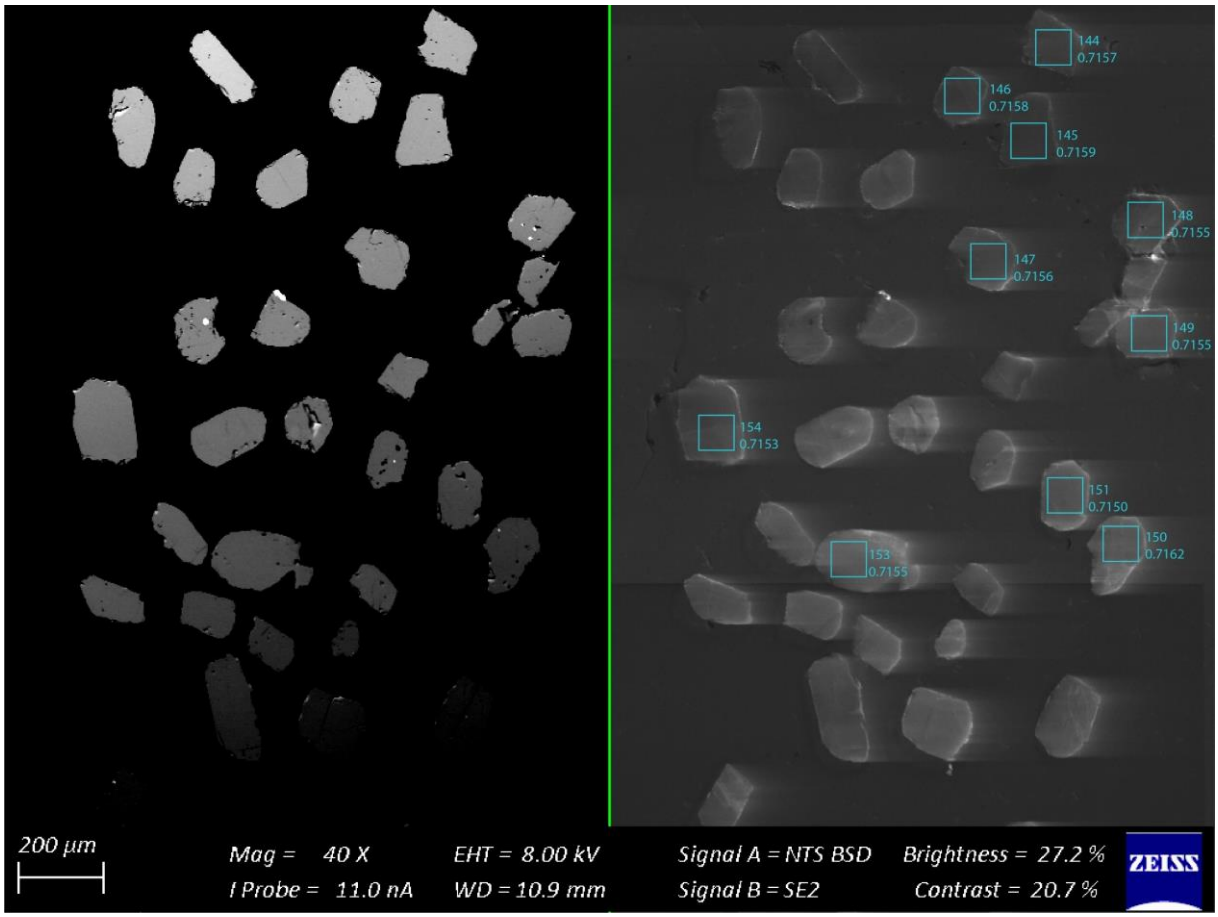

Figure 31 – Apatite spot analyses of sample s2A indicating the analysed spots with the obtained $^{87}Sr/^{86}Sr_{468}$ values

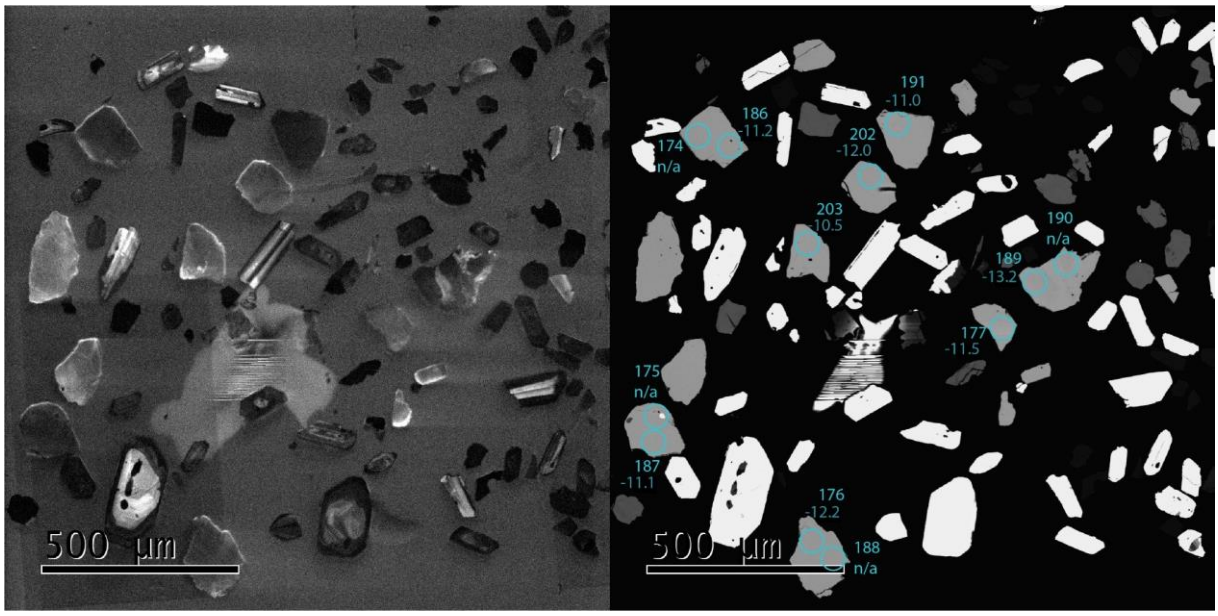

Figure 32 – Apatite εNd spot analyses of sample s2B indicating the analysed spots with the obtained εNd_{468} values

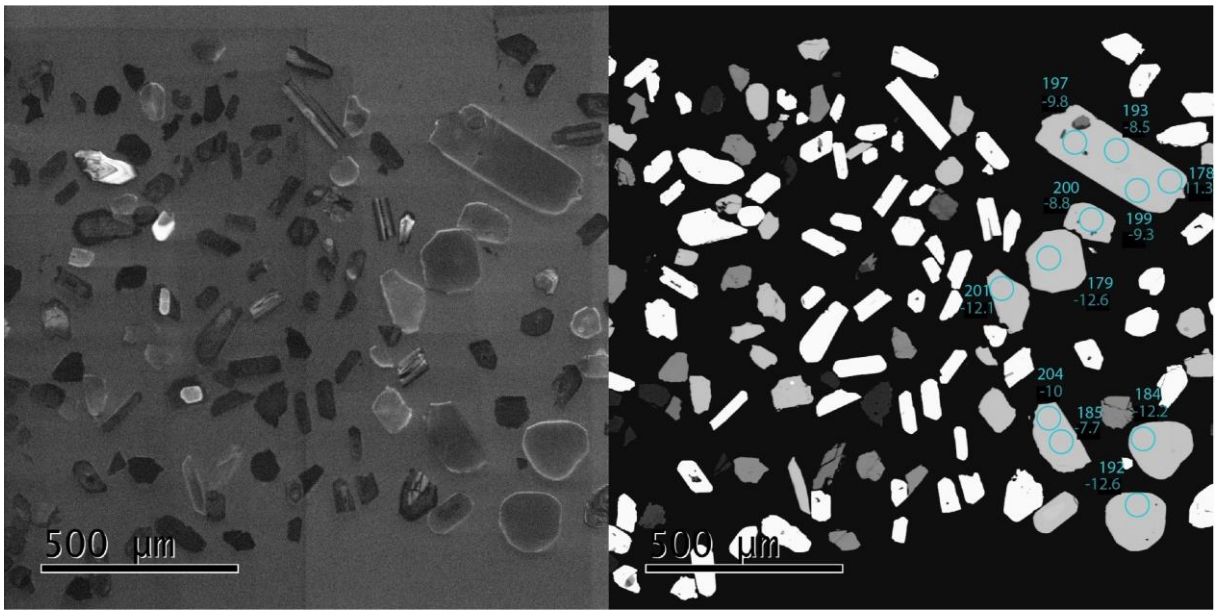

Figure 33 – Apatite εNd spot analyses of sample s2B indicating the analysed spots with the obtained εNd_{468} values

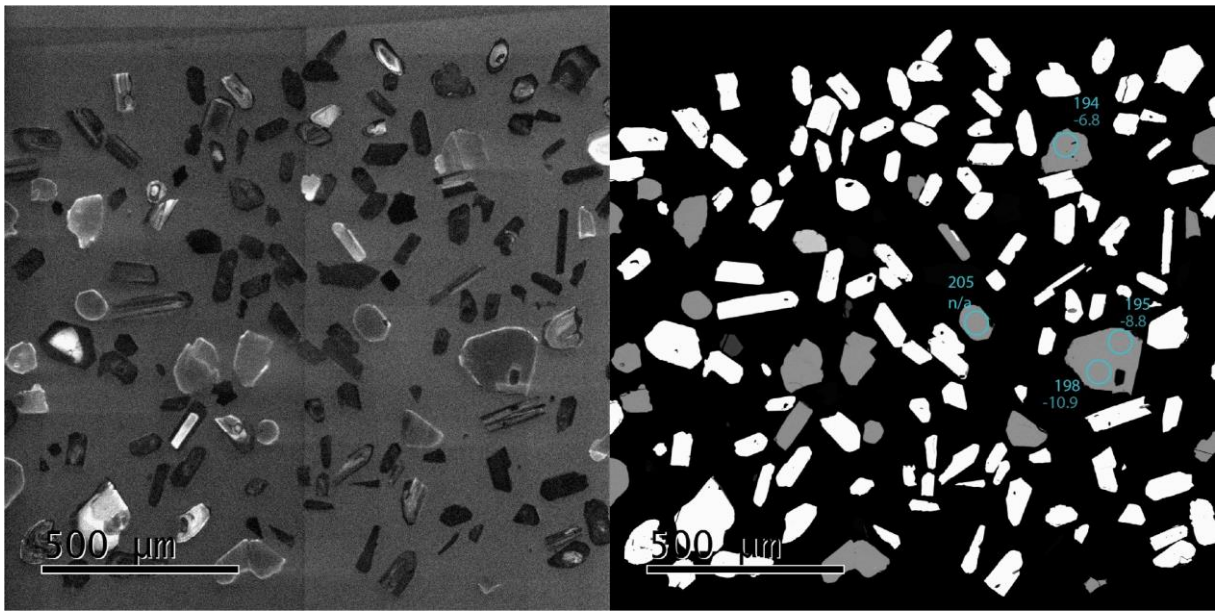

Figure 34 – Apatite εNd spot analyses of sample s2B indicating the analysed spots with the obtained εNd_{468} values

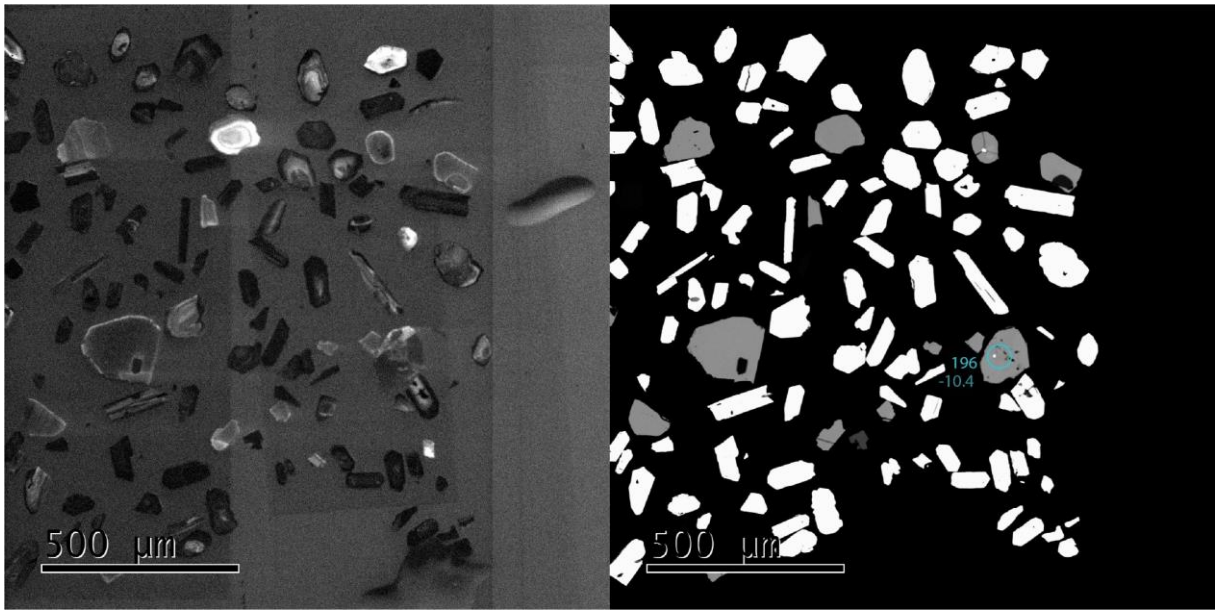

Figure 35 – Apatite εNd spot analyses of sample s2B indicating the analysed spots with the obtained εNd_{468} values

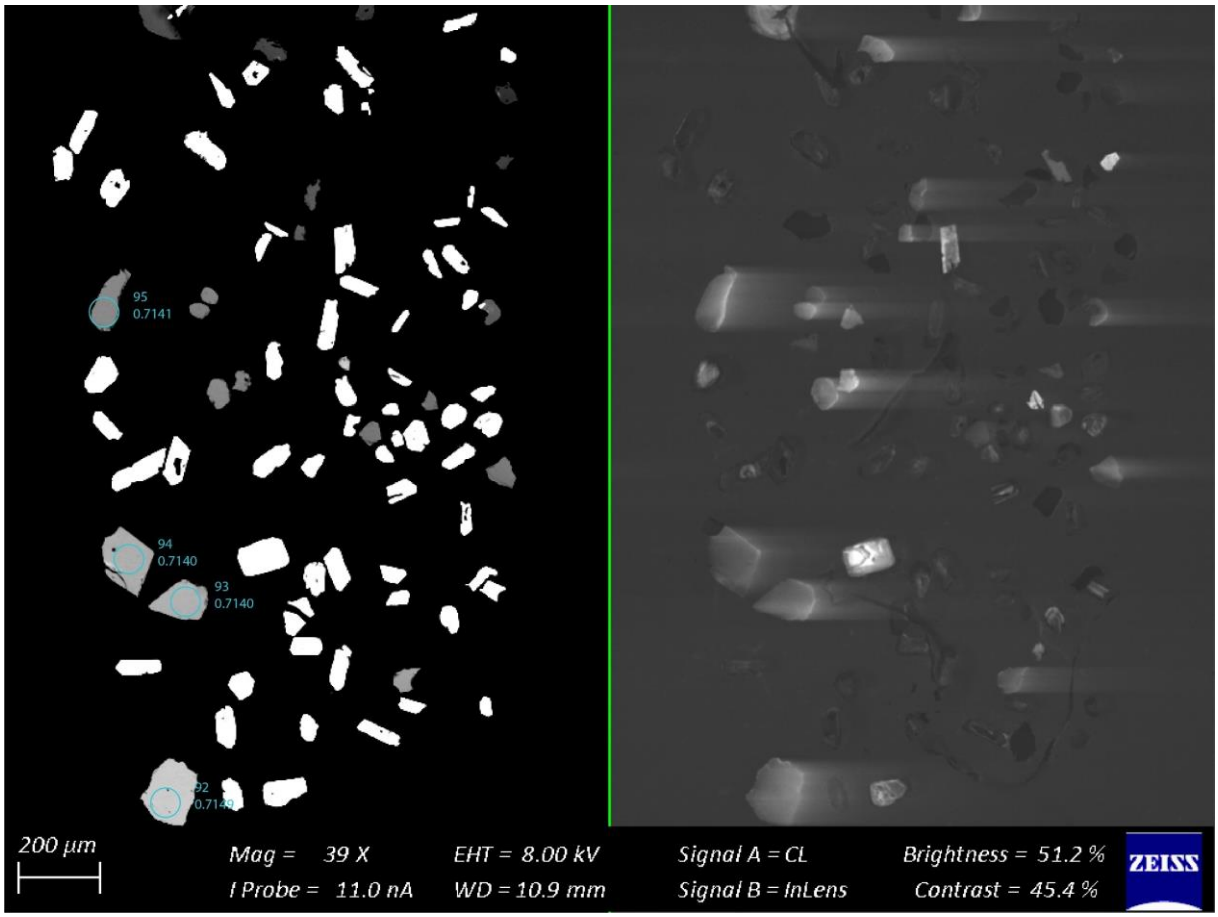

Figure 36 – Apatite spot analyses of sample s2B indicating the analysed spots with the obtained $^{87}Sr/^{86}Sr_{468}$ values

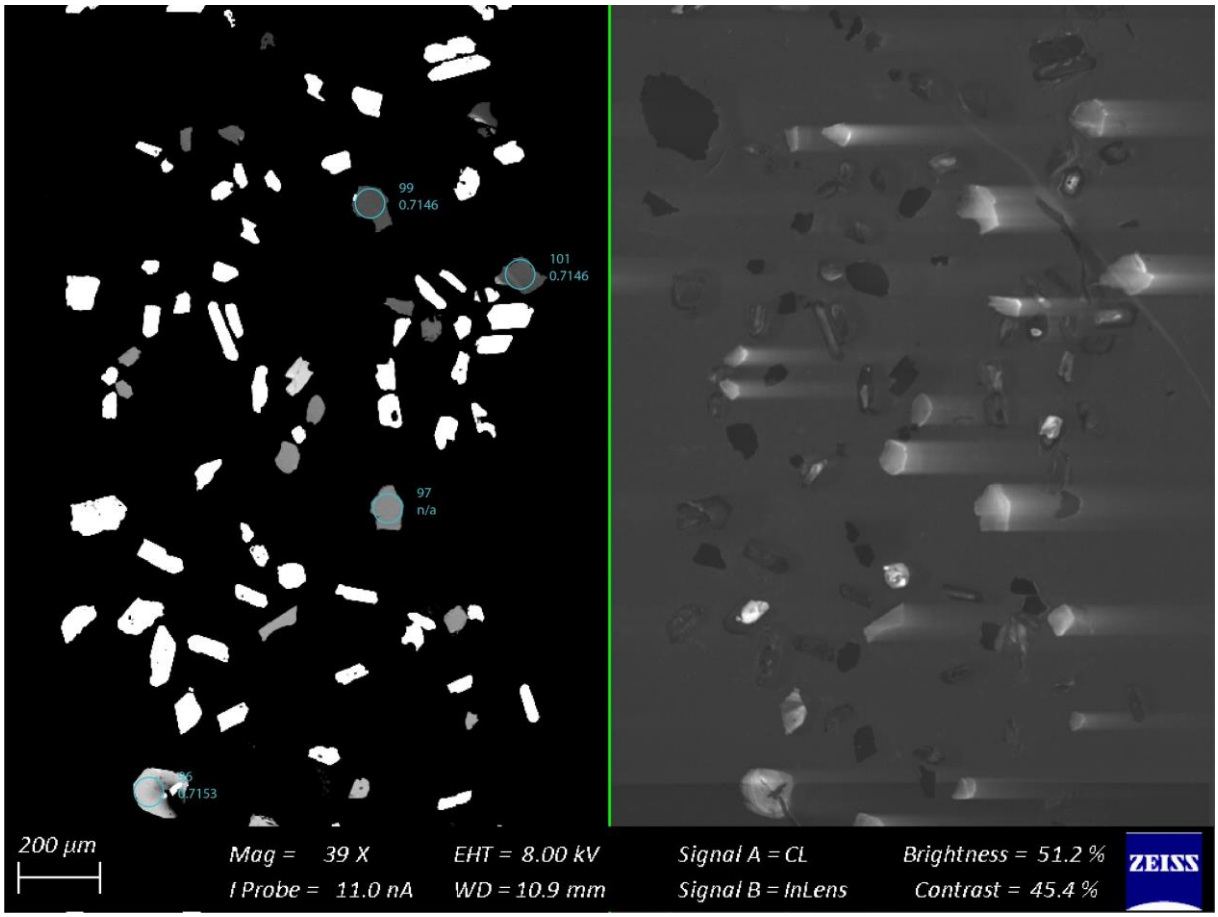

Figure 37 – Apatite spot analyses of sample s2B indicating the analysed spots with the obtained $^{87}Sr/^{86}Sr_{468}$ values

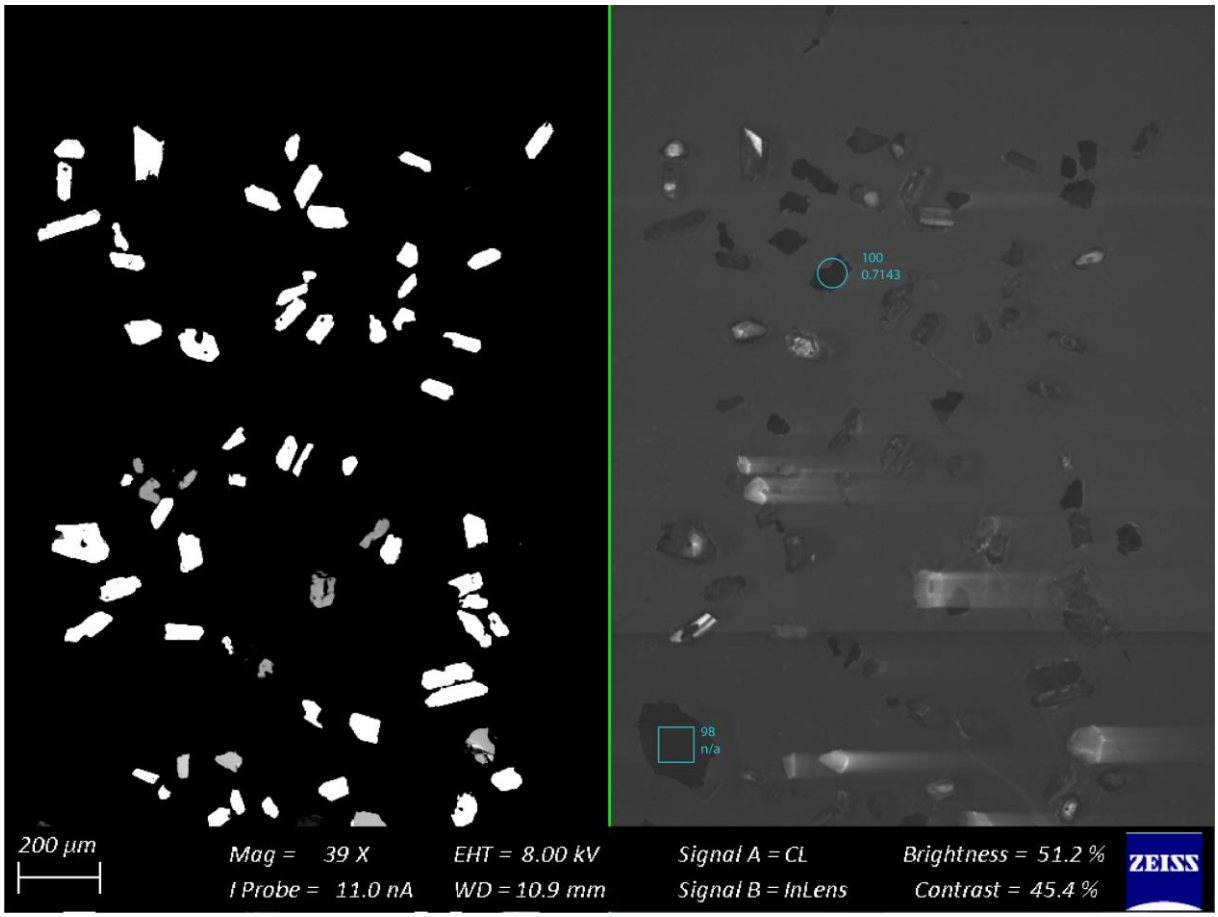

Figure 38 – Apatite spot analyses of sample s2B indicating the analysed spots with the obtained $^{87}Sr/^{86}Sr_{468}$ values

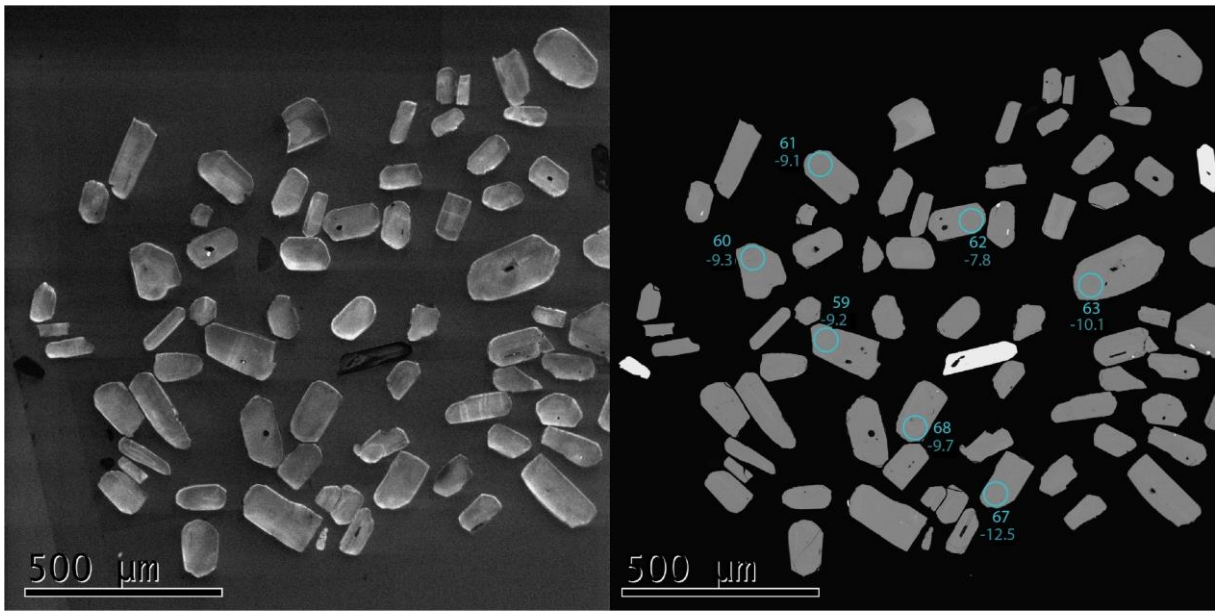

Figure 39 – Apatite εNd spot analyses of sample s3B indicating the analysed spots with the obtained εNd_{468} values

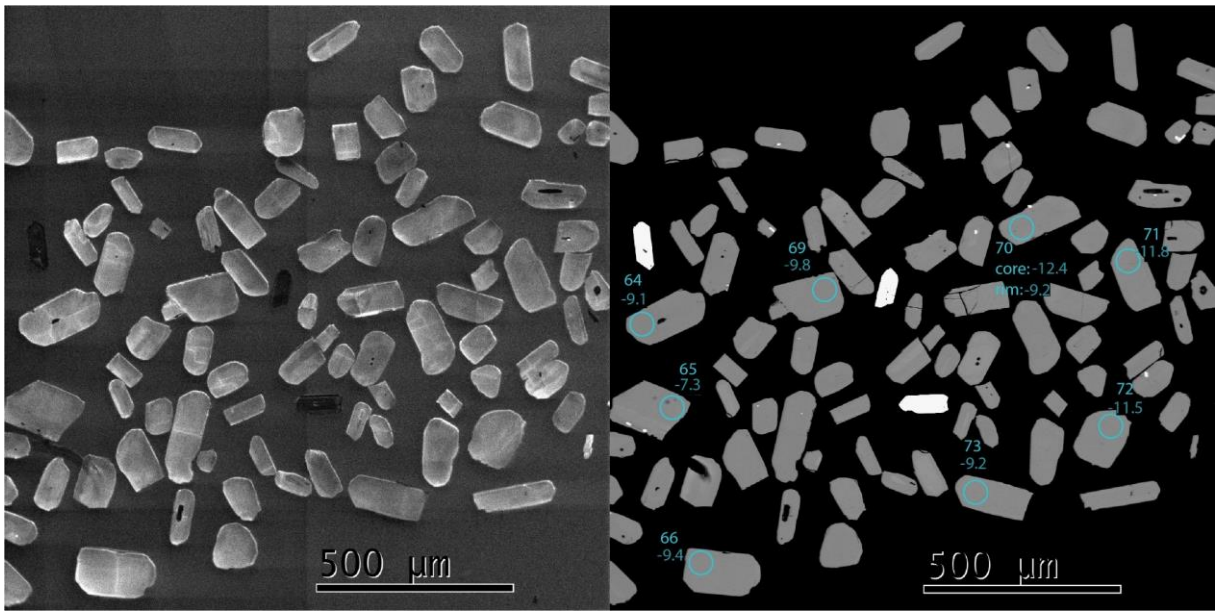

Figure 40 – Apatite εNd spot analyses of sample s3B indicating the analysed spots with the obtained εNd_{468} values

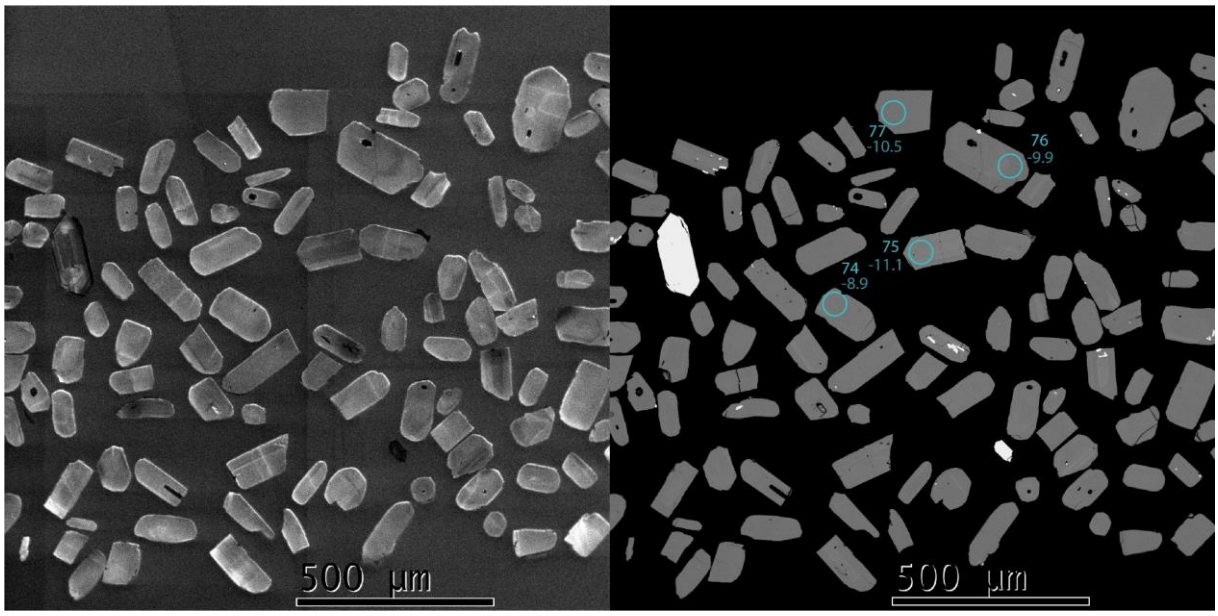

Figure 41 – Apatite εNd spot analyses of sample s3B indicating the analysed spots with the obtained εNd_{468} values

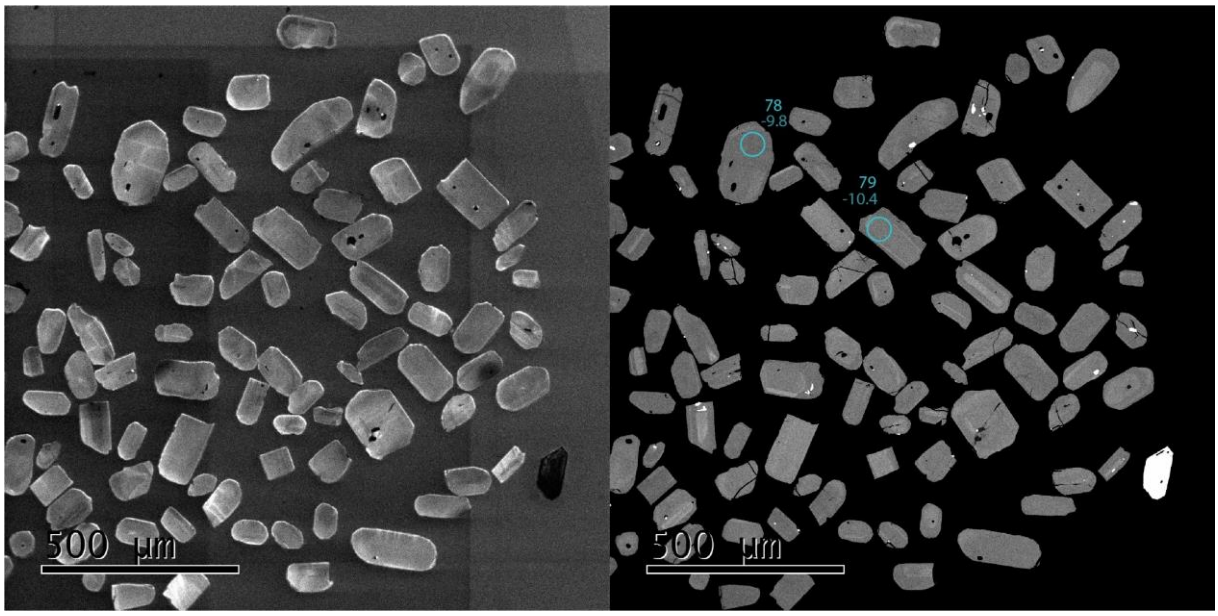

Figure 42 – Apatite εNd spot analyses of sample s3B indicating the analysed spots with the obtained εNd_{468} values

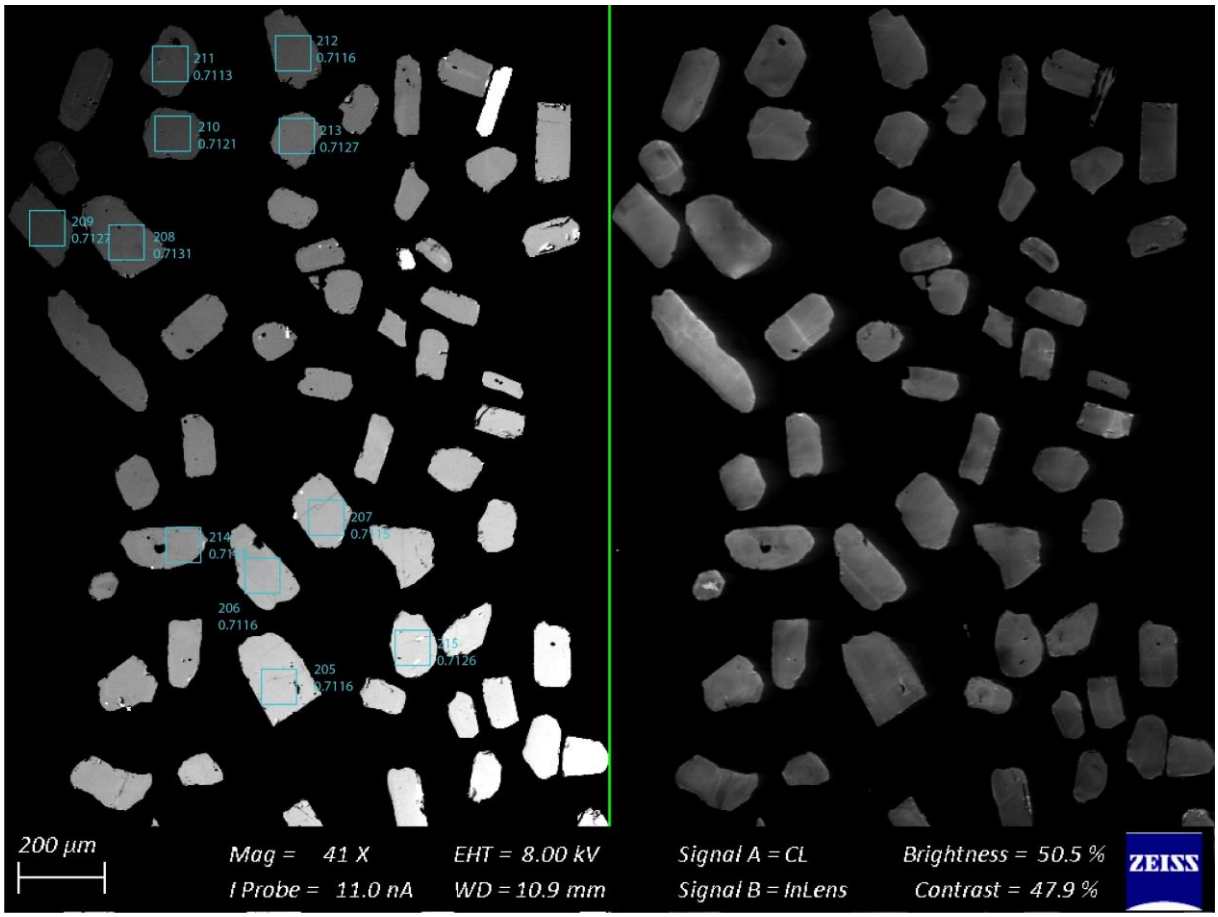

Figure 43 – Apatite spot analyses of sample s3B indicating the analysed spots with the obtained $^{87}Sr/^{86}Sr_{468}$ values

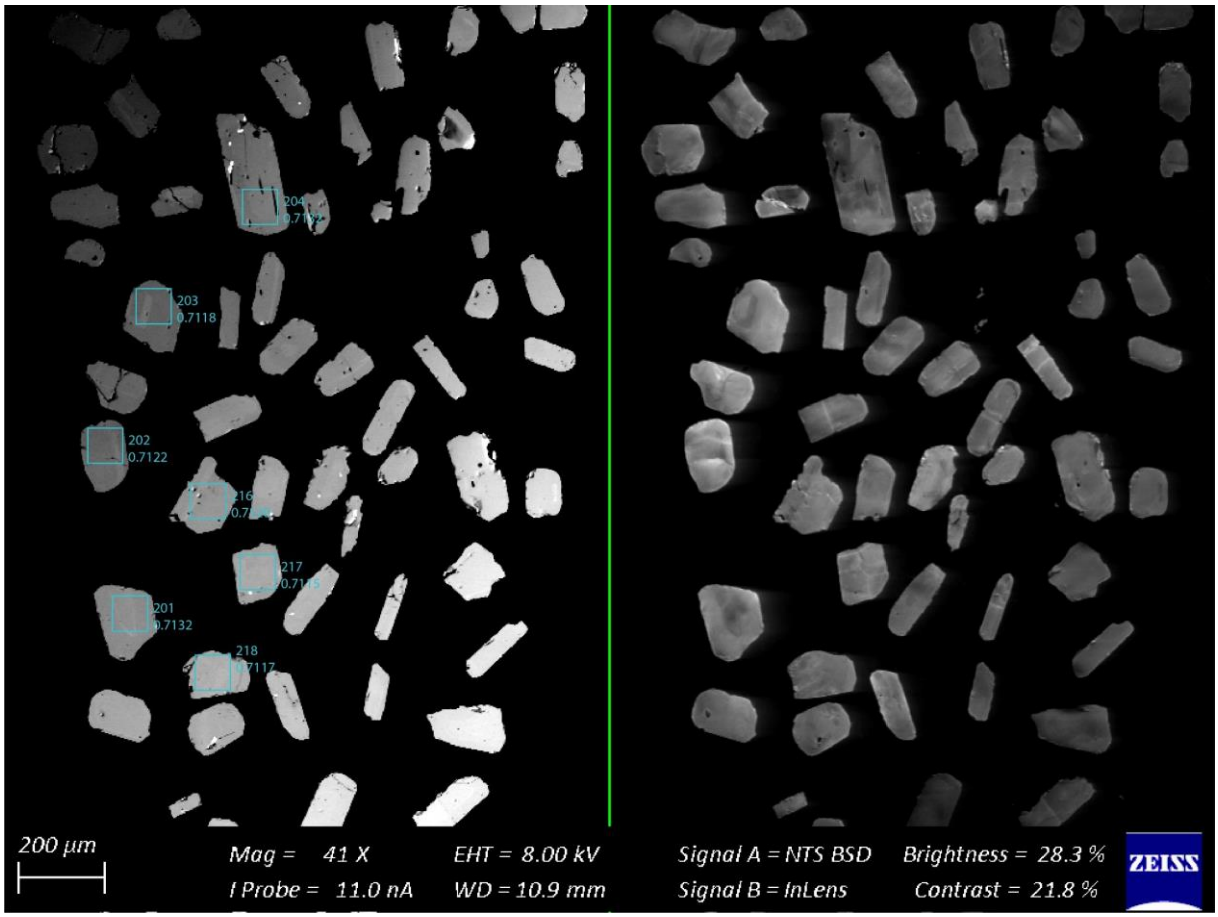

Figure 44 – Apatite spot analyses of sample s3B indicating the analysed spots with the obtained $^{87}Sr/^{86}Sr_{468}$ values

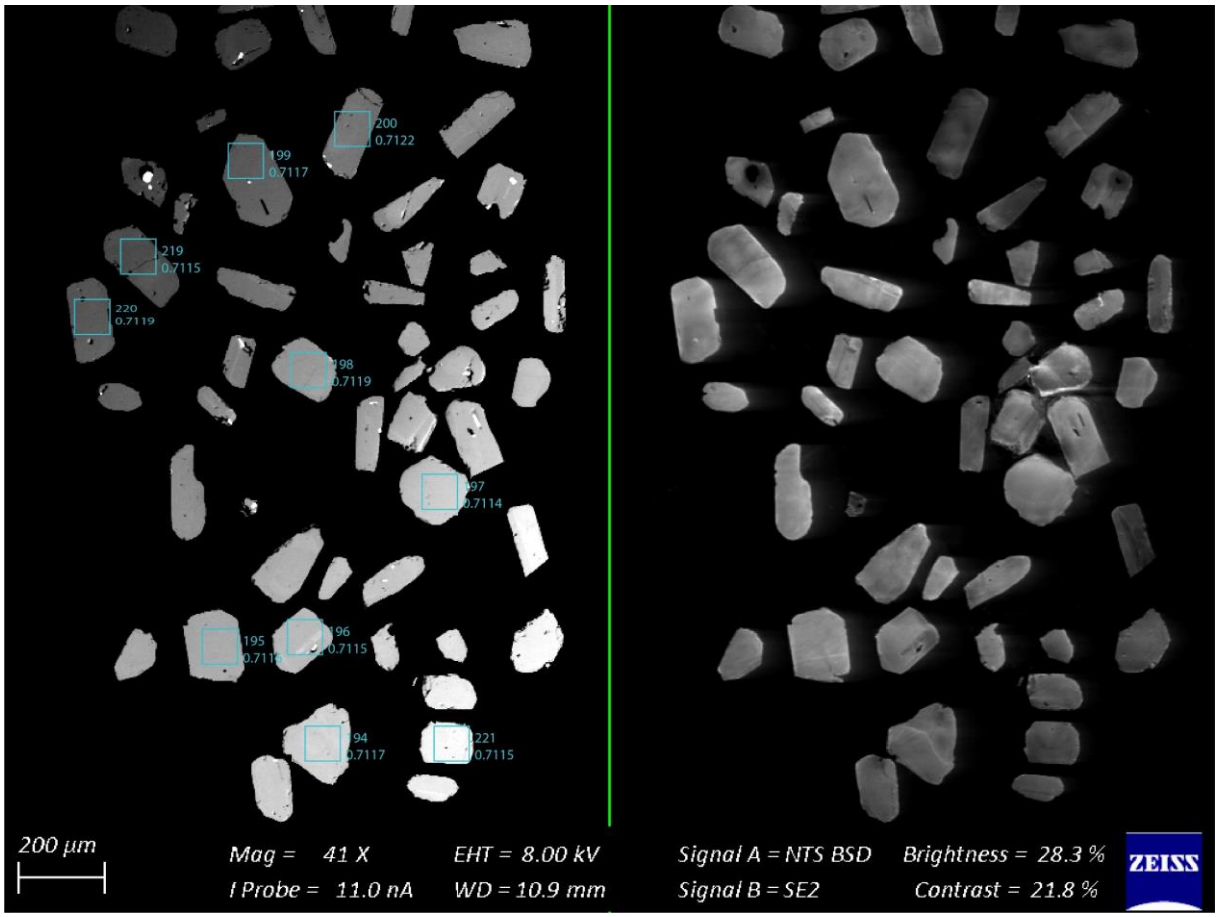

Figure 45 – Apatite spot analyses of sample s3B indicating the analysed spots with the obtained $^{87}Sr/^{86}Sr_{468}$ values

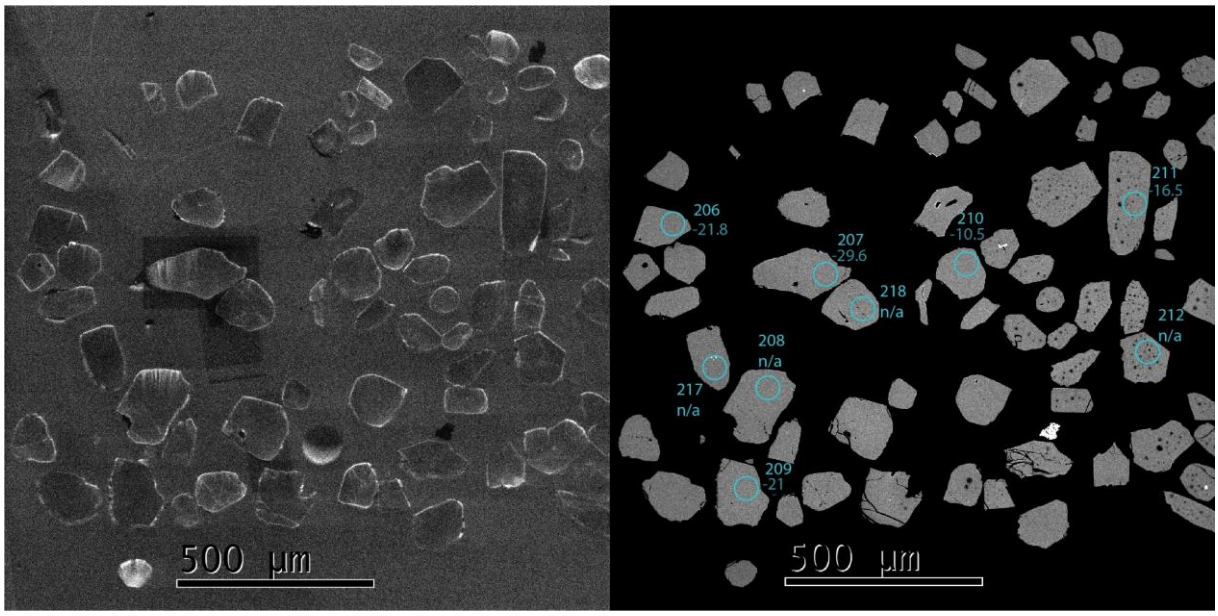

Figure 46 – Apatite εNd spot analyses of sample s4D indicating the analysed spots with the obtained εNd_{468} values

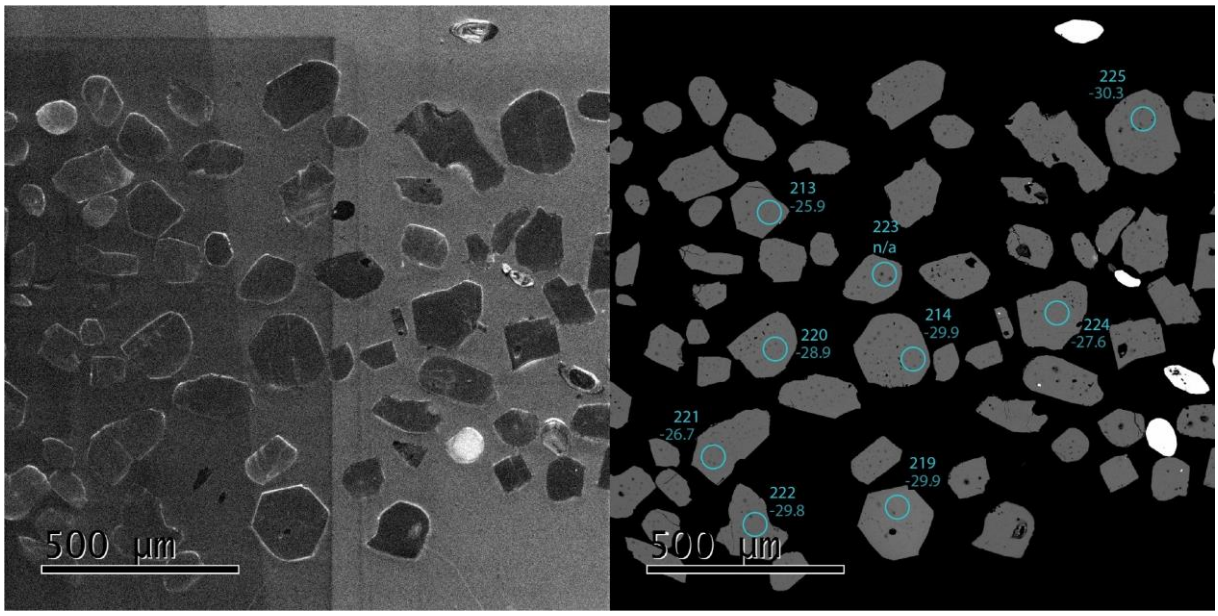

Figure 47 – Apatite εNd spot analyses of sample s4D indicating the analysed spots with the obtained εNd_{468} values

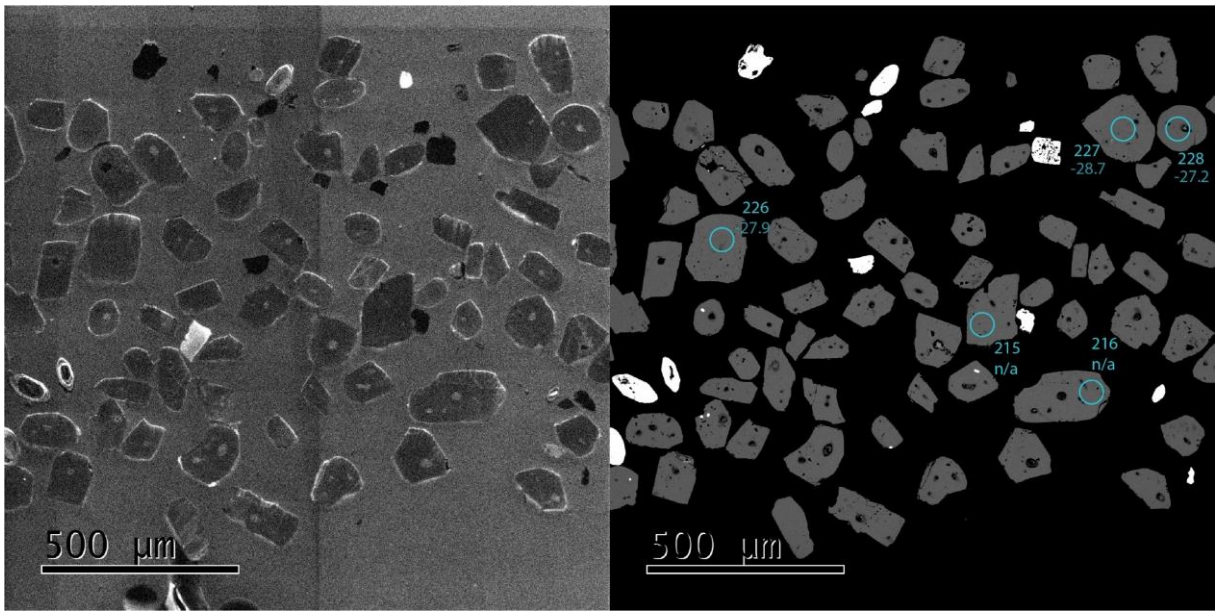

Figure 48 – Apatite εNd spot analyses of sample s4D indicating the analysed spots with the obtained εNd_{468} values

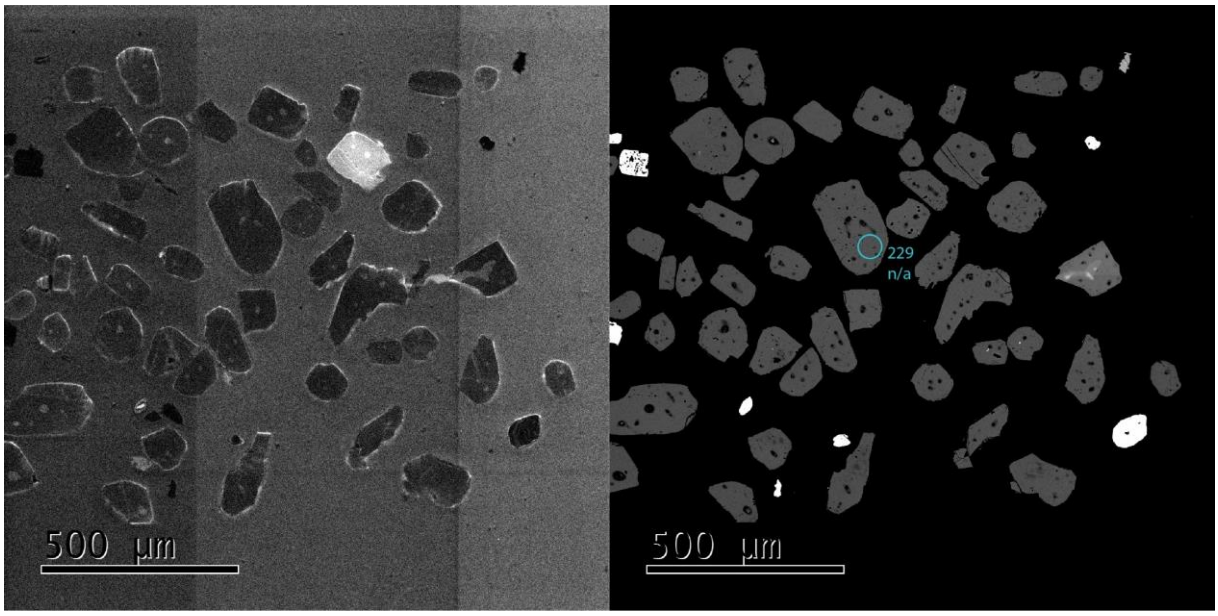

Figure 49 – Apatite εNd spot analyses of sample s4D indicating the analysed spots with the obtained εNd_{468} values

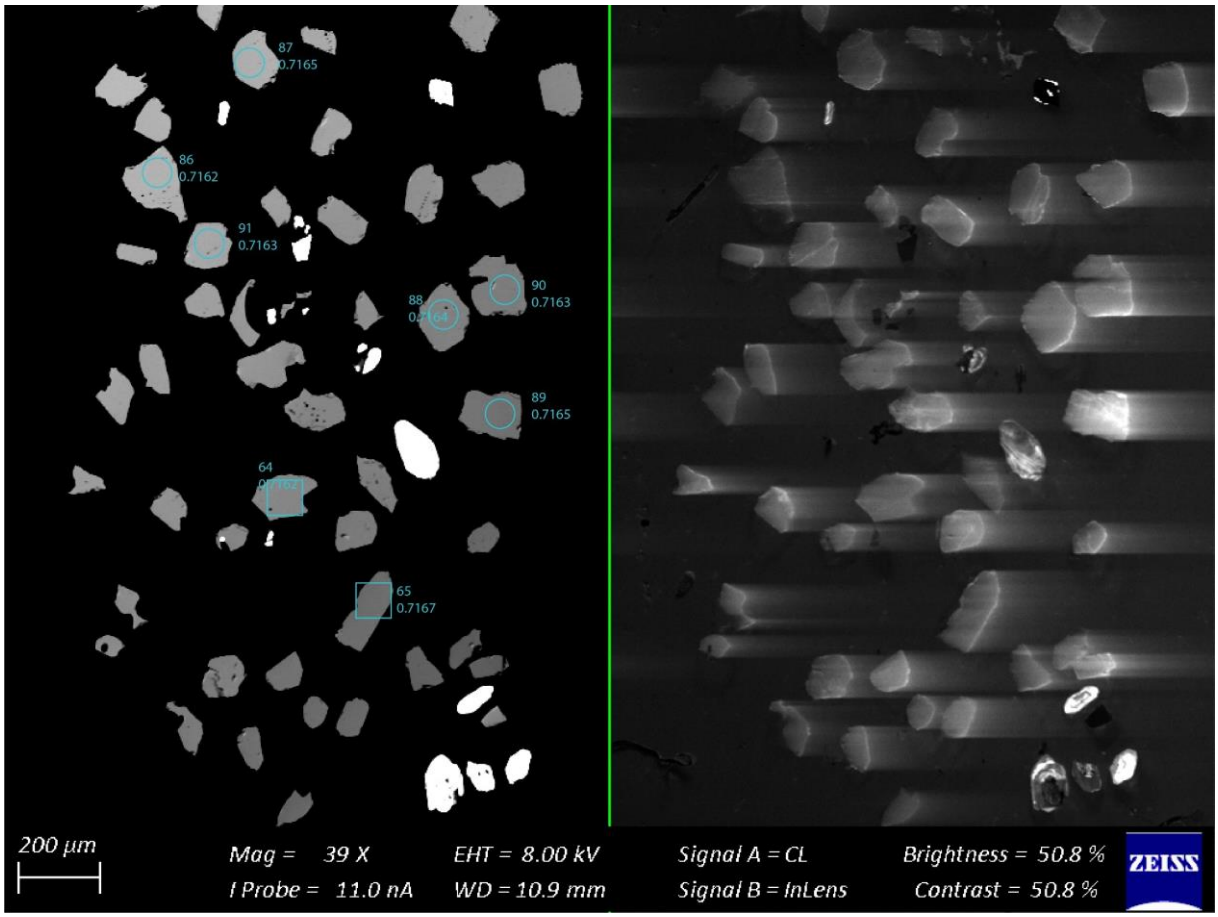

Figure 50 – Apatite spot analyses of sample s4D indicating the analysed spots with the obtained $^{87}Sr/^{86}Sr_{468}$ values

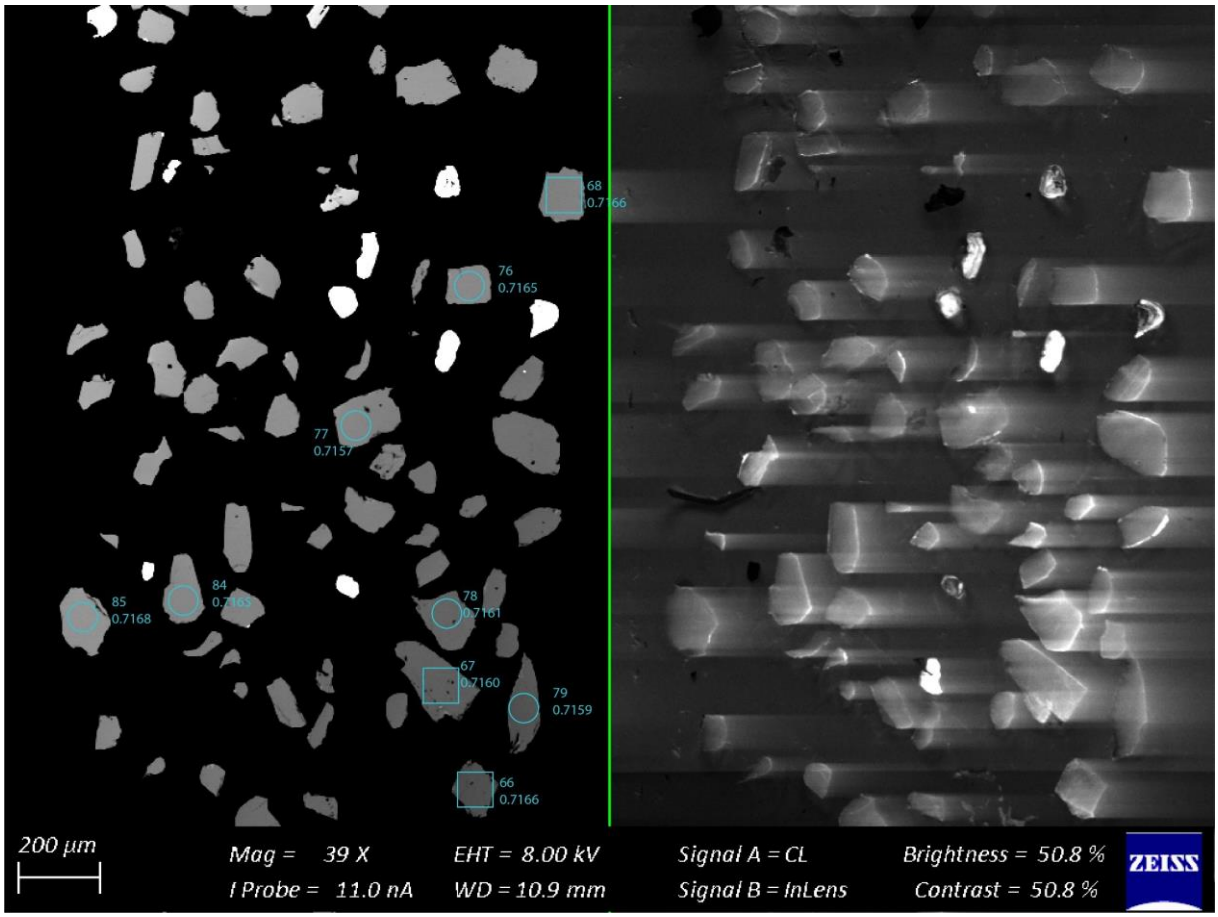

Figure 51 – Apatite spot analyses of sample s4D indicating the analysed spots with the obtained $^{87}Sr/^{86}Sr_{468}$ values

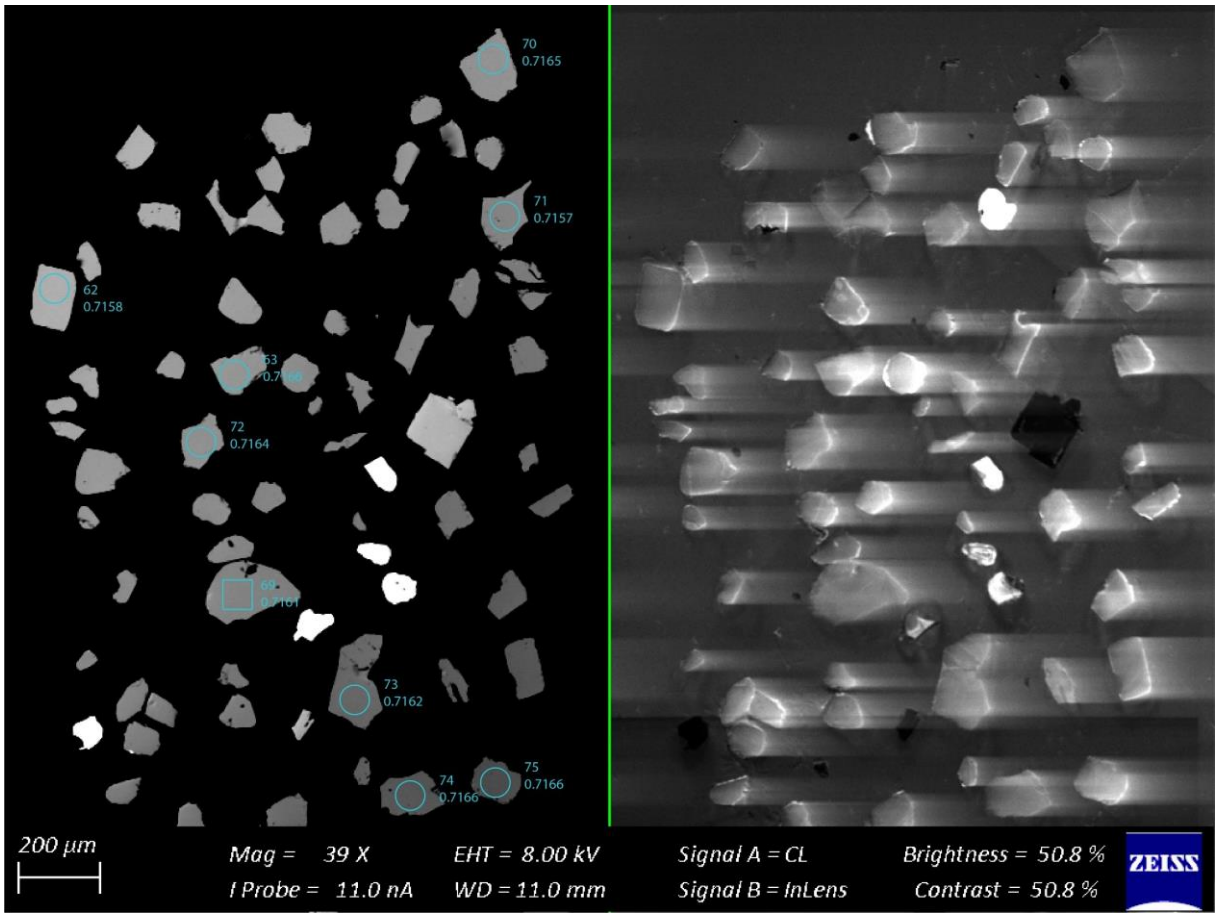

Figure 52 – Apatite spot analyses of sample s4D indicating the analysed spots with the obtained $^{87}Sr/^{86}Sr_{468}$ values

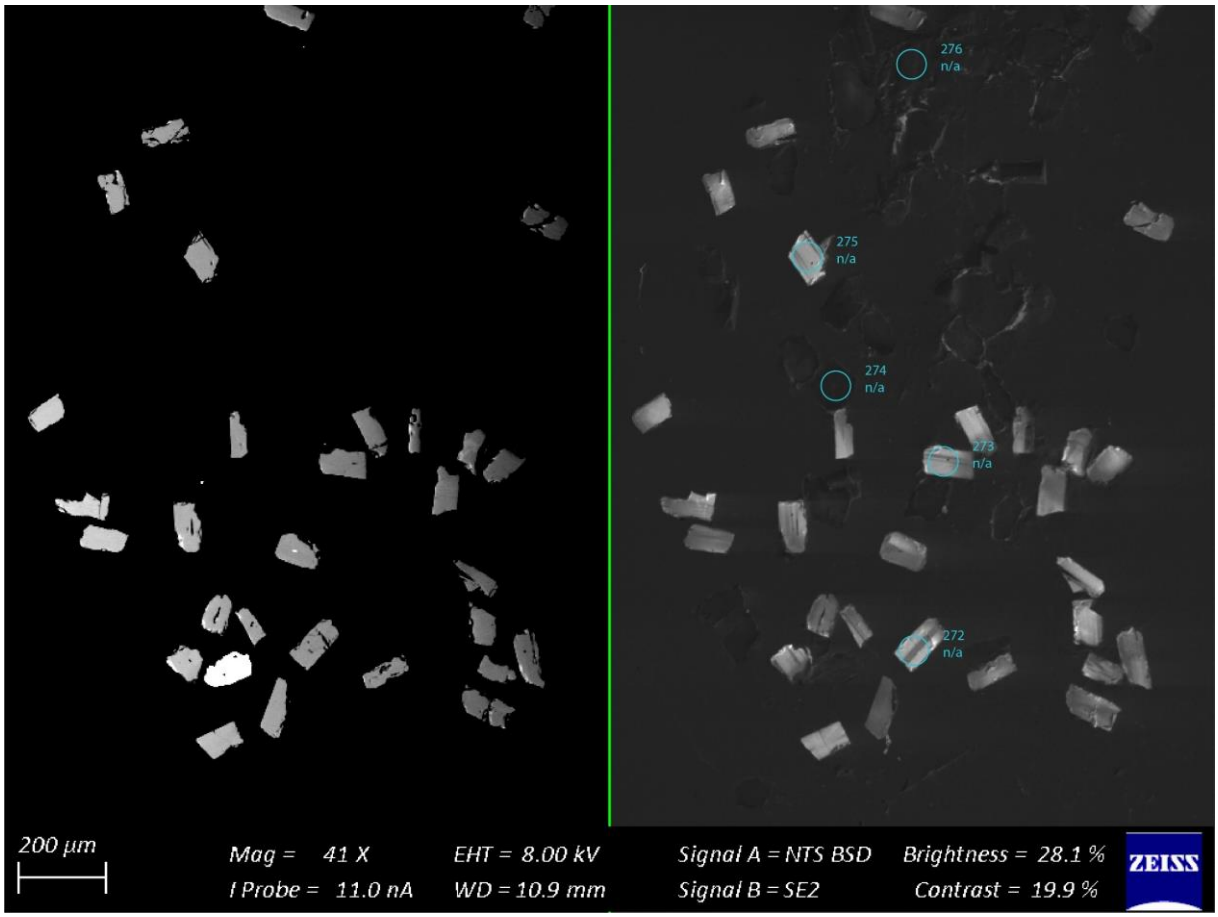

Figure 53 – Apatite spot analyses of sample s5A indicating the analysed spots with the obtained $^{87}Sr/^{86}Sr_{468}$ values

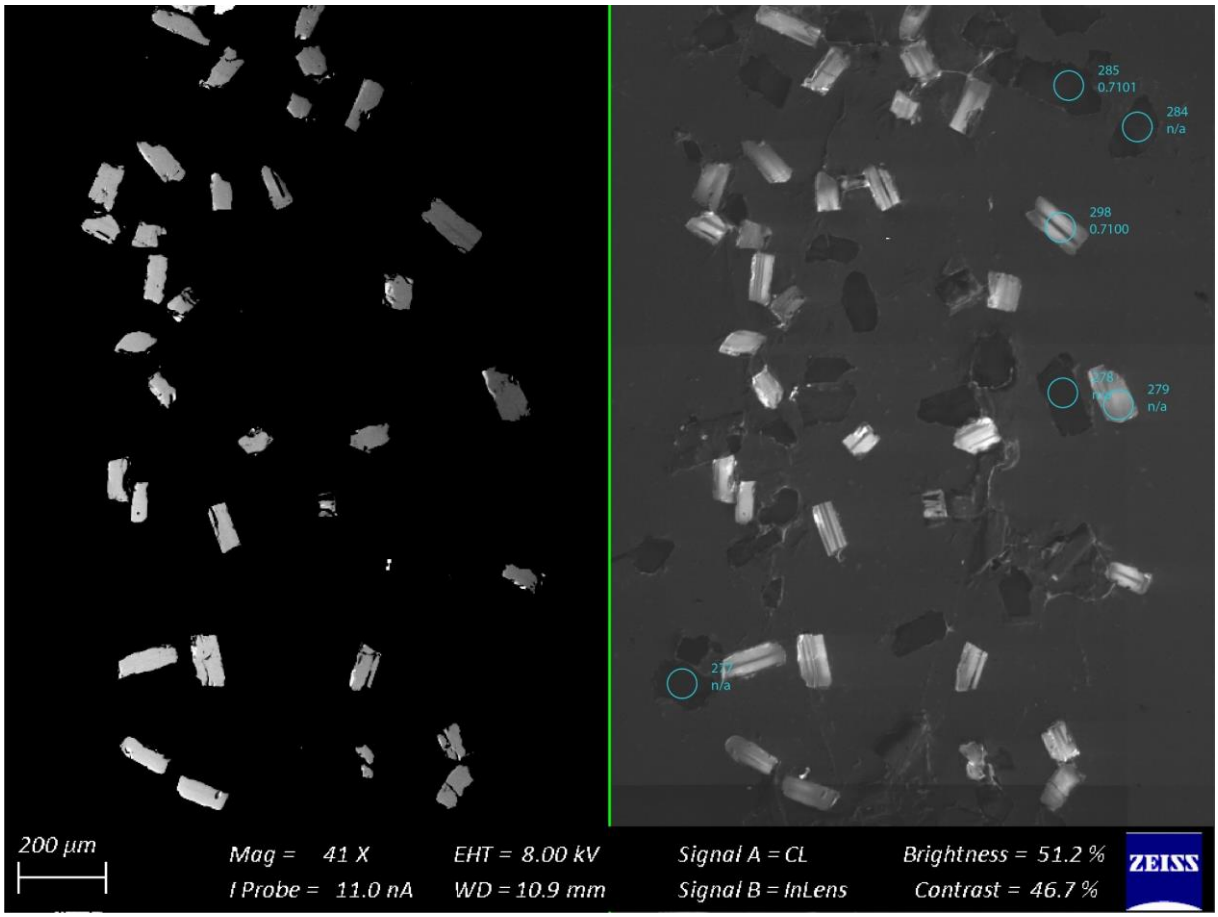

Figure 54 – Apatite spot analyses of sample s5A indicating the analysed spots with the obtained $^{87}Sr/^{86}Sr_{468}$ values

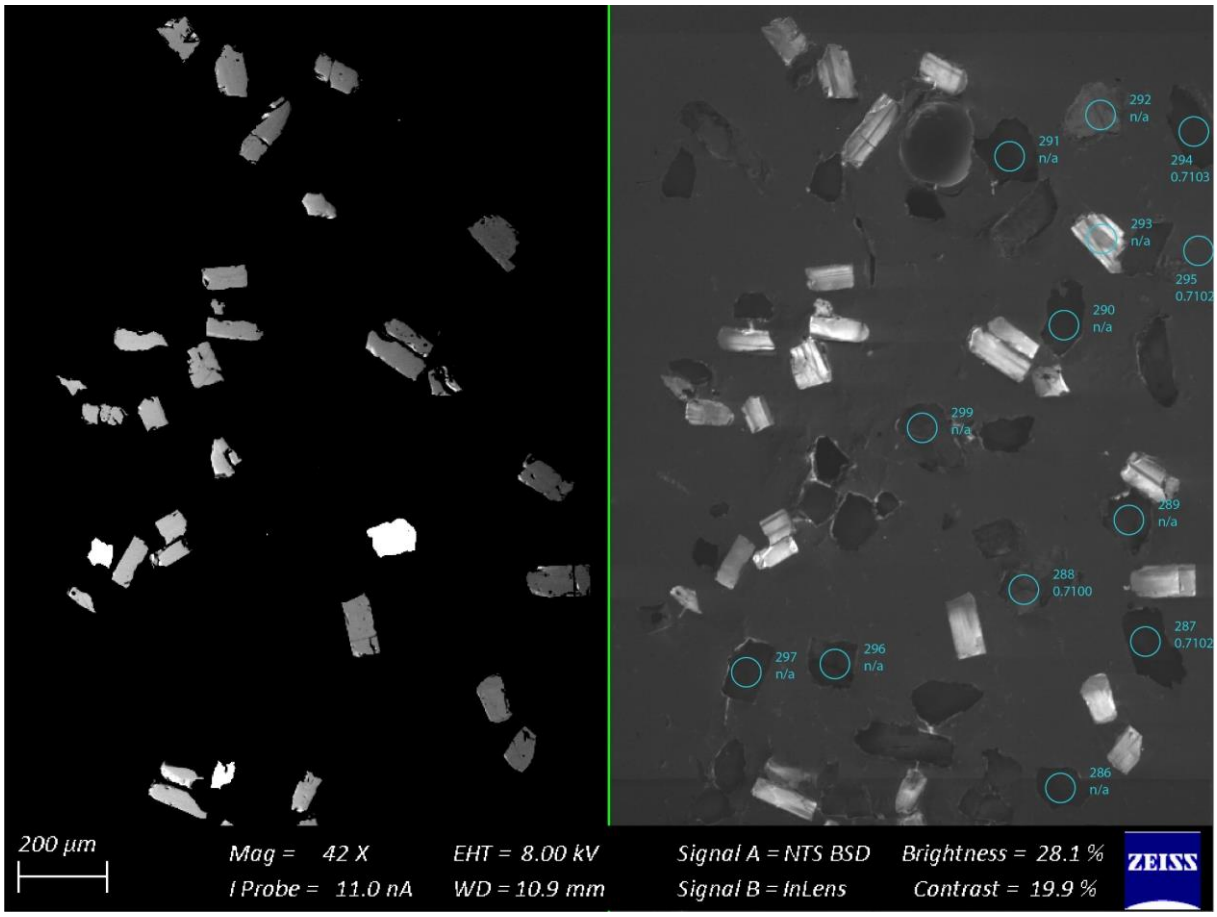

Figure 55 – Apatite spot analyses of sample s5A indicating the analysed spots with the obtained $^{87}Sr/^{86}Sr_{468}$ values

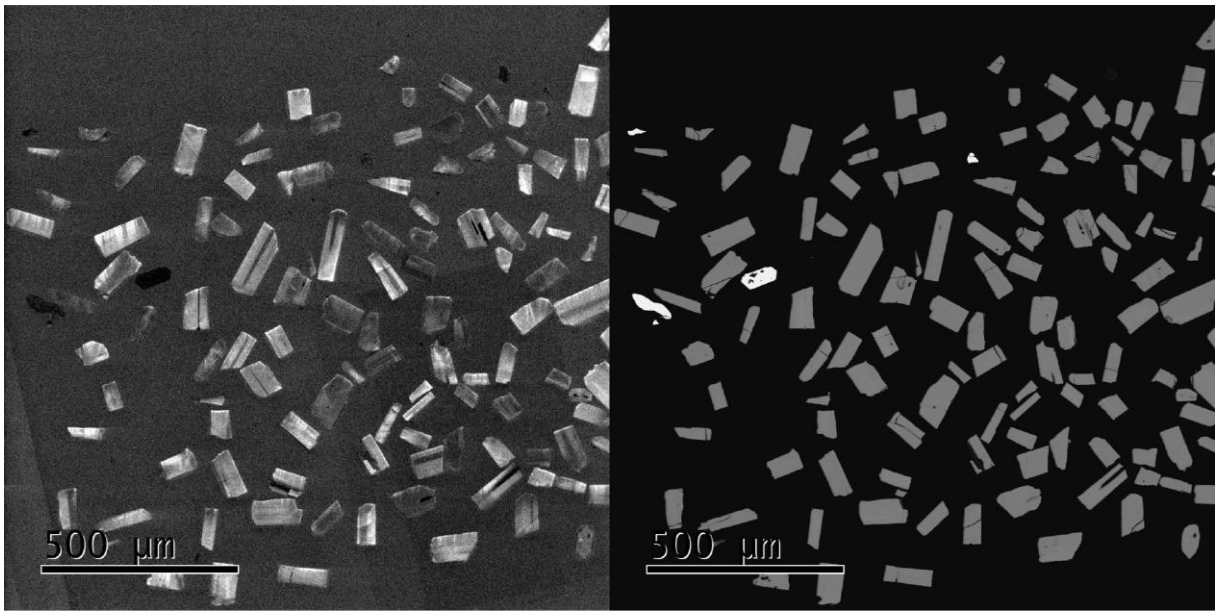

Figure 56 – Apatite εNd spot analyses of sample s5Ba indicating the analysed spots with the obtained εNd_{468} values

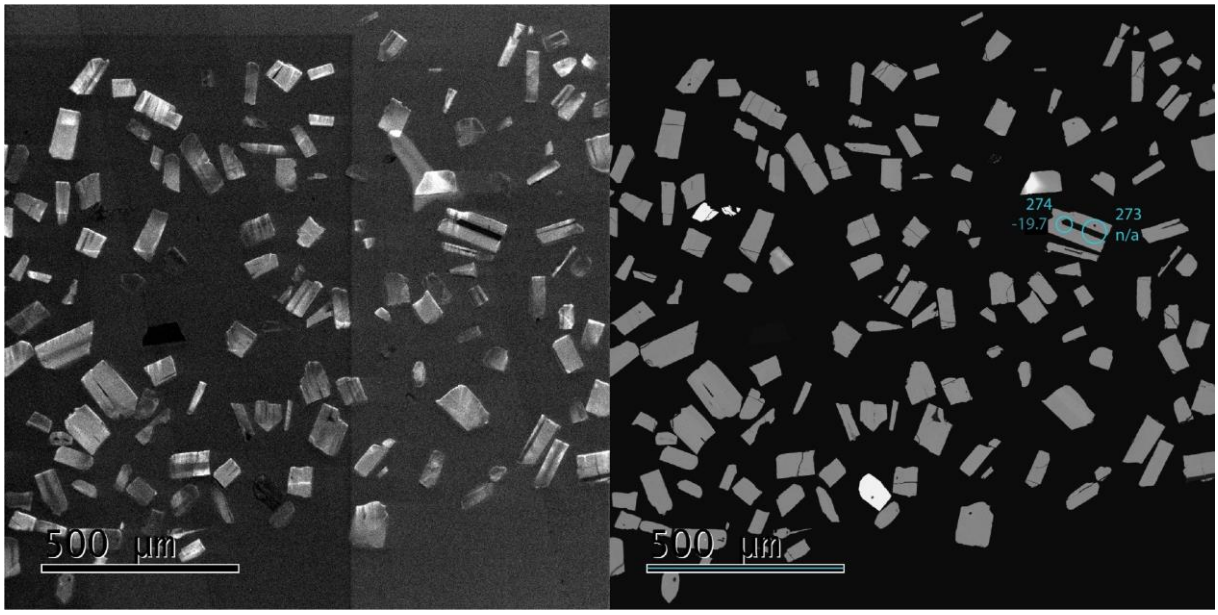

Figure 57 – Apatite εNd spot analyses of sample s5Ba indicating the analysed spots with the obtained εNd_{468} values

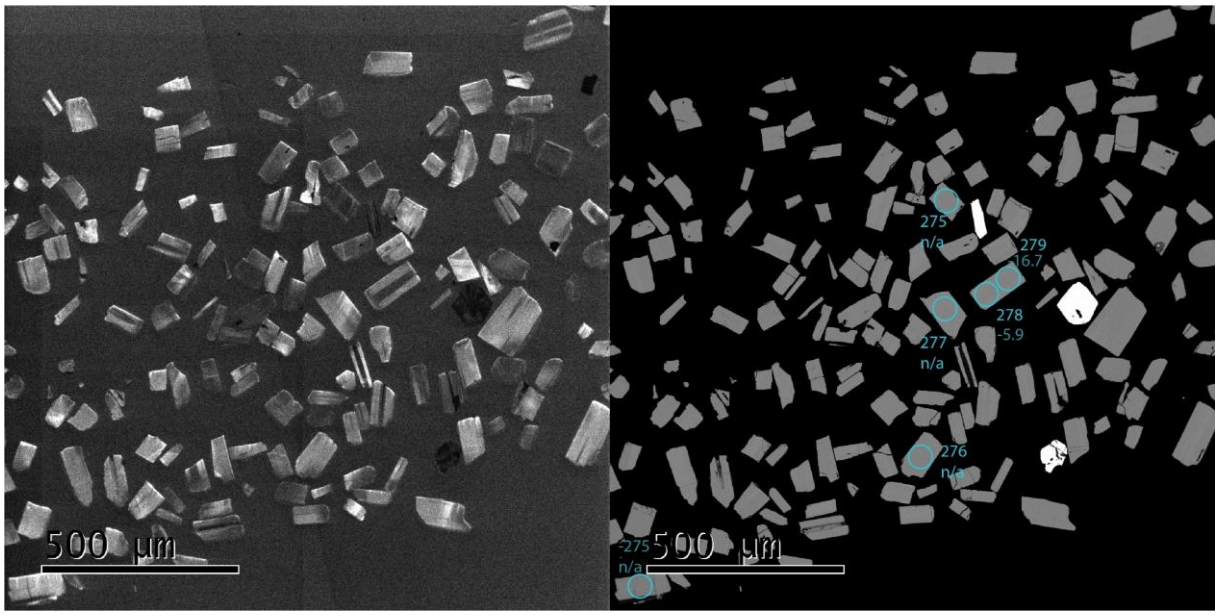

Figure 58 – Apatite εNd spot analyses of sample s5Ba indicating the analysed spots with the obtained εNd_{468} values

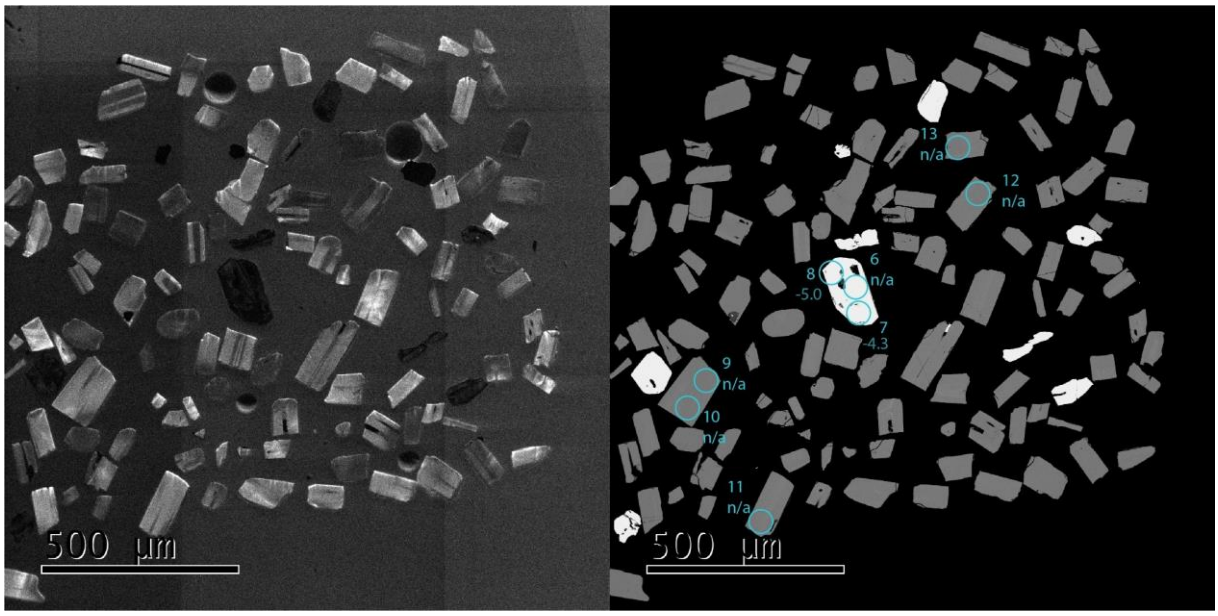

Figure 59 – Apatite εNd spot analyses of sample s5Ba indicating the analysed spots with the obtained εNd_{468} values

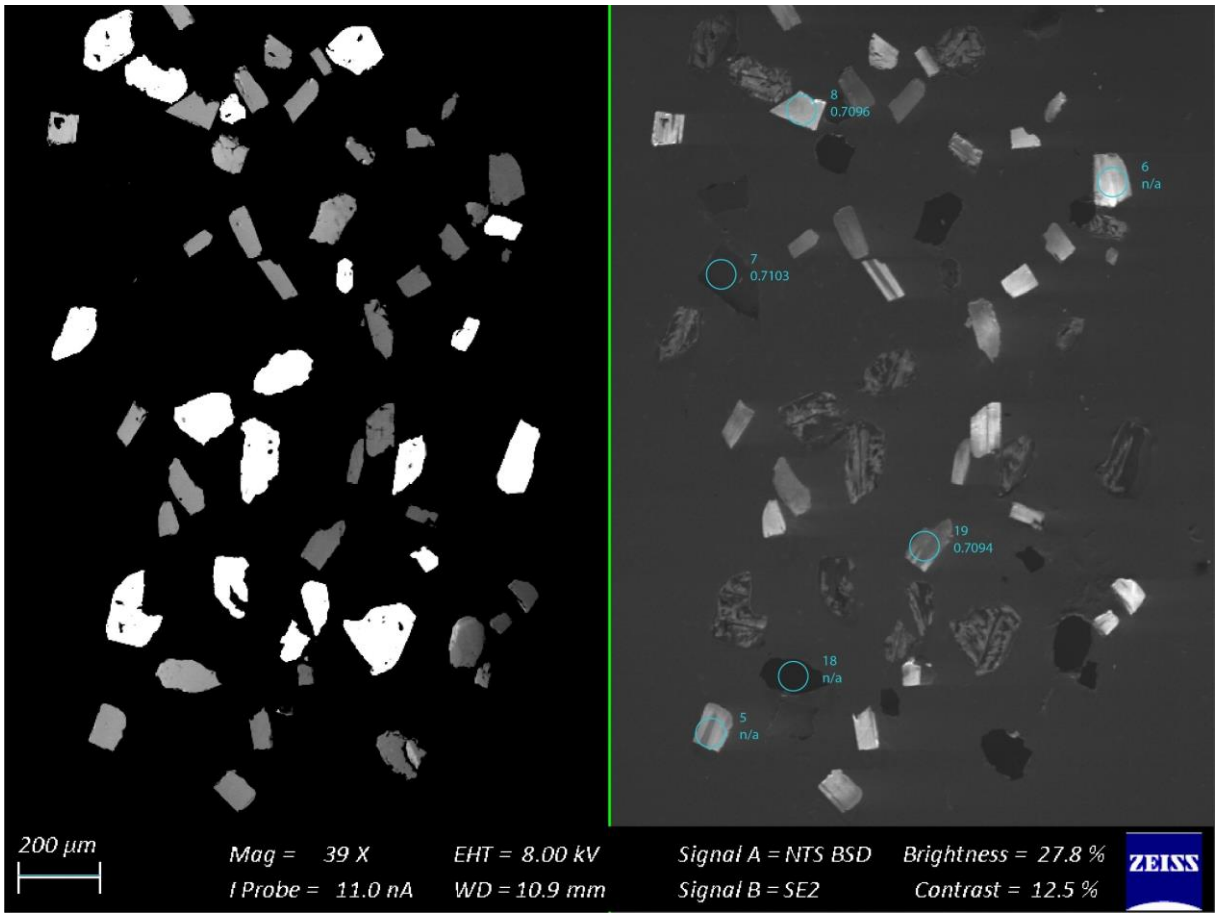

Figure 60 – Apatite spot analyses of sample s5Ba indicating the analysed spots with the obtained $^{87}Sr/^{86}Sr_{468}$ values

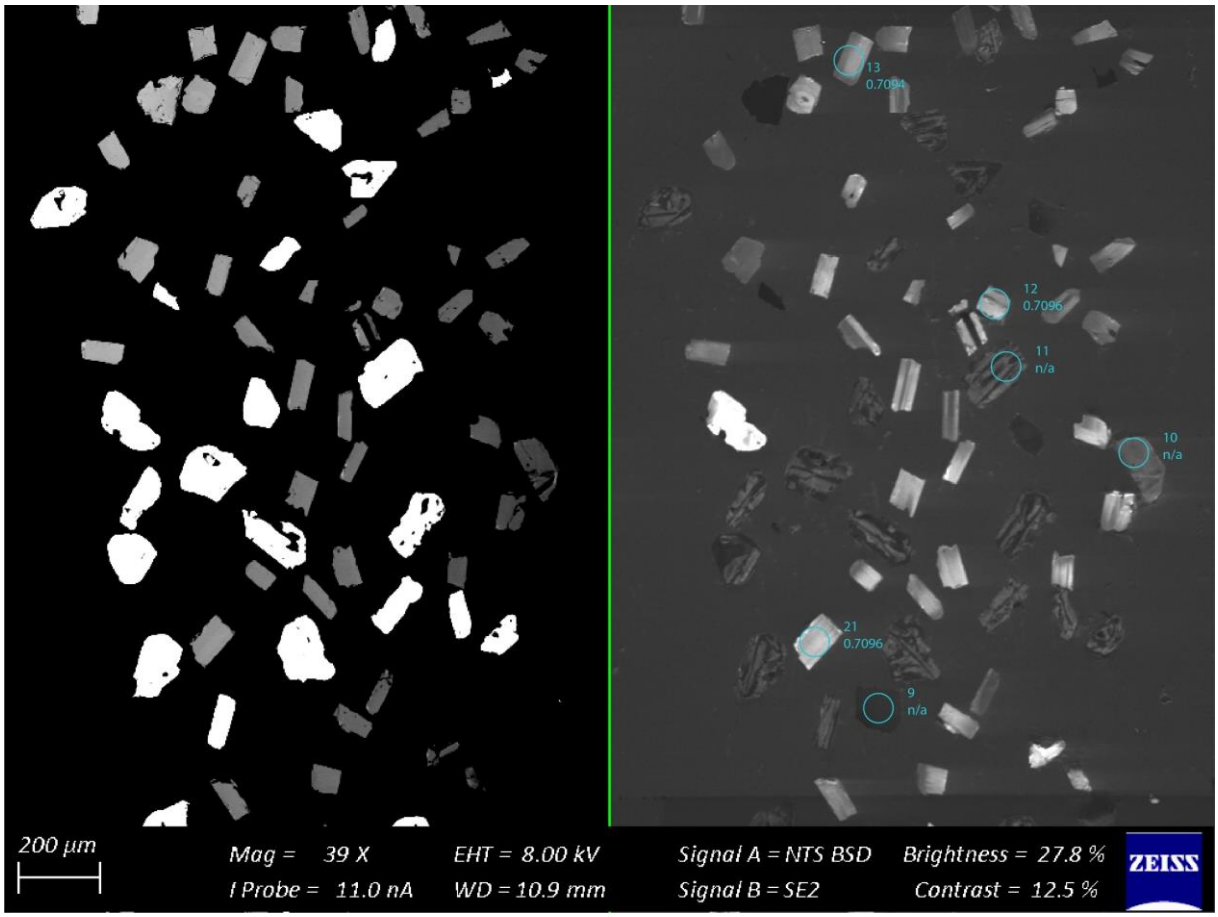

Figure 61 – Apatite spot analyses of sample s5Ba indicating the analysed spots with the obtained $^{87}Sr/^{86}Sr_{468}$ values

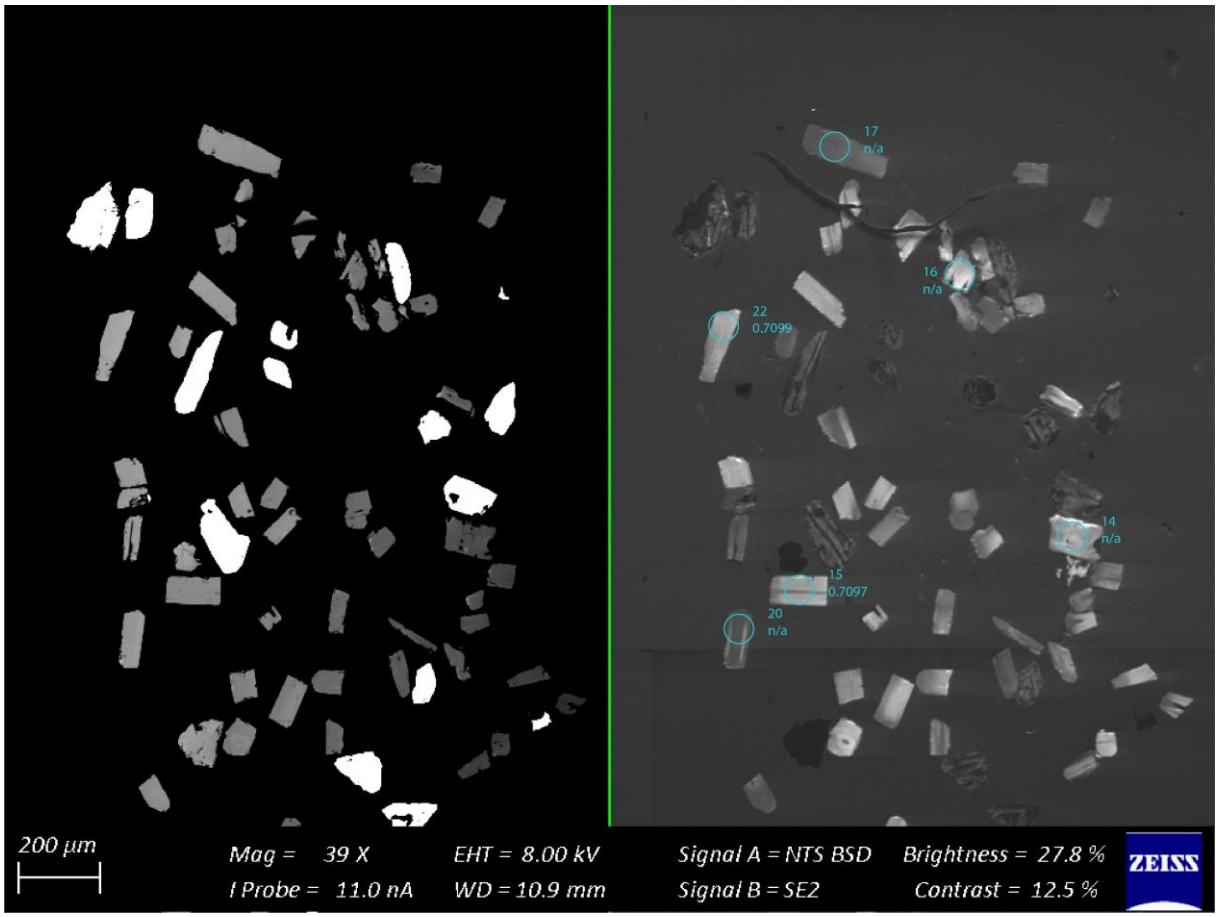

Figure 62 – Apatite spot analyses of sample s5Ba indicating the analysed spots with the obtained $^{87}Sr/^{86}Sr_{468}$ values

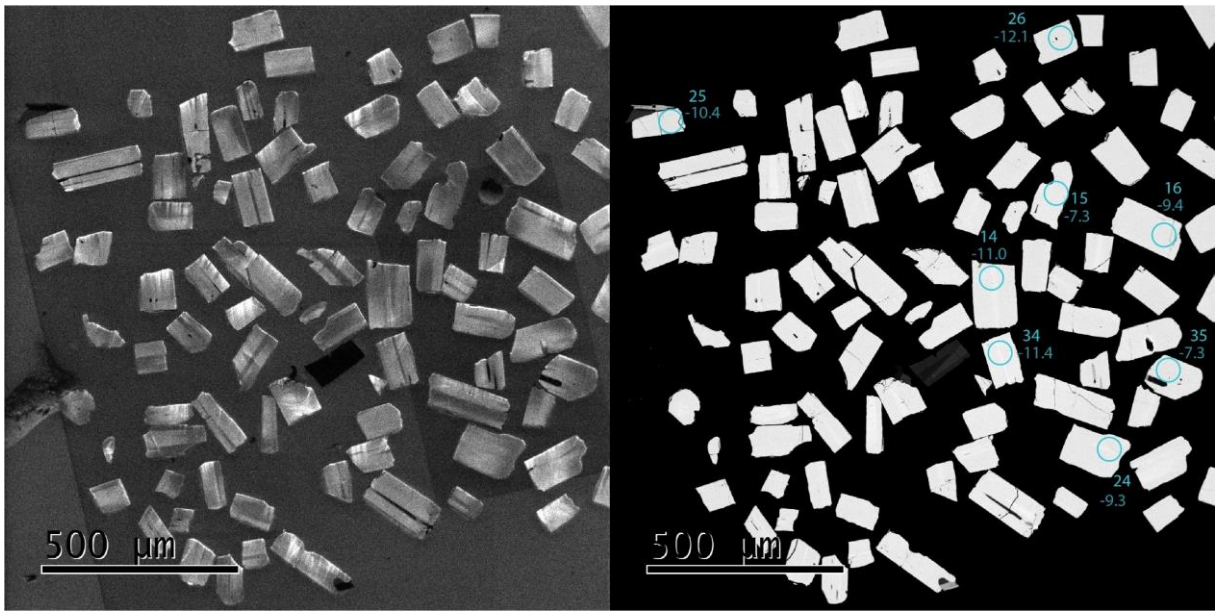

Figure 63 – Apatite εNd spot analyses of sample s5Bb indicating the analysed spots with the obtained εNd_{468} values

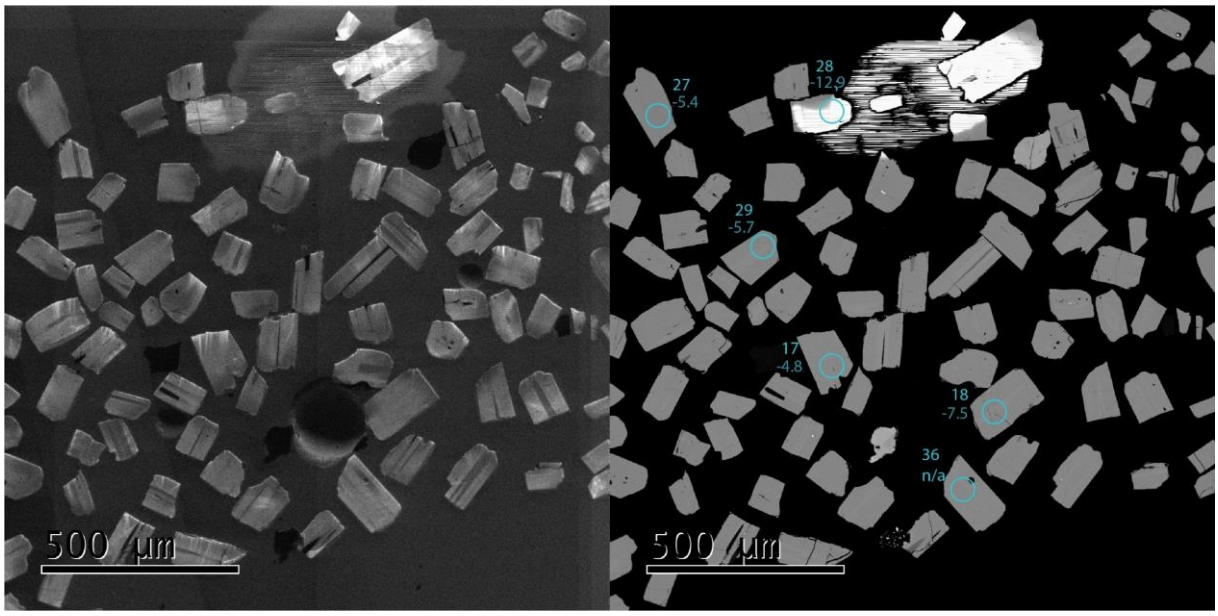

Figure 64 – Apatite εNd spot analyses of sample s5Bb indicating the analysed spots with the obtained εNd_{468} values

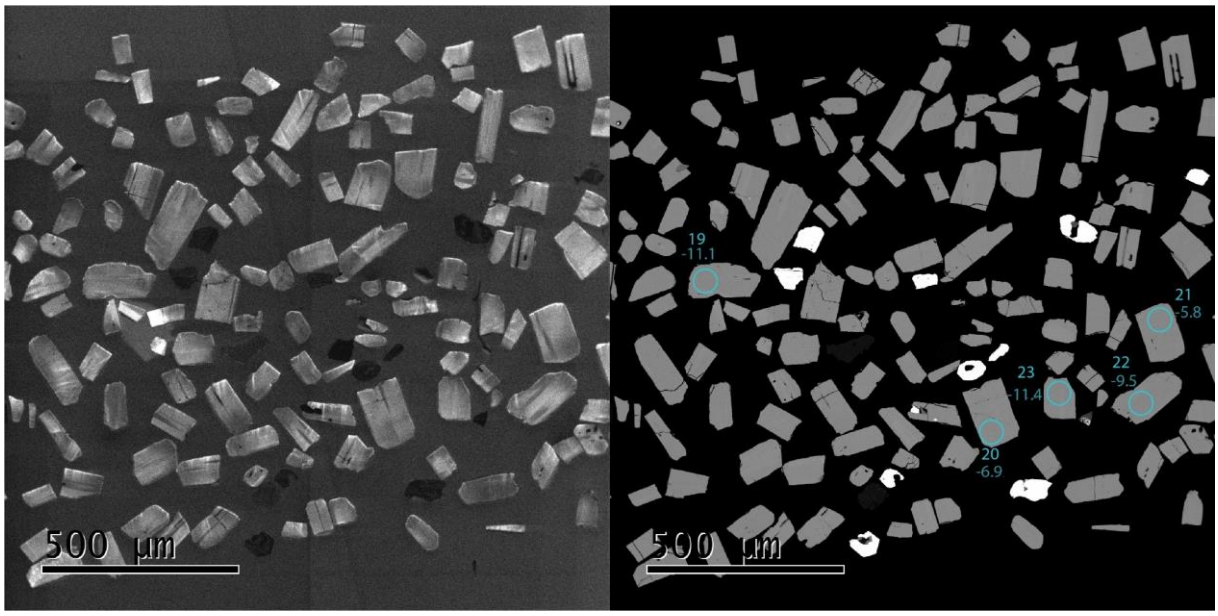

Figure 65 – Apatite εNd spot analyses of sample s5Bb indicating the analysed spots with the obtained εNd_{468} values

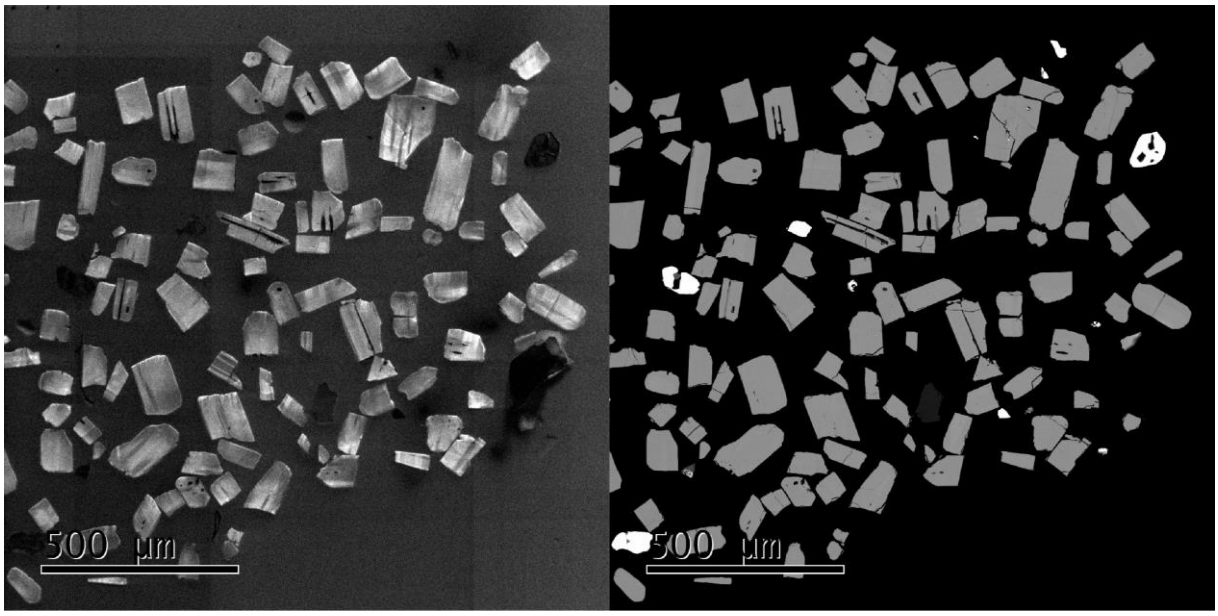

Figure 66 – Apatite εNd spot analyses of sample s5Bb indicating the analysed spots with the obtained εNd_{468} values

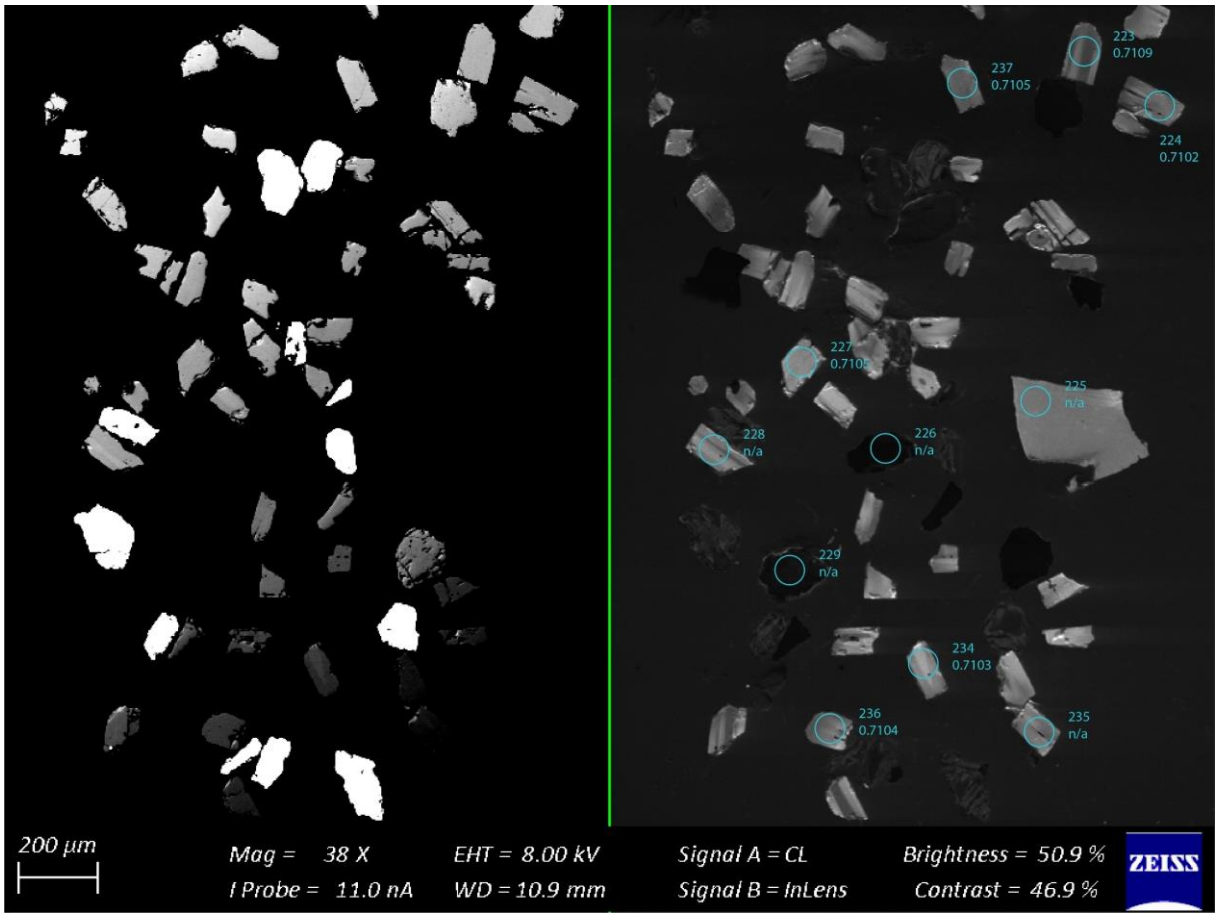

Figure 67 – Apatite spot analyses of sample s5Bb indicating the analysed spots with the obtained $^{87}Sr/^{86}Sr_{468}$ values

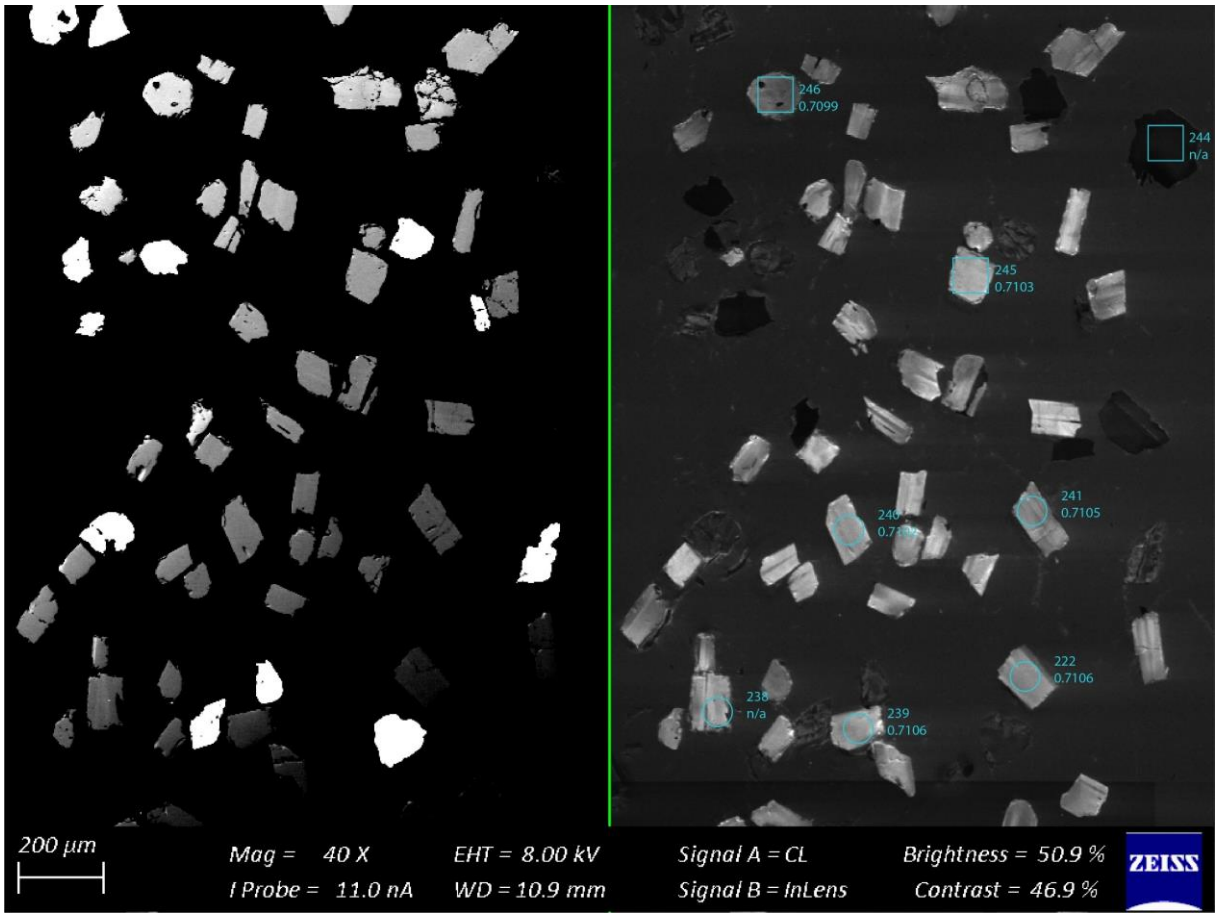

Figure 68 – Apatite spot analyses of sample s5Bb indicating the analysed spots with the obtained $^{87}Sr/^{86}Sr_{468}$ values

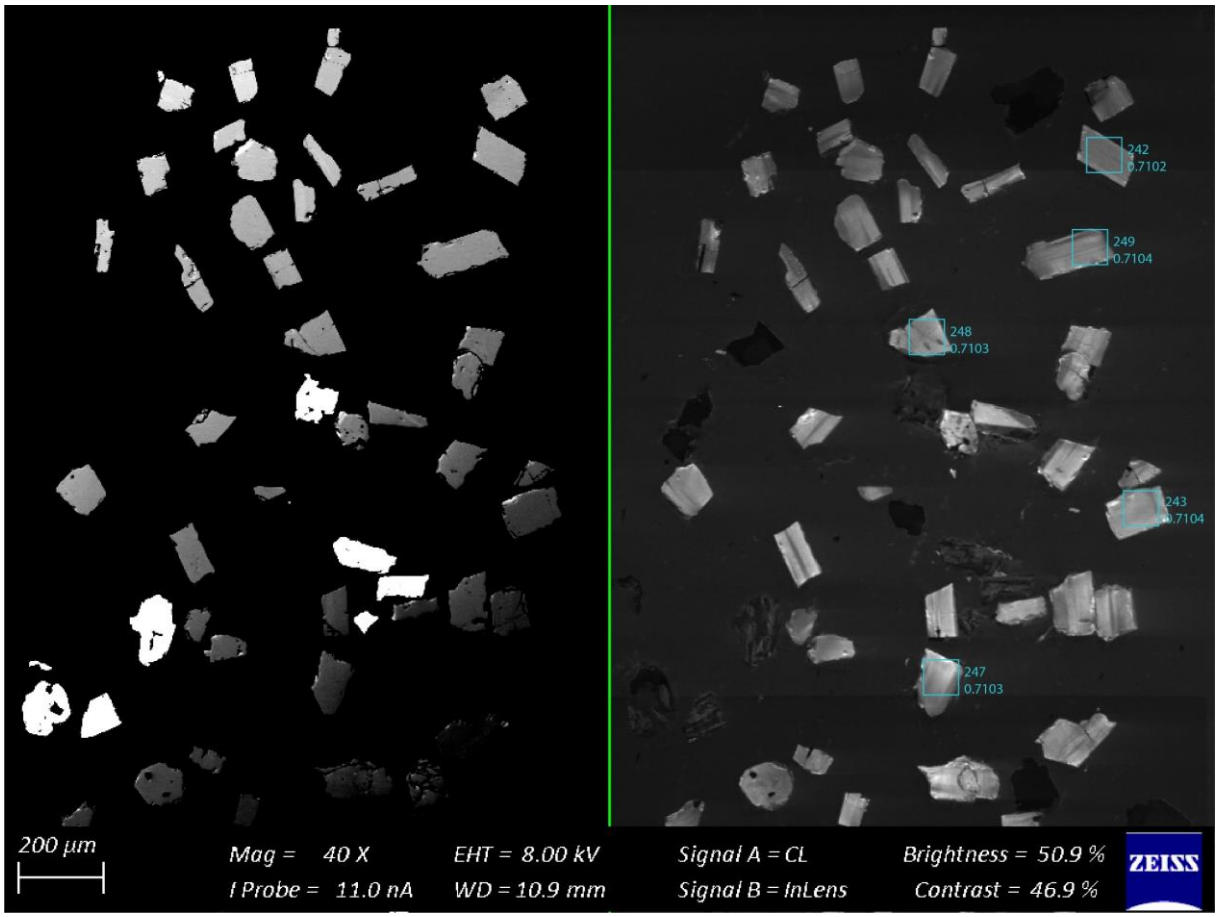

Figure 69 – Apatite spot analyses of sample s5Bb indicating the analysed spots with the obtained $^{87}Sr/^{86}Sr_{468}$ values

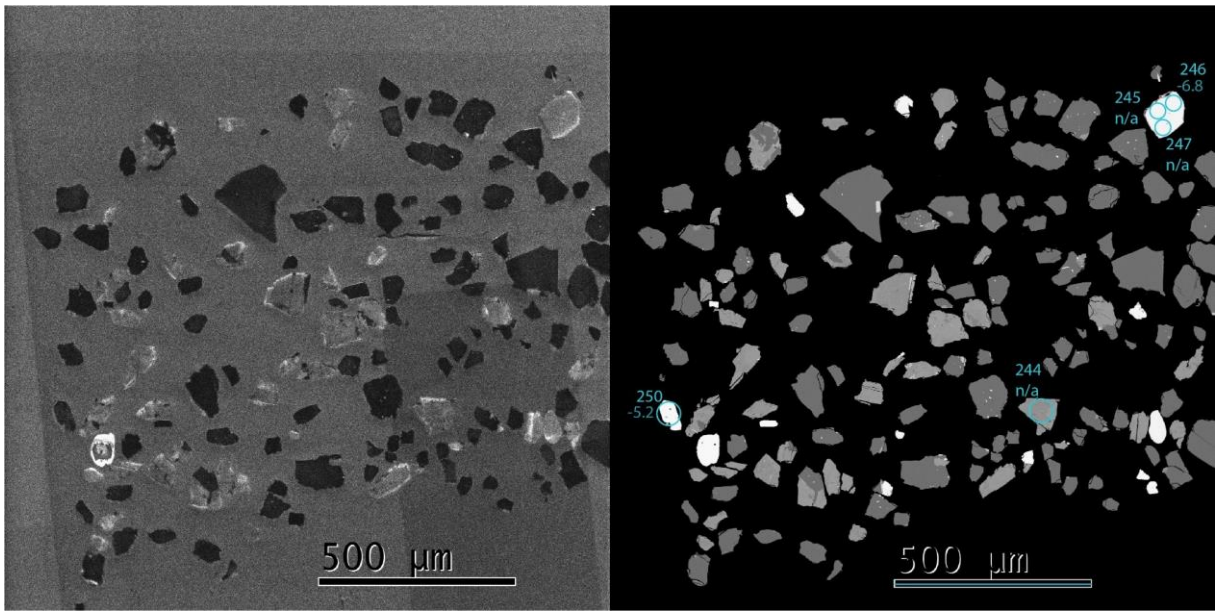

Figure 70 – Apatite εNd spot analyses of sample s7A indicating the analysed spots with the obtained εNd_{468} values

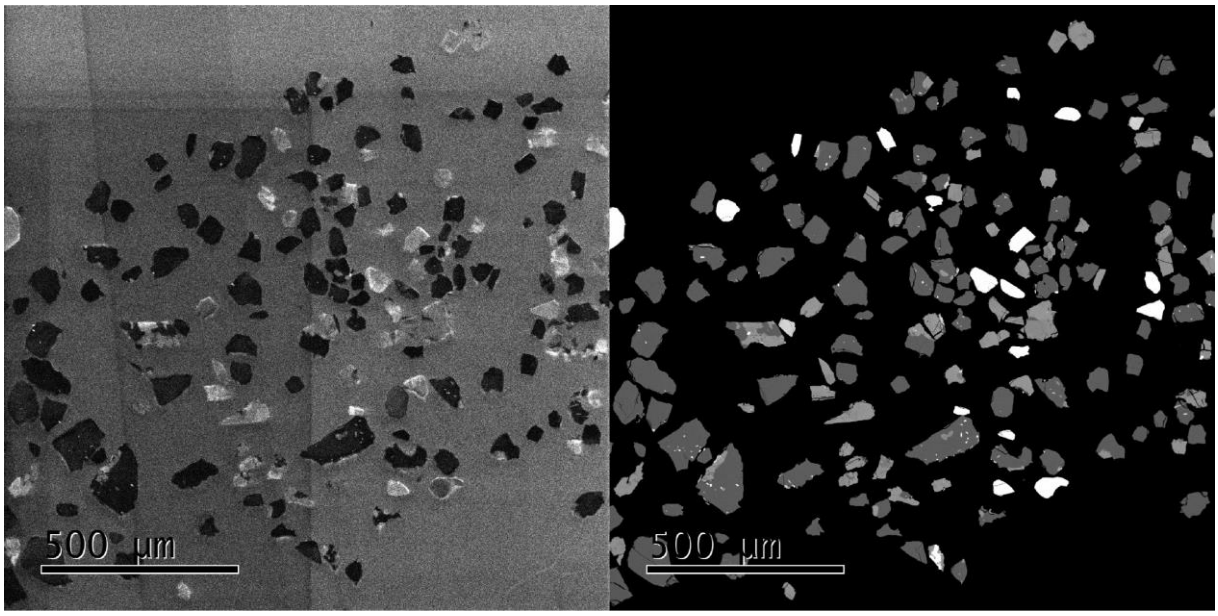

Figure 71 – Apatite εNd spot analyses of sample s7A indicating the analysed spots with the obtained εNd_{468} values

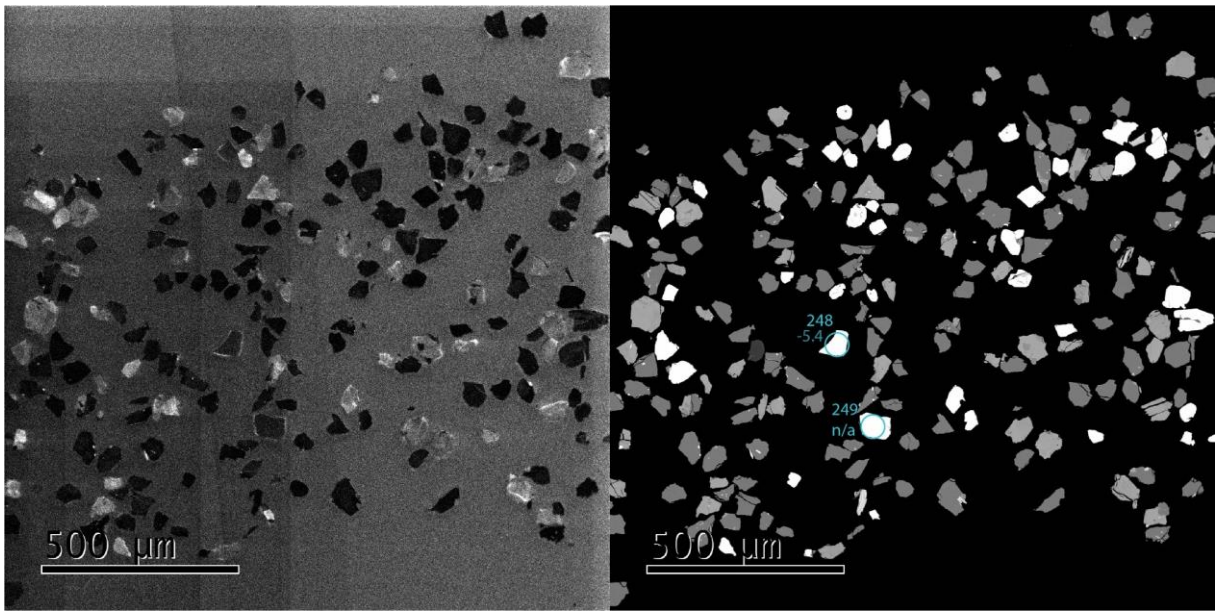

Figure 72 – Apatite εNd spot analyses of sample s7A indicating the analysed spots with the obtained εNd_{468} values

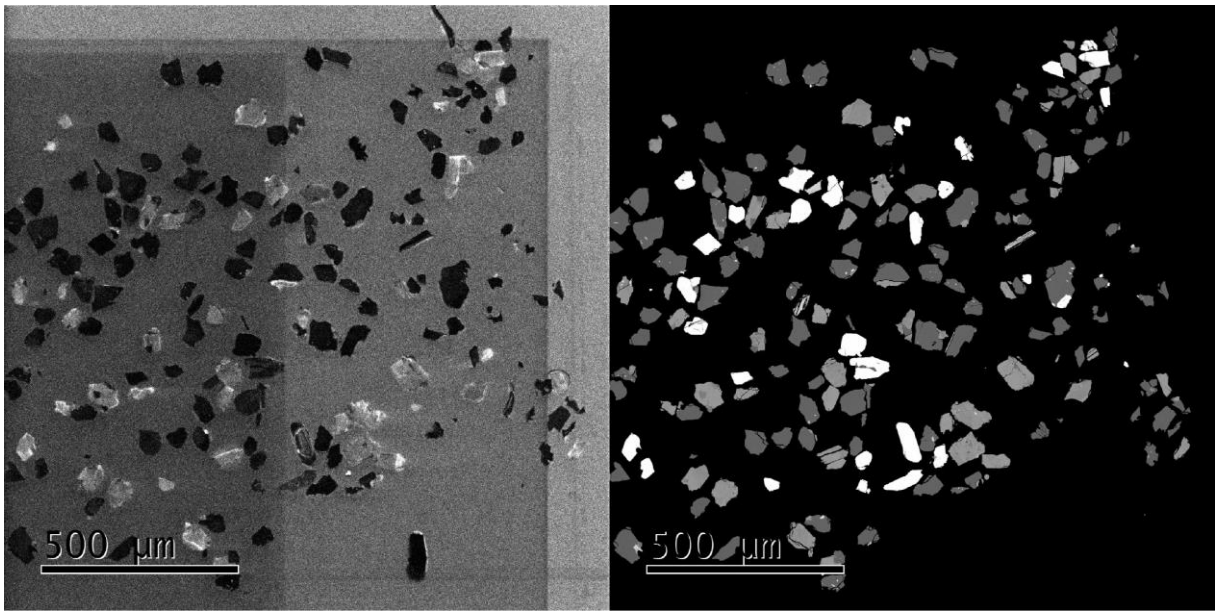

Figure 73 – Apatite εNd spot analyses of sample s7A indicating the analysed spots with the obtained εNd_{468} values

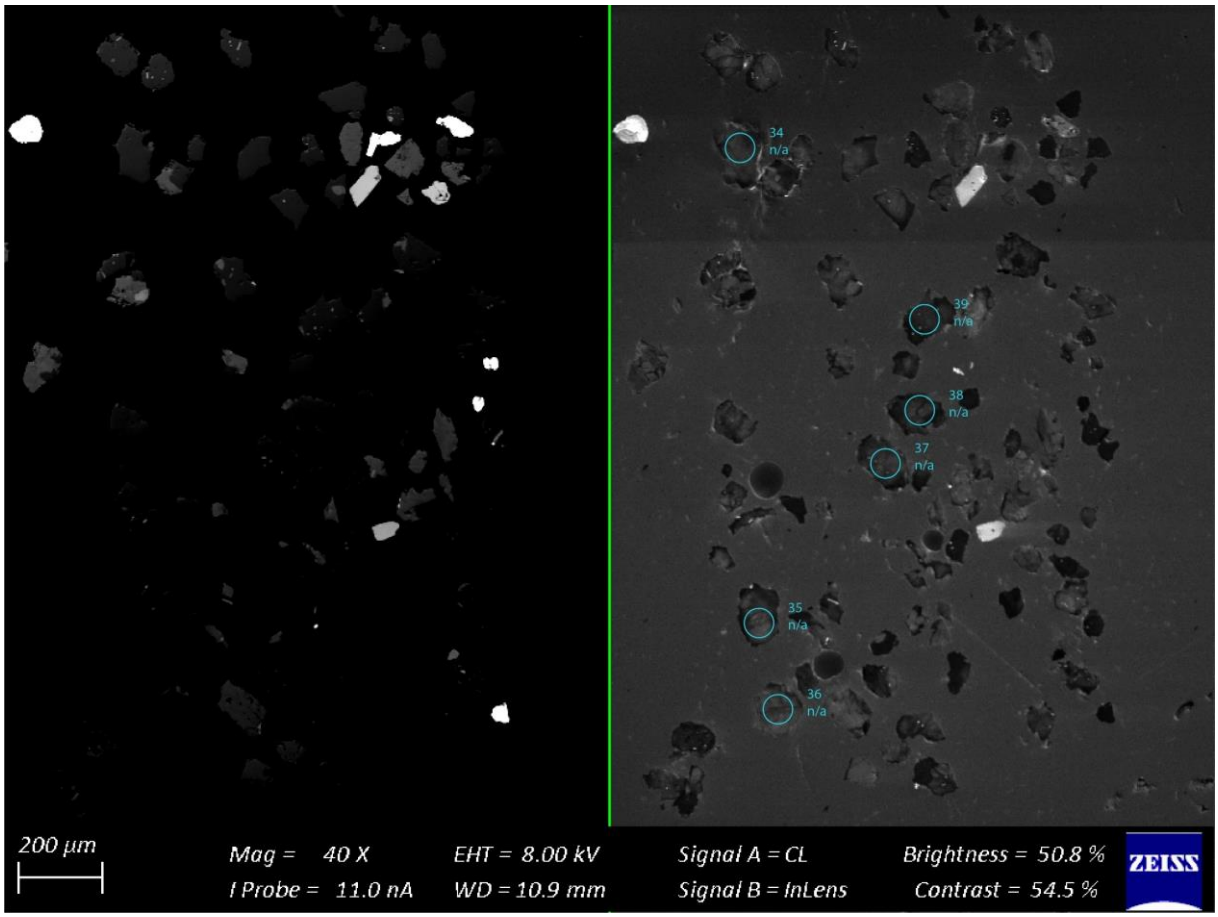

Figure 74 – Apatite spot analyses of sample s7A indicating the analysed spots with the obtained $^{87}Sr/^{86}Sr_{468}$ values

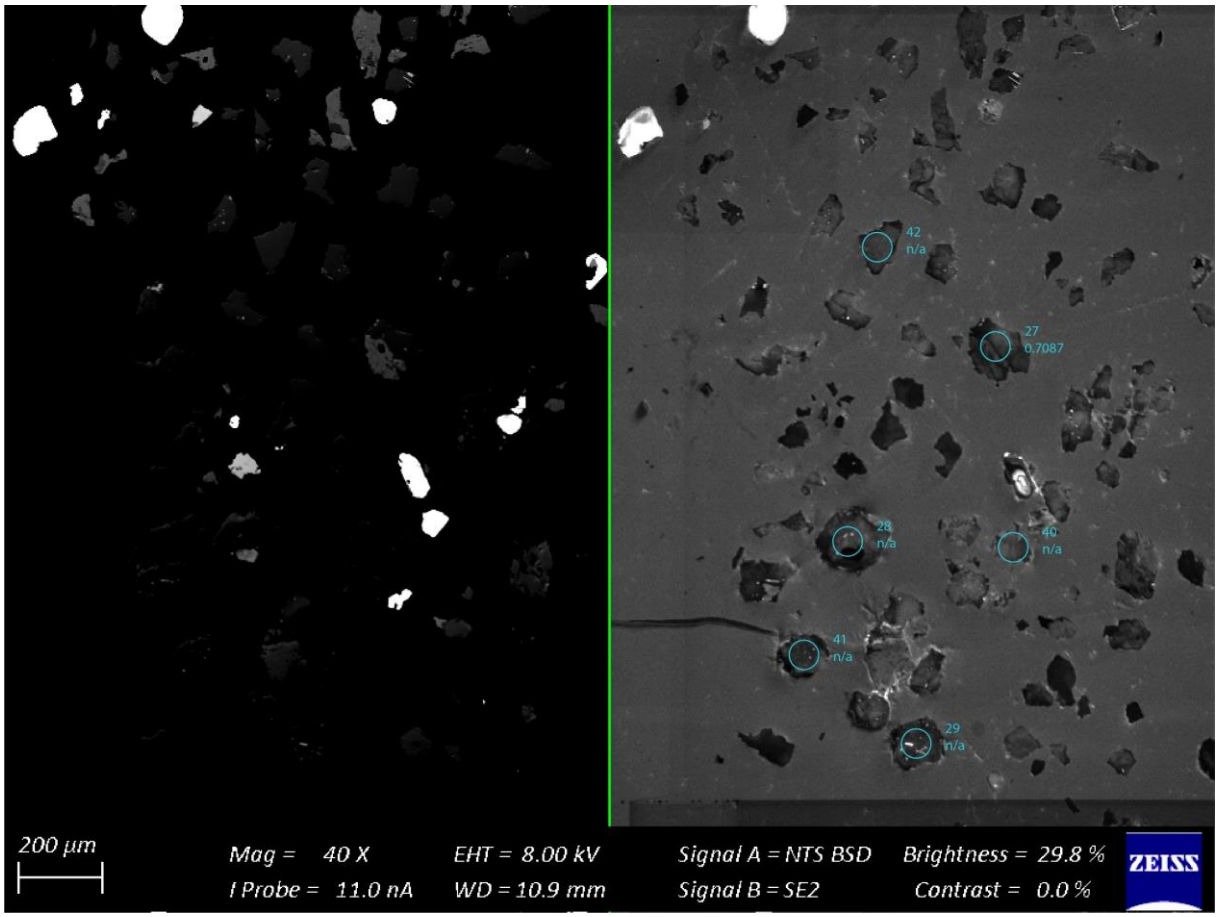

Figure 75 – Apatite spot analyses of sample s7A indicating the analysed spots with the obtained $^{87}Sr/^{86}Sr_{468}$ values

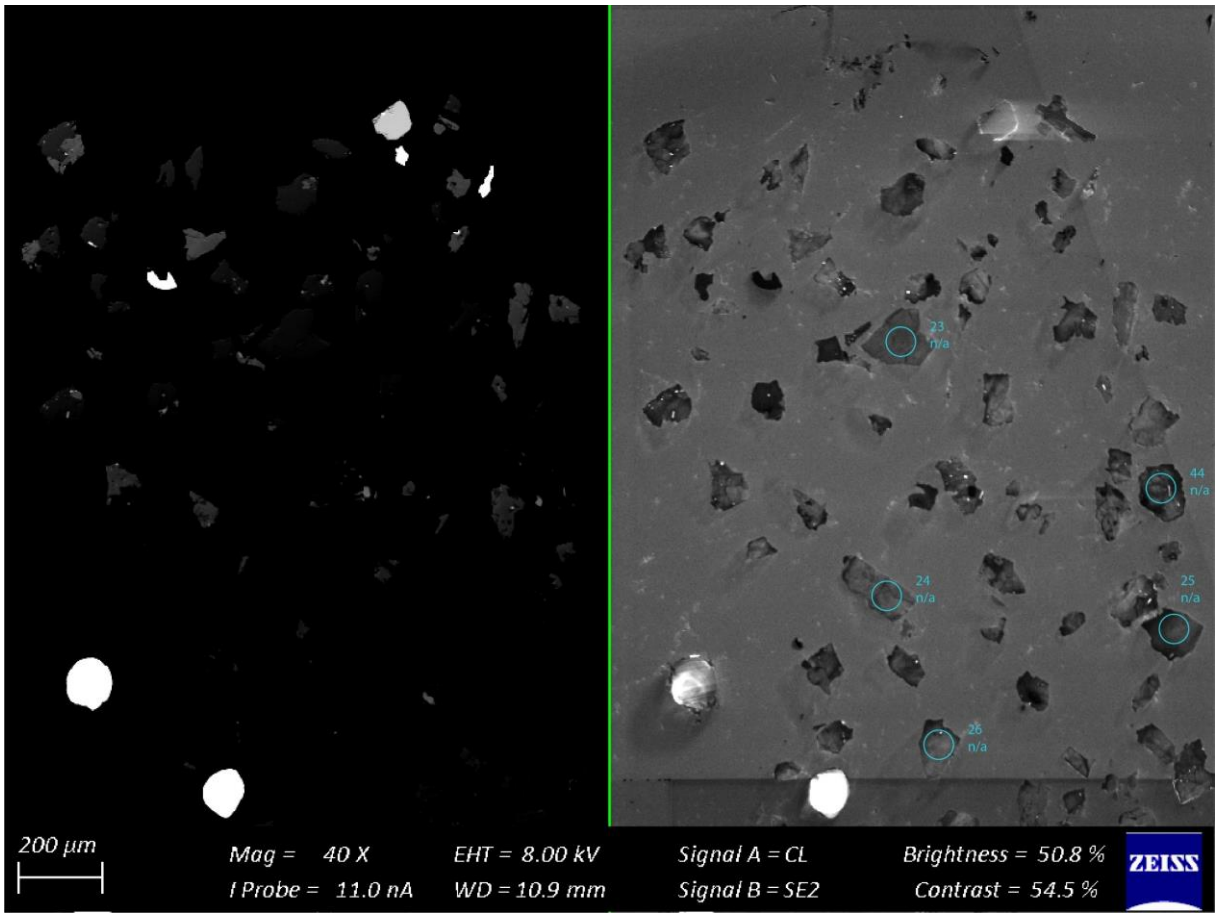

Figure 76 – Apatite spot analyses of sample s7A indicating the analysed spots with the obtained $^{87}Sr/^{86}Sr_{468}$ values

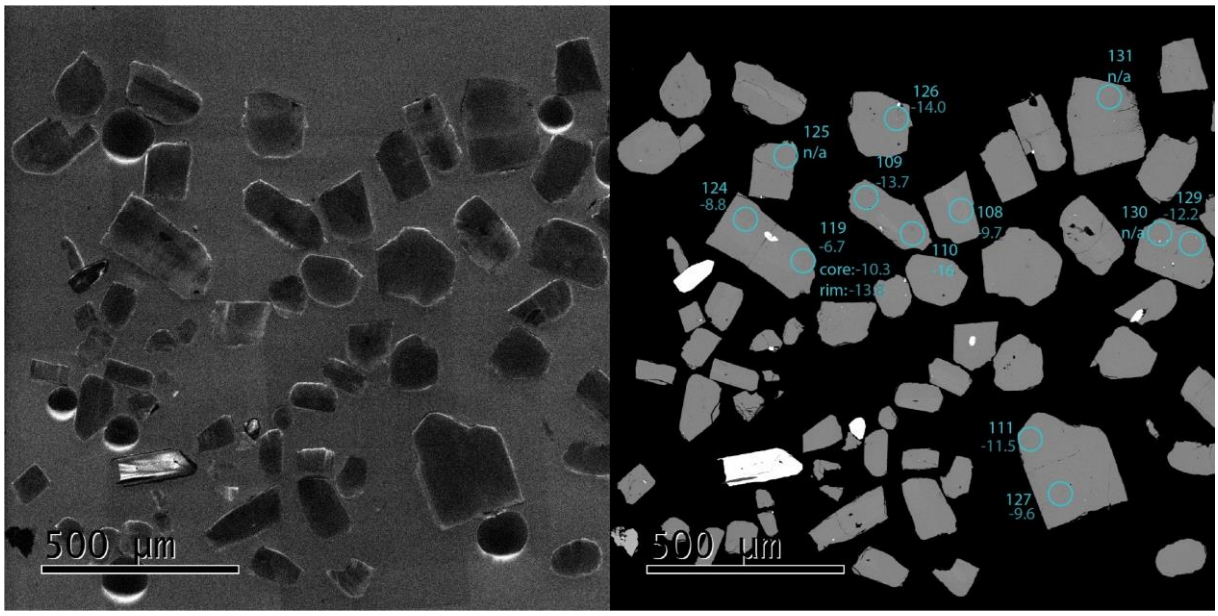

Figure 77 – Apatite εNd spot analyses of sample s7B indicating the analysed spots with the obtained εNd_{468} values

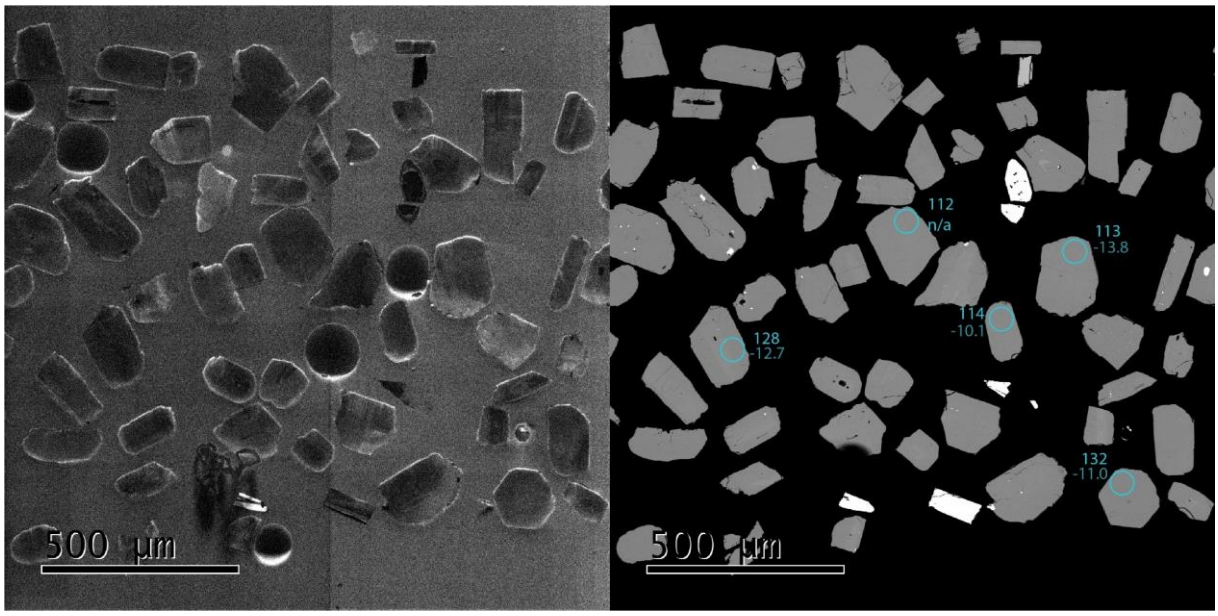

Figure 78 – Apatite εNd spot analyses of sample s7B indicating the analysed spots with the obtained εNd_{468} values

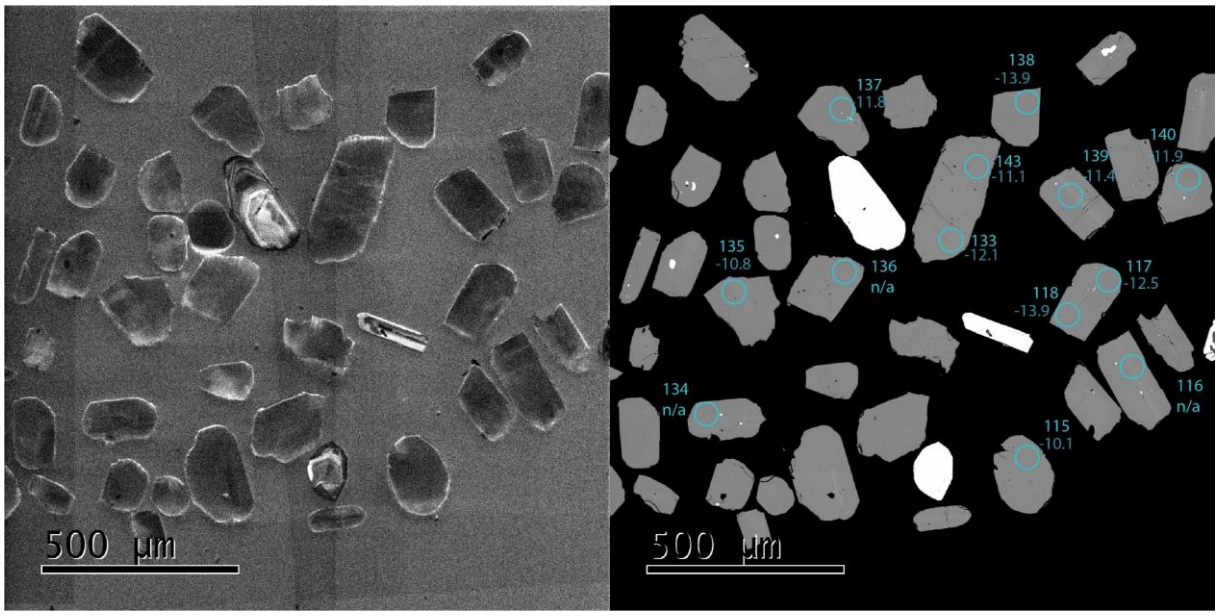

Figure 79 – Apatite εNd spot analyses of sample s7B indicating the analysed spots with the obtained εNd_{468} values

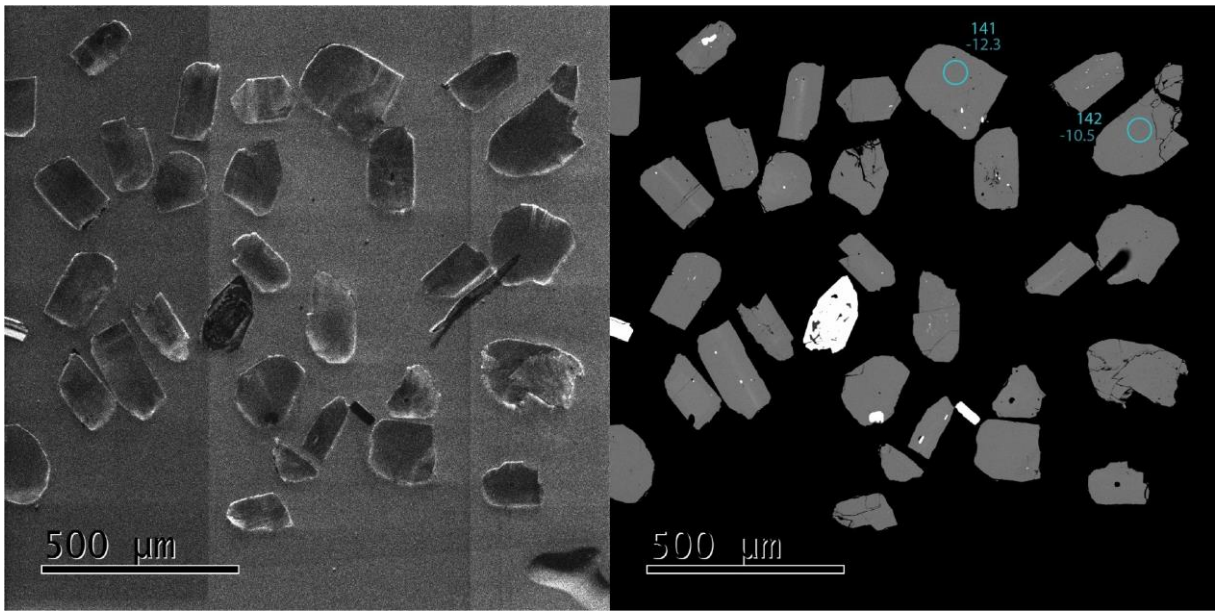

Figure 80 – Apatite εNd spot analyses of sample s7B indicating the analysed spots with the obtained εNd_{468} values

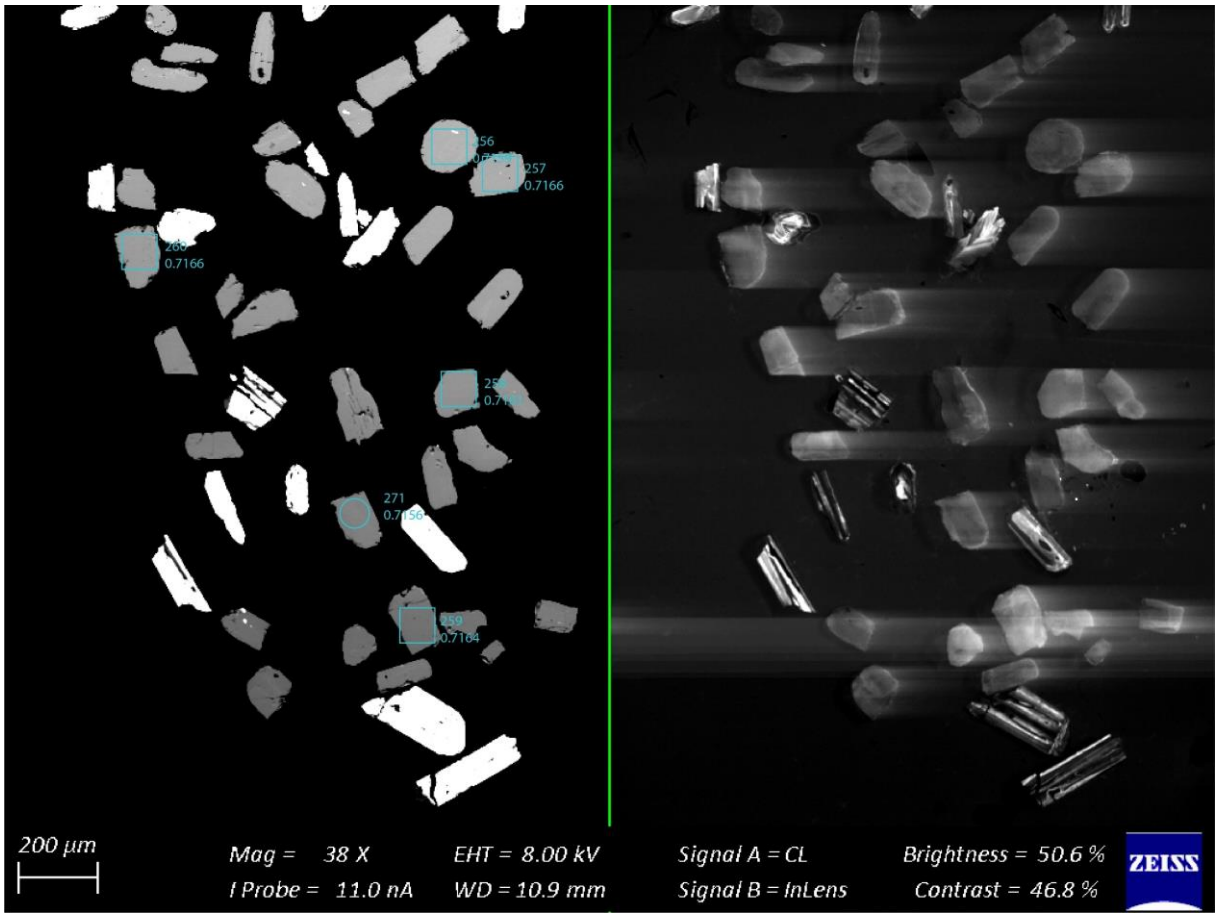

Figure 81 – Apatite spot analyses of sample s7B indicating the analysed spots with the obtained $^{87}Sr/^{86}Sr_{468}$ values

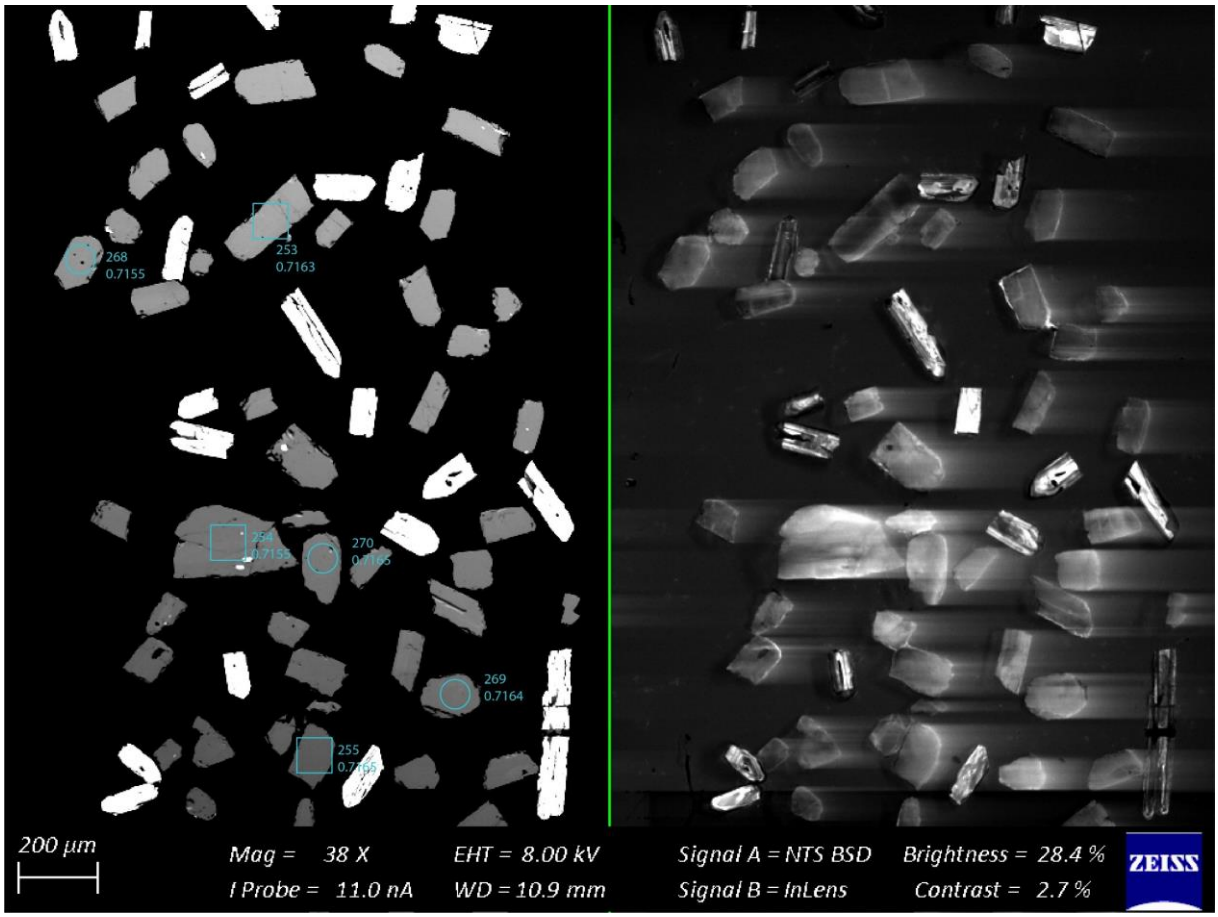

Figure 82 – Apatite spot analyses of sample s7B indicating the analysed spots with the obtained $^{87}Sr/^{86}Sr_{468}$ values

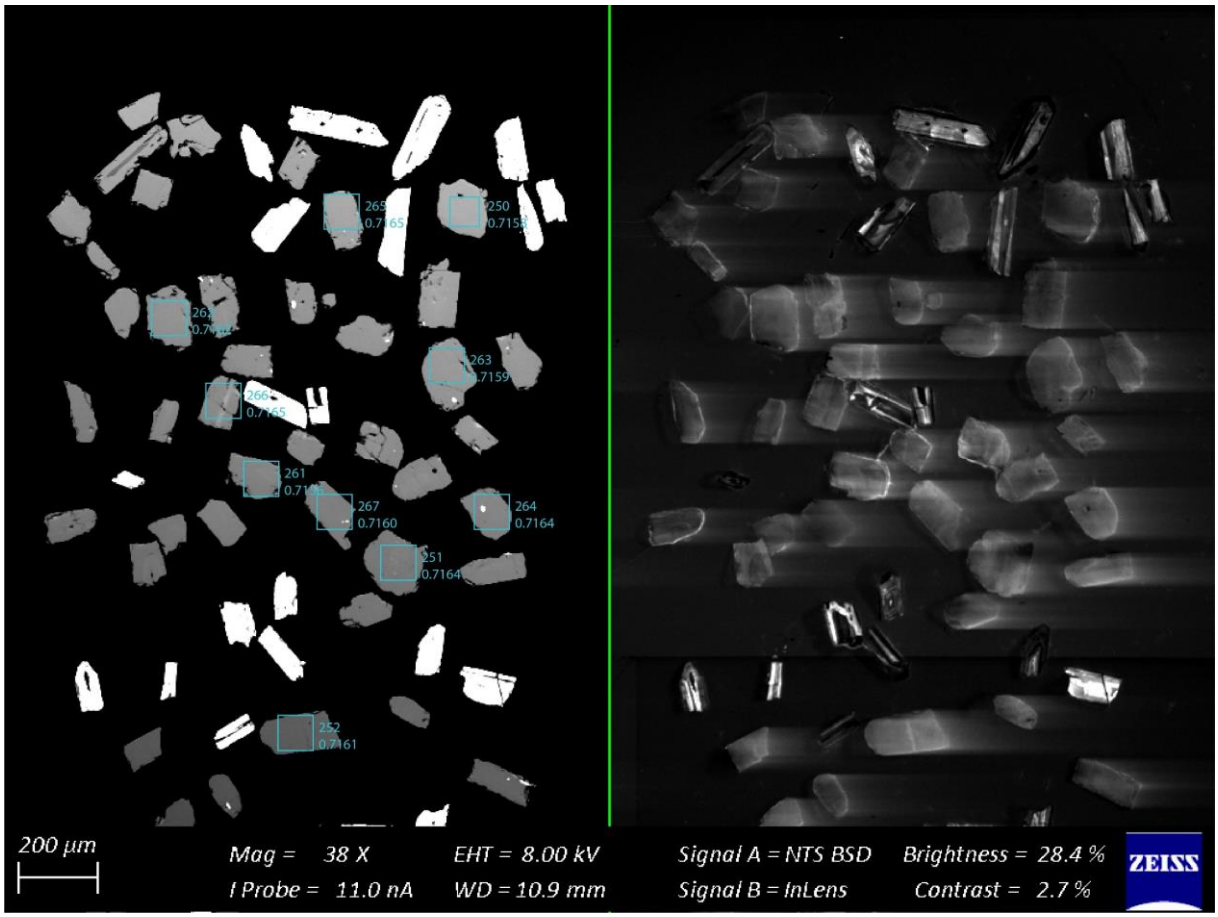

Figure 83 – Apatite spot analyses of sample s7B indicating the analysed spots with the obtained $^{87}Sr/^{86}Sr_{468}$ values

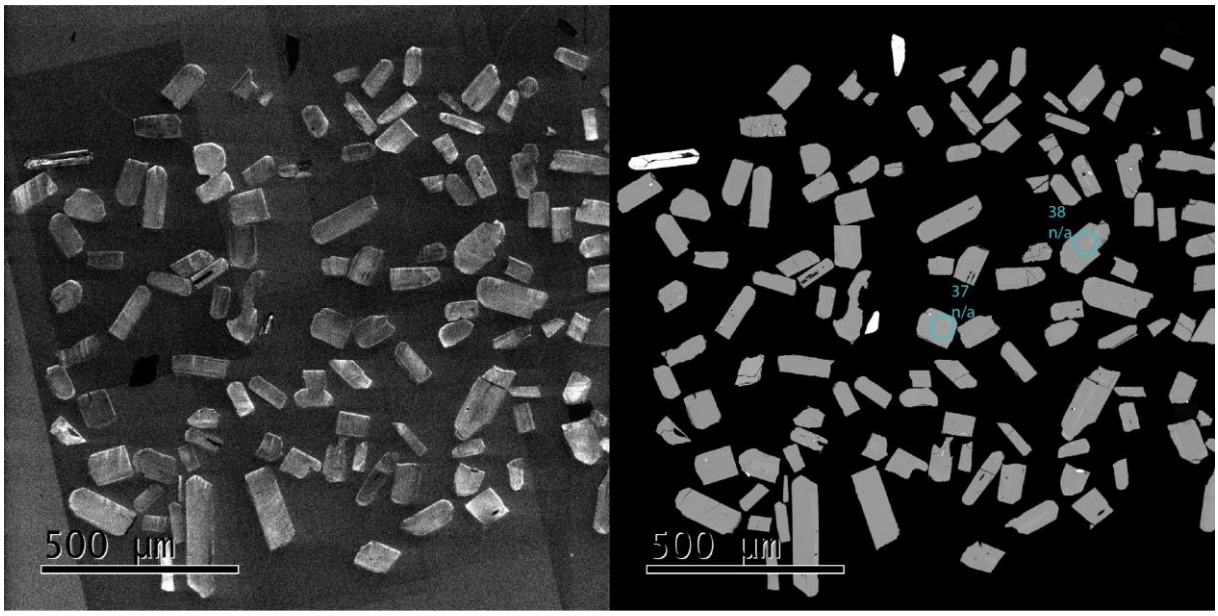

Figure 84 – Apatite εNd spot analyses of sample s8Da indicating the analysed spots with the obtained εNd_{468} values

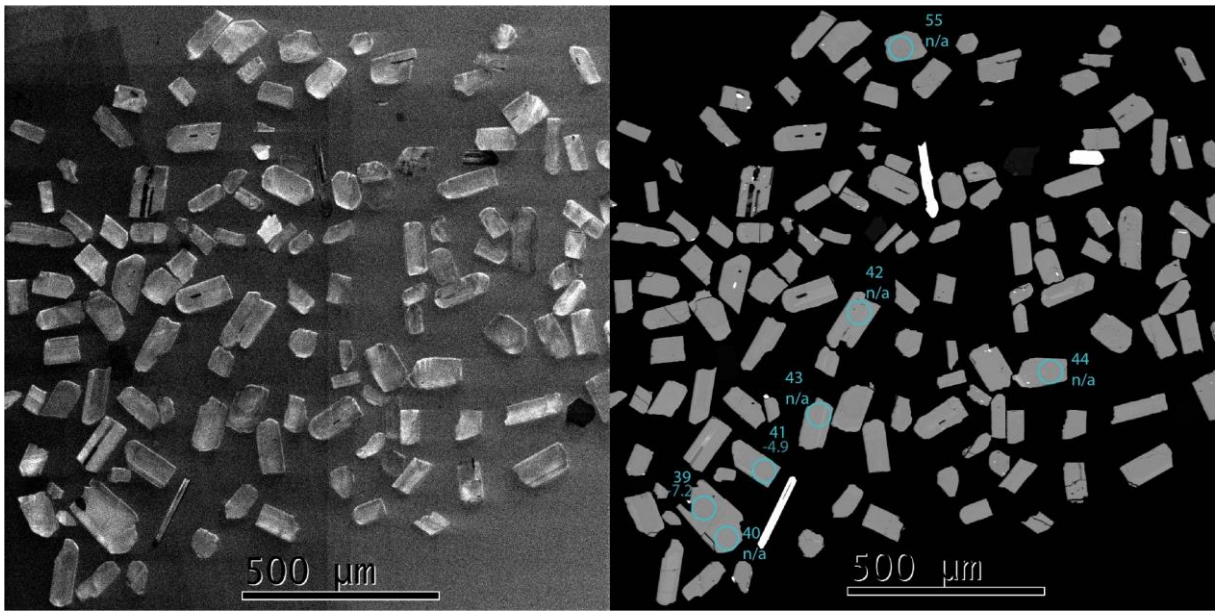

Figure 85 – Apatite εNd spot analyses of sample s8Da indicating the analysed spots with the obtained εNd_{468} values

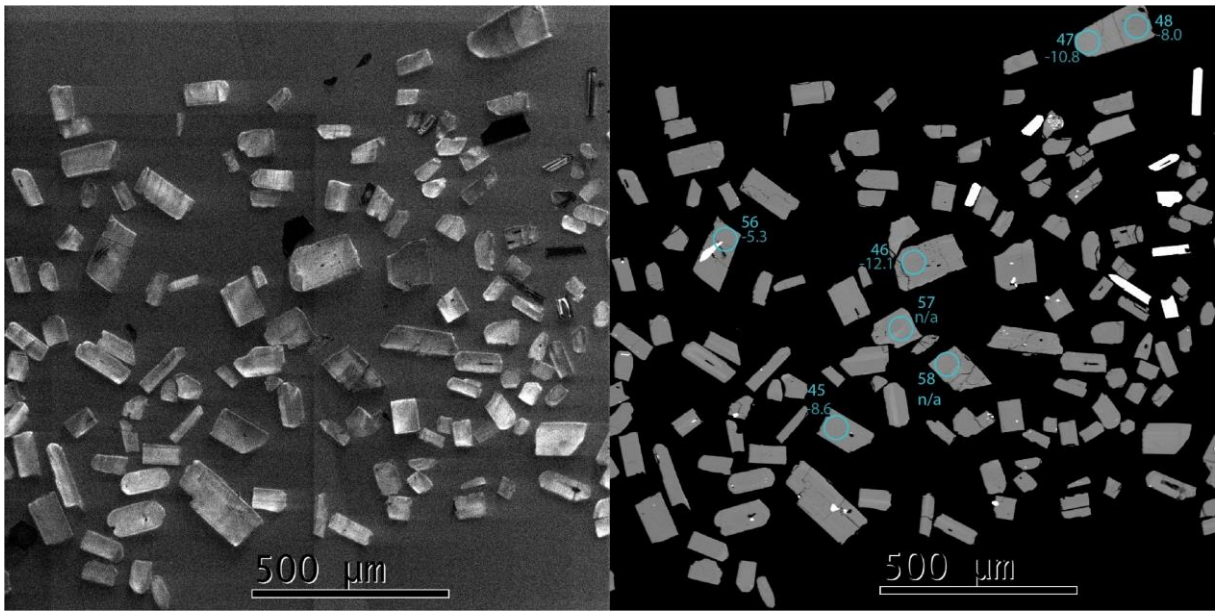

Figure 86 – Apatite εNd spot analyses of sample s8Da indicating the analysed spots with the obtained εNd_{468} values

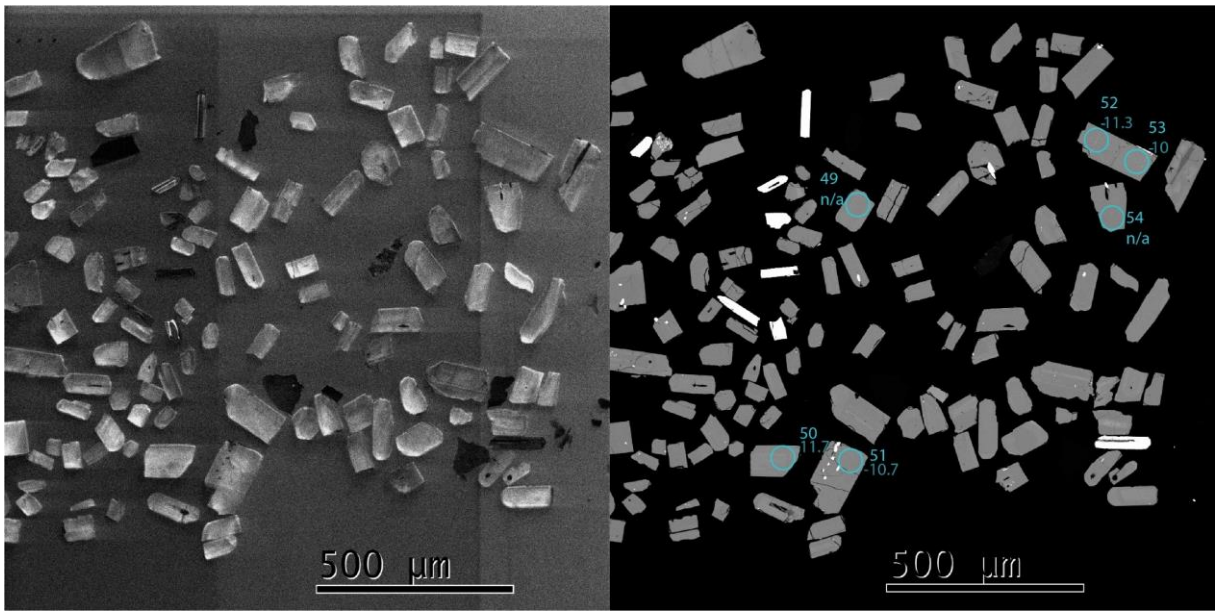

Figure 87 – Apatite εNd spot analyses of sample s8Da indicating the analysed spots with the obtained εNd_{468} values

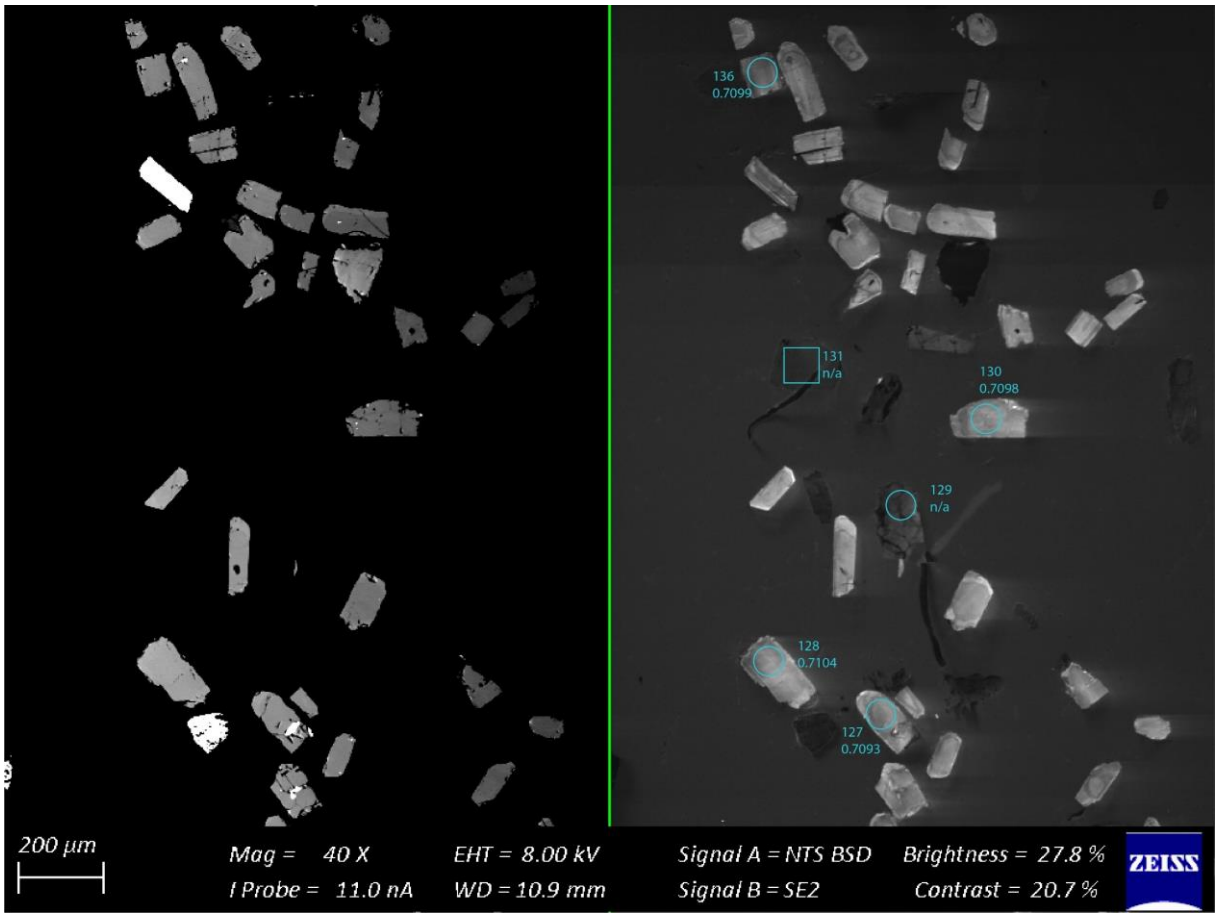

Figure 88 – Apatite spot analyses of sample s8Da indicating the analysed spots with the obtained $^{87}Sr/^{86}Sr_{468}$ values

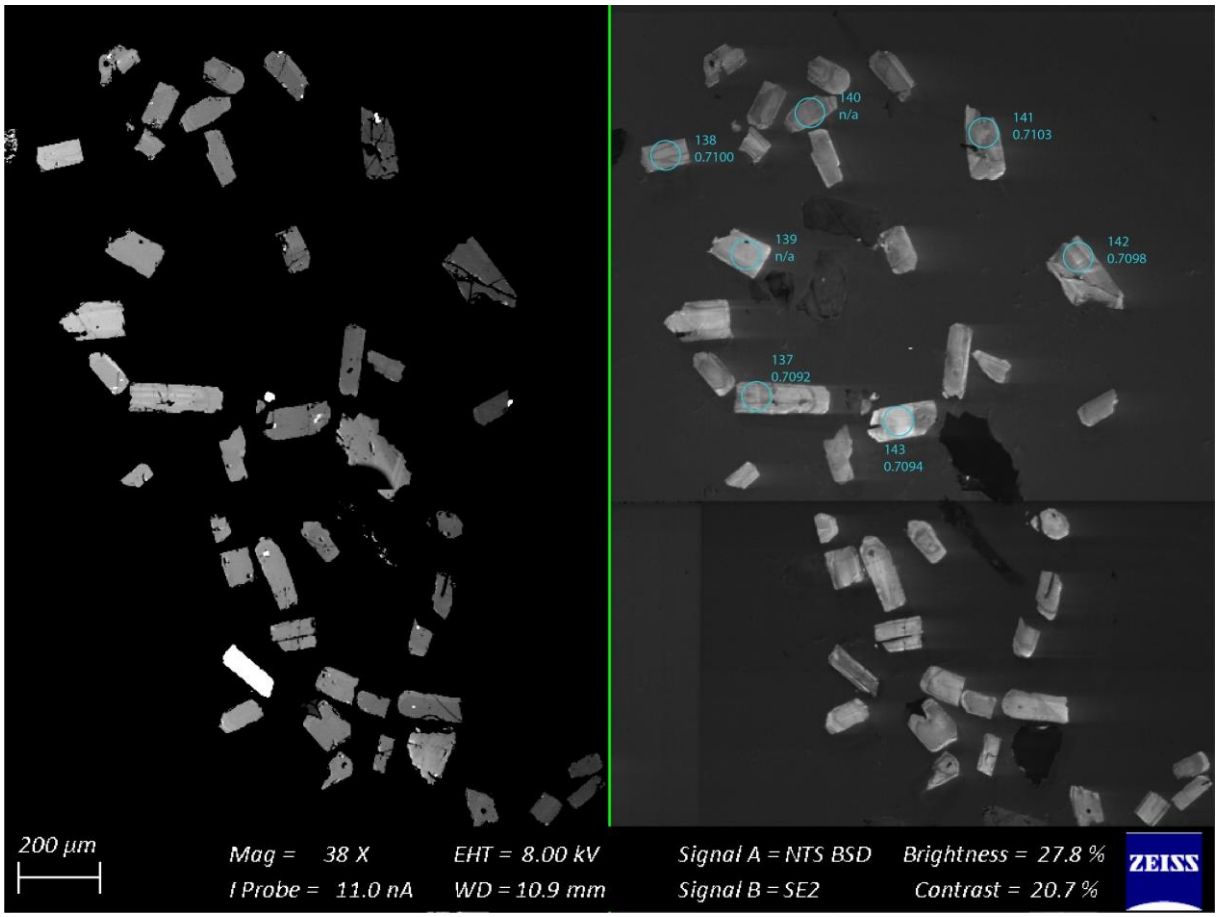

Figure 89 – Apatite spot analyses of sample s8Da indicating the analysed spots with the obtained $^{87}Sr/^{86}Sr_{468}$ values

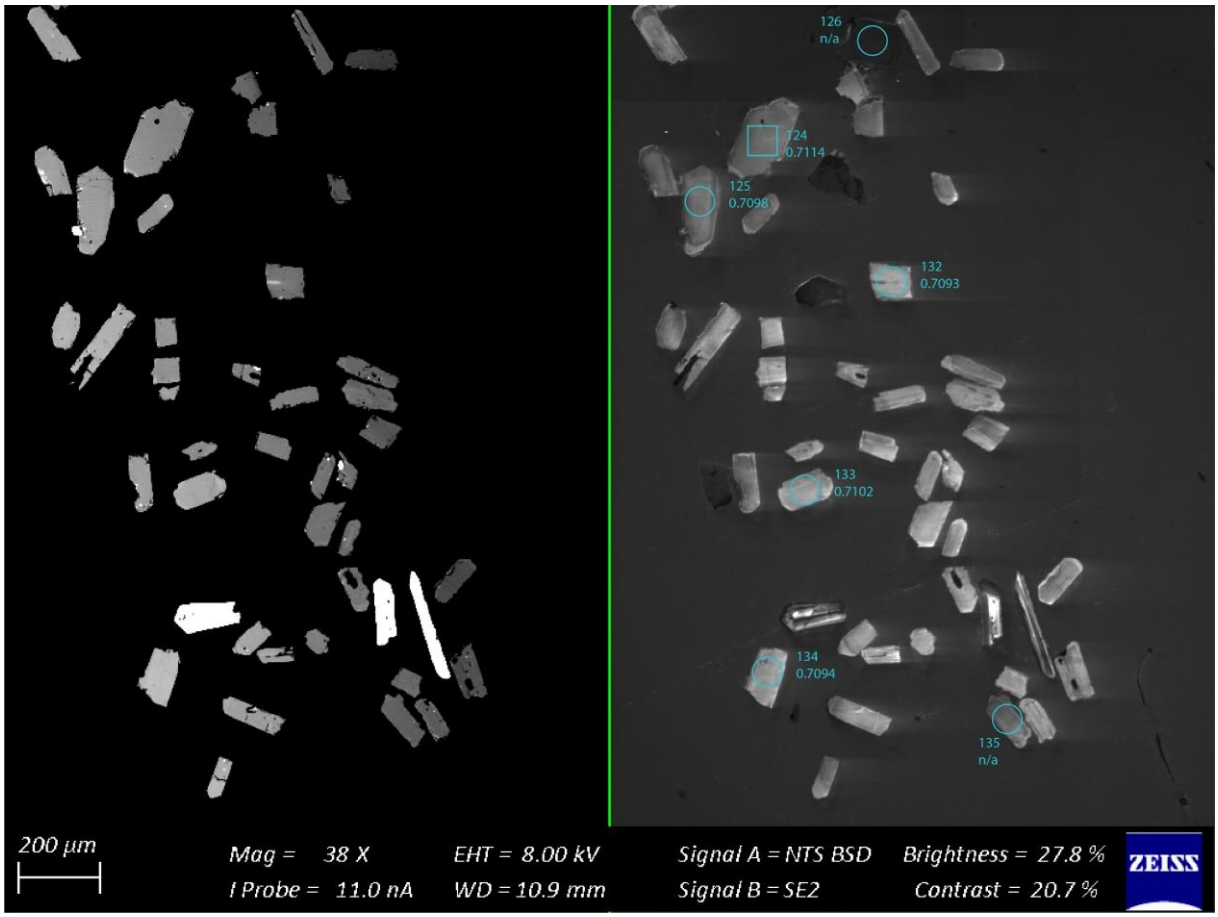

Figure 90 – Apatite spot analyses of sample s8Da indicating the analysed spots with the obtained $^{87}Sr/^{86}Sr_{468}$ values

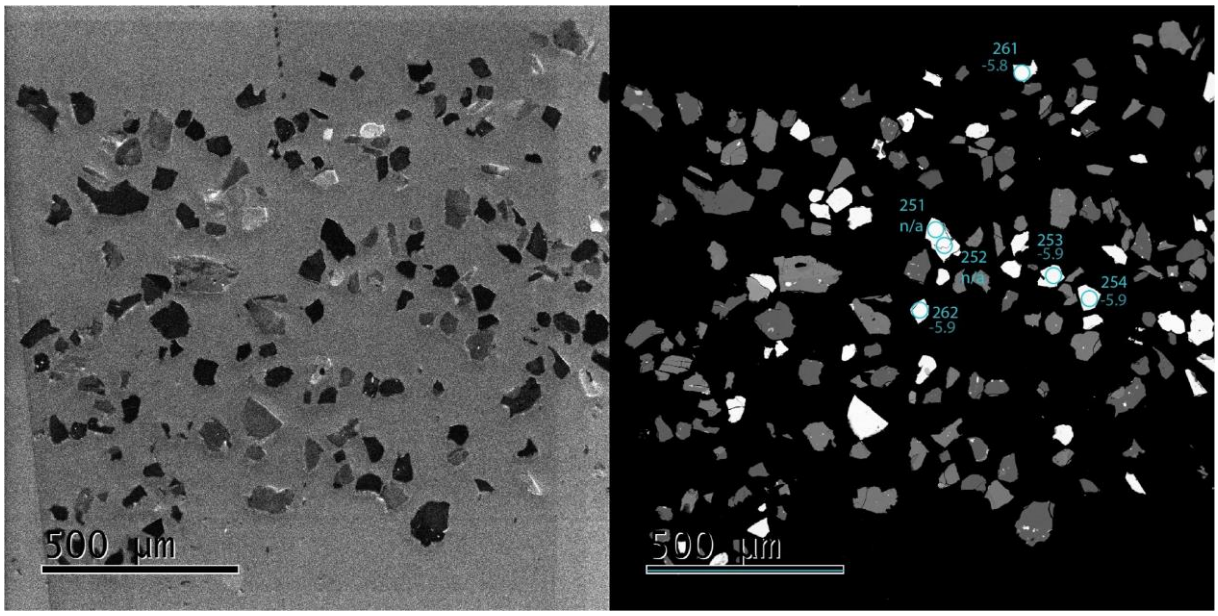

Figure 91 – Apatite εNd spot analyses of sample s8Db indicating the analysed spots with the obtained εNd_{468} values

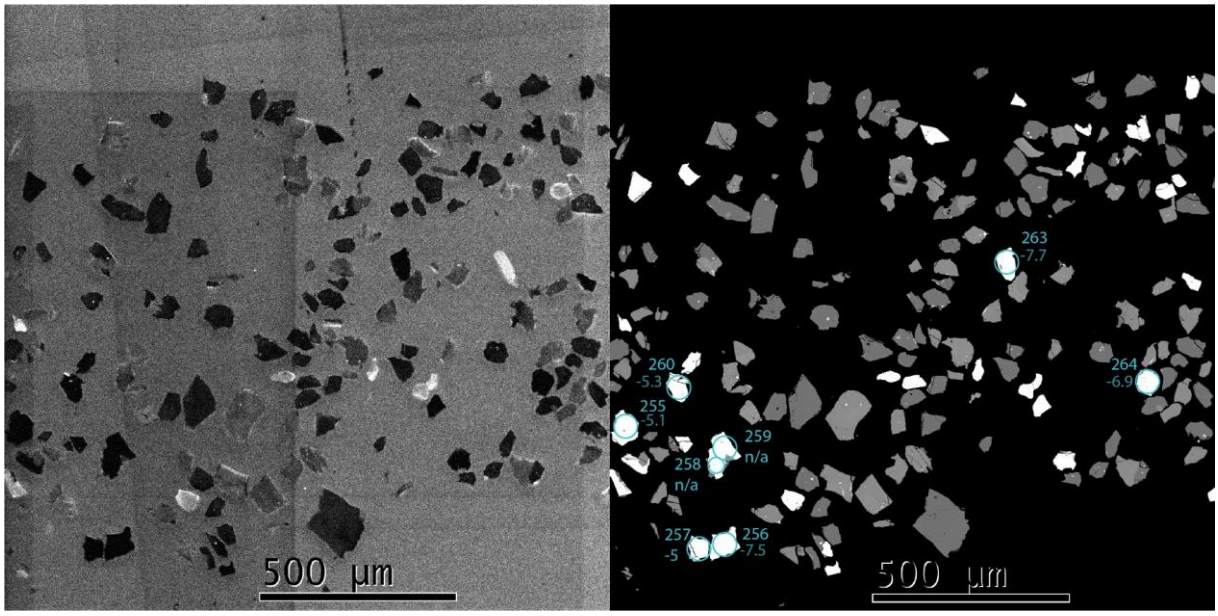

Figure 92 – Apatite εNd spot analyses of sample s8Db indicating the analysed spots with the obtained εNd_{468} values

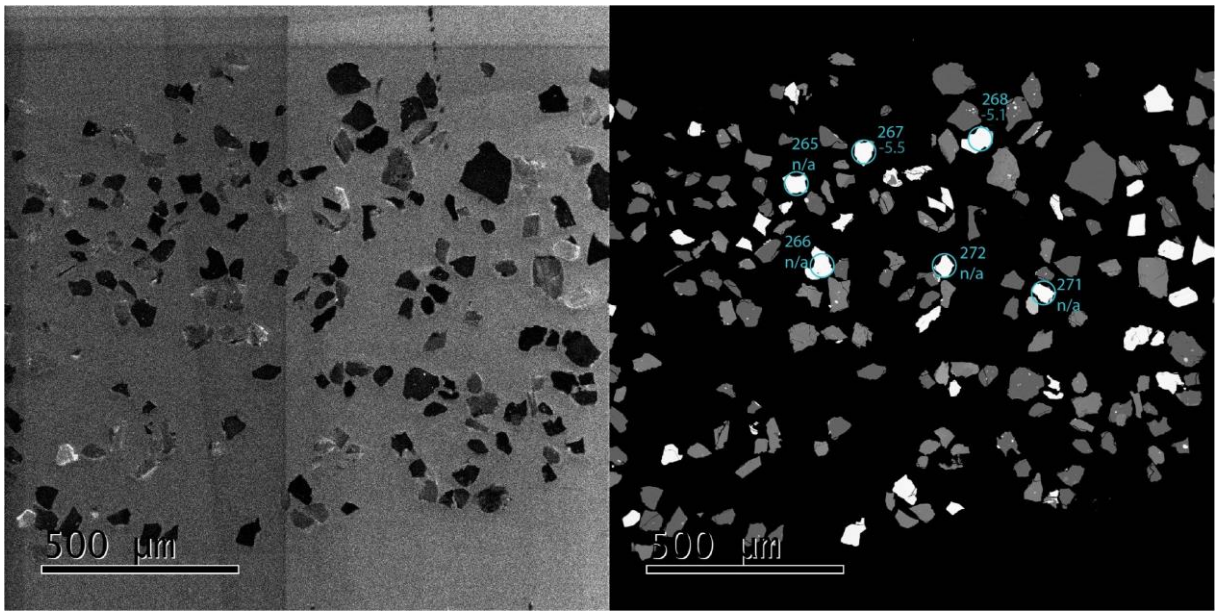

Figure 93 – Apatite εNd spot analyses of sample s8Db indicating the analysed spots with the obtained εNd_{468} values

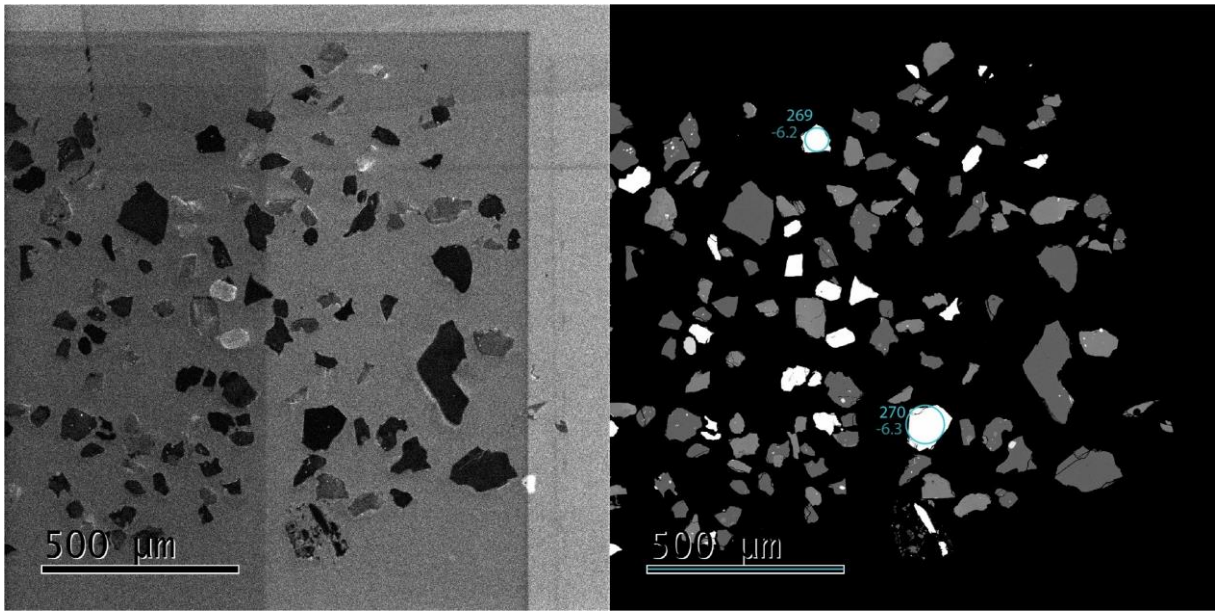

Figure 94 – Apatite εNd spot analyses of sample s8Db indicating the analysed spots with the obtained εNd_{468} values

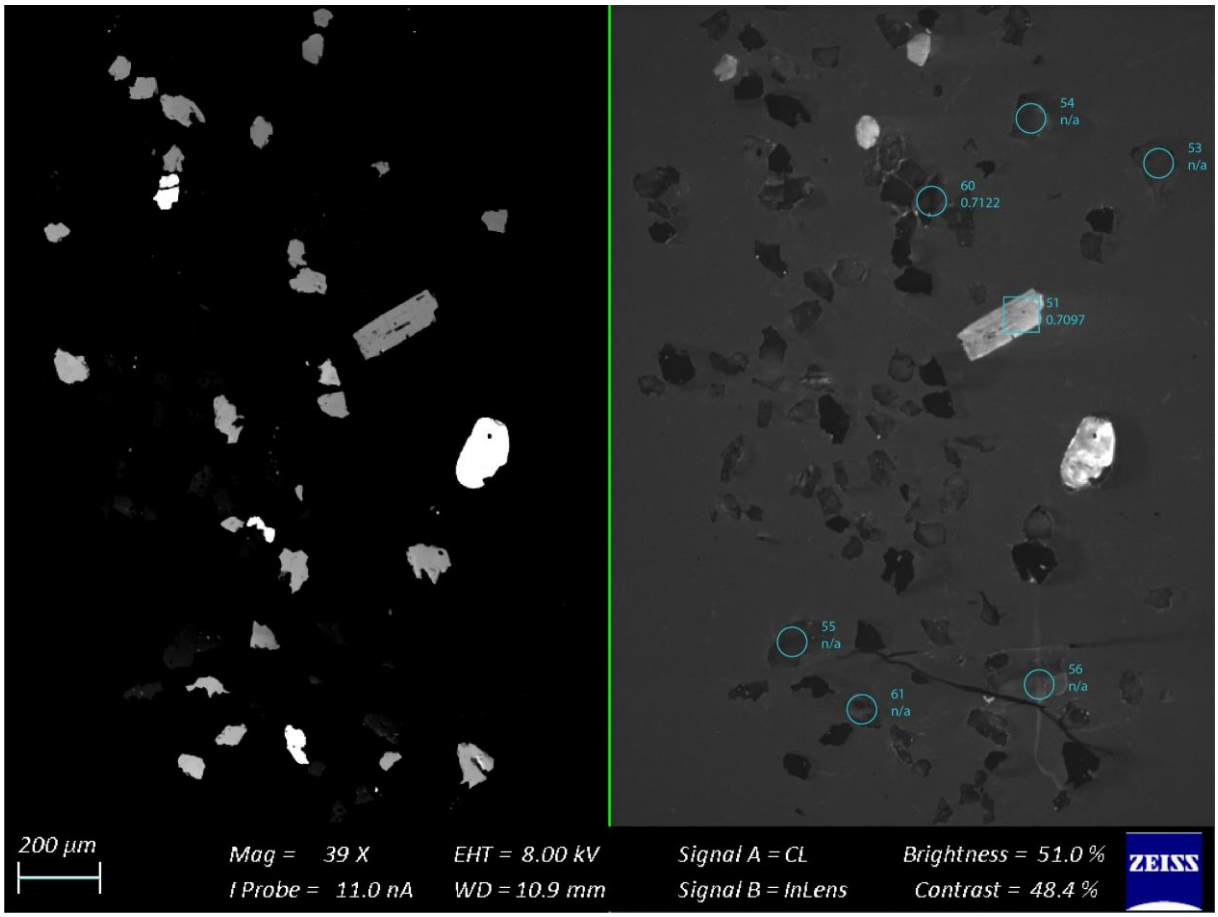

Figure 95 – Apatite spot analyses of sample s8Db indicating the analysed spots with the obtained $^{87}Sr/^{86}Sr_{468}$ values

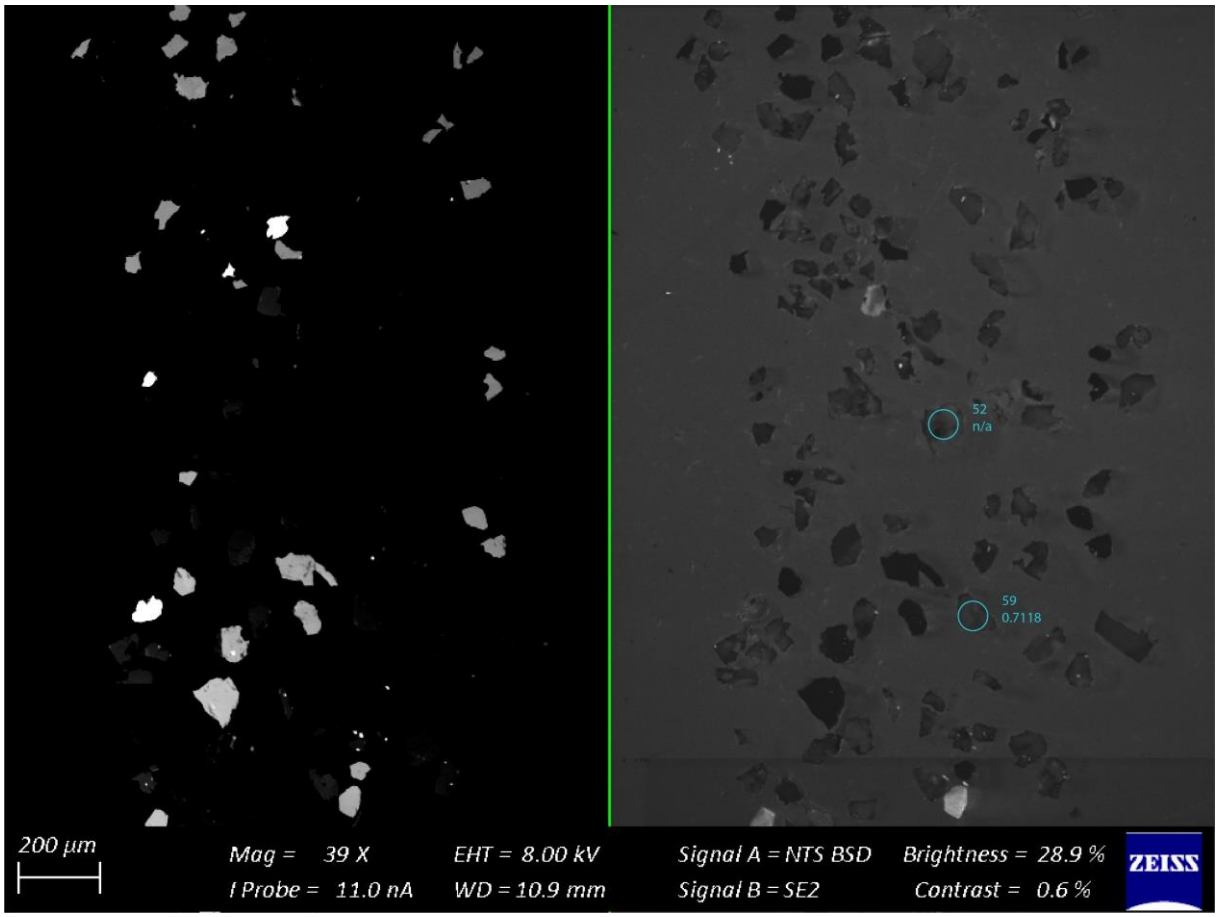

Figure 96 – Apatite spot analyses of sample s8Db indicating the analysed spots with the obtained $^{87}Sr/^{86}Sr_{468}$ values

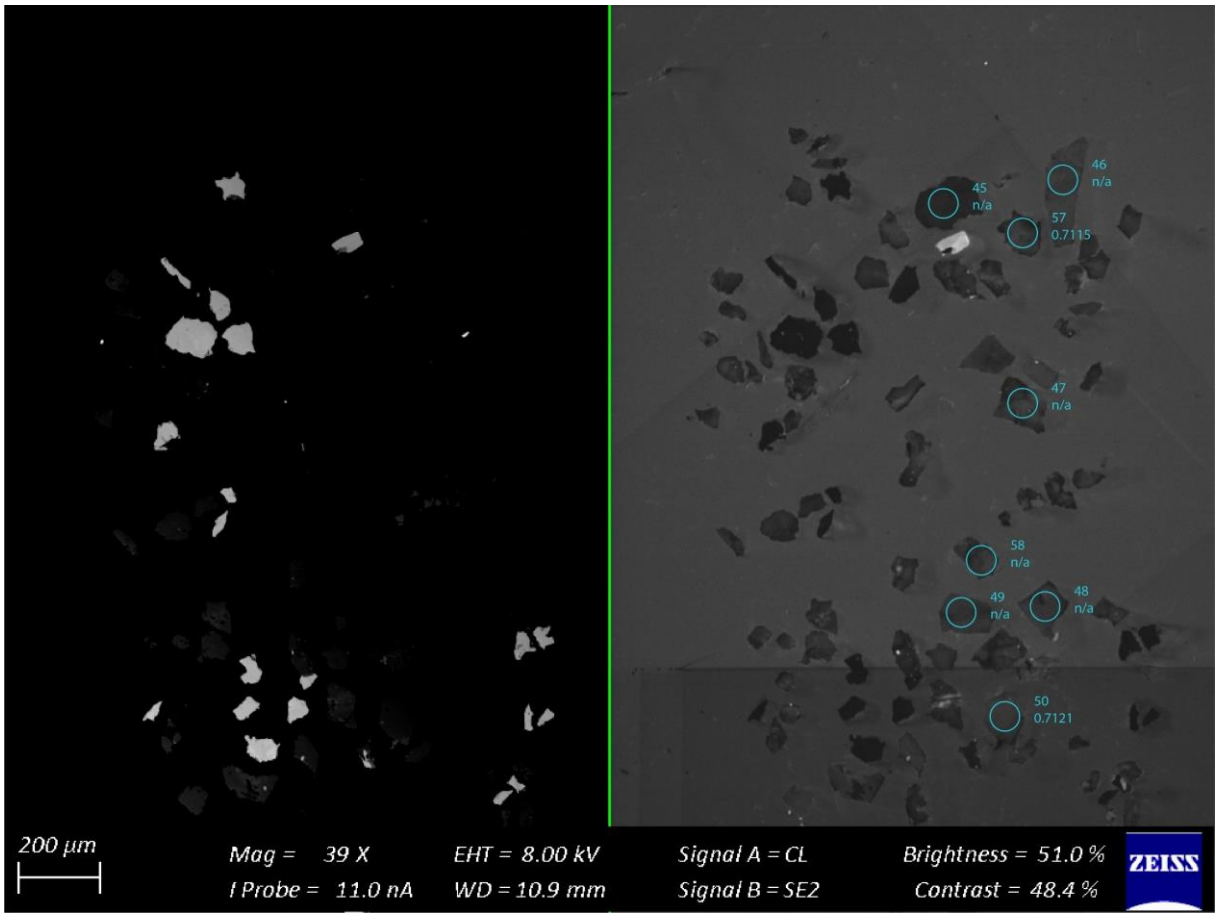

Figure 97 – Apatite spot analyses of sample s8Db indicating the analysed spots with the obtained $^{87}Sr/^{86}Sr_{468}$ values

APPENDIX V: ISOTOPE ANALYSES OF WHOLE ROCKS

TABLE 1: WHOLE ROCK ISOTOPE ANALYSES; INITIAL VALUES (I) ARE CALCULATED TO THE MEAN MAGMATIC AGE OF 468 MA

Sample	$^{87}Sr/^{86}Sr_i$	±2σ	$^{143}Nd/^{144}Nd_i$	±2σ	εNd_i	±2σ
s008	0.710192	0.000012	0.512067	0.000013	-7.3	0.3
s010	0.705924	0.000010	0.512606	0.000010	-0.6	0.2
s013	0.727537	0.000017	0.511933	0.000011	-8.8	0.2
s020	0.864175	0.000016	0.512514	0.000013	-8.2	0.3
s028	1.095306	0.000014	0.512284	0.000011	-8.4	0.2
s029	0.750728	0.000013	0.511172	0.000014	-22.8	0.3
s037	0.720749	0.000013	0.511181	0.000010	-22.2	0.2
s039	0.729712	0.000012	0.511669	0.000012	-14.6	0.2
s040	0.738600	0.000011	0.511298	0.000014	-20.6	0.3
s044	0.714297	0.000012	0.512097	0.000011	-6.5	0.2
s045	0.714327	0.000012	0.512059	0.000011	-7.4	0.2
s046	0.714495	0.000012	0.512064	0.000015	-7.6	0.3
s047	0.726213	0.000012	0.511893	0.000010	-10.8	0.2
s050	0.706367	0.000010	0.512529	0.000008	1.3	0.2

APPENDIX VI: PHASE COMPOSITION MODELLING

TABLE 1: MODELLED PHASE COMPOSITIONS OF SAMPLE S1A AS A FUNCTION OF TEMPERATURE; FEO INDICATES TOTAL FE

Phase	Bulk	Clinopyroxene1	Clinopyroxene2	Plagioclase	Ilmenite	Melt		Clinopyroxene1	Clinopyroxene2	Melt	Plagioclase	Ilmenite	
Temperature(°C)		900						890					
Na_2O	2.7	0.2	0.4	4.2	0.0	4.0		0.2	0.4	4.0	4.3	0.0	
MgO	6.4	13.1	17.6	0.0	3.8	1.3		12.9	17.7	1.3	0.0	3.8	
Al_2O_3	15.1	2.4	1.3	30.3	0.0	15.1		1.8	1.2	15.1	30.2	0.0	
SiO_2	54.7	52.0	51.9	52.6	0.0	63.7		52.6	51.9	63.9	52.7	0.0	
CaO	6.9	19.1	3.1	12.7	0.0	3.0		18.4	2.7	2.9	12.6	0.0	
TiO_2	1.7	0.2	1.6	0.0	54.2	0.4		0.3	1.6	0.4	0.0	54.2	
FeO	9.2	12.6	23.0	0.0	42.0	3.0		12.9	23.2	2.8	0.0	42.0	
H_2O	1.4	0.0	0.0	0.0	0.0	4.6		0.0	0.0	4.7	0.0	0.0	
K_2O	1.9	0.4	1.1	0.2	0.0	4.8		0.9	1.1	4.9	0.2	0.0	

Phase		Clinopyroxene1	Clinopyroxene2	Melt	Plagioclase	Ilmenite		Clinopyroxene1	Clinopyroxene2	Melt	Plagioclase	Ilmenite	
Temperature(°C)		880						870					
Na_2O	2.7	0.2	0.4	4.0	4.3	0.0		0.4	0.4	3.9	4.4	0.0	
MgO	6.4	12.9	17.6	1.2	0.0	3.8		12.8	17.5	1.1	0.0	3.8	
Al_2O_3	15.1	1.9	1.2	15.1	30.1	0.0		2.3	1.1	15.1	30.0	0.0	
SiO_2	54.7	52.6	51.9	64.1	52.8	0.0		52.3	52.0	64.3	53.0	0.0	
CaO	6.9	18.6	2.7	2.7	12.5	0.0		18.9	2.7	2.7	12.4	0.0	
TiO_2	1.7	0.3	1.7	0.4	0.0	54.2		0.2	1.7	0.4	0.0	54.2	
FeO	9.2	12.7	23.3	2.6	0.0	42.0		12.6	23.4	2.3	0.0	42.0	
H_2O	1.4	0.0	0.0	4.9	0.0	0.0		0.0	0.0	5.1	0.0	0.0	
K_2O	1.9	1.0	1.2	5.0	0.2	0.0		0.4	1.2	5.1	0.3	0.0	

Phase		Clinopyroxene1	Clinopyroxene2	Melt	Plagioclase	Ilmenite		Clinopyroxene	Melt	Biotite	Plagioclase	Ilmenite	Orthopyroxene
Temperature(°C)		860						850					
Na_2O	2.7	0.4	0.4	3.8	4.4	0.0		0.1	3.6	0.0	5.0	0.0	0.0
MgO	6.4	12.8	17.5	1.0	0.0	3.7		13.0	1.0	14.4	0.0	3.4	19.1
Al_2O_3	15.1	2.3	1.1	15.1	29.9	0.0		2.2	14.4	13.0	29.0	0.0	1.8
SiO_2	54.7	52.3	52.0	64.5	53.1	0.0		52.0	66.2	38.5	54.4	0.0	51.6
CaO	6.9	19.1	2.6	2.5	12.3	0.0		19.5	2.4	0.0	11.3	0.0	1.2
TiO_2	1.7	0.2	1.7	0.4	0.0	54.2		0.2	0.3	4.5	0.0	54.1	0.1
FeO	9.2	12.5	23.4	2.1	0.0	42.1		12.8	2.0	16.4	0.0	42.5	26.1
H_2O	1.4	0.0	0.0	5.3	0.0	0.0		0.0	4.8	2.9	0.0	0.0	0.0
K_2O	1.9	0.4	1.3	5.2	0.3	0.0		0.2	5.2	10.3	0.3	0.0	0.0

Phase		Clinopyroxene	Melt	Biotite	Plagioclase	Ilmenite		Clinopyroxene	Melt	Biotite	Plagioclase	Ilmenite	
Temperature(°C)		840						830					
Na_2O	2.7	0.1	3.7	0.0	5.2	0.0		0.1	3.6	0.0	5.3	0.0	
MgO	6.4	15.5	1.1	14.9	0.0	3.6		15.3	1.1	14.9	0.0	3.4	
Al_2O_3	15.1	3.2	13.1	13.6	28.8	0.0		2.8	11.9	13.6	28.8	0.0	
SiO_2	54.7	50.3	68.6	38.3	54.7	0.0		50.6	70.9	38.3	54.8	0.0	
CaO	6.9	7.6	2.1	0.0	11.0	0.0		7.9	1.9	0.0	10.9	0.0	
TiO_2	1.7	1.4	0.3	4.0	0.0	54.1		1.2	0.3	3.7	0.0	54.1	
FeO	9.2	21.2	2.2	15.8	0.0	42.3		21.3	2.0	16.1	0.0	42.5	
H_2O	1.4	0.0	5.0	3.1	0.0	0.0		0.0	5.1	3.1	0.0	0.0	
K_2O	1.9	0.8	3.9	10.4	0.2	0.0		0.8	3.2	10.4	0.2	0.0	

Phase		Clinopyroxene	Melt	Biotite	Plagioclase	Ilmenite		Clinopyroxene	Melt	Biotite	Plagioclase	Amphibole	Ilmenite	
Temperature(°C)		820						810						
Na_2O	2.7	0.1	3.5	0.0	5.3	0.0		0.1	2.7	0.0	5.5	0.2	0.0	
MgO	6.4	15.3	1.1	14.9	0.0	3.4		12.7	1.0	13.4	0.0	17.8	2.7	
Al_2O_3	15.1	2.8	12.0	13.5	28.7	0.0		2.0	10.8	12.9	28.3	1.2	0.0	
SiO_2	54.7	50.6	71.0	38.4	54.9	0.0		51.5	73.5	38.2	55.5	54.4	0.0	
CaO	6.9	7.9	2.0	0.0	10.8	0.0		16.4	2.2	0.0	10.4	2.6	0.0	
TiO_2	1.7	1.2	0.3	3.7	0.0	54.0		0.2	0.2	3.9	0.0	0.0	53.7	
FeO	9.2	21.3	1.9	16.0	0.0	42.6		17.0	2.1	18.3	0.0	21.7	43.6	
H_2O	1.4	0.0	5.2	3.1	0.0	0.0		0.0	3.9	3.0	0.0	2.1	0.0	
K_2O	1.9	0.8	3.2	10.4	0.2	0.0		0.2	3.4	10.3	0.3	0.0	0.0	

Phase		Clinopyroxene	Melt	Biotite	Plagioclase	Amphibole	Ilmenite		Clinopyroxene	Melt	Biotite	Plagioclase	Amphibole	Ilmenite	Quartz
Temperature(°C)		800							790						
Na_2O	2.7	0.1	2.6	0.0	5.6	0.2	0.0		0.1	2.7	0.0	5.6	0.2	0.0	0.0
MgO	6.4	12.6	1.0	13.4	0.0	17.8	2.6		12.7	0.9	13.5	0.0	17.8	2.5	0.0
Al_2O_3	15.1	1.9	10.6	12.8	28.3	1.1	0.0		1.9	10.6	12.8	28.2	1.1	0.0	0.0
SiO_2	54.7	51.5	74.1	38.3	55.6	54.4	0.0		51.5	74.5	38.3	55.6	54.4	0.0	100.0
CaO	6.9	16.4	2.2	0.0	10.3	2.6	0.0		16.4	2.1	0.0	10.3	2.6	0.0	0.0
TiO_2	1.7	0.2	0.2	3.8	0.0	0.0	53.7		0.2	0.2	3.7	0.0	0.0	53.7	0.0
FeO	9.2	17.1	1.9	18.4	0.0	21.8	43.7		17.1	1.7	18.4	0.0	21.8	43.8	0.0
H_2O	1.4	0.0	4.0	3.1	0.0	2.1	0.0		0.0	4.2	3.1	0.0	2.1	0.0	0.0
K_2O	1.9	0.2	3.4	10.3	0.3	0.0	0.0		0.2	3.3	10.3	0.2	0.0	0.0	0.0

TABLE 1 CONTINUED

Phase	Bulk	Clinopyroxene	Melt	Biotite	Plagioclase	Amphibole	Ilmenite	Quartz	Clinopyroxene	Melt	Biotite	Plagioclase	Amphibole	Ilmenite	Quartz
Temperature(°C)		780							770						
Na_2O	2.7	0.1	2.7	0.0	5.7	0.2	0.0	0.0	0.1	2.9	0.0	5.7	0.1	0.0	0.0
MgO	6.4	12.3	0.8	13.4	0.0	17.6	2.4	0.0	12.3	0.7	13.6	0.0	17.7	2.4	0.0
Al_2O_3	15.1	1.8	10.6	12.7	28.2	1.1	0.0	0.0	1.7	10.5	12.7	28.2	1.2	0.0	0.0
SiO_2	54.7	51.7	74.3	38.3	55.7	54.4	0.0	100.0	51.9	74.4	38.3	55.7	54.2	0.0	100.0
CaO	6.9	18.3	2.1	0.0	10.2	2.6	0.0	0.0	19.4	1.7	0.0	10.2	1.4	0.0	0.0
TiO_2	1.7	0.1	0.2	3.5	0.0	0.0	53.6	0.0	0.1	0.2	3.4	0.0	0.0	53.6	0.0
FeO	9.2	15.4	1.6	18.7	0.0	22.1	44.0	0.0	14.3	1.2	18.5	0.0	23.4	44.0	0.0
H_2O	1.4	0.0	4.6	3.1	0.0	2.1	0.0	0.0	0.0	5.2	3.2	0.0	2.1	0.0	0.0
K_2O	1.9	0.2	3.2	10.3	0.2	0.0	0.0	0.0	0.2	3.1	10.3	0.2	0.0	0.0	0.0

Phase		Clinopyroxene	Melt	Biotite	Plagioclase	Amphibole	Ilmenite	Quartz	Melt	Biotite	Plagioclase	Amphibole	Ilmenite	Quartz	
Temperature(°C)		760							750						
Na_2O	2.7	0.1	2.9	0.0	5.7	0.1	0.0	0.0	3.1	0.0	5.9	0.8	0.0	0.0	
MgO	6.4	12.3	0.6	13.6	0.0	17.6	2.3	0.0	0.6	11.8	0.0	15.1	1.8	0.0	
Al_2O_3	15.1	1.6	10.7	12.7	28.1	1.1	0.0	0.0	10.5	12.7	27.9	4.1	0.0	0.0	
SiO_2	54.7	52.0	73.9	38.3	55.8	54.2	0.0	100.0	73.7	37.7	56.1	52.4	0.0	100.0	
CaO	6.9	20.1	2.0	0.0	10.2	1.5	0.0	0.0	1.8	0.0	9.9	9.7	0.0	0.0	
TiO_2	1.7	0.1	0.2	3.2	0.0	0.0	53.6	0.0	0.2	2.9	0.0	0.0	53.4	0.0	
FeO	9.2	13.6	1.1	18.7	0.0	23.4	44.2	0.0	1.3	21.6	0.0	15.9	44.9	0.0	
H_2O	1.4	0.0	5.5	3.2	0.0	2.1	0.0	0.0	6.2	3.2	0.0	2.1	0.0	0.0	
K_2O	1.9	0.2	3.0	10.3	0.2	0.0	0.0	0.0	2.7	10.1	0.2	0.0	0.0	0.0	

Phase		Melt	Biotite	Plagioclase	Amphibole	Ilmenite	Quartz		Melt	Biotite	Plagioclase	Amphibole1	Amphibole2	Ilmenite	Quartz
Temperature(°C)		740							730						
Na_2O	2.7	3.1	0.0	5.9	0.8	0.0	0.0		3.1	0.0	5.9	0.1	0.7	0.0	0.0
MgO	6.4	0.5	11.8	0.0	15.1	1.7	0.0		0.4	11.8	0.0	15.6	15.4	1.7	0.0
Al_2O_3	15.1	10.7	12.8	27.9	4.2	0.0	0.0		10.8	12.7	27.9	1.1	3.3	0.0	0.0
SiO_2	54.7	73.5	37.7	56.2	52.3	0.0	100.0		73.1	37.7	56.1	53.5	53.2	0.0	100.0
CaO	6.9	2.0	0.0	9.9	9.9	0.0	0.0		2.0	0.0	10.0	1.4	10.6	0.0	0.0
TiO_2	1.7	0.2	2.7	0.0	0.0	53.3	0.0		0.2	2.7	0.0	0.0	0.0	53.3	0.0
FeO	9.2	1.0	21.6	0.0	15.7	45.0	0.0		0.9	21.6	0.0	26.2	14.9	45.0	0.0
H_2O	1.4	6.5	3.3	0.0	2.1	0.0	0.0		6.9	3.3	0.0	2.0	2.1	0.0	0.0
K_2O	1.9	2.5	10.1	0.1	0.0	0.0	0.0		2.6	10.1	0.1	0.0	0.0	0.0	0.0

Phase		Melt	Biotite	Plagioclase	Amphibole	Ilmenite	Quartz		Melt	Biotite	Plagioclase	Amphibole1	Amphibole2	Ilmenite	Quartz
Temperature(°C)		720							710						
Na_2O	2.7	3.3	0.0	6.0	0.7	0.0	0.0		3.2	0.0	5.9	0.1	0.6	0.0	0.0
MgO	6.4	0.4	11.8	0.0	15.1	1.6	0.0		0.4	11.8	0.0	15.6	15.4	1.5	0.0
Al_2O_3	15.1	10.8	12.9	27.8	4.1	0.0	0.0		10.8	12.9	27.9	1.1	3.3	0.0	0.0
SiO_2	54.7	72.9	37.6	56.3	52.5	0.0	100.0		72.6	37.7	56.2	53.5	53.2	0.0	100.0
CaO	6.9	1.9	0.0	9.8	10.0	0.0	0.0		2.0	0.0	9.9	1.3	10.6	0.0	0.0
TiO_2	1.7	0.2	2.5	0.0	0.0	53.3	0.0		0.2	2.5	0.0	0.0	0.0	53.3	0.0
FeO	9.2	0.8	21.7	0.0	15.5	45.1	0.0		0.7	21.7	0.0	26.4	14.8	45.2	0.0
H_2O	1.4	7.5	3.3	0.0	2.1	0.0	0.0		7.9	3.3	0.0	2.0	2.1	0.0	0.0
K_2O	1.9	2.3	10.1	0.1	0.0	0.0	0.0		2.3	10.1	0.1	0.0	0.0	0.0	0.0

Phase		Biotite	Plagioclase	Amphibole1	Amphibole2	Ilmenite	Quartz	H2O	Biotite	Plagioclase	Amphibole1	Amphibole2	Quartz	Ilmenite	H2O
Temperature(°C)		700							690						
Na_2O	2.7	0.0	6.0	0.1	0.6	0.0	0.0	0.0	0.0	6.0	0.1	0.6	0.0	0.0	0.0
MgO	6.4	11.8	0.0	15.5	15.5	1.5	0.0	0.0	11.9	0.0	15.6	15.6	0.0	0.0	0.0
Al_2O_3	15.1	12.9	27.8	1.1	3.2	0.0	0.0	0.0	13.0	27.8	1.1	3.2	0.0	0.0	0.0
SiO_2	54.7	37.6	56.3	53.5	53.3	0.0	100.0	0.0	37.6	56.3	53.5	53.4	100.0	0.0	0.0
CaO	6.9	0.0	9.8	1.2	10.6	0.0	0.0	0.0	0.0	9.8	1.2	10.7	0.0	0.0	0.0
TiO_2	1.7	2.4	0.0	0.0	0.0	53.3	0.0	0.0	2.3	0.0	0.0	0.0	0.0	52.6	0.0
FeO	9.2	21.8	0.0	26.5	14.7	45.3	0.0	0.0	21.7	0.0	26.5	14.5	0.0	47.4	0.0
H_2O	1.4	3.3	0.0	2.0	2.1	0.0	0.0	100.0	3.4	0.0	2.0	2.1	0.0	0.0	100.0
K_2O	1.9	10.1	0.1	0.0	0.0	0.0	0.0	0.0	10.1	0.1	0.0	0.0	0.0	0.0	0.0

Phase		Biotite	Plagioclase	Amphibole1	Amphibole2	Quartz	Ilmenite	H2O	Biotite	Plagioclase	Amphibole1	Amphibole2	Quartz	Ilmenite	H2O
Temperature(°C)		680							670						
Na_2O	2.7	0.0	6.0	0.1	0.6	0.0	0.0	0.0	0.0	6.0	0.1	0.6	0.0	0.0	0.0
MgO	6.4	11.9	0.0	15.5	15.6	0.0	0.0	0.0	11.9	0.0	15.5	15.6	0.0	0.0	0.0
Al_2O_3	15.1	13.1	27.8	1.2	3.1	0.0	0.0	0.0	13.1	27.8	1.1	3.1	0.0	0.0	0.0
SiO_2	54.7	37.6	56.3	53.5	53.5	100.0	0.0	0.0	37.5	56.4	53.5	53.5	100.0	0.0	0.0
CaO	6.9	0.0	9.8	1.1	10.7	0.0	0.0	0.0	0.0	9.8	1.1	10.8	0.0	0.0	0.0
TiO_2	1.7	2.2	0.0	0.0	0.0	0.0	52.6	0.0	2.1	0.0	0.0	0.0	0.0	52.6	0.0
FeO	9.2	21.7	0.0	26.6	14.4	0.0	47.4	0.0	21.8	0.0	26.6	14.4	0.0	47.4	0.0
H_2O	1.4	3.4	0.0	2.0	2.1	0.0	0.0	100.0	3.4	0.0	2.0	2.1	0.0	0.0	100.0
K_2O	1.9	10.1	0.1	0.0	0.0	0.0	0.0	0.0	10.1	0.1	0.0	0.0	0.0	0.0	0.0

Phase		Biotite	Plagioclase	Amphibole1	Amphibole2	Quartz	Ilmenite	H2O	Biotite	Plagioclase	Amphibole1	Amphibole2	Quartz	Ilmenite	H2O
Temperature(°C)		660							650						
Na_2O	2.7	0.0	6.1	0.1	0.6	0.0	0.0	0.0	0.0	6.1	0.1	0.5	0.0	0.0	0.0
MgO	6.4	11.9	0.0	15.5	15.6	0.0	0.0	0.0	11.9	0.0	15.5	15.7	0.0	0.0	0.0
Al_2O_3	15.1	13.2	27.8	1.2	3.0	0.0	0.0	0.0	13.3	27.7	1.2	3.0	0.0	0.0	0.0
SiO_2	54.7	37.5	56.4	53.5	53.6	100.0	0.0	0.0	37.4	56.4	53.4	53.7	100.0	0.0	0.0
CaO	6.9	0.0	9.7	1.0	10.8	0.0	0.0	0.0	0.0	9.7	1.0	10.8	0.0	0.0	0.0
TiO_2	1.7	2.0	0.0	0.0	0.0	0.0	52.6	0.0	2.0	0.0	0.0	0.0	0.0	52.6	0.0
FeO	9.2	21.8	0.0	26.7	14.3	0.0	47.4	0.0	21.8	0.0	26.8	14.2	0.0	47.4	0.0
H_2O	1.4	3.4	0.0	2.0	2.1	0.0	0.0	100.0	3.4	0.0	2.0	2.1	0.0	0.0	100.0
K_2O	1.9	10.1	0.1	0.0	0.0	0.0	0.0	0.0	10.1	0.1	0.0	0.0	0.0	0.0	0.0

Phase		Biotite	Plagioclase	Amphibole1	Amphibole2	Quartz	Ilmenite	H2O	Biotite	Plagioclase	Amphibole1	Amphibole2	Quartz	Ilmenite	H2O
Temperature(°C)		640							630						
Na_2O	2.7	0.0	6.1	0.1	0.5	0.0	0.0	0.0	0.0	6.1	0.1	0.5	0.0	0.0	0.0
MgO	6.4	11.9	0.0	15.4	15.7	0.0	0.0	0.0	11.8	0.0	15.4	15.7	0.0	0.0	0.0
Al_2O_3	15.1	13.4	27.7	1.2	3.0	0.0	0.0	0.0	13.5	27.7	1.2	3.0	0.0	0.0	0.0
SiO_2	54.7	37.4	56.4	53.4	53.7	100.0	0.0	0.0	37.3	56.4	53.4	53.8	100.0	0.0	0.0
CaO	6.9	0.0	9.7	1.0	10.9	0.0	0.0	0.0	0.0	9.7	0.9	10.9	0.0	0.0	0.0
TiO_2	1.7	1.9	0.0	0.0	0.0	0.0	52.6	0.0	1.8	0.0	0.0	0.0	0.0	52.6	0.0
FeO	9.2	21.9	0.0	26.9	14.1	0.0	47.4	0.0	21.9	0.0	27.0	14.1	0.0	47.4	0.0
H_2O	1.4	3.5	0.0	2.0	2.1	0.0	0.0	100.0	3.5	0.0	2.0	2.1	0.0	0.0	100.0
K_2O	1.9	10.1	0.1	0.0	0.0	0.0	0.0	0.0	10.1	0.1	0.0	0.0	0.0	0.0	0.0

Phase		Biotite	Plagioclase	Amphibole1	Amphibole2	Quartz	Ilmenite	H2O	Biotite	Plagioclase	Amphibole1	Amphibole2	Quartz	Ilmenite	H2O
Temperature(°C)		620							610						
Na_2O	2.7	0.0	6.1	0.1	0.5	0.0	0.0	0.0	0.0	6.1	0.1	0.5	0.0	0.0	0.0
MgO	6.4	11.8	0.0	15.4	15.7	0.0	0.0	0.0	11.8	0.0	15.3	15.7	0.0	0.0	0.0
Al_2O_3	15.1	13.6	27.7	1.2	2.9	0.0	0.0	0.0	13.7	27.7	1.2	2.9	0.0	0.0	0.0
SiO_2	54.7	37.3	56.4	53.4	53.9	100.0	0.0	0.0	37.2	56.5	53.3	53.9	100.0	0.0	0.0
CaO	6.9	0.0	9.7	0.9	10.9	0.0	0.0	0.0	0.0	9.7	0.9	11.0	0.0	0.0	0.0
TiO_2	1.7	1.7	0.0	0.0	0.0	0.0	52.6	0.0	1.7	0.0	0.0	0.0	0.0	52.6	0.0
FeO	9.2	22.0	0.0	27.0	14.0	0.0	47.4	0.0	22.0	0.0	27.1	13.9	0.0	47.4	0.0
H_2O	1.4	3.5	0.0	2.0	2.1	0.0	0.0	100.0	3.5	0.0	2.0	2.1	0.0	0.0	100.0
K_2O	1.9	10.1	0.1	0.0	0.0	0.0	0.0	0.0	10.1	0.0	0.0	0.0	0.0	0.0	0.0

TABLE 2: MODELLED PHASE COMPOSITIONS OF SAMPLE S1F AS A FUNCTION OF TEMPERATURE; FEO INDICATES TOTAL FE

Phase	Bulk	Garnet	Melt	Orthopyroxene	Cordierite	Plagioclase	Ilmenite	Quartz	Garnet	Melt	Orthopyroxene	Cordierite	Plagioclase	Ilmenite	Quartz
Temperature(°C)		890							880						
Na_2O	2.5	0.0	2.7	0.0	0.0	5.0	0.0	0.0	0.0	2.8	0.0	0.0	4.8	0.0	0.0
MgO	0.8	7.5	0.4	14.6	9.2	0.0	3.4	0.0	7.3	0.3	14.5	9.1	0.0	3.3	0.0
Al_2O_3	13.6	21.8	13.5	5.6	33.4	28.8	0.0	0.0	21.7	13.5	5.4	33.4	29.2	0.0	0.0
SiO_2	71.1	38.5	72.4	48.2	49.2	54.8	0.0	100.0	38.4	72.4	48.3	49.2	54.1	0.0	100.0
K_2O	4.8	0.0	5.2	0.0	0.0	0.5	0.0	0.0	0.0	5.3	0.0	0.0	0.4	0.0	0.0
CaO	0.8	1.2	0.8	0.2	0.0	10.9	0.0	0.0	1.2	0.7	0.2	0.0	11.4	0.0	0.0
TiO_2	0.4	0.0	0.0	0.0	0.0	0.0	54.0	0.0	0.0	0.0	0.0	0.0	0.0	54.0	0.0
FeO	2.9	29.2	1.9	30.8	7.0	0.0	41.7	0.0	29.9	1.8	31.1	7.2	0.0	42.1	0.0
H_2O	2.9	0.0	3.1	0.0	1.0	0.0	0.0	0.0	0.0	3.2	0.0	1.1	0.0	0.0	0.0
MnO	0.0	1.9	0.0	0.5	0.2	0.0	0.9	0.0	1.5	0.0	0.5	0.2	0.0	0.7	0.0

Phase	Bulk	Garnet	Melt	Orthopyroxene	Cordierite	Plagioclase	Ilmenite	Quartz	Garnet	Melt	Orthopyroxene	Cordierite	Plagioclase	Ilmenite	Quartz
Temperature(°C)		870							860						
Na_2O	2.5	0.0	2.8	0.0	0.0	5.0	0.0	0.0	0.0	2.8	0.0	0.0	5.3	0.0	0.0
MgO	0.8	7.3	0.3	14.4	9.2	0.0	3.2	0.0	7.2	0.3	14.3	9.2	0.0	3.1	0.0
Al_2O_3	13.6	21.7	13.5	5.4	33.4	28.8	0.0	0.0	21.7	13.5	5.4	33.4	28.3	0.0	0.0
SiO_2	71.1	38.4	72.4	48.2	49.2	54.8	0.0	100.0	38.4	72.2	48.2	49.2	55.4	0.0	100.0
K_2O	4.8	0.0	5.5	0.0	0.0	0.5	0.0	0.0	0.0	5.6	0.0	0.0	0.5	0.0	0.0
CaO	0.8	1.0	0.7	0.2	0.0	10.9	0.0	0.0	1.0	0.6	0.1	0.0	10.4	0.0	0.0
TiO_2	0.4	0.0	0.0	0.0	0.0	0.0	53.9	0.0	0.0	0.0	0.0	0.0	0.0	53.9	0.0
FeO	2.9	30.2	1.6	31.4	7.1	0.0	42.3	0.0	30.5	1.5	31.7	7.1	0.0	42.6	0.0
H_2O	2.9	0.0	3.3	0.0	1.1	0.0	0.0	0.0	0.0	3.4	0.0	1.1	0.0	0.0	0.0
MnO	0.0	1.3	0.0	0.3	0.1	0.0	0.6	0.0	1.1	0.0	0.3	0.1	0.0	0.4	0.0

Phase	Bulk	Garnet	Melt	Orthopyroxene	Cordierite	Plagioclase	Ilmenite	Quartz	Garnet	Melt	Orthopyroxene	Cordierite	Plagioclase	Ilmenite	Quartz
Temperature(°C)		850							840						
Na_2O	2.5	0.0	2.9	0.0	0.0	5.5	0.0	0.0	0.0	2.9	0.0	0.0	6.0	0.0	0.0
MgO	0.8	7.2	0.3	14.3	9.1	0.0	3.1	0.0	7.0	0.2	14.4	9.2	0.0	3.0	0.0
Al_2O_3	13.6	21.7	13.5	5.2	33.3	28.0	0.0	0.0	21.7	13.5	5.1	33.4	27.2	0.0	0.0
SiO_2	71.1	38.4	72.3	48.3	49.1	55.8	0.0	100.0	38.3	72.3	48.4	49.2	57.0	0.0	100.0
K_2O	4.8	0.0	5.7	0.0	0.0	0.6	0.0	0.0	0.0	5.9	0.0	0.0	0.7	0.0	0.0
CaO	0.8	1.0	0.6	0.1	0.0	10.1	0.0	0.0	1.0	0.5	0.1	0.0	9.1	0.0	0.0
TiO_2	0.4	0.0	0.0	0.0	0.0	0.0	53.9	0.0	0.0	0.0	0.0	0.0	0.0	53.9	0.0
FeO	2.9	30.8	1.4	31.8	7.1	0.0	42.6	0.0	31.1	1.3	31.8	7.0	0.0	42.8	0.0
H_2O	2.9	0.0	3.4	0.0	1.2	0.0	0.0	0.0	0.0	3.5	0.0	1.2	0.0	0.0	0.0
MnO	0.0	0.9	0.0	0.3	0.1	0.0	0.4	0.0	0.8	0.0	0.3	0.1	0.0	0.4	0.0

Phase	Bulk	Garnet	Melt	Orthopyroxene	Cordierite	Plagioclase	Ilmenite	Quartz	Garnet	Melt	Orthopyroxene	Cordierite	Plagioclase	Ilmenite	Quartz
Temperature(°C)		830							820						
Na_2O	2.5	0.0	2.9	0.0	0.0	6.3	0.0	0.0	0.0	2.8	0.0	0.0	6.6	0.0	0.0
MgO	0.8	7.0	0.2	14.4	9.2	0.0	2.9	0.0	7.0	0.2	14.4	9.2	0.0	2.9	0.0
Al_2O_3	13.6	21.7	13.4	4.9	33.4	26.6	0.0	0.0	21.7	13.4	4.7	33.3	26.0	0.0	0.0
SiO_2	71.1	38.3	72.2	48.5	49.1	57.9	0.0	100.0	38.3	72.2	48.6	49.1	58.7	0.0	100.0
K_2O	4.8	0.0	6.0	0.0	0.0	0.8	0.0	0.0	0.0	6.2	0.0	0.0	0.9	0.0	0.0
CaO	0.8	1.0	0.5	0.1	0.0	8.4	0.0	0.0	0.9	0.4	0.1	0.0	7.7	0.0	0.0
TiO_2	0.4	0.0	0.0	0.0	0.0	0.0	53.8	0.0	0.0	0.0	0.0	0.0	0.0	53.8	0.0
FeO	2.9	31.3	1.1	31.9	7.0	0.0	42.9	0.0	31.5	1.0	32.0	6.9	0.0	43.0	0.0
H_2O	2.9	0.0	3.6	0.0	1.2	0.0	0.0	0.0	0.0	3.7	0.0	1.3	0.0	0.0	0.0
MnO	0.0	0.8	0.0	0.3	0.1	0.0	0.4	0.0	0.7	0.0	0.3	0.1	0.0	0.3	0.0

Phase	Bulk	Garnet	Melt	Biotite	Cordierite	Plagioclase	Ilmenite	Quartz	Garnet	Melt	Biotite	Cordierite	Plagioclase	Ilmenite	Muscovite	Quartz
Temperature(°C)		810							800							
Na_2O	2.5	0.0	2.8	0.0	0.0	6.9	0.0	0.0	0.0	2.9	0.0	0.0	6.9	0.0	0.0	0.0
MgO	0.8	6.7	0.2	11.4	9.1	0.0	2.7	0.0	6.2	0.1	10.6	8.7	0.0	2.4	0.0	0.0
Al_2O_3	13.6	21.6	13.5	15.4	33.3	25.4	0.0	0.0	21.5	13.6	15.7	33.2	25.4	0.0	18.3	0.0
SiO_2	71.1	38.2	72.1	36.4	49.1	59.6	0.0	100.0	38.0	72.1	36.0	48.9	59.6	0.0	64.8	100.0
K_2O	4.8	0.0	6.3	10.2	0.0	1.1	0.0	0.0	0.0	6.3	10.1	0.0	1.1	0.0	16.9	0.0
CaO	0.8	0.9	0.4	0.0	0.0	7.0	0.0	0.0	0.7	0.3	0.0	0.0	7.0	0.0	0.0	0.0
TiO_2	0.4	0.0	0.0	4.0	0.0	0.0	53.8	0.0	0.0	0.0	3.9	0.0	0.0	53.6	0.0	0.0
FeO	2.9	31.8	0.9	19.6	7.1	0.0	43.3	0.0	32.8	0.8	20.6	7.7	0.0	43.7	0.0	0.0
H_2O	2.9	0.0	3.8	3.0	1.3	0.0	0.0	0.0	0.0	3.9	3.0	1.3	0.0	0.0	0.0	0.0
MnO	0.0	0.7	0.0	0.0	0.1	0.0	0.2	0.0	0.7	0.0	0.0	0.1	0.0	0.3	0.0	0.0

Phase	Bulk	Garnet	Melt	Biotite	Cordierite	K-feldspar	Plagioclase	Ilmenite	Quartz	Garnet	Melt	Biotite	Cordierite	K-feldspar	Plagioclase	Ilmenite	Quartz
Temperature(°C)		790								780							
Na_2O	2.5	0.0	3.1	0.0	0.0	3.2	6.7	0.0	0.0	0.0	3.1	0.0	0.0	3.2	7.0	0.0	0.0
MgO	0.8	5.7	0.1	10.3	8.6	0.0	0.0	2.2	0.0	5.0	0.1	9.5	8.2	0.0	0.0	2.0	0.0
Al_2O_3	13.6	21.5	13.5	15.9	33.1	18.9	26.0	0.0	0.0	21.3	13.5	16.2	33.0	18.9	25.5	0.0	0.0
SiO_2	71.1	37.9	71.8	35.8	48.8	65.5	58.8	0.0	100.0	37.7	71.7	35.4	48.6	65.5	59.5	0.0	100.0
K_2O	4.8	0.0	5.9	10.1	0.0	12.1	0.8	0.0	0.0	0.0	5.8	10.1	0.0	12.1	0.9	0.0	0.0
CaO	0.8	0.9	0.4	0.0	0.0	0.3	7.7	0.0	0.0	0.9	0.4	0.0	0.0	0.3	7.2	0.0	0.0
TiO_2	0.4	0.0	0.0	3.6	0.0	0.0	0.0	53.6	0.0	0.0	0.0	3.4	0.0	0.0	0.0	53.5	0.0
FeO	2.9	33.2	0.7	21.3	8.0	0.0	0.0	43.9	0.0	34.2	0.6	22.4	8.6	0.0	0.0	44.4	0.0
H_2O	2.9	0.0	4.5	3.1	1.5	0.0	0.0	0.0	0.0	0.0	4.8	3.1	1.5	0.0	0.0	0.0	0.0
MnO	0.0	0.8	0.0	0.0	0.1	0.0	0.0	0.3	0.0	0.9	0.0	0.0	0.1	0.0	0.0	0.2	0.0

TABLE 2 CONTINUED

Phase	Bulk	Garnet	Melt	Biotite	Cordierite	K-feldspar	Plagioclase	Ilmenite	Quartz		Garnet	Melt	Biotite	Cordierite	K-feldspar	Plagioclase	Ilmenite	Quartz
Temperature(°C)		770									760							
Na_2O	2.5	0.0	3.2	0.0	0.0	3.1	7.1	0.0	0.0		0.0	3.2	0.0	0.0	3.1	7.3	0.0	0.0
MgO	0.8	4.7	0.1	8.8	7.9	0.0	0.0	1.8	0.0		4.3	0.1	8.2	7.5	0.0	0.0	1.6	0.0
Al_2O_3	13.6	21.3	13.7	16.5	32.9	18.9	25.3	0.0	0.0		21.2	13.7	16.8	32.8	18.8	25.0	0.0	0.0
SiO_2	71.1	37.7	71.4	35.1	48.5	65.4	59.7	0.0	100.0		37.5	71.2	34.7	48.3	65.5	60.2	0.0	100.0
K_2O	4.8	0.0	5.7	10.0	0.0	12.2	0.9	0.0	0.0		0.0	5.7	10.0	0.0	12.3	0.9	0.0	0.0
CaO	0.8	0.9	0.4	0.0	0.0	0.3	7.0	0.0	0.0		0.9	0.3	0.0	0.0	0.3	6.5	0.0	0.0
TiO_2	0.4	0.0	0.0	3.3	0.0	0.0	0.0	53.4	0.0		0.0	0.0	3.0	0.0	0.0	0.0	53.3	0.0
FeO	2.9	34.4	0.5	23.2	9.1	0.0	0.0	44.5	0.0		34.8	0.4	24.2	9.6	0.0	0.0	44.7	0.0
H_2O	2.9	0.0	5.1	3.1	1.6	0.0	0.0	0.0	0.0		0.0	5.4	3.1	1.6	0.0	0.0	0.0	0.0
MnO	0.0	1.0	0.0	0.0	0.1	0.0	0.0	0.3	0.0		1.3	0.0	0.0	0.1	0.0	0.0	0.4	0.0

Phase	Bulk	Garnet	Melt	Biotite	Cordierite	K-feldspar	Plagioclase	Ilmenite	Microcline	Quartz		Garnet	Melt	Biotite	Cordierite	Plagioclase	Ilmenite	Microcline	Quartz
Temperature(°C)		750										740							
Na_2O	2.5	0.0	3.3	0.0	0.0	3.4	7.7	0.0	0.0	0.0		0.0	3.5	0.0	0.0	8.1	0.0	0.0	0.0
MgO	0.8	4.0	0.0	7.8	7.2	0.0	0.0	1.5	0.0	0.0		3.7	0.0	7.4	7.0	0.0	1.3	0.0	0.0
Al_2O_3	13.6	21.2	13.7	17.0	32.7	18.9	24.4	0.0	18.3	0.0		21.1	13.8	17.2	32.7	23.7	0.0	18.3	0.0
SiO_2	71.1	37.4	71.1	34.5	48.2	65.6	61.1	0.0	64.8	100.0		37.3	70.8	34.2	48.1	62.0	0.0	64.8	100.0
K_2O	4.8	0.0	5.5	10.0	0.0	11.8	1.0	0.0	16.9	0.0		0.0	5.3	9.9	0.0	1.0	0.0	16.9	0.0
CaO	0.8	0.7	0.3	0.0	0.0	0.3	5.9	0.0	0.0	0.0		0.7	0.3	0.0	0.0	5.1	0.0	0.0	0.0
TiO_2	0.4	0.0	0.0	3.0	0.0	0.0	0.0	53.3	0.0	0.0		0.0	0.0	2.8	0.0	0.0	53.2	0.0	0.0
FeO	2.9	35.2	0.4	24.7	10.1	0.0	0.0	44.8	0.0	0.0		35.5	0.3	25.2	10.4	0.0	45.0	0.0	0.0
H_2O	2.9	0.0	5.6	3.1	1.6	0.0	0.0	0.0	0.0	0.0		0.0	6.0	3.2	1.7	0.0	0.0	0.0	0.0
MnO	0.0	1.5	0.0	0.0	0.1	0.0	0.0	0.5	0.0	0.0		1.7	0.0	0.0	0.2	0.0	0.5	0.0	0.0

Phase	Bulk	Garnet	Melt	Biotite	Cordierite	Plagioclase	Ilmenite	Microcline	Quartz		Garnet	Melt	Biotite	Cordierite	Plagioclase	Ilmenite	Sillimanite	Microcline	Quartz
Temperature(°C)		730									720								
Na_2O	2.5	0.0	3.6	0.0	0.0	8.2	0.0	0.0	0.0		0.0	3.7	0.0	0.0	8.3	0.0	0.0	0.0	0.0
MgO	0.8	3.4	0.0	6.8	6.8	0.0	1.3	0.0	0.0		3.4	0.0	7.4	7.0	0.0	1.3	0.0	0.0	0.0
Al_2O_3	13.6	21.1	13.8	17.5	32.6	23.6	0.0	18.3	0.0		21.1	13.8	17.7	32.6	23.6	0.0	62.9	18.3	0.0
SiO_2	71.1	37.3	70.6	33.9	48.0	62.2	0.0	64.8	100.0		37.3	70.5	34.0	48.1	62.3	0.0	37.1	64.8	100.0
K_2O	4.8	0.0	5.0	9.9	0.0	1.0	0.0	16.9	0.0		0.0	4.9	10.0	0.0	0.9	0.0	0.0	16.9	0.0
CaO	0.8	0.7	0.3	0.0	0.0	5.0	0.0	0.0	0.0		0.7	0.2	0.0	0.0	4.9	0.0	0.0	0.0	0.0
TiO_2	0.4	0.0	0.0	2.7	0.0	0.0	53.2	0.0	0.0		0.0	0.0	2.6	0.0	0.0	53.2	0.0	0.0	0.0
FeO	2.9	35.5	0.3	25.8	10.6	0.0	45.0	0.0	0.0		33.6	0.2	24.9	10.1	0.0	44.5	0.0	0.0	0.0
H_2O	2.9	0.0	6.4	3.2	1.7	0.0	0.0	0.0	0.0		0.0	6.7	3.2	1.8	0.0	0.0	0.0	0.0	0.0
MnO	0.0	2.0	0.0	0.1	0.2	0.0	0.6	0.0	0.0		3.9	0.0	0.2	0.4	0.0	1.1	0.0	0.0	0.0

Phase	Bulk	Garnet	Melt	Biotite	Plagioclase	Ilmenite	Sillimanite	Microcline	Quartz		Garnet	Melt	Biotite	Plagioclase	Ilmenite	Sillimanite	Microcline	Quartz
Temperature(°C)		710									700							
Na_2O	2.5	0.0	3.7	0.0	8.4	0.0	0.0	0.0	0.0		0.0	3.8	0.0	8.5	0.0	0.0	0.0	0.0
MgO	0.8	3.2	0.0	7.5	0.0	1.3	0.0	0.0	0.0		3.1	0.0	7.5	0.0	1.2	0.0	0.0	0.0
Al_2O_3	13.6	21.1	13.7	17.9	23.4	0.0	62.9	18.3	0.0		21.0	13.5	17.9	23.4	0.0	62.9	18.3	0.0
SiO_2	71.1	37.2	70.3	34.0	62.6	0.0	37.1	64.8	100.0		37.2	70.1	33.9	62.7	0.0	37.1	64.8	100.0
K_2O	4.8	0.0	4.9	10.0	0.9	0.0	0.0	16.9	0.0		0.0	4.6	10.0	0.8	0.0	0.0	16.9	0.0
CaO	0.8	0.7	0.2	0.0	4.7	0.0	0.0	0.0	0.0		0.7	0.2	0.0	4.6	0.0	0.0	0.0	0.0
TiO_2	0.4	0.0	0.0	2.5	0.0	53.2	0.0	0.0	0.0		0.0	0.0	2.4	0.0	53.2	0.0	0.0	0.0
FeO	2.9	32.8	0.2	24.8	0.0	44.1	0.0	0.0	0.0		31.7	0.1	24.8	0.0	43.8	0.0	0.0	0.0
H_2O	2.9	0.0	7.1	3.3	0.0	0.0	0.0	0.0	0.0		0.0	7.5	3.3	0.0	0.0	0.0	0.0	0.0
MnO	0.0	4.9	0.0	0.2	0.0	1.4	0.0	0.0	0.0		6.2	0.0	0.2	0.0	1.8	0.0	0.0	0.0

Phase	Bulk	Garnet	Melt	Biotite	Plagioclase	Ilmenite	Sillimanite	Microcline	Quartz		Melt	Biotite	Plagioclase	Ilmenite	Sillimanite	Microcline	Quartz	H2O
Temperature(°C)		690									680							
Na_2O	2.5	0.0	3.8	0.0	8.7	0.0	0.0	0.0	0.0		4.0	0.0	9.0	0.0	0.0	0.0	0.0	0.0
MgO	0.8	3.0	0.0	7.5	0.0	1.2	0.0	0.0	0.0		0.0	7.4	0.0	1.1	0.0	0.0	0.0	0.0
Al_2O_3	13.6	21.0	13.4	18.0	23.2	0.0	62.9	18.3	0.0		13.4	18.1	22.7	0.0	62.9	18.3	0.0	0.0
SiO_2	71.1	37.2	69.9	33.9	62.8	0.0	37.1	64.8	100.0		69.8	33.8	63.6	0.0	37.1	64.8	100.0	0.0
K_2O	4.8	0.0	4.5	10.0	0.7	0.0	0.0	16.9	0.0		4.3	10.0	0.8	0.0	0.0	16.9	0.0	0.0
CaO	0.8	0.7	0.2	0.0	4.5	0.0	0.0	0.0	0.0		0.2	0.0	3.9	0.0	0.0	0.0	0.0	0.0
TiO_2	0.4	0.0	0.0	2.3	0.0	53.2	0.0	0.0	0.0		0.0	2.2	0.0	53.1	0.0	0.0	0.0	0.0
FeO	2.9	30.9	0.1	24.9	0.0	43.6	0.0	0.0	0.0		0.1	25.0	0.0	43.7	0.0	0.0	0.0	0.0
H_2O	2.9	0.0	8.0	3.3	0.0	0.0	0.0	0.0	0.0		8.3	3.3	0.0	0.0	0.0	0.0	0.0	100.0
MnO	0.0	7.1	0.0	0.2	0.0	2.1	0.0	0.0	0.0		0.0	0.3	0.0	2.1	0.0	0.0	0.0	0.0

Phase	Bulk	Biotite	Plagioclase	Ilmenite	Sillimanite	Microcline	Quartz	H2O		Biotite	Plagioclase	Ilmenite	Sillimanite	Microcline	Quartz	H2O
Temperature(°C)		670								660						
Na_2O	2.5	0.0	9.5	0.0	0.0	0.0	0.0	0.0		0.0	9.6	0.0	0.0	0.0	0.0	0.0
MgO	0.8	7.4	0.0	1.1	0.0	0.0	0.0	0.0		7.4	0.0	1.1	0.0	0.0	0.0	0.0
Al_2O_3	13.6	18.1	21.8	0.0	62.9	18.3	0.0	0.0		18.1	21.8	0.0	62.9	18.3	0.0	0.0
SiO_2	71.1	33.8	64.9	0.0	37.1	64.8	100.0	0.0		33.8	64.9	0.0	37.1	64.8	100.0	0.0
K_2O	4.8	10.0	0.9	0.0	0.0	16.9	0.0	0.0		10.0	0.8	0.0	0.0	16.9	0.0	0.0
CaO	0.8	0.0	2.8	0.0	0.0	0.0	0.0	0.0		0.0	2.9	0.0	0.0	0.0	0.0	0.0
TiO_2	0.4	2.2	0.0	53.1	0.0	0.0	0.0	0.0		2.1	0.0	53.1	0.0	0.0	0.0	0.0
FeO	2.9	25.0	0.0	43.7	0.0	0.0	0.0	0.0		25.0	0.0	43.7	0.0	0.0	0.0	0.0
H_2O	2.9	3.3	0.0	0.0	0.0	0.0	0.0	100.0		3.3	0.0	0.0	0.0	0.0	0.0	100.0
MnO	0.0	0.3	0.0	2.1	0.0	0.0	0.0	0.0		0.3	0.0	2.1	0.0	0.0	0.0	0.0

Phase	Bulk	Biotite	Plagioclase	Ilmenite	Sillimanite	Microcline	Quartz	H2O		Biotite	Plagioclase	Ilmenite	Sillimanite	Microcline	Quartz	H2O
Temperature(°C)		650								640						
Na_2O	2.5	0.0	9.6	0.0	0.0	0.0	0.0	0.0		0.0	9.7	0.0	0.0	0.0	0.0	0.0
MgO	0.8	7.4	0.0	1.1	0.0	0.0	0.0	0.0		7.5	0.0	1.0	0.0	0.0	0.0	0.0
Al_2O_3	13.6	18.2	21.8	0.0	62.9	18.3	0.0	0.0		18.2	21.9	0.0	62.9	18.3	0.0	0.0
SiO_2	71.1	33.8	64.9	0.0	37.1	64.8	100.0	0.0		33.8	64.9	0.0	37.1	64.8	100.0	0.0
K_2O	4.8	10.0	0.7	0.0	0.0	16.9	0.0	0.0		10.0	0.7	0.0	0.0	16.9	0.0	0.0
CaO	0.8	0.0	2.9	0.0	0.0	0.0	0.0	0.0		0.0	2.9	0.0	0.0	0.0	0.0	0.0
TiO_2	0.4	2.0	0.0	53.1	0.0	0.0	0.0	0.0		2.0	0.0	53.1	0.0	0.0	0.0	0.0
FeO	2.9	25.0	0.0	43.5	0.0	0.0	0.0	0.0		25.0	0.0	43.5	0.0	0.0	0.0	0.0
H_2O	2.9	3.4	0.0	0.0	0.0	0.0	0.0	100.0		3.4	0.0	0.0	0.0	0.0	0.0	100.0
MnO	0.0	0.3	0.0	2.3	0.0	0.0	0.0	0.0		0.3	0.0	2.3	0.0	0.0	0.0	0.0

Phase	Bulk	Biotite	Plagioclase	Ilmenite	Sillimanite	Microcline	Quartz	H2O		Muscovite	Biotite	Plagioclase	Ilmenite	Microcline	Quartz	H2O
Temperature(°C)		630								620						
Na_2O	2.5	0.0	9.7	0.0	0.0	0.0	0.0	0.0		0.9	0.0	9.7	0.0	0.0	0.0	0.0
MgO	0.8	7.5	0.0	1.0	0.0	0.0	0.0	0.0		0.2	7.5	0.0	1.0	0.0	0.0	0.0
Al_2O_3	13.6	18.2	21.9	0.0	62.9	18.3	0.0	0.0		37.5	17.9	22.0	0.0	18.3	0.0	0.0
SiO_2	71.1	33.8	64.9	0.0	37.1	64.8	100.0	0.0		46.0	33.9	64.8	0.0	64.8	100.0	0.0
K_2O	4.8	10.0	0.6	0.0	0.0	16.9	0.0	0.0		10.4	10.0	0.5	0.0	16.9	0.0	0.0
CaO	0.8	0.0	2.9	0.0	0.0	0.0	0.0	0.0		0.0	0.0	3.0	0.0	0.0	0.0	0.0
TiO_2	0.4	1.9	0.0	53.1	0.0	0.0	0.0	0.0		0.0	1.8	0.0	53.1	0.0	0.0	0.0
FeO	2.9	25.1	0.0	43.4	0.0	0.0	0.0	0.0		0.4	25.3	0.0	43.5	0.0	0.0	0.0
H_2O	2.9	3.4	0.0	0.0	0.0	0.0	0.0	100.0		4.5	3.4	0.0	0.0	0.0	0.0	100.0
MnO	0.0	0.3	0.0	2.5	0.0	0.0	0.0	0.0		0.0	0.3	0.0	2.5	0.0	0.0	0.0

Phase	Bulk	Muscovite	Biotite	Plagioclase	Ilmenite	Microcline	Quartz	H2O		Muscovite	Biotite	Plagioclase	Ilmenite	Microcline	Quartz	H2O
Temperature(°C)		610								600						
Na_2O	2.5	0.9	0.0	9.7	0.0	0.0	0.0	0.0		1.0	0.0	9.7	0.0	0.0	0.0	0.0
MgO	0.8	0.2	7.5	0.0	0.9	0.0	0.0	0.0		0.2	7.6	0.0	0.9	0.0	0.0	0.0
Al_2O_3	13.6	37.5	17.5	22.0	0.0	18.3	0.0	0.0		37.4	17.2	22.0	0.0	18.3	0.0	0.0
SiO_2	71.1	46.0	34.1	64.8	0.0	64.8	100.0	0.0		46.1	34.3	64.8	0.0	64.8	100.0	0.0
K_2O	4.8	10.4	9.9	0.5	0.0	16.9	0.0	0.0		10.3	9.9	0.4	0.0	16.9	0.0	0.0
CaO	0.8	0.0	0.0	3.0	0.0	0.0	0.0	0.0		0.0	0.0	3.0	0.0	0.0	0.0	0.0
TiO_2	0.4	0.0	1.8	0.0	53.0	0.0	0.0	0.0		0.0	1.7	0.0	53.0	0.0	0.0	0.0
FeO	2.9	0.4	25.4	0.0	43.5	0.0	0.0	0.0		0.4	25.6	0.0	43.5	0.0	0.0	0.0
H_2O	2.9	4.5	3.4	0.0	0.0	0.0	0.0	100.0		4.5	3.4	0.0	0.0	0.0	0.0	100.0
MnO	0.0	0.0	0.3	0.0	2.5	0.0	0.0	0.0		0.0	0.3	0.0	2.5	0.0	0.0	0.0

TABLE 3: MODELLED PHASE COMPOSITIONS OF SAMPLE S5BB AS A FUNCTION OF TEMPERATURE; FEO INDICATES TOTAL FE

Phase	Bulk	Melt	Orthopyroxene	Plagioclase	Ilmenite	Quartz	Melt	Orthopyroxene	Plagioclase	Ilmenite	Quartz
Temperature(°C)		890					880				
Na_2O	2.6	2.7	0.0	4.9	0.0	0.0	2.6	0.0	4.9	0.0	0.0
MgO	3.6	0.4	16.0	0.0	3.5	0.0	0.4	15.9	0.0	3.4	0.0
Al_2O_3	15.1	12.4	2.0	29.0	0.0	0.0	12.5	2.0	28.9	0.0	0.0
SiO_2	61.3	73.1	50.4	54.4	0.0	100.0	73.1	50.4	54.5	0.0	100.0
K_2O	1.9	5.8	0.0	0.5	0.0	0.0	6.0	0.0	0.5	0.0	0.0
CaO	4.6	0.7	0.6	11.2	0.0	0.0	0.7	0.6	11.1	0.0	0.0
TiO_2	1.7	0.0	0.0	0.0	54.1	0.0	0.0	0.0	0.0	54.0	0.0
FeO	8.2	2.0	30.5	0.0	40.9	0.0	1.8	30.6	0.0	41.1	0.0
H_2O	0.9	2.9	0.0	0.0	0.0	0.0	3.0	0.0	0.0	0.0	0.0
MnO	0.1	0.0	0.5	0.0	1.5	0.0	0.0	0.5	0.0	1.5	0.0

Phase	Bulk	Melt	Orthopyroxene	Plagioclase	Ilmenite	Quartz	Melt	Orthopyroxene	Plagioclase	Ilmenite	Quartz
Temperature(°C)		870					860				
Na_2O	2.6	2.6	0.0	5.0	0.0	0.0	2.5	0.0	5.0	0.0	0.0
MgO	3.6	0.3	15.9	0.0	3.3	0.0	0.3	15.9	0.0	3.3	0.0
Al_2O_3	15.1	12.5	1.9	28.8	0.0	0.0	12.5	2.0	28.7	0.0	0.0
SiO_2	61.3	73.1	50.4	54.7	0.0	100.0	73.0	50.4	54.7	0.0	100.0
K_2O	1.9	6.2	0.0	0.6	0.0	0.0	6.3	0.0	0.6	0.0	0.0
CaO	4.6	0.7	0.5	11.0	0.0	0.0	0.6	0.5	10.9	0.0	0.0
TiO_2	1.7	0.0	0.0	0.0	54.0	0.0	0.0	0.0	0.0	54.0	0.0
FeO	8.2	1.6	30.7	0.0	41.1	0.0	1.5	30.8	0.0	41.2	0.0
H_2O	0.9	3.1	0.0	0.0	0.0	0.0	3.2	0.0	0.0	0.0	0.0
MnO	0.1	0.0	0.5	0.0	1.5	0.0	0.0	0.5	0.0	1.5	0.0

Phase	Bulk	Melt	Orthopyroxene	Plagioclase	Ilmenite	Quartz	Melt	Orthopyroxene	Plagioclase	Ilmenite	Quartz
Temperature(°C)		850					840				
Na_2O	2.6	2.4	0.0	5.1	0.0	0.0	2.4	0.0	5.1	0.0	0.0
MgO	3.6	0.3	15.9	0.0	3.2	0.0	0.3	15.8	0.0	3.2	0.0
Al_2O_3	15.1	12.5	2.0	28.7	0.0	0.0	12.6	2.0	28.5	0.0	0.0
SiO_2	61.3	73.1	50.3	54.9	0.0	100.0	72.9	50.3	55.0	0.0	100.0
K_2O	1.9	6.5	0.0	0.6	0.0	0.0	6.7	0.0	0.7	0.0	0.0
CaO	4.6	0.6	0.5	10.8	0.0	0.0	0.6	0.5	10.7	0.0	0.0
TiO_2	1.7	0.0	0.0	0.0	54.0	0.0	0.0	0.0	0.0	54.0	0.0
FeO	8.2	1.3	30.8	0.0	41.4	0.0	1.2	30.9	0.0	41.4	0.0
H_2O	0.9	3.3	0.0	0.0	0.0	0.0	3.4	0.0	0.0	0.0	0.0
MnO	0.1	0.0	0.5	0.0	1.5	0.0	0.0	0.5	0.0	1.5	0.0

Phase	Bulk	Melt	Orthopyroxene	Plagioclase	Ilmenite	Quartz	Melt	Orthopyroxene	Biotite	Plagioclase	Ilmenite	Quartz
Temperature(°C)		830					820					
Na_2O	2.6	2.3	0.0	5.1	0.0	0.0	2.3	0.0	0.0	5.2	0.0	0.0
MgO	3.6	0.2	15.8	0.0	3.1	0.0	0.2	15.6	12.4	0.0	3.0	0.0
Al_2O_3	15.1	12.5	2.0	28.5	0.0	0.0	12.5	1.9	13.2	28.4	0.0	0.0
SiO_2	61.3	73.0	50.3	55.1	0.0	100.0	72.9	50.3	37.8	55.2	0.0	100.0
K_2O	1.9	6.8	0.0	0.7	0.0	0.0	6.8	0.0	10.2	0.7	0.0	0.0
CaO	4.6	0.5	0.5	10.6	0.0	0.0	0.5	0.5	0.0	10.5	0.0	0.0
TiO_2	1.7	0.0	0.0	0.0	53.9	0.0	0.0	0.0	4.5	0.0	53.9	0.0
FeO	8.2	1.1	30.9	0.0	41.5	0.0	1.0	31.2	18.8	0.0	41.6	0.0
H_2O	0.9	3.5	0.0	0.0	0.0	0.0	3.7	0.0	2.9	0.0	0.0	0.0
MnO	0.1	0.0	0.5	0.0	1.5	0.0	0.0	0.5	0.2	0.0	1.5	0.0

Phase	Bulk	Melt	Orthopyroxene	Biotite	Plagioclase	Ilmenite	Quartz	Melt	Orthopyroxene	Biotite	Plagioclase	Ilmenite	Quartz
Temperature(°C)		810						800					
Na_2O	2.6	2.5	0.0	0.0	5.3	0.0	0.0	2.9	0.0	0.0	5.4	0.0	0.0
MgO	3.6	0.2	15.0	12.0	0.0	2.8	0.0	0.2	14.7	11.8	0.0	2.6	0.0
Al_2O_3	15.1	12.3	1.7	13.0	28.3	0.0	0.0	12.2	1.6	12.9	28.2	0.0	0.0
SiO_2	61.3	72.7	50.2	37.7	55.4	0.0	100.0	72.4	50.1	37.7	55.5	0.0	100.0
K_2O	1.9	6.4	0.0	10.2	0.6	0.0	0.0	5.8	0.0	10.1	0.5	0.0	0.0
CaO	4.6	0.5	0.5	0.0	10.4	0.0	0.0	0.5	0.5	0.0	10.3	0.0	0.0
TiO_2	1.7	0.0	0.0	4.2	0.0	53.8	0.0	0.0	0.0	3.8	0.0	53.7	0.0
FeO	8.2	1.1	32.1	19.7	0.0	41.9	0.0	1.1	32.5	20.4	0.0	42.1	0.0
H_2O	0.9	4.2	0.0	3.0	0.0	0.0	0.0	4.8	0.0	3.0	0.0	0.0	0.0
MnO	0.1	0.0	0.6	0.2	0.0	1.5	0.0	0.0	0.6	0.2	0.0	1.5	0.0

Phase	Bulk	Melt	Orthopyroxene	Biotite	Plagioclase	Ilmenite	Quartz	Melt	Orthopyroxene	Biotite	Plagioclase	Ilmenite	Quartz
Temperature(°C)		790						780					
Na_2O	2.6	3.2	0.0	0.0	5.5	0.0	0.0	3.4	0.0	0.0	5.5	0.0	0.0
MgO	3.6	0.2	14.4	11.7	0.0	2.5	0.0	0.2	14.2	11.7	0.0	2.4	0.0
Al_2O_3	15.1	12.1	1.4	12.8	28.2	0.0	0.0	12.0	1.4	12.8	28.2	0.0	0.0
SiO_2	61.3	72.2	50.1	37.7	55.6	0.0	100.0	72.0	50.0	37.7	55.6	0.0	100.0
K_2O	1.9	5.2	0.0	10.1	0.4	0.0	0.0	4.8	0.0	10.1	0.4	0.0	0.0
CaO	4.6	0.5	0.5	0.0	10.3	0.0	0.0	0.5	0.6	0.0	10.3	0.0	0.0
TiO_2	1.7	0.0	0.0	3.6	0.0	53.7	0.0	0.0	0.0	3.4	0.0	53.6	0.0
FeO	8.2	1.1	32.8	20.8	0.0	42.4	0.0	1.1	33.0	20.9	0.0	42.5	0.0
H_2O	0.9	5.4	0.0	3.1	0.0	0.0	0.0	6.0	0.0	3.1	0.0	0.0	0.0
MnO	0.1	0.0	0.7	0.2	0.0	1.5	0.0	0.0	0.7	0.2	0.0	1.5	0.0

Phase	Bulk	Melt	Orthopyroxene	Biotite	Plagioclase	Ilmenite	Quartz	Melt	Orthopyroxene	Biotite	Plagioclase	Ilmenite	Quartz
Temperature(°C)		770						760					
Na_2O	2.6	3.7	0.0	0.0	5.6	0.0	0.0	3.9	0.0	0.0	5.6	0.0	0.0
MgO	3.6	0.2	14.2	11.7	0.0	2.3	0.0	0.2	14.1	11.7	0.0	2.3	0.0
Al_2O_3	15.1	11.9	1.3	12.8	28.2	0.0	0.0	11.8	1.3	12.8	28.2	0.0	0.0
SiO_2	61.3	71.7	50.1	37.7	55.7	0.0	100.0	71.4	50.1	37.7	55.7	0.0	100.0
K_2O	1.9	4.3	0.0	10.1	0.3	0.0	0.0	3.9	0.0	10.1	0.2	0.0	0.0
CaO	4.6	0.5	0.6	0.0	10.3	0.0	0.0	0.5	0.6	0.0	10.3	0.0	0.0
TiO_2	1.7	0.0	0.0	3.1	0.0	53.6	0.0	0.0	0.0	3.0	0.0	53.6	0.0
FeO	8.2	1.1	33.1	21.2	0.0	42.6	0.0	1.0	33.2	21.3	0.0	42.6	0.0
H_2O	0.9	6.6	0.0	3.2	0.0	0.0	0.0	7.2	0.0	3.2	0.0	0.0	0.0
MnO	0.1	0.0	0.7	0.2	0.0	1.5	0.0	0.0	0.8	0.2	0.0	1.5	0.0

TABLE 3 CONTINUED

Phase	Bulk	Melt	Orthopyroxene	Biotite	Plagioclase	Ilmenite	Quartz		Orthopyroxene	Biotite	Plagioclase	Ilmenite	Quartz	H2O
Temperature(°C)		750							740					
Na_2O	2.6	4.1	0.0	0.0	5.7	0.0	0.0		0.0	0.0	5.8	0.0	0.0	0.0
MgO	3.6	0.2	14.1	11.8	0.0	2.2	0.0		13.9	11.7	0.0	2.2	0.0	0.0
Al_2O_3	15.1	11.7	1.2	12.8	28.2	0.0	0.0		1.2	12.7	27.9	0.0	0.0	0.0
SiO_2	61.3	71.3	50.1	37.7	55.7	0.0	100.0		50.1	37.7	56.1	0.0	100.0	0.0
K_2O	1.9	3.5	0.0	10.1	0.2	0.0	0.0		0.0	10.1	0.2	0.0	0.0	0.0
CaO	4.6	0.5	0.6	0.0	10.3	0.0	0.0		0.6	0.0	10.0	0.0	0.0	0.0
TiO_2	1.7	0.0	0.0	2.8	0.0	53.6	0.0		0.0	2.7	0.0	53.5	0.0	0.0
FeO	8.2	0.9	33.3	21.4	0.0	42.7	0.0		33.5	21.6	0.0	42.6	0.0	0.0
H_2O	0.9	7.7	0.0	3.2	0.0	0.0	0.0		0.0	3.3	0.0	0.0	0.0	100.0
MnO	0.1	0.0	0.8	0.2	0.0	1.5	0.0		0.8	0.2	0.0	1.7	0.0	0.0

Phase	Bulk	Orthopyroxene	Biotite	Plagioclase	Ilmenite	Quartz	H2O		Orthopyroxene	Biotite	Plagioclase	Amphibole	Ilmenite	Quartz	H2O
Temperature(°C)		730							720						
Na_2O	2.6	0.0	0.0	5.8	0.0	0.0	0.0		0.0	0.0	5.8	0.1	0.0	0.0	0.0
MgO	3.6	14.0	11.7	0.0	2.1	0.0	0.0		13.6	11.6	0.0	13.7	2.0	0.0	0.0
Al_2O_3	15.1	1.1	12.7	28.0	0.0	0.0	0.0		1.1	12.6	28.0	1.6	0.0	0.0	0.0
SiO_2	61.3	50.1	37.7	56.0	0.0	100.0	0.0		50.0	37.7	56.0	52.5	0.0	100.0	0.0
K_2O	1.9	0.0	10.1	0.1	0.0	0.0	0.0		0.0	10.1	0.1	0.0	0.0	0.0	0.0
CaO	4.6	0.6	0.0	10.0	0.0	0.0	0.0		0.5	0.0	10.0	0.7	0.0	0.0	0.0
TiO_2	1.7	0.0	2.6	0.0	53.5	0.0	0.0		0.0	2.5	0.0	0.0	53.5	0.0	0.0
FeO	8.2	33.5	21.7	0.0	42.7	0.0	0.0		33.6	22.0	0.0	29.4	42.7	0.0	0.0
H_2O	0.9	0.0	3.3	0.0	0.0	0.0	100.0		0.0	3.3	0.0	2.0	0.0	0.0	100.0
MnO	0.1	0.8	0.2	0.0	1.7	0.0	0.0		1.2	0.2	0.0	0.0	1.9	0.0	0.0

Phase	Bulk	Orthopyroxene	Biotite	Plagioclase	Amphibole	Ilmenite	Quartz	H2O		Biotite	Plagioclase	Amphibole	Ilmenite	Quartz	H2O
Temperature(°C)		710							700						
Na_2O	2.6	0.0	0.0	5.8	0.1	0.0	0.0	0.0		0.0	5.8	0.1	0.0	0.0	0.0
MgO	3.6	13.2	11.4	0.0	13.5	1.9	0.0	0.0		11.4	0.0	13.5	1.8	0.0	0.0
Al_2O_3	15.1	1.1	12.6	28.0	1.6	0.0	0.0	0.0		12.6	28.0	1.5	0.0	0.0	0.0
SiO_2	61.3	49.8	37.7	56.0	52.4	0.0	100.0	0.0		37.7	56.0	52.5	0.0	100.0	0.0
K_2O	1.9	0.0	10.1	0.1	0.0	0.0	0.0	0.0		10.1	0.1	0.0	0.0	0.0	0.0
CaO	4.6	0.5	0.0	10.0	0.6	0.0	0.0	0.0		0.0	10.0	0.6	0.0	0.0	0.0
TiO_2	1.7	0.0	2.4	0.0	0.0	53.4	0.0	0.0		2.3	0.0	0.0	53.4	0.0	0.0
FeO	8.2	33.4	22.2	0.0	29.9	42.0	0.0	0.0		22.3	0.0	29.9	41.4	0.0	0.0
H_2O	0.9	0.0	3.3	0.0	2.0	0.0	0.0	100.0		3.3	0.0	2.0	0.0	0.0	100.0
MnO	0.1	2.0	0.4	0.0	0.0	2.7	0.0	0.0		0.4	0.0	0.0	3.4	0.0	0.0

Phase	Bulk	Biotite	Plagioclase	Amphibole	Ilmenite	Quartz	H2O		Biotite	Plagioclase	Amphibole	Ilmenite	Quartz	H2O
Temperature(°C)		690							680					
Na_2O	2.6	0.0	5.8	0.1	0.0	0.0	0.0		0.0	5.8	0.1	0.0	0.0	0.0
MgO	3.6	11.4	0.0	13.5	1.8	0.0	0.0		11.4	0.0	13.4	1.7	0.0	0.0
Al_2O_3	15.1	12.6	28.0	1.5	0.0	0.0	0.0		12.6	28.0	1.5	0.0	0.0	0.0
SiO_2	61.3	37.7	56.0	52.5	0.0	100.0	0.0		37.6	56.0	52.5	0.0	100.0	0.0
K_2O	1.9	10.1	0.1	0.0	0.0	0.0	0.0		10.1	0.1	0.0	0.0	0.0	0.0
CaO	4.6	0.0	10.0	0.6	0.0	0.0	0.0		0.0	10.0	0.7	0.0	0.0	0.0
TiO_2	1.7	2.3	0.0	0.0	53.4	0.0	0.0		2.2	0.0	0.0	53.4	0.0	0.0
FeO	8.2	22.3	0.0	29.9	41.4	0.0	0.0		22.3	0.0	29.8	41.5	0.0	0.0
H_2O	0.9	3.4	0.0	2.0	0.0	0.0	100.0		3.4	0.0	2.0	0.0	0.0	100.0
MnO	0.1	0.4	0.0	0.0	3.4	0.0	0.0		0.4	0.0	0.0	3.4	0.0	0.0

Phase	Bulk	Biotite	Plagioclase	Amphibole	Ilmenite	Quartz	H2O		Biotite	Plagioclase	Amphibole	Ilmenite	Quartz	H2O
Temperature(°C)		670							660					
Na_2O	2.6	0.0	5.9	0.1	0.0	0.0	0.0		0.0	5.9	0.1	0.0	0.0	0.0
MgO	3.6	11.5	0.0	13.4	1.7	0.0	0.0		11.5	0.0	13.4	1.6	0.0	0.0
Al_2O_3	15.1	12.6	28.0	1.5	0.0	0.0	0.0		12.6	28.0	1.5	0.0	0.0	0.0
SiO_2	61.3	37.7	56.0	52.4	0.0	100.0	0.0		37.7	56.0	52.5	0.0	100.0	0.0
K_2O	1.9	10.1	0.1	0.0	0.0	0.0	0.0		10.1	0.1	0.0	0.0	0.0	0.0
CaO	4.6	0.0	10.1	0.7	0.0	0.0	0.0		0.0	10.1	0.7	0.0	0.0	0.0
TiO_2	1.7	2.1	0.0	0.0	53.4	0.0	0.0		2.1	0.0	0.0	53.3	0.0	0.0
FeO	8.2	22.3	0.0	29.9	41.7	0.0	0.0		22.3	0.0	29.8	41.8	0.0	0.0
H_2O	0.9	3.4	0.0	2.0	0.0	0.0	100.0		3.4	0.0	2.0	0.0	0.0	100.0
MnO	0.1	0.4	0.0	0.0	3.3	0.0	0.0		0.4	0.0	0.0	3.3	0.0	0.0

Phase	Bulk	Biotite	Plagioclase	Amphibole	Ilmenite	Quartz	H2O		Biotite	Plagioclase	Amphibole	Ilmenite	Quartz	H2O
Temperature(°C)		650							640					
Na_2O	2.6	0.0	5.9	0.1	0.0	0.0	0.0		0.0	5.9	0.1	0.0	0.0	0.0
MgO	3.6	11.5	0.0	13.5	1.6	0.0	0.0		11.6	0.0	13.5	1.6	0.0	0.0
Al_2O_3	15.1	12.6	28.0	1.5	0.0	0.0	0.0		12.6	28.0	1.5	0.0	0.0	0.0
SiO_2	61.3	37.7	56.0	52.5	0.0	100.0	0.0		37.7	56.0	52.5	0.0	100.0	0.0
K_2O	1.9	10.1	0.1	0.0	0.0	0.0	0.0		10.1	0.1	0.0	0.0	0.0	0.0
CaO	4.6	0.0	10.1	0.7	0.0	0.0	0.0		0.0	10.1	0.7	0.0	0.0	0.0
TiO_2	1.7	2.0	0.0	0.0	53.3	0.0	0.0		1.9	0.0	0.0	53.3	0.0	0.0
FeO	8.2	22.3	0.0	29.8	41.8	0.0	0.0		22.3	0.0	29.8	41.9	0.0	0.0
H_2O	0.9	3.4	0.0	2.0	0.0	0.0	100.0		3.4	0.0	2.0	0.0	0.0	100.0
MnO	0.1	0.4	0.0	0.0	3.2	0.0	0.0		0.4	0.0	0.0	3.2	0.0	0.0

Phase	Bulk	Garnet	Biotite	Plagioclase	Amphibole	Ilmenite	Quartz	H2O		Garnet	Biotite	Plagioclase	Amphibole	Ilmenite	Quartz	H2O
Temperature(°C)		630							620							
Na_2O	2.6	0.0	0.0	5.9	0.1	0.0	0.0	0.0		0.0	0.0	5.9	0.1	0.0	0.0	0.0
MgO	3.6	2.6	11.7	0.0	13.3	1.5	0.0	0.0		2.5	11.7	0.0	13.4	1.5	0.0	0.0
Al_2O_3	15.1	21.2	12.6	28.0	1.5	0.0	0.0	0.0		21.2	12.6	28.0	1.4	0.0	0.0	0.0
SiO_2	61.3	37.6	37.7	56.0	52.5	0.0	100.0	0.0		37.5	37.7	56.0	52.5	0.0	100.0	0.0
K_2O	1.9	0.0	10.1	0.1	0.0	0.0	0.0	0.0		0.0	10.1	0.1	0.0	0.0	0.0	0.0
CaO	4.6	5.4	0.0	10.1	0.7	0.0	0.0	0.0		5.5	0.0	10.1	0.7	0.0	0.0	0.0
TiO_2	1.7	0.0	1.8	0.0	0.0	53.3	0.0	0.0		0.0	1.8	0.0	0.0	53.3	0.0	0.0
FeO	8.2	22.1	22.2	0.0	30.0	42.2	0.0	0.0		21.9	22.3	0.0	29.9	42.2	0.0	0.0
H_2O	0.9	0.0	3.5	0.0	2.0	0.0	0.0	100.0		0.0	3.5	0.0	2.0	0.0	0.0	100.0
MnO	0.1	11.1	0.4	0.0	0.0	3.0	0.0	0.0		11.3	0.4	0.0	0.0	3.0	0.0	0.0

Phase	Bulk	Garnet	Biotite	Plagioclase	Amphibole	Ilmenite	Quartz	H2O		Garnet	Biotite	Plagioclase	Amphibole	Ilmenite	Quartz	H2O
Temperature(°C)		610							600							
Na_2O	2.6	0.0	0.0	5.9	0.1	0.0	0.0	0.0		0.0	0.0	5.9	0.1	0.0	0.0	0.0
MgO	3.6	2.4	11.7	0.0	13.4	1.5	0.0	0.0		2.3	11.7	0.0	13.4	1.4	0.0	0.0
Al_2O_3	15.1	21.2	12.7	28.0	1.4	0.0	0.0	0.0		21.2	12.7	28.0	1.4	0.0	0.0	0.0
SiO_2	61.3	37.5	37.7	56.0	52.6	0.0	100.0	0.0		37.5	37.7	56.0	52.6	0.0	100.0	0.0
K_2O	1.9	0.0	10.1	0.1	0.0	0.0	0.0	0.0		0.0	10.1	0.1	0.0	0.0	0.0	0.0
CaO	4.6	5.8	0.0	10.1	0.7	0.0	0.0	0.0		5.8	0.0	10.1	0.7	0.0	0.0	0.0
TiO_2	1.7	0.0	1.7	0.0	0.0	53.3	0.0	0.0		0.0	1.6	0.0	0.0	53.3	0.0	0.0
FeO	8.2	21.7	22.3	0.0	29.9	42.2	0.0	0.0		21.9	22.3	0.0	29.9	42.3	0.0	0.0
H_2O	0.9	0.0	3.5	0.0	2.0	0.0	0.0	100.0		0.0	3.5	0.0	2.0	0.0	0.0	100.0
MnO	0.1	11.3	0.4	0.0	0.0	3.0	0.0	0.0		11.3	0.4	0.0	0.0	3.0	0.0	0.0